

21st Century COE Program
Evolution of Urban Earthquake Engineering

First International Conference on Urban Earthquake Engineering

*Center for Urban Earthquake Engineering
Tokyo Institute of Technology*

Tokyo Tech
CUEE

21st Century COE Program
Evolution of Urban Earthquake Engineering

First International Conference on Urban Earthquake Engineering

*Center for Urban Earthquake Engineering
Tokyo Institute of Technology*

Tokyo Tech
CUEE

PREFACE

As the leader of our 21st century COE (Center of Excellence) program, I am very pleased to have this international conference, inviting many distinguished guests and experts from inside and outside Japan. The COE program entitled “Evolution of Urban Earthquake Engineering” aims to develop effective strategies and technologies to enhance our present urban societies resilience against earthquakes and to train elite individuals in the related fields. This kind of effort is urgently needed, not only in Japan but also in other earthquake prone countries around the world. Just as an example, consider the 1995 Kobe earthquake: it demonstrated that modern cities are highly vulnerable to earthquakes and that the state of the practice of earthquake preparedness should be much advanced in order to prevent catastrophic disasters in the next big earthquake.

To carry out the COE program, which is sponsored by the Ministry of Education, Culture, Sports, Science and Technology (MEXT), in an effective manner the Center for Urban Earthquake Engineering (CUEE) was established in the Tokyo Institute of Technology (Tokyo Tech) on September 1, 2003, which marked the 80th anniversary of the 1923 Great Kanto Earthquake. The faculty members working in six departments in three of the Graduate Schools of Tokyo Tech are unified under CUEE to further strengthen the available resources. In the area of mitigation of urban earthquake disasters, CUEE serves as the home for extensive and in-depth research and development efforts (R&D) and also hosts special training programs prepared for doctoral and postdoctoral students. In addition to these research and educational activities, CUEE also offers the possibility of worldwide collaboration with research organizations, and industry and government partners.

Following a kick-off symposium which was held in last October, CUEE has organized this international conference to introduce our COE program and to facilitate the worldwide collaboration in the various fields related to urban earthquake engineering. In our quest for the success of the COE program at an international level, we would appreciate your creative and kind contribution and fruitful discussions.

Tatsuo Ohmachi
Program Leader
Professor, Department of Built Environment

TABLE OF CONTENTS

About the COE program

- 21st century COE programs in Tokyo Institute of Technology 1
Aizawa, M.
Outline of 21st COE program: evolution of urban earthquake engineering 3
Ohmachi, T. and Tokimatsu, K.

Keynote Presentations

- The Bam Earthquake: The Facts and the Lessons Learnt 7
Rofooei, F.

Keynote Presentations

- A framework for performance-based earthquake engineering 19
Moehle, J.
Overview of the Multidisciplinary Center on Earthquake Engineering 30
Research (MCEER).
Bruneau, M.
Considerations of site response in U.S. building code provisions 37
Borcherdt, R.

Seismic Resistant Steel Structures

- Fracture in steel bridge piers due to earthquakes 49
Miki, C. and Sasaki, E.
Required fracture toughness of steels to prevent brittle fracture during 57
earthquakes in steel bridge piers
Sasaki, E. and Miki, C.
Experimental study on ductility capacity of composite beams 64
Yamada, S., Oh, S.H. and Okada, K.
Effect of column flexural stiffness and strength on story drift concentration 71
for two story braced frame
Kimura, Y. and MacRae G.A.
Beam element for truss beam with elastoplastic-buckling behavior 79
Motoyui, S.

Seismic Resistant RC Structures (I)

- Enhancement of flexural ductility of reinforced concrete bridge columns 85
Kawashima, K.
An evaluation of the displacement amplification factors for seismic design 96
of bridges
Watanabe, G. and Kawashima, K.
Simplified nonlinear analysis procedure for single-story asymmetric 104
buildings subjected to bi-directional ground motion
Fujii, K., Nakano, Y. and Sanada, Y.

An experimental study on influence of mullion-type wall of predominant bending failure in reinforced concrete frame Hotta, H. and Tsunoda, T.	112
Experimental study on mechanical behavior of damage controlled precast-prestressed concrete frame with P/C mild-press-joint Sakata, H., Wada A., Matsuzaki, Y. and Nakano K.	119

Structural Control and Base Isolation

Current status of Japanese passive control scheme for mitigating seismic damage to buildings and equipments Kasai, K.	127
Passive vibration-control concept for truss frame structures Takeuchi, T.	138
Extended constitutive rules for various viscoelastic materials using fractional derivatives Ooki, Y. and Kasai, K.	146
Energy balance-based seismic response prediction methods for seismic isolated buildings with rubber bearings, dampers and low friction elastic sliding bearings. Satsukawa, K., Chiba, Y., Kitamura, H., and Koyama, Y.	154
Experimental study on mitigation of seismic response of a building by variable dampers Ruangrassamee, A., Srisamai, W., and Lukkunaprasit, P.	161
Enhanced performance of buildings retrofitted with friction dampers with restrainers Lukkunaprasit, P. and Wanitkorkul A.	169

Keynote Presentations

Opportunities for International Collaboration on earthquake engineering through the George Brown Jr. network for earthquake engineering Simulation Mahin, S.A.	181
Earthquake engineering research in shaking table testing laboratory of Tongji university, Shanghai, China Lu, X.L. and Jiang H.J.	192
Recent research activities in NCREC: developments of the earthquake loss estimate system and internet testing techniques Tsai, K.C. and Yeh C.H.	205

Seismic Resistant RC Structures (II)

Experimental study on tri-axial non-linear restoring force characteristics of R/C columns Takiguchi, K., Nishimura, K. and Okuda, T.	226
Stress-strain relationship for the localized compressive failure zone of concrete under cyclic loading Watanabe, K., Niwa, J., Yokota, H. and Iwanami, M.	232

New reinforcing method for reinforced concrete beam with web opening introduced prestressing force Katori, K. and Hayashi, S.	239
Shear crack control on reinforced concrete column by lateral prestressing Watanabe, H., Katori, K., Shinohara, Y. and Hayashi, S.	247
Seismic retrofit study of rectangular RC columns at NCREE Chang, K.C., Tsai, K.C., Chang, S.P. and Lin, M.L.	255

Ground Motions and Their Effects (I)

Seismic hazard mapping projects in Japan Midorikawa, S.	264
Several subjects still remained since the 1995 Kobe earthquake Seo, K., Motoki, K., Kurita, K., Momii, T., Shigeta, T. and Niwa, N.	270
Estimation of site amplifications in focal area of the 2003 Miyagiken-Hokubu earthquake using aftershock and microtremor records Yamanaka, H., Motoki, K., Komaba, N., Kamimura, Y. and Murayama, M.	278
An approximate method to represent the extreme values of non-stationary Gaussian white noise Morikawa, H.	286

Ground Motions and Their Effects (II)

Site amplification effects observed from moderate intensity earthquake records obtained in the SMASCH array Cruz, E.F., Valdivia, D. and Schmauk, R.	294
Disaster prevention by realtime earthquake information Takahashi, I. and Nambu, S.	302
Near field effects of a hidden seismic fault underlying concrete dam Ohmachi, T., Kojima, N., Murakami, A. and Komaba, N.	309

Keynote Presentation

Urban earthquake engineering: foundation characterization for performance based design Finn, L.	317
--	-----

Seismic Soil and Foundation Engineering

Effects of dynamic soil-structure interaction on pile stress in large shaking table tests Tokimatsu, K. and Suzuki H.	337
A method to evaluate the safety of the existing piled foundations against buckling in liquefiable soils Bhattacharya, S.	345
1-G model test on pile-soil interaction in lateral flow of liquefied ground Kuwano, J., Takahashi, A., Yano, Y. and Saruwatari, T.	353

Liquefaction remediation of sand with an existing oil tank by chemical grouting	361
Takemura, J., Imamura, S. and Hirano, T.	

Keynote Presentation

Integrated natural hazards risk reduction-emergence of a US approach	369
Scawthorn, C.	

Issues on Performance-Based Design for Future Earthquakes

Seismic design : From buildings to cities	387
Wada, A.	
An optimal design problem of infrastructure consistent with maintenance/replacement scheduling	391
Ueda, T. and Yamada, N.	
Evaluation of portfolio seismic risk due to different allocations of multiple buildings	398
Suwa, H., Nobata, A. and Seki, M.	

Papers Presented in the Poster Sessions

RC Structures

Seismic response of nonlinear controlled isolated bridges under near-field ground motions	406
Lee, T.Y. and Kawashima, K.	
Seismic performance of reinforced concrete C-bent columns based on a hybrid loading test	413
Nagata, S., Kawashima, K. and Watanabe, G.	
Three-dimensional non-linear earthquake response analysis of reinforced concrete structures	421
Nishimura, K., Takiguchi, K. and Nguyen, H.H.	
The proposal of simplified truss model for shear carrying capacity of prestressed concrete beams	429
Lertsamattiyakul, M., Niwa, J., Tamura, S. and Hamada Y.	
Nonlinear analysis of reinforced concrete viaducts subjected to seismic loads using 3D lattice model	437
Miki, T. and Niwa, J.	
Research on weight reduction of PC composite members using ultra high strength fiber reinforced cementitious composites (UFC)	445
Murata, H., Niwa, J. and Sivaleepunth, C.	
Mechanism of efflorescence on historical masonry buildings seismically reinforced with concrete	453
Matsuo, T. and Tanaka K.	

Steel Structures

- Development of planar array probes for detection of three-dimensional defect459
Rattanasuwannachart, N., Takahashi K., Miki C. and Hirose S.
- Proposal of new steel structures which limit damage to connection elements at the bottom flange of beam-ends467
Kishiki, S., Yamada, S., Takeuchi, T., Suzuki, K. and Wada, A.

Passive Control

- Applications of inelastic SPD method for estimating relative displacement to avoid pounding of adjacent buildings473
Tran, B.T. and Kasai, K.
- Simplified peak response evaluation and design for elasto-plastically damped structures481
Ito, H. and Kasai, K.
- Wind and seismic vibration characteristics of a tall building model using viscoelastic damper489
Sato, D., Kasai, K. and Tamura, T.

Soil & Foundation Dynamics

- Pore water pressure response around pile and its effects on p-y relation during liquefaction497
Suzuki, H. and Tokimatsu, K.
- Scattering of plane SH-waves by a circular cavity in a pre-stressed elastic medium504
Leungvichcharoen, S. and Wijeyewickrema, A.C

Evacuation

- Evacuation behavior in city fire following earthquake.....512
Meshitsuka, Y., Aoki, Y., Ohno, R., Osaragi, T. and Katayama, M.

Tsunami

- Relation between Rayleigh waves and uplift of the seabed for rapid tsunami detection520
Inoue, S. and Ohmachi, T.

Ground Motions

- Updating of GIS building inventory data for earthquake damage assessment using high-resolution satellite image527
Miura, H., Midorikawa, S. and Fujimoto, K.
- Preliminary evaluation of surface soil response applying the H/V spectral ratio technique to microtremor data within Dhaka city area, Bangladesh535
Kamal, M., Midorikawa, S., Yamazaki, F. and Ansary, M.
- A study on the effects of surface waves generated in deep sedimentary basins during a major earthquake543
Eto, K., Seo, K. and Motoki, K.

Effects of deep subsurface structures on seismic wave propagation near the edge of sedimentary plain	549
Saguchi, K., Motoki, K. and Seo, K.	
Modern urban seismic network in Bucharest, Romania.....	557
Aldea, A, Kashima, T., Lungu, D., Vacareanu, R., Koyama, S. and Arion, C.	

21ST CENTURY COE PROGRAMS IN TOKYO INSTITUTE OF TECHNOLOGY

Masuo Aizawa

President, Tokyo Institute of Technology, Japan

The 21st Century COE Program (Center of Excellence) has started as a new project sponsored by the Ministry of Education, Culture, Sport, Science, and Technology (MEXT) from the fiscal year 2002. It aims to form one of the most advanced international centers in every research field, which can focus research and education at an international level and foster potential leaders in the international community.

In the fiscal year 2003, proposals for this COE program were solicited in 5 research fields comprising 1) Medical Science, 2) Mathematics, Physics, Earth Science, 3) Mechanical, Civil, Construction Engineering and Others, 4) Social Science, 5) Interdisciplinary, Combined Fields, and New Disciplines and 611 research programs were submitted from 225 National/ Public/ Private Universities.

In the fiscal year 2003, 133 research programs were adopted, including 97 programs from the National universities (73%), 5 programs from Public universities (4%) and 31 programs from the Private universities (23%). Five research programs out of a total of 9 proposals from Tokyo Institute of Technology have been adopted for the fiscal year 2003, resulting in a total of 9 COE programs in our university including 4 programs adopted in the fiscal year 2002. Classifying by fields, we have 1 program in Mathematics, Physics, Earth Science, 3 programs in Mechanical, Civil, Construction Engineering and Others, and 1 program in Interdisciplinary, Combined Fields, and New Disciplines.

A budget of 960 million yen has been provided by MEXT for the 5 programs, which were adopted in the fiscal year 2003. It is noteworthy that the total provided budget for our 9 programs in the fiscal years 2003 and 2004 is over 1,580 million yen. Although MEXT will give us the midterm assessment, it will provide the budget for 5 years.

The 9 programs adopted in our Tokyo Institute of Technology listed below consist of strong research groups that are selected from the whole campus among the researchers who are internationally well known. We strategize making the global research basis as a key step towards realization of our university's objective of attaining the status of "World-leading university in science and technology".

Adopted Program and Project Leader in the fiscal year 2002

1. Prof. Hiroshi HANDA "Frontier System of Bioengineering"
2. Prof. Takakazu YAMAMOTO "Creation of Molecular Diversity and Development of Functionalities"
3. Prof. Hideo HOSONO "Nanomaterial Frontier Cultivation for Industrial Collaboration"
4. Prof. Shigehisa ARAI "Photonic Nano-Device Integrated Engineering"

Adopted Program and Project Leader in the fiscal year 2003

5. Prof. Tsuneya Ando “Nanometer-Scale Quantum Physics”
6. Prof. Shigeo Hirose “Innovation of Creative Engineering through the Development of Advanced Robotics”
7. Prof. Tatsuo OHMACHI “Evolution of Urban Earthquake Engineering”
8. Prof. Hiroshi SEKIMOTO “Innovative Nuclear Energy Systems for Sustainable Development of the World”
9. Prof. Sadaoki Furui “Framework for Systematization and Application of Large-scale Knowledge Resources”

OUTLINE OF 21ST CENTURY COE PROGRAM: EVOLUTION OF URBAN EARTHQUAKE ENGINEERING

T. Ohmachi¹⁾ and K. Tokimatsu²⁾

1) Professor, Department of Built Engineering, Tokyo Institute of Technology, Japan

*2) Professor, Department of Architecture and Building Engineering, Tokyo Institute of Technology, Japan
ohmachi@enveng.titech.ac.jp, kohji@o.cc.titech.ac.jp*

Abstract: Densely populated urban cities that comprise a complicated web of people, urban facilities and urban system are highly vulnerable to earthquake disasters. Once an earthquake strikes such a metropolitan city, catastrophic disasters and widespread disaster chain, which may even lead to chaos in the global economy, could be anticipated. This has led to the pressing need for improving the overall earthquake risk reduction technology for urban cities. The Center for Urban Earthquake Engineering has been established to carry out the 21st Century COE program entitled "Evolution of Urban earthquake Engineering," that aims not only to promote the above research objectives but also to strengthen the graduate education program as well as to launch international collaboration in research and education. This paper describes the outline of our COE program on Urban Earthquake Engineering.

1. INTRODUCTION

Since the 1995 Kobe Earthquake, various researches and proposals have been made for developing measures to reduce seismic risks in urban cities; however, there still remains much to be done to develop and disseminate feasible risk reduction technologies for the benefit of urban society. Densely populated urban cities that comprise a complicated web of people, urban facilities and urban system are highly vulnerable to earthquake disasters. Once an earthquake strikes such a metropolitan city, catastrophic disasters and widespread disaster chain, which may even lead to chaos in the global economy, could be anticipated. This has led to the pressing need for improving the overall earthquake risk reduction technology for urban cities.

The Center for Urban Earthquake Engineering (CUEE) was established on September 1, 2003, to carry out the 21st Century Center of Excellence (COE) program, entitled "Evolution of Urban Earthquake Engineering," which is sponsored by the Ministry of Education, Culture, Sport, Science, and Technology (MEXT).

CUEE program includes extensive and in-depth research and development (R & D) of new technologies for the prevention of urban disasters caused by earthquakes. CUEE will work towards making global contributions in the areas of research and education as well as aim to become one of the most advanced international centers for Urban Earthquake Engineering (Fig. 1).

2. OVERVIEW OF THE COE PROGRAM

The faculty working in six departments in three Graduate Schools of Tokyo Institute of Technology, which may be ranked as one of the world's top level faculty in the field of earthquake

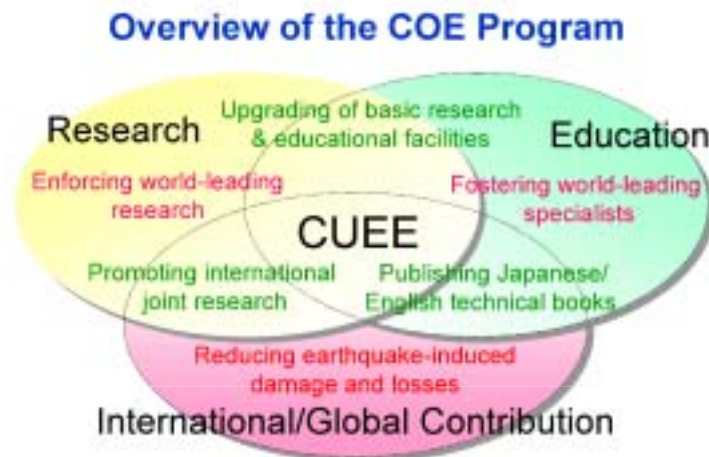


Fig. 1 Overview of the COE Program

engineering, shall be unified under CUEE together with its research and educational bases to further strengthen the resources. This would enable the research and study on Urban Earthquake Engineering to attain the world's highest standards, making CUEE a global hub, interconnecting North and South Americas, Asia and Europe, for international study on Urban Earthquake Engineering. To develop in-depth, strategic technologies on urban disaster mitigation, CUEE will focus on the following three major research topics:

- (1) *Advanced Technology for Earthquake Disaster Mitigation*
- (2) *Renovation Technology for Urban Earthquake Resilience*
- (3) *Strategic Plan for Urban Seismic Risk Reduction*

CUEE will also offer special doctoral courses involving overseas studies and OJT programs to foster potential leaders in the international community. CUEE will forge ahead with more active efforts in collaborating and interacting with foreign as well as local research institutions, government and non-government institutions and Non Profit Organizations (NPO) in order to promote the research on Urban Earthquake Engineering for practical applications.

3. PROMOTION OF RESEARCH ON URBAN EARTHQUAKE ENGINEERING

To effectively reduce the earthquake-induced damage and losses that are related to the people, buildings and infrastructures, CUEE will enforce studies from the following three viewpoints (Fig. 2):

3.1 Advanced Technology for Earthquake Disaster Mitigation:

To develop advanced technologies for the creation of safer cities and communities, R&D will be carried out on topics including: seismic hazard and risk simulation technology, smart material structures, intelligent passive and active control, real-time processing of ground profile survey, high seismic performance foundations, and real-time earthquake information system.

Research Themes & Topics



Fig. 2 Research themes and topics

3.2 Renovation Technology for Urban Earthquake Resilience

To reduce seismic risks in existing cities and communities, R&D will be carried out on topics including: seismic evaluation of existing facilities in urban areas, comprehensive disaster mitigation technology for ground and underground structures, seismic retrofit technologies with limited environmental impact, regional planning for mitigating fire spread, evacuation planning, and universal design for disaster mitigation.

3.3 Strategic Plan for Urban Seismic Risk Reduction

To develop basic strategies for reducing seismic risks of urban cities that are yet friendly to people and environment, R&D will be carried out on topics including: evaluation of urban seismic risks, evaluation of investment required for risk reduction, performance-based design, damage control design, and earthquake education.

4. FOSTERING YOUNG RESEARCHERS AND SPECIALISTS ON DISASTER PREVENTION

CUEE educational program (Fig. 3) aims to offer two special doctoral courses to foster world-leading specialists in the area of the disaster prevention, e.g., Academic course to foster researchers and Practical course to foster specialist engineers for immediate deployment.

In order to foster ability in international communication, teaching, research, creativity, and practice for doctoral and post-doctoral fellows, the CUEE education program includes the following implementations: (i) intensive lectures on English technical presentations, (ii) assignment to Research Assistant (RA) and Post-Doctoral Fellow (PD), (iii) scholarships for overseas school training and participation in international conferences, (iv) research awards to young researchers, (v) supervision by overseas visiting professors, and (vi) publication of technical books on Urban Earthquake Engineering in Japanese and English.

Urban Earthquake Engineering Education Implementation Plan

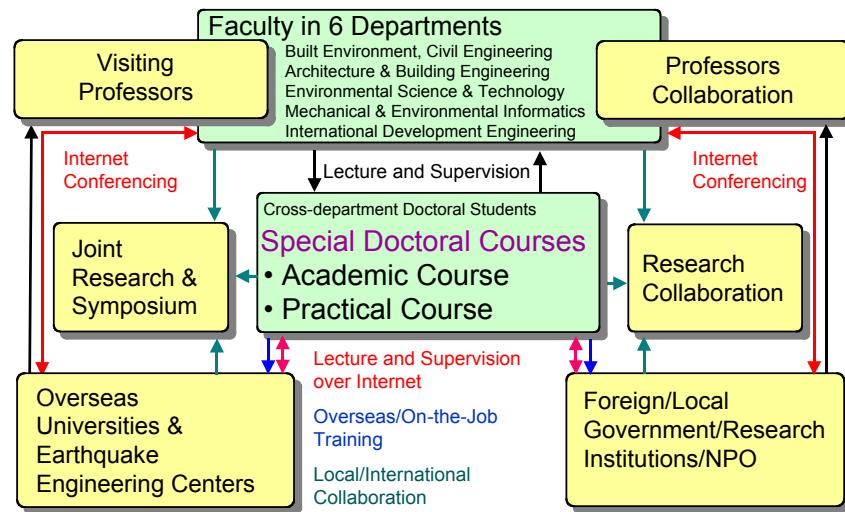


Fig. 3 Educational Implementation Plan

5. UPGRADING OF BASIC RESEARCH AND EDUCATIONAL FACILITIES

Basic research facilities such as high-precision dynamic experimental system and emergency assessment system will be introduced and/or upgraded. Advanced IT system, enabling internet conferencing and multimedia lectures not only within the university but also with local and foreign institutions, will be introduced, facilitating worldwide collaboration.

6. PROMOTION OF INTERNATIONAL RESEARCH COLLABORATION AND CONTRIBUTION

CUEE also aims to promote active international involvements through planning and sponsoring international joint researches, international symposia and exchange programs for young researchers and graduate students. CUEE would also make international contributions through conducting specialized seminars on earthquake engineering for developing countries as well as promote and develop the implementation of practical measures through collaboration with local and international government and non-government research institutions.

7. PROMOTION OF EDUCATION TO GENERAL PUBLIC ON DISASTER PREVENTION

Knowledge and information accumulated through the programs will be disseminated to the general public through seminars and Internet, to promote education on Urban Earthquake Engineering and enhance their awareness on disaster prevention.

THE BAM EARTHQUAKE: THE FACTS AND THE LESSONS LEARNT

Fayaz R. Rofooei¹⁾

*1) Associate Professor, Civil Engineering Department, Sharif University of Technology, Tehran, Iran,
rofooei@sharif.edu*

ABSTRACT At 5:28 am on December 26, 2003, a devastating earthquake with a moment magnitude around 6.5, leveled the historical city of Bam within few seconds. More than %80 of the city was destroyed and the dead toll was officially declared to be around 40000. The historical citadel of Arg-e-Bam, made entirely from mud bricks, was ruined and most of its ancient irrigation system, qanats, was ruptured. The 20 kilometers long Bam fault, silent for the last 2 millenniums, passes from the vicinity of the city. The hypocenter of the Bam earthquake has been estimated to be below the city itself, with a focal depth around 7 km, thus causing extensive damage to city. The preliminary investigation of the region indicates a rapid decay of the ground motion amplitude toward the suburbs of the city. Almost all of the mud brick buildings of the city were totally collapsed causing the heaviest life loss among the buildings of the city. Poor construction techniques together with low to none supervision were found to be the major reasons for the destruction of many newly designed and built buildings.

1. INTRODUCTION

The Bam 12/26/2003 earthquake with a moment magnitude around 6.5 struck at 01:58 GMT, 5:28 am local time. The epicenter was in Bam, a city of 80,000, with 200,000 in the surrounding area, in southern Iran, 620 miles southeast of Tehran. The earthquake flattened the old city and ruptured its qanats, the ancient water supply system that have been used in this area for centuries.

Bam is on major trade routes to India and the Far East. It's well known orange and date farms were a major source of income for its farmers and the country. Many of its population were involved in the booming tourism industry, serving a large number of tourists coming from different parts of the world to visit the ancient citadel of Bam. As the largest mud brick structure in the world, and a major historic site, it was on the Unesco's list of World Heritage Sites(Figure 1). The ruined citadel of Bam, known as the old Arg-e-Bam was made entirely of mud bricks, clay, straw and the trunks of palm trees. It was originally founded during the Sassanian period (224-637 AD) and while some of the surviving structures date from before the 12th century, most of it was built during the Safavid period (1502-1722). During Safavid times, it was expanded to six square kilometers, surrounded by a wall with 38 towers with 9000 to 13,000 inhabitants.

At the site of the Zoroastrian fire temple(dating to early Sassanian times), the Jame Mosque was built during the Saffarian period (866-903 AD) and adjacent to this mosque is the tomb of Mirza Naiim, a mystic and astronomer who lived three hundred years ago. Bam declined in importance following an invasion by Afghans in 1722 and another by invaders from the region of Shiraz in 1810. The city was used as a barracks for the army until 1932 and then completely abandoned. Intensive restoration work began in 1953, and was continued since then. This historic monument was mostly destroyed during this earthquake (Figure 2).



Figure 1 The ancient Arg-e Bam before earthquake.



Figure 2 The Arg-e Bam after earthquake.

2. Geological Setting of Iran

Earthquakes in Iran and neighboring regions (e.g., Turkey and Afghanistan) are closely connected to their position within the geologically active Alpine-Himalayan belt (Figure 3). In the Middle East region, modern tectonic activity is forced by the convergent movements between two plates: the Arabian plate, including Saudi Arabia, Persian Gulf and the Zagros Ranges of Iran, and the Eurasian plate that incorporates Europe, central and East Asia, as well as the interior Iran (Figures 3 and 4). The Zagros Thrust Zone (red line in Figure 4) constitutes the boundary between the two colliding plates[1-4].

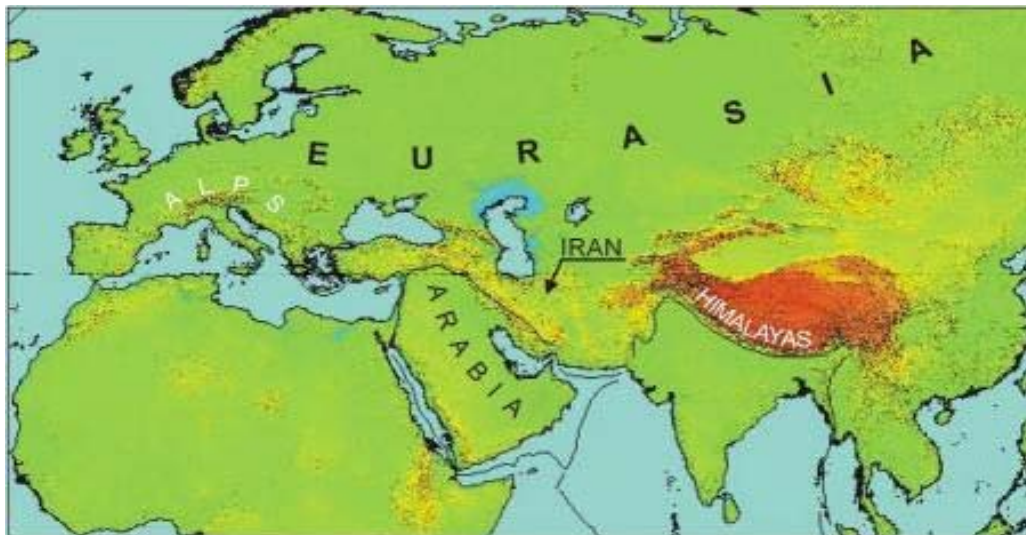
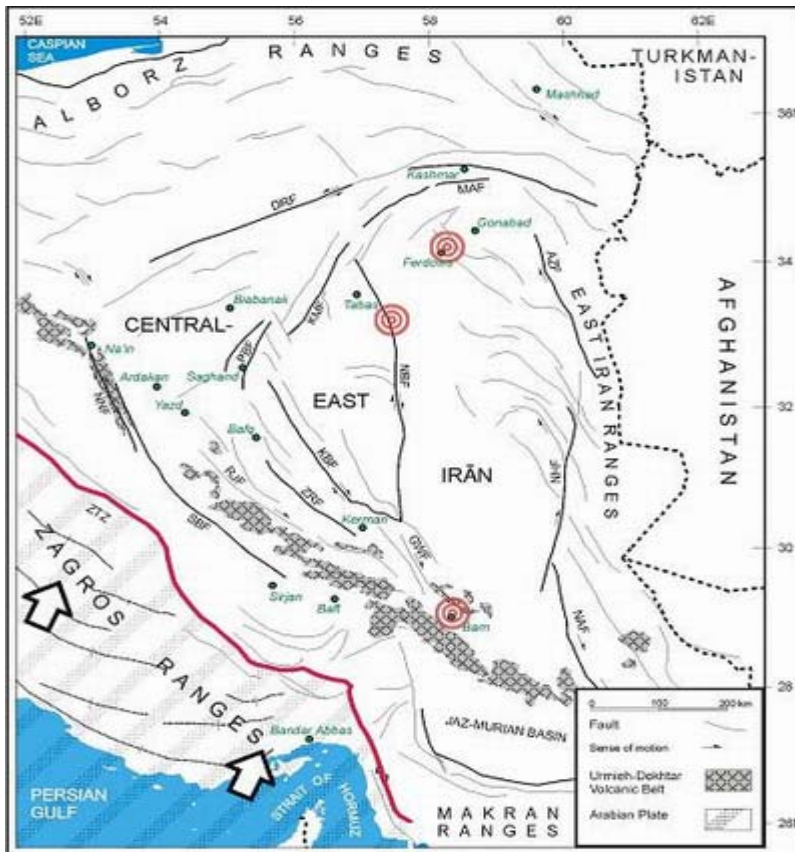


Figure 3 The Alpine-Himalayan Belt. Image from Cornell University/INSTOC[1-4]

Much of the mechanical deformation resulting from Arabia-Eurasia collision is accommodated by the Zagros Ranges in the form of folding of rocks and the rise of mountains in conjunction with fault movements at depth of the Earth. In fact, the highest frequency of earthquakes in Iran occurs in the Zagros region (Figure 5). However, because of the diffuse nature of this deformation (i.e. simultaneous movements along a number of sub-parallel faults over a wide area) the intensities of these tremors are generally low and are recordable only by sensitive seismic devices. The interior parts of Iran, however, respond to the plate collisional forces in a different manner. In the area known as Central-East Iran deformation takes place largely in the form of strike-slip (sideway) movements



- AZF= Abiz Fault,**
- DRF= Doruneh Fault,**
- GWF= Gowk Fault,**
- KBF= Kuhbanan Fault,**
- KMF= Kalmard Fault,**
- MAF= Mehdiabad Fault,**
- NAF= Nostratabad Fault,**
- NHF= Nehbandan Fault,**
- NNF= Naein Fault,**
- RJF = Rafsanjan Fault ,**
- SBF=Shahre-abak Fault,**
- ZRF= Zarand Fault,**
- ZTZ=Zagros Thrust Zone.**

Figure 4 The simplified structural map of Central-East Iran showing the location of major faults. Red line represents the boundary between Arabian and Eurasian plates. Large arrows indicate the direction of plate motion [1-4].

focused along a complex array of intersecting faults (Figure 4). In sharp contrast to that in Zagros, seismic activity associated with central Iranian faults is sporadic but much more localized and occurs with significantly higher magnitudes.

Many of Iran's powerful tremors, such as the recent Bam earthquake, have occurred in this area. By and large similar mechanisms are responsible for large magnitude earthquakes in other parts of the country, such as Zanjan and Azerbaijan, not shown here. Figure 4 illustrates major fault structures of the Central-East Iranian region along with large centers of population in their vicinity. The locations of three largest earthquakes of the modern times are also indicated by red circular symbols. These are the Ferdows earthquake of August 31, 1968 (Magnitude = 7.3, 12,000 – 20,000 deaths), Tabas earthquake of September 16, 1978 (M = 7.8, more than 1,500 deaths), and the recent Bam earthquake (M = 6.6, more than 30,000 deaths).

Preliminary analysis of the pattern of seismic-wave radiation from the December 26 earthquake is consistent with the earthquake having been caused by right-lateral strike-slip motion on a north-south

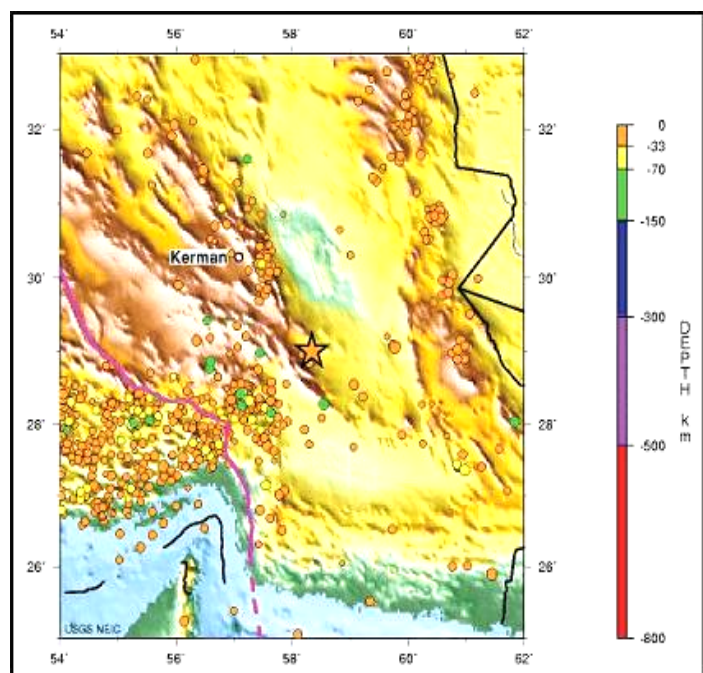


Figure 5 Record of seismicity in southeastern Iran from 1990 to 2003 [5]

oriented fault. The earthquake occurred in a region within which major north-south, right-lateral, strike-slip faults had been previously mapped, and the epicenter lies near the previously mapped, north-south oriented, Bam fault. However, field investigations will be necessary to determine if the earthquake occurred on the Bam fault or on another, possibly not yet mapped fault. The December 26 earthquake is 100 km south of the destructive earthquakes of June 11, 1981 (magnitude 6.6, approximately 3,000 deaths) and July 28, 1981 (magnitude 7.3, approximately 1,500 deaths). These earthquakes were caused by a combination of reverse-motion and strike-slip motion on the north-south oriented Gowk fault. Table 1 shows the major earthquakes occurred within a 100 kilometers distance from the city of Bam[6].

Table-1 Seismicity of the Bam region, within a 100km distance from the city of Bam[6].

Date			Time			Coordinates		FD	mb	Ms	Mw	Efa	Ref	Region
Y	M	D	HH	MM	SS	Lat.N	Lon.E							
1948	07	05	13	53		29.460	57.780	0	5.9	6.0	.0		Amb	Gowk
1962	09	29	06	54	00	28.290	57.480	83	5.5	.0	.0		N.US	
1964	05	11	06	07	38	28.220	57.390	73	5.3	.0	.0		N.IS	
1964	08	27	11	58	39	28.160	58.830	50	5.1	.0	.0		N.IS	
1976	11	13	10	12	36	28.250	57.340	62	5.0	.0	.0		ISC	
1981	06	11	07	24	25	29.895	57.718	30	6.6	6.0	.0	*	ISC	Golbaf
1981	07	28	17	22	23	29.987	57.770	11	5.9	7.0	.0	*	ISC	Sirch
1981	10	14	09	12	39	29.900	57.758	43	5.2	.0	.0		ISC	
1982	10	15	02	53	55	28.280	57.398	83	5.0	.0	.0		ISC	
1983	01	31	18	56	53	28.919	57.318	133	5.0	.0	.0		ISC	
1984	10	11	05	09	27	29.539	58.030	48	5.1	.0	.0		ISC	
1986	07	25	10	08	09	28.068	57.303	69	5.2	.0	.0		ISC	
1989	11	20	04	19	04	29.880	57.721	18	5.5	5.7	5.9		ISC	South Golbaf
1998	06	10	08	30	16	28.227	58.507	113	5.0	.0	.0		ISC	

3. Strong Ground Motion

There have been various recording of this earthquake in and around the city of Bam. The accelerogram located in the Governship's building in the middle of the city has recorded the strongest motion with the horizontal PGA's equal to 0.8g and 0.7g respectively, and a PGA around 1.0g in the vertical direction(Figure 6). The big velocity pulse caused by the directivity effect is shown in the Figure 7. It should be mentioned that around 1000 accelerograms are currently under operation by the Building and Housing Research Center of Iran(BHRC).[7]

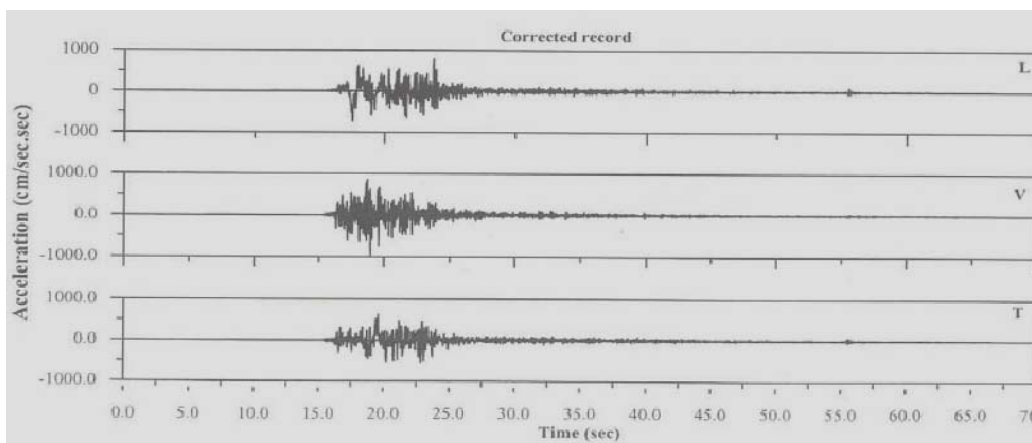


Figure 6 The corrected accelerograms of Bam Earthquake 2003(Record No. 3168-2)[7].

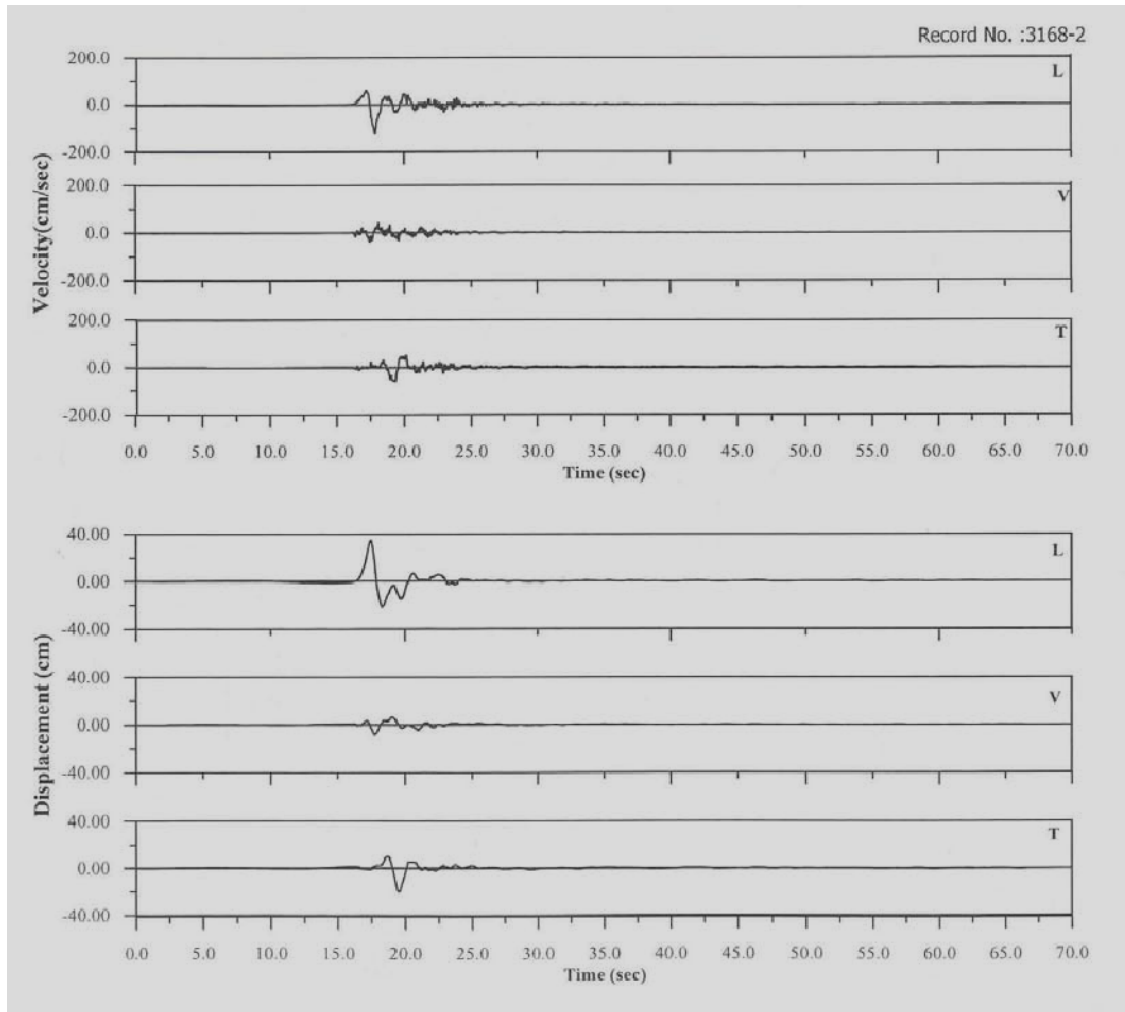


Figure 7 The Displacement and Velocity time histories of the corrected accelerograms of Bam earthquake recorded at the Governorship's building [7].

4. Structural Damages and Their Cause

The total number of Buildings in Bam and Baravat area has been estimated to be around 19000 units. The intense strong ground motion destroyed more than %80 of those buildings. In general these building can be categorized as the adobe buildings, un-reinforced masonry buildings, reinforced masonry buildings, semi-steel structures and steel and concrete structures. Based on the preliminary investigations, the following observation can be made for these different types of structures.

The adobe buildings that are made of mud bricks with dome shaped or arch type roofs, comprise more than %30 of the buildings within the Bam city and the Baravat (Figure 8). The thick walls and roofs in adobe buildings in the absence of bonding beams can not resist the lateral earthquake forces. More than %90 of adobe buildings, including the ancient citadel known as the Arg-e-Bam were destroyed by the earthquake. When collapsed, the mud brick crumbles into a heavy powder without air pockets. Consequently, casualties were much higher compared to other similar earthquakes in Iran or elsewhere in the world.

The un-reinforced masonry buildings still are the most built buildings, specially in the rural areas. These type of buildings are constructed mostly with certain type of heavy steel jack arch(shallow arch) roofs(Figure 9). No bonding beam is usually used to provide the masonry bearing walls with some ductile behavior. The steel profiles that are used for the steel jack arch are also placed on the walls without any tie beams to make them act as a diaphragm. Therefore, any failure of the bearing walls usually lead to the collapse of the heavy roofs, killing many people(Figures 9 and 10). About %35 of the buildings in city of Bam and Baravat belong to this type of buildings that were mostly destroyed.



Figure 8 The adobe buildings with dome or arched type roofs.



Figure 9 The un-reinforced masonry buildings and an example of steel jack arch type roofs.



Figure 10 collapsed un-reinforced masonry buildings with steel jack arch type roofs.

In reinforced masonry buildings, vertical and horizontal bonding beams are used to provide them with a better seismic behavior. The main problem with these type of buildings are the poor quality of the concrete used in the horizontal and vertical bonding beams. In some cases, there were not enough rebars in the bonding beams(Figure 11). That clearly shows the lack of an effective supervision, if any, during the construction process of those buildings. Weak connections between the vertical and horizontal ties(no anchorage of the steel bars) and no connection between the walls and the ties, non-standard hoop spacing and skipping the horizontal ties were among other problems encountered in these type of buildings. About %18 of the buildings in the earthquake effected area were from this category with many of them destroyed.



Figure 11 The reinforced masonry buildings with seperated vertical bonding beams, inappropriate connection detailing and poor concrete quality.

The third type of the buildings in this area is a combination of surrounding masonry bearing walls with some interior steel columns. Therefore, in these so-called semi-steel structures, there is basically no frame action. Again, the poor quality welding of the beam-column connections was the cause of many failures. The masonry bearing walls in these type of buildings were usually un-reinforced with no bonding beams. More than %17 of the buildings were in this group and as expected, most of them were destroyed.

The remaining %2 of the buildings in the city of Bam and Baravat, can be considered as concrete or steel structures with infilled masonry walls. Some of the main problems with the steel structures include, poor quality welding, use of non-standard steel with poor specification, weak connections, no connection between the infilled walls and the columns and in some cases, no lateral load resisting systems(bracing or moment resisting systems) (Figure. 12).



Figure 12 Steel Structures with inappropriate welding that led to the separation of the beam or bracing from the columns.

In concrete structures, non-professional construction procedures and poor quality concrete, were among the most common problems. In some cases, no rebars were used in beams and columns with non-standard hoop spacings(Figure 13).



Figure 13 Concrete structures without required hoop spacing or proper beam-column connection details.

After the Tabas earthquake in 1978, a new seismic design regulation were developed in Iran that was mainly adapted from the Uniform Building Code(UBC). It was updated about 4 years ago, and a new revision of that will be out for practitioners in a few months. As it is clearly shown by some of the remaining steel or concrete buildings in Bam, minimal observance of the country's seismic design code and the proper construction technics, could have saved many lives by preventing the total collapse of those buildings(Figure 14).



Figure 14 Minimum attention to the country's seismic code, or proper construction techniques, could have prevented many buildings from total collapse.

On the other hand, in well designed and built buildings, the damages were limited to nonstructural elements, like formation of cracks in interior partitions or exterior walls (Figure 15).

Traditional way of building new houses, almost in any part of the country including the Bam area is among other major problems to deal with. Inappropriate use of materials is frequently encountered. Many houses, especially in the rural regions, are built out of mud bricks and un-reinforced masonry, which do not stand up well to earthquakes. Therefore, the builders should be provided with the necessary education for proper construction methods to minimized further loss of lives in any future events.



Figure 15 Nonstructural damages to the well designed and built were minimal.

The preliminary investigation on the strong ground motion recorded in the Bam Governorship's office, as well as the inflicted damages observed in the city, is a clear indication of a very strong vertical component, compared to the horizontal ones in the Bam earthquake. That has led to some very peculiar type of destruction of the buildings. As it can be seen from the Figure 16, the folded columns could be seen in many damaged steel structures.



Figure 16 Folded columns caused by the vertical component of the earthquake.

5. Non- Building Structural Damages

The city's only elevated water tank was empty when the earthquake struck. There were minor damage in the form of cracking of the concrete cover at some of its joints. As it can be seen in Figure 17, smooth steel bars have been used as the reinforcement for the concrete.

No serious damage is reported with regard to the effect of earthquake on the major Mosques of the city. However, there was a slight buckling in the tower of one of these Mosques, plus falling of some of the bricks used as a cover as it is shown in Figure 18.

There were some damages to the Bam city's only substation. But the damaged equipments were



Figure 17 The Bam's elevated water tank and the cracking of its concrete cover at joints . As it can be seen from the picture, smooth steel bar has been used as the re-inforement .



Figure 18 Minor damages is reported for Bam's major Mosques.

repaired very rapidly to restore the electricity of the Bam(Figure 19).

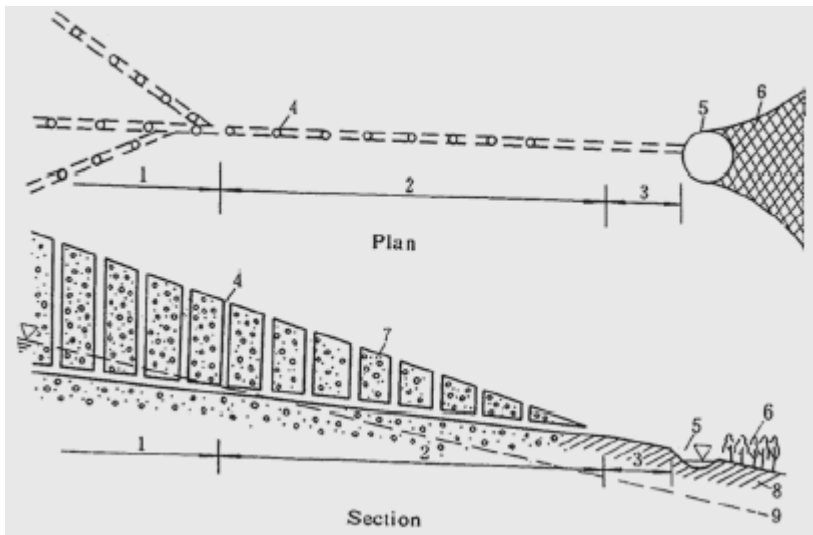
As it was mentioned before, the destruction of qanats, the ancient irrigation system used vastly in central and southern part of Iran, is of major concern. A qanat can be defined as a horizontal underground gallery that conveys water from an aquifer in pre-mountainous alluvial fans to lower-elevation irrigated fields[8]. As it can be seen from Figure (20), a qanat consists of a series of vertical shafts in sloping ground, interconnected at the bottom by a tunnel with a gradient less than that of the ground. The first shaft is usually sunk into an alluvial fan to a level below the groundwater

table.

Shafts are sunk at intervals of 20 to 30 meters in a line between the groundwater recharge zone and the irrigated land. From the air, the tunnel portion of a qanat system looks like a line of anthills leading from the foothills across the desert to the greenery of an irrigated settlement.



Figure 19 The damages inflicted to the city's only substation.



- (1) Infiltration part of the tunnel
- (2) Water conveyance part of the tunnel
- (3) Open channel
- (4) Vertical shafts
- (5) Small storage pond
- (6) Irrigation area
- (7) Sand and gravel
- (8) Layers of soil
- (9) Groundwater surface

Figure 20 General Schematic for a qanat[8]

In the Bam earthquake, many of the qanats located within the vicinity of city have been damaged. As the Figure 21 shows, the opening of many of the vertical shafts of the qanats have collapsed, blocking the flow of water. The restoration of some of these qanats has begun recently.



Figure 21 A view of the opening of vertical shafts of the qanats and their type of failure caused by the Earthquake[6].

6. CONCLUSION

On December 26, 2003, a devastating earthquake with a moment magnitude around 6.5, leveled the historical city of Bam. More than %80 of the city was destroyed and the dead toll was officially declared to be around 40000. The historical citadel of Arg-e-Bam, made entirely from mud bricks, was ruined and most of the city's ancient irrigation system, qanats, was ruptured. The hypocenter of the Bam earthquake has been estimated to be below the city with a focal depth around 8 km. Almost all of the mud brick buildings of the city were totally collapsed causing the heaviest life loss among the different types of buildings in the city. No observance of the country's seismic design code, poor construction techniques and low to none supervision during construction, were found to be the major reasons for the destruction of most of the buildings in Bam.

Acknowledgements

The author acknowledges support from Japan Ministry of Education, Culture, Sport, Science, and Technology (MEXT) for establishing the Center for Urban Earthquake Engineering (CUEE) in Tokyo Institute of Technology. The support has made possible this international conference, as well as international joint research projects and exchange programs with foreign universities. Also, The Financial support provided by the Center for Urban Earthquake Engineering of Tokyo Institute of Technology and its director, Professor Tatsuo Ohmachi, for presenting this paper in the first International Conference on Urban Earthquake Engineering is greatly appreciated.

References:

- [1] Alavi, M., 1991, "Tectonic map of the Middle East: Tehran", Geological Survey of Iran, scale 1:5,000,000.
- [2] Berberian, M., 1981, "Active faulting and tectonics of Iran: In Zagros-Hindu Kush-Himalaya Geodynamic Evolution" Editors H. K. Gupta and F.M. Delany, American Geophysical Union Geodynamic Series, v. 3, p. 33-69.
- [3] Haghypour, A. and Aghanabati, A., 1989, "Geological Map of Iran (2nd edition)", Tehran, Geological Survey of Iran, Scale 1:2,500,000.
- [4] Jackson, J. and McKenzie, D., 1984, "Active tectonics of the Alpine-Himalayan Belt, between western Turkey and Pakistan", Geophysical Journal of the Royal Astronomical Society, v. 77, p. 185-264.
- [5] U.S. Geological Survey, 2003, "Data on the Bam Earthquake", Iran.
- [6] International Institute of Earthquake Engineering and Seismology (IIEES), 2003, "Preliminary Report Bam Earthquake", Website. <http://www.iiees.ac.ir/>.
- [7] Building and Housing Research Center (BHRC), 2004. "2nd Quick Preliminary Report on the Bam Earthquake", Ministry of Housing and Urban Development, Iran.
- [8] <http://www.waterhistory.org/histories/qanats/qanats.pdf>

A FRAMEWORK FOR PERFORMANCE-BASED EARTHQUAKE ENGINEERING

J. P. Moehle¹⁾

*1) Professor and Director, Pacific Earthquake Engineering Research Center, University of California, Berkeley, USA
moehle@peer.berkeley.edu*

Abstract: The Pacific Earthquake Engineering Research Center (PEER) aims to develop a robust methodology for performance-based earthquake engineering. To accomplish this objective, the performance assessment and design process has been broken into logical elements that can be studied and resolved in a rigorous and consistent manner. Elements of the process include description, definition, and quantification of earthquake intensity measures, engineering demand parameters, damage measures, and decision variables. A consistent probabilistic framework underpins the methodology so that the inherent uncertainties in earthquake performance assessment can be represented. The methodology can be implemented directly for performance assessment, or can be used as the basis for establishing simpler performance metrics and criteria for performance-based earthquake engineering.

1. INTRODUCTION

Performance-based earthquake engineering seeks to improve seismic risk decision-making through assessment and design methods that have a strong scientific basis and that express options in terms that enable stakeholders to make informed decisions. A key feature is the definition of performance metrics that are relevant to decision making for seismic risk mitigation. The methodology needs to be underpinned by a consistent procedure that characterizes the important seismic hazard and engineering aspects of the problem, and that relates these quantitatively to the defined performance metrics.

The first generation of performance-based earthquake engineering assessment and design procedures for buildings in the United States (ATC 1996, FEMA 1997) made important steps toward the realization of performance-based earthquake engineering. These procedures conceptualized the problem as shown in Figure 1. A building was visualized as being loaded by earthquake-induced lateral forces that resulted potentially in nonlinear response and resulting damage. Relations were established between structural response indices (interstory drifts, inelastic member deformations, and member forces) and performance-oriented descriptions such as Immediate Occupancy, Life Safety and Collapse Prevention. Without belittling the remarkable accomplishments of these first-generation procedures, several shortcomings can be identified:

- Engineering demands were based on simplified analysis techniques, including static and linear analysis methods; where dynamic or nonlinear methods were used, calibrations between calculated demands and component performance were largely lacking.
- The defined relations between engineering demands and component performance were based somewhat inconsistently on relations measured in laboratory tests, calculated by analytical models, or assumed on the basis of engineering judgment; consistent approaches based on relevant data are needed to produce reliable outcomes.

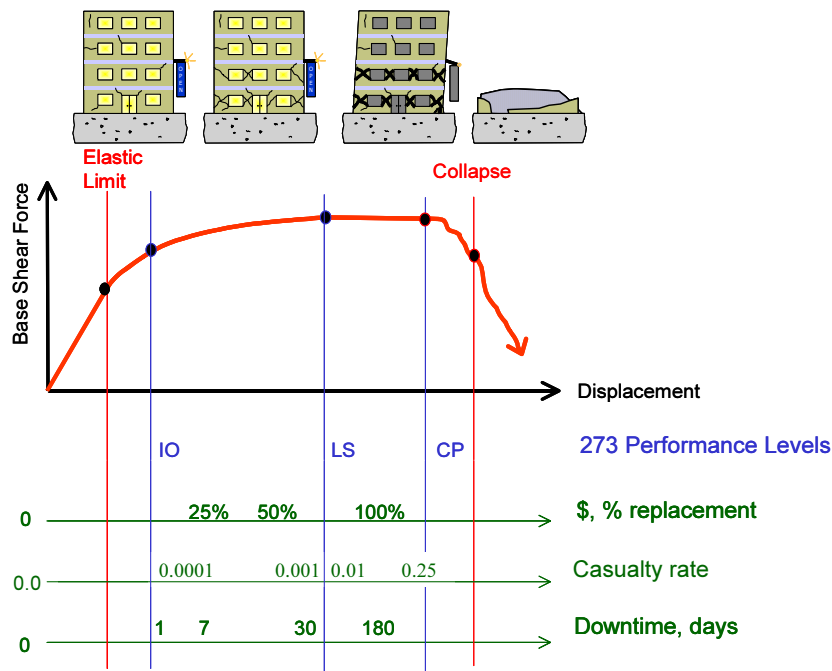


Figure 1 – A visualization of performance-based earthquake engineering (after Holmes).

- Structural performance was defined on the basis of component performance states; structural system performance was assumed to be equal to the worst performance calculated for any component in the building.

Although the shortcomings of the first-generation procedures were widely recognized by the developers, limitations in available technologies and supporting research did not permit further development at that time. Since then, the Pacific Earthquake Engineering Research Center (PEER) has embarked on a research program aimed at developing a more robust methodology for performance-based earthquake engineering. Recognizing the complex, multi-disciplinary nature of the problem, PEER has broken the process into logical elements that can be studied and resolved in a rigorous and consistent manner. The process begins with definition of a ground motion *Intensity Measure*, which defines in a probabilistic sense the salient features of the ground motion hazard that affect structural response. The next step is to determine *Engineering Demand Parameters*, which describe structural response in terms of deformations, accelerations, or other response quantities calculated by simulation of the building to the input ground motions. *Engineering Demand Parameters* are next related to *Damage Measures*, which describe the condition of the structure and its components. Finally, given a detailed probabilistic description of damage, the process culminates with calculations of *Decision Variables*, which translate the damage into quantities that enter into risk management decisions. Consistent with current understanding of the needs of decision-makers, the decision variables have been defined in terms of quantities such as repair costs, downtime, and casualty rates (Figure 1). Underlying the methodology is a consistent framework for representing the inherent uncertainties in earthquake performance assessment.

While full realization of the methodology in professional practice is still years away, important advances are being made through research in PEER. Some specific highlights are presented in the following text.

2. FORMALIZATION OF THE FRAMEWORK

Given the inherent uncertainty and variability in seismic response, it follows that a performance-based methodology should be formalized within a probabilistic basis. Referring to Figure 2, PEER’s probabilistic assessment framework is described in terms of four main analysis steps (hazard analysis, structural/nonstructural analysis, damage analysis, and loss analysis). The outcome of each step is mathematically characterized by one of four generalized variables: *Intensity Measure (IM)*, *Engineering Demand Parameter (EDP)*, *Damage Measure (DM)*, and *Decision Variable (DV)*. Recognizing the inherent uncertainties involved, these variables are expressed in a probabilistic sense as conditional probabilities of exceedance, i.e., $p[A|B]$. Underlying the approach in Figure 2 is the assumption that the performance assessment components can be treated as a discrete Markov process, where the conditional probabilities between parameters are independent.

The first assessment step entails a hazard analysis, through which one evaluates one or more ground motion *Intensity Measures (IM)*. For standard earthquake intensity measures (such as peak ground acceleration or spectral acceleration) *IM* is obtained through conventional probabilistic seismic hazard analyses. Typically, *IM* is described as a mean annual probability of exceedance, $p[IM]$, which is specific to the location (*O*) and design characteristics (*D*) of the facility. The design characteristics might be described by the fundamental period of vibration, foundation type, simulation models, etc. In addition to determining *IM*, the hazard analysis involves characterization of appropriate ground motion input records for response history analyses. PEER’s research on hazard analysis involves close coordination with the earth science and engineering seismology communities both to improve the accuracy of determining conventional scalar *IMs* and to investigate alternative seismic intensity measures that best correlate with earthquake-induced damage. These alternative measures may include vector representations of multiple intensity measures, such as multiple representations of spectral acceleration, spectral shape, and duration.

Given *IM* and input ground motions, the next step is to perform structural simulations to calculate *Engineering Demand Parameters (EDP)*, which characterize the response in terms of deformations, accelerations, induced forces, or other appropriate quantities. For buildings, the most common *EDPs* are interstory drift ratios, inelastic component deformations and strains, and floor acceleration spectra. Relationships between *EDP* and *IM* are typically obtained through inelastic simulations, which rely on models and simulation tools under development by PEER in areas of structural engineering, geotechnical engineering, SSFI (soil-structure-foundation-interaction), and non-structural component and system response. PEER has developed various approaches, such as the incremented dynamic analysis technique, to systematize procedures for characterizing the conditional probability, $p(EDP|IM)$, which can then be integrated with the $p[IM]$ to calculate mean annual probabilities of exceeding the *EDPs*.

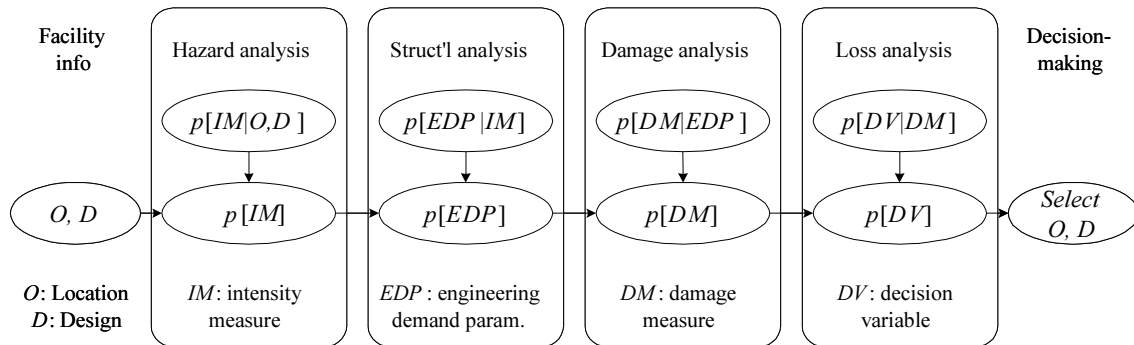


Figure 2 – Underlying probabilistic framework (after Cornell, Porter)

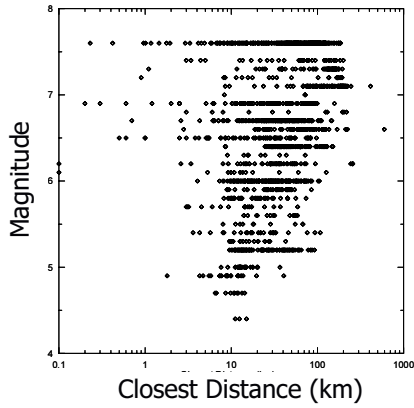


Figure 3 – Available ground motion data (after Stewart)

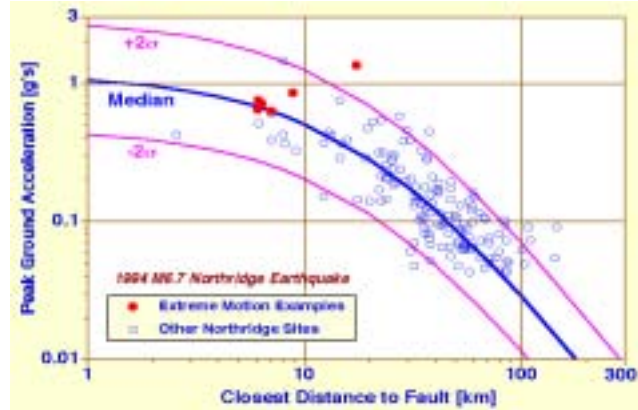


Figure 4 – Attenuation relations

The next step in the process is to perform a damage analysis, which relates the *EDPs* to *Damage Measures*, *DM*, which in turn describe the physical damage to a facility. The *DMs* include descriptions of damage to structural elements, non-structural elements, and contents, in order to quantify the necessary repairs along with functional or life safety implications of the damage (e.g., falling hazards, release of hazardous substances, etc.). PEER is developing conditional damage probability relationships, $p(DM|EDP)$, for a number of common and representative components, based on published test data, post earthquake reconnaissance reports, and tests of a few select components. These conditional probability relationships, $p(DM|EDP)$, can then be integrated with the *EDP* probability, $p(EDP)$, to give the mean annual probability of exceedance for the *DM*, i.e., $p(DM)$.

The final step in the assessment is to calculate *Decision Variables*, *DV*, in terms that are meaningful for decision makers. Generally speaking, the *DVs* relate to one of the three decision metrics discussed above with regard to Figure 1, i.e., direct dollar losses, downtime (or restoration time), and casualties. In a similar manner as done for the other variables, the *DVs* are determined by integrating the conditional probabilities of *DV* given *DM*, $p(DV|DM)$, with the mean annual *DM* probability of exceedance, $p(DM)$. PEER's previous research has served to, first, establish the choice of appropriate *DVs* and ways of presenting these performance metrics to stakeholders and, second, develop loss functions describing $p(DV|DM)$ relationships.

The methodology just described and shown in Figure 2 is an effective integrating construct for both the performance-based earthquake engineering methodology itself and the PEER research program. The methodology can be expressed in terms of a triple integral based on the total probability theorem, as stated in Equation 1.

$$v(DV) = \iiint G\langle DV|DM \rangle | dG\langle DM|EDP \rangle | dG\langle EDP|IM \rangle | d\lambda(IM) \quad (1)$$

Though the equation form of the methodology seems on the surface to be a minimalist representation of a very complex problem, it nonetheless serves a useful function by providing researchers with a clear illustration of where their discipline-specific contribution fits into the broader scheme of performance-based earthquake engineering and how their individual research results need to be presented. The equation also emphasizes the inherent uncertainties in all phases of the problem and provides a consistent format for sharing and integrating data and models developed by researchers in the various disciplines.

3. HAZARD INTENSITY MEASURE

The first assessment step in the methodology is a seismic hazard analysis. PEER currently is working with relatively conventional earthquake intensity measures such as peak ground acceleration or spectral acceleration, as well as some alternative measures. In the former case, the *IM* is obtained through conventional probabilistic seismic hazard analyses and is expressed as a mean annual probability of exceedance, $p[IM]$, which is specific to the location and design characteristics of the facility.

Current methods for estimating ground shaking intensity probabilities at a given site rely heavily on careful interpretation of the available empirical data from past earthquakes. The database of strong ground motion records has grown in the past several years to encompass a significant range of magnitudes, mechanisms, site conditions, and distances (Figure 3). When data are compiled into conventional attenuation relationships, the large degree of scatter leads to substantial uncertainty in the predicted motions (Figure 4). The PEER Strong Motion Database (<http://peer.berkeley.edu>) has been compiled to bring together over 1,500 records from 143 different earthquakes in a web-accessible format. Current developments for the database are expanding it by introducing more records and improving the information about the records. In conjunction with multiple other PEER projects, the database is including more detailed and accurate characterization of the site conditions at many of the important strong motion stations, and the details of the ruptures themselves. The new information is fostering the development of next-generation attenuation models that are more sophisticated and that will reduce the dispersion and bias associated with predicted levels of shaking.

PEER also is investigating the use of alternative hazard measures. Some promising examples include spectral ordinates at an elongated period (reflecting anticipated period elongation associated with inelastic response), spectral or roof displacement, duration; and vectors of these and other quantities. At present we have yet to settle on a specific, broadly accepted alternative to the conventional quantities.

In addition to determining the *IM* in terms of scalar or vector quantities that can be mapped or otherwise specified for a site given the geologic setting, hazard analysis also involves characterization of appropriate ground motion input records for response history analyses. Establishing input motions is especially important given the observation that accurate performance prediction can only be obtained through accurate dynamic simulation of system response. PEER currently is using industry-accepted procedures for generating *IM*-compatible input records, but continues to support research to advance procedures for developing consensus-based input records for performance analysis. Although the database of recorded strong ground motions has grown considerably in the past decade, there still are gaps in recordings for certain combinations of rupture mechanism, magnitude, distance, and site characteristics. Therefore, simulation of strong ground motion remains an important component of this part of the methodology.

4. ENGINEERING DEMAND PARAMETERS

Given the *IM* and input ground motions, the next step is to perform structural simulations to calculate *Engineering Demand Parameters (EDP)*, which characterize the response in terms of deformations, accelerations, induced forces, or other appropriate quantities. For buildings, the most common *EDPs* for the structural components and system are interstory drift ratios and inelastic component deformations and associated forces. For nonstructural components and contents, the most common *EDPs* are interstory drift ratios, floor accelerations, and floor velocities.

Relationships between *EDP* and *IM* are typically obtained through inelastic simulations, which are supported by PEER's research on simulation models and computational methods to assess the

performance of structural and geotechnical systems. Breaking the barriers of traditional methods and software development protocols, PEER has embarked on a completely new approach in the earthquake engineering community by developing an open-source, object-oriented software framework. *OpenSees* (Open System for Earthquake Engineering Simulation (<http://opensees.berkeley.edu>)) is a collection of modules to facilitate the implementation of models and simulation procedures for structural and geotechnical earthquake engineering. By shared development using well-designed software interfaces, the open-source approach has effected collaboration among a substantial community of developers and users within and outside of PEER. Unique among software for earthquake engineering, *OpenSees* allows integration of models of structures and soils to investigate challenging problems in soil-structure-foundation interaction. In addition to improved models for reinforced concrete structures, shallow and deep foundations, and liquefiable soils, *OpenSees* is designed to take advantage of the latest developments in databases, reliability methods, scientific visualization, and high-end computing.

PEER researchers have developed the incremented dynamic analysis procedure as a means of integrating structural simulations and ground motions to establish a relation between *EDPs* and *IMs*. The procedure is illustrated in Figure 5. According to the procedure, a numerical simulation is carried out in which a building structure is subjected to an input ground motion having a specified amplitude of the *IM* for which the response *EDP* is calculated. The process is repeated for increasing values of the *IM* by scaling the ground motion record, resulting in a continuous relation between the input *IM* and the resulting *EDP*. This process is repeated for a series of input ground motion records that have characteristics consistent with the site conditions, resulting in a series of relations between *IM* and *EDP*. One can calculate relevant statistical relations between *IM* and *EDP*, and establish the probability that the *EDP* will exceed a set value given *IM*. Given a seismic hazard analysis that establishes the probabilities of exceeding *IM*, one can integrate to obtain the hazard relation for *EDP*, which states the probability of exceeding *EDP* (Figure 6).

Prospects for accurate computation of the *EDP* relations vary with the target *EDP*. For example, procedures for calculation of nonlinear dynamic response of ductile frames are becoming increasingly routine with analytical models and computational procedures that have fairly comprehensive validations. Simulation of structural collapse, especially for less ductile systems, remains problematic because of the paucity of analytical models and the challenges of validating

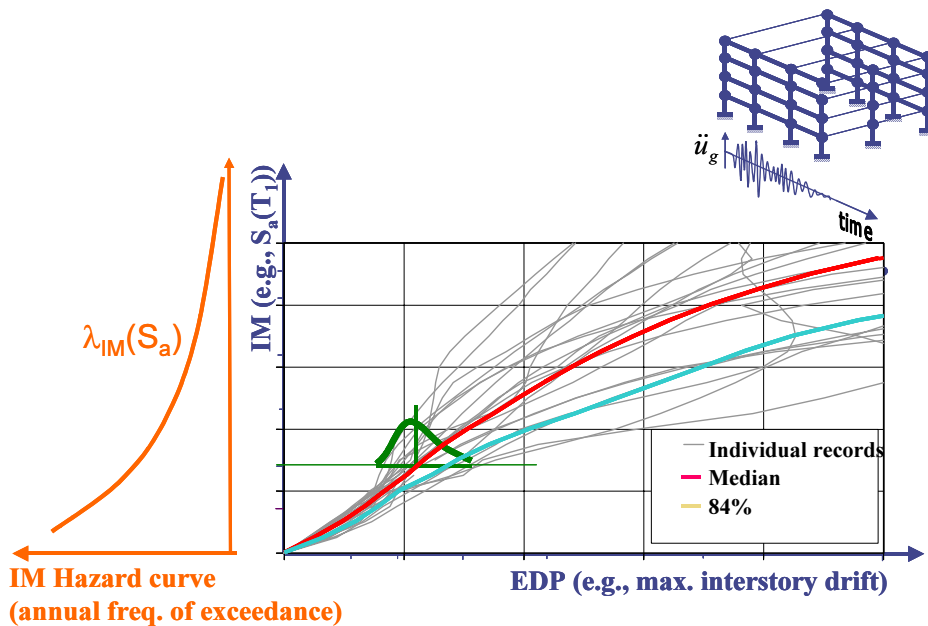


Figure 5 – IM hazard curve and incremented dynamic analysis results for an example structure (after Krawinkler)

simulation procedures for softening systems with large deformations. PEER has made considerable progress in this area, but the challenges here remain large.

5. DAMAGE MEASURES

The next step in the process is to perform a damage analysis, which relates the *EDPs* to *Damage Measures, DM*. The *DMs* include quantitative descriptions of damage to structural elements, non-structural elements, and contents. This quantification must be relevant and in sufficient detail to enable subsequent quantification of the necessary repairs, disruption of function, and safety hazards.

PEER is developing conditional damage probability relationships, $p(DM|EDP)$, for a number of common and representative components, based on published test data, post earthquake reconnaissance reports, and tests of a few select components. Some characteristic examples include the following:

- Damage models for structural collapse – Collapse of older existing reinforced concrete buildings commonly results from the loss of vertical load-carrying capacity of columns. Research on shear-critical columns has established relations between drift ratio at axial load failure and relevant parameters including column details and axial load (Figure 7). These models are useful not only for establishing the *DM* given a set of *EDPs*, but also for informing the structural simulation model so that it can compute the appropriate *EDP* - onset of axial load failure (a *DM*) in this case results in a significant change in the dynamic response characteristics of the building and therefore changes the *EDP*.
- To be useful within the probabilistic context of the PBEE framework, the *DMs* must be defined in terms of fragility relations. Figure 8 shows fragility relations for nonstructural partition walls, identifying probability of being in a given damage state as a function of the interstory drift ratio, and for various damage states. Importantly, the fragility relation is in terms of the most relevant *EDP*, in this case the interstory drift ratio. This is a departure from some approaches where fragilities are expressed as a probability of being in a certain damage state given an input ground motion parameter.

There exists a tremendous gap in knowledge to characterize all the necessary *DMs* and *EDP-DM* relations for buildings, for several reasons:

- Much prior testing emphasized strength and ductility capacity, with insufficient attention to damage measures such as residual crack width, spalling, permanent displacement, etc.
- There is a significant gap in research that relates *EDPs* as calculated by computer simulations and *EDPs* as measured in the laboratory and used as a basis for establishing *EDP-DM* relations (for example, strain is commonly used in experimental research as the *EDP* to define various damage states yet existing codes and simulation packages for nonlinear dynamic analysis of buildings are unable to provide accurate information on component strains).
- Nonstructural components and contents damage are the primary source of loss in most buildings during earthquakes, yet there is a paucity of experimental data on these.

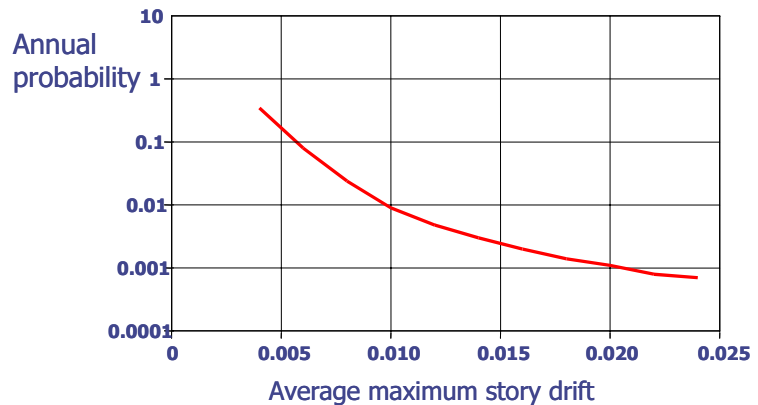


Figure 6 – Hazard curve for an EDP for an example structure (after Krawinkler)

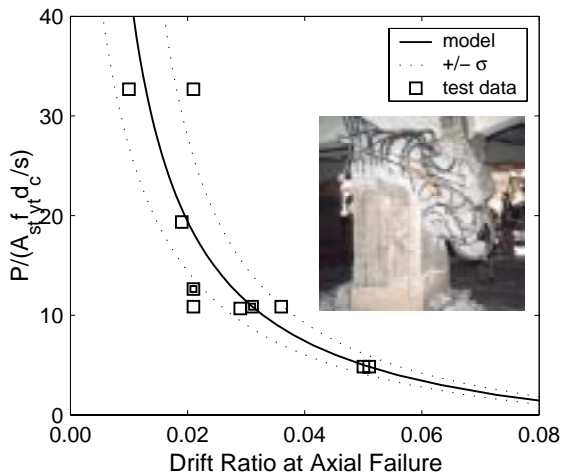


Figure 7 – DM for a column susceptible to axial failure (after Elwood and Moehle)

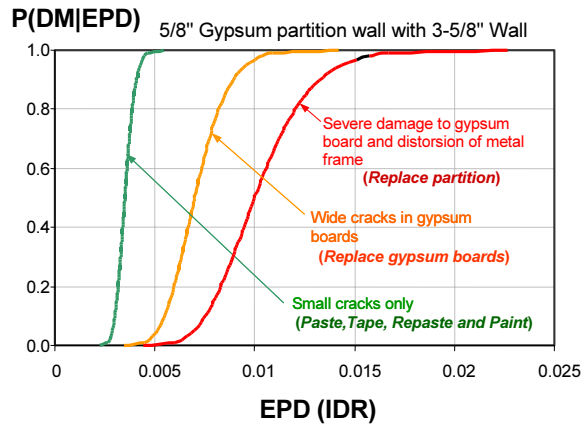


Figure 8 – Fragility relation for nonstructural component (after Miranda)

Increased awareness of the needs of PBEE methods may increase attention of researchers to these shortcomings. Furthermore, the availability of databases and database standards as part of the George E. Brown Network for Earthquake Engineering Simulation (NEES) also holds promise for needed advancements.

6. DECISION VARIABLES

The final step in the methodology is to calculate *Decision Variables*, *DV*, in terms that are useful to decision makers. Initial work within PEER aimed to express *DVs* in terms of mean annual probabilities of exceedance, $p[DV]$. However, work with various stakeholder groups indicated that this approach probably would not be of sufficient (or any) interest to many interest groups. Therefore, PEER has begun to think more broadly about the problem and to seek alternative ways of expressing losses. Examples include:

- Likely losses in the event of a single scenario (Figure 9a).
- Loss with a particular probability of exceedance (Figure 9b).
- Losses associated with a continuum of scenarios (Figure 9c)
- Probability of exceeding a given level of losses in a set period of time (Figure 9d).

While some of the distinction may seem mere semantics, getting the right language (e.g., “risk of ruin”) may be essential for getting PBEE on the agenda of a decision maker, let alone influencing their decisions.

These ways of expressing losses can all be accomplished within the general PBEE framework that is proposed. In a similar manner as done for the other variables, the *DVs* are determined by integrating the conditional probabilities of *DV* given *DM*, $p(DV|DM)$, with the mean annual *DM* probability of exceedance, $p(DM)$, for the selected seismic hazard, and then converting the results by appropriate analytics to the form that is required.

Addressing decisions in performance-based earthquake engineering involves more than calculation of *DVs*. It becomes important also to understand how these *DVs* relate to the different stakeholders that have potential interest in performance-based earthquake engineering, as illustrated in Figure 10. Business characteristics such as business size, occupancy tenure, and sector determine the vulnerability dimensions of greatest importance, including financial condition, location of customers, type of competition, and the location of competition. Other loss factors

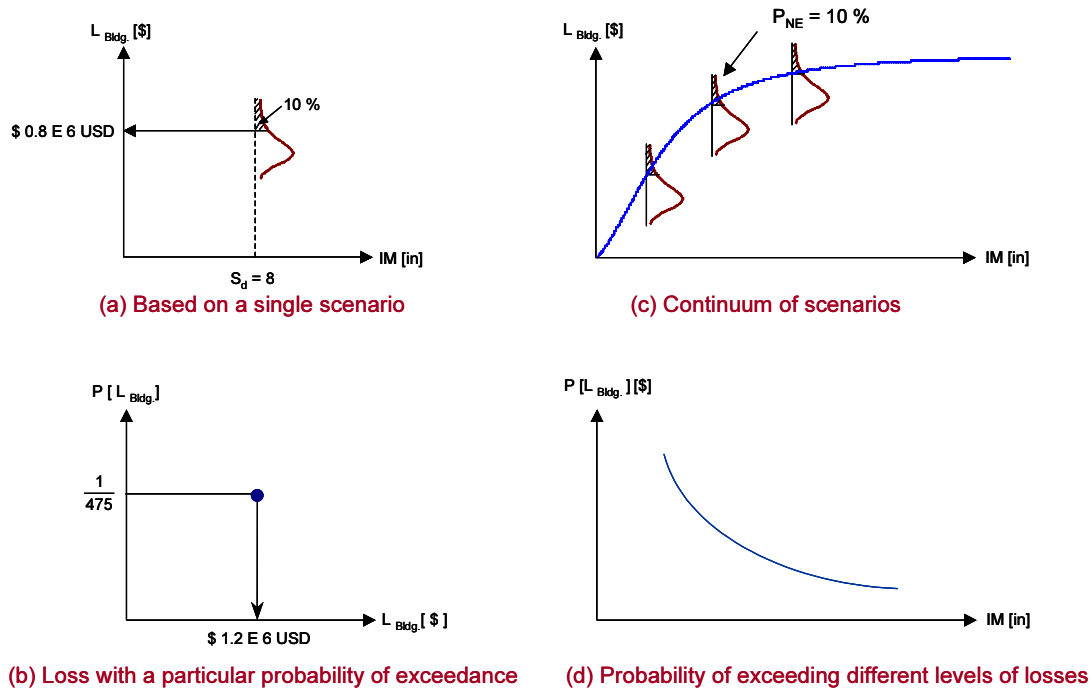


Figure 9 – Some ways of expressing losses (after Miranda)

related to the vulnerability dimensions determine how the various *DVs* relate to losses. For example, the loss of 90 percent of the air conditioning in a facility may represent a fixed cost of replacement for a range of occupancies, but the impact on functionality will vary greatly depending on the occupancy (a hospital would be completely nonfunctional while an office building may be able to continue operations). The methodology needs, therefore, to include a loss-modeling procedure that can represent the impacts of various *DVs* on different stakeholders.

7. METHODOLOGY APPLICATION

The proposed methodology is intended to serve two related purposes. The first of these is as a performance engine to be applied in full detail to the seismic performance assessment of a facility. As illustrated in Figure 1, the application would result in a comprehensive statement of the probabilities of various losses (in terms of dollars, downtime, and casualties) for events or timeframes of interest to the owner or decision maker for that facility. Though illustrated in an apparent static loading domain in Figure 1, this is for illustrative purposes only; the intent is to apply the methodology using a fully nonlinear dynamic analysis. Subsequent simplifications to a static or linear analysis domain awaits further study.

This leads to the second intended purpose of the methodology. Presuming it can be used to provide reliable results for a complete facility analysis, the methodology then can be used as a means of calibrating simplified procedures that might be used for advancement of future building codes. It is in this application that the methodology is likely to have its largest potential impact.

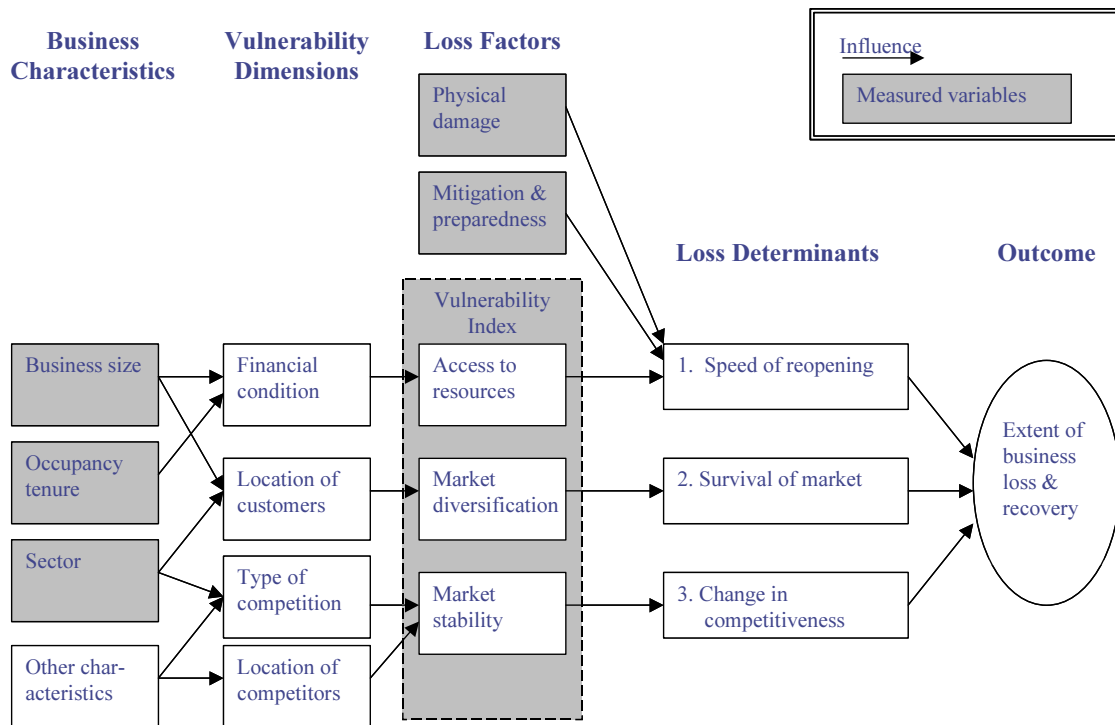


Figure 10 – Relating decision variables to various stakeholders (after Meszaros)

8. CONCLUSION

A methodology has been proposed by which to assess the expected performance of a facility subjected to earthquake hazard. The methodology breaks the assessment process into logical elements that can be studied and resolved in a rigorous and consistent manner. The process begins with definition of a ground motion *Intensity Measure*, uses advanced simulation procedures to establish *Engineering Demand Parameters*, relates these to *Damage Measures*, and finally calculates *Decision Variables* that can be used in risk management decisions. Importantly, the methodology addresses the shortcomings of the first generation PBEE methods in that it does away with simplified analysis techniques, tracks the overall problem in a consistent manner, and defines system performance on the basis of system measures rather than component measures. The methodology can be used for comprehensive performance assessment of an individual facility, and therefore is useful in assisting decision-makers who wish to target enhanced performance objectives. Alternatively, it can be used as a means of calibrating existing building code provisions, reducing dispersion and bias in results, and thereby achieving conventional performance targets in a more reliable and efficient way. It is in this latter capacity that the methodology holds the greatest potential for reducing losses in future earthquakes.

9. ACKNOWLEDGMENT

This work was supported primarily by the Pacific Earthquake Engineering Research Center through the Earthquake Engineering Research Centers Program of the National Science Foundation under Award number EEC-9701568. Key elements of the work were carried out by researchers funded and coordinated by PEER. Specific materials for this paper were derived from various works of PEER researchers, notably including Keith Porter (Caltech); Mary Comerio, Gregory Fenves, Stephen Mahin, and Michael Riemer (UC Berkeley); Jonathan Stewart (UCLA); Ahmed Elgamal (UC San Diego), Gregory Deierlein, Allin Cornell, Helmut Krawinkler, and Eduardo Miranda

(Stanford); and Peter May and Jacqueline Meszaros (U.Washington). Any opinions, findings, and conclusions or recommendations expressed in this material are those of the author and do not necessarily reflect those of the National Science Foundation or these other individuals.

10. REFERENCES

ATC, 1996, Methodology for Evaluation and Upgrade of Reinforced Concrete Buildings, Report No. ATC-40, California Seismic Safety Commission, Sacramento, California
FEMA, 1997, NEHRP Guidelines for Seismic Rehabilitation of Buildings, Report No. FEMA-273, Federal Emergency Management Agency, Washington, D.C.

OVERVIEW OF THE MULTIDISCIPLINARY CENTER FOR EARTHQUAKE ENGINEERING RESEARCH (MCEER)

Michel Bruneau

*Director of Multidisciplinary Center for Earthquake Engineering Research
and Professor of Engineering, University of New York at Buffalo
bruneau@mceermail.buffalo.edu*

Abstract: New strategies and technologies to reduce escalating losses are the thrust of MCEER's program. Center research seeks to define innovative approaches to improve performance assessment of engineered structures and infrastructure systems, and to develop cost-effective advanced techniques for the design of new construction and the rehabilitation of existing critical facilities—those that must remain operational after an earthquake—namely hospitals, lifeline systems (water and power distribution networks) and high-way systems.

1. INTRODUCTION

The Multidisciplinary Center for Earthquake Engineering Research (MCEER) is a national center of excellence that develops and applies knowledge and advanced technologies to reduce earthquake losses. Headquartered at the University at Buffalo, the Center was established in 1986 by the National Science Foundation (NSF) as the country's first National Center for Earthquake Engineering Research (NCEER). MCEER unites a group of leading researchers from numerous disciplines and institutions throughout the United States to integrate knowledge, expertise, and interdisciplinary perspective with state-of-the-art experimental and computational facilities in the fields of earthquake engineering and socioeconomic studies. The result is a systematic "engineered" program of basic and applied research that produces solutions and strategies to reduce the structural and socioeconomic impacts of earthquakes. Sponsored principally by NSF, the State of New York and the Federal Highway Administration (FHWA), MCEER garners additional support from the Federal Emergency Management Agency (FEMA), other state governments, academic institutions, foreign governments and private industry.

The Center's mission is to reduce earthquake losses through research, development and application of knowledge and advanced technologies that improve engineering, pre-earthquake planning, and post-earthquake response and recovery. In pursuit of this goal, MCEER coordinates a nationwide program of problem-focused, multidisciplinary team research, education and outreach activities that include collaboration with business, industry, consultants and government.

This paper describes some of MCEER's specific characteristics and current activities.

2. EARTHQUAKE-RESILIENT COMMUNITIES VIA USE OF ADVANCED TECHNOLOGIES

The Multidisciplinary Center for Earthquake Engineering Research (MCEER) seeks solutions to reduce earthquake losses, and help communities stand better prepared and increasingly resilient when faced with earthquakes. MCEER believes that the future of earthquake engineering and loss reduction lies in advanced and emerging technologies.

Therefore the center seeks to discover, nurture, develop, promote, help implement, and in some cases pilot-test innovative measures and advanced and emerging technologies to reduce losses in future earthquakes, in a cost-effective manner. Research includes innovative applications of engineered systems and materials, scientific methodologies, and concepts and analytical approaches not previously used in earthquake engineering and loss reduction. Projects focus on use of technologies to strengthen the most critical of facilities – hospitals, highways, and utilities – that communities become increasingly dependent upon in times of crisis, and to improve post-earthquake emergency response, crisis management, recovery and reconstruction efforts.

MCEER's nationwide program of problem-focused, multidisciplinary team research, education and outreach, includes collaboration with business, industry, and government. Advanced and emerging technologies being studied, include but are not limited to: Site remediation technologies; Structural control and simulation; Advanced systems analysis and high performance materials; Condition assessment technologies (including those for estimating potential and actual earthquake losses); Decision support systems

3. SAFEGUARDING LIFELINES, HOSPITALS, RESPONSE & RECOVERY SYSTEMS, AND HIGHWAYS

Advanced technologies are principally examined within four research programs – three funded by the National Science Foundation (NSF), and a fourth involving Federal Highway Administration (FHWA) contracts.

3.1 Seismic Evaluation and Retrofit of Lifeline Networks (NSF)

MCEER collaborates with Memphis Light, Gas and Water (MLGW) Division and the Los Angeles Department of Water and Power (LADWP) to study real-world systems, scenarios, and strategies to retrofit existing water and power systems. The objective is to identify, explore, and develop advanced technologies to rehabilitate critical water supply and electrical power networks to ensure a high level of performance following earthquakes. The goal is to substantially improve the reliability of these networks and demonstrate this through the Los Angeles and Memphis test beds.

3.2 Seismic Retrofit of Hospitals (NSF)

Hospitals must remain operational after an earthquake to render emergency medical care. This may require retrofit of the building, its foundation, and its non-structural components and contents. While other critical buildings house important emergency services (i.e., fire, police, etc.), hospitals pose

unique challenges, as they integrate complex structural and non-structural systems. Consequently, retrofit techniques developed for hospitals will apply in improving seismic performance of other less complicated critical facilities.

MCEER's hospital project involves a team with varying expertise, including representation from both the New York and California Offices of State Health Planning & Development (OSHPD), to account for differences in hospital construction types, seismic environments, and societal concern for earthquake risk in the eastern and western US.

3.3 Emergency Response and Recovery (NSF)

Emergency response and recovery represent a community's final line of support following a damaging earthquake. In contrast to more "routine" emergencies, earthquakes can produce multiple emergencies that overwhelm response and recovery authorities. Optimal response depends on quality advance planning and preparation.

The most significant challenge after an earthquake is to accurately assess the impact of the disaster, and to prioritize response needs accordingly. MCEER studies examine use of remote-sensing technologies for rapid damage assessment and loss estimation, and advanced decision support systems to ease and improve decision making in the immediate post-earthquake emergency period as well as during the following recovery and reconstruction.

3.4 Seismic Performance and Reliability of the Nation's Highway System (FHWA)

Improving seismic performance and reliability of the nation's highway system is the aim of MCEER's Highway Project. Initiated in 1992 with contracts from the Federal Highway Administration (FHWA), the project uniquely examines earthquake impacts on the highway system as an integrated network, rather than individual roads, bridges, embankments, etc.

Projects seek to ensure usability of highways following earthquakes by improving performance of interconnected components. Goals are to improve understanding of seismic hazards and improve and develop analysis methods, screening procedures and tools, retrofit technologies, design criteria, and methods to reduce vulnerability of existing and future highway infrastructure.

3.5 Engineering and Organizational Issues Related to The World Trade Center Terrorist Attack

With funding from the National Science Foundation (NSF), MCEER initiated a research project to collect perishable data in the aftermath of the WTC attack for later study to gain a better understanding of how resilience is achieved in physical, engineered systems, and in organizational systems. Reports on Engineering and Organizational Issues Related to The World Trade Center Terrorist Attack presents these findings. Each report in the series focuses on a narrow aspect of the disaster as studied by MCEER researchers. The series is based on the premise that the World Trade Center attack could be seen as a "proxy" for what a major earthquake might do in a complex, densely populated, modern urban environment. Like an earthquake, the terrorist attack occurred with virtually no warning. As would be expected in an earthquake, fires broke out and multiple structural collapses occurred. As has been observed in major urban earthquakes and in other disasters, structures that performed critical emergency functions were destroyed, heavily damaged, or evacuated for life-safety reasons.

4. DEMONSTRATION PROJECTS AND EARTHQUAKE RECONNAISSANCE INVESTIGATIONS

MCEER demonstration projects enable researchers and partners in industry and government to examine the promise of advanced technologies in real-world situations. For example, projects involving water supply and electrical power systems in California, infrastructure networks in Memphis, hospital facilities in New York and California, and bridge sites in Utah, provide opportunities to evaluate engineering and socioeconomic strategies for urban risk assessment and rehabilitation of critical facilities in a systematic integrated fashion.

Post-earthquake reconnaissance investigations offer additional real-world insight to MCEER's research. Though tragic in nature, the devastation of earthquakes in the U.S. and abroad serves as a real-life learning laboratory for Center investigators of all disciplines. Quickly dispatched to stricken regions, MCEER researchers learn valuable lessons from field investigations and on-site interviews which often bring new perspectives to the nation's and the Center's research agendas. Post-investigation technical briefings and reports contribute immeasurably to the worldwide body of knowledge in earthquake engineering and hazards mitigation.

5. MCEER OUTREACH

Center outreach efforts include broad-based dissemination of information and technology through research reports, national and international conferences and workshops, industry partnerships, and a national Information Service that provides convenient access to published, recorded and on-line materials on engineering, geological, social, political, and economic aspects of earthquakes. MCEER also engages in cooperative research programs with institutions outside the U.S., including Japan, the People's Republic of China, Mexico, Taiwan, and others. The international alliances promote global cooperation, collaborative experimental research, and information exchange that advance earthquake engineering and loss mitigation principles in the U.S. and abroad.

5.1 Partnerships

MCEER's partnerships program forges strategic alliances with manufacturers, consultants, end-users and other public- and private-sector stakeholders to develop, adapt, test and help implement the use of new and emerging technologies to mitigate earthquake losses. The program creates opportunities for cross-participation in collaborative research and demonstration projects enabling partners to widely examine and assess the reliability of new and emerging technologies. It also provides partners with access to a variety of research, education and technology transfer opportunities including state-of-the-art knowledge, experimental facilities, information resources, publications, meetings, seminars, short courses and distance learning.

5.2 Publications

MCEER publications foster knowledge and technology transfer by communicating the latest developments in earthquake engineering research and loss reduction practices to academic researchers, consultants, practitioners and policymakers in government and the private sector. Since its inception, the Center has published more than 300 technical reports, workshop and conference proceedings, special publications and monographs to address the needs of these important audiences.

Examples of practical research publications developed through MCEER include:

- Monographs that synthesize MCEER's technical achievements for a wider range of readers than the technical report series. Each book provides an in-depth view of the topic addressed, by summarizing the essence and significance of the problems investigated, the methods used, and the various solutions/issues proposed. Topics include passive energy dissipation systems for structural design and retrofit, engineering and socioeconomic impacts of earthquakes, and the response of buried pipelines to earthquakes.
- Research and Accomplishments volumes that summarize research and education achievements, highlighting MCEER work in progress on improving community resilience to earthquakes. MCEER researchers, practitioners and students, contribute reports on applications and development of a wide range of advanced technologies, conceptualizing decision support systems, modeling and loss estimation, and the research-education interface.
- A manual to help engineers retrofit major components of existing U.S. highways against earthquakes, developed with funding from the Federal Highway Administration (FHWA). The two-volume guide includes procedures to evaluate and retrofit all components comprising the nation's highway system. Guidelines apply to all regions and seismic zones in the U.S., and to all bridge construction projects that receive federal funding.
- Advanced design specifications aimed at improving strength and safety of U.S. bridges, developed through a joint venture between MCEER and the Applied Technology Council (ATC). The new specifications address all aspects of seismic design for highway bridges, defining the seismic hazard for each of the 50 United States, and including state-of-the-art design and performance criteria to help engineers better safeguard new highway bridges from damage and collapse during earthquakes.
- An MCEER-developed guide to improve and simplify screening of soils at highway bridge sites, for possible liquefaction problems. The guide, which includes simple state-of-the-art procedures, improves on other existing screening tools, which tend to be complex, difficult to apply in the field, and often produce inconsistent results. It is useful on any type of construction project, to reduce uncertainties in the design of foundations and the stability of underlying soils. The guide has been distributed to chief bridge engineers in all 50 states, and are widely used by engineers across the USA.
- Earthquake reconnaissance reports, workshop and conference proceedings, software users manuals, and many others.

5.3 Information Services

MCEER's national Information Service is a comprehensive source for earthquake engineering and loss reduction information. Housed in the University at Buffalo Science and Engineering Library, the Information Service provides reference services including literature searches and document delivery to academics, practitioners, policymakers and at-large publics worldwide. Information professionals on staff fulfill an average of 200 requests per week, and the Center's World Wide Web site, offering additional online information and resources, receives more than 56,000 distinct visits annually. MCEER's Quakeline database, updated monthly and also available online, provides easy access to tens of thousands of records on books, journals, technical reports and other earthquake engineering and natural hazards mitigation literature.

6. MCEER EDUCATION

MCEER's education initiatives provide learning opportunities for students and educators at the K-12 and university undergraduate and graduate levels, as well as practitioners seeking specialized training through continuing education. Consistent with the Center's goals, educational activities aim to stimulate interest in engineering and sciences at the earliest levels, develop future leaders in earthquake engineering and hazards mitigation at the undergraduate and graduate levels, and help today's engineering and emergency management practitioners keep pace with changes in their respective fields. Programs include an undergraduate internship program, providing students with extensive involvement in ongoing research; a professional Master of Engineering program that offers focused and intensive graduate study in earthquake engineering and the current state-of-practice; and Professional and Continuing Education (PACE) short courses to help practitioners gain new knowledge of advancements in research and application of emerging technologies in earthquake engineering and hazards mitigation.

7. EXPERIMENTAL RESEARCH FACILITIES AND THE GEORGE E. BROWN JR. NETWORK FOR EARTHQUAKE ENGINEERING SIMULATION (NEES)

The establishment of the National Science Foundation-funded George E. Brown, Jr. Network for Earthquake Engineering Simulation (NEES) is a milestone event in earthquake engineering. This network of 15 state-of-the-art experimental facilities will bring the U.S. experimental earthquake engineering capabilities to a leadership position worldwide. These facilities will make it possible to conduct advanced research and create new knowledge not possible until now.

Since its inception in 1986, MCEER has provided leadership in establishing a tradition of multi-institution distributed research programs. Currently, all MCEER-affiliated institutions with large-scale experimental testing capabilities are home to NEES equipment sites. These sites are located at the University at Buffalo (UB), University of Nevada, Reno (UNR), Rensselaer Polytechnic Institute (RPI) and Cornell University. The laboratories at UNR and RPI are already operational, as two of three early adopter sites of NEESgrid, a network infrastructure that will link earthquake engineering sites across the United States and create a national virtual earthquake engineering laboratory. The facilities at UB and Cornell are on schedule for completion in 2004. MCEER plans to become a major user of the NEES facilities, as well as a facilitator of multi-institute research using these facilities.

A brief description of the facilities underway at MCEER-affiliated institutions follows:

- The University at Buffalo's Structural Engineering and Earthquake Simulation Laboratory (SEESL), housed within the department of civil, structural and environmental engineering, will add twin six-degrees-of-freedom shake tables, as part of its \$10.5 million NSF grant. The new shake tables will be capable of seismic testing of structures up to 120 feet in length. The facility will also house two 30-foot high reaction walls, 41 and 23 feet in length. When complete, the \$20 million construction project will make the facility one of the most versatile in the world.

- Two shake tables at the University of Nevada, Reno (UNR) will be upgraded, and a third shake table will be added, as part of the institution's \$4.4 million NSF grant. The three shake tables, each measuring 14 square feet, will offer biaxial, or two directional testing of earthquake ground motions on structures. Each table can be operated independently of the others, or in-phase with the other two. The tables can also be moved together to form a single large table. The new and upgraded tables will more accurately simulate real earthquakes. Total cost of the expansion and upgrade is \$7 million.
- Rensselaer Polytechnic Institute's (RPI) 100-g ton Geotechnical centrifuge will undergo a \$2.5 million upgrade. This will include the installation of new equipment and software, including a two-dimensional in-flight earthquake simulator and a four dimensional in-flight robot, that will enable geotechnical engineers to better study earthquake impacts on soils.
- A \$2 million NSF grant will enable geotechnical engineers at Cornell University to for develop advanced experimental facilities for both full-scale and centrifuge-scale for testing, evaluation , and analysis of soil-structure- foundation interaction. This will dramatically enhance the ability to study the impact of this phenomenon on buried pipelines and other utilities. The upgrade will also include a new reaction wall 50 feet long and 24 feet high.

In a complementary way, the Center's Computational Network in Earthquake Engineering links computing facilities and resources at each of the MCEER member institutions, providing researchers and research partners with access to the most advanced computational tools for simulation and analysis of ground motion and structural behavior, loss and damage assessment, and emergency response.

8. CONCLUSIONS

The engineering of sound, cost-effective solutions to the problems posed by earthquakes, requires more than engineering alone. It requires a coordinated, unified effort of stakeholders from varied disciplines. Through a systematic integration of researchers, facilities and research partners in industry and government, research centers such as MCEER can engineer solutions to today's earthquake challenges, mobilizing expert multidisciplinary teams to investigate, test and develop strategies and technologies that lessen the impacts of earthquakes on society. This paper provided an overview of how a research center experience can help fulfill the goal of enhancing the seismic resilience of communities.

9. ACKNOWLEDGMENTS

The activities of the Multidisciplinary Center for Earthquake Engineering Research are in part funded by the Earthquake Engineering Research Centers Program of the National Science Foundation under Award No. ECC-9701471, the Federal Highway Administration under contract number DTFH61-98-C-00094, the Federal Emergency Management Agency, as well as many other sponsors. However, any opinions, findings, conclusions, and recommendations presented in this paper are those of the writer and do not necessarily reflect the views of the sponsors.

CONSIDERATIONS OF SITE RESPONSE IN U. S. BUILDING CODE PROVISIONS

Roger D. Borcherdt¹⁾

*1) Senior Research Seismologist, United States Geological Survey, Menlo Park, CA, USA
borcherdt@usgs.gov*

Abstract: Current provisions to account for local site-response in U.S. Building Code Provisions were adopted in 1994. No significant changes have occurred in these provisions since that time. These provisions provide new unambiguous definitions of seismically distinct site classes in terms of shear wave velocity and new amplitude-dependent site coefficients as a function of shear velocity and site class. The provisions are based on strong-motion measurements of the 1989 Loma Prieta, CA earthquake, numerical modeling, and a rather extensive set of borehole geotechnical data. Subsequent earthquakes have provided a significant increase in the number of strong-motion recordings at base accelerations in the 0.2-0.5 g range and corresponding borehole shear wave velocity measurements. Analyses of these data and subsequent research by several researchers resulted in a consensus that changes in the 2003 edition of the NEHRP building code provisions as adopted by the US National Provision Update Committee was not warranted. This paper will summarize the current site-response provisions in US Building Codes and summarize the basis for this recommendation.

1. INTRODUCTION

Exaggerated damage on soft soil deposits from the 1985 Mexico City earthquake, the 1988 Spitak, Armenia earthquake and the 1989 Loma Prieta earthquake emphasized the need to revise site response provisions in building codes adopted for use in the United States. Subsequent efforts resulted in a new set of provisions to account for the amplification effects of local soil deposits. These new provisions were first adopted in the 1994 Edition of the NEHRP (National Earthquake Hazard Reduction Program) "Recommended Provisions for Seismic Regulations for New Buildings and other Structures" and subsequently adopted in the 1997 and 2000 editions (NEHRP, 1994, 1997, 2000). They have been adopted with no significant changes in the 1997 and 2000 editions of the Uniform Building Code (UBC) and the 2000 edition of the International Building Code (IBC, 2000). Recently, they also have been adopted for the proposed 2003 edition of the NEHRP provisions and the new ASCE 7 2003 edition. The IBC and ASCE 7 represent a consensus effort to standardize seismic code provisions in the United States.

Reviews by several investigators of the theoretical and empirical evidence for the site coefficients as adopted in the 2000 editions of US seismic code provisions indicated that evidence available in 2002 confirmed provisions as written and that no change proposals were warranted for the 2003 NEHRP edition. This manuscript summarizes procedures and commentary as adopted in the 2003 NEHRP provisions. The manuscript reproduces pertinent NEHRP code provision material for readers not familiar with the provisions. A brief summary is provided of recent results derived by other investigators and their implications for change.

2. SITE-SPECIFIC DESIGN SPECTRA IN US BUILDING CODE PROVISIONS

In general, site-specific design spectra are specified in US building code provisions for each period as the product of an input ground motion level and an appropriate site coefficient intended to account for the amplification effects of local site conditions. The site coefficients are specified for a short-period and a long-period band as a function of site conditions and input ground motion level. The site conditions are specified in terms of site classes. The site classes are defined in terms of a minimum thickness and an estimate of shear velocity to 30 meters of the near-surface material. The input ground motion levels are specified from seismic design maps termed “Maximum Considered Earthquake Maps” developed from national probabilistic seismic hazard maps for a uniform ground condition of firm to hard rock. Details of the procedure are presented in subsequent sections.

2.1 Site Class Definitions

The seismic response of near surface deposits depends strongly on the geological character of the ground with the amplification effects of soft soil deposits at some periods being significantly larger than incoming base rock motions, especially if local site response resonances develop. Site classes are used in US building code provisions to define categories of geologic units with distinct seismic response characteristics. The classes are defined in terms of shear velocity to a depth of 30 m, denoted by \bar{v}_s (Borcherdt, 1992, 1994). For sites underlain by soils for which no measurements of \bar{v}_s to 30 m are feasible corresponding limits in terms of standard penetration resistance (\bar{N}_{ch}) and undrained shear strength (\bar{s}_u) have been added to facilitate identification of the site classes.

The site classes in US building code provisions (<http://www.bssconline.org/>) are defined as follows:

- A Hard rock with measured shear wave velocity, $\bar{v}_s > 5,000$ ft/sec (1500 m/s).
- B Rock with $2,500$ ft/sec $< \bar{v}_s < 5,000$ ft/sec (760 m/s $< \bar{v}_s < 1500$ m/s),
- C Very dense soil and soft rock with $1,200$ ft/sec $< \bar{v}_s < 2,500$ ft/sec (360 m/s $< \bar{v}_s < 760$ m/s) or with either $N > 50$ or $\bar{s}_u > 2,000$ psf (100 kPa),
- D Stiff soil with 600 ft/sec $< \bar{v}_s < 1,200$ ft/sec (180 m/s $< \bar{v}_s < 360$ m/s) or with either $15 < N < 50$ or $1,000$ psf $< \bar{s}_u < 2,000$ psf (50 kPa $< \bar{s}_u < 100$ kPa)
- E A soil profile with $\bar{v}_s < 600$ ft/sec (180 m/s) or with either $N < 15$, $\bar{s}_u < 1,000$ psf, or any profile with more than 10 ft (3 m) of soft clay defined as soil with $PI > 20$, $w \geq 40$ percent, and $\bar{s}_u < 500$ psf (25 kPa),
- F Soils requiring site-specific evaluations:
 - a) Soils vulnerable to potential failure or collapse under seismic loading such as liquefiable soils, quick and highly sensitive clays, collapsible weakly cemented soils.
Exception: For structures having fundamental periods of vibration less than or equal to 0.5 second, site-specific evaluations are not required to determine spectral accelerations for liquefiable soils. Rather, the Site Class may be determined according to preceding classes, assuming liquefaction does not occur,
 - b. Peat and/or highly organic clays ($H > 10$ ft [3 m] of peat and/or highly organic clay, where H = thickness of soil)
 - c. Very high plasticity clays ($H > 25$ ft [8 m] with $PI > 75$)
 - d. Very thick, soft/medium stiff clays ($H > 120$ ft [36 m]) with $\bar{s}_u < 1,000$ psf (50 kPa).

The values for \bar{v}_s , \bar{N} or \bar{N}_{ch} , and \bar{s}_u for site classes E, D, and C are summarized in Table 1.

Table 1 Definition of site classes in terms of \bar{v}_s , \bar{N} or \bar{N}_{ch} , and \bar{s}_u .

Site Class	\bar{v}_s	\bar{N} or \bar{N}_{ch}	\bar{s}_u
E	< 600 fps (< 180 m/s)	<15	<1000 psf (< 50 kPa)
D	600 to 1,200 fps (180 to 360 m/s)	15 to 50	1,000 to 2,000 psf (50 to 100 kPa)
C	1,200 to 2,500 fps (360 to 760 m/s)	> 50	> 2,000 psf (> 100 kPa)

Note: If the \bar{s}_u method is used and the \bar{N}_{ch} and the \bar{s}_u criteria differ, select the category with the softer soils (for example, use Site Class E instead of D).

2.2 Site Coefficients

Site response is characterized in current US building code provisions by average short-and long-period amplification factors F_a and F_v that are dependent on the type of local site condition and the amplitude of the incoming base motion. The site coefficients as specified in the provisions are tabulated as a function of site class and maximum considered spectral acceleration at short period (0.2 second, S_S) and at long period (1.0 second, S_I). The short and long period site coefficients as they appear in the 2003 NEHRP provisions (<http://www.bssconline.org/>) are tabulated in Tables 2 and 3.

Table 2 Values of Site Coefficient F_a

Site Class	Mapped MCE Spectral Response Acceleration Parameter at 0.2 Second Period ^a				
	$S_S \leq 0.25$	$S_S = 0.50$	$S_S = 0.75$	$S_S = 1.00$	$S_S \geq 1.25$
A	0.8	0.8	0.8	0.8	0.8
B	1.0	1.0	1.0	1.0	1.0
C	1.2	1.2	1.1	1.0	1.0
D	1.6	1.4	1.2	1.1	1.0
E	2.5	1.7	1.2	0.9	0.9
F	— ^b	— ^b	— ^b	— ^b	— ^b

Notes:
^a Use straight line interpolation for intermediate values of S_S .
^b Site-specific geotechnical investigation and dynamic site response analyses shall be performed.

Table 3 Values of Site Coefficient F_v

Site Class	Mapped MCE Spectral Response Acceleration Parameter at 1 Second Period ^a				
	$S_I \leq 0.1$	$S_I = 0.2$	$S_I = 0.3$	$S_I = 0.4$	$S_I \geq 0.5$
A	0.8	0.8	0.8	0.8	0.8
B	1.0	1.0	1.0	1.0	1.0
C	1.7	1.6	1.5	1.4	1.3
D	2.4	2.0	1.8	1.6	1.5
E	3.5	3.2	2.8	2.4	2.4

Table 3 Values of Site Coefficient F_v .

Site Class	Mapped MCE Spectral Response Acceleration Parameter at 1 Second Period ^a				
	$S_I \leq 0.1$	$S_I = 0.2$	$S_I = 0.3$	$S_I = 0.4$	$S_I \geq 0.5$
F	— ^b	— ^b	— ^b	— ^b	— ^b

Notes:
^a Use straight line interpolation for intermediate values of S_I .
^b Site-specific geotechnical investigation and dynamic site response analyses shall be performed.

2.3 Definition of Design Response Spectrum

The rigorous definition of the design response spectrum S_a as currently specified in recommended provisions for the 2003 edition of the NEHRP provisions may be written succinctly as:

$$S_a = \left\{ \begin{array}{ll} \left(0.6 \frac{T}{T_0} + 0.4 \right) S_{DS} & \text{for } T \leq T_0 = 0.2 \left(\frac{S_{D1}}{S_{DS}} \right) \\ S_{DS} = \frac{2}{3} S_{MS} = \frac{2}{3} F_a S_S & \text{for } T_0 \leq T < T_S = \frac{S_{D1}}{S_{DS}} \\ S_{D1} = \frac{2}{3} S_{M1} = \frac{2}{3} \frac{F_v S_1}{T} & \text{for } T_S \leq T \leq T_L \\ S_{D1} \left(\frac{T_L}{T^2} \right) & \text{for } T_L \leq T \end{array} \right\}, \quad (1)$$

where the notation is defined as follows:

- S_a The design spectral response acceleration for a given period T ,
- S_{aM} The maximum considered earthquake spectral response acceleration at a given period T ,
- S_{DS} The design, 5-percent-damped, spectral response acceleration parameter at short periods,
- S_{D1} The design, 5-percent-damped, spectral response acceleration parameter at a period of one second,
- S_{MS} The maximum considered earthquake, 5-percent-damped, spectral response acceleration parameter at short periods adjusted for site class effects,
- S_{M1} The maximum considered earthquake, 5-percent-damped, spectral response acceleration parameter at a period of one second adjusted for site class effects,
- F_a Short-period site coefficient specified in table 2,
- F_v Long-period site coefficient specified in table 3,
- S_S The mapped, maximum considered earthquake, 5-percent-damped, spectral response acceleration parameter at short periods as determined from the 0.2 sec Maximum Considered Earthquake maps included in the NEHRP provisions,
- S_I The mapped, maximum considered earthquake, 5-percent-damped, spectral response acceleration parameter at 1 second period as determined from the 1.0 sec Maximum Considered Earthquake maps included in the NEHRP provisions,

T = the fundamental period of the *structure* (sec),
 $T_0 = 0.2S_{D1}/S_{DS}$,
 $T_S = S_{D1}/S_{DS}$,
 T_L = Region dependent transition period as shown on maps of the coterminous US, California, Alaska, and Hawaii in Figures 3.3-4 through 3.3-5 of the proposed 2003 NEHRP provisions.

Notation used in the definition of the design response spectral acceleration is illustrated in Figure 1. The dashed curve represents the design response spectral acceleration estimated for a base motion spectrum for a site-class B site (firm to hard rock). The solid curve represents the design response spectral acceleration for a site class D site (stiff clays and sandy soils), where the appropriate short and long period site coefficients F_a and F_v have been multiplied by the spectra estimated for rock to obtain the resulting site class D spectra for an input maximum considered spectral acceleration at 0.2 seconds of $S_S = 0.25g$ and at one second of $S_1 = 1.0g$. The proposed 2003 NEHRP edition includes a new constraint to reduce design motions with periods longer than T_L , but no modifications of the site coefficients are proposed (see Figure 1).

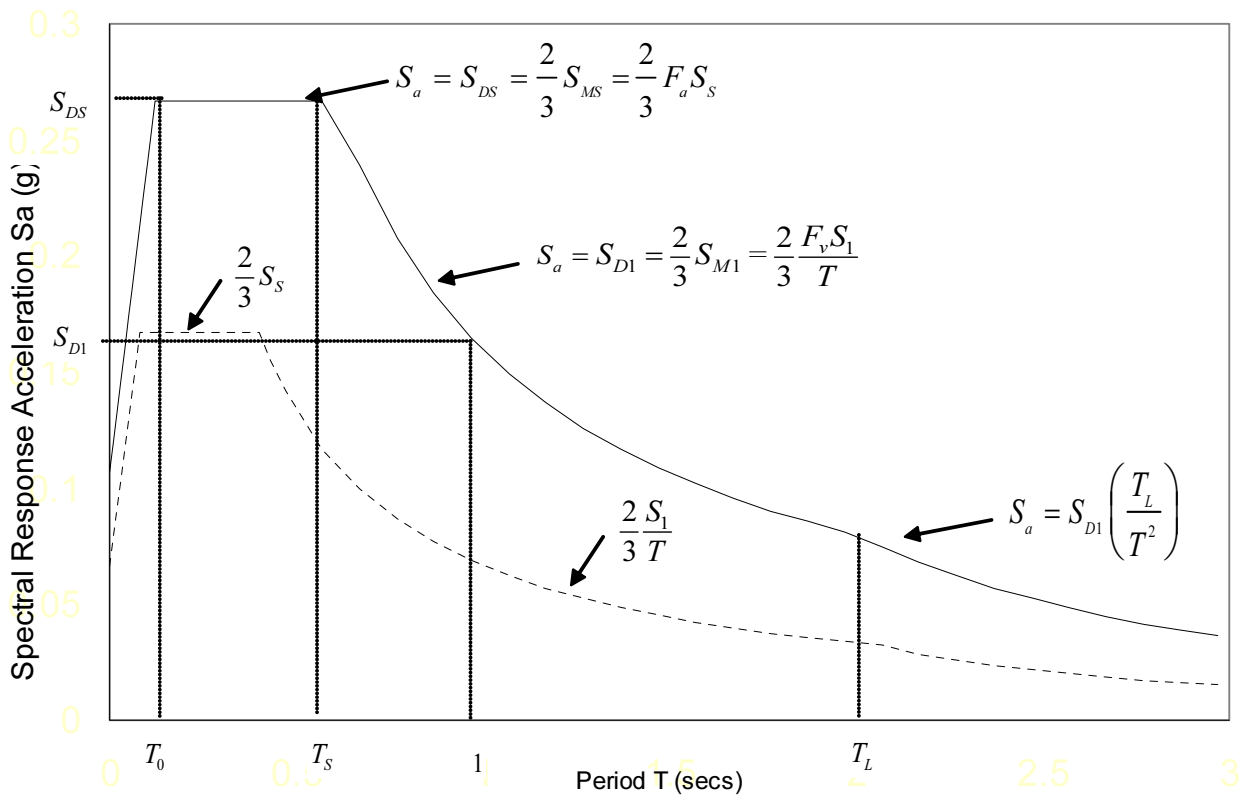


Figure 1 Illustration showing design response spectral acceleration versus period as defined in equation 1 (see text) for a base ground motion spectra (dashed curve) and a ground motion spectra modified from the base motion spectra to account for the local site effects. Parameters, as defined in equation 1, are illustrated.

2.4 Methodology for Estimating Design Response Spectrum

The methodology for estimation of design response spectral acceleration is easily understood in terms of equation 1, Figure 1, and Tables 1-3. The general steps in the methodology may be summarized as follows:

- 1) Classify the site according to the appropriate site class defined in Table 1 and section 2.1.

- 2) Determine the short-period and long-period site coefficients F_a and F_v appropriate for the determined site class from Tables 2 and 3.
- 3) Derive estimates of S_s and S_1 from the “Maximum Considered Earthquake” national design maps for 0.2 second and 1.0 second spectral acceleration for the site location of interest, (*The MCE maps are included in the building code provisions. They have been prepared for a uniform ground condition of site class B (firm to hard rock) from the national probabilistic seismic hazard maps showing 2% in 50 year probability of exceedance levels for spectral response acceleration with 5% damping for 0.2 and 1.0 second period motions (Frankel, and others, 1996;2003, <http://eqhazmaps.usgs.gov/html/us2002.html>) with deterministic upper bounds placed on the exceedance levels for some locations with short return periods (Leyendecker, and others, 2000)*)
- 4) Derive estimates of the short- and long-period design spectral parameters S_{DS} and S_{D1} as defined in equation 1 and shown in Figure 1.
- 5) Derive estimates of T_0 and T_s as defined in equation 1 and T_L as shown on new maps in 2003 NEHRP provisions,
- 6) Compute values of spectral response acceleration function S_a for values of period T of interest in the intervals $[0, T_0]$, $[T_0, T_s]$, $[T_s, T_L]$ and $[T_L, \infty]$ using equation 1.

3. BASIS FOR SITE COEFFICIENTS AS SUMMARIZED FROM COMMENTARY FOR 2003 EDITION OF NEHRP PROVISIONS

The basis for the site coefficients as provided in the commentary for the proposed 2003 edition of the NEHRP provisions is restated in summary here as explanatory information for the provisions (<http://www.bssconline.org/ReformattedProv.htm>).

Strong-motion recordings obtained on a variety of geologic deposits during the Loma Prieta earthquake of October 17, 1989 provided an important empirical basis for the development of the site coefficients F_a and F_v . Average amplification factors derived from these data with respect to “firm to hard rock” for short-period (0.1-0.5 sec), intermediate-period (0.5-1.4 sec), mid-period (0.4-2.0 sec), and long-period (1.5-5.0 sec) bands show that a short- and mid-period factor (the mid-period factor was later denoted the long-period factor in the NEHRP Provisions) are sufficient to characterize the response of the local site conditions (Borcherdt, 1994). This important result is consistent with the two-factor approach to response spectrum construction summarized in Figure 1. Empirical regression curves fit to these amplification data as a function of mean shear wave velocity at a site are shown in Figure 2.

The curves in Figure 2 provide empirical estimates of the site coefficients F_a and F_v as a function of mean shear wave velocity for input peak ground accelerations on rock (Borcherdt, 1994; Borcherdt and Glassmoyer, 1994). The empirical amplification factors predicted by these curves are in good agreement with those obtained from empirical analyses of Loma Prieta data for soft soils by Joyner et al. (1994). These short- and long-period amplification factors for low peak ground (rock) acceleration levels (~ 0.1 g) provided the basis for the values in the left-hand columns of Tables 2 (3.3-1) and 3 (3.3-2). Note that in Tables 2 and 3, peak ground (rock) acceleration of 0.1g corresponds approximately to a response spectral acceleration on rock at 0.2-second period (S_s) equal to 0.25g (Table 2) and to a response spectral acceleration on rock at 1.0-second period (S_1) equal to 0.1g (Table 3).

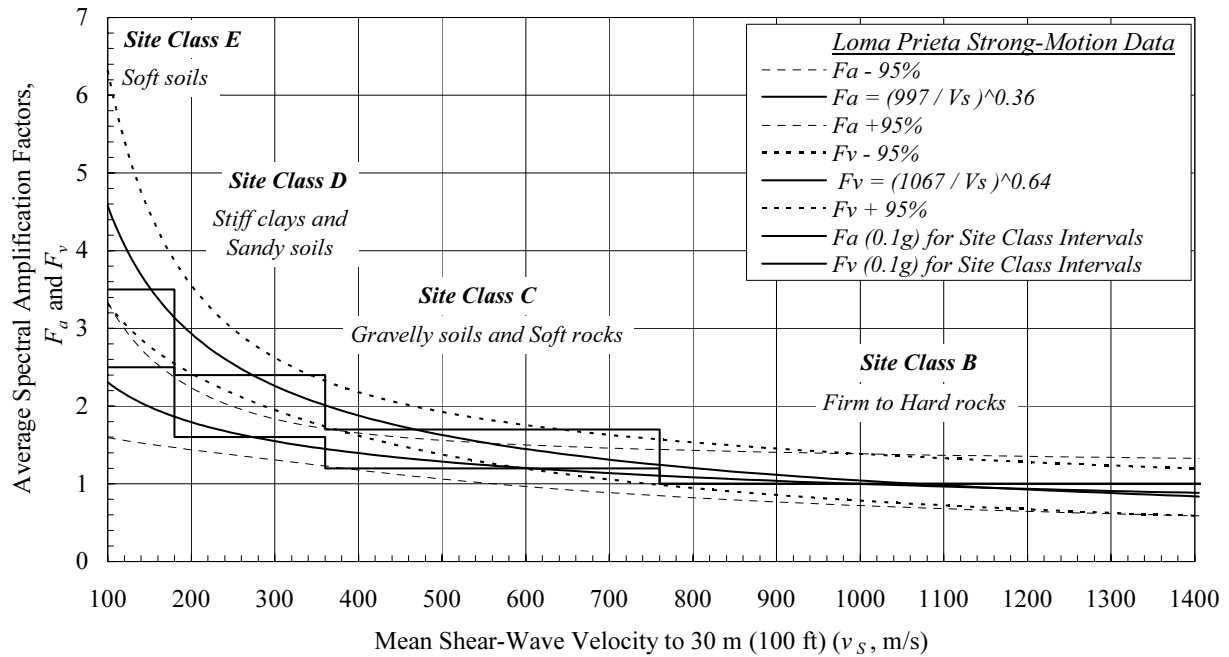


Figure 2 Short-period F_a and long-period F_v site coefficients with respect to site class B (firm to hard rocks) inferred as a continuous function of shear-wave velocity from empirical regression curves derived using Loma Prieta strong-motion recordings. The 95 percent confidence intervals for the ordinate to the true population regression line and the corresponding site coefficients in Tables 2 and 3 for 0.1g acceleration are plotted. The curves show that a two factor approach with short- and long-period site coefficients are needed to characterize the response of near surface deposits (modified from Borchardt 1994).

The values of F_a and F_v obtained directly from the analysis of ground motion records from the Loma Prieta earthquake were used to calibrate numerical one-dimensional site response analytical techniques, including equivalent linear as well as nonlinear programs. The equivalent linear program SHAKE (Schnabel et al. 1972), which had been shown in previous studies to provide reasonable predictions of soil amplification during earthquakes (e.g., Seed and Idriss 1982), was used extensively for this calibration. Seed et al. (1994) showed that the one-dimensional model provided a good first-order approximation to the observed site response in Loma Prieta, especially at soft clay sites. After calibration, these equivalent linear and nonlinear one-dimensional site response techniques were used to extrapolate the values of F_a and F_v to larger rock accelerations of as much as 0.4g or 0.5g. These results provided the basis for the values of F_a and F_v shown in the right-most four columns of Tables 2 and 3.

Graphs and equations that provide a framework for extrapolation of Loma Prieta results to larger input ground motion levels continuously as a function of site conditions (shear-wave velocity) are shown in Figures 3a and 3b. Site coefficients in Tables 2 and 3 are superimposed on each figure. These simple curves were developed to reproduce the site coefficients for site classes E and B and provide approximate estimates of the coefficients for the other site classes at various ground acceleration levels. The equations describing the curves indicate that the amplification at a site is proportional to the shear velocity ratio (impedance ratio) with an exponent that varies with the input ground motion level (derivation details are provided in Borchardt, 1994). The equations and graphs provide a simple framework for inference of F_a and F_v values as a continuous function of shear velocity at various input acceleration levels for sites requiring special investigations.

4. IMPLICATIONS OF RECENT ANALYSES FOR CHANGES IN SITE-COEFFICIENT PROVISIONS

Empirical and numerical estimates of F_a and F_v conducted on the basis of data collected since the Loma Prieta earthquake have been reported by a number of researchers, including Crouse and McGuire, 1996; Dobry et al., 1999; Silva et al., 2000; Joyner and Boore, 2000; Rodriguez-Marek et al., 2001; Stewart et al., 2001; and Borchardt, 2002. In particular, The Northridge earthquake provided the largest set of strong-motion recordings exceeding 0.2g yet obtained in the United States. These data provided an important basis to develop empirical estimates of site coefficients, F_a and F_v for comparison with those specified in current U.S. building code provisions for Site Classes C and D, but not E, due to a limited number of “soft-soil” sites in the area.

Recent estimates of site coefficients as derived by the various investigators are plotted in Figures 4 and 5 as a function of base acceleration level from a detailed comparison by Borchardt (2002). Figures 4a and 4b show results derived for site coefficient F_a for site class D and C sites.

Similarly, Figures 5a and 5b show results derived for site coefficient F_v for site class D and C sites. Superimposed on each figure are the best fitting regression curves and corresponding 95% confidence limits for the ordinate to the true population regression line as derived from the Northridge strong-motion recordings (Borchardt, 2002). Also, superimposed are the site coefficients as presented in Tables 2 and 3.

The estimates, as derived by various investigators, vary depending on the database, the reference ground motion, the site-classification method, and the procedure used to infer the resultant site factors. The regressions of the site coefficients on base acceleration as derived from the Northridge recordings (Figures 4 and 5) show that F_a and F_v as specified in current code provisions at the higher levels of base acceleration (≥ 0.3 g) are within the 95 percent confidence bands for the ordinates to the true population regression line. Hence, in a rigorous statistical sense this result implies that for the higher levels of base acceleration no changes in the present code provisions are justified at the 95 percent confidence level. For lower levels of base acceleration (< 0.3 g) these regressions suggest that the short-period factors could be increased at the 95 percent confidence level by percentages up to 13 percent; however, considerations of the base normalization velocity for reference sites indicates that such an increase is not warranted. The analyses show that no change in the slopes or the regression coefficients that specify the dependence of the site coefficients on base acceleration can be justified at the 95 percent confidence level. Consensus based on review of these results by the appropriate provision update committees indicated a change in the provisions was not warranted.

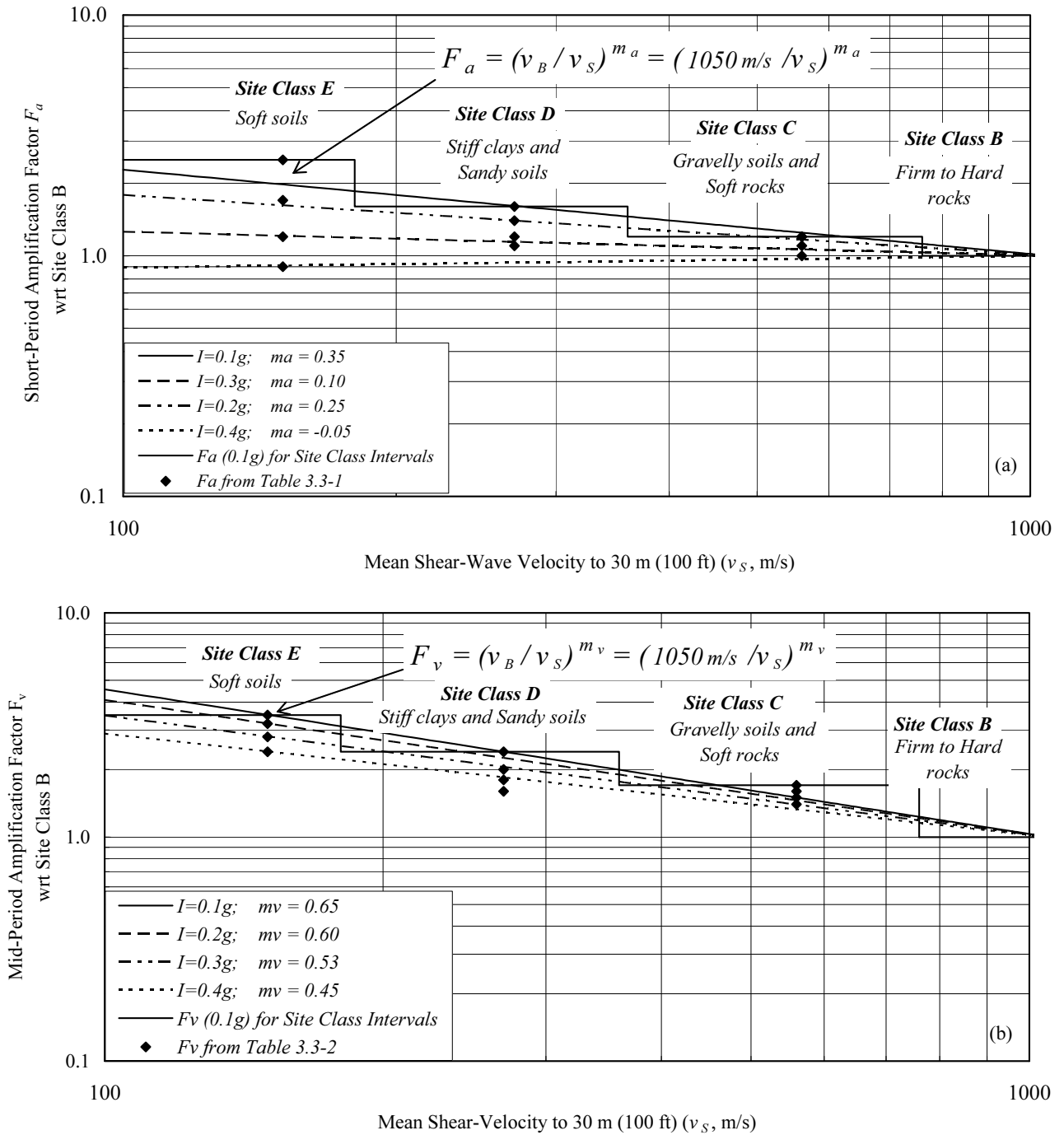


Figure 3 Graphs and equations that provide a simple framework for inference of (a) F_a and (b) F_v values as a continuous function of shear velocity at various input acceleration levels. Site coefficients in Table 2 and 3 are superimposed. These simple curves were developed to reproduce the site coefficients for site classes E and B and provide approximate estimates of the coefficients for the other site classes at various ground acceleration levels (from Borcherdt 1994).

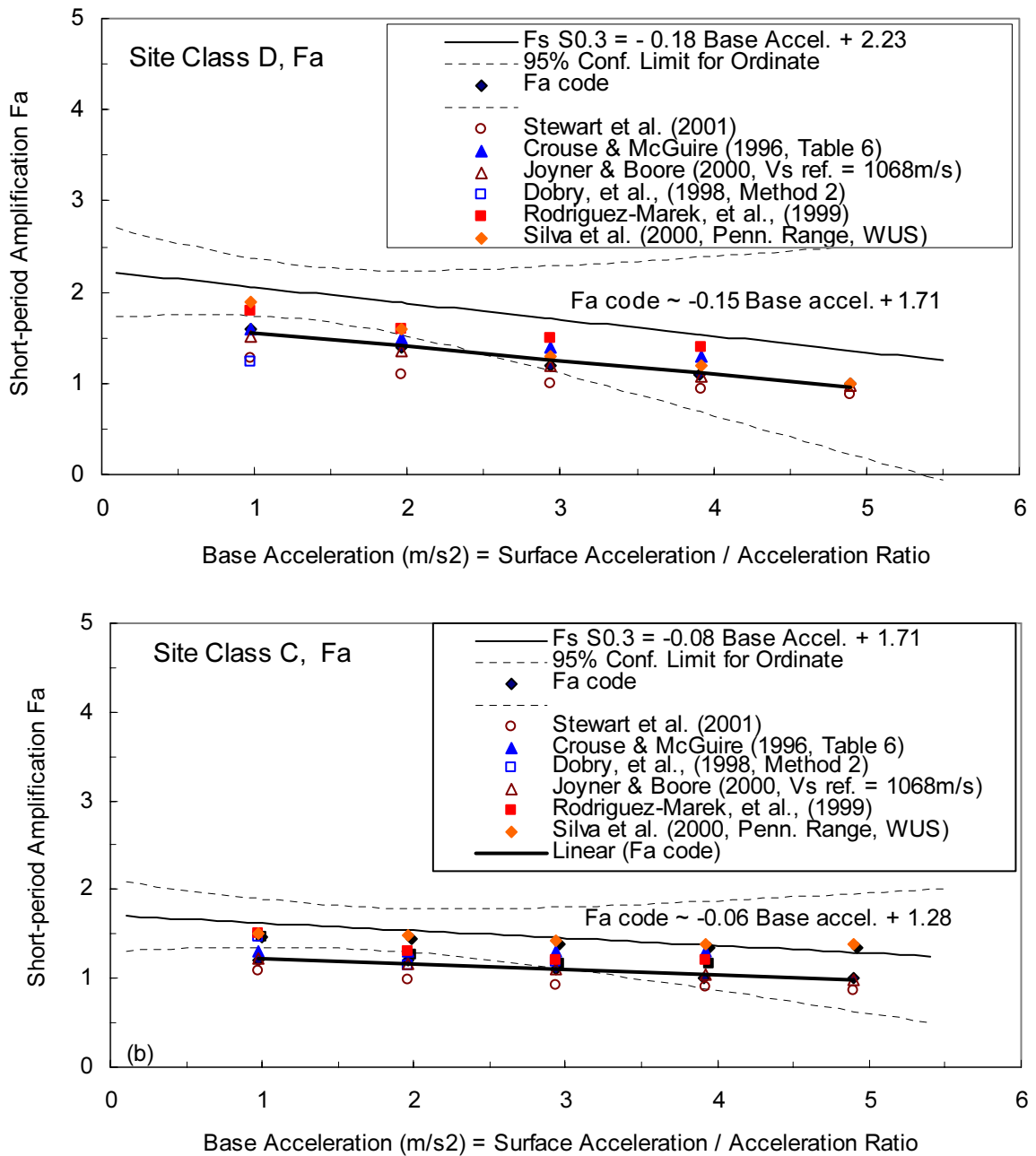


Figure 4 Estimates of site coefficient F_a for site class D (a) and C (b) sites as a function of base acceleration level and regression curves and corresponding 95 % confidence intervals for the ordinate to the true population regression line as derived from recordings of the Northridge earthquake (from Borchardt, 2002).

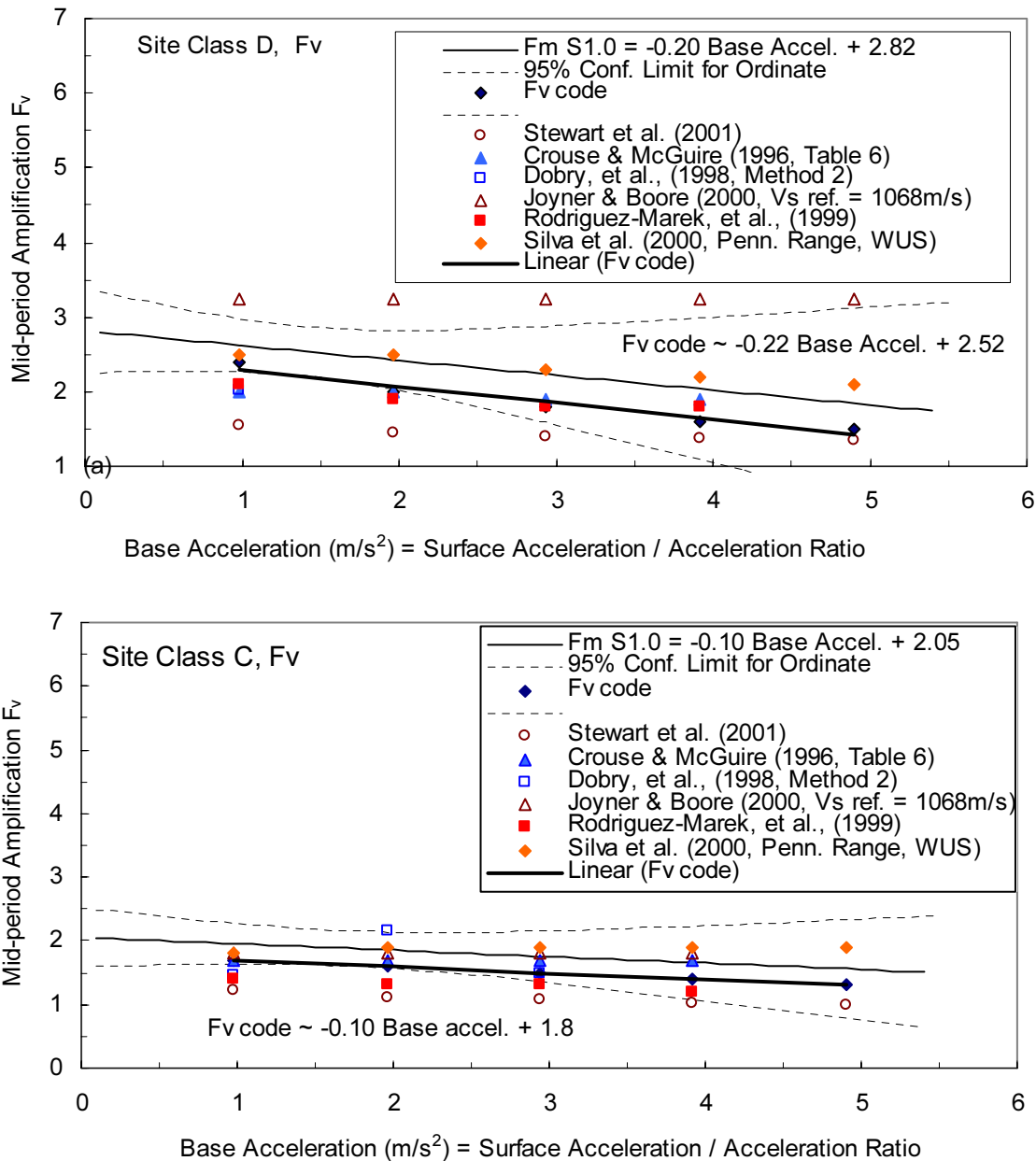


Figure 5 Estimates of site coefficient F_v for site class D (a) and C (b) sites as a function of base acceleration level and regression curves and corresponding 95 % confidence intervals for the ordinate to the true population regression line as derived from recordings of the Northridge earthquake (from Borchardt, 2002).

References:

- ASCE-7, 2003, Minimum Design Loads for Buildings and Other Structures, SEI/ASCE 7-02, *American Society of Civil Engineers*, 352p.
- Borchardt, R.D., 1994, Estimates of site-dependent response spectra for design (Methodology and Justification), *Earthquake Spectra*, **10**, 617-653.
- Borchardt, R.D., 2002, Empirical evidence for site coefficients in building-code provisions, *Earthquake Spectra*, **18**, 189-217.

- Borcherdt, R.D., 1994, Simplified site classes and empirical amplification factors for site-dependent code provisions, *Proceedings of the 1992 NCEER/SEAOC/BSSC Workshop on Site Response During Earthquakes and Seismic code Provisions*, G.R. Martin, ed., University of Southern California, Los Angeles, November 18-20, 1992, National Center for Earthquake Engineering Research Special Publication NCEER-94-SP01, Buffalo, NY, (1993, Simplified site classes and empirical amplification factors for site-dependent code provisions, in *Proceedings of International Workshop on Strong-Motion Data*, Menlo Park, CA, Port and Harbour Research Institute, S. Iai, and G Brady, eds., 1993).
- Borcherdt, R.D., and Glassmoyer, G., 1994, Influences of local geology on strong and weak ground motions in the San Francisco Bay region, California, and their implications for site-specific code provisions, in *The Loma Prieta Earthquake of October 17, 1989 – Strong Ground Motion*, R.D. Borcherdt, ed., U.S. Geological Survey Professional Paper 1551-A, A77-A108.
- Crouse, C.B., and McGuire, J.W., 1996, Site response studies for purposes of revising NEHRP Seismic Provisions, Earthquake Spectra, Earthquake Engineering Research Institute, **12**.
- Dobry, R., Borcherdt, R., Crouse, C.B., Idriss, I.M., Joyner, W.B., Martin, G.R., Power, M.S., Rinne, E.E., Seed, R.B., 2000, New Site coefficients and site classifications system used in recent building seismic code provisions, Earthquake Spectra **16**; 41-67.
- Dobry, R., Martin, G. R., Parra, E., and Bhattacharyya, A., 1994, Development of site-dependent ratios of elastic response spectra (RRS) and site categories for building seismic codes, *Proceedings of the 1992 NCEER/SEAOC/BSSC Workshop on Site Response During Earthquakes and Seismic Code Provisions*, G.R. Martin, ed., University of Southern California, Los Angeles, November 18-20, 1992, National Center for Earthquake Engineering Research Special Publication NCEER-94-SP01, Buffalo, NY.
- Dobry, R., Ramos, R., and Power, M. S., 1999, Site factors and site categories in seismic codes, *Technical Report MCEER-99-0010*, 81 pp.
- Frankel, A., Mueller, C., Barnhard, T., Perkins, D., Leyendecker, E.V., Dickman, N., Hanson, S., and Hopper, M., 1996, National Seismic Hazard Maps, June 1996, Documentation, <http://gldage.cr.usgs.gov/eq/hazmapsdoc/junecover/html>.
- International Council of Building Officials (ICBO), 2000, 2000 International Building Code, <http://www.icbo.org/>.
- Idriss, I. M., and Sun, J.I., 1992. *User 's Manual for SHAKE91*. Davis: Center for Geotechnical Modeling, Department of Civil and Environmental Engineering, University of California.
- Joyner, W.B., Fumal, T.E., and Glassmoyer, G., 1994, Empirical spectral response ratios for strong motion data from the 1989 Loma Prieta, California earthquake, *Proceedings for the 1992 NCEER/SEAOC/BSSC Workshop on Site Response During Earthquakes and Seismic Code Provisions*, G.R. Martin, ed., University of Southern California, Los Angeles, November 18-20, 1992, National Center for Earthquake Engineering Research Special Publication NCEER-94-SP01, Buffalo, NY.
- Joyner, W. B. and Boore, D. M., 2000, Recent developments in earthquake ground-motion estimation, Proc. Sixth International Conference on Seismic Zonation.
- Leyendecker, E. V., Hunt, J. R., Frankel, A. D., and Rukstales, K. S., 2000, Development of maximum considered earthquake ground motion maps, *Earthquake Spectra*, **1**, 21-40.
- NEHRP (National Earthquake Hazards Reduction Program) Recommended Provisions for Seismic Regulations for New Buildings, 1994, 1997, 2000 Ed., 1995, 1998, 2001 Federal Emergency Management Agency Reports FEMA 222A, 223A, 302, 303, 368, 369.
- Rodriguez-Marek, A., Bray, J.D., Abrahamson, N., 2001, An empirical geotechnical site response procedure, Earthquake Spectra, Earthquake Engineering Research Institute, v. 17, No. 1, p. 65-87.
- Silva, W., Darragh, R., Gregor, N., Martin, G., Abrahamson, N., and Kircher, C., 2000, Reassessment of site coefficients and near-fault factors for building code provisions, USGS EHRP program report 98-HQ-GR-1010.
- Seed, R. B. Dickenson, S.E., Rau, G.A., White, R.K., and Mok, C.M., 1994, Observations regarding seismic response analyses for soft and deep clay sites, *Proceedings of the 1992 NCEER/SEAOC/BSSC Workshop on Site Response During Earthquakes and Seismic Code Provisions*, G.R. Martin, ed., University of Southern California, Los Angeles, November 18-20, 1992, National Center for Earthquake Engineering Research Special Publication NCEER-94-SP01, Buffalo, NY.
- Stewart, J.P., Liu, A.H., Choi, Y., and Baturay, M.B., 2001, Amplification factors for spectral acceleration in active regions, Pacific Earthquake Engineering Research Center, PEER Report 2001/10.

FRACTURE IN STEEL BRIDGE PIERS DUE TO EARTHQUAKES

C. Miki¹⁾ and E. Sasaki²⁾

1) Professor, Department of Civil Engineering, Tokyo Institute of Technology, Japan

2) Research Associate, Department of Civil Engineering, Tokyo Institute of Technology, Japan

miki@cv.titech.ac.jp, esasaki@cv.titech.ac.jp

Abstract: The great Hanshin Earthquake of January 17, 1995 caused serious damage to various civil structures never before experienced. A particular emphasis is placed on the fracture in steel bridge piers, and the results of studies up to date are reviewed in this paper.

1. INTRODUCTION

During the Great Hanshin Earthquake of January 17, 1995, steel bridge structures suffered damage of various kinds never before experienced. They were collapse, buckling, fracture and cracking. All of these accidents were far more severe than contemplated in the conventional seismic design method and might essentially invalidate historical seismic design approaches and code provisions.

Steel bridge piers have been adopted to support elevated highways and over pass bridges. Particularly, the piers of expressway in urban areas are in the median strip zones or sidewalk zones of streets because these are placed on the existing streets and piers (Figure 1). There are more than 5000 piers including 2000 piers in Tokyo Metropolitan Expressway and some of these are decrepit. Fracture accidents in these structures during earthquakes may cause not only the service failure of expressways supported by these piers but also a muddle on streets underneath the expressway.



Figure 1 Existing Steel Bridge Piers

2. COLLAPSE

2.1 Cases of Steel Bridge Pier Shafts

These were the steel bridge pier shafts at Iwaya Viaduct (Figure 2) on the national highway No.43 and Tateishi Viaduct on the Hanshin Expressway. According to the report of the investigation committee, the damage mechanism of the pier shaft at Iwaya Viaduct is “estimated to have been due to

the occurrence of local buckling deformation of panels between diaphragms including splice plates, as deformation grew larger so that corner welds at this parts began to be torn, and load bearing capacity for supporting vertical force became lost and the collapse occurred directly below in the end.” This means that the cause was breaking of vertical stiffeners at field-joints with high strength bolts, but according to normal thinking in design, vertical stiffeners need not made continuous at this detail. However, the sudden change in rigidity due to the stiffeners being broken, and the stress concentrations at stiffener ends may be said to be cases showing that they can be causes of failure.

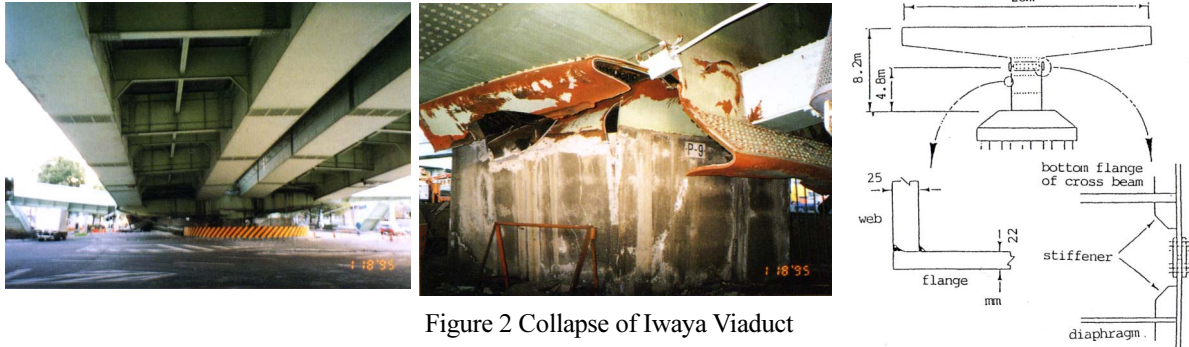


Figure 2 Collapse of Iwaya Viaduct

Corner welds are so-called stitch welds which are for the purpose of assembling members but do not expect loads to be transmitted. Therefore, these corner welds are composed of partial penetration welds and internal fillet welds except in the region of beam-to-column connections. It is conceivable that if the joints had been strong, it could not have led to such collapse. By making these corner welds as full penetration welds, it is possible for the strength to be increased more than the strength with the partial penetration welds and fillet welds detail actually used here. However, what is of importance is that in failure of corner welds this time either the insufficiency of weld size or the root faces as incomplete penetration zone remaining due to partial penetration was involved as cracks.

2.2 Large Size Column Tests (PWRI et-al, 1999)

Figure 3 shows the some of specimens in the cooperative study under the Public Works Research Institute. In order to improve the seismic performance of steel bridge piers and develop retrofitting methods for existing structures, 99 large size column type specimens were tested in total under incremental repeating loads and hybrid response loads.

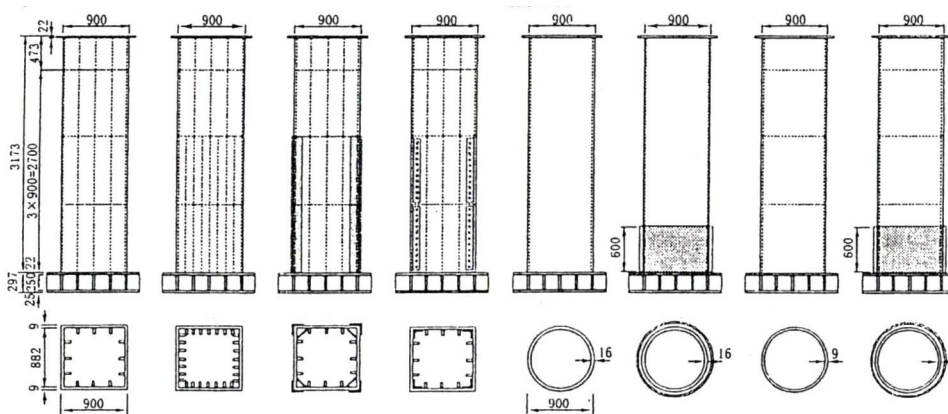
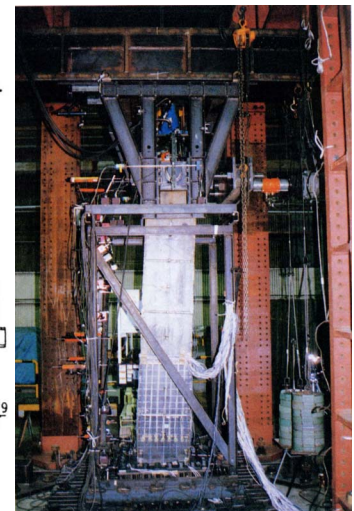


Figure 3 Specimens of Steel Bridge Piers



The followings are the objectives of this series of test specimens.

(a) Piers with rectangular columns

- *add corner plates at the four corners of the column by welds or high strength bolts
- *fill concrete inside of the column as a retrofitting work.
- *lower the width-thickness ratio of stiffened plates,

practically, increasing the number of stiffeners on flange plates and web plates of column.

(b) Piers with cylindrical pier shafts

*fill concrete inside of the column shaft as a retrofitting work

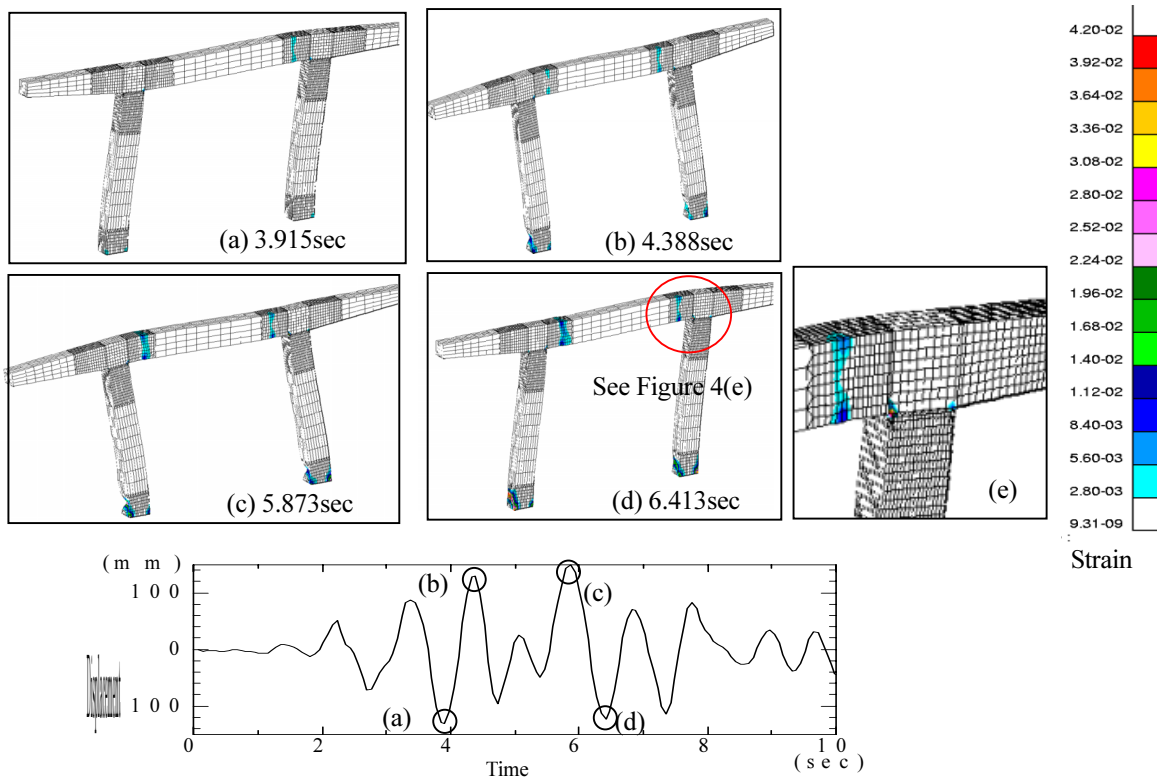
*cover the column shaft by a steel plate with narrow space

Based on these test results, the design specifications of highway bridges were revised (Japan Road Association, 1998). In order to insure adequate deformation capacity, to avoid collapse as brittle fracture mode including tearing of corner welds, and to satisfy the limitation of remaining deflection, provisions of structural details have been established. As the retrofitting works, the concrete fill method and corner plate addition method were adopted and applied to many actual piers. The result of dynamic response analysis is used to decide the necessity of retrofit and suitable retrofit method.

2.3 Seismic Performance as Rigid Frame of Thin Walled Members

In order to clarify the dynamic behaviors of steel bridge bents during earthquakes, the dynamic elasto-plastic FEM analysis was conducted. Some of actual steel bridge bents with general dimensions were chosen, and were modeled with shell elements for all the structural details including ribs and diaphragms. The measured acceleration data in the Kobe Great Earthquake were used in the analyses.

Figure 4 shows the representative result of the FEM analyses. In Figure 4, the time history of the displacement at the center of the beam upper flange was shown representatively, and the change of the deformations and the distributions of plastic equivalent strain were presented. As seen in the Figure 4, at two portions in the beam close to the beam-to-column connections, large plastic strain due to local buckling was occurred locally. Actually, the portions are just at the locations where the connections are there and the thickness of the plates is drastically changed. Especially, large plastic strain occurs at the corner joints of the beam. In contract, in the beam-to-column connections, no buckling occurs because of the large plate thickness due to the consideration in the elastic design of the local stress concentration by the shear-lag phenomenon. However, it should be noted that at the corner of the beam-to-column connections, large plastic strain occurs locally as shown in Figure 4(e) and that the local strain concentration can be one of the main causes of brittle fracture during earthquakes.



Time History of the Horizontal Displacement at the Center of the Beam
 Figure 4 Dynamic FEM Analysis Results of A Steel Bridge Bent (JR Takatori Wave)

3. BRITTLE FRACTURE

3.1 Cracking in the Connection Corner of Steel Rigid Frame Bridge Pier (K. Okashita, C. Miki et-al, 1998)

One of the important events of the Great Hanshin Earthquake was the occurrences of brittle fractures in steel bridge structures. A brittle fracture accident during the earthquake occurred in one of the steel rigid frame bridge piers called P75 in the Harbor Highway (Figure 5). Cracks started from the lower corner of the beam and the column shaft, and ran through almost the entire cross section of shafts. The Chevron pattern on the failure surface indicated that the cracks started at the west-north corner of shafts and propagated into both the north flange and the west web plate.

Detailed observations at the crack originated portion revealed that the cracks started from the unwelded-zone at the corner of column-beam connection, so-called delta-zone (see 3.3). There were two origins of crack, one was the toe of fillet weld on the north flange which was the origin of cracks propagated into the flange plate and another was just inside of fillet weld end on the web plate which was the origin of cracks in the web plate. The observations of fractographs indicated dimple patterns were remained in these areas and the sizes of these were about 0.7mm and 0.4mm. Outsidess of these areas are typical brittle fracture surfaces.

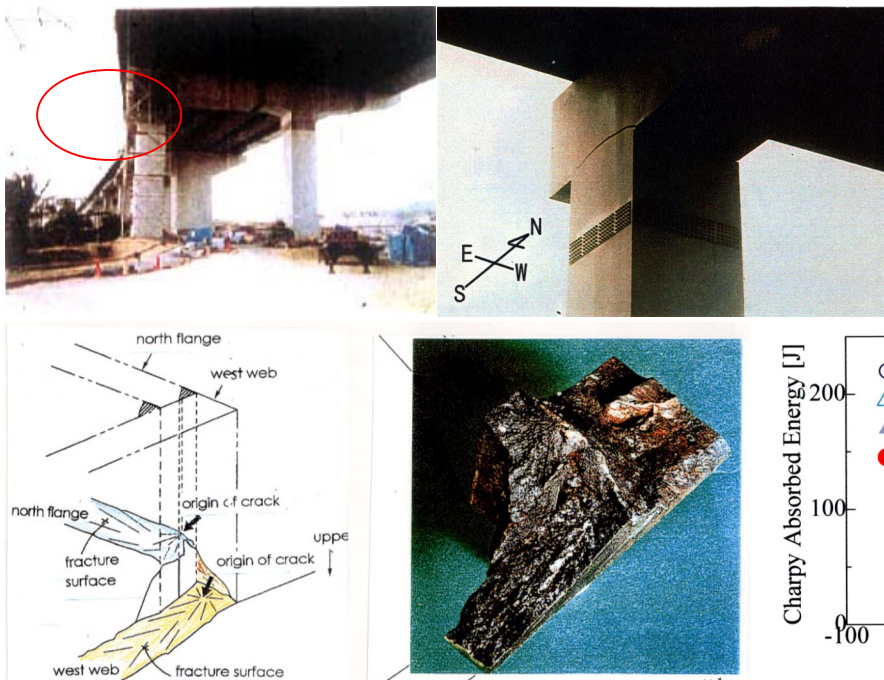


Figure 5 Brittle Fracture in P75 Rigid Frame Pier

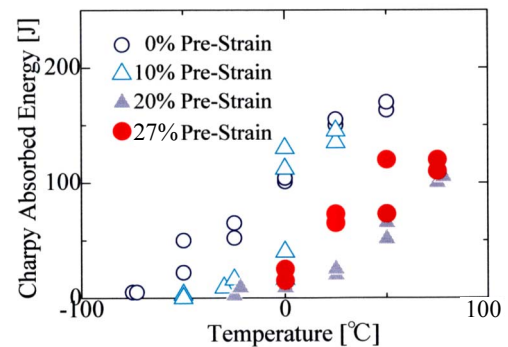


Figure 6 Results of Charpy Impact Tests

3.2 Fracture Toughness Properties of the Steel Used in Damaged Pier

In the vicinity of the corner, paint films were removed and a slight out-of-plane deformation due to local buckling was observed. The local buckling occurred at the welded joint where the plate thickness changed from original 19mm to about 17.4mm. The results of hardness tests indicated that plastic strain of about 20% to 30% occurred in these plates during the earthquake.

The used steels of this structure are SMA41 (SMA400). The tensile properties and the chemical composition satisfy the JIS requirements. Figure 6 shows the results of Charpy impact tests. Specimens were from the south flange plate of the shafts. In order to examine the deterioration of notch toughness due to plastic strain experience, specimens with pre-strain of 10%, 20% and 27% were tested beside as cut-out specimens. These test results indicate that notch toughness decrease significantly with increasing the experience of plastic strain.

Some more detailed investigations of the cause are necessary, but we can say that this brittle

fracture was the result of large plastic deformations at the corner due to shear lag during the earthquake and the deterioration of fracture toughness due to plastic strain. The large unwelded zone “delta zone” existed at the high stress region and the small weld defects acted the origin of brittle cracks.

3.3 Existence of “Delta Zone” at the Corner of Bridge Bent (C. Miki et-al, 2003)

The steel bridge rigid frame structures consist of box section or cylindrical column shafts and box section beams, all of these members are welded closed sections. Figure 7 shows the details of plate assembling of beams and columns. The structural details are roughly classified into two types, one is column pass type and another is beam pass type (Figure 7(a), (b)). However, plate assembling system are more various and complicated.

Detailed investigations of fatigue damaged piers in Tokyo Metropolitan Expressway revealed that un-welded cavities and metal-touch zones existed at the corner of beam to column connections. In most cases, these are kind of inherent defects coming from plate assembling system, poor accessibility and improvident welding sequences. Figure 7(c) and (d) show the remaining of delta zones in two different column pass type plate assembling methods. We call these inherent defects as “delta zones”. The delta zone is the dominant cause of fatigue cracks in many steel bridge piers and also may lead to brittle fractures in the case of suffering strong earthquakes. The combination of existences of delta zones and fatigue cracks more increases the possibility of the occurrence of brittle fracture.

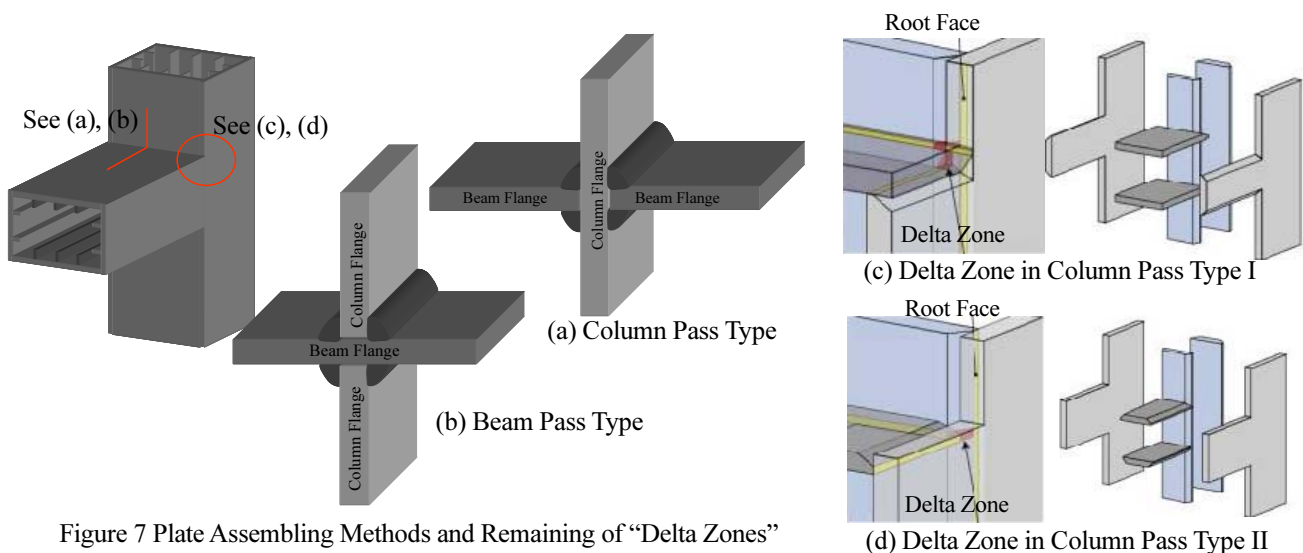


Figure 7 Plate Assembling Methods and Remaining of “Delta Zones”

4. LANTERN BUCKLING AND CRACKING

4.1 Cases in Cylindrical Steel Pier Shafts

In cylindrical steel bridge pier shafts on the Kobe route of Hanshin Expressway, there were cases where plastic deformation occurred and the wall of pier shafts bulged outward, so-called “lantern buckling”(Figure 8). The sections where lantern buckling occurred were close to the welded joints where the plate thickness was changed. Once these buckling incidents occurred, the load bearing capacity for supporting vertical forces became lost significantly.

Brittle fractures also occurred along the outward plastic deformation in two consecutive pier shafts. One of the pier shafts had exhibited large plastic deformation outward but the plastic deformation was not so large in another pier shafts. The crack seemed to start from the inside of shaft wall.

4.2 Deterioration of Fracture Toughness due to Lantern Buckling

Figure 9 shows the plate cut out from one pier which was suffered lantern buckling. Various

material tests were performed on specimens made from this plate. Figure 10 shows estimated plastic strain in the plates from buckled zone and unbuckled zone. The plastic strain on the inner surface of column wall is over 20%. This plastic strain caused deterioration of toughness of the plate, called embrittlement, as shown in Figure 11. Embrittlement due to plastic strain, particularly compressive strain becomes new problem for us to prevent the fatal condition of bridge piers.

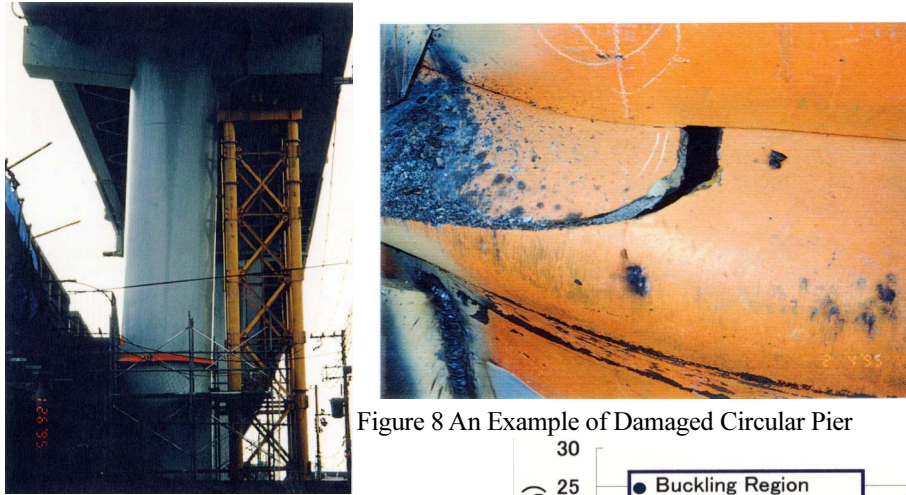


Figure 8 An Example of Damaged Circular Pier

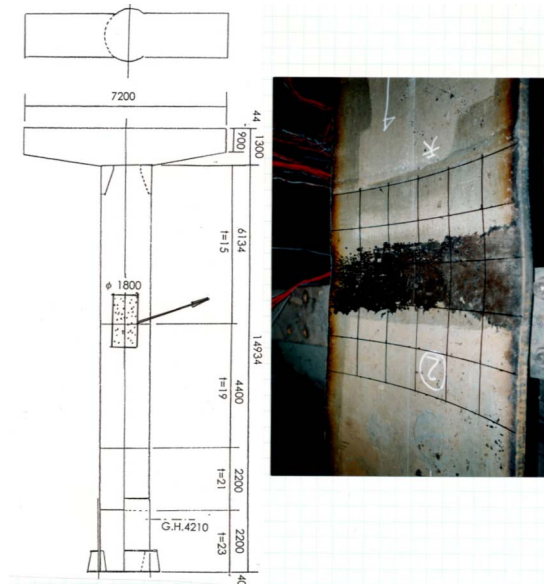


Figure 8 The Steel Plate Cut from the Damaged Pier

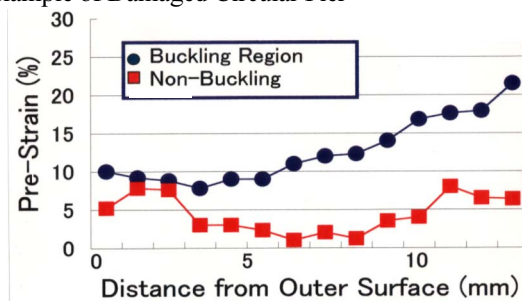


Figure 10 The plastic strain distribution in the plate thickness

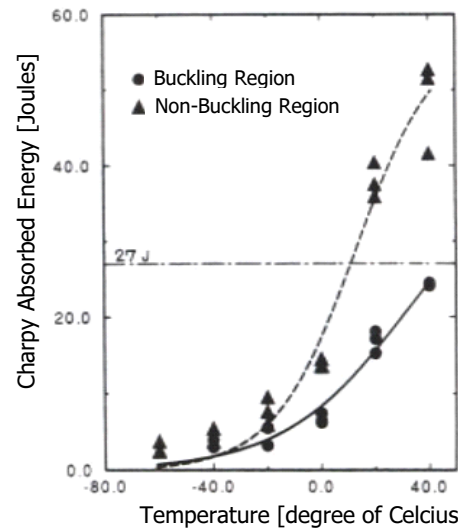


Figure 11 The Charpy impact test results of the steel plate

5. HISTORICAL REVIEW OF STRUCTURAL STEELS

JIS structural steels SM41 (SM400) and SM58 (SM570) have been commonly used for steel bridge piers from the middle of 1960s. Tensile properties of each of the steels have been the same level. However, various innovative technologies in steel making process including TMCP, continuous casting and removal of gases have been improving the performance of steels including notch toughness and weldability.

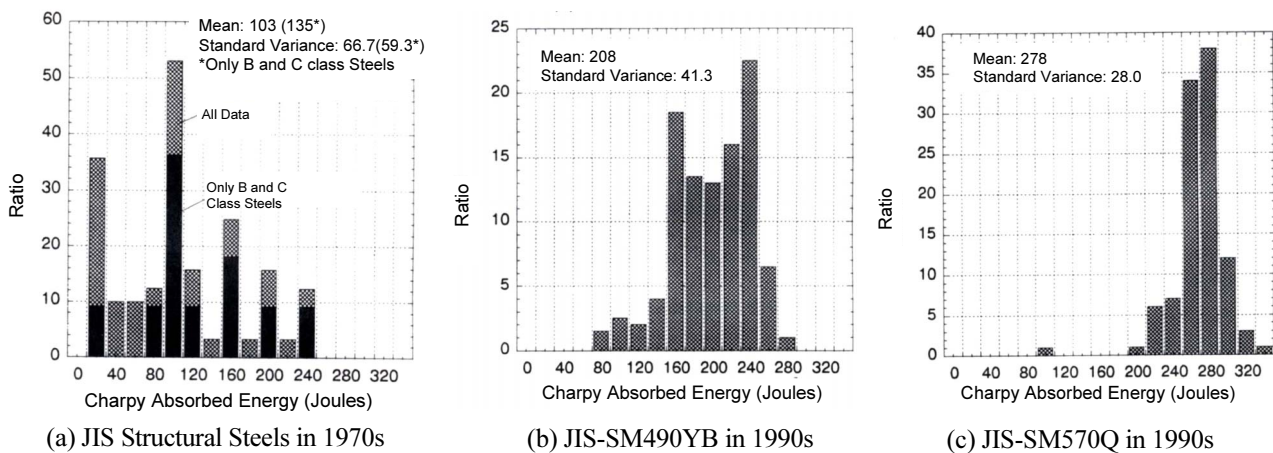


Figure 12 Distribution of Charpy Absorbed Energy of Steels Produced in 1970s and in 1990s

Figure 12 shows the results of Charpy impact tests in 1970s and 1990s. The notch toughness property of steels was significantly improved (K. Honma, C. Miki et-al, 1997). We also have to recognize that the fracture toughness of old steels is low in some cases.

Figure 13 shows the transition of capability for removing sulfur (S) from steels. All of steel making factories of the 5 major Japanese steel companies started to produce low S content steels since the middle of 1970s and the content of S in the recent steels is around 0.005%. However, the content of S in steels which were produced before the middle of 1970s might be over 0.01%. The high content of S leads to poor weldability and the occurrence of lamellar tearing in welded joints. In order to prevent the occurrence of lamellar tearing (Figure 14), the reduction of area in the plate thickness direction tensile tests (RAZ) have to be greater than 35%, and the content of S has to be less than 0.005%. That is to say, there is high risk of lamellar tearing in piers which were constructed before 1975. There are about 2000 steel bridge piers only in the Tokyo Metropolitan Expressway System and a half of them were constructed before 1975. We have to pay careful attention to the prevention of lamellar tearing in the retrofiting works against fatigue and earthquakes.

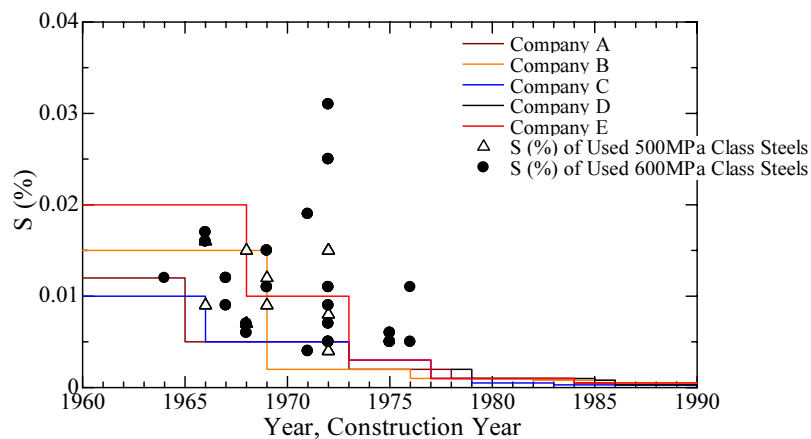


Figure 13 History of Sulfur Inclusion in Steels

4. CLOSING REMARKS

Since the Great Hanshin Earthquake, retrofiting of existing bridge structures has been recognized as urgent issues beside the improvements in the design of new structures. The ascertainment of the causes of experienced fracture accidents is essential to establish appropriate retrofit measures.

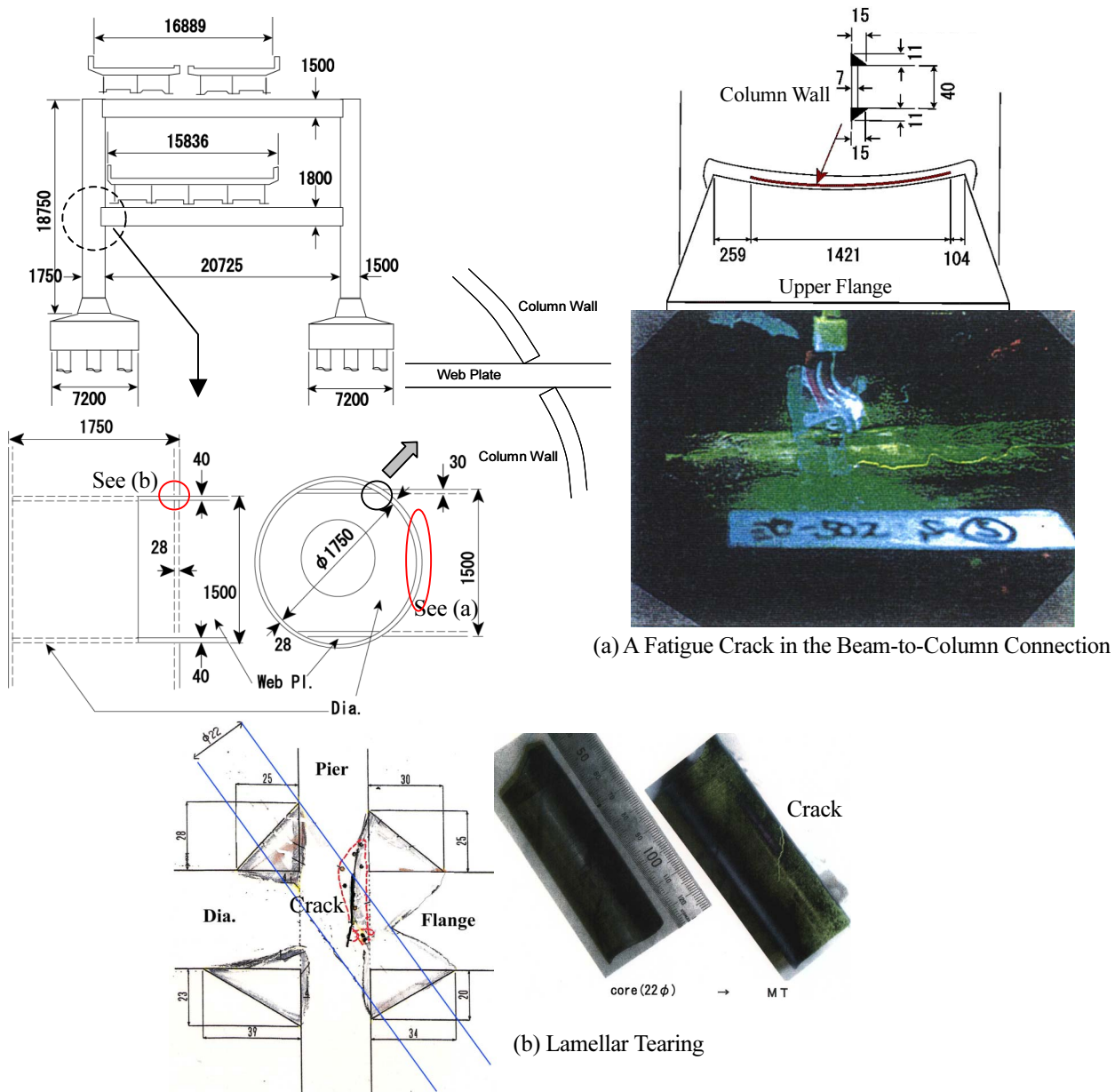


Figure 14 The Fatigue Crack and Lamellar Tearing during Retrofitting Works by Welding in a Steel Bridge Pier

The primary reason of damage is very strong ground motions never before experienced. Apart from this, many factors contributed to the damage such as material properties, structural systems, details, and qualities of structural elements. It is also important to evaluate structural responses due to earthquakes such as forces, displacements, stresses, and strains. It can be said that the cause has been ascertained only when the results of examinations from the external disturbance side and the structural resistance side have come together without contradiction.

References:

PWRI et-al (1999), Summary of the Cooperation Research on the Seismic Limit State Design of Highway Bridge Piers.
 Japan Road Association (1998), Design Specifications of Highway Bridges, Part V, Seismic Design.
 K. Okashita, C. Miki et-al (1998), "Investigation of the Brittle Fracture at the Corner of P75 Rigid Frame Pier in Kobe Harbor Highway during the Hyogoken Nanbu Earthquake", Proc. of JSCE, **I-43**, 243-261.
 C. Miki et-al (2003), "Beam-Column Connection Details of Steel Pier and Their Fatigue Damage Mode", Proc. of JSCE, **I-65**, 105-119.
 K. Honma, C. Miki et-al (1997), "A Study on Strain Aging of Cold Worked Structural Steel and Allowable Cold Forming Radius", Proc. of JSCE, **I-40**, 153-162.

REQUIRED FRACTURE TOUGHNESS OF STEELS TO PREVENT BRITTLE FRACTURE DURING EARTHQUAKES IN STEEL BRIDGE PIERS

E. Sasaki¹⁾ and C. Miki²⁾

1) Research Associate, Dept. of Civil Engineering, Tokyo Institute of Technology, Japan

2) Professor, Dept. of Civil Engineering, Tokyo Institute of Technology, Japan

esasaki@cv.titech.ac.jp, miki@cv.titech.ac.jp

Abstract: During the 1995 Hyogo-ken nanbu earthquake in Japan, brittle cracking accidents were occurred in several steel bridge piers. From the investigations on the cracked structures, deterioration of fracture toughness of steel by the effect of large plastic strain is considered as the dominate cause. This study is aiming to determine the required fracture toughness to prevent brittle fracture during earthquakes in steel bridge piers by discussing on the following objectives. 1) To identify the characteristics of strain history during large earthquakes in steel bridge piers by dynamic FEM analysis, and based on that, 2) to determine patterns of strain history that should be considered by discussing the process of the occurrence of brittle fracture, and 3) to evaluate the extent of deterioration of fracture toughness of steel by various patterns of large plastic strain including reversed patterns by CTOD tests.

1. INTRODUCTION

During the 1995 Hyogo-ken nanbu earthquake in Japan, many civil structures were damaged and also in steel bridge piers. Brittle cracking accidents were occurred in some steel bridge piers (JSCE 1995), which were the first experience in steel bridge piers. Figure 1 shows the cracks occurred during the earthquake. Many investigations have been conducted to prevent local buckling from the viewpoint of structural details and to ensure high ductility of steel columns, and the limitation of the parameters like width-thickness ratio have been suggested for design of new steel piers (T. Usami et al 1995). Also, some investigations (C. Miki et al 1998, 1999, 2000, I. Okura et al 1996, JWES 1999) on the prevention against brittle fracture accidents in bridge piers were conducted and concluded that deterioration of fracture toughness of steel due to effect of introduced large plastic prestrain could be considered as the main cause of brittle fracture. Therefore, in order to prevent brittle fracture, it is necessary to use the steels that have enough fracture toughness even after plastic prestrain experience. However, the required level of fracture toughness of the steel to prevent brittle fracture during earthquakes in steel bridge piers has not been clear until so far. This study is aiming to determine it, and so the followings were considered as the objectives.

- 1) To identify the characteristics of plastic strain history during earthquakes in steel bridge piers and to determine the patterns of strain history that should be considered by discussing the process of the occurrence of brittle fracture.
- 2) To evaluate the extent of deterioration of fracture toughness of steel by various patterns of plastic prestrain.

Finally, the discussions for suggesting the required fracture toughness of steel to prevent brittle fracture were made by organizing all the results of fracture toughness tests.

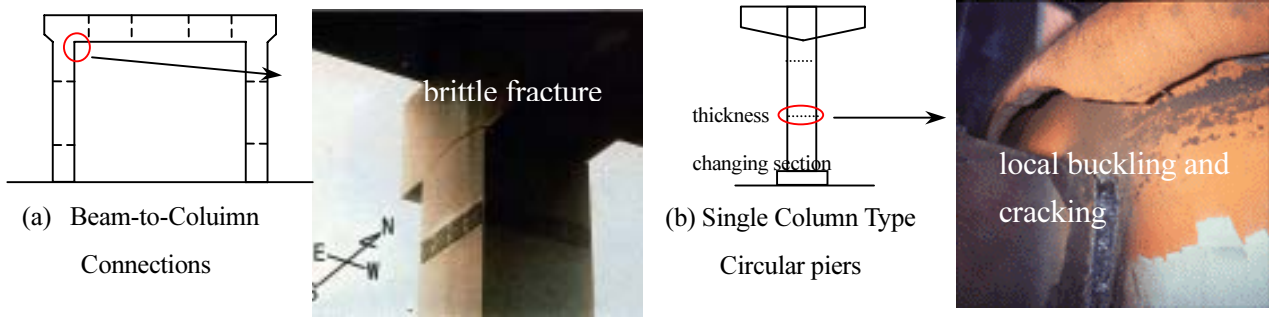


Figure 1 Cracks occurred in Steel Bridge Piers during the Kobe Great Earthquake

2. CHARACTERISTICS OF THE STRAIN HISTORY DURING EARTHQUAKES IN STEEL BRIDGE PIERS

In order to identify the characteristics of strain history during large earthquakes in steel bridge piers, elasto-plastic dynamic FEM analyses on typical bridge pier structures were carried out. Figure 2 shows the shape and size of the target pier and the FEM mesh of the model. The FEM model was built by half model by assuming symmetry in the direction of out-plane of the frame. The smallest mesh size is around 5mm that is nearly equal to one third of the plate thickness. The steel bridge pier considered here was designed by modifying the parameters of the used stiffened plates of an existing bridge pier according to the limitation for new structures (T. Usami et al 1995). The limitation of the width-thickness ratio of plate elements has been suggested to ensure superior ductility up to the specific displacement level δ_{95} beyond δ_{max} . δ_{95} is the displacement at which the strength decreases up to 95% of the maximum strength P_{max} (at the displacement δ_{max}). Recently, the displacement level of δ_{95} has been considered as the level to verify seismic performance of steel bridge piers. In this study, also, δ_{95} was taken into consideration as the limit level to ensure the prevention of brittle fracture. Therefore, the strain history during large earthquakes and the strain level at δ_{95} are mentioned here.

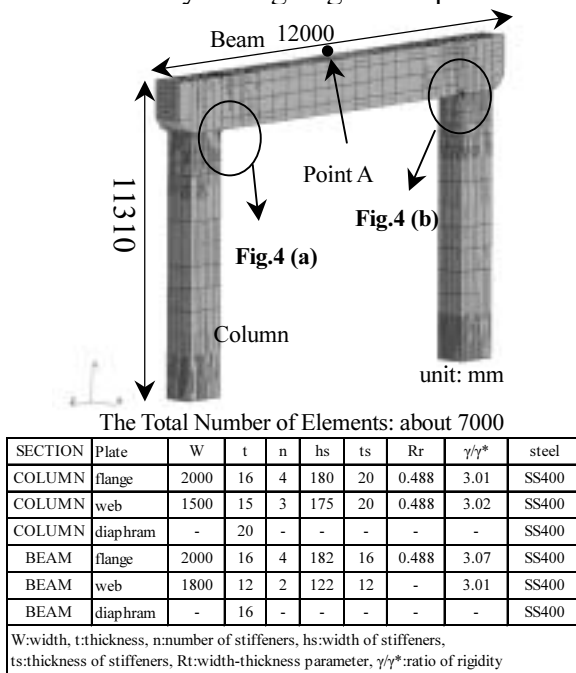


Figure 2 The FEM model of the target steel bridge pier

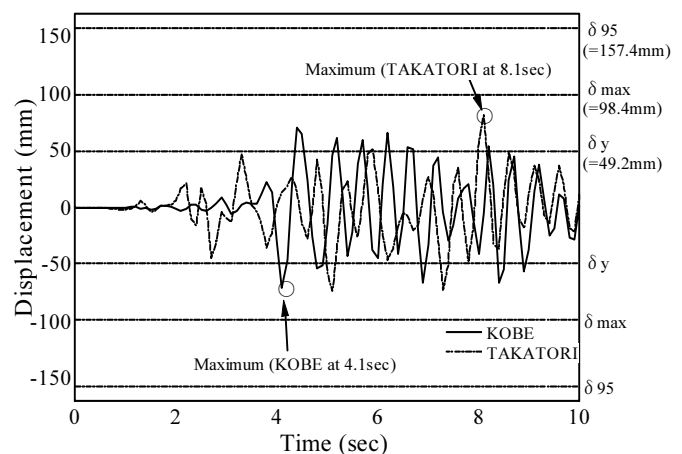


Figure 3 Displacement History at the center of the beam (Point A in Figure 2)

The seismic acceleration waves measured at JR Takatori station and at Kobe Marine Observatory in Hyogo-ken nanbu earthquake were used in the analyses. Figure 3 shows the displacement history at the center of the beam. The values of the yield displacement δ_y and δ_{95} in Figure 3 were obtained by the analyses of cyclic static loading under displacement control at point A. Figure 4 illustrates the strain history in direction of component axis near the corner of beam-to-column connections. In both of the cases of Takatori and Kobe, the maximum displacement was in the level over δ_y and the maximum value of strain during the earthquake was observed at that portion and reached almost 10%. And it can be found that the strain history has the tendency to be one-sided to the region of tension or compression and vary in that region. Finally, according to our previous experimental study (E. Sasaki et al 2001), the measured maximum strain at δ_{95} near the corner of beam-to-column connections reached less than 10%.

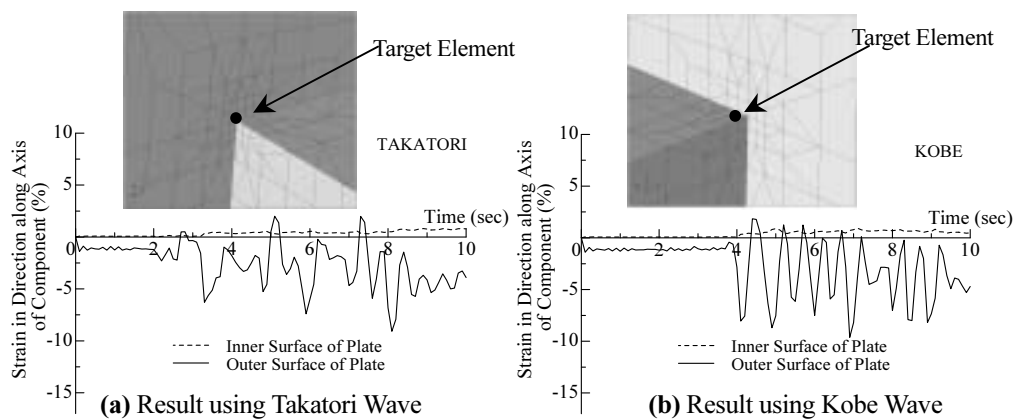


Figure 4 Strain History

3. SCENARIOS OF BRITTLE FRACTURE DURING EARTHQUAKES

As the scenarios of brittle fracture during earthquakes, the following four types shown in Figure 5 were considered. In case of Type I, cracks will be occurred by large compressive plastic strain, for example, in the compressive side of local buckling zone (H. Inoue et al 1986). The size of the cracks is small. In case of Type II, cracks are occurred by tensile strain and the following compressive strain makes them sharp. The cracks in Type III and IV occur by fatigue induced by live load like traffic load. Actually, many fatigue cracks were found in steel bents recently (H. Morikawa et al 2002). The deterioration of steels due to plastic strain history, initial cracks and their size and sharpness become our interests.

4. DETERIORATION OF FRACTURE TOUGHNESS OF STEELS BY LARGE PLASTIC PRESTRAIN

The used structural steels were JIS-SM490YB and JIS-SM570Q. They have been commonly used in construction of steel bridge piers. The chemical composition and the mechanical properties of them are shown in Table 1 and Table 2, respectively. Various patterns of plastic prestrain shown in Table 3 were considered and the effects of them on the fracture toughness of steels were evaluated by CTOD

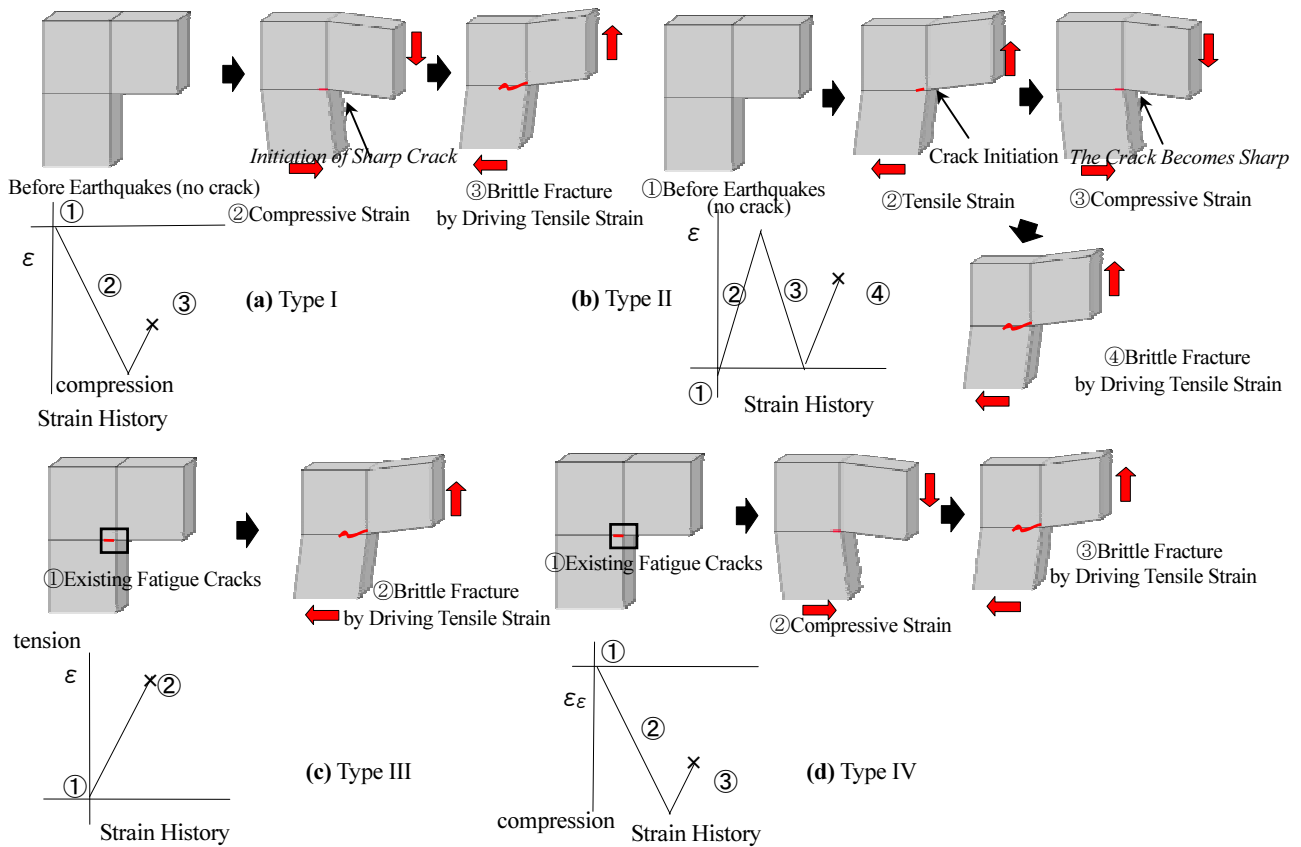


Figure 5 Scenarios of Brittle Fracture

Table 1 Chemical Compositions

Steel	C	Si	Mn	P	S	Cu	Ni	Cr	V
JIS-SM490YB	0.14	0.46	1.56	0.02	0.005	0.01	0.01	0.02	0.04
JIS-SM570Q	0.14	0.23	0.012	0.005	0.005				

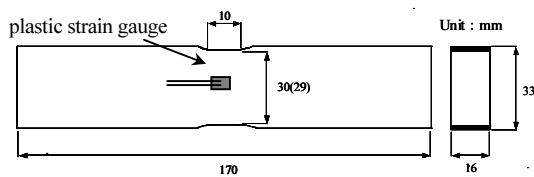
Table 2 Mechanical Properties

Steel	Y.P. (MPa)	T.S. (MPa)	Elongation (%)	CVN (Joul)
JIS-SM490YB	407	547	26	154 (0°C)
JIS-SM570Q	560	651	39	299(-5°C)

Table 3 Patterns of Plastic Prestrain

Pattern	Prestrain	Comment
AP0, BP0	0%	no prestrain
AP1, BP1	+10%	uniform tensile prestrain (10%)
AP2, BP2	-10%	uniform compressive prestrain (10%)
AP3, BP3	+10%	cyclic prestrain in tensile region (10%)
AP4, BP4	-10%	cyclic prestrain in compressive region (10%)
AP5, BP5	-5%	uniform compressive prestrain (5%)
AP6, BP6	+5%	cyclic prestrain in tensile region (5%)

*The initial letter of the pattern name shows type of steel.
(A: JIS-SM490YB, B: JIS-SM570Q)



The value closed by parenthesis is concerned with SM570Q

Figure 6 The Specimen for Introducing of Prestrain

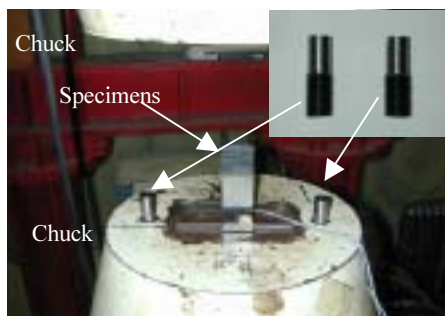


Photo 1 The Fixtures to Prevent Slips Between the Chucks

tests. As the levels of prestrain, two levels of 10% and 5% were taken into consideration because reversed patterns of prestrain up to 10% level could be introduced in this study. In order to introduce all the prestrain patterns, the specimens shown in Figure 6 were used to make deformation concentrated at the center. Furthermore, it was needed to invent the fixtures for the direction guides for the chucks in the testing machine shown in Photo 1 to prevent the local buckling of specimens in compressing processes. After the introducing plastic prestrain, bar specimens for tensile tests (Figure 7) and CTOD specimens (Figure 8) were cut from the specimens as shown in Figure 9.

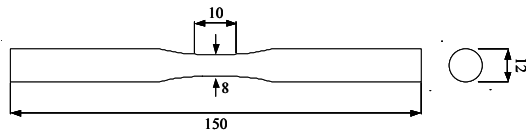


Figure 7 Bar Specimen For Tensile Test

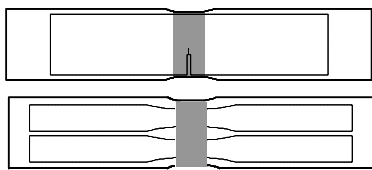
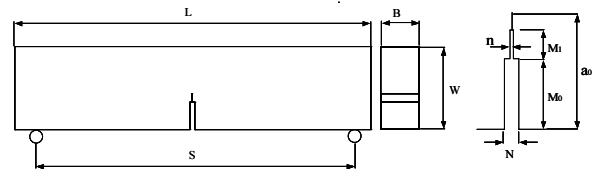


Figure 9 Cutting Techniques



Unit: mm									
B	W	S	L	a ₀	n	N	M ₁	M ₂	M ₀
14.0	28.0	112.0	126.0	0.5W	0.15	1.8	9.0	3.0	

Figure 8 CTOD Specimen

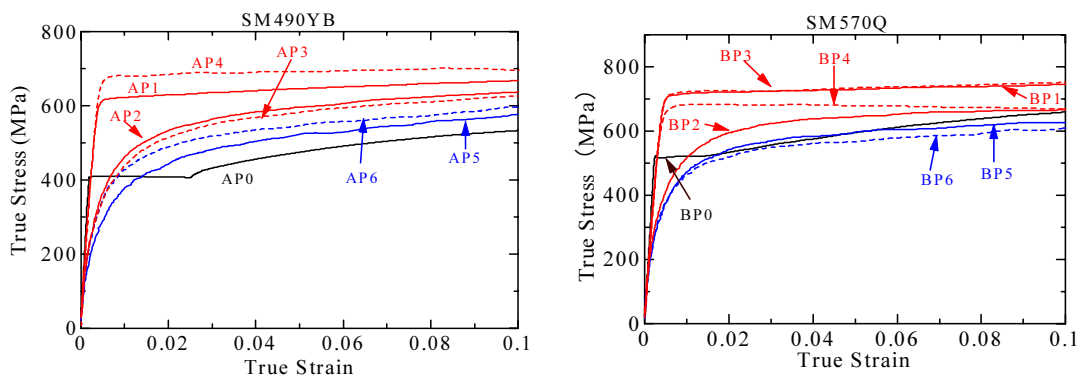


Figure 10 Stress-Strain Relationship

Figure 10 shows the stress-strain relationship after introduction of prestrain for both of the steels. The stress-strain relationship changed by the effect of the prestrain, and so the yield point also varied with the patterns of prestrain.

Figure 11 shows the relationship between test temperature and critical CTOD values. The significant and characteristic deterioration behaviors of the two types of steels were demonstrated. On SM490YB steel, the patterns of prestrain in compression region and the reversed patterns caused more deterioration of fracture toughness than those in tensile region and the uniform patterns, respectively. Also, the difference of the level of prestrain, the extent of deterioration of fracture toughness in case of 10% is larger than that in case of 5%. However, in SM570Q steel, no remarkable changes of fracture toughness were observed in most patterns of prestrain, and only in case of uniform compressive, much deterioration of fracture toughness occurred. From these results, among the patterns showed in the process of brittle fracture, uniform compressive prestrain can be considered as the critical pattern to fracture toughness of steel. As mentioned here, the extent of deterioration of fracture toughness depends on the types of steel and the patterns of prestrain.

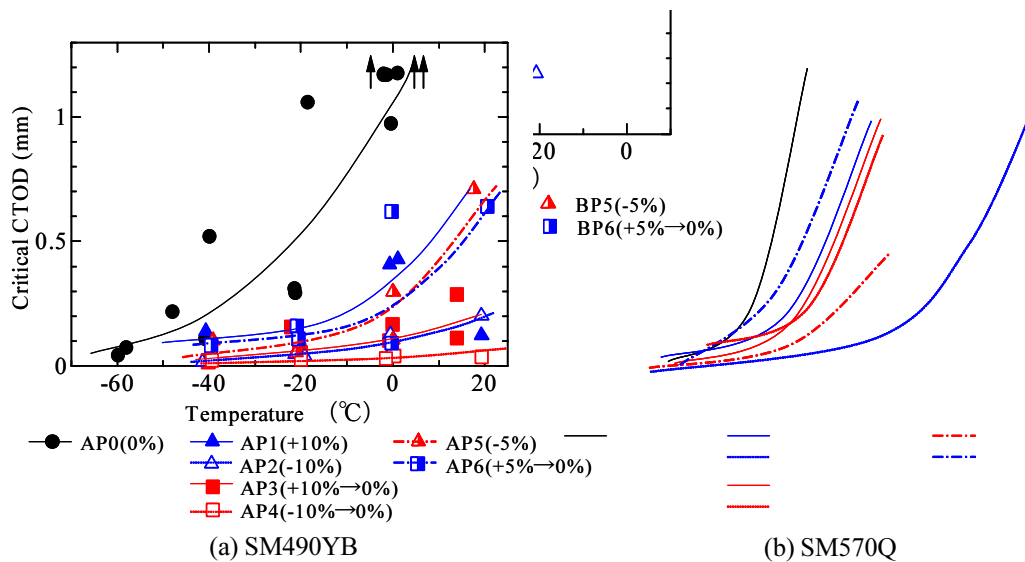


Figure 11 The Critical CTOD Curves

5. DISCUSSIONS ON THE REQUIRED FRACTURE TOUGHNESS TO PREVENT BRITTLE FRACTURE

Figure 12 shows the relationship between prestrain and the amount of temperature shift of CTOD curves by the prestrain. Figure 12 includes all the results for the various types of steel including the results of this study and our previous studies [2]. The temperature shift was defined at the critical CTOD value of 0.1mm and it shows quantitatively how much extent of deterioration of fracture toughness occurred. The results of the reversed patterns of prestrain were plotted on the same position in the value of prestrain. Let us consider 10% level of prestrain corresponding to the displacement level δ_{95} . In Figure 12, it can be found that the temperature shift reaches at most 50 degrees of Celsius in 10% level of prestrains with considering all kinds of steels. For that reason, it can be said that in order to prevent brittle fracture in steel bridge piers up to the displacement level δ_{95} , the used steel has to have enough fracture toughness even after the temperature shift of 50 degrees of Celsius.

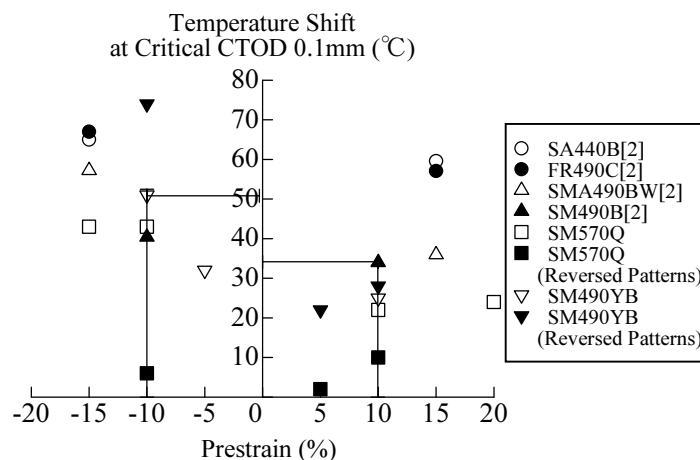


Figure 12 Relationship between Prestrain and Temperature Shift of CTOD Curves

6. CONCLUSIONS

The conclusions of this study can be summarized as follows.

- 1) By the elasto-plastic dynamic FEM analysis, the strain histories in steel bridge piers during large earthquakes were investigated. The strain histories have the tendency of being one-sided to the region of tension or compression and varying in that region.
- 2) The plastic strain patterns that should be considered were explained by discussing the processes of brittle fracture, and the effects of the various patterns of plastic prestrain including them on fracture toughness of steels were investigated by CTOD tests. The extent of deterioration of fracture toughness depends on the types of steel and the patterns of prestrain. On SM490YB steel, compressive prestrain and reversed prestrain make fracture toughness more deteriorated than tensile prestrain and uniform prestrain, respectively, and the deterioration of fracture toughness by prestrain in 10% level was more than that by prestrain in 5% level. On SM570 steel, in all the prestrains but uniform compressive prestrain in 10% level, no remarkable deterioration of fracture toughness were not observed.
- 3) By arranging all the results of this study and our previous investigations concerned with the effects of plastic prestrain, the temperature shift of 50 degrees of Celsius was suggested as the extent of deterioration of fracture toughness of steels due to the effects of plastic prestrain that should be considered in determination of the required fracture toughness of steels to prevent brittle fracture in steel bridge piers to the displacement level δ_{95} .

References:

- JSCE: Committee of Steel Structures (1995): Survey Reports on Safety of Steel Structures
- T. Usami et al: A Proposal for Check of Ultimate Earthquake Resistance of Partially Concrete Filled Steel Bridge Piers, Proceedings of JSCE, 525 (1995), p.69.
- C. Miki et al: Investigation of the Brittle Fracture at the Corner of P75 Rigid-Frame Pier in Kobe Harbor Highway During the Hyogoken-Nanbu Earthquake, Proceedings of JSCE, 591 (1998),p.243., A Study on the Material of the Brittle Fractured Bridge Pier, Proceedings of JSCE, 612 (1999), p.45., Deterioration of Fracture Toughness of Steel by Effect of Tensile and Compressive Prestrain, Proceedings of JSCE, 640/ (2000), p.165-175.
- I. Okura et al: Effects of Cyclic Plastic Strains on Fracture Toughness of Structural Steels, Steel Construction Engineering, Vol.3, No.11 (1996), p.1.
- JWES(1999): Seminar on Brittle fracture in Steel Building Frames and Fracture Toughness of Steels.
- E. Sasaki et al: Influences of Stiffening Methods on Elasto-Plastic Behavior of Beam-to-Column Connections of Steel Rigid Frame Piers, Proceedings of JSCE, 689 (2001), p.201.
- H. Inoue et al: Journal of Marine Science and Technology, JSNA, 160 (1986), p.450.
- H. Morikawa et al.: The Investigation and The Temporally-repair of fatigue cracks on the steel bridge piers with box sections, Proceedings of JSCE, 703 (2002), p.177.

EXPERIMENTAL STUDY ON DUCTILITY CAPACITY OF COMPOSITE BEAMS

S. Yamada¹⁾, S.H. Oh²⁾, K. Okada³⁾

1) Associate Professor, Structural Engineering Research Center, Tokyo Institute of Technology, Japan
naniwa@serc.titech.ac.jp

2) Research Institute of Industrial Science and Technology, Korea
oshoon@rist.re.kr

3) JSPS Research Fellow, Tokyo Institute of Technology, Japan
kokada@serc.titech.ac.jp

Abstract: Ductility capacity of composite beams which have conventional type of scallops has been investigated by cyclic loading tests. The results of the tests have shown that ductility capacity of composite beams is nearly half of that of steel beams without slabs. The effectiveness of application of improved connection details to a composite beam has been investigated. The improved connection details applied to the composite beams are No-weld-access-hole detail and RBS detail. They have improved ductility capacity of composite beams sufficiently.

1. INTRODUCTION

In Hyogo-ken Nanbu Earthquake, many fractures of bottom flanges occurred at beam-to-column connections of steel framed structures. After the earthquake, many researchers tried to resolve the issues about fractures and ductility capacity of steel members. However, most of them ignored effects of slabs even though composite beams, which consist of steel beams and RC slabs strongly connected each other by stud connectors, are generally used for actual buildings.

A schematic diagram of beam-to-column connections subjected to seismic force is shown in Fig. 1. In positive bending, because of the RC slab resisting compression, the full section of the beam is subjected to tensile force and the tensile strain in the bottom flange becomes excessive, so that the ductility capacity of the composite beams is considered to reduce. However, in current structural design, ductility capacity of composite beams is supposed to be equal to that of steel beams without slabs.

In this study, ductility capacity of composite beams is investigated experimentally, focusing on flange fractures which mainly determine ductility capacity of these beams.

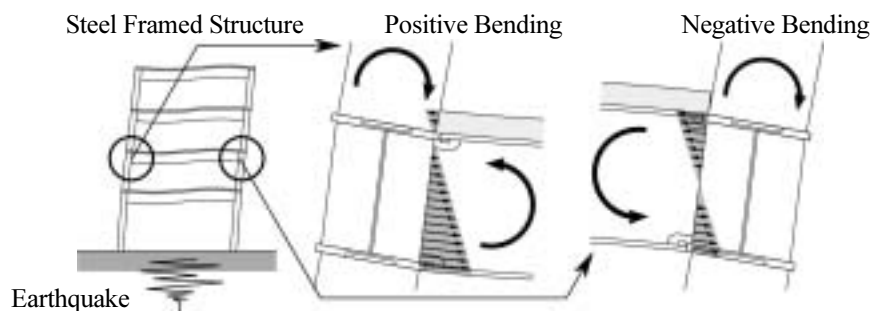


Fig. 1. Strain in Beam-to-column Connection under Earthquake

2. EXPERIMENTAL

A list of the specimens is shown in Table 1, and the standard specimen (No.1) is shown in Fig. 2. The scale and the shape of the specimens were designed based on those of beam-to-column connections of medium-rise steel buildings. The columns and the panels are composed of thick plates over 22mm so that they have sufficient strength to remain elastic during the tests. A list of mechanical properties of the materials used for the specimens is given in Table 2.

The specimens are divided into two series, Series A and Series B.

Series A (No.1~No.5) consists of four composite beam specimens (No.1, No.3~No.5) and one steel beam specimen without slabs (No.2). They have conventional type of weld access holes in their beam-to-column connections. The main purposes of the tests using Series A specimens are: (a) to demonstrate fractures of composite beams in Hyogo-ken Nanbu Earthquake; (b) to investigate ductility capacity of composite beams for fracture; and (c) to clarify the effects of slabs on ductility capacity of composite beams. Experimental parameters for Series A are as follows: (1) existence of a slab; (2) section properties; and (3) loading patterns.

Series B (No.6, No.7) consists of two composite beam specimens, beam-to-column connection details of which are modified to improve their ductility capacity. The details applied to Series B specimens are No-weld-access-hole detail (No.6) and RBS detail (No.7). No-weld-access-hole detail is shown in Fig. 3, and RBS detail is shown in Fig. 4. Many researchers have studied the effectiveness of these details in steel beams without slabs [Suita, et al]. The purpose of the tests using Series B specimens is to demonstrate their effectiveness in composite beams.

The experimental setup is shown in Fig. 5. During the tests, lateral deformation is restricted by frames positioned at the ends of the lateral beams and the free end of the main beam.

The deformation of the specimens is defined in Fig. 6 as the rotation angle θ . The actuator is controlled so that θ follows the target deformation shown in Fig. 7. Pattern 1 is applied to all specimens except No.5, and pattern 2 is applied to No.5 to investigate effects of the difference in the loading patterns.

Table 1. List of Specimens

	No.	Parameter	Beam	${}_cM_p$ [kN·m]	${}_sM_p$ [kN·m]	${}_s\theta_p$ [rad.]	t_c [mm]	Weld Access Holes	Loading Pattern
A	1	Standard	R-H-612×202×13×23	2.24×10^3	1.41×10^3	0.0082	200	Conventional	1
	2	(1) Existence of a slab without Slab	R-H-612×202×13×23	---	1.41×10^3	0.0082	0	Conventional	1
	3	(2) Section properties Small Section Beam	R-H-596×199×10×15	1.69×10^3	0.99×10^3	0.0087	200	Conventional	1
	4	(2) Section properties Thinner Slab	R-H-612×202×13×23	2.07×10^3	1.41×10^3	0.0082	140	Conventional	1
	5	(3) Loading pattern Pattern 2	R-H-612×202×13×23	2.24×10^3	1.41×10^3	0.0082	200	Conventional	2
B	6	(4) Improved connection details Non-Scallop detail	R-H-612×202×13×23	2.07×10^3	1.33×10^3	0.0077	200	Non-scallop	1
	7	(4) Improved connection details RBS detail	B-H-610×240×12×22 RBS: B-H-610×160×12×22	2.13×10^3 2.33×10^3	1.43×10^3 1.12×10^3	0.0077 ---	200	Conventional	1

${}_cM_p$: full plastic moment calculation for composite beams [AIJ], ${}_sM_p$: full plastic moment calculation for bare steel beams, ${}_s\theta_p$: elastic rotation angle of bare steel beams subjected to ${}_sM_p$, t_c : thickness of slabs

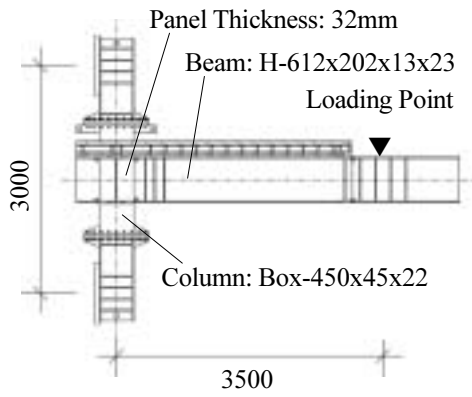


Fig. 2. Configuration of Specimen (No.1)

Table 2. Results of Material Tests

Material		σ_y	σ_u	Y.R.	ϵ_u	
		[N/mm ²]	[N/mm ²]	[%]	[%]	
SM490	H-612x202x13x23 (No.1,2,4,5)	Flange	386	535	72.2	14.4
		Web	444	551	80.6	14.6
	H-612x202x13x23 (No.6)	Flange	351	522	67.3	17.6
		Web	353	539	65.5	17.4
	H-596x199x10x15 (No.3)	Flange	414	556	74.5	14.4
		Web	445	565	78.8	14.4
	PL-22(No.7)	Flange	376	501	75.0	13.9
PL-12(No.7)	Web	357	565	63.2	14.4	
Concrete ($F_c=23.5\text{N/mm}^2$)	28days	---	26.0	---	---	

σ_y : yield stress, σ_u : maximum stress, Y.R.: yield ratio, ϵ_u : elongation

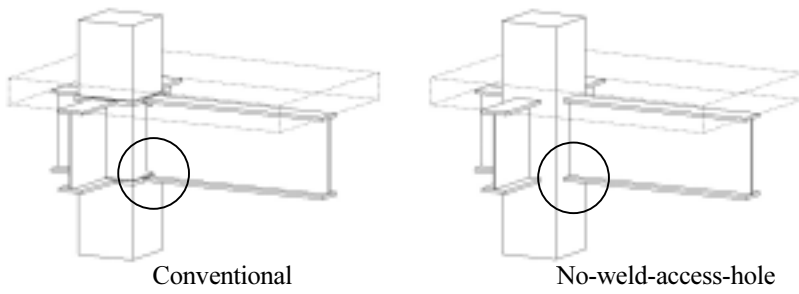


Fig. 3. No-weld-access-hole Detail

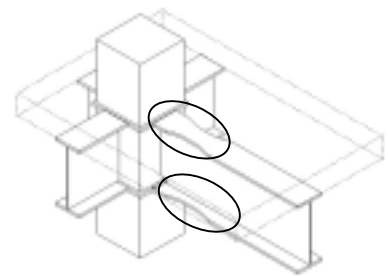


Fig. 4. RBS Detail

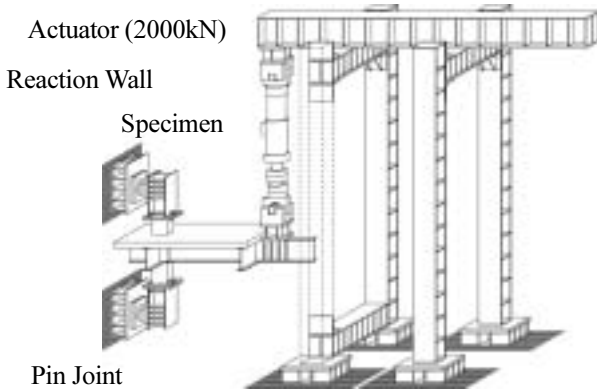


Fig. 5. Testing Setup

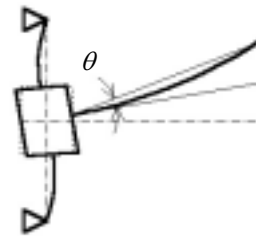


Fig. 6. Rotation Angle θ

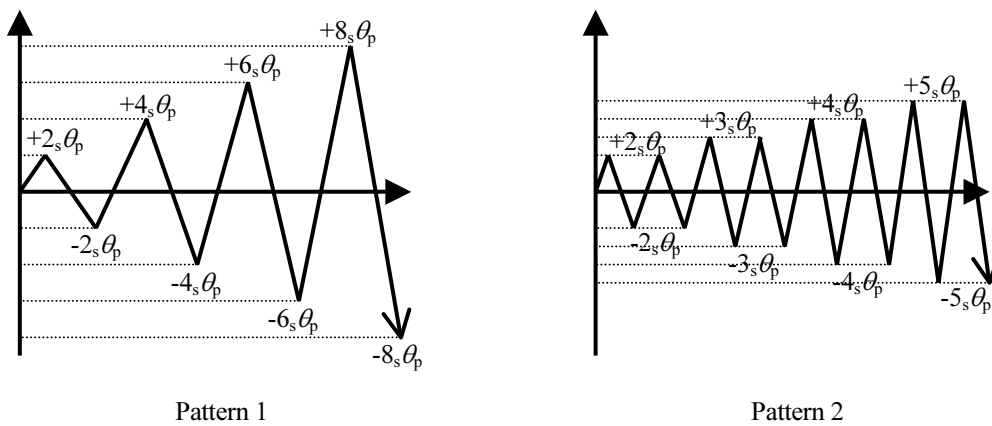


Fig. 7. Loading Patterns

3. RESULTS & DISCUSSION

3.1. Experimental results & Ductility capacity

Moment (M) versus rotation angle (θ) relationships are shown in Fig. 8, where \blacktriangledown shows the point where the flange fracture occurred. Full plastic moment calculations for composite beams and steel beams are shown by dashed lines as ${}_cM_p$ and ${}_sM_p$. Some experimental results are listed in Table 3.

The failure mode of all the specimens in Series A is flange fracture initiated by a crack which occurred at the tip of a weld access hole. The flange fractures of the composite beam specimens occurred in positive bending state.

The ductility capacity of specimens in Series A is compared by θ_{max}^+ and ${}_s\theta_{max}^+$, where θ_{max}^+ is the maximum rotation angle in positive bending state in M - θ relationships, and ${}_s\theta_{max}^+$ is the maximum rotation angle in positive bending state in skeleton curves. The skeleton curves are converted from M - θ relationships in the way shown in Fig. 9, and they are shown in Fig. 10. θ_{max}^+ and ${}_s\theta_{max}^+$ of specimens in Series A are compared in Fig. 11. θ_{max}^+ of the composite beams are 50~60% and ${}_s\theta_{max}^+$ of them are 40~50% when comparing to steel beam without slabs (No.2). Differences in section properties and loading patterns have little effect on their deformation capacity.

The specimens in Series B (No.6, No.7) were tested until flange fractures occurred. The deformation capacity of them is higher than that of the composite beams in Series A, and even that of the steel beam specimen without slab (No.2).

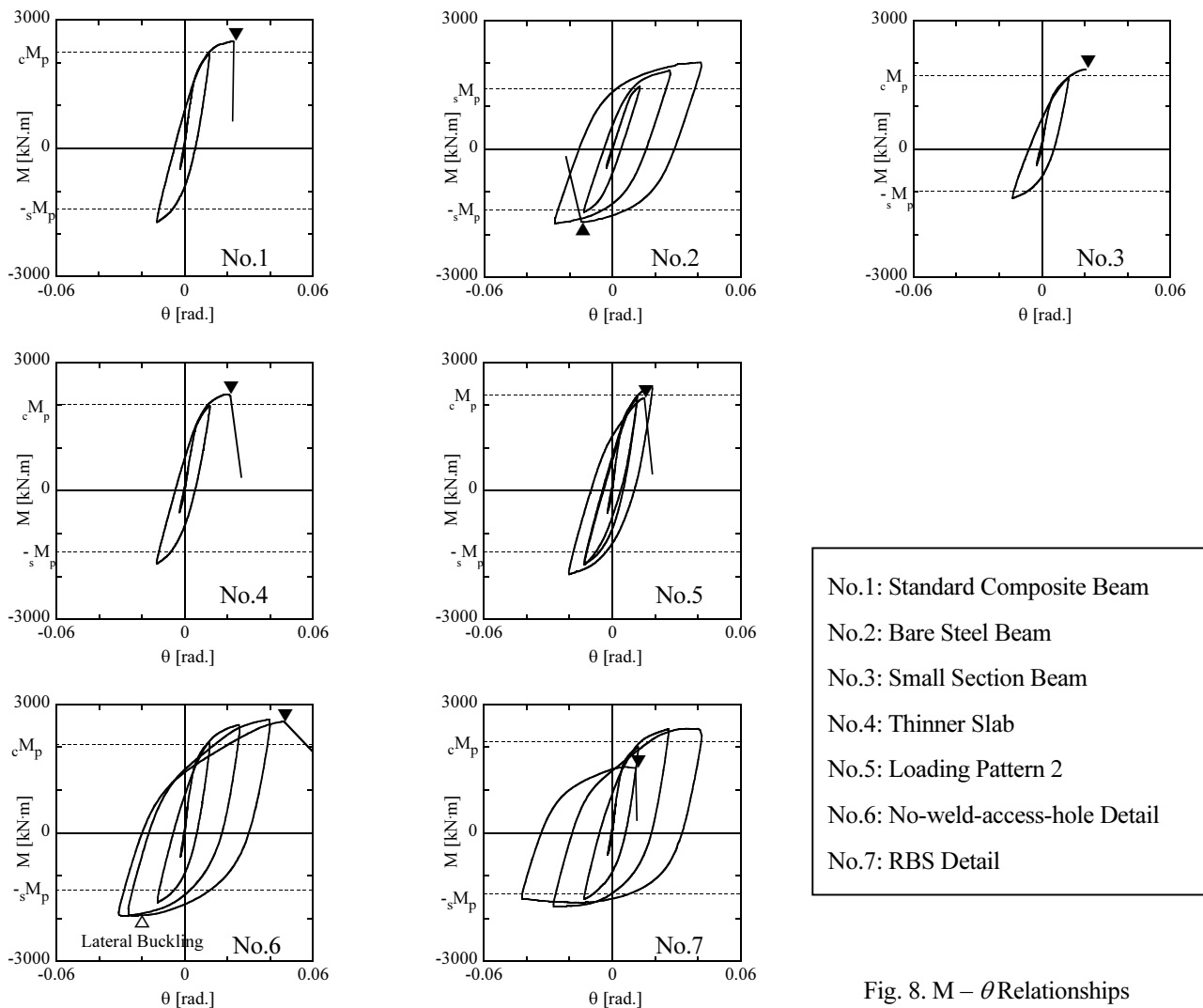


Fig. 8. $M - \theta$ Relationships

Table 3. Results of Tests

No.	K_e^+ [kN/m/rad.]	K_e^- [kN/m/rad.]	M_{max}^+ [kN·m]	M_{max}^- [kN·m]	θ_{max}^+ [rad.]	θ_{max}^- [rad.]	Fracture Part	Failure Mode	Temp. [°C]
1	412000	262000	2500	-1730	0.0231	-0.0129	Bottom Flange	Brittle Fracture	29.0
2	157000	----	2020	-1710	0.0416	-0.0268	Top Flange	Brittle Fracture	29.0
3	307000	185000	1860	-1150	0.0206	-0.0138	Bottom Flange	Ductile Fracture	29.0
4	314000	233000	2250	-1710	0.0214	-0.0131	Bottom Flange	Brittle Fracture	28.5
5	377000	262000	2440	-1950	0.0187	-0.0203	Bottom Flange	Brittle Fracture	28.5
6	477000	312000	2650	-1930	0.0470	-0.0308	Bottom Flange	Ductile Fracture	19.5
7	423000	279000	2430	-1720	0.0419	-0.0423	Bottom Flange	Brittle Fracture	28.5

K_e^+ : initial stiffness under positive bending, K_e^- : initial stiffness under negative bending, M_{max}^+ : maximum moment under positive bending, M_{max}^- : maximum moment under negative bending, θ_{max}^+ : maximum rotation angle under positive bending, θ_{max}^- : maximum rotation angle under negative bending, Temp.: temperature

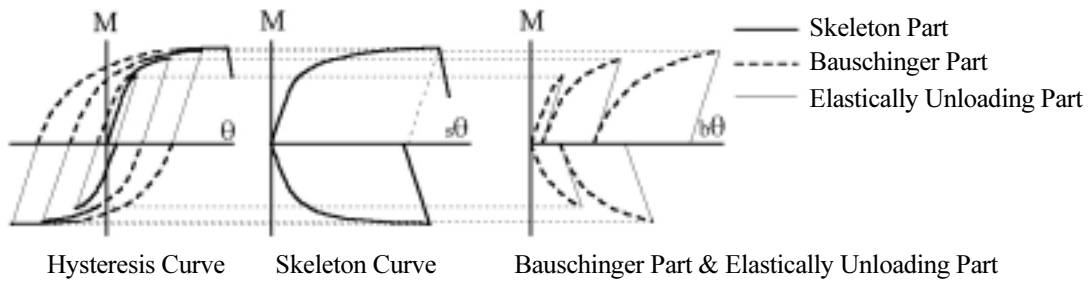


Fig. 9. Concept of Skeleton Curves

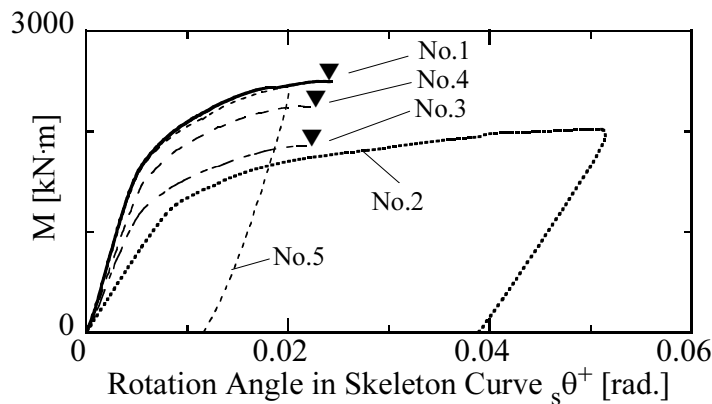


Fig. 10. Skeleton Curves (Series A)

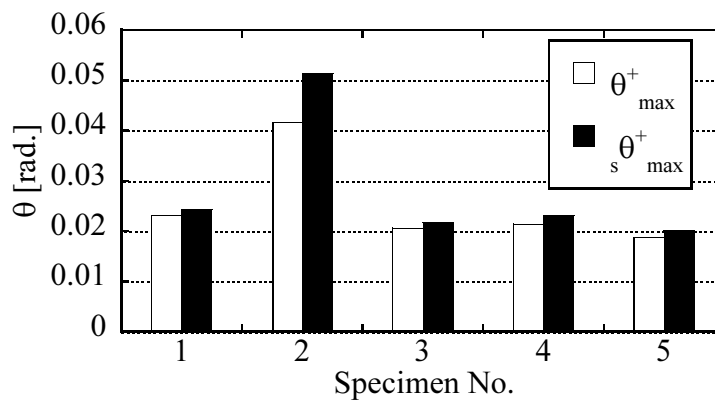


Fig. 11. Ductility Capacity (Series A)

3.2. Effects of a slab on ductility capacity of composite beams

Focusing on the existence of slabs, the effect of the slab on ductility capacity is investigated from the result of No.1 and No.2. The strain data are measured in two sections, Section A and Section B, shown in Fig. 12. The examples of strain distributions for Section A under positive bending are also shown in Fig. 12. The strain in the bottom flange of No.1 is larger than that of No.2, so that the neutral axis of No.1 seems to have moved to the upper flange side. This is the main reason for reduction of ductility capacity of composite beams.

Moment (M) versus curvature (ϕ) relationships can be obtained from the strain data in each section. The positive bending part of the skeleton curves of M - ϕ relationships are shown in Fig. 13. The ductility capacity around Section A (near the fracture point) is compared by the maximum curvature. The ductility capacity around Section A of No.1 is 65% of that of No.2.

As shown in Fig. 13, a restoring force of Section A is higher than that of Section B at same curvature. The difference in restoring forces between Section A and Section B of No.1 is about 35%, and that of No.2 is about 20%. This indicates that Section A of No.1 is relatively weaker than that of No.2, and that the deformation around the beam-to-column connection tends to be larger in No.1 than No.2, so that No.1 has reduced the ductility capacity. The curvature distribution diagrams for No.1 and No.2 specimens are shown in Fig. 14, and these are obtained at the maximum rotation angle of Fig. 10. It is shown that the plastic zone of No.1 was narrow and concentrated to the beam-to-column connection when flange fracture occurred.

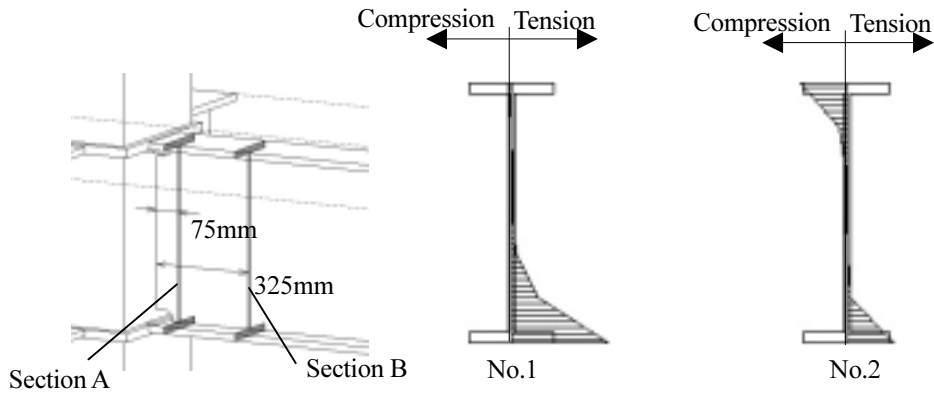


Fig. 12. Strain Distribution Diagrams

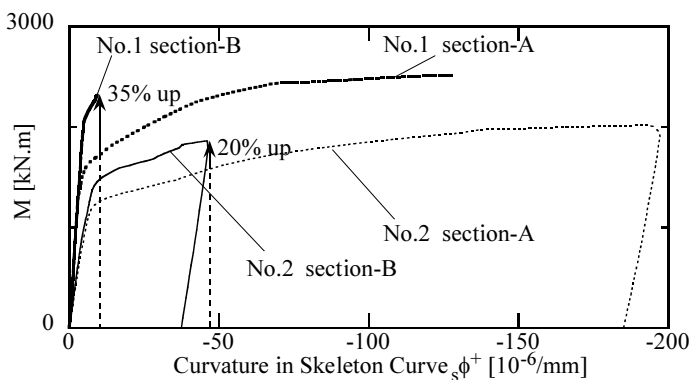


Fig. 13. Skeleton Curves of Moment versus Curvature Relationships
(No.1, No.2)

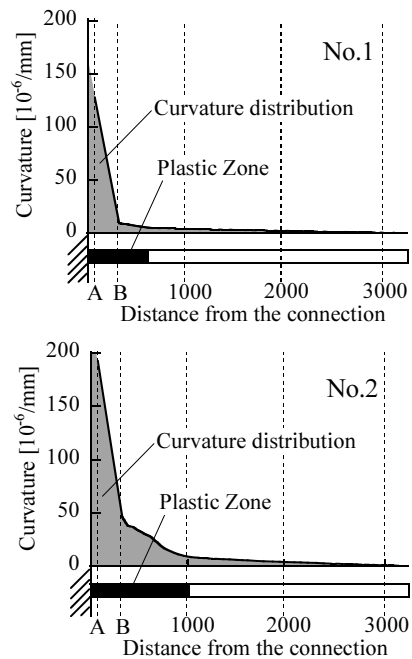


Fig. 14. Curvature Distribution

3.3. Effectiveness of improved connection details in composite beams

Skeleton curves of $M-\phi$ relationships for No.6 and No.7 specimens are shown in Fig. 15. For No.6, a restoring force of Section A is 25% larger than that of Section B, and for No.7, a restoring force of Section A is equal to that of the smallest section in RBS area. This data implies that if beam-to-column connections are protected from concentration of deformation, the deformation capacity of composite beams is improved.

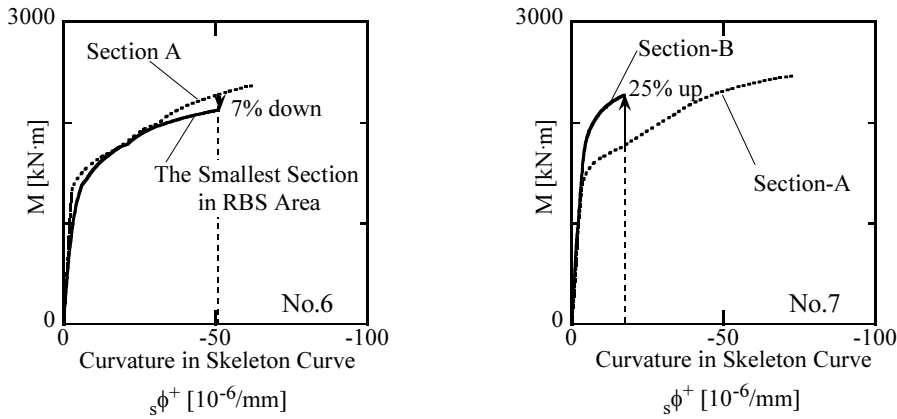


Fig. 15. Skeleton Curves of Moment versus Curvature Relationships (No.6, No.7)

4. CONCLUSION

In this study, ductility capacity of composite beams is investigated by cyclic loading tests. The results indicate that ductility capacity of composite beam is nearly half of that of steel beams without slabs. This is due to slabs, the effects of which are considered as the strain concentration to the bottom flange and the deformation concentration to the beam-to-column connection. And, No-weld-access-hole detail and RBS detail improve ductility capacity of composite beams sufficiently.

References:

- A.I.J. (1998) Recommendation for Limit State Design of Steel Structures, Architectural Institute of Japan.
- Suita, K. et al (1999), "Plastic rotation capacity of steel beam-to-column connections using a reduced beam section and no weld access hole design -Full scale tests for improved steel beam-to-column subassemblies -part 1-", *J. Struct. & Const. Eng.*, A.I.J., No. 526, 177-184.

Effect of Column Flexural Stiffness and Strength on Story Drift Concentration for Two Story Braced Frames

Y. Kimura¹⁾ and G. A. MacRae²⁾

1) *Research Associate, Dept. of Structural Engineering, Tokyo Institute of Technology, Japan*

2) *Associate Professor, Dept. of Civil Engineering, University of Washington, USA*

kimura@arch.titech.ac.jp, macrae@u.washington.edu

Abstract: Columns in concentrically braced steel frames are generally designed for axial force and column moment demands do not affect the member sizes. In the case that no column flexural stiffness is provided, a soft-story mechanism may occur in a braced frame as soon as the braces in one level reach their strength. Real frames often possess sufficient column flexural stiffness and strength that large concentrations of damage do not generally occur.

In a previous paper, the effect of the column flexural stiffness on 2 story braced frames with pinned column bases was quantified using direct mathematical formulation, frame push-over analysis and dynamic analysis. It was shown that increased column stiffness and strength tend to reduce the story drift concentration. This paper evaluates the effect of column base fixity, as well as column stiffness and strength, on drift concentration in two story braced frames.

1. INTRODUCTION

Methods to evaluate the effect of column strength and stiffness on the story drift concentration of yielding braced frame structures have been evaluated by MacRae, Kimura and Roeder (2004) when the columns have pinned connections to their foundation. It was shown that increased column flexural stiffness tends to decrease the story drift concentration.

In real frames, columns are not pinned at the foundation and do carry moment. Also, other types of system in which a shear-type frame (such as a moment frame or braced frame) is placed in parallel with a cantilever column (such as a slender structural wall) exist. In both of these cases, estimation of the drift demand of the system can be modeled as the combination of a shear-frame with that of a cantilever column. While the base condition of any column in a frame is probably not fully fixed, the assumption of the fixed base, together with the pinned base assumption, provide bounds on the base fixity for the evaluation of story drift concentration.

This paper investigates the behavior of systems consisting of both braced frames and continuous flexural columns. It quantifies the effect of column flexural stiffness and strength on the drift concentration using a direct mathematical formulation, frame push-over analysis and dynamic analysis. The base of the column is assumed to be fully fixed to the foundation. Minimum values of column stiffness and strength to limit the story drift concentration to specific values are proposed.

2. PUSHOVER BEHAVIOR OF FRAME WITH FIXED BASE COLUMN

2.1 Comparison between Braced Frame with Pinned and Fixed Base Column

Fig. 1(a) shows the two story frame with same stiffness and strength at each level. There is one “continuous column”, representing the flexural stiffness of all gravity seismic columns in the building. It is assumed that the connections of the left braced frame are totally pinned and the continuous column is fixed at the base. Only the column resists the concentration of deformation in one story. Drift concentration describes the ratio of the maximum story drift, Δ_1/h to maximum roof drift, Δ_2/H , in Fig. 1(b). In the real structures, the boundary conditions of the columns at the base are never pinned or fixed, and their rotational stiffnesses are almost during pin and fix. But if the drift concentrations for both extreme boundary conditions are clarified, that for the conditions during pin and fix can be approximately calculated.

The drift concentration factor, DCF is calculated from Eq. (1) and Eq. (2) (MacRae, Kimura and Roeder, 2004) in a braced frame with a pinned base column. Eq. (1) is valid when the bottom story yields and Eq. (2) is valid when both the top and bottom stories yield. Eq. (1) and Eq. (2) can respectively estimate the DCF for small and large column stiffness ratios, α . Here, μ_t is total roof ductility when the brace at first story yields, k is the frame shear stiffness, and EI/h^3 is the column flexural stiffness.

$$DCF = \frac{10\mu_t + 55\alpha\mu_t - 4 - 10\alpha + 75\alpha^2\mu_t}{5\mu_t(1+5\alpha)(1+3\alpha)} \quad (1)$$

$$DCF = 1 + \frac{1}{15\alpha\mu_t} \quad (2)$$

$$\text{where } \alpha = \frac{EI_c}{kh^3} \quad (3)$$

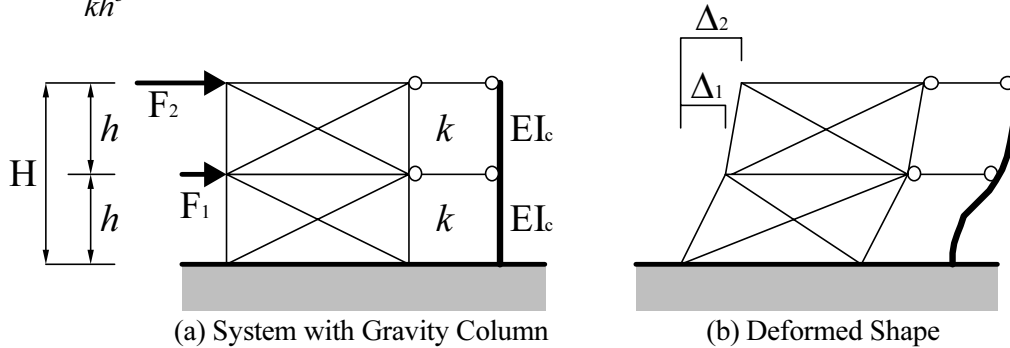


Figure 1 Idealization of Two Story Frame with Continuous Column
Deformation and Forces

Fig. 2(a) compares the behavior of a DCF for the braced frame with pinned or fixed base columns. The lines are drawn by Eq. (1) or Eq. (2) for pinned column base at $\mu_t=4$, and plots are the pushover analysis results. The columns are assumed to keep elastic to compare only the difference of boundary condition. μ_t is the total roof ductility when any brace yields in the frame.

Pushover analysis was carried out using the computer program DRAIN-2DX (Prakash, Powell and Campbell, 1993). When α is very low, DCFs for pinned and fixed base columns are almost same. As α increases, DCF for fixed base column suddenly decreases and converges about 1.4, even though DCF for pinned base column decreases and converges to 1.0. The difference of boundary conditions of the columns is influenced with DCFs especially for very high α , because the column at pinned base moves linearly, and that at fixed base is like a cantilever for very high α .

Fig. 2(b) shows compares the yield moment strength of steel column for DCF. The moment strength, M_c is calculated the following.

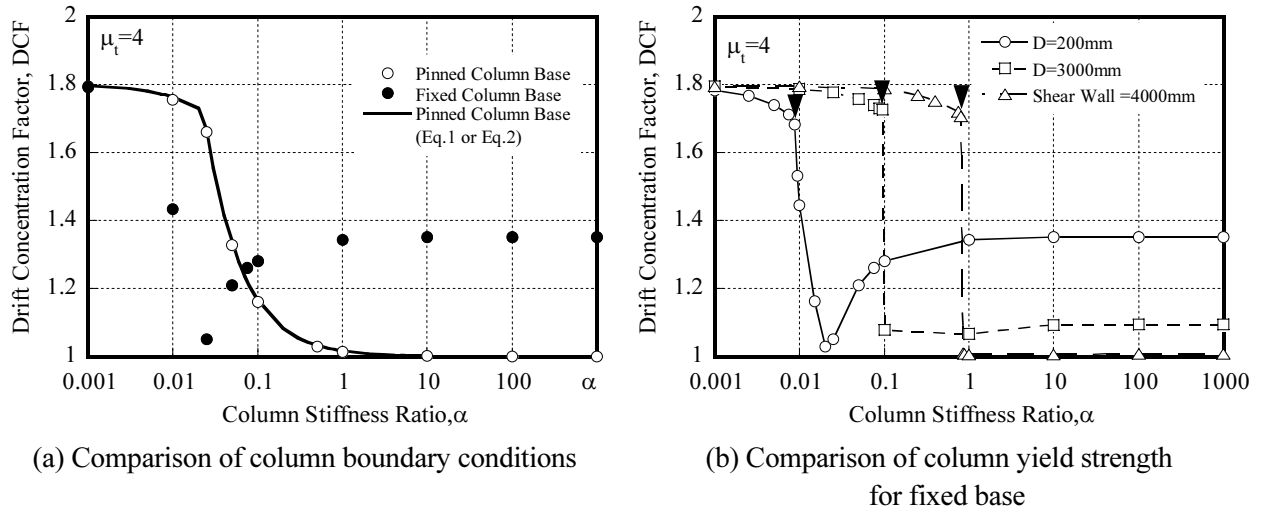


Figure 2 DCF of Two Story Shear Structure with Various Column Flexural Stiffness, α , and Roof Ductility, μ_t , using Static Pushover Analysis

$$M_c = \varepsilon_y EI_c / (D/2) \quad (4)$$

Here, D is column diameter, and ε_y is yield strain.

Three kinds of all column capacity in the frame were selected corresponding to steel column diameter 1) 200mm, 2) 3000mm and 3) RC shear wall with depth 4000mm. The column for case 1) almost keeps elastic, and that for case 3) becomes yield as soon as α increases. The column strength is influenced with DCF. Making the closed form solution for DCF of the braced frames with fixed column base, it may be shown using the non-dimensional new parameter for column moment strength ratio, χ_c .

$$\chi_c = \frac{M_c h}{EI_c} \quad (5)$$

In Fig.2 (b), the kink, the black triangle point, in the curve shows where column behavior changes from first story only to both stories yields. Its value is different among 3 kinds of lines.

Fig.3 shows the relationship between α_c and χ_c . The plots are the analytical results, and the line is approximated by the analytical results. α_c is α when the kink occurs, as α increases. The approximate equation for α_c and χ_c is defined as the following.

$$\alpha_c = \frac{4.0 * 10^{-4}}{\chi_c} \quad (6)$$

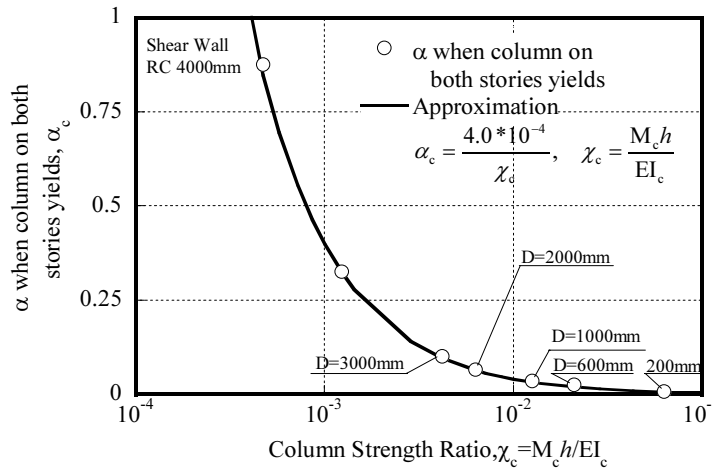


Figure 3 Relationship between α_0 and χ_c

The line is very fitting to the plots, so Eq. (6) is available to find their relationship.

2.2 Estimation for Drift Concentration Factor for Fixed Base Column in range of lare α

The value of DCF for the braced frame with fixed base column also consists of 2 kinds of closed form solution. When α is larger than α_c , it is shown that DCF is almost same as shown Fig. 2(b). Eq. (7) is the approximation of DCF when α is larger than α_c . Eq. (7) is consists of 3 equations with the value of χ_c . First equation of Eq. (7) is for the case of small column strength, and Third equation is for the case of large column strength. χ_{c1} and χ_{c2} are the range for changing the tendency of DCF. χ_{c1} is constant, and χ_{c2} is the value calculated from Fig.4.

$$DCF = \begin{cases} 1 & \chi_c < \chi_{c1} \\ 1 + 0.35 \frac{\chi_c - \chi_{c1}}{\chi_{c2} - \chi_{c1}} & \chi_{c1} < \chi_c < \chi_{c2} \\ 1.35 & \chi_{c2} < \chi_c \end{cases} \quad (7)$$

$$\chi_{c1} = 4.75 * 10^{-4}, \quad \chi_{c2} = 4.0 * 10^{-3} \mu_t \quad (8)$$

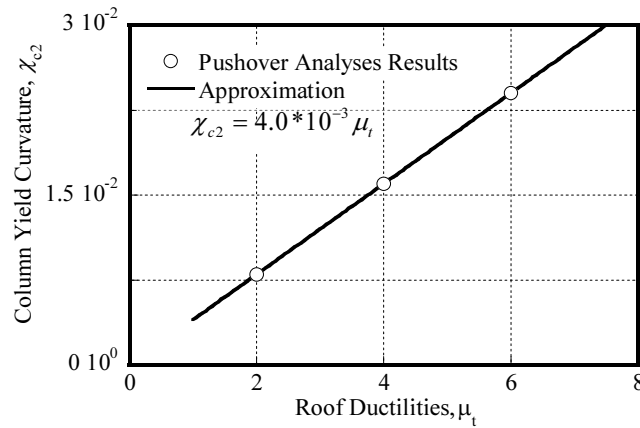


Figure 4 Relationship between χ_{c2} and μ_t

χ_{c2} depends on the roof ductility, μ_t , and is linearly related to μ_t . Plots are pushover analysis results, and the line is approximated from them.

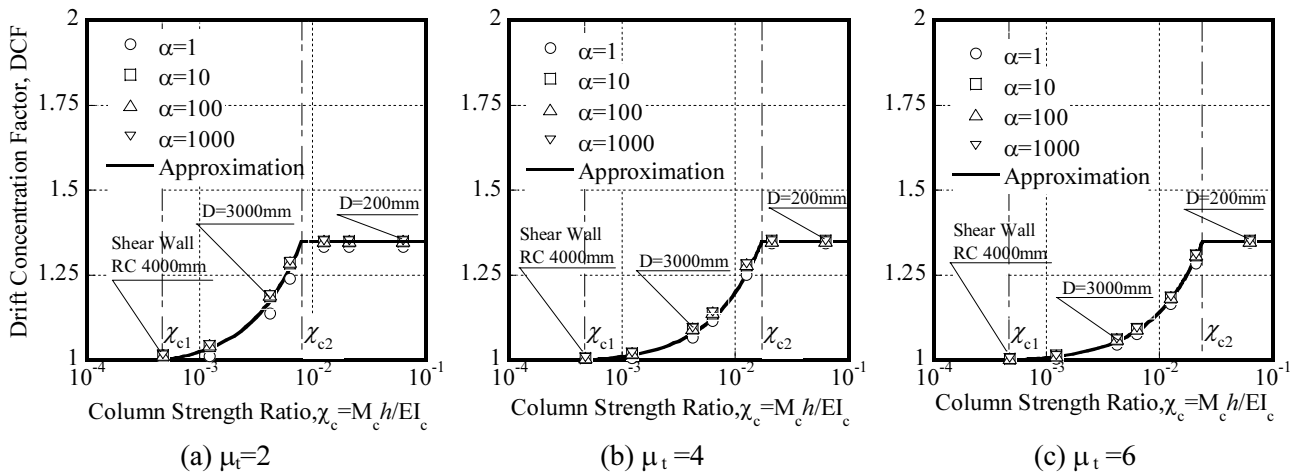


Figure 5 Relationship between DCF and χ_c

Equations derived above for DCF are given in Fig.5 (a)~(c) respectively for ductilities of 2, 4 and 6. The derived equations are referred to as pushover analyses results. Results of approximation and pushover analyses are almost same as would be expected.

2.3 Estimation for Drift Concentration Factor for Fixed Base Column in range of small α

When α is smaller than α_c , DCF is calculated using Eq. (1) which is modified from α to α' . α' is the modified coefficient of α , as shown in Eq. (10).

$$DCF = \frac{10\mu_t + 55\alpha'\mu_t - 4 - 10\alpha' + 75\alpha'^2\mu_t}{5\mu_t(1 + 5\alpha')(1 + 3\alpha')} \quad (9)$$

$$\text{where } \alpha' = \alpha \left(\frac{\alpha_0}{\alpha_c} \right) \quad (10)$$

α_c is the value calculated from Eq. (6). α_0 is the kink in the curve for the frame with pinned column base in Fig.2 (a). And α_0 is calculated from the value of α when Eq. (1) and Eq. (2) are equal.

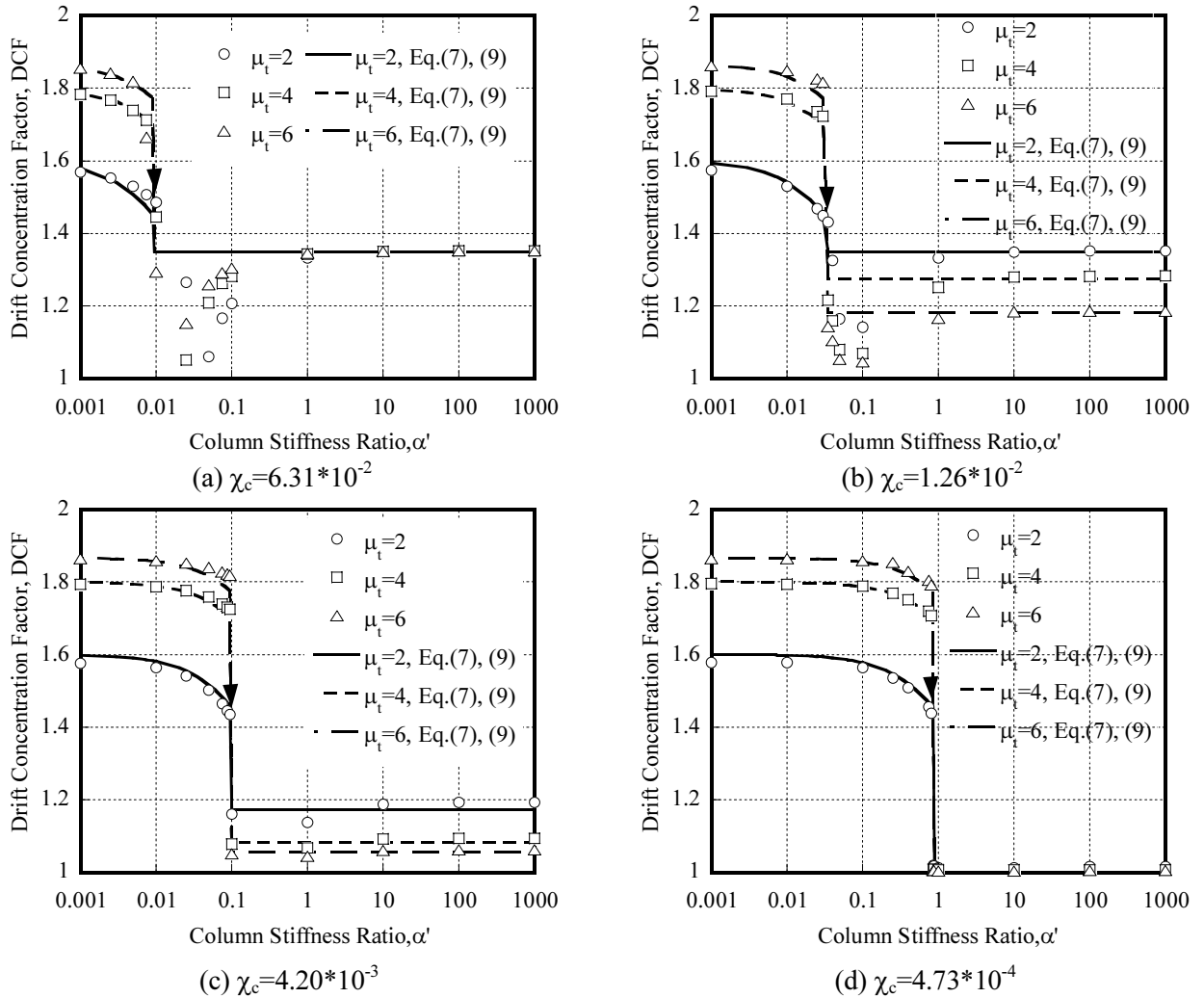


Figure 6 Relationship between DCF and modified α'

Fig.6 (a)~(d) show the relationship between DCF and modified α' respectively for $\chi_c=6.31 \cdot 10^{-2}$, $1.26 \cdot 10^{-2}$, $4.20 \cdot 10^{-3}$ and $4.73 \cdot 10^{-4}$. The curves are the approximation for Eq. (7) and (9), and the plots are pushover analyses results respectively for $\mu_t=2, 4$ and 6 . In the diagrams, the black triangle is the boundary point between Eq. (7) and Eq. (9). Eq. (7) is used to calculate DCF at less than the point, and

Eq. (9) is at more than the point. They are similar and DCF can be estimated by these equations well. It is shown in Fig.6 (d) that when χ_c is low, DCF keeps high value by α of about 1. DCF suddenly decreases at the point, and it becomes unity. But it is shown in Fig.6 (a) that when χ_c is high, DCF suddenly decreases at α of about 0.01 and it converges about 1.4. χ_c and α are important to estimate DCF for the braced frame with fixed base columns.

2.4 Estimation for DCF with Strength Distribution of Braced Frame

In section 2.1~2.3, it is assumed that the strength distribution of braced frame is unity over height in order to lead the equation for DCF with column stiffness ratio α and column yield curvature ratio χ_c . But the frame shear demand and frame shear capacity are different and are independent of the α and χ_c . Their difference is represented by the parameter, β which is the ratio of second story strength to first story strength.

Fig.7 shows the relationship between α_c and χ_c respectively for $\beta=3/4, 5/6, 11/12$ and 1. The plots are the analytical results, and the lines are drawn by Eq. (11) which is closed form solution for α_c with χ_c and β as the following.

$$\alpha_c = \frac{4.0 \cdot 10^{-4} \cdot (3\beta - 2)}{\chi_c} \quad \left(\frac{2}{3} \leq \beta \leq 1\right) \quad (11)$$

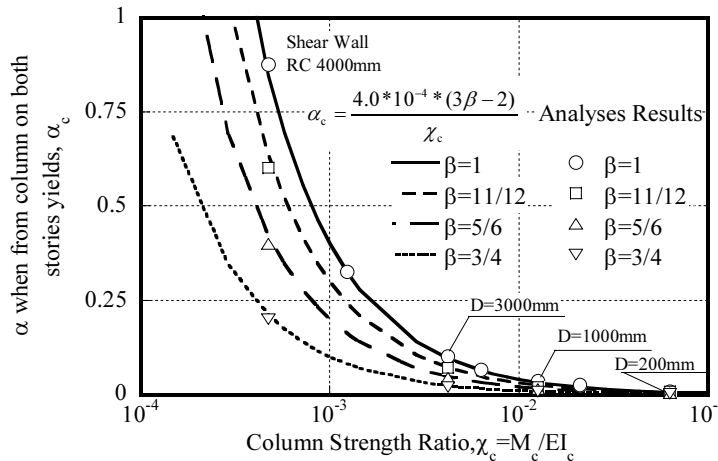


Figure 7 Relationship between α_0 and χ_c respectively for $\beta=3/4, 5/6, 11/12$ and 1

The equations for DCF of brace frame with pinned column base were developed for β and shown to fit the pushover analysis results (Kimura and MacRae, 2002). Using modified Eq. (9), the equation for DCF including β is shown as following.

$$DCF = \frac{4\beta(\mu_t - 1) + 10\alpha'(\mu_t - 1) + 6\beta^2\mu_t + 45\alpha'\beta\mu_t + 75\alpha'^2\mu_t}{\mu_t(2 + 3\beta + 15\alpha')(\beta + 5\alpha')} \quad (12)$$

Here, α' is calculated from Eq. (10) and Eq. (11). Eq. (7) can also be useful in the range of large α , changing β .

3. DYNAMIC ANALYSIS BEHAVIOR OF FRAME WITH FIXED BASE COLUMN

It was shown that the static drift concentration of two story braced frame is lead with column flexural stiffness and strength. In the relationships above, lateral loading distribution was assumed to be inverse triangular. Since the inertial loads change with time during earthquake, DCF may be different than that by pushover analysis. The two story frames with fixed column base are analyzed, whose models are 3 types of frame with $\beta=1, 5/6$ and $2/3$ same as the frames with pinned column base

(Kimura, MacRae and Roeder, 2002). Modeling was also carried out using the computer program DRAIN-2DX. The earthquake records used were El Centro NS, Hachinohe NS and Kobe NS whose acceleration was twice. Before the dynamic time history analysis, the modal analysis of the frames gives a fundamental period, T , as shown in Table 1. The period for the braced frame with pinned column base is almost same, even though α for the frame is different. But that with fixed column base is significantly different, because both the braced frame stiffness and the continuous column stiffness are added to the structure stiffness for the period. It is seen that the column stiffness ratio, α increases, the period decreased. In this paper, the reduction in the period of the structure due to increasing α , is not discussed, so the frames for α of less than 1 were carried out.

Table 1 Natural Period of the Braced Frames with Continuous Column

Frame Model	α	0.0	0.01	0.1	1	10	100
Case1 ($\beta=1$)	T	0.336	0.330	0.300	0.220	0.098	0.033
Case2 ($\beta=5/6$)		0.336	0.341	0.314	0.228	0.090	0.033
Case3 ($\beta=2/3$)		0.336	0.356	0.331	0.237	0.100	0.033

Fig.8 shows dynamic DCF_d plotted against static value, DCF. Circular, square and triangle respectively indicate the case of $\chi_c = 0.0631$, 0.0126 and 0.0042. The dynamic drift concentration factor, DCF_d was computed from the peak story drift and the peak roof drift, even though these occurred different times. Dynamic DCF is compared to static DCF at same roof ductility, μ_r . It may be seen that DCF_d is almost similar to DCF.

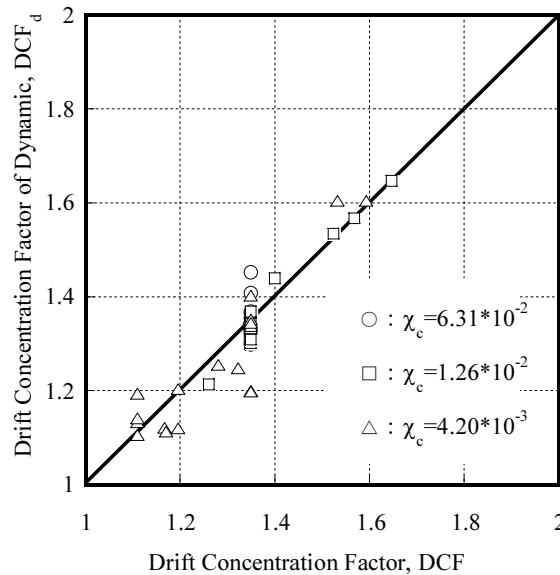


Figure 8 Comparison between dynamic DCF_d and static DCF

4. CONCLUSIONS

Pushover and dynamic inelastic time history analyses are performed on concentrically braced frames with continuous columns fixed at base to investigate the effect of column flexural stiffness and strength. It was shown that:

- 1) Continuous columns over the height of the structure may be seismic and gravity columns. These boundary conditions at the base, are influenced with the drift concentration of the structure. DCF for the braced frames with pinned column base, gradually decreases as column stiffness ratio, as α increases. But DCF for those with fixed column base, suddenly decreases and converges a value, as

column stiffness ratio, α , increases.

- 2) The drift concentration fixed at base is related to the strength of the continuous columns. DCF for low column strength ratio, χ_c , early becomes low, as α increases. And DCF for high χ_c , keeps high even though α increases.
- 3) Equations (7) and (9) approximately estimate static DCF for the brace frame with fixed column base.
- 4) Peak drift concentration is almost equal to the static demand for the same roof ductility. So Equations (7) and (9) are available to estimate the dynamic drift concentration for two story frames with fixed column base.

References:

- MacRae G. A., Kimura Y., and Roeder C. W. (2004), "Effect of Column Stiffness on Braced Frame Seismic Behavior," *Journal of Structural Engineering*, American Society of Civil Engineers, **130**(2), Accepted for Publication.
- Kimura Y., MacRae G., and Roeder C. (2002), "Column Stiffness Effects on Braced Frame Seismic Behavior," 7th National Conference on Earthquake Engineering, CD-ROM, 1-9.
- Prakash V., Powell G. H. and Campbell S. (1993), "DRAIN-2DX Base Program Description and User Guide Version 1.10," Department of Civil Engineering, University of California, Berkeley, Report No. UCB/SEMM-93/17&18.
- Kimura Y. and MacRae G. (2002), "the Effect of the Column Flexural Stiffness on Story Drift Concentration Mechanism of 2 Story Braced Frames," *Journal of Structural Construction Engineering*, AII, 560, 189-195.

BEAM ELEMENT FOR TRUSS BEAM WITH ELASTOPLASTIC-BUCKLING BEHAVIOR

S. Motoyui¹⁾

*1) Department of Built Environment, Tokyo Institute of Technology, Japan
motoyui@enveng.titech.ac.jp*

Abstract: In this paper, we will suggest the useful beam element which enables us to analyze truss beams involving the elastoplastic buckling behavior of chord members without constructing discrete model. In this element, multi-surfaces for the yielding and buckling behavior are considered in the space of (M_i, M_j, N) . Each couple of surfaces corresponds to the yielding and buckling strength of each chord member in a truss beam. It is assumed that total nodal displacement can be expressed in the form of additive decomposition of elastic, plastic and buckling components. Furthermore, we describe that it is possible to evaluate the effect of buckling behavior of a chord member as the isotropic softening behavior for only a couple of surfaces in the space of (M_i, M_j, N) . Finally we will examine the validity of our beam element through a numerical example.

1. INTRODUCTION

We consider a truss beam as shown in Figure 1(a). This truss beam belongs to the Warren truss type. Usually structural designers do not directly analyze such huge structures as are composed with many truss beams since such analytical models have much more freedom degree number and are very costly. Then an effective continuous model in which a truss beam is replaced with a single beam element shown in Figure 1(b), is usually used when analyzing the dynamic behavior of such a huge structure. The continuous model could not applied to the plastic problem until we developed a truss beam element which enabled us to simulate elastoplastic problem (Motoyui et al.(2000b)). However, chord members buckle and can not carry an axial force as soon as they yield in compression. In this paper, we will describe the consistent and convenient truss beam element to consider the elastoplastic buckling behavior of chord members in the continuous model.

At first, we explain that the elastoplastic buckling behavior of a chord member can be approximately represented as the plastic behavior with softening under the assumption that its slenderness ratio is the less(Motoyui et al.(2000a)). Next, we formulate the truss beam element based on the thermodynamics approach. Finally we show the validity of the present element by comparison with results by a discrete model of which chord members are divided by standard beam elements.

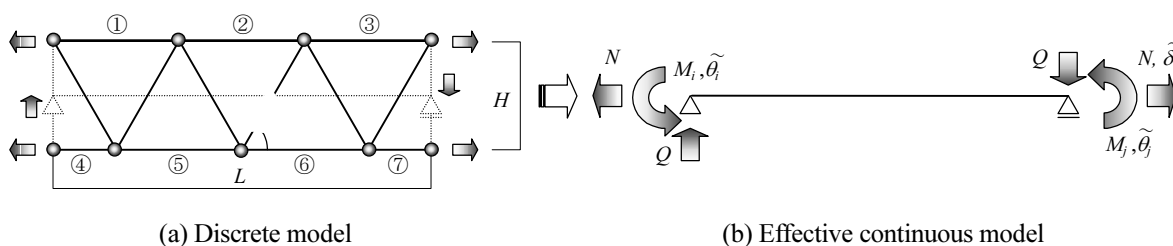


Figure 1 Two types of truss model

2. BASIC EQUATIONS FOR CHORD MEMBER

It is assumed that the Helmholtz free energy ψ_α for the α th chord member which consist of an elastic straight bar and a perfect elastoplastic rotary spring in Figure 2(b) can be written by

$$\psi_\alpha(u_\alpha, \theta_\alpha, u_\alpha^p, \theta_\alpha^p) = \left\{ \frac{1}{2} n k_\alpha \left(\frac{u_\alpha}{2} - \frac{u_\alpha^p}{2} - \frac{l_\alpha}{4} \theta_\alpha^2 \right)^2 + \frac{1}{2} m k_\alpha (\theta_\alpha - \theta_\alpha^p)^2 \right\} \times 2 \quad (1)$$

where u_α and θ_α are a total stretch and total rotation, u_α^p and θ_α^p are plastic components of a stretch and a rotation, and $n k_\alpha$ and $m k_\alpha$ are an elastic stiffness of a bar and an elastic stiffness of a rotary spring. The sub-suffix α means the value of the α -th member. In this paper, it is asumed that θ is always positive and a chord member does not buckle until its member yields.

Substituting in the Clausius-Duhem inequality; $-\dot{\psi}_\alpha + n_\alpha \dot{u}_\alpha \geq 0$ from Eq.(1) gives

$$n_\alpha = \frac{1}{2} n k_\alpha \left(u_\alpha - u_\alpha^p - \frac{l_\alpha}{2} \theta_\alpha^2 \right), \quad n_\alpha l_\alpha \theta_\alpha = 2 m k_\alpha (\theta_\alpha - \theta_\alpha^p) \Rightarrow 2 m_\alpha, \quad \Gamma_\alpha = n_\alpha \dot{u}_\alpha^p + n_\alpha l_\alpha \theta_\alpha \dot{\theta}_\alpha^p \geq 0 \quad (2)$$

where Γ_α is called the plastic dissipation term and this expression mean variables of n_α and $n_\alpha l_\alpha \theta_\alpha$ are thermodynamic force to u_α^p and θ_α^p respectively. The yield function at the rotary spring; $\Phi_\alpha(n_\alpha, m_\alpha) = (n_\alpha/n_y)^2 + |m_\alpha|/m_p - 1 \leq 0$ can be rewritten in the form

$$\Phi_\alpha(n_\alpha, \theta_\alpha) = \frac{|n_\alpha|}{n_y} - \bar{\tau}_\alpha(\theta_\alpha) \leq 0 \quad \text{where} \quad \bar{\tau}_\alpha(\theta_\alpha) = \bar{\sigma}_\alpha(\theta_\alpha) - \frac{n_y l_\alpha \theta_\alpha}{4 m_p}, \quad \bar{\sigma}_\alpha(\theta_\alpha) = \sqrt{1 + \left(\frac{n_y l_\alpha \theta_\alpha}{4 m_p} \right)^2} \quad (3)$$

Here, the principle of maximum plastic dissipation is introduced to specify the post-buckling behavior. So consider the Lagrangian; $L_\alpha = -\Gamma_\alpha + \lambda_\alpha^p \Phi_\alpha$ where λ_α^p is a plastic consistent parameter. Differentiation of the Lagrangian with respect to n_α or θ_α gives

$$\dot{u}_\alpha^p = \frac{n_\alpha}{n_y} \frac{1}{\bar{\sigma}_\alpha} \dot{\lambda}_\alpha^p, \quad \dot{\theta}_\alpha^p = \frac{1}{4 m_p} \frac{n_\alpha}{|n_\alpha|} \frac{1}{\bar{\sigma}_\alpha} \dot{\lambda}_\alpha^p \quad (4)$$

These equations are called evolution equations. Furthermore, if the yield condition of Eq.(3-a) is active then the following Kuhn-Tucker complementary conditions must be satisfied

$$\Phi_\alpha = 0, \quad \dot{\Phi}_\alpha = 0 \quad \text{and} \quad \dot{\lambda}_\alpha^p \geq 0 \quad (5)$$

Now consider the case that member's slenderness ratio is much less. In this case, the assumption that θ_α is approximately equal to θ_α^p is satisfied. Then the yield function of Eq.(3) can be rewritten in the form

$$\Phi_\alpha(n_\alpha, \lambda_\alpha^p) = \frac{|n_\alpha|}{n_y} - \bar{\tau}_\alpha(\lambda_\alpha^p) \leq 0 \quad \text{where} \quad \bar{\tau}_\alpha(\lambda_\alpha^p) = \bar{\sigma}_\alpha(\lambda_\alpha^p) - \frac{n_y l_\alpha \theta_\alpha^p(\lambda_\alpha^p)}{4 m_p}, \quad \bar{\sigma}_\alpha(\lambda_\alpha^p) = \sqrt{1 + \left(\frac{n_y l_\alpha \theta_\alpha^p(\lambda_\alpha^p)}{4 m_p} \right)^2} \quad (6)$$

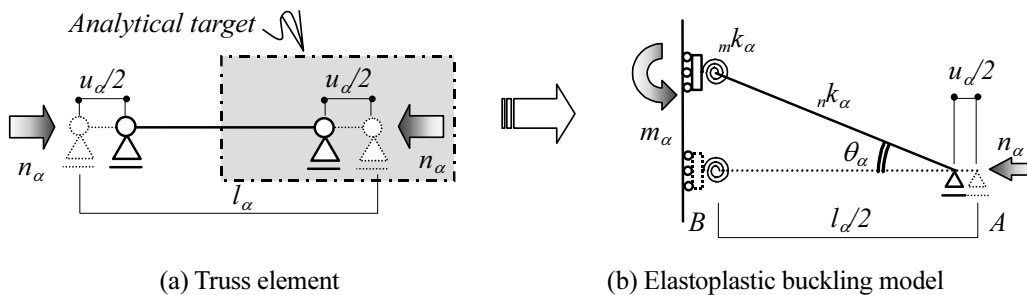


Figure 2 Single chord member

We introduce an effective plastic-buckling component u_α^{pb} which is defined by the form of additive decomposition.

$$u_\alpha^{pb} = u_\alpha^p + u_\alpha^b, \quad u_\alpha^b = \frac{l_\alpha}{2} \theta_\alpha^p, \quad \dot{u}_\alpha^{pb} = \dot{u}_\alpha^p + l_\alpha \theta_\alpha^p \dot{\theta}_\alpha^p = \frac{1}{n_y} \frac{n_\alpha}{|n_\alpha|} \dot{\lambda}_\alpha^p \quad (7)$$

From the third loading condition of Eq.(5-c), the necessary condition to satisfy the second law of thermodynamics is given by

$$\frac{1}{n_y} \frac{n_\alpha k_\alpha}{2} - \frac{n_\alpha l_\alpha}{16m_p^2 \bar{\sigma}_\alpha^2} > 0 \quad (8)$$

3. EXTEND TO TRUSS BEAM

3.1 Basic Equations for Truss Beam

The Helmholtz free energy Ψ for the whole of a truss beam can be given by the sum of each member's Helmholtz free energy ψ .

$$\Psi = \sum_{\alpha=1}^{all} \psi_\alpha(u_\alpha, \theta_\alpha, u_\alpha^p, \theta_\alpha^p) \quad (9)$$

This equation can be rewritten in the form

$$\Psi = \frac{1}{2} \tilde{\mathbf{u}}^{efT} \mathbf{k}^e \tilde{\mathbf{u}}^{ef} + \frac{1}{2} \sum_{\alpha=1}^{all} \left\{ k_\alpha (\theta_\alpha - \theta_\alpha^p)^2 \times 2 \right\} \quad (10)$$

where $()^T$ signifies transpose, \mathbf{k}^e is an elastic stiffness matrix for an effective continuous model and $\tilde{\mathbf{u}}^{ef}$ is the effective elastic component of the nodal relative displacement $\tilde{\mathbf{u}}$. And we assume that total component $\tilde{\mathbf{u}}$ can be rewritten by the form of additive decomposition.

$$\tilde{\mathbf{u}} = \tilde{\mathbf{u}}^{ef} + \tilde{\mathbf{u}}^p + \tilde{\mathbf{u}}^b, \quad \tilde{\mathbf{u}}^T = \langle \tilde{\delta} \quad \tilde{\theta}_i \quad \tilde{\theta}_j \rangle \quad (11)$$

where $\tilde{\mathbf{u}}^p$ and $\tilde{\mathbf{u}}^b$ are the plastic and buckling components of the nodal relative displacement. Furthermore, the assumption of $\tilde{\mathbf{u}}^p \equiv \tilde{\mathbf{u}}^p(u_\alpha^p)$ and $\tilde{\mathbf{u}}^b \equiv \tilde{\mathbf{u}}^b(\theta_\alpha)$ is introduced.

$$\dot{\tilde{\mathbf{u}}}^p(u_\alpha^p) = \sum_{\alpha=1}^{all} \frac{\partial \tilde{\mathbf{u}}^p}{\partial u_\alpha^p} \dot{u}_\alpha^p \equiv \sum_{\alpha=1}^{all} \mathbf{h}_\alpha^p \dot{u}_\alpha^p, \quad \dot{\tilde{\mathbf{u}}}^b(\theta_\alpha) = \sum_{\alpha=1}^{all} \frac{\partial \tilde{\mathbf{u}}^b}{\partial \theta_\alpha} \dot{\theta}_\alpha \equiv \sum_{\alpha=1}^{all} \mathbf{h}_\alpha^b \dot{\theta}_\alpha \quad (12)$$

In this case, the Clausius-Duhem inequality can be rewritten as $-\dot{\Psi} + \mathbf{f}^T \dot{\tilde{\mathbf{u}}} \geq 0$. \mathbf{f} is the nodal forces; $\mathbf{f}^T = \langle N \quad M_i \quad M_j \rangle$. Then substituting in this inequality from Eq.(10) gives

$$\left\{ \mathbf{f} - \mathbf{k}^e \tilde{\mathbf{u}}^{ef} \right\}^T \dot{\tilde{\mathbf{u}}} + \sum_{\alpha=1}^{all} \left[\mathbf{f}^T \mathbf{h}_\alpha^b - 2_m k_\alpha (\theta_\alpha - \theta_\alpha^p) \right] \dot{\theta}_\alpha + \sum_{\alpha=1}^{all} \left[\mathbf{f}^T \mathbf{h}_\alpha^p \dot{u}_\alpha^p + 2_m k_\alpha (\theta_\alpha - \theta_\alpha^p) \dot{\theta}_\alpha^p \right] \geq 0 \quad (13)$$

For this inequality equation to be true for all values of $\tilde{\mathbf{u}}^{ef}$ or θ_α , their coefficients must be zero, giving

$$\mathbf{f} = \mathbf{k}^e \tilde{\mathbf{u}}^{ef}, \quad \mathbf{f}^T \mathbf{h}_\alpha^b = 2_m k_\alpha (\theta_\alpha - \theta_\alpha^p), \quad \sum_{\alpha=1}^{all} \left[\mathbf{f}^T \mathbf{h}_\alpha^p \dot{u}_\alpha^p + \mathbf{f}^T \mathbf{h}_\alpha^b \dot{\theta}_\alpha^p \right] \geq 0 \quad (14)$$

The third equation represents the dissipation term. By comparison with Eq.(2-c), it is understood that both \mathbf{h}_α^p and \mathbf{h}_α^b can be represented by \mathbf{h}_α which is defined by $n_\alpha = \mathbf{f}^T \mathbf{h}_\alpha$ (as shown in Figure 3).

$$\mathbf{h}_\alpha^p = \mathbf{h}_\alpha, \quad \mathbf{h}_\alpha^b = \mathbf{h}_\alpha l_\alpha \theta_\alpha \quad (15)$$

And from Eq.(3), the yield function for a truss beam model can be expressed in the form

$$\Phi_\alpha(\mathbf{f}, \theta_\alpha) = \frac{|\mathbf{f}^T \mathbf{h}_\alpha|}{n_y} - \bar{\tau}_\alpha(\theta_\alpha) \leq 0 \quad (16)$$

The expression of Eq.(15) and Eq.(16) means that both plastic and buckling component rate are

proportional to the gradient of the yield surface. Namely the associate flow rule is satisfied in this model. It is noted that Eq.(12) is similar to the extended Koiter's form.

For simplicity, assume that the case that member's slenderness ratio is much less. In this case, the assumption that θ_α is approximately equal to θ_α^p is satisfied. Then the yield function of Eq.(16) can be rewritten in the form

$$\Phi_\alpha(\mathbf{f}, \lambda_\alpha^p) = \frac{|\mathbf{f}^T \mathbf{h}_\alpha|}{n_y} - \bar{\tau}_\alpha(\lambda_\alpha^p) \leq 0, \quad \bar{\tau}_\alpha(\lambda_\alpha^p) = \bar{\sigma}_\alpha(\lambda_\alpha^p) - \frac{n_y l_\alpha \theta_\alpha^p}{4m_p}, \quad \bar{\sigma}_\alpha(\lambda_\alpha^p) = \sqrt{1 + \left(\frac{n_y l_\alpha \theta_\alpha^p}{4m_p}\right)^2} \quad (17)$$

where $\bar{\tau}_\alpha$ is an effective yield stress. Consequently the above assumption enables to treat the elastoplastic buckling problem as the plastic problem with the hardening (softening) specified with Eq.(17-b). And the yield surface becomes to be so-called multi-surface in (M_i, M_j, N) space as Eq.(17-a) must be satisfied at $\alpha=1, \text{all}$. Here we introduce an effective plastic-buckling component $\tilde{\mathbf{u}}^{pb}$ which is defined by $\tilde{\mathbf{u}}^{pb} = \tilde{\mathbf{u}}^p + \tilde{\mathbf{u}}^b$ and $\dot{\tilde{\mathbf{u}}}^{pb} = \dot{\tilde{\mathbf{u}}}^p + \dot{\tilde{\mathbf{u}}}^b$. Substituting in the latter equation from Eq.(12) and comparing with Eq.(7) gives

$$\dot{\tilde{\mathbf{u}}}^{pb} = \sum_{\alpha=1}^{\text{all}} \frac{1}{n_y} \frac{\mathbf{f}^T \mathbf{h}_\alpha}{|\mathbf{f}^T \mathbf{h}_\alpha|} \mathbf{h}_\alpha \dot{\lambda}_\alpha^p \Leftrightarrow \sum_{\alpha \in \text{active}} \frac{1}{n_y} \frac{\mathbf{f}^T \mathbf{h}_\alpha}{|\mathbf{f}^T \mathbf{h}_\alpha|} \mathbf{h}_\alpha \dot{\lambda}_\alpha^p \quad \because \dot{\lambda}_\beta^p = 0 \quad \text{for} \quad \Phi_\beta < 0 \quad (18)$$

This equation is the plastic flow rule for the present method. Furthermore, the hardening (softening) coefficient can be calculated by

$$\dot{\bar{\tau}}_\alpha = \frac{\partial \bar{\tau}_\alpha}{\partial \theta_\alpha^p} \frac{\partial \theta_\alpha^p}{\partial \lambda_\alpha^p} \dot{\lambda}_\alpha^p = -\frac{n_\alpha l_\alpha}{16m_p^2} \frac{1}{\bar{\sigma}_\alpha(\theta_\alpha^p)^2} \dot{\lambda}_\alpha^p \quad (19)$$

The yield function, the plastic flow rule and the hardening (softening) property are clarified.

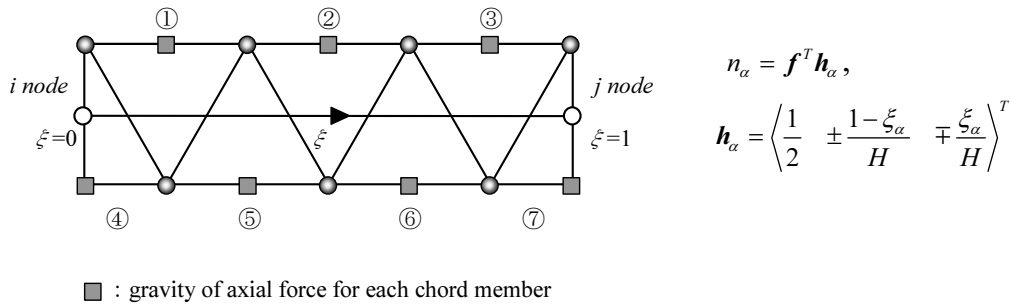


Figure 3. Local coordinate system

3.2 Consistent Tangent Stiffness Matrix

Since $\dot{\Phi}_\alpha = 0$ for $\alpha \in \text{active}$, substituting in it from Eq.(18) and Eq.(19),

$$\begin{aligned} \dot{\Phi}_\alpha &= \left\{ \frac{\partial \Phi_\alpha}{\partial \mathbf{f}} \right\}^T \dot{\mathbf{f}} - \frac{\partial \bar{\tau}_\alpha}{\partial \lambda_\alpha^p} \dot{\lambda}_\alpha^p = \frac{1}{n_y} \frac{n_\alpha}{|n_\alpha|} \mathbf{h}_\alpha^T \mathbf{k}^e \left\{ \dot{\tilde{\mathbf{u}}} - \dot{\tilde{\mathbf{u}}}^{pb} \right\} - \frac{\partial \bar{\tau}_\alpha}{\partial \lambda_\alpha^p} \dot{\lambda}_\alpha^p \\ &= \frac{1}{n_y} \frac{n_\alpha}{|n_\alpha|} \mathbf{h}_\alpha^T \mathbf{k}^e \left\{ \dot{\tilde{\mathbf{u}}} - \sum_{\beta \in \text{active}} \frac{1}{n_y} \frac{n_\beta}{|n_\beta|} \mathbf{h}_\beta \dot{\lambda}_\beta^p \right\} - \frac{\partial \bar{\tau}_\alpha}{\partial \lambda_\alpha^p} \dot{\lambda}_\alpha^p = 0 \end{aligned} \quad (20)$$

Then we have the simultaneous equations respect to $\dot{\lambda}_\alpha$ as follows;

$$\sum_{\beta \in \text{active}} G_{\alpha\beta} \dot{\lambda}_\beta^p = \frac{1}{n_y} \frac{n_\alpha}{|n_\alpha|} \mathbf{h}_\alpha^T \mathbf{k}^e \dot{\tilde{\mathbf{u}}} \quad \text{for} \quad \alpha \in \text{active} \quad (21)$$

$$\text{where} \quad G_{\alpha\beta} = \frac{1}{n_y^2} \frac{n_\alpha}{|n_\alpha|} \frac{n_\beta}{|n_\beta|} \mathbf{h}_\alpha^T \mathbf{k}^e \mathbf{h}_\beta - \frac{n_\alpha l_\alpha}{16m_p^2 \bar{\sigma}_\alpha^2} \delta_{\alpha\beta} \quad \delta_{\alpha\beta} : \text{kroncker's delta symbol} \quad (22)$$

By solving this simultaneous equation, we can find the plastic consistency parameter $\dot{\lambda}_\alpha$.

$$\dot{\lambda}_\alpha^p = \frac{1}{n_y} \sum_{\beta \in active} G^{\alpha\beta} \frac{n_\beta}{|n_\beta|} \mathbf{h}_\beta^T \mathbf{k}^e \dot{\tilde{\mathbf{u}}} \quad (23)$$

where $G_{\alpha\beta}$ is the inverse of $G^{\beta\alpha}$. And from the nodal force rate the consistent tangent stiffness matrix \mathbf{k}^{epb} is given

$$\dot{\mathbf{f}} = \left[\mathbf{k}^e - \frac{1}{n_y} \sum_{\alpha \in active} \sum_{\beta \in active} \frac{n_\alpha}{|n_\alpha|} \frac{n_\beta}{|n_\beta|} G^{\alpha\beta} (\mathbf{k}^e \mathbf{h}_\alpha) \otimes (\mathbf{k}^e \mathbf{h}_\beta) \right] \dot{\tilde{\mathbf{u}}} \equiv \mathbf{k}^{epb} \dot{\tilde{\mathbf{u}}} \quad (24)$$

where \otimes signifies tensor product.

3.3 Numerical implementation to calculate nodal force vector

The present calculation method of a nodal force vector belongs to the Return Mapping Algorithm for the Multi-surface yield function (Simo et al.(1988)). The values of ${}^t \tilde{\mathbf{u}}^p$, ${}^t \lambda_\alpha^p$ and ${}^t \theta_\alpha^p$ in the configuration at $t=t$ and ${}^{t+\Delta t} \tilde{\mathbf{u}}$ at $t=t+\Delta t$ are assumed to be known.

Elastic predictor : Any incremental plastic deformation is frozen; $\Delta \tilde{\mathbf{u}}^{pb} = \mathbf{0}$, ${}^{trial} \tilde{\mathbf{u}}^{pb} = {}^t \tilde{\mathbf{u}}^{pb}$, $\Delta \lambda_\alpha^p = 0$, ${}^{trial} \lambda_\alpha^p = {}^t \lambda_\alpha^p$, ${}^{trial} \theta_\alpha^p = {}^t \theta_\alpha^p$. By using these values, trial values can be calculated by

$${}^{trial} \mathbf{f} = \mathbf{k}^e ({}^{t+\Delta t} \tilde{\mathbf{u}} - {}^{trial} \tilde{\mathbf{u}}^{pb}), \quad {}^{trial} \bar{\tau}_\alpha = \sqrt{1 + \frac{n_y^2 l_\alpha^2 ({}^{trial} \theta_\alpha^p)^2}{16 m_p^2} - \frac{n_y l_\alpha ({}^{trial} \theta_\alpha^p)}{4 m_p}} \quad (25)$$

Thus, the trial value of the yield function is given by

$${}^{trial} \Phi_\alpha ({}^{trial} \mathbf{f}, {}^{trial} \theta_\alpha^p) = \frac{|{}^{trial} \mathbf{f}^T \mathbf{h}_\alpha|}{n_y} - {}^{trial} \bar{\tau}_\alpha \quad (26)$$

If ${}^{trial} \Phi_\alpha$ is greater than zero, then the plastic corrector must be execute since the rotary spring is in plastic loading. Otherwise, it is in elastic state including unloading state.

Plastic corrector : The stress by the actual plastic deformation is relaxed. The value of the nodal force vector and the effective yield stress at $t=t+\Delta t$ can be rewritten in the form

$${}^{t+\Delta t} \mathbf{f} = {}^{trial} \mathbf{f} - \mathbf{k}^e \Delta \tilde{\mathbf{u}}^{pb}, \quad {}^{t+\Delta t} \bar{\tau}_\alpha = \sqrt{1 + \frac{n_y^2 l_\alpha^2 ({}^{trial} \theta_\alpha^p + \Delta \theta_\alpha^p)^2}{16 m_p^2} - \frac{n_y l_\alpha ({}^{trial} \theta_\alpha^p + \Delta \theta_\alpha^p)}{4 m_p}} \quad (27)$$

Inserting Eq.(27) into the yield function gives the nonlinear simultaneous equations with respect to $\Delta \lambda_\alpha^p (\alpha \in active)$. Then we solve them by Newton method.

$$\begin{aligned} & {}^{t+\Delta t} \Phi_\alpha \cong {}^{t+\Delta t} (k) \Phi_\alpha + \sum_{\beta \in active} \frac{\partial {}^{t+\Delta t} \Phi_\alpha}{\partial \Delta \lambda_\beta^p} \delta \Delta \lambda_\beta^p \\ & = {}^{t+\Delta t} (k) \Phi_\alpha - \sum_{\beta \in active} \left(\frac{1}{n_y} \frac{{}^{t+\Delta t} (k) n_\alpha}{{}^{t+\Delta t} (k) |n_\alpha|} \frac{{}^{t+\Delta t} (k) n_\beta}{{}^{t+\Delta t} (k) |n_\beta|} \mathbf{h}_\alpha^T \mathbf{k}^e \mathbf{h}_\beta - \frac{{}^{t+\Delta t} (k) n_\alpha l_\alpha}{{}^{t+\Delta t} (k) \bar{\sigma}_\alpha^2} \delta_{\alpha\beta} \right) \delta \Delta \lambda_\beta^p \end{aligned} \quad \text{for } \alpha \in active \quad (28)$$

Solving these linear equations and updating each values.

$${}^{t+\Delta t} (k+1) \tilde{\mathbf{u}}^{pb} = {}^{t+\Delta t} (k) \tilde{\mathbf{u}}^{pb} + \sum_{\alpha \in active} \frac{1}{n_y} \frac{{}^{t+\Delta t} (k) n_\alpha}{{}^{t+\Delta t} (k) |n_\alpha|} \mathbf{h}_\alpha \delta \Delta \lambda_\alpha^p, \quad {}^{t+\Delta t} (k+1) \theta_\alpha^p = {}^{t+\Delta t} (k) \theta_\alpha^p + \frac{{}^{t+\Delta t} (k) n_\alpha}{|{}^{t+\Delta t} (k) n_\alpha|} \frac{1}{4 m_p (k) \bar{\sigma}_\alpha} \delta \Delta \lambda_\alpha^p \quad (29)$$

$${}^{t+\Delta t} (k+1) \mathbf{f} = \mathbf{k}^e ({}^{t+\Delta t} \tilde{\mathbf{u}} - {}^{t+\Delta t} (k+1) \tilde{\mathbf{u}}^{pb}), \quad {}^{t+\Delta t} (k+1) n_\alpha = {}^{t+\Delta t} (k+1) \mathbf{f}^T \mathbf{h}_\alpha, \quad {}^{t+\Delta t} (k+1) \bar{\tau}_\alpha = \sqrt{1 + \frac{n_y^2 l_\alpha^2 ({}^{t+\Delta t} (k) \theta_\alpha^p)^2}{16 m_p^2} - \frac{n_y l_\alpha ({}^{t+\Delta t} (k) \theta_\alpha^p)}{4 m_p}} \quad (30)$$

where lower index (k) signified iteration number. Repeat these calculations until $|{}^{t+\Delta t} (k+1) \Phi_\alpha| \leq Tolerance$.

4. NUMERICAL EXAMPLES

Finally we show two numerical examples in Figure 4 and Figure 5 to valid the present method. One example is subjected to monotonic loading and another is subjected to cyclic loading. The present results are calculated with only one element, and another is done with the model of which chords are divided by 10 elastoplastic beam elements. The mechanical properties of analytical model: Truss length; 34.6m, Height; 10m, Slenderness ratio of chord members; 40 (partially 20). The material properties: Young’s modulus; 206GPa, Elastic-perfectly plastic material, Yield stress; 235MPa. Two equilibrium paths are close and this means the present method is valid.

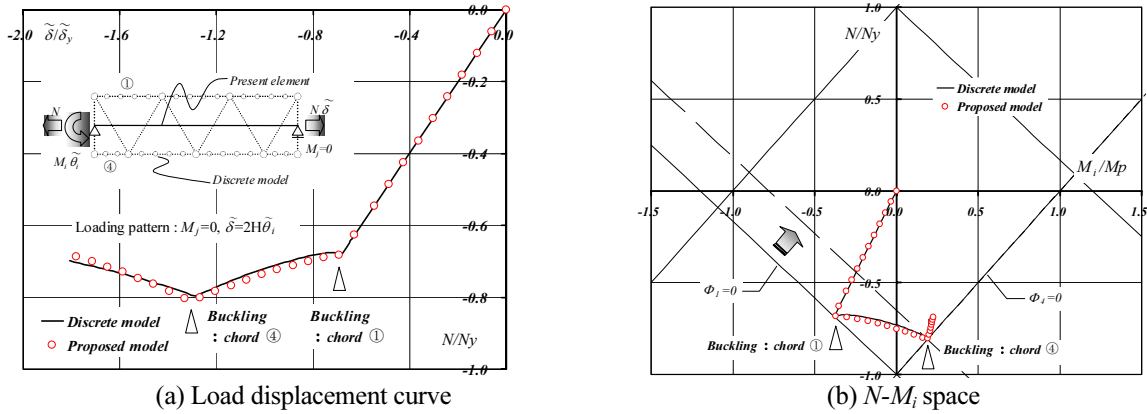


Figure 4 Numerical results (monotonic loading)

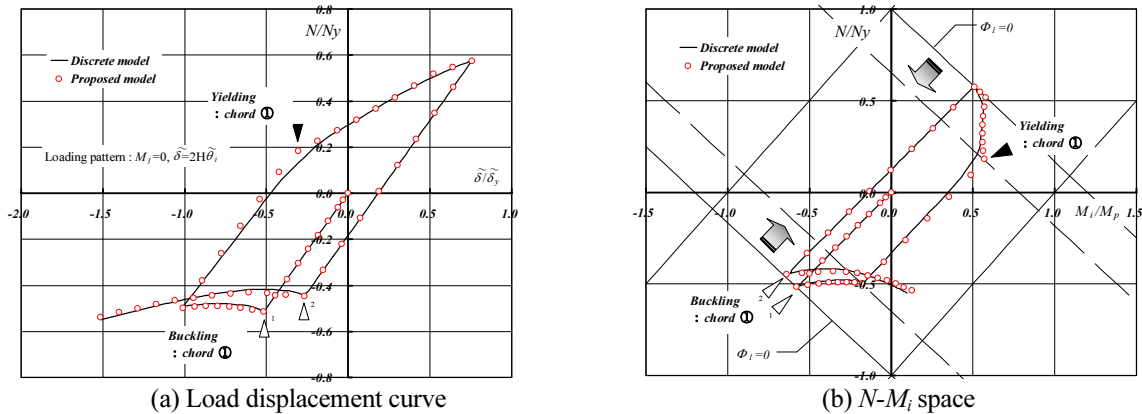


Figure 5 Numerical results (cyclic loading)

5. CONCLUSIONS

In this paper, we described the consistent and convenient analytical method to simulate truss beam problems including with the elastoplastic buckling behavior of chord members, and clarified that such problems reduce to the pure elastoplastic problem under the condition that a chord member’s slenderness ration is much less. Furthermore the validity of the present method was examined through the numerical examples.

References:

Simo, J. C., Kennedy, J. G., Govindjee , S., “Non-smooth Multisurface Plasticity and Viscoplasticity. Loading/Unloading Conditions and Numerical Algorithms”, International Journal of Numerical Methods in Engineering, 1988, Vol.26, pp.2161-2185

Motoyui, S., Ohtsuka, T., “Consistent and Convenient Analytical Method for Elastoplastic Buckling Problem of Compression Members”, ASCS01 Proceedings, 2000, Vol.II, pp.969-976, Seoul, Korea.

Motoyui, S., Ohtsuka, T., “ Analytical Method for Elasto-plastic Behavior of Truss Girder Based on the Theory of Plasticity”, Journal of Structural and Construction Engineering (Transaction of Architectural Institute of Japan), 2000, No.538, pp.109-114(in Japanese).

ENHANCEMENT OF FLEXURAL DUCTILITY OF REINFORCED CONCRETE BRIDGE COLUMNS

K. Kawashima

Professor, Department of Civil Engineering, Tokyo Institute of Technology, Japan
kawasima@cv.titech.ac.jp

Abstract: This paper introduces some new technologies aiming of enhancing the seismic performance of reinforced concrete bridge columns. Introduced are the interlocking spiral columns with a large cross section, effect of unbonding of longitudinal bars at the plastic hinge, prestressed concrete columns, and an isolator built-in column. Although they are still in the research and preliminary implementation stage, it is expected to extend the new technology into practice.

1. INTRODUCTION

The extensive damage to bridges during the recent earthquakes in Northridge, USA (1994), Kobe, Japan (1995), Chi-Chi, Taiwan (1999), and Kocaeli and Duzce, Turkey (1999), revealed the vulnerability of bridges under extreme ground motions. A number of bridges suffered extensive damage as a result of the insufficient shear strength and ductility capacity of reinforced concrete columns. Based on the lessons from the recent earthquakes, the seismic design methodology was extensively revised worldwide.

Since the enhancement of reinforced concrete piers/columns was one of the most important aspects in the revision of the seismic design codes, various unique technical developments for reinforced concrete columns with verification through loading tests have been conducted. Several new technologies are presented in this paper. Although most of them are still in the research stage, it is important to extend the current technology.

2. INTERLOCKING SPIRAL COLUMNS WITH LARGE CROSS SECTIONS

Interlocking columns have been extensively implemented in New Zealand, USA and other countries (Tanaka and Park 1993, Priestley et al 1996). The interlocking spirals confine the core concrete to enhance the ductility of reinforced concrete columns. Prior to the 1995 Kobe earthquake, spirals were not used in Japan because rectangular columns were generally preferred and because column diameters are generally larger. Since the 1995 Kobe earthquake, the interlocking spiral columns have been recommended in the design codes (Japan Road Association 1996 and 2002), and various studies have been conducted (Yagishita et al 1997, Fujikura et al 2000).

Interlocking spiral columns with large sections were constructed at Kamanashi bridge. Each column consists of 2 spirals with a diameter of 6 m and is 8.5 m wide and 6 m long in the transverse and the longitudinal directions, respectively. Since these columns were much larger in size than the interlocking columns which had ever been constructed elsewhere, a unique experimental test was

conducted by the Japan Highway Public Corporation (JH) in conjunction with the construction of the bridge. Since assemblage of the interlocking spirals requires a special skill, an onsite assemblage test of large diameter interlocking spirals was conducted (Shito et al 2002).

In the cyclic loading test, several model columns with interlocking spirals were loaded independently in the transverse and the longitudinal directions. The model columns were 2.7 m tall (effective column height) and 900 mm wide and 600 mm long in the transverse and longitudinal directions, respectively. They consisted of two spirals with a diameter of 600 mm. They were about 1/10 geometrically scaled models. The concrete strength was 28.1-39.7 MPa. The volumetric tie reinforcement ratio was varied 0.19%, 0.29% and 0.52% with the longitudinal reinforcement ratio being 1.63%. A 900 mm wide and 600 mm long standard rectangular column was also constructed for comparison. In addition to ties, cross ties were laterally spaced at every 158-196 mm interval in the standard rectangular column. The concrete strength of the rectangular column was 39.8 MPa. The longitudinal reinforcement ratio was 1.18% and the volumetric tie reinforcement ratio including the cross ties was 0.88%.

Fig. 1 compares the lateral force vs. lateral displacement hysteresses of the interlocking spiral column (volumetric tie reinforcement ratio is equal to 0.29%) and the standard rectangular column under a cyclic loading in the longitudinal direction. The lateral restoring force is stable until 4.5% drift in the rectangular column, while it is stable until 5% drift in the interlocking spiral column. A similar test was conducted to verify that the interlocking columns exhibit stable hysteresis under a cyclic loading in the transverse direction.

Since the diameter of the interlocking spirals is large at Kamanashi bridge, an onsite assemblage test of the interlocking spirals was conducted, using a 4.5 m wide and 3 m long column consisting of two interlocking spirals with a diameter of 3 m. Two spirals were interlocked after being hung separately using a balanced lever, and they were set in position from the top of longitudinal bars. The spirals were temporally fixed to hanging cables so that they were set with an expected vertical interval. This construction procedure was successfully implemented on the interlocking column.

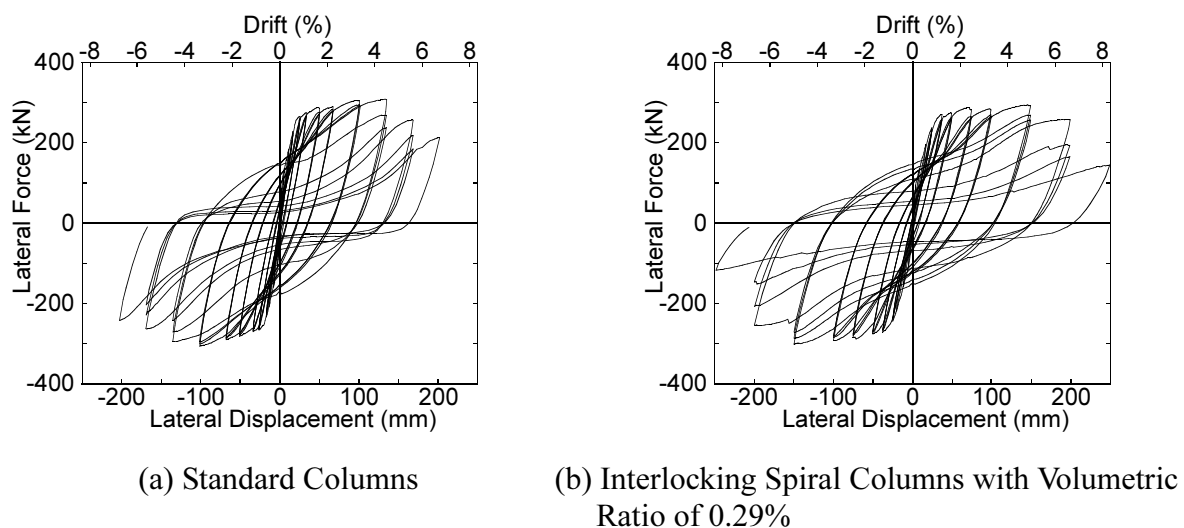


Fig. 1 Effect of Interlocking Spirals

3. UNBONDING OF LONGITUDINAL BARS AT THE PLASTIC HINGE

In a reinforced concrete column, damage of the longitudinal bars progress from local bucklings to rupture in the plastic hinge under an extreme earthquake excitation. The bond between the longitudinal bars and the concrete results in the concentration of damage to the longitudinal bars at a specific localized interval where the local buckling occurs.

One of the measures of mitigating such a concentration of damage to the longitudinal bars is to unbond the longitudinal bars from the concrete at the plastic hinge (Takiguchi et al 1976). By appropriately unbonding the longitudinal bars at the plastic hinge region with a length L_{ub} as shown in Fig. 2, the deformation of the longitudinal bars may be reduced by avoiding the concentration of strain as a result of averaging the strain in the interval L_{ub} . The unbonding may be achieved by wrapping the longitudinal bars with plastic materials. Protection is required for corrosion of the unbonded longitudinal bars.

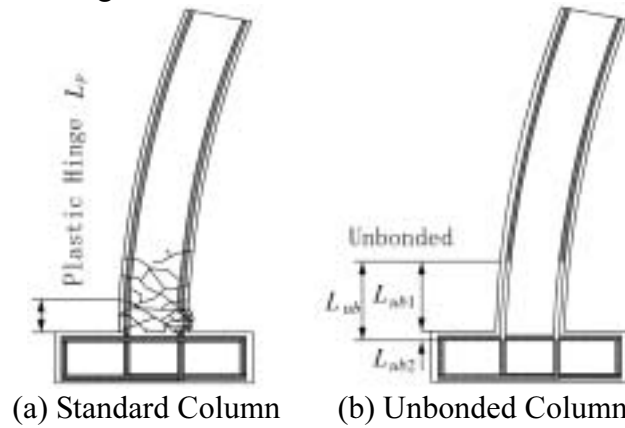


Fig. 2 Unbonding of Longitudinal Bars

Fig. 3 shows the effect of unbonding the longitudinal bars in a 1.45 m tall square column with a width D equal to 400 mm (Kawashima et al 2001). Although several tests were conducted, only two cases are presented here. The concrete strength was 24 MPa. The longitudinal reinforcement ratio was 0.95%, and the volumetric tie reinforcement ratio was 0.77%. The longitudinal bars were unbonded within a distance equivalent to the column width D . In the standard column, the covering concrete started to significantly spall off at $8\delta_y$, in which δ_y is the yield displacement of the standard column. Since δ_y is equal to 6 mm, 1% drift corresponds to $2.3\delta_y$. The column was cyclically loaded 3 times at each loading displacement δ_y , $2\delta_y$, $3\delta_y$, ..., until failure. The same loading hysteresis was used for both the standard and the unbonded columns.

The concrete failed within about 200 mm from the bottom after $11\delta_y$ (=4.8% drift) in the standard column. On the other hand, the failure of concrete was much less in the unbonded column than the standard column. The covering concrete failed no higher than 120 mm from the bottom even after $13\delta_y$ (=5.7% drift). The strain measured at 25 mm from the bottom built up over the yield strain at the first load excursion of $2\delta_y$. On the other hand, the strain on a longitudinal bar that was unbonded within a length of D was much smaller than the strain on a longitudinal bar in the standard column. The strains were similar, although not the same, at 25 mm and 175 mm from the bottom in the longitudinal bar in the unbonded column. The strains on the longitudinal bars became larger than $6,000\mu$ at 25 mm and 175 mm from the bottom at the first excursion of $2\delta_y$ and $3\delta_y$ loadings, respectively.

An important feature of the unbonded column is a rocking response of the column relative to the footing. Since the longitudinal bars were unbonded within a length of L_{ub} , the longitudinal bars in tension pulled out from the column, which resulted in a dominant rocking response of the column. As a result of the small flexural deformation, the flexural failure of the column was limited.

Fig. 4 compares the lateral force vs. lateral displacement hystereses. The restoring force of the standard column started to deteriorate at $9\delta_y$ (=3.9% drift), while the restoring force was stable until $11\delta_y$ (=4.8% drift) in the unbonded column.

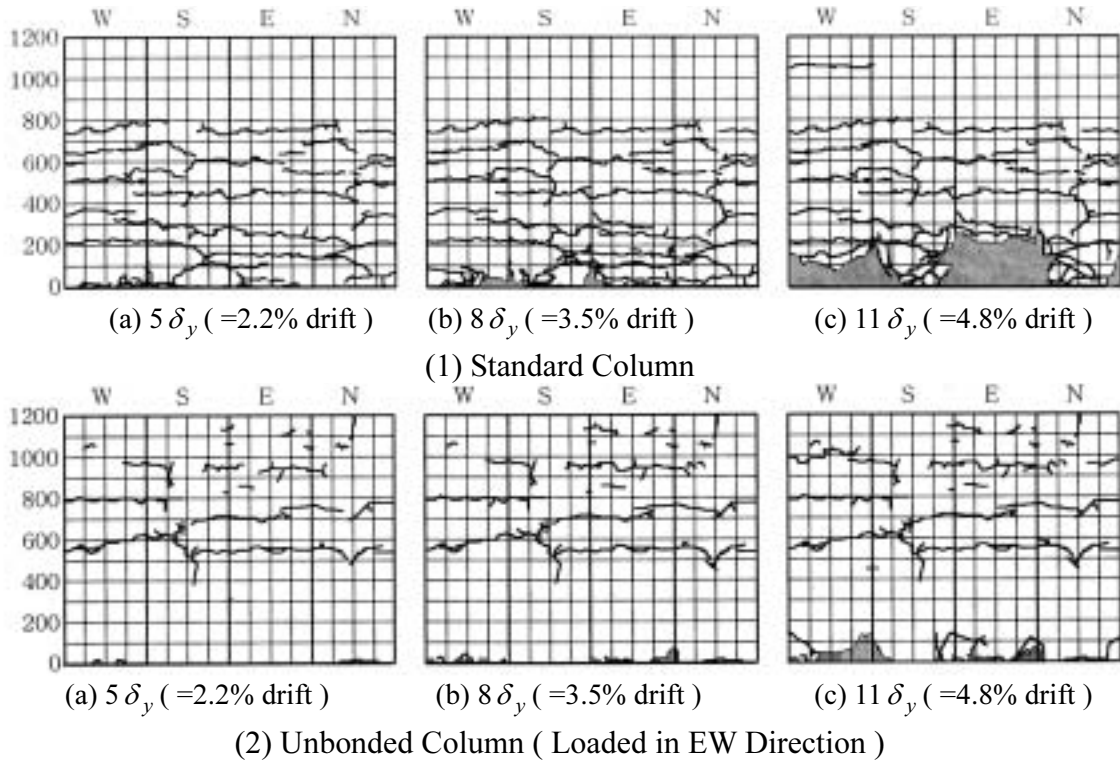


Fig. 3 Progress of Damage

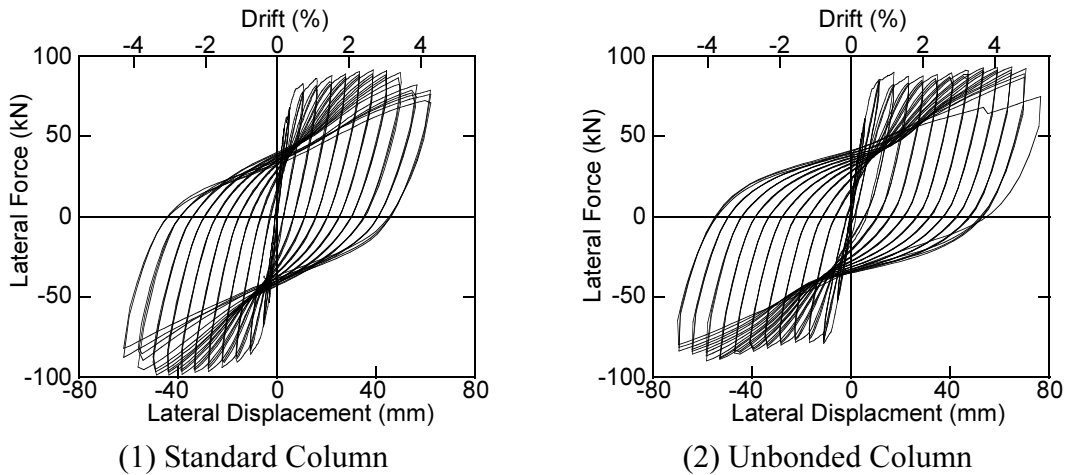


Fig. 4 Lateral Force vs. Lateral Displacement Hystereses

As a result of the deformation of the unbonded longitudinal bars in the plastic hinge, the initial lateral stiffness is slightly smaller in the unbonded column than the standard column. Fig. 5 compares the equivalent lateral stiffness and the accumulated energy dissipation between the unbonded and standard columns. The equivalent lateral stiffness is defined here as the secant stiffness between the maximum and minimum displacements in a hysteresis loop at each loading displacement. Although the equivalent lateral stiffness is slightly smaller in the unbonded column than the standard column when the lateral displacement is smaller than 1% drift, the difference between the two columns becomes small as the lateral displacement increases. This is due to the larger deterioration of the standard column. The difference of the accumulated energy dissipation between the two columns is negligible.

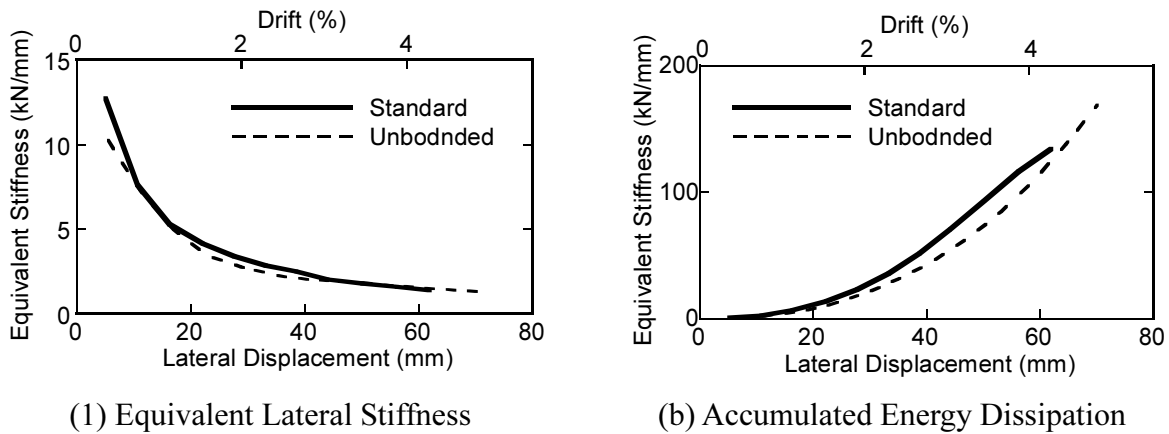


Fig. 5 Equivalent Lateral Stiffness and Energy Dissipation

Although the longitudinal bars were unbonded in the plastic hinge of the column in the above example, it is feasible to unbond the longitudinal bars in the footing or partly above and below the footing. Similar results were obtained by unbonding the longitudinal bars inside a footing (Hoshikuma et al 2000).

Based on the studies, it is considered that the unbonding is an effective means to increase the ductility capacity of columns by properly choosing the unbond length L_{ub} .

4. PRESTRESSED CONCRETE COLUMNS

It is well known that prestressed concrete members exhibit stable seismic performance under a combined action of shear and flexure. Consequently, it is anticipated that the flexure and the shear capacities can be enhanced in the prestressed concrete columns in comparison to the standard reinforced concrete columns. It is also anticipated that residual displacements after an extreme earthquake may be smaller in prestressed concrete columns than reinforced concrete columns. It is expected to reduce construction periods by using precast concrete segments.

However, the prestressed concrete columns have been seldom constructed throughout the world in spite of their merits. Lack of practice and possible cost increase may be the reasons for limiting the implementation of prestressed concrete columns. It is also sometimes pointed out that the energy dissipation is less in prestressed concrete columns than reinforced concrete columns because fewer concrete cracks dissipate less energy.

To verify the seismic performance of prestressed concrete columns, an extensive experimental and analytical study was conducted (Ikeda 1998, Ikeda et al 1998, Mutsuyoshi et al 2001). In the loading test, rectangular prestressed concrete columns with an effective height of 1.5 m and a section of 400 mm by 400 mm were constructed. The concrete strength, the prestress and bond/unbond of the PC cables were studied as parameters.

Fig. 6 shows the effectiveness of the prestressed concrete columns in terms of the lateral force vs. lateral displacement hysteresis. The columns were subjected to an axial load (dead load of the superstructure) equivalent to 1MPa, and the prestress was either 4 or 8 MPa. They failed in flexure. The hysteresis of a standard reinforced concrete column is also presented here for comparison. A remarkable feature of the prestressed concrete columns is the rest-position oriented unloading hysteresees. If one defines the unloaded residual displacement as a residual lateral displacement of a column when the lateral force is equal to zero after unloaded from a maximum lateral displacement, then the unloaded residual displacement is significantly smaller in the prestressed concrete columns than the standard reinforced concrete column. Fig. 7 shows how the unloaded residual displacement decreases as the prestress increases in the prestressed concrete columns. It is obvious from a

nonlinear dynamic response analysis that the limited unloaded residual displacement contributes to reduce the residual displacement of a bridge after an extreme earthquake. This contributes to satisfy the requirement of residual drift after an earthquake (Kawashima et al 1998, Japan Road Association 1996 and 2002).

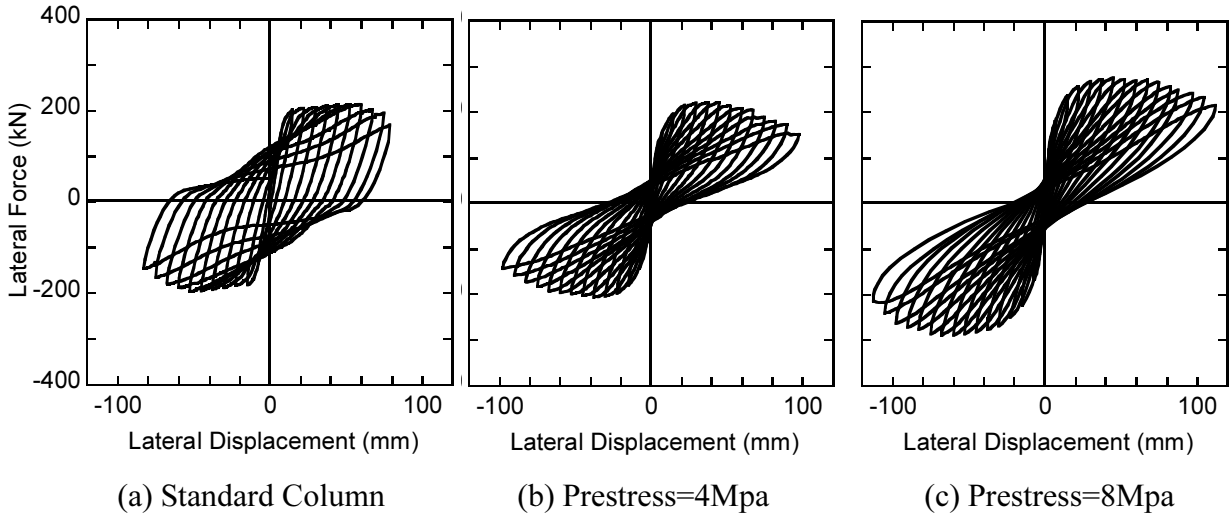


Fig. 6 Effect of Prestressing on the Hysteretic Behavior [Ikeda 1998, Ikeda et al 1998]

Number and size of concrete cracks were smaller in the prestressed columns than the standard reinforced concrete column during the loading and unloading reversals. The restoring force remarkably decreases when longitudinal bars locally buckle in the standard reinforced concrete, while such a remarkable deterioration of restoring force does not occur in the prestressed columns. Fig. 8 shows that the accumulated energy dissipation normalized by the peak restoring forces is smaller in the prestressed columns than the standard reinforced concrete columns as anticipated inherent to the rest-position oriented hysteretic behavior. This effect has to be considered in design based on the total response of a bridge system.

From the study, various merits of certain prestressed concrete columns were found. Those merits support the implementation of prestressed concrete columns.

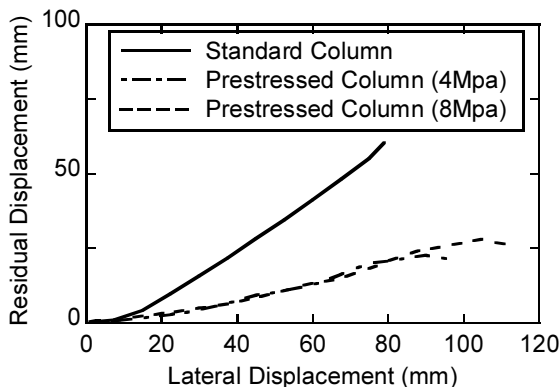


Fig. 7 Effect of Prestressing on the Residual Displacement of Unloaded Columns [Ikeda 1998, Ikeda et al 1998]

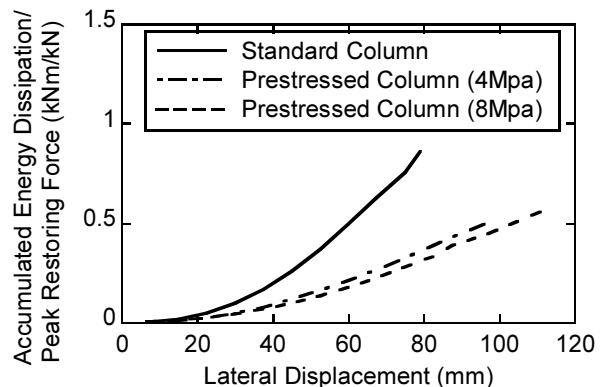


Fig. 8 Effect of Prestressing on the Accumulated Energy Dissipation/Peak Restoring Force [Ikeda 1998, Ikeda et al 1998]

5. ISOLATOR BUILT-IN COLUMNS

Since the hysteretic behavior of a reinforced concrete column occurs only at the plastic hinge, it is interesting to replace the concrete in the plastic hinge by an appropriate material that provides enough deformation and energy dissipation so that the flexural deformation in the rest of a column is limited. The material has to be sufficiently softer than the reinforced concrete column in order to reduce the flexural deformation of the column. By appropriately choosing the stiffness and strength of the material, it is expected that the reinforced concrete column at the plastic hinge becomes free from damage under an extreme earthquake excitation. Several efforts have been already initiated for such a purpose. The major technical importance is what material should be used for the replacement of reinforced concrete at the plastic hinge. It must be sufficiently stable under repeated seismic loading with large strains, and durable for long term use. It is preferable if energy dissipation is available associated with the deformation of the material.

A material studied is a high damping rubber that is used for standard high damping rubber bearings for seismic isolation. The high damping rubber meets several requirements described above. The high damping rubber may be provided in the form of a rubber block or a laminated rubber. If one sets a high damping rubber unit at the bottom of a cantilever column, the column deforms as shown in Fig. 9 under a lateral seismic force. The longitudinal bars are continuous through the rubber unit. Prestressed tendons may be effective to prevent a sudden deterioration of the restoring force and decrease the residual displacement.

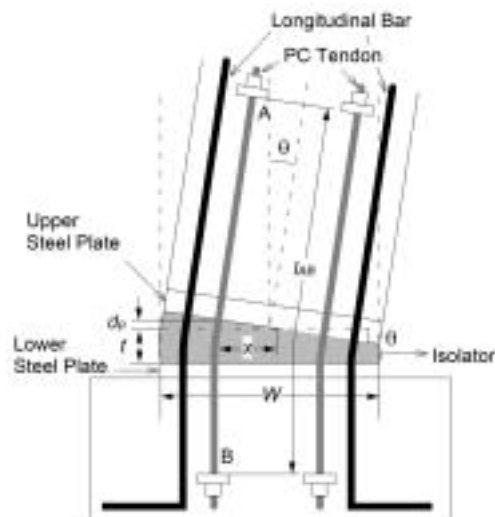


Fig. 9 Isolator Built-in Column

The rubber unit does not resist tension if it is not anchored to the column and the footing. Since contact of the rubber unit with the column and the footing is limited if the rubber unit is not anchored to the column and the footing, slippage and rotation of the column relative to the footing occurs once the longitudinal bars yield under a cyclic lateral loading. Hence, the upper and lower steel plates which are galvanized to the rubber unit are anchored to the column and the footing by anchor bolts. The longitudinal bars need to be continuous through holes in the steel plates and the rubber unit.

Laminated rubber units may be used if the rubber unit is thick. The steel plates in the laminated rubber unit may prevent the local buckling of the longitudinal bars when they are subjected to alternative tension and compression. Shear-keys may be required to prevent an excessive lateral displacement of the column relative to the footing when the rubber unit is thick. Since such a column is nearly equivalent to a built-in high damping rubber isolator, it is called here an *isolator built-in column* (Kawashima and Nagai 2002, Yamagishi and Kawashima 2004).

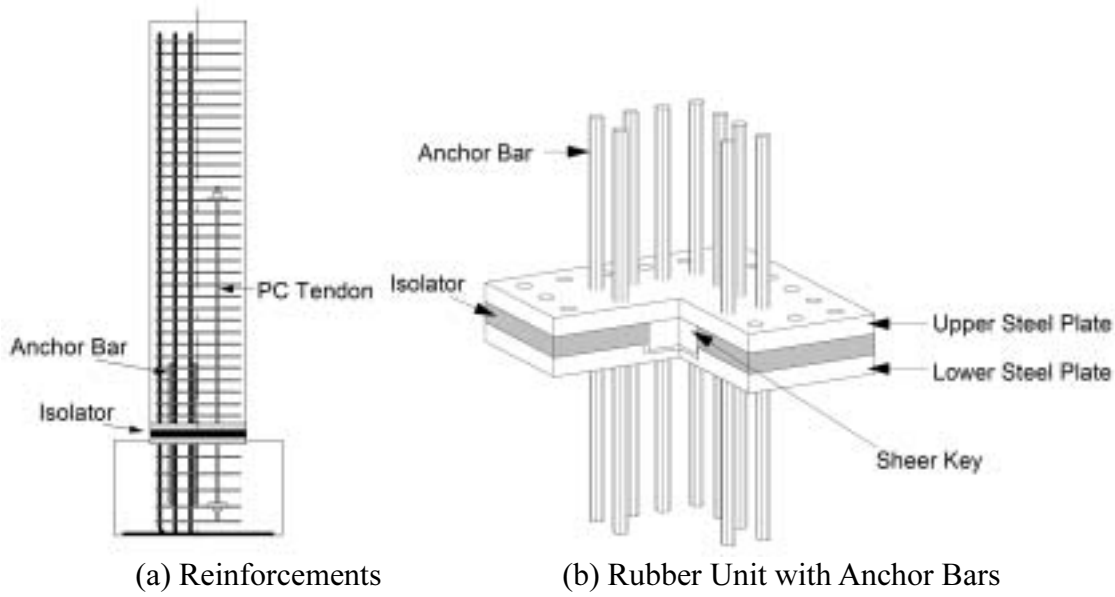


Fig. 10 Model Columns

A difficult barrier of the isolator built-in column is the deformation of the longitudinal bars. As a consequence that the column is supported by a flexible rubber unit, the longitudinal bars in the rubber unit are subjected to compression due to the self-weight of the structure. The longitudinal bars in the rubber unit are also subjected to repeated tension and compression with larger strain amplitude than a standard reinforced concrete column under an extreme earthquake excitation. Hence, it is likely that the longitudinal bars locally buckle and rupture in the rubber unit. Consequently a special attention has to be paid to prevent the premature failure of the longitudinal bars in the rubber unit. Use of special steels with the enhanced ductility may be effective.

If the stiffness of the rubber unit is sufficiently smaller than the stiffness of the column, major deformation under a lateral seismic force occurs in the rubber unit with the deformation of the column being limited. This results in the rocking response of the column similar to the unbonded column. Representing a rotation of the column as θ , the lateral displacement of the column at the top is $H \cdot \theta$ under a lateral force, in which H represents the column height. Since the drift $d_r \approx H \cdot \theta / H = \theta$, if one expects to have stable response of the column until a drift of d_r , the strain at the compression fiber of the rubber unit ε_r is

$$\varepsilon_r = \frac{\alpha W}{t} \theta \quad (1)$$

where W is the column width, t is the thickness of the rubber unit, and α is defined as $\alpha = x/W$ in which x is the distance from the neutral axis to the compression fiber. Since the rubber unit shows the extensive strain hardening under high compression, its effect has to be included in the evaluation of stress $\sigma_r = f(\varepsilon_r)$ corresponding to the strain by Eq. (1). Deformation characteristics of rubber units under high compression as high as 120 MPa was studied to determine $f(\varepsilon_r)$.

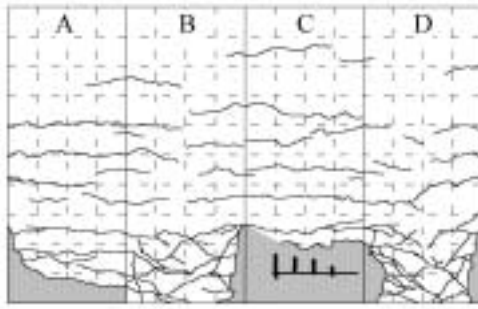
Consequently, the following relation has to be satisfied to avoid failure of concrete of the column

$$\sigma_r < \sigma_{cc} \quad (2)$$

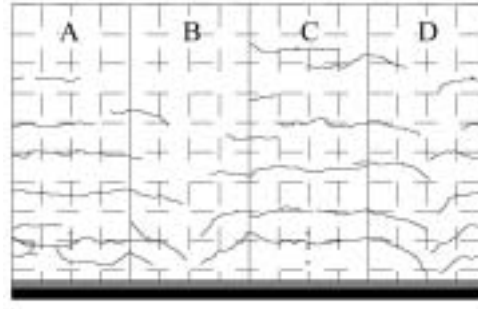
where σ_{cc} represents the concrete strength.

On the other hand, from Eq. (1), the rubber unit must be thicker than the following value so that it is stable under the repeated compression corresponding to the lateral drift d_r .

$$t_{\min} > \frac{\alpha W}{\varepsilon_r} \cdot d_r \quad (3)$$

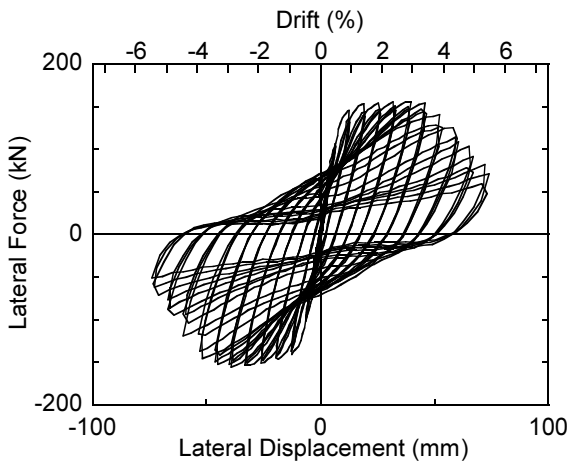


(a) Standard Column

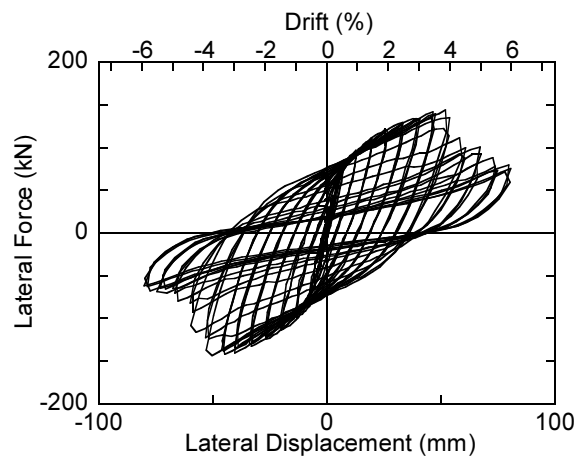


(b) Isolator Built-in Column

Fig. 11 Failure of Columns after 4% Drift (Loaded in AC Direction)



(a) Standard Column



(b) Isolator Built-in Column

Fig. 12 Lateral Force vs. Lateral Displacement Hystereses

A series of seismic loading tests was conducted to verify the performance of the isolator built-in columns. Constructed were 1350mm tall (effective height) model columns with a 400mm by 400mm rectangular section as shown in Fig. 10. They were designed so that the hystereses are stable until 4% drift. As a consequence, 30 mm and 60 mm thick damping rubber units were used with an initial shear modulus of 1.2 MPa. Those rubber units are often used for seismic isolators in bridges. The longitudinal reinforcement ratio was 1.58%, and the volumetric tie reinforcement ratio was 0.79%. A shear-key was provided at the center, and four prestressed tendons were provided at the four corners.

Fig. 11 compares the failure of the isolator built-in column and the standard column after 4% drift loadings. Extensive failure of the concrete occurs until 4% drift at the compression fiber in the standard column. The longitudinal bars start to rupture at 5.5% drift, which results in the significant deterioration of restoring force. On the other hand, the failure of concrete is much limited in the isolator built-in column until 4% drift. However the longitudinal bars start to rupture in the rubber unit at 4.5% drift. The use of ductile steel is required to mitigate the rupture of the longitudinal bars as a result of concentration of strain at the bars in the rubber unit.

Fig. 12 compares the lateral force vs. lateral displacement relations of the two columns. A remarkable change of the shape of the hysteresis loops is seen. The lateral force is almost the constant in the post-yield zone in the standard column, while it increases as the lateral displacement increases in the isolator built-in column. The extensive deterioration of the restoring force at 4.5% drift results from the rupture of longitudinal bars in the isolator built-in column. An important difference of the isolator built-in column is the smaller initial stiffness, as shown in Fig. 13 (a), due

to the soft deformation of the rubber unit. However, since the stiffness of the standard column deteriorates due to failure of the concrete, the lateral stiffness of the standard column becomes close to that of the isolator built-in column over 2.5% drift. The energy dissipation per load reversal is nearly the same between the isolator built-in column and the standard column as shown in Fig. 13 (b).

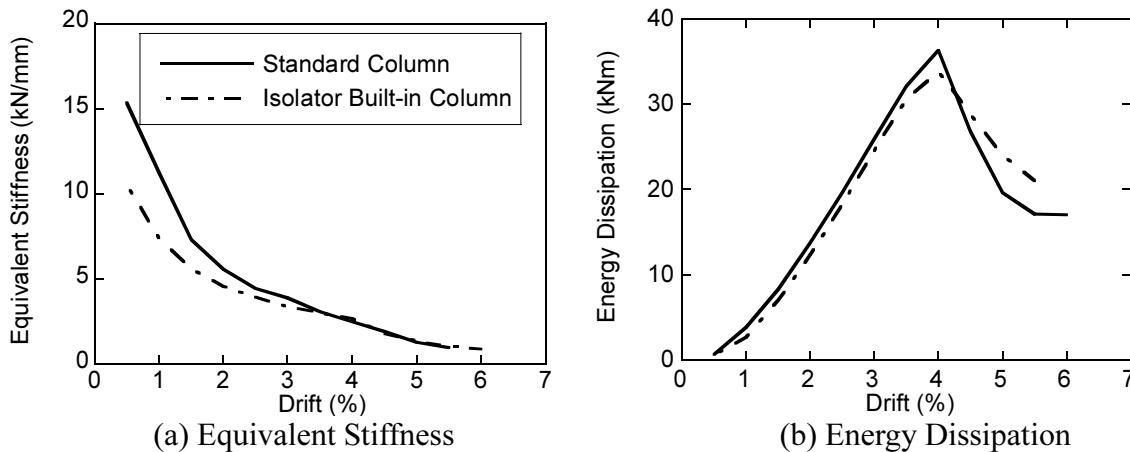


Fig. 13 Effect of Isolator on the Equivalent Stiffness and Energy Dissipation

6. CONCLUDING REMARKS

The preceding pages introduced some new attempts to enhance the ductility capacity of reinforced concrete columns. It is noted that they are only a part of the efforts, and that many other practical and effective measures are being developed. Since 1995, the seismic design practice has extensively changed based on the technical development conducted in the last two decades. It was the major lesson of the recent earthquakes that it is important to have an insight to hold account in great un-experienced damage of bridges in the past.

Acknowledgements:

The author expresses his sincere appreciation to Professor Katsuki Takiguchi for introducing the concept of unbonding longitudinal bars. The author also expresses his sincere appreciation to Dr. Shoji Ikeda, Professor Emeritus, Yokohama National University, Mr. Yoshinori Igase, Japan Highway Public Corporation, and Mr. Takuya Mori, PS Concrete for providing him with the variable information and materials.

References:

- Fujikura, S., Kawashima, K., Shoji, G., Jiandong, Z. and Takemura, H. (2000) "Effect of the interlocking ties and cross ties on the dynamic strength and ductility of rectangular reinforced concrete bridge piers," *Structural and Earthquake Engineering, Proc. JSCE*, No. 640/I-50, 71-88.
- Hoshikuma, J., Unjoh, S., and Nagaya, K. (2000) "Experimental study for enhancement of seismic performance of reinforced concrete columns," *1st Symposium for Enhancement of Seismic Disaster Prevention*, 135-140.
- Ikeda, S. (1998) "Seismic behavior of reinforced concrete columns and improvement by vertical prestressing," *Proc. 13th FIP Congress on Challenges for Concrete in the Next Millennium*, Vol. 2. pp. 879-884.
- Ikeda, S., Mori, T., and Yoshioka, T. (1998) "Seismic performance of prestressed concrete columns," *Prestressed Concrete*, 40-5, pp. 40-47 (in Japanese).
- Japan Road Association (1996 and 2002) "Seismic design specifications of highway bridges," Maruzen, Tokyo, Japan
- Kawashima, K., MacRae, G. A., Hoshikuma, J. and Nagaya, K. (1998) "Residual displacement response spectrum," *Journal of Structural Engineering, ASCE*, 124-5, pp. 523-530.
- Kawashima, K. (2000) "Seismic design and retrofit of bridges," (Key note presentation), *12th World Conference on Earthquake Engineering*, Paper No. 1818 (CD-ROM), Auckland, New Zealand
- Kawashima, K. (2002) "Seismic design of concrete bridges," (Key note presentation), *1st fib Congress*, Osaka, Japan

- Kawashima, K., Hosoiri, K., Shoji, G. and Sakai, J. (2001) "Effects of unbonding of main reinforcements at plastic hinge region on enhanced ductility of reinforced concrete bridge columns," Structural and Earthquake Engineering, Proc. JSCE, 689/I-57, 45-64.
- Kawashima, K. and Nagai, M. (2002) "Development of a reinforced concrete pier with a rubber layer in the plastic hinge region," Structural and Earthquake Engineering, Proc. JSCE, 703/I-59, 113-128.
- Mutsuyoshi, H., Zatar, W. A. and Maki, T. (2001) "Seismic behavior of partially prestressed concrete piers," Proc. JSCE, 669/V-50, 27-38.
- Priestley, N.M.J., Seible, F. and Calvi, M. (1996) "Seismic design and retrofit of bridges," John Wiley & Sons.
- Shito, K., Igase, Y., Mizugami, Y., Ohasi, G., Miyagi, T. and Kuroiwa, T. (2002) "Seismic performance of bridge columns with interlocking spiral/hoop reinforcements," First fib Congress, Osaka, Japan
- Takiguchi, K., Okada, K. and Sakai, M. (1976) "Ductility capacity of bonded and unbonded reinforced concrete members," Proc. Architectural Institute of Japan, 249, 1-11
- Tanaka, H. and Park, R. (1993) "Seismic design and behavior of reinforced concrete columns with interlocking spirals," ACI Structural Journal, pp. 192-203.
- Yagishita, F., Tanaka, H. and Park, R. (1997) "Cyclic behavior of reinforced concrete columns with Interlocking spirals," Proc. JSCE, 19-2.
- Yamagishi, M. and Kawashima, K. (2004) "Development of a rubber layer built-in reinforced concrete column in the plastic hinge region," Structural and Earthquake Engineering, Proc. JSCE, 752/I-62, 43-62.

An Evaluation of the Displacement Amplification Factors for Seismic Design of Bridges

G. Watanabe¹⁾ and K. Kawashima²⁾

1) Research Associate, Department of Civil Engineering, Tokyo Institute of Technology, Japan

2) Professor, Department of Civil Engineering, Tokyo Institute of Technology, Japan

gappo@cv.titech.ac.jp, kawasima@cv.titech.ac.jp

Abstract: This paper presents an analysis of the displacement amplification factors in seismic design of bridges. The displacement amplification factors are evaluated based on 70 free-field ground motions. Scattering of the displacement amplification factors depending on ground motions and natural periods are clarified. A new empirical formulation of the displacement amplification factors is proposed.

1. INTRODUCTION

In the force based seismic design, the force demand is generally determined based on a linear response of a structure divided by the force reduction factor. In the similar way, the displacement demand of a structure is estimated by multiplying a linear displacement response by the displacement amplification factor (Ye and Otani 1999, Miranda and Ruiz-Garcia 2002, 2003, and Lin, Chang and Wang 2004). The force reduction factors are worldwide used, and it plays an important role in the force based design of a structure. However, in spite of the importance of the displacement demand in seismic design of bridges, less attention has been paid to the estimation of a displacement amplification factor.

This paper presents an analysis on the displacement amplification factors based on 70 free-field ground motions. The dependence of displacement amplification factors on natural periods and ground motions is clarified.

2. DEFINITION OF DISPLACEMENT AMPLIFICATION FACTOR

If one idealizes a structure in terms of a single-degree-of-freedom (SDOF) oscillator with an elastic perfect plastic bilinear hysteretic behavior as shown in Fig. 1, the displacement amplification factor D_μ may be defined as

$$D_\mu = \frac{\delta_{NL}(T, \mu_T, \xi_{NL})}{\delta_{EL}(T, \xi_{EL})} \quad (1)$$

where T : natural period, δ_{EL} and δ_{NL} : maximum displacement in an oscillator with a linear and a bilinear hysteresis, respectively, μ_T : target ductility factor, and ξ_{EL} and ξ_{NL} : damping ratio assumed in the evaluation of linear and bilinear responses, respectively. The natural period T may be

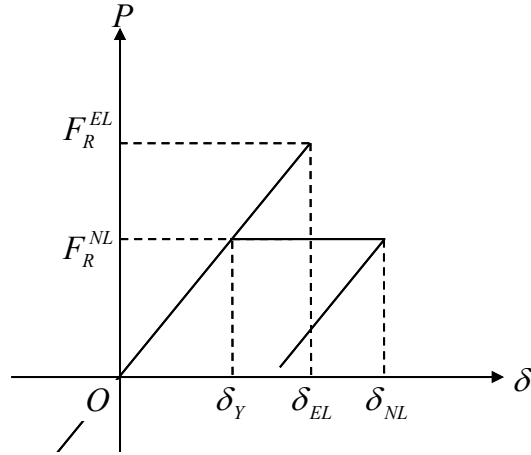


Fig. 1 Linear or Nonlinear Response of an SDOF oscillator

evaluated based on the initial elastic stiffness of columns. Representing u_y the yield displacement where the stiffness changes from the initial elastic stiffness to the post-yield stiffness, a target ductility factor μ_T may be defined based on the yield displacement u_y as

$$\mu_T = \frac{u_{\max}}{u_y} \quad (2)$$

where u_{\max} is the maximum displacement response of an oscillator. The post-yield stiffness is assumed to be 0 in the present study.

An important point in Eq.(1) is what value should be assigned to ξ_{EL} and ξ_{NL} . It is general to assume $\xi_{EL} = 0.05$, which may be validated from the fact that standard structures have a damping ratio of nearly 0.05. On the other hand, because an energy dissipation occurs in the bilinear oscillator resulted from the hysteretic response, assuming $\xi_{NL} = 0.05$ results in larger energy dissipation in the bilinear oscillators than the linear oscillator. Because taking account of the hysteretic energy dissipation, it is often the practice to assume a damping ratio which is slightly smaller than ξ_{EL} in the nonlinear always, ξ_{NL} is assumed 0.02 here.

3. DISPLACEMENT AMPLIFICATION FACTOR FOR BILINEAR OSCILATORS

Displacement amplification factors were evaluated at the target ductility factor μ_T of 2, 4, 6 and 8 assuming an elastic perfected-plastic bilinear hysteresis. Seventy free-field ground accelerations by 64 shallow earthquakes with depth less than 60 km were used in analysis. They were classified into three soil conditions depending on the fundamental natural period of subsurface ground T_g ; stiff ($T_g < 0.6$ s), moderate ($0.2 < T_g < 0.6$ s) and soft ($0.6 < T_g$) (Japan Road Association 2002). Number of records in the stiff, moderate and soft categories is 16, 39 and 15, respectively. Distribution of peak ground accelerations on the earthquake magnitudes and epicentral distances is shown in Fig. 2. The peak accelerations are in the range of 0.1-8 m/sec², and the epicentral distances are in the range of 10-500 km.

Fig. 3 shows the displacement amplification factors for the 70 ground motions. Only the results for $\mu_T = 4$ and 6 are presented here since the results for other target ductility factors show the similar characteristics. It is seen in Fig. 3 that scattering of the displacement amplification factors depending on ground motions is considerable. For example, the displacement amplification factors at natural

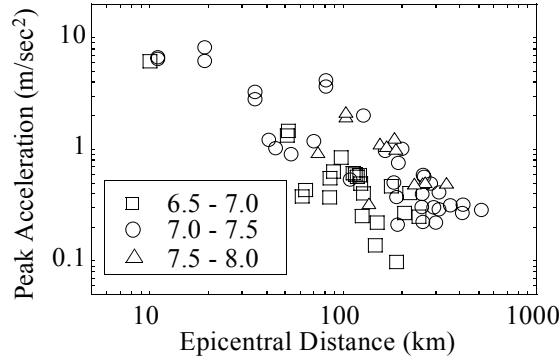


Fig. 2 Classification of Ground Acceleration in terms of Earthquake Magnitudes

period of 1 second varies from 0.29 to 3.41 depending on ground motions at $\mu_T = 4$. The dependence of displacement amplification factors on the soil condition is less significant.

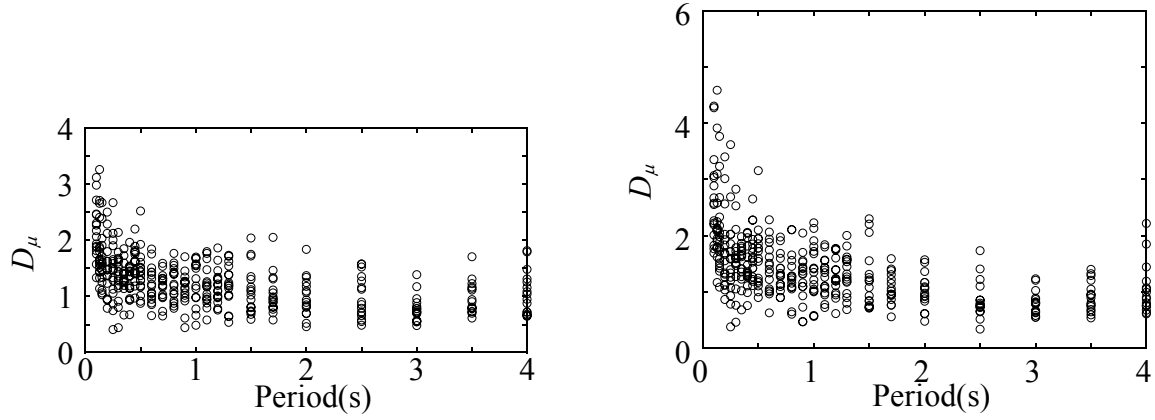
Since the scattering of the displacement amplification factors depending on ground motions is considerable, the averages \pm one standard deviations of the displacement amplification factors were obtained at each target ductility factor, natural period and soil condition. Fig. 4 shows the average values and the average values \pm one standard deviations of the displacement amplification factors at $\mu_T = 4$. The following displacement amplification factors predicted by the equal displacement and the equal energy assumptions are presented here for comparison.

$$D_\mu = \begin{cases} 1 & \text{Equal Displacement Assumption} \\ \mu / \sqrt{2\mu - 1} & \text{Equal Energy Assumption} \end{cases} \quad (3)$$

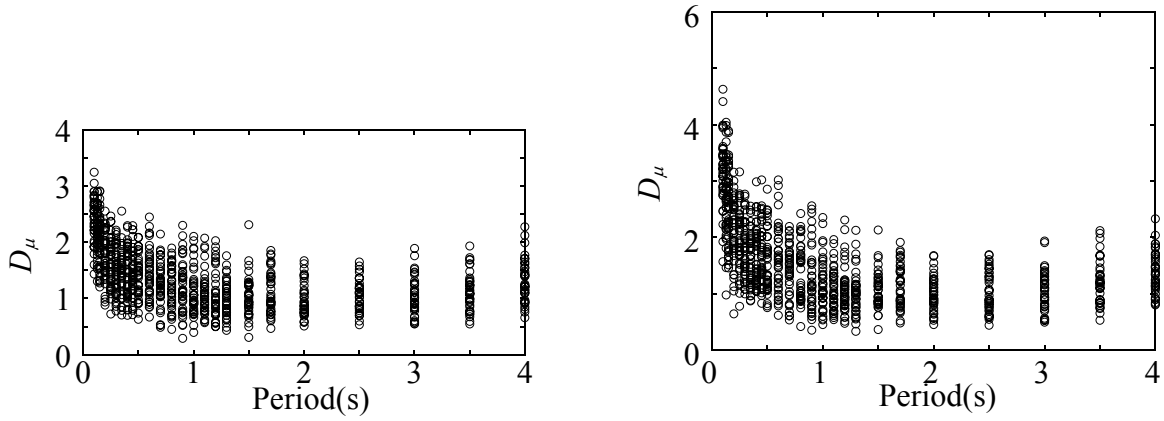
The average values of displacement amplification factors sharply increase as the natural periods decrease, while they approach to 1.0 at the periods longer than about 1.5s. The equal displacement assumption provides a good estimate to the average values at the natural periods longer than about 1.5 s. But if we take account of the considerable scattering in terms of the average plus one standard deviation, the equal displacement assumption considerably underestimates the displacement amplification factors. On the other hand, the equal energy assumption provides an overestimation to the average values but better estimation to the average values plus one standard deviations. Taking the considerable scattering of the displacement amplification factors depending on ground motions into account, it seems reasonable to consider a certain redundancy in the estimate of the displacement amplification factors in design. For such a purpose, it seems appropriate to assume the equal energy assumption instead of the equal displacement assumption.

Fig. 5 shows the dependence of the standard deviations of displacement amplification factors $\sigma(D_\mu)$ on the natural periods T and the soil condition. Different to the average values, the standard deviations $\sigma(D_\mu)$ are less dependent on the natural periods T . Fig. 6 shows the dependence of the standard deviations $\sigma(D_\mu)$ on the target ductility factors μ_T . The standard deviations $\sigma(D_\mu)$ increase as the target ductility factors increase. The relation may be approximated by a least square fit as

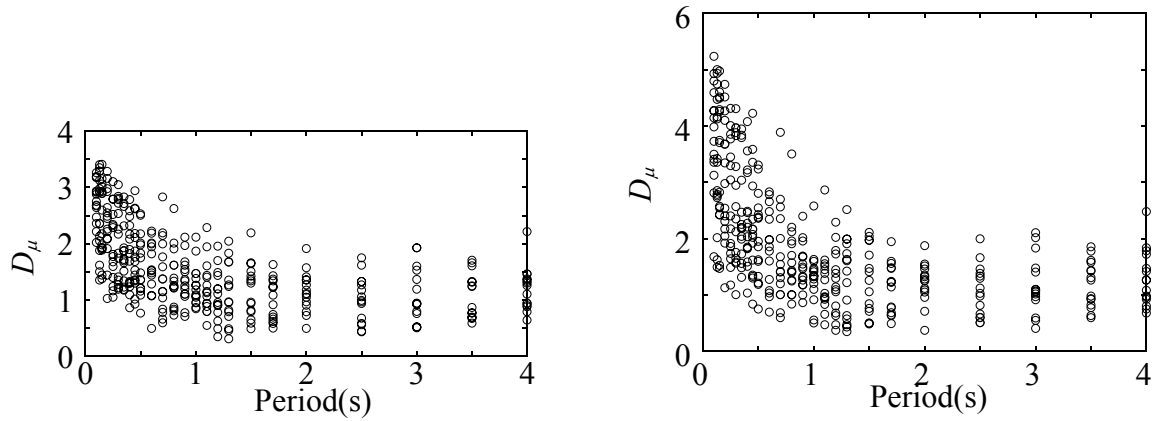
$$\sigma(D_\mu) = \begin{cases} 0.145 + 0.053 \cdot \mu_T & (\text{Stiff}) \\ 0.170 + 0.049 \cdot \mu_T & (\text{Medium}) \\ 0.061 + 0.101 \cdot \mu_T & (\text{Soft}) \end{cases} \quad (4)$$



(a) Stiff (Type-I)



(b) Moderate (Type-II)



(c) Soft (Type-III)

(1) $\mu_T = 4$

(2) $\mu_T = 6$

Fig. 3 Displacement Amplification Factor

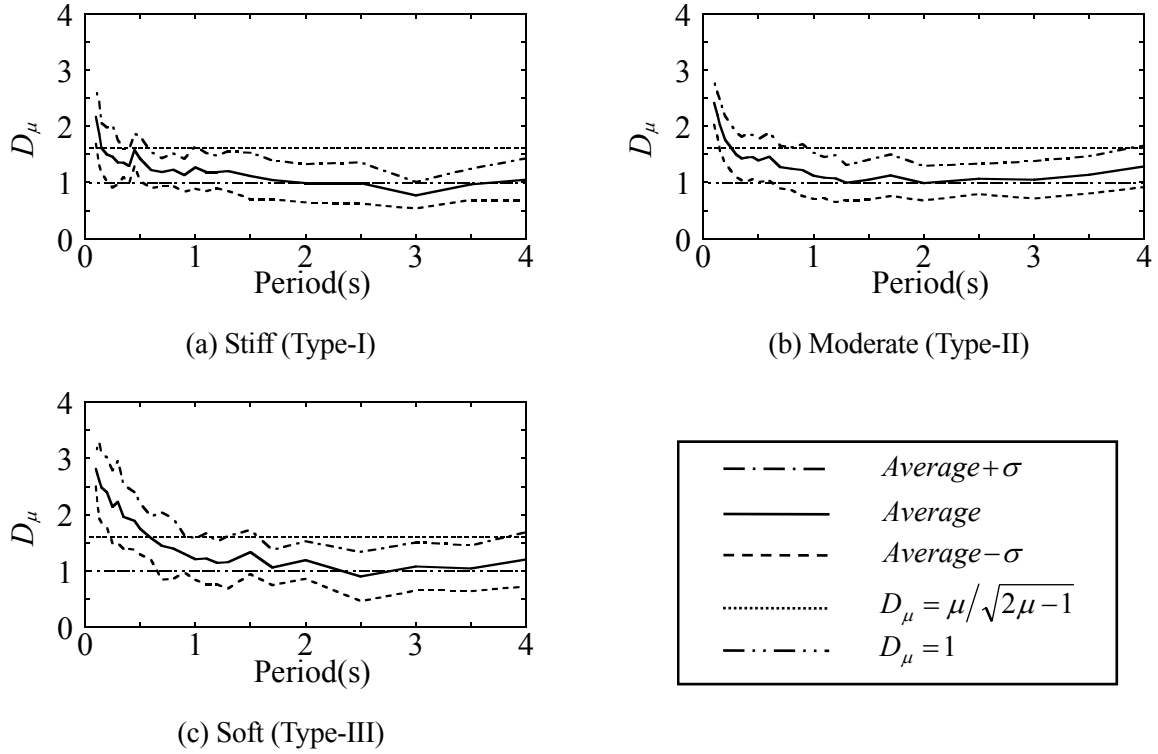


Fig. 4 Average and Average +/- One Standard Deviation of the Displacement Amplification Factor ($\mu_T = 4$)

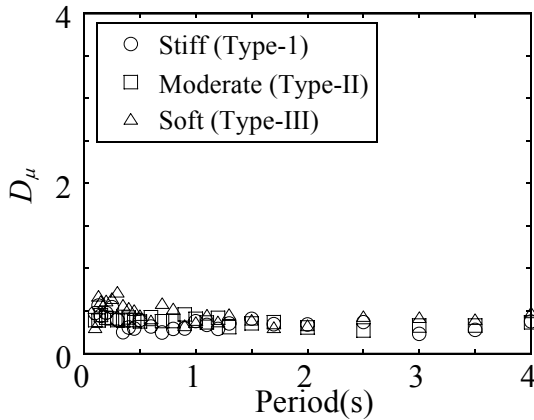


Fig. 5 Natural Period Dependencies of the Standard Deviations of the Displacement Amplification Factors

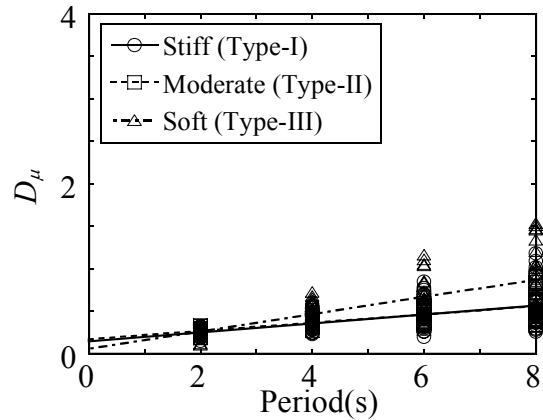


Fig. 6 Target Ductility Factor Dependencies of the Standard Deviations of the Displacement Amplification Factors

4. DISPLACEMENT AMPLIFICATION FACTOR FOR BILINEAR OSCILATORS

To idealize the average values of the displacement amplification factors, they are formulated as

$$D_\mu = \Psi(T) + 1 \quad (5)$$

where,

$$\Psi(T) = -(c-1) \cdot \frac{T-a}{ae^{b \cdot T}} \quad (6)$$

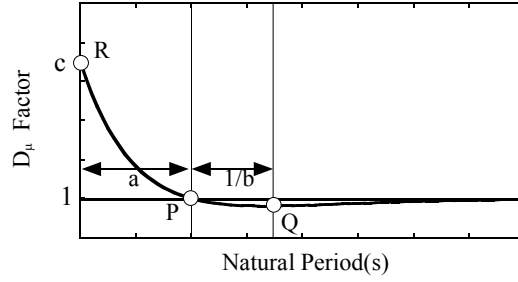


Fig. 7 Idealization of Force Reduction Factors

Table. 1 Parameters a , b and Regression Coefficients R

μ_T	a, b, c and R	Soil Conditions			μ_T	a, b, c and R	Soil Conditions		
		Stiff	Moderate	Soft			Stiff	Moderate	Soft
2	a	1.19	1.37	1.51	4	a	1.34	1.31	1.64
	b	1.50	2.28	1.30		b	1.69	2.42	1.46
	c	1.39	1.74	1.71		c	2.02	2.66	2.96
	R	19.6	46.6	55.1		R	54.1	65.6	70.2
6	a	1.32	1.32	1.68	8	a	1.27	1.36	1.76
	b	1.66	1.89	1.53		b	1.99	1.91	1.73
	c	2.50	3.29	4.19		c	3.17	4.02	5.48
	R	57.9	72.6	72.9		R	59.9	74.7	75.2

in which a , b and c are parameters depending on the natural periods and the soil conditions. Since $D_\mu = \mu$ at $T = a$ and $D_\mu = c$ at $T = 0$ in Eqs. (5) and (6), the parameter a and c represent the period where D_μ is equal to 1 (point P) and the displacement amplification factor D_μ at $T = 0$ as shown in Fig. 7, respectively. Since the gradient of D_μ is

$$\frac{dD_\mu}{dT} = -(c-1) \cdot \frac{1-b(T-a)}{a \cdot e^{-bT}} \quad (7)$$

representing Q as the point where D_μ takes the minimum value, $1/b$ represents the period between points P and Q.

Based on the definition, Eqs. (5) and (6) automatically satisfy the following conditions

$$\lim_{T \rightarrow 0} D_\mu = \mu \quad (8)$$

$$\lim_{T \rightarrow \infty} D_\mu = 1 \quad (9)$$

The average values of the displacement amplification factors in Fig. 4 were fitted by Eq. (5) using a nonlinear least square method (Press et al 1996). Table 1 represents the parameters a , b and c as well as the regression coefficients R . Since the regression coefficients R are not high enough at some combinations of the target ductility factors and soil conditions, such as the combination of $\mu_T = 2$ and stiff sites, this should be noted in the interpretation of the following results.

Fig. 8 shows the parameters a , $a+1/b$ and c . The parameter a is in the range of 1.3-1.4 second at the stiff and the moderate sites, and 1.5-1.8 second at the soft sites. They are less sensitive to

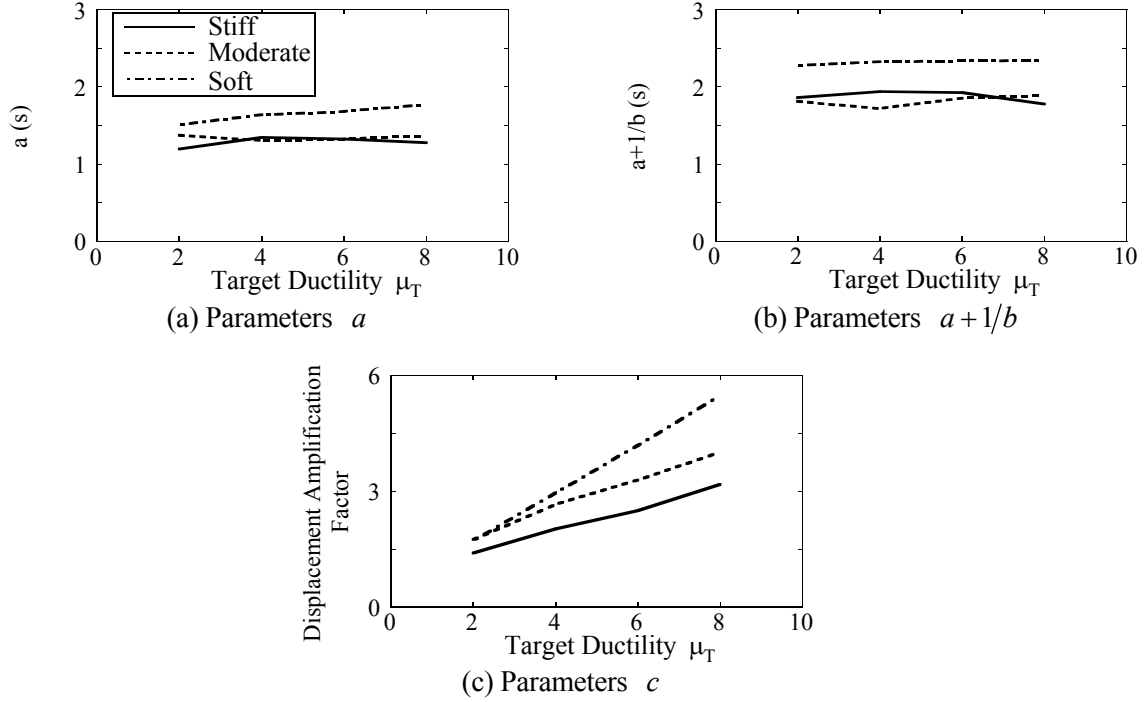


Fig. 8 Parameters a , $a+1/b$ and c in Eq.(6)

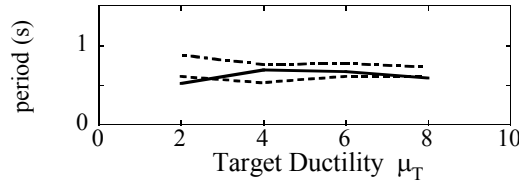


Fig. 9 Natural period where $D_\mu = \mu/\sqrt{2\mu-1}$

the target ductility factor μ_T . As described above, a represents the period where $D_\mu = 1.0$, which implies that the equal displacement assumption provides the best estimate at this period. Consequently, the accuracy of the equal displacement assumption is high at 1.0-1.4 second at the stiff and the moderate sites, and 1.5-2.4 second at the soft site. On the other hand, $a+1/b$ represents the natural period where D_μ takes the minimum value. It is 1.8-1.9, 1.7-1.9 and 2.3 second at the stiff, moderate and soft sites, respectively. The parameter c is in the range of 1.3-3.2, 1.7-4.0 and 1.7-5.5 at the stiff, moderate and soft sites, respectively. It increases as the target ductility μ_T increases.

The natural periods T where D_μ is equal to $\mu_T/\sqrt{2\mu_T-1}$ are obtained as shown in Fig. 9, based on Eq.(3), the equal energy assumption provides the best estimate in the range of 0.52-0.69, 0.53-0.62 and 0.72-0.88 at the stiff, the moderate and the soft sites, respectively. They are much shorter than the natural periods where the equal displacement assumption provides the best approximation.

Fig. 10 compares the average displacement amplification factors presented in Fig. 4 and the values predicted by Eqs. (5) and (6). Although slightly discrepancies are observed at larger target ductility factors, Eqs. (5) and (6) provides a good estimation for the average displacement amplification factors.

5. CONCLUSIONS

An analysis was conducted on the displacement amplification factors of SDOF oscillators based on the 70 free-field ground motions. Based on the analysis presented herein, the following conclusions may be deduced:

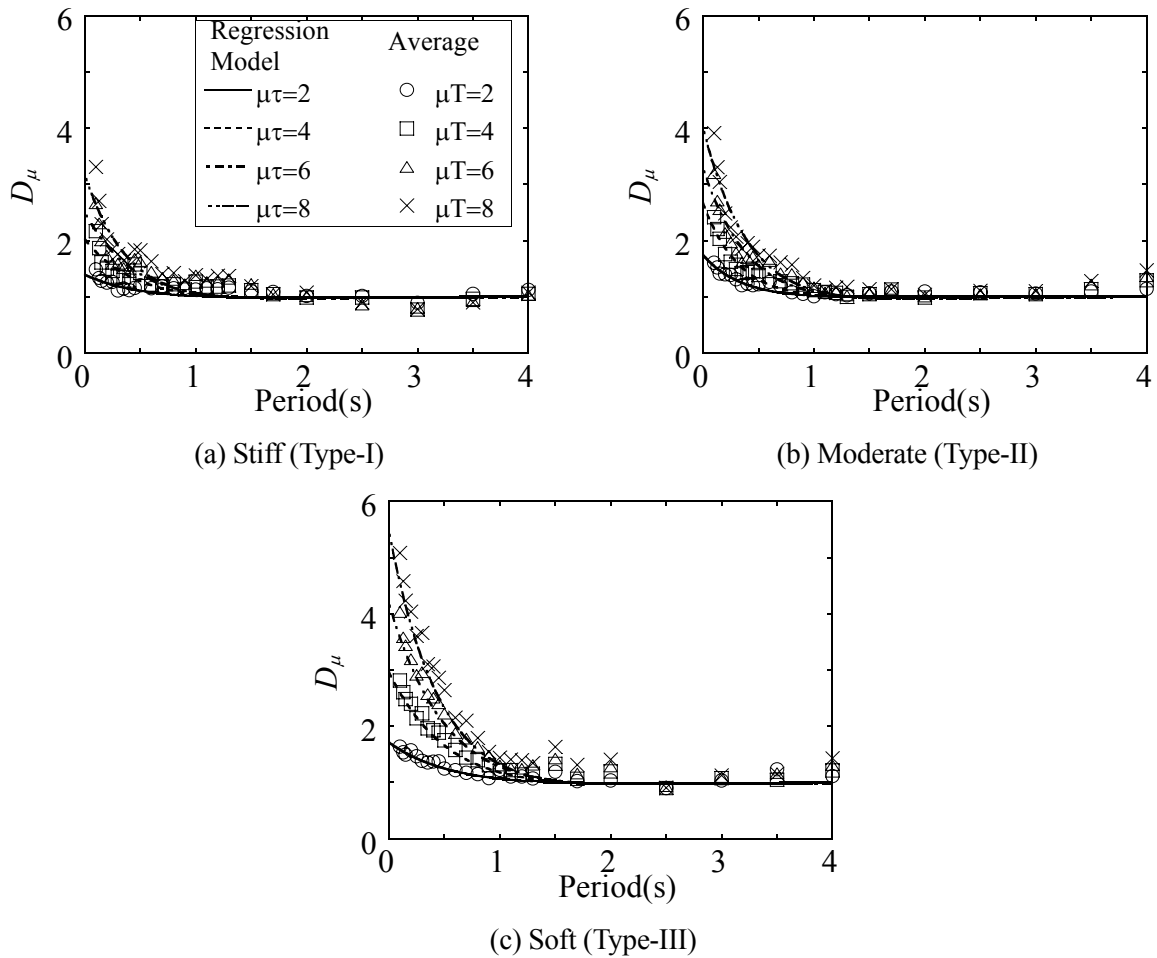


Fig. 10 Displacement Amplification Factor

- 1) Scattering of the displacement amplification factors depending on the ground motions is considerable.
- 2) The equal displacement assumption and the equal energy assumptions provide a good estimate to the average and average plus one standard deviation of the displacement amplification factors, respectively. Taking account of the considerable scattering, it seems appropriate to assume the equal energy assumption instead of the equal displacement assumption for the evaluation of the displacement amplification factors in seismic design.
- 3) An empirical equation to predict the displacement amplification factors was proposed as shown in Eqs. (5) and (6). The parameters a and $a + 1/b$ express the natural period where D_μ is equal to μ and D_μ becomes the minimum, respectively.

References:

Priestley, M. J. N., Seible, F. and Calvi, G. M. (1996). "Seismic design and retrofit of bridges," John Wiley & Sons, New York, USA.

Ye, L. and Otani, S. (1999). "Maximum Seismic Displacement of Inelastic Systems Based On Energy Concept," Earthquake Engineering and Structural Dynamics, John Wiley & Sons, 28, 1283-1499.

Miranda, E. and Ruiz-Garcia, J. (2002). "Evaluation of approximate methods to estimate maximum inelastic displacement demands," Earthquake Engineering and Structural Dynamics, John Wiley & Sons, 31, 539-560.

Ruiz-Garcia, J. and Miranda, E. (2003). "Inelastic displacement ratios for evaluation of existing structures," Earthquake Engineering and Structural Dynamics, John Wiley & Sons, 32, 1237-1258.

Lin, Y. Y., Chang, K. C. and Wang, Y. L. (2004). "Comparison of displacement coefficient method and capacity," Earthquake Engineering and Structural Dynamics, John Wiley & Sons, 33, 35-48.

SIMPLIFIED NONLINEAR ANALYSIS PROCEDURE FOR SINGLE-STORY ASYMMETRIC BUILDINGS SUBJECTED TO BI-DIRECTIONAL GROUND MOTION

K. Fujii¹⁾, Y. Nakano²⁾, and Y. Sanada³⁾

1) Post-doctoral Research Fellow, Institute of Industrial Science, University of Tokyo, Japan

2) Associate Professor, Institute of Industrial Science, University of Tokyo, Japan

3) Research Associate, Earthquake Research Institute, University of Tokyo, Japan

kfujii@iis.u-tokyo.ac.jp, iisnak@iis.u-tokyo.ac.jp, sanada@iis.u-tokyo.ac.jp

Abstract: A simplified procedure for single-story asymmetric buildings subjected to bi-directional ground motion is proposed. In this procedure, their responses are predicted through a nonlinear static analysis of MDOF model considering the effect of bi-directional excitation and a nonlinear dynamic analysis of equivalent SDOF model. The results are compared with those of the nonlinear dynamic analysis of MDOF models, and satisfactory prediction can be found in nonlinear response of asymmetric buildings.

1. INTRODUCTION

The estimation of nonlinear response of buildings subjected to a strong ground motion is a key issue for the rational seismic design of new buildings and the seismic evaluation of existing buildings (ATC-40, 1996). For this purpose, the nonlinear time-history analysis of Multi-Degree-Of-Freedom (MDOF) model might be one solution, but it is often too complicated whereas the results are not necessarily more reliable due to uncertainties involved in input data. To overcome such shortcomings, several researchers have developed simplified nonlinear analysis procedures (Saiidi and Sozen 1981, Fajfar and Fischinger 1988). This approach consists of a nonlinear static (pushover) analysis of MDOF model and a nonlinear dynamic analysis of the equivalent Single-Degree-Of-Freedom (SDOF) model, and it would be a promising candidate as long as buildings oscillate predominantly in the first mode. Although these procedures have been more often applied to planar frame analyses, only a few investigations concerning the extension of the simplified procedure to asymmetric buildings have been made.

In this paper, a simplified procedure for single-story asymmetric buildings (one mass three degree of freedom model) subjected to bi-directional ground motion is proposed. The procedure proposed in this paper is aimed to extend the studies by the authors (Fujii et al. 2003). It consists of a pushover analysis of MDOF model and a nonlinear dynamic analysis of equivalent SDOF model as is in the previous studies (Fajfar et al. 2002), but the effect of bi-directional excitations is taken into account in the pushover analysis. The results obtained by the proposed procedure are compared with those obtained by the nonlinear dynamic analysis of MDOF models. Since the simplified nonlinear analysis procedure under unidirectional excitation proposed in the previous study (Fujii et al. 2003) is applicable only to torsionally stiff (TS) buildings (Fajfar et al. 2002, Fujii et al. 2003), the discussion in this paper is also limited to TS buildings. This discussion made in this paper is the basis to predict the earthquake response of multi-story asymmetric building with simplified procedure, and the applicability of the proposed procedure to multi-story asymmetric buildings will be discussed elsewhere.

2. BUILDING AND GROUND MOTION DATA

2.1 Building Data

Buildings investigated in this paper are idealized single-story asymmetric buildings (one mass three degree of freedom model): they are assumed to be symmetric about the X-axis as shown in Figure 1. Their height is assumed 10.8m and the total building weight is 21.2 MN and the weight is uniformly distributed. In this study, four analytical models are studied considering following parameters: **(1) type of structural plan, (2) yield strength in X and Y-direction.**

(1) Type of structural plan: Two structural plans are studied as shown in Figure 1. Both models are symmetric about X-axis and asymmetric about Y-axis. Figure 2 shows the envelope curve of restoring force-displacement relationship of each element. The envelopes are assumed symmetric in both positive and negative loading directions. The Takeda hysteretic model (Takeda et al. 1970) is employed for both column and wall elements, assuming that they behave in a ductile manner. For column elements, the effect of bi-axial moment is neglected for the simplicity of the analysis.

(2) Yield strength in X and Y-direction: Two series of the yield strength in X and Y-direction are studied for each structural plan. Table 1 shows the yield strength of each element and model parameters, where E is the eccentricity ratio ($= e / r$, e : elastic eccentricity, r : radius of gyration of floor), and J is the radius ratio of gyration of story stiffness ($= j / r$, j : radius of gyration of story stiffness with respect to the center of mass), Re is the eccentricity ratio in accordance with the Japanese Standard of Seismic Design of Buildings.

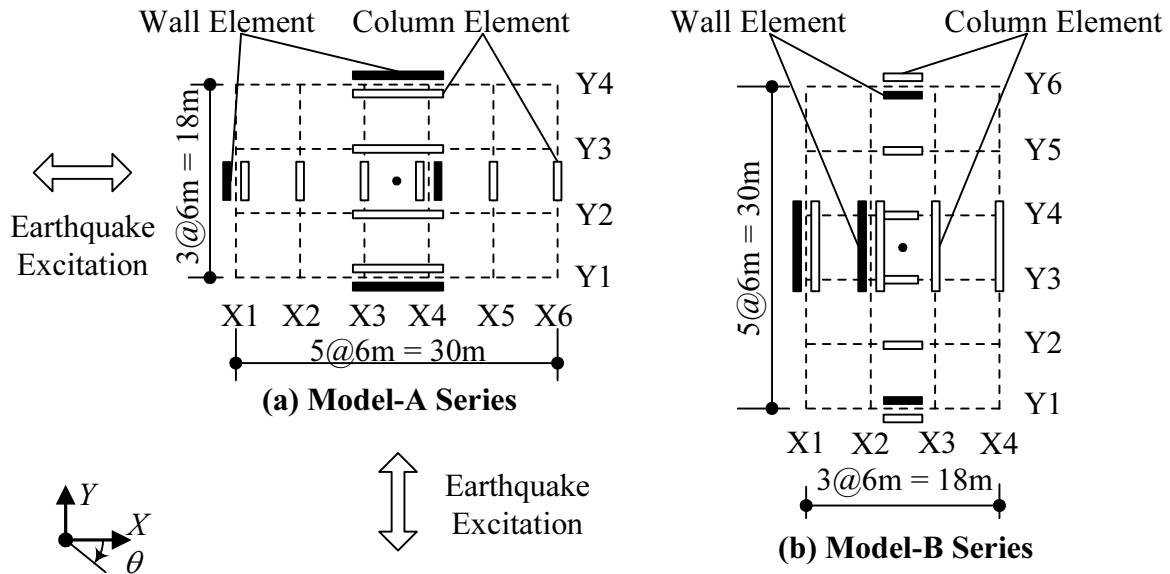


Figure 1 Plan of the Model Building

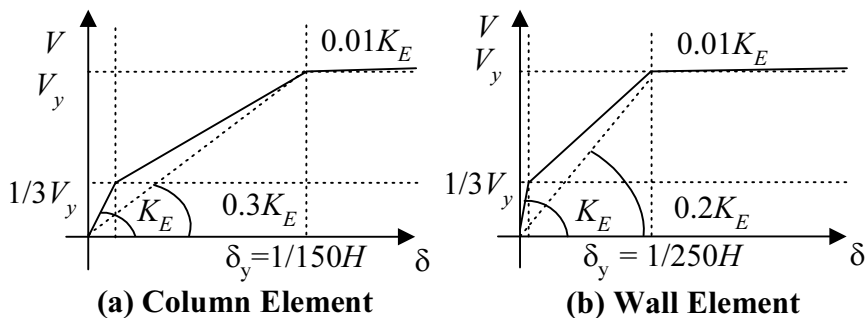


Figure 2 Envelope of Restoring Force-Displacement Relationship

Table 1 Model Parameters

	Yield Strength of Element				E	J	Re
	X-direction		Y-direction				
	Column	Wall	Column	Wall			
Model-A-W1	0.06W	0.24W	0.04W	0.24W	0.495	1.365	0.389
Model-A-W2		0.48W				1.589	0.328
Model-B-W1	0.04W	0.24W	0.06W			1.566	0.333
Model-B-W2		0.48W				2.071	0.246

Model-A-W1			Model-A-W2		
1st Mode	2nd Mode	3rd Mode	1st Mode	2nd Mode	3rd Mode
$T_1=0.279s$	$T_2=0.245s$	$T_3=0.170s$	$T_1=0.266s$	$T_2=0.181s$	$T_3=0.150s$
$m_{1X}^*=0.000, m_{1Y}^*=0.829$	$m_{2X}^*=1.000, m_{2Y}^*=0.000$	$m_{3X}^*=0.000, m_{3Y}^*=0.171$	$m_{1X}^*=0.000, m_{1Y}^*=0.913$	$m_{2X}^*=1.000, m_{2Y}^*=0.000$	$m_{3X}^*=0.000, m_{3Y}^*=0.150$
Model-B-W1			Model-B-W2		
1st Mode	2nd Mode	3rd Mode	1st Mode	2nd Mode	3rd Mode
$T_1=0.267s$	$T_2=0.245s$	$T_3=0.170s$	$T_1=0.267s$	$T_2=0.181s$	$T_3=0.170s$
$m_{1X}^*=0.000, m_{1Y}^*=0.913$	$m_{2X}^*=1.000, m_{2Y}^*=0.000$	$m_{3X}^*=0.000, m_{3Y}^*=0.171$	$m_{1X}^*=0.000, m_{1Y}^*=0.979$	$m_{2X}^*=1.000, m_{2Y}^*=0.000$	$m_{3X}^*=0.000, m_{3Y}^*=0.118$

Where m_{iX}^* , m_{iY}^* are the equivalent modal mass ratio of i -th mode in X- and Y-axis, respectively (see Ch. 3).

Figure 3 Mode Shapes of Model Buildings

Model-W1 Series: The yield strengths in X and Y-direction are assumed $0.72W$. The total yield strengths of column and wall elements are assumed $0.24W$, $0.48W$, respectively, in each direction.

Model-W2 Series: The yield strengths of the wall elements in X-direction are assumed twice of that in Y-direction. Therefore, the yield strength of those models is $1.20W$ in X-direction and $0.72W$ in Y-direction, respectively.

Figure 3 shows the mode shapes of each model. As shown in this figure, the first and second modes of all models are governed by translational component in Y- and X-direction, respectively, while their third modes is governed by the torsional component. Consequently, all models can be classified as torsionally stiff (TS) buildings (Fajfar et al. 2002, Fujii et al. 2003).

2.2 Ground Motion Data

In this study, the earthquake excitation is considered bi-directional in X-Y plane, and six sets of artificial ground motions are used. Target elastic spectrum with 5% of critical damping $S_A(T, 0.05)$ is determined by Eq. 1:

$$S_A(T, 0.05) = \begin{cases} 4.8 + 45T & \text{m/s}^2 & T < 0.16s \\ 12.0 & & 0.16s \leq T < 0.864s \\ 12.0 \cdot (0.864/T) & & T \geq 0.864s \end{cases} \quad (1)$$

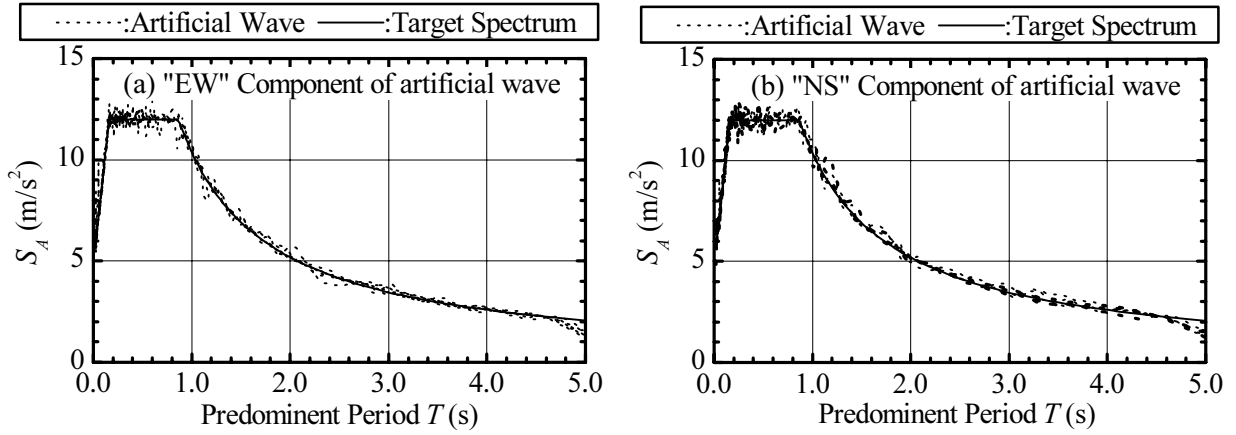


Figure 4 Acceleration Response Spectra

where T is the natural period of the SDOF model. The first 40.96 seconds ($2^{12} = 4096$ data, 0.01 second sampling) of EW and NS components of the following records are used to determine phase angles of the ground motion: El Centro 1940 (referred to as ELC), Taft 1952 (TAF), Hachinohe 1968 (HAC), Tohoku University 1978 (TOH), Kobe Meteorological Observatory 1995 (JKB) and Fukiai 1995 (FKI). Elastic acceleration response spectra of artificial ground motions with 5% of critical damping are shown in Figure 4. In this study the “EW” and “NS” components of those artificial ground motions are applied simultaneously.

2.3 Numerical Analysis Procedure

In this study, the damping matrix is assumed proportional to the instant stiffness matrix and 3% of the critical damping for the first mode. Newmark- β method ($\beta = 1/4$) is applied in numerical integrations. The time increment for numerical integration is 0.005 sec. The unbalanced force due to stiffness change is corrected at a next time step during analysis.

3. EQUATIONS OF MOTION OF THE EQUIVALENT SDOF MODELS

The equation of motion of a single-story asymmetric building model can be expressed by Eq. (2):

$$[M]\{\ddot{d}\} + [C]\{\dot{d}\} + \{R\} = -[M](\{\alpha_X\} \cdot a_{gX} + \{\alpha_Y\} \cdot a_{gY}) \quad (2)$$

where $[M]$: mass matrix, $[C]$: damping matrix, $\{d\} = \{x, y, \theta\}^T$: displacement vector (displacement at the C.M. and rotation), $\{R\} = \{V_X, V_Y, T_Z\}^T$: restoring force vector (shear forces in X- and Y-direction and torque at the C.M.), m : mass, I : moment of inertia, $\{\alpha_X\} = \{1, 0, 0\}^T$, $\{\alpha_Y\} = \{0, 1, 0\}^T$: vector defining the directions of ground motion, a_{gX} , a_{gY} : ground acceleration in X- and Y-direction, respectively.

The displacement vector $\{d\}$ and restoring force vector $\{R\}$ are assumed in the form of Eq. (3) even if the building responds beyond the elastic range:

$$\{d\} = \sum_{i=1}^3 \{\phi_i\} \cdot (\Gamma_{iX} D_{iX}^* + \Gamma_{iY} D_{iY}^*), \{R\} = [M] \sum_{i=1}^3 \{\phi_i\} \cdot (\Gamma_{iX} A_{iX}^* + \Gamma_{iY} A_{iY}^*) \quad (3)$$

$$\Gamma_{iX} = \frac{\{\phi_i\}^T [M] \{\alpha_X\}}{\{\phi_i\}^T [M] \{\phi_i\}}, \Gamma_{iY} = \frac{\{\phi_i\}^T [M] \{\alpha_Y\}}{\{\phi_i\}^T [M] \{\phi_i\}} \quad (4)$$

where Γ_{iX} , Γ_{iY} : i -th modal participation factor, $\{\phi_i\}$: i -th mode shape vector, D_{iX}^* , D_{iY}^* : i -th mode equivalent displacement, A_{iX}^* , A_{iY}^* : i -th mode equivalent acceleration.

It is assumed that a building oscillates predominantly in the first mode under Y-directional (unidirectional) excitation, and under X-directional excitation it oscillates predominantly in the second mode. Eq. (3) is rewritten as Eq. (5), assuming the predominant oscillation of the fundamental modes in both X- and Y-directions under bi-directional excitation and neglecting minor modal responses.

$$\{d\} = \Gamma_{2X} \{\phi_2\} \cdot D_{2X}^* + \Gamma_{1Y} \{\phi_1\} \cdot D_{1Y}^*, \{R\} = [M] \left(\Gamma_{2X} \{\phi_2\} \cdot A_{2X}^* + \Gamma_{1Y} \{\phi_1\} \cdot A_{1Y}^* \right) \quad (5)$$

By substituting Eq. (5) into Eq. (2) and by multiplying $\Gamma_{1Y} \{\phi_1\}^T$ from the left side, Eq. (6) is obtained:

$$\ddot{D}_{1Y}^* + \frac{C_{1Y}^*}{M_{1Y}^*} \cdot \dot{D}_{1Y}^* + A_{1Y}^* = - \left(\sqrt{\frac{m_{1X}^*}{m_{1Y}^*}} \cdot a_{gX} + a_{gY} \right) \quad (6)$$

$$m_{1X}^* = M_{1X}^* / m, m_{1Y}^* = M_{1Y}^* / m \quad (7)$$

$$M_{1X}^* = \Gamma_{1X}^2 \left(\{\phi_1\}^T [M] \{\phi_1\} \right) = \Gamma_{1X} \{\phi_1\}^T [M] \{\alpha_X\}, M_{1Y}^* = \Gamma_{1Y}^2 \left(\{\phi_1\}^T [M] \{\phi_1\} \right) = \Gamma_{1Y} \{\phi_1\}^T [M] \{\alpha_Y\} \quad (8)$$

$$C_{1Y}^* = \Gamma_{1Y}^2 \left(\{\phi_1\}^T [C] \{\phi_1\} \right) \quad (9)$$

where m_{1X}^* , m_{1Y}^* are first equivalent modal mass ratio in X- and Y-axis, respectively, and C_{1Y}^* is first equivalent damping coefficient in Y-axis. In the Eq. (6), m_{1X}^* is zero in elastic range if the building considered is symmetric about X axis as shown in Figure 3. Therefore, assuming that m_{1X}^* is negligibly small even building responds beyond the elastic range, Eq.(6) can be rewritten as Eq.(10).

$$\ddot{D}_{1Y}^* + \frac{C_{1Y}^*}{M_{1Y}^*} \cdot \dot{D}_{1Y}^* + A_{1Y}^* = -a_{gY} \quad (10)$$

Eq. (11) is obtained similarly by substituting Eq. (5) into Eq. (2) and by multiplying $\Gamma_{2X} \{\phi_2\}^T$ from the left side.

$$\ddot{D}_{2X}^* + \frac{C_{2X}^*}{M_{2X}^*} \cdot \dot{D}_{2X}^* + A_{2X}^* = -a_{gX} \quad (11)$$

Eqs. (10) and (11) are the equations of motion of equivalent SDOF models and they are the same as the equation of motion of equivalent SDOF models under unidirectional excitation (Fujii et al. 2003). It should be pointed out that it is rigorous in case of unidirectional excitation, however in case of bi-directional excitation, Eqs. (10) and (11) are approximate: in these equations, the influence of the orthogonal ground motions to response of equivalent SDOF model are neglected by assuming m_{1X}^* and m_{2Y}^* are negligibly small.

4. DESCRIPTION OF SIMPLIFIED NONLINEAR ANALYSIS PROCEDURE

In this chapter, a simplified nonlinear analysis procedure for single-story asymmetric buildings subjected to bi-directional ground motion is proposed. The outline of the proposed procedure is described as follows.

- STEP 1: Pushover analysis of MDOF model
- STEP 2: Determination of equivalent SDOF model properties
- STEP 3: Estimation of seismic demand of equivalent SDOF model
- STEP 4: Estimation of drift demand in each frame of MDOF model

The procedure required in each step is described below.

STEP 1: Pushover analysis of MDOF model: Pushover analysis of a MDOF model is carried out to obtain the force – displacement relationship, considering the change in the mode shape at each nonlinear stage. The pushover analysis is carried out independently in both X- and Y-directions (first and second modes), respectively. The numerical procedure of the pushover analysis can be found in previous work by the authors (Fujii et al. 2003).

STEP 2: Determination of equivalent SDOF model properties: The properties of two equivalent SDOF models representing the first and second mode responses are determined from the results of STEP 1, as is in the previous work by the authors (Fujii et al. 2003). For building of which the first and second modes are governed by the translational component in Y- and X-direction, respectively, the equivalent acceleration A_{1Y}^* (or A_{2X}^*) - equivalent displacement D_{1Y}^* (or D_{2X}^*) relationship of the equivalent SDOF models are determined from pushover analysis in STEP 1. A_{1Y}^* , A_{2X}^* and D_{1Y}^* , D_{2X}^* are determined by the Eqs. (12) and (13), respectively:

$$D_{1Y}^* = \frac{\{d_1\}^T [M] \{d_1\}}{\{d_1\}^T [M] \{\alpha_Y\}}, D_{2X}^* = \frac{\{d_2\}^T [M] \{d_2\}}{\{d_2\}^T [M] \{\alpha_X\}} \quad (12)$$

$$A_{1Y}^* = \frac{\{d_1\}^T \cdot \{R_1\}}{\{d_1\}^T [M] \{\alpha_Y\}}, A_{2X}^* = \frac{\{d_2\}^T \cdot \{R_2\}}{\{d_2\}^T [M] \{\alpha_X\}} \quad (13)$$

where $\{d_1\}$, $\{d_2\}$ and $\{R_1\}$, $\{R_2\}$ are the displacement and restoring force vector obtained by the pushover analyses in STEP 1.

The $A_{1Y}^*-D_{1Y}^*$ and $A_{2X}^*-D_{2X}^*$ relationships, referred as to capacity diagram, are idealized by elasto-plastic bi-linear curve so that the hysteretic dissipation enclosed by the original curve and the bi-linear idealized curve is same.

STEP 3: Estimation of seismic demand of equivalent SDOF model: The seismic demand of two equivalent SDOF models $D_{1Y}^*_{MAX}$, $D_{2X}^*_{MAX}$, $A_{1Y}^*_{MAX}$, $A_{2X}^*_{MAX}$ are obtained by the equivalent linearization procedure (Otani 2000) in this study. The equivalent period T_{eq} and damping ratio h_{eq} of the equivalent SDOF model at each nonlinear stage is calculated by Eq. (14).

$$T_{eq} = 2\pi\sqrt{D^*/A^*}, h_{eq} = 0.25(1 - 1/\sqrt{\mu}) + h_0 = 0.25(1 - \sqrt{D_Y^*/D^*}) + h_0 \quad (14)$$

where μ is the ductility of the equivalent SDOF model, D_Y^* is the yield displacement of the equivalent SDOF model determined from bi-linear curve, and h_0 is the initial damping ratio. In this study, h_0 is assumed 0.03, because in the dynamic analysis of MDOF model the damping is assumed also 3% of critical damping for the first mode as described in section 2.3. The response spectral acceleration and displacement are reduced by following factor F_h calculated by Eq. (15) (Otani, 2000).

$$F_h = 1.5/(1 + 10h_{eq}) \quad (15)$$

The demand spectrum of an earthquake excitation is constructed by plotting an SDOF response acceleration $S_A(T_{eq}, h_{eq})$ in vertical axis and corresponding displacement $S_D(T_{eq}, h_{eq})$ in the horizontal

axis. The seismic demand of equivalent SDOF model is determined by comparing the capacity diagram and the demand spectrum. The intersection of the capacity diagram and demand spectrum represents the maximum response of the equivalent SDOF model.

STEP 4: Estimation of drift demand in each frame of MDOF model: The drift demand in each frame of the MDOF model is determined from the four pushover analyses summarized below.

- 1) Determination of the four combined force distributions $\{P_{1X}\}$, $\{P_{1Y}\}$, $\{P_{2X}\}$, $\{P_{2Y}\}$ from Eq. (16):

$$\begin{aligned} \{P_{1X}\} &= [M] \left(\Gamma_{2Xie} \{\phi_{2ie}\} \cdot A_{2X}^*_{MAX} + \gamma \cdot \Gamma_{1Yie} \{\phi_{1ie}\} \cdot A_{1Y}^*_{MAX} \right) \\ \{P_{2X}\} &= [M] \left(\{\alpha_X\} \cdot A_{2X}^*_{MAX} + \gamma \cdot \Gamma_{1Yie} \{\phi_{1ie}\} \cdot A_{1Y}^*_{MAX} \right) \\ \{P_{1Y}\} &= [M] \left(\gamma \cdot \Gamma_{2Xie} \{\phi_{2ie}\} \cdot A_{2X}^*_{MAX} + \Gamma_{1Yie} \{\phi_{1ie}\} \cdot A_{1Y}^*_{MAX} \right) \\ \{P_{1X}\} &= [M] \left(\gamma \cdot \Gamma_{2Xie} \{\phi_{2ie}\} \cdot A_{2X}^*_{MAX} + \{\alpha_Y\} \cdot A_{1Y}^*_{MAX} \right) \end{aligned} \quad (16)$$

where $\Gamma_{1Yie} \{\phi_{1ie}\}$: first mode shape at $D_{1Y}^*_{MAX}$, $\Gamma_{2Xie} \{\phi_{2ie}\}$: second mode shape at $D_{2X}^*_{MAX}$ and γ : coefficient considering the combination of the first and second.

- 2) Pushover analysis using $\{P_{1X}\}$ and $\{P_{2X}\}$ until the equivalent displacement D^* calculated by Eq. (17) reaches $D_{2X}^*_{MAX}$ obtained from STEP 3 (referred to as Pushover-1X, Pushover-2X, respectively).

$$D^* = \frac{\Gamma_{2Xie} \{\phi_{2ie}\}^T [M] \{d\}}{\Gamma_{2Xie} \{\phi_{2ie}\}^T [M] \{\alpha_X\}} \quad (17)$$

- 3) Pushover analysis using $\{P_{1Y}\}$ and $\{P_{2Y}\}$ until the equivalent displacement D^* calculated by Eq. (18) reaches $D_{1Y}^*_{MAX}$ obtained from STEP 3 (Pushover-1Y, Pushover-2Y, respectively).

$$D^* = \frac{\Gamma_{1Yie} \{\phi_{1ie}\}^T [M] \{d\}}{\Gamma_{1Yie} \{\phi_{1ie}\}^T [M] \{\alpha_Y\}} \quad (18)$$

- 4) Determination of the drift demand by the envelope of (a) Pushover-1X and 2X obtained from 2) and (b) Pushover-1Y and 2Y obtained from 3).

The value of γ is a key parameter to predict the drift at each frame. If A_{2X}^* equals to zero when $A_{1Y}^*_{MAX}$ occurs, γ is taken as 0.0, while if $A_{1Y}^*_{MAX}$ and $A_{2X}^*_{MAX}$ occurs simultaneously, γ is taken as 1.0. In this study, $\gamma = 0.0, 0.5$ and 1.0 are studied.

5. ANALYSIS RESULTS

Figure 5 shows the comparisons of the maximum drift at each frame obtained from time-history analysis of MDOF models (mean value of the 12 analyses, and mean \pm standard deviation are shown) and the proposed procedure. This figure shows that in case of $\gamma = 0.5$, the proposed procedure can estimate the drift at each frame satisfactory. However, in case of $\gamma = 0.0$, the torsional response is underestimated and therefore the drift at stiff side (Frame X1) is overestimated and the drift at frame Y1 are underestimated, while in case of $\gamma = 1.0$, the torsional response is overestimated and therefore the drift at stiff side is underestimated and the drift at flexible side (frame X6 for Model-A series, and frame X4 for Model-B series, respectively) and frame Y1 are significantly overestimated. Therefore the proposed procedure with $\gamma = 0.5$ provides the most reasonable predictions in three cases.

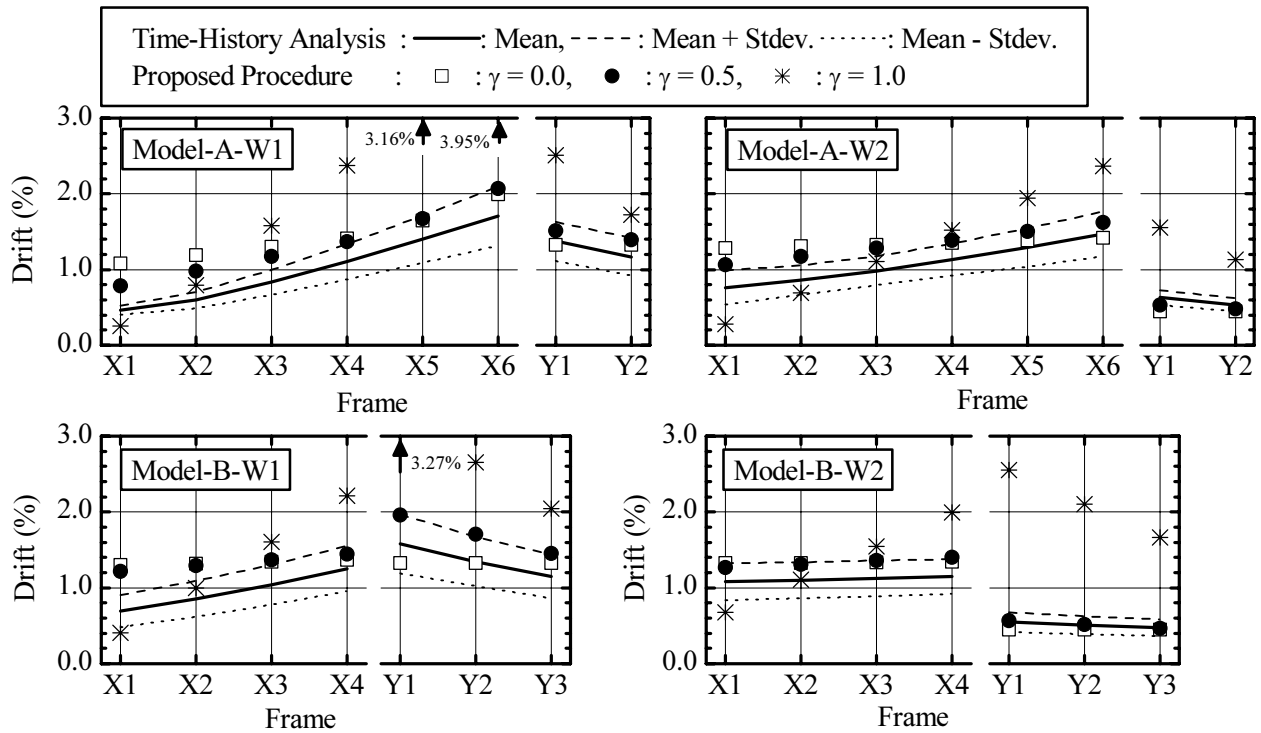


Figure 5 Prediction of the Maximum Drift at Each Frame

6. CONCLUSIONS

In this paper, a simplified procedure for single-story asymmetric buildings subjected to bi-directional ground motion is proposed, and the results obtained by the proposed procedure are compared with the results obtained by the nonlinear dynamic analysis. The results show that the nonlinear response of asymmetric buildings subjected to bi-directional ground motion can be satisfactorily estimated by the simplified procedure proposed in this study.

References:

- ATC-40 (1996), "Seismic Evaluation and Retrofit of Concrete Buildings", Vol. 1, ATC-40, Applied Technology Council
- Saiidi M, Sozen MA. (1981), "Simple Nonlinear Seismic Analysis of R/C Structures," *Journal of the Structural Division*, ASCE, Vol. 107, ST5: 937-952
- Fajfar P., Fischinger M. (1988), "N2-A Method for Non-Linear Seismic Analysis of Regular Buildings", *Proceedings of Ninth World Conference on Earthquake Engineering*, Vol. V, V-111-116
- Fujii, K., Nakano, Y. and Sanada, Y. (2003), "A Simplified Nonlinear Analysis Procedure for Single-Story Asymmetric Buildings", *Journal of JAEE*, Received by Japan Association for Earthquake Engineering
- Fajfar P., Kilar V., Marusic D., Perus I., Magliulo G. (2002), "The Extension of The N2 Method to Asymmetric Buildings", *Proceedings of the Fourth Forum on Implications of Recent Earthquakes on Seismic Risk*, TIT/EERG02-1, 291-308
- Takeda T, Sozen MA, Nielsen NN. (1970), "Reinforced Concrete Response to Simulated Earthquakes", *Journal of the Structural Division*, ASCE, Vol. 96, No. ST12: 2557-2573
- Otani, S. (2000), "New Seismic Design Provision in Japan", *The Second U.S.-Japan Workshop on Performance-Based Earthquake Engineering Methodology for Reinforced Concrete Structures*, PEER Report 2000/10, 3-14

An Experimental Study on Influence of Mullion-type Wall of Predominant Bending Failure in Reinforced Concrete Frame

Hisato HOTTA¹⁾ and Takuya TSUNODA²⁾

1)Assoc.Prof., Graduate School of Science and Engineering, Tokyo Institute of Technology, Dr.Eng

2)Graduate Student, Graduate School of Science and Engineering, Tokyo Institute of Technology
hotta@arch.titech.ac.jp, ttsund2@arch.titech.ac.jp

Abstract: Mullion-type walls, which are not regarded as structural elements in general, joined to RC frames may raise horizontal load-carrying capacity of the structure. However there is some probability that the axial elongation of them after their yielding due to bending moment has a bad influence on a behavior of RC frames. In this paper, one eighth scale two story and three story specimens were made and tested. Those consist of 1 span RC frame and the mullion-type walls at every story. The conclusions are as follows. The mullion-type wall elongates axially in each story after it yields due to bending moment, and the beams connected with the walls at the upper story are forcibly and more conspicuously deformed by the elongation of the walls. Consequently the rotation angle of the upper beams is about one and a half times as large as the drift angle. Experimental horizontal load-carrying capacity corresponds to the value calculated as the elongation produces plastic hinge in beams. These verification indicates that the mullion-type wall joined to RC frame raises horizontal load-carrying capacity unless the elongation causes brittle failure of beams.

1. INTRODUCTION

Continuous mullion-type walls are very popular as exterior walls of structures for condominiums in Japan. In general, they are not regarded as structural elements, because they do not satisfy the requirements for bearing walls, and their existence are ignored in structural calculation. However, if slightly, they have a certain lateral stiffness and strength, therefore, they have some influence on the behavior of the structure in which they are installed. They may raise the ultimate lateral strength of the structure. On the other hand, they will yield due to bending moment at both the ends and will axially extend after yielding. The end moment and the elongation of them may have bad influence on the behavior of main structure. Nowadays, under performance-based design, it becomes more important to fully grasp load-displacement curves of the structure including inelastic region. The purpose of this paper is to show the influences above mentioned through an empirical examination.

2. OUTLINE OF THE EXPERIMENT

2.1 Specimens

Two specimens, one of which was 1 span-2 story plain frame(MW2) and the other was 1 span-3 story one(MW3), were made and tested. As shown in Fig.1, both of them were about 1/8

scale models of actual structures. They had the story height of 40cm and the span of 80cm, and a continuous mullion-type wall was installed at the center of the span. The dimensions of the columns, the beams and the wall are indicated in Fig.2. Their reinforcements are indicated in Table 1. Longitudinal reinforcements were deformed bars with the nominal diameter of 6mm and shear reinforcements were round bars with the diameter of 3mm. The beams and the walls were strengthened laterally almost until the limit of strengthening as shown in Table 1. The center hole of the column is for PC bar provided to induce axial force. Mechanical characteristics of the reinforcements and the concrete are indicated in Tables 2 and 3.

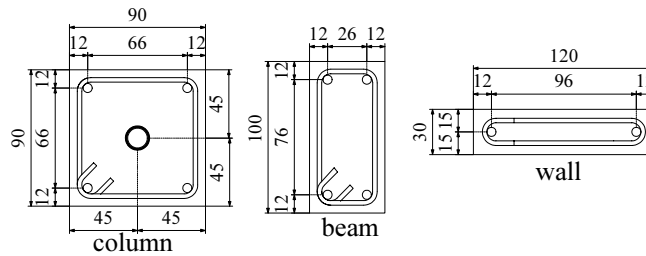
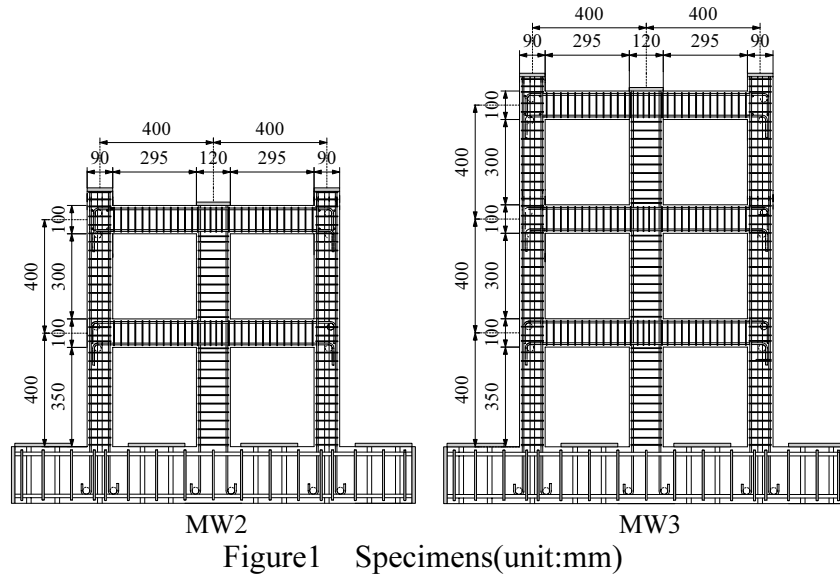


Figure2 Sections of members(unit:mm)

Table1 Reinforcement

	Longitudinal Reinforcing Bars	Hoop Reinforcing Bars
beam	D6(2.6%)	3 ϕ @25(1.1%)
column	D6(1.6%)	3 ϕ @30(0.53%)
wall	D6(1.8%)	3 ϕ @30(1.5%)

Table2 Mechanical Characteristics of the Reinforcements

	Yield Strength (MPa)	Tensile strength (MPa)	Young's modulus (MPa $\times 10^4$)
D6	374	486	18.2
3 ϕ	500	616	18.7

Table3 Mechanical Characteristics of the Concrete

age	Compressive Strength(MPa)	Tensile strength(MPa)	Young's modulus(MPa $\times 10^4$)
28	29.1	2.81	2.67
45	30.7	2.86	2.60

2.2 Loading setup and method of loading

The specimens were fastened to the basement by 16 PC bars at the center of the loading frame, as shown in Fig.3. A constant axial force equivalent to $0.2bD\sigma_B$ was loaded to both the columns by two center-hole jacks set under the specimen and PC bars piercing the columns vertically. The top of the specimen was horizontally pulled and pushed with the same forces by the upper two oil jacks, and the lower ones were to load reacting forces. By means of them, the PC bars to fasten the specimen did not share the lateral reacting force at all.

Cyclic loading test was carried out under controlling the story drift angle of the first story. The controlled drift angles were positive and negative 0.005rad, 0.01rad, 0.02rad, 0.04rad 0.06rad and positive 0.08rad.

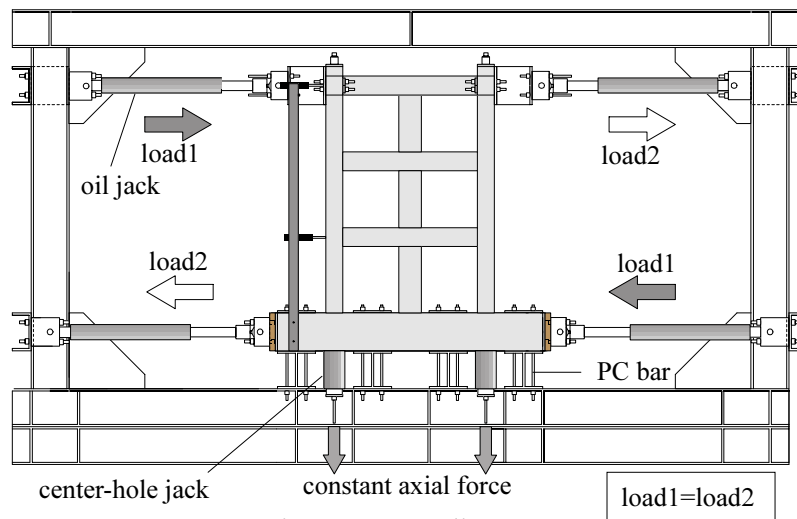


Figure3 Loading Setup

3. TESTING RESULTS

3.1 Load-displacement curves and development of cracking and destruction

Relationships between the lateral load and the story drift angle of the first story are indicated in Fig.4. In the figure, broken lines stand for the strength calculated neglecting the existence of the walls. The maximum strength of the specimen MW2 was 31.1kN at the drift angle of 0.02rad, and that of the specimen MW3 was 28.1kN at the drift angle of 0.018rad. They significantly exceeded the calculated ones. Until the drift angle when the specimens showed the maximum strength, all the ends of the beams and the walls were yielded due to bending. As for the columns, the yielding was recognized at only bottom ends of the first story columns. Crack distributions of both the specimens at the drift angle of 0.02rad are illustrated in Fig.5. At that time, many flexural cracks were observed in the beams and the walls, and many shear cracks were observed in the beam-column joint and the beam-wall joint, however, there were no cracks inducing brittle failure in the members. After they showed the maximum strength, both ends of the walls were crushed, and the strength degraded gradually. However, the strength exceeded the ultimate lateral strength calculated neglecting the existence of the walls until the drift angle of 0.04rad. Crack distributions at the drift angle of 0.06rad are shown in Fig.6. As for the specimen MW3, the top end of the top wall was fatally crushed and deformed to out-of-plane at 0.04rad, and the plastic hinge was observed at the bottom ends of the second story columns.

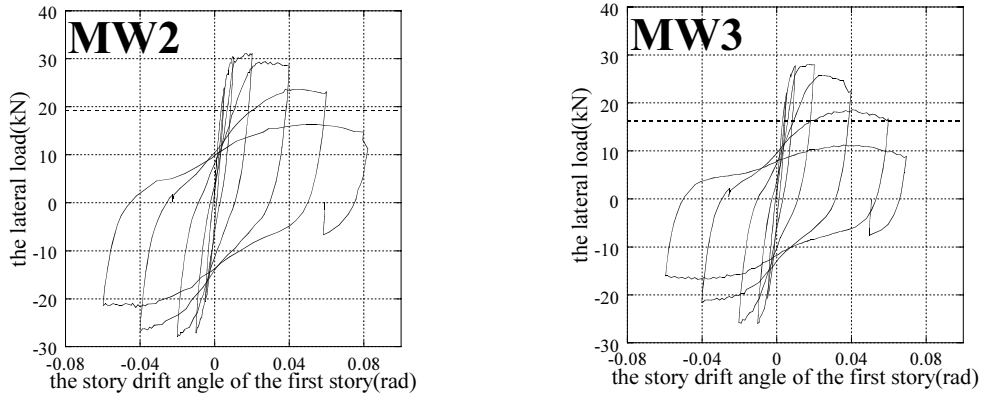


Figure4 Relationships Between the Lateral Load and the Story Drift Angle of the First Story

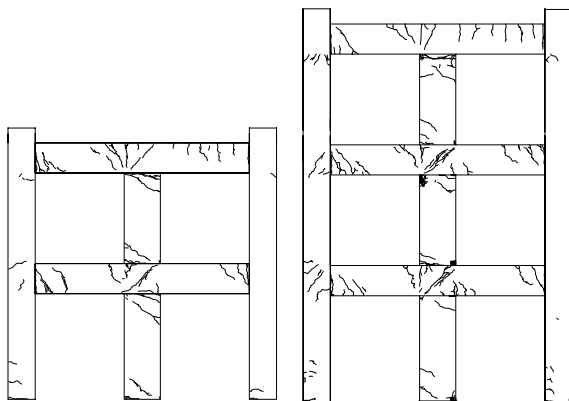


Figure5 Crack Distribution(0.02rad)

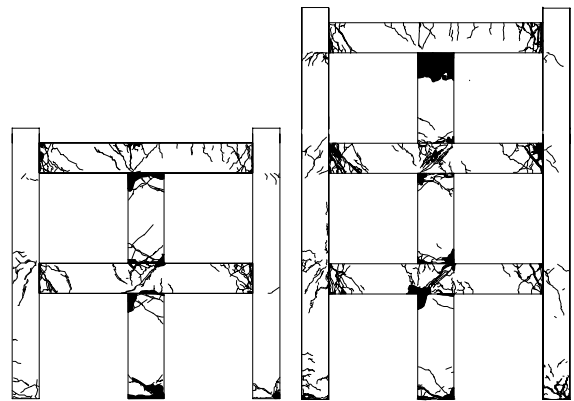


Figure6 Crack Distribution(0.06rad)

3.2 Two dimensional deformation of the specimens

An apparatus to measure the nodal displacements as illustrated in Fig.7 was set at one side of the specimens, and two dimensional shape of the grids consisted of the horizontal members and the vertical ones was calculated by means of the least squares method. The results are illustrated in Fig.8. In the figure, the displacement is enlarged 10 times as large as the actual one.

The story drift angles of every story was almost same as each other until the drift angle was 0.02rad, however, after that, the angle at the upper story became larger than that at the lowest story. Some elongation of the mullion-type walls began to be observed at about 0.02rad, and it became significant gradually. The beams were enforced to deform upward at the beam-wall joint due to the elongation of the walls.

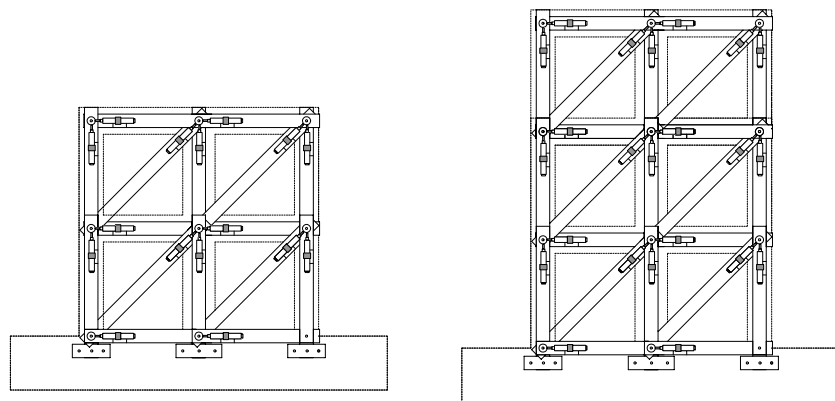


Figure7 MW2 MW3 The Apparatus to Measure the Nodal Displacements

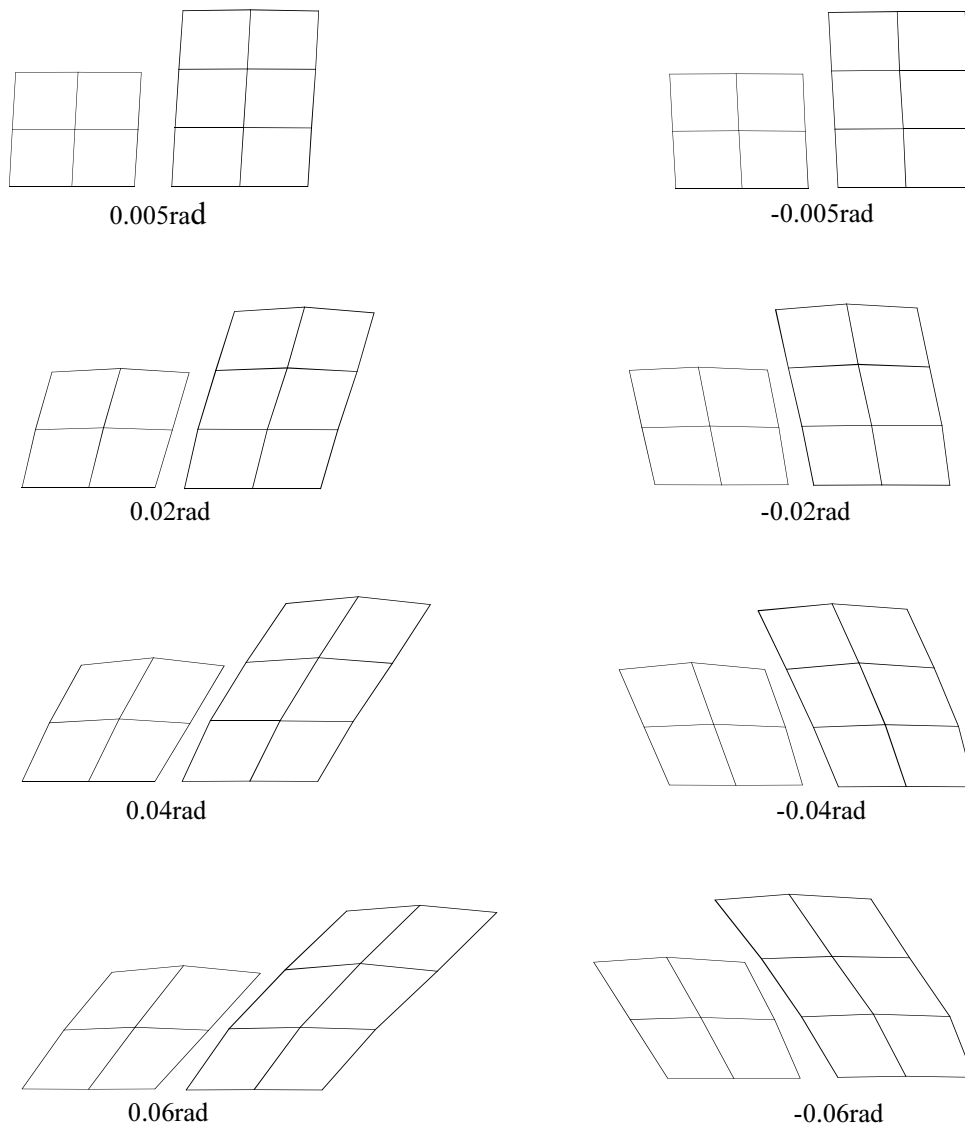


Figure8 Two Dimensional Diformation

3.3 Elongation of mullion-type walls and its influence on beams

How the difference between the vertical displacement of the column and that of the wall at the top of the specimens developed are shown in Fig.9. This figure shows that the walls extend before they yield. The difference declined at 0.06rad as for the specimen MW2 and at 0.04rad as for the specimen MW3. The walls in the upper story were crushed at those angles and they finished to play a role of bearing the lateral load.

The member angles of the beams to the connected columns are compared with the drift angle of the first story in Fig.10. If the drift angles of the whole stories are the same and the members do not extend axially, both the angles ought to be equal. However, the member angle of the beam in the top story of the specimen MW2 was 0.031rad and that of the specimen MW3 was 0.035 when the drift angle was 0.02rad. That indicates the beams are required to be more strengthened laterally so as to deform with ductility until larger deformation in the case that the deformation capacity of the structure is expected to be 0.02rad

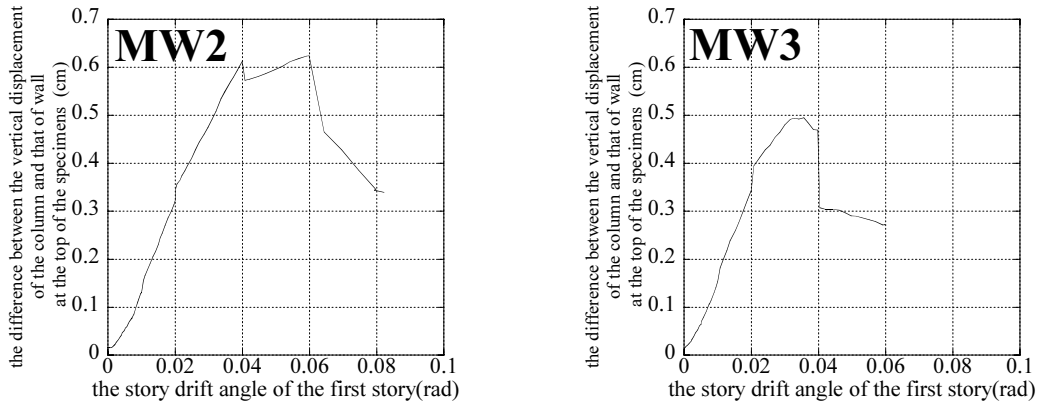


Figure9 The Difference between the Vertical Displacement of the Column and that of the Wall at the Top of the Specimens

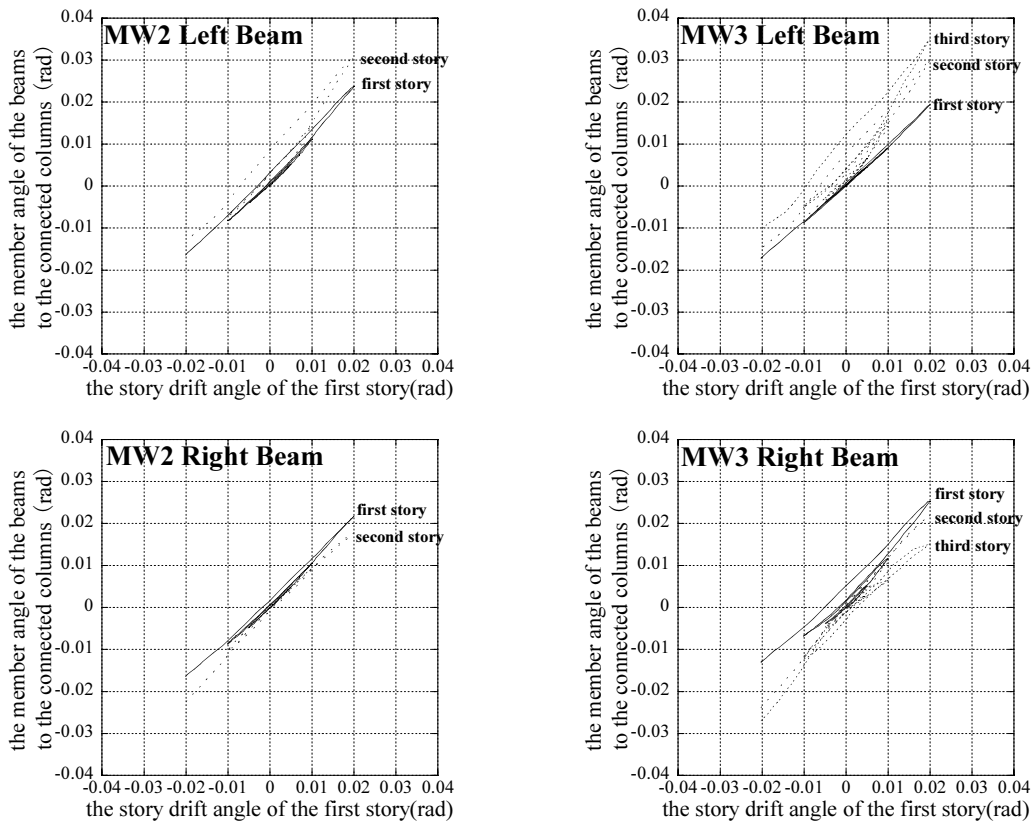


Figure10 Relationship Between the Member Angle of the Beams to the Connected Columns and the Drift Angle of the First Story

4. EVALUATION OF THE ULTIMATE LATERAL STRENGTH

The ultimate lateral strengths of the specimens are calculated under the following 3 cases, and they are compared with the experimental results.

Case 1: in the case of neglecting the existence of the mullion-type walls.

Case 2: in the case of neglecting the elongation of the walls.

Case 3: in the case of considering the elongation of the walls.

As for the above cases, collapse mechanisms are illustrated in Fig.11. In the case of considering the elongation of the walls, the situation of Case 2 is not the ultimate state. In this case, plastic hinges occur at one end of the beams connected to the walls as shown in the figure,

because the elongation of the walls forcibly deform the beams.

The calculated ultimate strengths are compared with the experimental one in Table 4. It is confirmed that the ultimate strength of the frame with continuous mullion-type walls can be evaluated to be the calculated one in the case 3 in 2 or 3 story frames, when the members exhibit ductile behaviors.

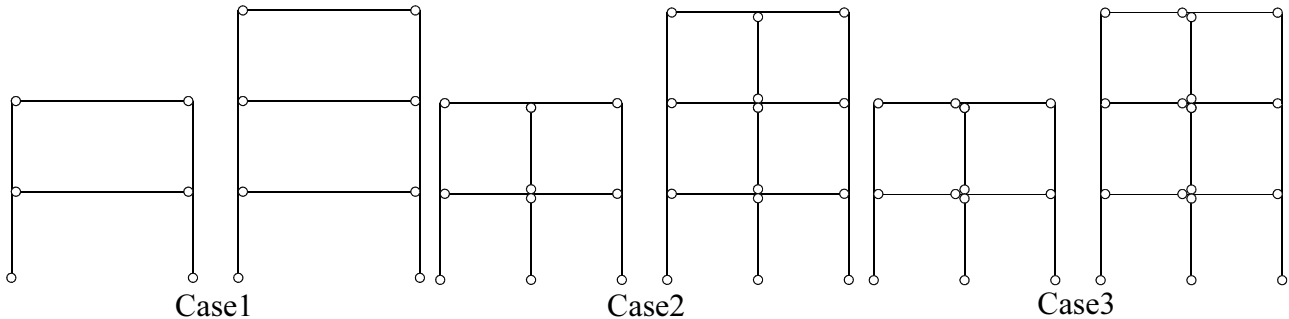


Figure11 Collapse Mechanisms

Table4 The Calculated Ultimate Strength and the Experimental One

	Exiperimental value	Case1	Case2	Case3
MW2(kN)	31.1	19.2	27.0	30.2
MW3(kN)	28.1	16.3	24.3	28.0

5. CONCLUSIONS

- 1) In the case beams and walls are sufficiently strengthened against shear force and their ductile behaviors are warranted, the ultimate lateral strength of frames with mullion-type walls are estimated by the calculated one considering elongation of the walls.
- 2) However, beams are required to be strengthened laterally considering not only the existence of mullion-type walls but also that the beams are more deformed due to the elongation of the walls.

References:

- 1)Hotta, H., Tsunoda, T., Kimura, T., “A Study on Influence of Mullion-type wall on Reinforced concrete Frame”, Summaries of Technical Papers of Annual Meeting Architectural Institute of Japan, C-2, Sep., 2003, pp.845-848.(In Japanese)
- 2)Suga, H., Katori, K., Hayashi, S., “Study on Seismic Performance of Reinforced Concrete Frames with Mullion-type Walls-The Influence of Mullion-type Wall on the Beam-”, Summaries of Technical Papers of Annual Meeting Architectural Institute of Japan, C-2, Aug., 2002, pp.833-834. (In Japanese)
- 3)Sugiyama, T., Matsuzaki, Y., Nakano, K., “Structural Performance of Reinforced Concrete Frame with Non-Structural Reinforced Concrete Walls”, Trans.of Architectural Institute of Japan, No.551, Jan., 2002, pp.111-118. (In Japanese)
- 4)Ebisugi, K., Uchida, K., Iwata, Y., Yamamoto, T., “Analytical Study on Reinforced Concrete Moment Resisting Frames with non-structural walls”, Summaries of Technical Papers of Annual Meeting Architectural Institute of Japan, C-2, Sep., 2000, pp.553-554. (In Japanese)
- 5)Nakayama, H., Ohkubo, M., Yoshioka, T., “Earthquake damage of R/C non-structural mullion-type walls in beam-yielding type frame”, Summaries of Technical Papers of Annual Meeting Architectural Institute of Japan, C-2, Sep., 1999, pp.659-660. (In Japanese)
- 6)Ikeda, K., “Failure Properties of Reinforced Concrete Mullion-type Walls Isolated by Non-structural Joints”, Summaries of Technical Papers of Annual Meeting Architectural Institute of Japan, C-2, Sep., 1996, pp.591-592. (In Japanese)

EXPERIMENTAL STUDY ON MECHANICAL BEHAVIOR OF DAMAGE CONTROLLED PRECAST-PRESTRESSED CONCRETE FRAME WITH P/C MILD-PRESS-JOINT

H. Sakata¹⁾, A. Wada²⁾, Y. Matsuzaki³⁾, and K. Nakano⁴⁾

1) Associate Professor, Structural Engineering Research Center, Tokyo Institute of Technology, Japan

2) Professor, Structural Engineering Research Center, Tokyo Institute of Technology, Japan

3) Professor, Department of Architecture, Tokyo University of Science, Japan

4) Managing Director, Nakano Building Research & Associate., Japan

hsakataq@serc.titech.ac.jp, wada@serc.titech.ac.jp, ymatsu@rs.kagu.tus.ac.jp

Abstract: This paper presents results of the experiment to certify the mechanical behaviors of the frame structures by precast-prestressed concrete with MILD-PRESS-JOINT. The specimen is cruciform model of prototype frame with MILD-PRESS-JOINT. The beam and column members precast-prestressed concrete are connected by prestressing strand that go through the beam and column, and anchored at the end of beam. Specimens have following parameter, with or without corbel of column and strand arrangement. The following conclusions were drawn from the study where partial frame experiments were conducted using prestressing strands and verification was obtained by comparison with RC frames. 1) The frame using the PC Mild Press Joint has extremely small residual deformation showed high restoration capability. 2) Damage was limited to the part near the beam column interface. Damage could be controlled.

1. INTRODUCTION

1.1 Background and Purpose of Study

In the light of depleting natural energy resources, global environmental issues, etc. there are important issues in future seismic design for rarely occurring large earthquake ground motions. It will be necessary not only to avoid building collapse and to protect human lives, but also to determine post-earthquake building damage, to minimize such damage and to continue using the buildings.

A PC Mild Press Joint¹⁾ has been used to control damage to concrete structures during earthquakes. This joint press binds prestressed concrete columns and beams. It thus controls damage by limiting cracks and utilizing the characteristics of origin-restoration capability, etc. It is expected to be effective in future seismic designs. However, there have been almost no experimental studies on PC Mild Press Joints. Thus, full understanding has not been gained on their mechanical characteristics. The purpose of this study is to clarify the mechanical characteristics of the frames using PC Mild Press Joints.

1.2 Overview of PC Mild Press Joint Method

The columns and beams are assembled with high quality precast and prestressed concrete members ($F_c > 50\text{N/mm}^2$) using the PC Mild Press Joint method. The members are press-bound and integrated using prestressing steel (prestressing strands) for jointing. The prestress force introduced for the press binding is set at 50% of the nominal yield strength of prestressing strand (P_y). Conceptual skeleton curves of the frame for prestress forces $0.75P_y$, $0.5P_y$ and $0.25P_y$ are shown in Figure 1. The PC Mild Press Joint method practices the control by setting the prestress force introduced to prestressing steel at $0.5P_y$, as shown in Figure 1. Control is attained so as not to cause yield of the prestressing strands, as shown in the $0.75P_y$ case, or excess deformation, as shown in the $0.25P_y$ case, at maximum strength until the targeted story deformation angle ($R = 1/75$ rad) is reached.

2. EXPERIMENT PROGRAM

2.1 Specimen

The specimen configurations and bar arrangement details are shown in Figure 2. The specimen parameters and material characteristics are shown in Table 1. Specimen Series I were beam yield preceding type. Specimen Series II suffered larger shear force in the joint panel. Both Series I and Series II were of two kinds, i.e. a partial frame using PC Mild Press Joint (hereinafter called PC specimen) and an RC-structured partial frame (hereinafter called RC specimen). Settings for beam shear span-to-depth ratio 3.0 and column shear span-to-depth ratio 2.2 were made common for all the test pieces. In each PC specimen, prestressing strands were placed in two rows on the beam cross-section and the main beam bars (normal reinforcing bars) did not penetrate the joint panel. Series I and II has one RC specimen, respectively. The beam flexural strengths of each of them were made the same as those of the PC specimen in Series I and II. Column flexural strengths of all specimens were made about 1.4 times the beam flexural strength. The ration of shear strength to flexural strength of the beams and column was about 1.7.

2.2 Experiment Method

The loading apparatus and loading cycle are shown in Figure 3. A shear force was applied to the right and left beams using two hydraulic of 490 kN jacks, as shown in Figure 3. The vertical displacements at the loading point were controlled keeping the same when the shear force was applied. Increasing cyclic loading was carried out according to the loading cycle shown in Figure 3. An axial force of about 745 kN (axial force ratio = 0.08 [F_c : 90 N/mm²], =0.15 [F_c : 50 N/mm²]) was applied to the column using an unbonded prestressing rod built into the column member.

The Jack load, displacement, strain of the steel member and crack width were measured. The widths of cracks across the

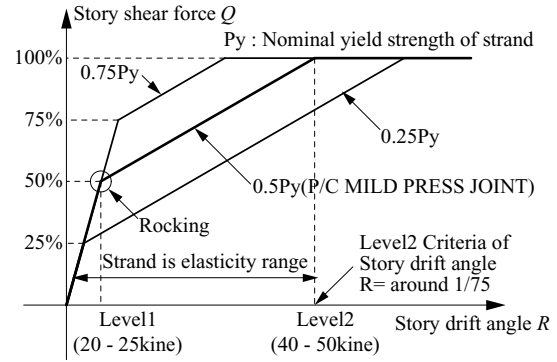


Figure 1 Conceptual Skeleton Curve of The Frame for Various Level of Prestress Forces

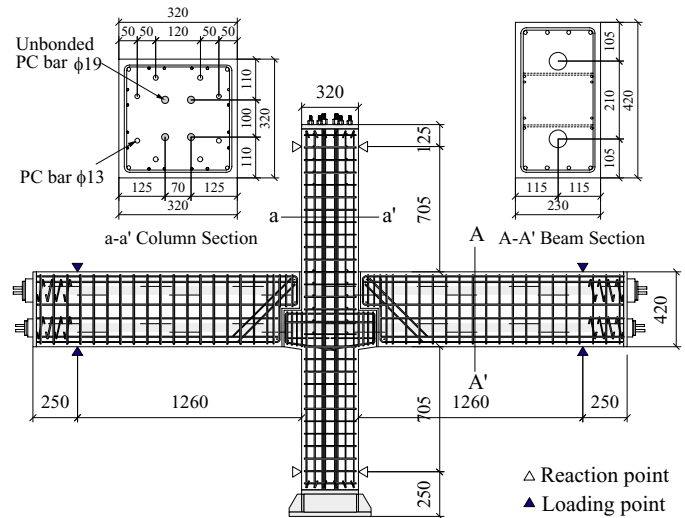


Figure 2 Specimen (PC-42-C-90)

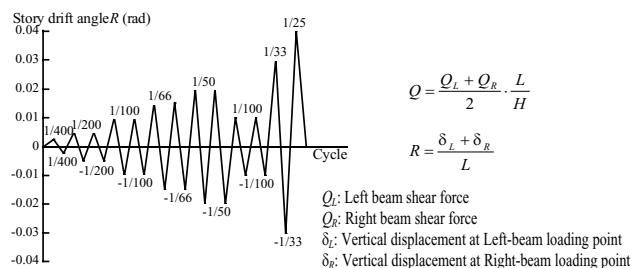
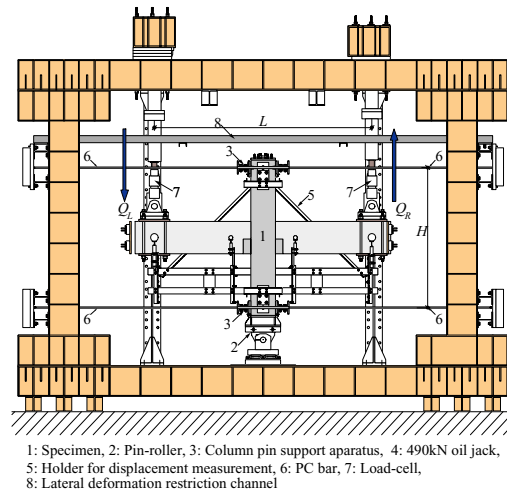


Figure 3 Loading Apparatus and Loading Cycle

shear reinforcing bar where strain gauges were attached were measured for Series II at the time of peak story drift angle using a digital microscope with a minimum scale of 0.01mm.

Table 1 Specimen parameters and material characteristics

Series	Specimen	Number of Strand *1 (Main Reinforcement)		Corbel	$c\sigma_B$	E_c	$c\sigma_t$	$p\sigma_y(s\sigma_y)$	$E_p(E_s)$	σ_p
		Upper	Lower		beam/ column	beam/ column	beam/ column			
		Number of Strand			N/mm ²	kN/mm ²	N/mm ²			
I	PC42-C-90	4	2	with	92.0	44.6	4.3	1762	195	4.84
	PC42-N-90	4	2	without	92.4	43.6	3.5			
	PC33-C-90	3	3	with	87.5	43.1	3.3			
	RC33-50	(7-D16*2)	(7-D16*2)	—	58.0	37.0	3.5	(357)	(195)	—
II	PC55-C-90	5	5	with	91.5	42.5	3.9	1628	212	8.07
	PC55-C-50	5	5	with	86.3/55.8	40.4/35.2	3.8/3.3			
	RC55-50	(7-D16*3)	(7-D16*3)	—	56.8	37.2	3.2			

*1:PC Strand (SWPR7B), *2:SD295A, *3:SD490, $c\sigma_B$: Concrete Compressive Strength,

E_c : Concrete Young's Modulus, $c\sigma_t$: Concrete Tensile Strength,

$p\sigma_y$: Strand Yield Strength (0.2%offset), $s\sigma_y$: Beam Main Reinforcement Yield Strength,

E_p : Strand Young's Modulus, E_s : Beam Main Reinforcement Young's Modulus

3. EXPERIMENT RESULTS AND DISCUSSIONS

3.1 Characteristics of Failure and Deformation

Figure 4 shows the part in the vicinity of the column/beam joint at the time of maximum deformation. Figure 5 shows the relationship of story shear Q – story drift angle R . Only one of the PC specimens shows whole hysteresis. Envelopes are shown for the other specimens, since the characteristics were almost the same. The Q – R relationship of the PC specimens indicates that their hysteresis characteristics belonged to the origin-oriented type having small residual deformation for both Series I and II. No yielding of the prestressing strands was observed. Damage was only observed near the press joint. Yield of shear reinforcing bars at the joint was observed at $R = 1/66$ rad in PC55-C-50. The RC specimens showed spindle-shaped hysteresis with narrow hysteresis up to $R = 1/66$ rad and slip type restoration characteristics after about $R = 1/50$ rad in RC33-50. Considerable damage occurred at the joint. RC33-50 reached the maximum story shear force at $R = 1/100$ rad and the main reinforcing bar of the beam yielded. The shear reinforcing bar at the joint yielded at the same cycle. For the RC55-50, the shear reinforcing bar of the joint yielded at $R = 1/100$ rad. The main reinforcing bar of the beam yielded at $R = 1/50$ rad. PC55-C-50 was designed so that joint failure preceded others. However, little damage occurred at the joint, because the shear force input to it reached the ceiling due to beam end crushing. Decreasing strength was observed after $R = 1/66$ rad where beam end crushing was observed.

3.2 Conditions of Joint Damage

Figure 6 shows the strain of the shear reinforcing bar used in the joint at peak story drift angle. Figure 7 shows the sum of crack widths at peak story drift angle at the joint. Figure 8 shows the sum of widths of residual cracks. As crack widths in the joint increased, strain of shear reinforcing bars of the joint increased. The crack widths of PC55-C-50 and RC55-50 were compared. In PC55-C-50, the shear reinforcing bars of the joint reached yield. The sum of crack widths at the peak was about 10 times larger in RC55-50 than in PC55-C-50. Meanwhile, the sum of widths of residual cracks during unloading was about 25 times larger in RC55-50. This indicates that more cracks closed in PC55-C-50 than in RC55-50 during unloading.

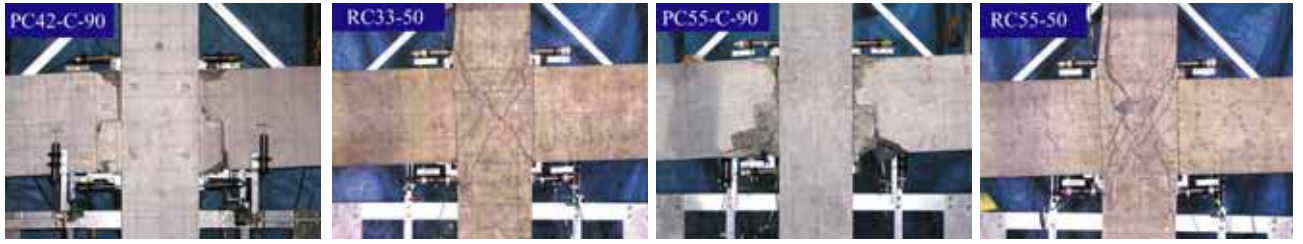


Figure 4 Ultimate Stage ($R=1/25\text{rad}$)

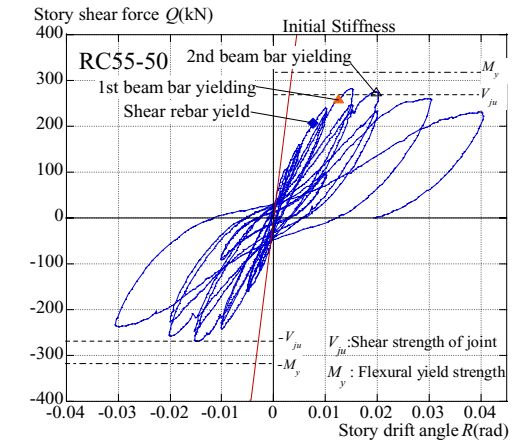
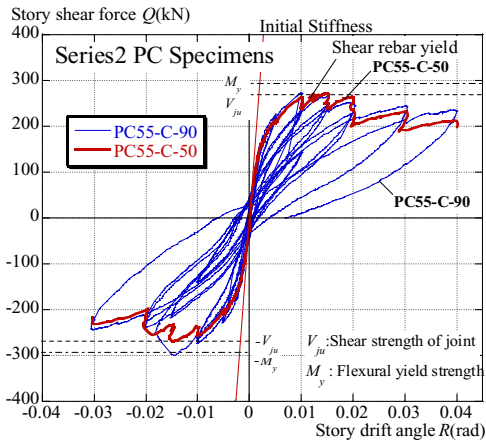
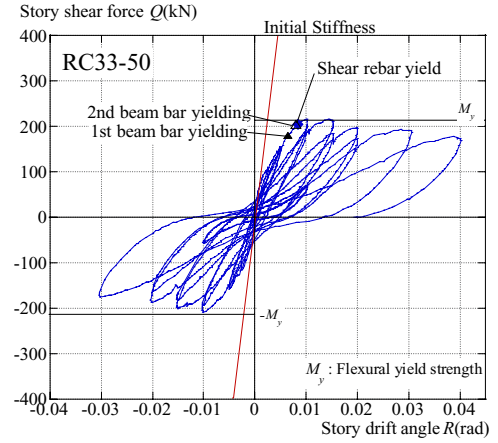
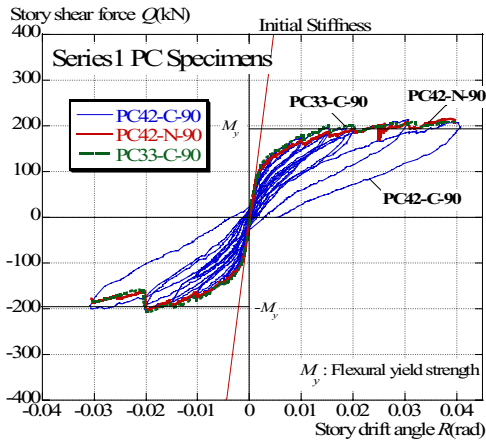


Figure 5 Story Shear Force Q – Story Drift Angle R Relationships

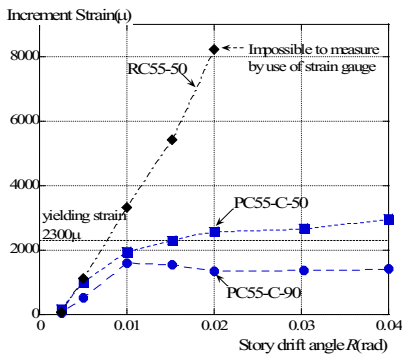


Figure 6 Strain of Shear Reinforcement in Joint Panel

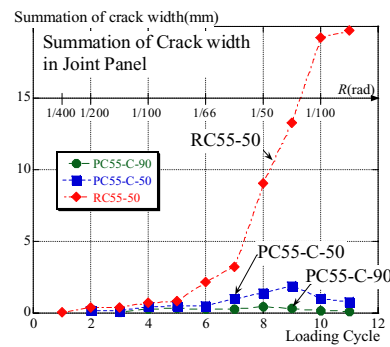


Figure 7 Summation of Crack Width at Peak Point of Each Cycle

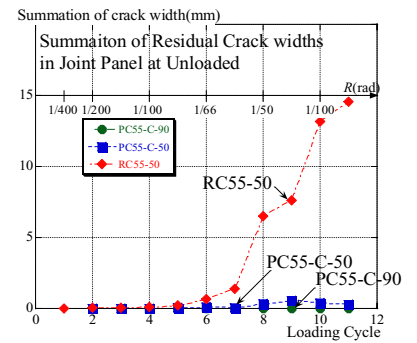


Figure 8 Summation of Residual Crack Width

3.3 Studies on Strength of Joint

To study the strength of the joint, the shear crack strength $ex \tau_{cr}$ of the joint during the experiments was first estimated. $ex \tau_{cr}$ was obtained from Equation (1). V_{jcr} is the shear force input to the joint when the crack first occurs at the joint, as obtained from Equation (2). The tensile force was obtained from Equation (3). The shear crack strength of the joint of the RC specimen was obtained from Equation (4).

$$ex \tau_{cr} = \frac{V_{jcr}}{b_j D_j} \quad (1)$$

$$V_{jcr} = 2T - V_c \quad (2)$$

$$RC \tau_{cr} = \sqrt{f_t^2 - \sigma_0 f_t} \quad (3)$$

$$T = \frac{M_b}{j} = \frac{Q_b \cdot a}{j} \quad (4)$$

where [b_j : Effective joint width, D_j : Column height, T : Tensile force of prestressing steel or tensile force of normal reinforcing bar, V_c : Column shear force (story shear force), M_b : Moment of beam end, Q_b : Beam shear force, a : Shear span, j : Distance between tension and compression resultants ($= 7/8 d$, d : Effective depth), f_t : Tensile strength of concrete, σ_0 : Column axial stress]

$ex \tau_{cr}$ obtained from Equation (1) and $RC \tau_{cr}$ obtained from Equation (4) are shown with solid lines in Figure 9. $ex \tau_{cr}$ and Equation (4) were compared. RC33-50 () and RC55-50 () showed general matching with Equation (4). However, $ex \tau_{cr}$ of all PC specimens became larger than that from Equation (4). Shear crack strength in the PC specimens was evaluated using $PC \tau_{cr}$, showing that the shear crack strength incorporated the beam prestress. $PC \tau_{cr}$ was obtained from Equation (5).

$$PC \tau_{cr} = \sqrt{f_t^2 - (\sigma_0' + \sigma_p) \cdot f_t + \sigma_0' \cdot \sigma_p} \quad (5)$$

[f_t : Tensile strength of concrete, σ_0' : Axial stress of column taking into account the column prestress, σ_p : Stress due to beam prestress (Series I: $\sigma_p = 4.02 \text{ N/mm}^2$, Series II: $\sigma_p = 7.61 \text{ N/mm}^2$)]

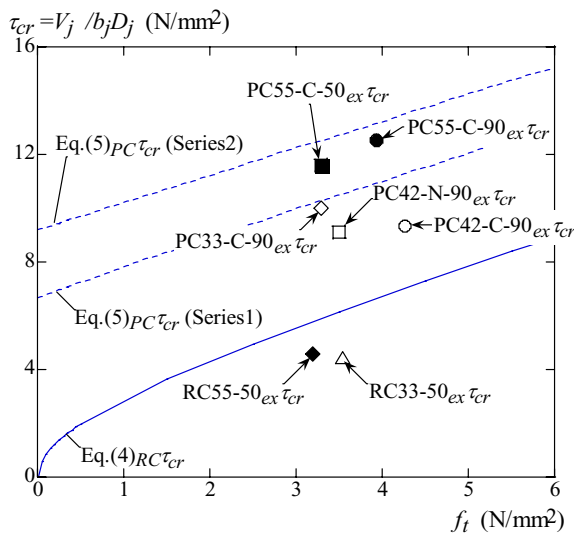


Figure 9 Shear Crack Strength

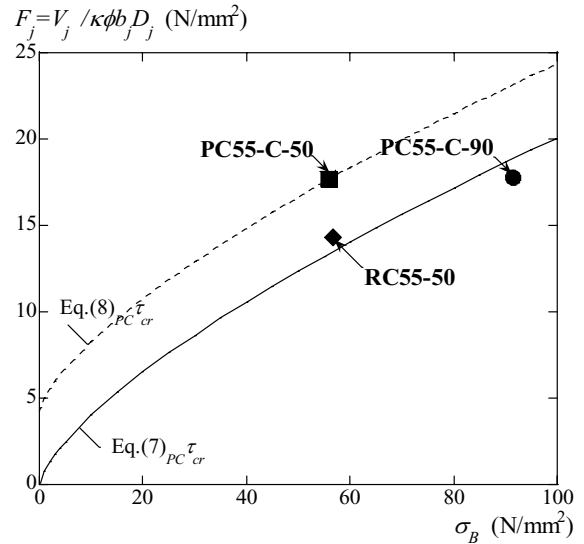


Figure 10 Shear Strength

Shear crack strength $PC \tau_{cr}$ calculated from Equation (5) is shown with a dashed line in Figure 9. $ex \tau_{cr}$ of the PC specimen was compared with that from Equation (5). The experimental results showed general agreement with the calculated results from Equation (5).

Next, the joint strength was investigated for the specimens where joint failure occurred. The joint strength during the experiments was obtained from Equation (6). V_{jmax} is the maximum shear force input to the joint during the experiments. It is obtained using the same method as used for V_{jcr} . The joint shear strength was obtained from Equation (7).

$${}_{ex}F_j = \frac{V_{jmax}}{\kappa \cdot \phi \cdot b_j \cdot D_j} \quad (6)$$

$$F_j = 0.8\sigma_B^{0.7} \quad (7)$$

[κ : Shape factor of joint ($\kappa = 1.0$), ϕ : Correction factor due to whether there are orthotropic beams or not ($\phi = 0.85$), σ_B : Compressive strength of concrete]

Experimental results complied with Equation (6) and F_j estimated from Equation (7) are shown in Figure 10. The experimental and calculated results were compared. RC55-50 showed agreement with Equation (7). However, the PC55-C-50 results were about 20% larger, exceeding the joint shear strength. The equation of joint strength where it is assumed that beam prestress force should bear part of shear strength input to the joint is defined by Equation (8).

$${}_{PC}F_j = 0.8\sigma_B^{0.7} + \frac{\alpha \cdot P_{ini}}{\kappa \cdot \phi \cdot b_j \cdot D_j} \quad (8)$$

[α : Correction factor due to beam prestress, P_{ini} : Initial prestressing force]

Results obtained when $\alpha = 0.4$ in Equation (8) are shown with a dashed line in Figure 10. Good agreement was seen in the results obtained from Equation (8) and those of PC55-C-50 where the shear reinforcing bar at the joint reached yield. Only one PC specimen reached shear failure. The conditions of the damaged joint of the other PC specimens showed that the joint had larger strength than estimated from Equation (7). About a 40% Increase from the initial anchoring force was expected. Accumulation of further experimental data is necessary in the future.

4. MODELING OF ENVELOPE

The $Q - R$ relationship envelope for the frame using PC Mild Press Joint was modeled. It was assumed that the envelope moved to secondary rigidity during release of the initial press binding and it should become tri-linear when the rigidity became zero when the frame reached yield. The first inflection point in the envelope was shown to be at the intersection of the initial rigidity and the moment when release of press binding occurred. The initial rigidity was calculated taking into account only bending deformation, assuming the rigidity region specified in RC standard²⁾ in the beam/column joint at the cross-shaped part of the frame. The moment at press binding release (the first inflection point in the envelope) M_1 was calculated from Equation (9). This is the moment when a force equivalent to the initial force was applied to the tensile side of the prestressing strand. M_1 was converted to the story shear force Q_1 .

$$M_1 = \Sigma T \cdot j = (E_p \cdot \varepsilon_{pt} \cdot A_{pt} + E_p \cdot \varepsilon_{pc} \cdot A_{pc}) \cdot j = (E_p \cdot \varepsilon_{pini} \cdot A_{pt} + E_p \cdot \varepsilon_{pc} \cdot A_{pc}) \cdot j \quad (9)$$

$$Q_1 = \frac{M_1}{a} \cdot \frac{L}{H} \quad (10)$$

[A_{pt} : Cross-sectional area of tensile side of prestressing strand, A_{pc} : Cross-sectional area of compression side of prestressing strand, E_p : Young's modulus of prestressing strand, ε_{pt} : Strain of tensile side of prestressing strand, ε_{pc} : Strain of compressive side of prestressing strand, j : Distance between tension and compression resultants, ε_{pini} : Initial strain of prestressing strand at the time of anchoring, a : Shear span, L : Beam span, H : Elevation between stories]

ε_{pc} was obtained by applying Popovics' Equation³⁾ for the stress - strain relationship of the concrete and from the cross-sectional analysis using Navier's hypothesis taking into account ε_{pini} . Next, the second inflection point in the envelope was obtained. It was assumed that the strain in the tensile side prestressing strand was the strain for 90% of the load against 0.2% permanent elongation in the tensile test for the prestressing strand. The moment M_2 at the second inflection point in the envelope was calculated by setting $\varepsilon_{pt} = \varepsilon_{pini} + \Delta\varepsilon_p = \varepsilon_{0.9}$ in Equation (9). Story drift angle at the second inflection point R_2 in the envelope was obtained from Equation (12) where the rotational angle of the press joint was obtained from Equation (11). It was judged that Equation (12) could be applied to the frames using the PC Mild Press Joints. This is because the deformation due to the rotational angle of the press joint occupied almost 100% of the story drift angle for the region larger than $R = 1/100$ rad. Also, δ_2 as an extracted quantity of prestressing strand was obtained from Equation (13)

$$\theta_2 = \frac{\delta_2}{\alpha} \quad (11)$$

$$R_2 = \frac{2(\theta_2 \cdot a)}{L} \quad (12)$$

$$\delta_2 = 2 \int \varepsilon(x) dx = \Delta\varepsilon_p \cdot l_x \quad (13)$$

[α : Distance from the neutral axis to the tensile side prestressing strand, δ_2 : Extract quantity of prestressing strand, $\Delta\varepsilon_p$: Incremental strain of prestressing strand on the beam column interface]

It was assumed that strain used for the extract quantity of prestressing strand δ_2 was in the symmetrical triangle distribution having a beam column interface at the center, as shown in the lower part of Figure 11. Results of the bond tests⁴⁾ carried out for the prestressing strands used in the experiments were reviewed for the strain distribution. The bond length l_x was defined by Equation (14).

$$l_x = \frac{\Delta\varepsilon_p \cdot E_p \cdot A_p}{\tau_{ave} \cdot \psi} \quad (14)$$

[τ_{ave} : $\tau_{ave} = 1.43 \text{ N/mm}^2$ from the average bond stress of the prestressing strand and grout material (Bond test⁴⁾), ψ : Periphery of prestressing strand surface (= 53.34 mm)]

Results obtained from the method employed in this study are shown by a bold solid line in Figure 12. As a result, it can be generally concluded that the method can model the envelope.

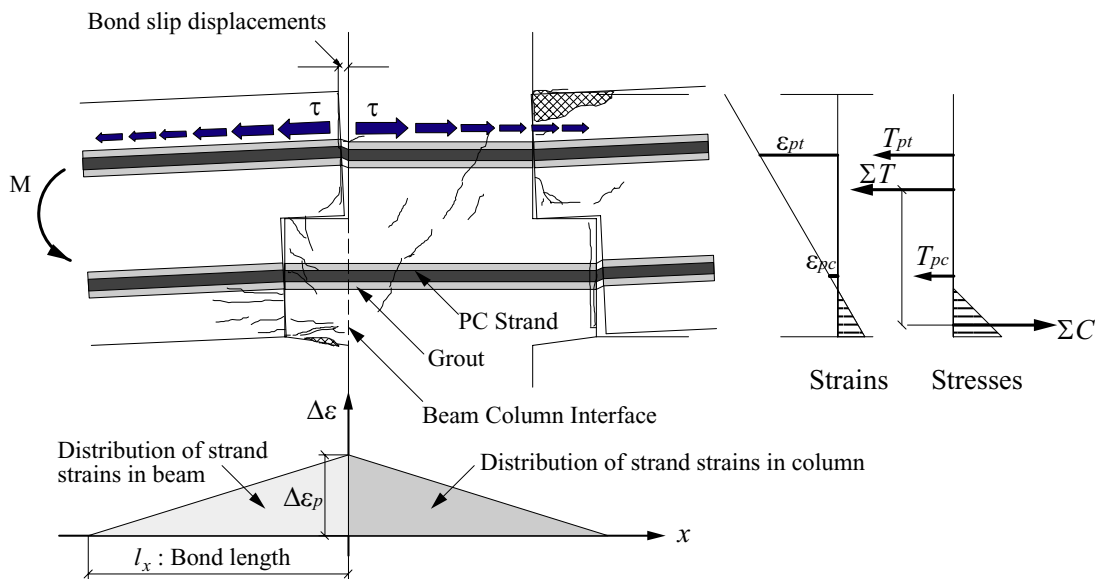


Figure 11 Strains of PC Strands and Bond Slip Displacement

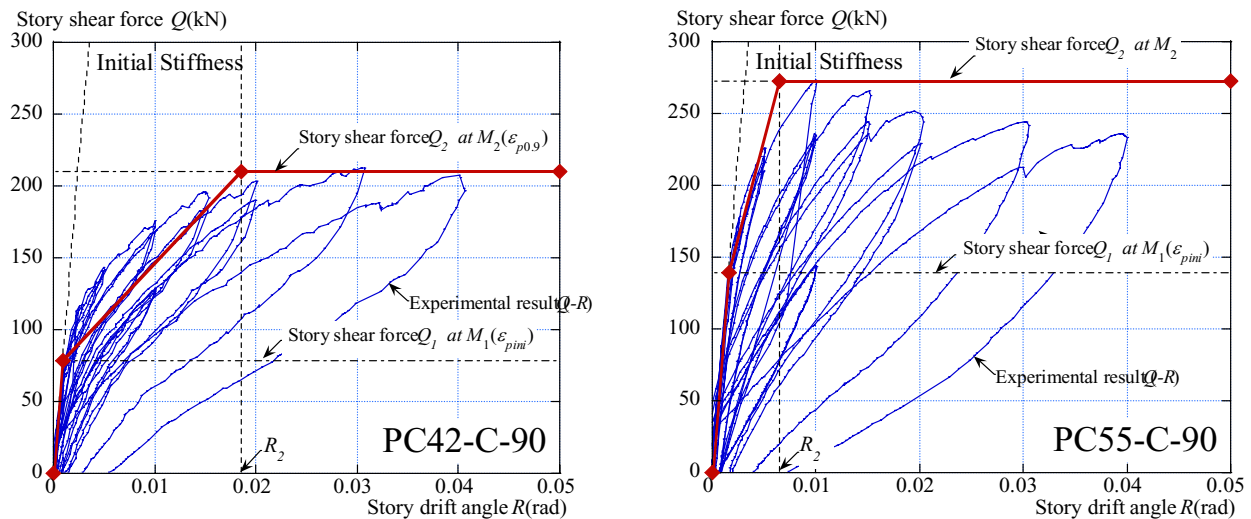


Figure 12 Experiment Results and Tri-Linear Envelope

5. CONCLUSIONS

The following conclusions were drawn from the study where partial frame experiments were conducted using prestressing strands and verification was obtained by comparison with RC frames.

- 1) Hysteresis characteristics of the frame using the PC Mild Press Joint were noted. Extremely small residual deformation showed high restoration capability.
- 2) Damage was limited to the part near the beam column interface. Damage could be controlled.
- 3) Shear crack strength of the joint could be evaluated by taking into account the beam prestress.
- 4) Increase in shear strength of the joint by about 40% of the initial anchoring force can be expected for the current specimens.
- 5) Envelope of rigidity and strength of the frames with PC Mild Press joints could be modeled using the proposed method.

References:

- 1) Matsuzaki, Y., Wada, A. et. Al. (2001), "Damage Control Design by Precast-Prestressed Concrete Structure with MILD-PRESS-JOINT (Part1-Part4)", Summaries of Technical Papers of Annual Meeting Architectural Institute of Japan C-2, pp.893-900
- 2) Architectural Institute of Japan (1999), "All Standard for Structural Calculation of Reinforced Concrete Structures –Based on Allowable Stress Concept- revised 1999"
- 3) Popovics, S. (1973), "A Numerical Approach to The Complete Stress-Strain Curve of Concrete, *Cement and Concrete Research*, 3, pp583—559
- 4) Matsuzaki, Y., Wada, A., Sakata, H. et. Al. (2003), "Study on Damage Control Design by Precast-Prestressed Concrete Structure with MILD-PRESS-JOINT (Part3. Bond Behavior) Summaries of Technical Papers of Annual Meeting Architectural Institute of Japan C-2, pp.991-992

CURRENT STATUS OF JAPANESE PASSIVE CONTROL SCHEME FOR MITIGATING SEISMIC DAMAGE TO BUILDINGS AND EQUIPMENTS

K. Kasai ¹⁾

*1) Professor, Structural Engineering Research Center, Tokyo Institute of Technology, Japan
kasai@serc.titech.ac.jp*

Abstract: Due to the recent earthquakes in the U.S. and Japan, many modern buildings ceased functioning and required costly structural and nonstructural repairs, although they successfully protected the lives of the occupants. Because of these, most major buildings constructed after the earthquakes utilize either passive-control scheme or base-isolation scheme in order to better protect the building and its contents. This paper addresses current status of passive control technology being implemented in Japan. Four major groups of dampers and their basic mechanisms are discussed. Three groups of frames are explained, referring to different connection schemes and deformation lags between the frame and damper. A unified approach to assess effectiveness of various dampers and frames will be presented.

1. INTRODUCTION

Passive control scheme has established its status as a viable means to enhance seismic performance of buildings (JSSI 2003, JSCA 2000). In this scheme, the damper connected to the structural frame dissipates the seismic input energy, thereby reducing the kinetic energy and vibration of the building. Japanese desire for adopting this scheme has increased considerably, especially after the recent earthquakes caused serious socio-economical problems in the metropolitan areas of the United States (Northridge) and Japan (Kobe). Due to these earthquakes, many modern buildings ceased functioning and required costly structural and nonstructural repairs, although they successfully protected the lives of the occupants. Because of these, a number of Japanese major buildings constructed after the earthquakes utilize the passive control scheme to better protect buildings and their contents. The number of such buildings increased to about three hundred in the year of 2002, and has been growing rapidly in Japan (e.g., JSCA 2000).

Considering the above circumstances, the writer has been conducting research into various issues for producing passively controlled buildings of high reliability and performance. The writer was also involved in development of design and construction manual of such buildings, leading the Response Control Committee, Japan Society of Seismic Isolation (JSSI). This so-called "JSSI manual" was published recently (JSSI 2003), and refers to mechanism, design, fabrication, testing, quality control, analytical modeling of dampers, as well as design, construction, and analysis of passively controlled buildings. It was developed by more than 50 members who are university researchers, structural designers, and engineers from about twenty damper manufacturing companies.

This paper describes current status of the Japanese passive control technology, including overview of the writer's research (Kasai et al. 1998-2004) and committee's accomplishments (JSSI 2003). Some of the issues abovementioned are not included in this paper due to page limitation. Such issues are described in detail in the JSSI Manual (2003).

2. MAJOR DAMPER TYPES

Numerous dampers are being produced and developed in Japan, and they are categorized into four types; oil damper, viscous damper, viscoelastic damper, and steel damper, as shown in Fig. 1.

Viscous damper produces the hysteresis loop of combined ellipse and rectangle. The material used is polymer liquid, and its resistance against flow produces the damper force. The damper possesses configurations of vertical panel, box, or cylinder (Furukawa et al. 2002, JSSI 2003).

Oil damper produces the hysteresis loop of ellipse. The material used therein is oil, and its resistance against flow at orifice produces the damper force. The damper possesses the configurations of cylinder, and it is usually provided with a relief mechanism that prevents increase in force, making the hysteresis like a rectangle shape (Tsuyuki et al. 2002, JSSI 2003).

Viscoelastic damper produces the hysteresis loop of inclined ellipse. In some material, the hysteresis is close to bilinear especially when it is under large deformation. The material used is polymer composite of acryl, butadiene, silicon, or others, and resistance against loading is produced from the molecular motion. Typical damper has configurations of vertical panel or tube, but it could be designed for many other configurations as well (Okuma et al. 2002, JSSI 2003).

Steel damper produces bi-linear hysteresis. The material is steel, but those using lead or friction pad can exhibit similar behavior. These materials produce elasto-plastic resistance due to yielding or slipping. Typical damper has configuration of vertical panel or tube, but it could be designed for many other configurations as well. This damper is the least expensive among the four types (Nakata .2002, JSSI 2003)

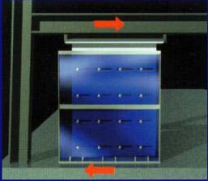
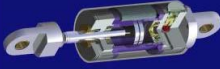
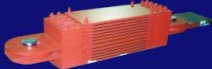

Viscous Damper	Oil Damper	Viscoelastic Damper	Steel Damper
			
$F = C \dot{u}^\alpha$	$F = C \dot{u}$	$F = K(\omega) \cdot u + C(\omega) \cdot \dot{u}$	$F = K \cdot f(u)$
Combined Ellipse and Rectangle Hysteresis	Ellipse Hysteresis	Inclined Ellipse Hysteresis	Bilinear Hysteresis
Silicon Fluid etc.	Oil	Acryl, Butadiene etc.	Steel, Lead, Friction Pad, etc.
Shear Resistance, Flow Resistance	Orifice Flow Resistance	Shear Resistance	Yielding Resistance Slipping Resistance
Plane, Box, and Tube Shapes	Tube Configuration	Tube and Plane Shapes	Tube and Plane Shapes

Figure 1 Major Damper Types

3. MAJOR FRAME TYPES

Figure 2 shows various frame types being used in Japan. The frame types are categorized into directly connected system, indirectly connected system, and special system. More systems are expected to appear in the near future, having better control performance and architecturally superior configurations.

Directly connected system is wall type, brace type, or shear link type. In such a system, the ends of the combined damper and relatively stiff supporting member are connected to the upper and lower floor levels. In other words, the damper is effective in directly controlling the drifts of the frame.

Indirectly connected system is stud type, bracket type, or connector type. In such a system, both ends of the damper are connected to the beams and columns that could deform locally and absorb a portion of the deformations that otherwise could be imposed to the damper. Thus, the damper is generally less effective than those of the directly connected system mentioned above (Kasai and Jodai 2002). However, since the system has an advantage of offering greater freedom for architectural planning, it has been much favored currently by the structural engineers and architects in Japan.

Special system considered herein is either column type or beam type. In such a system, the damper is inserted into intentionally disconnected zone of a beam or a column, and becomes a part of those members. Thus, it does not create any obstacle in the floor plan, but its control effectiveness depends on how rigid the rest of the frame is. Similarly to the indirectly connected system, the frame must be very stiff such that the deformation takes a place in the damper. Kanada et al. (2002) for instance described a real application of the column type, which turned out to be very effective in controlling both displacements and forces including uplift force of the foundation.

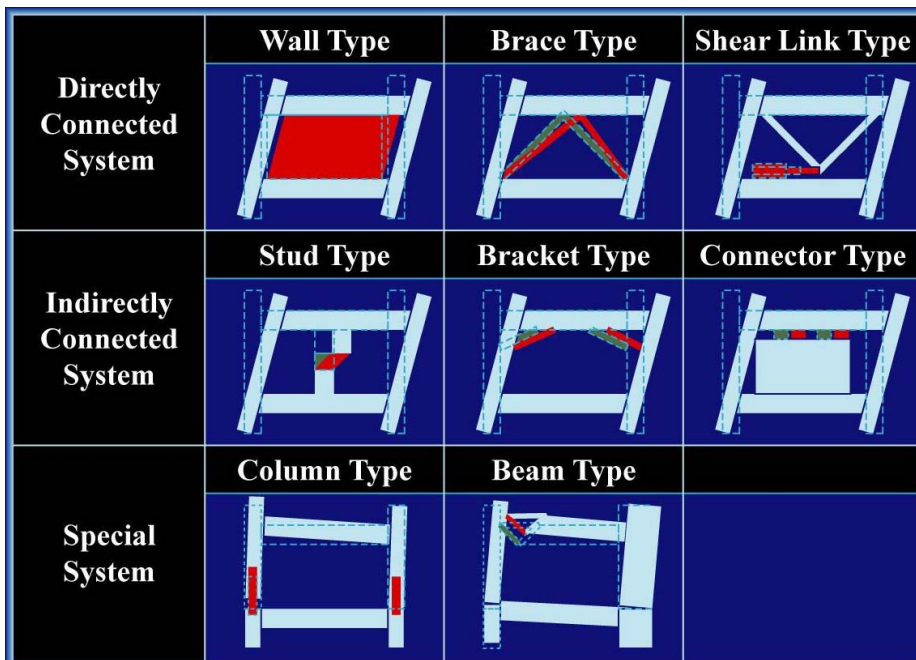


Figure 2 Major Frame Types

4. UNIFIED MODELING OF VARIOUS SYSTEMS FOR DESIGN

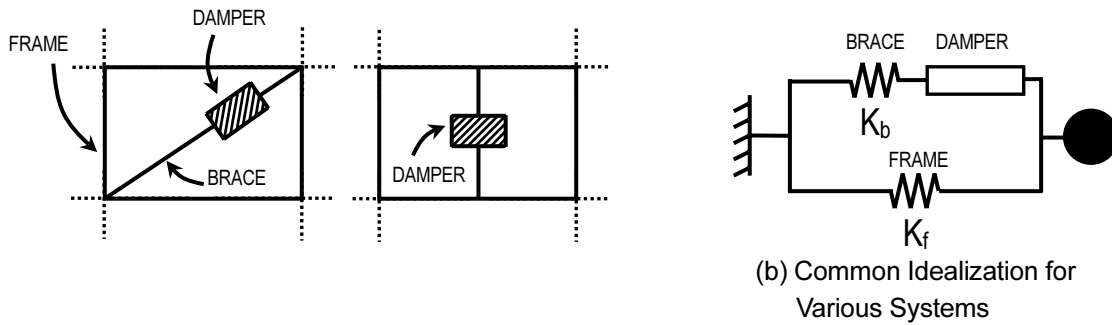
4.1 Model Idealization

Previous chapters described 4 types of dampers and 8 different frames. About 20 combinations of the dampers and frames are used currently in Japan (Kibayashi et al. 2002, JSSI 2003). More combinations are expected, since new dampers and/or frames are being developed in Japan. Thus, it is important to develop common methodology that evaluates various passive control systems having different dampers and frames. Such methodology would enable engineers to understand and directly compare control mechanisms, performance ranges, and element interactions of various systems.

Pursuant to these, the writer proposed a common model to represent properties and characteristics of various passive control systems (e.g., Kasai et al. 1998, Kasai and Okuma 2001b, Kasai et al. 2003c). Figure 3 shows an example, where two distinct systems, directly- and indirectly-connected

systems (Chapter 3), are commonly considered as an equivalent SDOF (single-degree-of-freedom) system. The SDOF system consists of damper and supporting member (e.g., brace) connected in series, as well as a frame connected to these components.

As depicted by Figure 3(b), the parameters affecting control are the mass, elastic stiffness of the frame and brace, and damping and stiffness of the damper. As a general term, “*added component*” is defined for the damper and brace connected in series. In this component, the brace deformation can reduce the damper deformation, and consequently energy dissipation. Hence, appropriate modeling of the added component is an essential step toward correct performance evaluation.



1 Figure 3 (a) Example Configurations of Passive Control Systems, and (b) Common SDOF Model

Figure 4 shows four added components containing different dampers. The brace is considered to be elastic and its stiffness is defines as K_b . Following comments are given for each added component:

- (a) Energy dissipater of *steel damper* is expressed by an elasto-plastic spring, and its elastic stiffness is defined as K_d . Added component elastic stiffness K_a is expressed simply by K_d and K_b only.
- (b) Energy dissipater of *oil damper* is expressed by a bilinear dashpot, and its viscous coefficient C_d switches between high and low values when the “relief load” (Chapter 2) is exceeded. The damper also has elastic stiffness K_d , due to compressive modulus of the oil. Thus, equivalent brace stiffness K_b^* , putting K_d and K_b together, is sometimes used for the ease of modeling.

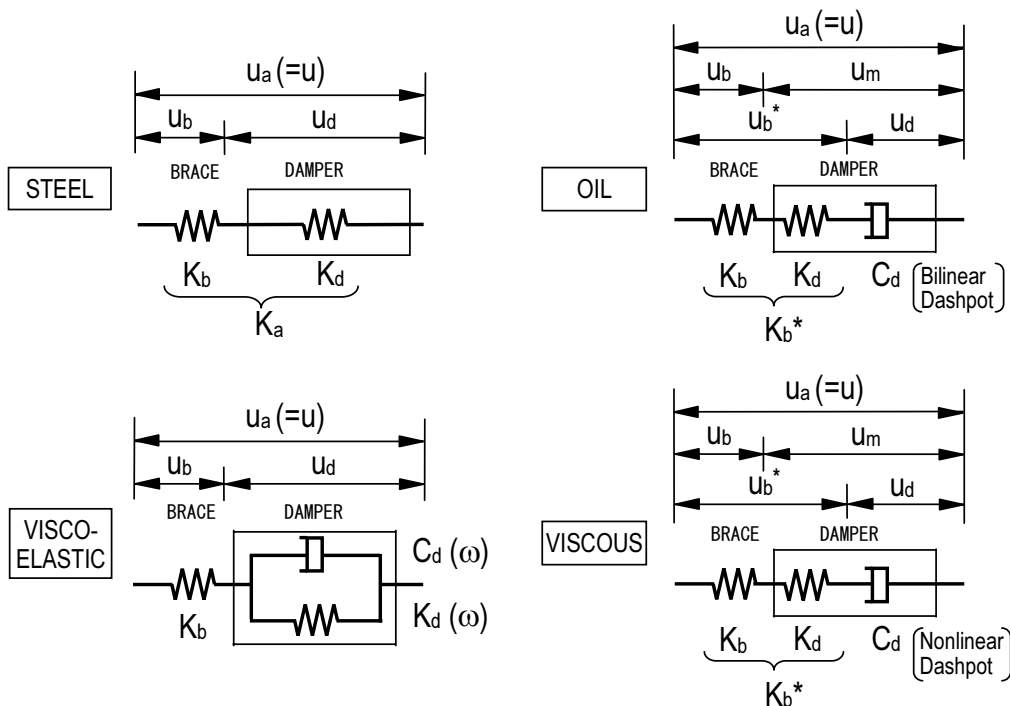


Figure 4 Four Types of Dampers and Added Components

- (c) Energy dissipater of *viscoelastic damper* is expressed by a dashpot and a spring connected in parallel. Their viscous coefficient C_d and elastic stiffness K_d , respectively, depend on the excitation frequencies. This added component, unlike others, includes parallel elements, and the brace having elastic stiffness K_b is the only element attached in series.
- (d) Energy dissipater of *viscous damper* is expressed by a nonlinear dashpot. The dashpot force equals the viscous coefficient C_d times the fractional power of the velocity. Like the oil damper, it has elastic stiffness K_d due to compressive modulus of the viscous polymer liquid, and equivalent brace stiffness K_b^* , putting K_d and K_b together, is sometimes used for the ease of modeling.
- Except for a case using steel damper, each of stiffness and damping properties of the added component is expressed by K_d , K_b , C_d , and excitation frequencies.

4.2 Hysteretic Characteristics of Passive Control Systems

Figure 5 shows hysteresis curves of the energy dissipater, added component, and system (including frame), for the cases using four different dampers. Sinusoidal deformation of a given peak deformation magnitude is imposed to each, and the figure plots the steady-state responses.

Note the black dot (●) indicating the point of peak deformation, where the “*storage stiffness*”, or so-called equivalent stiffness, is defined as the corresponding force divided by the deformation. Likewise, “*loss stiffness*” is defined as the force at the white dot (○) divided by the peak deformation. From now on, the storage stiffness K_d' , K_a' , and K' , the loss stiffness K_d'' , K_a'' , and K'' will be considered for the energy dissipater, added component, and system, respectively.

These stiffnesses can be mathematically expressed in terms of K_d , K_b , C_d , and excitation frequencies mentioned in Section 4.1. Based on this, one can determine the forces at the peak and zero displacements, respectively, and subsequently the peak force, energy dissipated, deformation lag and magnitudes at each component, making evaluation of the control system possible.

Energy dissipater of the *viscous damper*, when its force for instance is proportional to 0.4th power of velocity (Section 4.1), exhibits hysteresis of a rectangle shape with round corners. The force is relatively large at small deformation, resulting in almost rigid response of the dissipater. At large deformation, the force is almost bounded, preventing overstress of the damper, connections, and surrounding members. Added component deforms more and shows diametrically longer hysteresis loop (Figure 5) because of the elastic springs (Figure 4), and develops non-zero storage stiffness unlike the dissipater. As for the system, its storage stiffness is sum of those of the added component and the frame due to their parallel combination, whereas the loss stiffness equals that of the added component, since the frame is considered to be elastic (Kasai et al. 2003c, JSSI 2003).

Energy dissipater of the *oil damper* shows an elliptical hysteresis curve at small deformation and almost a rectangle shape at large deformation. It produces the force of a relatively high magnitude at small deformation, but it does not behave as rigid as the viscous damper mentioned above. The trends of storage and loss stiffnesses of the added component as well as system are similar to those observed from the case of viscous damper (JSSI 2003, Kasai and Nishimura 2004d).

Energy dissipater of the *viscoelastic damper*, when it is a linear type as shown (Sec. 3.1), exhibits hysteresis of an inclined ellipse. Unlike the nonlinear dampers above, the shape of the hysteresis remains the same regardless of the peak deformation, which makes dissipater’s force unbounded and storage and loss stiffnesses constant. The hysteresis of the added component is more slender due to the spring attached (Figure 4), and the storage and loss stiffnesses are smaller than those of the dissipater. As for the system, its storage stiffness is sum of those of the added component and the frame, whereas the loss stiffness equals that of the added component (Kasai et al. 1998, Kasai and Okuma 2001b, 2002a, JSSI 2003).

The energy dissipater of the *steel damper* exhibits hysteresis of a parallelogram shape approximately. Refined modeling of the hysteresis and its dependency on the strain rate will be given in the near future. In contrast to the other dampers, the dissipater does not absorb energy during small deformation. At large deformation, it absorbs energy by yielding of the material, cumulating damage

to the material. Therefore, unlike the other dampers, effect of such damage must be considered when using this damper. This does not, however, prohibit the use of the steel damper, since it can sustain large number of inelastic cyclic excursions when adequately detailed, and it is inexpensive than other dampers. The trends of storage and loss stiffnesses of the added component and system are similar to those observed from the case of the viscous damper (Kasai et al. 1998, Kasai et al. 2003b, JSSI 2003).

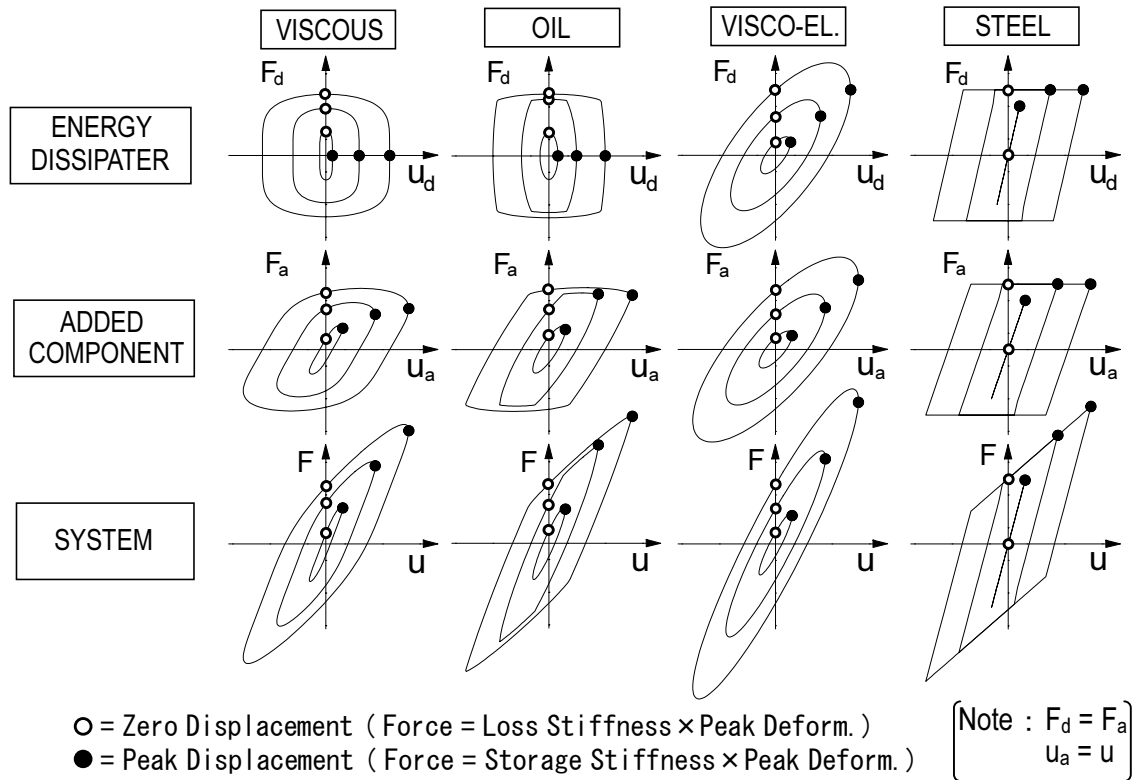


Figure 5 Steady-State Responses of Energy Dissipaters, Added Components, and Systems for 4 Different Dampers and 3 Different Peak Deformations

5. PERFORMANCE CURVES AND DESIGN

5.1 Use of Storage Stiffness and Loss Stiffness

To date, design and performance prediction of passive control systems have typically been based on iterations involving extensive response time history analyses or equivalent static analyses using various types and sizes of dampers. The analysis methods are also different between the various systems; these make direct comparison of the systems difficult. Moreover, they offer limited information about the possible range of seismic performance variations and the complex interactions between the dampers, their supporting members, frame, seismic input, and response.

Using mathematical expressions for the storage stiffness and the loss stiffness (Section. 4.2), the writer developed formulas to evaluate dynamic properties and responses for different dampers and systems. Based on this and using idealized seismic response spectra, the writer also proposed a method to commonly express the seismic peak responses of systems and local members by a continuous function of the structural and seismic parameters. The method promotes understanding of the commonalities and differences between various systems having distinct energy dissipation mechanisms. It requires only simple calculations, and its prediction agrees well with the results of the extensive multi-degree-of-freedom dynamic analyses performed.

Figure 6 shows examples for evaluating multi-story passive control systems using the four types of

dampers mentioned in Chapters 2 and 4. The curves are named as *performance curves* which model buildings as an equivalent SDOF system explained in Sec. 3.1. The curves show both *displacement reduction ratio* R_d and *force (or acceleration) reduction ratio* R_a that are defined as the values of the peak responses normalized to those having no dampers (e.g., Kasai et al. 1998, JSSI 2003). In these examples, pseudo-velocity response spectrum is assumed to be constant over different periods, as often considered when designing moderate to tall buildings. The response reduction ratios appear to vary widely, depending on balance among the frame, the damper, and the supporting member such as a brace. Note the following for each figure:

- (a) When using *steel dampers*, K_d/K_f and μ govern the response reduction. The former is a ratio of the added component elastic stiffness to the frame elastic stiffness, and the latter is a ductility ratio of the system.
- (b) When using *oil dampers*, K_{dl}''/K_f and K_b/K_f govern the response reduction. The former is a ratio of the dissipater loss stiffness (defined when peak force is below the relief load) to the frame elastic stiffness, and the latter is a ratio of the brace elastic stiffness to the frame elastic stiffness. Relief load of the dissipater (Section 4.1) is already set optimum in the curves.
- (c) When using *viscoelastic dampers*, K_d''/K_f and K_b/K_f govern the response reduction. The former is a ratio of the dissipater loss stiffness to the frame elastic stiffness, and the latter is a ratio of the brace elastic stiffness to the frame elastic stiffness.

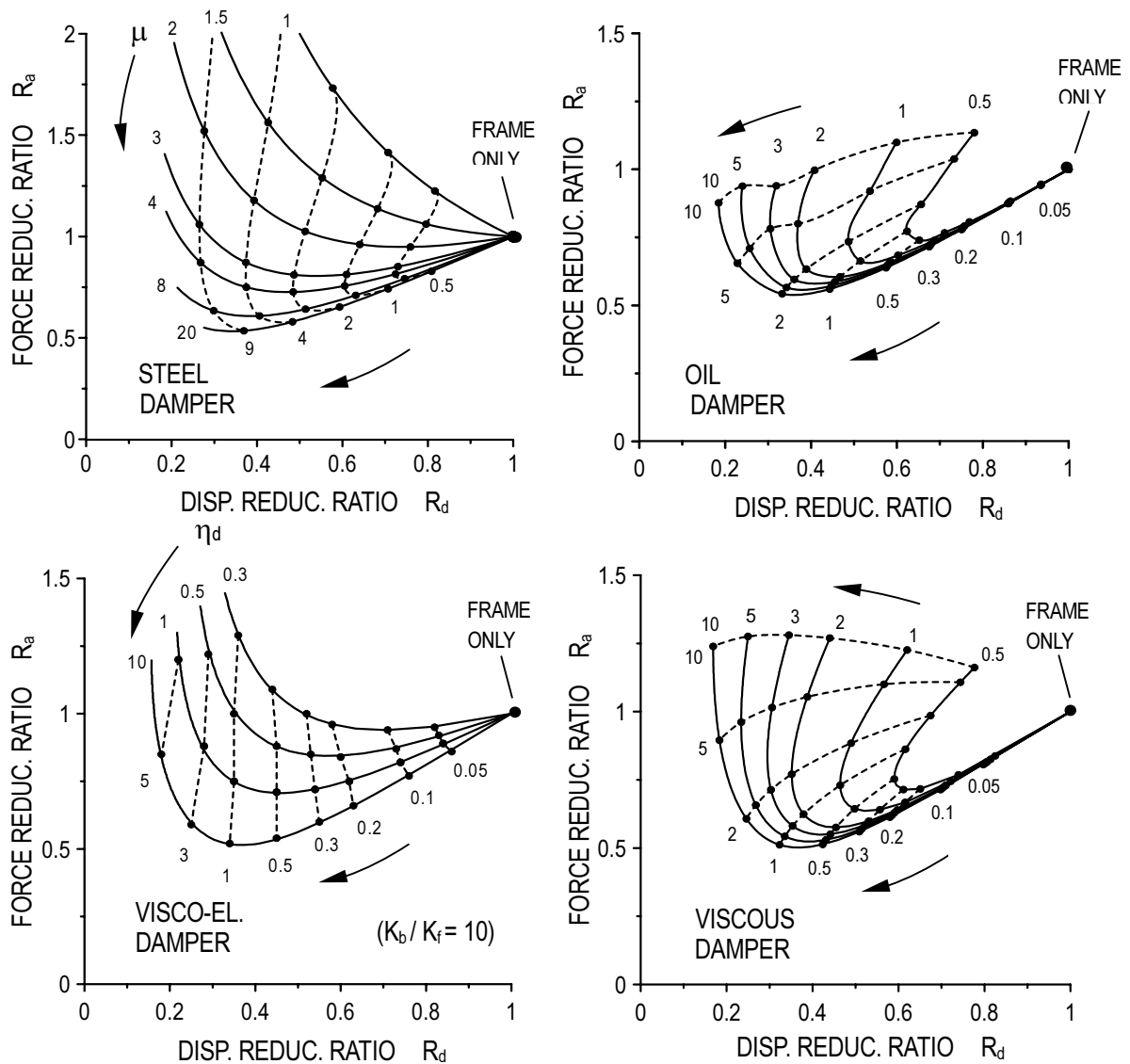


Figure 6 Performance Curves for Passive Control Systems Using 4 Different Damper Types

(d) When using *viscous dampers*, K_d^*/K_f and K_b^*/K_f govern the response reduction. The former is a ratio of the dissipater loss stiffness to the frame elastic stiffness, and the latter is a ratio of the equivalent spring stiffness to the frame elastic stiffness. The equivalent spring stiffness is obtained from the damper elastic stiffness and brace elastic stiffness (Figure 4). The curves plotted in Figure 6 are for a case where dissipater force is proportional to 0.4th power of velocity.

Figure 6 enables the users to quickly evaluate response reduction: To a certain extent, larger damper leads to more reduction of displacement and force. However, excessively large damper appears to be ineffective for displacement control, and detrimental in force control, as observed from sharply rising curves. Figure 6 also shows decrease of control effectiveness by smaller brace stiffness: brace deforms more, and damper deformation as well as energy dissipation becomes smaller.

5.2 Design of Passive Control Systems

The performance curves (Figure 6) can be used effectively for determining necessary sizes of damper and brace for the required performance. For instance, given an earthquake input of a smooth response spectrum, the peak displacement and base shear of the frame prior to damper installment can be predicted easily from the response spectrum. Then, one can estimate target reduction ratios of displacement and base shear based on the required performance. Considering the target reduction ratios and the performance curve, one can determine the necessary stiffness of the damper and brace. Optimum design solution to control both displacement and force can also be found from the performance curve.

This design result for the SDOF system (Figure 3) can be equally applied to sizing of the dampers in the multistory case as well. That is, one could size the damper and brace such that the ratios of their stiffnesses to the frame story stiffness satisfy the ratios determined from the SDOF approach explained above. When modeling the MDOF frame by the SDOF system, one could use the first mode effective mass approximately equal to 0.8 times total mass for a regular building, and effective height based on the static deflected shape of the frame.

Since the steel damper, viscoelastic damper, and some of the viscous dampers possess considerable storage stiffness, they could be used to tune the storage stiffness of the system at each story level. This can result in the MDOF system having adequate overall storage stiffness distributions throughout the building height. The technique is useful when the frame has undesirable stiffness distributions and tendency to suffer from concentration of deformation at particular story levels. It has been proved to assure relatively uniform story drift distributions in spite of the undesirable frame stiffness distributions (e.g., Kasai et al. 1998, JSSI 2003).

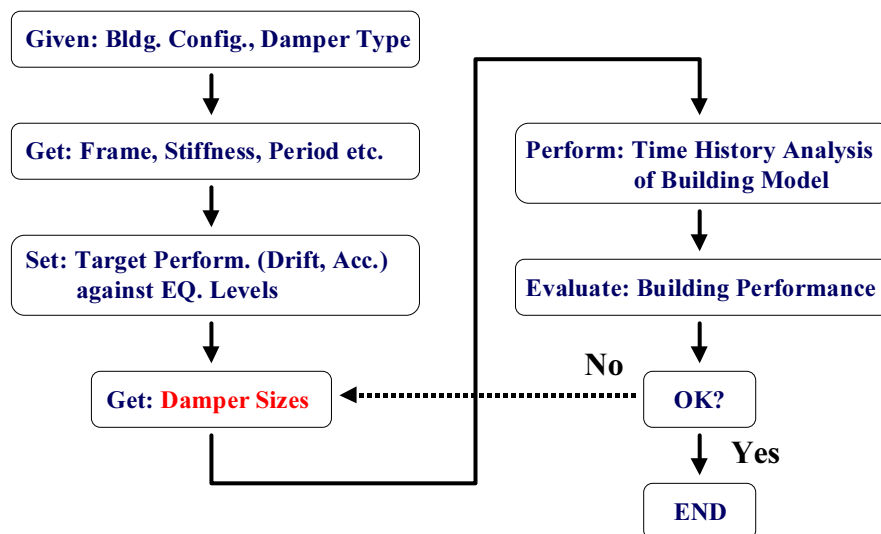


Figure 7 Summary of Damper and System Design Procedures

After completion of design, one can create a MDOF analytical model, and perform time-history analyses using appropriately selected ground motions. Analytical results will be used to confirm or make modifications in design. Fig. 5 summarizes the design procedures. Numerous examples and details for the design procedures are documented in the JSSI manual (2003).

6. TIME HISTORY ANALYSIS AND DISSEMINATION OF COMPUTER CODES

In Japan, significant progress is being made in numerical modeling of the dampers (Figures 1, 4, and 5) for time-history analysis of passively controlled systems. However, the new models, in spite of enhanced accuracy and efficiency, have not necessarily been implemented into the computer programs of software companies or construction companies.

The writer and JSSI members, therefore, intended to accelerate implementations, by publishing model algorithms and computer codes. This should lead to more reliable and fair assessment of the passive scheme, thereby promoting sound growth in the technology. In general, proposed analytical elements simulate the added components (Fig. 4) rather than dampers alone. Such modeling is advantageous for reducing the degree of freedom as well as maintaining numerical stability. The following briefly describes the models, and detailed information can be found from the references.

The element involving *oil damper* rests the viscous coefficient of energy dissipater to a small value when subjected to a large deformation rate, in order to simulate the relief mechanism explained in Section 4.1 (Takahasi and Sekiguchi 2002, JSSI 2003).

The element involving *viscous damper* uses, unlike the oil damper above, a nonlinear dashpot whose force is a fractional power of deformation rate (Oohara and Kasai 2002, JSSI 2003). For some types possessing elastic stiffness, the model considers an in-series combination of the spring and the nonlinear dashpot (Sekiguchi and Takahashi 2002, JSSI 2003). The elastic stiffness may be a nonlinear function of the deformation. Sensitivity against temperature must be modeled for some types.

The element involving *viscoelastic damper* could be either linear type, softening type, and stiffening type. Hysteresis loops of the three types show commonly an inclined ellipse at relatively small deformation, but they differ considerably at larger deformation. In order to simulate this and sensitivities against frequency and temperature, some models consist of in-series as well as parallel combinations of dashpots and springs (Kasai and Okuma 2001b, 2002a, JSSI 2003), and another model directly expresses the constitutive equation of the damper using fractional time-derivatives of the force and deformation (Kasai et al. 2001a, 2002e, 2003a, Ooki et al. 2002, JSSI 2003).

The element involving *steel damper* is proposed by utilizing the constitutive equations of steel material readily known from the past research (Ono et al. 2002), in contrast to the typical Japanese model assuming purely bi-linear behavior. The analysis results must be cross-referenced to cumulative damage of the damper, since the damper is typically designed to yield under the small and frequent seismic loads. Special model is developed for some dampers designed to a post-buckled range.

7. CONCLUSIONS

Passive control scheme has established its status as a viable means to enhance seismic performance of buildings. For the sake of further growth in this technology, it is necessary to promote understanding of the passive control schemes, as well as to create a uniform basis for assessment of the various stages to be followed during the design and construction process.

Pursuant to this, the writer and JSSI Response Control Committee have formulated Design and Construction Manual for Passively-Controlled Buildings (JSSI 2003). The committee consists of more than fifty members who are the researchers from universities and research institutes, the designers from general construction companies and design offices, and the engineers from more than twenty

device manufacturing companies.

Due to these efforts, various issues regarding Japanese passive control technology have been documented. Such issues are mechanism, design, fabrication, testing, quality control, and analytical modeling of various passive control devices, as well as design, construction, and analysis of passively controlled buildings. This paper has given brief overview of design and analysis part of the manual. More detailed information can be obtained from the writers' papers as well as the Manual. Furthermore, the abovementioned issues not discussed in this paper are described in detail in the Manual.

Acknowledgements:

The writer acknowledges support from Japan Ministry of Education, Culture, Sport, Science, and Technology (MEXT) for his research on various passive control systems. The writer also thanks the students at Kasai Laboratory, Tokyo Institute of Technology for their dedications to this research. Special gratitude is given to Mr. Kibayashi, the Senior Manager of Building Structural Design Division, Takenaka Corporation, for his close collaboration with the writer as well as significant contribution during the entire period of formulating the JSSI manual.

References:

- JSSI Manual (2003), Design and Construction Manual for Passively Controlled Buildings, Japan Society of Seismic Isolation (JSSI), First Edition, Tokyo, JAPAN, October (in Japanese, 405 pages).
- JSCA Specifications (2000), Design Methodologies for Response Controlled Structures, Japan Structural Consultants Association (JSCA), Tokyo, JAPAN, December, 2000 (in Japanese, 445 pages).
- Kasai, K., Fu, Y., and Watanabe, A. (1998), "Passive Control Systems for Seismic Damage Mitigation," *Journal of Structural Engineering*, American Society of Civil Engineers, **124**(5), 501-512.
- Fu, Y. and Kasai, K., 1998, "Comparative Study of Frames Using Viscoelastic and Viscous Dampers", *J. Struct. Eng.*, American Society of Civil Engineers, 122 [10], pp. 513-522
- Kasai, K., Teramoto, M., Okuma, K., and Tokoro, K. (2001a), "Constitutive Rule for Viscoelastic Materials Considering Temperature, Frequency, and Strain Sensitivities (Part 1: Linear Model with Temperature and Frequency Sensitivities)", *Journal of Structural and Construction Engineering (Transactions of AIJ)*, No. 543, pp. 77-86, May. (in Japanese)
- Kasai, K. and Okuma, K. (2001b), "Kelvin-Type Formulation and Its Accuracy for Practical Modeling of Linear Viscoelastic Dampers (Part 1: One-Mass System Having Damper and Elastic / Inelastic Frame)", *Journal of Structural and Construction Engineering (Transactions of AIJ)*, No. 550, pp. 71-78, Dec. (in Japanese)
- Kasai, K. and Okuma, K. (2002a), "Accuracy Enhancement of Kelvin-Type Modeling for Linear Viscoelastic Dampers (A Refined Model Including Effect of Input Frequency on Material Property)", *Journal of Structural Engineering*, Architectural Institute of Japan (AIJ), **48B**, pp.545-553, March. (in Japanese)
- Kasai, K., Teramoto, M., and Watanabe, Y. (2002b), "Behavior of a Passive Control Damper Combining Visco-Elastic and Elasto-Plastic Devices in Series", *Journal of Structural and Construction Engineering (Transactions of AIJ)*, No. 556, pp. 51-58, June. (in Japanese)
- Kasai, K. and Jodai, A. (2002c), "Dynamic Property, Behavior, and Their Simplified Estimation Rules for a Passive Control System with Stud-Type Viscoelastic Damper", *Journal of Structural and Construction Engineering (Transactions of AIJ)*, No. 558, pp. 125-132, Aug. (in Japanese)
- Kasai, K., Motoyui, S., and Ooki, Y. (2002d), "Application of Viscoelastic Dampers to Space Frames and Response Prediction Methods for a Single-Directional Earthquake", *Journal of Structural and Construction Engineering (Transactions of AIJ)*, No. 561, pp. 125-135, Nov. (in Japanese)
- Kasai, K. and Tokoro, K. (2002e), "Constitutive Rule for Viscoelastic Materials Having Temperature, Frequency, and Strain Sensitivities (Part 2: Nonlinear Model Based on Temperature-Rise, Strain, and Strain-Rate)", *Journal of Structural and Construction Engineering (Transactions of AIJ)*, No. 561, pp. 55-63, Nov. (in Japanese)
- Kasai, K., Ooki, Y., Amemiya, K., and Kimura, K. (2003a), "A Constitutive Rule for Viscoelastic Materials Combining Iso-Butylene And Styrene Polymers (Part 1: Linear Model Considering Temperature And Frequency Sensitivities)", *Journal of Structural and Construction Engineering (Transactions of AIJ)*, No. 569, pp.47-54, July. (in Japanese)
- Kasai, K., Ito, H., and Watanabe, A. (2003b), "Peak Response Prediction Rule for a SDOF Elasto-Plastic System Based on Equivalent Linearization Technique", *Journal of Structural and Construction Engineering (Transactions of AIJ)*, No. 571, pp.53-62, Sep. (in Japanese)
- Kasai, K., Suzuki, A., and Oohara, K. (2003c), "Equivalent Linearization of a Passive Control System Having Viscous Dampers Dependent on Fractional Power of Velocity", *Journal of Structural and Construction Engineering (Transactions of AIJ)*, No. 574, pp.77-84, Dec. (in Japanese)
- Kasai, K. and Okuma, K. (2004a), "Evaluation Rule and Its Accuracy for Equivalent Period and Damping of

- Frequency-Dependent Passive Control Systems —Global Damping Model of One-Mass System Having Elastic Frame and Either Viscoelastic or Oil Damper—”, *Journal of Structural and Construction Engineering (Transactions of AIJ)*, (in Review)
- Ooki, Y., Kasai, K., and Takahashi, O. (2004b), “Performance of Velocity-Dependent Dampers under Extremely Small Excitations”, *Journal of Structural Engineering*, Architectural Institute of Japan (AIJ), **50B**, March (in Print). (in Japanese)
- Kasai, K., Sakata, H., Komehana, S., and Miyashita, Y. (2004c), “Experimental Study on Daynamic Behavior of Timber Frame with Viscoelastic Damper”, *Journal of Structural Engineering*, Architectural Institute of Japan (AIJ), **50B**, March (in Print). (in Japanese)
- Kasai, K. and Nishimura, T. (2004d), “Equivalent Linearization of Passive Control System Having Oil Damper Bi-Linearly Dependent on Velocity”, *Journal of Structural and Construction Engineering (Transactions of AIJ)*, (in Review). (in Japanese)
- Kasai, K., Kibayashi M., Takeuchi T., Kimura Y., Saito Y., Nagashima I., Mori H., Uchikoshi M., Takahashi O., and Oohara K. (2002), “Principles and Current Status of Manual for Design and Construction of Passively-Controlled Buildings: Part-1: Background Scope, and Design Concept”, *Proc. Structural Engineers World Congress (SEWC)*, Yokohama, JAPAN, CD-ROM, T2-2-a-1
- Kibayashi, M., Kasai, K., Tsuji, Y., Kato, S., Kikuchi, M., Kimura, Y., and Kobayashi, T. (2002), “Principles and Current Status of Manual for Design and Construction of Passively-Controlled Buildings: Part-2 JSSI Criteria for Implementation of Energy Dissipation Devices”, *Proc. Structural Engineers World Congress (SEWC)*, Yokohama, JAPAN, CD-ROM, T3-3-1
- Takeuchi, T., Kasai, K., Ohara, K., Nakajima, H., and Kimura, Y. (2002), “Performance Evaluation and Design of Passively Controlled Buildings Using Equivalent Linearization”, *Proc. Structural Engineers World Congress (SEWC)*, Yokohama, JAPAN, CD-ROM, T2-2-a-2
- Ichikawa, Y., Takeuchi, T., Morimoto, S., and Sugiyama, M. (2002), “Practical Design of High-Rise Structure Using Viscoelastic Dampers and Hysteretic Dampers”, *Proc. Structural Engineers World Congress (SEWC)*, Yokohama, JAPAN, CD-ROM, T2-2-a-3
- Kanada, M., Kasai, K., and Okuma, K. (2002), “Innovative Passive Control Scheme: a Japanese 12-Story Building with stepping Columns and Viscoelastic Dampers”, *Proc. Structural Engineers World Congress (SEWC)*, Yokohama, JAPAN, CD-ROM, T2-2-a-5
- Ono, Y., Kaneko, H., and Kasai, K. (2002), “Time-History Analysis Models for Steel Dampers”, *Proc. Structural Engineers World Congress (SEWC)*, Yokohama, JAPAN, CD-ROM, T2-2-b-1
- Ooki, Y., Kasai, K., and Tokoro, K. (2002), “Time-History Analysis Models for Linear and Nonlinear Viscoelastic Dampers”, *Proc. Structural Engineers World Congress (SEWC)*, Yokohama, JAPAN, CD-ROM, T2-2-b-2
- Oohara, K., and Kasai, K. (2002), “Time-History Analysis Models for Nonlinear Viscous Dampers”, *Proc. Structural Engineers World Congress (SEWC)*, Yokohama, JAPAN, CD-ROM, T2-2-b-3
- Sekiguchi, Y., and Takahashi, O. (2002), “Time-History Analysis Models for Nonlinear Viscous Damping Wall”, *Proc. Structural Engineers World Congress (SEWC)*, Yokohama, JAPAN, CD-ROM, T2-2-b-4
- Takahashi, O. and Sekiguchi, Y. (2002), “Time-History Analysis Models for Nonlinear Oil Dampers”, *Proc. Structural Engineers World Congress (SEWC)*, Yokohama, JAPAN, CD-ROM, T2-2-b-5
- Tsuyuki, Y., Kamei, T., Gofuku, Y., Iiyama, F., and Kotake, Y. (2002), “Performance and Quality Control of Oil-Damper”, *Proc. Structural Engineers World Congress (SEWC)*, Yokohama, JAPAN, CD-ROM, T3-3-2
- Furukawa, Y., Kawaguchi, S., Sukagawa, M., Masaki, N., Sera, S., Kato, N., Washiyama, Y., and Mitsusaka, Y. (2002), “Performance and Quality Control of Viscous Dampers”, *Proc. Structural Engineers World Congress (SEWC)*, Yokohama, JAPAN, CD-ROM, T3-3-3
- Okuma, K., Ishikawa, K., Oku, T., Sone, Y., Nakamura, H., and Masaki, N. (2002), “Performance and Quality Control of Viscoelastic Dampers”, *Proc. Structural Engineers World Congress (SEWC)*, Yokohama, JAPAN, CD-ROM, T3-3-4
- Nakata, Y. (2002), “Performance and Quality Control of Steel Hysteretic Damper”, *Proc. Structural Engineers World Congress (SEWC)*, Yokohama, JAPAN, CD-ROM, T3-3-5

PASSIVE VIBRATION-CONTROL CONCEPT FOR TRUSS FRAME STRUCTURES

T.Takeuchi¹⁾

1) Associate Professor, Dept. of Architecture & Building Engineering, Tokyo Institute of Technology, Japan
ttoru@arch.titech.ac.jp

Abstract: Truss frame generally had to be designed elastically even against large seismic force, because of fragile characteristics led by member buckling. In this paper, damage tolerant design for truss frame structures using energy dissipation members in critical positions are discussed. Detailed designs for high-rise rack warehouses and communication towers are studied and tested, followed by simple method for evaluating the effect of these members.

1. INTRODUCTION

In seismic area, plastic design with moment frames have been popular for long time, with the concept of ductile characteristics led by plastic-hinges on bending beam ends. On the other hand, truss frame structures, popularly used for long-span roofs or industrial facilities, had to be designed elastically against design loads, because of less-ductile characteristics due to the axial member's buckling. However, designing truss structures elastically against large earthquake is not economic, not elegant in design, and remaining risks for fragile collapse in the event of seismic level exceeding the design criteria.

Recently, passively controlled buildings have become popular in Japan, and various types of passive energy dissipation devices are put in practical use. Many of them are incorporated within moment frames, achieving damage tolerant design, which keeps main structures in elastic even with great earthquake. The same concept can be applied for truss frame structures by incorporate energy dissipation members in critical positions, plasticize them firstly while other truss members are kept before buckling, and control entire structure ductile (Fig.1). This design concept will enable truss frame structures to be slender, elegant, economic and safe from buckling even in heavy seismic areas.

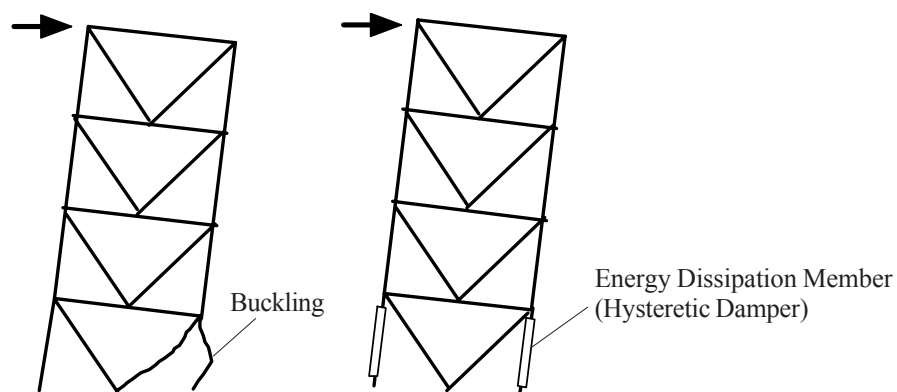


Figure 1. Damage Tolerant Concept for Truss Frame

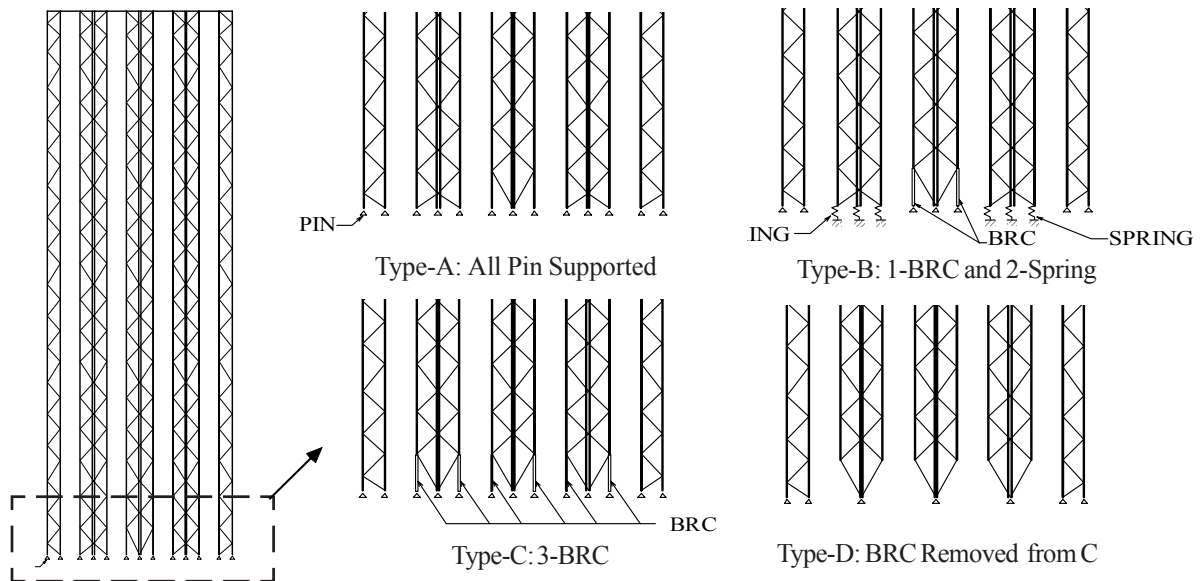


Figure 2. Rack Structure and Supporting Options

In this paper, above design concept is applied to practical design of high-rise automatic rack warehouse and communication tower using hysteretic energy-dissipation members, introducing their details and effects.

2. APPLICATION FOR RACK WAREHOUSES

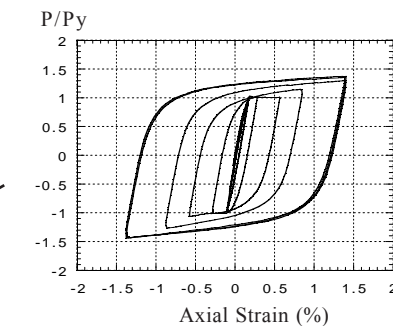
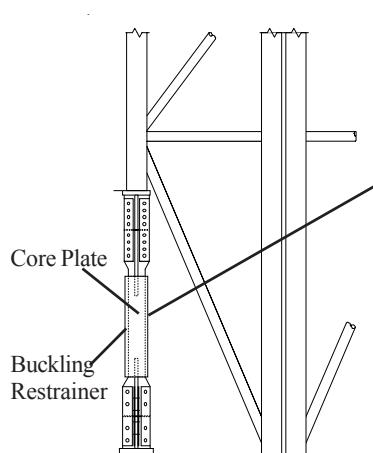
The high-rise automatic rack warehouse are composed of 52m high, 5 lines of 1.3m-2.6m wide trussed structures connected each other at their top by horizontal beams (Fig.2). Each line of trusses is independent between the ground level and the top to keep spaces for vertical cranes, the aspect ratios of each set of trusses reaches 20 to 40. As diagonal braces stiffen the frames in longitudinal direction, this transverse direction is critical in strength and deflections. Walls are attached on the side trusses and roofs are on top beams, the rack structure itself composes the warehouse frame. The critical members against horizontal forces are the base-chords of the trusses, and buckling of these members lead to the collapse of entire structure. For the sake of ductile design, these chords are replaced by Buckling-Restrained Columns (BRC; e.g. Unbonded Braces), which perform as axial elasto-plastic dampers.

In this study, four types of truss structures as shown in Figure 2 are studied.

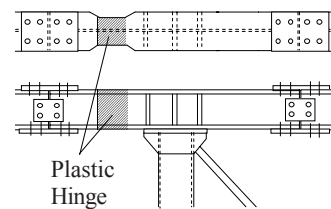
Type-A: Normal truss structure whose bases are all pin-supported.

Type-B: Side base chords of the center truss are replaced by BRC, while other chords are supported by pin or spring to concentrate reaction forces into BRC.

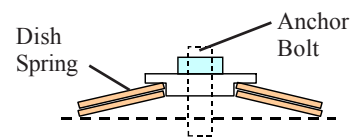
Type-C: Side chords of all trusses except for side trusses are replaced by BRC.



(a) Buckling Restrained Column (Unbonded Brace) and its Hysteresis Loop



(b) Dog-bone Plastic Hinges at Top Beams



(c) Dish Springs at Anchor Bolts

Figure 3 Details of the Rack Structure

Type-D: All BRC are removed from Type-C.

In Type-B and Type-C, axial yielding of BRC and plastic hinges of the top beams decide collapsing mechanism of the entire structure. The side trusses are kept in elastic while BRC are going into plastic, and pull back the structure from residual deformation after earthquake being finished.

Detailed design of each part is shown in Figure 3. Detail of BRC at bases are in Figure 3(a). The base-side chords of the truss are replaced by Unbonded Braces, which are composed of core plates and concrete-filled tube restrainer (Fujimoto et.al. 1990). Because of restrainer keep core-plate from buckling even in plastic zone, they show symmetrical hysteretic loops and excellent characteristics as energy dissipation members. They are connected to the truss members with bolts, which enables replacement of BRC after earthquake.

The top beams have dog-bone shape at truss sides, which realizes stable plastic hinges (Fig.3(b)). For spring supports in Type-B frame, dish springs are inserted for anchor bolts at column bases (Fig.3(c)).

To verify the performance of these structures against large seismic vibrations, time-history analyses are carried out on each types of structure. The analytical models are two-dimensional composed of each member as beam element, considering axial forces and bending moments. For seismic vibrations, El Centro NS, Taft EW, Hachinohe NS, and Artificial wave using site ground conditions are used for design loads with the level of 50 cm/sec in maximum velocity. The maximum responses for Type-A, Type-B and Type-C are shown in Figure 4. In shear forces, additional forces of each line of trusses are shown. In story drift, horizontal displacement of the side trusses, which are the most critical in each truss, are represented.

The ultimate capacity of the frame is about 450 kN at base, and maximum response at Type-A frame exceeds the ultimate capacity. This means Type-A frame will collapse with foresaid seismic vibration caused by the buckling of base columns. On the other hand, maximum story drift is about 42mm in 3365mm unit

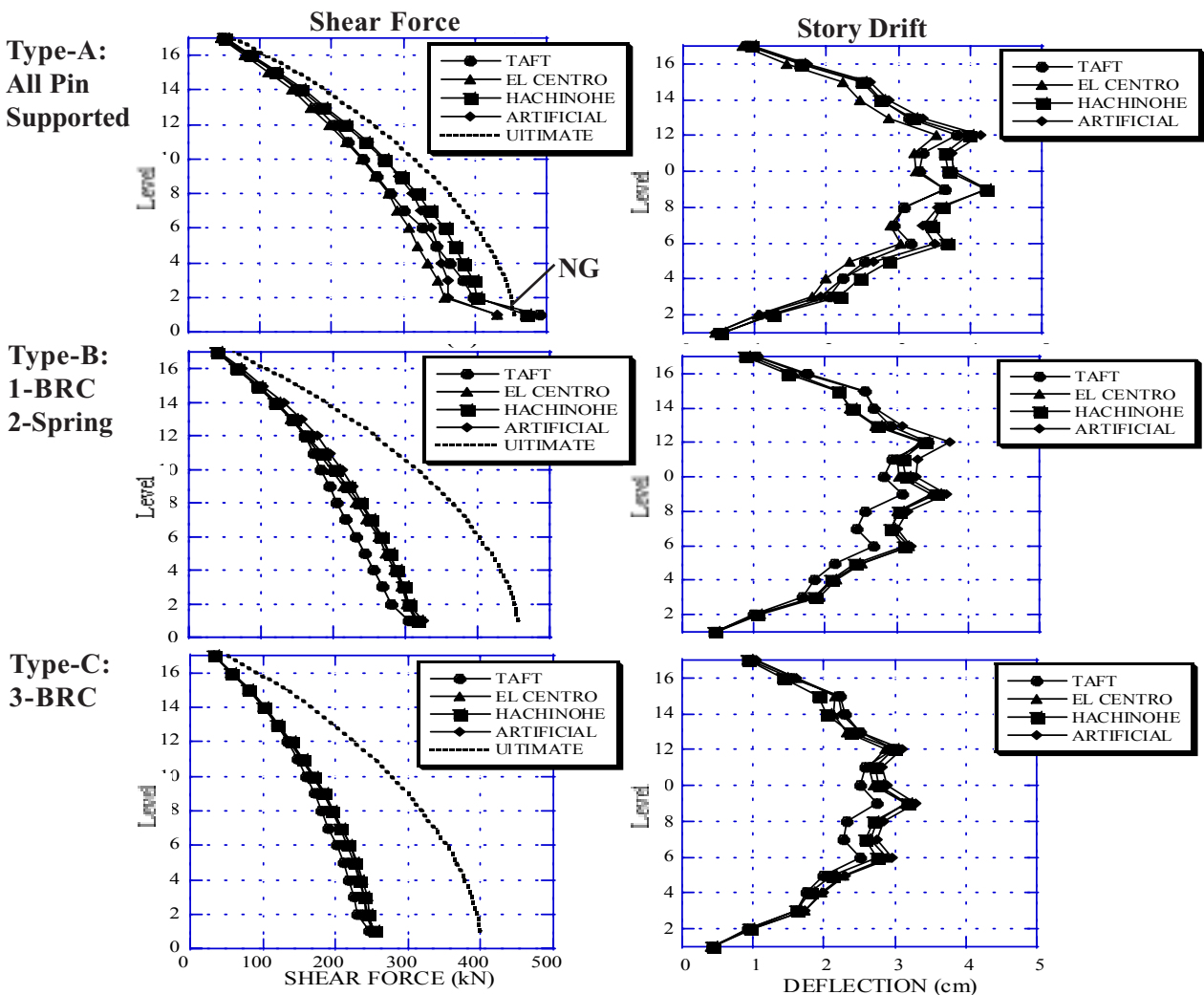


Figure 4 Effects of Energy Dissipation Devices

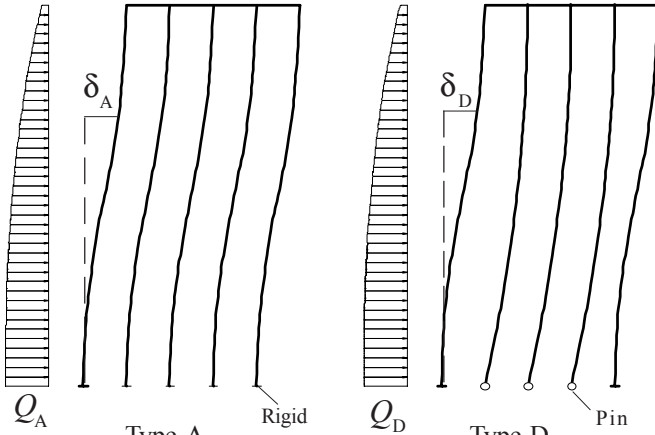


Figure 5 Models for Stiffness Evaluation

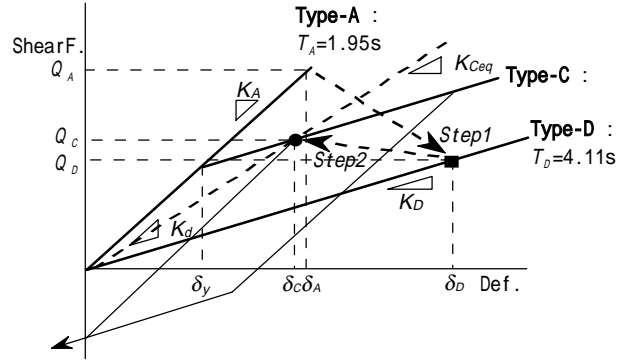


Figure 6 Maximum Response Conversion

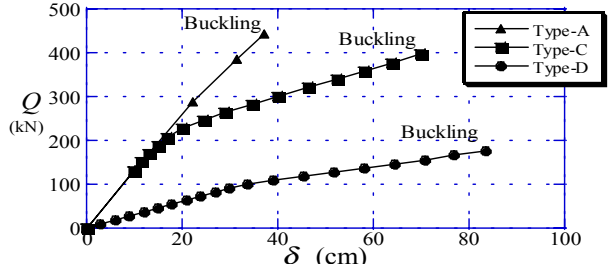


Figure 7 Q - δ Relationship by Pushover Analyses

height, which is acceptable for the limit of 1/60 in drift angle.

In type-B, maximum shear forces are reduced to about 75% of Type-A, which secure some margin in strength. Maximum displacement in each story is slightly reduced to about 90%.

In Type-C, the reduction effect of BRC is more significant, and the maximum shear forces are reduced to about 55% of Type-A. Maximum displacement is reduced to about 80%.

Consequently, introduction of BRC is effective to reduce maximum shear forces and avoid local buckling at base chord members. The more BRC are introduced, the more reduction effect is obtained. Although reductions in deflection are not significant, they are also contributes to decrease the deflection of the entire structure.

3. ESTIMATION OF RESPONSE REDUCTION EFFECTS

In this section, a simple method for estimating the maximum response of the frames with energy dissipation members, using linearization techniques are proposed. When each set of truss is modeled as an equivalent fragile single member, a end of truss with energy dissipation elements on side chords can be modeled as a plastic hinge in the equivalent single member. Then the entire truss frames can be modeled as equivalent beam-column frames with plastic hinges as Figure 5. Simplified response estimation methods developed for moment frames with dampers (Kasai et.al. 1998) can be applied to truss frames, which enable easy structural design avoiding try-and-error basis study in preliminary stages. In this section, response of Type-C frame is estimated using stiffness of Type-A and D frames.

When each type of frames are plotted by horizontal forces (Q) and displacement (δ), their relationship can be led as shown in Figure 6. Where, Q is the shear force at the base, and δ is the equivalent displacement defined as following.

$$\delta = \frac{\sum_{i=1}^N m_i \delta_i^2}{\sum_{i=1}^N m_i \delta_i} \quad (1)$$

In these frames, δ is represented by the displacement at the height of 68-75% of the total height.

In Fig.6, Type-D has much lower stiffness than Type-A, and Type-C is considered to have the same stiffness as Type-A while BRC is elastic, then transferred to the same stiffness as Type-D after BRC yielding. Pushover analyses in Figure 7 proves this assumption. In this condition, the equivalent stiffness ratio of Type-C/Type-D is the function of $\mu = \delta_c / \delta_y$, where δ_c is the maximum deflection of Type-C, and δ_y is the deflection

where BRC start yielding, expressed as following.

$$\frac{K_{Ceq}}{K_D} = 1 + \frac{K_d}{K_D \mu} = 1 + \frac{K_A / K_D - 1}{\mu} \quad (2)$$

The equivalent damping ratio can be estimated as the following equation by taking the average of integral to the maximum amplitude (Kasai et.al 1998).

$$h_{ceq} = h_0 + \frac{2(1+K_d/K_D)}{\pi\mu} \ln \frac{\mu+K_d/K_D}{(1+K_d/K_D)\mu^{\frac{1}{1+K_d/K_D}}} = h_0 + \frac{2K_A/K_D}{\pi\mu} \ln \frac{\mu+K_A/K_D-1}{(K_A/K_D)\mu^{\frac{K_A/K_D}{1+K_A/K_D}}} \quad (3)$$

where, T_A : own period of Type-A, T_D : own period of Type-D. Consequently, to estimate the maximum response of Type-C, the following two steps are required.

- 1) Response of Type-A (in Fig.6) is estimated by response spectrums. Where $T_A > 0.6$ sec, the response of Type-D (in Fig.6) is estimated by Q being multiplied by (T_A/T_D) , and δ being multiplied by (T_D/T_A) . (Step1)
- 2) Response of Type-C (in Fig.7) is estimated with the effect of K_{Ceq}/K_D and h_{ceq} . (Step2).

In detail, the response of Type-C/Type-A is expressed by the following equations.

Shear force and displacement response ratio is, respectively :

$$\frac{a_c}{a_A} = D_h \left(\frac{T_A}{T_D} \right) \sqrt{\left(\frac{K_{Ceq}}{K_D} \right)} \quad \frac{\delta_c}{\delta_A} = D_h \left(\frac{T_D}{T_A} \right) \sqrt{\left(\frac{K_D}{K_{Ceq}} \right)} \quad (4, 5)$$

$$\text{where, } D_h = \sqrt{\frac{1+25h_0}{1+25h_{ceq}}} \quad T_{A,D} = 2\pi \sqrt{\frac{M_{A,D} \delta_{A,D}}{Q_{A,D}}} \quad M = \frac{\left(\sum_{i=1}^N m_i \delta_i \right)^2}{\sum_{i=1}^N m_i \delta_i^2} \quad (7, 8, 9)$$

The evaluated responses by these equations are calculated in spread sheets, and maximum shear forces and story drift led by this results are plotted with time-history analyses in Figure 8. In these figures, dotted line is evaluated response without dampers (Type-A), and solid line is response with dampers (Type-C), both led by the proposed method, and marks are the results of time-history analyses.. From these comparison, the results of proposed evaluation method is considered to be consistent with the results of time-history analyses.

In Fig.7, the critical deflections of Type-A,C, D frames are 35cm, 87cm, and 70cm respectively, and the rate of safety in each structure estimated by proposed evaluation is 1.1 in Type-A, 1.2 in Type-D, and 2.3 in Type-C. This means the frame with almost collapse limit (Type-A) is improved in performance to more than double-safe frame just by replacing base chords to BRC (Type-C).

From these studies, proposed evaluation method is considered to be effective for deciding the suitable volume and position of energy dissipation members in preliminary design stages. Advantage of this method includes that no elasto-plastic analyses or time-history analyses are required, and suitable amount of energy dissipation members is directly given without try-and-error analyses.

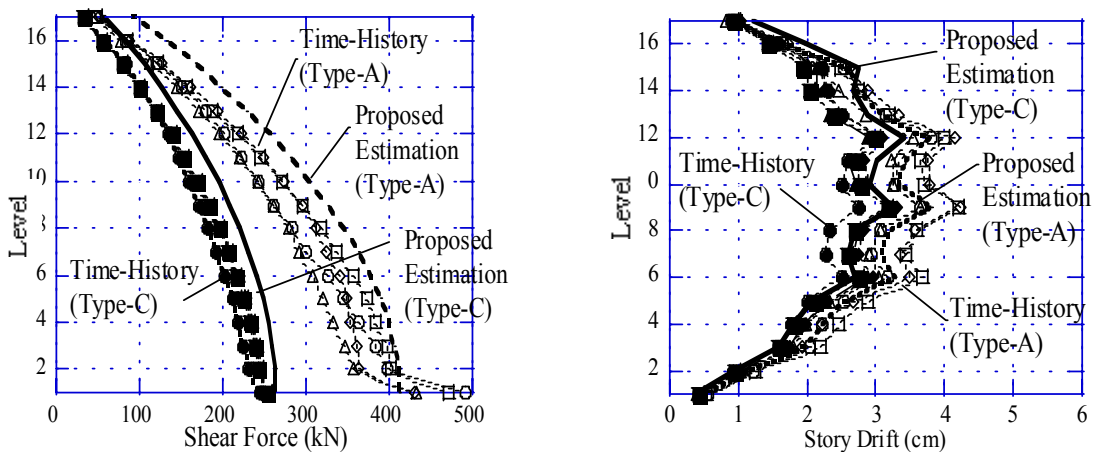


Figure 8 Comparison of Proposed Estimation and Time-History Analyses

4. APPLICATION FOR COMMUNICATION TOWERS

Instead of replacing column, replacing diagonal members to buckling restrained members is another way to reduce seismic responses. In this section, application for communication towers are discussed and tested. The concept of structural system is shown in Fig.9, which is planned as seismic refinement. The towers are usually designed against wind forces, however, seismic response accelerated by standing buildings can be exceed the wind forces. In this study, critical diagonal members are replaced by Buckling Restrained Braces (BRB), aims at saving all other members from buckling.

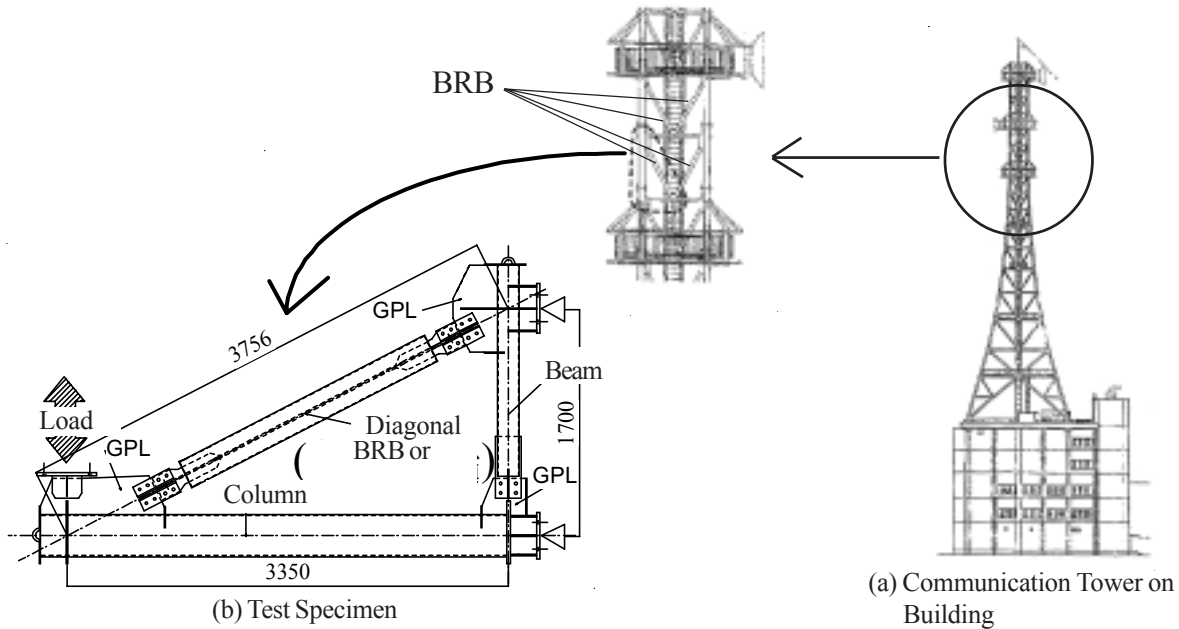


Figure 9 Application for Communication Towers

To verify the reality of energy dissipation mechanism, three types of real-size mock-up tests are carried -out using single truss elements consists of a chord, a beam, and a diagonal member. In the existing tower, all truss members have pipe (CHS) sections (Type-TO). In strengthen reinforcement option, concrete is in-filled within the diagonal member (Type-TC). In BRB reinforcement option, diagonals are replaced by BRB whose yield strength are meeting with the buckling strength of original pipe diagonals (Type-TA). Each truss is cyclically loaded up to 1/25 story drift . The configuration of the test is shown in Fig.10, the detail of BRB in Fig. 11, and loading program is shown in Fig. 12.

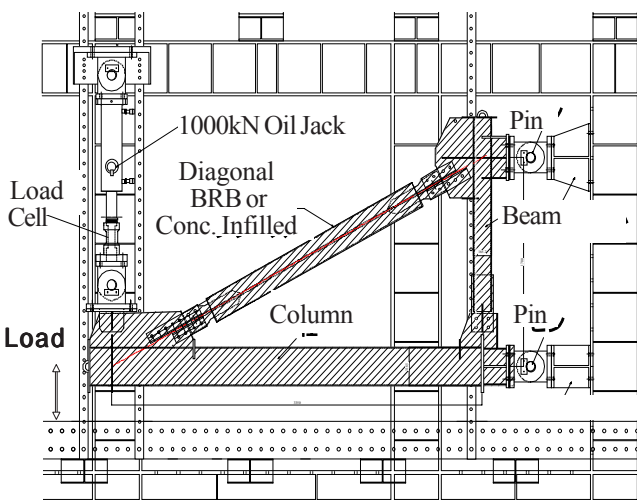


Figure 10 Test Configuration

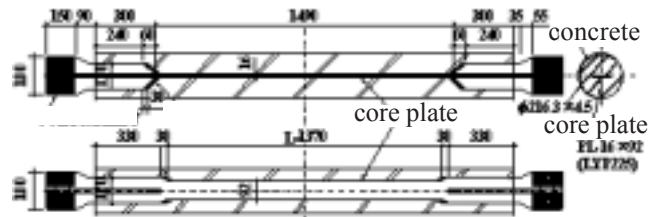


Figure 11 Detail of BRB

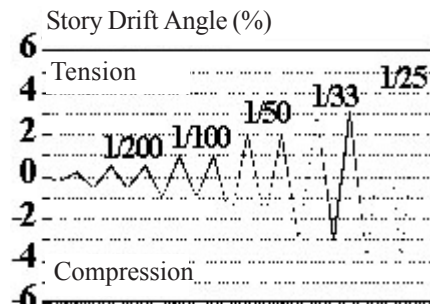


Figure 12 Loading Program

The test results for Type-TO, Type-TC, Type-TA are shown in Fig.13, 14 and 15, respectively. In each figure, (a) are load-relationship of truss structures, (b) are axial force-deformation of diagonal members, (c) are figures at the end of tests.

For Type-TO, story drift up to 1/100 is accepted by slip of connection bolts, then the diagonal started buckling at 1st 1/50 cycle in compression. elbow was created at 2nd 1/50 cycle in compression, and torn off at 1st 1/25 cycle in tension. The maximum axial force to start buckling was about 800kN.

For Type-TC, buckling strength was increased more than 1000kN, the gusset plate at diagonal-to-beam connection was buckled to out-of-plane direction. From this result, it is found that only strengthen diagonal member will cause collapse in other parts as connections.

For Type-TA, BRB keeps its maximum force between 400 kN and 600kN, and shows quite stable and symmetrical hysteresis loop up to 1/25 story drift both in Fig. 15(a) and 15(b). After 3rd 1/25 cycles, BRB fractured at its core plate. Their cumulative plastic deformation and dissipated energy until its fracture are shown in Fig. 16 and Fig. 17, respectively. The cumulative equivalent strain (axial deformation/ length) capacity in BRB diagonal (Type-TA) was about 5.5 times of normal pipe tests (Type-TO). The dissipated energy until fracture is also has the same tendency.

From these results, replacement of diagonals to BRB is considered to have the best performance as seismic refinement and saving other members.

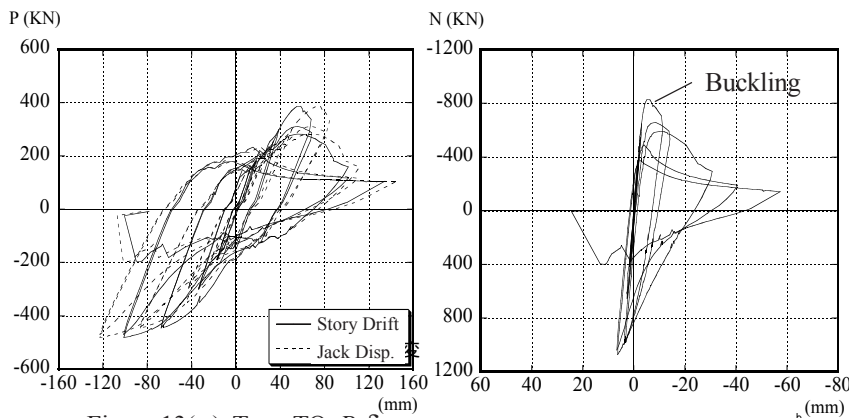


Figure 13(a) Type-TO $P-\delta$

Figure 13(b) Type-TO $N-\delta_B$



Figure 13(c) Diagonal buckling

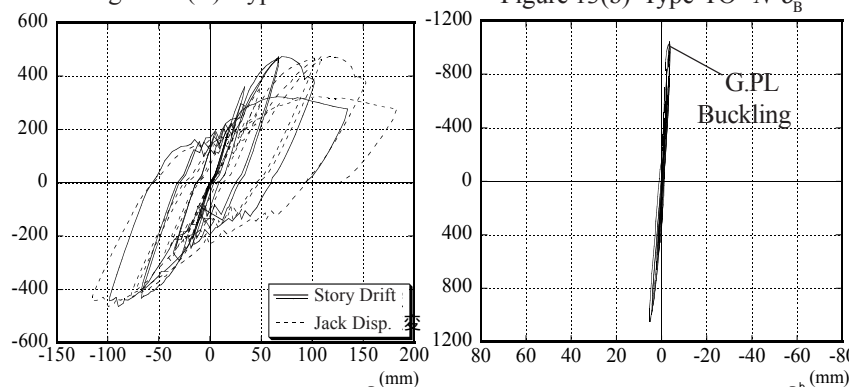


Figure 14(a) Type-TC $P-\delta$

Figure 14(b) Type-TC $N-\delta_B$



Figure 14(c) G.PL buckling

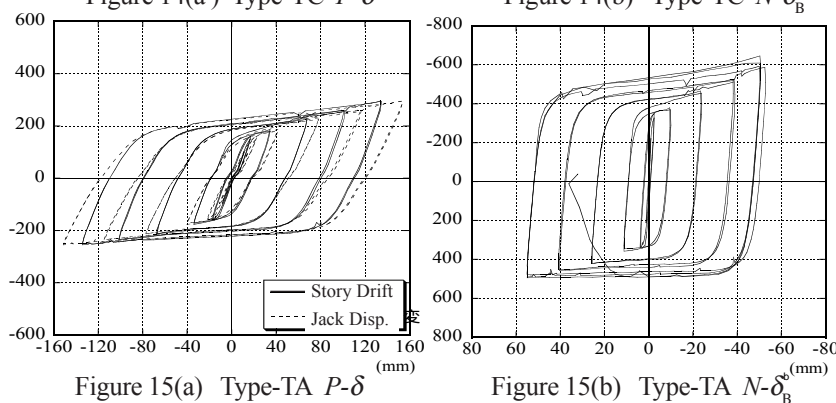


Figure 15(a) Type-TA $P-\delta$

Figure 15(b) Type-TA $N-\delta_B$



Figure 15(c) Diagonal at Test End

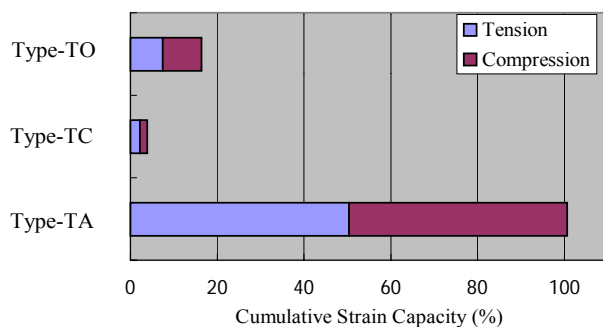


Figure 16 Cumulative Equivalent Strain Capacity until Fracture

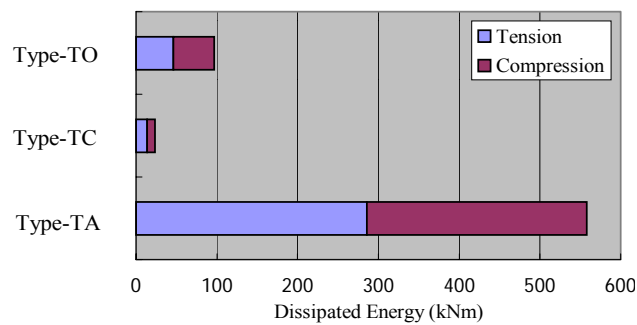


Figure 17 Dissipated Energy until Fracture

5. CONCLUSIONS

Concept of damage-tolerant design for truss frames with elasto-plastic energy dissipation members are introduced, and applications for high-rise automatic-rack warehouse and communication towers are described. Using linearization techniques, the simple method for evaluating maximum response of rack warehouse structures against large earthquake is proposed, and compared with time-history analyses. Also cyclic loading tests for the truss for communication towers are carried out with real-size mock-ups. By these studies, the following points become clear.

1) In truss frames, incorporating energy dissipation members (e.g. buckling restrained members) into critical positions in truss frames are effective to improve the performance of the rack warehouse structure against large earthquake. In the case of 52m high rack warehouse structures, replacing 2/13 base chords to BRC reduces the maximum shear forces to 75%, and replacing 6/13 base chords to BRC reduces the maximum shear forces to 55%.

2) The above reduction effects evaluated by proposed evaluation method are consistent with time-history analyses, and effective to predict maximum responses. For the proposed method requires only elastic analyses, it is useful for deciding the volume of energy-dissipation members in preliminary design stages.

3) From the real size cyclic-loading tests modeling communication towers, replacement of diagonals to BRB is considered to have the best performance as energy dissipation system. strengthening diagonal pipes by infilling concrete will increase the buckling strength, however, other members or connections might be critical instead. BRB frame has stable hysteresis loop, and has over 5 times of cumulative strain than normal pipe diagonal.

References

- Fujimoto, M., Wada, A., Sacki, E., Takeuchi, T., & Watanabe, A., (1990), "Development of Unbonded Braces", *Quarterly Column*, pp.91-99
- Kasai, K., Fu, Y. & Watanabe A., (1998) "Two Types of Passive Control Systems for Seismic Damage Mitigation", *ASCE Journal of Structural Engineering*
- Takeuchi, T. & Aoki, H., (2000), "Design of Vibration-Controlled Building, II-2", Design Recommendation for the Building with Passive Energy Dissipation Devices, *Japan Structural Consultants Association, Syokokusya*
- Kasai, K., & Jodai, A., (2002), "Dynamic property, Behavior, and Their Simplified Estimation Rules for a Passive Control System with Stud-Type Viscoelastic Damper, *J. Struct. Constr. Eng., A.I.J.*, No.558, pp.125-132
- Takeuchi, T., Kasai, K., Oohara, K., Kimura, Y., & Nakajima, H., (2002), "Performance Evaluation and Design of Passively Controlled Building using Equivalent Linearization", *Struct. Eng. World Congress 2002, Nagoya*, T2-2-a-2
- Watanabe, H., Zhu, L., Suzuki, K., Maeda, Y., & Takeuchi, T., (2002), "A Seismic Behavior of Steel Truss Structure Loaded with Sliding Baggages", *Proceedings of Annual Meeting of A.I.J.*, No. 21216-7, pp.431-434 (S-II)
- T.Uchiyama, T.Takeuchi, K.Suzuki, Y.Ookouchi, T.Ogawa, S.Kato (2004), "Seismic Refinement for Communication Toewrs", *Proceedings of Annual Meeting of A.I.J. Kanto*, 2004.3

EXTENDED CONSTITUTIVE RULES FOR VARIOUS VISCOELASTIC MATERIALS USING FRACTIONAL DERIVATIVES

Y. Ooki¹⁾ and K. Kasai²⁾

1) *Research Associate, Structural Engineering Research Center, Tokyo Institute of Technology, Japan*

2) *Professor, Structural Engineering Research Center, Tokyo Institute of Technology, Japan*

ooki@serc.titech.ac.jp, kasai@serc.titech.ac.jp

Abstract: This paper discusses the constitutive rule including the fractional time-derivatives of the strain and stress. We have modeled four kinds of constitutive rules of viscoelastic materials based on this, and introduce the typical material of acrylic and styrene material here. Although viscoelastic material has temperature and frequency sensitivity, accurate modeling is possible by using temperature-frequency equivalency principle. Furthermore, efficient modeling is conducted to reproduce the behavior under large strain without spoiling accuracy. The behavior of the material under sinusoidal or random excitation was examined by comparing the experiment and analysis results. The proposed model showed high accuracy.

1. INTRODUCTION

Dynamic characteristics of viscoelastic (VE) material used for dampers are linear under small strain loading but vary according to the ambient temperature and frequency. In addition, the material shows nonlinear behavior when it is subjected to large strain loading. Since the loading strain in VE material varies in time especially under seismic loading, accurate analytical models for time-history analysis are required for the design of viscoelastically-damped buildings.

The linear VE model based on the fractional time-derivatives of the stress and strain (fractional derivative model) is proposed (Kasai et al, 2001) and this model shows high accuracy compared with the traditional integer derivative models. Based on the temperature-frequency equivalency principle (Ferry, 1980) of VE material, “equivalent frequency” is proposed to consider the complex interactions between the temperature and frequency sensitivities efficiently. On the other hand, various nonlinear models have been proposed (Soda et al, 2002). Usually in those models, the temperature, frequency, and strain sensitivities are considered separately, and it has been difficult to model the accurate constitutive rule which reproduce those three sensitivities in wide range.

In this paper, linear and nonlinear models including the fractional time-derivatives of the stress and strain are discussed. Further more, the use of temperature-frequency equivalency principle has lead to excellent model accuracy. The accuracy is examined compared with the various loading test results and time-history analyses under various excitations. We have modeled four kinds of constitutive rules of VE materials, and will discuss the typical two types, acrylic and styrene material.

2. LINEAR CONSTITUTIVE RULES FOR SMALL STRAIN

2.1 Temperature-Frequency Equivalency Principle

Consider a given damper deformation $u(t)$ and force $F(t)$, corresponding shear strain $\gamma(t)$ and stress $\tau(t)$ are

$$\gamma(t) = u(t)/d, \quad \tau(t) = F(t)/A_s \quad (1a, b)$$

where d and A_s are VE material thickness and shear area, respectively. Fig. 1 shows typical linear steady-state response of a VE material subjected to sinusoidal shear deformation. VE material is often characterized by the storage modulus G' and the loss factor η .

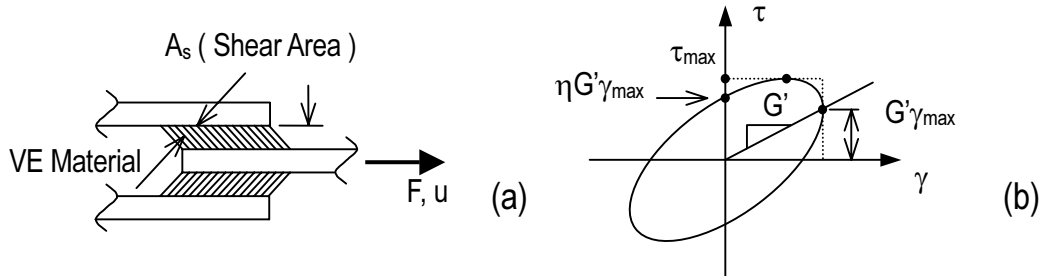


Figure 1 (a) Shear Deformation and (b) Stress-Strain Curve of VE Material

Fig. 2 shows the G' and η at 10% strain. Material properties vary according to the temperature and frequency. G' and η are large at low temperature or high frequency, and small at high temperature or low frequency. The test results at 0, 10, 20, 30, 40 °C are shown and all data can be overlapped into a curve at 20 °C by moving parallel to the horizontal axis. This characteristic is known as “temperature-frequency equivalency principle” and observed in the materials which we have ever treated.

$$G'(\omega, \theta) = G'(\lambda\omega, \theta_{ref}), \quad \eta(\omega, \theta) = \eta(\lambda\omega, \theta_{ref}) \quad (2a, b)$$

where λ is shifting factor and $\lambda\omega/(2\pi)$ ($=f_{eq}$) is defined as “equivalent frequency”. The amount of movements in Fig. 2 is equivalent to $\log\lambda$. By using the temperature-frequency equivalency, we have only to take into account the sensitivities for the equivalent frequency.

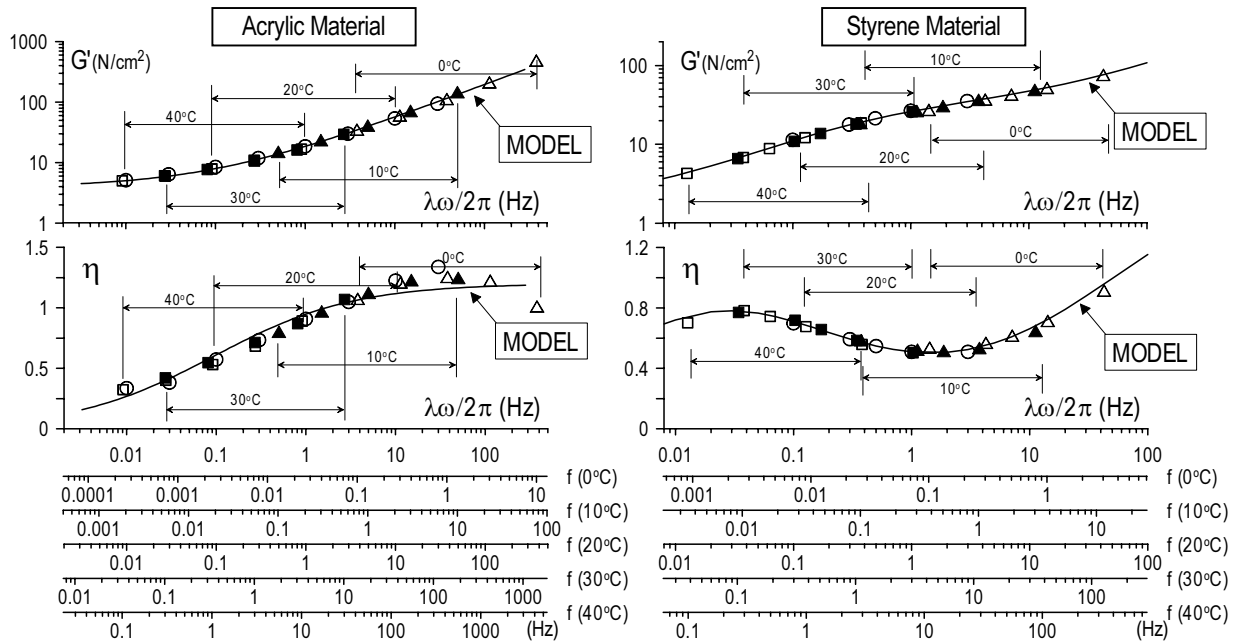


Figure 2 Experimental Results and Model at 20 °C, and Relationships between Temperature, Frequency, and Equivalent Frequency ($\gamma_{max} = 10\%$)

2.2 Linear Constitutive Rules Using Fractional Derivatives

The advantage of the fractional derivative rule as opposed to the more conventional integer derivative rule is the ability to model the VE material accurately over a large range of frequency with a small number of constants. The following is generalized model using fractional derivatives.

$$\tau(t) + \sum_n a_n D^{\alpha_n} \tau(t) = G [\gamma(t) + \sum_n b_n D^{\beta_n} \gamma(t)] \quad (3)$$

where a_n and b_n are constants, G is elastic parameter, and α_n and β_n is the order of fractional derivative of stress and strain. D^α ($= d^\alpha/dt^\alpha$) is the fractional derivative operator. To satisfy the temperature-frequency equivalency shown in Eq. (2),

$$a_n = a_{n,ref} \lambda^{\alpha_n}, \quad b_n = b_{n,ref} \lambda^{\beta_n}, \quad \lambda = \exp[-p_1(\theta - \theta_{ref}) / (p_2 + \theta - \theta_{ref})] \quad (4a, b)$$

where $a_{n,ref}$ and $b_{n,ref}$ are constants at reference temperature θ_{ref} (20 °C). Eq. (5) and (6) are applied to acrylic and styrene material under small strain, and model for the acrylic material has four parameters; $a_{ref} = 5.60 \times 10^{-5}$, $b_{ref} = 2.10$, $G_{ref} = 3.92 \times 10^{-2}$ (N/mm²), and $\alpha = 0.56$ (Kasai et al. 2001). On the other hand, model for the styrene material has seven parameters; $a_{ref} = 0.84$, $b_{1,ref} = 0.94$, $b_{2,ref} = 15.1$, $G = 1.63 \times 10^{-2}$ (N/mm²), $\alpha = 0.57$, $\beta_1 = 1.24$, and $\beta_2 = 0.63$ (Kasai et al. 2003). Solid lines in Fig. (2) show the frequency sensitivities of the materials by the proposed models, and match well with experimental results.

$$\text{Acrylic Material:} \quad \tau(t) + aD^\alpha \tau(t) = G [\gamma(t) + bD^\alpha \gamma(t)] \quad (5)$$

$$\text{Styrene Material:} \quad \tau(t) + aD^\alpha \tau(t) = G [\gamma(t) + b_1 D^{\beta_1} \gamma(t) + b_2 D^{\beta_2} \gamma(t)] \quad (6)$$

3. EXTENDED CONSTITUTIVE RULES USING FRACTIONAL DERIVATIVES

3.1 Temperature-Frequency Equivalency Principle under Large Strain

Fig. 3 shows hysteresis loops under different strain with same equivalent frequency (See Section 2.1). Nonlinearities such as softening and hardening are observed and the shape of hysteresis loops

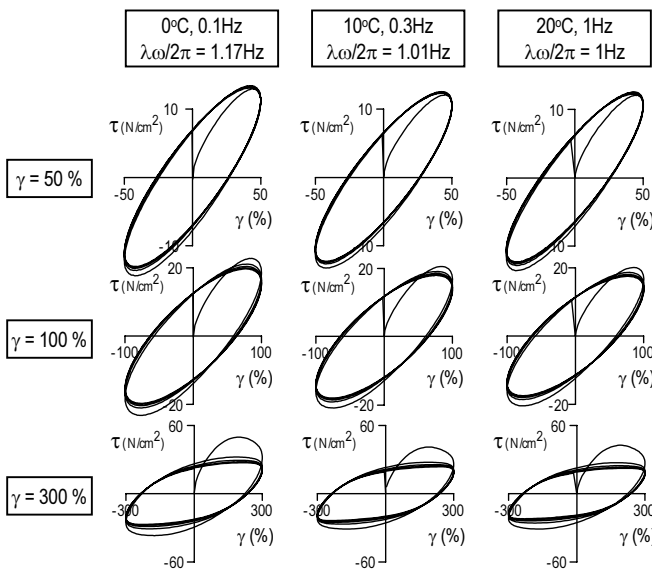


Figure 3 Temperature-Frequency Equivalency under Large Strain

look very similar. This indicates that the temperature-frequency equivalency is also applicable to nonlinear VE material modeling. Utilizing this finding, we have to only take into account the strain and equivalent frequency sensitivities (Fig. 4).

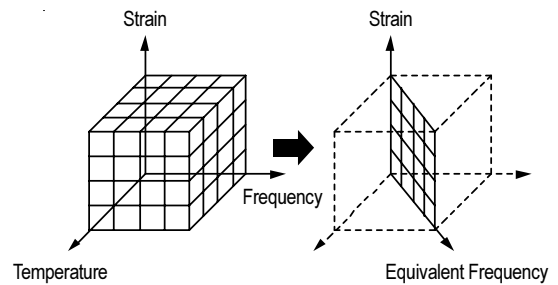


Figure 4 Reduction of Parameter Using Temperature-Frequency Equivalency

3.2 Source of Nonlinearity

Four kinds of nonlinearity of VE material have been found from the experiment and are discussed in this paper. Fig. 5 shows the comparison of time-history responses and hysteresis loops between small and large strain tests, and strain is normalized by maximum value. In small strain test, temperature-rise is negligibly small and VE material behaves linearly. Characteristics of these nonlinearities are as follows;

a) Softening by temperature-rise:

Temperature-rise of VE material is significant under low ambient temperature. The G' and η gradually decreases with number of cycles.

b) Softening by large strain:

Reduction of G' is significant under large strain and η rises relatively in this case. This occurs without the temperature-rise and characterized difference softening mentioned above.

c) Hardening by high strain-rate: At the beginning of loading, the strain suddenly increases in very large rate, and abrupt increase in shear stress is observed. Especially, this occurs under high equivalent frequency with large strain.

d) Hardening by large strain: Hysteresis shows pinching if the shear strain advances further, This behavior is remarkable in the materials which have strong strain sensitivities.

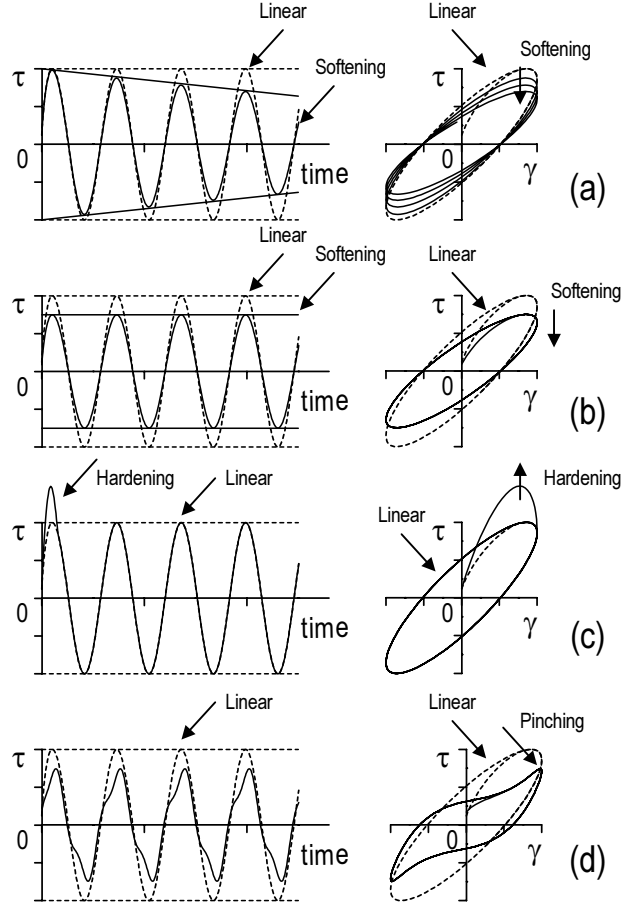


Figure 5 Nonlinearity of VE Material: (a) Softening by Temperature, (b) Softening by Large Strain, (c) Hardening by High Strain-Rate, and (d) Hardening by Large Strain (Pinching)

3.3 Additional Components for Nonlinear Model

Acrylic Material: The temperature $\theta(t)$ in the VE material is evaluated using the shear stress, strain, density ρ , and specific heat, s , of the material as (Kasai et al, 1993)

$$\theta = \theta_0 + \int \tau d\gamma / (s\rho) \tag{7}$$

where $\theta_0(t)$ is initial temperature. In Eq. (7), it is assumed that the heat generated in the VE material is all contained in VE material and heat loss due to heat conduction is ignored. This assumption is applied since the external loading time is short and the thermal conductivity of the material is small. Temperature-rise is calculated by using Eq. (7), shifting factor λ is changed by Eq. (4c), and a and b are updated by Eq. (4a) and (4b). Thus softening by temperature-rise is reproduced in numerical analysis.

In contrast with the softening phenomenon examined above, even when the temperature-rise is very small, the softening is seen at large strain with high temperature or low frequency, i.e., low equivalent frequency $f_{eq} = \lambda\omega / (2\pi)$. This is a softening caused by large strain shown in Fig. 5 previously. In the softening by the temperature-rise previously mentioned, η decreases with decreasing of G' . By increasing b and decreasing G , vice versa, in Eq. (5), the behavior can be reproduced, and this modeling is applied at $\theta \geq 25$ °C and $\gamma_{max} \geq 100$ % because softening by temperature-rise dominates in low temperature. The b and G vary almost linearly with respect to maximum strain at $\gamma_{max} \geq 100$ % and modeled as follows;

$$b = b_{ref} \lambda^\alpha \lambda_1, \quad G = G_{ref} \lambda_2 \tag{8a, b}$$

$$\lambda_1 = 1 + C_1(\gamma_{max} - 1), \quad \lambda_2 = 1 + C_2(\gamma_{max} - 1) \tag{9a, b}$$

where $C_1 = 0.124$ and $C_2 = -0.182$.

From temperature-frequency equivalency principle, strain-rate $\gamma\omega$ at θ is equivalent to $\lambda\gamma\omega$ at θ_{ref} . Accordingly, $\lambda\gamma\omega = \lambda\dot{\gamma}$ is defined as “equivalent strain-rate”, and its maximum is $\lambda\dot{\gamma}_{max}$. Under sinusoidal loading, $\lambda\dot{\gamma}_{max}$ occurs at the beginning of loading, and the hardening is effectively modeled by utilizing the data at the 1st half cycle. Nonlinear spring element is adopted parallel to the fractional derivative model to reproduce this phenomenon. Required spring stiffness G_s is written as

$$\tau_s = G_s \cdot \gamma \quad (10a)$$

$$G_s = C_3 \beta \min[\lambda\dot{\gamma}_{max}, 100], \quad \beta = \exp[C_4(\gamma_0 - 0.5)] \leq 1 \quad (10b)$$

where $C_3 = 0.278$ (N·sec/cm²) and $C_4 = -0.549$. γ_0 is absolute value of the strain when the sign of strain-rate changes. G_s is set to 0 after the unloading and not used until $\lambda\dot{\gamma}_{max}$ is updated again.

The stress of the VE element τ_v is obtained by substituting Eq. (8) for Eq. (5), and total stress τ_{tot} considering the nonlinearity of the material is shown as follows.

$$\tau_{tot} = \tau_v + \tau_s \quad (11)$$

Styrene Material: Softening by the large strain of styrene material is reproduced by applying the parameter which is dependent on maximum strain γ_{max} to Eq. (6) same as the case of acrylic material.

$$a = a_{ref} \lambda^\alpha \lambda_2, \quad b_1 = b_{1,ref} \lambda^{\beta_1} \lambda_3, \quad b_2 = b_{2,ref} \lambda^{\beta_2} \lambda_4, \quad G = G_{ref} \lambda_1 \quad (12a, b, c, d)$$

$$\lambda_i = A_i \exp[B_i \gamma_{max}] \quad , \quad i = 1 \sim 4 \quad (13)$$

where A_i ($i = 1 \sim 4$) = 1.11, 1.06, 1.081, and 1.03, B_i ($i = 1 \sim 4$) = -0.58, -0.56, -0.78, and -0.30. λ_i decreases further by repeating cyclic loading with large strain. (Kasai et al, 2004)

Under large strain with low equivalent frequency, the material becomes stiff and pinching is observed in the hysteresis. To reproduce this, a spring is added parallel to the VE element and its stiffness depends on the strain. Stress with this spring is set to τ_s .

$$\tau_s = G_s \cdot \gamma \quad (14a)$$

$$G_s = m_1 \gamma^3 + m_2 \gamma^2 + m_3 \gamma \quad (14b)$$

where m_i ($i = 1 \sim 3$) = -0.23, 1.16, and -0.44.

Setting up the parameters as shown in Eq. (8), acrylic material can reproduce change of the loss factor under large strain, but in this material, which has strong strain sensitivities, a nonlinear dashpot is required to reproduce the behavior under large strain. Stress with this element is set to τ_d .

$$\tau_d = C_1 \cdot C_2 [\lambda\dot{\gamma}]^\zeta \quad (15a)$$

$$C_1 = n_1 \gamma_0^3 + n_2 \gamma_0^2 + n_3 \gamma_0 \quad (15b)$$

$$C_2 = \min(C_t, \dot{\gamma} / \dot{\gamma}_{pk}) \quad , \quad C_t = |\sin \pi(\gamma - \gamma_0) / (2\gamma_0)|^\zeta \quad (15c, d)$$

where n_i ($i = 1 \sim 3$) = -0.37, 1.55, and 0.89, C_1 = function of γ_0 ($-3.0 < \gamma_0 < 3.0$) used in Eq. (10b). C_2 = coefficient which starts from 0 and ends by 0 in a half cycle, and can take 1 as maximum. $\dot{\gamma}_{pk}$ is strain-rate in a half cycle and set to 0 when the sign of strain-rate changes. C_t and $\dot{\gamma}_{pk}$ are updated until it reaches maximum in a half cycle. $\zeta = 0.26$.

Eq. (7) is also applied for reproducing the softening by temperature-rise. The stress of the VE element τ_v is obtained by substituting Eq. (12) for Eq. (6), and total stress τ_{tot} considering the nonlinearity of the material is shown as follows;

$$\tau_{tot} = \tau_v + \tau_s + \tau_d \quad (16)$$

4. COMPARISON BETWEEN ANALYSIS AND EXPERIMENT

Fig. 6 and 7 show the sinusoidal responses of two materials. The softening by temperature-rise is remarkable at low temperature or high frequency. Softening by large strain as well as hardening by high strain-rate is also reproduced in high accuracy by proposed model. The test at 0 °C is not conducted as for Acrylic material because of the limit of the performance of the testing machine. In Table 1, the accuracy of these two models is examined. Storage modulus and loss factor are compared between experiment and analysis. Not only the average of the ratio of the experiment and analysis is almost equal to 1, but also standard deviation is very small.

Fig. 8 and 9 show the case of random loading considering the events of JMA Kobe, El Centro and Taft earthquake. The ambient temperature 20 °C is considered and the maximum strains are set to 300 %. The deformation history is obtained from analyses of 3, 12, and 24 story buildings having fundamental vibrations of 0.35, 1.41, and 2.84 seconds. Note that the material stiffness and number of cyclic excursions differ significantly with respect to building's vibration periods. The analytical prediction matches extremely well with the experimental results.

5. CONCLUSIONS

- 1) The temperature-frequency equivalency principle, the typical characteristic of VE material, is applicable not only under small strain range but also large strain range. It is possible to express the sensitivity of temperature and frequency as that of equivalent frequency.
- 2) The nonlinear behavior of the VE material characterized by softening by temperature-rise of material, softening by large strain, and hardening by high strain-rate. And pinching is observed if the material has strong strain sensitivity. The tendency of nonlinearity is effectively expressed by the equivalent frequency, which combines the effects of both temperature and frequency.
- 3) High accuracy of proposed analysis model was proved by performing comparison with the experiment over wide range temperature, frequency, and peak shear strain. This model also showed high accuracy for the random waves.

References:

- Kasai, K., Teramoto, M., Okuma, K., and Tokoro, K., "Constitutive Rule for Viscoelastic Materials Considering Temperature and Frequency Sensitivity", *Journal of Structural and Construction Engineering*, AIJ, No. 543, May, 2001, pp. 77-86 (in Japanese)
- Ferry, J.D., *Viscoelastic Properties of Polymers*, John Wiley & Sons Inc., Third Ed., New York, 1980
- Soda, S., Kakimoto, K., and Sekiya, E., "Mechanical Models for Softening and Hardening Type Nonlinear Viscoelastic Dampers", *Journal of Structural and Construction Engineering*, AIJ, No. 551, 2002, pp. 45-52 (in Japanese)
- Kasai, K., Munshi, J. A., Lai, M-L, and Maison, B.F., "Viscoelastic Damper Hysteresis Model: Theory, Experiment, and Application", ATC-17-1 Seminar, Applied Technology Council, Vol. 2, 1993, pp.521-532
- Kasai, K., Ooki, Y., Amemiya, K., and Kimura, K., "A Constitutive Rule for Viscoelastic Materials Combining Iso-Butyrene and Styrene Polymers", *Journal of Structural and Construction Engineering*, AIJ, No. 569, July, 2003, pp. 47-54 (in Japanese)
- Kasai, K., Ooki, Y., and Amemiya, K., "Principles of Manual for Design and Construction of Passively-Controlled Buildings Part-11 Time-History Analysis Model for Viscoelastic Dampers Combining Iso-Butylene and Styrene Polymers", *Proceedings of 13th World Conference on Earthquake Engineering*, Vancouver, BC Canada, Aug. 1-6, 2004

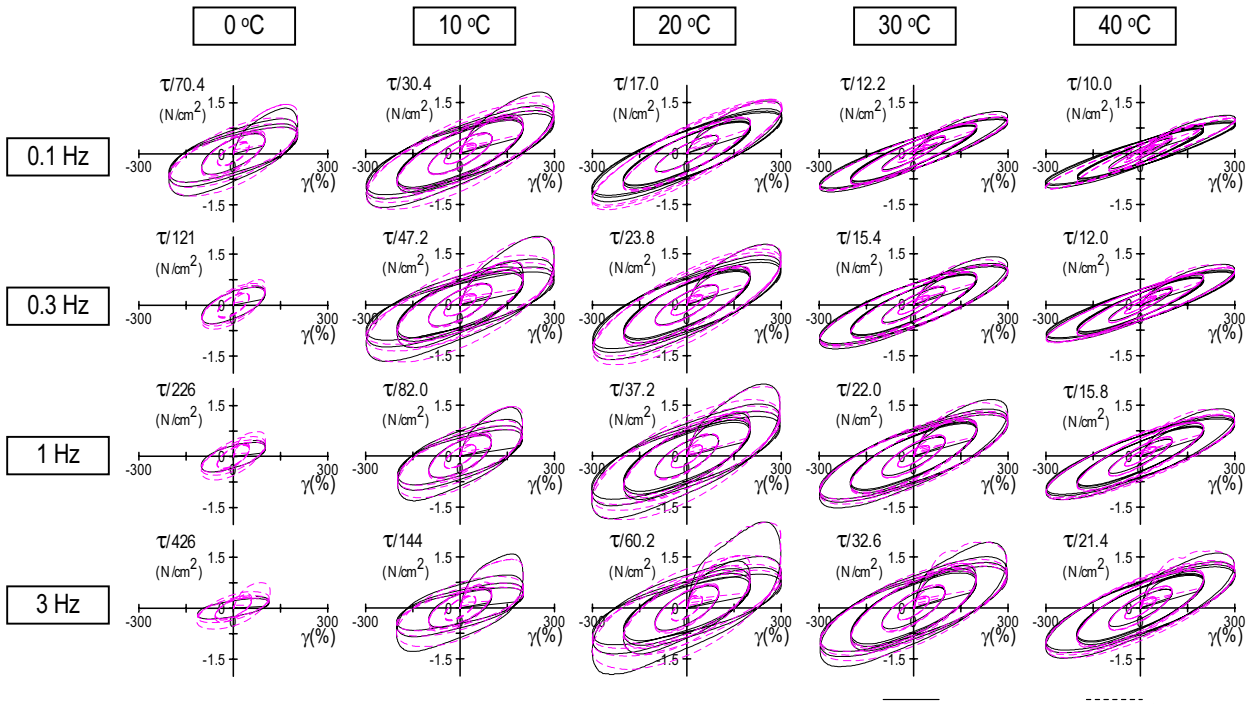


Figure 6 Sinusoidal Responses of Acrylic Viscoelastic Material ($\gamma_{max} = 50, 100, 200, 300\%$)

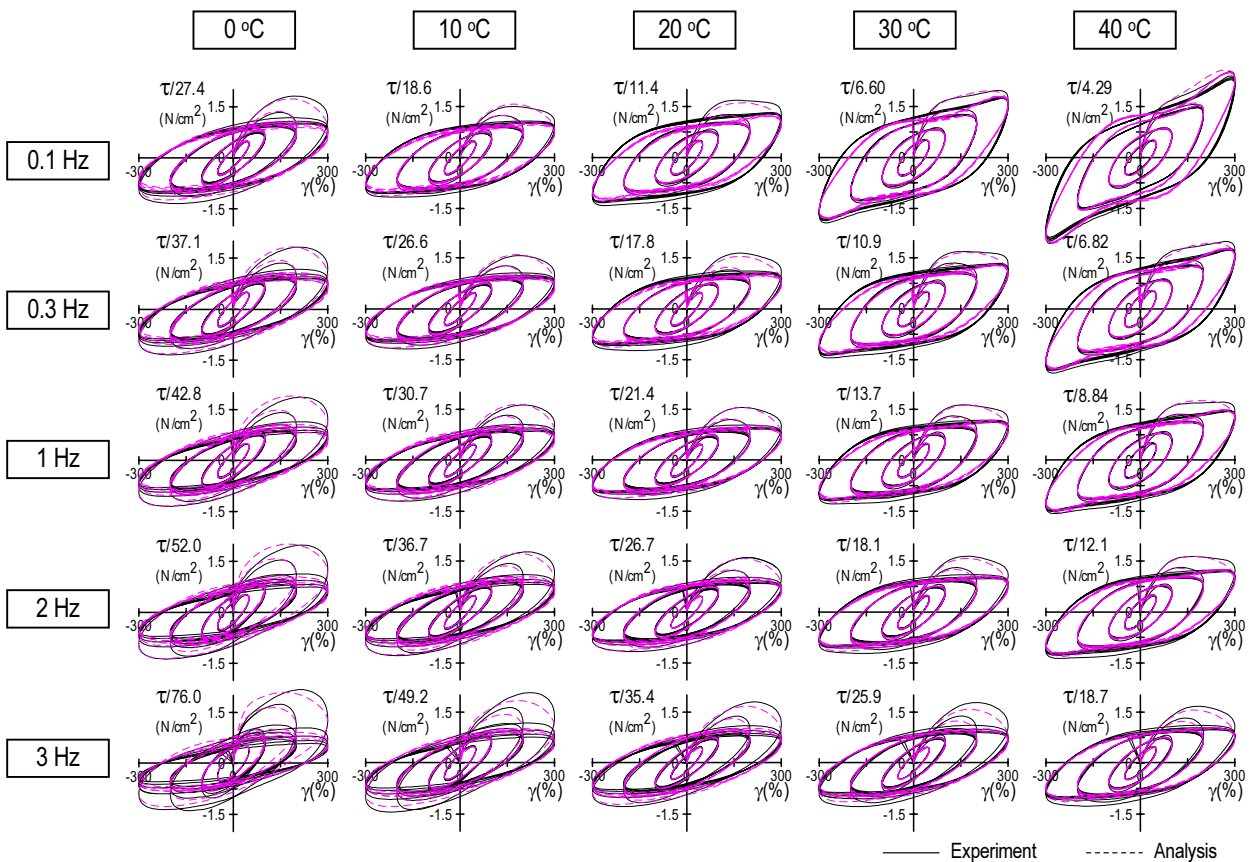


Figure 7 Sinusoidal Responses of Styrene Viscoelastic Material ($\gamma_{max} = 50, 100, 200, 300\%$)

Table 1 Accuracy Verification of Sinusoidal Responses: (a) Acrylic Material, (b) Styrene Material

Analysis/Test	$\gamma = 10\%$		$\gamma = 50\%$		$\gamma = 100\%$		$\gamma = 200\%$		$\gamma = 300\%$		(a)
	G'	η	G'	η	G'	η	G'	η	G'	η	
Average	1.02	1.02	1.02	0.98	1.04	0.99	0.99	1.05	0.96	1.08	
Standard Dev.	0.050	0.090	0.033	0.077	0.054	0.074	0.098	0.108	0.087	0.125	

Analysis/Test	$\gamma = 10\%$		$\gamma = 50\%$		$\gamma = 100\%$		$\gamma = 200\%$		$\gamma = 300\%$		(b)
	G'	η	G'	η	G'	η	G'	η	G'	η	
Average	0.99	1.00	0.99	1.00	1.03	0.97	1.05	0.97	0.96	1.02	
Standard Dev.	0.019	0.028	0.020	0.037	0.044	0.038	0.060	0.029	0.034	0.047	

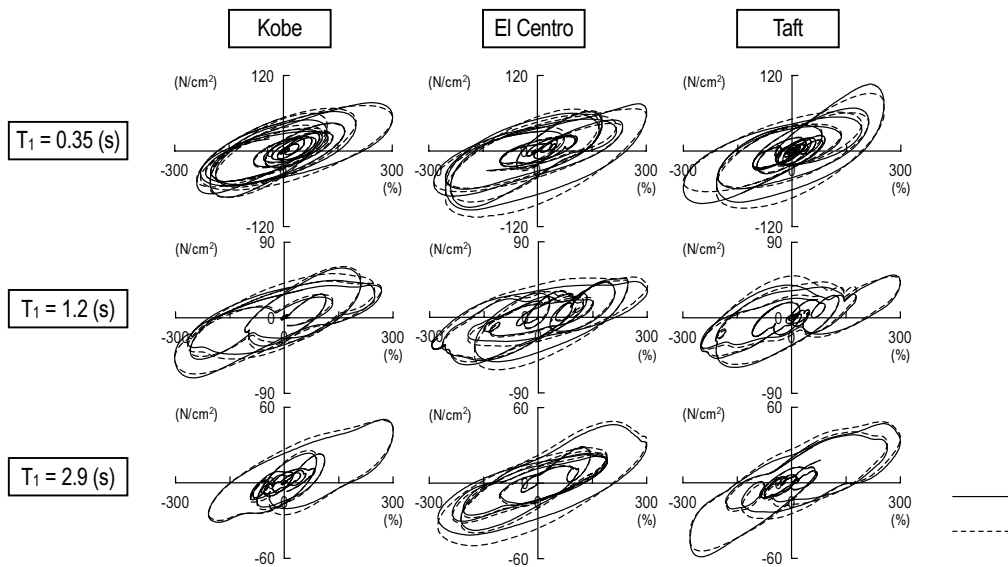


Figure 8 Responses of Acrylic Viscoelastic Material (Deformation history is obtained from analyses of 3, 12, and 24 story buildings having fundamental period of 0.35, 1.2, and 2.9 seconds)

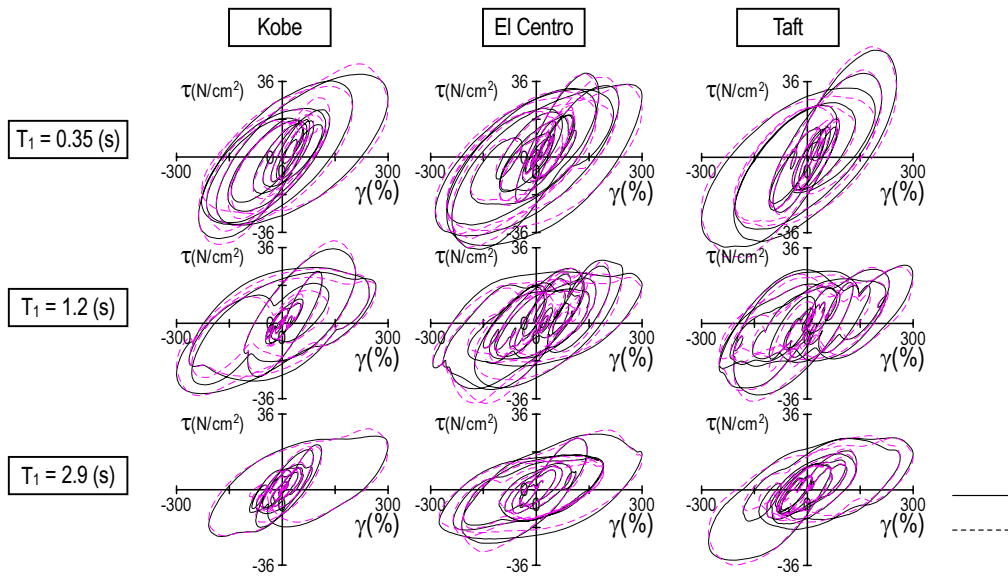


Figure 9 Responses of Styrene Viscoelastic Material (Deformation history is obtained from analyses of 3, 12, and 24 story buildings having fundamental period of 0.35, 1.2, and 2.9 seconds)

ENERGY BALANCE-BASED SEISMIC RESPONSE PREDICTION METHODS FOR SEISMIC ISOLATED BUILDINGS WITH RUBBER BEARINGS, DAMPERS AND LOW FRICTION ELASTIC SLIDING BEARINGS

K. Satsukawa¹⁾, Y. Chiba²⁾, H. Kitamura³⁾, and Y. Koyama²⁾

1) *Research Assoc., Dept. of Architecture, Faculty of Science and Engineering, Tokyo Univ. of Science, Dr. Eng., Japan*

2) *Graduate Student, Tokyo Univ. of Science*

3) *Professor, Dept. of Architecture, Faculty of Science and Engineering, Tokyo Univ. of Science, Dr. Eng., Japan
k-satsu@rs.noda.tus.ac.jp, 7102633@rs.noda.tus.ac.jp, kita-h@rs.noda.tus.ac.jp, 7103622@rs.noda.tus.ac.jp*

Abstract: Recently, low friction elastic sliding bearings are installed seismic isolated buildings with rubber bearings and dampers. Low friction elastic sliding bearings enable the base isolation system with longer natural period than the buildings with rubber bearings and dampers. A method to predict the response of this type of structures based energy balance theory is introduced in this paper. Natural period should be estimated energy spectrum and maximum deformation in consideration of effect of energy absorption and residual deformation. A design methodology of seismic isolated buildings with low friction elastic sliding bearings, that is based an energy balance, is presented.

1. INTRODUCTION

The base-isolated structure is widely recognized as the damage control structure, because structural engineers can control the concentration of earthquake energy to the isolation layer at the design stage. The major advantage of the structure is that the seismic responses can be easily and effectively decreased by elongating the period and increasing the damping. Therefore, the natural period of the base-isolated structure recently tends to be longer. The elastic sliding bearings and the rolling bearings with the laminated rubber bearings are currently predominant strategies for the base-isolated structures. In the case of the elastic sliding bearings, the high frictional type and the low frictional type are provided as the system. The high friction elastic sliding bearings have the capability of energy absorption. However, the low friction elastic sliding bearings have a little capability. Therefore, it is used for only elongating the natural period and it is necessary to use the damper along with the laminated rubber bearings.

If elastic sliding bearings are excessively used, the amount of the laminated rubber bearings (the flexible element) unreasonably decreased. Akiyama indicated that the flexible elements for the base-isolated structure are required to retain at appropriate quantity for increasing the energy absorption effectively and for decreasing the residual deformation in base-isolated structure.

2. Analysis model and Parameter

Fig.1 shows Analysis model in this study. This model is shear force-deformation relationship model of five –mass-system. Mass distribution is equal in each mass. Stiffness distribution sets trapezoid form with which the top layer is half of the lower layer. The natural period of the mass system is 0.5

second without base isolation. If base isolation is installed in the mass-system, the value of stiffness is changed and damping coefficient is zero. Fig.2 shows hysteresis characteristics of each member in the base isolation. k_f is horizontal modulus of isolator, ${}_f Q_{max}$ is shear force of isolator, k_{s1} is elastic modulus of dumper, ${}_{s1} Q_y$ is yield shear force of dumper. ${}_{s1} \delta_y$ is yield displacement. The hysteresis characteristics of low friction elastic sliding bearings is perfect elasto-plastic model, k_{s2} is elastic modulus, ${}_{s2} Q_y$ is yield shear force ${}_{s2} \delta_y$ is horizontal displacement when this bearings slide. Q is shear force of base isolation, δ_{max} is maximum horizontal displacement. Residual deformation of base isolation defines δ_r when 40 seconds pass after the input of seismic wave. Mass of the buildings (Mg) is supported by the isolator and the low friction elastic sliding bearings. R is the ratio of Mass of the buildings supported by the low friction elastic sliding bearings. The yield shear force of the low friction elastic sliding bearings, ${}_{s2} Q_y$, defined by equation.

$${}_{s2} Q_y = \zeta R M g \quad (1)$$

The shear coefficient of isolator (α_f), the yield shear coefficient of dumper (α_{s1}), the yield shear coefficient of the low friction elastic sliding bearings (α_{s2}) is defined by equation.

$$\alpha_f = \frac{{}_f Q_{max}}{Mg}, \quad \alpha_{s1} = \frac{{}_{s1} Q_y}{Mg}, \quad \alpha_{s2} = \frac{{}_{s2} Q_y}{Mg} = \zeta R \quad (2)$$

${}_m k_f$ is horizontal stiffness of base isolation when supporting entirely weight of buildings by isolator. ${}_m k_{s2}$ is horizontal stiffness of base isolation when supporting entirely weight of buildings by the low friction elastic sliding bearings. ${}_m r_{ks}$ is the ratio of ${}_m k_f$ to k_{s1} , ${}_m r_{kf}$ is the ratio of ${}_m k_f$ to ${}_m k_{s2}$.

$${}_m r_{ks} = {}_m k_f / k_{s1}, \quad {}_m r_{kf} = {}_m k_f / {}_m k_{s2} \quad (3)$$

$$k_f = (1 - R) {}_m k_f = \left(\frac{2\pi}{m T_f} \right)^2 \cdot M \cdot (1 - R) \quad (4)$$

$$k_{s1} = \frac{{}_m k_f}{{}_m r_{ks}} = \left(\frac{2\pi}{m T_f} \right)^2 \cdot \frac{M}{{}_m r_{ks}} \quad (5)$$

$$k_{s2} = R \cdot {}_m k_{s2} = \left(\frac{2\pi}{m T_f} \right)^2 \cdot \frac{M}{{}_m r_{kf}} \cdot R \quad (6)$$

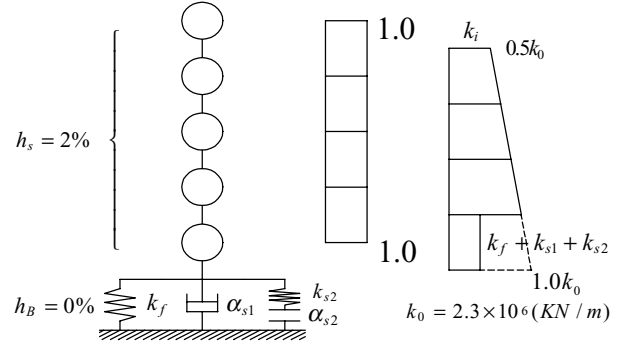


Fig.1 Analysis Model

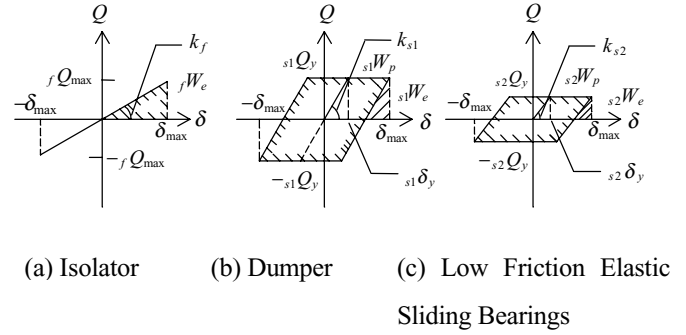


Fig.2 Restoring force of each member

Table.1 Parameter of Analysis

Natural Period ${}_m T_f$ (sec)	2.0,3.0,4.0
Friction Coefficient ζ	0.01,0.05
${}_m r_{ks}$	0.1,0.2,0.5
${}_m r_{kf}$	0.05,0.10,0.20,0.50,1.00
R	0.0,0.1,0.2,0.3,0.4,0.5,0.6,0.7,0.8,0.9,1.0
α_{s1}	0.00,0.02,0.04,0.06,0.10

$$mTf = 2\pi\sqrt{\frac{M}{mk_f}}, \quad Tf = 2\pi\sqrt{\frac{M}{k_f}} \quad (7)$$

Using natural period mTf without dumper, stiffness of isolator k_f , stiffness of dumper ks_1 , stiffness of low friction elastic sliding bearings ks_2 is defined by equation. Relationship between Tf and mTf is defined by equation (8) from equation (4), (7).

$$\frac{mTf}{Tf} = \sqrt{\frac{k_f}{mk_f}} = \sqrt{1-R} \quad (8)$$

3. Distribute Energy of Member

3.1 Comparison of Absorb Energy

This chapter examines the absorb energy of base isolation member, to calculate response prediction method based on energy balance under system of the subject of this study.

fWe is the vibration elastic energy of isolator. s_1We , s_1Wp are the vibration elastic energy and the inelastic strain energy of dumper. s_2We , s_2Wp are the vibration elastic energy and the inelastic strain energy of the low friction elastic sliding bearings. In the analysis, response of the analytical model is calculated for two imitate seismic wave. The analytical model is mass-system set up by $\alpha_{s1} = 0.02, 0.04, 0.06, 0.10$, $m r k_s = 0.1$, $\zeta = 0.01$, $m r k_f = 0.05, 1.00$. $R = 0 \sim 1.0$. The relationship between the values which divide absorbed energy of each member in the base isolation by input energy and the value of R is shown in Fig.3. The values of absorbed energy of the each energy show the maximum value by analytical result. s_1We and s_2We are always minute value, these elements can ignore in energy balance.

3.2 Equivalent Number of Cycles

To deduce the response prediction method based on the energy balance of the seismic isolation structure, the equivalent number of cycles n_l which is absorbed energy efficiency of the base isolation is verified. The shear force ratio r_q , which laminated rubber and damper, and low friction sliding bearing, is given by Equation (10)

$$r_q = \frac{f Q_{max}}{s_1 Q_y + s_2 Q_y} \quad (10)$$

Equivalent number of cycles is proposed value from the relationship between the shear force ratio in equation (11) by Akiyama.

$$\left. \begin{array}{l} r_q < 1.0 \quad n_l = 1.0 + r_q \\ r_q \geq 1.0 \quad n_l = 2.0 \end{array} \right\} \quad (11)$$

In this study, equivalent number of cycles n_l is evaluated by equation (11). n_l is calculated by equation (12) with the response prediction method. The difference between all input energy and elastic

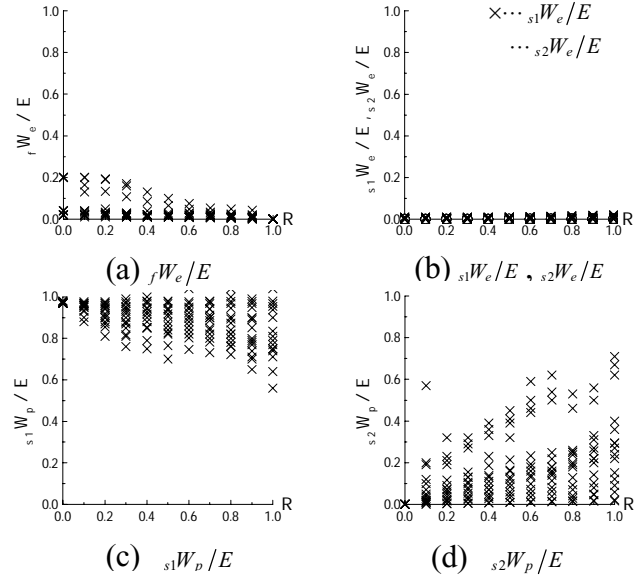


Fig.3 Absorb Energy of Each Member

strain energy of laminated rubber is hysteretic damping energy which the elasto-plasticity element absorbs. n_l is the value which divided this hysteretic damping energy by the area of equivalent hysteresis loop of dumper and low friction sliding bearing at the largest horizontal displacement generation. E 、 fQ_{max} 、 δ_{max} use the result got by this analysis.

$$n_l = \frac{2E - fQ_{max} \cdot \delta_{max}}{\delta_{s1}Q_y \cdot \delta_{max} + \delta_{s2}Q_y \cdot \delta_{max}} \quad (12)$$

The relationship between n_l and r_q in the difference between mT_f is shown in Fig.4(a), (b) and (c), the relationship between n_l and r_q in the difference between $m r_{kf}$ is shown in figure 4(b), (d) and (e). n_l shows large dispersion from Fig.4. n_l and r_q are approximately correlation, regardless of $m r_{kf}$ and seismic wave. Equation (11) which shown in bold continuous line approximately envelopes the lower limit of the response analysis result. Equation (11) of equivalent number of cycles n_l in earthquake-resistant design method can be applied to the base isolation.

4. Proposed Response Prediction

Method Based on Energy Balance

On the assumption of the upper structure with rigid body, the balance method of the energy of seismic isolation structure is given by Equation (13). v_E is the equivalent velocity.

$$fW_{e+s1}W_{e+s1}W_{p+s2}W_{e+s2}W_p = E = MV E^2 / 2 \quad (13)$$

s_1W_e , s_2W_e is small absorb energy referenced by Chapter 3.1, Equation (13) simplifies Equation(14).

$$fW_{e+s1}W_{p+s2}W_p = MV E^2 / 2 \quad (14)$$

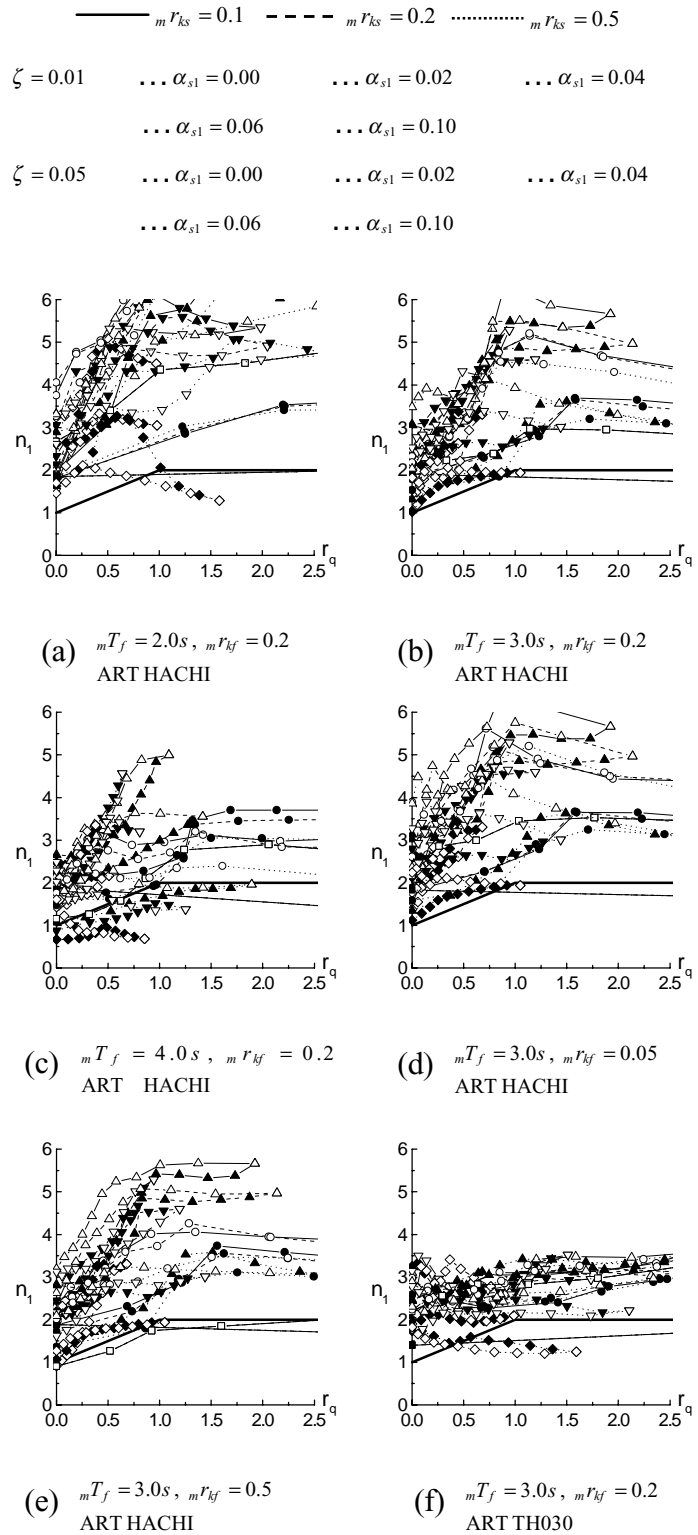


Fig.4 n_l and r_q relationship

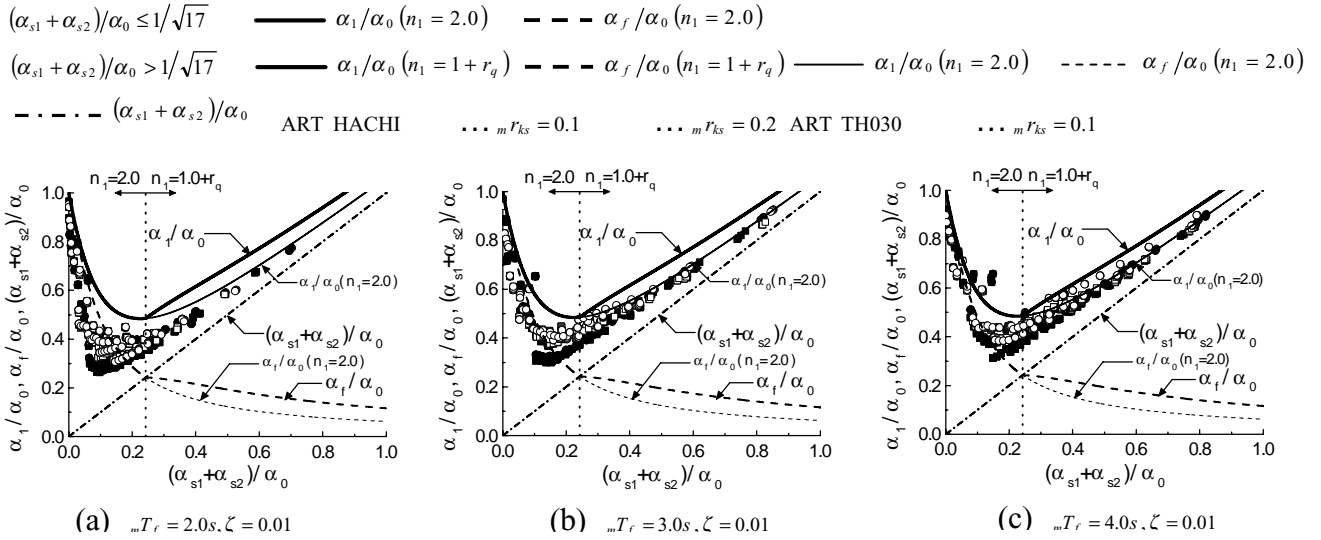


Fig.5 α_1/α_0 and $(\alpha_{s1} + \alpha_{s2})/\alpha_0$ Relationship

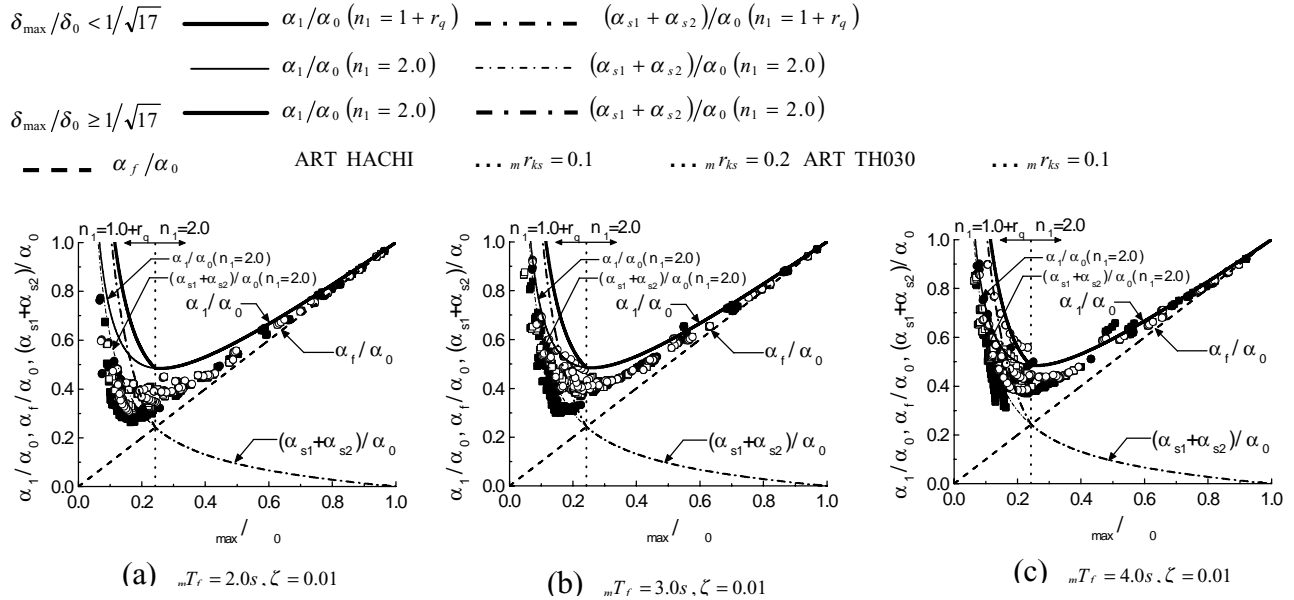


Fig.6 α_1/α_0 and δ_{max}/δ_0 Relationship

Seismic response prediction method is deduced by Equation (14). When dumping is zero, Shear force efficient α_0 and the horizontal displacement of base isolation δ_0 is given by Equation (15).

$$\alpha_0 = \frac{2\pi VE}{T_f \cdot g}, \quad \delta_0 = \frac{T_f \cdot VE}{2\pi} \quad (15)$$

Elastic strain energy of isolator fW_e is given by Equation (16).

$$fW_e = \frac{1}{2} f Q_{max} \cdot \delta_{max} = \left(\frac{\alpha_f}{\alpha_0} \right)^2 \cdot \frac{MVE^2}{2} \quad (16)$$

Hysteretic dumping energy of dumper sIW_p is given by Equation (17). $sI\delta_y \cong 0$ is assumed because sIW_e is very small absorb energy.

$$\begin{aligned}
s1W_p &= 4n1 \cdot s1 Q_y \cdot (\delta_{max} - s1 \delta_y) \\
&= 8n1 \left(\frac{\alpha_f}{\alpha_0} \right) \left(\frac{\alpha_{s1}}{\alpha_0} \right) \cdot \frac{MVE^2}{2} \quad (17)
\end{aligned}$$

Hysteretic dumping energy of low friction elastic sliding bearings $s2W_p$ is given by Equation (18). $s2\delta_y \cong 0$ is assumed because $s2W_e$ is very small absorb energy.

$$\begin{aligned}
s2W_p &= 4n1 \cdot s2 Q_y \cdot (\delta_{max} - s2 \delta_y) \\
&= 8n1 \left(\frac{\alpha_f}{\alpha_0} \right) \left(\frac{\alpha_{s2}}{\alpha_0} \right) \cdot \frac{MVE^2}{2} \quad (18)
\end{aligned}$$

Equation (16),(17),(18) is substituted in Equation (14) And Equation (19) is obtained.

$$\left(\frac{\alpha_f}{\alpha_0} \right)^2 + 8n1 \left(\frac{\alpha_{s1} + \alpha_{s2}}{\alpha_0} \right) \left(\frac{\alpha_f}{\alpha_0} \right) = 1 \quad (19)$$

Shear coefficient of isolator α_f is given by Equation (19)

$$\frac{\alpha_f}{\alpha_0} = -4n1 \left(\frac{\alpha_{s1} + \alpha_{s2}}{\alpha_0} \right) + \sqrt{16n1^2 \left(\frac{\alpha_{s1} + \alpha_{s2}}{\alpha_0} \right)^2 + 1} \quad (20)$$

Shear coefficient of base isolation α_1 is given by Equation (20)

$$\frac{\alpha_1}{\alpha_0} = \frac{\alpha_f}{\alpha_0} + \frac{\alpha_{s1}}{\alpha_0} + \frac{\alpha_{s2}}{\alpha_0} = -4n1 - 1 \left(\frac{\alpha_{s1} + \alpha_{s2}}{\alpha_0} \right) + \sqrt{16n1^2 \left(\frac{\alpha_{s1} + \alpha_{s2}}{\alpha_0} \right)^2 + 1} \quad (21)$$

Using α_f , maximum horizontal displacement of base isolation is given by Equation (22), (23).

$$\delta_{max} = \frac{f Q_{max}}{k_f} = \frac{\alpha_f g}{(1-R)} \left(\frac{mT_f}{2\pi} \right)^2 = \frac{\alpha_f \cdot \delta_0}{\alpha_0} \quad (22)$$

$$\frac{\delta_{max}}{\delta_0} = \frac{\alpha_f}{\alpha_0} = -4n1 \left(\frac{\alpha_{s1} + \alpha_{s2}}{\alpha_0} \right) + \sqrt{16n1^2 \left(\frac{\alpha_{s1} + \alpha_{s2}}{\alpha_0} \right)^2 + 1} \quad (23)$$

5. Certificated Response Prediction Method Based on Analysis Result

The analytical result obtained from time history analysis is evaluated, and response prediction method, Equation (21) is verified. The value of equivalent number of cycles in Equation (21) is calculated by Equation (11). The relationship between response shear coefficient of base isolation α_1/α_0 and shear coefficient of elastic element $(\alpha_{s1} + \alpha_{s2})/\alpha_0$ on the difference between mT_f is shown in Fig.5. The relationship between α_1/α_0 and maximum horizontal displacement of base isolation δ_{max}/δ_0 on the difference between mT_f is shown in Fig.6. The response prediction method approximately envelops upper limited values of result of analysis. The value of the analytical result is larger than the value α_1/α_0 of prediction method written in fine continuous line ($n_1 = 2.0$) within $r_q < 1.0$. But it is shown that the response prediction method written in bold continuous line ($n_1 = 1 + r_q$) is estimated in safe side.

6. CONCLUSIONS

The proposed method is verified with numerical simulation and good agreement is observed. The equivalent number of cycles and the residual deformation are evaluated using the shear stress ratio of

flexible element and stiff element obtained from numerical simulation. Besides the design equation, which Akiyama proposed for Shear-type Multi-Story Frame, can be applied for base-isolated structures.

References:

Akiyama, H., (1991) , “Earthquake-Resistant Design Method for Buildings Based on Energy Balance” Gihodo Inc.

EXPERIMENTAL STUDY ON MITIGATION OF SEISMIC RESPONSE OF A BUILDING BY VARIABLE DAMPERS

A. Ruangrassamee¹⁾, W. Srisamai²⁾, and P. Lukkunaprasit³⁾

1) Lecturer, Department of Civil Engineering, Chulalongkorn University, Thailand

2) Graduate Student, Department of Civil Engineering, Chulalongkorn University, Thailand

3) Professor, Department of Civil Engineering, Chulalongkorn University, Thailand

fcearr@eng.chula.ac.th, nokweerasit@hotmail.com, lpانيتan@chula.ac.th

Abstract: In this study, the damping force algorithm called the viscous-plus-variable-friction damping force algorithm is proposed by combining advantageous features of typical viscous and friction dampers. The variable damper with the proposed algorithm can be represented by a viscous element placed in series with a variable-friction element. As a piston velocity increases from zero, the damping force is generated by the viscous element. This is aimed to allow energy dissipation at a small velocity. When the damping force reaches a peak value of the viscous element or a preset force limit, the sliding of the variable-friction element occurs, resulting in a constant damping force. A variable damper with the proposed damping force algorithm was developed using a magnetorheological (MR) damper. A series of cyclic loading tests of a MR damper was conducted to develop the mathematical model of the MR damper for control purpose. It is found that the proposed algorithm can be realized by the MR damper with a good accuracy. Subsequently, the MR damper was installed in the first story of a three-story steel model building. The model building is excited by a shaking table under a one-directional ground motion. It is found that the proposed damping force algorithm is effective in controlling the displacement, acceleration, and column displacement of the model building.

1. INTRODUCTION

Passive control systems have been widely applied to mitigate seismic response (Constantinou et al. 1998). Typical passive control devices are viscous dampers and friction dampers. The damping force of a viscous damper is linearly proportional to a piston velocity. The smooth change in a damping force leads to energy dissipation even when a piston velocity is small. However, a damping force is small at the end of a stroke due to a decrease in a velocity. It results in a large relative displacement of a structure in which the damper is installed. On the other hand, a friction damper provides a constant level of a damping force over an entire stroke, resulting in a large amount of energy dissipation if properly designed. However, at a slightly large damping force level, the amount of energy dissipation decreases significantly (Ruangrassamee and Kawashima 2002). And the friction damper tends to cause larger acceleration due to sudden changes of damping forces. With an emerging semi-active control technology (Spencer et al. 1997 and Sunakoda et al. 2000), the benefits of both damping force patterns can be combined. In this study, the damping force algorithm called the viscous-plus-variable-friction damping force algorithm is proposed. The variable damper with the proposed damping force algorithm was developed using a magnetorheological (MR) damper. Then, the MR damper was installed in the first story of a three-story steel model building. The model building was excited by a shaking table under a one-directional ground motion. The effectiveness of the proposed damping force algorithm in controlling the seismic response of the model building was investigated.

2. DEVELOPMENT OF VARIABLE DAMPERS

2.1 Concept of Viscous-Plus-Variable-Friction Damping Force Algorithm

The combination of viscous and friction damping force algorithms called as “viscous-plus-variable-friction (VVF) damping force algorithm” is proposed. The model representing the proposed damping force algorithm is illustrated in Fig. 1. A viscous damping element is connected in series with a variable-friction element having a variable slipping force level. As a velocity increases from zero, the viscous damping element is mobilized to dissipate energy. Once the damping force of the viscous damping element reaches its peak value in each loading direction or a force limit, the slipping force of the variable-friction element is set equal to the value, resulting in the sliding of the variable-friction element. In the reverse direction, the damping force changes in the similar manner. Fig. 2 shows the damping force vs. velocity relationship and the damping force vs. stroke relationship of the proposed damping force algorithm. The damping force algorithm is characterized by two parameters: the damping coefficient of the viscous damping element and the force limit of the variable-friction element. The force limit may represent the force capacity of a variable damper.

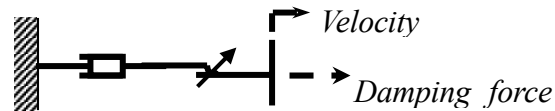
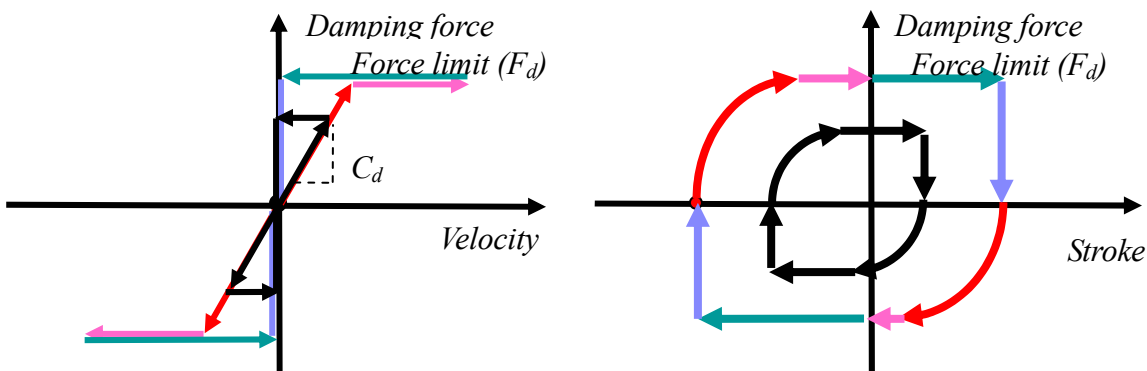


Fig. 1 Model representing the proposed damping force algorithm



(a) Damping force vs. velocity relationship

(b) Damping force vs. stroke relationship

Fig. 2 Hysteresis of the viscous-plus-variable-friction damping force algorithm

2.2 Dynamic Properties of MR Dampers

To realize the proposed damping force algorithm, a RD-1084 MR damper developed by Lord Corporation was used in this study. The damper is 237 mm long in its extended position and 197 mm long in its compressed position. So, the stroke of the damper is +/- 20 mm. The cylinder is 28 mm in diameter. The force capacity of the damper is about 60 N. The damper operates at the current of 0-400 mA. The current is supplied to the damper by a Lord RD-3002 current driver. The current driver outputs a current proportional to an input voltage in the range of about 0.5-1.5 V. In order to apply the MR damper as a semi-active control device, it is necessary to identify the damping properties of the MR damper. A series of cyclic loading tests was conducted for various loading conditions. The damping force was measured by a load cell. The load cell was connected between the reaction frame and the damper. The displacement was measured by a laser displacement transducer. The current to the damper was controlled by a microcomputer. The voltage was generated by an I/O board which was installed in the computer. Then, the current driver supplied a current proportional to the voltage. A hydraulic actuator with displacement control was used to load the damper. The damper was subjected

to sinusoidal excitations. The loading frequencies were 0.01, 1, 2, and 3 Hz. The loading amplitudes were 7.5 and 15 mm. The current levels were varied as 0, 100, 200, 300, and 400 mA. The force-displacement relationships of the MR damper are presented in Fig. 3. It is seen that the damping force increases as the current to the damper increases. The force-displacement relationship of the MR damper is close to that of a friction damper. It is seen that the shape of force-displacement relationship is slightly affected by the loading conditions.

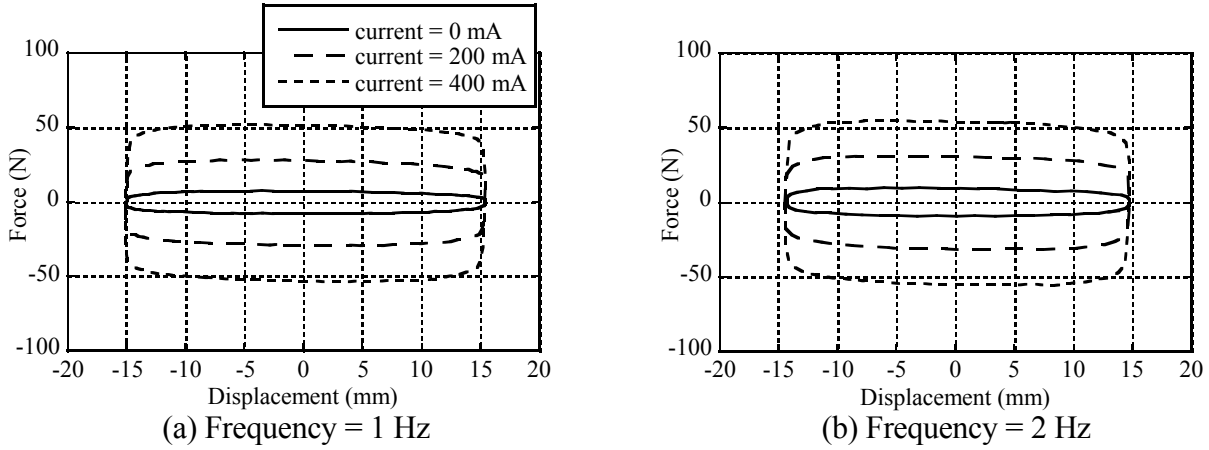


Fig. 3 Force vs. displacement relationship of the MR damper

2.3 Control of Damping Force

To control the MR damper, the mathematical model of the MR damper is required. The MR damper was modeled from the relationship between the maximum damping force and maximum velocity as shown in Fig. 4. From a linear regression analysis, the following equation is obtained:

$$f = (3.78 + 0.123c) + (0.03 - 0.0000577c)v \quad (1)$$

where c is the current to the MR damper (mA), v is the piston velocity (mm/s), and f is the damping force (N). The current commanded to achieve a damping force can be computed from the back calculation of Eq. (1) with a known piston velocity. As it has been realized that there is a discrepancy in the damping force, a simple correction of the damping force was introduced after the back calculation. An additionally-supplied voltage (ΔV) is set as a function of the instantaneous difference between the commanded and actual (measured) damping force (Δf), as shown in Fig. 5. The effect of the slope k was investigated. Fig. 6 shows the damping force-displacement relationship of the MR damper for $k = 0.04$ V/N. It is found that the damping force algorithms can be realized by the MR damper with a good accuracy. For a frequency of 2 Hz, small spikes in damping forces occur after the direction of excitation is reversed. It is due to a delay in predicting the velocity of the MR damper. This may limit the application of the control algorithm for a high-frequency excitation.

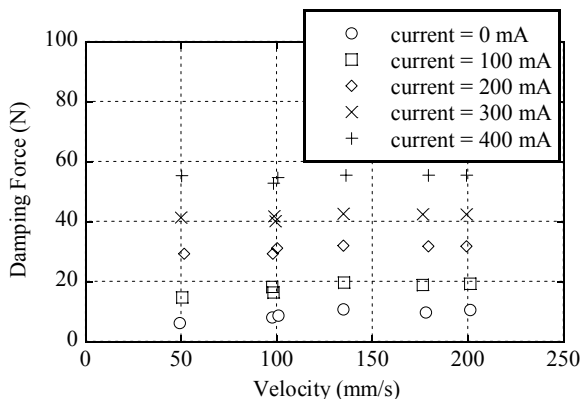


Fig. 4 Damping force vs. velocity relationship

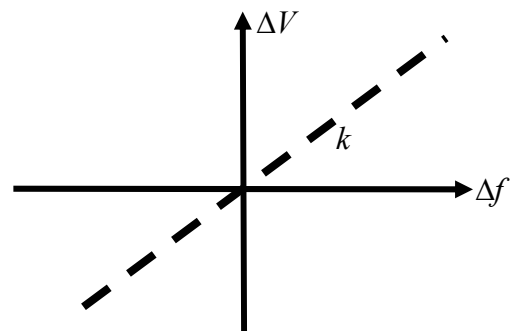


Fig. 5 Function for correcting a damping force

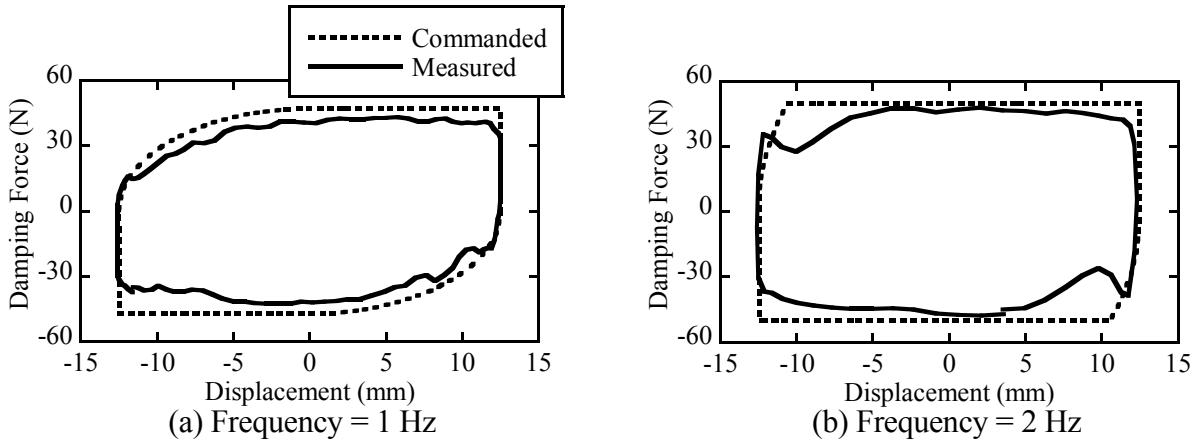


Fig. 6 Damping force vs. displacement relationship for the VVF damping force algorithm

3. SHAKING TABLE TEST OF A MODEL BUILDING

3.1 Properties of Model Building

To investigate the effectiveness of the damping force algorithm, a shaking table test was conducted on a three-story steel model building. The model building was fabricated from steel plates as shown in Fig. 7. The masses of the 1st, 2nd, and 3rd floors are 37.5 kg, 37.4 kg, and 30.6 kg, respectively. There are four columns in each story connected to the floors by steel angles. The height of the model building is approximately 1 m. The floor size is 0.8 m by 0.4 m. From a free vibration test, the natural periods of the 1st, 2nd, and 3rd modes are 0.73, 0.25, and 0.17 s, respectively. The model building was designed to have a fundamental natural period within a typical period range of three-story steel buildings. The displacement of each floor was measured by a displacement transducer and the acceleration of each floor was measured by an accelerometer.



Fig. 7 Setup of shaking table test

3.2 Cases of Shaking Table Test

The model building was constructed on a shaking table and was excited by a ground motion in the long direction of the model building. The El Centro record was used in the test. The ground motion was recorded at the Imperial Valley Irrigation District substation in El Centro, California, during the M7.1 Imperial Valley, California earthquake of May 18, 1940. The peak ground acceleration is 0.35 g. The intensity of the ground motion record in the test is about 40% of the original ground motion record. The time scale of the ground motion is equal to one. It is interesting to investigate the response of the variable damper under a realistic excitation frequency. The damping force algorithm was varied as listed in Table 1.

Table 1 Cases of shaking table test

Case	Damping force algorithm	Parameters of damping force algorithm
1	No damper	No MR damper was installed.
2	No current	A MR damper was installed but there was no input current.
3	Viscous damping	Damping coefficient = 0.35 N.s/mm
4	Friction damping	Friction force = 25 N
5	VVF damping	Damping coefficient (C_d) = 0.35 N.s/mm, Friction force (F_d) = 25 N

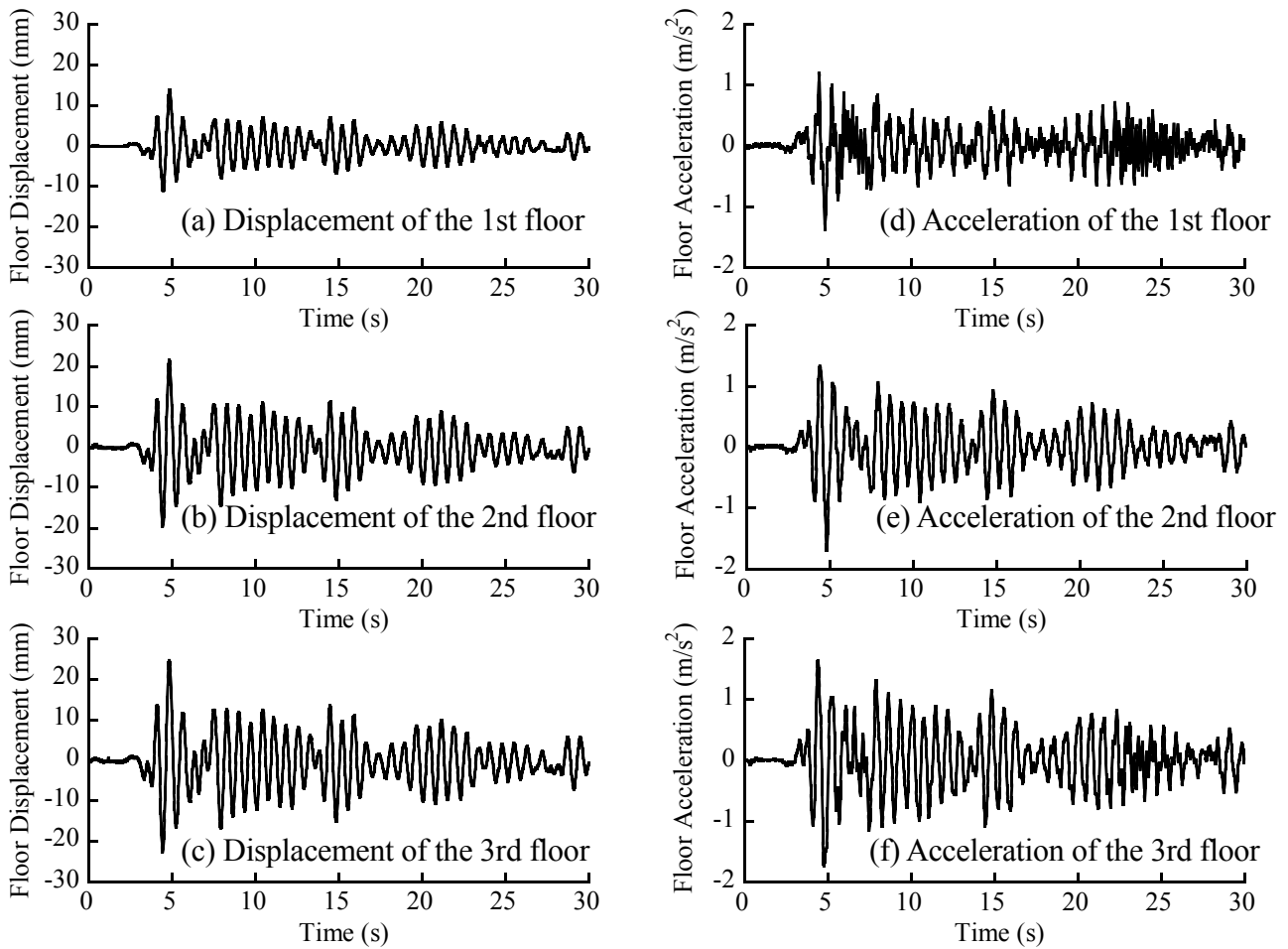


Fig. 8 Response of the model building without damper

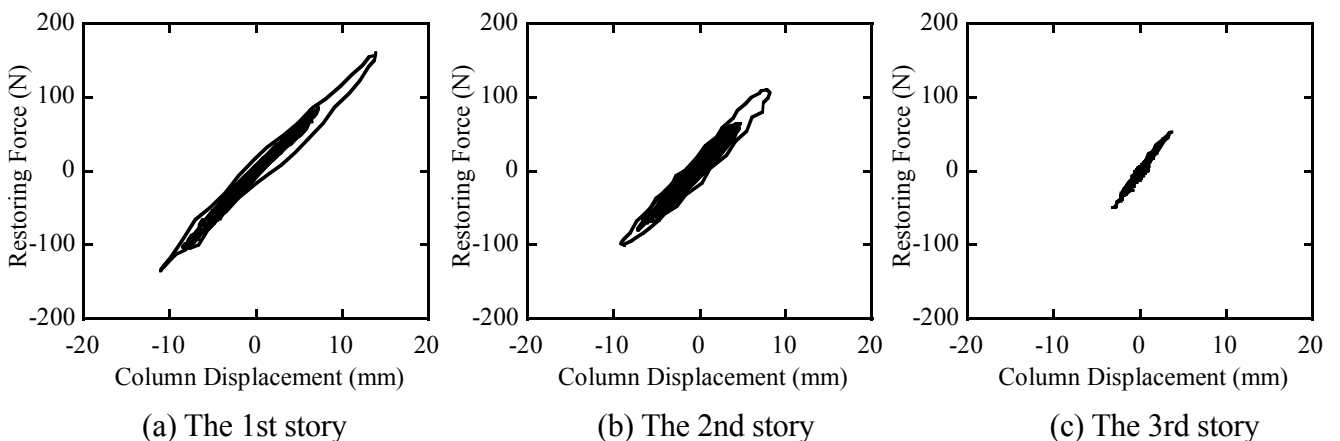


Fig. 9 Restoring force vs. column displacement relationship of the model building without damper

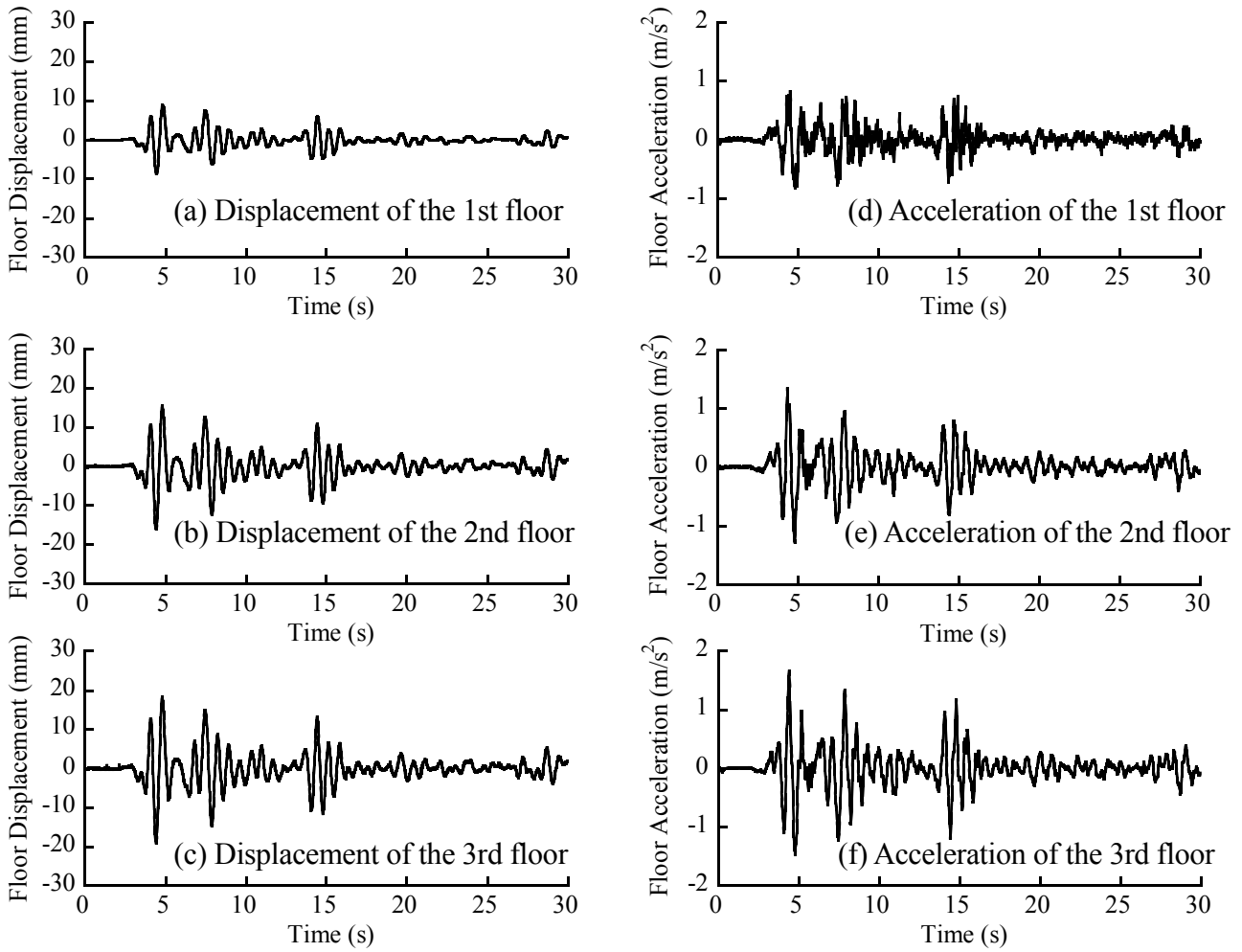


Fig. 10 Response of the model building controlled by the VVF damping force algorithm

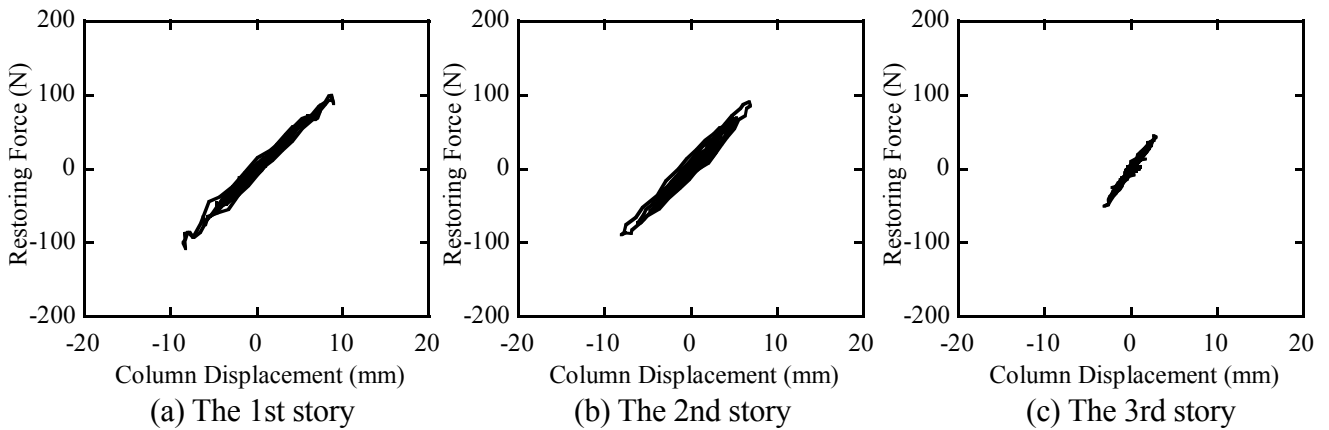


Fig. 11 Restoring force vs. column displacement relationship of the model building controlled by the VVF damping force algorithm

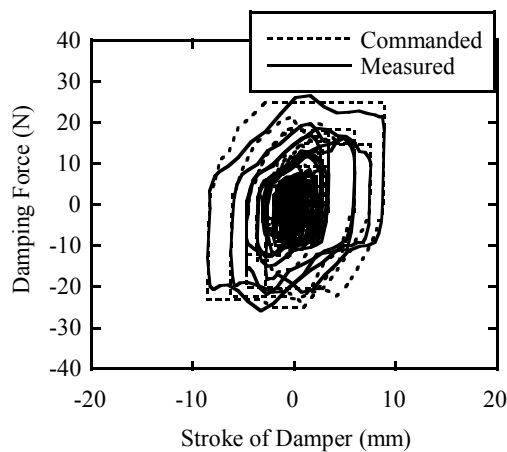
3.3 Experimental Results

Fig. 8 shows the response of the model building without damper. The maximum displacements of the 1st, 2nd, and 3rd floors are 13.9, 21.5, and 24.6 mm, respectively. The maximum accelerations of the 1st, 2nd, and 3rd floors are 1.36, 1.69, and 1.73 m/s^2 , respectively. The restoring force of columns in each story was computed from the equations of motion of a three-degree-of-freedom system with the measured acceleration and displacement. The relationship between the restoring force and column

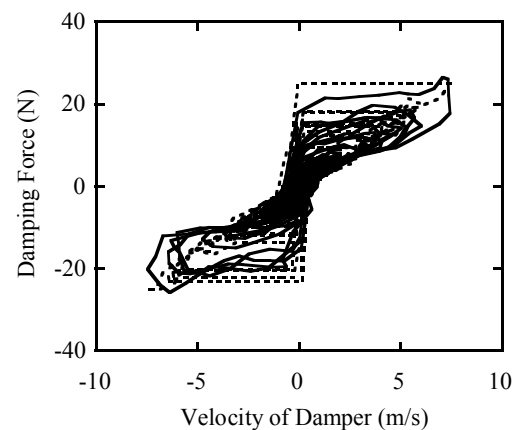
displacement in each story is shown in Fig. 9. The displacement of columns is 13.9 mm in the 1st story and varies to 3.7 mm in the 3rd story. It is seen that slight nonlinearity occurs in the columns in the 1st and 2nd stories. Fig. 10 shows the response of the model building controlled by the VVF damping force algorithm. The maximum displacements of the 1st, 2nd, and 3rd floors are 8.9, 16.0, and 19.1 mm, respectively. The maximum accelerations of the 1st, 2nd, and 3rd floors are 0.83, 1.34, and 1.66 m/s^2 , respectively. Fig. 11 shows the relationship between the restoring force and column displacement in each story. The displacements of columns are 8.9, 8.1, and 3.2 mm in the 1st, 2nd, and 3rd stories, respectively. It corresponds to the percentage of reduction of 36.0%, 12.0%, and 13.5%, respectively. It is obvious that the nonlinearity is less than the case without damper. Fig. 12 shows the damping force vs. stroke relationship and the damping force vs. velocity relationship. It is seen that the damping force can be controlled with a good accuracy. For comparison, the maximum response of all cases is summarized in Table 2. The friction damping force algorithm results in more reduction of floor displacements but it causes larger accelerations. It is important to note that the maximum damping force of the friction damping force algorithm is larger than the commanded value of 25 N due to the delay in predicting the velocity as mentioned. It is seen that the VVF damping force algorithm provides slightly more reduction of displacements than the viscous damping force algorithm while yields more reduction of accelerations of the 1st and 2nd floors than other damping force algorithms. The VVF damping force algorithm is effective in controlling the response of the model building.

Table 2 Summary of experimental results

Case	Damping force algorithm	Maximum acceleration of each floor (m/s^2)			Maximum displacement of each floor (mm)			Maximum column displacement of each story (mm)			Maximum damping force (N)
		1st	2nd	3rd	1st	2nd	3rd	1st	2nd	3rd	
1	No damper	1.36	1.69	1.73	13.9	21.5	24.6	13.9	9.2	3.7	-
2	No current	1.00	1.47	1.61	12.3	19.8	22.9	12.3	8.2	3.2	7.5
3	Viscous	1.04	1.37	1.70	9.8	16.1	19.4	9.8	7.9	3.4	27.9
4	Friction	1.37	1.59	1.57	6.9	13.0	15.0	6.9	6.6	3.5	41.4
5	VVF	0.83	1.34	1.66	8.9	16.0	19.1	8.9	8.1	3.2	26.5



(a) Damping force vs. stroke relationship



(b) Damping force vs. velocity relationship

Fig. 12 Hysteresis of the VVF damping force algorithm from the shaking table test

4. CONCLUSIONS

In this study, the damping force algorithm called the viscous-plus-variable-friction (VVF) damping force algorithm was proposed. A series of cyclic loading tests of a MR damper was conducted to develop the mathematical model of the MR damper for control purpose. It is found that the proposed damping force algorithm can be realized by the MR damper with a good accuracy. Then, the MR damper was installed in the first story of a three-story steel model building for the shaking table test. It is found that the VVF damping force algorithm provides slightly more reduction of displacements than the viscous damping force algorithm while yields more reduction of accelerations of the 1st and 2nd floors than viscous and friction damping force algorithms. The nonlinearity of columns can be reduced by the VVF damping force algorithm. The VVF damping force algorithm is effective in controlling the response of the model building. The issue related to the application of MR dampers for high-frequency excitations was noted.

Acknowledgements:

The authors acknowledge the financial support from the Thailand Research Fund (TRF).

References:

- Constantinou, M. C., Soong, T. T., and Dargush, G. F. (1998), "Passive Energy Dissipation System for Structural Design and Retrofit." *Technical Report of Multidisciplinary Center for Earthquake Engineering Research.*, SUNY, Buffalo, New York, USA.
- Ruangrassamee, A. and Kawashima, K. (2002), "Seismic Response Control of a Benchmark Cable-Stayed Bridge by Variable Dampers." *Proceedings of the American Control Conference*, Anchorage, Alaska, USA.
- Spencer, B. F., Jr., Dyke, S. J., Sain, M. K., and Carlson, J. D. (1997), "Phenomenological Model of a Magnetorheological Damper." *Journal of Engineering Mechanics*, American Society of Civil Engineers, **123**(3), 230-238.
- Sunakoda, K., Sodeyama, H., Iwata, N., Fujitani, H., and Soda, S. (2000), "Dynamic Characteristics of Magneto-Rheological Fluid Damper." *Proceedings of SPIE 7th Annual International Symposium on Smart Structures and Materials*. Newport Beach, USA.

ENHANCED PERFORMANCE OF BUILDINGS RETROFITTED WITH FRICTION DAMPERS WITH RESTRAINERS

P. Lukkunaprasit¹⁾, and A. Wanitkorkul²⁾

1) Professor, Department of Civil Engineering, Chulalongkorn University, Thailand

2) Former Graduate Student, Department of Civil Engineering, Chulalongkorn University, Thailand
lpanitan@chula.ac.th, assawin78@hotmail.com

Abstract: The behaviour of slotted-bolted connections when the maximum slip travel exceeds the available slot length is presented. The drastic degradation behaviour of slotted-bolted connections under bolt impact is demonstrated. Remedy by means of the concept of restrainers is proposed, which is also advantageous in suppressing the build-up of resonance motion by virtue of the change in system stiffness at different stages. Nonlinear dynamic analyses are performed on two buildings equipped with the friction dampers with and without restrainers. The first structure, a 6-storey steel building with moment-resisting frame, is subjected to strong near-field earthquakes. The second one, a typical 6-storey reinforced concrete building in Bangkok with non-seismic design, is investigated under moderate ground motions induced by distant earthquakes. In the worst loading cases, the damper with restrainers is superior to that without restrainers, resulting in reduction of the peak inter-storey drift in the order of 16-20% and the peak slip travel 15-30%. The shorter slip travel obviously provides extra safety to the damper against bolt impact. Although the peak inter-storey drift and the peak slip travel of the device decrease with increasing in the restraining force limit, the extra gain has to be balanced with the potential of buckling of the bracing at the high restraining force in the case of retrofitting with bracings.

1. INTRODUCTION

The slotted-bolted connection (SBC) has been recognized as a low-cost passive friction-damping system for reduction of damages caused by strong motions (e.g. FitzGerald et al. 1989, Grigorian et al. 1993, Tremblay and Stierner 1993). Most studies, except the one by Roik et al. (1988), do not address the situation when the slip travel of the SBC reaches the provided slip length. However, Roik et al. (1988) did not investigate the effect of stiffening due to the restraining action. Since earthquake characteristics are unpredictable, it cannot be guaranteed that in the most severe case the bolts would slide freely in the 'finite length' slot available. Furthermore, it is not practical, or even impossible in some cases, to provide long slots. It is thus significant to investigate the behavior of such a damping system in the event of bolt impact and the restraining effect thereafter. Advantages of the limited-slip friction damper over the conventional one are demonstrated through performance assessments of two buildings, one subjected to strong motion earthquakes, and the other to moderate ground motions induced by distant earthquakes.

2. CONVENTIONAL SBC UNDER BOLT IMPACT

Wanitkorkul (2003) performed a series of displacement controlled, cyclic tests on slotted-bolted

connections, with and without impact on high-strength bolts. The damper specimen consisted of three A36 steel plates, i.e. one central plate and two cover plates each with a thickness of 11 mm. Brass plates were inserted between the central plate and the cover plates to create steel-on-brass contacting surfaces. The damper was designed to have two slots symmetrically placed on the central plate. All plates were clamped together using two 12-mm-diameter A325 high-strength bolts with “Belleville washers”. The total clamping force on each sliding surface was 108 kN (70% of bolt tensile strength). The test assembly was subjected to 30 displacement cycles without bolt impact, followed by 10 displacement cycles with impact on high-strength bolts, in general. Testing frequencies of 0.1, 0.5, and 1 Hz were used in the cyclic tests.

Figure 1 shows the hysteresis of a SBC specimen under the first thirty displacement cycles without bolt impact. Generally, the hysteresis under each testing frequency is similar, hence only the results from the testing frequency of 0.1 Hz are demonstrated. The resulting force-displacement relationships were nearly rectangular in shape, which was consistent with the results obtained from many past researches. The initial friction forces were around 45 kN, and they became stable around 95 kN after approximately 20 displacement cycles. Despite the fluctuation of the friction forces, steel-on-brass friction type specimens were acceptable because the variation of frictions was in the initial stage, therefore it would not affect the behaviour of damper when the specified slip travel was reached upon bolt impact. The stiffness increased sharply as can be seen in Fig. 2 which illustrates the portion of the hysteresis of a SBC specimen during bolt impact. From the figure, the first yield-plateau indicates the level of friction, while the second one shows the yield strength of the connection. During cycling of bolt impact, degradation of the friction force is evident. More than 50% of friction force was lost after only 4-mm of displacement was imposed beyond the provided slot length. Bearing caused permanent deformations in the clamping bolts, with the consequence of the friction loss.

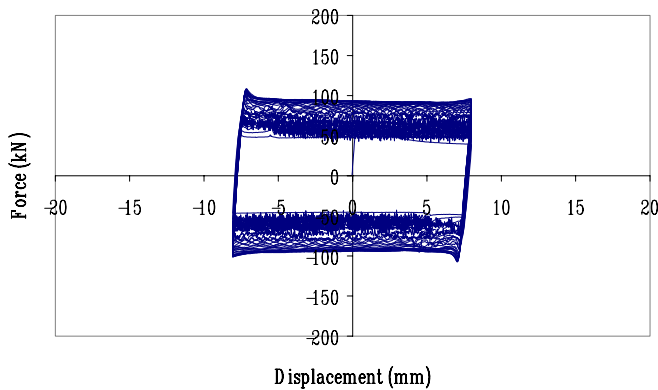


Figure 1 Force-Displacement Relationship of SBC: 30 Cycles, 0.1 Hz, without Bolt Impact

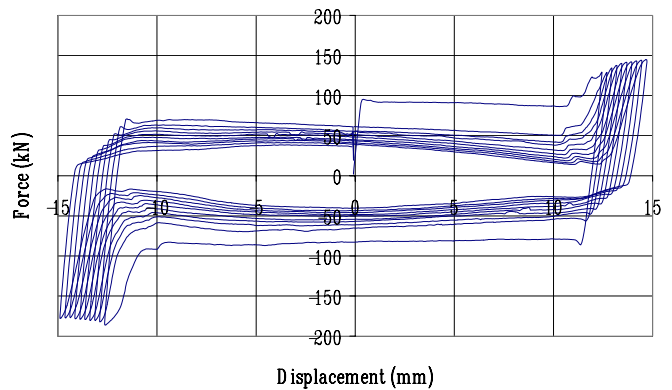


Figure 2 Force-Displacement Relationship of SBC: 10 Cycles, 0.1 Hz, with Bolt Impact

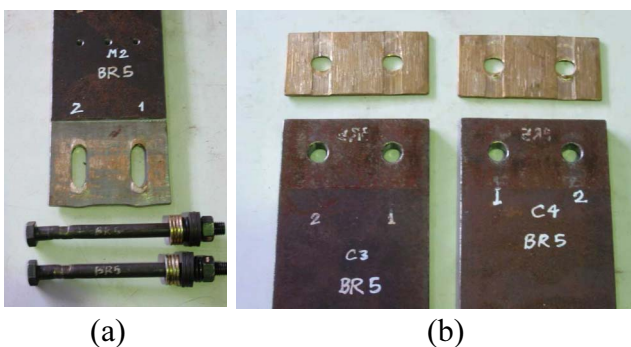


Figure 3 SBC Specimen after Bolt Impact: (a) Central Plate and Bolts; (b) Cover Plates and Brass Plates

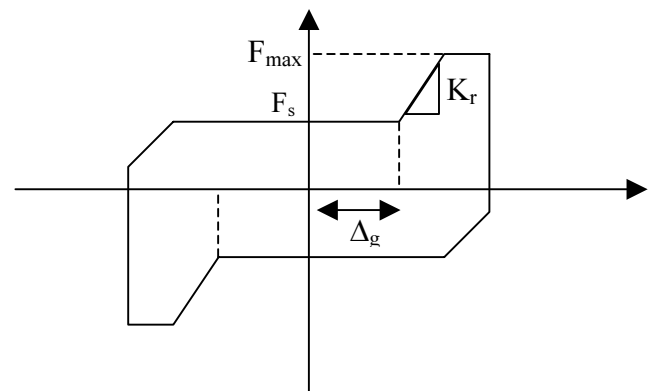


Figure 4 Damper Force-Slip Travel Relationship of Slotted-Bolted Connection with restrainers

Figure 3 shows each component of the specimen after test. Damages of the clamping bolts can be clearly seen in the figure. More experimental results can be found in the original document by Wanitkorkul (2003).

3. THE SLOTTED-BOLTED CONNECTION WITH RESTRAINERS

With the unacceptable behaviour of SBC under bolt impact witnessed, it is obvious that remedy is needed to prevent bolt impact. The restraining concept proposed by Roik et al. (1988) to prevent undesirable bolt impact is adopted in this study, with slight modification. The device with restrainers will slip at the predetermined slip load F_s . The restrainers will be activated when the slip travel is larger than the provided slip distance Δ_g , which results in increasing of the resisting force of the device at a stiffness K_r . This restraining force is further limited to a threshold value F_{max} which remains constant at the second yield plateau. Figure 4 shows the force-slip travel relationship of a slotted-bolted connection with restrainers. The restraining stiffness K_r of the device can be selected as suggested by Roik et al. (1988). It should be noted that the change in stiffness at different stages is advantageous in suppressing the build-up of resonance, should there be a tendency for such an event.

4. STEEL BUILDING

4.1 Building Model

We first take the case study of the steel structure considered by Filiatrault et al. (2001). The building is a 6-storey steel structure, rectangular in plan, and is braced by two exterior moment-resisting frames. Gravity loads acting on the frame during the earthquake are assumed equal to 3.8 kPa from roof dead load, 4.5 kPa from floor dead load, 0.7 kPa from floor live load, and 1.7 kPa from weight of the exterior cladding. Steel grade A36 is used for all members. The building, designed for seismic zone 4 in the United States, would not survive strong earthquakes when weld fractures occur in the welded beam-to-column connections. For retrofit, chevron-brace members are introduced in the central bay of the two exterior moment-resisting frames as shown in Fig. 5. The steel section HSS 300 mm x 300 mm x 15 mm is used for all chevron-brace elements. Slotted-bolted connections are incorporated at one end of all bracing members. Both conventional SBC and slotted-bolted connections with restrainers (SBC-R) are considered. The fundamental vibration period of the original building was 1.30 sec and was reduced to 0.67 sec after retrofitted with the proposed system.

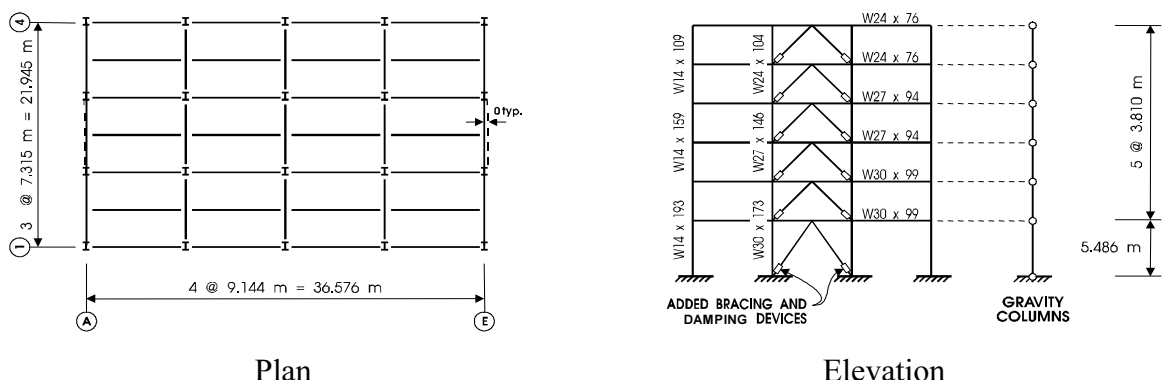


Figure 5 Steel Building Model and Retrofit Scheme

Because of symmetry, only one exterior moment-resisting frame was modeled as a two-dimensional structure. Floor slabs and architectural elements were excluded. The panel zones of the beam-column joints were assumed to have no panel shear deformation and yielding during strong excitations. Large displacement effect was also considered in the analyses. P- Δ effect from interior columns was included by introducing a pin-ended gravity column into the building model, which represents all interior columns. Total gravity loads acting on the interior columns were applied to the gravity columns. Both the exterior frames and the gravity columns were constrained to undergo the same lateral displacement at each floor, representing a rigid floor diaphragm assumption. Bilinear moment-curvature relation with a curvature-hardening ratio of 2% was assigned to all columns.

The flexural strength degradation model suggested by Filiatrault et al. (2001) was introduced at both ends of all beams to account for the brittle behaviour of welded beam-to-column connections. It was assumed that the strength degradation was independent in positive and negative bending. Only fractures at the beam-to-column interfaces were considered. An elasto-plastic moment-curvature relation was specified for all beam elements. The connections were assumed to have no loss in shear capacity when weld fractures occurred. More details on the building model can be found in the original paper.

4.2 Parameters for Conventional Slotted-Bolted Connection (SBC) and Slotted-Bolted Connection with Restrainers (SBC-R) Model

For SBC, a slip load value (F_{s1}) of 1524-kN was assigned for the device on the first floor, which was equal to 40% of the buckling strength (P_{b1}) of the corresponding bracing element. In the case of SBC with restrainers, the maximum restraining force (F_{max}) was limited to 60% of bracing buckling load to avoid damages to the bracing members, Based on the design procedure proposed by Filiatrault and Cherry (1990), slip loads of the connections on the second to the sixth floor were assigned a value equal to 80% of slip load on the first floor. Similarly, limits on restraining forces on the other floors were also assigned to be 80% of the maximum restraining force of the device on the first floor. The restraining stiffness was set equal to the corresponding bracing stiffness on each floor. A limit on slip travel was selected based on the maximum slip required in the most severe case, which will be discussed later. Axial springs with an elasto-plastic axial force-displacement relationship were used for all bracing members.

4.3 Earthquake Ground Motions

Three near-field earthquakes were considered in the nonlinear dynamic analyses, i.e. the 1989 Loma Prieta and the 1966 Parkfield earthquakes, which have the same peak ground acceleration of 0.48g, and the 1940 El Centro record with PGA's of 0.34g. Figure 6 depicts the accelerograms and the pseudo-acceleration response spectra with 5% damping associated with these earthquakes.

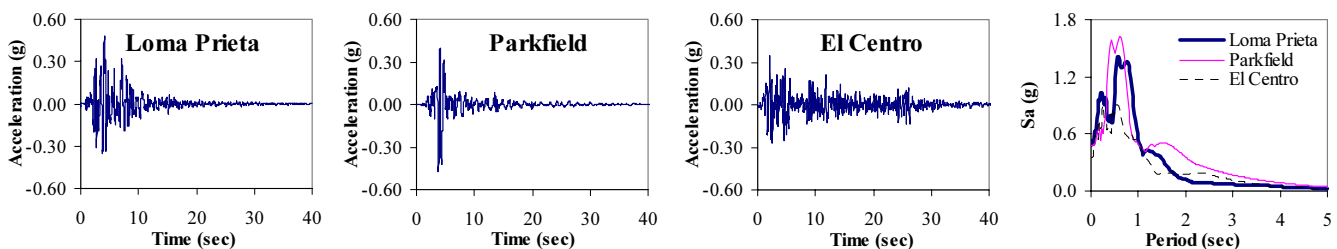


Figure 6 Accelerograms and Pseudo-Acceleration Response Spectra with 5% Damping

4.4 Performance

Nonlinear dynamic analyses were performed using the computer program RUAUMOKO (Carr

2000). The unretrofitted building collapses under all earthquakes considered with the peak inter-storey drift greater than 5% which indicates that retrofit is required for this structure.

4.4.1 Performance of Building with SBC

The most severe scenario results from the Parkfield earthquake, which results in the peak inter-storey drift of about 1.2% on the ground floor and the maximum curvature ductility of 3.8 in the ground floor columns. Damage is concentrated only on the first two floors with no yielding taking place on the others. The Loma Prieta earthquake, having the second highest spectral value, results in the maximum inter-storey drift of 0.8% and a peak curvature ductility of 2.7 in the ground floor columns with less damage compared with Parkfield. For the El Centro motion, it causes the least damage which is consistent with its lowest spectral value compared with other near-field records. Figure 7 illustrates the peak slip travels of the device obtained from analyses. The maximum slips of the device on the first and second floors are 35 and 20 mm, respectively, which result from the case of the Parkfield earthquake. These slip values are used for calculation of slip limits as discussed in the next section.

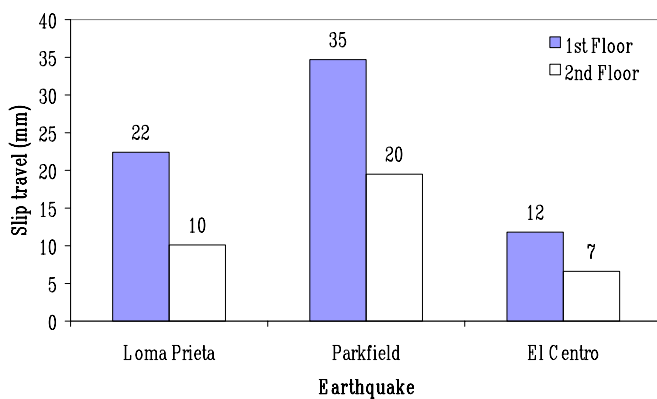


Figure 7 Maximum Slip Travel of SBC:
 $F_{s1}/P_{b1} = 0.40$

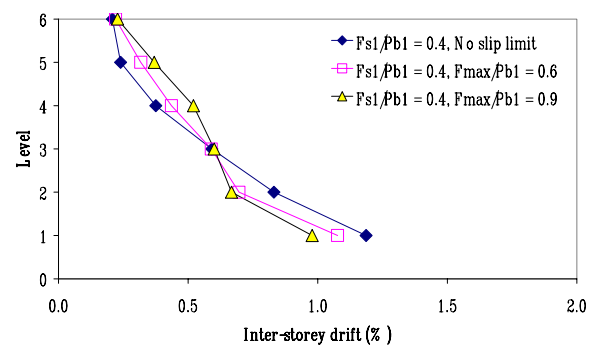


Figure 8 Peak Inter-Storey Drifts:
Parkfield Earthquake

4.4.2 Performance of Building with SBC-R

Half of the maximum slip travel resulted from the case of Parkfield earthquake was applied to the SBC-R model as the slip threshold for activating the restrainers in the SBC-R model. Hence, the slip travel of the SBC-R on the first floor was limited to 17.5 mm when restraining effect takes place. However, rather than using different slip limits on each floor, the slip limit assigned to all devices on the other floors was 10 mm which was half of the maximum slip occurred on the second floor.

Figure 8 presents the peak inter-storey drifts of the structure subjected to the Parkfield earthquake. For the case of Loma Prieta, the maximum slip travel is close to the limit value; hence, responses from the system without and with limited slip are similar. For Parkfield excitation, with limited slip, the peak floor displacement is reduced by 11%. The inter-storey drifts on the first and the second floors are reduced by 9 and 16%, respectively, while those on the other floors increases by 6-33% because restraining actions stiffen the lower floors compared to other floors. Although the inter-storey drifts in those upper floors increase, the maximum value is still less than the immediate occupancy limit of 0.7% as per ATC (2000). The maximum curvature ductility in the ground floor columns is reduced to 3.5 which amounts to 8% reduction while there are no yielding of columns on the other floors.

It seems that the advantage of restrainers in terms of response reduction is not promising.

However, it is worth noting that, without restrainers, bolt impact may occur should the intended slip travel be accidentally reduced by, for instance, error in workmanship. Significant degradation of the friction force of the device would result as mentioned earlier, which can result in much worse performance or even collapse of the structure. The advantage of the restraining action is evident from the damper force-slip travel plot shown in Fig. 9. With the maximum normalized restraining force (F_{max}/P_{b1}) of 0.60, the maximum slip travel is reduced by 15% from the case without restrainers. Further reduction of 20% results when F_{max}/P_{b1} is increased to 0.90. The shorter travel obviously provides extra safety against the undesirable bolt impact. Hence, utilization of restrainers in slotted-bolted connections is desirable and beneficial.

Although the benefits of SBC-R are evident, the device also induces larger base shear to the system. Figure 10 shows the peak base shear with different slip loads and restraining force limits. With restrainers, the total base shear of the retrofitted structure increases, which directly affects the foundation system. The magnitude of the additional base shear induced by SBC-R depends on the level of slip load and restraining-force limit, and the earthquake considered. For the case of the Parkfield earthquake with a 40% normalized slip load, the total base shear increases by 15% and 39% with the normalized restraining force of 60% and 90%, respectively, while the corresponding increase for the case of Loma Prieta excitation is about 15% only.

It should be noted that the selected parameters, i.e. slip load, maximum restraining force, etc., are for demonstration purposes. To determine the optimum values, more parametric studies are required. This is out of scope of this study.

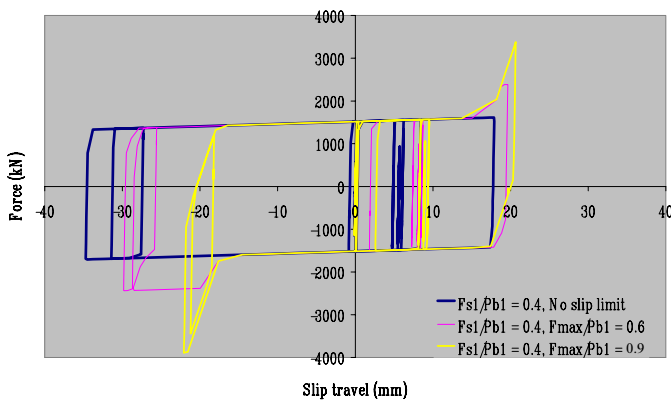


Figure 9 Damper Force- Slip Travel of SBC and SBC-R: Parkfield Earthquake

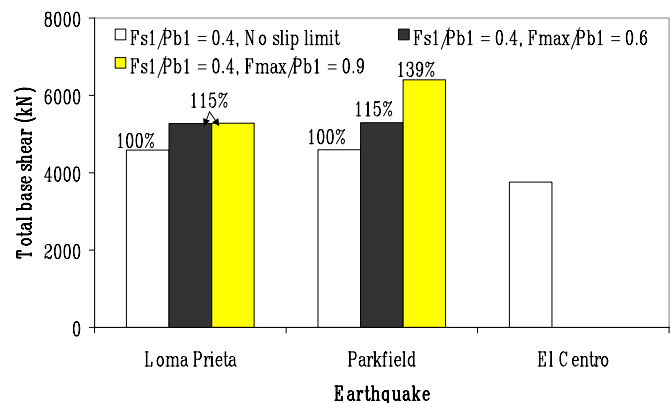


Figure 10 Total Base Shear for Retrofitting with Different Restraining Force Limits

5. RC BUILDING

5.1 Building Model

An existing 6-storey reinforced concrete building with brick masonry, which has been in use as an apartment building in suburban Bangkok (Bang Na area), Thailand since 1989, is next considered for seismic performance evaluation. It has typical details which represent many buildings in Bangkok. The exterior frames have masonry walls in all spans and all storeys except the ground floor level while the interior frames have masonry walls only in the exterior spans from the second to the fifth floors. Figure 11 shows the plan and elevation views of the building. Because of symmetry, only half of the building was modeled. The reinforcement details of the beams and columns are typical of non-ductile design in Thailand (Wanitkorkul 2003).

The Takeda hysteretic model was assigned for all beams and columns. A flexural strength degradation model was also introduced to the inelastic springs of all beam and column elements

when the ultimate section capacity was reached to simulate the post peak behaviour of the member. The model simulating the brick masonry wall proposed by Crisafulli (1997) was also included. Figure 12 depicts the masonry wall model. The strength of each spring representing masonry can be calculated as follows:

For shear spring,
$$P_{u, shear} = \frac{\tau_m L_m t}{\cos \alpha} \quad (1)$$

For axial spring,
$$P_{u, axial} = \frac{f'_m A_{ms}}{2} \quad (2)$$

where $P_{u, shear}$ and $P_{u, axial}$ are the strengths of the equivalent shear and axial springs, respectively; τ_m and L_m are the shear strength and the horizontal length of the masonry wall, respectively; t is the thickness of the wall; α is the inclination angle of the equivalent shear spring; f'_m is the compressive strength of the masonry; and A_{ms} is the area of the equivalent masonry strut. More details can be found in the original document.

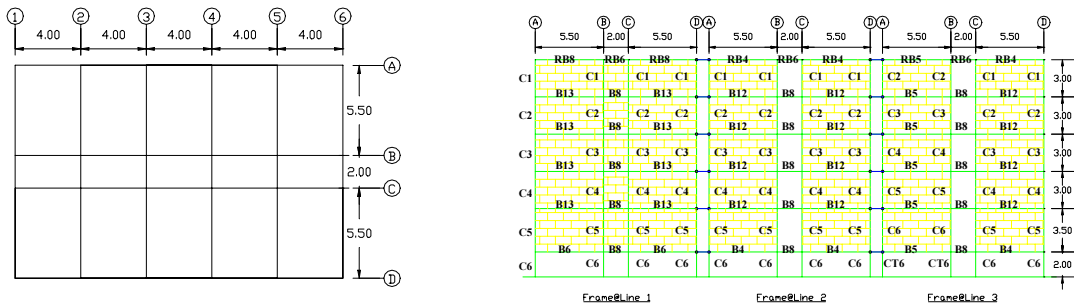


Figure 11 Plan and Elevation of the RC Building

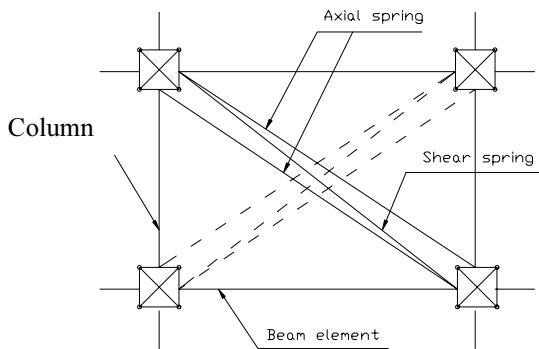
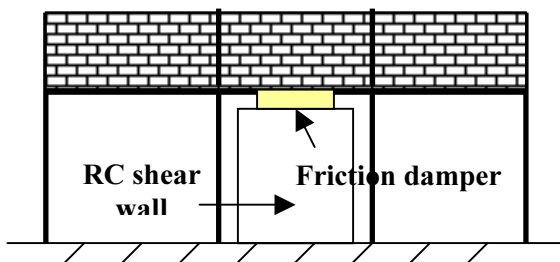


Figure 12 Masonry Wall Modeling



Exterior frame

Figure 14 Retrofit Scheme

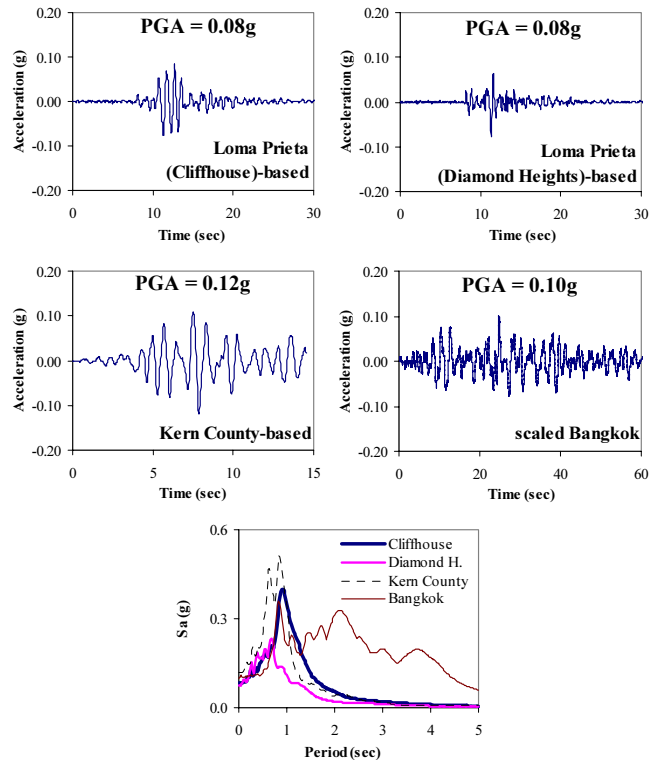


Figure 13 Accelerograms and Pseudo-Acceleration Response Spectra with 5% Damping

5.2 Earthquake Ground Motions

The ground motions induced by distant earthquakes were simulated using the available soil properties from field tests in Bangkok area (Wanitkorkul 2003). Three strong rock outcrop motions were selected as input motions for the analyses, namely, the 17 October 1989 Loma Prieta earthquake records at the Cliffhouse and the Diamond Heights stations and the Pasadena signal from the 1952 Kern County, California earthquake. Figure 13 depicts the resulting ground motions and their response spectra. The 1995 Bangkok excitation with scaled peak acceleration of 0.10g was also included in the investigation.

5.3 Performance

5.3.1 Response of Unretrofitted Building

For all the earthquakes considered, the damages are concentrated on the first few floors due to the poor structural system. Failure of two thirds of the ground floor columns occur at the storey drift level of less than 0.8%. This indicates non-ductile behaviour of the system. The Loma Prieta (Cliffhouse)-based excitation put the most severe demand on the building. So results will be presented based mainly on those from the Loma Prieta-based earthquake.

The maximum curvature ductility of 9.7 occurs in a few ground floor columns of the interior frames which is about 139% of the curvature capacity at ultimate moment resistance. These columns can be regarded as totally collapsed. However, no failures occur in ground floor columns of the exterior frames because of the lower level of axial load. High axial load level increases the strength of the column; however, it also decreases the ductility capacity. As for the brick walls, some infilled panels on the second and the third floor fail in the sliding-shear failure mode because of the low-strength of the mortar used in their bed joints.

5.3.2 Retrofit Scheme

The proposed retrofit scheme consists of incorporating a reinforced concrete shear wall on the ground floor with a frictional damping device connecting the wall and the beam in the central bay of the exterior frame (Fig. 14). This system has the advantage over the bracings with friction dampers system in that it does not require strengthening of the existing foundations, as will be explained later. Of course, the wall itself has to be constructed on a (new) separate foundation. This would be easier to build and also more economical. This scheme also does not induce high forces into the vulnerable beam-column joints. The 225-mm thick x 1200-mm wide shear wall is designed to respond without any yielding to avoid the pinching behaviour that would result in poor performance. This can be achieved with the use of the friction dampers which can limit the force transferred to the wall and provide an additional source of energy dissipation.

5.3.3 Performance of Building Retrofitted with SBC

After a couple of trials, a value of 3% of the total seismic weight (W), or 320 kN, was selected as the slip load of the device. The peak inter-storey drifts of the unretrofitted and retrofitted buildings are compared in Fig. 15. Only the results from the most severe earthquake, i.e. the Loma Prieta (Cliffhouse)-based excitation, are shown here. In general, retrofit reduces responses on the first floor. The retrofit system reduces the peak inter-storey drifts by 20%, compared with the unretrofitted building. However, stiffening the first floor induces more damage on the upper floors. Damage is distributed to the other storeys instead of concentrating on the first floor as indicated by the increase in the inter-storey drifts on those upper floors. However, even with an increase in the peak inter-storey drifts ranging between 3-17%, the resulting curvatures on the upper storeys are still small that neither the beams nor columns reach flexural failures.

Considering only the inter-storey drifts, it seems that the retrofit system is not so effective. However, in terms of collapse prevention, the retrofit system proves beneficial in preventing

failures of the ground floor columns. The maximum curvature ductility of the ground floor columns is reduced from 9.7 in the unretrofitted system to 6.5 with the presence of the retrofit system in the worst scenario earthquake. This amounts to a reduction of 33% in the maximum curvature ductility demand of the ground floor columns compared with the unretrofitted building whose columns fail under the same excitation.

The maximum slip travel of the device resulting from each excitation, when no restrainer is provided to limit the slip travel, is shown in Fig. 16. The maximum slip travel of 8.4 mm results from the case of earthquake simulated by using the Loma Prieta (Cliffhouse station) record.

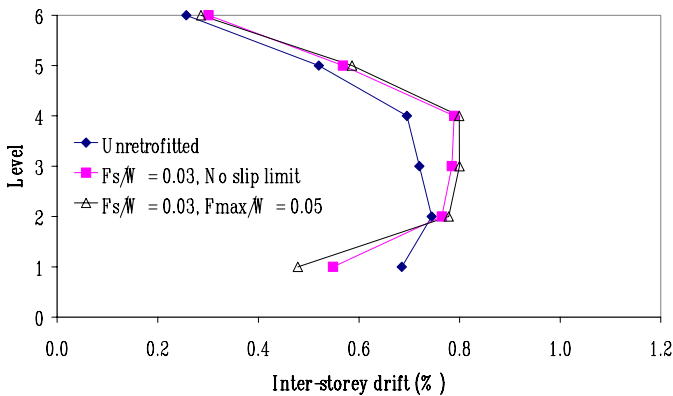


Figure 15 Peak Inter-Storey Drifts: Loma Prieta (Cliffhouse)-Based Earthquake

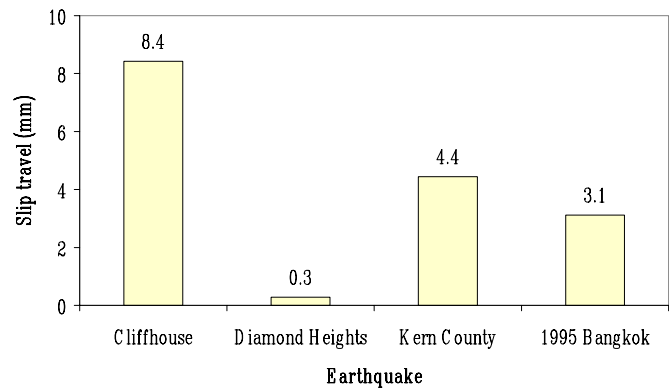


Figure 16 Peak Slip Travel of Friction Damper

5.3.4 Performance of Building Retrofitted with SBC-R

Half of the maximum slip required by the case of the earthquake generated from the scaled Loma Prieta earthquake (Cliffhouse station), or 4.2 mm, is assigned as the threshold slip for activating the restraining action, and hence additional restraining force. This will be referred to as the limited-slip case. With this value of slip limit, the other generated signals cause (practically) no impact in the device. Thus, only the excitation simulated by using the scaled Loma Prieta (Cliffhouse station) record is considered in the analyses. Since a high maximum restraining force induces high demand on the foundations, only 5% of total seismic weight of the building, or 510 kN, is assigned as the limit on the maximum restraining force.

Figure 15 compares the computed peak inter-storey drifts of the building for different cases. Similar to the previous case, retrofit with limited-slip friction damper reduces the peak inter-storey drift response on the first floor by about 13% but slightly increases those on the upper floors by 1-3% compared with the case of conventional damper. No flexural failures occur in any structural element. With slip limit, the maximum deformation of the ground floor column is reduced; hence, less damage occurs. The maximum curvature ductility of the ground floor column is reduced to 5.1 which is decreased by 22% compared with the case of no slip limit.

Comparison of the base shears for different building systems is shown in Fig. 17. The base shear resisted by the original frames is reduced by 7% compared with the retrofitted structure with no slip-limit friction damper, while the total base shear increases by 3%. The decrease in base shear in the original frames when retrofitted with SBC-R (or even without restrainers) makes it unnecessary to strengthen the existing foundations, which is an advantage. Figure 18 shows the force-slip travel of the device. With slip limit, maximum slip travel decreases to 5.3 mm which is a 37% reduction compared with the case without limit on slip travel (8.4 mm). Again, the restrainers provide extra safety to the device against bolt impact, which is an advantage over the conventional one.

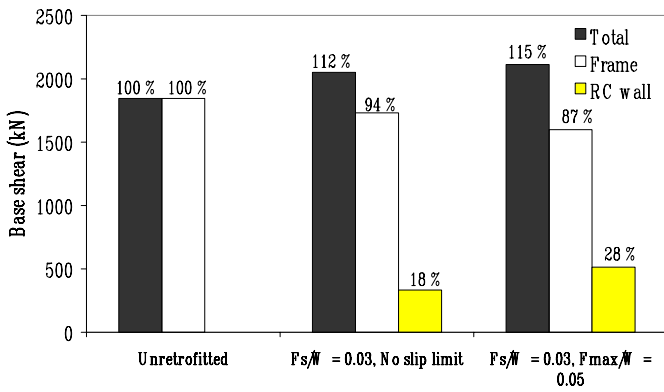


Figure 17 Base Shear Distributions: Loma Prieta (Cliffhouse)-Based Earthquake

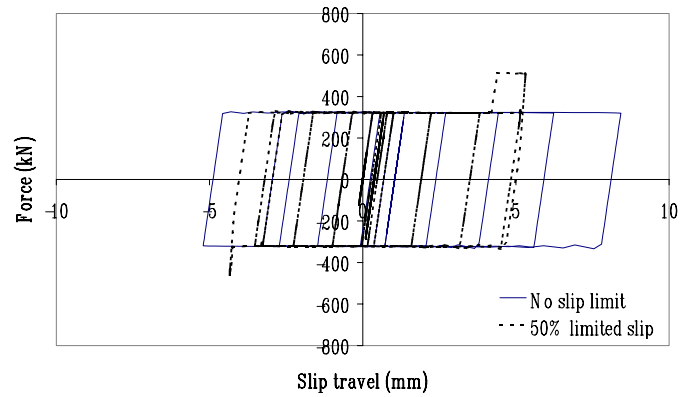


Figure 18 Force-Slip Travel of Friction Damper: Loma Prieta (Cliffhouse)-Based Earthquake, $F_s/W = 0.03$, $F_{max}/W = 0.05$

5.3.5 Storey-Level Damage Index

To quantify damage on each floor the Park and Ang (1985) damage index (DI) is adopted with slight modification to determine the storey-level damage index of each storey as follows:

$$DI = \left(\frac{U_{max}}{U_u} \right)_{storey} + \left[\frac{\beta_s \left(\int dE_{h,s} \right)_{storey} + \beta_m \left(\int dE_{h,m} \right)_{storey}}{(F_u \times U_u)_{storey}} \right] \quad (3)$$

where U_{max} and U_u are the maximum floor displacement and the ultimate floor displacement capacity, respectively; F_u is the ultimate shear strength of the storey associated with U_u , obtained from the pushover analysis; $dE_{h,s}$ and $dE_{h,m}$ are the incremental hysteretic energies absorbed by structural components and masonry panels, respectively; and β_s and β_m are the model constant parameters for structural components and masonry, respectively. A value of 0.1 for β_s was suggested by Valles et al. (1996). Ang and Kwok (1987) suggested a value of 0.075 for unreinforced brick masonry. Hence, these values were adopted for damage index calculation.

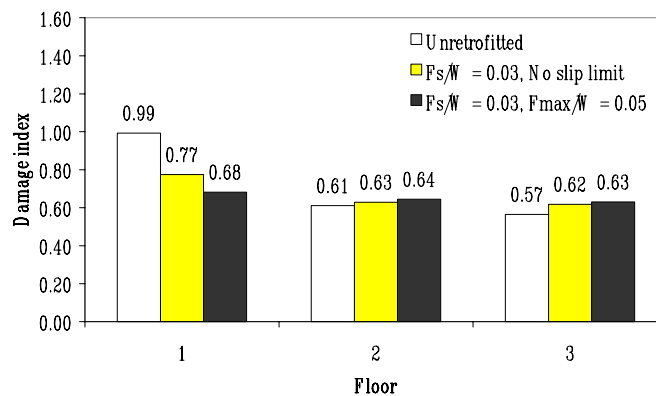


Figure 19 Storey Damage Index: Loma Prieta (Cliffhouse)-Based Earthquake

Figure 19 depicts the calculated damage indices for buildings subjected to Loma Prieta (Cliffhouse)-based earthquakes. Since damages generally concentrate on the first three floors, only damage indices of these storeys are presented. It should be noted that for the unretrofitted building under the worst scenario earthquake (Loma Prieta (Cliffhouse)-based ground motion with PGA of

0.08g), the ground-floor damage index is 0.99 which indicates that the storey is on verge of collapse. The damage indices of the other storeys are much less than 1, indicating no failure is imminent. Upon retrofitting with no slip limit friction damper, the damage index of the ground level is reduced to 0.77, a reduction of 23% compared with the unretrofitted building, while the damage indices of the other storeys are increased insignificantly. Further reduction in ground-floor damage index is achieved by utilizing slip limit with the maximum normalized force of 0.05. In this case, the ground-floor damage index is reduced to 0.68, which is 12% lower than the case without slip limit. These results are consistent with the findings described earlier.

6. CONCLUSIONS

This study focuses on the behaviour of the slotted-bolted connections (SBC) when the slip travel exceeds the provided slot length. The effectiveness of the dampers with restrainers (SBC-R) is demonstrated. Nonlinear dynamic analyses on two prototype buildings equipped with SBC and SBC-R were performed to evaluate the performance of the SBC-R as a seismic protection device. The following conclusions can be drawn from this study:

Bolt impact causes severe damage to the clamping bolts with significant degradation of the friction force of the device. Loss of friction can be more than 50%. Therefore, accidental impact of bolts in an unforeseen event can lead to disastrous result.

For the steel building under strong ground motions, the SBC-R is superior to the conventional SBC in the worst loading case, resulting in reduction of the peak inter-storey drift by 9-16% and the peak slip travel by 15-30% depending on the maximum normalized restraining force.

Although the peak inter-storey drift and the peak slip travel of the device decrease with increasing in the restraining force limit, the extra gain has to be balanced with the potential of buckling of the bracing at the high restraining force.

For the RC building under moderate ground motions, the limited-slip friction damper can reduce the peak curvature ductility demand by 22% compared with the conventional damper, which results in less damage in the ground floor columns.

The peak slip travel of the device is reduced by 37% with the use of restrainers, similar to the case of the steel building. This provides extra safety against bolt impact which can damage the damper.

Higher restraining force induces higher base shear; hence the adequacy of the foundations has to be properly addressed as well in retrofitting of buildings.

Acknowledgements:

The writers are grateful to the Thailand Research Fund (TRF) for the support for this project. The contributions of Prof. Dr. A. Filiatrault, Prof. Dr. J.I. Restrepo, and Assoc. Prof. Dr. S.A. Ashford are also acknowledged.

References:

- Ang, A.H.-S and Kwok, Y.H. (1987), "Seismic Damage Analysis and Damage-limiting Design of Masonry Buildings," *US-Asia Conference on Engineering for Mitigating Natural Hazards Damage*, Bangkok, Thailand, D3-1 – D3-14.
- Applied Technology Council (ATC) (2000), "NEHRP guidelines for the seismic rehabilitation of buildings," *Federal Emergency Management Agency (FEMA 354)*.
- Carr, A.J. (2000), "RUAUMOKO User's manual," Department of Civil Engineering, University of Canterbury, New Zealand.
- Crisafulli, F.J. (1997), "Seismic Behaviour of Reinforced Concrete Structures with Masonry Walls," *Doctoral Dissertation*, Department of Civil Engineering, University of Canterbury, New Zealand.
- Filiatrault, A. and Cherry, S. (1990), "Seismic design spectra for friction-damped structures," *Journal of Structural Engineering*, American Society of Civil Engineers, **116**(5), 1334-1355.
- Filiatrault, A., Tremblay, R., and Wanitkorkul, A. (2001), "Performance evaluation of passive damping systems for the seismic retrofit of steel moment resisting frames subjected to near field ground motions," *Earthquake Spectra*, **17**(3), 427-456.

- FitzGerald, T.F., Anagnos, T., Goodson, M., and Zsutty, T. (1989), "Slotted bolted connections in a seismic design for concentrically braced connections," *Earthquake Spectra*, **5**(2), 383-391.
- Grigorian, C.E., Yang, T.S., and Popov, E.P. (1993), "Slotted bolted connection energy dissipators," *Earthquake Spectra*, **9**(3), 491-504.
- Park, Y.J. and Ang, A.H.-S. (1985), "Mechanistic Seismic Damage Model for Reinforced Concrete," *Journal of structural Engineering*, American Society of Civil Engineers, **111**(4), 722-739.
- Roik, K., Dorka, U., and Dechent, P. (1988), "Vibration Control of Structures Under Earthquake Loading by Three-Stage Friction-Grip Elements," *Earthquake Engineering and Structural Dynamics*, **16**, 501-521.
- Tremblay, R. and Stiemer, S.F. (1993), "Energy dissipation through friction bolted connections in concentrically braced steel frames," *Proceedings of Seminar on Seismic Isolation, Passive Energy Dissipation, and Active Control*, ATC17-1, San Francisco, CA. Applied Technology Council, **2**, 557-568.
- Valles, R.E., Reinhorn, A.M., Kunnath, S.K., Li, C., and Madan, A. (1996), "IDARC2D: A Computer Program for the Inelastic Damage Analysis of Buildings," *Technical Report NCEER-96-0010*, State University of New York at Buffalo.
- Wanitkorkul, A. (2003), "Seismic Response of Braced Frames with Slotted-Bolted Friction Dampers Considering Limited Slip," *Doctoral Dissertation*, Department of Civil Engineering, Chulalongkorn University.

OPPORTUNITIES FOR INTERNATIONAL COLLABORATION ON EARTHQUAKE ENGINEERING THROUGH THE GEORGE BROWN JR. NETWORK FOR EARTHQUAKE ENGINEERING SIMULATION

Stephen A. Mahin, Ph.D.

*Byron and Elvira Nishkian Professor of Structural Engineering
University of California, Berkeley 94720-1710
mahin@ce.berkeley.edu*

Abstract: In late 1999, the US National Science Foundation (NSF) launched a major new research initiative known as the George E. Brown, Jr. Network for Earthquake Engineering Simulation (NEES). This initiative substantially upgrades resources available in the US for experimental and computational research related to the simulation of earthquake effects on the engineered environment. Importantly, these resources are interconnected and linked to the earthquake engineering community via a state-of-the-art, network-enabled infrastructure for information management and communication. The NEES infrastructure is expected to become fully operational in late 2004, and a ten-year program of collaborative research and education is being planned utilizing these resources. The NEES program raises numerous, important new opportunities for international cooperation and collaboration in the field of earthquake engineering, not only in terms of cooperative activities focused on technical problems of global importance, but also in terms of the prospects at the international level for enhanced communication, archiving of data and exchange of information and personnel.

BACKGROUND

The George E. Brown, Jr. Network for Earthquake Engineering Simulation (NEES) is intended to transform America's ability to carry out earthquake engineering research. This program involves capital outlays from NSF and host institutions in excess of \$100 million. Research and operating expenditures are likely to exceed four times this amount over the planned ten-year operation of the facilities. NEES is intended to accelerate substantially progress in earthquake engineering, leading to technically sound and cost-effective guidelines for the design, analysis and evaluation of engineered facilities and systems. Specific goals generally cited for NEES include generating new engineering knowledge vital to reducing the vulnerability of the engineered environment to catastrophic earthquakes, and educating a more diverse and capable workforce.

The NEES initiative is part of the Major Research Equipment and Facilities Construction (MREFC) program at NSF. The intent of this program is to provide the NSF research community with major world-class research tools, on a shared-use basis, that can enable them to address problems of critical importance to the United States and the world. Similar major research facilities programs at NSF include the South Pole Station, Laser Interferometer Gravitational-Wave Observatory (LIGO), National Radio Astronomy Observatory, and the National Center for Atmospheric Research. NEES is the first MREFC initiative to be undertaken by the Engineering Directorate, and as such, incorporates several new and unique features.

When fully operational in October 2004, the NEES program will provide the US earthquake engineering community with an unprecedented infrastructure for research and education. This infrastructure consists of networked and integrated resources for experimentation, computation, model-based simulation, data management, idea generation, and communication. Rather than placing all of these resources at a single location, NSF is leveraging its investment and fostering the integration of research and education by distributing the new shared-use equipment among approximately 15 universities throughout the US. To insure that researchers can effectively use this equipment, the new NSF-funded equipment sites will be operated as shared-use facilities, and NEES will be implemented as a network-enabled collaboratory. As such, members of the broad earthquake engineering community will be able to access unique, next generation instruments and equipment, interact with one another, share data and computational resources, and retrieve information from extensive digital libraries, without regard to geographic location.



Fig. 1 Shared Use Field Test Equipment, Univ. of Texas, Austin

In this paper, some of the unique features of NEES are described, focusing on those related to operating NEES as a collaboratory. Opportunities for international collaboration are also highlighted.

CURRENT ACTIVITIES

Currently, four major activities are being undertaken to bring the NEES program on line. These include (1) constructing the shared-use equipment sites, (2) developing standards and advanced networking capabilities to connect experimental, computational and other resources with the earthquake engineering community as well as to the public at large, (3) developing a community-backed research collaboratory and consortium to carryout and help manage NEES activities, and (4) identifying a research agenda that addresses high priority needs. The status of these activities is briefly summarized below.

The portfolio of new shared-use, test equipment being developed within NEES includes major new or upgraded shaking tables, reaction wall facilities, geotechnical centrifuges, tsunami wave tanks, and field test capabilities (a few of the facilities are shown in Figs. 1 through 5). Many next-generation capabilities and features have been incorporated in these facilities, enabling types of experimentation and tests not previously possible in the US. Shared-use sites are currently under construction at:

- Actuator-based Hybrid Simulation Facilities: Lehigh University, University of Buffalo, University of California at Berkeley, University of Colorado at Boulder, University of Illinois at Champaign-Urbana, and University of Minnesota at Minneapolis
- Field Test Facilities: Bingham Young University, University of California at Los Angeles, and University of Texas at Austin
- Geotechnical Simulator Facility: Cornell University, Rensselaer Polytechnic Institute, and University of California at Davis

- Shaking Table Simulation Facilities: University of Buffalo, University of California at San Diego, and University of Nevada at Reno
- Tsunami Wave Basin Simulator Facility: Oregon State University

At each site, participation by off-site collaborators is being encouraged through the development and installation of advanced capabilities for tele-observation and tele-operation. Information on the objectives and capabilities at each site may be found at: <http://www.nees.org>.

To enable broad-based collaboration by the earthquake engineering community, recent advances in information technology and computer science are being adapted and extended as a central feature of the NEES program. The systems being implemented will provide convenient, secure and dependable access to NEES resources and data. Integral to this system is a high-performance (>1Ghz) network with integrated services providing secure access to computational resources, software, databases and communication capabilities. In addition, it is providing a common infrastructure and set of protocols and tools for defining, sharing, analyzing and storing data and metadata, and carrying out hybrid simulations drawing concurrently upon experimental and computational resources at several geographically distributed sites. This system integration effort is led by the National Center for Supercomputer Applications (NCSA) headquartered at the University of Illinois at Urbana-Champaign, in conjunction with a consortium of other universities and national laboratories. In addition, the NEES IT infrastructure will provide a capability for grid-based, high performance computing. This will involve a special implementation of the open source computational framework known as OpenSees (see <http://www.opensees.edu>) and other similar applications for numerical simulation. Special emphasis will be placed on software for introducing high performance computing within an educational context (see: <http://www.ce.berkeley.edu/~filippou/Courses/FEDEASLab.htm>). More information on the NEES network and related services may be found at <http://www.neesgrid.org>.

The overall NEES infrastructure is being administered and managed by a single community-based and community-led not-for-profit entity, known as the NEES Consortium, Inc. (NCI). The NEES program will be operated as a collaboratory serving the needs of the entire earthquake engineering community. As such, NCI will be responsible for the management, operations and maintenance of the various laboratories, computational, network, database, software, and other resources that are part of the overall NEES program, and for facilitating the participation of the earthquake engineering community in NEES related activities. Additional information on the NEES Consortium, including the by-laws and charges to various standing committees, may be found at <http://www.nees.org/>.



Fig. 2 Shared Use Shaking Platforms,
Univ of Nevada, Reno

NSF has funded two national projects to help identify and prioritize the long-term uses of NEES resources. The Earthquake Engineering Research Institute (EERI) undertook one of these efforts, which focused on identifying the overall research needs for reducing earthquake losses in the US. The National Research Council, and focuses on the specific uses of NEES carried out the other effort. The results of the EERI effort (EERI, 2003) may be found on line at <http://www.eeri.org>. The report of the National Research Council (NRC, 2003) is available at <http://www.nas.edu/nrc/>.

SPECIAL FEATURES OF NEES

While several NSF programs have general goals similar to those articulated for NEES, there are several features that make NEES unique. Clearly, the unprecedented array of new next-generation resources will increase the ability of researchers in the US to carry out cutting-edge research. However, other features are likely to have even more profound long-term impacts. These include the intent of programs organized within NEES to (1) integrate and serve the entire earthquake engineering community and (2) and explicitly incorporate aspects of experimentation, theory formulation and validation, data curation, model-based simulation, high performance computing and education. As such, in solving challenging earthquake engineering problems, NEES programs will employ a comprehensive array of methodologies and tools as well as a diversity of backgrounds, disciplines and expertise.

Another unique feature of NEES is the “shared use” nature of the new experimental facilities being funded by NSF. While a portion of the use of these facilities is reserved for investigators at the host institution, the majority of use is intended for NEES projects by off-site investigators.

An important aspect of the NEES program is that the majority of the efforts and costs associated with managing, operating and maintaining NEES resources are directed by NSF to NCI. NEES research projects using these shared-use facilities are funded directly by NSF, and awards are made on the basis of competitive reviews of proposals received from the entire earthquake engineering community. Thus, NCI has no specific input into the nature of the research programs undertaken. Since NSF will fund (through NCI) the shared-use aspects of operating these new equipment sites, the cost to NEES research projects of conducting tests or other activities at shared use facilities should be substantially reduced. In addition, each shared-use facility will provide on- and off-site researchers with an array of services, including (1) on-site and on-line training on use of the facilities, (2) extensive capabilities for tele-communication, tele-observation and tele-operation; (3) personnel to assist with planning and conduct of tests; (4) help in locating local contractors and support personnel necessary conducting the tests; (5) assistance with documenting and storing data; (6) well-written on-line manuals, help desks and knowledge bases and (7) educational opportunities for participants while on site. NCI will provide a number of critical services, including archiving data and metadata, providing support for the development of shared-risk tools, such as various software applications, and encouraging broad-based collaboration within the earthquake engineering community.



Fig. 3 Shared-Use, Reconfigurable Reaction Wall, UC Berkeley

The shared-use aspect of NEES will allow investigators from universities, other research and educational institutions, industry and business to propose (or participate in) research programs even if their home institutions do not have the necessary research resources. Similarly, students interested in conducting experimental research following graduation can join a university or organization that does not have its own laboratory or computational facilities, and be assured of ready access to world-class resources.

One of the major features of NEES is that it is to be implemented as a collaboratory. This strategy is intended to accelerate progress through the integration and synergism associated with collaboration. It also builds upon specific advances in information technology that facilitate the interaction of collaboratory participants with each other, with research equipment and instrumentation, with large and diverse data sets, and with software and other applications. The Collaboratory may well prove to be the primary catalyst within NEES for transformation of the earthquake engineering community.



Fig. 4 Shared Use Tsunami Wave Tanks, OSU

THE NEES COLLABORATORY

The collaboratory concept utilized in NEES refers in part to the harnessing of information technology to: (1) bring researchers, educators and students together with members of the broad earthquake engineering community and public, (2) provide them ready access to powerful experimental, computational, database, information management and communication tools, and (3) facilitate their collaboration, without regard to geographic location, as if they were “just across the hall.” This builds upon the well-known concept initially proposed by William Wulf [NRC, 1993]. To achieve this ideal, collaboratories incorporate a number of specific capabilities to facilitate sharing of data, sharing of software, sharing of research facilities, developing “shared risk” community-based resources, and communicating with remote colleagues. In this context, a collaboratory is not a “research center” per se, but rather, a proactive and supportive virtual environment that facilitates the research activities of its participants.

It is intended that NEES incorporate other facilities for experimentation, computation, data analysis, and visualization beyond the new shared-use sites, both nationally and internationally. Efforts are currently underway by NCI to identify minimum resources, policies and costs associated with a resource provider or group becoming affiliated with NEES.

A World Forum on Collaboration in Earthquake Engineering Research is planned later in 2004 to discuss such opportunities amongst the international community. This Forum will focus on large, multidisciplinary programs underway globally related to earthquake engineering research, specific infrastructure requirements for implementing NEES-like networking services among international collaborators, and policies and protocols for carrying out collaborative research within the NEES environment.

An important aspect of the NEES Collaboratory is the integration of experimental and computational forms of simulation, and a shifting of focus in the long-term from the mechanics of simulation, to information and information technology. Thus, one might view NEES and the NEES Collaboratory as a means of “getting information to those who need it in a form most useful to them.” Experimentation and computation are powerful means to advancing understanding; stimulating innovation and generating needed information. However, ready access to information and promoting information literacy are high priority goals of the NEES Collaboratory.

The Collaboratory Vision

Much of the background related to the development of the NEES program, and the vision for its implementation may be found in a white paper [Mahin, 2002] entitled “Towards a Vision for the NEES Collaboratory.” This

document includes an extensive discussion of similar projects at NSF, organizational and practical aspects of operating a network-enabled collaboratory, and metrics often used in assessing the performance of such ventures. In addition, the white paper includes a discussion of the NEES participant community and an assessment of the strengths, weaknesses, opportunities and threats of this community that need to be considered in developing the NEES program. The document also proposes draft mission and vision statements for the NEES collaboratory as well as specific goals. The overarching goal of the NEES Collaboratory is the integration of people, ideas, and tools within a collaboratory environment to accelerate progress in earthquake engineering. To achieve this, the NEES Consortium is being implemented to enable the mission identified for the Collaboratory; this mission includes:

OVERARCHING GOAL OF THE NEES COLLABORATORY

Integration of people, ideas, and tools within
a collaboratory environment to accelerate
progress in earthquake engineering

1. facilitate collaboration by the earthquake engineering community in research and education, nationally as well as internationally;
2. enhance the research capabilities of the US earthquake engineering community;
3. foster innovative research leading to technically sound and cost-effective approaches to earthquake loss reduction and otherwise serving the critical needs of society;
4. promote the use of engineering knowledge through curated data repositories and programs of information dissemination; and
5. integrate research and education in support of effective programs of education at all levels.

The vision for the NCI and the NEES Collaboratory is to synergistically blend information technology with earthquake engineering, to promote the widespread acquisition and use of engineering knowledge through curated digital libraries, and proactively facilitate programs of information dissemination. NEES research programs are expected to integrate significant aspects of experimentation, theory formulation and validation, data curation, model-based simulation, high performance computing and education, and involve experts from a diversity of technical disciplines. To realize this vision, it is expected that NCI will partner with government entities, academia, industry and business, nationally and internationally. In addition, outreach and educational activities being formulated by NCI are intended to serve the public in numerous ways, including helping develop improved policies and more effective regulations for earthquake loss reduction, attracting and training a more diverse and capable workforce, and developing effective learning programs across the full educational spectrum.

Collaboratory Services

Collaboratory capabilities are being developed to assist investigators before, during and after projects. At the core, these include services for sharing of information, software, facilities, and communication with remote colleagues. These would support activities related to generating of ideas and support for research projects, developing of proposals, planning of research activities, executing the research plan, analyzing and interpreting the results obtained, and incorporating

findings in various education and outreach efforts. A wide variety of activities are possible, depending on the needs of the participants, and the nature of the project. Various collaboration functions, tools and enabling technologies are needed to offer such services.

NEES PROJECTS

As mentioned previously, NSF will determine the type and nature of projects to be undertaken by NEES through a competitive peer-review process. Specific details of the NEES research solicitation may be found at:

<http://www.nsf.gov/pubsys/ods/getpub.cfm?nsf03589>.

Projects undertaken will consist of an array of: (1) traditional single investigator grants; (2) grants to small groups of investigators addressing specific problems; and (3) larger multidisciplinary, multiple institution programs involving several investigators.



Fig. 5 Shared Use Geotechnical Centrifuge, UC Davis

NEES research projects will differ from current efforts in that investigators will need to utilize at least one of the shared-use experimental facilities and take advantage of the next-generation network infrastructure to interact with (1) other investigators; (2) the shared-use or other resources within the NEES federation of resources; (3) data of various sorts, or (4) NEES software and computer applications. Projects funded through NEES will be required to document and share data obtained from experimental and computational investigations in accordance with community-based policies, procedures and formats. Details are currently being developed by the NEES Site Operations and Shared Use Committee and the Data Sharing Committee regarding the types of data and metadata to be archived, and time frame for the release of information to the public.

It is anticipated that the NEES program will more than double funding for earthquake engineering research in the US during the 2004-2015 time frame. As such, there are tremendous opportunities to solve major technical and social problems associated with earthquake engineering.

Single Investigator Grants

Single investigator grants provide the backbone of NSF's research program. By employing competitive peer review, NSF is able to identify the most promising, innovative and technically sound ideas for research. They would be expected to remain an important and vital component of the NEES program.

Such projects may be particularly useful to explore and develop new concepts and methodologies, identify and fill gaps in existing knowledge. Significantly, such grants may be particularly useful in gathering existing experimental and analytical data/metadata and processing it into the format required by the NEES data repository. Like all NEES projects, single investigator grants must utilize one of the NEES shared-use experimental facilities. It is likely, given the nature of NEES, that there will be, even with single investigator type projects, a high level of collaboration with other investigators.

Group investigations

The telecommunication and other collaboration features of the NEES Collaboratory are particularly well suited to assist small groups of investigators wishing to collaborate on a particular problem. Often, these may involve geographically separated investigators having different expertise and backgrounds. For example, experimentalists, theorists and analysts might unite to advance a particular aspect of model-based analysis. Other projects may integrate individual investigations across scales (for example, investigations characterizing behavior at the material, component and subassemblage level) and disciplines (e.g., involving tsunami- and geo-engineers in the investigation of coastal structures). Similarly, groups of investigators might band together to devise testbeds for comparing different approaches to the solution of a common problem (e.g., devising a benchmark structural test platform to assess different active control algorithms, sensors, actuators, etc.).

A special type of group collaboration may involve “mission payload” type investigations, where investigators leverage the efforts of others to conduct research of their own. For instance, investigators working on health monitoring systems and damage assessment algorithms (or investigators focusing on the response of non-structural systems and contents, approaches for improving the performance of vulnerable structures, methods for post-earthquake repair, and so on) may simply want to install special instrumentation on another investigators test specimen, access another investigators analytical model, or to use these models following the studies undertaken by the primary investigator. The NEES Collaboratory will focus on maximizing opportunities for leveraging the impact of individual investigations through such symbiotic and potentially synergistic activities.

Group collaborations involving expertise from information technology and earthquake engineering may also be appealing. For example, groups may unite to develop community-backed resources, such computational environments and applications for high performance computing and visualization. Other multidisciplinary groups may form to advance experimental methodologies or to enhance data management and mining capabilities.

Grand Challenge Multi-investigator Programs

As important as individual and group investigations are expected to be, it is anticipated that NEES resources will have the largest impact when directed towards “Grand Challenge” projects that address issues of national and international importance. Such projects are ones of substantial scope, and that require, by necessity, large numbers of investigators, consultants, and participants from a variety of disciplines.

A recent example in the US of such a project is the Program to Reduce Earthquake Hazards in Steel Moment Frame Structures [FEMA, 2000]. This project was funded by the US Federal Emergency Management Agency (FEMA), with additional support from other federal and state agencies, industry and a variety of professional and trade associations. This program was initiated in response to the 1994 Northridge earthquake, which caused brittle fractures in the critical beam to column connections of many welded steel moment frame buildings. The types of fractures observed were unexpected, and counter to highly ductile behavior anticipated by building codes. This six year, \$12.5 million program involved more than 100 individual research projects, testing at eleven different institutions, and more than 250 individual participants. Using a performance-base reliability framework, it integrated wide-ranging activities, including research, economic, social

and political studies, and guideline development, and training (see Fig. 6). The resources being developed within NEES for analytical and experimental analysis, communication and education would have substantially benefited this program.

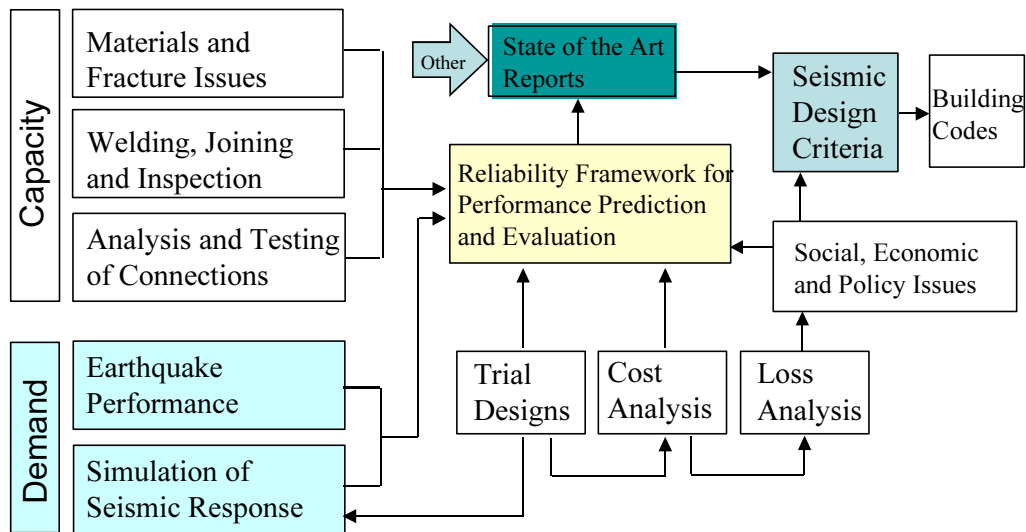


Fig. 6 Logical Network Diagram for the FEMA Project on Steel Moment Frame Buildings

Similar grand challenge efforts could be developed to address and extend performance-based criteria for design, evaluation, retrofit and repair other types of new and existing systems. For example, studies could focus on

1. General and regional applications of braced steel frames; composite, reinforced concrete and timber structures; systems incorporating various protective systems, such as seismic isolation and supplemental energy dissipation devices; special occupancy structures employing unusual performance criteria; etc.
2. Various types of nonstructural systems and components as well as critical contents and equipment housed in structures
3. Infrastructure components and systems, including various transportation and utility systems,
4. Geo-structures of various types;
5. Soil-foundation-structure interaction, including the impact of soils and foundations on seismic response and the development and evaluation of various design methodologies,
6. Coastal structures of various types to earthquake ground shaking and the effects of tsunami,
7. Development and evaluation of new and innovative technologies and methodologies (active control, optimum design, high performance materials, hybrid and other special structural systems, etc.)
8. Improved methods for post-disaster condition assessment, safety assessment, loss estimation, repair, including response to unanticipated and undesirable modes of behaviors.

It is clear that the facilities and collaboratory concepts embedded in NEES are applicable to many other forms of natural and man-made hazards, including homeland security. The precise nature and scope of the grand challenge projects undertaken within the NEES program will be developed by NSF on the basis of recommendations contained in the research agenda developed for

NEES and earthquake engineering by EERI and the National Research Council, as well as through various workshops involving various segments of the overall community. Based on anticipated funding levels, between one- and two-dozen grand challenges might be undertaken during 2004-2015.

OPPORTUNITIES FOR INTERNATIONAL COLLABORATION

Tremendous opportunities will arise due to the research infrastructure and programs to be incorporated within NEES. Because earthquake engineering is a worldwide problem, NEES provides special opportunities for international cooperation. This is associated with a number of possible activities, including conduct of international cooperative and collaborative research programs, development of international standards and capabilities for documenting, archiving and sharing information, and exchange of personnel.

While there are regional differences in construction, seismic hazard, performance criteria, building technology and materials, and economic circumstances, many issues are fundamental to all nations. Where major issues of mutual interest can be identified, it is possible that special cooperative or collaborative projects can be facilitated by the technology incorporated within the NEES Collaboratory. Numerous examples of bi-lateral and tri-lateral cooperative programs exist where an international perspective has substantially helped advance achievement of the goals of the program. Importantly, significant opportunities exist to use on an international cooperative basis some of the unique experimental and computational facilities coming on line in the US through NEES, as well as in Asia, Europe and elsewhere in the Americas.

To maximize potential benefits, considerable effort is needed to develop international agreements regarding the basic network services and protocols for sharing information, applications, and implementing tele-presence, tele-observation and tele-operation capabilities. This would include identification of computer and network equipment requirements, resources for data storage and computation, basic user requirements for services, security standards, various definitions, formats and protocols for data and metadata, and so on.

With the acceleration of activities expected in the US related to earthquake engineering research, substantial opportunities should be anticipated related to the exchange of students, faculty, and others in the earthquake engineering community at an international level.

CONCLUDING REMARKS

By bringing researchers, educators and students together with members of the broad earthquake engineering and information technology communities, providing them ready access to powerful experimental, computational, information management and communication tools, and facilitating their interaction as if they were " just across the hall," the NEES and the NEES Collaboratory will be a powerful catalyst for transforming the face of earthquake engineering, nationally and international. The diversity of talents, backgrounds, experience and disciplinary concerns to be represented within the NEES Collaboratory will provide an unparalleled stimulus to intellectual inquiry and education. The NEES Collaboratory will transform the processes by which earthquake engineering research is initiated and performed, accelerate the generation and dissemination of basic knowledge, facilitate the development of effective educational programs, minimize the lag

between knowledge development and its application, and hasten the attainment of universal goals for earthquake loss reduction.

Substantial opportunities exist for cooperation and collaboration at the international level. To this end, it appears desirable to convene a series of international meetings or workshops to begin to lay the foundations for these activities. In addition to experts in earthquake engineering, information technology, and computer science, it is necessary to involve individuals from funding agencies interesting in reducing the threat posed by earthquakes.

Acknowledgements

Preparation of this paper was supported primarily by the George E. Brown, Jr. Network for Earthquake Engineering Simulation of the National Science Foundation under Award Number CMS-0126366. The authors serve as co-Principal Investigators for the NEES Consortium Development project, and greatly appreciate the time and contributions of all those who have contributed ideas, offered suggestions, and participated in various efforts to develop NEES. Because the NEES program is still in the development phase, many of the ideas presented herein are subject to revision. The materials presented in this paper do not represent the policy or views of the National Science Foundation, the NEES Consortium Development Project, other groups or individuals.

References

- EERI, 2003. Securing Society from the Catastrophic Earthquake Losses, Earthquake Engineering Research Institute, Oakland, CA.
- Mahin, S., 2002. "White Paper: Towards a Vision for the NEES Collaboratory, George E. Brown Jr. Network for Earthquake Engineering Simulation," Task Group on Collaboratory Research, NEES Consortium Development Project, Consortium of Universities for Research in Earthquake Engineering, Richmond, CA, Version 2.0, June 6, 2002.
- NRC, 1993. National Collaboratories: Applying Information Technology for Scientific Research, National Academies Press, Washington DC.
- NRC, 2003. Preventing Earthquake Disasters: The Grand Challenge in Earthquake Engineering: A Research Agenda for the Network for Earthquake Engineering Simulation (NEES) , Committee to Develop a Long-Term Research Agenda for the Network for Earthquake Engineering Simulation (NEES), National Academies Press, Washington DC

EARTHQUAKE ENGINEERING RESEARCH IN SHAKING TABLE TESTING LABORATORY OF TONGJI UNIVERSITY, SHANGHAI, CHINA

X. L. Lu¹⁾, and H. J. Jiang²⁾

1) Professor, State Key Laboratory for Disaster Reduction in Civil Engineering, Tongji University, Shanghai, P. R. China

2) Associate Professor, State Key Laboratory for Disaster Reduction in Civil Engineering, Tongji University, Shanghai, P. R. China

xlst@mail.tongji.edu.cn, jianghuanjun@hotmail.com

Abstract: The research work in the field of earthquake engineering conducted in Shaking Table Testing Laboratory of Tongji University, Shanghai, China in recent years is reviewed briefly in this paper. It includes structural control study of high-rise buildings with application, base isolation study with application, development of new seismic energy-dissipation shear walls, study on dynamic soil-structure interaction, study on concrete-filled rectangular tubular structures, and seismic behavior of reinforced concrete high-rise buildings and towers. It can be seen that the basic research work is combined with engineering practice and most of the research accomplishments have been applied in practice successfully.

1. INTRODUCTION

Since China is an earthquake prone area, research in the field of earthquake engineering has been highlighted by the government and researchers all along, especially after the Tangshan earthquake in 1976. Quite a few research projects in this field have been carried out in Shaking Table Testing Laboratory of Tongji University, Shanghai, China, since it was founded in 1983. Up to 2003, 390 and more experiment projects including 20 and more state key projects have been conducted on the shaking table. Now, it is one of the most renowned laboratories in civil engineering in China. In this laboratory the basic research is generally combined with engineering application and can be transformed for the actual needs of engineering practice. The tradition of continuous contact and good cooperation with other institutions and companies allows it to remain abreast of the latest developments in this field. In this paper the main research work in the field of earthquake engineering completed by this laboratory in recent years are reviewed, and some topics that are being investigated now or will be investigated in the future are also presented.

2. STRUCTURAL CONTROL STUDY OF HIGH-RISE BUILDINGS WITH APPLICATION

2.1 Development of A New TMD Control System

A new TMD control system using servomotor as tuned damper shown in Figure1 was proposed to control earthquake response of buildings by Lu and Fang (1994). The system is composed of tuned mass, tuned springs, and tuned damper. The parameters of these three components can be tuned according to the dynamic characteristics of the controlled structure so as to get the optimal control

effect. The dynamic behavior and the control effect of the new system were studied through a series of free vibration tests with variant damping values. Then shaking table tests were carried out on a 3-story steel frame structure equipped with this system under various seismic inputs by Lu, Ye and Fang (2000). The test results showed that the earthquake responses of the structure with the control system were reduced significantly, compared with the structure without the control system. It was discovered that the damping value and the characteristics of frequency spectrum of the seismic input had significant effect on the control efficiency of this system. Moreover, the analytical model is developed for the tested structure as shown in Figure2, and the calculation results agree well with the test results.

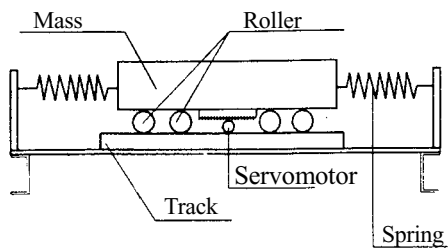


Figure1 Servomotor TMD System

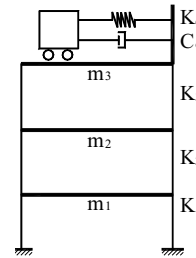


Figure2 Analytical Model for The Tested Structure

2.2 Development of A New Combined Energy-dissipation System

Although various single energy-dissipation system has been studied more extensively during the last 20 years, it still has some limitations in engineering practice. In order to meet the different requirements of structures to reduce earthquake response, a new combined energy-dissipation system was developed by Lu and Zhou (2002). It consists of lead rubber damper, oil damper, and conventional steel brace. The installation of this system in a frame is shown in Figure3. Under wind load or minor earthquake, the lead rubber damper behaves elastically and oil damper provides small damping force and stiffness. Under strong earthquake the lead rubber damper develops elasto-plastic deformation and the stiffness to the structure is decreased, and the oil damper provides larger damping force but smaller stiffness. As a result, the seismic force to the whole structure is reduced and its response decreased.

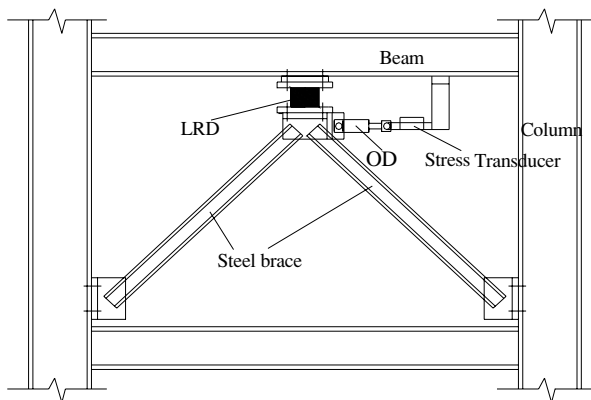


Figure3 Combined Energy-dissipation System Installed in A Frame



Figure4 Tested Model

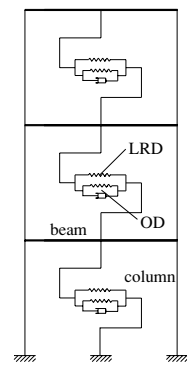


Figure5 Analytical Model

Shaking table tests were carried out on a 3-story steel frame structure equipped with the energy-dissipation system in each story, as shown in Figure4. To make comparison the structure was tested in three conditions, unbraced frame, frame braced with lead rubber damper and steel brace, frame braced with this system. The test results show that the system can increase the damping ratio and stiffness of the entire structure and so has good control effect on the earthquake response of the structure. The analytical model for this system is developed as shown in Figure5, and optimal analysis is conducted for the design parameters of the system. This new energy-dissipation system has been

applied to seismic retrofit of existing old buildings. One application example is presented here. The structural plane layout of a 9-story old building with reinforced concrete frame is shown in Figure6. After evaluation of its seismic performance, the seismic capacity of this structure is considered not able to meet the seismic demand, especially in the longitudinal direction the seismic capacity is severely insufficient. By being added six energy-dissipation devices as shown in Figure6, the earthquake responses of this structure are reduced efficiently and within the limitations specified by the seismic design code. The in-site installation of this system is shown in Figure7.

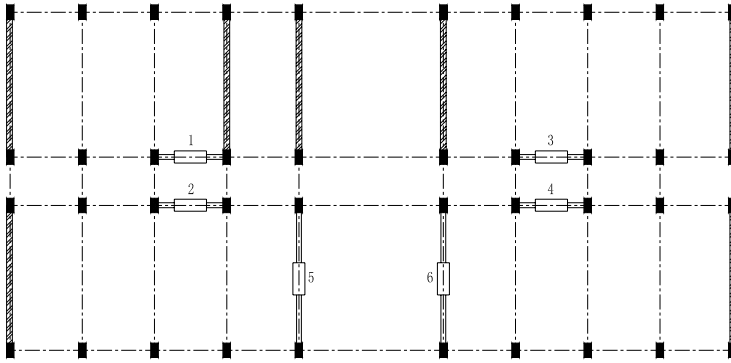


Figure6 Plane Layout of The Structure and The Energy-dissipation System

Figure7 In-site Installation of This System

2.3 Coupling-structure System Connected by Fluid Dampers

Buildings in a modern city are often built closely to each other because of limited land available and centralized services preferable. In most cases these buildings are built separately without any structural connections. Under strong earthquakes, the pounding of two adjacent buildings often occurs. In other cases, two adjacent buildings are linked together in different ways to meet the requirements of architectural function or esthetic needs. A series of theoretical and experimental studies are carried out to study the feasibility of the concept of linking adjacent buildings or connecting podium structures to a main building by fluid dampers to improve their seismic performance and to prevent the pounding between them. Shaking table tests were conducted on a 1/4-scale coupling-structure system composed of one 6-story steel frame and one 5-story steel frame by Lu, Yang and Xu (2002), as shown in Figure8. Three connection conditions between the two frames were involved: connected by rigid steel rods, connected by fluid dampers, or without any connections. In the case of being connected by fluid dampers, the influence of different connection locations, different linking forms, that is, parallel linking form and oblique linking form, were also investigated in the tests. The test results showed that the modal damping ratios of both buildings could be increased significantly and so their seismic responses could be reduced effectively if fluid dampers with appropriate parameters were installed to link the two buildings. General finite element software Ansys5.5 is used to set up the analytical model and calculate the nonlinear earthquake response of the tested structure, and good agreement is obtained between the test results and calculated results.

A standardized 3-D model of two stories, surrounded by a 3-D one-story model, as shown in Figure9, is first proposed to simulate a high tower with a podium structure based on several simplified principles. The equations of motion of the tower-damper-podium system are derived using this model. Recently, this concept has been applied to an actual 60-story ultra-tall building with 10-story large podium connected by fluid dampers to reduce their torsional seismic response. An extensive analysis on the structure and a series of experiment on the fluid dampers have been carried out to get the optional parameters for the fluid dampers, and to achieve the best structural performance under various seismic excitations. Finally 40 fluid dampers with maximum capacity of 600kN were used to connect the podium structure to the main building at different floor levels on and below the roof of podium structures, so as both the podium structure and the main building can meet the seismic design

requirements for low and higher intensity of earthquake actions. The layout of the fluid dampers is shown in Figure10, and the perspective picture of this building is shown in Figure11.



Figure8 Adjacent Structure Linked by Fluid Dampers

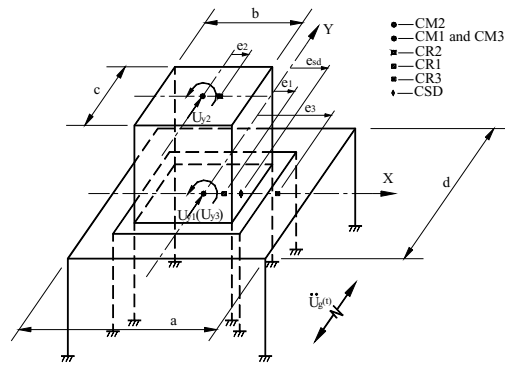


Figure9 Standardized Analytical Model

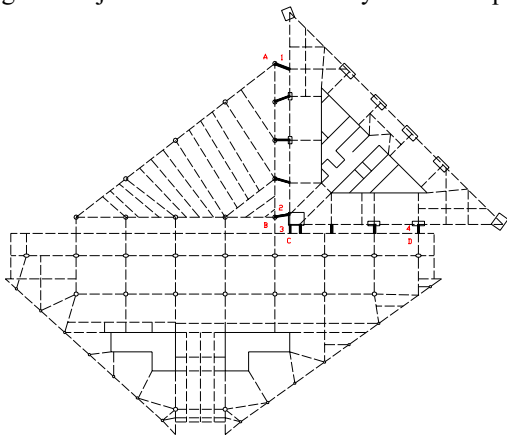


Figure10 Plane Layout of The Structure and The Fluid Dampers



Figure11 Perspective Picture of The Building

3. BASE ISOLATION STUDY WITH APPLICATION

3.1 Development of A New Type of Base Isolation System with Restrained Sliding Mechanism

In the past three decades several base isolation systems have been developed, among which sliding isolation system is one of the most attractive systems due to its effectiveness for a wide range of frequency inputs and good control of seismic force. However, the biggest disadvantage is excessive sliding and residual displacement of the isolator under strong earthquakes. A new type of base isolation system with restrained sliding mechanism was proposed by Shi and Li (1998). It consists of common friction isolator and rubber block with specified distance to friction isolator. The sliding isolator can slide freely when the maximum sliding displacement is within the control range at minor or moderate intensity earthquake excitations. The sliding lateral stiffness will increase due to the contribution of the rubber block comes into operation when the sliding displacement exceeds the pre-defined distance and the sliding isolator collides with the rubber block at high intensity earthquake excitations. The analytical model is developed for this base isolation system, as shown in Figure12. By taking the contribution of both the friction isolator and the rubber block into account, the hysteretic model of this system can be obtained, as shown in Figure13. Earthquake time history response analysis demonstrated that compared with the structure installed with common sliding isolator, the earthquake responses of the structure installed with this system were reduced considerably and the maximum sliding displacement during the earthquake as well as the residual displacement after the earthquake was more satisfactory.

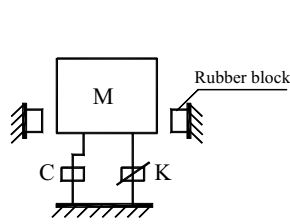


Figure12 Analytical Model

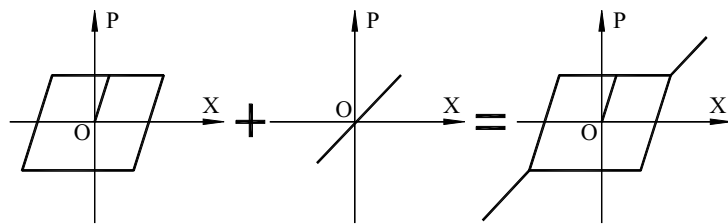


Figure13 Hysteretic Model for The Developed Base Isolation System

3.2 Research on A Hybrid Isolation System

A hybrid isolation system, composed of frictional slider isolation system and rubber bearing re-centering the isolation system, was studied by Lu, Zhu et al. (2002). To verify the effectiveness of this system, a 1/12-scale and three-story steel frame model was tested on the shaking table with base fixed (FIX) and isolated (SLD) separately for comparison. The isolation system was composed of four rubber bearings and two frictional sliding bearings. The layouts of the isolation system and the superstructure are illustrated in Figure14 and Figure15. Compared with FIX, the responses of SLD were reduced significantly. In addition, the isolation system was of good re-centering capability with a small residual displacement. For each piece of ground motion input, the total input energy and the constitutive energy components were calculated by integration, which showed that in FIX most of the total input energy was dissipated by the superstructure itself while in SLD, by the sliding isolators. A new simplified analytical model for the tested model is developed. The superstructure and the rubber bearing are supposed to be elastic, the frictional force in the slider is simulated by the Coulomb-friction characteristics, and the damping of the rubber bearing and slider is taken as viscous damping. By using this analytical model, the earthquake responses of the tested model are calculated through finite element program Ansys5.5.

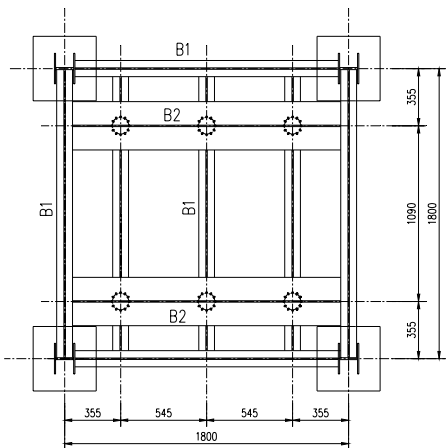


Figure14 Layout of Base Isolators



Figure15 Base Isolated Structural Model on The Shaking Table

3.3 Inter-story Seismic Isolation

The new method of inter-story seismic isolation was developed to improve the seismic performance of the existing old buildings, especially in the case of adding story to original buildings by Shi and Zhu (1994). The principle of inter-story isolation is to add an additional energy-dissipation system, composed of the top mass block and rubber bearings installed between the top mass block and original roof, at the top of the building. After being installed this system, the damping ratio of the building can be increased significantly, and so the earthquake responses are decreased considerably. In practice, there are three forms of this system, as shown in Figure16. Shaking table tests were carried out on one 1/7-scale 6-story flying-ash concrete block masonry structure model and one 1/6-scale

3-story reinforced concrete frame structure model with inter-story isolation system as shown in Figure17. The test results showed that compared with common structures without this system, the earthquake responses of the structures with this system were reduced by 20%~40%. The calculation and design method has been developed to analyze and design the inter-story isolation system. This new method has been applied to strengthen twenty and more old buildings in China.

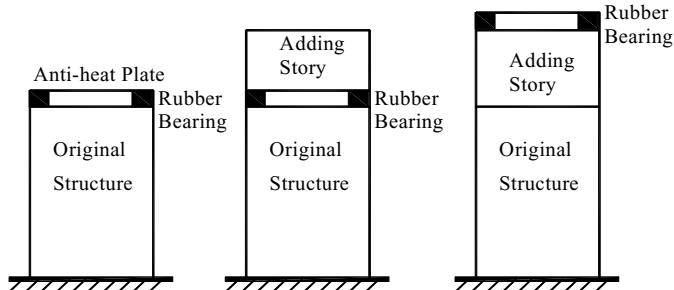


Figure16 Inter-story Isolation System



Figure17 Comparing Shaking Table Tests on Frame Structure Model

4. DEVELOPMENT OF NEW SEISMIC ENERGY-DISSIPATION SHEAR WALLS

4.1 Reversed Cyclic Tests on Interfaces between Concrete and Rubber

To prevent R. C. shear walls suffering damage concentrating at the base and to improve the seismic performance, a new type of energy-dissipation shear wall was proposed by Lu and Wu (2000). It is one with vertical slit purposely cast within the wall, and the rubber belt penetrated by a part of web shear reinforcement as seismic energy-dissipation device was filled in the slit. A series of experimental and theoretical studies were carried out. As the first stage of investigation, reversed cyclic tests on the energy-dissipation device were carried out to study its energy-dissipation mechanism and analytical model. Each specimen was divided into three parts, four steel bars passed through the middle rubber belts. The testing setup is shown in Figure18. The tests proved that the device had large capacity of dissipating energy and good ductility.

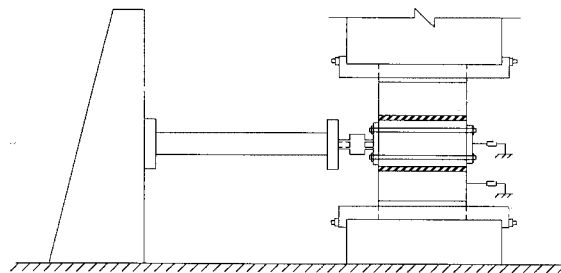


Figure18 Testing Setup for The Energy-dissipation Device

4.2 Reversed Cyclic Tests on Low-rise Shear Wall and High-rise Shear Wall Models

To compare the different seismic performance between the solid wall and the new shear wall, low-rise wall models and high-rise wall models were tested under reversed cyclic loads respectively by Jiang and Lu (2003). The vertical compressive load was applied on the top loading beam in advance of the application of the horizontal cyclic load. At the beginning of loading the behavior of solid wall models was similar to that of the solid wall models, and then different failure process took place in two different types of wall models. In solid wall models damage concentrated at the base while in slit wall models the damage at the base was much lightened and damage dispersed along the slit. The final failure modes of these models are shown in Figure19. Compared with solid wall models, the ductility and energy-dissipation capacity of slit wall models was enhanced significantly.



(a)



(b)



(c)



(d)

Figure19 Failure Modes of The Shear Wall Models: (a) Solid Low-rise Shear Wall, (b) Slit Low-rise Shear Wall, (c) Solid High-rise Shear Wall, and (d) Slit High-rise Shear Wall

4.3 Shaking Table Tests on Slit Shear Wall Models

In order to further verify this concept of slit wall, shaking table tests were carried out on a 10-story 1/5-scale shear wall model. The model consisted of two pieces of 40 mm thick walls connected by floor slabs and four foundation beams. Under minor earthquake ground motions, the model was in elastic stage, and its responses were very much like those of solid wall model. Under moderate earthquake ground motions, the relative sliding along the slits between the rubber belts and wall piers took place to dissipate the input seismic energy, and damage appeared along the slits. Under severe earthquake ground motions, slight flexural failure occurred at the base of the wall. The good seismic performance of slit wall was proved once again by the tests.

4.4 Finite Element Analysis on Slit Shear Walls

The slit shear walls are analyzed by finite element method. To reflect the seismic energy-dissipation mechanism on the sliding friction interfaces between concrete and rubber, a contact element is derived from the joint element that is conventionally used in the rock mechanics. The contact element is composed of two sliding surfaces. The analytical model is shown in Figure20. Cyclic shear-sliding relationships for the interface is shown in Figure21. The steel reinforcement is treated as a uniaxially stressed material and smeared among the concrete element. Nonlinear time history analysis is conducted by the finite element models for the slit shear wall model tested on the shaking table. The numerical results are in good agreement with test results. This new slit shear wall was applied in two actual tall buildings in Shanghai in 1997.

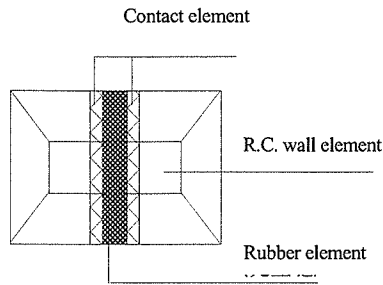


Figure20 Analytical Model

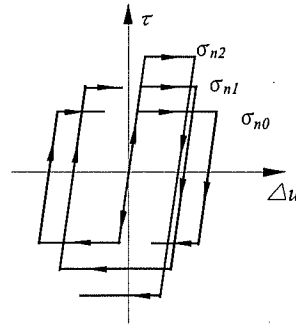


Figure21 Shear-sliding Relationships for The Interface

5. STUDY ON DYNAMIC SOIL-STRUCTURE INTERACTION

5.1 Shaking Table Tests on Interaction System Including Soil-pile-structure

In order to reduce the box effect, a flexible container and the proper construction details were designed by Lu, Chen et al (2002). The ratio of ground plane diameter D to structure plane size was taken as 5. The cylindrical container was 3000 mm in diameter and its lateral rubber membrane was 5 mm in thickness. The reinforcement of $\Phi 4@60$ along the outside perimeter of the container was used to strengthen the container. The foundation of the model consisted of 3X3 group piles capped by a slab. Shanghai soft soil was used as model soil. From top to bottom, three kinds of model soil, silty clay, sandy silt, and medium sand, were stacked. Two 12-story R.C. frame structure models, with the scale of 1/10 and 1/20 respectively, were tested. Accelerometers and strain gauges were installed on the models to measure the earthquake responses of the superstructure, foundation, and soil. Soil pressure gauges were also installed to measure the contact pressure between the piles and soil. The tested model is illustrated in Figure22.



Figure22 Shaking Table Tests on SSI model



Figure23 Analytical Model

5.2 Computer Simulation on Soil-pile-structure Interaction Considering Soil Liquefaction

Analytical model was developed by finite element program Ansys5.5 for numerical analysis by Chen and Lu (2002), as shown in Figure23. The lateral rubber membrane of the container is meshed by shell element. The bottom of soil is considered as fixed. Soil is meshed by three-dimensional solid element, and the equivalent linearization model is adopted. The effect of effective confining pressure of soil on initial shear modulus is considered when the initial shear modulus of each layer soil is chosen. The equivalent linearity model is realized in Ansys program by using the APDL, so the calculation of material nonlinearity is realized automatically. In Ansys program contact analysis is

realized by overlaying a thin layer of elements upon the contact interface of analysis model to reflect sliding and splitting phenomena on the soil-structure interface. The soil surface is taken as contact surface, and the structure (foundation) surface due to its larger rigidity, as target surface. A material-damping input method is used, and different damping ratio can be input for different materials.

The effect of the material nonlinearity of soil and the changing-status nonlinearity of soil-structure interface on the computational results is studied. The computational analysis is carried out under three conditions, not considering material nonlinearity, considering material nonlinearity, and considering both material nonlinearity and changing-status nonlinearity. By using the above analytical model, the calculation results agree with the test results approximately. Along the height of the piles in different location in the group piles the distribution of the strain amplitude, contact pressure amplitude on soil-pile interface, and sliding amplitude between soil and pile are studied. Along the height of the pile, the strain amplitude at the top is larger than in the middle, and that at the tip, smaller. The contact pressure amplitude at both ends is larger than in the middle. The strain amplitude of corner pile is larger than that in other location; the sliding amplitude of the pile in the side row is larger than that in the middle row.

6. STUDY ON CONCRETE-FILLED RECTANGULAR TUBULAR (CFRT) STRUCTURES

6.1 Ultimate Strength and Confinement Mechanism of Axially Compressed CFRT Stubs

Six CFRT columns and two square steel tubes without infilled concrete were tested for comparison. The width-to-thickness ratio of steel plate and the concrete grade were variant parameters. In steel tubular columns local buckling failure of the plate panels occurred before the yielding stress was reached. Compared with the steel tubular columns, the CFRT columns had better ductility because the infilled concrete increased the stability and slowed down the development of the local buckling. A constitutive model for concrete subjected to triaxial compressive stresses is developed, which is based on hypoelastic orthotropic approach. The criterion proposed by Ottosen is adopted herein and the equivalent uniaxial strain concept of Darwin and Pecknold is incorporated further into the nonlinear three-dimensional incremental stress-strain relationship. A 3D nonlinear F.E.M. analytical model was developed to analyze the steel-concrete composite structures and corresponding computer program was completed by Lu and Yu (2000). The concrete material model, where Sargin's stress-strain expression and corresponding tension and compression failure surfaces are adopted, is based on a hypo-elastic orthotropic approach. Von Mises elasto-plastic isotropic hardening model is employed for steel element. Smeared crack approach is applied. In order to trace pre- and post-collapse response of structure, the arc-length method is used to solve nonlinear equations. The calculation results agree well with the test result

6.2 Seismic Behavior of CFRT Columns

Eleven CFRT columns were subjected to cyclic lateral loads, while one subjected to monotonic load for comparison, as shown in the work by Lu and Lu (2000). The width-to-thickness ratio of plate, concrete grade, and axial force ratio are variant parameters. The analysis method is based on finite slices model. In analysis, Bernoulli-Euler hypothesis and planar assumption are adopted, and the slippage between the infilled concrete and steel tube and the buckling of the steel plate are ignored.

6.3 Connections between CFRT Columns and Beams

The Seismic behavior of connections between CFRT columns and beams was studied through sub-assembly loading tests by Lu, Yu et al. (2000). Cruciform tensile tests for modeling connections of column-to-tension part of beam on CFRT connection was conducted, and then the transfer mechanism was investigated by Li and Lu (2002). Simple stress transfer mechanism is assumed to

compute yielding and ultimate tension strength of the joint, which is based on yielding line theory and takes the contribution of the inner diaphragm and flange of CFRT columns into account. The computational and experimental results are in good agreement. Secondly, tests on CFRT column and steel beam sub-assemblages were conducted. The tests showed that the infilled concrete and inner diaphragm improved the behavior of connections, i.e., reducing the deformation of joint panel and enhancing the strength and rigidity.

Present types of CFRT joints are concerned on the connection between CFRT columns and steel beams. But in China, the floors of high-rise buildings are mostly composed of R.C. beams and R.C. slabs. In order to accomplish the connection between CFRT columns and reinforced concrete floors, two new types of joint, the one that reinforcements are put through the CFRT column; and the other one that the beam reinforcements are located outside the column and connected by R.C. ring beams around the column, are developed, shown in Figure24.

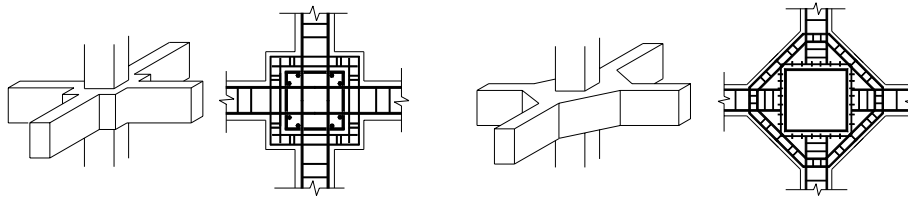


Figure24 New Types of Connections

7. SEISMIC BEHAVIOR OF R.C. HIGH-RISE BUILDINGS AND TOWERS

7.1 R. C. Coupled Shear Walls

Three 1/4-scale 5-story R.C. coupled shear wall models shown in Figure25 were tested under cyclic loading. The only difference between the models was the height of coupling beams, which brought forward different stiffness ratio of coupling beams to wall piers. After constant vertical loads were applied on the top beam, the horizontal cyclic loads were applied through two points, with the ratio of 2, to simulate the reversed triangular load. The failure process and mechanism were studied.

A nonlinear macro model is proposed to simulate coupled shear walls, as shown in Figure26. This model consists of multi-vertical-element model for wall piers and a combined model for coupling beams. In the model for wall piers, some key characters, such as shifting of neutral axis within wall section, interaction among flexure, shear and axial forces, can be taken into account. In the model for coupling beams, the deformation of flexure and shear, and the interface bond-slip action are considered by using different elements. The analytical results agree well with the test results.

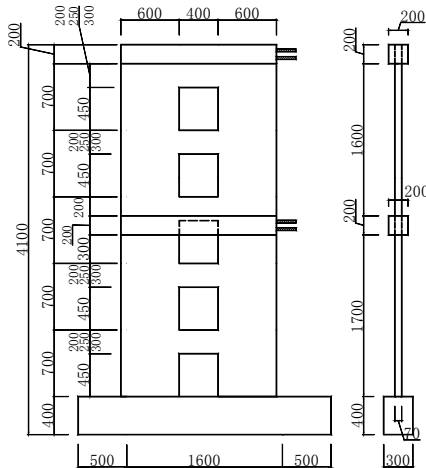


Figure25 Profile of The Tested Models

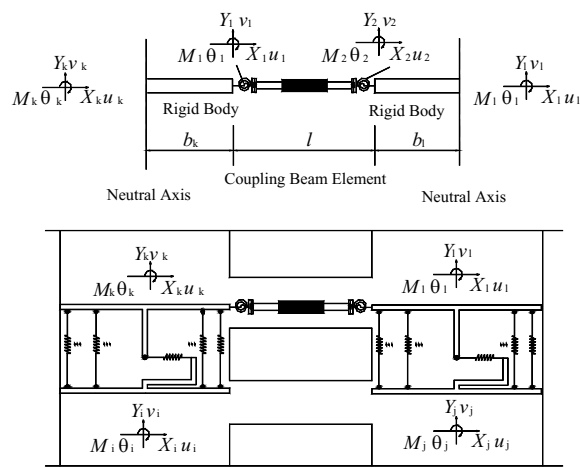


Figure26 Analytical Model

7.2 R. C. Core Walls

Three 1/5-scale 3-story core wall models (the first group) and two 1/6-scale 5-story core wall models (the second group) were tested under cyclic loading, as shown in the work by Li and Lu (2003). For the first group, the vertical loads were exerted by hydraulic jacks, and the horizontal loads acted on the top floor level. For the second group, the vertical loads were applied by prestressed strands, and the horizontal loads acted on the top floor level and second floor level simultaneously. The testing setups for the two groups are shown in Figure27 and Figure28. The failure process and mechanism were studied. The phenomenon of shear lag of the core wall was observed distinctly.

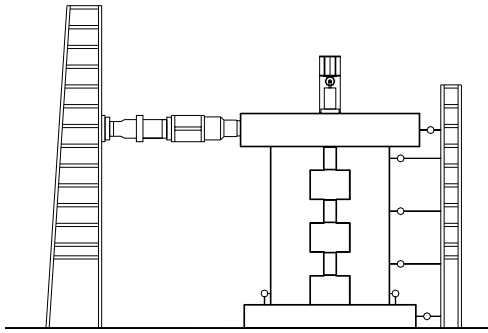


Figure27 Testing Setup for The First Group



Figure28 Testing Setup for The Second Group

A nonlinear finite element analytical model is developed using eight-joint plane-stress elements, as shown in Figure29. A simple and reliable constitutive model of reinforced concrete under cyclic loading as shown in Figure30, and the concept of a smeared crack approach with orthogonal cracks are utilized. Using this analysis model, the behavior of reinforced concrete core walls under cyclic loading with different axial load ratio, different height-width ratio and different coupled-beam stiffness is studied. The comparison of the experimental and computational results shows that the analytical model is reasonable and reliable.

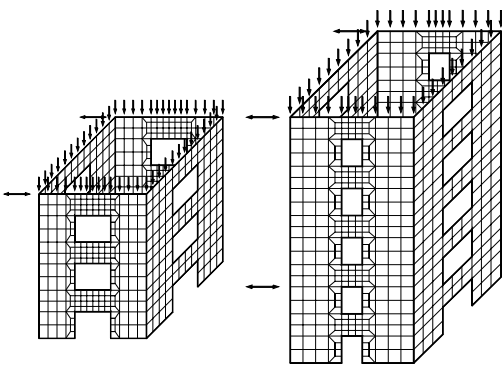


Figure29 Analytical Model for Core Wall Models

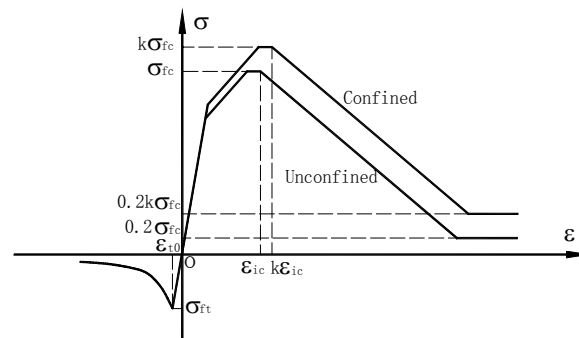


Figure30 Cyclic Stress-strain Relationships for Concrete

7.3 Shaking Table Tests on Models for Various Complicated Buildings and Towers to Guide The Engineering Design

Physical testing is important to structural engineering because it helps establish fundamental understanding about the behavior and failure mechanism of structures. Structural model testing is often used to help structural engineers to directly acquire the knowledge about the prototype, especially in the case of complicated buildings for which the numerical simulations are considered unreliable. Shaking table model tests has been considered an economic, accuracy, and practical way to evaluate the seismic performance of structures. To ensure that the model behaves in a similar manner

as the prototype, the model designed should meet the requirements of dynamic similitude theory. It is no doubt that dynamic similitude theory is the most important basis in shaking table model test. To verify the validity of dynamic similitude theory in shaking table model test, two 6-story R C. frame models, one with 1/4 scale and the other with 1/8 scale, designed according to the same prototype, were tested on the shaking table. The test results demonstrated that there existed good consistency with the similarity on natural frequency, failure mechanism, and restoring force model between the two scale models.

On the basis of the above research, more than twenty structural models of complicated tall buildings and TV towers, such as Shanghai TV tower, Tianwang Tower, China Southern Airline Tower and so forth, have been tested on shaking table in the past two decades. Two tested structural models are shown in Figure31 and Figure32. The model design and construction method, testing and analysis procedures, and measure techniques have been developed maturely. By these shaking table tests, the earthquake responses and dynamic characteristics were derived, the failure process, failure mechanism, and structural weak points were discovered, and then the overall seismic performance of the prototype was evaluated accordingly. Advices or suggestions were proposed as references for structural design to improve the seismic performance of structures. Some test results were also verified by in-site testing on completed actual structures.



Figure31 Shanghai Join-by Department Store



Figure32 Shanghai Jinghua Garden Apartment

8. FURTHER RESEARCH

Based on the previous research work, the following topics are being investigated now or will be investigated in the future in this laboratory:

1. Performance-based seismic design of building structures
2. Smart material and smart structural system
3. Seismic behavior of composite ultra-tall buildings and nonlinear earthquake response analysis
4. Development of new structural control devices and engineering application
5. Development of new evaluation and strengthening methodology for old buildings
6. Development of computer software for nonlinear seismic analysis of tall building and ultra-tall building structures

References:

- Chen, B. and Lu, X.L. (2002), "Modelling of Dynamic Soil-structure Interaction by ANSYS Program," *2nd Canadian Specialty Conference on Computer Applications in Geotechnique*, Canada, 21-26.
- Jiang, H.J., Lu, X.L. *et al.* (2003), "Study on A Seismic Slit Shear Wall with Cyclic Experiment and Macro-model

- Analysis," *Structural Engineering and Mechanics-An International Journal*, **16**(4), 371-390.
- Li, J.L. and Lu, X.L. (2003), "Study on The Seismic Behavior of Reinforced Concrete Core Walls," *International Conference on Concrete Structures in Seismic Regions*, Athens, Greece, Paper No. 133.
- Li, X.P. and Lu, X.L. (2002), "Shear-resistant Capacity of Interface of Ring-beam Connection Located outside Concrete-filled Rectangular Tubular Column," *Journal of Tongji University*, China, **30**(1), 11-17.
- Lu, X.L., Chen, Y.Q. *et al.* (2002), "Shaking Table Model Test on Dynamic Soil-structure Interaction System," *Journal of Asian Architecture and Building Engineering*, **1**(1), 55-63.
- Lu, X.L. and Fang, Z. (1994), "Servo-motor Control System with Application in Seismic Control of Buildings," *Proceedings of 1st World Conference on Structural Control*, Los Pasadena, California, USA, 33-40.
- Lu, X.L. and Lu, W.D. (2000), "Seismic Behavior of Concrete Steel Composite Columns under Cyclic Loading," *12th WCEE*, Auckland, Paper No. 1416.
- Lu, X.L. and Wu, X.H. (2000), "Study on A New Shear Wall System with Shaking Table Test and Finite Element Analysis," *Earthquake Engineering and Structural Dynamics*, **29**(7), 1425-1440.
- Lu, X.L., Yang, Z., and Xu, Y.L. (2002), "Seismic Response Control of Adjacent Buildings Linked by Fluid Dampers," *Proceedings of the International Symposium on Safety Science and Technology*, Tai'an, China, 3, 480-487.
- Lu, X.L., Ye, H., and Fang, Z. (2000), "Shaking Table Test of A Servomotor TMD System for Structural Control," *Journal of Vibration Engineering*, China, **13**(1), 61-70.
- Lu, X.L., Yu, Y. *et al.* (2000), "Experimental Study on The Seismic Behavior in The Connection Between CFRT Column and Steel Beam," *Structural Engineering and Mechanics-An International Journal*, **9**(4), 365-374.
- Lu, X.L. and Yu, Y. (2000), "Nonlinear Analysis on Concrete-filled Rectangular Tubular Composite Columns," *Structural Engineering and Mechanics-An International Journal*, **10**(6), 577-587.
- Lu, X.L. and Zhou, Q. (2002), "Dynamic Analysis Method of A Combined Energy Dissipation System and Its Experimental Verification," *Earthquake Engineering and Structural Dynamics*, **31**(6), 1251-1265.
- Lu, X.L., Zhu, Y.H. *et al.* (2002), "Shaking Table Test and An Analytical Model for Base Isolated Buildings with Combined Isolation System," *IABSE Symposium*, Melbourne, Austria, CD-Rom Version.
- Shi, W.X. and Li, Z.S. (1998), "An Experimental Study on Seismic Response of Sliding Isolated Building," *Advances in Structural Engineering*, **2**(1), 17-24.
- Shi, W.X. and Zhu, B.L. (1994), "The Seismic Response of Story Isolation Masonry Building," *International Workshop on Use of Rubber Based Bearing for Earthquake Protection of Building*, Shantou, China, 41-48.

RECENT RESEARCH ACTIVITIES IN NCREE: DEVELOPMENTS OF THE EARTHQUAKE LOSS ESTIMATE SYSTEM AND INTERNET TESTING TECHNIQUES

K. C. Tsai¹⁾ and C.H. Yeh²⁾

1) Professor and Director, National Center for Research on Earthquake Engineering, Taiwan

2) Research Fellow, National Center for Research on Earthquake Engineering, Taiwan

kctsai@ncree.gov.tw, chyeh@ncree.gov.tw

Abstract: This paper describes two team efforts on the research of earthquake loss estimate system and networked internet testing techniques in the National Center for Research on Earthquake Engineering (NCREE). The application software "Taiwan Earthquake Loss Estimation System (TELES)" is developed in NCREE to simulate earthquake scenarios and estimate induced damages and losses. This paper focuses on demonstrating the analysis models, software features and applications of the Early Seismic Loss Estimation (ESLE) module which is contained in TELES. The second part of the paper presents an effort in developing an Internet-based environment, entitled "Internet-based Simulations for Earthquake Engineering", for collaborative networked structural experiments among geographically distributed structural laboratories. Two approaches, the Database Approach and the Application Protocol Approach, are described to provide different solutions for network communication as well as collaborative framework in networked hybrid testing. Database Approach shows that the network and data processing costs about 0.2 seconds and 2 seconds per time step in domestic and transnational experiments, respectively. Application Protocol Approach testing results show that it took less than 0.2 seconds for two data packets to travel back and forth between NCREE laboratory in Taiwan and Stanford University in USA.

1. INTRODUCTION

The National Science Council of Taiwan started HAZ-Taiwan project in 1998 to promote researches on seismic hazard analysis, structural damage assessment, and socio-economic loss estimation. The associated application software, "Taiwan Earthquake Loss Estimation System (TELES)", integrates various inventory data and analysis modules to fulfill three objectives. Firstly, it helps to obtain reliable estimates of seismic hazards and losses soon after occurrence of large earthquakes. Secondly, it helps to simulate earthquake scenarios and to provide useful estimates for local governments or public services to propose their seismic disaster mitigation plans. Thirdly, it helps to provide catastrophic risk management tools, such as proposing the seismic insurance policy for residential buildings. The first part of this paper focuses on the development and application of analysis modules used in early loss estimation system. These modules include assessments of ground motion intensity, soil liquefaction potential, building damage and casualty. The second part of the paper presents an effort in developing an Internet-based environment, called ISEE (Internet-based Simulations for Earthquake Engineering), for collaborative networked structural experiments among geographically distributed structural laboratories. Two approaches, the Database Approach and the Application Protocol Approach, have been employed to provide different solutions for network communication as well as collaborative framework in ISEE. This paper presents the ISEE environment for collaborative networked structural experiments among geographically distributed structural laboratories. Several networked pseudo dynamic tests have been conducted to investigate the feasibility and efficiency of ISEE. Based on these test results, the

feasibility of ISEE for collaborative networked tests is presented. A series of networked pseudo-dynamic test examples using the Database Approach shows that the network and data processing costs about 0.2 seconds and 2 seconds per time step, around 20% and 70% of total elapsed time in domestic and transnational experiments, respectively, which is feasible for most of the low-speed pseudo-dynamic experiments. Application Protocol Approach testing results show that significant laboratory events were promptly reflected and data transmission was satisfactorily efficient since less than 0.2 seconds for two data packets to travel back and forth between NCREE laboratory in Taiwan and Stanford University in USA.

2. EARTHQUAKE LOSS ESTIMATE SYSTEM

Taiwan is located at the circum-pacific earthquake belt and has suffered from devastating earthquakes in almost every decade. In 21 September 1999, Chi-Chi earthquake attacked central Taiwan due to the rupture of Chelongpu fault. Its Richter magnitude was 7.3 with a focal depth of 7 kilometers. This earthquake has resulted in about 2,500 deaths, 11,000 injuries, and caused more than 100 thousand households severely wounded due to various degrees of building damages. The total economic losses were about US\$11.5 billions. Since then, the central government of Taiwan has devoted efforts on reconstructing the disastrous regions and implementing the seismic disaster reduction systems against future earthquakes. Several coordinated projects are undertaken in Taiwan to identify the hazard sources, reinforce the civil infrastructures, integrate information and scenario simulation systems, improve communication capabilities, and to educate as well as disseminate these information to the general public.

In general, risk can be defined by occurrence probability of a seismic event, exposure of people and property to the event, and consequences of that exposure. Based on the previous definition of risk, an earthquake loss-estimation methodology, integrated with geographic information system (GIS) and designed to run on personal computers, has been developed in the United States. The methodology and associated application software are contained in HAZUS (RMS, 1997). The National Science Council (NSC) of Taiwan started HAZ-Taiwan project in 1998 to promote researches on seismic hazard analysis, structural damage assessment, and socio-economic loss estimation. After gaining experiences on simulation of earthquake scenarios for several years, the National Center for Research on Earthquake Engineering (NCREE) has completed the prototype of "Taiwan Earthquake Loss Estimation System (TELES)" in 2002 to fulfill the objectives of HAZ-Taiwan Project.

The HAZ-Taiwan project and associated application software TELES follow a similar approach used in HAZUS. However, TELES has made major modifications in analysis models, parameter values and software architecture, not only to accommodate the special environment and engineering practices in Taiwan, but also to reflect the state-of-the-art technology. Furthermore, through modular approach and step-by-step improvement, TELES has added a new feature of early seismic loss estimation to estimate automatically the disaster scale and its distribution soon after the occurrence of large earthquakes. In order to serve as a seismic risk assessment and management tool, TELES plans to integrate probabilistic seismic hazard analysis in the near future. HAZUS does not have the features of early seismic loss estimation and probabilistic seismic risk assessment.

The results of the HAZ-Taiwan project help to plan and stimulate efforts to reduce risk from earthquakes, and to prepare for emergency response and recovery from an earthquake. It also provides a standard risk assessment and loss estimation methodology to evaluate the performance of seismic hazard mitigation efforts and to set the priorities of local, regional or nation-wide public works/services. Expected benefits of a standard methodology also include more economic use of available resources and improved sharing of knowledge.

2.1 Analysis Framework of TELES

The HAZ-Taiwan project is mainly consisted of three parts:

- collection of seismic sources, geologic and inventory database;
- development and modification of analysis modules in hazard analysis, vulnerability assessment and loss estimation;
- improvement of the application software TELES.

To collect complete and useful database is one of the key factors leading to the success of HAZ-Taiwan project. Nonetheless, database collection is often the most time consuming and expensive aspect in performing a comprehensive loss study. The analysis modules contained in TELES can be roughly divided into four groups, namely the potential earth science hazards (PESH), the direct physical damages, the indirect physical damages, and the socio-economic losses, as shown in Figure 1. In general, the civil infra-structures are classified into general building stocks, essential facilities, transportation and utility systems by their usage and functionality. Each general category of inventory data is further divided into several specific categories according to their specific usages. The inventory data are also classified according to their structural types, seismic resistant characteristics, etc. in order to assess damage-state probabilities based on site specific ground motion intensity and ground failure extent. The data classification schemes as well as the associated analysis models should depend on the content of inventory database.

The analysis modules and sub-modules are interdependent. The output from one module may act as input to another. The modular approach allows estimates based on simplified models and limited inventory data. Addition or replacement of existing modules may be done without reworking the entire methodology. The modular approach also facilitates information exchange and technology transfer between the research communities and the end users. Although development of each module may require a comprehensive study, the degree of sophistication and the associated cost often varies greatly by user and application.

Like HAZUS, TELES can simulate earthquake scenario due to single event. The Central Weather Bureau (CWB) of Taiwan is currently in charge of earthquake monitoring networks and has developed "Taiwan Rapid Earthquake Information Release System (TREIRS)", which can obtain earthquake magnitude, epicenter location and focal depth within 90 seconds after occurrence of earthquakes. CWB will automatically send out the earthquake alerts to all clients by mail, fax, etc. Combining functionalities of TREIRS and TELES, an Early Seismic Loss Estimation (ESLE) module has been developed and integrated in TELES. It monitors the mailbox continuously and will be triggered and start analysis automatically when a large earthquake is detected. Applications of ESLE will be further explained in the following sections.

As shown in Figure 1, the probabilistic seismic hazard analysis will be integrated in the analysis framework of TELES. Addition of this feature helps to identify the maximum probable earthquake for each county/city, to evaluate seismic risk of various facilities and lifeline systems in different regions, to propose reasonable risk management policies such as seismic insurance for residential buildings and high-tech industrial plants, to evaluate performance and to set priority of seismic retrofit of public works, etc.

In summary, the analysis framework of TELES provides basis for applications on emergency responses, local disaster mitigation plans and risk management tools. However, this paper focuses on the analysis modules related to ESLE.

2.2 Prediction of Ground Motion Intensity

The PESH module calculates estimates of ground motion intensity and ground failure extent. Based on the source parameters of a scenario earthquake and the local geologic conditions, ground motion demands are in terms of response spectra and peak values (PGA and PGV). The response spectra are simplified and expressed in terms of S_{as} and S_{a1} , which denote the spectral accelerations with structural periods 0.3 and 1.0 seconds, respectively. The occurrence probability

of soil liquefaction and the induced permanent ground deformation (PGD) are also estimated. Other related earth science hazards, such as tsunami and inundation, may affect social/economic environment, but are not considered in the current framework of TELES.

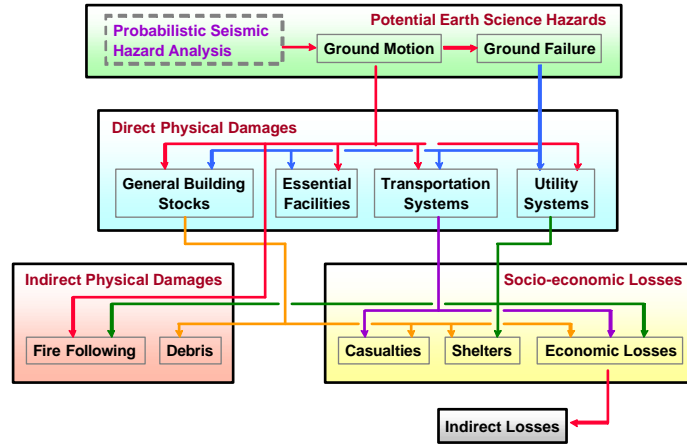


Figure 1. Methodology framework of Taiwan Earthquake Loss Estimation System.

The first step in simulating earthquake scenario is to set source parameters of a seismic event. The basic source parameters include event date, time, magnitude, epicenter location and focal depth. If the earthquake has large magnitude and shallow focal depth, it often accompanies surface fault rupture. The fault mechanism (reverse, normal or strike), the orientation of fault trace, the dip angle, length and width of rupture plane are required to define the source parameters. In case there is no actual fault information, the rupture plane can be assumed as a rectangle with certain orientation, dip angle, and passing through the hypocenter of scenario earthquake. If actual faults are used in defining the seismic source, the surface fault trace may compose of many line segments, though not necessarily continuous, to depict reality. Default rupture length and width are provided by using Wells et al (1994) empirical formula; however, they can be customized to match the actual observation.

Different attenuation laws for ground motion intensity parameters use different definitions for earthquake magnitude and source-to-site distance. Furthermore, different definitions for earthquake magnitude may be used in different analysis modules. Since both moment magnitude (M_w) and Richter local magnitude (M_L) are often used in Taiwan, TELES internally converts them by using the following equation (Wu et al, 2001),

$$M_L = 4.533 \ln M_w - 2.091. \quad (1)$$

Depending on the attenuation laws chosen by the user, TELES automatically selects corresponding definition for source-to-site distance. For example, Jean (2001) uses Richter local magnitude and shortest distance to rupture plane, while Boore et al (1994) uses moment magnitude and shortest distance to the horizontal projection of rupture plane. If the rupture length reduces to zero, focal distance is automatically used in the attenuation laws. The effect of seismogenic rupture zone is also taken into consideration when evaluating the source-to-site distance.

Estimation of ground motion intensity due to a scenario earthquake may divide into three steps. Referring to Figure 2, the first step uses the attenuation laws to predict the intensity at bedrock level. The second step uses the local site modification factors to obtain the intensity at ground surface. When the monitored data at strong-motion stations are available, for example, in early seismic loss estimation, the local intensity can be updated accordingly.

The local site conditions are classified into six categories in HAZUS by using properties of the

soil profile such as shear wave velocity, SPT-N value, etc. The site modification factors depend on the soil type as well as the ground motion intensity. However, topography and geology are very complex in Taiwan, basin effects or topographic conditions may influence the ground motion intensity significantly. To overcome the shortage of rough classification scheme of soil types, micro-zonation of the site modification factor is necessary. Since the strong-motion stations installed by CWB are dense enough, the site modification factors for each region are studied by using historical earthquake records and local geologic conditions at the strong-motion stations (Yeh et al, 2003).

2.3 Estimation of Soil Liquefaction Potential and Settlement

The influence factors in soil liquefaction are the intensity level and the time duration of ground excitation and the ground water depth. The peak ground acceleration (PGA) is commonly used to indicate the excitation intensity, while the earthquake magnitude is used to indicate the duration of excitation. Following the methodology of HAZUS, the soil liquefaction susceptibility is classified into six categories, that is, “very high”, “high”, “moderate”, “low”, “very low” and “none”. Yeh et al (2002a) analyzed more than 11,000 sets of borehole data in Taiwan and proposed a classification scheme to identify the liquefaction susceptibility category of each borehole. Based on the knowledge of liquefaction susceptibility for each borehole and a small-scale geologic map, the liquefaction susceptibility map of Taiwan has been roughly estimated. As an example, Figure 3 shows the soil liquefaction susceptibility map in Taipei city.

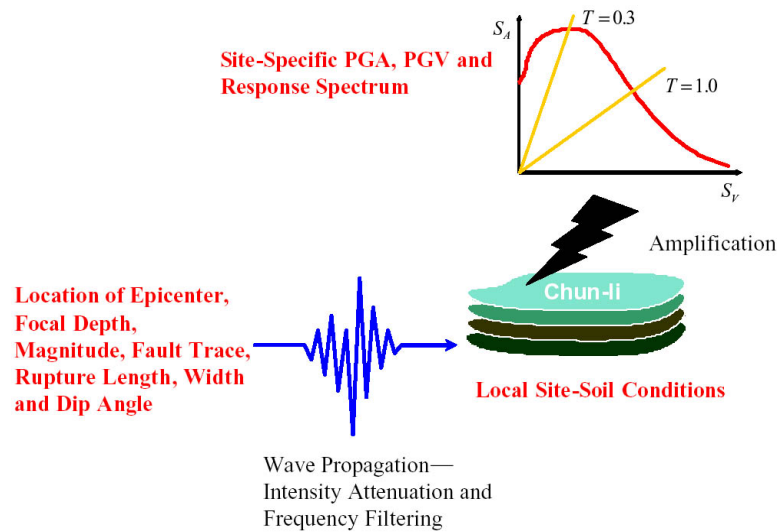


Figure 2. Procedures in estimation of ground motion intensities.

The semi-empirical formulas to estimate the liquefaction probability and the amount of settlement are obtained from nonlinear regression analysis (Yeh et al, 2002b). They are summarized as follows. It is assumed that the liquefaction potential index P_L (Iwasaki et al, 1982) is proportional to liquefaction potential and the liquefaction probability is greater than 0.8 when $P_L \geq 15$. The P_L for susceptibility category i can be estimated by

$$(P_L)_i = \alpha_i \cdot f(M) \cdot g(d_w)(PGA) + \beta_i \quad (2)$$

$$f(M) = 0.0353M^2 - 0.1855M + 0.4069 \quad (3)$$

$$g(d_w) = 0.0002d_w^4 - 0.0051d_w^3 + 0.0535d_w^2 - 0.2758d_w + 1.3105 \quad (4)$$

where $f(M)$ and $g(d_w)$ are correction functions for earthquake magnitude and ground water depth, respectively; α_i and β_i are constants and listed in Table 1.

Using the approach in Ishihara (1993), it was observed that the relationship of average settlement

S_i for category i and PGA, when the earthquake magnitude and the ground water depth are kept constant, is similar to a lognormal distribution with two parameters m_i and σ_i indicating median and coefficient of variation, respectively. When PGA becomes larger and larger, the average settlement S_i approaches a limiting value \bar{S}_i , which is not influenced by varying earthquake magnitude and ground water depth. Thus, the average settlement can be expressed as

$$S_i = \bar{S}_i \cdot \int_0^A \frac{1}{\sqrt{2\pi}\sigma_i x} e^{-\frac{[\ln(x/m_i)]^2}{\sigma_i^2}} dx = \bar{S}_i \cdot \Phi \left[\frac{\ln(A/m_i)}{\sigma_i} \right] \quad (5)$$

$$m_i = \mu_i \cdot \bar{f}(M) \cdot \bar{g}(d_w) \quad (6)$$

$$\sigma_i = \lambda_i \cdot \bar{h}(d_w) \quad (7)$$

$$\bar{f}(M) = 0.1231M^2 - 2.2052M + 10.5954 \quad (8)$$

$$\bar{g}(d_w) = -0.007188d_w^2 + 0.145195d_w + 0.7919 \quad (9)$$

$$\bar{h}(d_w) = 0.003208d_w^2 - 0.042231d_w + 1.0611 \quad (10)$$

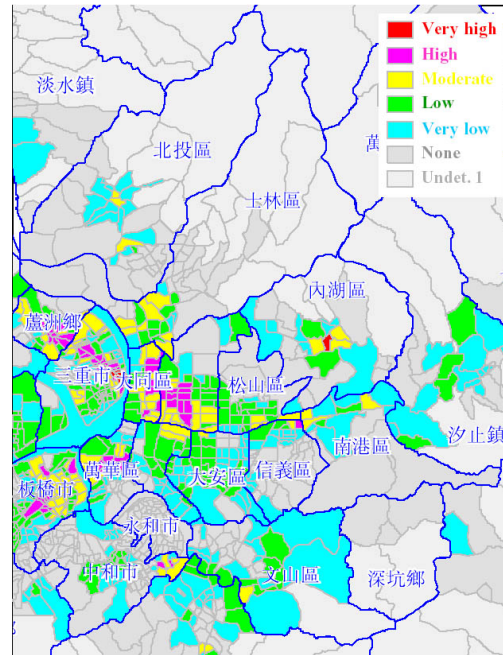


Figure 3. Soil liquefaction susceptibility map of Taipei city.

Table 1 Coefficients in empirical formula for estimating liquefaction potential index.

Category	α_i	β_i
Very High	227.52	-13.63
High	188.30	-18.45
Moderate	157.35	-20.51
Low	103.02	-14.95
Very Low	66.95	-10.64

Table 2 Coefficients in empirical formulas for estimating settlement due to soil liquefaction.

Category	\bar{S}_i (cm)	m_i (g)	I_i
Very High	47.43	0.0872	0.4522
High	50.22	0.1292	0.3657
Moderate	46.21	0.1613	0.3433
Low	35.89	0.1875	0.3430
Very Low	25.66	0.2104	0.3764

where $\bar{f}(M)$, $\bar{g}(d_w)$ and $\bar{h}(d_w)$ are correction functions for earthquake magnitude and ground water depth, respectively; \bar{S}_i , m_i and I_i are constants as shown in Table 2.

2.4 Damage Assessment of General Building Stocks

The general building stocks consist of many buildings of different structural types, seismic behavior and usages. These buildings are grouped into several model building types, seismic design levels, and occupancy classes in order to facilitate damage, casualty and loss estimations. The building tax data from ministry of finance and local governments have been used to calculate various kinds of statistics of general building stocks, since it is the only database that provides consistent format and up-to-date information of buildings in Taiwan.

Based on the content of the building tax data, the general building stocks are grouped into several model building types according to their construction material and building height. There are 15 model building types, namely, wood (L), steel (L, M, H), light steel (L), reinforced concrete (L, M, H), pre-cast concrete (L), reinforced masonry (L, M), un-reinforced masonry (L), and steel reinforced concrete (L, M, H) buildings. The letters L, M and H in the parenthesis indicate low-rise, mid-rise and high-rise buildings, respectively. Each model building type is further divided into four seismic design levels according to their construction years, seismic zoning factors, and local site conditions.

Some inventory data, such as bridges and tunnels, may be treated as point objects. Some others, such as highway segments and airport runway, may be treated as line objects. However, for general building stocks, it is neither necessary nor practical to evaluate individual building. In this case, the mapping scheme of specific occupancy to model building type plays an important role in the framework to estimate various social impacts and economic losses. The mapping scheme for each town in Taiwan has been calculated from building tax data.

TELES evaluates the damage state probabilities for each model building type and seismic design level due to ground motion and liquefaction-induced settlement. The procedures in building damage assessment are depicted in Figure 4, where damages in structural system and nonstructural component are evaluated separately. The effects of hysteretic damping and system degradation are considered in calculating the seismic demand. The seismic capacity and fragility curves for each model building type and seismic design level are determined by reference to seismic design codes in various periods, nonlinear push-over analysis, and historical data collected after Chi-Chi earthquake.

2.5 Casualty Estimation

TELES considers only the casualties due to severe damage or collapse of buildings. Although other factors, such as fire following earthquakes, sudden failure of critical dams, unseat of bridges, etc may cause significant casualties, they are not considered in the current methodology. Referring to Figure 5, the first step in casualty assessment is to estimate spatial distribution of population at different times. For simplicity, only three population migration patterns are taken into consideration, that is, daytime, nighttime, and commute time. It is assumed that the

population density (number of persons per unit floor area) can be estimated for all specific occupancies at three different times. The population can be obtained by multiplication of the population density and the floor area. Assuming the population is uniformly distributed within the same occupancy class, the mapping schemes are used to calculate the number of people in each model building type.

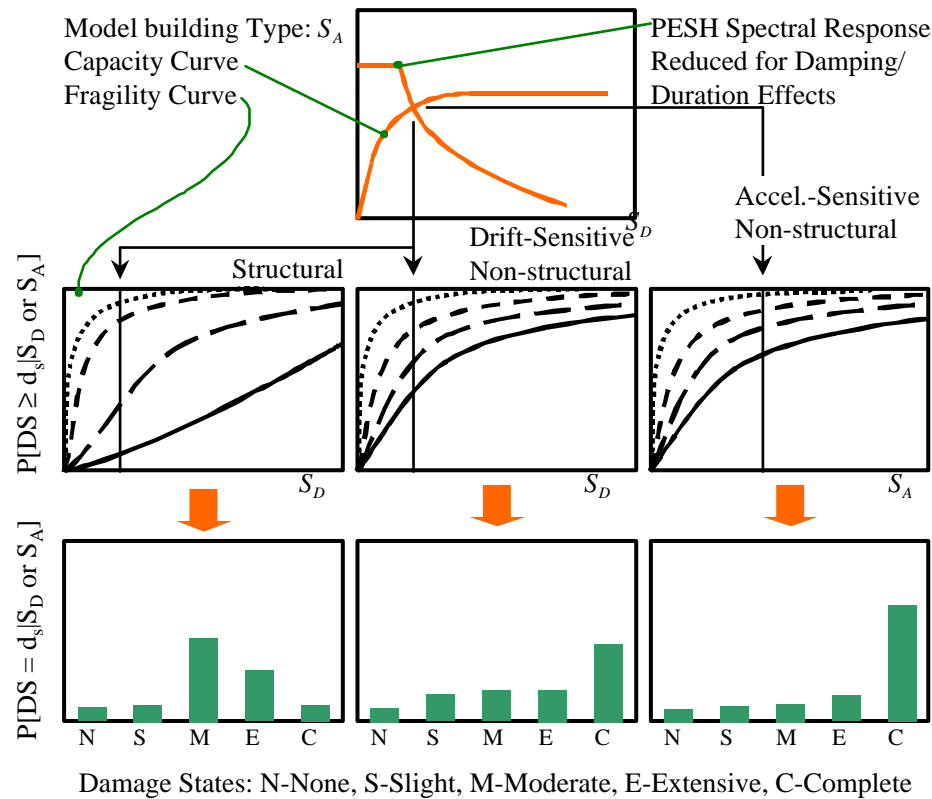


Figure 4. Damage assessment of general building stocks.

The output of casualty module contains estimates breakdown into four injury severity levels, namely, "injuries requiring basic medical aid without hospitalization," "injuries requiring a greater degree of medical care but not expected to threaten life," "injuries requiring adequate and expeditious treatment to avoid loss-of-life," and "instantaneous killed or mortally injured." The casualty rates for different model building types and under various damage states are calibrated considering the effects of structural and nonstructural damages. Complete damage state of buildings is further divided into collapse and without collapse. By combining casualty information with loss-of-function estimates for hospitals, alternate plans may be prepared for treatment of victims outside of the affected area.

2.6 Software Features

The application software, TELES, is written in Visual C++, which is an object-oriented programming (OOP) language, and MapBasic, which is the language used to communicate with MapInfo. Through the object linking and embedding (OLE) technology, the TELES integrates the functionalities and custom usages of MapInfo, which is famous application software of geographical information system (GIS). The main functions of MapInfo in TELES are to view and to edit records and map objects in various kinds of database. All the numerical analysis is written in C++ and FORTRAN. The software architecture of TELES has modular design, so addition and modification of individual module will not affect the other modules. TELES allows

users to open multiple documents and multiple map windows at the same time, so the users can compare different thematic maps and obtain in-depth understanding of the relationships between input and output database. TELES also allows users to monitor the earthquake occurrence and run scenario simulation in separate application windows at the same time. HAZUS and the first version of HAZ-Taiwan software do not have these features.

2.7 Application of Early Loss Estimation System

Having the functionality of early loss estimation which can be auto-trigger after occurrence of large earthquakes, TELES can act as a decision making support system in emergency responses. The time delay between earthquake occurrence and analysis start is normally within two minutes. The affected region of the earthquake is determined by ground motion intensity. All the towns with PGA greater than 80 cm/sec^2 are selected in the study region. The ground motion intensity, soil liquefaction potential and induced settlement, damage state probability and quantity of general building stocks and casualty assessment of each town are calculated one by one. Some of the important results are automatically output in raster maps and tables, which can be used in the presentation to chief commander of emergency response center, or in dispatching the rescue forces and medical resources, etc. Since the required work force and equipment are different to rescue people in low-rise or high-rise buildings, the statistics of at-least-severe damage building counts are obtained for low-rise, med-rise and high-rise buildings, separately.

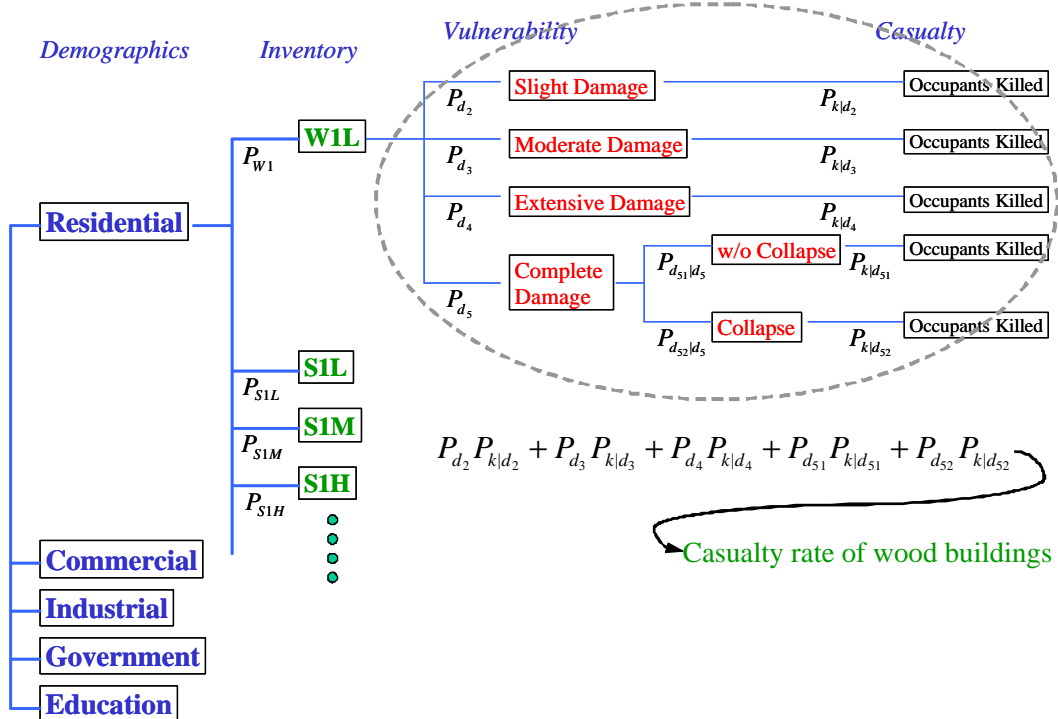


Figure 5. Assessment of casualties caused by building damages.

In practice, application of early loss estimation system divides into three stages. The first stage automatically uses a point-source model to predict the ground motion intensity and associated disasters, when TELES receives email from CWB. Since using a point-source model often under-estimates ground motion intensity and disaster scale, before the actual source mechanism is available, reasonable assumptions can be made about the orientation, dip angle, length and width of the rupture plane. Therefore, the second stage uses several artificial sets of source parameters to

calculate probable range of disaster scale and distribution. In the meantime, actual disaster information are gathered and studied to identify the true source mechanism. Once the true source mechanism and rupture fault are identified, early loss estimation enters the third stage and obtains the most reliable results.

As examples, Figures 6, 7 and 8 show the estimations of PGA, building damage count and induced casualty in Chi-Chi Taiwan Earthquake. These figures are only part of the raster maps that are automatically generated by TELES after occurrence of strong earthquakes.

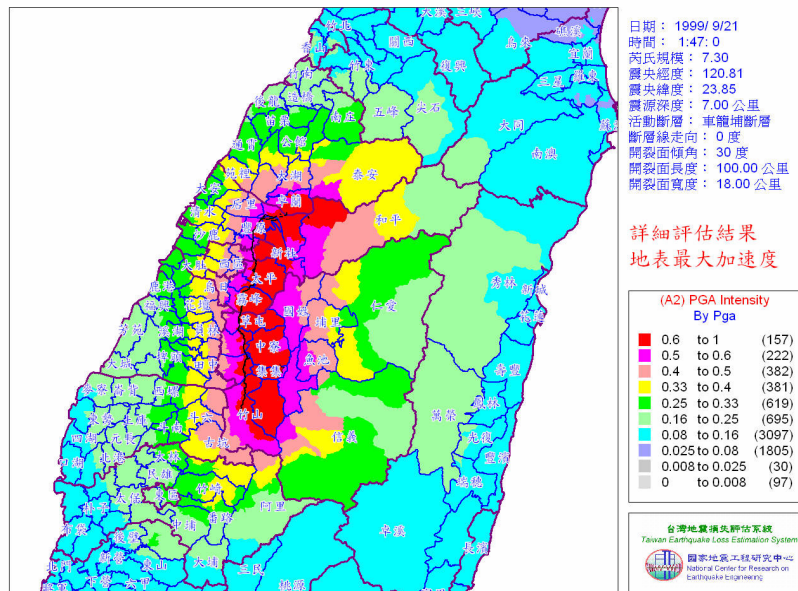


Figure 6. Estimated distribution of peak ground acceleration in Chi-Chi Taiwan earthquake. The black line represents the trace of Chelungpu fault.

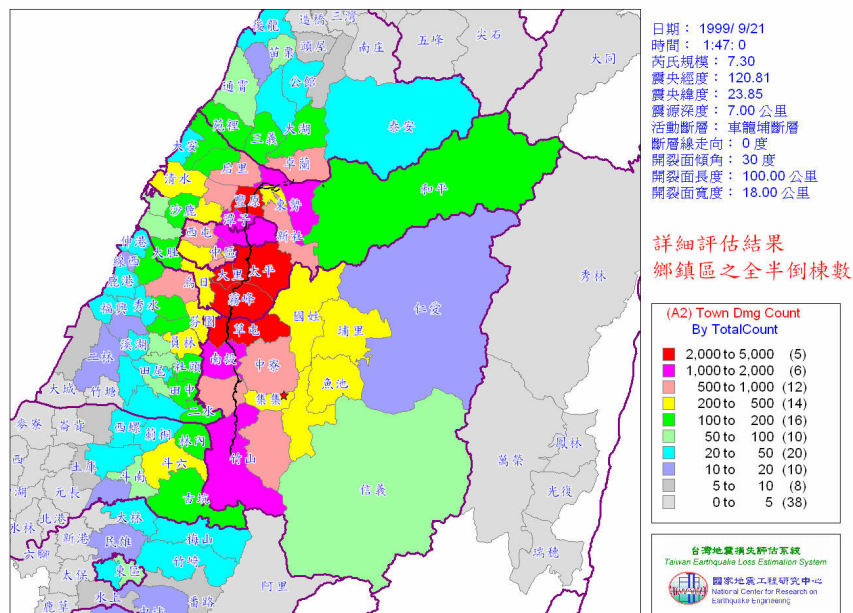


Figure 7. Estimated distribution of building counts in at least severe-damage state in Chi-Chi Taiwan earthquake.

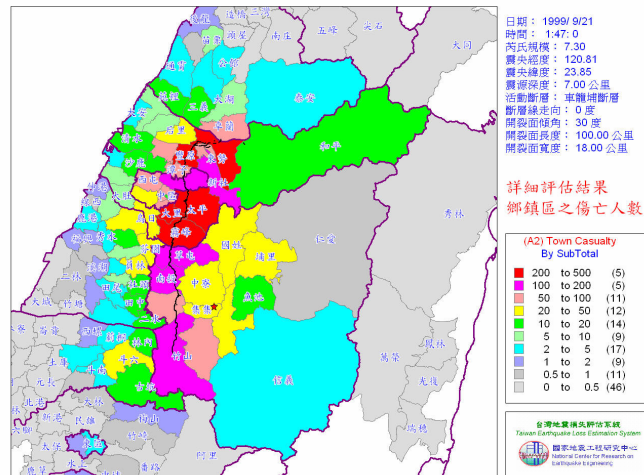


Figure 8. Estimated distribution of casualties in injury levels 3 and 4 in Chi-Chi Taiwan earthquake.

2.8 Summary

Taiwan Earthquake Loss Estimation System (TELES) is part of research accomplishment of HAZ-Taiwan project. It can be applied in proposing local seismic disaster mitigation plans and act as a decision-making support system soon after occurrence of strong earthquakes. In the near future, TELES will also integrate probabilistic seismic hazard analysis and may have applications in proposing maximum probable earthquakes for each county, in proposing adequate seismic insurance policies, etc.

3. INTERNET-BASED SIMULATION ON EARTHQUAKE ENGINEERING

Structural experiment plays an important role in the earthquake engineering research. In view of the continuous changes in structural engineering and the increasing awareness of cost in today's society, the existing large-sized structural laboratories are gradually becoming incapable of satisfying the various types of demand of the experiments. Besides endlessly increasing the capacity of each laboratory, alternatively it would be more cost effective for different laboratories to collaboratively conduct such experiment. In addition, it would be more productive and can make most out of the experiment resources and results if experts around the world can participate in. Such demand can be accommodated by the virtual laboratory. In the concept of virtual laboratory, each laboratory sited around the globe with different facilities becomes part of this virtual laboratory and participate jointly in the experiment. The participating researchers or general viewers could concurrently view the experimental results and launch discussions in a timely manner. Considering the benefits of international cooperation, the concept of virtual laboratory should be applied to transnational collaborative experiment capability.

Some research efforts have been made on developing the technology of collaborative structural experiments, allowing more than one laboratory can jointly conduct a test involving more than one specimen at different test sites. The network technique was applied to a pseudo-dynamic test of a viaduct consisting of different types of piers performed at two experiment stations exchanging experimental data and visualization data through a shared file system in Kyoto University in Japan (Sugiura et al., 1998.) A networked numerical simulation of a pseudo-dynamic test of a base-isolated bridge is then carried out at three laboratories hundreds of kilometers apart in Korea (Yun et al., 2000.) A transnational pseudo-dynamic test is then successfully simulated between Kyoto University (Japan) and Korea Advanced Institute of Science and Technology (KAIST,

Korea), which exchanging data through shared disk units, demonstrating the capability and feasibility of future international collaborative experiments between Japan and Korea (Watanabe et al., 2001; Part et al., 2003) In an under-constructing 3-D full-scale earthquake testing facility in Japan, E-Defense, an ED-Net is being constructed, which may provide tele-observation and tele-discussion capability to both domestic and international research institutes, universities, or private sectors in the near future (Ohtani et al., 2002)

A NEES (Network for Earthquake Engineering Simulation) project, which has been launched by the National Science Foundation in USA. About fifteen universities or laboratories will be connected by high-performance network to explore the benefits of sharing and integrating laboratory resources, including expensive equipments, experiment data, and simulation codes, via network. Not only various types of experiment facilities will be updated or constructed, but also a network system, NEESgrid, will be developed to provide remote operation and observation of experiment equipment, real-time or time-independent data sharing and visualization, data linking among facilities, data repository and numerical simulation programs, and robust security management (NEES, 2003; Mahin, 2002.)

In this work, an Internet-based environment, named ISEE (Internet-based Simulation for Earthquake Engineering) is being developed for collaborative networked pseudo-dynamic experiments among geographically distributed laboratories. The key task in this research work is to develop the capability to perform distributed pseudo-dynamic experiments, which will be particularly valuable for evaluating the seismic performance of large-scale structure systems or components. The application focuses on slow pseudo-dynamic experiments, which the possible time lag among different laboratories collaboratively performing a distributed pseudo-dynamic experiment is acceptable. Two different approaches, namely, the Database Approach and the Application Protocol Approach, are prototyped to provide different solutions for network communication as well as collaborative framework in the ISEE. Database Approach employs a database server for data exchange and data repository; while the Application Protocol Approach directly uses point-to-point TCP/IP-based communication to transfer experimental data. This paper introduces the framework of the two approaches and the validation experiments.

3.1 Database Approach in ISEE

The ISEE framework with the database approach is composed of three major parts: the Data Center, the Facility Controllers, and the Analysis Engine (as shown in Fig. 9). The Data Viewers and the Cameras are accessory parts of the ISEE framework.

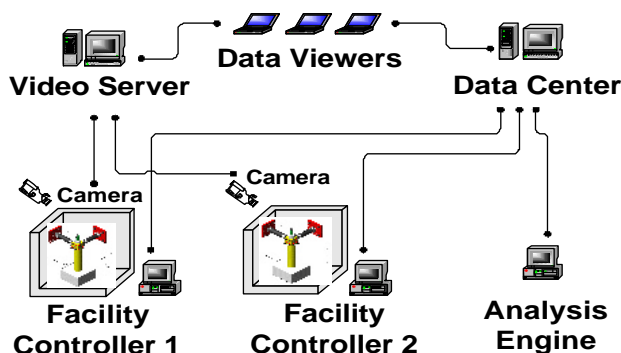


Figure 9 Database Approach in ISEE

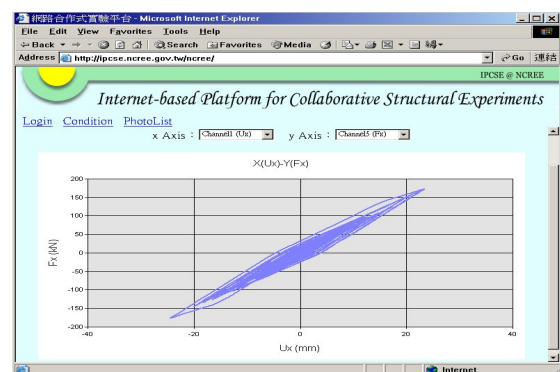


Figure 10 Web representation of real-time experiment data using Database Approach in ISEE

The Data Center

The Data Center serves as a data exchange hub and repository in ISEE database approach. All

the experiment data and analysis data are gathered to the Data Center during and after a pseudo-dynamic test. The Data Center employs a database server to facilitate exchange of experimental or analysis data among different ISEE parts (or components) that may reside in laboratories at different geographical locations. The Data Center also provides a WWW (World-Wide Web) interface for viewers to browse the experiment data (Fig. 10) or researchers to setup required experimental parameters for collaborative networked structural tests before the experiment starts. In this work, the Data Center employs the Microsoft SQL Server database and the IIS web server. In addition, for the C++ programs of the Analysis Engine and the Facility Controllers to easily communicate with the Data Center, a C++ class, named SQLAccess, is developed (Hsu, 2002) for incorporation into those C++ programs.

For the flexibility issue, this work uses a three-layer framework to construct the Database Approach (see Fig. 11.) The top layer is the user layer includes components for data viewers or researchers, including www browsers, analysis engine, and facility controllers. The bottom layer is the data layer, which is the database engine. Although the user-layer components get or exchange data with the database, they do not communicate with it directly, instead, through a middle layer. All the user layer components are database independent. Researchers maintaining the analysis engine or facility controllers do not need to worry about the detail of access the database. In addition, few extra efforts will be required on the user-layer components if we upgrade or change the database engine, for example, to a distributed or even transnational database system.

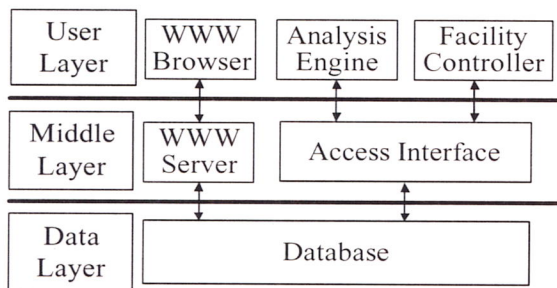


Figure 11 Three-layer framework of the Database Approach

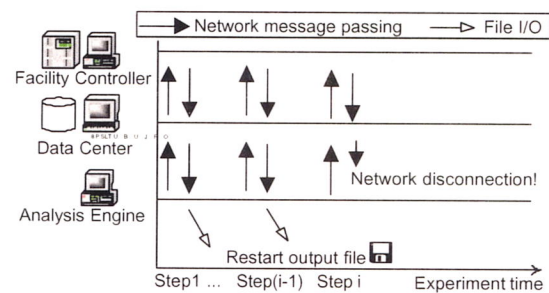


Figure 12a Experiment encountering an accident network disconnection

The Analysis Engine

The Analysis Engine computes the dynamic responses of a structure by considering both the finite element analytical responses and the real experimental responses of the specimen. In a collaborative pseudo-dynamic test, the Analysis Engine performs a finite element dynamic analysis, in which the resisting forces of one or more elements are obtained from the measured specimen resisting forces in the laboratory. The Analysis Engine sends the computed displacements to the Data Center for sharing with the Facility Controller(s) or Data Viewers.

In this work, the Analysis Engine is based on a finite element analysis program, named OpenSees (OpenSees, 2003), which allows researchers to add new components (e.g., new element types or material models). Two new element types, called pseudoGen1 and pseudoGen2, respectively, are implemented and added into the OpenSees framework (both derived from the 'Element' class in OpenSees.) The pseudoGen1 is superseded by pseudoGen2 because the latter one costs less elapsed time for a multiple-sited networked pseudo-dynamic experiment. More detail about the differences between the two types of pseudo-dynamic elements can be found in Tsai et al. (2003.) These pseudoGen elements act as actual specimen components in the finite element model by exchanging displacement and resisting forces with a Facility Controller through the Data Center. When each pseudoGen element is requested to return the resisting forces, it sends the element's displacements to the Facility Controller through the Data Center, waits for the resisting forces returned from the Facility Controller through the Data Center, and returns it to the OpenSees

component which sends the request.

A pseudoGen element acts as an actual specimen component in the finite element model by exchanging displacement and resisting forces with a Facility Controller through the Data Center. During each time step of the pseudo-dynamic analysis, the OpenSees calculates a predicted response, including the displacements, velocities, and accelerations of each node. Each pseudoGen element is then requested to return the dynamic resisting force in the predicted response. It gets the predicted displacements, sends them to the Data Center (so that the Facility Controller can push the specimen and measure the stiffness resisting forces), and gets the stiffness resisting forces. The dynamic resisting force of the pseudoGen is assembled with the stiffness resisting force, inertia forces, and the damping force. The inertia forces and damping forces are calculated by multiplying the acceleration and velocity vectors by the element mass and damping matrices, respectively, read from the user-specified file. The stiffness resisting force is the measured specimen resisting force, which reflects the nonlinear behavior of the specimen. After responding the dynamic resisting force, OpenSees calculates the displacement, velocity, and acceleration response of all nodes in the structures.

In this study, the Newmark-based Operator-Splitting (OS) method is employed by the Analysis Engine for the time integration of a pseudo-dynamic experiment. The concept of the OS method (Hughes and Liu, 1978) is to separate the damping and stiffness matrices into the implicit part and the explicit part. In the viewpoint of implementation, the only difference between the Newmark's method and the OS method is that the latter one considers the nonlinear effects only on the unbalanced force, i.e., the parts in Eq. (1), but not on the effective matrix. In a pseudo-dynamic experiment, the explicit part denotes the nonlinear part of the damping and stiffness matrices of the specimen(s), while the implicit part is the rest of the damping and stiffness matrices. The effective matrix (see Eq. 11) does not change during an analysis. There is no nonlinear iteration solution scheme (such as Newton Raphson's iteration) used in this work.

$$\{\Delta a_{i+j}\} = ([M] + \gamma\Delta t[C] + \beta\Delta t^2[K^I])^{-1} (\{p_{i+j}\} - \{\tilde{f}_{i+j}\}) \quad (11)$$

The Facility Controller

The Facility Controller is a software layer that can be used to drive the corresponding experimental facility in the laboratory. In a networked pseudo-dynamic experiment, the Facility Controller gets the displacement data from the Data Center, sends the displacements to the experimental facilities (servo hydraulic actuators), then receives restoring force data and sends them back to the Data Center. The control systems employed in NCREE Lab and NTU Lab are the MTS FlexTest IIm and MTS 407 controllers, respectively.

Network Fault Tolerance

A successful networked pseudo-dynamic experiment relies on network stability. Even a short period of network disconnection during an experiment may cut off the procedure of the experiment. In case of network disconnection during a network pseudo-dynamic experiment, the Analysis Engine and/or all Facility Controllers can not get the data they need, and the experiment will get suspended, even after the network is re-connected. It is not good to re-do a suspended experiment from the beginning if the specimen has been in nonlinearity status which behavior and properties may not be restored. However, typically the network between laboratories is Internet, which connection quality is not the focus of this research. To avoid of the failure of network pseudo-dynamic experiments caused by Internet disconnection, this research focuses on providing fault tolerance mechanism. A network fault tolerance solution is necessary for a network pseudo-dynamic test.

The fault tolerance solution in the Database Approach allows a re-start experiment to link with

a previous suspended one. By setting the initial condition (including displacements, velocities, accelerations, material stress-strain histories) to the re-start experiment, we provide a solution so that a broken-off experiment can be followed by a re-start experiment. The initial condition of the re-start experiment is just the final condition of the suspended experiment. After the re-start experiment finishes, a complete experiment result is available by combining the experiment result of the suspended experiment and the re-start experiment.

In this research, both pseudoGen1 and pseudoGen2 element types provide a restart function to link with a previous suspended experiment. During a network pseudo-dynamic analysis, the pseudoGen element(s) export the element resisting forces and displacements step-by-step to restart output files, including the data flowing through the Analysis Engine, Data Center, Facility Controller(s), then back to Data Center, and Analysis Engine in each time step. After the data (of resisting force) flows back to the Analysis Engine, the pseudoGen1 or pseudoGen2 elements append the displacements and forces to a restart file. In case of accident network disconnection, the experiment breaks off (see Fig. 12a), say, at the i -th step, the restart output file would then contain the displacements and forces data of at least the previous $(i-1)$ time steps. Also, the specimens are at the status of the $(i-1)$ -th or the i -th step (depends on where the network disconnection happens.) To restart the suspended experiment, a new restart experiment has to be constructed in the Data Center. In the restart experiment, the Analysis Engine imports resisting forces from the restart output file of the suspended experiment, instead of the Data Center, from the first step through the $(i-1)$ -th step (see Fig. 12b.) It is supposed that the analysis result before the $(i-1)$ -th step is exactly the same as those of the previous suspended experiment because the resisting forces fed into the Analysis Engine are exactly the same. After the i -th step, the Analysis Engine begins to send and receive data to Data Center, as it does in a normal experiment, until it completes the experiment. If the network disconnection happens again in a restart experiment, the restart solution can be applied again, until the whole experiment completes.

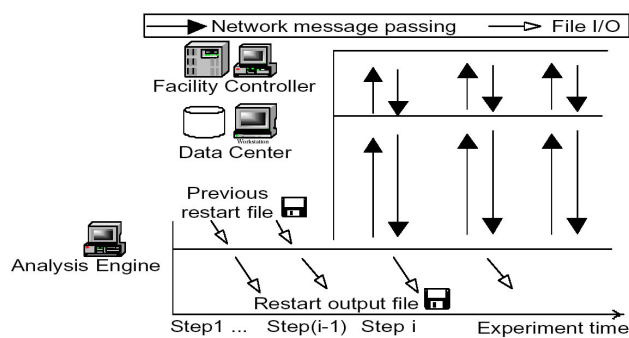


Figure 12b A restart experiment completing a previously disconnected experiment



Figure 13 A real-time video image through a WWW browser

Other Accessory Parts

Anyone on the Internet can access the experimental data from the Data Center using a Data Viewer (actually a WWW browser, such as Microsoft Internet Explorer or Netscape Navigator) without installing any additional software. The viewers can browse the time history curves of displacements or resisting forces, or the hysteresis loop of the displacements and resisting forces of any specimens of any completed or in-progress experiments using the Database Approach of ISEE (for example, see Fig. 10) With proper authorization, users can also get the plain numerical data of these displacements and resisting forces data from the Web page. With proper setup of Cameras and the Video Server, users can also see the real-time video images of the experiments. The Video

Server also provides a WWW interface to the Data Viewers (see Fig. 13)

3.2 Application Protocol Approach in ISEE

Platform Architecture

The Transmission Control Protocol/Internet Protocol (TCP/IP) suite was designed as an open standard to meet the demand of data transmission on rigorous network conditions (Postel 1981.) It connects a number of different networks designed by different vendors into a network of networks (the Internet). TCP guarantees reliable data transmission by providing services such as acknowledged delivery, error detection, retransmission if necessary, data sequence preservation, and flow control. IP provides addressing, routing, fragmentation and reassembly for data packets. TCP/IP stack thus handles robustly all those tedious works for data transmission between hosts on heterogeneous networks. Simply put, an application protocol is a set of predefined rules that defines the constitution and content of information to be shared and transmitted, as well as the sending/receiving behaviors to be obeyed by the applications.

The Application Protocol Approach proposed a TCP/IP-based platform, the “Platform for Networked Structural Experiments” (PNSE, see Fig. 14) on which data transmission is implemented by transferring predefined data packets defined by a preliminarily proposed application protocol, the “Networked Structural Experiment Protocol” (NSEP), to realize the goal of Internet collaborative structural experimentation. A series of transnational pseudo dynamic tests upon a specimen composed of two double-skinned concrete filled in tube (DSCFT) columns located in two different laboratories were conducted to verify the validness and efficiency of PNSE. The characteristic of environment independency of PNSE was also verified by a series of networked pseudo dynamic tests were also performed upon a full scale 3-story 3-bay concrete filled steel tube (CFT) and buckling restrained braced (BRB) composite frame.

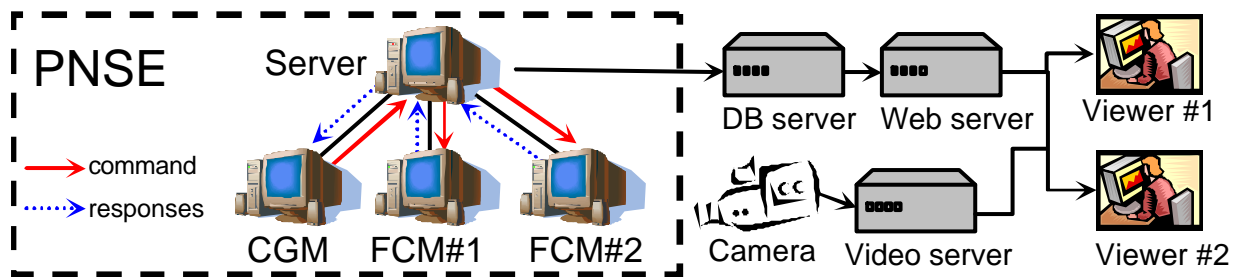


Figure 14 The Architecture of the Application Protocol Approach

Platform for Networked Structural Experiments

This study proposed a platform, PNSE, to meet the goal of networked collaborative structural experimentation. The architecture of PNSE is illustrated in Fig. 14. PNSE concentrates on the core tasks related to successful and robust progression of the networked experiment and excludes functionalities of digital and video data storage and display on the Internet, which can be implemented by commercially available software such as Microsoft SQL server or Windows Media Player. The PNSE is a multi-client system with all the clients connected to the server with a TCP point-to-point connection. The PNSE server is essentially the center of the system and provides services of message dispatch and data delivery for all clients. PNSE has two kinds of clients: the Command Generation Module (CGM) and the Facility Control Module (FCM). The CGM generates command to be imposed on the specimen located at different laboratories by all the FCMs. It can be a numerical integration algorithm in the scenario of pseudo dynamic testing, an input module that queues predefined command profile in the case of quasi-static testing, or simply a remote application with an user interface that allows its users to enter command promptly. The

CGM prepares the commands for all FCMs in a single packet and sends the packet to the server. After receiving the packet, the server forwards them to corresponding FCMs. The FCMs then control the actuators to impose the individual command received from the server on the specimen located in their laboratories. After the command is successfully executed, an FCM measures or calculates the response and sends it back to the server. When the server receives all the packets, it integrates them and sends it to the CGM as a notification of the completion of command execution. Those actions performed by the PNSE server, CGM and FCMs described above constitute a cycle, which is the smallest unit to be executed repeatedly until the collaborative experiment finishes.

On PNSE, human communication is still necessary but not as easy to implement as in a traditional structural laboratory since all the participants (including test operators and interested individuals on the Internet) are scattered around at different locations. However, it is very difficult or even impossible to clearly define all possible events (such as the detailed damage condition of the specimen or any action taken by the laboratory staffs to fix the specimen, etc.) that can occur in a networked structural experiment in the application protocol. To address this issue, a feature of instant discussion is included in the application protocol for all PNSE participants to promptly transfer relevant information about the experiment by means of sending and receiving human readable texts.

Characteristics of PNSE

PNSE is an environment independent platform since it is constructed based on the TCP/IP suite which is supported by almost all currently available operating systems and programming languages. High interoperability can be assured regardless of the diverse environment composed of computer hardware, operating system, and programming language. This suggests only minimum programming work has to be done to incorporate existing numerical analysis programs and facility control programs on PNSE.

The PNSE server sits the central position in the star-topology connection system. However, except for maintaining a simple login procedure for each connection attempt, it does not behave as an “administrator” of the system for any purpose other than security concern. That is, it does not mandate any clients to perform any specific task during the course of the experiment and only serves as a “spokesman” for all clients. For example, the server never actively queries the CGM for command to be executed nor it ever queries the running state of any of its clients. It is the CGM’s responsibility to actively send the command to the server, and similarly, it is every client’s responsibility to send a notification of change of its running state to the server when necessary. Actually, both the PNSE server and clients are stipulated to make “active notifications,” meaning that the one who owns relevant information should actively inform the other side of the connection, when necessary. This stipulation naturally makes the PNSE an event-reflective platform, provided that all significant events that can occur in experiments are clearly defined in the application protocol.

In other words, for any PNSE client, any information that comes from the server is actually originally sent or caused by other clients. This characteristic actually makes the PNSE a truly cooperative platform because every client plays an indispensable role and has its responsibility to behave as stipulated to jointly make the progression of the experiment. This leads PNSE to an event-driven system. The progression of the experiment can be thought of a series of responsive behaviors to all events defined in the application protocol. The characteristic of event-driven enhances the extensibility of PNSE since when events and interactions get more and more complex in the future, all that has to be done is to add more message handler functions in programs without drastically modifying the program architecture.

In addition to make the PNSE an event-driven and a truly cooperative platform, the stipulation of active notification actually increases the overall data transmission efficiency of PNSE. Other than the active notification stipulation proposed in this study, an “information query mechanism

(IQM)” can be an alternative approach to realize an event-reflective platform. This mechanism basically stipulates that the one who need relevant information should actively query for that information from the one who owns it repeatedly until the information is acquired. Techniques utilizing IQM to exchange data over the networks have been employed in other research works due to its simplicity. Examples include accessing shared-used disk files (Sugiura et al. 1998, Yun et al. 2000, and Watanabe et al. 2001) and depositing and retrieving data from a database repository (Tsai et al. 2003). However, IQM generally decreases the overall system efficiency since the polling operations have to be done frequently enough so that information can be acquired promptly enough, but frequent query wastes a lot of time and network resources especially when the information queried has not been updated at the moment of query. As for the active notification stipulation proposed in this study, the system efficiency could be drastically increased since all the PNSE modules (both the server and the clients) have to do is to wait for the information to come automatically without spending any time and network resources to poll from the other side of the connection continuously.

PNSE is designed and constructed in a start-topology connection system to simplify the network topology and hence the communication flow. Instead of connected to any other client, a PNSE client is designed to connect to the server only. Consequently all data packets must be directed to the server first and then can they be dispatched to their destination by the server. This would cause additional time consumed in data transferring but this architecture tremendously simplifies the network communication flow since for each client program it only has to handle information that comes from the server, instead of the many other clients. This design can save large amount of efforts needed in programming especially when events and interactions get more and more complex in the future. Since all the information must be directed to the server first, the PNSE server appears to be the best candidate to publicize all valuable information on the Internet, including the general information (metadata) of the current experiment, all the open signal values, running state of the experiment, running states of all client programs.

In any traditional structural laboratory, due to various reasons such as damage examination, photographing, minor specimen or instrumentation adjustment, or safety concerns, an experiment can be suspended, resumed or even stopped prematurely. In the scenario of virtual laboratory, privilege of change of the running state is still preserved for each participating laboratory, although all the FCMs are stipulated to report any change of its running state to the system.

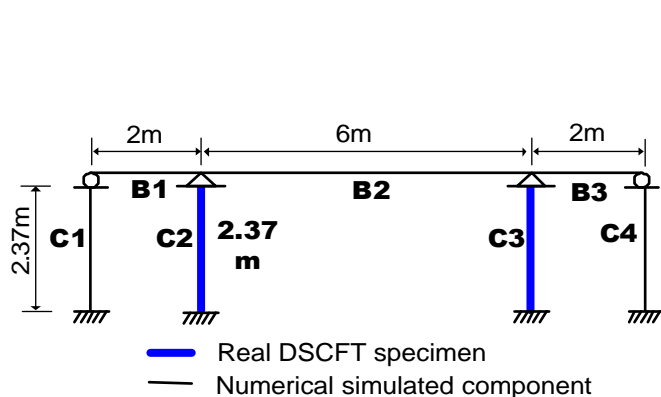


Figure 15 Substructure Pseudo-dynamic DSCFT Tests using Database Approach

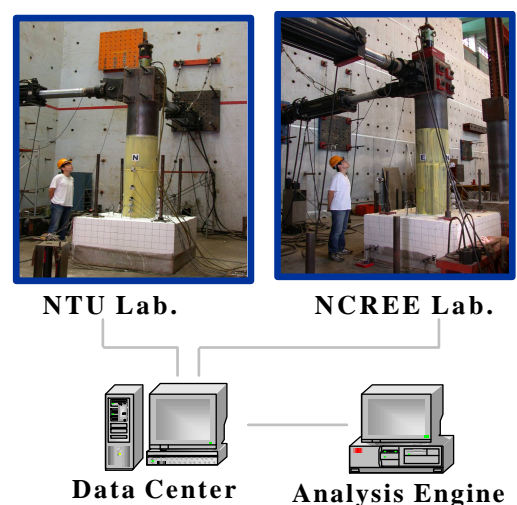


Figure 16 Configuration of the DSCFT Tests using Database Approach

3.3 Experimental Validation

To verify the validness and efficiency of the Database Approach and Application Protocol Approach, a series of domestic and transnational collaborative experiments were conducted upon a bridge with two double-skinned concrete-filled tube (DSCFT) bridge specimens. More details of these tests can be found in (Tsai et al., 2003). The two columns were fixed to the ground and pin-connected to the rigid superstructure with earthquake ground motions along two horizontal directions, hence each pier has two controlled degrees of freedom assigned at the top. Two piers of the structure are constructed and located at National Taiwan University Laboratory (NTU Lab.) and National Center for Research on Earthquake Engineering Laboratory (NCREE Lab.) respectively.

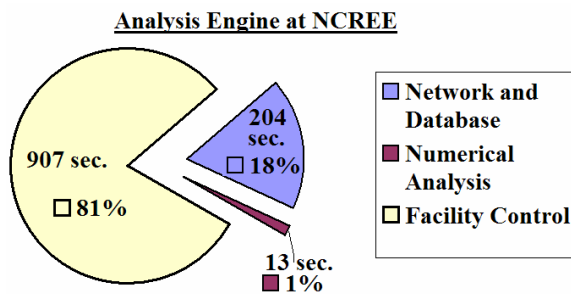


Figure 17a NCREE-NTU Testing Result using Database Approach

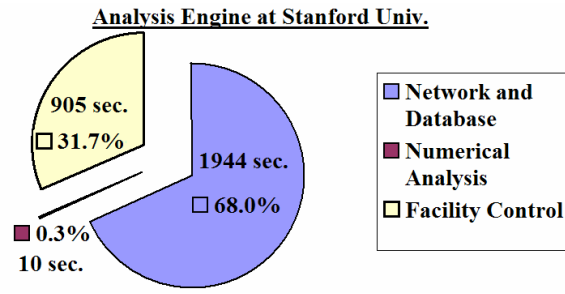


Figure 17b NCREE-NTU-Stanford Testing Result using Database Approach

A series of 1000-time-step substructure pseudo-dynamic tests demonstrates the feasibility of the Database Approach. A four-pier bridge subjected to a bi-directional earthquake is simulated (see Fig. 15), while two of the four piers are real specimens and other components are numerically simulated by the OpenSees-based analysis engine (see Fig. 16.) In average, the time cost on network transmission costs 204 seconds of the total elapsed time of 1124 seconds (see Fig. 17a), less than 20% of total time in domestic tests (across NTU and NCREE, while the Data Center and the Analysis Engine are placed at NCREE.) The network costs less than 70% of total elapsed time in transnational tests, (see Fig. 17b) in which the Analysis Engine is moved to Stanford University in USA.

A series of transnational pseudo-dynamic tests are also conducted using Application Protocol Approach for a two-pier bridge system (see Figs. 18 and 19.) In the tests, the server resided in Stanford University, while the CGM runs at the NCREE Lab. A 1999 Chi-Chi earthquake motion is selected as the excitation, which PGA is reduced so that the specimens keep in elastic status for the networked tests. The test results reasonably agrees with the one obtained from pure numerical analysis, indicating that all signals including commands and responses were correctly transmitted over the Internet. Time consumed for a data packet to make a round trip between NCREE and Stanford is 0.17 seconds in average, which is nearly the same as the network performance tested by using an operating system ping-pong network testing program (0.16 seconds.)

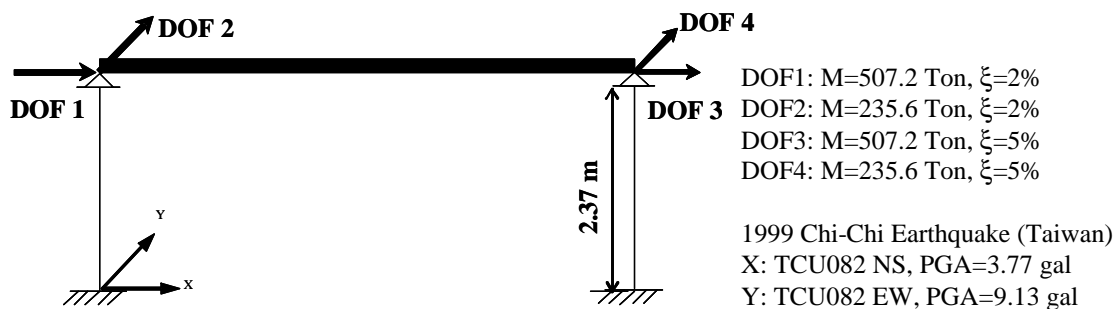


Figure 18 Pseudo-dynamic DSCFT Tests using Application Protocol Approach

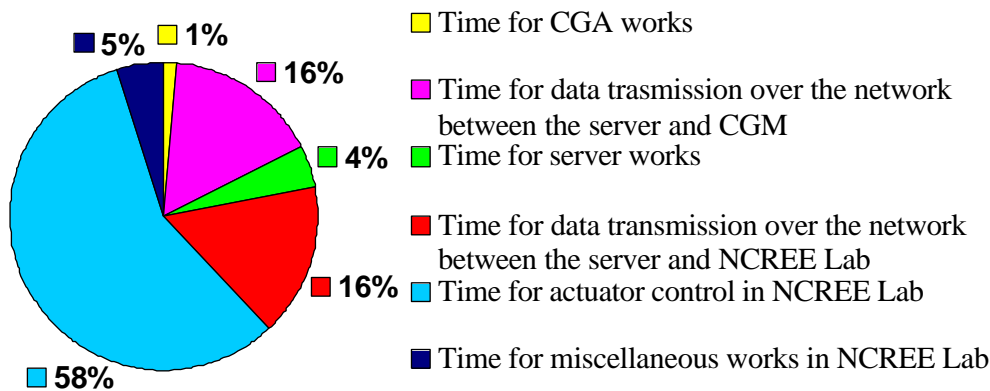


Figure 19 A Restart Experiment Completing a Previously Disconnected Experiment

3.4 Summary

An Internet-based environment, called ISEE, has been prototyped in this work for collaborative networked structural experiments among geographically distributed structural laboratories. Two approaches, the Database Approach and the Application Protocol Approach, have been prototyped and employed to provide different solutions for network communication as well as collaborative framework in ISEE. The Database Approach employs a database server with a World-Wide Web service as a data center to serve as a data exchange and repository center, and all network communications are performed by calling SQL commands. The Application Protocol Approach develops a communication protocol based on TCP/IP suite for direct exchange of messages in ISEE. Several networked pseudo-dynamic tests have been conducted to investigate the feasibility and efficiency of ISEE. The tested experiment sites include the NCREE Lab and the NTU Lab. A series of networked experiments using Database Approach and Application Protocol Approach, which the components of the experiments are placed at the NTU Lab, NCREE Lab and Stanford University (in USA) has been completed and validates the feasibility of the ISEE for future networked collaborative pseudo-dynamic experiments.

Acknowledgements

The authors are deeply grateful to the National Science Council for financial support, the Ministry of Finance for building tax data, Central Weather Bureau for complete earthquake records, and the technical supports provided by the researchers at National Center for Research on Earthquake Engineering.

References

- Boore, D. M., Joyner, W. B., and Fumal, T. E., 1997. "Equations for estimating horizontal response spectra and peak acceleration from western north American earthquakes: a summary of recent works," *Seismological Research Letter*, 68, 128-153.
- Hsu, C. W. (2002), "Internet-based Platform for Collaborative Structural Experiments," Master Thesis, Department of Civil Engineering, National Taiwan University, Taiwan ROC. (in Chinese)
- Hughes, T. J. R. and Liu, W. K. (1978), "Implicit-Explicit Finite Element in Transient Analysis: Stability Theory," *Journal of Applied Mechanics*, Vol. 45, pp. 371-374.
- Ishihara, K., 1993. "Liquefaction and flow failure during earthquake", *Geotechnique*, 43 (3), 315-415.
- Iwasaki, T., Arakawa, T., and Tokida, K., 1982. "Simplified procedures for assessing soil liquefaction during earthquake", *Proceedings of the Conference on Soil Dynamics & Earthquake Engineering*, 2, 925-939.
- Jean, W. Y., 2001. "A study on the characteristic earthquake and site effects and its application to the hazard evaluation", Report of National Center for Research on Earthquake Engineering, NCREE-01-036.
- Mahin, S. (2002), "White Paper: Towards a Vision for the NEES Collaboratory," NEES Consortium Development Project, Consortium of Universities for Research in Earthquake Engineering, USA.
- NEES (2003). "Network for Earthquake Engineering Simulation," Homepage web site: <http://www.nees.org/>
- Ohtani, K, Ogawa, N., Katayama, T. and Shibata, H. (2002). "3-D Full-Scale Earthquake Testing Facility and Earthquake Engineering Network," *Proceedings of the Third World Conference on Structural Control*, Italy, pp.

1019-1024.

- OpenSees (2003), "Open System for Earthquake Engineering Simulation," Homepage web site: <http://opensees.berkeley.edu/>
- Park, D-U., Yun, C-B., Lee, J-W., Nagata, K., Watanabe, E. and Sugiura, K. (2003). "On-Line Pseudo-Dynamic Network Testing on Base-Isolated Bridge Using Internet and Wireless Internet," Proceedings of the Sixteenth KKCNN Symposium on Civil Engineering, Korea, pp. 121-128.
- Postel Jon. (1981a), "Transmission Control Protocol – DARPA Internet Program Protocol Specification", RFC-793, DARPA.
- Risk Management Solutions, Inc., 1997. Earthquake Loss Estimation Method – HAZUS 97 Technical Manual, National Institute of Building Sciences, Washington, D.C.
- Sugiura, K., Nagata, N., Suzuka, Y., and Watanabe, E. (1998), "Internet Related Structural Testing," Proceedings of The Eighth KKNN Seminar on Civil Engineering, Singapore, pp. 219-224.
- Tsai, K. C., Hsieh, S. H., Yang, Y. S., Wang, K. J., Wang, S. J., Yeh, C. C., Cheng, W. C., Hsu, C. W., and Huang, S. K. (2003), "Network Platform for Structural Experiment and Analysis (I)," Technical report NCREE-03-021, National Center for Research on Earthquake Engineering, Taiwan ROC.
- Watanabe, E., Yun, C. B., Sugiura, K., Park, D. U., and Nagata, K. (2001), "On-Line Interactive Testing between KAIST and Kyoto University," Proceedings of The Fourteenth KKNN Symposium on Civil Engineering, Kyoto, Japan, pp. 369-374.
- Wells, D. L. and Coppersmith, K. J., 1994. "New empirical relationships among magnitude, rupture length, rupture width, rupture area, and surface displacement," *Bulletin of Seismological Society of America*, 84, 4, 974-1002.
- Wu, Y. M., Shin, T. C., and Chang, C. H., 2001. "Near real-time mapping of peak ground acceleration and peak ground velocity following a strong earthquake," *Bulletin of Seismological Society of America*, 91, 5, 1218-1228.
- Yeh, C. H., Jean, W. Y., and Chung, L. L., 2003. "Development of early estimation system for seismic disasters in Taiwan", submit to review in *Journal of the Chinese Institute of Civil and Hydraulic Engineering*.
- Yeh, C. H., Hsieh, M. Y., and Loh, C. H., 2002a. "Classification and parametric study on soil liquefaction potential", Proceedings of the Second Japan-Taiwan Workshop on Lifeline Performance and Disaster Mitigation, Kobe, Japan, May 13-15.
- Yeh, C. H., Hsieh, M. Y., and Loh, C. H., 2002b. "Estimations of soil liquefaction potential and settlement in scenario earthquakes", Proceedings of the Canada-Taiwan National Hazards Mitigation Workshop, Ottawa, Canada, July 17-19.
- Yun, C. B., Lee, I. W., Part, D. U, and Watanabe, E. (2000), "Remote Parallel Pseudo-Dynamic Testing on Base-Isolated Bridge Using Internet," Proceedings of The Thirteenth KKNN Symposium on Civil Engineering, Taipei, Taiwan, pp. 87-92

EXPERIMENTAL STUDY ON TRI-AXIAL NON-LINEAR RESTORING FORCE CHARACTERISTICS OF R/C COLUMNS

K. Takiguchi¹⁾, K. Nishimura²⁾, and T. Okuda³⁾

1) Professor, Dept. of Mechanical and Environmental Informatics, Tokyo Institute of Technology, Japan

2) Assistant Professor, Dept. of Architecture and Building Engineering, Tokyo Institute of Technology, Japan

3) Graduate Student, Dept. of Built Environment, Tokyo Institute of Technology, Japan

ktakiguc@tm.mei.titech.ac.jp, knishimu@tm.mei.titech.ac.jp, tokuda@tm.mei.titech.ac.jp

Abstract: Four reinforced concrete column specimens were prepared for tri-axial loading test. The specimens had 150x150mm square section and 600mm clear span. A new experimental apparatus that allows tri-axial translation and restricts tri-axial rotation of head of the specimens was developed. The specimens were subjected to three-directional cyclic loading in the range of 0.1 to 0.4 axial force ratio. As a result, it was verified that rotation of head of the specimens could be restricted, experimental data for understanding and modeling restoring force characteristics of the R/C columns subjected to anti-symmetric bending and varying axial force were obtained, and considerations regarding restoring force model by using the theory of plasticity were carried out.

1. INTRODUCTION

It is necessary to formulate restoring force characteristics of structures or members for earthquake response analysis, and tri-axial response analysis have been appealed. Experimental tests of structures or members are indispensable for understanding the restoring force characteristics. One-axial restoring force characteristics of R/C members are understood fairly well. Experiments of R/C members subjected to two-directional loading have been made in the past researches (for example, Takiguchi et al. 1979, and Takiguchi et al. 2001). However there are few experimental research focused on tri-axial behaviors of R/C structures and members.

Four reinforced concrete column specimens were prepared for tri-axial loading test. The specimens had 150x150mm square section and 600mm clear span. A new experimental apparatus that allows tri-axial translation and restricts tri-axial rotation of head of the specimens was developed. The specimens were subjected three-directional cyclic loading in the range of 0.1 to 0.4 axial force ratio. The purposes of this study are to verify validity of the new experimental apparatus, and to understand the tri-axial behaviors of R/C columns for modeling the restoring force characteristics by using the theory of plasticity, which is one of the macro modeling (for example, Takizawa and Aoyama 1976, and Nishimura and Takiguchi 2003).

2. EXPERIMENTAL PROGRAM

2.1 Apparatus

A new experimental apparatus for a column specimen subjected to tri-axial loading was developed.

Figure 1 represents loading and measuring system. Base of the column was fixed horizontally, and head of the column was allowed tri-axial translation and restricted tri-axial rotation. A system that consists of a cross of steel beams and eight hydraulic cylinders restricts lean of the head, and a parallel rule of link mechanism (Takiguchi et al. 1979) restricts rotation that causes torsion of the column. As shown in Figure 2, the system with hydraulic cylinders allows vertical translation and keeps horizontal. The eight hydraulic cylinders have capacity of 500kN, and were connected by sixteen ultra-high-pressure hoses of the same size. Strain gages were pasted to the beams of the cross at a distance of 1600mm from joints of beams and cylinders to measure loading of the each beam. The specimen is subjected to horizontal loading by two hydraulic jacks of 200kN capacity through loading beams, and axial force by one hydraulic jack of 500kN capacity. Load cells on the hydraulic jacks measure loading of these three jacks.

Five displacement transducers measured tri-axial rotation of head of the specimen as shown in Figure 1. The displacement transducers of No.1 to 3 decide the lean of the head, and No.4 and 5 measure the rotation regarding torsion. Four measuring instruments measured tri-axial translation. The measuring instrument connects head of the specimens and the other end through ball bearing of self-aligning rod-ends, and measures distance between the ends with displacement transducer. Tri-axial relative displacement of head to base of the specimen is calculated with these five displacement transducers and three out of four measuring instruments. Two measuring instruments regarding vertical direction make two results of relative displacement, and we take an average.

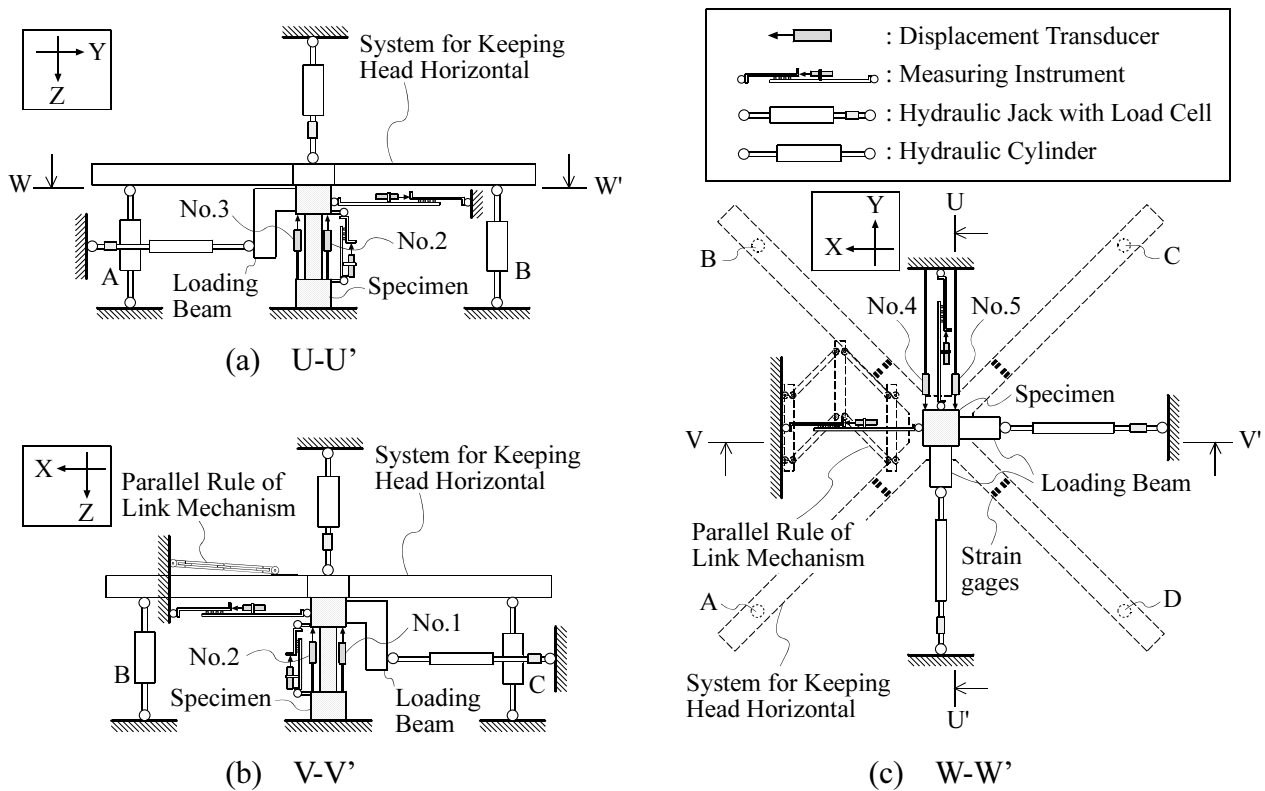


Figure 1 Loading and Measuring System

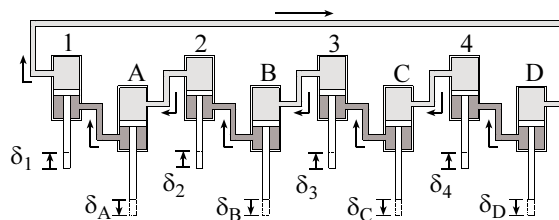


Figure 2 System of Eight Hydraulic Cylinders

2.2 Specimens and Loading Plan

Four reinforced concrete column specimens were prepared for the test. Table 1 shows dimensions of specimens and mechanical properties of concrete and reinforcements, and Figure 3 shows details of specimen. Shear span-to-depth ratios of specimens are equal to 2.0. Deformed bar and round bar, D10 and 4ϕ , are used for longitudinal bars and shear reinforcements, respectively. The specimens were designed to yield in flexural and not to fail in shear. The specimens were subjected to tri-axial cyclic loadings. Axial force was varied in the range of 0.1 to 0.4 axial force ratios.

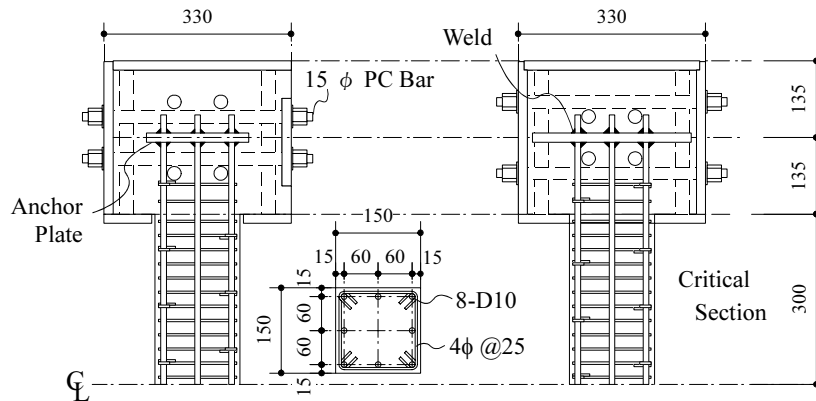


Figure 3 Detail of Specimen

Table 1 Dimension of Specimens and Properties of Reinforcements and Concrete

Name of Specimen	Section b×D (mm)	Length of Clear span (mm)	Reinforcements		Concrete			Axial Force Ratio (%)
			Main Reinf.	Shear Reinf.	Age at Column Test (days)	Compressive Strength σ_B (N/mm ²)	Splitting Tensile Strength σ_T (N/mm ²)	
CBS-3D-1	150×150	600	8-D10 $\sigma_y = 356 \text{ N/mm}^2$ $p_g = 2.56 \%$	$4\phi @25$ $\sigma_y = 411 \text{ N/mm}^2$ $p_w = 0.67 \%$	51-54	33.56	2.97	32
CBS-3D-2					57-60	33.56	2.94	10-40
CBS-3D-3					56-60	31.14	2.93	10-40
CBS-3D-4					63-66	31.78	2.81	15.5-33.4

Curing in air after 7 days moist curing

3. TEST RESULTS AND CONSIDERATION

3.1 Verification of Apparatus

Displacements and forces of test results are expressed on rectangular coordinate, and compressive axial displacement and force are taken as positive, as shown in Figure 4.

Figure 5 shows rotation of the test results. It can be said that the system with hydraulic cylinders and the parallel rule of link mechanism could restrict the rotation of head of specimen, and those had equal ability. The maximum rotations of four specimens were 0.0012 rad, 0.0027 rad, and 0.0035 rad in r_x , r_y , and r_z , respectively.

The maximum forces, which acted on hydraulic cylinders through the beams of system for keeping horizontal the head of specimens, were 2.5 kN, 3.7 kN, 2.7 kN, and 1.6 kN compressive force on the tests of CBS-3D-1, CBS-3D-2, CBS-3D-3, and CBS-3D-4, respectively. These maximum forces were quite smaller than axial force that the specimens were subjected. The force, which acted on the hydraulic cylinder, was obtained by calculating curvature of beam of the cross with Navier's assumption and strain measured by strain gages posted on the beam. The system for keeping horizontal the head of specimens could restrict rotation of the head without bearing axial force.

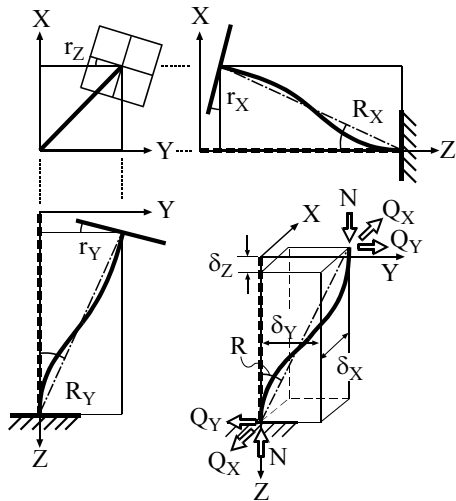


Figure 4 Displacements and Forces

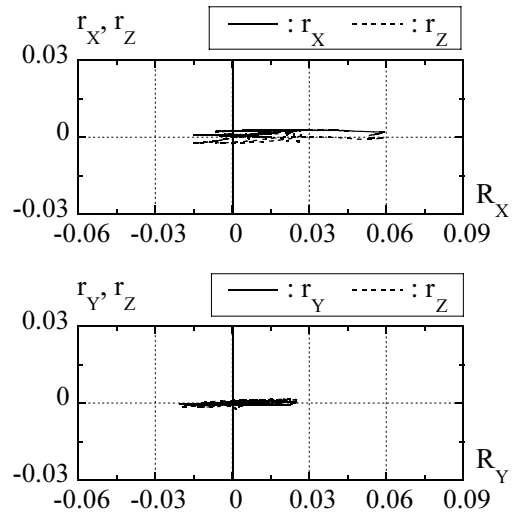


Figure 5 Rotation of Head of CBS-3D-2

3.2 Test Results and Consideration

Figure 6 to 9 show test results of four specimens. The maximum R , which was lean of axis of member to Z -axis as shown in Figure 4, were 0.032 rad, 0.043 rad, 0.061 rad, and 0.081 rad in CBS-3D-1, CBS-3D-2, CBS-3D-3, and CBS-3D-4, respectively. Loading history influenced the maximum lateral displacement. Tendency could be seen that cyclic lateral loading under higher axial force made the lower maximum lateral displacement.

Dotted lines shown in Q_X - N and Q_Y - N relationships of Figure 7 to 9 represent strength curve that have parabola in Q_X - N and Q_Y - N relationships and circle in Q_X - Q_Y relationship. The parabola is approximated curve of strength given by the additional theorem, perfectly rigid-plastic assumption on stress-strain relationships of concrete and reinforcement, and anti-symmetric bending moment distribution of the specimen. Compressive strength of concrete and yield strength of reinforcement obtained through test of material are used for calculation. It can be said that strength of the column specimens can be estimated with the strength curve as shown in Figure 7 to 9 and the strength curve can be regarded as yield surface.

CBS-3D-1 was subjected to alternate one-directional lateral loading in X and Y direction under a constant axial force, as shown in Figure 6. First, X -directional loading was dealt in the range of -6 mm to 6 mm with no Y -directional loading, and next Y -directional loading was dealt in the same range with no X -directional loading. These processes were repeated as displacement was increased. Figure 10 shows the results of CBS-3D-1, which Q_X - δ_X and Q_Y - δ_Y relationships are drawn on the same sheet. It can be said that restoring force characteristics aren't influenced by loading history in the direction lied at right angle because Q_X - δ_X and Q_Y - δ_Y relationships are almost equal.

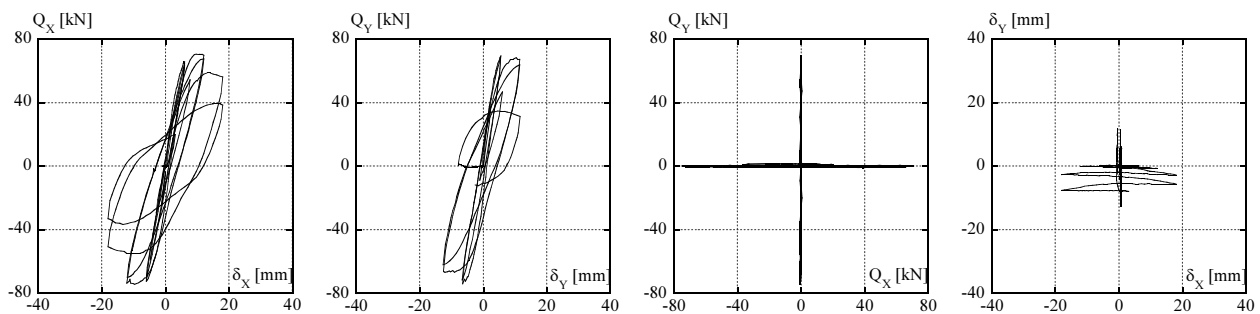


Figure 6 CBS-3D-1

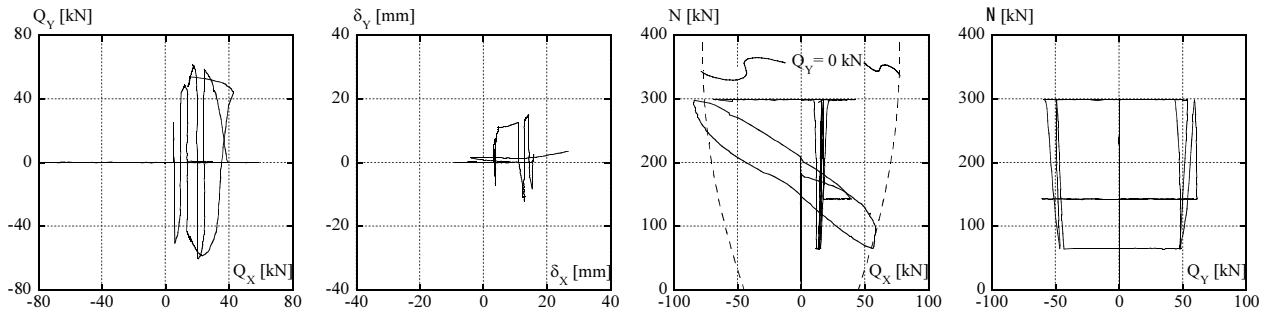


Figure 7

CBS-3D-2

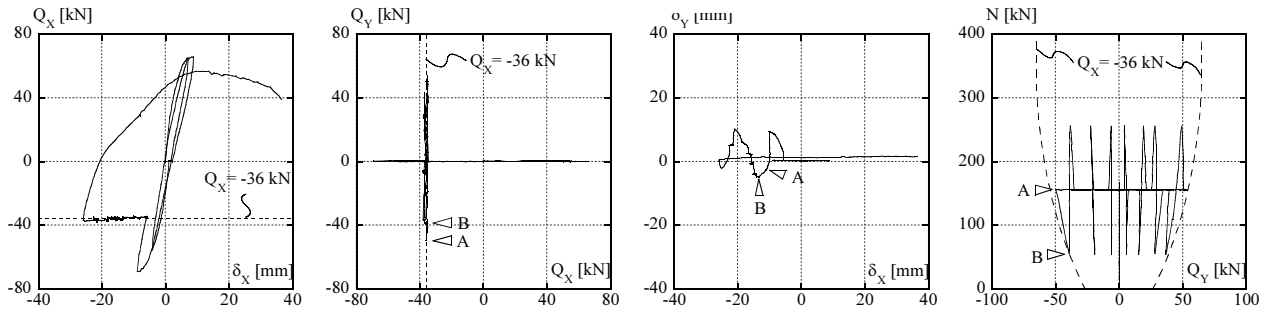


Figure 8

CBS-3D-3

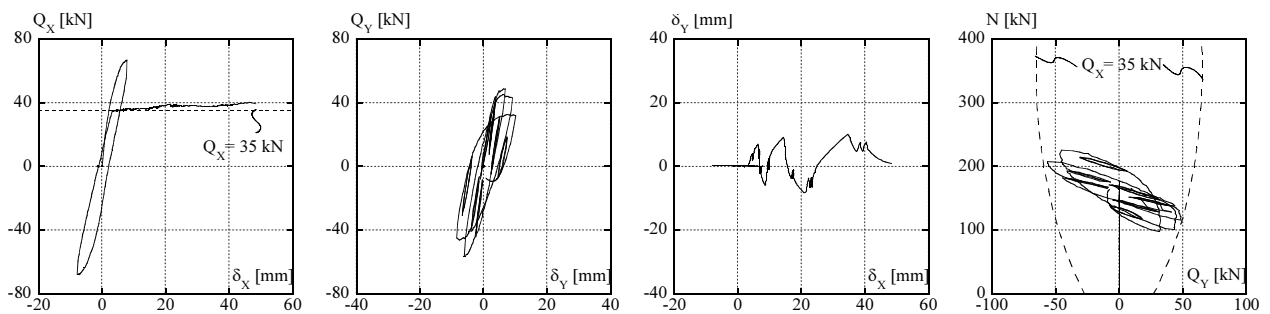


Figure 9

CBS-3D-4

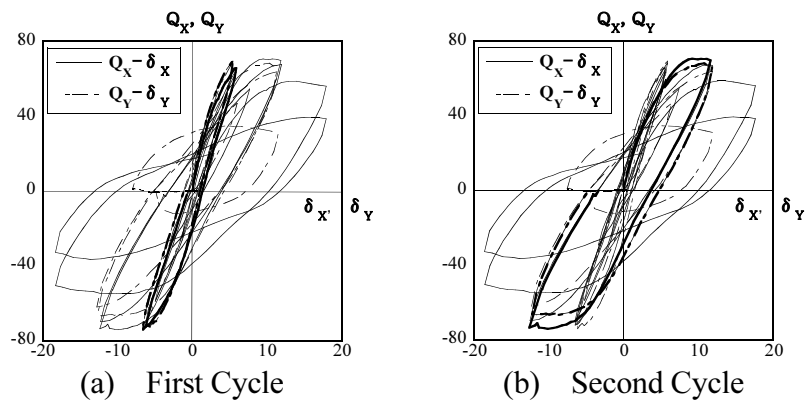


Figure 10 Hysteresis Loops

Figure 11 shows a stage from A to B the test result of CBS-3D-3 shown in Figure 8. In the stage, axial force was decreased after the specimen was yielding. displacement increment vector of the test result lied in direction of loading in the stage from A to B. When the column specimen was yield and its displacement directed toward loading, force-displacement relationship were analogous to the theory of plasticity (for example, Chen 1994), because plastic displacement increment vector of calculation roughly lied in normal direction of yield surface, as shown in Figure 11. The plastic displacement increment was given by subtracting elastic displacement increment from total displacement increment

of the test result, where elastic displacement increment was calculated by multiplying force increment of the test result and inverse of elastic rigidity together. Elastic rigidity was decided on inclination of line that was regarded as linear relationship on initial force-displacement curve of the test result.

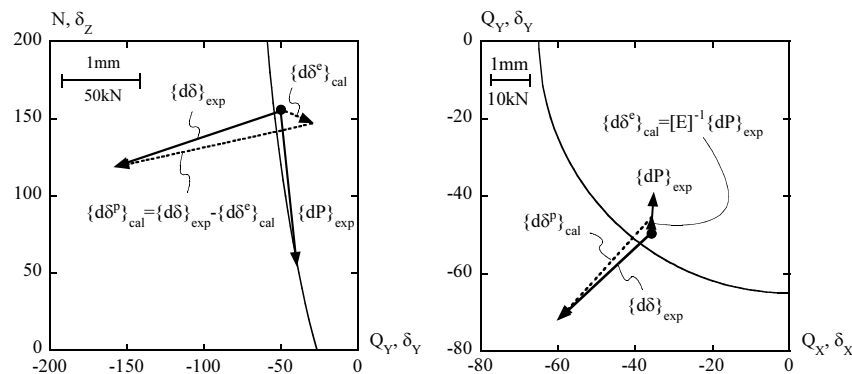


Figure 11 Plastic Flow

4. CONCLUSIONS

Four reinforced concrete column specimens were prepared for tri-axial loading test. The specimens had 150x150mm square section and 600mm clear span. A new experimental apparatus that allow tri-axial translation and restrict tri-axial rotation of head of specimens was developed. The specimens were subjected to three-directional cyclic loading in the range of 0.1 to 0.4 axial force ratio. As a result, the following conclusions were found.

- [1] Rotation of head of specimens could be restricted, and experimental data for understanding and modeling restoring force characteristics of the R/C columns subjected to anti-symmetric bending and varying axial force were obtained.
- [2] Surface, which was calculated with the additional theorem, perfectly rigid-plastic assumption on stress-strain relationships of concrete and reinforcement, and anti-symmetric bending moment distribution of a column, could estimate strength of the R/C columns, where compressive strength of concrete and yield strength of reinforcement obtained through test of material were used.
- [3] One-axial restoring force characteristics under a constant axial force weren't influenced by loading history in the direction lied at right angle.
- [4] When the R/C columns were yielding and those displacements directed toward loading, force-displacement relationships were analogous to the theory of plasticity.

References:

- Takiguchi, K., Nishimura, K., and Hirai, K. (2001), "Experimental study on two-dimensional restoring force characteristics of R/C columns under varying axial force," *Journal of Structural and Construction Engineering*, Architectural Institute of Japan, 539, 111-118, (in Japanese).
- Takiguchi, K., Kokusho, S., Kobayashi, K., Ishida, A., and Kimura, M. (1979), "Study on the Restoring Force Characteristics of Reinforced Concrete Columns to Bi-Directional Displacements, Part 1 Development and Examination of Loading Apparatus for Testing Reinforced Concrete Columns Subjected to Bi-directional Horizontal Forces and Axial Force," *Journal of Structural and Construction Engineering*, Architectural Institute of Japan, 286, 29-35, (in Japanese).
- Takizawa, H., and Aoyama, H. (1976), "Biaxial effects in modeling earthquake response of R/C structures," *Earthquake Engineering and Structural Dynamics*, 4, 523-552.
- Nishimura, K. and Takiguchi, K. (2003), "Tri-Axial Non-Linear Restoring Force Model of R/C Structures by Using an Analogy to the Plastic Theory," *Journal of Structural and Construction Engineering*, Architectural Institute of Japan, 566, 113-120, (in Japanese).
- Chen W.F. (1994), "Constitutive Equations for Engineering Materials, 2," Elsevier.

Stress-Strain Relationship for the Localized Compressive Failure Zone of Concrete under Cyclic Loading

Ken Watanabe¹⁾, Junichiro Niwa²⁾, Hiroshi Yokota³⁾, and Mitsuyasu Iwanami⁴⁾

1) Doctoral student, Department of Civil Engineering, Tokyo Institute of Technology, Japan

2) Professor, Department of Civil Engineering, Tokyo Institute of Technology, Japan

3) Chief research engineer, Structural Mechanics Division, Port and Airport Research Institute, Japan

*4) Research engineer, Structural Mechanics Division, Port and Airport Research Institute, Japan
96b31400@cv.titech.ac.jp, jniwa@cv.titech.ac.jp, hiroy@pari.go.jp, iwanami@pari.go.jp*

Abstract: To predict the behavior of a concrete structure under seismic loading, the stress-strain curve of concrete in compression is important material characteristic. Current models are including the influence of compressive strength. By the way, the localization of failure of concrete in compression is also influential on the stress-strain curve; hence, the stress-strain curve is strongly changing with the aspect ratio of a concrete specimen. The objective of this study is to establish the hysteresis model of concrete in compression considering the localization and compressive strength of concrete. To overcome the localization of failure, it is assumed that the zone of strain softening (failure zone) of a specimen is coupling in series to “transition zone” and “unloading zone”, such that the stresses carried by these 3 zones are equal and their strains are superimposed with considering the extent of each zone. In this paper, the hysteresis loop model for a failure zone, which governs the overall behavior of concrete structures, was presented in comparison with the experimental loop.

1. INTRODUCTION

To predict the behavior of a concrete structure under seismic loading, the model for the stress-strain relationship of concrete under cyclic loading (hysteresis loop) is important material characteristic. Current models (i.e., Karsan and Jirsa 1969) are including various influential factors and experimental conditions on the hysteresis loop. Especially, the influence of compressive strength has been discussed. By the way, Figure 1 shows the failed concrete specimen and stress-strain relationship with diameter D of 100 mm and varied height H ; height to diameter ratio H/D is changing (Watanabe et al. 2003). The localization of failure in compression is clearly observed. And the localization is also influential on the stress-strain relationship; hence, the stress-strain relationship is strongly changing with the aspect ratio of a concrete specimen (Figure 1 (a)). However, the model involving an influence of the localization has not been formulated.

The objective of this study is to establish the hysteresis model of concrete in compression considering the localization and compressive strength of concrete. A series of uniaxial one-directional repeated load test (specimens have been loaded up to the maximum load, then turned to be unloaded) has been conducted with measuring stress-strain relationships (hysteresis loop) at each local portion of the specimen by the acrylic-rod method (the experiment was detailed in section 2). To overcome the localization of failure, it is assumed that the zone of strain softening (failure zone) of a specimen is coupling in series to “transition zone” and “unloading zone”, such that the stresses carried by these 3 zones are equal and their strains are superimposed with considering the extent of each zone (Watanabe et al. 2003). Similar concepts are proposed previously (i.e., a series coupling model, Bazant (1989)). The length of a failure zone was calculated from the cross-sectional area of a concrete specimen (Lertsrisakulrat et al. 2001). Then,

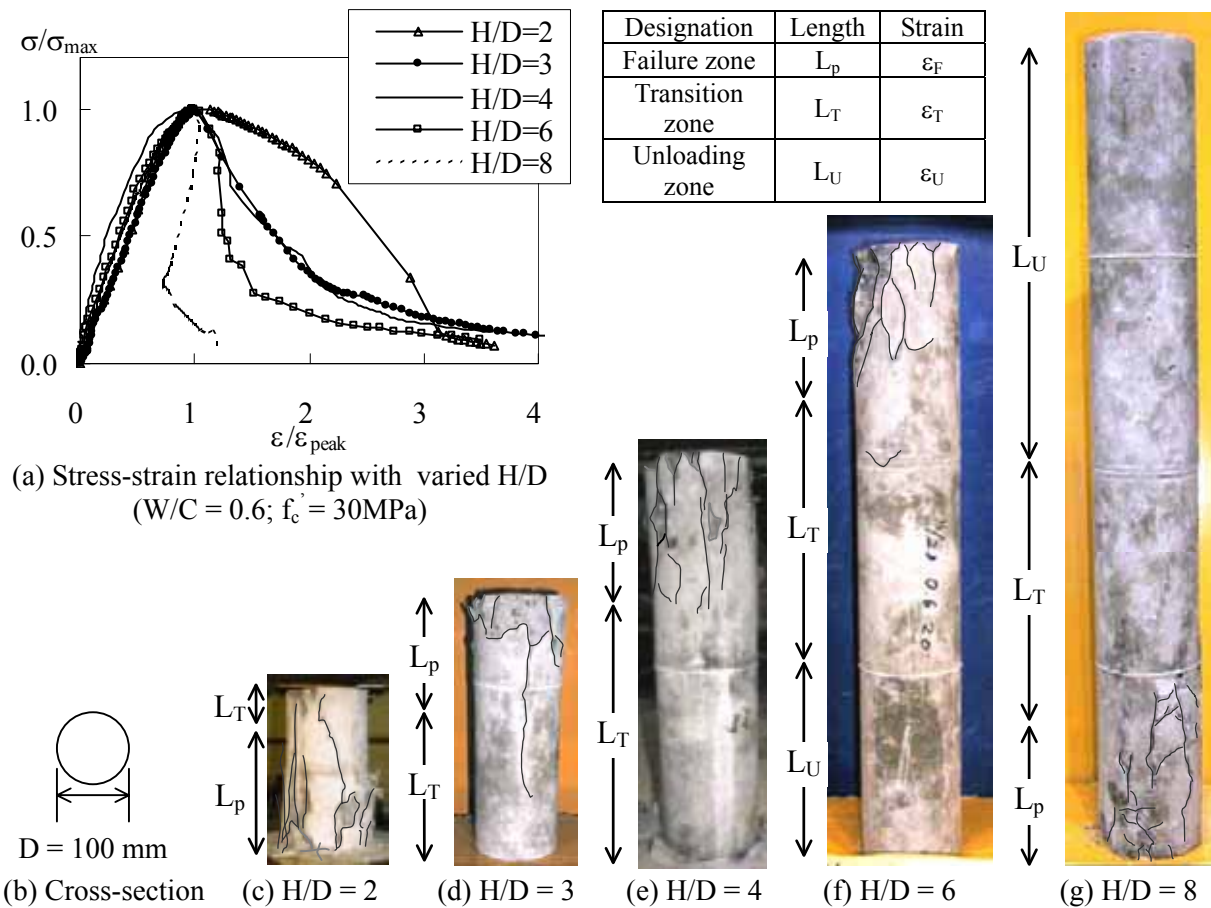


Figure 1 Failed specimen and stress-strain relationship with varied H/D (Watanabe et al. 2003). (black lines indicate crack observed clearly)

the model for an envelope curve involving a characteristic of compressive strength of concrete was formulated for each zone (Watanabe et al. 2003). By combining 3 models considering the extent of each zone, a new model to express an experimental value of envelope curve of the specimen can be obtained regardless the aspect ratio.

Finally, a hysteresis loop model for overall behavior of a concrete specimen with any aspect ratio was established. Each hysteresis loop model for failure, transition and unloading zones was formulated. In this paper, the hysteresis loop model for a failure zone, which governs the overall behavior of concrete structures, was presented in comparison with the experimental loop.

2. OUTLINE OF UNIAXIAL COMPRESSIVE TEST

2.1 Specimen

Tested specimens are listed in Table 1. Two specimens were used for each case. Cylindrical specimens were made with diameter (D) of 100 mm. To investigate the effect of concrete strength on the hysteresis loop, water-to-cement ratios of concrete are set to 0.4, 0.5, 0.6 and 0.7. Coarse aggregate with the maximum size (G_{max}) of 13 mm and 20 mm were used in these specimens. Height of specimens was 400 mm (H/D=4), which indicates the localized failure clearly (Lertsrisakulrat et al. 2001). The compressive strength of concrete (f'_c) ranged from 26.2 to 48.4 MPa at the time of test. The value of f'_c was determined from the standard cylindrical specimen of 200 mm in height and 100 mm in diameter.

Table 1 Tested Specimen.

H/D	G_{max} (mm)	Water to Cement ratio	f'_c (MPa)	σ_{max} (MPa)	L_p (mm)	Designation
4	13	0.4	47.3	41.9	120	A13-0.4-4
		0.5	42.0	39.3	120	A13-0.5-4
		0.6	32.2	27.7	120	A13-0.6-4
		0.7	26.2	22.0	160	A13-0.7-4
	20	0.4	48.4	47.5	120	A20-0.4-4
		0.5	39.0	34.9	120	A20-0.5-4
		0.6	36.7	30.7	120	A20-0.6-4
		0.7	28.4	22.5	120	A20-0.7-4

σ_{max} : maximum stress, L_p : the failure zone length.

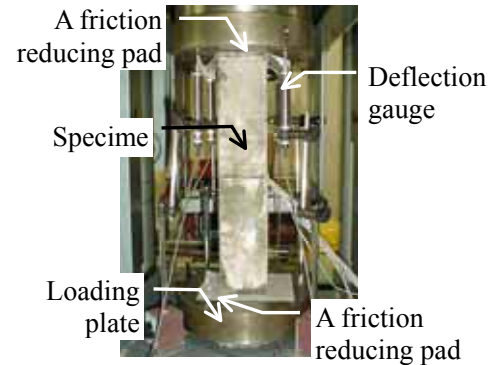


Figure 2 Loading set up.

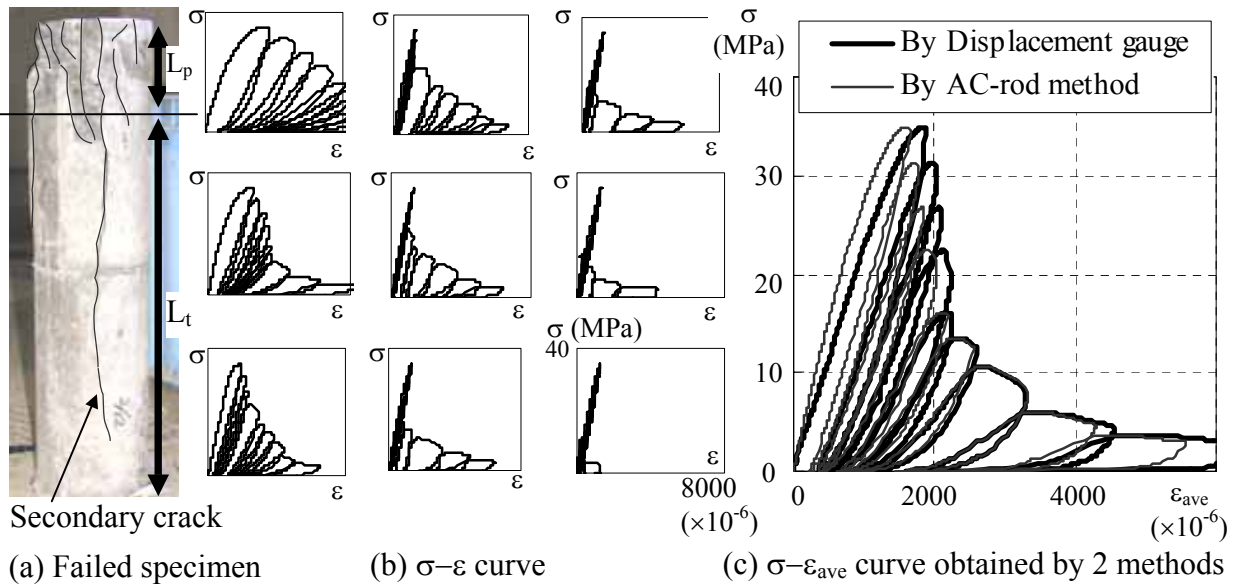


Figure 3 Experimental results (A13-0.5-4).

2.2 Loading Test and Measurement

The loading set up is shown in Figure 2. To decrease a friction, friction reducing pads, i.e., two Teflon sheets (0.05 mm thickness) sandwiching silicon grease were inserted between the specimen and loading plates. The specimen was loaded up to the maximum load, then unloaded until 0 kN. With controlled displacement rate of 0.002 mm per second, the load was applied until decreasing to 10% of the maximum load after the peak.

In the loading test, the load (P) is measured by a load-cell. The value P divided by the cross-section area A_c denotes the stress (σ). Deformations (d) in the specimen were externally measured by deflection gauges, and internal strains were measured by strain gauges (3 mm long) pasted on the acrylic rod with 40 mm interval embedded in the specimen (AC-rod method). The acrylic rod was embedded vertically into a specimen. The strain measured by each gauge denotes a local strain (ϵ), which was assumed to be uniform within 40 mm region of each strain gauge. Average strain (ϵ_{ave}) for the whole of the specimen is obtained by averaging all the value ϵ or by dividing the measured value d with the initial specimen height (H).

2.3 Experimental Results

The failure mode, a stress-local strain loop ($\sigma-\epsilon$) and a stress-average strain loop ($\sigma-\epsilon_{ave}$) of the specimen A13-0.5-4 are shown in Figure 3. Figure 3(c) suggested that the value ϵ_{ave} measured by AC-rod method shows the similar behavior to the strain measured by deflection gauges; hence, a concrete bonded to the acrylic rod and the value ϵ can express the strain at the local portion of a

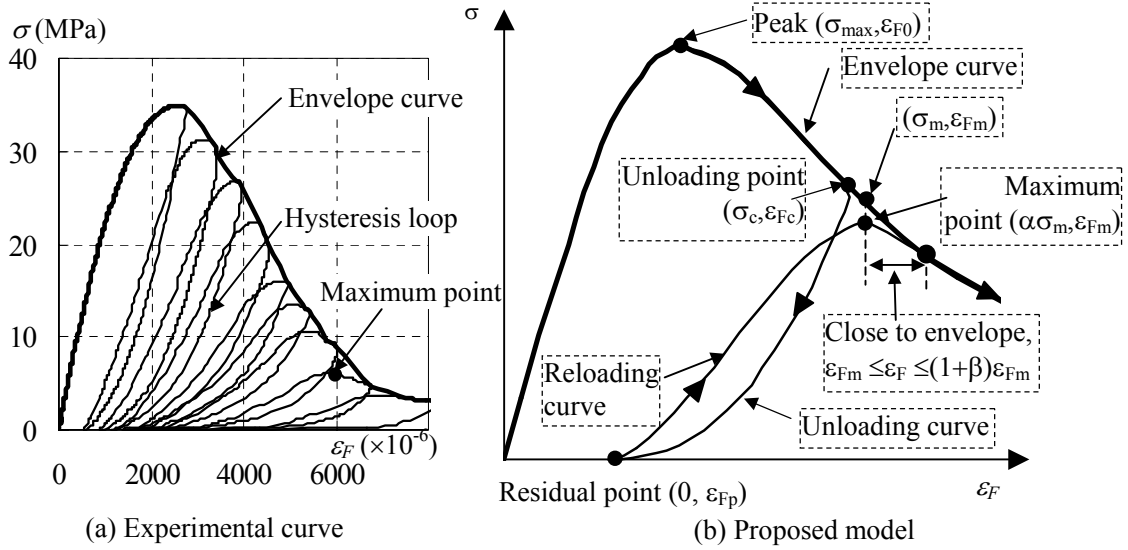


Figure 4 Experimental curve and proposed model of hysteresis loop for the failure zone.

concrete specimen accurately. Based on the existing criterion (Lertsrisakulrat et al. 2001), failed specimens with H/D of 4 are divided into 2 parts; namely a failure zone (length, L_p) of the strain softening, and a transition zone (length, L_T) where decreasing strain turns to increase in the post-peak region.

3. HYSTERESIS LOOP FOR THE FAILURE ZONE

3.1 Definition

Averaging the local strain ε measured in the failure zone gives the strain in the failure zone (ε_F). An experimental curve and the proposed model for hysteresis loop in the failure zone (σ - ε_F) are shown in Figure 4. The characteristics of the loop are denoted by the following symbol and schematically shown in Figure 4(b). If the value ε_F in the post-peak region decreases with the stress (σ), the traced curve is called an unloading curve (σ - ε_{Fu}): between the unloading point ($\sigma_c, \varepsilon_{Fc}$) (a deviation from the envelope curve) and the residual point ($0, \varepsilon_{Fp}$) (the stress reached 0 kN). After completely unloaded, the strain and stress increased again from the residual point, then, approaches to the maximum point ($\alpha\sigma_m, \varepsilon_{Fm}$). The curve is called a reloading curve (σ - ε_{Fr}). The locus joining the end of the reloading curve and the start of the unloading curve will be called the envelope curve.

3.2 Envelope Curve

By referring the existing model (Popovics 1973), Watanabe et al. (2003) reported the numerical expression for the envelope curve for the failure zone as follows:

$$\frac{\sigma}{\sigma_{\max}} = \frac{n_F \times \left(\frac{\varepsilon_F}{\varepsilon_{F0}}\right)}{n_F - 1 + \left(\frac{\varepsilon_F}{\varepsilon_{F0}}\right)^{n_F}} \quad (1)$$

where, $\varepsilon_{F0} = (1.72 \times 10^2 \times \sigma_{\max}^{2/3}) \times 10^{-6}$, $n_F = 3.00 \times 10^{-4} \times \sigma_{\max}^2 + 3.47 \times 10^{-2} \times \sigma_{\max} + 1.86$.

3.3 Unloading Curve

Figure 5 shows the experimental value and the prediction of the unloading curve; those of the stress and strain are expressed as a ratio between the unloading point and the residual point. At the

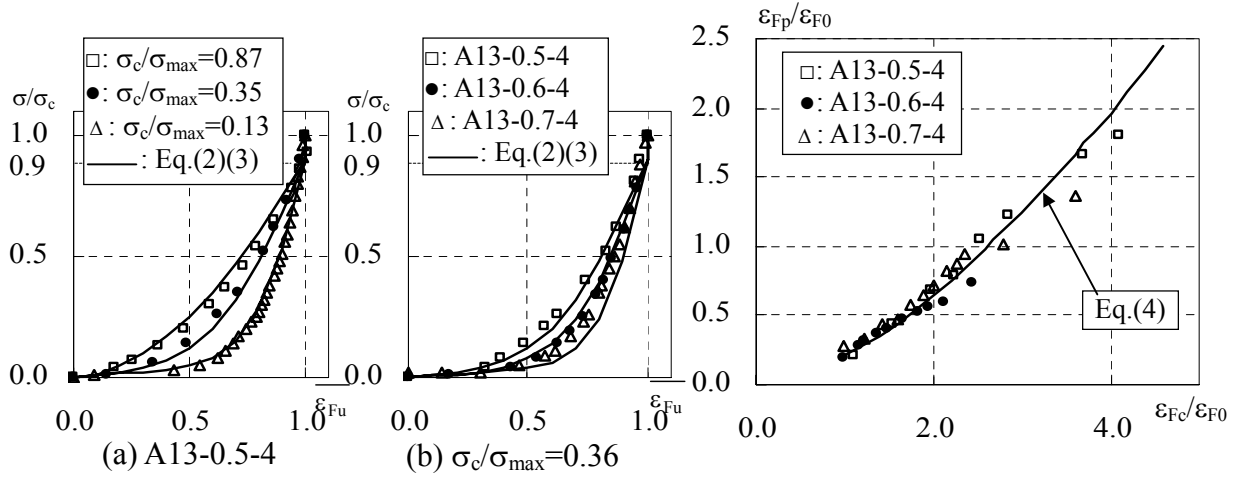


Figure 5 Experimental value and prediction of the unloading curve. Figure 6 $(\varepsilon_{F_c}/\varepsilon_{F_0})-(\varepsilon_{F_p}/\varepsilon_{F_0})$ relationship.

beginning of unloading, all unloading curves show that the strain (ε_{F_c}) is constant during the stress decreasing from σ_c to $0.9\sigma_c$. On the other hand, after the point $(0.9\sigma_c, \varepsilon_{F_c})$, a shape of the convex curve is not unique. As shown in Figure 5(a), a curvature increased with the decrease in the stress at the unloading point (σ_c). In addition, Figure 5(b) shows that the value σ_{max} also affected the unloading curve, even if the value σ_c/σ_{max} of each unloading point is the same.

In traditional empirical equations (Karsan and Jirsa 1969), the convex curve was expressed by using a power function. However, the convex curve near the horizontal axis became flat as the value σ_c/σ_{max} decreased. Therefore, it would be difficult to express the experimental results by a single expression. Here, a polynomial expression was adopted as follows:

$$\overline{\varepsilon_{Fu}} = 1.0 \quad (0.9\sigma_c \leq \sigma \leq \sigma_c) \quad (2)$$

$$\frac{\sigma}{\sigma_c} = 0.9 \left\{ (\overline{\varepsilon_{Fu}})^{u_F} + 0.1 \overline{\varepsilon_{Fu}} \left(1 - \frac{\sigma_c}{\sigma_{max}}\right) (1 - \overline{\varepsilon_{Fu}})^{0.1} \right\} \quad (0 \leq \overline{\varepsilon_{Fu}} \leq 1.0) \quad (3)$$

where, $\overline{\varepsilon_{Fu}} = (\varepsilon_F - \varepsilon_{F_p}) / (\varepsilon_{F_c} - \varepsilon_{F_p})$, $u_F = 1.73 \times (\sigma_c/\sigma_{max})^{(-21/\sigma_{max})}$.

To predict the strain at the residual point, the relationship of the strain between the unloading point ($\sigma_c, \varepsilon_{F_c}$) and the residual point ($0, \varepsilon_{F_p}$) is plotted in Figure 6. Both strains are divided by the peak strain (ε_{F_0}). There are slight differences caused by σ_{max} . However, the identical equation could be applied to express the experimental curve. Previous studies (Karsan and Jirsa 1969) argued that the relationship could be predicted by an exponential function or a quadratic function. According to the JSCE (2002), the relationship in Figure 6 is formulated as follows:

$$\varepsilon_{F_p} = \varepsilon_{F_c} - 2.7\varepsilon_{F_0} \left(1 - \exp\left(-0.35 \frac{\varepsilon_{F_c}}{\varepsilon_{F_0}}\right) \right) \quad (4)$$

3.4 Reloading Curve

Figure 7 shows the experimental value and the prediction of the reloading curve; those of the stress and strain are expressed as a ratio between the residual point and the maximum point. Figure 7(a), obtained by the specimen A13-0.5-4, indicates that the shape of the unloading curve changes with the strain ratio between the residual point and the peak point ($\varepsilon_{F_p}/\varepsilon_{F_0}$). In addition, Figure 7(b) shows the curve of 3 specimens reloaded from the residual point with the identical $\varepsilon_{F_p}/\varepsilon_{F_0}$. It is

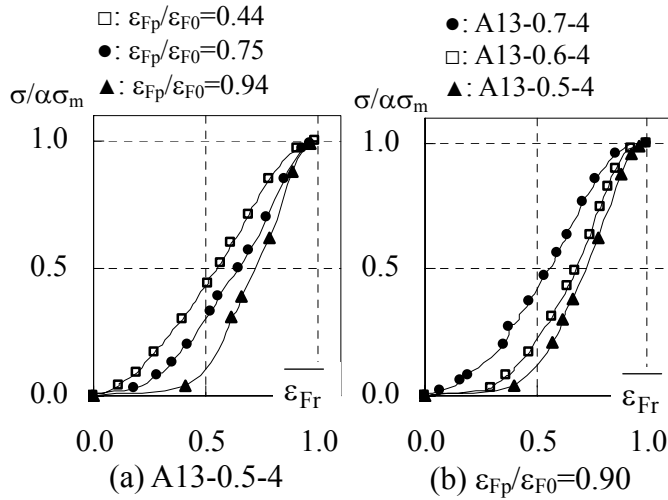


Figure 7 Experimental value and prediction of the reloading curve.

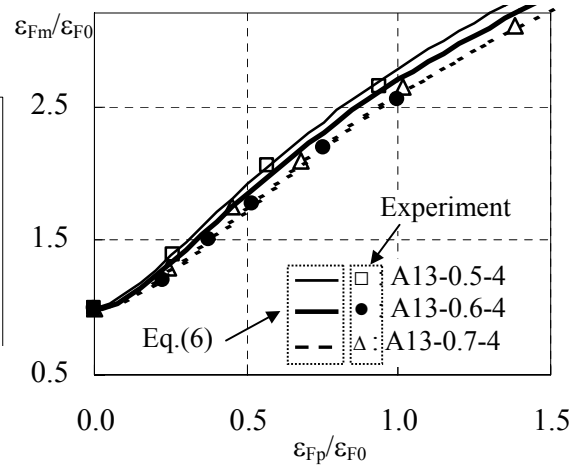


Figure 8 $(\epsilon_{Fp}/\epsilon_{F0}) - (\epsilon_{Fm}/\epsilon_{F0})$ relationship.

clarified that the influence of the value σ_{max} exists on a shape of the reloading curve. Therefore, the reloading model involving σ_{max} and $\epsilon_{Fp}/\epsilon_{F0}$ should be formulated. Based on Eq. (1), a new value (n_{fb}) is added as the power, which is corresponding to the bending degree of the reloading curve. The value n_{fb} is captured as fitting the calculation by the equation with the experimental curve for each case, and approximated with relation to σ_{max} and $\epsilon_{Fp}/\epsilon_{F0}$.

By the way, Figure 4(a) implies that the maximum point $(\alpha\sigma_m, \epsilon_{Fm})$ does not exist on the envelope curve. A stress of the maximum point is slightly lower than the value σ_m : the stress of the point on the envelope curve and corresponding to the identical strain (ϵ_{Fm}). When cracked concrete is subjected to loading and unloading, the strength of concrete may decrease with closing and opening of cracks. Experimental results indicated that the value α might depend on σ_{max} and $\epsilon_{Fp}/\epsilon_{F0}$.

By summarizing these discussions, the reloading curve from the residual point to the maximum point is formulated as follows:

$$\frac{\sigma}{\sigma_m} = \frac{n_F \left(\frac{\epsilon_{Fr}}{\epsilon_{F0}} \right)^{n_{fb}}}{n_F - 1 + \left(\frac{\epsilon_{Fr}}{\epsilon_{F0}} \right)^{n_F \times n_{fb}}} \times \alpha \quad (5)$$

where, $\overline{\epsilon_{Fr}} = (\epsilon_F - \epsilon_{Fp}) / (\epsilon_{Fm} - \epsilon_{Fp})$, $n_{fb} = \exp(0.025\sigma_{max}(\epsilon_{Fp}/\epsilon_{F0}))$, $\alpha = 1 - 0.2(\sigma_{max}/50)(\epsilon_{Fp}/\epsilon_{F0})$.

To predict the strain at the maximum point (ϵ_{Fm}), the relationship between the value ϵ_{Fp} and ϵ_{Fm} is plotted in Figure 8. By comparing 3 results, there is just a difference depending on σ_{max} . An approximation without the difference is not adequate to express a common point (Karsan and Jirsa 1969). Therefore, each relationship is predicted by the function of σ_{max} as follows:

$$\frac{\epsilon_{Fm}}{\epsilon_{F0}} = a \exp\left(-2b \frac{\epsilon_{Fp}}{\epsilon_{F0}}\right) - (a + 0.8) \exp\left(-b \frac{\epsilon_{Fp}}{\epsilon_{F0}}\right) + c \frac{\epsilon_{Fp}}{\epsilon_{F0}} + 1.8 \quad (6)$$

where, $a = 6.7 \times 10^{-3} \sigma_{max} + 9.7 \times 10^{-1}$, $b = -2.0 \times 10^{-2} \sigma_{max} + 3.2$, $c = -4.0 \times 10^{-3} \sigma_{max} + 1.2$.

After the maximum point of the reloading curve, the hysteresis loop is gradually getting close to the envelope curve (Figure 4(a)). To consider the behavior after the reloading curve, the value β is added to Eq.(1) while the strain is ϵ_{Fm} to $(1+\gamma)\epsilon_{Fm}$. In this range, the value β gradually increases

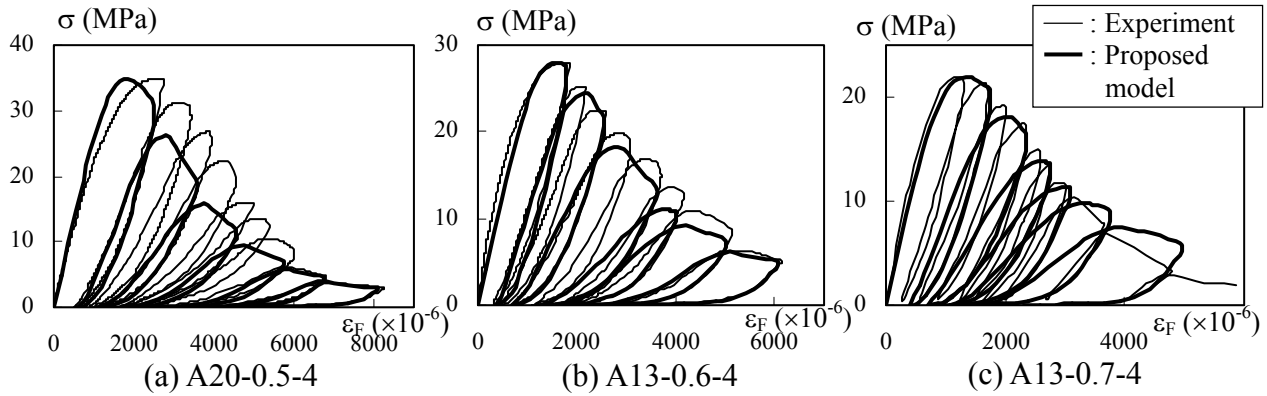


Figure 9 Comparison of proposed model with experimental curve in the failure zone.

from α to 1. Based on the experimental data, the value γ is decided by the value α and $\varepsilon_{Fm}/\varepsilon_{F0}$: a strain at the maximum point divided by ε_{F0} . The equation to express the curve getting close to the envelope curve is formulated as follows:

$$\frac{\sigma}{\sigma_m} = \frac{n_F(\varepsilon_F)}{n_F - 1 + (\varepsilon_F)^{n_F}} \times \beta \quad (\varepsilon_{Fm} \leq \varepsilon_F \leq (1+\gamma)\varepsilon_{Fm}) \quad (7)$$

where, $\beta = \alpha + (\varepsilon_F - \varepsilon_{Fm})(1-\alpha)/\gamma\varepsilon_{F0}$, $\gamma = 1.4(1-\alpha)(\varepsilon_{Fm}/\varepsilon_{F0})$.

3.5 Comparison of Proposed Model with Experimental Curve

Hysteresis loop in the failure zone (σ - ε_F) is predicted by substituting σ_{max} into Eqs. (1) to (7). In Figure 9, the proposed model and experimental results in the failure zone are compared based on σ_{max} . The calculation by the proposed model has a good relation with the experimental curve regardless of σ_{max} .

4. CONCLUSION

This paper discusses the hysteresis loop in the localized compressive failure zone of concrete, which governs the behavior for a whole of concrete structure. Then, it is confirmed that the proposed model in this paper can simulate the experimental loop in the failure zone accurately.

Acknowledgements:

The authors would like to thank ‘Taiheiyo Cement Corporation Research & Development Center’ and ‘Kuraray Co., LTD.’ for their kind supports of the loading test and providing acrylic-rods.

References:

- Karsan, I.D. and Jirsa, J.O. (1969) “Behavior of Concrete under Compressive Loading,” *Journal of the Structural Division, Proceeding of the American Society of Civil Engineers*, 95(ST12), 2543-2563.
- Watanabe, K., Niwa, J., Yokota, H. and Iwanami, M. (2003) “Formulation of Stress-Strain Relationship of Concrete Considering the Localized Compressive Failure Zone,” *Journal of Materials, Concrete Structures and Pavements*, Japan Society of Civil Engineers, 725/V-58, 197-211.
- Bazant, Z. P. (1989) “Identification of Strain-Softening Constitutive Relation from Uniaxial Tests by Series Coupling Model for Localization,” *Cement and Concrete Research*, 19(6), 973-977.
- Lertsrisakulrat, T., Watanabe, K., Matsuo, M. and Niwa, J. (2001) “Experimental Study on Parameters in Localization of Concrete Subjected to Compression,” *Journal of Materials, Concrete Structures and Pavements*, Japan Society of Civil Engineers, 669/V-50, 309-321.
- Popovics, S. (1973) “A Numerical Approach to the Complete Stress-Strain Curve of Concrete,” *Cement and Concrete Research*, 3(5), 583-599.
- JSCE (2002) “Standard Specifications for Concrete Structures. 2002, Seismic Performance Verification,” Japan Society of Civil Engineers.

NEW REINFORCING METHOD FOR REINFORCED CONCRETE BEAM WITH WEB OPENING INTRODUCED PRESTRESSING FORCE

K. Katori¹⁾, and S. Hayashi²⁾

1) Assistant Professor, Structural Engineering Research Center, Tokyo Institute of Technology, Japan

2) Professor, Structural Engineering Research Center, Tokyo Institute of Technology, Japan

katori@serc.titech.ac.jp, hayashi@serc.titech.ac.jp

Abstract: The authors originated new reinforcing methods for reinforced concrete beams with web opening. Those new methods consist of using unbonded prestress tendons, which are arranged near web opening. Prestressed force is introduced to each tendon. The authors made two arranging ways of unbonded tendons near web opening. The authors aim that both new methods will be suitable not only for seismic retrofit of existing reinforced concrete buildings having beam with web opening, but also new buildings. In this study the authors performed shear-bending experiments of reinforced concrete beams with those new reinforcing methods for web opening, and tried to confirm effectiveness of those methods and make clear shear characteristics of those beams.

From specimens the following facts were taken;

1. Shear strength of specimens could be calculated by well-known formula by regarding prestress tendons near web opening as reinforcing bars for web opening.
2. When sufficient prestressed force was introduced to each tendons, crack width under allowable shear force for sustained loading could be controlled to lower than 0.2mm.

1. INTRODUCTION

Reinforced concrete (R/C) beams with web opening have some loss in their section caused by web opening, so their section loss may cause large crack width around web opening. Sometimes their large crack width may exceed beyond design assumption. To improve that situation the authors has proposed new reinforcing method, named “the IC reinforcing method; the IC reinforcing method is made up of unbonded-type prestress tendons arranged around web opening and introducing prestressed tensile force to prestress tendons. The authors intend that the IC reinforcing method may be adopted for new construction buildings for restraint of crack width being small.

In this research the authors intended to investigate effects of amount of prestressed tensile force to prestress tendons, ratio of web opening reinforcement by prestress tendons and compressive strength of concrete, for ability of restraint of crack width and shear ultimate strength of reinforced concrete beams having the IC reinforcing method.

The authors, furthermore, have proposed new reinforcing method, named “the OC reinforcing method”, for beams with web openings in existing building; the OC reinforcing method is made up of prestress tendons placed on the surface of beam roundly, and introducing prestressed tensile force to the tendons. In this study the authors also intended to investigate effect of the OC reinforcing method.

2. EXPERIMENTAL PROGRAM

2.1 Specimens

Specimen's details are shown in *Fig. 1*, and *Table 1*. Twelve specimens were tested in this study. Eleven of specimens were made as specimens of the IC reinforcing method, and one of specimen was as the OC reinforcing method. All specimens had 300mm in width b and 450mm in depth D of section, 150mm in diameter of web opening (equal to $D/3$) and 1.54 of shear span ratio M/Qd .

Three pieces of D22 high strength bar having screw-type knot were used as longitudinal reinforcement. Three pieces of U8, which were arranged as stirrup and unbonded-type prestress tendons of $\phi 7.1$, $\phi 9.2$ and $\phi 11$ were all approved in JIS (Japan Industrial Standard) as "C-1 class".

On the IC reinforcing method, four pieces of unbonded-type prestress tendons were arranged symmetrically having 40 degree of inclined angle against longitudinal direction. On specimen of the OC reinforcing method (No.3), a pair of prestress tendons was placed round on the surface of specimen near web opening. Those round tendons were connected each other by steel corner blocks, and same amount of prestressed tensile force was loaded to those tendons, not only tendons placed to beam-depth direction but also beam-width direction. On all specimens, prestressed tensile force for tendons, not only the IC reinforcing method but also the OC reinforcing method, were loaded by the post tension-style loading. To normalize the effects of prestressed tensile force, which may be varied by reinforcing method, the authors defined σ_D as an average prestress suffer to crack occurred near web opening which were assumed that crack angle against longitudinal direction was equal to 45 degree, which is shown in *Fig. 2*.

On the specimens of the IC reinforcing method, specimens had 0.23%, 0.38% and 0.54% of ratio of reinforcement for web opening p_p calculated by diameter of prestress tendons arranged near web opening.

2.2 Shear-Bending Loading System

Fig. 3 shows loading setup. Specimens were suffered from multi-cyclic shear-bending force. So-called "Kenken-style shear-bending loading system" was adopted. By using that loading system, specimens were suffered from reversal bending moment against mid-point of specimens on longitudinal axis. Peak point of each loading cycle were decided by deformed angle of specimen R ; R were decided to $\pm 1/500\text{rad.}$, $\pm 1/200\text{rad.}$, $\pm 1/100\text{rad.}$, $\pm 1/67\text{rad.}$ and $\pm 1/50\text{rad.}$

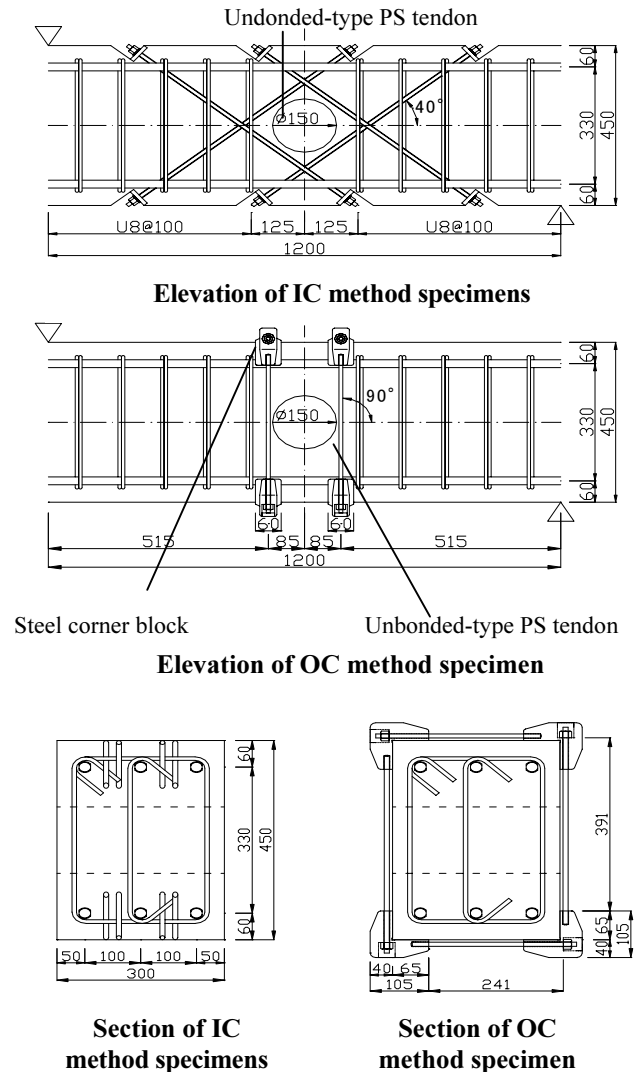


Fig. 1: Details of specimens

Table 1: List of specimens

Spec. No.	Tendons' diameter, mm	Reinf. method	F_c , MPa	P_p , %	P_l , kN	P_l/P_y	σ_D , N/mm ²
No.1	7.1	IC	30	0.23	---	---	---
No.2					31	0.7	0.8
No.3	9.2	OC		0.27	40	0.5	---
No.4		IC		0.38	15	0.2	0.4
No.5					31	0.4	0.8
No.6	11	IC		60	0.54	61	0.8
No.7			---			---	---
No.8			31		0.3	0.8	
No.9			61	0.6	1.7		
No.10			---	---	---		
No.11			31	0.3	0.8		
No.12				61	0.6	1.7	

IC: IC reinforcing method OC: OC reinforcing method

F_c : Specified concrete strength

p_p : Ratio of reinforcement for web opening by prestress tendons arranged near web opening;

$$p_p = \sum (a_s \cdot (\sin \theta_p + \cos \theta_p)) / b \cdot c$$

P_l : Prestressed tensile force per one piece of prestress tendon

P_y : Yield tesile force of prestress tendon ($= \sigma_y/A$)

σ_D : average prestress suffer to crack occurred near web opening which are assumed that crack angle against longitudinal direction is equal to 45° ; $\sigma_D = n \cdot P_l \cdot \cos(\theta_p \cdot -\pi/4) / (b \cdot (\sqrt{2} \cdot D - H))$

n : Number of prestress tendons which cross section having 45 degree of inclined angle

θ_p : Inclined angle of prestress tendons against longitudinal axis of specimens

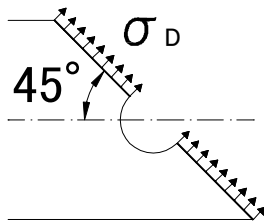


Fig. 2: Definition of σ_D

Table 2: Mechanical properties of steel bars and concrete

Steel bar	$s\sigma_y, p\sigma_y$ (N/mm ²)	$s\sigma_t$ (N/mm ²)	E_s (GPa)	A (mm ²)
Longitudinal, D22	1152	1279	190	387
Stirrup, U8	874	943	195	50
PS Tendon for the IC method, 7.1φ	1182	1192	185	40
PS Tendon for the IC method, 9.2φ	1244	1282	193	66
PS Tendon for the OC method, 9.2φ	1273	1312	196	66
PS Tendon for the IC method, 11φ	1220	1292	195	95
Concrete	F_c (MPa)	σ_B (MPa)	σ_t (MPa)	E_c (GPa)
Spec. No.1-3	30	42	3.0	25
Spec. No.4-6		39	2.8	24
Spec. No.7-9		35	2.6	24
Spec. No.10-12		60	66	3.8

$s\sigma_y, p\sigma_y$: Yield strength
 E_s, E_c : Elastic modulus
 F_c : Designed strength

$s\sigma_t, \sigma_t$: Tensile strength
 A : Section area
 σ_B : Compressive strength

2.3 Crack Observation

To observe crack near web opening, the authors decided the area of 330mm × 330mm near web opening, shown in **Fig. 3**, and width of crack occurred in that area were measured frequently. Crack width W was defined as width perpendicular to longitudinal direction of crack which occurred diagonally.

3. RESULT AND DISCUSSION

3.1 General Behavior

Experimental results are shown in **Table 3**, and relations between shear force Q and deformation angle R and crack pattern are shown in **Fig. 4**. On specimens of the IC reinforcing method width of

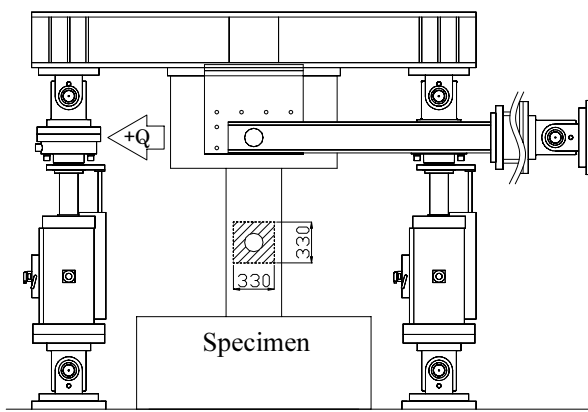


Fig. 3: Loading setup
(Hatched area shows crack-observing area)

crack occurred near web opening became wide and specimens became failure.

On spec. No.1 and No.2, unbonded-type tendons yielded and reached to maximum shear force just before R was equal to $+1/67$ rad.. But on other specimens of the IC reinforcing method, shear force became the maximum at the point that R was equal to $+1/67$ rad.. On spec. No.3 of the OC reinforcing method, shear failure were occurred on upper and lower area of web opening when R was equal to $-1/50$ rad., then Q had fallen.

Relations between shear crack strength near web opening τ_{sco} and average prestress σ_D are shown in Fig. 5. As figure shows, generally τ_{sco} increased according to growth of σ_D , that is growth of prestressed tensile force. And figure shows that τ_{sco} may not be influenced by p_p and concrete compressive strength σ_B .

After shear crack occurred, number of shear crack near web opening became smaller according to growth of σ_D , and other shear cracks were occurred outside of web opening area.

Table 3: Experimental result

Spec. No.	eQ_{bu} (kN)	eQ_{AL} (kN)	eQ_{AS} (kN)	eQ_{suo} (kN)	eQ_{sco} (kN)	eQ_{max} (kN)	eQ_{max}/eQ_{suo}
No.1	783	179	346	294	66	343	1.17
No.2					101	356	1.21
No.3					308	475	1.54
No.4		175	339	325	55	387	1.19
No.5					106	401	1.23
No.6					129	449	1.38
No.7		168	329	347	58	408	1.18
No.8					113	422	1.22
No.9					141	424	1.22
No.10		218	403	395	63	478	1.21
No.11					98	515	1.31
No.12					138	507	1.29

eQ_{bu} : Calculated maximum bending strength eQ_{AL} : Allowable shear strength for sustained loading by AIJ approved formula for reinforced concrete beam not having web opening eQ_{AS} : Allowable shear strength for temporary loading by AIJ approved formula for reinforced concrete beam not having web opening eQ_{suo} : Shear strength calculated by the Hirose's formula¹⁾:

$$eQ_{suo} = \left\{ \frac{0.092 \cdot k_u \cdot k_p \cdot (F_c + 18)}{M/Q \cdot d + 0.12} \cdot \left(1 - \frac{1.61 \cdot H}{D} \right) + 0.85 \cdot \sqrt{p_s \cdot \sigma_y + p_p \cdot \sigma_y} \right\} \cdot b \cdot j \quad \dots(1)$$

a_s : Sectional area of prestress tendons θ_p : Inclined angle of prestress tendons against longitudinal axis of specimens $p\sigma_y$: Yield strength of prestress tendon eQ_{sco} : Shear cracking load near web opening taken in experiments eQ_{max} : Maximum shear strength taken in experiments

3.2 Crack Width near Web Opening

Relations between average shear stress τ and maximum crack width W_{max} are shown in Fig. 6, 7, and 8. On those figures range of τ were positive. As figure shows, crack width, both width when shear loading and unloading, became small according to growth of σ_D and p_p . For example, if σ_D is equal to 1.7MPa, that is to say that σ_D is a small value, crack width became about 1/20 as small as that if σ_D is equal to zero, when specimen is under situation of allowable shear stress for long sustained loading. As compared between spec. No.2 and No.3, strength when shear crack occurred were approximately equal, but crack width of spec. No.3 was smaller than that of spec. No.2. Reason why that may be that stiffness for axial direction of prestress tendon used for spec. No.3 was larger

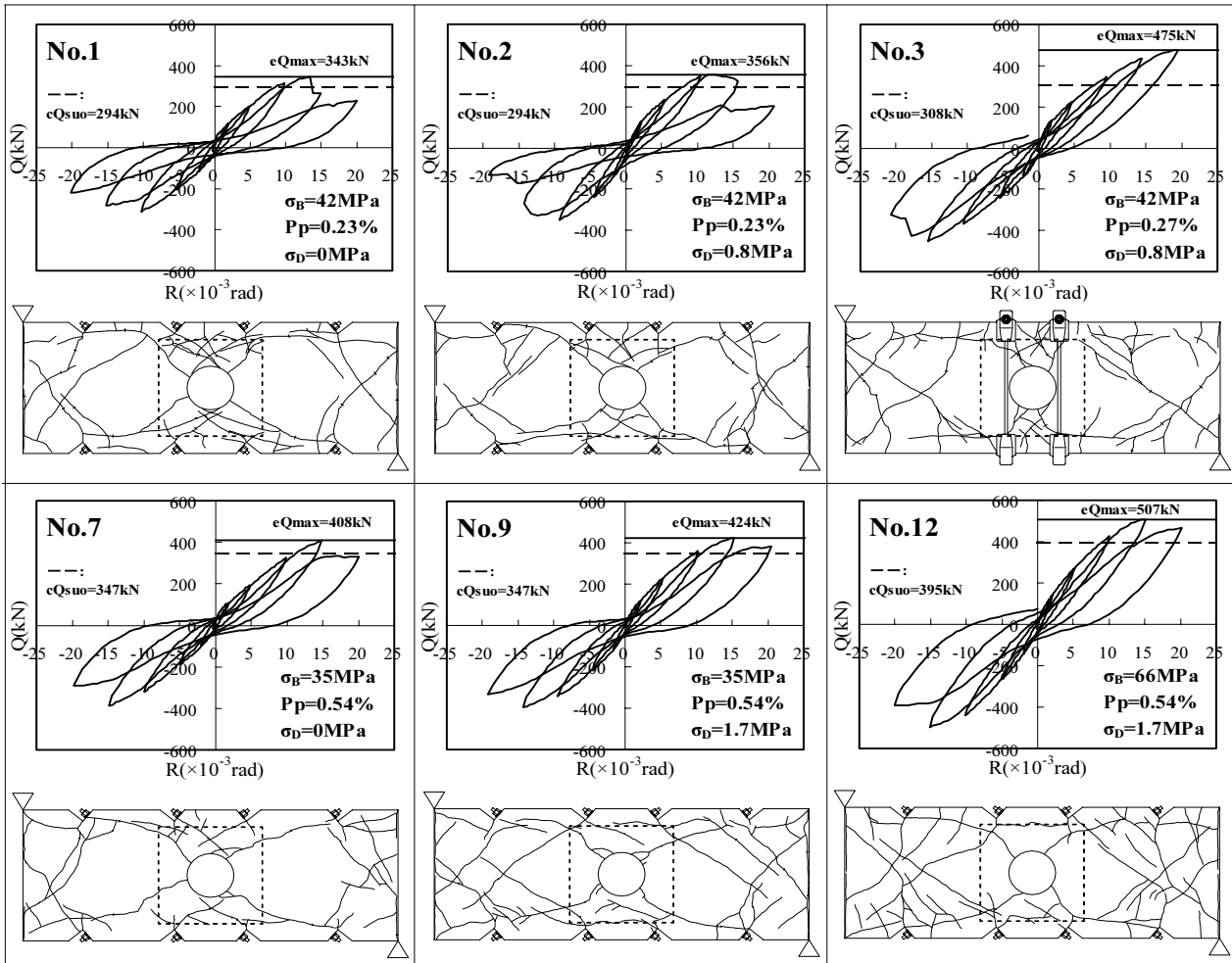


Fig. 4: Q-R relations and crack patterns

than that of spec. No.2, because tendon for spec. No.3 had larger area of section and shorter length than those of spec. No.2.

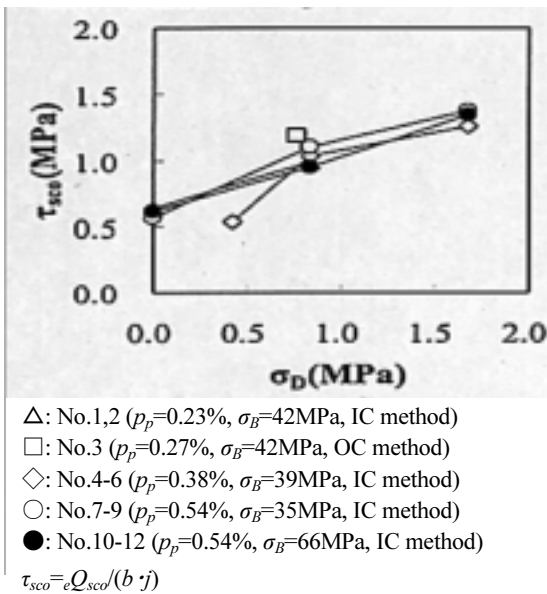


Fig. 5: τ_{sco} - σ_D relation

Relations between σ_D and crack width when specimens were under situation of allowable shear stress for long sustained loading ALW_{max} are shown in Fig. 9. Generally in Japan, maximum crack width when prestressed concrete structures are under situation of allowable shear stress for long sustained loading may be recommended to 0.2mm or below. But as shown in figure, crack width ALW_{max} of specimens which had no prestressed tensile force for prestress tendons reached between 1.10mm and 1.31mm. Those values are approximately six times as large as 0.2mm. So those facts show that it is estimated that maximum crack width of normal reinforced concrete beam with web opening, not having the IC or OC reinforcing method, may be exceed to 0.2mm, when beam is under situation of allowable shear stress for long sustained loading.

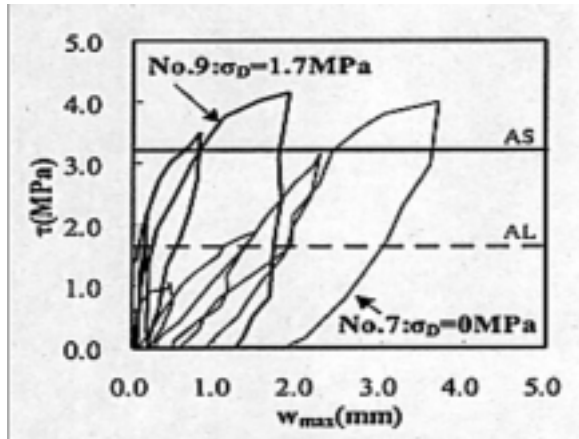


Fig. 6: τ - W_{max} relation
(Spec. selected by the scope of variable of σ_D)

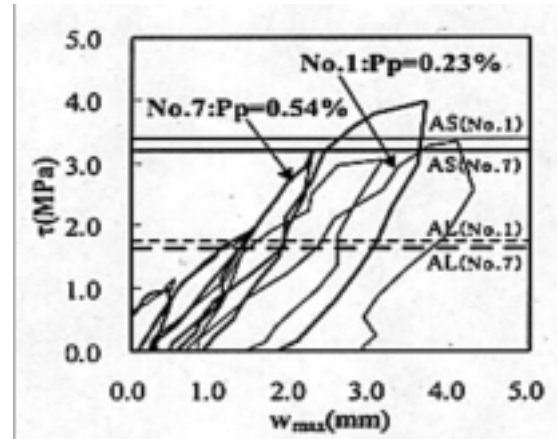


Fig. 7: τ - W_{max} relation
(Spec. selected by the scope of variable of p_p)

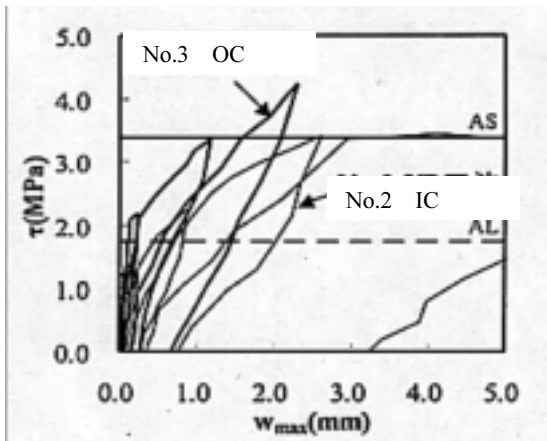


Fig. 8: τ - W_{max} relation
(Spec. selected by the scope of reinforcing method)

In Fig. 6-8;

$$\tau = Q/(b \cdot j)$$

AL: Allowable shear stress for long sustained loading;

$$AL = c_{AL}/(b \cdot j)$$

AS: Allowable shear stress for temporary loading;

$$AS = c_{AS}/(b \cdot j)$$

j : Distance between centers of tension and compression;

$$j = 341.25 \text{ mm}$$

3.3 Behavior of Reinforcing Bar near Web Opening

Relations between shear force Q and vertical shear force loaded by prestress tendons V_p , vertical shear force loaded by stirrup arranged near web

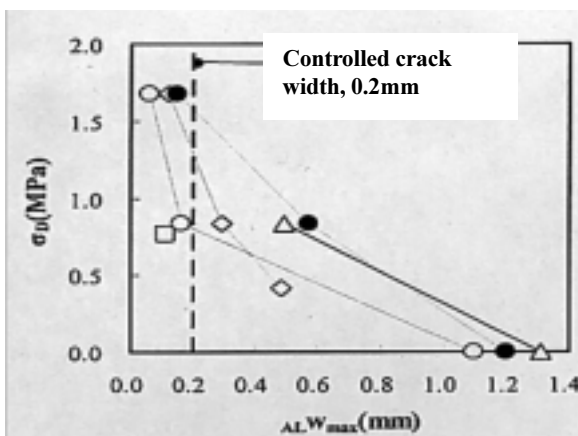


Fig. 9: σ_D - $AL W_{max}$ relation

- △: No.1,2 ($p_p=0.23\%$, $\sigma_B=42\text{MPa}$, IC)
- : No.3 ($p_p=0.27\%$, $\sigma_B=42\text{MPa}$, OC)
- ◇: No.4-6 ($p_p=0.38\%$, $\sigma_B=39\text{MPa}$, IC)
- : No.7-9 ($p_p=0.54\%$, $\sigma_B=35\text{MPa}$, IC)
- : No.10-12 ($p_p=0.54\%$, $\sigma_B=66\text{MPa}$, IC)

opening V_s , which are defined on Fig. 10, are shown in between Fig. 11 to 14. As figure shows, point that shear force loaded by stirrup arranged near web opening became to grow may appear later according to growth of prestressed tensile force. That is because large prestressed tensile force prevents to become width of shear crack near web opening wide.

Among specimens not having prestressed tensile force,

characteristics between σ_D and V_p , V_s are similar to each other even if concrete compressive strength may vary. But on specimen having σ_B is equal to 66MPa and having prestressed tensile force, shear force not only loaded by prestress tendon but also loaded by stirrup arranged near web opening tend to

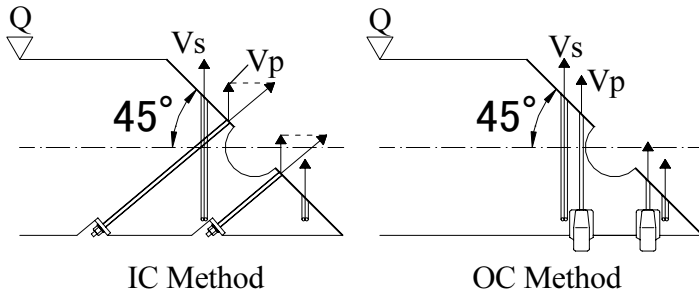


Fig. 10: Shear force at PS tendons and stirrup

the OC and IC reinforcing method, but in this section the authors tried to apply that formula to each specimen. Relation between shear strength calculated by the Hirosawa's formula eQ_{suo} and that taken in experiments eQ_{max} are shown in Fig. 15. In this figure, it is assumed that prestress tendons were considered as reinforcement for web opening like stirrup. As figure shows, eQ_{max} exceeded eQ_{suo} . Value of eQ_{max}/eQ_{suo} , that is safety factor, became between 1.14 and 1.38 on specimens with the IC reinforcing method, and became 1.54 on specimen with the OC reinforcing method. Safety factor for

grow. So it became clear that prestressed tensile force makes prestress tendon and stirrup arranged near web opening act effectively.

3.4 Shear Strength between Experiment and Calculation

In Japan the formula suggested by Dr. Hirosawa (eq.1)¹⁾ is well-known for calculation of shear strength of reinforced concrete beam with web opening. Exactly that formula is not following to beam with

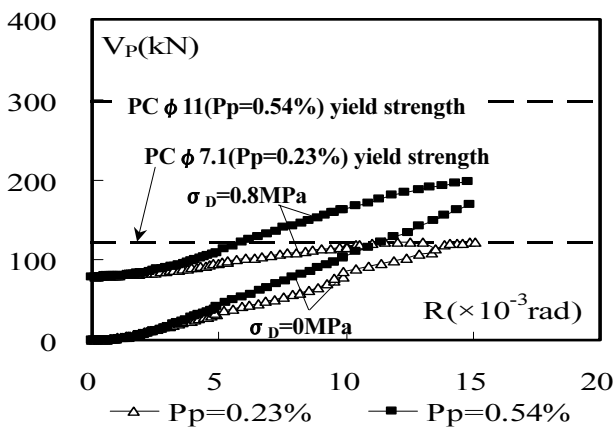


Fig. 11: V_p -R relation
(Spec. selected by the scope of variable of p_p and σ_D)

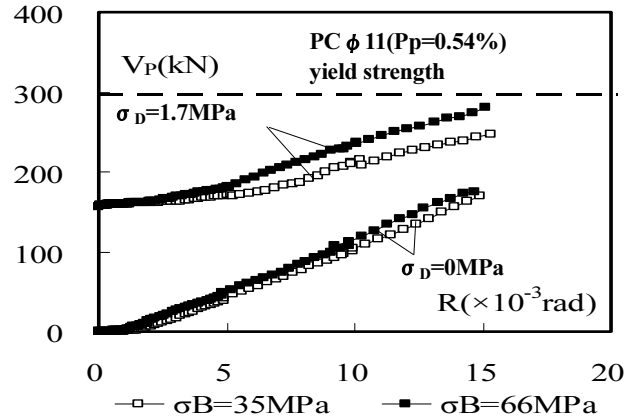


Fig. 12: V_p -R relation
(Spec. selected by the scope of variable of σ_B and σ_D)

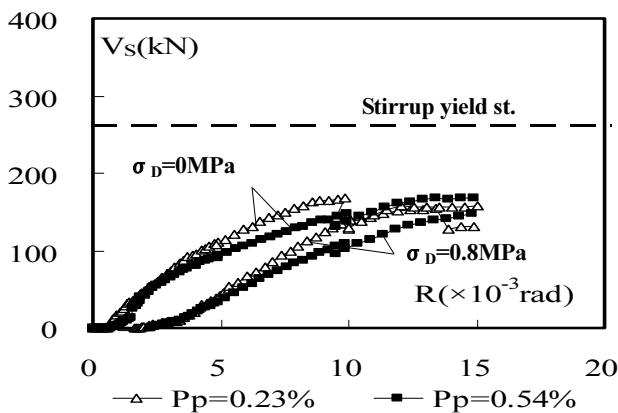


Fig. 13: V_s -R relation
(Spec. selected by the scope of variable of p_p and σ_D)

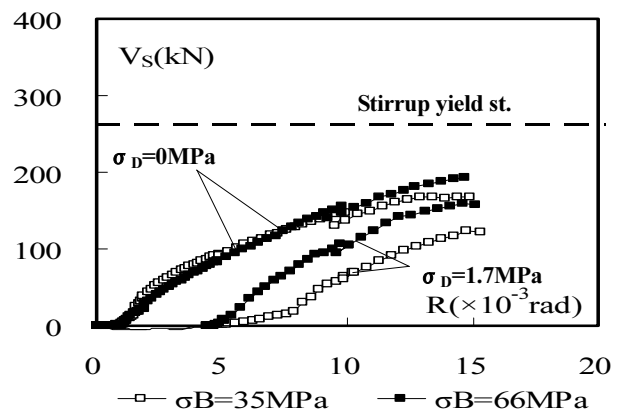


Fig. 14: V_s -R relation
(Spec. selected by the scope of variable of σ_B and σ_D)

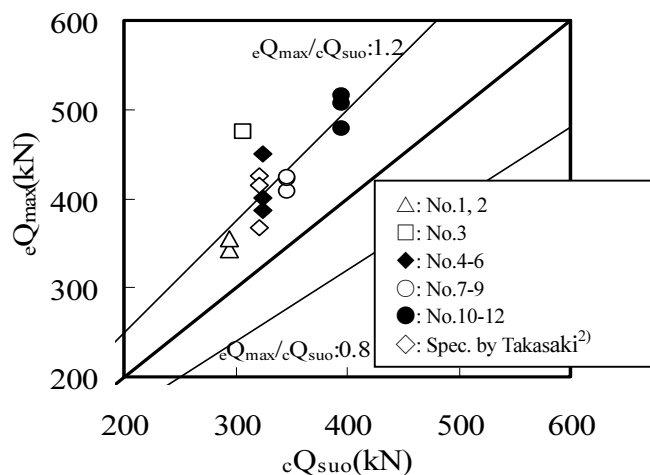


Fig. 15: eQ_{\max} - cQ_{suo} relation

specimen with the OC reinforcing method was larger than that for specimens with the IC reinforcing method. It may be thought that the reason above is that prestress tendon for the OC reinforcing method has larger effects for shear strength than that of the IC reinforcing method.

4. CONCLUSION

This study examined the effects of new reinforcing method of reinforced concrete beam with web opening. The following conclusion can be made:

1. Shear crack strength near web opening increases according to growth of prestressed tensile force for prestress tendons arranged or placed near web opening.
2. Crack width become small according to growth of prestressed tensile force for prestress tendons arranged or placed near web opening. Moderate prestressed tensile force for prestress tendons and amount of reinforcement for web opening may lead crack width under controlled width value.
3. If specimens are made of high strength concrete, prestressed tensile force may make prestress tendon and stirrup arranged near web opening act effectively.
4. The Hirosawa's formula, which is famous in Japan to estimate shear strength of reinforced concrete beam with web opening, is applicable to specimens having the IC and OC reinforcing methods.

Acknowledgements:

The authors acknowledge support from the Structural Engineering Research Center (SERC) in Tokyo Institute of Technology. The authors also thank Mr. Daisuke Akagi, engineer of Takenaka Corporation, for his great help.

References:

- 1) Architectural Institute of Japan (1999), "AIJ Standard for Structural Calculation of Reinforced Concrete Structures -Based on Allowable Stress Concept- Revised 1999,"
- 2) Takasaki, Y., Katori, K. and Hayashi, S. (2002), "Study on Shear Reinforcement for RC Beam with Web Opening under Consideration of Crack Control," *Proc. of Japan Concrete Institute*, Japan Concrete Institute, **24**(2), 295-300.
- 3) Akagi, D., Yanase, T., Katori, K. and Hayashi, S. (2003), "Experimental Study on Shear Behavior of Prestressed Reinforced Concrete Beams with Web Openings," *Proc. of Japan Concrete Institute*, Japan Concrete Institute, **25**(2), 409-414.
- 4) Architectural Institute of Japan (1986), "Recommendations for Design and Construction of Partially Prestressed Concrete (Class 3 of Prestressed Concrete) Structures,"
- 5) Yanase, K., Ono, Y., Li, Z. and Minami, H. (2002), "Shear Crack Width of Reinforced Concrete Beams," *Proc. of Japan Concrete Institute*, Japan Concrete Institute, **24**(2), 343-348.

SHEAR CRACK CONTROL ON REINFORCED CONCRETE COLUMN BY LATELAL PRESTRESSING

H. Watanabe¹⁾, K. Katori²⁾, Y. Shinohara³⁾, and S. Hayashi⁴⁾

1) Research Student, Structural Engineering Research Center, Tokyo Institute of Technology, Japan

2) Research Associate, Structural Engineering Research Center, Tokyo Institute of Technology, Japan

3) Associate Professor, Structural Engineering Research Center, Tokyo Institute of Technology, Japan

4) Professor, Structural Engineering Research Center, Tokyo Institute of Technology, Japan

hwatanab@serc.titech.ac.jp, katori@serc.titech.ac.jp, yshinoha@serc.titech.ac.jp, hayashi@serc.titech.ac.jp

Abstract: This paper describes the investigation of the influence of lateral prestress on the crack opening within reinforced concrete column by experiments. From the experiments, it is found that either shear crack strength and allowable shear force which makes residual shear crack opening into target value increased with lateral prestressing.

1. INTRODUCTION

According to building design based on structural performance, damage on reinforced concrete building such as crack must be controlled to implement required performance. On the reinforced concrete column, from views of durability, waterproof and appearance, shear crack should be prevent or its residual opening should be controlled. Shear crack opening also should be controlled to keep residual strength of the column, since its transverse reinforcements stresses and residual deformation become larger due to increasing of the crack width.

When design was performed to control residual shear crack opening within reinforced concrete column, it is seem that allowable shear force for temporary loading formula in Architectural Institute of Japan Standard of Reinforced Concrete Structures (1999) might be available. However, AIJ Standard does not describe clearly on residual crack width control. Based on experimental results in beam, residual shear crack width was predicted by using allowable shear force formula above as index of damage by Fukuyama et al. (2000). Crack widths could not be controlled in some member, and verification based on other index was required. An axial load could not be neglect, although the effect of the axial load was not considered in the formula, when shear crack strength was examined. Thus, it might be needed:

- (a) Method of restricting residual shear crack opening.
- (b) To control residual crack opening, evaluation index at design.

This paper develops effect of lateral prestressing into column (Watanabe et al. 2002 and 2003) on shear design for minor earthquake, as preventing method on shear crack occur, or as control method on the residual shear crack width, based on experimental results. An evaluation method of allowable shear force which makes residual shear crack width within the column as control target value, as control index, was also considered.

Table 1 List of Test Specimens

No.	b, D (mm)	d_w (mm)	σ_0 $/f_c$	s (mm)	p_w (%)	p_{wp}^* (%)	Longitudinal bars	f_c (N/mm ²)	f_{ct} (N/mm ²)	f_{wp} (N/mm ²)	σ_L (N/mm ²)
1	340	6.4*, and D16**	0.30	60	2.54	0.29*	8-D22	40.1	2.09	859	2.5
2								45.0	2.21	528	1.6
3								48.0	2.29	0	0.0
4		6.4*, and D13**			0.29			35.4	1.96	876	2.6
5		35.3						1.96	0	0.0	

*pretensioned hoop, **sub hoop, b is breadth of column, D is depth of column, d_w is nominal diameter of transverse hoop, σ_0 is axial stress of column, f_c is compressive strength of concrete, s is spacing of transverse hoops in longitudinal direction, p_w is ratio of transverse hoop $(=(A_{wn}+A_{wp})/(b \cdot s))$, p_{wp} is ratio of transverse hoop used in prestressing $(=A_{wp})/(b \cdot s)$, f_{ct} is tensile strength of concrete, A_{wn} is cross area of one pair of transverse reinforcement without prestressing, A_{wp} is cross area of one pair of transverse reinforcement with prestressing and σ_L is lateral prestress $(=p_{wp} \cdot f_{wp})$

2. TEST PROGRAM

2.1 Test Specimens

Table 1 lists test specimen, and Fig. 1 shows details of the specimens. The test specimens were total five specimens which have square shaped section 340mm×340mm, height 900mm. Five specimens were designed as which occur shear failure in ultimate condition, before longitudinal reinforcement had been yielded, without bond splitting failure, based on AIJ Guidelines for Reinforced Concrete Buildings (1999). Principal variables were effective tensile stress into a piece of transverse

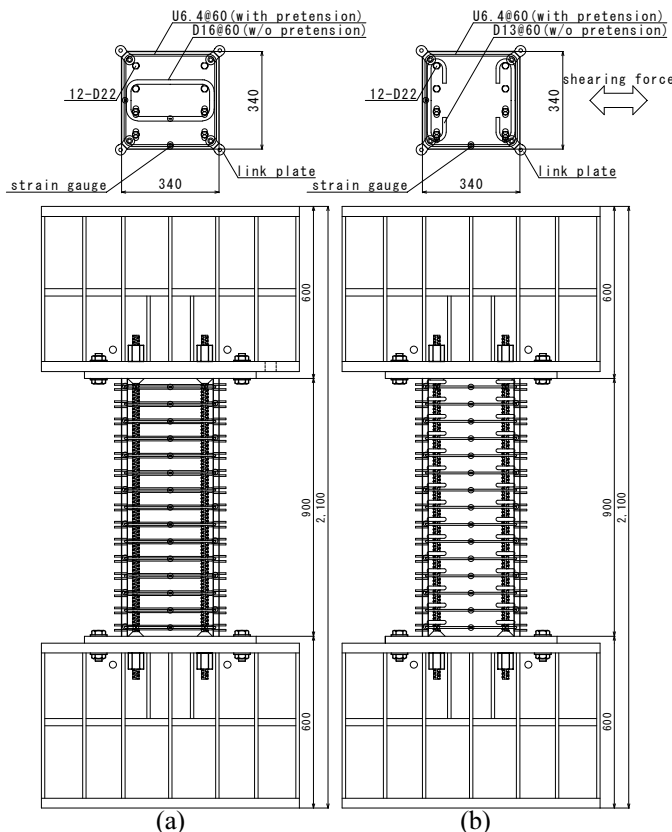


Fig. 1 Details of Test Specimens: (a) No.1-3, and (b) No.4 and 5

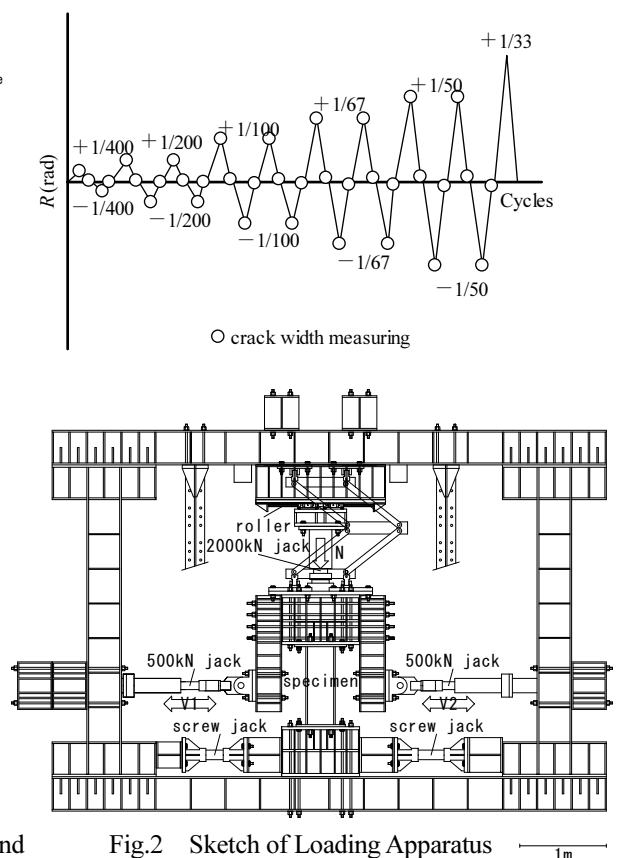


Fig.2 Sketch of Loading Apparatus

Table 2 Mechanical Properties of Steel used in the Experiments

Type	Material	f_{sy}, f_{wy} (N/mm ²)	f_{st} (N/mm ²)	E_s (kN/mm ²)
D22	—	1016*	1162	206
U6.4	—	1441	1465	197
D13	SD345	378	535	198
D16	SD295A	344	513	202

*0.2% offset, f_{sy} and f_{wy} are yield strength of steel, f_{st} is tensile strength of steel, and E_s is steel Young's modulus

reinforcement f_{wp} (60, 37 and 0% of its yield). Two types of sub reinforcements were used (see Figs. 1(a) and (b)). In this experiment, the transverse hoop used for prestressing was only outer one. Cover to transverse reinforcements was 12mm. Maximum particle size of coarse aggregate was 25mm. Cement was high early strength Portland cement. Mechanical properties of steel used in the experiments were shown in Table 2.

2.2 Loading and Measuring Method

The loading apparatus is shown as Fig. 2. Vertical force on the test specimen was supplied by one hydraulic jack capacity 2MN, and axial load ratio (on assumption that this axial load equal to dead load without consideration of steel) was kept constant as 0.30 controlled in the load during test. To comparison among shear crack strength of columns with different prestress, so that absolute value of difference among specimens become larger, higher axial force ratio was adopted. Horizontal forces on test specimen was supplied by two hydraulic jacks capacity 500kN, and controlled in displacement during test. Horizontal forces were applied in cyclic, and made an unsymmetrical moment. Tests repeated, once at deformation angle of member $R = \pm 400$, two times, at $R = \pm 1/200$, $\pm 1/100$, $\pm 1/67$ and $\pm 1/50$, once at $R = \pm 1/33$, and finished at $+1/25$. R is horizontal relative displacement between top and bottom of the column divided by its height. Shear crack openings were measured by using digital micro scope (which had minimum divisions of a scale, 0.01mm) at deformation peak and horizontal force unloaded (added shear force due to dead load was still residual) of each cycle until $\pm 1/50$, after cracks occurring. Shear cracks upon transverse reinforcement and the middle point between two transverse reinforcements were measured.

2.3 Lateral Prestressing Method

Lateral prestress is applied into the concrete with high strength transverse hoops pretensioned mechanically. Reacting forces of pretension is taken with steel cast, and the cast is removed after concrete hardening. Lateral prestress is introduced just before axial force due to dead load of assumed upper structure loaded into the column, such as Precast column. Lateral prestress σ_L was defined as value which was product of ratio of transverse reinforcement used in prestressing and transverse reinforcement stress before column had been loaded axially.

3. EXPERIMENTAL RESULTS

3.1 $V-R$ Curves

Each hysteresis of specimens were shown in Fig. 3. For typical damage process observed on the specimens, after flexural crack, flexural shear crack, and shear crack occurred, reached maximum strength with increasing of the input shear force.

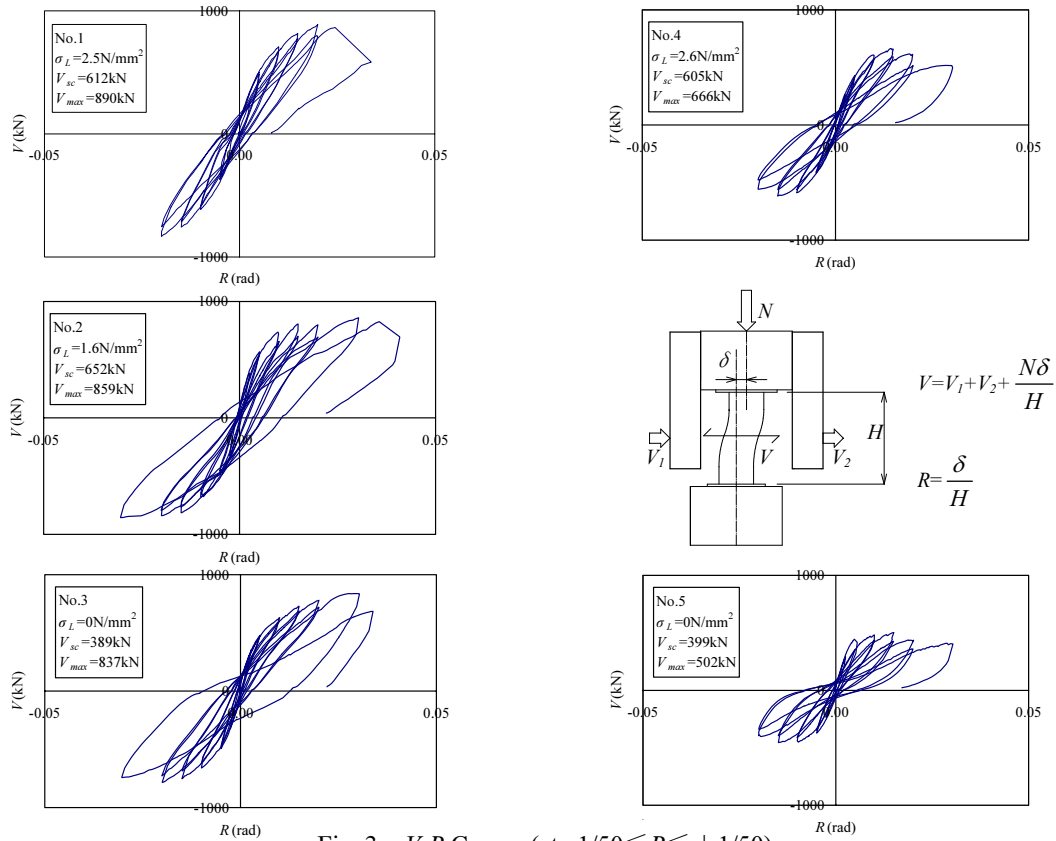


Fig. 3 V-R Curves (at $-1/50 \leq R \leq +1/50$)

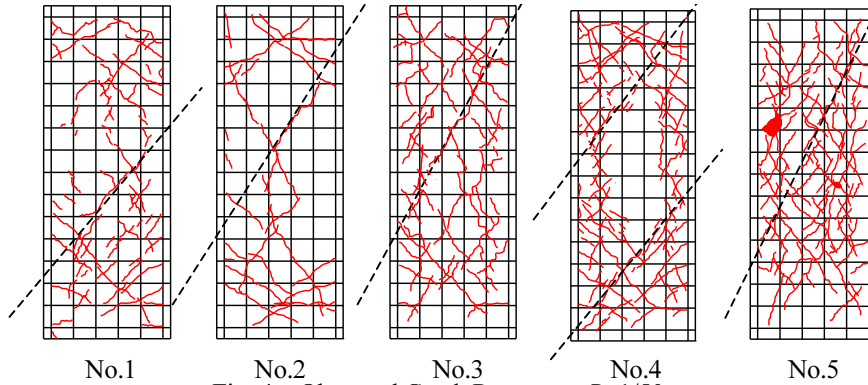


Fig. 4 Observed Crack Patterns at $R=1/50$

3.2 Failure Mode

Observed crack patterns at $R=1/50$ were shown in Fig. 4. Here, an angle of crack which reached severe opening was indicated in a broken line. According to increase of lateral prestress, these angles at crack relative to axis of the column approximated 45 degrees from axial direction of the column. Finally, all specimen represented shear compression failure without flexural yield.

3.3 Effects of Lateral Prestress on Shear Crack Strength

Relations between shear crack strength $_{exp}V_{sc}$ and lateral prestress was considered. Relations between shear crack stress $_{exp}\tau_{sc} (=_{exp}V_{sc}/bD)$ and lateral prestress were plotted in Fig. 5, together with data from literature (Watanabe et al. 2002). Shear crack strength improved with increasing of prestress.

3.4 Evaluation of Shear Crack Strength

Verification of precision was estimated by evaluation equation of shear crack strength based on

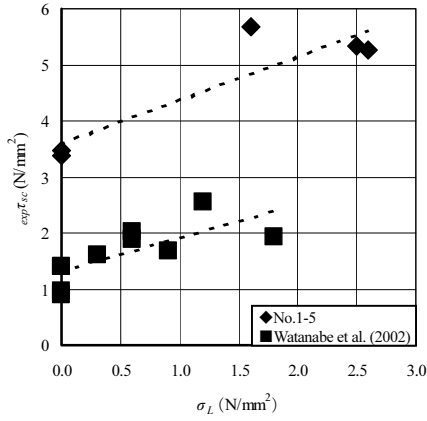


Fig.5 Relations Between Shear Crack Stress and Lateral Prestress

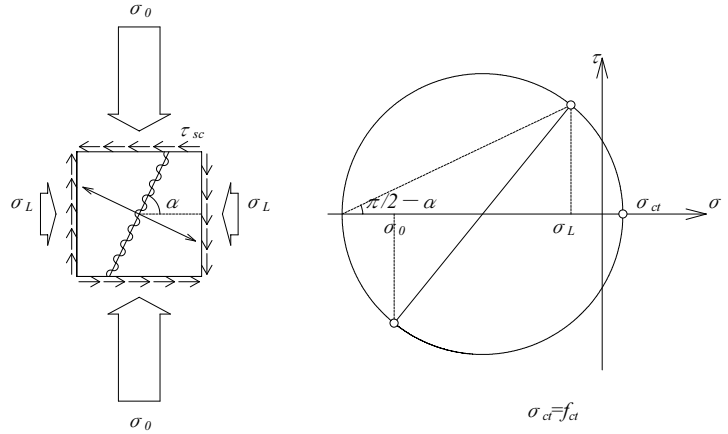


Fig.6 Assumption of Mohr's Circle due to Lateral Prestressing

maximum principal stress theory which proposed in literature (Watanabe et al. 2003). Equation was not derived empirically from statistics of experimental results, based on the hypothesis which could be explained theoretically. Eq. (1) adopted in AIJ Design Guidelines for Reinforced Concrete Buildings (1999) and AIJ Standard of Prestressed Concrete Structures (1998). Actually, lateral prestressed reinforced concrete column was seated under three dimensional stresses condition with combination of lateral prestress and axial load added column, but here, projected into two dimensions like Fig. 6. Comparison estimated precisions of calculated values between usual evaluation Eq. (1) of shear crack strength without consideration of lateral prestress and evaluation Eq. (2) with consideration of prestress, was examined, adding 10 columns from literature (Watanabe et al. 2002).

$$\tau_{sc} = \sqrt{(f_{ct})(\sigma_0 + f_{ct})} / \kappa \quad (1)$$

$$\tau_{sc} = \sqrt{(\sigma_L + f_{ct})(\sigma_0 + f_{ct})} / \kappa \quad (2)$$

where f_{ct} is concrete tensile strength, σ_0 is axial stress of the column and κ is constant ($\kappa = 1.5$). f_{ct} was calculated by Eq. (3) which was adopted from literature (Collins and Mitchell 1991) same as AIJ Design Guidelines (1999). Unit of f_c is in N/mm^2 .

$$f_{ct} = 0.33\sqrt{f_c} \quad (3)$$

Fig.7 shows estimated precision on shear crack stress both calculated by original Eq. (1) and proposal Eq. (2). Proposed Eq. (2) takes accounts of lateral prestress, which had coefficient of variation 21%, estimate in safely with smaller dispersion than original Eq. (1), which had coefficient of variation 27%. Thus, prediction accuracy was given by using Eq. (2), more than using present design formula.

3.5 Effect on Damage

Fig. 8 shows envelopes of hysteresis of shear force V - shear crack width W . Here crack width W is maximum shear crack width, which had been measured on surface of the specimens. Starting from shear crack strength, and W at shear force reaching almost zero (added shearing force due to dead load was still residual) represents residual shear crack width W_r . For lateral prestressed reinforced concrete column, W_r is prevented in smaller value, even if the column had experienced larger shear force or crack opening than usual reinforced concrete column had experienced.

Relations between residual shear crack widths and shear stresses which apply the widths are shown in Fig. 9. The shear stress applied residual shear crack width as 0.2mm, which increased with

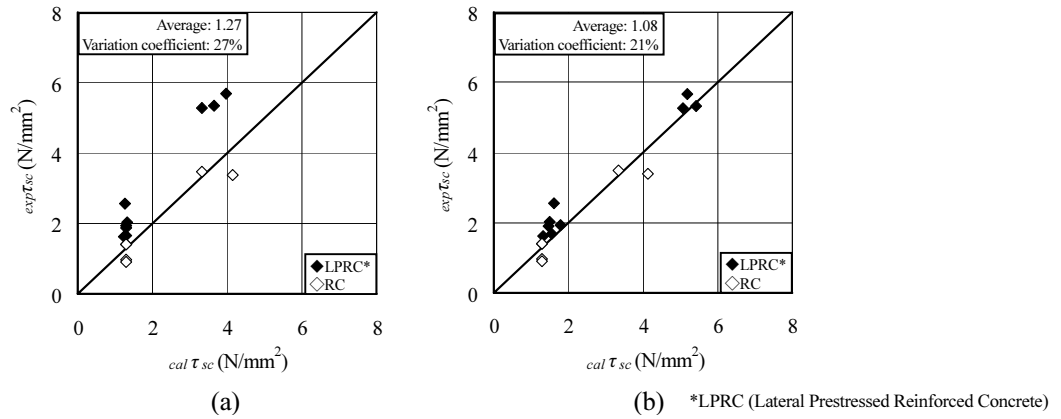


Fig. 7 Comparisons of Shear Crack Stress Between Experimental Results and Calculations: (a) by Eq.(1), and (b) by Eq.(2)

lateral prestress. For column with larger quantity of transverse reinforcements, shear stress increased with prestress from occurring of shear crack to residual shear crack width reaching 0.2mm, for column with smaller quantity of transverse reinforcements, shear stress at residual shear crack width reaching 0.2mm within lateral prestressed reinforced column was equal to shear cracking stress of non-prestressed column. For columns had smaller quantity of transverse reinforcement, when shear crack occurred, then residual crack opening reached 0.2mm.

3.6 Definition of Shear Damage Strength

The shear stress is defined as “*shear damage stress*” τ_{sd} which applies control target value on residual shear crack width. Here, control target value on crack width was indicated by AIJ Recommendations for Design of Partially Prestressed Concrete (2003), as 0.2mm. From a viewpoint of durability, the absolute value of crack width is adopted as 0.2mm without its reduction in scale-downed specimen used in this experiment. However, when total depth of a member becomes two times, also residual crack width becomes about two times, even if the member had been experienced coordinate shear stress, experimental results were reported (Honjou et al. 2001). The control target value of crack width should be given attention in actual design. Relations between shear crack stress τ_{sc} and lateral prestress σ_L , and relations between *shear damage stress* τ_{sd} and lateral prestress σ_L were shown in Fig. 10. Both shear crack strength and *shear damage strength* increased with lateral prestress. Residual crack width is defined under the following condition, as inputted horizontal load into column is unloaded and added shear force due to dead load is still residual.

In particular, for specimen with large quantity of transverse reinforcement, under same shear stress, residual shear crack width on reinforced concrete column with no prestress reached 0.2mm, while lateral prestressed reinforced concrete column ($\sigma_L=2.5\text{N/mm}^2$) had no shear crack. *Shear damage stress* increased in lateral prestressed column one and a half times than reinforced concrete column.

3.7 Evaluation of Shear Damage Strength

To control damage on reinforced concrete column, estimate method of shear damage strength V_{sd} which makes residual shear crack width into control target value, is expressed in this paper. It is always after cracking that residual shear crack occurs. Since the tensile force due to horizontal load becomes impossible to be subjected by concrete after cracking occur, therefore, be supported by transverse reinforcements instead. Transverse reinforcement subjected tensile force was required tensile strain. When transverse reinforcement is in elastic condition, tensile stress in a single piece of the reinforcement is taken as

$$f_w = W_r \cdot E_s / (j \cdot \sin \alpha) \quad (4)$$

where, j is distance between corner longitudinal reinforcement bars, and α is an angle at diagonal crack plane relative to horizontal plane. The crack width used in Eq. (4) is crack width at *shear damage strength*. Correctly, residual crack width differs from crack width in Eq. (4). Here, crack width in Eq. (4) is assumed that equal to residual crack width, since crack width in Eq. (4) equal to sum total of crack width and strain distribution in transverse reinforcements is un-uniform.

By assuming *shear damage strength* equals to total subjected load by all transverse reinforcement across shear crack surface, *shear damage strength* $calV_{sd1}$ given by

$$calV_{sd1} = (f_w + f_{wp})A_{wp} \cdot n + f_w \cdot A_{wn} \cdot n \quad (5)$$

where, A_{wp} is cross area of one pair of transverse reinforcement with prestressing, A_{wn} is cross area of one pair of transverse reinforcement without prestressing, and n is the number of pieces of transverse reinforcement which crossing shear crack surface. Eq. (5) takes account of lateral prestress by including transverse reinforcement effective tensile stress f_{wp} .

Eq. (5) required number of transverse reinforcement crossing crack surface. Judging from crack patterns, the number of transverse reinforcement was defined. Since residual crack width do not

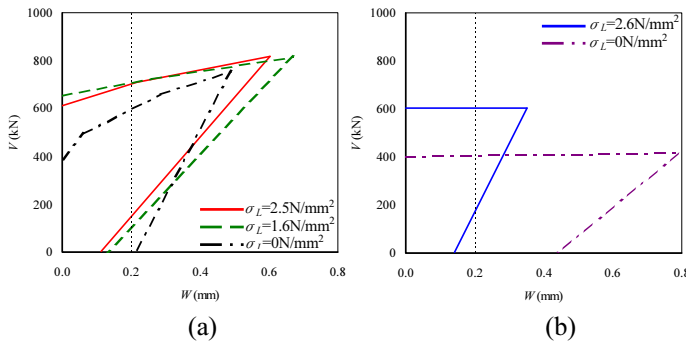


Fig. 8 Relations Between Shearing Force and Shear Crack Width: (a) $p_w=2.54\%$, and (b) $p_w=0.29\%$

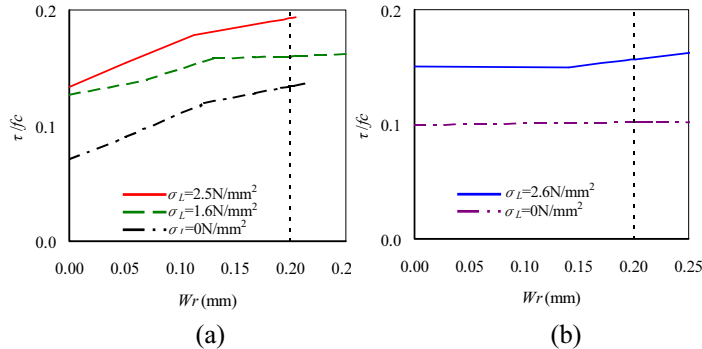


Fig. 9 Relations Between Shearing Stress and Residual Shear Crack Width: (a) $p_w=2.54\%$, and (b) $p_w=0.29\%$

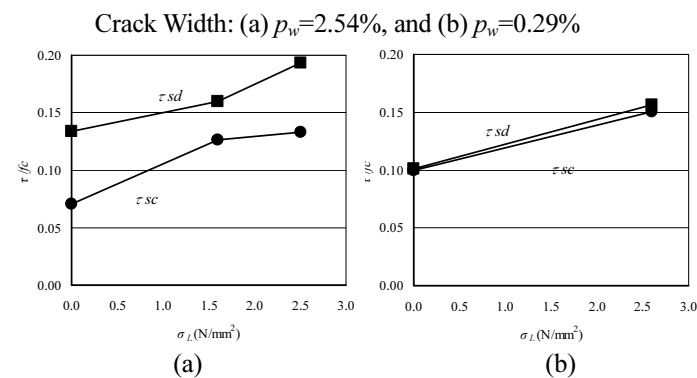


Fig.10 Relations Between *Shear Damage Strength* and Lateral Prestress: (a) $p_w=2.54\%$, and (b) $p_w=0.29\%$

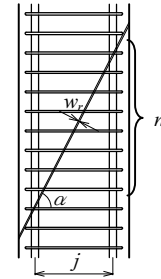


Table 3 Calculated Results of Shear Damage Strength

No.	n	$calV_{sd1}$ (kN)	$calV_{sc}$ (kN)	$expV_{sc}$ (kN)	$calV_{sd}$ (kN)	$expV_{sd}$ (kN)	$expV_{sd} / calV_{sd}$
1	6	850	622	612	850	886	1.04
2	7	819	595	652	819	827	1.01
3	9	738	476	389	738	738	1.00
4	6	384	582	605	582*	629	1.08
5	10	106	382	399	382*	407	1.07

Bold number shows the bigger value. (* $calV_{sd1} < calV_{sc}$)

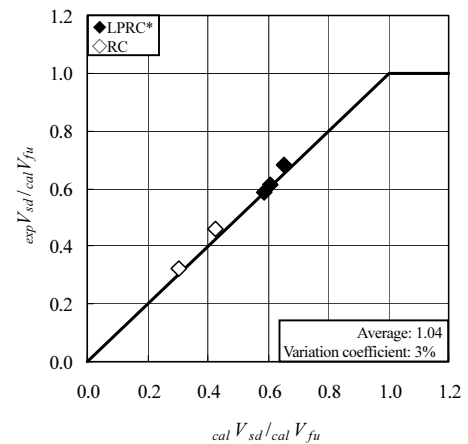


Fig.11 Comparisons of *Shear Damage Strength* Between Experimental Results and Calculations

occur before crack occur, V_{sd} is calculated as the larger one, ${}_{cal}V_{sd1}$ or ${}_{cal}V_{sc}$ (which calculated by Eq. (2)).

Calculating *shear damage strength* of specimens of this experiment, Fig. 11 and Table 3 were obtained. Both axes are normalized by ${}_{cal}V_{fu}$, the shear force when the bending moment at column end section reaches the theoretical flexural capacity. V_{sd} was defined as ${}_{cal}V_{sd1}$ for No.1-3, while V_{sd} was defined as ${}_{cal}V_{sc}$ for No.4 and 5. This phenomenon corresponded to results of Fig. 9.

Average of experimental value/calculated value was 1.04 and coefficient of variation was 3%. Above is evaluated with sufficient accuracy and safely.

4. CONCLUSIONS

From the behavior observed during the flexure-shear experiment on lateral prestressed reinforced concrete column and results presented above, the following conclusions can be drawn:

Shear crack strength on column able to be improved by introduction of lateral prestress. Moreover, based on a consistent theory, evaluation method of shear crack strength of usual Reinforced Concrete column and Lateral Prestressed Reinforced Concrete column was shown.

By introducing of lateral prestress, improvement of the *shear damage strength* could be recognized, which makes residual shear crack width to control target value is newly defined. By taking account of lateral prestress as transverse reinforcements stresses which crossing shear crack surface, *shear damage strength* was evaluated. The design could allow larger shear force into the columns by lateral prestressing, when occurrence of shear crack is prevented or residual shear crack width is controlled.

By using evaluation method of *shear damage strength* which takes accounts of only load subjected by transverse reinforcements, input shear force into column makes residual crack width to control target value was calculated safely with sufficient accuracy.

Acknowledgements:

The authors acknowledge support from Neteuren Co., Ltd. The financial support of Structural Engineering Research Center, Tokyo Institute of Technology, as a part of the Collaborative Research Projects, is also gratefully acknowledged.

References:

- Architectural Institute of Japan (1999), "AIJ Standard for Structural Calculation of Reinforced Concrete Structures –Based on Allowable Stress Concept–"
- Fukuyama, H., Suwada, H., Iso, M., Matsuzaki, Y., Nakano, K., and Kasahara M. (2000), "Evaluation of Damage Limit State of RC Elements Due to Shear Crack Width (Part. 1 In case of beams and columns)," *Summaries of Technical Papers of Annual Meeting Architectural Institute of Japan*, C-2, 13-14
- Watanabe, H., Makitani, E., Ito, Y., and Arima, H. (2002), "Mechanical behaviors of laterally prestressed concrete columns by high strength hoops under compressive or shear conditions," *Journal of Structural and Construction Engineering*, No.552, 133-140
- Watanabe, H., Katori, K., Shinohara, Y., and Hayashi, S. (2003), "Effects of Lateral Prestress on Damage of Reinforced Concrete Columns," *Proceedings of the Japan Concrete Institute*, Vol.25, No.2, 193-198
- Architectural Institute of Japan (1999), "Design Guidelines for Earthquake Resistant Reinforced Concrete Buildings Based on Inelastic Displacement Concept," 91-137
- Architectural Institute of Japan (1998), "Standard for Structural Design and Construction of Prestressed Concrete Structures"
- Collins, M.P. and Mitchell, D.(1991), "Prestressed Concrete Structures," *Prentice Hall*, Englewood Cliffs, NJ, 766
- Architectural Institute of Japan (2003), "Recommendations for Design and Construction of Partially Prestressed Concrete (Class III of Prestressed Concrete) Structures"
- Honjou, M., Nagae, T., Yanase, T., and Hayashi, S. (2001), "Experimental Study on Size Effect in Shear Failure of Reinforced Concrete Pile," *Proceedings of the Japan Concrete Institute*, Vol.23, No.3, 979-984

SEISMIC RETROFIT OF RECTANGULAR RC COLUMNS AT NCREE

K. C. Chang¹⁾, Keh-Chyuan Tsai²⁾, S. P. Chang³⁾, and M.L. Lin⁴⁾

1) Professor, Department of Civil Engineering, National Taiwan University, Taipei 106, Taiwan

2) Director, National Center for Research on Earthquake Engineering, Taipei 106, Taiwan

3) Graduate Assistant, Department of Civil Engineering, National Taiwan University, Taipei 106, Taiwan

4) Associate Research Fellow, National Center for Research on Earthquake Engineering, Taipei 106

kcchang@ncree.gov.tw, kctsai@ncree.gov.tw, kilin5@sinamail.com, mllin@ncree.gov.tw

Abstract: One of the major collapse modes of RC structures during the 1999 Taiwan Chi-Chi earthquake is the failure of columns due to lap-splicing at the plastic hinge zone. It has been shown that directly apply the CFRP or steel jacket to large rectangular RC column is ineffective in providing confinement to concrete except at the corners of the cross-section. This paper summarizes experimental results of two effective methods using steel jacketing and FRP wrapping to retrofit the existing RC columns with the above mentioned problems. For steel jacketing methods, the octagonal steel jacketing scheme for seismic retrofitting the rectangular RC bridge columns is presented in this paper. For applying the CFRP, a new retrofit method -“CS retrofit method” is proposed. Experimental results show that both the octagonal steel jacketing and the CS retrofit methods can greatly improve the lateral strength, displacement ductility, and energy dissipation of the columns lap spliced at the plastic hinge zone.

Key word : Rectangular RC column, Lap-spliced, Octagonal steel jacketing, CS Retrofit

1. INTRODUCTION

Significant amount of retrofit research and actual implementations to enhance the seismic performance of existing bridges have been made in the United States (Gates 1988), Japan (Kawashima 1990) and New Zealand (Priestley and Park 1987). Recent studies indicate that under a severe earthquake some existing bridges in Taiwan can be severely damaged in bridge columns due to a number of factors (Chang et al. 1999). Among many others, (1) inadequate design strength, (2) inadequate confinement at potential plastic hinge region, and (3) inadequate shear strength due to the change of lateral steel spacing, have been identified as the most possible sources for seismic hazard. Therefore, a coordinated research effort on seismic retrofit of reinforced concrete bridge columns has been launched in the National Center for Research on Earthquake Engineering (NCREE). This coordinated research program aims at reviewing and developing effective measures in seismic retrofit of the existing rectangular and circular RC bridge piers. The joint research effort has applied several retrofit techniques in the tests, including the steel jacketing, reinforced concrete jacketing, and the advanced composite material wrapping using the FRP jackets. The purposes of the program are to gather additional data for seismic bridge engineering applications and accelerate retrofit programs to be implemented for seismically deficient bridges in Taiwan. As part of the aforementioned joint research program, this paper focuses on the flexural and shear retrofit techniques for rectangular RC bridge columns using steel and CFRP jackets.

The objectives of this study, in the context of a joint research with other researchers, include: (1) collecting additional data on seismic retrofit of rectangular RC columns using the elliptical steel jacket,

and (2) seeking other cost-effective steel or FRP jacketing schemes for rectangular RC columns. In this paper, the experimental results of the rectangular RC columns retrofitted with the octagonal steel jackets and the combined CFRP wrapping and steel plates (CS) are critically compared with other schemes.

2. STEEL JACKETING RETROFIT

2.1 Experimental Program

A total of eleven 0.4 scale specimens were tested. All the test specimens were subjected to constant axial load and cyclic lateral displacements. The test setup is shown in Figure 1 and Photo 1. All test specimens were loaded in the strong bending direction and subjected to the same displacement pattern of increasing magnitude as shown in Figure 2. Displacement control method was used in the test. The vertical stress was kept approximately at $0.15f'_c$ during the tests.

In order to gain insight into the three most possible seismic failure modes of RC bridge column in Taiwan, three as-built specimens were tested. All the test specimens have the same cross-sectional dimensions. The rectangular cross section of the specimens is 600 by 750 mm, a 2/5 scale of the prototype column using the pre-1987 details. A double U-shaped, alternation arrangement of the transverse reinforcements was adopted in all specimens. This type of transverse reinforcing details is rather common in the construction of bridge columns in Taiwan, therefore, is one of the key items studied in this research. Table 1 shows the details and design parameters of the specimens. The steel jacketing details for the retrofitted specimens were shown in Table 2. To ensure that the jacket does not bear against the footing when in compression, a nominal gap of 30 mm is provided between the toe of the jacket and the footing.



Photo 1. Test setup

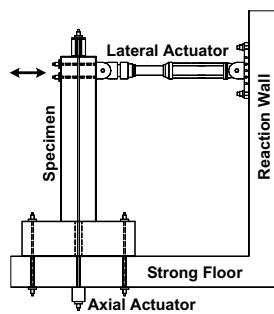


Figure 1. Test setup

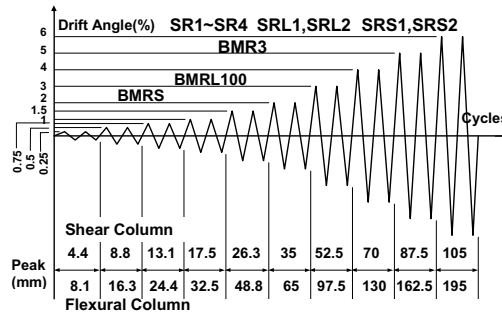


Figure 2. Lateral loading history

Table 1. Design parameters of test specimen

Parameter	BMR3	BMRL100	BMRS
Dimensions (mm)	600x750	600x750	600x750
Column Height (mm)	3250	3250	1750
Concrete Stress (MPa)	21	21	21
Longitudinal Steel	32#5	32#6	32#6
Longitudinal Stress (MPa)	280	420	420
Transverse Steel	#3@130mm #3@240mm	#3@130mm #3@240mm	#3@300mm
Transverse Stress (MPa)	420	280	280

Table 2. Steel jacketing details and experimental results

Specimen	Steel Jacketing Details (A36 Steel)			Ductility		Failure Mode
	Scheme	Thickness	Height	Push	Pull	
BMR3	NA	NA	NA	4	4	Confinement
SR1	Octagonal	3 mm	2800 mm	10.7	11	Low Cycle Fatigue
SR2	Elliptical	3	2800	13.1	9.4	Low Cycle Fatigue

SR3	Octagonal	6	2800	11.8	10.1	Low Cycle Fatigue
SR4	Elliptical	3	2800	11.7	13.9	Low Cycle Fatigue
BMRL100	NA	NA	NA	NA	NA	Lap-Splice
SRL1	Octagonal	6	2800	6.6	6.7	Low Cycle Fatigue
SRL2	Elliptical	3	2800	10.6	7.3	Low Cycle Fatigue
BMRS	NA	NA	NA	1.3	1.9	Shear
SRS1	Octagonal	3	1400	8.2	6.9	Low Cycle Fatigue
SRS2	Rectangular	3	1400	6.6	5.5	Low Cycle Fatigue

2.2 Test Results of Lap-Spliced Deficient Specimens

According to a rather common reinforcing detail found in Taiwan, as-built Specimen BMRL100 shown in Fig. 3 adopted a 76cm (equal to 40 times of the longitudinal bar diameter) lap-splice length for the longitudinal reinforcing bars in the plastic hinge region. For the retrofitted specimens (Fig. 4), SRL1 was retrofitted with a 6mm thick octagonal steel jacket while SR2 was retrofitted with a 3mm thick elliptical steel jacket.

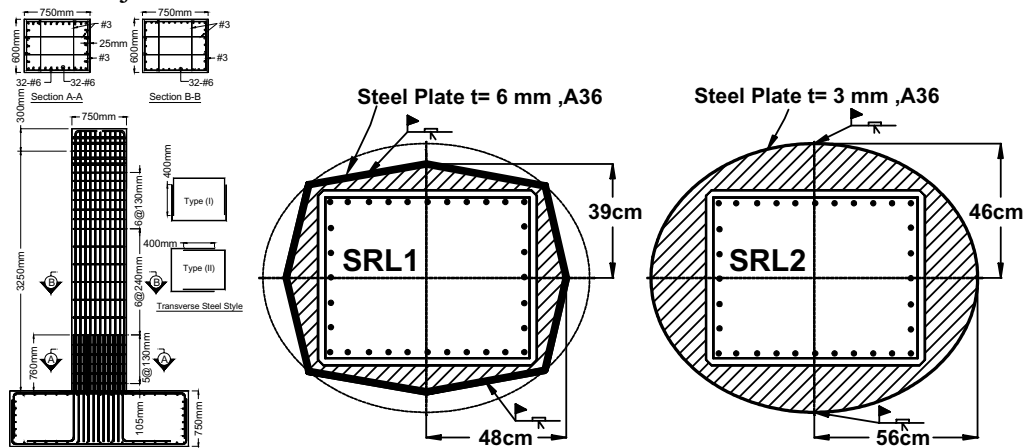


Figure 3. Details of Lap-splice specimen Figure 4. Details of the steel jackets for Lap-splice specimens

All specimens were subjected to the same cyclically increasing lateral displacement history until significant strength degradation was observed. The cyclic lateral load-deformation relationships for all specimens are shown in Figure 5. The energy dissipation histories are given in Figure 6. For the BMRL100, this lap-splice deficient bridge column can not develop full flexural strength to the nominal design level, and the strength degradation resulted from bond slip occurred prematurely and severely in the small displacement range.

Test results given in Figures 5 and 6 confirm that the seismic performance of rectangular RC bridge columns can be significantly and equally enhanced by properly designed elliptical or octagonal steel jacket following the procedures noted above. Bridge columns retrofitted with the octagonal or the elliptical steel jacket exhibit stable lateral force-displacement hysteretic response, possess excellent displacement ductility and energy dissipation capacities.

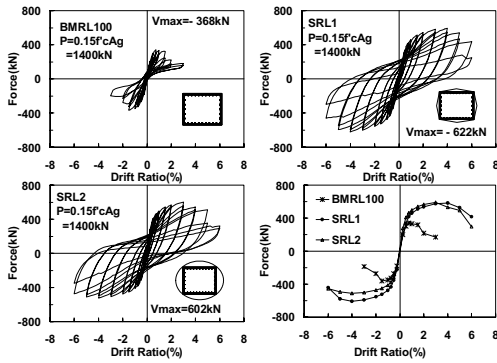


Figure 5. Cyclic lateral load vs. deflection relationships

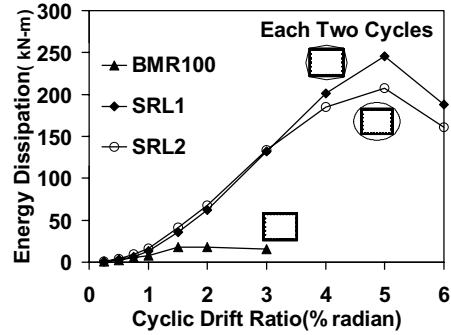


Figure 6. Energy dissipation curves

2.3 Full Scale Testing

One full-scale specimen with lap splice retrofit using the octagonal steel jacket was testing in order to verify the seismic performance of the octagonal steel jacketing. The details and design parameters of the full-scale specimen was shown in Fig. 7. The rectangular cross section of the columns is 1500 by 1875 mm, a full scale of the prototype column using the pre-1987 details. The column height is 8500 mm from the top of footing to the center of horizontal actuator. The footing is 1500-mm thick. A 1270-mm (equal to 40 times of the longitudinal bar diameter) lap splice length for all longitudinal reinforcement bars right above the top of the footing in the potential plastic hinge region was detailed and constructed. Ready mixed concrete providing a target compressive strength of 17.5 MPa at 28 days was adopted. This was to consider the effects of possible insufficient strength of concrete commonly observed in the existing old bridge columns constructed with a design strength of 21 MPa. Octagonal steel jacket (9 mm thick) was applied as shown in Fig. 8. The lap splice failure was completely prevented in LSRL-R. Fig. 9 shows the hysteretic responses.

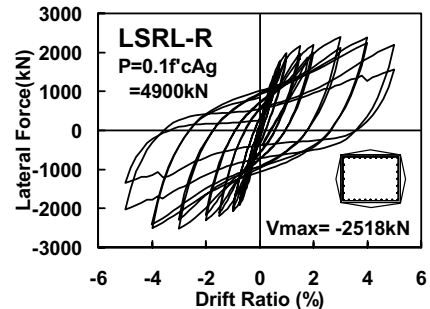
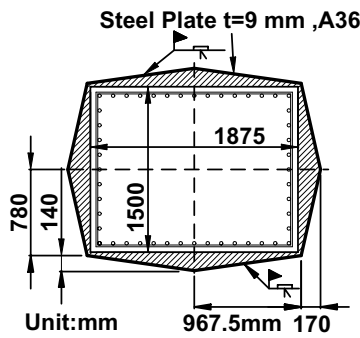
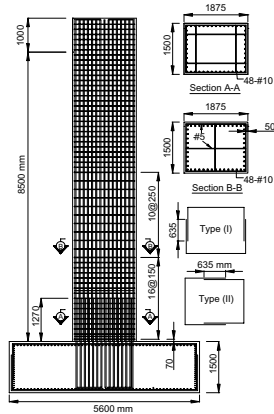


Figure 7 Reinforcing details of a full scale specimen	Figure 8 Retrofit design	Figure 9 Hysteretic response
---	--------------------------	------------------------------

3. THE “CS” RETROFIT

The reinforce concrete is composed of steel and concrete material. While using lap-spliced design, it's very important that the interface strength between concrete and the lap splicing reinforcements is sufficient. Because the lap-spliced steels strongly affect the column ductility, the ACI 318-95 (1995) specifies the construction detail in section 21.4.3.2 that no lap-spliced should be used in the joint and probable places of plastic hinge zone. However, it has been a common practice for the existing RC columns in Taiwan to lap-spliced the main steel bars at the plastic hinge zone. Fig.10 and 11 show the failure mode lap-spliced column in two collapsed buildings during the 1999 Chi-Chi earthquake.



Fig.10 Lap splices failure of rectangular Column



Fig.11 Lap splices failure in a collapsed building

In 1977, Orangun et. al (1997) proposed the well known O.J.B model based on 254 development length tests. This model considers concrete strength, clear cover, reinforcement spacing, reinforcement dimension, and confinement effect of lateral reinforcement. Besides, Orangun found that the O.J.B model can be applied to estimate the lap splices strength based on 286 test specimens. Another model was proposed by Paulay (1982) in 1982. The best way to improve columns ductility is to increase confinement stress by lateral reinforcements. Both the peak stress and ultimate strain of concrete will increase. This paper provides a new retrofit method, named “CS method” to improve the behavior of rectangular RC columns lap spliced at the plastic hinge zone.

The CS method combines the advantages of steel plates and CFRP jackets to provide more efficient confinement effect. The procedure of CS method is described as follows. First, clean the column surface; then, apply suitable steel plates on the surface; finally, wrap the CFRP jacket around the column. Fig.12 shows the drawing of the proposed CS method.

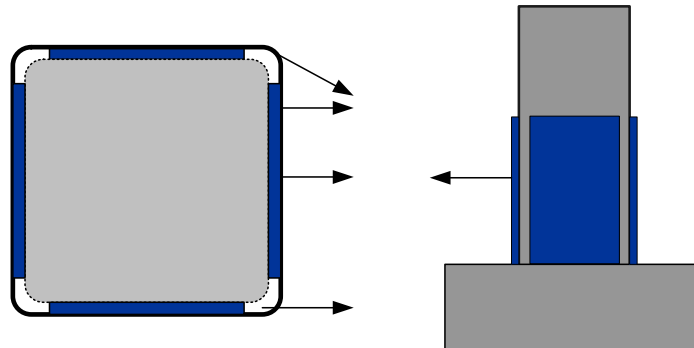


Fig12. Design drawing of CS method

3.1 Experimental Program

Table 2 shows the details and design parameters of the test specimens. These specimens represent the as-built, CFRP wrapped, and combined steel plate and CFRP.

For all the specimens, the lap spliced length is 40 times of the longitudinal bar diameter in the plastic hinge zone. This type of longitudinal reinforcing details was common in the construction of buildings in Taiwan. In addition to the lap splice steel, the double U-shaped, transverse reinforcement was used as the ties in each specimen. For retrofitted specimens, the design parameters are summarized in Table 3.

Table 2 The retrofitted Design parameter of Steel Jakets method

	Name	Failure Type	Lap Height (cm)	Section (cm ²)	Height (cm)	Concrete Strength (kg/cm ²)	Main Bar Strength (kg/cm ²)	Main Bar Ratio (%)	Axial Load (f'cAg)
1	B1L17-BM	Lap Spliced	76	60×75	325	170	4339	2.02	0.19~0.25
2	B2L21-BM	Lap Spliced	89	60×75	325	208	5188	2.07	0.27~0.42
3	B3L17-C8	Lap Spliced	76	60×75	325	170	4339	2.02	0.19~0.25
4	B4L21-B30S6	Lap Spliced	89	60×75	325	208	5188	2.07	0.27~0.44
5	B5L17-C8S10	Lap Spliced	76	60×75	325	170	4339	2.02	0.19~0.25
6	B6L21-C12S10	Lap Spliced	89	60×75	325	208	5188	2.07	0.28~0.43
7	B7L21-C12S5	Lap Spliced	89	60×75	325	208	5188	2.07	0.27~0.41
8	W1L19-B30S6	Lap Spliced	89	75×60	325	193	5188	2.07	0.30~0.43
9	W2L19-C15S10	Lap Spliced	89	75×60	325	193	5188	2.07	0.29~0.43
10	S1L19-C5S10	Lap Spliced	76	30×50	110	186	5273	1.90	0.41~0.47
11	S2L19-C5S10	Lap Spliced	76	30×50	200	186	5273	1.90	0.41~0.46
12	M1L19-C10S10	Lap Spliced	127	50×80	200	186	5467	1.98	0.15~0.21

Table 3-1 Design parameters of Steel Jacketing Method

Name	Section (cm ²)	Steel thickness (Height) : (mm)	Bolt diameter (mm)	Bolt distane (cm)
B4L21-B30S6	60×75	Under 100 cm : 6	22	vertical : 30
W1L19-B30S6	75×60	Under 100 cm : 6	22	vertical /transversely: 30/25

Table 3-2 Design parameters of the CS Method

Name	Section (cm ²)	CFRP thickness (Height) : (layer)	Steel size (cm ²)	Steel thickness (mm)
B3L17-C8	60×75	Under 100 cm : 8		
B5L17-C8S10	60×75	Under 100 cm : 8	50×100	10
B6L21-C12S10	60×75	Under 50 cm : 12	50×100	10
B7L21-C12S5	60×75	Under 50 cm : 12	50×100	5
W2L19-C15S10	75×60	Under 50 cm : 15	50×100	10
S1L19-C5S10	30×50	Under 80 cm : 5	14× 86	10
S2L19-C5S10	30×50	Under 100 cm : 5	14× 86	10
M1L19-C10S10	50×80	Under 150 cm : 10	34×138	10

3.2 Instrumentation and Testing Procedures

Fig. 13 shows the test setup in this study. Fig. 14 shows the displacement control cycles. The test began with the application of the axial load at the target value, and ended when the lateral force dropped more than 80% of the maximum experienced capacity.

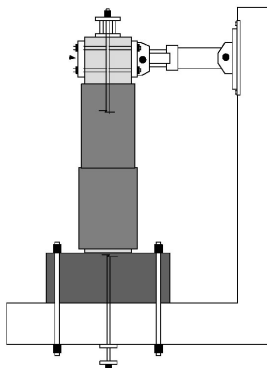


Fig.13 Test setup

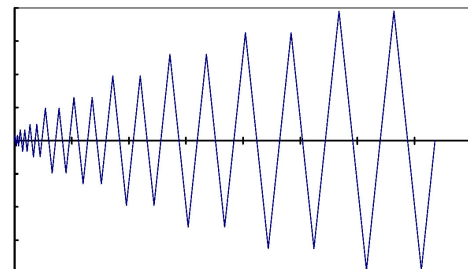


Fig.14 Lateral displacement control history

3.3 Test Results and Discussion

- (1) Fig. 15 shows the different failure types at the bottom of the column before and after retrofit. For the as-built specimens B1L17-BM, B2L21-BM, the specimens failed when the cover concrete was spalled and large concrete block were crushed at the corner. The longitudinal bars experienced no buckling. For the retrofitted specimens, it can be observed that, after removing the CFRP, the internal lap spliced reinforcements buckled under combined axial and lateral force.



(a) specimen B2L21-BM



(b) specimen B7L21-C12S5

Fig15. Photographs of damaged region at plastic hinge zone

- (2) The load-displacement hysteresis loops are given in Figure 16. The failure of lap spliced column (B1L17-BM · B2L21-BM) at low ductility =1.5 and 2.0 ,was caused by the bond failure at the splices of longitudinal bars. From the hysteresis loops, the strength of the as-built specimens decreased rapidly after failure. However, highly ductile behavior was observed in the retrofitted rectangular column (B6L21-C12S10 · B7L21-C12S5 · W2L19-C15S10,etc.).
- (3) In the lap spliced models, specimens S1L19-C5S10 · S2L19-C5S10 · M1L19-C5S10 are short columns. The CS method was used for enhancing the shear resistance to avoid the shear failure mode. The test results showed that such columns can be effectively retrofitted with the new retrofit technique.
- (4) The efficiency of using direct steel jackets to retrofit the lap spliced column can be improved by augmented a small number of adhesive anchor bolts. Comparing with CS method, they both have excellent performance.
- (4) To analyze the test result of specimens B6L21-C12S10 · B7L21-C12S5, although their plate thickness are different (10 mm / 5 mm), they have similar highly ductile behavior.

4. CONCLUSIONS

1. Test results confirmed that the seismic performance of the rectangular RC bridge columns can be significantly and equally enhanced by properly constructed elliptical or octagonal steel jacket.
2. The thickness of the steel jacket can be determined from the static equilibrium assuming a specific confinement pressure is to be developed. Using a reduced elliptical shape but a thickened steel jacket can reduce the cross-sectional area of an octagonal steel jacketed rectangular RC bridge column.
3. Octagonal steel jacketing scheme is cost-effective. It can provide lateral confinement and the shear strength to mitigate seismic failure of rectangular RC bridge columns due to a lack of lateral confinement, improper lap-splice or inadequate shear capacity.
4. A smaller cross-sectional area and better seismic performance than the elliptical steel jacketing scheme have been achieved from the octagonal steel jacketing.
5. The CS method is an effective method to improve the strength, ductility, and energy dissipation of rectangular RC columns, including those columns with main steels lap spliced at the plastic hinge zone.

6. Further analytical studies are necessary to better understand the mechanisms and critical parameters for the combined steel plate and CFRT retrofit method.

Acknowledgements:

The financial supports provided by the National Science Council and the National Center for Research on Earthquake Engineering (NCREE) are gratefully acknowledged. The experimental facilities and the technical supports provided by the NCREE are very much appreciated.

References:

Building Code Requirements for Reinforced Concrete and Commentary (ACI 318-95, 1995). American Concrete Institute, Detroit, Mich.

Chang, K.C., Chung, L.L., Hwang, S.J., Hwang, J.S., Lee, Y.F. and Tsai, K.C. (1999), "Seismic Retrofit of Reinforced Concrete Bridge Columns," Proceedings of the International Workshop on Mitigation of Seismic Effects on Transportation Structures, Taipei.

Chai, Y.H., Priestley, M.J.N. and Seible, F. (1990), "Retrofit of Bridge Columns for Enhanced Seismic Performance", Proceedings, First U.S.-Japan Workshop on Seismic Retrofit of Bridges.

Chang K.C., Liu K.Y., and Chang, S.B., "Seismic Retrofit Study of RC Columns Lap-Spliced at the Plastic Hinge Zone", proceeding of FRP Composites in Civil Engineering, pp.869-876, 12-15 December 2001, Hong Kong, China.

Kawashima, K. (1990), "Seismic Design, Seismic Strengthening and Repair of Highway Bridges in Japan," Proceedings of the First U.S.-Japan Workshop on Seismic Retrofit of Bridges.

Orangun, C. O.; Jirsa, J. O.; and Breen, J. E., (1997) "A Reevaluation of Test Data on Development Length and Splices," ACI Journal, Proceedings V. 74, No. 3, pp. 114-122.

Paulay, (1982), "Lapped Splices in Earthquake-Resisting Columns", ACI Journal, Proceedings, V. 79, No. 6, November-December 1982, pp.458-469, American Concrete Institute.

Priestley, M.J.N. and Park, P. (1987) Strength and Ductility of Concrete Bridge Columns under Seismic Loading. Structure Journal, ACI, 84(1):61-76.

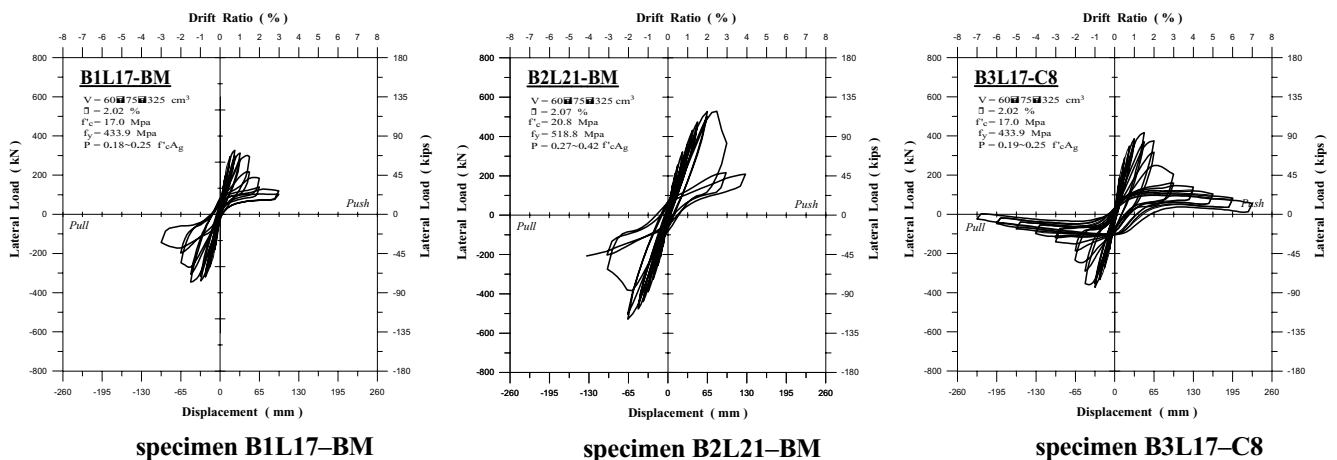
Priestley, M.J.N., Seible, F. and Calvi, G.M. (1996) Seismic Design and Retrofit of Bridges. John Wiley & Sons, Inc., New York.

Sun, Z.L., Seible, F. and Priestley, M.J.N. (1993) Flexural Retrofit of Rectangular Reinforced Concrete Bridge Columns by Steel Jacketing. Structural System Research Project, Report No. SSRP-93/01, Department of Applied Mechanics and Engineering Science, U.C. San Diego.

Tsai, K.C. and Lin, M.L. (2002) Steel Jacketing for Seismic Retrofit of RC Rectangular Columns. National Center for Research on Earthquake Engineering, Technical Report.

Verma, R., Priestley, M.J.N., and Seible, F., Assessment of Seismic Reponse and Steel Jacket Retrofit of Squat Circular Reinforced Concrete Bridge Columns, Report No. SSRP-92/05, Department of Applied Mechanics and Engineering Sciences, University of California at San Diego, June 1993.

Xiao, Y. and Ma, R., (1997), "Seismic Retrofit of RC Circular Columns Using Prefabricated Composite Jacketing", Journal of Structural Engineering,, ASCE Vol. 123, No. 10, pp.1357-1364.



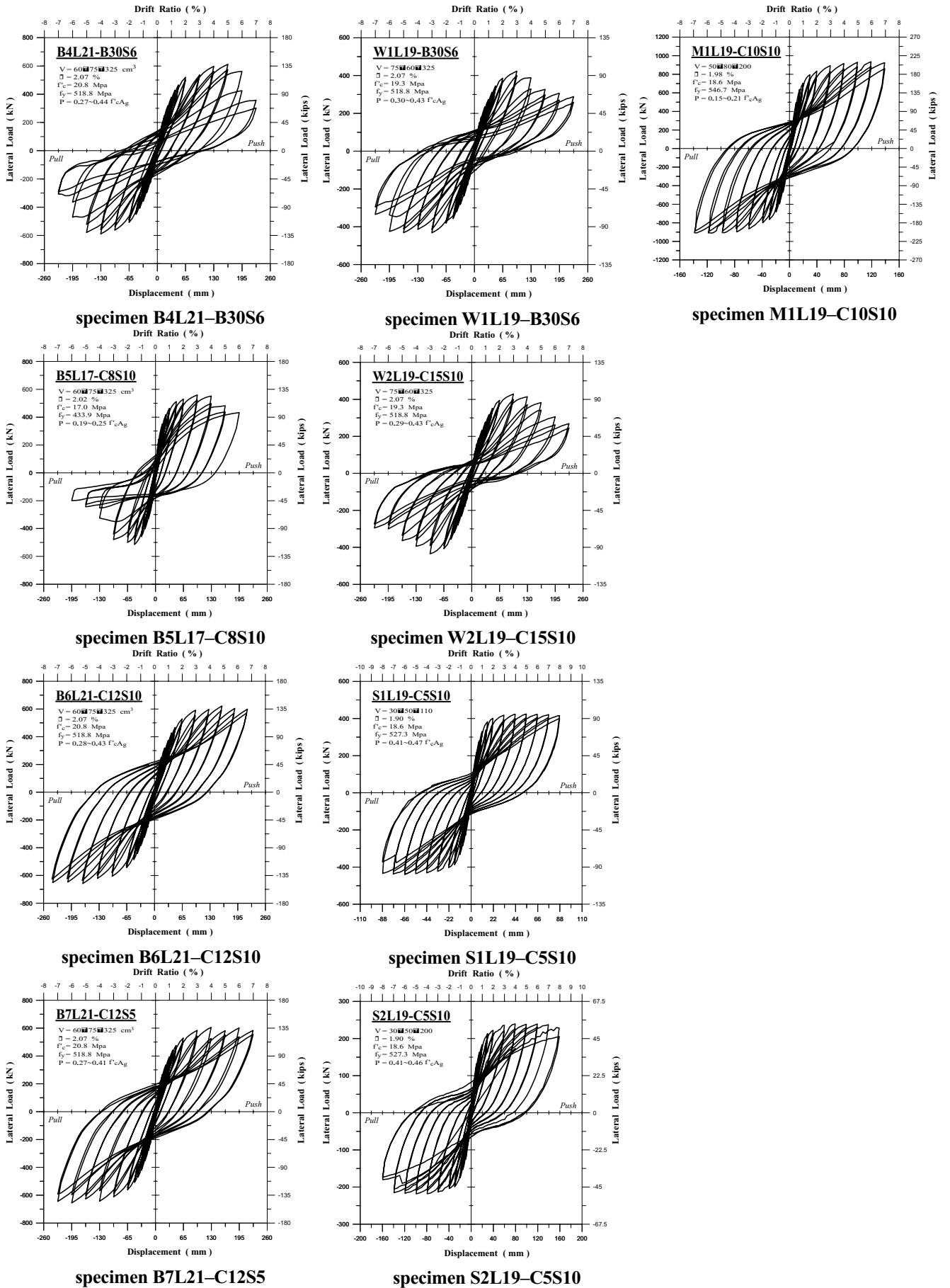


Fig.16 Load-Displacement hysteretic curve

SEISMIC HAZARD MAPPING PROJECTS IN JAPAN

S. Midorikawa¹⁾

*1) Professor, Department of Built Environment, Tokyo Institute of Technology, Japan
smidorik@enveng.titech.ac.jp*

Abstract: The national seismic hazard mapping project of Japan started in 1999. In the project, two types of the maps such as the deterministic and probabilistic maps will be produced by March, 2005. The maps provide the general view of seismic hazard in the whole of Japan, and are considered as the basic map. The project by a local government is also going on in order to produce the advanced regional map for improvement of disaster consciousness and preparedness of citizens. Applications of the maps should be further discussed not only in the engineering community but also in the general public.

1. INTRODUCTION

Following on the lessons learned from the Great Hanshin-Awaji Earthquake disaster, the Special Measure Law on Earthquake Disaster Prevention sponsored by legislators was enacted in July 1995 to promote a comprehensive national policy on earthquake disaster prevention. The Headquarters for Earthquake Research Promotion, a special governmental organization attached to the Prime Minister's office (now belongs to the Ministry of Education, Culture, Sports, Science and Technology), was established in accordance with this law. In April 1999, the Headquarters established its fundamental mission statement on research over the next ten years, where initiatives for development of national seismic hazard maps were proposed. Following the proposal, the Earthquake Research Committee, which is one of the committees in the Headquarters, started the national seismic hazard mapping project of Japan in order to produce seismic hazard maps covering the whole of Japan by March, 2005 (Fujiwara et al., 2003). This paper introduces the national seismic hazard mapping project and the related projects in Japan.

2. NATIONAL SEISMIC HAZARD MAPS

2.1 Outline of the Project

The Headquarters for Earthquake Research Promotion have promoted surveys of major active faults, long-term evaluations of the possibility of occurrence of large earthquakes, and surveys of deep sedimentary basin structures. In order to utilize the results for disaster mitigation, the Headquarters decided to start the project for producing the national seismic hazard maps based on most recent knowledge and techniques on strong motion prediction.

For this project, the subcommittee for evaluation of strong ground motion was established in the Earthquake Research Committee. To examine the strong motion prediction techniques to be used, the working group was also established under the subcommittee. The National Research Institute for Earth Science and Disaster Prevention (NIED) was selected to be the responsible institution for the

project. To support their work, the technical committee for probabilistic seismic hazard map was established in the NIED.

In the project, to understand the general view of seismic hazard in the whole of Japan, two types of the maps will be produced. One is a deterministic ground shaking map with specified seismic source fault. This type of the map is also called a scenario earthquake ground shaking map. Another is a probabilistic ground shaking map that shows possibility with which a certain area is attacked by strong shaking in a certain period by means of probability. The reason for adopting two types of the maps is that these two maps have different merits and should be selected according to the objectives. The deterministic maps will be produced for ten to twenty scenario earthquakes which have high potential of occurrence or may give high impact to urban areas. The probabilistic maps with different probabilities of occurrence will be produced for the whole of Japan.

2.2 Deterministic Ground Shaking Map

For the deterministic map, the hybrid simulation method (eg. Irikura and Kamae, 1999) is mainly employed. The empirical method (eg. Si and Midorikawa, 2000) is also used as supplementary one. In the hybrid simulation method, the shorter period ground motion is computed by the stochastic Green's function method, and the longer period motion is computed by the theoretical finite difference method considering the three-dimensional deep underground structure. The heterogeneous source model is adopted, considering asperities with larger slip and higher stress drop on the fault plane. The source parameters are determined following the standardized recipe (Irikura, 2002). The deep underground structure is modeled based on the available data including the results from surveys of deep sedimentary basin structures initiated by the Headquarters.

By this procedure, the time history of the ground motion at engineering bedrock where shear-wave velocity is about 400 m/s is computed for each element of the 1km-mesh system. Since surface soils vary strongly site by site, it is difficult to prepare the surface soil models with adequate spacing. Therefore, the peak ground velocity on surface is simply computed by multiplying the peak velocity at engineering bedrock and the amplification factor estimated from the site geomorphological condition (eg. Matsuoka and Midorikawa, 1995). The peak ground velocity is converted to the JMA seismic intensity using the empirical relationship.

As of February, 2004, the deterministic maps have been published for five active fault earthquakes such as the Yamagata Basin, Miura Peninsula, Futagawa-Hinata, Morimoto-Togashi, and Itoigawa-Shizuoka fault earthquakes and for three subduction earthquakes such as the Miyagi-ken-oki, Nankai, and Tonankai earthquakes. As example, the deterministic seismic intensity maps for the Yamagata Basin fault earthquake are shown in Figs. 1. In this earthquake, the results for four cases with different locations of the asperities on the fault are shown in order to indicate variability of the prediction.

2.3 Probabilistic Ground Shaking Map

A probabilistic ground shaking map is presented by three parameters such as intensity, time period and probability of strong shaking. On the map reflected are long-term evaluations of the possibility of occurrence of large active fault and subduction earthquakes which have been published by the Headquarters. In the calculation, the earthquakes are classified into seven different types (Ishi et al., 2003):

- 1) characteristic earthquakes along the major 98 active fault zones in Japan;
- 2) earthquakes along the other active faults,
- 3) earthquakes in the major 98 active fault zones except the characteristic earthquakes,
- 4) characteristic inter-plate earthquakes along the subduction zones,
- 5) inter-plate earthquakes along the subduction zones except the characteristic earthquakes,
- 6) intra-plate earthquakes along the subduction zones,
- 7) crustal earthquakes whose fault planes could not be identified in advance.

The time-dependent model of earthquake occurrence is used for earthquakes whose occurrence patterns have been investigated, but the Poisson model is used for most earthquakes. The logic tree is not used for simplicity. With the probabilistic models of earthquake occurrence for these earthquake types, seismic hazard curves are computed in terms of ground motion intensity and probability of exceedance at each element of the 1km-mesh system. The empirical attenuation relationships of ground motion and the amplification factor based on the site geomorphological condition are used in the calculation. At several principal sites, the contribution factors of major earthquakes on the hazard curves at each probability level are presented in order to show the impact of each earthquake. The preliminary probabilistic maps have been published for the northern part of Japan. Figures 2 show the seismic intensity maps with 5%, 10% and 39% probabilities of exceedance in 30 years, respectively.

3. ADVANCED REGIONAL MAPS

3.1 Detailed Seismic Hazard Map

The seismic hazard maps will provide basic information for;

- 1) improvement of earthquake awareness of citizens,
- 2) seismic design of structures,
- 3) strategies of disaster mitigation planning,
- 4) seismic risk evaluation of facilities, and so on.

When a citizen look the seismic hazard map, he thinks that a) Is my house in the red zone ? and b) If my house is in the red zone, what should I do ? (Olshansky, 2000). To reply his questions, the map should be the micro-scale one. The national seismic hazard maps are basic ones and too large in scale to catch citizen's strong interest. As an advanced map for citizens, the detailed hazard map for the region will be necessary.

For this purpose, the city of Yokohama (2001) published "Yokohama City Shake Map" in June, 2001. More than 15,000 borehole data in the city were compiled. The soil profile sections were drawn from the borehole data and the geomorphological information, and the soil condition of the city is classified into 268 types. The data from borings or measurements of S-wave velocity are used to build up the generalized underground model for each soil type. For the mapping, the 50m mesh system is adopted because of strong spatial variation of the geomorphological conditions in the city.

Using the detailed subsoil data, the deterministic ground shaking maps are computed for several scenario earthquakes including the recurrence of the 1923 Kanto earthquake. Figures 3 are the map for the Kanto earthquake and its close-up, respectively. About 100,000 copies were printed and distributed to citizens. As the results, the numbers of applicants for seismic performance appraisal of wooden house and for seismic retrofitting subsidies by the city increased to about 2000 and 150 in 2001, respectively. These numbers are twice of those in the previous year. This is an evidence of improvement of earthquake awareness of citizens by the map.

3.2 Information Map for Earthquake Emergency Preparedness

As mentioned above, the detailed seismic hazard map is useful for easy understanding the regional seismic risk. However, if we focus our objectives on improvement of citizen's emergency preparedness, the detailed hazard map does not provide sufficient information. An Information map for earthquake emergency preparedness should be developed. The information map may consist of three kinds of maps, such as a risk map, evacuation aid map, and fire fighting and rescue aid map (Ishizawa and Midorikawa, 2002). Figures 4 shows preliminary evacuation aid and fire fighting and rescue aid maps. In the maps, the items which are related to evacuation actions, such as evacuation place, road width, slope failure potential and building damage. Now the city of Yokohama is being developed this kind of the map.

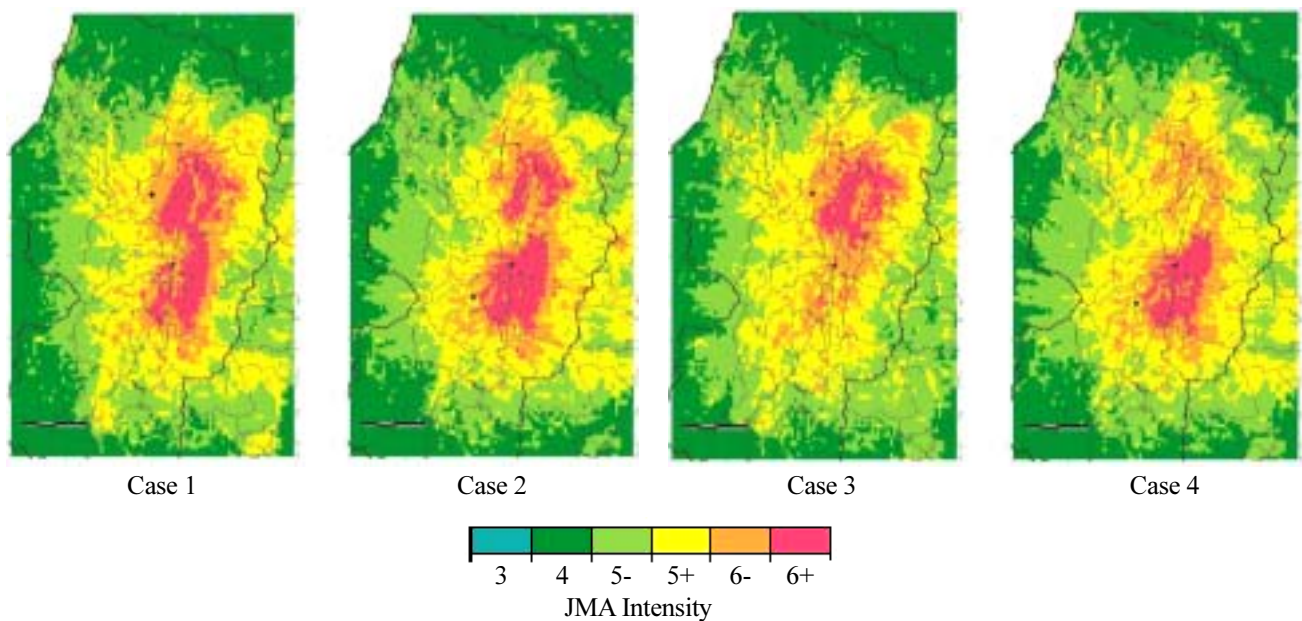
The maps will be provided on the web GIS system.

4. CONCLUDING REMARKS

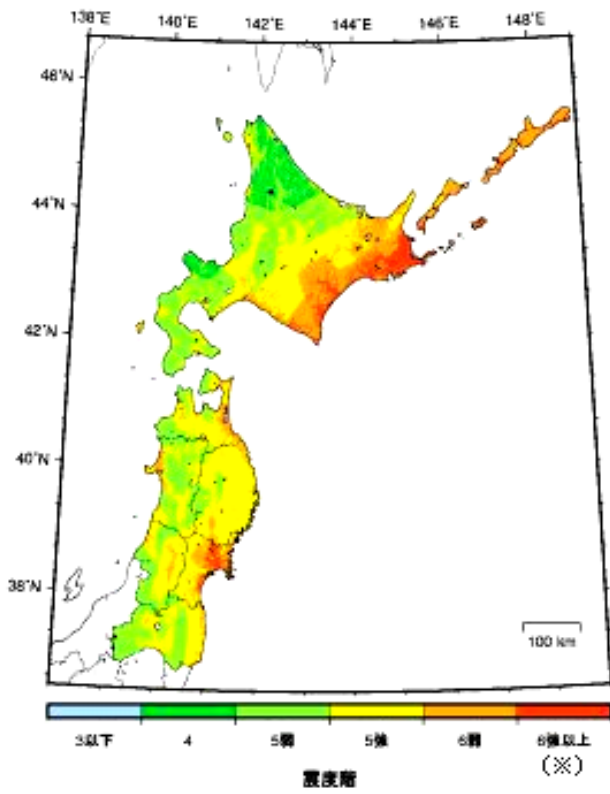
The national project on seismic hazard mapping of Japan started in 1999. In the project, two types of the maps such as the deterministic and probabilistic maps will be provided by March, 2005. The maps are to understand the general view of seismic hazard in the whole of Japan, and to be considered as the basic map. The project by a local government is also going on in order to produce the advanced regional map for improvement of disaster consciousness and preparedness of citizens. Applications of the maps should be further discussed not only in the engineering community but also in the general public.

References:

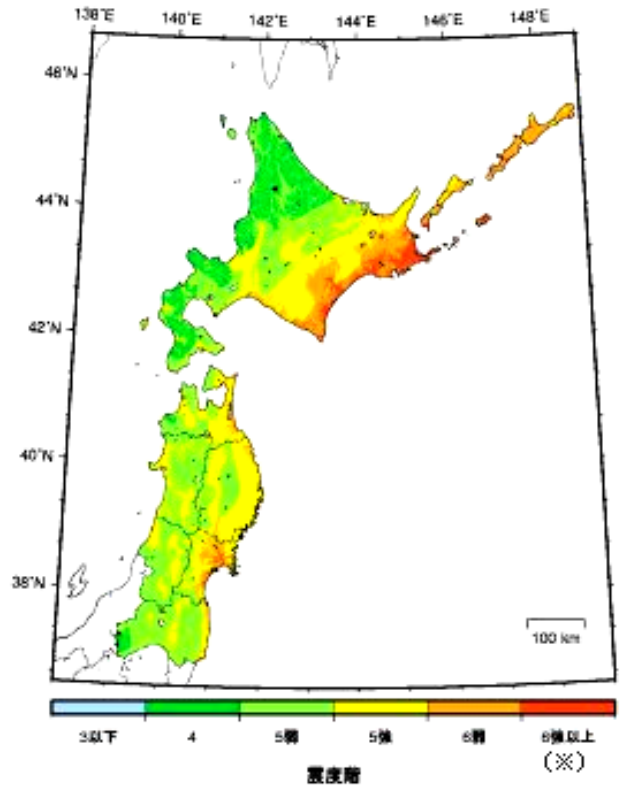
- City of Yokohama (2001), *Yokohama City Shake Map*, Yokohama City Brochure B-BE152.
- Fujiwara, H. et al. (2003), "National Seismic Hazard Mapping Project of Japan," *IUGG2003*, SS04b/10P/D-015.
- Irikura, K. (2002), "Recipe for Estimating Strong Ground Motions from Active Fault Earthquakes," *Seismotectonics in Convergent Plate Boundary*, 45-55.
- Irikura, K. and K. Kamae (1999), "Strong Ground Motions during the 1948 Fukui Earthquake –Estimation of Broad-band Ground Motion Using a Hybrid Simulation Technique-,“*Journal of the Seismological Society of Japan*, **52**(1), 129-150.
- Ishii, T. et al. (2003), "A Study on Probabilistic Seismic Hazard Maps in Japan," *IUGG2003*, SS04b/10P/D-023.
- Ishizawa, E. and S. Midorikawa (2002), "A Guide Map for Earthquake Disaster Management in Order to Improve Citizen's Disaster Consciousness," *Proceedings of the Eleventh Japan Earthquake Engineering Symposium (CD-ROM)*, Paper #406.
- Matsuoka, M. and S. Midorikawa (1995), "GIS-Based Integrated Seismic Hazard Mapping for a Large Metropolitan Area," *Proceedings of the Fifth International Conference on Seismic Zonation*, **2**, 1334-1341.
- Olshansky, R.B. (2000), "Is My House in the Red Zone? Local Communities and Seismic Hazard Mapping," *Proceedings of the Sixth International Conference on Seismic Zonation (CD-ROM)*.
- Si, H. and S. Midorikawa (2000), "Attenuation Relationships of Peak Ground Acceleration and Velocity Considering Effects of Fault Type and Site Condition," *Proceedings of the Twelfth World Conf. on Earthquake Engineering (CD-ROM)*, Paper #532.



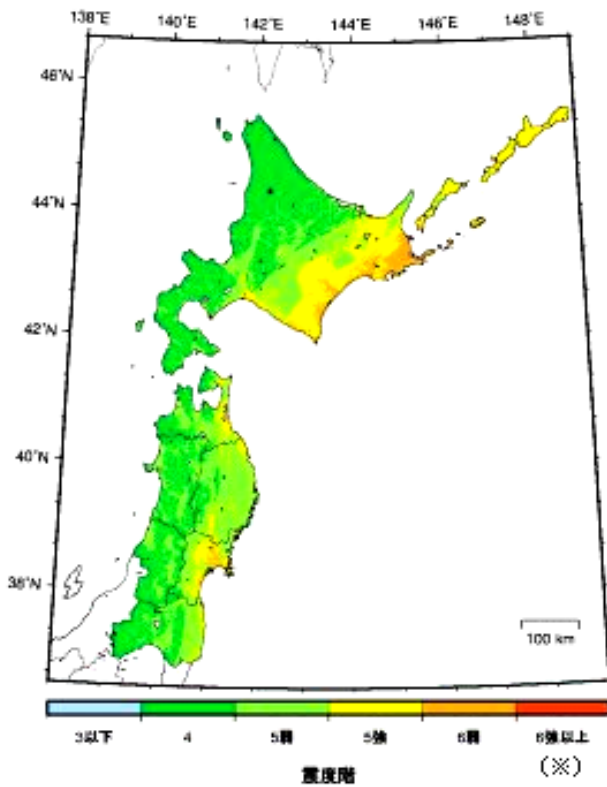
Figures 1 Deterministic Seismic Hazard Maps for the Yamagata Basin Fault Earthquake



(a) seismic intensity with 5% probability of exceedance in 30 years



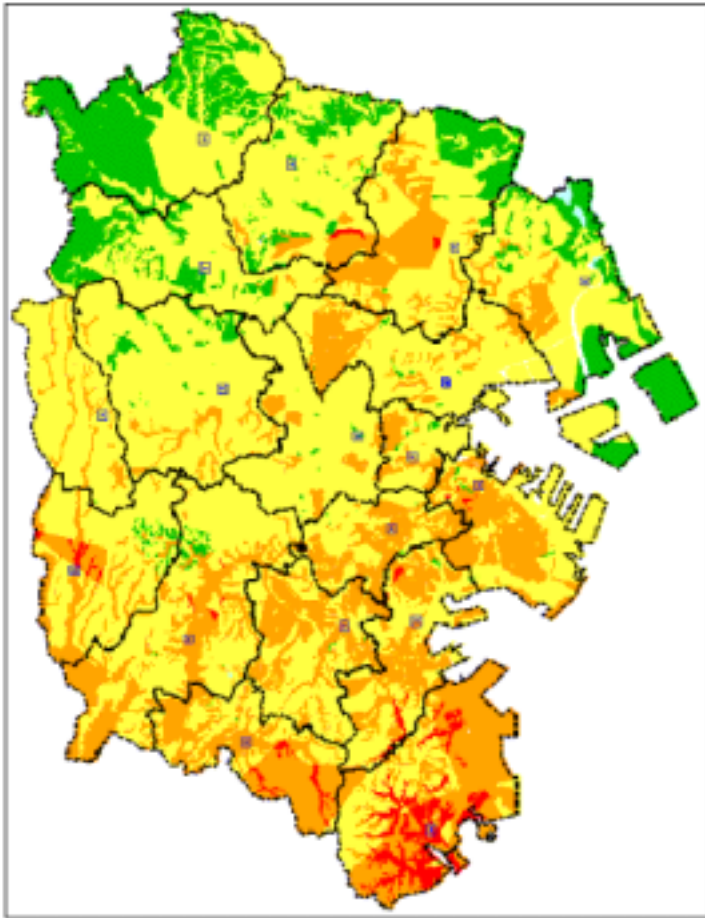
(b) seismic intensity with 10% probability of exceedance in 30 years



(c) seismic intensity with 39% probability of exceedance in 30 years

Figures 2 Probabilistic Ground Shaking Maps

南関東地震

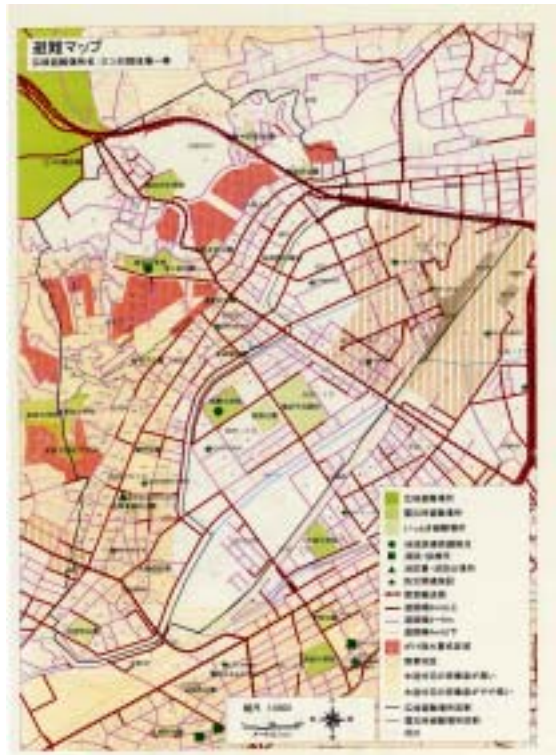


(a) whole area map



(b) close-up map

Figures 3 Yokohama City Shake Map



(a) evacuation aid map



(b) fire fighting and rescue aid map

Figures 4 Information Map for Earthquake Emergency Preparedness

SEVERAL SUBJECTS STILL REMAINED SINCE THE 1995 KOBE EARTHQUAKE

K. Seo¹⁾, K. Motoki²⁾, K. Kurita³⁾, T. Momii⁴⁾, T. Shigeta⁵⁾, and N. Niwa⁶⁾

1) Professor, Urban Earthquake Engineering Center, Tokyo Institute of Technology, Japan

2) Research Associate, Department of Built Environment, Tokyo Institute of Technology, Japan

3) Researcher, Department of Computer Science and Informatics, Tokyo Gakugei University, Japan

4) Researcher, Department of Built Environment, Tokyo Institute of Technology, Japan

5) Pipeline Engineer, Pipeline Design Section, Tokyo Gas Co., LTD, Japan

6) Teacher, Science Course, Kobe Municipal Rokko Island Senior High School, Japan

seo@enveng.titech.ac.jp, kmoto@enveng.titech.ac.jp, katsumi@sanga.u-gakugei.ac.jp,
mtakashi@enveng.titech.ac.jp, tshigeta@tokyo-gas.co.jp, minaminiwaebi@hi-net.zaq.ne.jp

Abstract: The 1995 Kobe earthquake brought serious problems from the earthquake disaster mitigation point of view. In this paper, several important subjects will be discussed after reviewing what happened during and after the earthquake. Most of all, the following subjects will be discussed in this paper.

1) Source model of the earthquake could be understood in detail using observed strong motions and damage direction of distributed structures. There is a possibility that one of asperities near Kobe city contributed to have brought heavy damage in Kobe city.

2) Significant later phase could be seen in the seismic record obtained in the coastal region of Kobe city. It can be explained as a surface wave that could be reflected at the southern boundary of Osaka basin. This later phase with long period component has the possibility to trigger the failure of Hanshin highway.

3) Two residential buildings, one was constructed with the older Japanese seismic code and the other one was constructed with the new seismic code that had been issued in 1981, showed different behavior during the earthquake. The former one suffered serious damage and the latter one did not suffer damage so much.

After all, such experiences should be taken into account in the future strategy about earthquake disaster mitigation.

1. INTRODUCTION

The Kobe (Hyogoken-Nanbu) earthquake of January 17, 1995, brought a serious disaster in Kobe and Hanshin districts including northern Awaji island. It was the worst that none of governors, reporters in mass communication, and even researchers, could estimate total amount of victims just after the earthquake. For this reason, we lost very important several hours in confusion not knowing what to do. Even after several days or several weeks from the earthquake, we were not sure that the most adequate countermeasures had been taken for the damaged area or not.

We have visited Kobe city many times, mainly in 1995 for field works to observe aftershocks, measuring microtremors and to perform refraction survey of deep underground structures using explosions. After that, we have also visited the area almost twice a year just to watch around the condition of restoration and reconstruction. In such occasion, we often found some of new subjects those were still remained without solving. Therefore we would like to report the following subjects because they could be very serious and important experiences when we consider earthquake disaster mitigation strategies in the future.

2. WHAT HAPPENED DURING AND AFTER THE EARTHQUAKE?

We have examined to draw a temporal flowchart as Table 1, to confirm what happened in and around Kobe city just after the earthquake. In this table, an item showing reported human victims was the most impressive one for us. The number of victims counted only a few at the beginning stage, and it showed rapid increase up to 5,000 within a week. Another very sad story was that additional 1,000 people had to die in sick and mental problem until seven years after the earthquake.

Most of residential people were in bed during the earthquake, and crashed in such condition as shown in Photos.1-3. Urgent rescue activity might be very hard because of the condition like Photos.2 and 4. Every transportation system was quit including JR Super Express (Shinkansen) as Photo.5 and Hanshin Highways as Photo.6. Therefore the only way was just to walk or to take bicycles or motorbikes as shown in Photo.7. Fortunately there were no big aftershocks, but local governors and polis men did not control the people passing through very dangerous areas like Photo.8. Residential people made temporal evacuation mainly into neighboring school buildings (Photo.9). But the term of temporal evacuation continued for a few months or several months. After they moved to temporal houses those were prepared by local governments, they had to live there for five years in maximum. Residential people living around the foot of Rokko Mountains had to repeat quick evacuation when the weather forecast predicted heavy rainfall. As Photo.10 shows such condition, it took almost two years to have completed Sabo-protection.

From earthquake engineering point of view, JR-Shinkansen exposed its vulnerable circumstances, in some case because of exceedingly heavy structure (Photo.11) and in another most of cases because of lack of binding hoops at the top of columns (Photo.12). It took four months to start working by repairing those columns like Photo.13. The other ordinary JR and private railways also suffered heavy damage mainly in embankment parts. Take Photo.14 for instance, it shows a very clear contrast between the enforcement of collapsed Hankyu railway (left) and remaining old houses without damage (right). Hanshin Highways were very quick to have reconstruction. It took only 20 months to have the condition as Photo.15. We remember that there was a very serious discussion about Embarcadero Freeway in San Francisco after the 1989 Loma Prieta earthquake, whether it should be reconstructed or not. Unfortunately there was no time for discussion in Kobe, although there was another opinion to abolish it.

Reinforced concrete buildings also suffered various kinds of structural damage. As shown in Fig.1, the discussion was made using statistical analyses to point out the fact that most of damaged buildings were constructed following to the older building code, and that others based on the 1981 newer code did not have serious damage. Then there is no reason to improve the existing building code. The only problem is how to maintain such remaining buildings with the older code. Here we have just two typical examples to show shear failures in columns (Photo.16) and a failure of middle floor (Photo.17). The upper floors of the latter building, Bldg. No.2 of Kobe municipality office, has demolished after a couple of years as shown in Photo.18, although it could be an educational monument to keep this earthquake disaster without forgetting.

From seismological point of view, we have also learned many things. Strong motions were observed in and around the damaging area as shown in Fig.2, and moreover a tendency was very clear that very large amplitudes were observed in the normal direction against the fault. At the beginning stage, strong motion in Kobe was regarded exceptionally large, but good understanding appeared very soon that the attenuation characteristics looked quite reasonable compared with past experiences like Fig.3. Inversion analyses with neighboring strong motions have been examined by many researchers to show the source mechanism in detail as shown in Fig.4. Some geologist doubted the existence of

submerged fault just beneath the heavily damaged belt zone, but the general understanding after a while was to imagine two-dimensional or three-dimensional underground topography like Fig.5. Measured microtremors across this heavily damaged belt zone also showed very systematic change of characteristics as shown in Fig.6.

Table 1 TEMPORAL FLOWCHART SHOWING WHAT HAPPENED IN AND AROUND KOBE CITY JUST AFTER THE 1995 KOBE EARTHQUAKE

	Earthquake	one hour after	6 hours after	one day after	one week after	2 weeks after	one month after
Countermeasures							
National Gov.	Origin time: 5:46m (JST), Jan. 17, 1995 Origin coordinates: 34.6°N, 135.0°E, M7.3	Fire-Defense Agency sent emergency teams (10:35)	Cov. installed Emerg. Headquarter (11:04)	Natl. Disaster Relief Act installed (1/17)	Natl. Gov. defined the Disaster Zone (1/24)	Minister for earthquake installed (1/20)	Reconsideration of Natl. Disaster Prevention Plan (1/22 to May)
Hyogo Pref. Office		Self-Defense Force arrived at Itami Railway-St. (8:30)	Natl. Police Agency installed Emerg. Headquarter (8:30)				Defense Agency renewed Disaster Rescue Plan (1/26) from Disaster. (2/4)
Kobe City Office	Damage: Death 6433 (Dec. 2002) Injured 43,792 Totally collapsed houses 104,906	Kobe city ofc. installed Emerg. Headquarter (8:30)		Call for volunteers (3000 applied in 2 days)	Serious problem about garbage (1/22)	Kobe city ofc. presented reconstruction plan (1/29)	New Law on Reconstruction from Disaster. (2/4)
Information and Evacuation Services							
TV, Radio Program	TV was the most reliable information source even for National Headquarters						
Newspapers	Main bldg of Kobe Newspaper suffered severe damage unable to issue papers.				Rumor and false information appeared that big aftershock will attack again, Guys serving water have AIDS virus, Evacuators may be kicked out when schools start open, Volunteers will have the advantage to get temporary houses, and so on.		
Human Victims Reported	No information about the amount of victims	Death 22 Buried 223 (9:50)	Death 203 Missing 331 (12:00)	Death 1407 Missing 1043 (23:00)	Death 1885 Missing 1071 (1/18)	Death 4057 Missing 732 (1/20)	Death 5060 Missing 96 (1/24)
Lifeline Facilities							
Telephone Service	Telephone worked only for minutes	Interruption of phones about 226,000 circuits		Interruption of phones about 160,000 circuits	646 places, 2,650 circuits	Temporal phone service in 1843,000 families	610,000 families (1/26)
Water Supplies	Water supply was out			No water among 3,600,000 person	324,000 families (1/20)		450,000 families (2/1)
Electric Power	Power failure among 660,000 houses			Power failure among 500,000 houses	1120,000 houses (1/18)	80,000 houses (1/20)	
Gas Supplies	Gas leak happened in wide area		Gas service stopped for 834,000 houses			There was no improvement on gas service	Gas service became available after one month and half.
Transportation Systems							
Railways	Shinkansen railway collapsed with other JR-lines and private lines		Shinkansen started working except Kyoto-Himeji section (1/18)		Kyoto-Shinosaka was open (1/20)		Shinkansen was completely restored after 4 months.
Roads and Highways	15 trains derailed with 39 injured		Cracks were found in Shinkansen tunnel	A subway station in Kobe was crushed	Bus system was substituted for trains in many places	JR lines recovered to work (1/30)	Hanshin highways were surely reconstructed after 20 months.
Harbors & Airports	Bridges in highways heavily collapsed		Heavy confusion of traffics by police	Bicycle and motorbike were very convenient			
Buildings and Houses	RC-buildings collapsed including hospitals and other important ones		Rescue activities by residential people	50 people were rescued from a damaged hospital	Emergent judgement for damaged buildings and houses	More than 50% of hospitals & schools suffered the damage	It took almost one year for rubble disposal. Buildings constructed around 1970 suffered heavy damage.
Industry Facilities	Hanshin industrial belt suffered heavy economic loss		Typical household industries in damaged area were SANE and chemical shoes.		Red labels showing very dangerous were out for 1268 in Kobe.		
Fire and its Extinguishment	Fire was very serious in some area because of no water to extinguish it		Fire spread to wide area	Total number of fires was counted as 308 in Kobe (1/20)			
Liquefaction & Flood	Liquefaction took place in reclaimed land area		Warning against toxic gas leaking	80,000 people had to evacuate (1/18)			
Land Failures	Land failures killed people at the foot of Rokko mountains		Rescue fighting by local fire brigade against 150 families	Landslide warning	Number of dangerous slopes was estimated as 1,000 sites	Warning of heavy rain against 1,500 people	
Ground Motion due to Main and Aftershocks	Intensity 6 was reported in Kobe and Sumoto(Awaji Is) but delayed information to tell "no tsunami"		Warning against aftershocks with M6 aftershocks (1/18)	M6 aftershocks (1/18)	M7 was applied in severe damage zone in Kobe and Awaji Is. (1/23)	M7 was applied in severe damage zone in Kobe and Awaji Is. (1/25)	JMA will make quick warning using estimated intensity
Remarks and Subjects Pointed out		Vertical motion might bring heavy damage.		Strong motion at Awaji Is. Fault was renewed from Northern Awaji Is. to Akashi straits	Seismic force was 4 times twice of the 1923 Kanto earthquake. Fault was found in Awaji Is. Vertical motion was bigger than horizontal one.		Wrong construction induced big damage in structures.



Photo.1 Typical example of collapsed wooden houses (Nishinomiya)



Photo.2 Collapsed houses disturbed rescue activities (Uozaki, Kobe)



Photo.3 Soft first story suffered heavy damage in many places (Motoyama, Kobe)



Photo.4 Such condition even after a couple of months (Uozaki, Kobe)



Photo.5 Failure of JR-Super Express called Shinkansen (Nishinomiya)



Photo.6 Overturning failure of Hanshin Highway (Fukae, Higashinada, Kobe)



Photo.7 Side-walks filled with bicycles and motorbikes (Root-43)



Photo.8 Walking people did not care about collapsed buildings (Motomachi, Kobe)



Photo.9 Evacuation to school buildings (Motomachi, Kobe)



Photo.10 Land failures protected after two years (Sumiyoshi-Yamate, Kobe)



Photo.11 JR-Shinkansen with heavy Beams and columns (Nishinomiya)



Photo.12 Failures of the top of columns in JR (Nishinomiya)



Photo.13 JR-Shinkansen after temporary repairs (Nishinomiya)



Photo.14 Restored railway (left) and old houses alive (right) (Okamoto, Kobe)



Photo.15 Restored Hanshin Highway after 20 months (Fukae, Kobe)

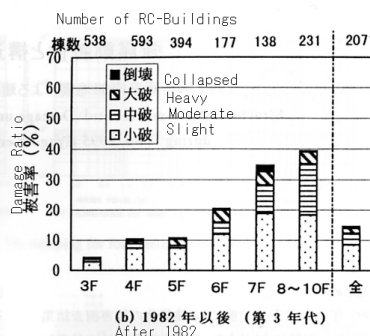
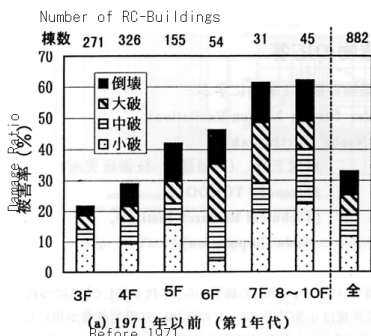


Fig. 1 Statistics of damaged RC-buildings. (a) old structures before 1971, and (b) recent structures after 1982. (after Tohdo in AIJ, 1998)



Photo.16 One directional shear failure of a school building (Okamoto, Kobe)



Photo.17 Kobe municipal office just after the earthquake



Photo.18 The same building with Photo.17 after a couple of years

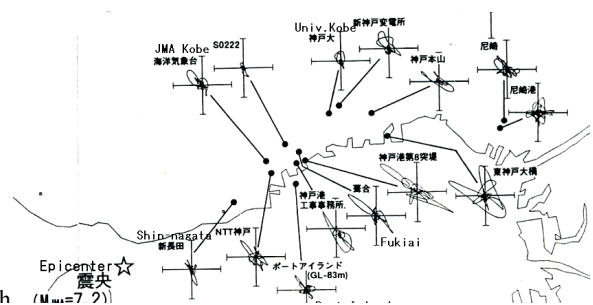


Fig. 2 Observed strong motions (after Wakamatsu in AIJ, 1995)

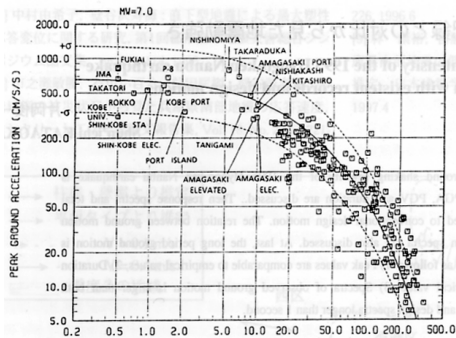


Fig.3 Attenuation of PGA during the 1995 Kobe earthquake (after Kataoka in AIJ, 1997)

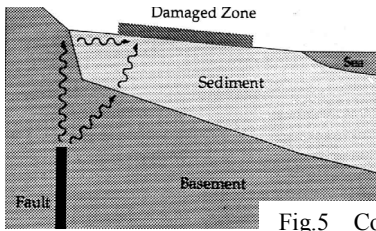


Fig.5 Concept to explain damaged zone with underground topography (after Koketsu et al. in AIJ, 1996)

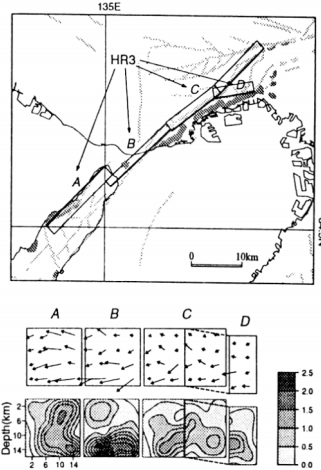


Fig.4 Source model and slip distribution for the 1995 Kobe earthquake (after Koketsu et al. in AIJ, 1997)

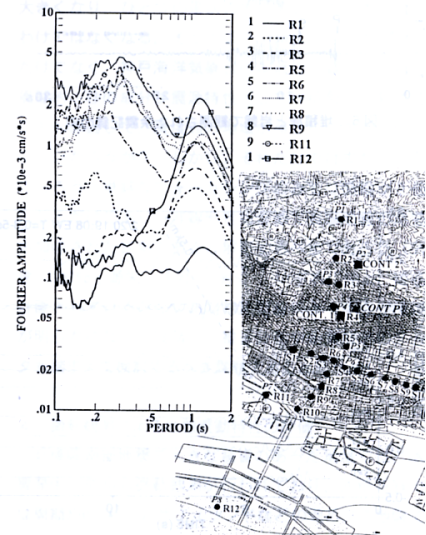


Fig.6 Measured microtremors across heavily damaged belt zone (after Seo et al. in AIJ, 1995)

3. SOURCE MODEL ESTIMATED BY OBSERVED STRONG MOTIONS AND DAMAGE DIRECTION OF DISTRIBUTED STRUCTURES

While we walked around Kobe and Hanshin districts many times, we noticed that the direction of failures for individual collapsed buildings, other structures including Hanshin Highways and overturned trains, looked very systematic as showing Fig.7. The direction was always towards the normal axis against the fault, to the northwest in the eastern side from Hyogo ward of Kobe city, on the contrary to the southeast in the western side. There was no exception in this tendency as if there were a node in Hyogo ward. Such direction of failures can be explained using neighboring strong motions like Fig.8 by assuming 1DOF response analyses. And to explain the polarity characteristics of strong motions, a source model for the 1995 seismic fault could be presented like Fig.9. The most important point is that the observed strong motion at JR-Takatori (TKT) will not accept the current rupture from the hypocenter. We need an effective asperity just beneath Hyogo ward in Kobe city to collapse structures distributed in Nagata and Takatori wards. Of course we need more careful consideration about this subject, but it is required in deed to prepare a synthetic interpretation throughout the source mechanism, underground structures, observed strong motions, and the behavior or damage of buildings and houses.

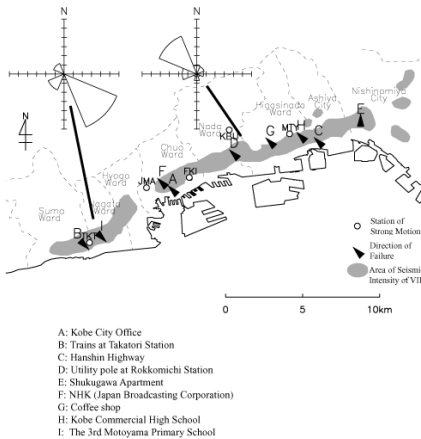


Fig.7 Direction of collapsed buildings and other structures including Photos.6, 16 and 17.

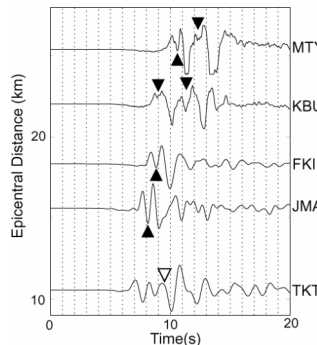


Fig.8 Velocity strong motions with effective phases contributed to the failure of structures

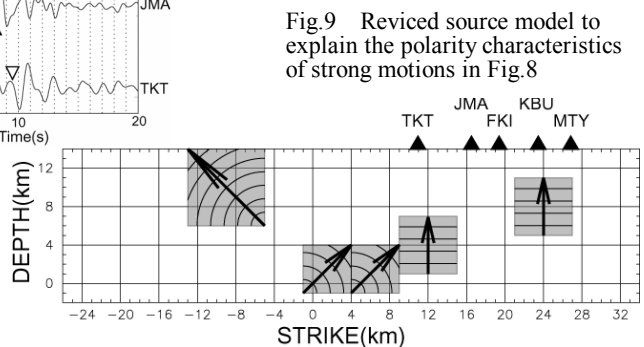


Fig.9 Revised source model to explain the polarity characteristics of strong motions in Fig.8

4. EXISTENCE OF LONG-PERIOD LATER PHASE AS A BASIN EFFECT

When we were thinking about the failure direction of damaged structures mentioned above, Kobe No.3 of Hanshin Highways (Photo.6), overturned toward the north direction with more than 600m in length, was one of targets to be taken into account. At first we believed that it must have collapsed quite soon during the strong shaking, and we estimated that the failure had been triggered at the west end and transmitted toward the east following to the seismic wave propagation from the source. Then we wanted to find people just watching the failure because no other information was expected. But we hesitated to ask neighboring people about this matter, as they did not like remembering the catastrophic condition anymore.

After all we started the survey in 2001, after 6 years from the earthquake. We found two persons who were watching the failure by checking reliabilities very carefully. One person was working in front of gas station located just on the northern side from the highway (Photo.19). According to his explanation in our interview, he fell and landed during the strong shaking, and was watching the behavior of the highway. At that time the highway was shaking without falling down. After a couple of minutes from the strong shaking, the highway started falling down against his side (north) from the west toward the east grading up the speed. He also found an empty truck had landed from the highway to the ground level and run away.

According to Kawashima(2003 and 2004), he does not believe this person because he talked inconsistent experiences for different newspapers just after the earthquake. But we have a quite different understanding that the person was in an abnormal state of mind just after the earthquake, and he was able to make any kinds of replies against the different questions made by newspaper reporters. On the contrary our interview was made in his stable psychological condition after 7 years and we found nothing strange at all from his talking. Another person, a young guy, was watching the highway from the opposite side (south). He met the earthquake on the tenth floor of a residential building (Photo.19). He opened the entrance steel door during the strong shaking to keep the evacuation route, and got back inside of his home to recommend the evacuation for his family. When they went out to the passage, the highway was still standing. And then they found the failure of the highway after they arrived to the ground level.

Therefore we tried to find the possibility meeting with such experiences. We checked the nearest observed strong motion as shown in Fig.10 very carefully. There were no effective aftershocks in the record, but we found a later phase with about 6 seconds in period that was very clear in velocity seismogram. We could assume a possibility that the later phase might be Love wave as a result of two-way reflection across the Osaka bay like Fig.11. An examination has been tried with 2-dimensional finite differential method as shown in Fig.12.

On the other hand, the highway structure could be evaluated with Fig.13(top) at the original stage before the earthquake. The fundamental natural period in rectangular direction of the highway could be about 0.6 second. During the strong shaking, the dynamic characteristics would change the condition as shown in Fig.13(bottom) because of bending failure at the foot of the highway. In this case, the fundamental period could be around 6 seconds. Such drastic shifting of the natural period may be possible if the floor panels on the top of the highway are jointed each other without missing the connection. And it becomes possible to consider the resonance between a very soft highway and a later phase with very long period. Needless to say we are just proposing a hypothesis to explain the failure of Hanshin Highways. If the hypothesis is acceptable, it will be so good for related responsible people, because the highway might keep standing in the case such later phase did not appear.



Photo.19 Overturning failure of Hanshin Highway and the location of watchers

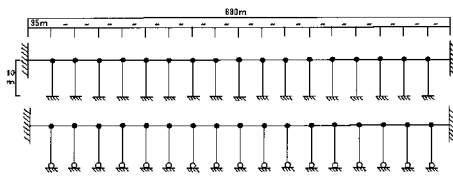


Fig.13 Structure model for Hanshin Highway

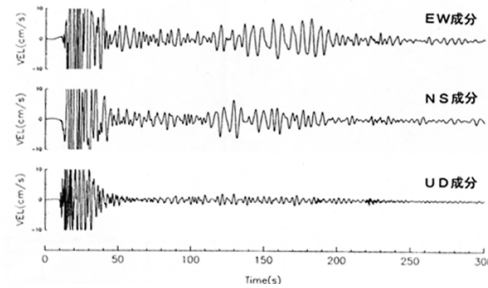


Fig.10 The nearest strong motion in velocity. A later phase appeared after two minutes with 6 seconds in period.



Fig.11 Concept to explain a possibility of long-period later phase in Fig.10 with surface waves across the Osaka bay.

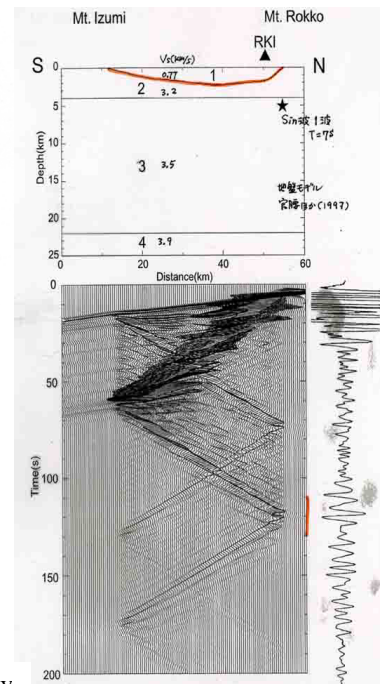


Fig.12 A trial of 2-DFDM analysis for Fig.11 by assuming basin structure.

5. DAMAGE EVALUATION OF SIMILAR RC-STRUCTURES BUILT WITH DIFFERENT SEISMIC CODES

As we mentioned before, we have full of statistical data about damaged building structures such like Fig.1. But we do not have any practical case studies to compare building structures between the older and the newer building codes. When we were visiting the highway mentioned above, we met with a set of similar RC-structures in the same field, one was already repaired with steel frames (Photo.20) and the other without repairs (Photo.21). They were residential buildings constructed by Hyogo prefecture, the local government. It was quite interesting for us because the former one was built just before the revision of Japanese Building Code in 1981 and the latter one was built just after the revision. Therefore they were constructed following to the different building codes in spite of the similarity in plan, number of stories and even the appearance.

According to the results of our questionnaire to living people, the older building suffered much heavier damage than the newer one. For example, the people in the older building felt much harder shaking, suffered heavier damage on furniture, heavier cracks including seismic walls and around entrance steel doors. Therefore they could not open the doors for evacuation. Such people had to stay much longer duration in other evacuation places because it looked very dangerous to live there (Fig.14). The local government repaired these buildings without moving the living people using additional seismic walls on the ground level. The steel frames mentioned above were put only for the older building, because the government judged the damage of the older one looked much harder although they were not sure such countermeasures were good enough or not.

Then we made a comparison of these two buildings using measured ambient motions on the top of both buildings. Some of measured dataset was quite interesting to explain their dynamic behaviors. The natural period of longitudinal direction was about 0.60s for both buildings. It meant that the steel frames of the older building worked well to have similar characteristics with the newer one, and such natural period looked quite reasonable for general RC-building with 11 floors. In the rectangular direction, the older building showed much longer natural period as 0.54s, while the newer one showed

0.48s. It was also reasonable that the older building might be softer than the newer one, maybe due to the different building code. After the enforcement with steel frames for the older building, it became much easier to have torsions. As we have just examined such features with only ambient motions, we recommended the local governors to make more careful surveys for both buildings. They should have made such surveys just after the earthquake or at least before the repairs.



Photo.20 RC-building built with the older building code

Photo.21 Similar building built with the newer building code

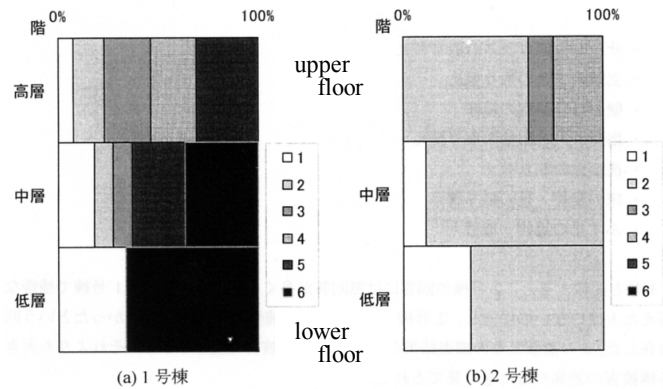


Fig.14 One of questionnaire results showing different degree of damage between the older (left) and the newer (right) buildings. Question was how long time you had to evacuate from your home. 1: not evacuated, 2: within one week, 3: within two weeks, 4: within one month, 5: within two months, 6: more than two months.

6. CONCLUSIONS

The 1995 Kobe earthquake brought really serious problems in the damaged districts. In this paper, after we reviewed what happened during and after the earthquake very quickly, we pointed out several important subjects. Most of all, the following subjects were discussed.

- 1) A source model for the 1995 earthquake was presented using damage direction of distributed structures and observed strong motions. There is a possibility, we are sure, that one of asperities just beneath the central Kobe city contributed to have brought heavy damage in some part of Kobe city.
- 2) Significant later phase could be seen in the seismic record obtained in the coastal region of Kobe city. It can be explained as a surface wave that might be reflected at the southern boundary of Osaka basin. This later phase with long period component as 6 seconds has the possibility to trigger the overturning failure of Hanshin highway.
- 3) Two residential buildings, one was constructed with the older Japanese building code and the other one was constructed with the newer code that had been issued in 1981, showed different behavior during the earthquake. The former suffered serious damage and the latter did not suffered so much. After all, such experiences should be taken into account in the future earthquake disaster mitigation.

Acknowledgements:

This field investigation research was made with full of cooperations and supports by the local governors and the residential people including victims in Kobe. Hereby we will never forget the 1995 Kobe earthquake. We will try our further efforts to make clear the reason of heavy damage and to prepare the better condition for future earthquakes.

References:

- Seo, K. et al. (1995a, 1995b, 1997, 1999, 2001, 2002), "Damage and Countermeasures about the 1995 Kobe Earthquake, Part 1-6.", Research Reports on Earthquake Engineering, through No.53 to 84, Tokyo Institute of Technology (in Japanese)
- Architectural Institute of Japan (1995-1998), "Recent Earthquake Ground Motion Researches Examined by the 1995 Hyogo-ken Nanbu Earthquake. Part 1-4", 23rd to 26th Symposia of Earthquake Ground Motion, AIJ (in Japanese)
- Kawashima, K. (2004), "Did the 18-Span Hanshin Expressway Viaduct Collapse by an Aftershock in the 1995 Kobe Earthquake?", Bridges and Foundations, Issued in January 2004, pp.41-47 (in Japanese)

ESTIMATION OF SITE AMPLIFICATIONS IN FOCAL AREA OF THE 2003 MIYAGIKEN-HOKUBU EARTHQUAKE USING AFTERSHOCK AND MICROTREMOR RECORDS

H. Yamanaka¹⁾, K. Motoki²⁾, N. Komaba³⁾, Y. Kamimura³⁾ and M. Murayama³⁾

1) Associate Professor, Dept. of Environmental Sci. and Tech, Tokyo Institute of Technology, Japan

2) Assistant Professor, Dept. of built environments, Tokyo Institute of Technology, Japan

3) Graduate Student, Interdisciplinary Graduate School of Sci. and Tech., Tokyo Institute of Technology, Japan
yamanaka@depe.titech.ac.jp, kmoto@enveng.titech.ac.jp, komaban@depe.titech.ac.jp,
kamimura@enveng.titech.ac.jp, mmrym@enveng.titech.ac.jp

Abstract: The 2003 Miyagiken-Hokubu earthquake (M_j=6.2) generated heavy damage in the northern part of Miyagi prefecture, Japan. Because of the shallow depth of the event, the damage was so limited in small area. In order to know ground motion characteristics and site effects in the focal area, we conducted observations of aftershocks and microtremors. The aftershocks were observed at 19 sites in 4 days just after the main shock on the 26th, July. We also conducted array observations of microtremors to know S-wave profiles down to the basement at 4 sites. The site amplification factors calculated from the deduced profiles agree with those estimated from the aftershock observations.

1. INTRODUCTION

Three major events (M5.5, M6.2, M5.3) occurred on the 26th, July, 2003, in the north of the Miyagi prefecture, Japan. Although these events are not so large as compared with the past destructive earthquakes, shallow depths of these events generated strong shaking in the focal area. Thus, sever damage was experienced in local cities in the focal area. In particular, some of old reinforced-concrete buildings and wooden houses were totally collapsed (e.g., Sato et al., 2003). Seismic intensities observed with seismic intensity meters in the focal area was 5-upper to 6 on the JMA scale during the main shock with M_j of 6.2. It is also reported that maximum accelerations at some sites were more than 1G. The maximum acceleration was 2.0G at the city office of Maruse-cho. However, strong ground motion records are not available at most of the seismic intensity stations. This also makes it difficult to understand relation between the damage and strong motion characteristics.

In this study, we conducted aftershock observations and microtremor array explorations in the focal area and the Ishinomaki plain to estimate strong motion characteristics with a focus on site effects.

2. GEOLOGICAL SETTING

Map of the studies area is shown in Fig. 1. Most of the area is covered with Quaternary soft soils. In the east of the area, pre-Tertiary granitic rock can be seen as an outcrop. We can see sedimentary layers in Tertiary age in the Asahiya hill area that corresponds to the focal area of the main shock as

shown by broken lines in Fig.1. The thickness of the Quaternary layers over the Tertiary rock is estimated in the Ishinomaki plain in the east of the fault. It forms a basin structure whose maximum depth is about 80 meters at the center of the plain. The layers become shallower in the eastern and western sides of the plain. The depth to the pre-Tertiary basement in the plain is not well-known. However, we can qualitatively understand the basement depth distribution in the area from Bouguer anomaly map as shown in Fig.2. The positive gravity anomaly in the east of the area corresponds to outcrop of the pre-Tertiary basement.

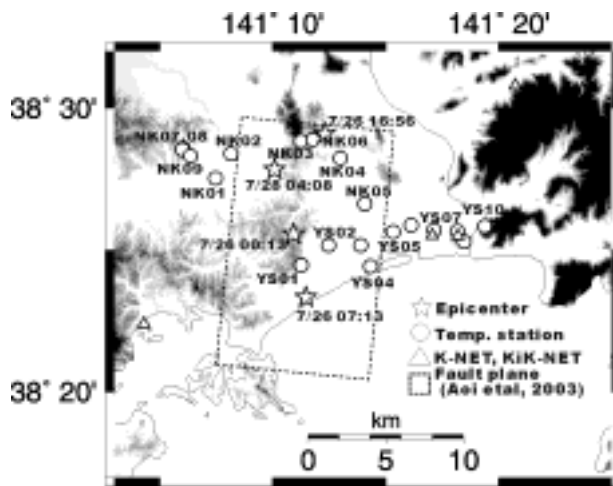


Fig.1 Map of studied area with aftershock observation stations.

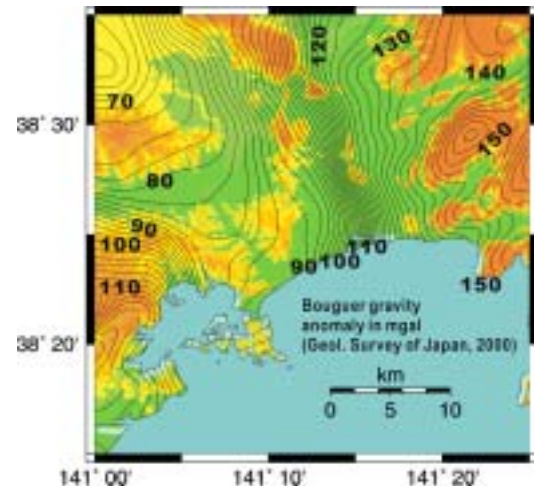


Fig.2 Bouguer gravity anomaly map

3. OBSERVATIONS OF AFTERSHOCKS AND MICROTREMORS

Aftershock observation was continued in four days starting on 27, September, 2003 at 19 stations which are indicated by circles in Fig.1. These stations are deployed with the following two viewpoints. The 10 stations from YS01 to YS10 were served to know nature of a layer phase seen in strong motion records at K-NET Ishinomaki station during the main shock. The station YS01 is situated at the foot of the Asahiya hill covered with Tertiary layers. The stations of YS08 and 09 are also located on Tertiary layers, while pre-Tertiary basement can be seen near YS10. The other stations are on Quaternary layers in the Ishinomaki plain. The other objective is to estimate strong motion characteristics in the northern part of the focal area where the damage was so heavy. The stations from NK01 to NK09 were prepared for this purpose. It is noted that some of the stations were installed near the damaged buildings as explained later. A data recorder and a three-component accelerometer were installed at each station. Since we prepared 10 sets of the observational equipments, observational periods at some of the stations were only a half day. However, high activity of the aftershock sequences allows us to obtain enough number of seismic records to assess local site effects.

Observations of vertical microtremors in arrays were conducted at four sites in the area to explore subsurface S-wave profiles of the sediments over the pre-Tertiary basement. Most of the sites are located near the aftershock observation stations as shown in Fig.3. At each sites, two arrays were temporarily deployed in triangular or cross shape in different array sizes as shown in Fig.4. We observed vertical microtremors simultaneously at 7 stations in each array in 30 to 60 minutes.

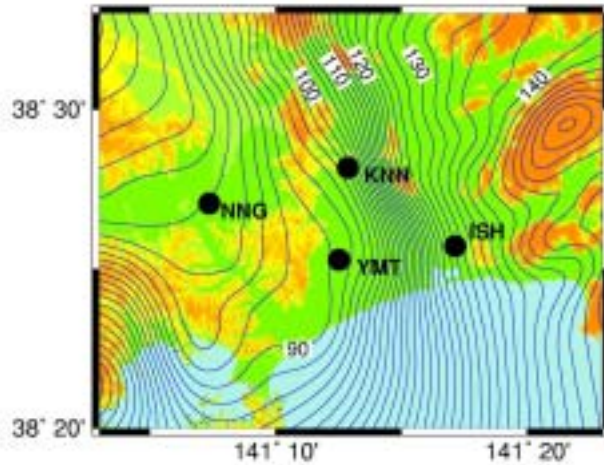


Fig.3 Locations of sites of microtremor array explorations

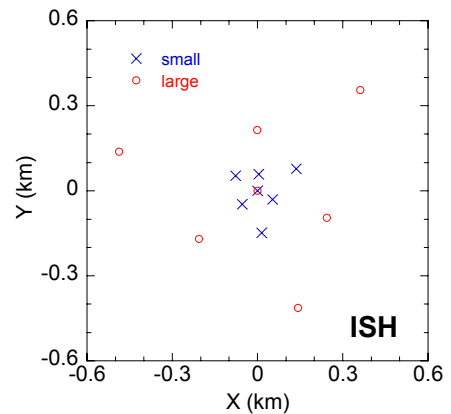


Fig.4 Example of microtremor arrays

4. ESTIMATION OF S-WAVE PROFILES

S-wave velocity profiles were deduced from analysis of the observed array data of vertical microtremors. Fig.5 shows the flow for data processing in the microtremor array exploration. Details can be seen in Yamanaka et al (2000). We, first, apply a frequency-wavenumber (f-k) spectral analysis (Capon, 1969). Then, a wavenumber vector for the maximum peak is found in f-k spectrum to estimate phase velocity at each period. These processes were repeated for all the segments of the array data. The final frequency-dependent phase velocity was obtained from averaging phase velocities for all the data in an array.

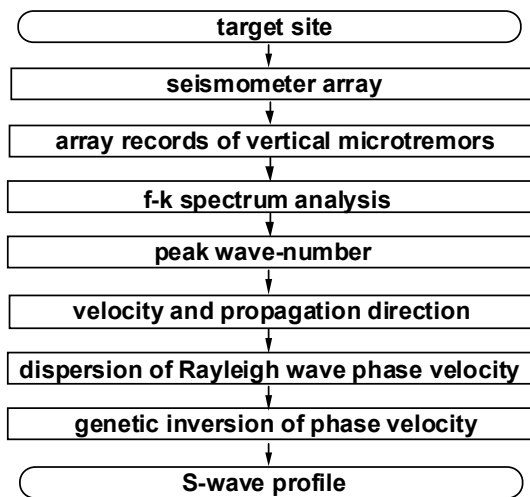


Fig.5 Flow for data processing in microtremor array exploration

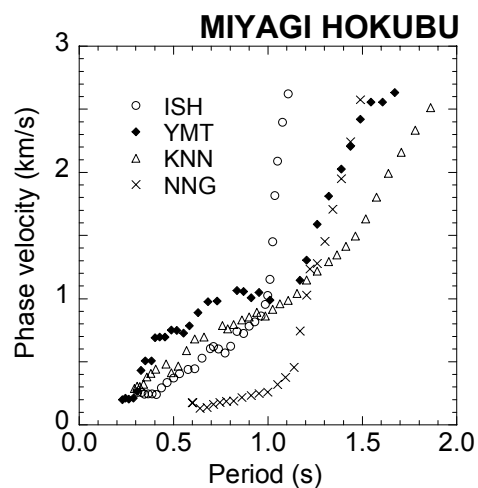


Fig.6 Phase velocity of vertical microtremors

The obtained phase velocities are shown in Fig.6. All the phase velocities clearly indicate dispersive features and can be regarded as that of Rayleigh waves. The phase velocity at ISH becomes rapidly large at periods of more than 1 second, indicating shallow depth to the basement. On the other hand, phase velocity at KNN is the lowest at periods of the more than 1.3 seconds. It is noted that the phase velocity at periods shorter than 1 second is extremely small at NNG, indicating the existence of low velocity layers near the surface.

We, next, invert the phase velocity at each site to a 1D S-wave velocity profile using an inversion technique. We apply a genetic inversion technique by Yamanaka and Ishida (1996). This method were successfully applied in many microtremor explorations in Japan (e.g., Yamanaka et al, 2000), because it does not require any specific initial model that must be usually prepared in least square methods. This method searches models with low misfit that is defined as L1-norm of differences between observed and synthetic phase velocities for fundamental Rayleigh wave. In the inversion, we assumed a 4-layers model and optimize S-wave velocity and thickness of each layer. Fig. 7 displays the inverted S-wave models. The depth basement with an S-wave velocity of 3.5 km/s is well correlated with the gravity anomaly map in Fig.2. The comparisons of the observed phase velocities with calculated ones for the inverted models are shown in Fig.8. The observed data can be well explained with inverted models.

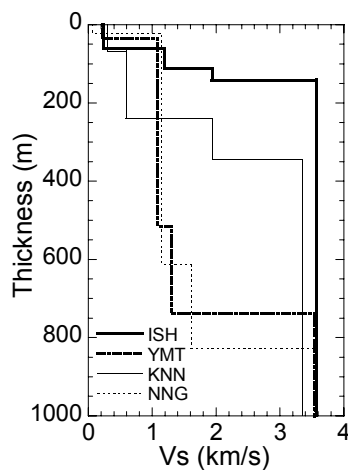


Fig.7 S-wave velocity profiles

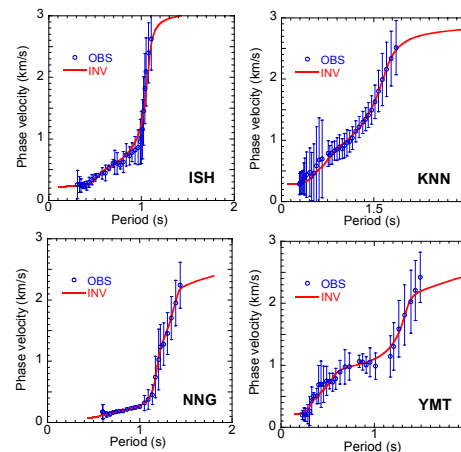


Fig.8 Comparison between observed and calculated phase velocities

5. ANALYSIS OF AFTERSHOCK RECORDS

5.1 Strong motion from large aftershock

In the aftershock observation, many events were recorded. However, most of them are small events with magnitudes of less than 2 and the maximum accelerations of less than 1 cm/s/s. The largest aftershock that we obtained is the event at 4:08 on 28th of July with an M_j of 5.0. The peak ground accelerations and velocities at YS01 to YS10 in our aftershock observations are shown in Fig.9 together with those from the K-NET. PGA and PGV calculated from the attenuation relations by Shi and Midorikawa (1999) are also shown in the figure. The observed PGAs for the aftershock are slightly larger than the calculated ones except for those in the focal area with a distance of less than 10 km. The observed PGVs are similar to those estimated from the attenuation equation for sites with surface S-wave velocities of 200 or 600 cm/s. These features of the PGA and PGV were also pointed out for the main shock (Motosaka, 2003). Therefore, it is indicated the PGV was normal to an event with similar size and only PGA in the focal area was extremely large. It is also noted that the PGVs in the Ishinomaki plain from our observations show a large variation by the differences of local geology. Such variation of the PGV must be appropriately incorporated in estimating strong motion in the area during the main shock.

North-south oriented ground velocities at YS01 to YS10 from the aftershock are displayed in Fig.10. The stations are almost situated in a line from the west to the east as can be seen in Fig.1. The development of the later phases is clearly identified in the stations in the Ishinomaki plain (YS02 to

YS07) indicating the strong effects of the sedimentary layers. In particular, the ground motion at YS07 is well dispersive and dominant at a period of 1 second. This later phase cannot be seen in the record at YS08 that is 1km apart in the east. Since YS08 is located on the hill with Tertiary layers, the later phases can be interpreted as effects of the Quaternary layers. In addition of the disappearance of the later phases, amplitude of the S-wave is much smaller at YS10 than that at YS08, because pre-Tertiary basement exists near the surface at YS10. These features can be also seen in the strong motion during the main shock. Fig. 11 shows the ground velocities during the main shock. The JMA and K-NET stations are located very close to YS08 and YS07 as shown in triangles in Fig.1, respectively. Since the ground motion features are very similar between the main shock and aftershocks, we can expect the existence of the later phases in Fig.10 during the main shock, too.

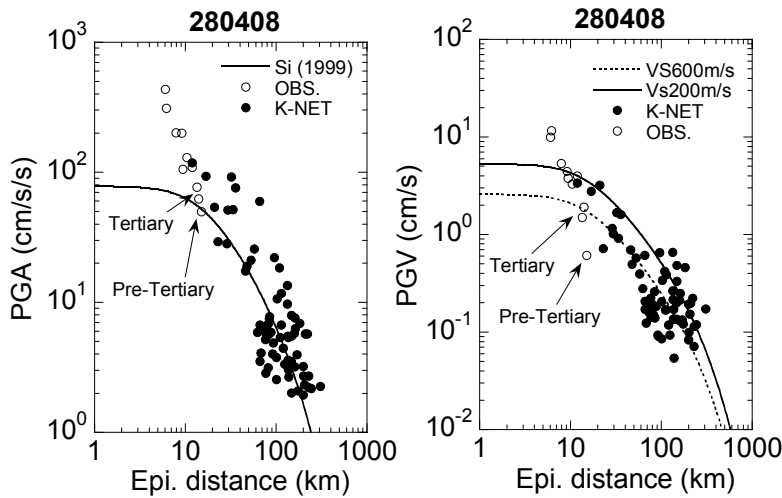


Fig. 9 Attenuations of PGA and PGV

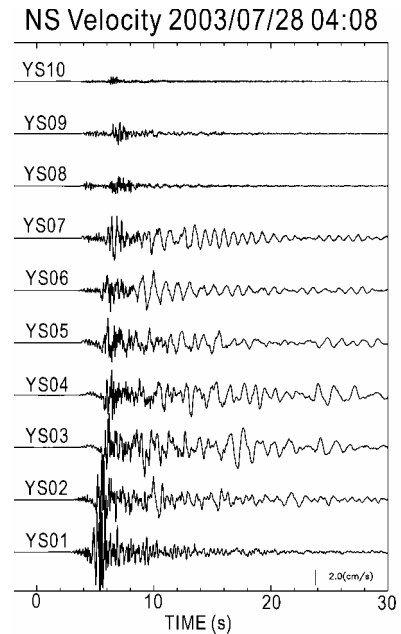


Fig.10 Observed ground velocity

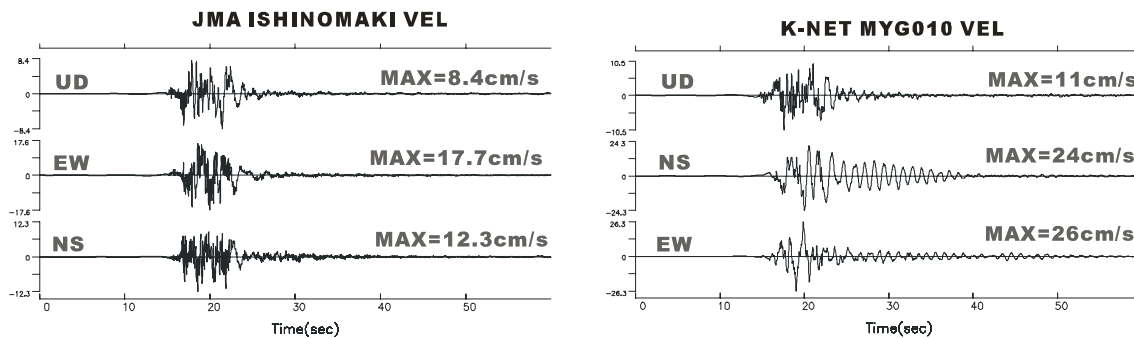


Fig.11 Strong ground motion during the main shock at JMA and K-NET

5.2 Spectral ratios at adjacent stations

As explained above, we installed our instruments at two adjacent stations with and without local soft soils. Fig. 12a shows the spectral ratios between YS07 and YS08. Two dominate peaks were found at periods of 1.0 and 0.4 seconds in the ratio. In the figure, the ratio for the strong motions from the main shock is also shown by a broken line. Although the ratios are not completely the same, similar peaks can be seen at a period of about 1 second. As explained above, the spectral ratio can be interpreted as amplification of S-wave in shallow Quaternary soft soils.

Next station pair is NK03 and NK06 in the Kanan-cho in the northern part of the focal area. NK06 is located in Kitamura Primary School where the most of columns at the first floor were heavily

damaged, while NK03 is 1 km apart from NK06 on the surface with no local soft soils. The spectral ratios of NK06 to NK03 in Fig.12b show amplification at periods of 0.1 to 0.3 seconds. Since this school is a three-story RC building, the amplification is one of the reasons for the heavy damage.

The last station pair consists of NK07 and NK08 in Kashimadai-cho. The distance between the two stations is just 100 meters as shown in Fig.13. NK07 is located close to 4-story RC building of Kashimadai Primary School that was moderately damaged. On the other hand, NK08 is located near the wooden school building. Although this wooden building is much older than the RC building, the wooden building has no damage at all. The spectral ratio between the two stations is shown in Fig. 12c. The amplification is dominant at a period of 0.3 seconds. Probably this spectral ratio can be interpreted as amplification of artificial fills at NK07. Since the RC building stands between the filling and cutting parts of ground, this difference of site effects can be one of the reasons for its damage.

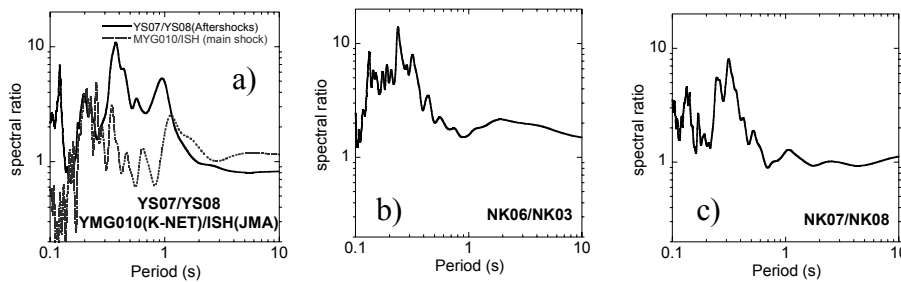


Fig.12 Spectral ratios at adjacent stations



Fig.13 Locations of aftershock observation station of NK07 and NK08 in Kashimadai Primary School.

6. SITE AMPLIFICATIONS

The spectral ratio in Figs.12 suggests local site effects. However, they are regarded amplification of shallow Quaternary layers with low velocity. We can estimate site amplification for the shallow and deep sedimentary layers over the pre-Tertiary basement with an S-wave velocity of 3.5 km/s by taking the spectral ratio to records at YS10. Fig. 14 shows the spectral ratio of YS06 and 07 to that of YS10 for the aftershock discussed above. Although the spectral shape is similar to that in Fig.12a, absolute amplification is different from each other. This indicates that effects of deep sedimentary layers are necessary to estimate amplification factors. In the figure, theoretical amplification of S-wave in the S-wave profile deduced from the microtremor array exploration is also displayed. It agrees with the observed amplification.

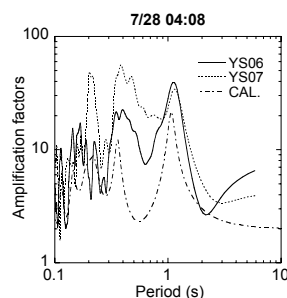


Fig.14 Ratio of spectra at YS06 and YS07 to that at YS10

There exist four layers in the S-wave profiles including the basement with an S-wave velocity of 3.5 km/s. We examine the effects of S-wave velocity of the bottom layer in calculation of theoretical amplification factors. The theoretical amplification factors are calculated with different S-wave velocity of the bottom layer in the models. Fig.15 shows the variation of the theoretical amplifications calculated for models at ISH from the microtremor array explorations. The thick solid line indicates the amplification of the model with a bottom layer velocity of 3.5 km/s. The amplification shown by the dotted line is calculated for the model where the 3rd layer is assumed as half space. Similarly, the amplification by thin line means the amplification for the model whose bottom layer has an S-wave velocity of 1.2 km/s. The comparisons of the amplifications clearly indicates that the importance of top Quaternary velocity layer in determining the amplification factors. We must pay special attention to model the Quaternary layer in strong motion calculation. Similar examination is conducted for the model at NNG shown in Fig.7. The spectral peak at 1 second can be modeled by considering the top Quaternary layers. However, amplification at periods of longer than 2 seconds can not be explained with consideration of only the top two layers. Therefore, deep sedimentary layers over the basement must be incorporated in synthetics of long-period motions in the area.

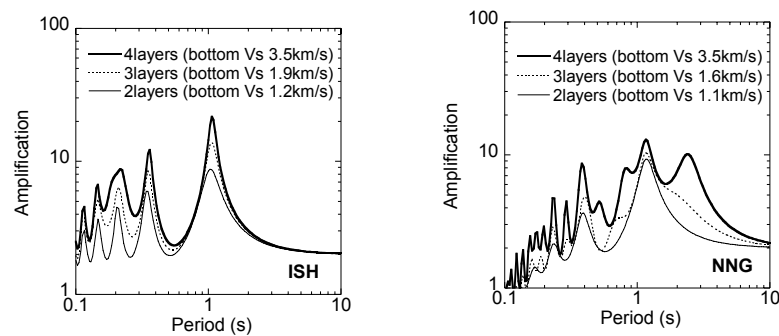


Fig.15 Variation of amplification factors with different S-wave velocity for the bottom layers in computational models at ISH (left) and NNG (right)

7. CONCLUSIONS

We conducted observation of aftershocks of the 2003 Miyagiken-Hokubu earthquake in Miyagi prefecture, Japan, to estimate local site effects. Strong motion instruments were temporarily deployed at 19 stations in the focal area of the main shock. We also conducted microtremor array observations at four sites in the area to know S-wave velocity profiles over the basement. The four-layer models for shallow and deep sediments are deduced from the microtremor array explorations. We estimate site amplification from spectral ratios of observed records from aftershocks. The amplification estimated is in agreement with the calculated one from the S-wave profiles deduced in the microtremor explorations.

Acknowledgements:

We thank people to allow us observation of aftershocks and microtremors. The strong motion data used in this study are provided by the K-NET and KiK-net of the National Research Institute for Earth Science and Disaster Prevention, and by Japan Meteorological Agency. This study supported by Grant-in-Aid for General Scientific Research (#15800009) from Japan Ministry of Education, Culture, Sport, Science, and Technology, Japan.

References:

- Capon, J.(1969), "High resolution frequency wavenumber spectrum analysis", *Proc. IEEE*, 57, pp1408-1418.
Motosaka, M. (2003), "Report of damage of July 26, 2003 Miyagiken-hokubu earthquake –earthquake and ground

- motion-," Earthquake Disaster Prevention, 193, 41-46 (in Japanese).
- Sato, T., S. Phno, and M. Motosaka (2003), "A quick report of seismic disaster for the Earthquake (July 26, 2003) occurred on northern part of Miyagi prefecture, J. of Japan Soc. For Natural Disaster Science, 22, 149-157 (in Japanese).
- Si H. and S. Midorikawa, S. (1999), "New attenuation relationships for peak ground acceleration and velocity considering effects of fault type and site conditions," *J. Struct. Constr. Eng., Arch. Inst. Jap.*, 523, 63-70 (in Japanese).
- Yamanaka, H. N. Yamada, H. Sato, S. Oikawa, Y. Ogata, K. Kurita, K. Seo, and Y. Kinugasa (2000) "Exploration of basin structure by microtremor array technique for estimation of long-period ground motion," *The 12th World Conf. Earthq. Eng., CDROM* No.1484.
- Yamanaka, H. and H. Ishida (1996) Application of genetic algorithms to an inversion of surface-wave dispersion data, *Bull. Seism. Soc. Am.* Vol.86, No.2, 436-444.

AN APPROXIMATE METHOD TO REPRESENT THE EXTREME VALUES OF NON-STATIONARY GAUSSIAN WHITE NOISE

H. Morikawa¹⁾

*Associate Professor, Department of Built Environment, Tokyo Institute of Technology, Japan
morika@enveng.titech.ac.jp*

Abstract: The statistics for extreme values of non-stationary processes are critical to designing structures in some engineering fields, such as earthquake engineering, coastal engineering, wind engineering, and so on. However, it is not easy to estimate the extreme values of non-stationary processes whose stochastic properties depend on time, because we have to deal with the i.n.n.i.d. (independent not necessarily identically distributed) random variables to solve problems of this type. Thus, we will discuss a probabilistic distribution for the extreme values of non-stationary Gaussian white noise as the simplest and most primary problem for i.n.n.i.d. random variables. Firstly, the closed form solutions are derived for the extreme values of i.n.n.i.d. Gaussian variables with two different properties and the qualitative properties are determined. Next, we propose an approximate representation of the distribution for the extreme values of i.n.n.i.d. random variables using these obtained properties, and confirm the appropriateness of the result through Monte Carlo simulations.

1. INTRODUCTION

The statistics for extreme values of non-stationary processes are critical to designing structures in some engineering fields, such as earthquake engineering, coastal engineering, and so on. Thus, many researchers have proposed various methods for this purpose. For example, Vanmarcke (1972) has developed a method to estimate the extreme values of a given system's response to random excitation using the spectral moments in a frequency domain. Furthermore, this method was extended by Kiureghian (1980).

While we may deal with this problem in time domain, most research on this type of problem has been limited to stationary processes. Especially, in a case where a time series is stationary Gaussian white noise with zero mean, we can directly apply the asymptotic representation for the extreme values of i.i.d. (independent identically distributed) Gaussian variables. Thus, the closed form solutions are easily obtained. This asymptotic representation of extreme values was introduced to the engineering fields by Gumbel and most classic and basic formulation as known as Gumbel's distribution (Gumbel 1958, Galambos 1978).

However, it is not easy to estimate the extreme values of non-stationary processes whose stochastic properties depend on time, because we have to deal with the i.n.n.i.d. (independent not necessarily identically distributed) random variables in a case of the simplest problem such as white noise. Although general representations for this type of problems can be obtained (Reise 1989, Ahsanullah and Nevzorov 2001), it is difficult to derive the closed form or asymptotic solutions for any specific distributions such as Gaussian distribution, etc. If such solutions

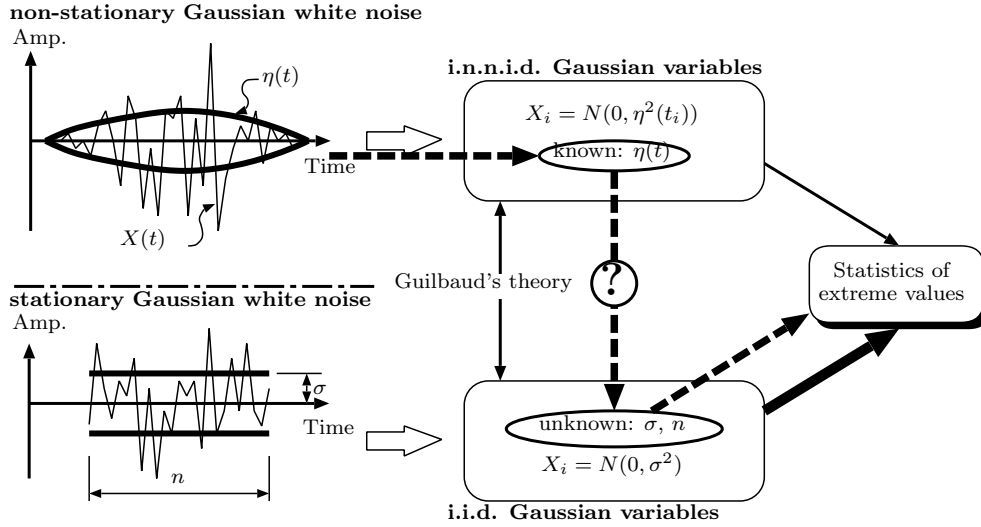


Figure 1 Schematic diagram to show the relationship between i.n.n.i.d. and i.i.d. Gaussian variables and concept to derive the statistics of extreme values of non-stationary Gaussian white noise.

are derived, their representations will be complicated and it is not suitable to apply them to the problems in the engineering fields.

The asymptotic representation of extreme values for i.i.d. random variable were derived on the basis of the ingenious ideas. As following this way, it is important to find an approximate representation for the extreme values of i.n.n.i.d. random variables using simple formulations. Unfortunately, nobody can propose appropriate representations for this type of problems, even though the problem is described for i.n.n.i.d. Gaussian variables.

Therefore, we will discuss a probabilistic distribution for the extreme values of non-stationary Gaussian white noise as the simplest and most primary problem: the extreme values of i.n.n.i.d. Gaussian are treated. Furthermore, we will limit the property of non-stationarity to the simple case keeping the application to the earthquake ground motion in mind: specifically, we will deal with the discrete white noise whose mean is zero, and standard deviation depend on time. The standard deviation has one peak and predominates the peak value over the time. Hereafter, we call “white noise” instead of the “discrete white noise” for the simplicity.

2. PROBLEM SETTING

We will deal with the asymptotic distribution, $F_Y(y)$ for maximum value of i.n.n.i.d. Gaussian variables X_i ($i = 1, 2, \dots$), as the simplest non-stationary process: that is,

$$X_i \equiv X(t_i) = \eta(t_i) \cdot W(t_i) \quad (1)$$

where, t_i stands for i-th discrete time, $W(t_i)$ for Gaussian white noise with zero mean and unit variance, and $\eta(t_i)$ for standard deviation which depends on time and varies smoothly with one extreme peak and $\eta(t; t \leq 0) = \eta(\infty) = 0$. The variations of $\eta(t_i)$ will be set much smaller than the time increments Δt . It is noted that $\eta(t_i)$ will play the role of a kind of envelop function of $X(t_i)$.

Generally speaking, the order statistics of i.n.n.i.d. random variables can be represented by using that of i.i.d. random variables because of the Guilbaud’s theory (Reiss 1989). However, this theory does not give any information how we can find the appropriate i.i.d. random variable corresponding with i.n.n.i.d. random variables with a specific probability distribution of X_i . As shown as question mark, $\textcircled{?}$ in Figure 1, although the asymptotic distribution should

be replaced by one of i.i.d. random variables in a case where the function $\eta(t)$, which is the probabilistic characteristics of i.n.n.i.d. random variable X_i , is given, there is no way to find parameters for the corresponding i.i.d. random variables.

To find the appropriate parameters for i.i.d. random variables are easier than to derive directly any asymptotic representation for the extreme values of i.n.n.i.d. random variables, because the asymptotic representation are already obtained for the extreme values for i.i.d. random variables.

From the above discussion, we will consider the approximate representations for the maximum values of non-stationary Gaussian white noise following the thick arrows in Figure 1. In this procedure, most significant problem is to represent the relationships between the parameters of i.i.d. and i.n.n.i.d. random variables. Thus, we will concentrate our concern into this problem, that is, to find the relationships as shown as $\textcircled{?}$ in Figure 1.

Firstly, it will be confirmed that we can replace i.n.n.i.d. variables with i.i.d. variables. Then, we will derive analytically the asymptotic representation for the maximum values of i.n.n.i.d. Gaussian variables with two distributions: we consider a case where $\eta(t_i)$ takes only two values. From this analysis, we discuss the relationships between the parameters for two types of variables and determine the qualitative properties to examine the possibility of the approximate representation for maximum values of i.n.n.i.d. variables. Finally, we will propose an approximate representation for our problem using the properties obtained from the above discussion, and confirm the appropriateness of the result through Monte Carlo simulations.

3. DISTRIBUTION FOR EXTREME VALUES OF GAUSSIAN VARIABLES WITH TWO DIFFERENT PROPERTIES

Let us consider X_i ($i = 1, 2, \dots, n_1 + n_2$) which consists of n_j independent Gaussian variables, X_{jk} with zero mean and variance σ_j^2 ($j = 1, 2, k = 1, 2, \dots, n_j$): that is, X_{jk} is $N(0, \sigma_j^2)$ and X_i should be X_{1k} or X_{2k} . Since X_i ($i = 1, 2, \dots, n_1 + n_2$) are independent mutually, we can renumber X_i without loss of generality. Thus, let us set X_{1k} ($k = 1, \dots, n_1$) for X_i ($i = 1, \dots, n_1$) and X_{2k} ($k = 1, \dots, n_2$) for X_i ($i = n_1 + 1, \dots, n_2$).

Then, the probability distributions for maximum value Y_j of X_{jk} ($j = 1, 2$) can be approximately written for large n_j as follows (Ahsanullah and Nevzorov 2001):

$$F_{Y_j}(y) = P(X_{jk} < y) \approx \exp[-\exp[-\alpha_j(y - u_j)]], \quad (2)$$

where $P(A)$ denotes the probability of A , and

$$\alpha_j = \sqrt{2 \ln n_j} / \sigma_j \quad (3a)$$

$$u_j = \left\{ \sqrt{2 \ln n_j} - \frac{\ln(\ln n_j) + \ln(4\pi)}{2\sqrt{2 \ln n_j}} \right\} \sigma_j. \quad (3b)$$

Thus, the probability distribution for maximum values of X_i is represented as

$$F_Y(y) = P(X_i < y) = \prod_{j=1}^2 P(X_{jk} < y) = \prod_{j=1}^2 F_{Y_j}(y) \approx \exp \left[- \sum_{j=1}^2 \exp[-\alpha_j(y - u_j)] \right]. \quad (4)$$

Eq.(4) gives an approximate representation from the meaning of the asymptotic distribution for a special case of i.n.n.i.d. random variable with large n_j .

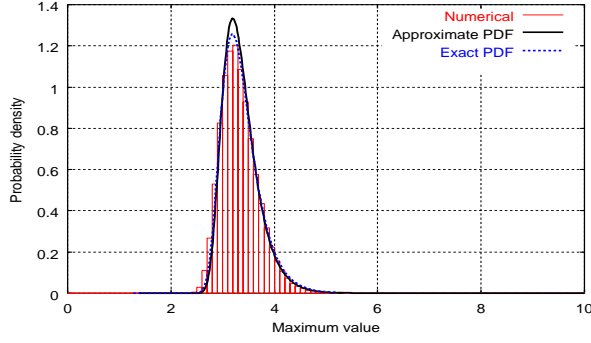


Figure 2 An example of distribution for extreme values of Gaussian white noise ($n_1 = n_2 = 500$, $\sigma_1 = 1.0$, $\sigma_2 = 1.05$).

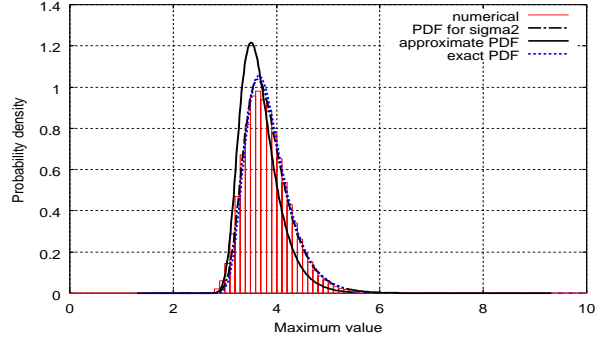


Figure 3 An example of distribution for extreme values of Gaussian white noise ($n_1 = n_2 = 500$, $\sigma_1 = 1.0$, $\sigma_2 = 1.25$).

According to Guilbaud's theory, Eq.(4) can be represented by the asymptotic distribution for the maximum values of i.i.d. random variable: namely, Eq.(4) can be replaced by

$$F_Y(y) \approx \exp[-\exp[-\alpha(y - u)]] \quad (5)$$

As pointed out above, this theory does not give any information about the relationships between α and u of Eq.(5), and α_j and u_j ($j = 1, 2$) of Eq.(2). Thus, we will discuss how α and u can be represented by α_j and u_j ($j = 1, 2$) in this section.

Calculating the Eq.(4) with various values of the parameters n_j and σ_j ($j = 1, 2$) of Eqs.(3a) and (3b), we obtained the following relationships as $\sigma_1 \approx \sigma_2$ and $n_1 \approx n_2$ by trial and error:

$$\alpha \approx \sqrt{2 \ln n} / \sigma \quad (6a)$$

$$u \approx \left\{ \sqrt{2 \ln n} - \frac{\ln(\ln n) + \ln(4\pi)}{2\sqrt{2 \ln n}} \right\} \sigma, \quad (6b)$$

where

$$n = \sum_{j=1}^2 n_j \quad (7a)$$

$$\sigma = \frac{\sum_{j=1}^2 n_j \sigma_j}{n}. \quad (7b)$$

Although this is not the mathematical consequence, these results may be expected instinctively under the above condition of σ_j and n_j . σ of Eq.(7b) is given by the weighted mean of σ_j with respect to n_j . Considering the general characteristics of the standard deviation, σ^2 should be represented by the weighted mean of σ_j^2 ($j = 1, 2$) with respect to n_j^2 , though Eq.(7b) gives good approximation as $\sigma_1 \approx \sigma_2$ as $n_1 \approx n_2$.

In other cases such as $\sigma_\ell \ll \sigma_j$ ($\ell, j = 1, 2$, $\ell \neq j$) and $n_1 \approx n_2$, $\alpha \approx \alpha_j$ and $u \approx u_j$ can be applied. This means that the distribution function, $F_Y(y)$ for the maximum values of i.n.n.i.d. Gaussian variables, X_i is approximately rewritten by the distribution for the maximum values of i.i.d. Gaussian variables with larger values of σ_j . Furthermore, in a case where σ_j is more than only 1.1 to 1.2 times of σ_ℓ , the effect from the maximum values of X_i with σ_ℓ is negligible. Thus, it is enough to treat the two cases of $\sigma_1 \approx \sigma_2$ and $\sigma_\ell \ll \sigma_j$ as $n_1 \approx n_2$.

Figures 2 and 3 show the numerical examples of the approximation of probability distribution for maximum value, Y , of X_i as $n_1 = n_2$. In this figures, the histogram of Y , which are obtained from the Monte Carlo simulation of 10000 times, is also shown. Figure 2 gives

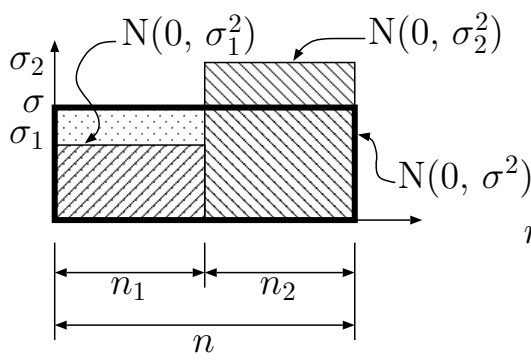


Figure 4 Concept to replace i.n.n.i.d. Gaussian variable with i.i.d. Gaussian variable.

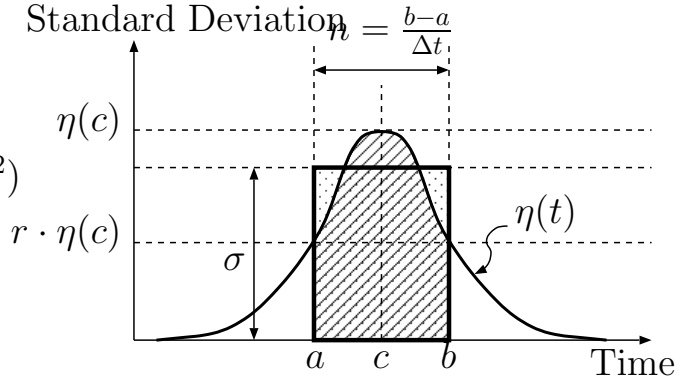


Figure 5 Concept to calculate the distribution of extreme value of non-stationary Gaussian white noise using the i.i.d. Gaussian variable.

the result as $\sigma_1 \approx \sigma_2$ and it is observed that the shapes of Eq.(4) and Eq.(5) obtained by using Eqs.(6a) and (6b) coincide. On the other hand, Figure 3 shows the case for $\sigma_1 \ll \sigma_2$. In this case, Eq.(4) coincides with the distribution for the maximum value of X_i with σ_2 : $F_{Y_2}(y)$. However, the distribution estimated by the weighted mean of σ_j ($j = 1, 2$) fails to represent the histogram.

From the above numerical calculations, we can confirm the Guilbaud's theory: the probability distribution for maximum values of i.n.n.i.d Gaussian variables are replaced by one of i.i.d. Gaussian distribution. Furthermore, the results give an instructions how to determine the values of α and u of Eq.(5).

As a result, we can conclude the method to determine the parameters for substitute i.i.d. distribution as follows. In a case of $\sigma_1 \approx \sigma_2$, we can choose the value of σ to satisfy the equation

$$\sigma \left(\sum_{j=1}^2 n_j \right) = \sum_{j=1}^2 (n_j \sigma_j). \quad (8)$$

This means that the area obtained by σ and $n = \sum_{j=1}^2 n_j$ should be same as the total area from n_j and σ_j ($j = 1, 2$) as shown in Figure 4. On the other hand, in a case of $\sigma_\ell \ll \sigma_j$ ($\ell, j = 1, 2$; $\ell \neq j$), we can use the probability distribution for the maximum value, Y_j , of i.i.d. Gaussian variable with $N(0, \sigma_j^2)$.

4. APPROXIMATE DISTRIBUTION FOR EXTREME VALUES OF NON-STATIONARY GAUSSIAN WHITE NOISE

We discussed the relationships between the parameters of i.n.n.i.d. and i.i.d. Gaussian variable for a special case in the previous section. Then, we will apply the obtained properties to approximate the probabilistic characteristics for maximum values of Eq.(1). Since we assume the standard deviation, $\eta(t)$ varies smoothly over the time as shown in Figure 5, we can approximate $\eta(t_i) \approx \eta(t_{i+1})$ at t_i and $t_{i+1} = t_i + \Delta t$, respectively, where Δt stands for the small increment of the discrete time. This suggests the possibility that the probability distribution for the maximum value, $F_Y(y)$, of X_i of Eq.(1) will be replaced with the asymptotic distribution for an i.i.d. Gaussian variable of Eq.(5) with parameters given by Eqs.(6a) and (6b).

On the basis of this daring (and mathematically baseless) assumption, we will determine the parameters for an i.i.d. Gaussian variable substituting the i.n.n.i.d. Gaussian variable. The parameters to determine are σ and n of Eqs.(6a) and (6b). Since we considered the area formed

by the number of variables and standard deviation to determine σ as shown in Figure 4, the same concept will be introduced as shown in Figure 5. The remaining part of this section is devoted to explain the procedure to obtain the probability distribution approximately using the Figure 5.

Let us consider $\eta(t)$ takes maximum value $\eta(c)$ at $t = c$. Then, introducing a real number r ($0 < r < 1$), we will determine parameters a and b which satisfy $r \cdot \eta(c) = \eta(a) = \eta(b)$, where $a < c < b$. The area of $\eta(t)$, S_r , are obtained as a function of r at $[a, b]$. To replace the probability distribution for the maximum value of i.n.n.i.d. Gaussian variable with one of i.i.d. Gaussian variable, we will consider a Gaussian variable with constant standard deviation at $[a, b]$. For the standard deviation of this i.i.d. Gaussian variable, we adopt the height σ of the rectangle whose area and length of the base are S_r and $b - a$, respectively. Applying the obtained σ and $n = (b - a)/\Delta t$ to Eqs.(6a) and (6b) and using Eq.(5), we can obtain the approximate probability distribution for the maximum values of i.n.n.i.d. Gaussian variable X_i .

The above procedure is rewritten mathematically as follows: the parameters a and b are determined by

$$a = \sup_{t < c} \{t; \eta(t) = r\eta(c)\} \quad (9a)$$

$$b = \inf_{t > c} \{t; \eta(t) = r\eta(c)\}, \quad (9b)$$

where $\eta(a) = \eta(b)$. Then, the area surrounded by $\eta(t)$ at $[a, b]$ is

$$S_r = \int_a^b \eta(t) dt. \quad (10)$$

n is obtained from $n = (b - a)/\Delta t$, and σ is determined by

$$\sigma = \frac{S_r}{n}. \quad (11)$$

Substituting n and σ for Eq.(5) derives the approximate probability distribution for the maximum value of X_i .

In this procedure, we did not mention the value of r . Generally speaking, since any function can be used for $\eta(t)$, we cannot examine the sensitivity of Eq.(5) with respect to r , exhaustively. We can say, in our calculations, Eq.(5) is not sensitive toward r . However, in a case where r is too small, the approximation of $\eta(t_i) \approx \eta(t_{i+1})$ is not assured. Thus, we can use the value of 0.8 to 0.9 as r . Since this suggests that the optimal value of r may depend on the time increment, Δt , Δt should be small with respect to the variance of $\eta(t)$ to satisfy the approximation $\eta(t_i) \approx \eta(t_{i+1})$.

5. A NUMERICAL EXAMPLE

To confirm the availability of the proposed method, we carried out a simple numerical calculation using the Monte Carlo simulation. The pseudo-random numbers are generated by the Mersenne Twister (Matsumoto and Nishimura 1998) and the Fortran code based on this method (Matsumoto 2002) are used. Since the generated random values follow the uniform distribution, they are transformed to Gaussian distribution (Evans et al. 1993). In this calculation, $\Delta t = 0.01$ are used as small value regarding to the variance of $\eta(t)$.

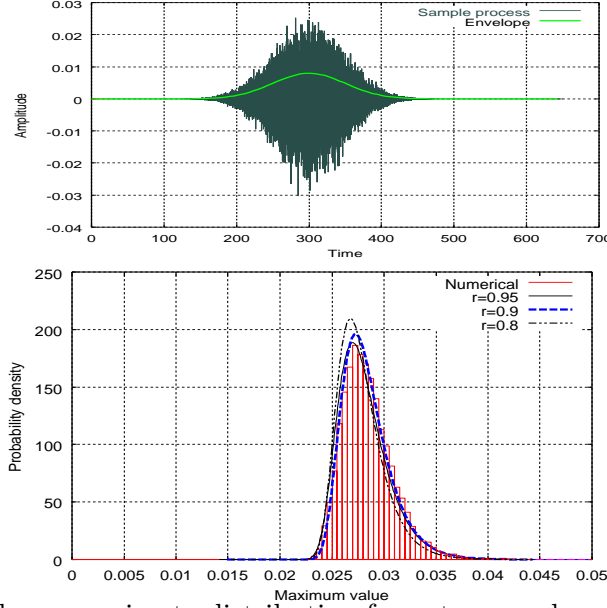


Figure 6 An example of the approximate distribution for extreme values of non-stationary Gaussian white noise. The upper panel shows a sample process and $\eta(t) = \frac{1}{\sqrt{2\pi}50} \exp\left[-\frac{1}{2}\left(\frac{t-300}{50}\right)^2\right]$. The approximate distributions for $r = 0.95, 0.9,$ and 0.8 are compared with the result of numerical simulation in the lower panel.

Table 1 Comparison of the parameters for Gumbel's distribution for Eq.(5)

	Numerical	$r = 0.95$	$r = 0.9$	$r = 0.8$
u	0.02733	0.02699	0.027270	0.02678
α	530.74	512.65	532.90	569.92

Figure 6 shows an example of the probability distribution for maximum value of X_i with $\eta(t)$ which is Gaussian type function. The upper panel of this figure compares a realization with the shape of $\eta(t)$. In the lower panel, the estimated distribution are shown with the histogram obtained from Monte Carlo simulation of 10000 times. The lines show the results from the different value of r of Eqs.(9a) and (9b): 0.8, 0.9, 0.95. It is noted that these lines approximate the histogram well. This means that the proposed method gives good approximation to represent the probability distribution for maximum value of i.n.n.i.d. Gaussian value.

Furthermore, to examine the accuracy of the approximation, the values of parameters α and u of Eq.(5) are listed in Table 1. From this, it is observed that the statistical parameters are consistent values with the results from Monte Carlo simulation. This means that the we can set the value of r roughly, because the approximation is not so sensitive to r .

6. CONCLUSIONS

We have analytically derived the asymptotic representation for maximum values of Gaussian variable with two different properties and found qualitative properties. Using these properties, an approximate representation were proposed for maximum values of non-stationary Gaussian white noise and the appropriateness was also confirmed through the numerical simulation.

Acknowledgments:

The author wish to express our special thanks to Professor A. Zerva (Drexel University, USA) for reading the draft and making a number of valuable advice and helpful suggestions. This research was partially supported by the Assistance to International Exchange of Scientist Fund of the Kajima Foundation, and the Ministry of Education, Science, Sports and Culture, Grants-in-Aid for the Encouragement of Young Scientists (A), No.15681010, 2003–2005.

References:

- Ahsanullah, M. and Nevzorov, V.B. (2001), “*Ordered Random Variables*,” Nova Science Publishers.
- Evans, M., Hastings, N., and Peacock, B. (1993), “*Statistical Distributions*,” 2nd edition, John Wiley & Sons.
- Galambos, J. (1978), “*The Asymptotic Theory of Extreme Order Statistics*,” John Wiley & Sons.
- Gumbel, E.J. (1958), “*Statistics of Extremes*,” Columbia University Press.
- Kiureghian, A.D. (1980), “Structural response to stationary excitation,” *Journal of Engineering Mechanics Division*, Proc. of ASCE, **106**(EM6), 1195–1213.
- Matsumoto, M. and Nishimura, T. (1998), “Mersenne Twister: A 623-dimensionally equidistributed uniform pseudorandom number generator,” *ACM Trans. on Modeling and Computer Simulation*, **8**(1), 3–30.
- Matsumoto, M. (2002), <http://www.math.keio.ac.jp/~matumoto/mt.html>
- Reiss, R.-D. (1989), “*Approximate Distributions of Order Statistics: With Applications to Nonparametric Statistics*,” Springer Verlag, p.36.
- Vanmarcke, E.H. (1972), “Properties of spectral moments with applications to random vibration,” *Journal of Engineering Mechanics Division*, Proc. of ASCE, **98**(EM2), 425–446.

SITE AMPLIFICATION EFFECTS OBSERVED FROM MODERATE INTENSITY EARTHQUAKE RECORDS OBTAINED IN THE SMASCH ARRAY

E. F. Cruz¹⁾, D. Valdivia²⁾, and N. Schmauk³⁾

1) Professor, Dept. of Structural and Geotechnical Engineering, P. Universidad Católica de Chile, Santiago, Chile

2) Seismic Engineer, GHD-Promina Ltda., Av. Apoquindo 4775, Of. 601, Santiago, Chile

3) Research Assistant, Dept. of Structural and Geotechnical Engineering, P. Universidad Católica de Chile, Santiago, Chile
ecruz@ing.puc.cl, Dania_Valdivia@ghdpromina.cl, nschmauk@puc.cl

Abstract: The SMASCH array for the observation of strong ground motion has been operating in the Santiago area since 1989. One of the objectives of this instrumentation project is to study the influence of local site conditions on observed earthquake ground motions. The array consists of seven free-field sites located on different soil conditions ranging from a reference rock outcrop site to a site located on soft silty ground.

Using data from low to medium intensity events which occurred between 1989 and 2001, an evaluation of site amplification effects has been carried out. Fourier Amplitude spectra of the accelerograms for each site, for several different events, were computed. For this purpose only a limited portion of the record was used: that containing predominantly S waves. The spectral shapes were smoothed and amplitude ratios with respect to the rock site were calculated.

For each site the averages of the amplification ratios were computed after grouping the events in three different sets: all events, events in two different magnitude ranges (4 to 5 and 5 to 6), and events having different epicenter location (NW azimuth and NE azimuth relative to the array location). From the results obtained it is apparent that there is a noticeable influence of the site soil conditions on the amplification value and also that this amplification can be quite different depending on the period range considered. The influence of magnitude is not very large, but is noticeable for several sites. The influence of azimuth is clear at some sites and not noticeable at others.

1. CONFIGURATION OF THE SMASCH ARRAY

The overall purpose of the instrumentation program is the study of earthquake motion in Santiago as a basis for improving the specification of earthquake design requirements for buildings and other structures. A specific objective towards this general goal is to obtain a thorough knowledge of ground motion in sites with various soil conditions.

The SMASCH array consists of seven stations as listed in Table 1. The location of the sites in the Valley of Santiago is shown in Figure 1. The sites are located on a range of soils and cover most of the city of Santiago, with spacing of 5 to 10 km. SMAC-MD digital accelerographs, manufactured by Akashi Seisakusho Inc., Japan, are installed at five sites; since this instrument has an A/D converter with resolution of 16 bits, it can record not only strong motion but also weak motion with high accuracy. At one site there is an SSA-1 instrument, manufactured by Kinematics Inc., USA, with characteristics similar to the SMAC-MD, although with only 12 bits resolution in the A/D converter. The instrument at site No.8 was originally an analog type instrument, that has been removed and is presently being replaced by a new instrument, that is not yet fully operational.

To record free-field earthquake ground motions, small instrument shelters were constructed at all

sites except CSL. The CSL site is a rock cave in the Santa Lucía hill in downtown Santiago; where the instrument is installed directly on a concrete floor in the cave. A detailed description of the instruments and of the shelters characteristics can be found in (Midorikawa et al., 1990).

2. GEOLOGICAL CONDITIONS IN SANTIAGO AND AT INSTRUMENT SITES

Santiago is situated in a narrow valley between the Andes and the coastal mountains. The altitude of the city is about 600 m above sea level. The valley originated from the depression of an area between two major faults, which are parallel to the two mountain chains. The depression was caused by tectonic movements in the Tertiary.

Most of the sediments which cover the valley were transported from the Andes mountains, mainly by streams. Some deposits are believed to be the result of volcanic mud flows or glaciers. The formation of the sediments is different in each area of the city. The surface geology of the city can be divided into several types, as shown in Figure 1 (Valenzuela, 1978). In the central and southern parts of the city, sediments consist of very dense coarse gravel with cobbles. In the northwest part of the city, recent alluvial deposits, consisting of loose silty soils, cover the area. Between these two areas a transition zone exists. At the foot of the mountains, in the eastern part of the city, the ground surface is covered by colluvial deposits from the mountains. Stiff pumice of volcanic origin, which is called Pomacite, is found in the western part of the city. Outcrops of basement rock are found in the mountains and outliers form the hills which exist in the plain.

To investigate soil conditions at the sites, bore hole tests were carried out at PTP, PCQ, and AES and small pits were excavated at UC1 and UC2. Below is a brief description of the soil conditions at the sites based on these explorations and on previous investigations compiled in (Valenzuela, 1978).

Site 1, CSL (Cerro Santa Lucía): Igneous rock surrounded by the alluvial deposits of the Mapocho river. The Santa Lucía hill rises about 60 m above the surrounding alluvial plain. The cave housing the instrument is about 20 m above the plain. Significant topographic effects from the hill are not expected in records at this site.

Site 2, UC1 (U. Católica, Campus Casa Central): Alluvial deposits of the Mapocho river. Dense to very dense gravel is found at a depth of 2.4 m. An S wave velocity for the gravel deposits of approximately 700 m/s was measured. The superficial layers consist of artificial fills, silts and clay deposits. The depth to water table is approximately 50 m and the depth to base rock is approximately 100 m. This site is about 300 m away from CSL.

Site 3, UC2 (U. Católica, Campus San Joaquín): Alluvial deposits. The soil conditions are similar to those of site 2, but dense gravel is found at a depth of 0.9 m. A thin clayey layer overlies the gravel deposits. The depth to water table is 80 m and the depth to base rock is approximately 400 m.

Site 4, PTP (Planta Toyota, Rotonda Pudahuel): "Pomacite" deposits formed of volcanic pumice and ash. Standard penetration test (SPT) N value is 50-75. The fine content is between 6 and 32%. Pomacite overlies the gravel layer which is the typical soil in the city. The thickness of the layer of Pomacite is 40m or less. S wave velocities of 300 m/s in the upper 6 m and 550 m/s at depths of 6 to 16 m were measured. The water table is deeper than 20 m, the depth to rock is approximately 300 m.

Site 5, PCQ (Planta Cervecería Santiago, Quilicura): Alternating layers of low to medium plasticity silts and clays, interbedded with gravel layers. From the surface to about 9 m depth the deposits have a soft consistency, low relative density and SPT N value of 2 to 4. The S wave velocity is around 200 m/s from the surface to a depth of 10 m. Below about 9 m the strata have a firm to hard consistency and medium to very high relative density and the SPT N value is 35. The depth to water table is about 2 m, the depth to base rock is about 100 m.

Site 6, ESM (Escuela Militar): Alluvial deposits of the Mapocho river. Dense to very dense gravel and unsaturated soil. The depth to water table is 25 m and the depth to base rock is 100 to 200 m.

Site 7, AES (Aeródromo Eulogio Sánchez, Tobalaba): Colluvial deposits. Inorganic silt of medium plasticity, firm, interbedded with 5 to 10 cm layers of dense silty gravel. Unsaturated soil. Estimated thickness of the stratum is more than 20 m. The depth to water table is about 90 m and the depth to rock is about 100 m. The S wave velocity profile was obtained using seismic refraction. It varies from 300 m/s at the top layer (considered to be 4m thick), to 480 m/s for the next layer (considered to be 6 m thick) with a final value of 1000 m/s for the infinite layer below that depth.

3. LOCAL SITE EFFECTS ON OBSERVED GROUND MOTIONS

Only events that have triggered three or more stations have been considered for this study. Detailed information regarding each event can be obtained from the report that is published every year with the corresponding data (see for example Cruz et al, 2001). Alternatively, the data can be obtained from the web page www.ing.puc.cl/~wwwice/sismologia, of the Strong Motion Seismology Laboratory. A summary of the events considered is presented in Table 2.

Three components are recorded at each site: two horizontal components aligned with the East-West (X) and North-South (Y) directions and a vertical component (Z). The epicenter locations for the events considered are shown in Figure 2, and in Figure 3 the focii locations are shown in terms of Longitude and Depth, where the inclination (dip angle) of the subduction zone, the predominant source of earthquake events in the area is clearly observed. Each event is identified with a label that includes the year in which it occurred and the sequence number of the event in the SMASCH Report of that year (Cruz et al., 2001).

It is clear that the observed ground motion is a consequence of source, path, and site effects. Only the amplitude ratio of the motion on soil ground to that on rock is representative of site effects, because the site effects can be ignored for a base rock site. A section of S waves in the record is used to calculate the spectral amplitude ratio, because the main portion of strong ground motion is mainly due to S waves. On each of the records and sites considered this is done for all the recorded components.

For each event the Fourier Amplitude Spectrum was computed for the selected portion of each record and the spectrum was smoothed using a simple average of the amplitudes over overlapping windows of 0.78 Hz. Then the ratio of the spectrum for each soil site to that of the reference rock site (CSL) was calculated.

Amplitude-ratio spectra for the various records available for each site were obtained. The ratios from different records are similar at each site, indicating that each site has particular properties regarding spectral amplification of ground motions. Simple statistics were performed for each site considering the full set of records available for the site, and plotted as shown in Figures 4 and 5 for sites 3 and 5.

These figures show that the soil conditions at the different sites have a significant influence in the amplifications ratios. Some trends can be observed, and even though the difference between the average curves (solid lines) and the average plus one standard deviation curves (dashed lines) are rather large at some period ranges, the results are considered adequate for identifying the major trends in the behavior of the amplitude ratios over the period range considered.

Some of the trends observed can be summarized as follows:

1. At UC1 (Site 2) and UC2 (Site 3) on gravel, the amplification of ground motion was generally small. At UC1, however, a large amplification was found in the period range 0.05 to 0.1 seconds. This effect is probably due to the artificial fill which exists locally at the site just below the instrument location. When the effects of the artificial fill are ignored, the amplification is found to be around 2.5 in the period range 0.1 to 2 seconds for UC1, and 1.5 between 0.05 and 2 seconds for UC2. A measure of the rather large scatter of the data is given by the difference of the two curves shown (solid and dashed) over the period range (Figure 4).

2. At PTP (Site 4) on the Pomacite deposits site, the amplification was small for periods shorter than 0.2 s and became larger in the longer period range. At a period of around 0.8 seconds, the ratio shows its maximum. The amplification on this site is about 2 for periods shorter than 0.2 seconds, and between 3 and 4 for periods larger than 0.4 seconds.
3. At PCQ (Site 5) on the silty soil site, a large amplification was obtained over a wide period range. The amplification tends to increase more or less linearly from 0.05 to about 0.1 seconds and then it remains fairly constant with an average value of about 6 (Figure 5).
4. At AES (Site 7) on the colluvial deposits site, limited amplification was found for periods in the range 0.10 to 0.25 seconds with an average value of about 3.5. For shorter periods the went up to about 7 at 0.05 seconds, and for longer periods it increased (more or less linearly) to about 9 or 10 at about 2 seconds, and then remains constant.

4. EFFECT OF MAGNITUDE AND OF EPICENTER LOCATION

The second part of this investigation deals with the identification of the effects on the amplitude ratios of two parameters: the magnitude of the event, and the epicenter location relative to the site (azimuth). For this purpose the events at each site were divided into two sets: magnitude between 4 and 5, and between 5 and 6 for the study of the effect of magnitude; and North-West azimuth and North-East azimuth for the study of the effect of epicenter location. The statistics for the results (amplitude ratios) for these groups were then computed and typical results are shown in Figures 6 through 9 for site 5. Although the number of events considered in these groups is smaller than in the previous results they still provide some significant insight in the effect of the parameters considered.

The results need to be analyzed further, but preliminary analysis of them shows that the effect of azimuth can be significant, especially for Sites 4 and 7. The effect of magnitude is not very significant in most of the sites, except may be in Site 7, but this may change if the magnitude ranges increase as larger magnitude events are likely to induce nonlinear effects in the soil, especially at the softer soil sites. More definitive conclusions will be obtained only when several strong earthquake records with higher acceleration levels are available.

5. RESULTS OBTAINED FROM MICROTREMOR MEASUREMENTS

In order to have a procedure that can be extended to other sites, and thus allowing to establish a micro-zoning of the region based on actual measurements of ground motions, the ratios of the amplitude spectra computed in a similar fashion as those for the earthquake records, were obtained for several different sites where micro-tremor measurements were performed. Several campaigns of micro-tremor observation have been carried out, especially in the softer soils areas. The results from these observations are expressed in terms of horizontal to vertical velocity amplitude spectral ratios and sample results are shown in Figures 10 and 11 for micro-tremor measurements performed at site 3 and site 5 respectively.

The results obtained show rather large dispersion, but in general it is observed that the magnitudes of the amplitude ratios have some correlation to the thickness of the deposits at the different sites, and also to the existence of soft soil layers.

6. SUMMARY AND CONCLUSIONS

Data from a strong ground motion monitoring array in Santiago, Chile (SMASCH array) has been used to study local site effects on ground motion. The spectral amplitude ratios of the observed

earthquake motions at soil sites with respect to a reference rock site were calculated to examine the local site effects. The spectral amplitude ratios from different records are similar at each site, and the spectral amplification of ground motion is unique at each site. The amplification values observed can be quite large reaching values as high as 9 or 10 for some period ranges in the softer soil sites. The effects of event magnitude and event epicenter location with respect to site location on the amplitude ratios are studied and are found to have some influence on the shape and the value of the amplification ratios observed.

The results are complemented with others obtained from micro-tremor measurements that have shown that the magnitude of the amplitude ratios have some correlation to the thickness of the deposits, and also to the existence of soft soil layers.

Acknowledgements:

This study was started as a part of the "Chile-Japan Joint Study Project on Seismic Design of Structures in Chile" sponsored by the Japan International Cooperation Agency (JICA) and conducted at the Department of Structural and Geotechnical Engineering of the P. Universidad Católica de Chile. The aid from JICA in providing the five SMAC-MD accelerographs, the support from Fundación Andes, which allowed the acquisition of two SSA-I accelerographs, and the support from the Seismographic Station of the University of California at Berkeley, which provided the two RFT-250 accelerographs that started our instrumentation program are gratefully acknowledged. The basic methodology for this investigation was initially used by Dr. S. Midorikawa, of the Tokyo Institute of Technology, and presented at a Workshop organized in Santiago in 1991 (Cruz et al, 1993).

References:

- Cruz, E., Riddell, R., and Midorikawa, S. (1993) "A study of site amplification effects on ground motions in Santiago, Chile." *Tectonophysics*, 218, pp 273-280.
- Cruz, E, Riddell, R., and Valdivia, D. (2001) "Annual Report on Strong Motion Records from SMASCH Array (2000)." DIE 98-1, Depto. Ingeniería Estructural y Geotécnica, P. Universidad Católica de Chile.
- Midorikawa, S., Riddell, R., and Cruz, E. (1992) "Strong-motion array observation in Santiago, Chile (SMASCH Array)." DIE 90-2, Depto. Ingeniería Estructural y Geotécnica, P. Universidad Católica de Chile.
- Valenzuela, G.B., (1978) "Suelo de fundación del Gran Santiago". Instituto de Investigaciones Geológicas. Santiago, Chile, *Boletín* 33, 105 pp..

TABLE 1. List of Strong Motion Sites of the SMASCH Array

Site Name	Site Code	Site No.	Soil Condition	Coordinates	Instrument Type	Installation Date
Cerro Santa Lucía	CSL	1	Rock	33°26'25"S 70°38'32"W	SMAC-MD	13/07/1989
U. Católica, Campus Casa Central	UC1	2	Dense Gravel	33°26'29"S 70°38'19"W	SMAC-MD	12/07/1989
U. Católica, Campus San Joaquín	UC2	3	Dense Gravel	33°29'59"S 70°36'49"W	SMAC-MD	11/07/1989
Planta Toyota, Rotonda Pudahuel	PTP	4	Stiff Fine Volcanic Sediment	33°27'01"S 70°46'34"W	SMAC-MD	14/07/1989
Planta Cervecera Santiago, Quilicura	PCQ	5	Alluvial Sediments	33°21'52"S 70°42'08"W	SMAC-MD	14/07/1989
Aeródromo Eulogio Sánchez, Tobalaba	AES	7	Colluvial Deposits	33°27'31"S 70°32'54"W	SSA-1	31/01/1990
Escuela Militar	ESM	8	Dense Gravel	33°24'43"S 70°34'55"W		

Table 2. Summary of Earthquake Events Considered.

Site No.	M ≤ 5	M > 5	Azimuth N-W	Azimuth N-E	Total
1	-	-	-	-	80
2	50	16	16	20	66
3	43	14	15	14	57
4	54	17	17	18	71
5	53	17	16	19	70
7	24	9	5	8	33

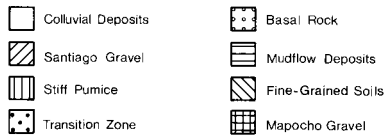
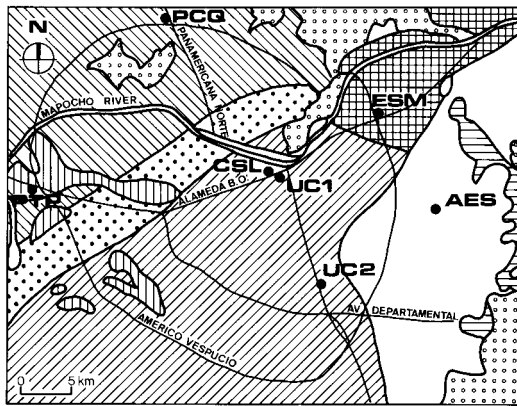


Figure 1. Geological map of Santiago and location of the stations of the SMASCH Array.

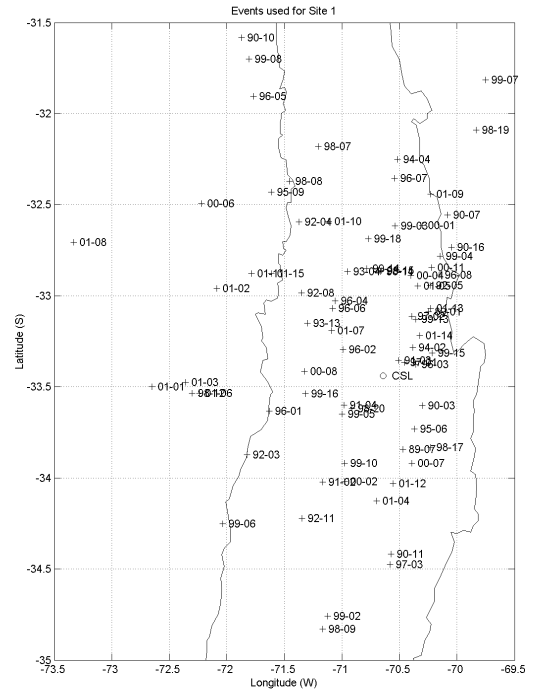


Figure 2. Epicenter Location for Events Used (Coast line and Chile-Argentina border are shown).

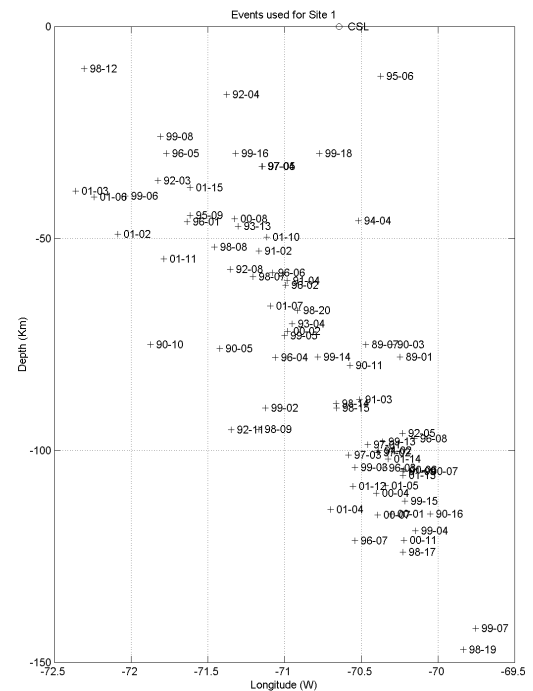


Figure 3. Hypocenter Locations for Events Used.

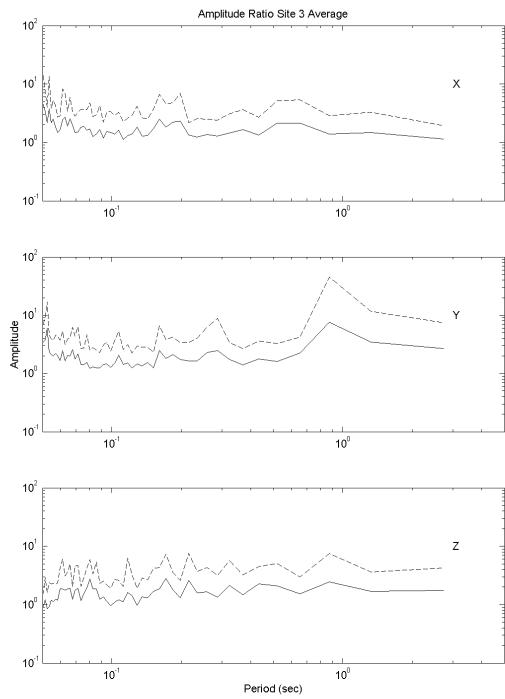


Figure 4. Amplitude Ratio Spectra for Site 3.

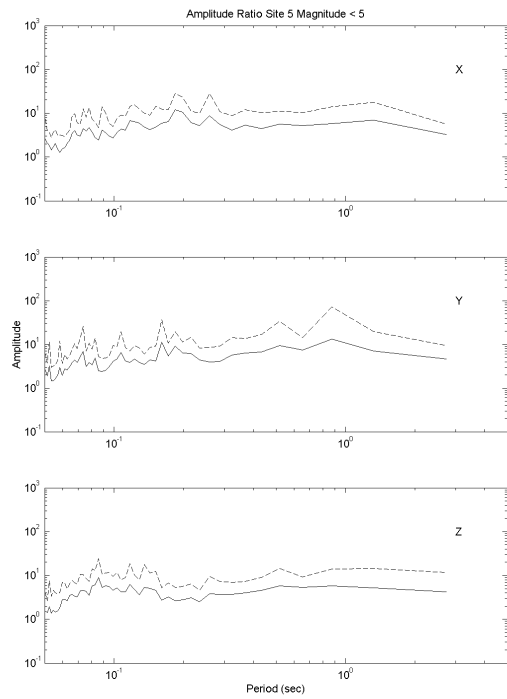


Figure 6. Amplitude Ratio Spectra for Site 5, $4 \leq \text{Magnitude} \leq 5$.

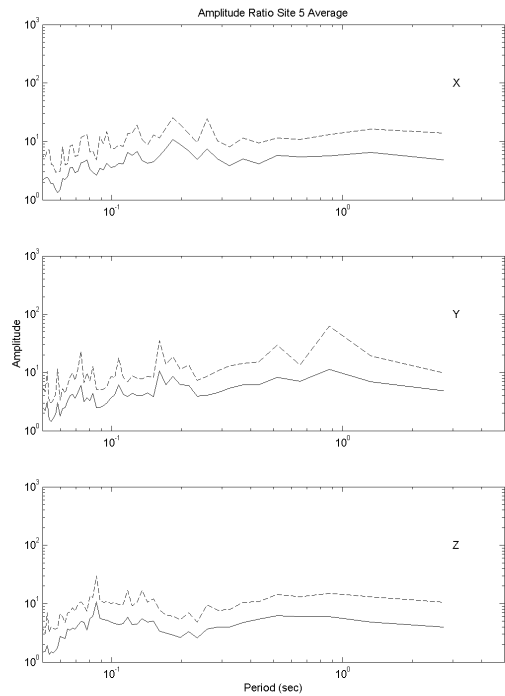


Figure 5. Amplitude Ratio Spectra for Site 5.

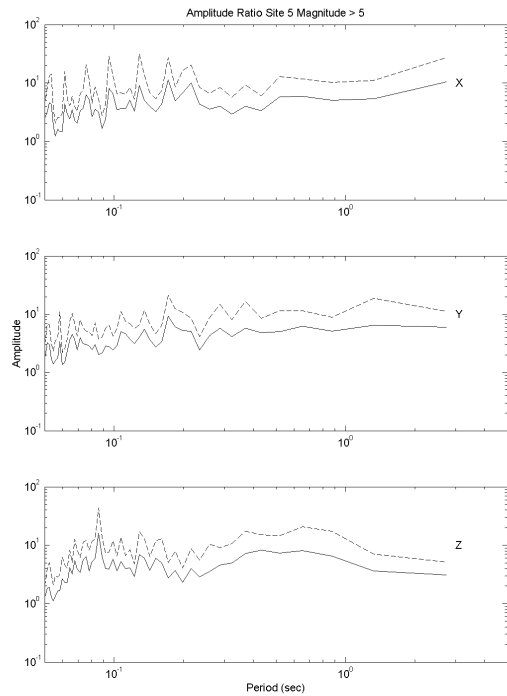


Figure 7. Amplitude Ratio Spectra for Site 5, $5 \leq \text{Magnitude} \leq 6$.

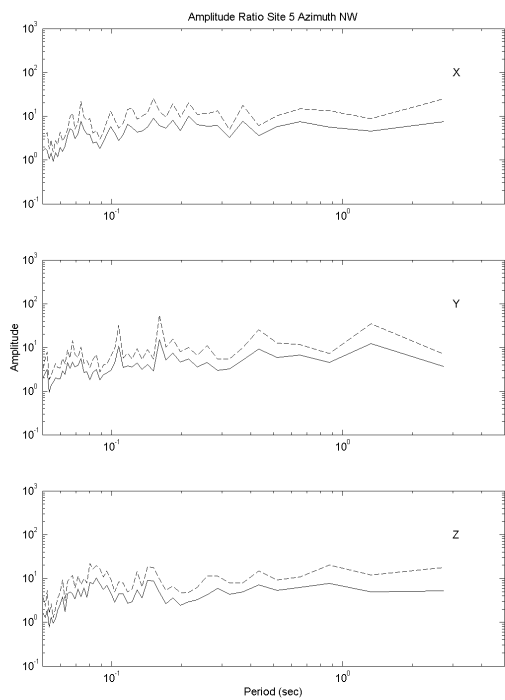


Figure 8. Amplitude Ratio Spectra for Site 5, NW Azimuth.

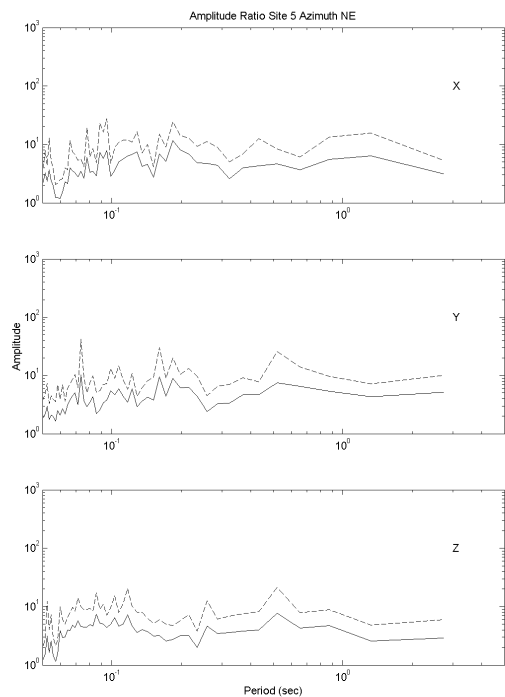


Figure 9. Amplitude Ratio Spectra for Site 5, NE Azimuth

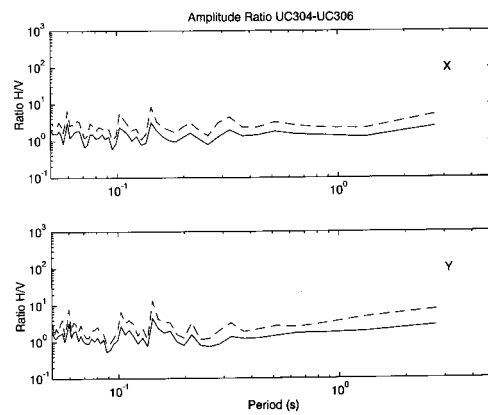


Figure 10. Amplitude Ratio Spectra for Site 3, Micro-tremors.

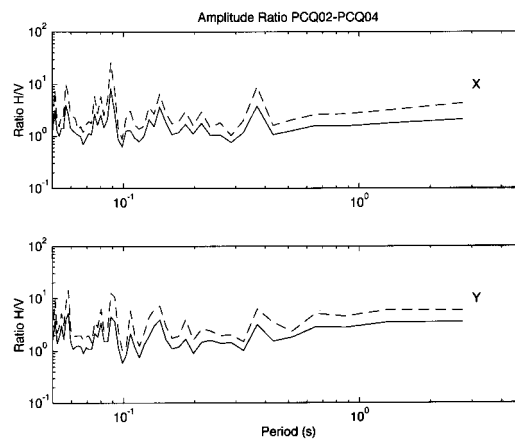


Figure 11. Amplitude Ratio Spectra for Site 5, Micro-tremors.

Disaster Prevention by Realtime Earthquake Information - Study on Practical Use in Private Enterprise -

I.Takahashi¹⁾ and S. Nambu²⁾

1) Senior Research Engineer, Innovation Center, Institute of Technology, Shimizu Corporation, Japan
 2) Deputy Senior Research Engineer, Innovation Center, Institute of Technology, Shimizu Corporation, Japan
ikuo@shimz.co.jp, nambu@shimz.co.jp

Abstract: The system of the “Nowcast Earthquake Information” is being developed, which will send us the realtime information about the hypocenters or the seismic intensity of big earthquakes before the main shocks reach. The development for practical use of the information has started. The information is expected to mitigate the disasters to human lives and structures when big earthquakes occur. In this paper, the practical use of the information is discussed mainly from the viewpoint of private enterprises through the concrete examples and tests. The points and the subjects of the use are also investigated.

1. INTRODUCTION

The big earthquakes occurred continually in the Tohoku and the Hokkaido districts last year. The occurrence of the Tokai, Tonankai, or Nankai Earthquake is a matter of anxiety in near future. Under the circumstances, there are a lot of things to do before such big earthquakes attack Japan.

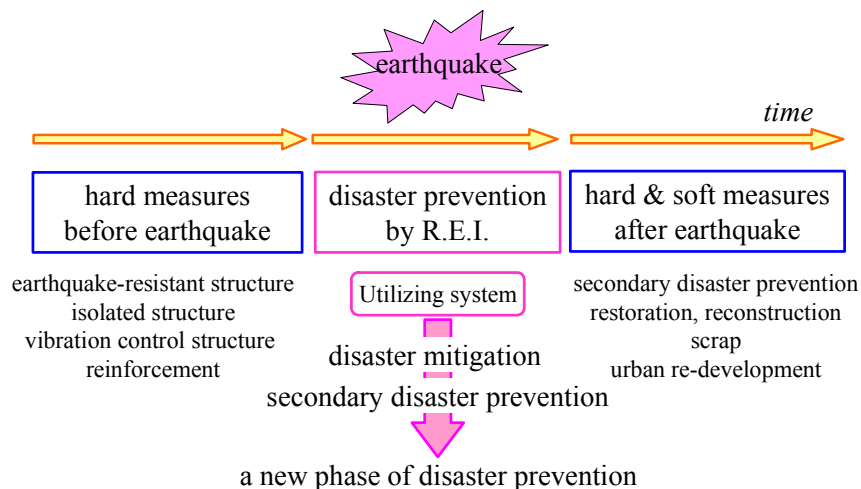


Figure 1 Disaster Prevention by Realtime Earthquake Information

The Japan Meteorological Agency (JMA) has been developing the iNowcast Earthquake Information system, which offers the realtime earthquake information about the epicenters or the seismic intensity before the main shocks reach. The study on the practical use of the information has been in progress simultaneously. It will be possible to make measures according to the information just before the main shocks reach or just after they calm down as shown in Figure 1.

In this paper, the practical use of the information is discussed mainly from the viewpoint of private enterprises through the concrete examples and tests. The points and the subjects of the practical use of the information are also investigated.

2. OUTLINE OF REAL TIME INFORMATION

The UrEDAS (Urgent Earthquake Detection and Alert System) of Japan Railway Company and the SUPREME (Super-dens Realtime Monitoring of Earthquake) of Tokyo Gas Company are known as the application system using the realtime earthquake information in Japan. The former is applied for the safe operation of the Shinkansen Lines as shown in the work by Nakamura (2000). The latter is the control system of city gas supply as shown in the work by Shimizu et al. (2001). The both are developed according to the needs of the business and utilize their own earthquake observation networks.

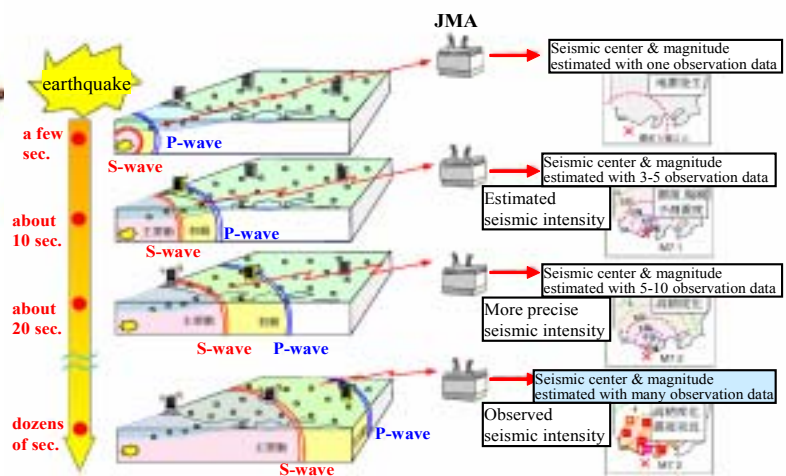
The realtime earthquake information system using the public earthquake observation networks has been studying mainly by JMA, The National Research Institute for Earth Science and Disaster Prevention (NIED) as shown in the work by Kamigaichi et al. (2004), Uhira (2004). The information will be offered to the world from JMA in near future. Sending tests have already started between JMA and several universities or companies. The system started using data from the five observatories around the Tokai district in 2003. The regular sending tests will start in 2004 because the eighty seismographs have been provided for the system from the Kanto to the Kyusyu districts as shown in Figure 2. The observation network is expected to expand to the Hokkaido, the Tohoku districts before long. NIED has been developing the technology of the information system as shown in the work of Horiuchi (2004) in combination of JMA and practical systems in the cooperation with the Real Earthquake Information Consortium (nonprofit organization) as shown in the work of Fujiwara (2004).

The system of the Nowcast Earthquake Information estimates the epicenters and the magnitudes according to the data obtained from the nearest observatories, and sends the information quickly. The



(supplied by JMA)

Figure 2 Distribution of Seismographs for Nowcast Earthquake Information



(supplied by JMA)

Figure 3 Wave Propagation and Nowcast Earthquake Information

information reaches before S-wave propagates because the estimation is made based on the observed P-waves. The several seconds before the main shocks can be used for the preparedness of the earthquakes. The forecasts of the seismic intensity and the arrival time of the main shocks are included in the information. The accuracy of the information can be improved as the data from the observatories increases as shown in Figure 3.

3. APPLICATION OF INFORMATION

3.1 Characteristics of Nowcast Realtime Earthquake Information

Taking all things into consideration, the Nowcast Earthquake Information has the characteristic as follows:

- 1) Certainty of Earthquake Occurrence: The information that earthquakes have occurred somewhere can be reliable unless noise is mixed in the data, because it is based on the observation, which is much different from the prediction.
- 2) Accuracy and Rapidity: The first information is based on the P-wave observed first at the nearest observatory to the epicenter. The rapidity of the first information is much valuable. On the other hand, the degree of the accuracy of the first information can't be very high. More accurate information can be given based on the data from several observatories in a few seconds. At that time, the S-waves have propagated to some extent. The accuracy of the realtime earthquake information is not compatible with the rapidity.
- 3) Time Margin: If a big earthquake occurs near or under cities, the main shock attacks the cities as soon as the realtime earthquake information reaches or before it does. In those cases, time is not left in preparing for the earthquake.
- 4) Information Before and After: The accuracy and the rapidity of the information are variable according to the epicenters of every earthquake. On the other hand, the information of observed seismic intensity sent after the shocks calm down is effective to prevent cities and citizens from the secondary damage in every big earthquake.

3.2 Capability in Past Earthquakes

It is very interesting to estimate how effective the realtime earthquake information should be to the disaster prevention if the information system existed when the past big earthquakes occurred.

Figure 4 shows the ratios of cause of death in the 1978 Miyagi-Ken-Oki Earthquake, the 1993 South-West off Hokkaido Earthquake and the 1995 Hyogo-Ken-Nambu Earthquake as shown in the

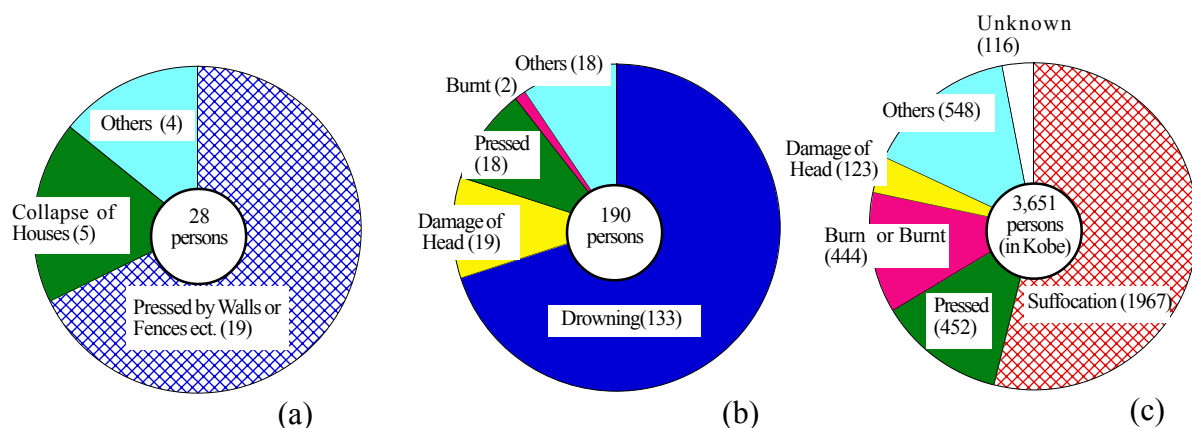


Figure 4 Cause of Death in Past Earthquakes: (a) 1978 Miyagi-Ken-Oki Earthquake, (b) 1993 South-West off Hokkaido Earthquake, and (c) 1995 Hyogo-Ken-Nambu Earthquake

work of A.I.J. (1980), A.I.J. (1995) and A.I.J. et al. (2000). In case of the Hyogo-Ken-Nambu Earthquake, the dead in Kobe is shown in the figure. In the Miyagi-Ken-Oki Earthquake, the fact is remarkable that many people died by fall down of walls or fences etc. This earthquake occurred in the evening when the most of people were in active. If they caught the realtime earthquake information somehow several seconds before, the dead should be decreased. Many people were killed by the tsunami in the South-West off Hokkaido Earthquake. It is conjectured that the most of the dead persons were not able to escape or fail. If they knew the possibility of tsunami occurrence, the scale or the arrival time, the victims of the tsunami should be decreased. In the Hyogo-ken Nambu Earthquake about two thirds of dead persons were pressed by houses or furniture. It can be thought that the sharp main shocks collapsed the houses or fell down furniture in a moment. If the realtime earthquake information was sent, the main shocks should attack Kobe before the information reached there because the epicenter was very close to Kobe. If the information was sent a few seconds before, it should not be possible to save their lives because the most of people were sleeping.

Those tell us that while the information is not almighty, it can save human lives if the information is utilized cleverly. The efficiency of the information would depend on usual training or consciousness of disaster prevention.

3.3 Disaster Prevention in Private Enterprises and Realtime Information

In the national anti-disaster plan, the roles of private enterprises are:

- securing the employees and the customers,
- maintaining the business activity and the economic stabilization,
- making contribution to the disaster mitigation in the local community.

Figure 5 shows the relation in the disaster between the companies and the local community. It is difficult for the companies to rescue the community if they are suffered from the disaster. Maintaining the business activity leads to the disaster mitigation in the local community and securing the community leads to the stability of the business.

3.3.1 Practical Use of Realtime Information

Some Examples of the practical use of the realtime information in private enterprises are shown in this section.

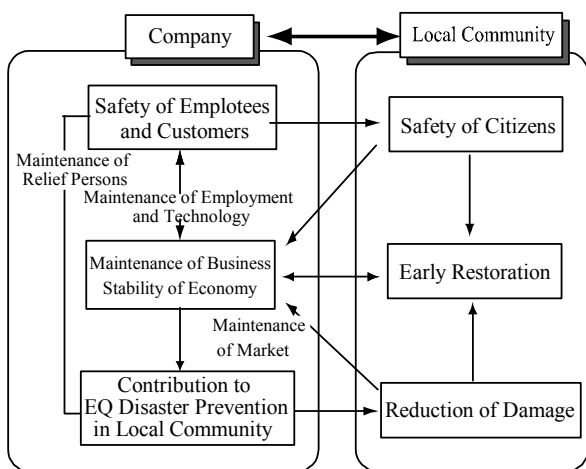


Figure 5 Relation between Private enterprise and Local Community in Disaster Mitigation

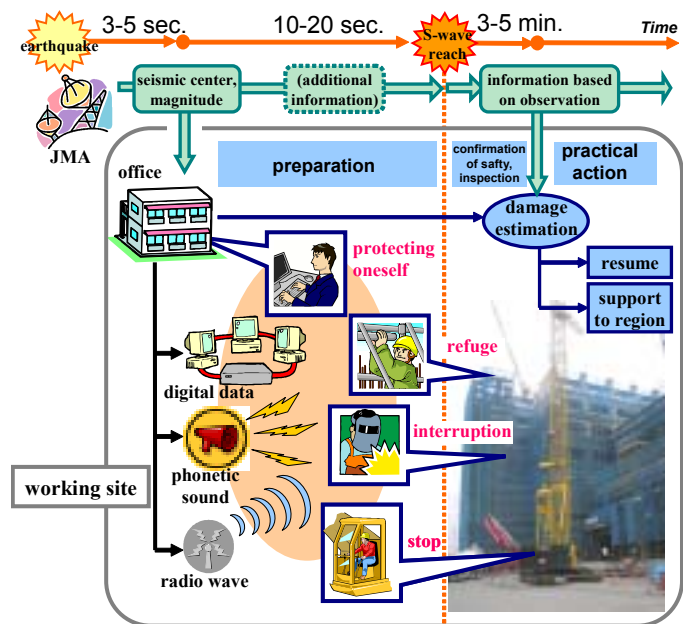


Figure 6 Example of Practical Use of Realtime Earthquake Information in Company

1) Securing Factories or Workplaces

Employees sometimes work at dangerous places or operate dangerous tools or machines in factories or workplaces. There may be toxic substances such as chemicals or combustible oil etc. It is necessary to secure the employees and the facilities by their escaping from heights, interrupting the dangerous works or stopping the dangerous operation of machines as shown in Figure 6. If the realtime information is sent to the employees before the arrival of the main shocks, preparing for the earthquakes is easy. It would be better to take action without being nervous of the scales of earthquakes if safety is prior to all, because there is little economic loss if the information is false. It is important to use the information considering the balance of safety and economic loss, the accuracy, or the contents if economic loss can be caused once a manufacturing process is stopped. In this case, employees may meet the emergency through the judgment according to the information.

2) Safety Confirmation of Employees

It is easy to confirm the safety of the employees within an office building, while it is difficult to confirm the safety of the employees in the disaster when they work here and there in factories or workplaces. If the disaster prevention center established in the company that can take the realtime earthquake information, and the employees have portable terminals such as cellular phones or PHS that can be used for both on business and in emergency, they can obtain the information from the center. When the center sends the earthquake information, it transmits the message at the same time instructing the employees to send the information about their safety after the earthquake. The employees can prepare for the earthquake by the information before it comes. It becomes easy for the center to grasp the safety of the employees in the sites after the earthquake. The point is the instruction of safety confirmation is included in the information and the escape from concentration and confusion of communication lines.

3.3.2 Test of Practical Use

The tests of control of machines and tools or confirmation of the employees' whereabouts using the realtime earthquake information are in progress in the Institute of Technology in Shimizu Corporation.

1) Record of Base Isolation Device Movement

The new office building of the institute has the base-isolation system that is supported by isolation devices on six columns at the first floor as shown in Picture 1. There is a video camera beside one of the devices for monitoring the movement when the earthquake occurs. Picture 2 is the image from the



Picture 1 Appearance of Office Building (Institute of Technology in Shimizu Cor.)



Picture 2 Image by Video Camera Beside Isolation Device



Figure 7 Result of Whereabouts Confirmation of Employees in Office Building

camera. Recording by the camera based on the realtime earthquake information is in the experimental stage. If the information is sent from JMA to the institute, the signal is made to start recording before the main shocks come. Originally the recording system is traceable by connection with the seismograph established in the institute. The control system by the realtime earthquake information works as a backup.

2) Confirmation of Employees' Whereabouts

All the employees have personal handyphones usable within the institute. There is a rule in the institute that they always take the handyphones with them during working, turns off when they go home. Those handyphones are used not only for communication on business but also for monitoring their whereabouts regularly for the purpose of effective air condition control etc. The plan will be considered on a trial basis that the realtime earthquake information is used for starting the monitoring system before the earthquakes come. It makes sure of the monitoring by avoidance of electrical or mechanical troubles. Figure 7 shows the employees' whereabouts on one occasion by the monitoring system. The monitoring system can be effective to the safety confirmation of the employees because there are a few buildings and a lot of facilities in the site.

3.3.3 Point of Practical Use

The points of the practical use of the information as it stands may be as shown bellow:

- 1) The measures based on the information of an earthquake occurrence or rough estimation of the epicenter are the first step of the practical use because the accuracy of the epicenter or the magnitude estimated varies according to the earthquakes.
- 2) It is difficult to apply the information if great economic loss is generated by the practical use, e.g. the control system of production processes by the information, when the estimated errors are included in it. The practical use that does not much depend on the accuracy of the information would be better.
- 3) When an epicenter is close to relevant cities, e.g. an epicentral earthquake, the preparedness by the information is limited because the time margin is small or none. On the other hand, the measures using the information for tall buildings or towers can be effective to the earthquakes which occur in the far, because the ground motion includes long periods components and they take long time to come in such cases.
- 4) After big earthquakes, the communication concentration or the network confusion is easy to generate as the Hyogo-Ken-Nambu Earthquake. The information is useful for the application with the aim of avoidance of such communication troubles because in many cases the information is sent before earthquakes come.
- 5) Preparing the application using the information leads to the multiplicity of the disaster prevention measures, as shown in the previous section, because the applications using the information sent before earthquakes come have not been existed up to now.

4. SUBJECTS FOR FUTURE STUDY

In order for the realtime earthquake information to be widespread and useful for disaster mitigation, the subjects as shown bellow should be investigated.

- 1) Finding Needs: Where or when the realtime earthquake information can be used has not been investigated enough. Finding needs in various scenes considering the characteristics of the information is one of the most important problems.
- 2) Ascertainment of Accuracy: Verification of the accuracy and improvement of the information are the problems of the sender. The users of the information should understand the system and ascertain the accuracy from the viewpoint of the practice.
- 3) Means of Communication: Economical, rapid and reliable communication is needed for popularization. Communication using private lines or satellites is not popular at present because of expensiveness.

- 4) Contents of Information: When the earthquake information is given directly to ordinal people such as employees or customers, the contents should be examined considering the states of human mind to avoid confusion or panic.
- 5) Usual Use and Training: It is easy for the users to receive the information by the experienced ways. The means of communication which can be used both in usual and in emergency is expected. The practical measures by the information should be incorporated into the disaster manuals and be used repeatedly in the disaster prevention training. The efforts of bringing emergency close to usual are needed.
- 6) Avoidance of Communication Concentration: Communication concentration is generated frequently just after earthquakes and it leads the situations to the worse. It is difficult to evaluate or simulate such situations. Various means of communication should be prepared for emergency to use the information certainly.

5. CONCLUSIONS

While the improvement of earthquake-resistance performance of buildings or house is one of the most important problems in regard to safety of human lives or minimization of economical loss, it is possible to save many human lives or prevent the damage to spread by using the real time earthquake information. Realization of the practical use of the information is expected before big earthquakes occur in near future.

Reference

- Nakamura, Y. (2000), "Status Quo and Future Prospects of the First Practical Alert System by P-wave (UrEDAS) in the World (in Japanese)," *Proceedings of the Second Symposium of Real Time Earthquake Disaster Prevention of Japan Society of Civil Engineering*.
- Shimizu, Y., Koganemaru, K., Nakayama, W., and Yamazaki, F. (2001), "Super-dens Realtime Monitoring of Earthquake (SUPREME) in City Gas Supply Facilities (in Japanese)," *Proceedings of the First Annual Meeting of Japan Association for Earthquake Engineering*, 255.
- Kamigaichi, O., Tsukada, S., Morimoto, M. and Hasebe, D. (2004), "Development of JMA's Nowcast Earthquake Information (in Japanese)," *Tsuchi-to-kiso (Journal of Japanese Geotechnical Society)*, 52(1), 19-21.
- Uhira, K. (2004), "On JMA's Nowcast Earthquake Information (in Japanese)," *Material of the Third Land Safety Net Symposium*, 1-3.
- Horiuchi, S., "For Advancement of Real Time Earthquake Information (in Japanese)," *Material of the Third Land Safety Net Symposium*, 15-20.
- Fujinawa, Y. (2004), "For Practical Use of Real Time Earthquake Information (in Japanese)," *Material of the Third Land Safety Net Symposium*, 21-25.
- Architectural Institute of Japan (1980), "Report on the Damage Investigation of the 1978 Miyagi-ken-oki Earthquake (in Japanese)."
- Architectural Institute of Japan (1995), "Report on the Damage Investigation of the 1994 Hokkaido-Toho-Oki Earthquake and the 1994 Sanriku-Haruka-Oki Earthquake (in Japanese)."
- Architectural Institute of Japan, Japan Society of Civil Engineering, Japanese Geotechnical Society, Seismological Society of Japan, The Japan Society of Mechanical Engineering (2000), "Report on the Hanshin-Awaji Earthquake Disaster General Issue Volume 1, Compendium of Earthquake Disaster including Stochastics Description (in Japanese)."

Near Field Effects of a Hidden Seismic Fault underlying Concrete Dam

T. Ohmachi¹⁾, N. Kojima²⁾, A. Murakami³⁾, and N. Komaba⁴⁾

1) Professor, Department of Built Environment, Tokyo Institute of Technology, Japan

2) Civil Engineer, Metropolitan Expressway Public Corporation, Japan (Formerly, Graduate Student, Ditto)

3) Engineer, Sumisho Electronics Co. Ltd, Japan (Formerly, Graduate Student, Ditto)

4) Graduate Student, Department of Environmental Science and Technology, Tokyo Institute of Technology, Japan
ohmachi@enveng.titech.ac.jp, kojima.n@mex.go.jp, murakamiatushi@kuramae.ne.jp, komaban@depe.titech.ac.jp

Abstract: The 2000 Western Tottori earthquake (M_J 7.3), Japan, was caused by a hidden seismic fault underlying Kasho Dam, a 46 m-high concrete gravity dam. Strong-motion accelerometers registered peak accelerations of 2051 and 531 gal at the top of the dam and in the lower inspection gallery, respectively. Integration of the acceleration records in the gallery gives a permanent displacement of 28 cm to the north, 7 cm to the west, and uplift of 5 cm. The dam survived the earthquake without serious damage, but the reservoir water level dropped suddenly by 6 cm, followed by damped free vibration that continued for several hours. Based on numerical simulation and field observation, the water level change is attributed to ground displacement in the near field followed by seiching of the reservoir. The vibration period in the upstream-downstream direction of the dam changed noticeably during the main shock, probably due to hydrodynamic pressure variations.

1. INTRODUCTION

The 2000 Western Tottori earthquake (M_J 7.3), Japan, occurred at 13:30 (local time) on October 6, 2000. Kasho Dam which lies in the near field of this earthquake, is a concrete gravity dam with height of 46.4 m and crest length of 174 m, constructed in 1989. The full water level of the reservoir is EL 118 m; at the time of the main shock the water level was EL 112 m.

Strong motion accelerometers at the dam registered peak accelerations of 2051 and 531 gal at the top of the dam and in the lower inspection gallery, respectively (Japan Commission on Large Dams, 2002). Despite such high acceleration, the dam body escaped serious damage. Although no increase in water leakage was observed, the reservoir water level of the dam recorded a sudden drop of 6 cm immediately after the main shock, followed by damped free vibration that continued for several hours. The drop in reservoir water level was not only a mystery but also raised concern among dam engineers.

The location of the dam is shown in Fig. 1, along with the locations of hypocenters of the main

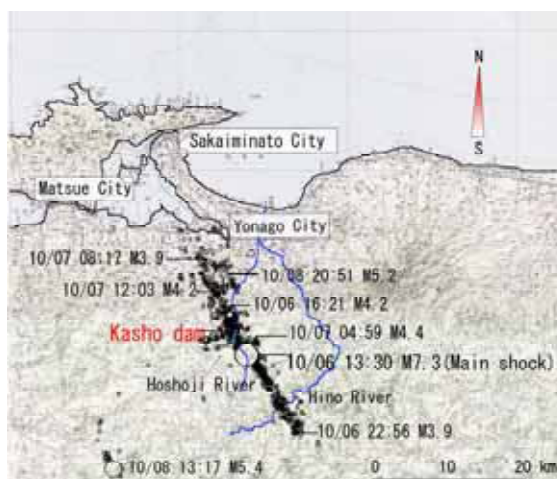


Fig. 1 Map showing locations of the main shock, aftershocks, and Kasho Dam

shock and aftershocks. The seismic fault appears to run through the Kasho Dam site. No clear trace of fault rupturing was observed on the ground surface in the epicentral area (Inoue et al., 2002). The earthquake therefore appears to have been caused by seismic rupturing of a hidden fault underlying the dam site. This paper is reproduction of the authors' publication (Ohmachi et. al., 2003).

2. NEAR-FIELD GROUND DISPLACEMENT

2.1 Ground displacement inferred from strong-motion records

Three-component strong-motion accelerometers (seismometers) are installed firmly with bolts on the concrete floor of the upper elevator room at EL 124.4 m, and on the concrete floor of the lower inspection gallery at EL 87.0 m, as shown in Fig. 2. The horizontal components of both accelerometers are set N-S and E-W (the dam axis is oriented N110°E). A floating reservoir water-level meter is also installed in a concrete well 0.8 m in diameter.

Acceleration records of the main shock captured at the two seismometer installations are shown in Fig. 3. The earthquake acceleration was sampled at 100 Hz with 24-bit resolution, with a reliable frequency range of DC to 41 Hz. Seismic ground displacement was estimated by integrating the acceleration histories at the lower inspection gallery twice with respect to time.

The result in Fig. 4 shows that the dam underwent different modes of displacement in the three directions. In the N-S direction, the dam displaced linearly to the north with a final permanent displacement of 27.6 cm. In the E-W direction, the displacement varied sinusoidally, with a final permanent displacement of 6.5 cm to the west. In the vertical direction, the displacement exhibited a sharp upward peak, with a final permanent uplift of 4.7 cm.

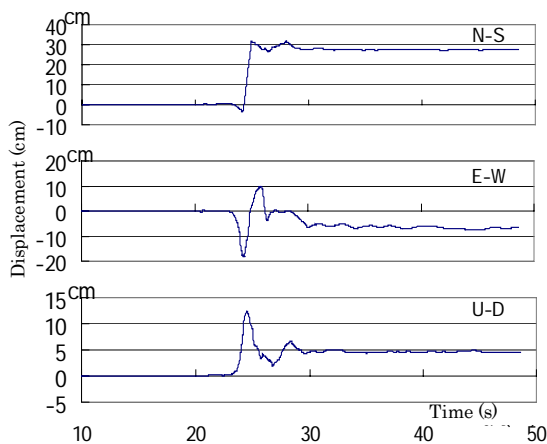


Fig. 4 Displacement histories obtained by integration of acceleration records

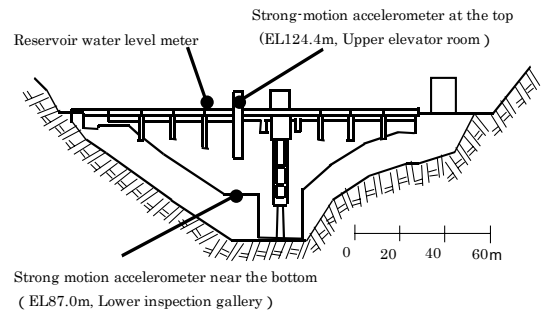


Fig. 2 Locations of strong-motion accelerometers and water level meter at Kasho Dam

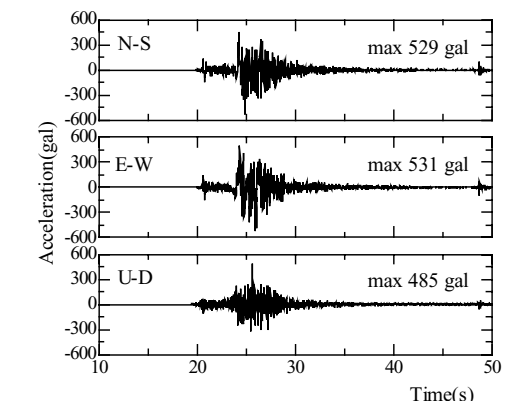
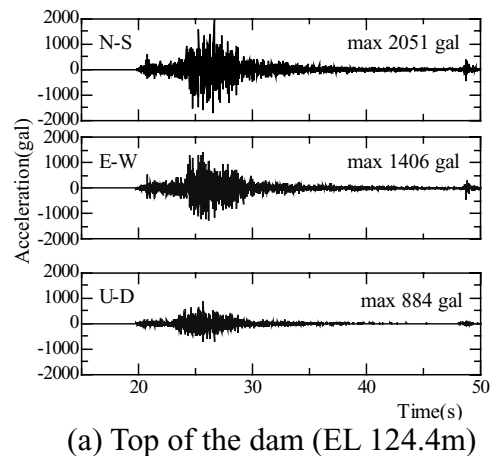


Fig. 3 Strong-motion acceleration of the main shock recorded at Kasho Dam

2.2 Ground displacement from numerical simulation

Using the fault parameters shown in Table 1 (Geographical Survey Institute, 2000), the ground displacement associated with the seismic faulting event was simulated using the 3D boundary element method (BEM). The seismic fault of the main shock was a left lateral strike slip fault with strike of N152°E.

The simulation was conducted for a rectangular area of 23 km long (N-S) by 17 km wide (E-W), encompassing Kasho Dam and its reservoir. The ground was simplified as a half-space of homogenous elasticity with shear wave velocity of 4 km/s. In the first step of the simulation, seismic ground displacement was calculated at every node of a 500 m × 500 m mesh. The result is shown in Fig. 5, where thick broken lines indicate the projection of the fault plane, thick solid lines denote the reservoir, and thin solid lines are the lines of equal displacement. The iso-displacement lines are almost parallel to the fault projection in the vicinity of the reservoir, indicating uplift to the northeast of the reservoir and settlement to the southwest.

The displacement in the area indicated by the solid lines in Fig. 5(a) was interpolated, with the result as shown in Fig. 5(b). The profile of the reservoir is drawn along the altitude of the design flood water level (EL123.2 m). Kasho Dam is located at the north end of the reservoir.

The histories of ground displacement around the dam obtained from the interpolation of the simulated displacement are plotted in Fig. 6. The histories appear very similar to the recorded displacement histories in Fig. 4, although the amplitudes are slightly smaller. The simulated permanent ground displacement at the dam is 10.9 cm to the north and 0.1 cm to the west, with uplift of 2.5 cm. The horizontal displacements shown in Figs. 4 and 6 are plotted in Fig. 7 in terms of motion trajectories. It is interesting to note that both trajectories in Fig. 7 have common features, such as the direction of initial motion, elliptic motion in the final stage, and a large transient shift to the NE or NNE.

Table 1 Fault parameters used for simulation

Strike (deg.)	152
Dip (deg.)	86
Rake (deg.)	-7
Dislocation (m)	1.4
Depth of fault (m)	1
Fault length (km)	20
Fault width (km)	10

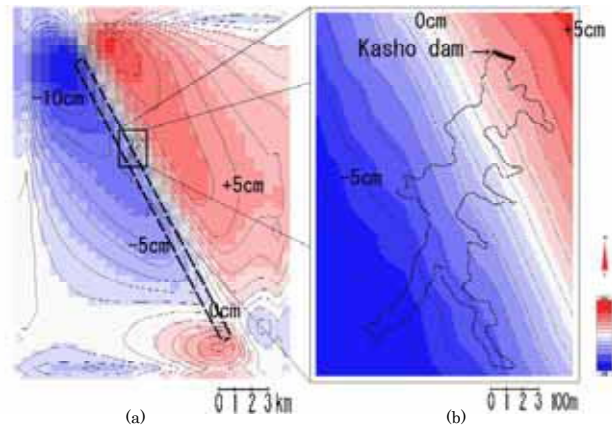


Fig. 5 Vertical ground displacement evaluated from simulation by (a) BEM and (b) its interpolation

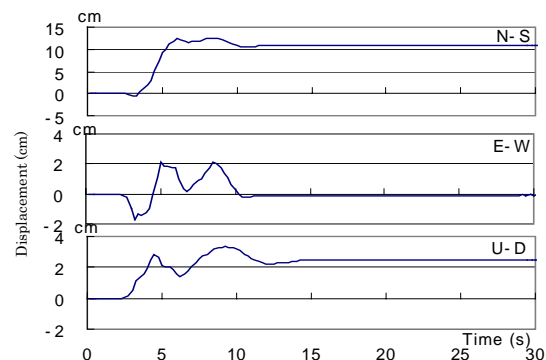


Fig.6 Ground displacement at Kasho Dam simulated by BEM

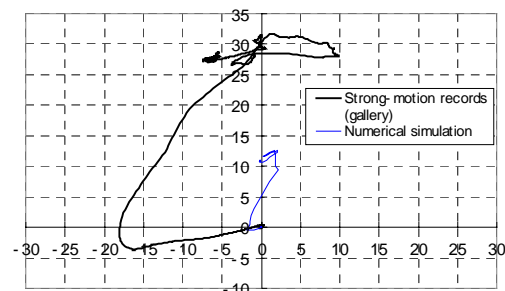


Fig. 7 Horizontal displacement motion trajectories estimated from strong-motion records and the simulation

2.3 Comparison of vertical displacements from simulation and ground survey

Following the main shock, a ground survey was conducted at 65 points along the reservoir as shown in Fig. 8, in which straight lines A to D are parallel to the fault projection shown in Fig. 5. Taking the distance from line A as a reference, the vertical displacements from the simulation and the survey are shown in Fig. 9. The displacements from the survey are almost three times that indicated by the simulation, and larger particularly between lines B and C. The differences could be attributed to several factors such as inaccurate parameters used in the simulation and the effects of local site conditions, as well as the effect of the many aftershocks, which were not considered in the simulation.



Fig. 8 Observation points along the reservoir for the ground survey

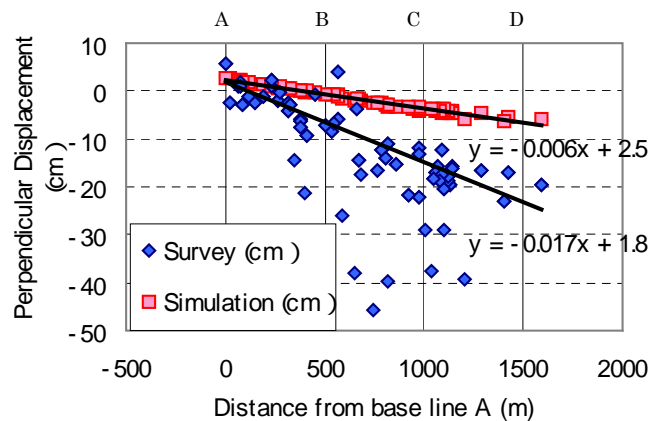


Fig. 9 Comparison of vertical displacements evaluated from the simulation and survey

2.4 Comparison with readings of a plumb line

To detect relative displacement between the top and bottom of the dam, a plumb line is installed in a vertical shaft 30 cm in diameter. The upper end of the steel plumb line is fixed to the floor of the upper elevator room, next to the strong motion accelerometer, and the weight on the lower end is housed in a measurement device located at EL 89.5 m in the lower inspection gallery. Automatic measurement is usually conducted only a few times a day. Readings from the measurement during October 3 and October 13 are plotted in Fig. 10. The main shock induced a relative displacement of -2.8 mm in the x (right-bank) direction, and 0.7 mm in the y (upstream) direction, with a resultant displacement of 2.9 mm.

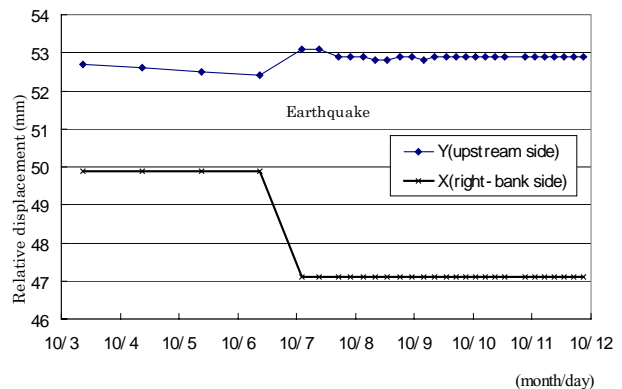


Fig. 10 Relative displacement evaluated from plumb line readings

If the relative displacement indicated by the plumb line readings is attributed to an inclination of the dam body caused by earthquake-induced ground displacement of the dam foundation, the inclination will be quantitatively given by the resultant displacement divided by the length of the plumb line; $2.9/34900 = 8.3 \times 10^{-5}$. In the vicinity of the dam, the inclination of the earthquake-induced ground displacement estimated from the simulation is 6×10^{-5} , as shown in Fig. 9. Although this differs slightly from the inclination determined from readings of the plumb line in terms of magnitude and direction of inclination, it is reasonable to surmise that the dam site was

displaced by the seismic faulting of the main shock, as inferred from integration of the strong-motion acceleration.

3. CHANGE IN RESERVOIR WATER LEVEL

3.1 Records of reservoir water level

The reservoir water level is continuously recorded, and the history around the time of the earthquake is shown in Fig. 11. The upper and lower histories in Fig. 11 are the records with low and high resolutions, respectively. The records indicate that the water level dropped suddenly by about 6 cm at the time of the main shock, followed by damped free vibration that continued for several hours.

The water level record was roughly reproduced from the readings of successive peaks and troughs of the original record. The Fourier spectrum of the reproduced history is shown in Fig. 12, which shows the free-vibration period of 6.5 min and a damping ratio of 2%.

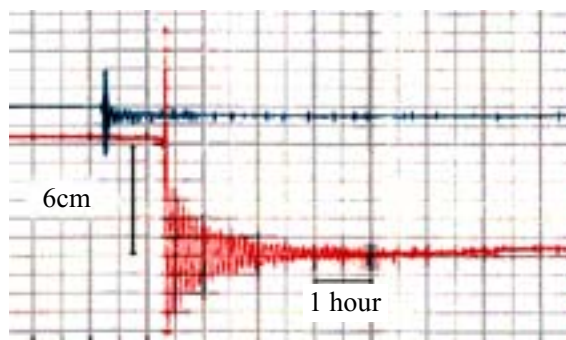


Fig. 11 Records of reservoir water level at Kasho Dam

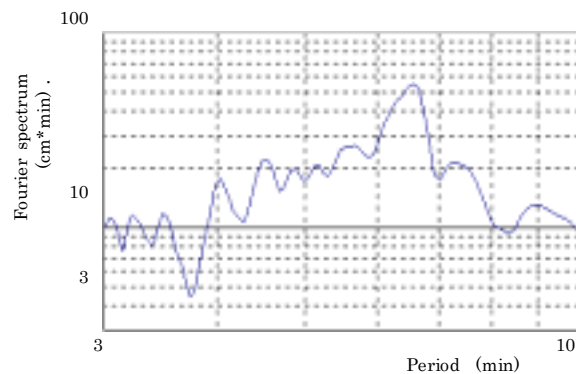


Fig. 12 Reproduced free-vibration history of the corresponding spectrum

3.2 Cause of the sudden drop in reservoir water level

The seismic faulting gave rise to uplift of the dam body and a change in the ground slope of the base of the reservoir as a result of near-field ground displacement. These factors are regarded to be the main cause of the sudden drop in reservoir water level. A schematic explanation is shown in Fig. 13, where the dam and ground slope before and after the main shock are indicated by thin and thick lines, respectively. In the figure, ΔH_1 is the water level change due to the increased reservoir capacity estimated from the average settlement of the reservoir area, and ΔH_2 is the water level change due to uplift of the dam. Using the simulated displacement shown in Fig. 5, ΔH_1 and ΔH_2 are -1.5 and 2.5 cm, respectively, with a corresponding water level change of -4.0 cm ($\Delta H = \Delta H_1 + \Delta H_2$), in reasonable agreement with the observation of -6.0 cm.

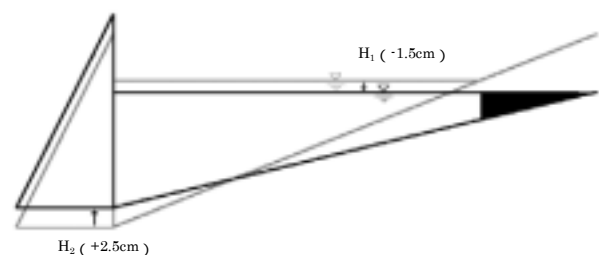


Fig. 13 Schematic explanation of water level change caused by ground displacement

3.3 Seiching of the reservoir

Free vibration of a water body such as a reservoir is referred to as seiching (Lamb, 1932). The fundamental period T for a rectangular reservoir is approximated by

$$T = \frac{2a}{\sqrt{gh}} \quad (1)$$

where a and h are the length and depth of the reservoir, and g is acceleration due to gravity. Introducing $a = 2$ km and $h = 10$ m into Eq. (1) for Kasho Dam gives a period of $T = 7.0$ min, which is fairly close to the observed period of free vibration (6.5 min). Accordingly, the free vibration is thought to be mainly due to the fundamental mode of the seiche. Based on this result, the seiching was simulated using a numerical technique recently developed for tsunami simulation (Ohmachi et al., 2001). The technique basically involves solving the Navier-Stokes equation for the system using a 3D finite difference method (FDM).

In the present simulation, for the sake of simplicity, the dam and ground were assumed to be rigid. The initial water surface was supposed to have the same slope as that given from the simulated ground displacement, and then it was released under the force of gravity to induce free vibration of the reservoir. The water level history at the dam is shown in Fig. 14, from which the period of the simulated seiche is found to be 7.5 min (450 s).

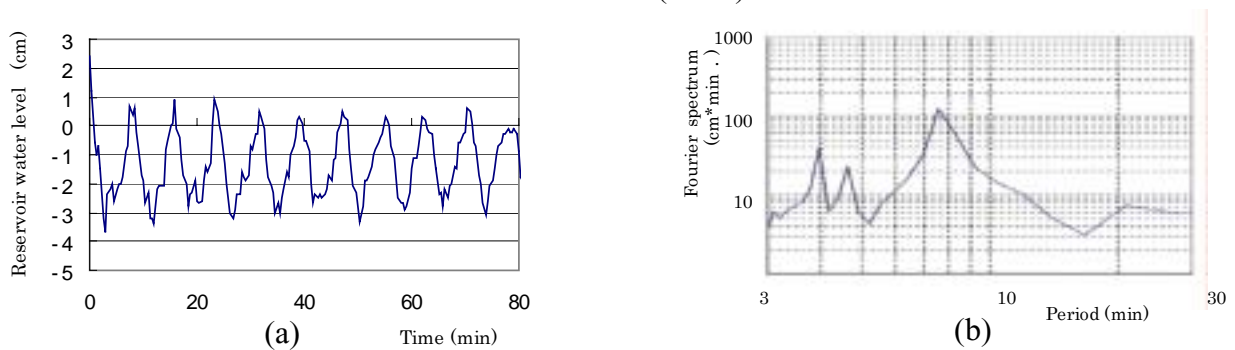


Fig. 14 History of simulated seiche at Kasho Dam

4. CHANGE IN VIBRATION PERIOD OF THE DAM

The response characteristics of the dam were analyzed by transforming the two horizontal components of the strong-motion records in the N-S and E-W directions shown in Fig. 3 into the upstream-downstream and dam-axis directions. The transformed acceleration histories are shown in Fig. 15. After transformation, the peak accelerations at the top of the dam were 2100 and 1684 gal in the upstream-downstream and dam-axis directions, respectively, and the peak accelerations in the lower inspection gallery were 503 and 570 gal.

The acceleration histories were divided into four 5.12-s samples as indicated in Fig. 15. At the top of the dam, peak accelerations in the upstream-downstream direction in these time segments were 491, 2100, 531 and 227 gal. The amplification factors between the top and the lower gallery, calculated by taking the Fourier spectral ratios between pairs of segments, are

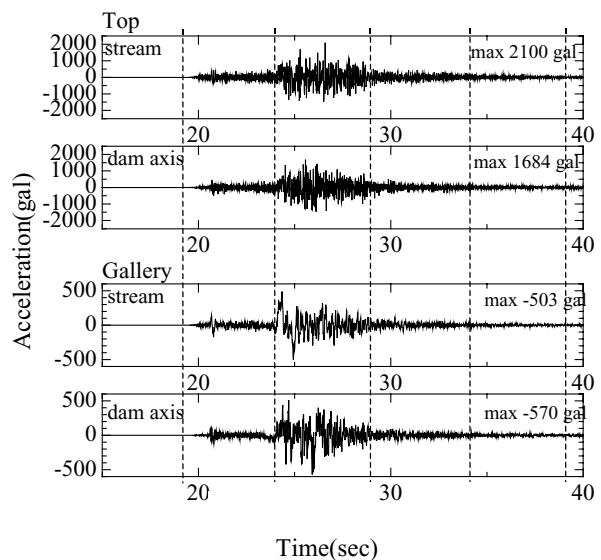


Fig. 15 Horizontal strong-motion records rotated with the azimuth of Kasho Dam

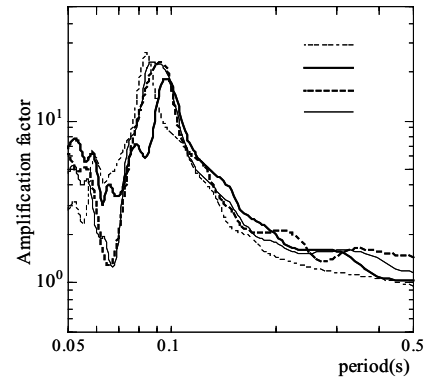
shown in Fig. 16. In the upstream-downstream direction shown, the main peak is at around 0.1 s, which appears to be associated with the fundamental mode of dam vibration. The peak periods of these amplification factors are 0.84, 0.96, 0.92 and 0.87 s for segments 1 through 4. Thus, during the main shock, the peak period was initially lengthened and then shortened, with a change exceeding 10%.

Lengthening of the vibration period during strong earthquake shaking is often caused by non-linearity of material properties. In the present case, however, because the lengthening is seen in the upstream-downstream direction only, and the period shortened shortly after, factors other than the non-linear properties seem to be responsible for the change in the period. One of the probable factors is hydrodynamic pressure acting on the upstream face of the dam, which would change in proportion to the intensity of earthquake acceleration (Westergaard, 1933).

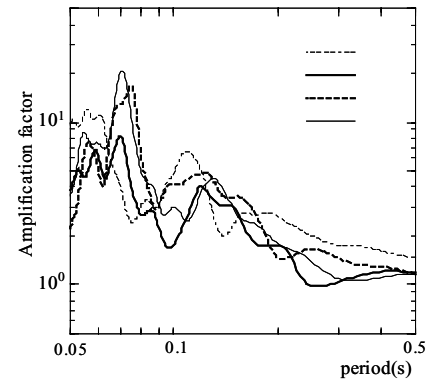
At Kasho Dam, strong-motion acceleration was well recorded during not only the main shock but also aftershocks as listed in Table 2 (Japan Commission on Large Dams, 2002), which shows peak accelerations for the upstream-downstream direction. It should be noted in Table 2 that the reservoir water level at the time of the earthquakes was almost at the same, between EL 112.20 m and EL 110.93 m. From the acceleration records of the aftershocks, the peak periods in the upstream-downstream direction were similarly obtained and plotted against peak accelerations at the top of the dam, with the result as shown in Fig. 17. The peak period tends to increase with peak acceleration, as indicated by a broken line in the figure, although the plotted periods are somewhat scattered. Further study is therefore necessary in order to identify with certainty the factors responsible for the period change.

Table 2 Main shock and aftershocks recorded at Kasho Dam in the 2000 Western Tottori earthquake

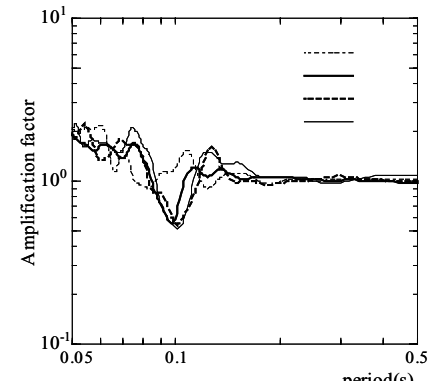
Date and time (M/Day)	M _J	Peak Acceleration (gal)		Water Depth (m)
		Top	Gallery	
10.06 13:30:00	7.3	2100	503	34.20
10.07 12:14:10	3.5	332	48	34.18
10.07 18:32:00	3.9	410	73	34.18
10.08 20:51:00	5.3	142	27	34.13
10.09 19:49:40	3.5	212	33	33.95
10.10 02:26:00	3.4	247	36	33.92
10.10 21:57:50	4.4	247	57	33.73
10.12 03:53:20	3.6	52	7	33.33
10.12 08:41:40	3.6	45	6	33.28
10.12 17:07:20	3.5	126	14	33.16
10.13 10:44:10	3.6	91	16	32.93



(a) Upstream-downstream direction



(b) Dam-axis direction



(c) Vertical direction

Fig. 16 Amplification factors between the dam top and the lower inspection gallery

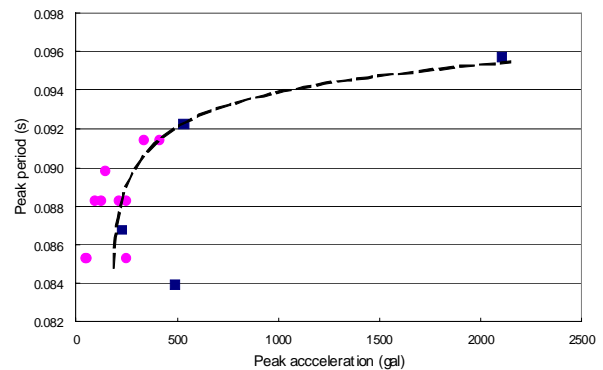


Fig. 17 Peak periods of the dam in the upstream-downstream direction

5. CONCLUSIONS

Kasho Dam, a concrete gravity dam, was located in the near field of the 2000 Western Tottori earthquake (M_J 7.3), which was caused by a hidden seismic fault. The strong-motion acceleration at the dam exceeded 2000 gal at the top of the dam and 500 gal in the lower inspection gallery during the main shock. Despite such large acceleration, the dam survived the earthquake without serious damage. However, the reservoir water level dropped considerably immediately after the main shock, and the vibration period of the dam varied by more than 10% during the main shock. The causes and effects of these observations were investigated in the present study, with the following conclusions.

The seismic rupturing of the hidden fault gave rise to not only dynamic but also permanent displacements at the dam site. Integration of the strong-motion acceleration observed in the lower inspection gallery gave a permanent displacement of 28 cm to the north, 7 cm to the west, and uplift of about 5 cm.

The sudden 6-cm drop in reservoir water level observed immediately after the main shock has been attributable to the permanent displacement of the ground in the near field of the earthquake. The free vibration of the reservoir water level following the sudden drop is interpreted as seiche of the reservoir water, characterized by a period of 6.5 min with a damping ratio of 2%.

The plumb line installed at the dam indicated a relative displacement of 2.9 mm between the top of the dam and the lower inspection gallery. This relative displacement is attributable to the incremental inclination of the dam foundation induced by the near-field ground displacement.

During the strong shaking of the main shock, the vibration period of the dam body exhibited a noticeable transient increase in the upstream-downstream direction. It is probable that the change in the period resulted from changes in the hydrodynamic pressure acting on the upstream face of the dam. Further study will be required in order to examine this effect in more detail.

Acknowledgements:

The authors would like to express their thanks to the Department of Civil Engineering, Tottori Prefecture for providing valuable information regarding the effects of the 2000 earthquake on Kasho Dam. This study was partly supported by the Ministry of Education, Science, Sport and Culture of Japan through Grants-in-Aid for Scientific Research Nos. 13480119 (T. Ohmachi) and 12555134 (K. Kawashima).

References:

- Geographical Survey Institute, <http://www.gsi.go.jp/wnew/press-release/2000/1007-2.htm>.
- Inoue, D., Miyakoshi, K., Ueta, K., Miyawaki, A., and Matsuura, K. (2002), "Active fault study in the 2000 Tottori-ken seibu earthquake area, Zisin," *Journal of the Seismological Society of Japan*, **5**(4), 557-573 (in Japanese).
- Japan Commission on Large Dams, (2002) Acceleration records on dams and foundations No. 2 (CD-ROM version).
- Lamb, H. (1932), "Hydrodynamics", *Cambridge Univ. Press*, 190-191.
- Ohmachi, T., Kojima, N., and Murakami, A. Komaba, N. (2003), "Near-Field Effects of Hidden Seismic Faulting on a Concrete Dam," *Jour. of Natural Disaster Science*, **25**(1), 7-15.
- Ohmachi, T., Tsukiyama, H., and Matsumoto, H. (2001), "Simulation of tsunami induced by dynamic displacement of seabed due to seismic faulting," *Bull. Seism. Soc. Am.*, **91**(6), 1898-1909.
- Westergaard, H. M., (1933) "Water pressure on dams during earthquakes," *Trans. ASCE* **95**, 418-433.

Urban Earthquake Engineering: Foundation Characterization for Performance Based Design

W. D. Liam Finn, Anabuki Professor,
Kagawa University, Takamatsu, Japan

ABSTRACT: The major development in urban earthquake engineering in the last 10 years is the concept of performance based design. A crucial feature of this new design approach is recognition of the impact of flexibility of foundations on the seismic demand and seismic response of structures. The challenge for geotechnical engineers is to characterize the actions of the foundation-soil system effectively in a manner compatible with commercial software used in design practice. The state of practice for characterization of the actions of the foundations on structural response is reviewed and the effectiveness of various approximate approaches are evaluated.

1.0 INTRODUCTION

Traditionally the objectives of seismic design codes for structures were to protect life safety under the extreme events envisioned by the codes and to maintain serviceability under the smaller events with a greater probability of occurring during the life of the structure. During the 1985 Loma Prieta earthquake in California the life protection objective was met but the level of damage was considered high for such a short duration, moderate earthquake. The direct costs of repair or replacement of buildings and in many cases huge indirect losses due to business interruption motivated the progressive structural engineers of California to critically review the design concepts and propose the idea of performance based design.

The concept underlying performance based design is to design for an acceptable damage level specified by the owner. The range of performance options is illustrated in Fig.1. Note that along the capacity curve for the structure, potential performance options are defined in terms of global displacement. The effectiveness of a performance based design is assessed by an appropriate nonlinear analysis that establishes the demand on capacity in terms of global displacement. The location of the calculated performance point on the capacity curve relative to the desired performance point is a measure of how design meets the design criteria.

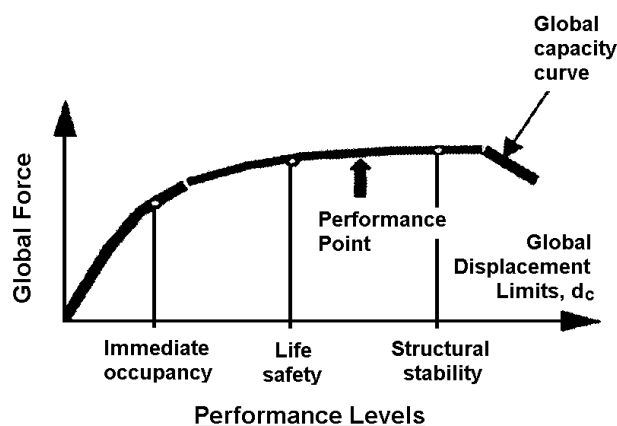


Fig. 1. Performance levels for seismic design (modified from (1))

A nonlinear pushover analysis is commonly advocated but it is recognized that in some cases a nonlinear dynamic analysis may be required. For an evaluation analysis to be valid, the structural model must include all elements of the building-foundation-soil system that significantly affect the seismic demand and response of the structure. Hitherto the seismic demand for code designed buildings was determined assuming that the structure rested on a rigid base. The actions of the foundations were completely ignored. The demands of performance based design make it imperative to include the effects of soils and foundations on seismic demand and structural response.

The first detailed examination of how to include the actions of the soils-foundation system in code design provisions was presented in a report by the Applied Technology Council (2) in which tentative provisions for seismic regulations were advanced. This procedure was based on the work of Veletsos and Wei (3). Veletsos et al (4) presented an updated review of these issues in a state of the art paper to the 9th World Conference on Earthquake Engineering in Tokyo. They noted that a proper analysis of the physical system of structure, foundation and foundation soils was necessary to get reliable estimates of structural demand and seismic response. They evaluated the relative contributions of kinematic and inertial interactions and concluded that inertial interaction had the greatest influence. These studies were based on analyses of a simple elastic structure on a rigid mat foundation welded to a homogeneous, elastic half space. Today the technology is available to consider flexible foundation elements and nonlinear soil response.

Investigations of structural performance during earthquake loading have confirmed the importance of treating the structure, foundation and foundation soils as a complete system. Wallace et al. (5) analyzed the seismic response of two 10-storey buildings designed and built in the 1970's. The buildings were instrumented to record strong motions. One building, in Northern California, was analyzed for the motions recorded during the 1984 Morgan Hill earthquake ($M_s=6.2$). The second building, in Southern California, was analyzed for the motions recorded during the Whittier earthquake ($M_s=5.9$). Good correlation was achieved between computed and recorded motions, when the flexibility of the foundation-soil system and cracked section properties were taken into account. Otherwise the correlation was poor.

The authors also evaluated the response of shear wall buildings in Chile that performed unexpectedly well during the 1985 Chilean earthquake. On the basis of conventional rigid base analysis these buildings had a ductility demand of 3 and should have suffered appreciable damage. However, when the effects of foundation flexibility were taken into account, the ductility demand dropped to 2. The beneficial effects of foundation flexibility were an important factor leading to the good performance.

Foundation flexibilities in the cases discussed above were all based on treating the soil response as elastic. More recent developments consider the nonlinear response of the soil to strong shaking. Furthermore allowing uplift during rocking and permitting yielding of the foundation soils is being advocated to reduce seismic demand on structures. These new advances are important developments for performance based design of new buildings but are even more important for developing cost effective retrofit strategies. Retrofitting to meet current code demand levels can be prohibitively expensive. The inclusion of foundation flexibility gives a more realistic picture of where retrofits are critical and can lead to lower seismic demand. These benefits result in more cost effective retrofits.

Clearly to evaluate a performance based design or the capacity of retrofitted building requires a realistic computational model of the structural system. This, in turn, requires a way of characterizing the actions of foundations and supporting soils on structural response that is compatible with available commercial computational software for structural analysis.

In this paper methods of characterizing both shallow and pile foundation will be presented.

2.0 CHARACTERIZATION OF SHALLOW FOUNDATIONS FOR STRUCTURAL MODELS

2.1 Spring models

The simplest way of modeling the force–displacement behavior of a shallow foundation to the seismic actions imposed on it by the structure is by means of discrete uncoupled elastic springs as shown in Fig. 2 (7). The footing is assumed to be a rigid plate, welded to a semi-infinite, homogeneous, elastic half-space. The stiffnesses of the translational and rotational springs are determined from published solutions. Surface stiffnesses for a rigid, circular plate on a semi-infinite homogeneous half space, published by Gazetas (6), are frequently used. Charts of shape and embedment factors to modify the surface stiffnesses of the circular plate for the effects of noncircular shape and depth of embedment are given in NEHRP (8).

It is more common to use Winkler springs, shown also in Fig. 2. These eliminate the rotational spring and facilitate the study of foundation uplift. The vertical springs in the Winkler model must be selected to represent both the vertical and rotational stiffnesses, if both stiffnesses are to be included in the analysis at the same time. One method for doing this

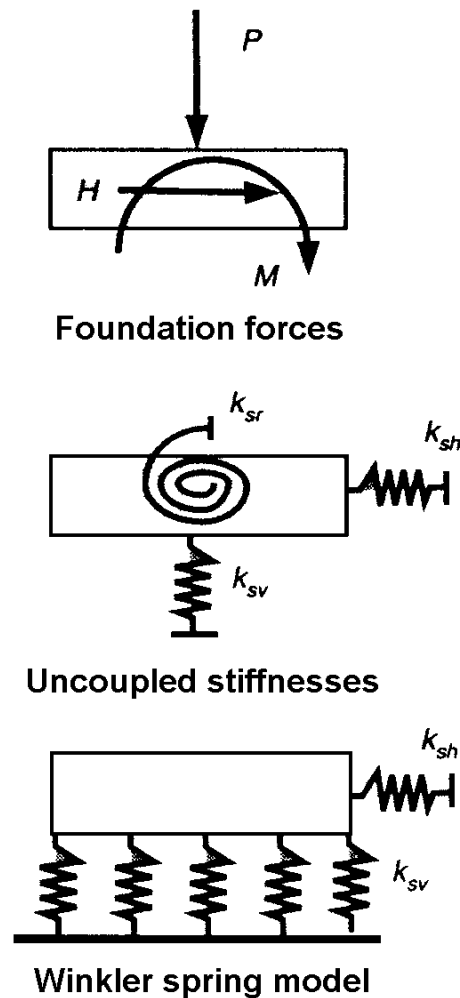


Fig. 2. Spring models for a spread footing (after (7))

is shown in Fig. 3 (8). The exterior stiffnesses in the $B/6$ wide end zones of the footing are assigned a stiffness of

$$k_{end} = 6.83G / (1 - \mu)B \quad (1)$$

and, in the mid-section, of

$$k_{mid} = 0.73G / (1 - \mu)B \quad (2)$$

Here k represents the stiffness/unit area, G is the shear modulus, μ is the Poisson ratio and B is the width of the footing. The distributed unit stiffnesses may be converted to individual spring stiffnesses, K_i , as shown in Fig.3, where K_i is given by

$$K_i = L_i k B \quad (3)$$

Here L_i is the length contributing to the stiffness of spring K_i .

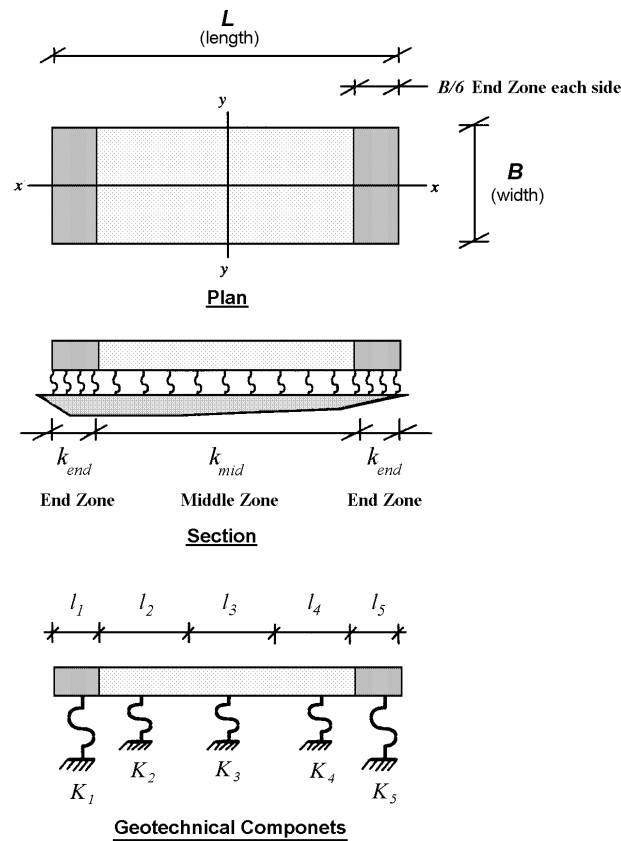


Fig. 3. Combined translation and rocking model for a footing (modified from (8))

In practice the modulus G is not constant with depth. Selection of a single representative value requires experience and a good knowledge of the dynamic response of surface footings. Little direct guidance is provided in the literature.

The response of soils to strong shaking is nonlinear, therefore the modulus used in the formulae to compute the translational and rotational stiffnesses should reflect the average effective moduli in the ground during shaking. An approximate way of modifying the effective, small strain elastic modulus, G_o , to the effective modulus, G , during to account for nonlinearity is to estimate the ratio, G/ G_o , from Table 1 (adapted from (8)).

Table 1 Effective shear moduli G as a function of shaking intensity (8)

Modulus Ratio	Effective Peak Acceleration	
	0.10	0.70
G/ G _o	0.50	0.20 *

- * 1. Site specific values from a geotechnical site investigation may be used
- 2. Use linear interpolation for intermediate values

2.2 Rocking with Uplift and Yielding

The effect of incorporating rocking, without uplift, into the computational model of a structure is to increase the fundamental period of vibration. This leads to a reduction in seismic base shear for taller buildings in designs based on code response spectra because the fixed based periods of these structures are associated with the longer period region of the code spectrum where spectral amplitudes decay with increasing period.

It is very expensive to prevent uplift in taller building on fully occupied city lots. Typically it involves massive foundation slabs and/or soil anchors. Structural engineers consider that uplift can be allowed. Housner (9) was one of the first to study in detail the behavior of rocking structures with uplift. One important conclusion of his work was that the evaluation of the stability of rocking structures could not be based on the static application of the dynamic forces causing rocking.

Rocking can be evaluated using the Winkler model by allowing separation to occur between structure and the spring with the onset of tension. The analysis may be conducted keeping the springs elastic. Uplift response is highly geometrically nonlinear. It results in an increase of period and damping. Uplift may result in a reduction in demand but it does so at the expense of increased global displacements.

Idealized stress distributions that may occur under a rocking foundation are shown in Fig.4 The stress at the compressive edge is limited by the yield pressure q_u of the soil. Rocking with uplift and yield was investigated in detail by Bartlett (10).for a clay foundation. He developed the theory for the relationships between overturning moment and foundation rotation. A very detailed and lucid description of uplift with soil yielding and how it affects seismic demand and response is given by Martin and Lam (11). They discuss at length how to incorporate uplift with soil yield into seismic design procedures.

From Fig. 4 it may be seen that, when the ratio of applied pressure, q , from a concentric load, P , to the yield pressure, q_u , is $q/q_u < 0.5$, uplift occurs before yielding takes place. Otherwise soil yielding occurs first. The moment capacity of the footing, M_c , when full yielding occurs is given by

$$M_c = PL (1-q/q_u)/2 \tag{4}$$

Martin and Lam studied the impact of uplift with soil yielding on the seismic demand and retrofit strategy for a 8-storey building. They found that rocking and compressional yielding occurred early in the response and over two thirds of the deformation demand was absorbed by the foundation soils. This reduced the demand on the capacity of a shear wall so that the structure met life safety requirements. One surprising and significant finding from their study was that variations in stiffness and strength between 67% and 150% did not lead to a significant change in behavior. They concluded from this that the response was much more

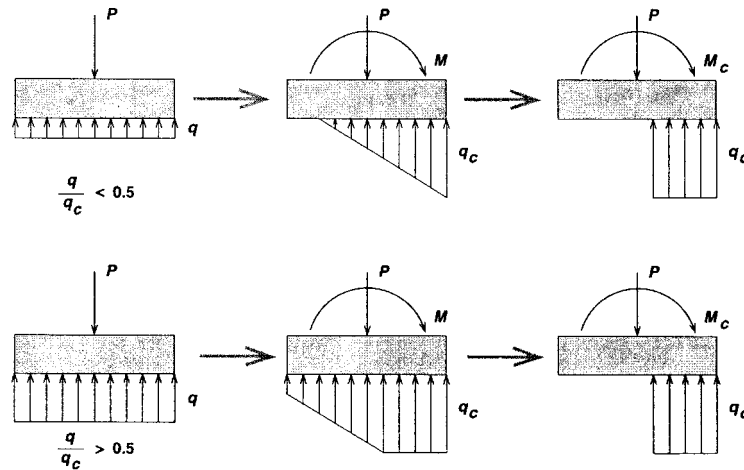


Fig. 4. Idealized stress distributions for rigid footings subjected to overturning moment (after (8))

sensitive to nonlinear rocking than to exact soil properties.

The benefits of rocking and uplift come at the price of increased displacement. Most of the analyses of the effects of rocking have been conducted on structures with one dominant structural system. For structures with combined systems such as shear walls and moment resisting frames, the reduction in demand in one system may transfer demand to the other system.

3.0 CHARACTERIZATION OF PILE FOUNDATIONS

. A major weakness in some models is the inadequate representation of the effects of the foundations on the structure, especially of pile foundations. The actions of pile foundations are represented by discrete, single valued springs to model rotational and translational stiffnesses and any coupling between these springs is usually ignored. The spring stiffnesses are frequently estimated using approximate, simplified methods of unknown reliability. This is a natural consequence of the complexity of a full 3-D nonlinear dynamic analysis of pile foundations. Even for the elastic case, only a limited number of 3-D parametric studies have been published. These have focused mainly on providing dynamic interaction factors between piles in small groups or frequency dependent stiffnesses and damping for single piles.

A complete picture of the effects of the foundation on the structure during strong earthquake shaking requires taking simultaneously into account many factors such as soil non-linearity, seismically induced pore water pressures, kinematic interaction between piles and soil, inertial interaction of the superstructure with soil and piles and dynamic interaction between the piles themselves. All of these factors can be taken into account by a non-linear, effective stress, dynamic, continuum analysis. Such an analysis provides time histories of direct and coupled foundation stiffnesses and demonstrates the effects of kinematic and inertial interactions, the effects of pore water pressures and soil nonlinearity. One prime benefit of such analyses, in addition to their use in the context of a specific design, is that results of parametric studies provide the data base for evaluating the effectiveness of the various approximate methods in use.

A comprehensive overview of the behavior of pile foundations during earthquakes using non-linear dynamic effective stress continuum analysis is presented here. The presentation is

limited to nonliquefiable soils. It is hoped that the overview will be useful in providing a framework for exercising judgment and an understanding of the limitations of approximate methods that facilitates the selection of an appropriate method for a particular application.

4.0 METHODS OF ANALYSIS

The pile foundation-structure system vibrates during earthquake shaking as a coupled system. Logically it should be analyzed as a coupled system. However this type of analysis is generally not feasible in engineering practice. Many of the popular structural analysis programs do not include the pile foundation directly into a computational model. Therefore the pile head stiffnesses are typically calculated by analyzing the pile foundation without any mass contribution from the superstructure. The analysis is done usually for a single pile and the group stiffnesses are evaluated using pile interaction factors, often static factors, or a group reduction factor.

Seismic analysis of a pile foundation for design purposes is often conducted by applying the base shears and moments from a fixed base analysis of the structure to the pile head and using a static analysis to estimate moments, shears and displacements in the piles. The most common approach to such an analysis is to use a Winkler spring computational model. A general Winkler model is shown in Fig. 5 which can be used for static or dynamic analysis. For static analysis, only the pile and the near field springs are used.

The springs may be elastic or nonlinear. Some organizations, such as the American Petroleum Institute [12], gives specific guidance for the development of nonlinear load-deflection (p - y) curves as a function of soil properties to represent nonlinear springs. The API (p - y) curves, which are widely used in engineering practice, are based on data from static and slow cyclic loading tests in the field. Murchison and O'Neill [13] suggest that the reliability of the Winkler (p - y) model may not be high.

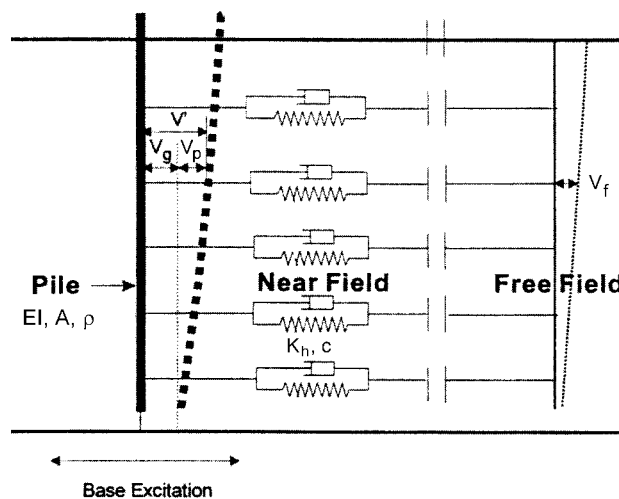


Fig. 5: Dynamic Winkler computational model for pile analysis.

The simple static analysis neglects many important factors that affect the seismic response of the structure-soil-foundation pile system. Inertial interaction between structure and foundation is neglected. This interaction increases the nonlinear behavior of the soil and reduces pile head stiffnesses. These effects increase the period of the system and change the spectral response and hence the base shears and moments. The kinematic moments are also neglected. These moments arise from the pressures generated against the pile to ensure that the seismic displacements of soil and pile are compatible at points of contact along the pile. These moments, which can be captured by a full dynamic analysis, can be significant in layered soils

with soft or liquefiable layers, especially for large diameter piles. Finally the effects of high pore water pressures and liquefaction on the base moments and shears are treated very approximately. The effects of the neglected factors on pile design vary with the intensity of shaking, site conditions and the details of the pile foundation. As will be seen later, sometimes these factors are important and sometimes not. Intelligent use of such approximate methods requires a good understanding of how pile foundations behave during earthquakes. The prime objective of this paper is to provide such an understanding.

A more realistic computational model that is still relatively simple to use is the dynamic Winkler model in Fig. 5 [14]. The free field accelerations may be computed using a 1-D program such as SHAKE [15] and applied to the ends of the near field springs. This ensures that the kinematic interaction of the vibrating ground with the pile is taken into account approximately. The problem with this method is that the reliability of the p-y curves used in practice for dynamic analysis has not been established.

Finn and Thavaraj [16] have shown that a dynamic analysis version of the Winkler model using cyclic p-y curves may prove quite unreliable for seismic response analysis during strong shaking on the basis of centrifuge tests on model piles in dry sand. Several investigators have studied the applicability of the standard North American p-y curves to pile foundations in liquefiable soils and found them unsatisfactory also [17-20]. To take the effects of high pore water pressures into account, the p-y curves were degraded by multiplying the ordinates by a factor p , called the p-multiplier which ranged in value from 0.3 to 0.1 [17-19]. While it was possible to calibrate the p-y curves for a specific test [7], it was not possible to develop a general curve that could be used for all tests [20].

An alternative to the Winkler type computational model is to use a finite element continuum analysis based on the actual soil properties. Dynamic nonlinear finite element analysis in the time domain using the full 3-dimensional wave equations is not feasible for engineering practice at present because of the time needed for the computations. However, by relaxing some of the boundary conditions associated with a full 3-D analysis, Finn and Wu [21] and Wu and Finn (22,23) found it possible to get reliable solutions for nonlinear response of pile foundations with greatly reduced computational effort. The results are accurate for excitation due to horizontally polarized shear waves propagating vertically. Wu and Finn [22,23] give a full description of this method and of numerous validation studies. The method is incorporated in the computer program PILE-3D. An effective stress version of this program, PILE-3D-EFF that can generate and incorporate seismic pore water pressures, has been developed by Thavaraj and Finn [24] and validated by Finn et al [25] and Finn and Thavaraj [16], in cooperation the geotechnical group at the University of California at Davis.

Seismic response analysis is usually conducted assuming that the input motions are horizontally polarized shear waves propagating vertically. The PILE-3D model retains only those parameters that have been shown to be important in such analysis. These parameters are the shear stresses on vertical and horizontal planes and the normal stresses in the direction of shaking. The soil is modeled by 3-D finite elements as shown in Fig. 6. The pile is modeled using beam or volume elements.

The pile is assumed to remain elastic, though cracked section moduli are used for concrete piles, when displacements exceed specified threshold values. This assumption is in keeping with the philosophy that the structural elements of the foundation should not yield. This requirement cannot always be met. If the pile shaft is projected upwards prismatically to act as a column, then any yielding is likely to occur in the buried portion of the shaft.

The constitutive soil model is equivalent linear with strain dependent shear modulus and damping. The strain dependence relations developed by Seed and Idriss [26] were used in the analyses described later. The equations of motion are formulated in the time domain. This allows the modulus and damping to be updated continually during earthquake shaking to maintain compatibility with shear strain level for the duration of analysis. A yield condition

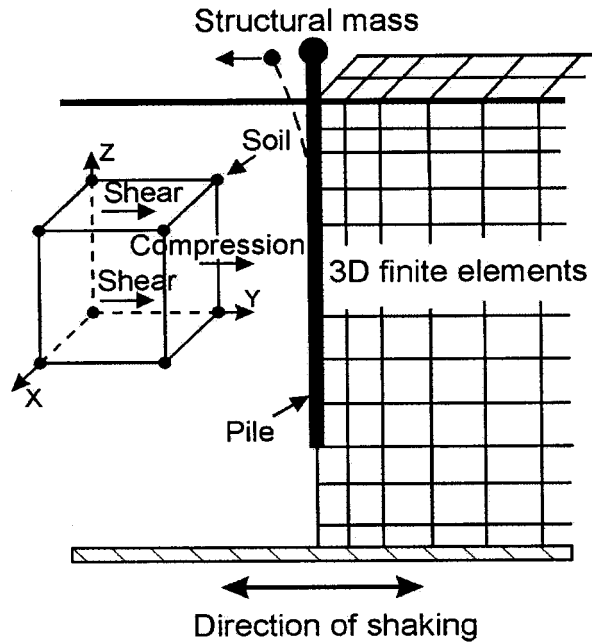


Fig. 6: Soil-pile model for analysis.

is incorporated consistent with the shear strength of the soil and no tension is allowed to develop between the soil and the pile.

A comprehensive picture of the behavior of pile foundations during earthquakes and how pile foundations affect structural response will be developed by detailed analyses of specific practical examples. The behavior of pile foundations in non-liquefiable soils will be examined in the context of the seismic response of a bridge on pile foundations.

5.0 SEISMIC RESPONSE ANALYSIS OF AASHTO (1983) CODE BRIDGE

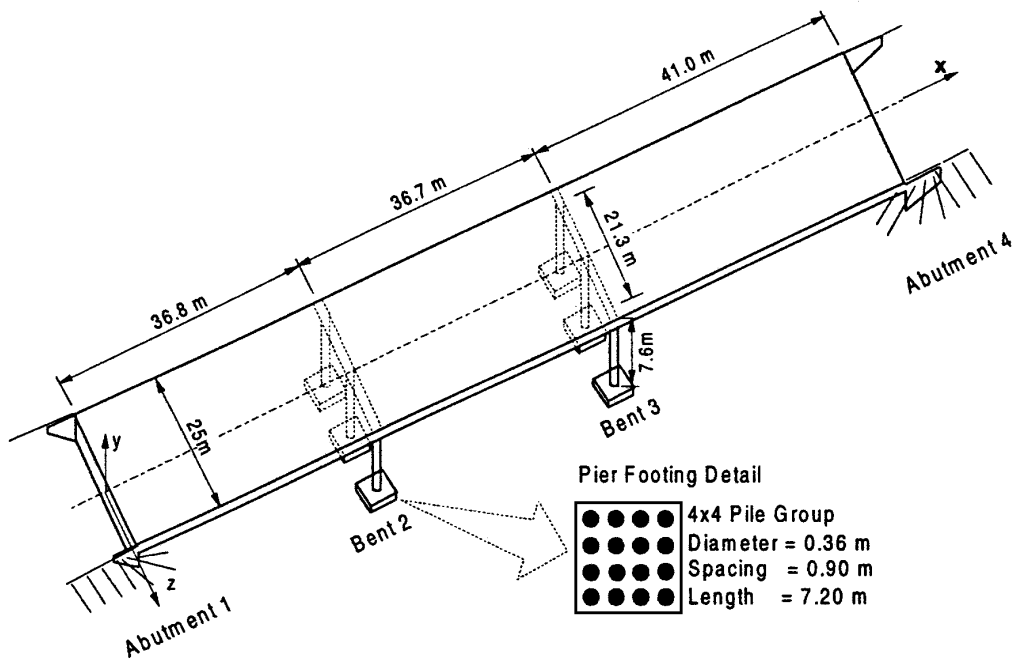


Fig. 7: Three span box girder bridge on pile foundations (after (27)).

A three span continuous box girder bridge structure, shown in Fig. 7, was chosen for the numerical studies of pile foundations in non-liquefiable ground. A rigid base version of this bridge is used as an example in the guide to the seismic design of bridges published by the American Association of State and Transportation Highway Officials [27]. The sectional and physical properties of the superstructure and the piers were taken from [27].

Each pier is supported on a group of sixteen (4×4) concrete piles. The diameter and length of each pile are 0.36 m and 7.2 m respectively. The piles are spaced at 0.90 m, center to center. The Young's modulus and mass density of the piles are $E = 22,000$ MPa and $\rho = 2.6$ Mg m⁻³ respectively.

The soil beneath the foundation is assumed to be a nonlinear, hysteretic continuum with unit weight, $\gamma = 18$ kNm⁻³ and Poisson's ratio, $\mu = 0.35$. The low strain shear modulus of the soil varies as the square root of the depth with values of zero at the surface and 213 MPa at 10 m depth. The variations of shear moduli and damping ratios with shear strain are those recommended by Seed and Idriss [26] for sand. The surface soil layer overlies a hard stratum at 10 m. For the Pile-3D finite element mesh, the foundation soil was divided into 10 sub-layers of varying thicknesses. The thickness decreased towards the surface where soil-pile interaction effects are stronger. Brick elements were used to model the soil around the piles and beam elements were used to model the piles.

The input acceleration record used in the study was the first 20 seconds of the N-S component of the free field accelerations recorded at CSMIP Station No.89320 at Rio Dell, California during the April 25, 1992 Cape Mendocino Earthquake. The power spectral density of this acceleration record shows that the predominant frequency of the record is approximately 2.2 Hz.

6.0 PILE CAP STIFFNESSES

The pile cap stiffnesses of the pile foundation shown in Fig. 7 will be determined for two different ratios of the column/foundation stiffness ratio, 7% and 50%. A PILE 3-D analysis is conducted first and the spatially varying time histories of modulus and damping are stored. Then an associated program PILIMP calculates the time histories of dynamic pile head impedances using the stored data. The dynamic complex impedances are calculated at any desired frequency by applying a harmonic force of the same frequency to the pile head and calculating the generalized forces for unit generalized displacements. In this paper, discussion will focus on the stiffnesses, the real parts of the complex impedances, as these are the parameters of primary interest for current practice. The stiffnesses are calculated first without taking into account inertial interaction between the superstructure and the pile foundation. This is the usual condition in which stiffness is estimated either by elastic formulae, static loading tests, or static analysis. The stiffnesses are calculated also taking the inertial effects of the superstructure into account. In this latter case, both kinematic and inertial interactions are taken into account at the same time. Since the entire pile group is being analyzed, pile-soil-pile interaction is automatically taken into account under both linear and non-linear conditions. Therefore the usual difficult problem of what interaction factors to use or what group factor to apply is avoided.

Time histories of lateral and cross coupling stiffnesses are shown in Figure 8; rotational stiffness in Fig. 9. These stiffnesses, resulting from kinematic interaction only, were calculated for the predominant frequency of the input motions, $f = 2.2$ Hz. It is clearly not an easy matter to select a single representative stiffness to characterize a discrete single valued spring to be used in structural analysis programs to represent the effects of the foundation. In

the absence of a nonlinear analysis, probably a good approach to including the effects of soil nonlinearity on stiffness is determine the vertical distribution of effective moduli using a

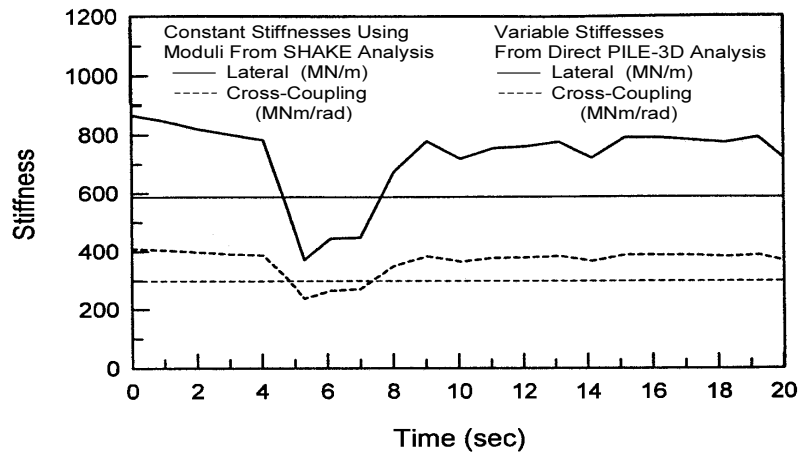


Fig. 8: Time history of lateral and cross-coupled stiffness under strong shaking.

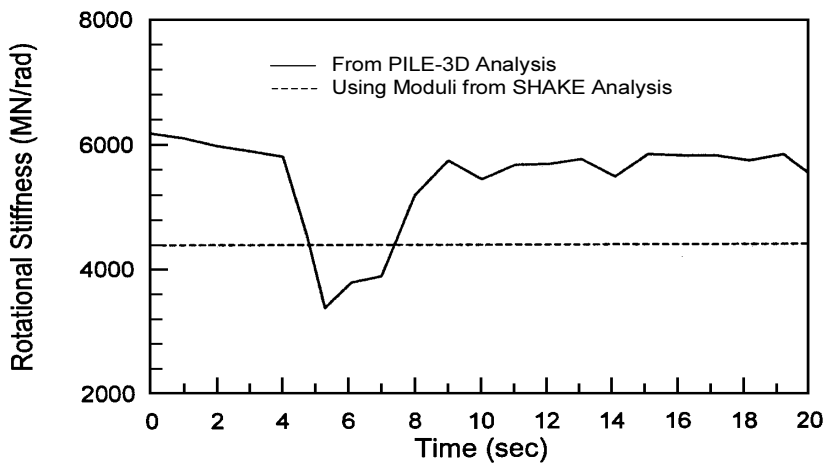


Fig. 9: Time history of rotational stiffness under strong shaking.

SHAKE [15] analysis of the free field and calculate the stiffnesses at the appropriate frequency using these moduli. The constant stiffnesses calculated in this way are shown also in Figs. [8] and [9]. These are kinematic stiffnesses. .

7.0 RESPONSE OF CODE BRIDGE TO TRANSVERSE EARTHQUAKE LOADING

7.1 Finite Element Model of the Bridge Structure

A three dimensional space frame model of the bridge is shown in Fig. 10. At the abutments, the deck is free to translate in the longitudinal direction but restrained in the transverse and vertical directions. Rotation of the deck is allowed about all three axes. The space frame members are modeled using 2-noded 3-D beam elements with twelve degrees of freedom, six degrees at each end. The bridge deck was modeled using 13 beam elements and each pier was modeled by 3 beam elements. The cap beam that connects the tops of adjacent piers was modeled using a single beam element. The sectional and physical properties of the deck and the piers are those provided in the AASHTO guide [27]. The pier foundation is modeled

using a set of time-dependent nonlinear springs and dashpots that simulate exactly the time histories of stiffnesses and damping from the PILE-3D analyses. The response of the bridge structure was analyzed for different foundation conditions to study the influence of various approximations to foundation stiffnesses and damping using the computer program BRIDGE-NL [28].

The free field acceleration was used as the input acceleration and the peak acceleration was set to 0.5g.

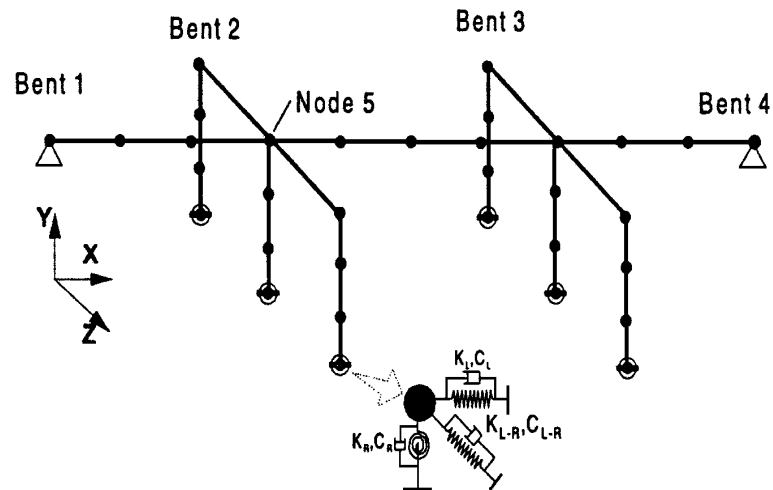


Fig. 10: Stick model of the bridge with the foundation springs and dashpots.

7.2 Foundation Conditions for Analyses

The seismic response of the bridge to transverse earthquake loading was analyzed for the four different foundation conditions listed below.

1. Rigid foundation and fixed base condition is assumed
2. Flexible foundation with elastic stiffness and damping
3. Flexible foundation with kinematic time dependent stiffness and damping
4. Flexible foundation with stiffness and damping based on the ‘SHAKE’ effective moduli.

The fundamental transverse mode frequency of the computational model of the bridge with a fixed base was found to be 3.18 Hz. This is the frequency quoted in the AASHTO-83 guide [27]. This agreement in fundamental frequencies indicates an acceptable structural model. In this analysis, the lateral stiffness of the bridge pier is only 7% of the foundation stiffness. For this extremely low stiffness ratio, the columns control the fundamental frequency of the bridge and the influence of the foundation is negligible. Results from analyses in which the column/foundation stiffness ratio is 50% will be presented here. The stiffness ratio was raised by increasing the stiffness of the piers only, with no changes to the super-structure. Normally much stiffer piers would imply a heavier superstructure and therefore higher inertial forces.

For a 50% stiffness ratio, the fixed base fundamental frequency of the bridge is 5.82 Hz. When the stiffnesses associated with low strain initial moduli are used, the fundamental frequency is 4.42 Hz, a 24% reduction from the fixed base frequency. With kinematic strain dependent stiffnesses, the frequency reached a minimum value of 3.97 Hz during strong shaking, a 32% reduction from the fixed base frequency. When the foundation stiffnesses are based on effective shear moduli from a ‘SHAKE’ analysis of the free field, the frequency is 4.18 Hz, a 28% change from the fixed base frequency. Fig. 11 shows the variation with time in fundamental transverse modal frequency for the different foundation conditions.

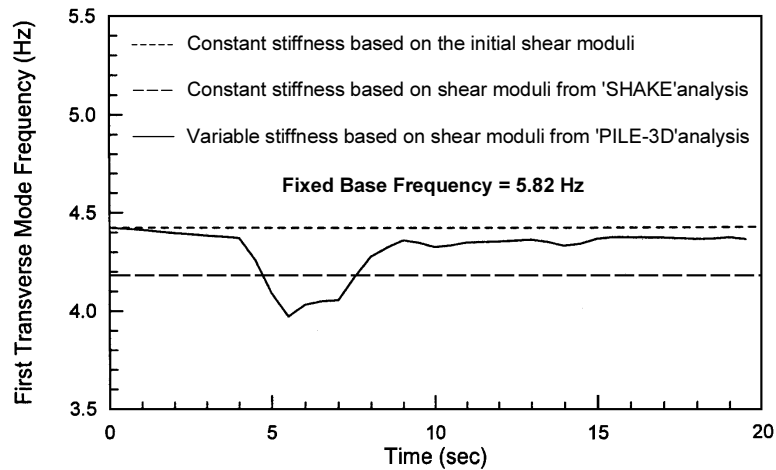


Fig. 11: Time history of the frequency of first transverse mode.

The response of the bridge deck at Bent 2 (Node No. 5 in Fig. 10) was computed for two cases: the fixed base case and a flexible foundation with kinematic time dependent stiffnesses. The effect of including the foundation flexibility is shown in Fig. 12. There is a dramatic change in the deck displacement during the strong shaking, when the foundation flexibility is included in the model. The peak displacement increased from 7mm to 17mm.

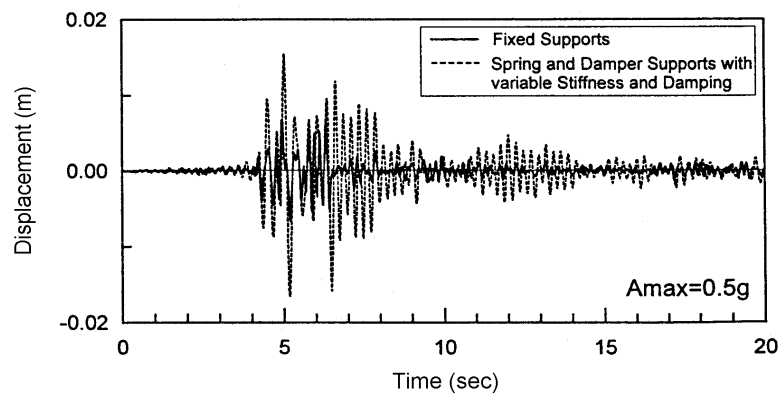


Fig. 12: Effects of foundation flexibility on deck displacement.

8.0 INERTIAL INTERACTION OF STRUCTURE AND PILE

The time dependent stiffnesses used in the analyses described above were computed without taking the inertial interaction of superstructure and foundation into account. The primary effect of this interaction is to increase the lateral pile displacements and cause greater strains in the soil. This in turn leads to smaller moduli and increased damping. The preferred method of capturing the effect of superstructure interaction is to consider the bridge structure and the foundation as a fully coupled system in the finite element analysis. However, such a fully coupled analysis is not possible with current commercial structural software. Even if it were, it would not be feasible in practice because it would require enormous amounts of computational storage and time.

An approximate way of including the effect of superstructure interaction is to use the model shown in Fig. 13. In this model, the superstructure is represented by a single degree of freedom (SDOF) system. The mass of the SDOF system is assumed to be the portion of the

superstructure mass carried by the foundation. The stiffness of the SDOF system is selected so that the system has the period of the fixed base bridge structure in the mode of interest.

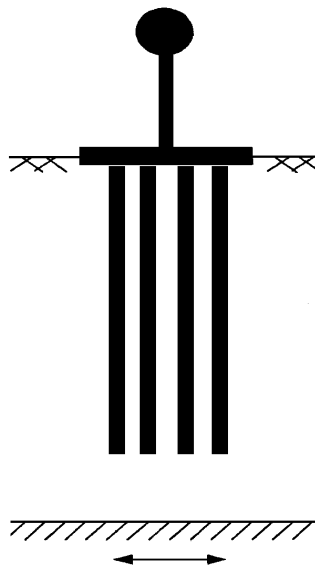


Fig. 13: Pile foundation with structure.

This approximate approach will be demonstrated by the analysis of the center pier at Bent 2. The fundamental transverse mode frequency of the fixed base model was found earlier to be 5.82Hz. The static portion of the mass carried by the center pier is 370 Mg. The superstructure can be represented by a SDOF system having a mass of 370 Mg at the same height as the pier top and frequency 5.82Hz. The corresponding stiffness of the SDOF system is 495 MN/m.

A coupled soil-pile-structure interaction analysis can be carried out using PILE3-D by incorporating the SDOF model into the finite element model of the pile foundation. The pile foundation stiffnesses derived from this finite element model incorporate the effects of both inertial and kinematic interactions and are called total stiffnesses. The time histories of stiffnesses with and without the superstructure are shown in Fig. 14. The reduction in lateral stiffness is greater throughout the shaking when the inertial interaction is included. There is a similar reduction in the rotational and cross-coupling stiffnesses.

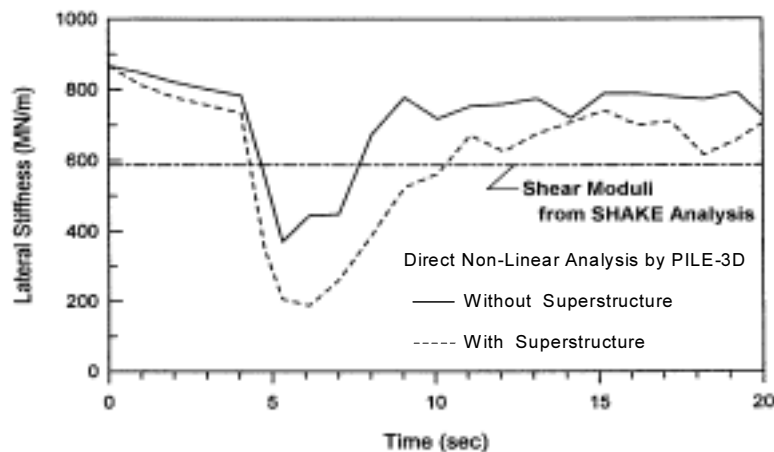


Fig. 14: Effects of inertial interaction on lateral pile cap stiffness.

When inertial interaction is included, the lateral stiffness reached a minimum of 188 MN/m which is 78% lower than the initial value. This minimum was 20% lower than the minimum that was attained, when the inertial interaction was not included. This analysis probably underestimates the effects of inertial interaction because the column stiffness of the AASHTO code bridge was increased from 7% to 50% without any increase in superstructure mass. Such a stiffness ratio would normally be associated with a heavier super-structure.

An eigenvalue analysis of the complete bridge structure was carried out, using the total foundation stiffnesses. The variation in first mode transverse frequency with time is shown in Fig. 15. This figure also shows the frequency variation for the case in which the inertial interaction was not considered. The frequency reached a minimum of 3.62Hz, when the inertial interaction was included and 3.97Hz, when the interaction was ignored. Figs. 16 and 17 show the effects of superstructure interaction on the time histories of acceleration and displacement respectively. For this particular case, when the superstructure interaction effect is included, it leads to greater acceleration and displacement. The increase in peak displacement is approximately 72%, a major increase.

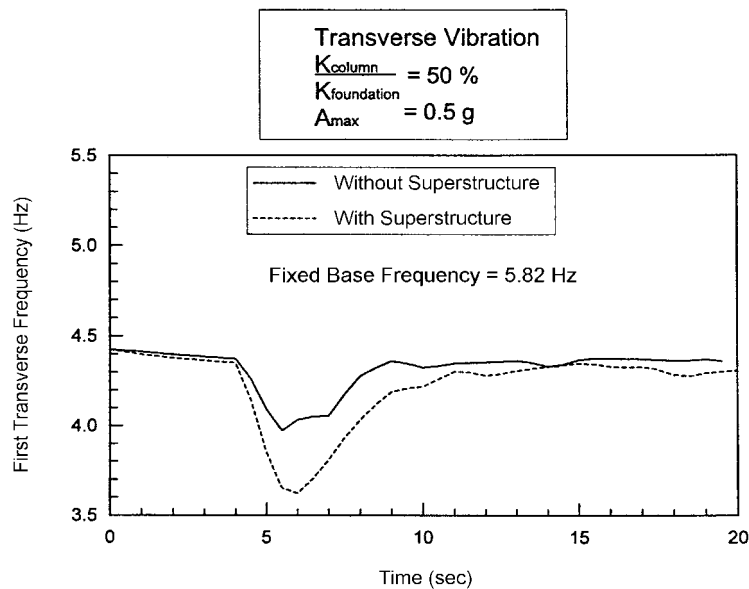


Fig. 15: Effects of inertial interaction on foundation frequency.

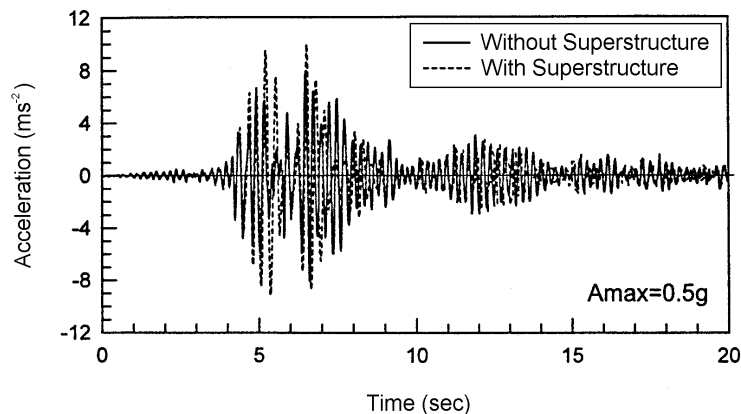


Fig. 16: Effect of superstructure interaction on deck acceleration.

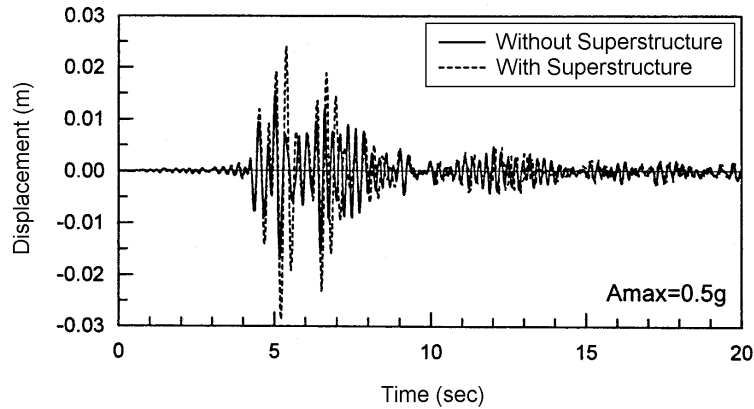


Fig. 17: Effect of superstructure interaction on deck displacement.

The results of the analyses for the four different foundation conditions are summarized in the acceleration and displacement spectra for transverse vibration of the bridge, shown in Figs. 18 and 19 respectively. The fixed base model for estimating response is clearly inadequate in this case. If the effects of inertial interaction are neglected, and only kinematic stiffness are taken into account, the seismic response obtained using effective moduli from a SHAKE analysis of the free field gives almost identical results to the PILE-3D response. However when the inertial interaction is included, there is significant difference in response.

9.0 PILE CAP STIFFNESSES AND SYSTEM FREQUENCIES

This study has shown that different approximations to foundation conditions of a bridge and in the evaluation of pile cap stiffnesses can make large differences in the estimated pile cap stiffness matrix. These differences will affect the mode frequencies of the bridge foundation system. It is these system frequencies that control response. The impact that pile cap stiffnesses have on system frequencies depends on the relative stiffnesses of the superstructure supports and the pile foundation. This effect can be estimated by the period shift in the first mode frequency. A parametric study was conducted to define the dependence of period shift on relative superstructure/ pile cap stiffness. The results are shown in Fig. 20, where the non-dimensional period ratio, T_p/T_F , is plotted against the non-dimensional stiffness ratio, K_p^S/K_L^F . In these ratios, T_p is the system period for a fixed base,

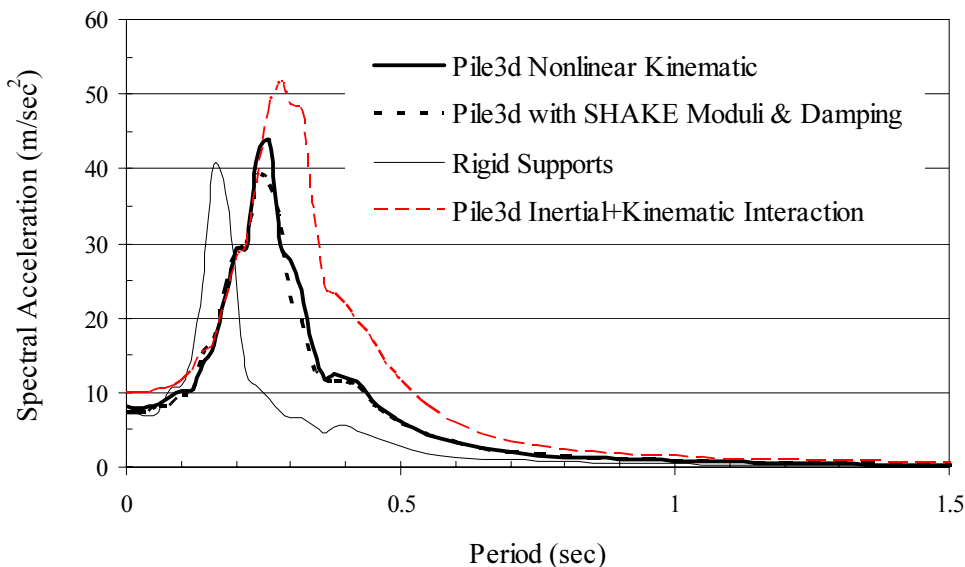


Fig. 18. Spectral accelerations of AASHTO bridge for four different approximations to foundation conditions.

T_F is the system period for a flexible base, K_P^S is the superstructural lateral stiffness and K_L^F is the lateral stiffness of the pile foundation.

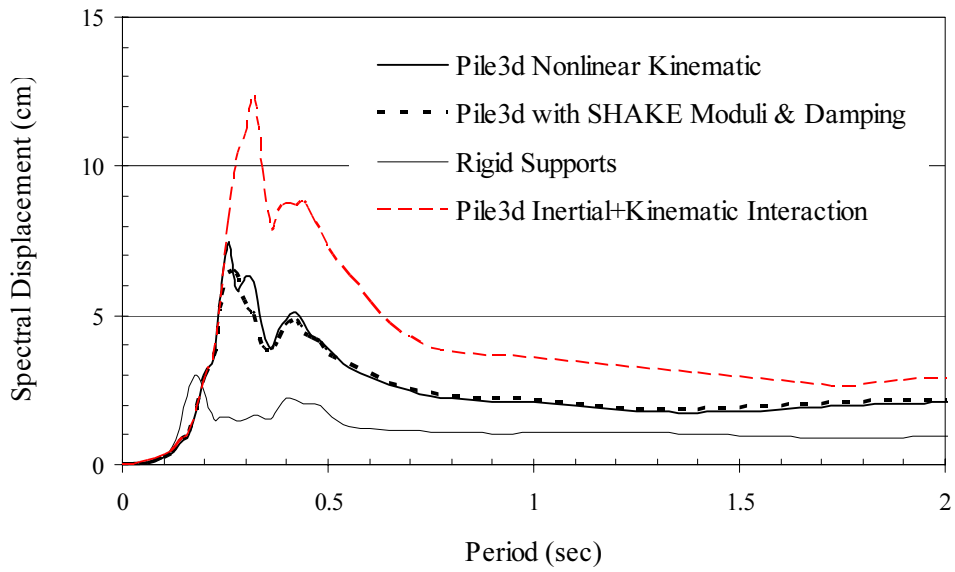


Fig. 19. Spectral displacements of AASHTO bridge for four different approximations to foundation conditions.

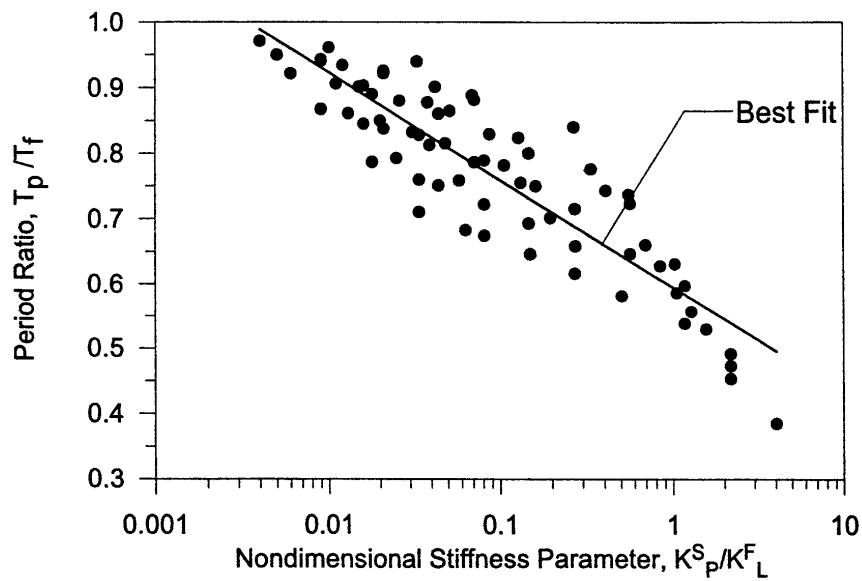


Fig. 20. Period shift for bridge-foundation system as a function of relative superstructure – foundation lateral stiffness.

10.0 CLOSING REMARKS

Performance based design demands an appropriate computational model of the structure in order to check whether the design meets the performance criterion. This requirement is a challenge for geotechnical engineers to provide effective models of the actions of foundations

on the structure during shaking. A constraint on such modeling is that the models must be compatible with the commercial software used in structural design practice.

The paper describes the modeling of shallow foundations as recommended by NEHRP (1997). NEHRP recommends Winkler spring models. The stiffnesses of these models are based for the most part on stiffness formulations related to rigid footing. Large mat footings may have flexibilities that make the rigidity assumption invalid.

The new development with a major impact on the modeling of shallow foundations is the acceptance of footing uplift, with or without soil yielding. To accommodate uplift and soil yielding, the Winkler springs must not be allowed to develop tension and must have compression stress limits that match the yield pressure of the soil. Reaching the yield capacity moment of a foundation is not synonymous with failure because of the ductility capacity of soil. The real indices of failure are the increased displacements and their effects on global stability and on seismic demand.

The reliable modeling of pile foundations in a manner suitable for design requires simplified methods but there is very little hard numerical data from past earthquakes to validate current methods. Also because the fully coupled analysis of pile groups is difficult and time consuming with commercial software not many analytical investigations of pile foundations have been conducted for realistic soil properties.

The reliability of approximate methods for representing the rotational and translational stiffnesses of pile foundations in the computational structural model of a superstructure are investigated in the paper, using a pseudo-3-D nonlinear continuum soil model. The study is focused on a 4x4 pile group supporting a bridge pier.

Some of the assumptions of the approximate methods in use for evaluating foundation stiffnesses were incorporated into 3-D nonlinear analyses of the foundations and the foundations-bridge system. Most of the approximate methods in use are based on single pile analysis and further assumptions must be made to establish the group response. They often neglect both the kinematic interaction between pile and foundation soils and inertial interaction between superstructure and foundations. The problems in selecting appropriate single valued springs to represent the actions of pile foundations on a superstructure are illustrated by time histories of pile cap stiffnesses during strong earthquake shaking. The consequences of using various approximations to pile cap stiffnesses are investigated by examining their effects on the first modal frequencies of the pile foundation - bridge system and on the accelerations and displacements of the deck. The effects of ignoring inertial or kinematic interactions, as some methods do, are also evaluated. The effects of inertial interaction can be very significant in reducing the stiffness factors and hence the frequency of the pile foundation-bridge system.

Parametric studies are continuing in order to provide a larger data base for a comprehensive evaluation of the many approximate methods in use for the evaluation of pile stiffnesses.

11.0 ACKNOWLEDGEMENTS

The research project on the seismic design and analysis of pile foundations is funded by Anabuki Komuten, Takamatsu, Japan. The support of the company is gratefully acknowledged. The help of Noboru Fujita, Research Assistant, was invaluable in the preparation of this paper.

12.0 REFERENCES

- [1] Daniel Shapiro, Christopher Rojahn, Lawrence D. Reavely, James R. Smith and Ugo Morelli, "NEHRP Guidelines and Commentary for Seismic Rehabilitation of Buildings," *Earthquake Spectra*, 16 (1), pp227-240, 2000.
- [2] ATC-3, "Tentative Provisions for the Development of Seismic Regulations for Buildings" (ATC-3-06), The Applied Technology Council, Redwood, California, 1978.
- [3] A. S. Veletsos and Y. T. Wei, "Lateral and rocking vibration of footings," *J. of Soil Mechanics and Foundation Division*, ASCE, New York, NY, 97 (SM9), pp 1227-1248, 1971.
- [4] A. S. Veletsos, A. M. Prasad and Y. Tang, "Design approaches for soil-structure interaction," *Proc. 9th World Conference on Earthquake Engineering*, Tokyo, 1988
- [5] J. W. Wallace, J. P. Moehle and J. Martinez-Cruzado, "Implications for the design of shear wall buildings using data from recent earthquakes," *Proc. 4th U.S. National Conference on Earthquake Engineering*, Palm Springs, CA, 1990
- [6] G. Gazetas, "Foundation Vibrations," *Foundation Engineering Handbook*, H. Y. Fang, Editor, VanNostrand-Reinhold, New York, 1991.
- [7] NEHRP, "National Earthquake Hazard Reduction Guidelines for the Seismic Rehabilitation of Buildings, Building Seismic Safety Council, Washington, DC, 1997a
- [8] NEHRP, "National Earthquake Hazard Reduction Commentary on the Guidelines for the Seismic Rehabilitation of Buildings, Building Seismic Safety Council, Washington, DC, 1997b
- [9] G. W. Housner, "The behavior of inverted pendulum structures during earthquakes," *Bulletin of the Seismological Society of America*, 53 (2), 1963.
- [10] P. E. Bartlett, "Foundation rocking on a clay soil," University of Auckland, School of Engineering, Report No. 154, M. E. Thesis, 1976.
- [11] Geoffrey R. Martin and Ignatius Po Lam, "Earthquake resistant design of foundations-retrofit of existing foundations," *Proc. GeoEng2000*, Melbourne, 1, pp1025-1047, Technomic Publishers, Lancaster, PA, 2000.
- [12] API, "Recommended practice for planning, designing, and constructing fixed offshore platforms," *API RP 2A*, American Petroleum Institute, 1995.
- [13] J. M. Murchison and M. W. O'Neill, "An evaluation of p-y relationships in cohesionless soils," *Proc. ASCE Sym. Analysis and Design of Pile Foundations*, *ASCE National Convention, San Francisco, California*, J. R. Meyer, Editor, pp. 174-191, 1984.
- [14] T. Thavaraj, and W. D. Liam Finn, "A program for dynamic analysis of a single pile using a Winkler model and p-y curves," *Anabuki Chair of Foundation Geodynamics*, Kagawa University, Japan, 2000
- [15] P. B. Schnabel, J. Lysmer and H. B. Seed, "SHAKE: A computer program for earthquake response analysis of horizontally layered sites," *Earthquake Engineering Research Center*, University of California, Berkeley, CA, Report No. EERC72-12, 1972.
- [16] W. D. Liam Finn, and T. Thavaraj. "Deep foundations in liquefiable soils: Case histories, centrifuge tests and methods of analysis," *CD-ROM Proceedings, 4th Int. Conf. on Recent Advances in Geotechnical Earthquake Engineering and Soil Dynamics*, San Diego, CA, 2001.

- [17] L. Liu, and R. Dobry, "Effect of liquefaction on lateral response of piles by centrifuge tests," *Nat. Ctr for Earthquake Engrg. Res. (NCEER) Bull.*, 9 (1), pp. 7-11.
- [18] Thomas. J. Weaver, Scott A. Ashford and Kyle M. Rollins, "Development of p-y curves for a 0.6 m diameter CISS pile in liquefied sand," *CDROM Proc. 6th CALTRANS Seismic Research Workshop*, Sacramento, CA, 2001.
- [19] D. W. Wilson, R. W. Boulanger, and B. L. Kutter, "Observed lateral resistance of liquefying sand," *J. of Geotech. And Geoenviron. Engrg.*, ASCE, 126 (10), pp. 898-906.
- [20] Scott J. Brandenburg, Priyanshu Singh, Ross W. Boulanger, and Bruce L. Kutter, "Behavior of piles in laterally spreading ground during earthquakes," *CDROM Proc. 6th CALTRANS Seismic Research Workshop*, Sacramento, CA, 2001
- [21] W. D. Liam Finn and G. Wu. Recent developments in the static and dynamic analysis of pile groups. *Proc. Annual Sym. Vancouver Geotechnical Society*. Vancouver, B. C. Canada , 1994, pp. 1-24.
- [22] G. Wu, and W. D. Liam Finn, "Dynamic elastic analysis of pile foundations using the finite element method in the frequency domain," *Canadian Geotechnical Journal*, (34), 34-43, 1997.
- [23] G. Wu, and W. D. Liam Finn, "Dynamic nonlinear analysis of pile foundations using the finite element method in the time domain," *Canadian Geotechnical Journal*, (34), 144-152, 1997.
- [24] T. Thavaraj and W. D. Liam Finn "Pile-3D-EFF: A program for nonlinear dynamic effective stress analysis of pile foundations," Anabuki Chair of Foundation Geodynamics, Kagawa University, Japan, 1999.
- [25] W. D. Liam Finn, T. Thavaraj, D. W. Wilson, R. W. Boulanger and B.L Kutter, "Seismic analysis of piles and pile groups in liquefiable sand," *Proc. 7th Intern. Sym. Numerical Models in Geomechanics, NUMOG VI*, Graz, Austria, pp. 287-292, 1999.
- [26] H. B. Seed and I. M. Idriss, "Soil moduli and damping factors for dynamic response analysis," Earthquake Engineering Research Center, University of California, Berkeley, CA, Report No. EERC70-10, 1970.
- [27] AASHTO, "Guide specifications for seismic design of highway bridges," American Association of State Highway and Transportation Officials, Washington, DC, USA, 1983.
- [28] T. Thavaraj, and W. D. Liam Finn, "A program for dynamic analysis of bridges incorporating foundation springs with specified time histories of stiffnesses," Anabuki Chair of Foundation Geodynamics, Kagawa University, Japan, 2001.

EFFECTS OF DYNAMIC SOIL-STRUCTURE INTERACTION ON PILE STRESS IN LARGE SHAKING TABLE TESTS

K. Tokimatsu¹⁾ and H. Suzuki²⁾

1) Professor, Dept. of Architecture and Building Engineering, Tokyo Institute of Technology, Japan

*2) Graduate Student, Dept. of Architecture and Building Engineering, Tokyo Institute of Technology, Japan
kohji@o.cc.titech.ac.jp, hsuzuki@arch.titech.ac.jp*

Abstract: Large shaking table tests are conducted to investigate the effects of dynamic soil-pile-structure interaction on pile stresses. A 2x2 pile group founded in either dry or liquefiable sand deposit is shaken with or without a superstructure, whose natural period is either less or greater than that of the ground. The test results show that, if the natural period of the superstructure is less than that of the ground, the kinematic and inertial forces tend to be in phase, increasing the stress in the pile. If the natural period of the superstructure is greater than that of the ground, they tend to be out of phase, restraining the pile stress from increasing. Pseudo-static analysis is conducted to estimate pile stresses in the tests. It is assumed that the pile stress is either the sum of the two stresses caused by the inertial and kinematic effects or the square root of the sum of the squares of the two, depending on the relationship between natural periods of the superstructure and ground. The estimated pile stresses are in good agreement with the observed ones regardless of the occurrence of soil liquefaction.

1. INTRODUCTION

Field investigation and subsequent analyses after recent earthquakes confirmed that not only the inertial effects of superstructures but also the kinematic effects arising from the ground movement had significant impact on the damage to pile foundations, particularly in the areas where soil liquefaction and/or lateral ground spreading occurred (BTL Committee 1998). Little is known, however, concerning the degree of contribution of the two effects.

The object of this paper is to examine the effects of inertial and kinematic components on pile stresses based on the results of large shaking table tests on pile-structure models constructed in either dry or saturated sand deposit and to discuss how these two effects are taken into account in the pseudo-static analysis such as Beam-on-Winkler-springs method.

2. LARGE SHAKING TABLE TESTS

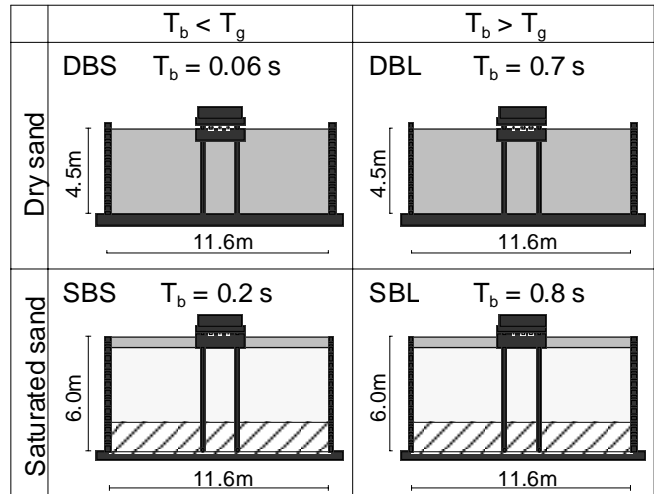
To investigate qualitatively the effects of inertial and kinematic forces, several series of shaking tests were conducted on soil-pile-structure systems using the shaking table facility at the National Research Institute for Earth Science and Disaster Prevention (NIED) (Tamura et al. 2000, 2001). Fig. 1 summarizes the test series in which a pile-structure system was constructed in either dry or saturated liquefiable sand in a large laminated shear box. The dimensions of the shear box were 4.6 or 6.1 m high, 12.0 m wide and 3.5 m long.

Model series IDs starting D and S indicate dry and saturated liquefiable sands, respectively. The

soil used for dry sand deposit was Nikko Sand ($e_{\max} = 0.98$, $e_{\min} = 0.65$, $D_{50} = 0.42$ mm). The relative densities were about 80% for the tests. The soil profile in the liquefaction tests consisted of three layers including a top dry sand layer 0.5 m thick, a liquefiable sand layer 4 m thick and an underlying dense gravelly layer about 1.5 m thick. The sand used was Kasumigaura Sand ($e_{\max} = 0.961$, $e_{\min} = 0.570$, $D_{50} = 0.31$ mm, $F_c = 5.4$ %). The cone penetration test was made before each shaking table test to characterize the density profile of the deposit with depth.

A 2x2 steel pile group that supported a foundation of 20.6 kN with a superstructure of 139.3 kN was used. All the piles had a diameter of 16.52 cm with a 0.37 cm wall thickness and their tips were connected to the container base with pin joints. The natural period of the superstructure for series ID containing S at the end was shorter than that of the ground. The natural period for series ID containing L was longer than that of the non-liquefied ground but shorter than that of the liquefied ground.

The soil-pile-structure system was heavily instrumented with accelerometers, displacement transducers, strain gauges, and, if saturated, pore pressure transducers, as shown in Fig. 2. In these tests, an artificial ground motion called Rinkai, produced as an earthquake in Southern Kanto district in Japan was used as an input base acceleration to the shaking table. The test results estimated in this paper are those having a peak input acceleration of 2.4 m/s^2 .



T_b : Natural period of superstructure
 T_g : Natural period of ground before liquefaction

Fig. 1 Model layout

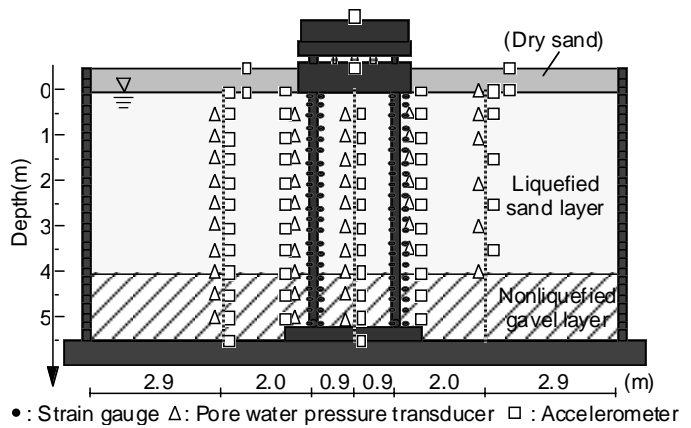


Fig. 2 Soil-pile-structure system

3. EFFECT OF SOIL DISPLACEMENT AND INERTIAL FORCE ON PILE STRESS IN DRY SAND

Fig. 3 shows time histories of acceleration of ground surface, foundation and superstructure, and bending moment at the pile head in DBS and DBL, together with the input base acceleration. In spite of similar acceleration response of the ground and superstructure, the bending moments in two tests are quite different. Namely, the moment in series DBS is almost twice that in series DBL. This suggests that the bending moment is affected not only by the inertial force from the superstructure but also other factors such as the ground displacement of dry sand.

To investigate factors affecting stress in piles, the forces acting on the foundation are modeled as shown in Fig. 4. Neglecting the friction between foundation and soil, the total earth pressure acting on the foundation is defined as:

$$P_e = P_{ep} \Phi P_{ea} = Q \Phi F \quad (1)$$

in which P_E is total earth pressure, P_{Ep} and P_{Ea} are earth pressures on the passive and active sides, Q is shear force at the pile heads computed from the differentiation of observed bending moment, and F is total inertial force computed from the accelerations of superstructure and foundation.

Fig. 5 compares the relations of the inertial force with bending moment, shear force, total earth pressure and ground surface displacement in DBS and DBL. The shear force is almost equivalent to the inertial force in series DBS (c), while the former is significantly smaller than the later in series DBL (d). This indicates that most of the inertial force is transmitted to the shear force in pile in series DBS, contributing to the large bending moment; however, this is not the case in series DBL. The difference in transmitted shear stress between the two tests is probably caused by the different actions of earth pressure against the inertial force, as shown in (e)(f). Namely, the earth pressure in DBS is out of phase with the inertial force and does not contribute toward reducing the shear force transmitted to the pile. In series DBL, in contrast, the earth pressure is in phase with and acts against the inertial force, reducing the shear force transmitted to the pile.

It is interesting to note that the inertial force is in phase in DBL and out of phase in DBS with ground displacement ((g)(h)). This indicates that the effects of inertial force and ground displacement become significant at the same time, inducing a large bending moment, in DBS. In contrast, the effects of the two do not become significant at the same time, yielding a small bending moment, in DBL.

4. EFFECTS OF SOIL DISPLACEMENT AND INERTIAL FORCE ON PILE STRESS DURING LIQUEFACTION

To investigate whether the findings in dry sands are valid in liquefiable sands, a similar examination was made for the other test series conducted with saturated sands. Fig. 6 shows the time histories of the accelerations of superstructure and foundation, soil displacement, bending moment at the pile head and pore pressure ratio, for series SBS, and SBL. The pore water pressure ratios in both tests begin to rise in 10 s and approaches 1.0 in about 20 s. After liquefaction, the bending moments in SBL as well as SBS get significantly larger than those before liquefaction. In addition, they are larger

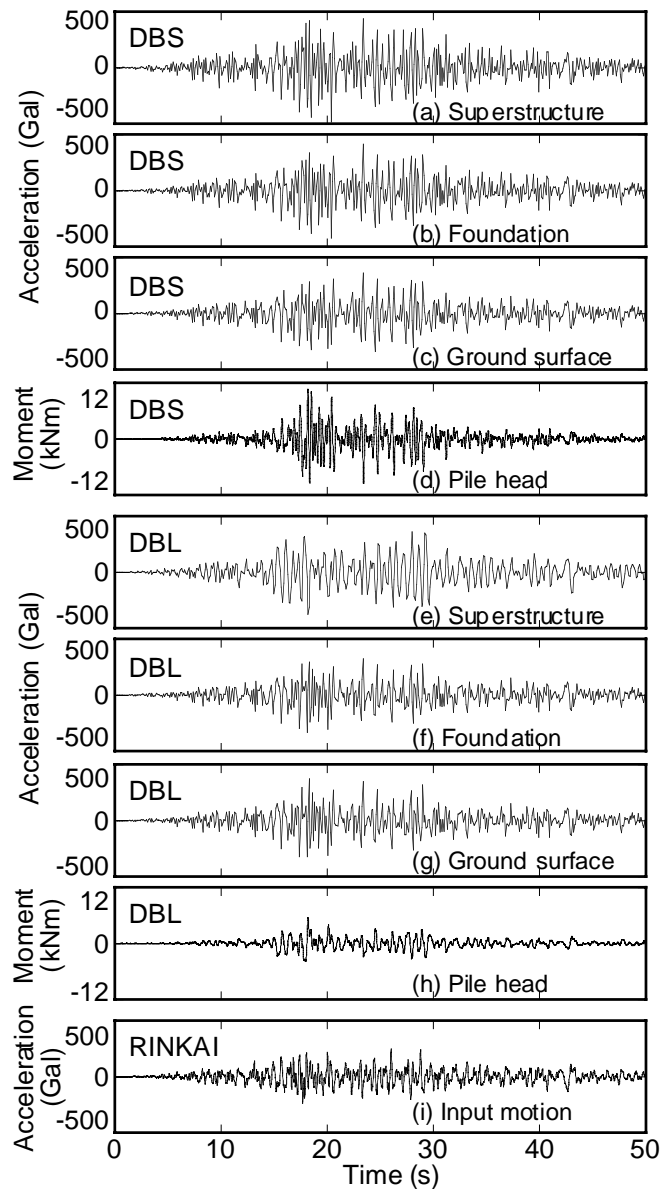


Fig. 3 Time histories in dry sand shaking tests

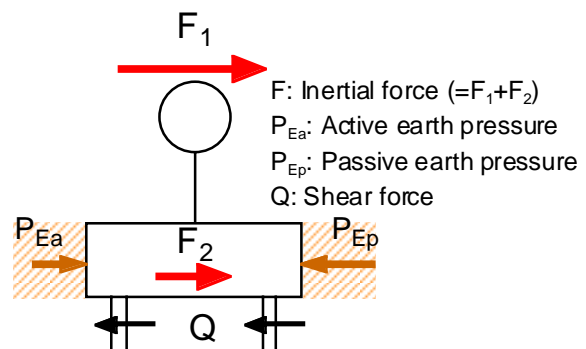


Fig. 4 Forces acting on foundation

than the bending moments in DBS and DBL, shown in Fig. 3. Considering that the acceleration of superstructure decreases and the soil displacement increases with the development of liquefaction, the contribution of inertial and kinematic forces on pile stresses might have changed during liquefaction.

Figs. 7 and 8 compare the relations of the inertial force with bending moment, shear force, total earth pressure and ground displacement for three time segments (0-10, 10-20, and 20-50s) in SBS and SBL. The circle in plates (j)-(l) corresponds to the time at which the bending moment at the pile head is the largest within a time segment of 0.5 s. The bending moments after liquefaction in both cases are larger than those before liquefaction. This is probably because the shear force, which is less than the inertial force before liquefaction, becomes equal to or greater than the inertial force

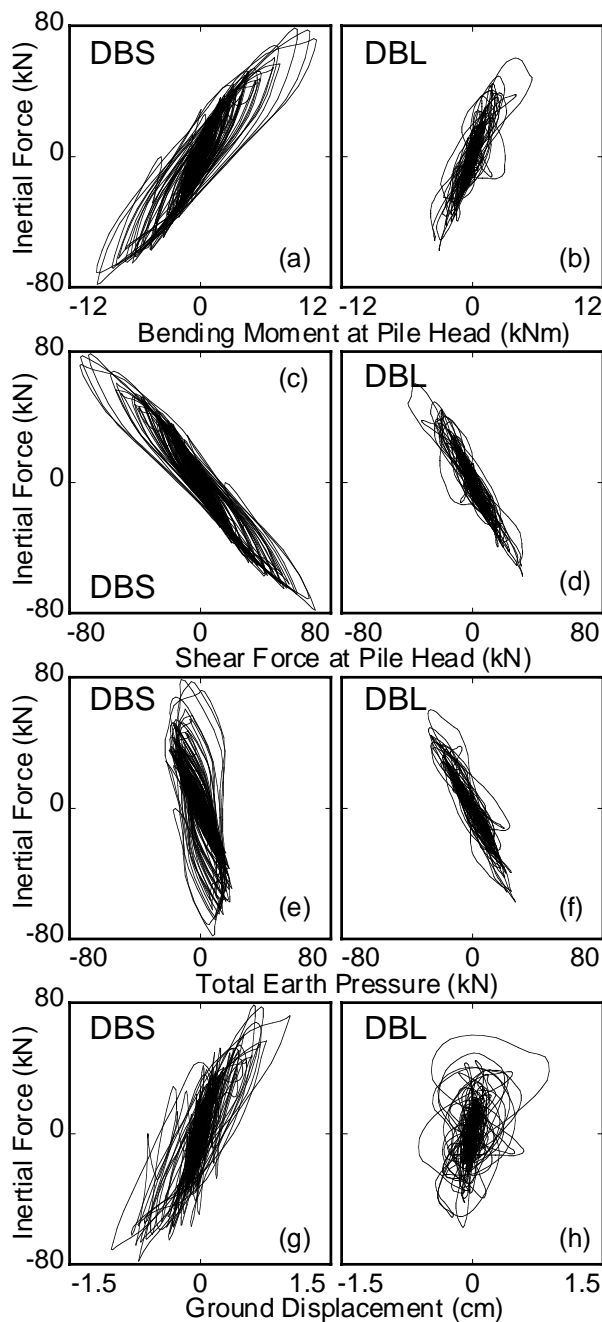


Fig. 5 Relation of inertial force with bending moment, shear force, earth pressure and ground displacement in DBS and DBL

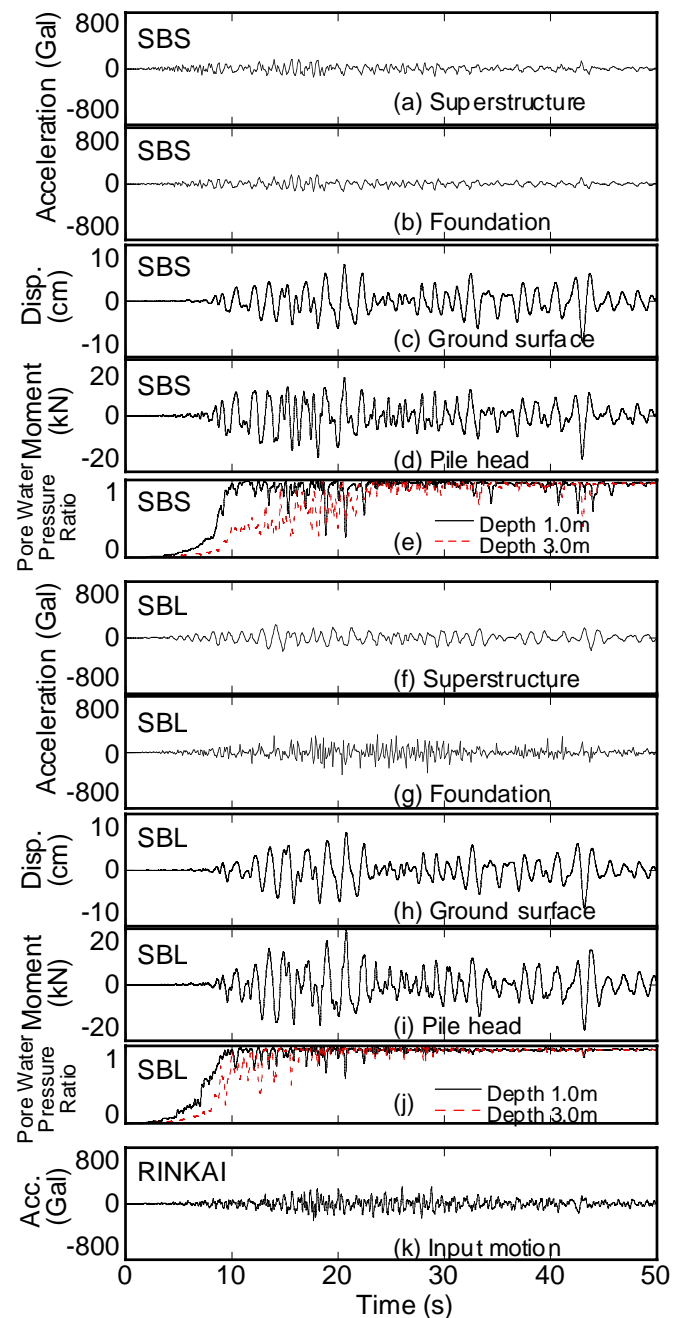


Fig. 6 Time histories in SBS and SBL

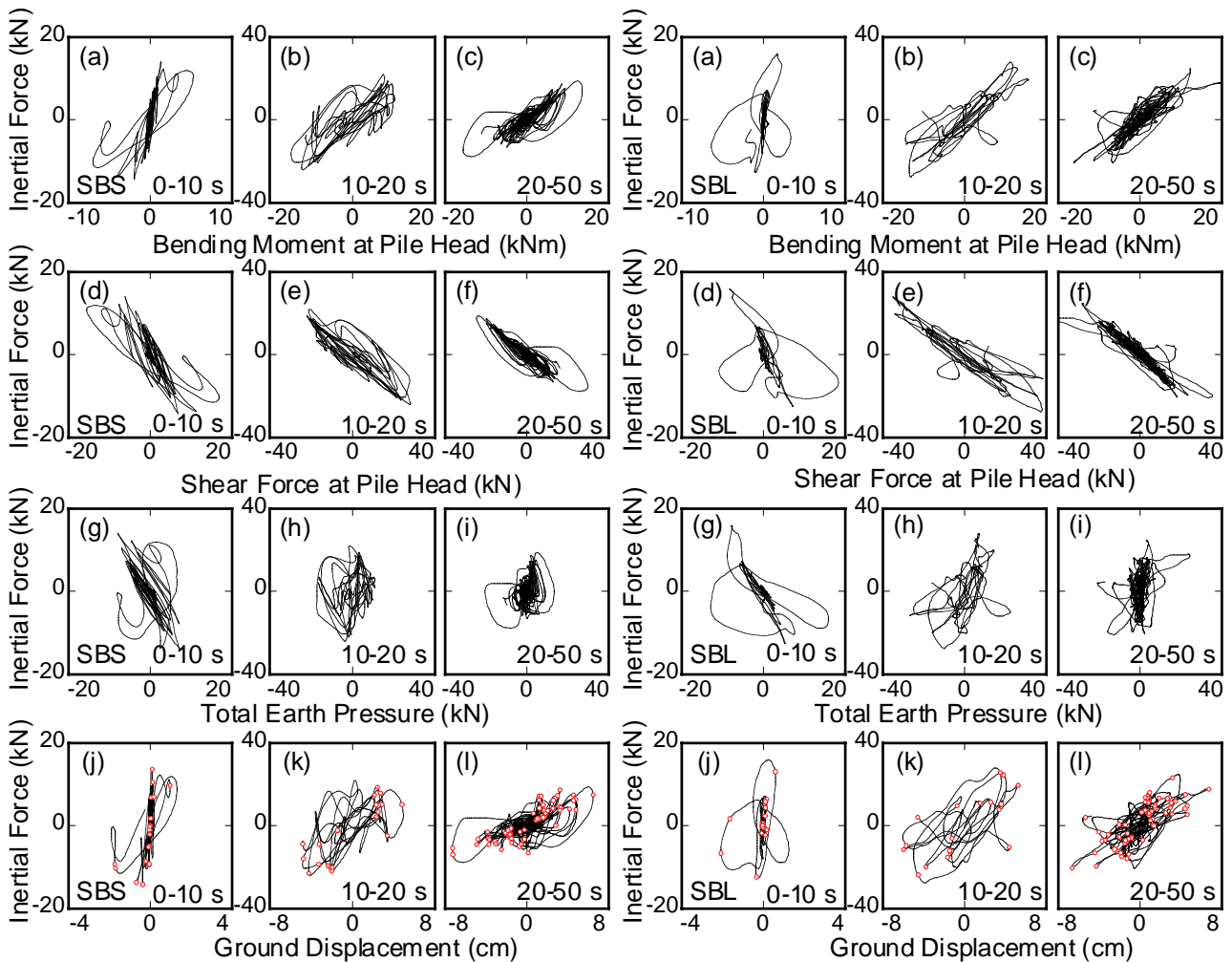


Fig. 7 Relation of inertial force with bending moment, shear force, earth pressure and ground displacement in SBS

Fig. 8 Relation of inertial force with bending moment, shear force, earth pressure and ground displacement in SBL

after liquefaction, as shown in (d)-(f). The drastic change in shear stress transfer to the pile with the development of liquefaction might have been induced by the change in action of earth pressure against the inertial force, as shown in (g)-(i). Namely, the earth pressure that acts against the inertial force before liquefaction and reduces the shear force transmitted to the pile acts with the inertial force after liquefaction, increasing the shear force to the pile.

It is interesting to note that the inertial force and ground displacement after liquefaction are in phase in both SBS and SBL, as shown in (j)-(l). This is because the natural period of the liquefied soil is always greater than that of the superstructure. It is conceivable therefore under such a condition that the effects of soil displacement and inertial force are in phase, increasing the bending moment in piles. The trend is consistent with that observed in dry sand.

5. PSEUDO-STATIC ANALYSIS

5.1 Contribution of inertial and kinematic components

Seismic design of foundations may be made based on either dynamic response or pseudo-static analyses. In this study, a pseudo-static analysis based on Beam-on-Winkler-springs method is conducted to examine its effectiveness in estimating pile stresses in the shaking table tests. Simplified

pseudo-static design methods using p-y curves for pile foundations (Architecture Institute of Japan 2001, Nishimura 1978, and Tokimatsu & Asaka 1998) are based on the following equation:

$$EI \frac{d^4 y}{dz^4} = \Phi k_h B_p (y - \Phi y_g) \quad (2)$$

in which E and I are Young's modulus and moment of inertia of pile, y and y_g are horizontal displacement of pile and ground, z is depth, k_h is coefficient of horizontal subgrade reaction, and B_p is pile diameter.

When the natural period of the ground is longer than that of the superstructure, the pile stress can be estimated assuming that both soil displacement and inertial force are in phase and act on the pile at the same time (Method 1 in Fig. 9).

When the natural period of the ground is smaller than that of the superstructure, the pile stress can be given by square root of the sum of the squares of the two values estimated, assuming that the soil displacement and inertial force are out of phase and act on the pile separately (Method 2 in Fig. 9).

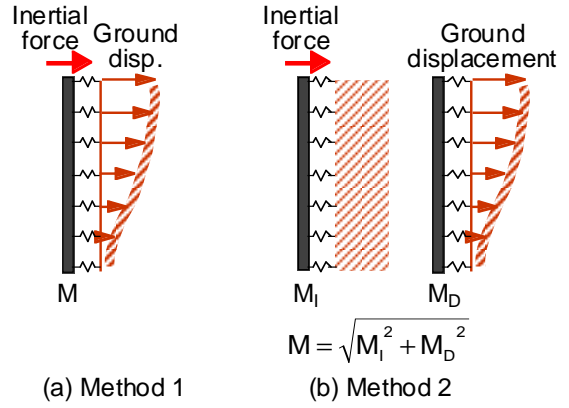


Fig. 9 Combination between inertial and kinematic forces

5.2 p-y curve

To estimate pile stresses, k_h in p-y curve (Eq. (2)) is defined as (Tokimatsu et al. 2002):

$$k_h = k_{h1} \frac{2\epsilon}{1 + |y_r / y_1|} \quad (3)$$

in which y_r is relative displacement between ground and pile ($= y - y_g$), y_1 is reference value of y_r , ϵ is scaling factor for liquefied soil, and k_{h1} is reference value of k_h and can be estimated by (Architecture Institute of Japan 2001, and Japan Road Association 1997):

$$k_{h1} = 80 E_0 B_0^{40.75} \quad (4)$$

$$E_0 = 0.7N \quad (5)$$

in which E_0 (MN/m²) is modulus of deformation, N is SPT N-value, and B_0 is pile diameter in cm.

5.3 Earth pressure acting on foundation

Based on the studies (Zhang et al. 1998 and Tokimatsu et al. 2003) on earth pressure acting on the foundation, the total earth pressure P_E defined in Fig. 4 may be given as:

$$P_E = P_{Ep} \Phi P_{Ea} = \frac{1}{2} \mathfrak{H}^2 B (K_{Ep} \Phi K_{Ea}) \quad (6)$$

in which \mathfrak{H} is unit weight of soil, H and B are height and width of foundation, and K_{Ea} and K_{Ep} are the coefficients of active and passive earth pressures and may be expressed by the following equations:

$$K_{Ea} = \frac{2 \cos^2(\nabla \Phi i)}{\cos^2(\nabla \Phi i)(1 + R) + \cos i \cos(\beta_{mob} + i)(1 - \Phi R) I_{E.1}} \quad (7)$$

$$K_{Ep} = 1 + \frac{1}{2} (R \Phi) \left[\frac{\cos^2(\nabla \Phi i)}{\cos i \cos(\beta_{mob} + i) I_{E.2}} \Phi \right] \quad (8)$$

$$\left[\frac{I_{E.1}}{I_{E.2}} \right] = \left[1 \pm \sqrt{\frac{\sin(\nabla + \beta_{mob}) \sin(\nabla \Phi i)}{\cos(\beta_{mob} + i)}} \right]^2 \quad (9)$$

$$\tan i = k_i \quad (10)$$

$$R = \max \left\{ \Phi, \Phi \left[\frac{O_r}{O_a} \right]^{0.5} \right\} \quad (\text{Active Side}) \quad (11)$$

$$R = \min \left\{ 3, 3 \left[\frac{O_r}{O_p} \right]^{0.5} \right\} \quad (\text{Passive Side}) \quad (12)$$

$$\delta_{mob} = \frac{1}{2} (1 \Phi R) \delta_a \quad (\text{Active Side}) \quad (13)$$

$$\delta_{mob} = \frac{1}{2} (R \Phi) \delta_p \quad (\text{Passive Side}) \quad (14)$$

in which \forall is internal friction angle of sand, i is angle of seismic coefficient in the horizontal direction (k_i), R is lateral strain constraint and is smaller than or equal to 0 in active side and larger than or equal to 0 in passive side, O_r is relative displacement between soil and foundation, δ is friction angle of the surface of the foundation, δ_a and δ_p are friction angles of sand at the active and passive states, and O_a and O_p are reference relative displacements at active and passive states, expressed as:

$$O_a = aH \quad (15)$$

$$O_p = bH \quad (16)$$

in which a is equal to 0.001-0.005, and b is equal to 0.05-0.1.

6. ESTIMATION OF PILE STRESSES IN SHAKING TABLE TESTS BASED ON PSEUDO-STATIC ANALYSIS

To demonstrate the effectiveness of the pseudo-static analysis, the bending moment distributions of the shaking table tests with dry and saturated sands are simulated by the method. The pile stresses in DBS, SBS, and SBL are estimated by method 1 as the natural period of the ground is longer than that of the superstructure while those in DBL is estimated by method 2 as the natural period of the ground is shorter than that of the superstructure. It is assumed that the soil displacement at the ground surface and the inertial force are the maximum values observed in the tests. In this analysis, the N-values in the deposit were estimated by CPT-values measured prior to the shaking table test. It is assumed that ϵ is 0.1, y_1 in Eq. (3) is 1.0 % of pile diameter (Japan Road Association 1997), \forall is 30 degrees, δ_a and δ_p are 15 degrees, and O_a and O_p are 0.5 % and 5 % for the height of the foundation.

Fig. 10 compares the observed and computed moment distributions of the four tests. The com-

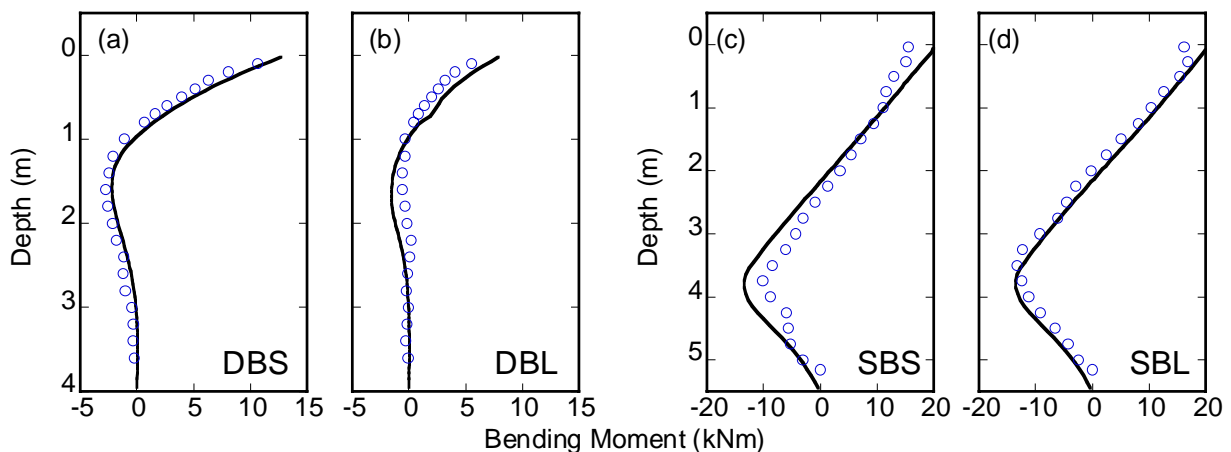


Fig. 10 Distribution of observed and estimated bending moments

puted moment distributions agree reasonably well with the observed ones, indicating that the pseudo-static analysis together with the consideration of effects of ground displacement is promising to estimate pile stress.

7. CONCLUSIONS

The large shaking table tests were conducted to estimate the effects of dynamic soil-pile-structure interaction on pile stress in both dry and saturated sands. The results and analysis have shown the following:

- 1) If the natural period of the structure is less than that of the ground, the kinematic force tends to be in phase with the inertial force, increasing the stress in piles. The maximum pile stress occurs when both inertial force and ground displacement become maxima at the same time and act in the same direction.
- 2) If the natural period of the structure is greater than that of the ground, the kinematic force tends to be out of phase with the inertial force, restraining the pile stress from increasing. The maximum pile stress tends to occur when both inertial force and ground displacement do not become maxima at the same time.
- 3) Above findings are valid for liquefiable sand as well as dry sand. During liquefaction, the kinematic effect becomes significant due to large ground displacement, increasing pile stress.
- 4) The pseudo-static analysis has been proposed, in which the combination of the inertial and kinematic effects is taken into account. The estimated bending moments are in good agreement with the observed values both in dry and saturated liquefied sands. This suggests that the pseudo-static analysis is promising to estimate pile stress with a reasonable degree of accuracy.

Acknowledgments

The study described herein was made possible through two research projects related to soil-pile-structure interaction using the large shaking table at the NIED, including Special Project for Earthquake Disaster Mitigation in Urban Areas, supported by Ministry of Education, Culture, Sports, Science and Technology (MEXT). The authors express their sincere thanks to the above organization.

References

- BTL Committee (1998), "Research Report on liquefaction and lateral spreading in the Hyogoken-Nambu earthquake" (in Japanese).
- Tamura, S., Tsuchiya, T., Suzuki, Y., Fujii, S., Saeki, E. & Tokimatsu, K. (2000), "Shaking table tests of pile foundation on liquefied soil using large-scale laminar box (Part 1 Outline of test)" (in Japanese), *Thirty-fifth Japan National Conference on Geotechnical Engineering*, 1907-1908.
- Tamura, S., Miyazaki, M., Fujii, S., Tsuchiya, T. & Tokimatsu, K. (2001), "Earth pressure acting on embedded footing during soil liquefaction by large-scale shaking table test", *Forth International Conference on Recent Advances in Geotechnical Earthquake Engineering and Soil Dynamics*, Paper No. 6.19.
- Architectural Institute of Japan (2001), "Recommendations for design of building foundations" (in Japanese).
- Nishimura, A. (1978), "Design of structures considering ground displacement" (in Japanese), *Kisoko*, **6**(7), 48-56.
- Tokimatsu, K. & Asaka, Y. (1998), "Effects of Liquefaction-induced ground displacements on Pile Performance in the 1995 Hyogoken-Nambu Earthquake", *Soils and Foundations, Special Issue*, 163-177.
- Tokimatsu, K., Suzuki, H. & Saeki, S. (2002), "Modeling of horizontal subgrade reaction of pile during liquefaction based on large shaking table" (in Japanese), *Journal of Structural and Construction Engineering*, **559**, 135-141.
- Japan Road Association (1997), "Specifications for road bridges, Vol. IV" (in Japanese).
- Zhang, J. -M., Shamoto, Y. & Tokimatsu, K. (1998), "Evaluation of earth pressure under any lateral displacement", *Soils and Foundations*, **38**(2), 143-163.
- Tokimatsu, K., Tamura, S., Miyazaki, M. & Yoshizawa, M. (2003), "Evaluation of seismic earth pressure acting on embedded footing based on liquefaction test using large scale shear box" (in Japanese), *Journal of Structural and Construction Engineering*, **570**, 101-106.

A METHOD TO EVALUATE THE SAFETY OF THE EXISTING PILED FOUNDATIONS AGAINST BUCKLING IN LIQUEFIABLE SOILS

S. Bhattacharya

*Fellow, Centre for Urban Earthquake Engineering, Tokyo Institute of Technology (Japan), Previously Schofield Centre,
University of Cambridge (U.K)*

bhattacharya@cuee.titech.ac.jp; S.Bhattacharya.00@cantab.net

Abstract: Recent research into the pile failure mechanism has shown that there is a fundamental omission in the seismic pile design in liquefiable areas. The current codes of practice for pile design such as EC 8, NEHRP 2000, JRA1996 and IS1893 is based on a bending mechanism where lateral loads due to inertia or slope movement induces bending failure in the pile. These codes omit considerations necessary to avoid buckling of a pile due to the axial load acting on it at all times in an event of soil liquefaction due to the diminishing soil support. These codes are inadequate and buckling needs to be addressed. Bending and buckling require different approaches in design. Bending is a stable mechanism and is dependent on strength whereas buckling is dependent on geometric stiffness and is almost independent of strength. Designing against bending would not automatically suffice the buckling requirements. For pile design, to avoid buckling there is a need to have minimum diameter depending on the depth of liquefiable soil. Thus there is a need to reconsider the safety of the existing piled foundations designed based on the current codes of practice. This paper discusses a way to identify the existing unsafe structures.

1. INTRODUCTION

1.1 Pile-supported Structures still collapse during earthquakes!

Collapse of pile-supported structures in liquefiable soils is still observed after strong earthquakes despite the fact that a large factor of safety against bending due to lateral loads is employed in their design. The failure of the structure is often accompanied by tilting and or settlement of the overall structure without any damage to the superstructure. During excavation following an earthquake, the piles are often observed to form plastic hinges, see for example the piles of NHK building, NFCH building and Showa Bridge Hamada (1992) or a three storied building, Tokimatsu (1997). It has been shown by Bhattacharya (2003) that using "Limit State Design Philosophy", the factor of safety against plastic yielding of a typical concrete pile ranges between 4 and 8. This high factor of safety is due to the multiplication of the partial safety factors due to load (1.5), material stress (1.5), plastic strength factor (ratio of Z_p/Z_E which is 1.67) and practical factors like minimum percentage of reinforcements due to shrinkage or creep in concrete. This suggests that unless wrong foundation design concepts are employed, failure by plastic yielding of piles is unlikely.

It is worth noting that study of failure of structures shows that when failure occurred in structures, they most often resulted due to loads that have been overlooked by the designer or regarded as secondary, rather than inadequate factor of safety. To cite an example is the collapse of 5km of 750mm diameter gas pipe line during testing from the Jamuna Bridge in Bangladesh on 11th June 1998. It has been reported (NCE, 1998) that the main cause of the collapse was the failure to allow in design the weight of the water in the pipe for testing purposes. Bhattacharya (2003), Bhattacharya and Bolton (2004a, 2004b) has shown that there is also a fundamental omission of a load effect in seismic pile design that has contributed to the failure of the many pile foundations. The current method of pile design under earthquake loading, for example JRA 1996, Eurocode 8, NEHRP 2000 is based on a bending mechanism where inertia and slope movement (lateral spreading of soil) induce bending moments in the pile. The next section of the paper aims to show that this hypothesis of pile failure is

inconsistent with some of the observed mode of failure.

1.2 Inconsistency in Observations of Pile Failure with the Current Understanding

This section of the paper highlights some of the inconsistencies of observations of pile failure with respect to the current understanding. They are summarized below:

After the detailed investigation of the failure of piles during 1995 Kobe earthquake, Tokimatsu and Asaka (1998) reports that:

“In the liquefied level ground, most PC piles (Prestressed Concrete pile used before 1980’s) and PHC piles (Prestressed High Strength Concrete piles used after 1980’s) bearing on firm strata below liquefied layers suffered severe damage accompanied by settlement and/or tilting of their superstructure,”.

If lateral spreading is the main cause of failure, why would most of high strength PHC piles collapse in level grounds i.e. in the absence of lateral spreading?

It is a common observation in seismic bridge failure that piers collapse while abutments remain stable, for example Figures 1 (a&b). Figure 1 (a) shows the collapse of one the piers of the Million Dollar Bridge leading to bridge failure. Similar failures were also observed of the Showa Bridge during the 1964 Niigata earthquake; see Figure 1(b).



Figure 1: Failure of bridges in earthquakes; (a): Million Dollar Bridge after the 1964 Alaska earthquake; (b): Showa Bridge after the 1964 Niigata earthquake. Photo courtesy NISEE.

Bhattacharya and Bolton (2004a) notes that in a bridge design, the number of piles required to support an abutment is governed by lateral load due to the fact that the abutment, as well as carrying the dead load of the deck, has to retain earth and fills of the approach roads to the bridge (see Figure 2). On the other hand, the bridge piers (intermediate supports) predominantly support the axial load of the deck. The lateral load acting on the pier during an earthquake is primarily the inertial force. The lateral capacity of a pile is typically 10 to 20% of the axial load capacity. Thus, for a multiple-span bridge having similar span lengths, the number of piles supporting an abutment will be more than that of a pier. It is worthwhile to note that in these examples only bridge piers collapsed while the abutments remained stable. This hints that the failure of bridge pier foundations may be influenced by axial load. In contrast, the current seismic design methods for pile foundations only concentrate on lateral loads.

Furthermore, the lateral loads acting on a bridge pier are only due to the drag force of the liquefied soil and any loads due to non-liquefied crust are unlikely to act. It is surprising that most often only bridge piers fail. This observation is in contradiction to the hypothesis of pile failure by Berrill et al (2001), Hamada (2000). Berrill (2001) analyzed the good performance of the Landing Bridge during the 1987 Edgecumbe earthquake and remarked that the chief threat to the piled foundations comes from the non-liquefied crust and not from the drag force of the liquefied soil.

Hamada (2000) in the 12th World Congress concludes that permanent displacement of non-liquefied soil is a governing factor for pile damage.

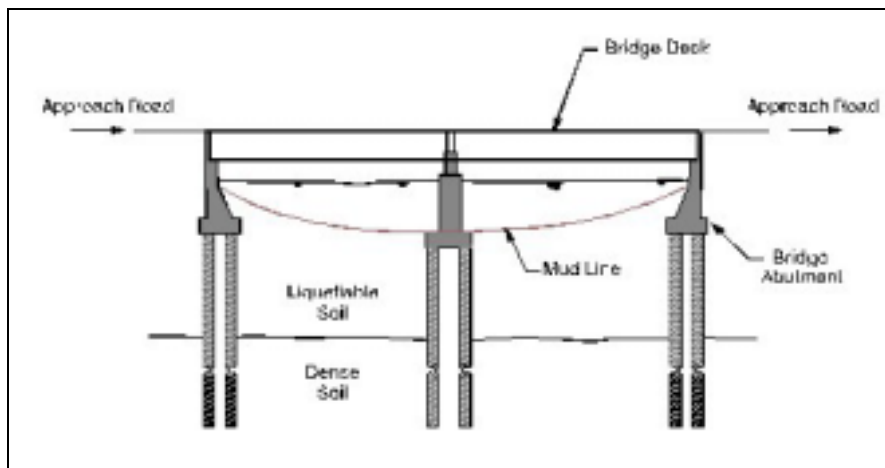


Figure 2: Schematic diagram of a bridge

Bhattacharya (2003), Bhattacharya et al (2004b), Bhattacharya and Bolton (2004a) studied in-depth the well known failure of the Showa Bridge, see Figure 1(b). This bridge was only one month old when the earthquake of Niigata occurred and the bridge collapsed. Details of the failure can be seen in Hamada (1992), Takata et al (1965), and Ishihara (1993). This bridge was studied in-depth as the bridge had steel tubular piles and was only one month old when it collapsed. Thus it is unlikely that the material of the pile corroded and it can be used as a benchmark problem for validation and verification of hypothesis or mechanisms. Figure 3 shows the schematic representation of the failure of the bridge which can be compared with Figure 1(b). As can be seen from Figure 3, piles under pier no. P₅ deformed towards the left and the piles of pier P₆ deformed towards the right, Takata et al (1965). Had the cause of pile failure been lateral spreading, the piers should have deformed identically in the direction of the slope. Furthermore, the piers close to the riverbanks did not fail, whereas the lateral spread is seen to be most severe at these places.

It must be mentioned here that this failure has been widely used as an example of piled foundations collapsed due to lateral spreading, Hamada (1992), Ishihara (1993). Bhattacharya (2003), Bhattacharya et al (2003) has shown that the piles of the Showa Bridge are safe against the JRA (1996) clause about the checks against lateral spreading by a factor of about 1.84. The bridge collapsed in 1964 which is safe against 1996 code and between these years the code was revised at least 3 times viz. 1972, 1980 and 1996.

It has been revealed after the excavation of the NHK building, Showa Bridge, Hamada (1992) and the three-storied building, Tokimatsu et al (1997) that hinges formed in piles occurred within the top third of the pile. Had the cause of pile failure been lateral spreading, the location of the plastic hinge would have been expected at the interface of liquefiable and non-liquefiable layer as this section would experience the highest bending moment. This observation also does not quite match with the current understanding of pile failure.

To summarize, the limitations of the current understanding of pile failure are:

1. The effect of axial load as soil liquefies is ignored.
2. Some observations of pile failure cannot be explained by the current hypothesis.
3. It has been shown, Bhattacharya (2003) that the pile foundation of Showa Bridge, which is considered safe by the JRA (1996) code, actually failed in 1964.

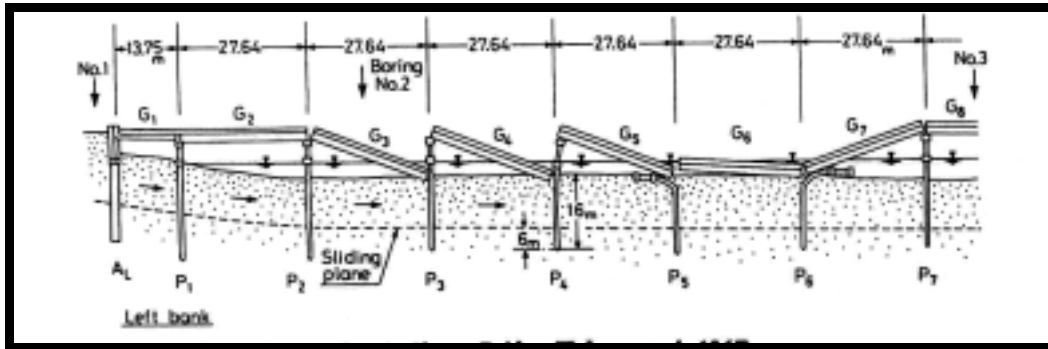


Figure 3: Schematic diagram of the failure of the Showa Bridge after Takata et al (1965). The diagram only shows half of the bridge. It must be noted that the direction of deflection of the piers P5 and P6 contradicts the current understanding.

Earthquakes induce lateral loads on the pile through inertia or slope movement (lateral spreading). But it must also be remembered that piles are normally used to carry vertical loads. These axial loads act at all times on the pile. Piles are long slender members having length to diameter ratio between 25 and 100 or even more, Bond (1989). The piles receive support from the surrounding soil and thus engineers did not see any problem of buckling. But during liquefaction, the stiffness of the soil surrounding the pile comes to near zero value and what will be the effect on these slender members? This is not addressed in the current understanding or codes of practice. An axial load has two distinct effects to a slender member being single or in a framework of many slender columns? They are (1) Reduces the bending strength of the member (Plastic moment capacity); (2) Causing a premature failure due to instability. This effect of axial load has been studied carefully and the missing link in the observations of pile failure and the current understanding could be bridged. Details can be seen in Bhattacharya and Bolton (2004a, 2004b and 2004c), Bhattacharya (2003).

2. A NEW THEORY OF PILE FAILURE

This section will describe a new theory of pile failure. A hypothesis of pile failure was formed based on the analysis of 15 reported case histories of pile foundation performance during earthquakes. This hypothesis was verified using dynamic centrifuge modeling; see Bhattacharya et al (2004a, 2004b), Bhattacharya (2003). Analytical studies also support the hypothesis, Bhattacharya and Bolton (2004a). The hypothesis being verified independently by three different approaches is thus called a theory of pile failure. This theory is based on the combination of two critical phenomena, such as Euler's elastic Critical Load and Critical State Soil Mechanics. The theory is described in Bhattacharya (2003), Bhattacharya and Bolton (2004b), Bhattacharya (2004). This section of the paper describes the basic ingredients of the theory.

2.1 Structural nature of pile

From a structural perspective, axially loaded piles are long slender columns with lateral support provided by the surrounding soil. If unsupported, these columns will fail in buckling instability and not due to crushing of the pile material. Figure 4(a) shows the failure pattern of structures resting on slender columns which would represent a piled building or a bridge in the absence of soil. Thus in the absence of soil, we would expect a pile-supported structure to fail in a similar pattern but it remains to be seen if liquefied soil behaves like "absence of soil". It must be mentioned that this failure is due to the effect of axial load alone. The static axial load at which a frame supported on slender columns (Figure 4(a)) becomes laterally unstable is commonly known as the "Elastic Critical Load" of the frame or the buckling load. The simplest way is to estimate the buckling load of the frame is to find out the Critical Load (P_{cr}) of one pile and multiply by the number of piles. P_{cr} is estimated using Equation 1 where L_{eff} is the "Euler's effective length of an equivalent pin-ended strut". Figure 4(b) shows the concept of effective length of pile adopted from column stability theory to normalise the

different boundary conditions of pile tip and pile head.

$$P_{cr} = \frac{\pi^2 EI}{L_{eff}^2} \quad (1)$$

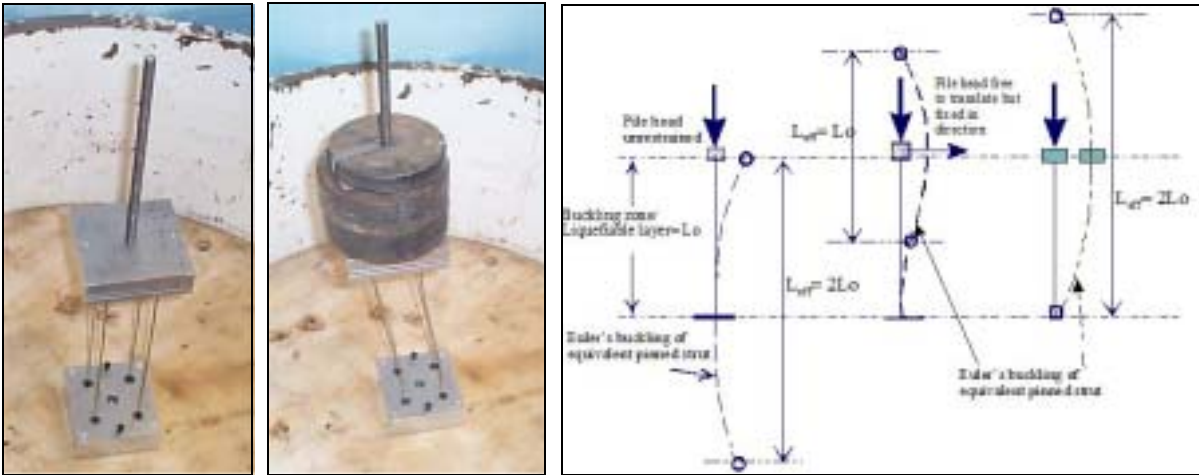


Figure 4: Simple concepts; (a): Buckling of slender columns; (b): Concept of Effective length for different boundary conditions of pile above and below the liquefiable layer.

Stability analysis of elastic columns, Timoshenko and Gere (1961) shows that the lateral deflections caused by lateral loads are greatly amplified in the presence of axial loads. In other words, in the presence of lateral loads a frame will buckle at a much lower load. Figure 5(a) shows a graph of buckling amplification factor plotted against the normalized axial load (P/P_{cr}) where P denotes the applied axial load. It can be observed from the graph that at 50% "Critical Load" the amplification of lateral deflection due to lateral loads is about 1.5 times. At these large deflections, secondary moments will generate which will lead to more deflections and thus more moment. It is thus advisable to keep the axial load within 35% of Euler's load and in these cases there are no chances of amplification. This is the approach of the structural engineers. It must be mentioned here that structural engineers generally prefer to keep a factor of safety of about 3 against linear elastic buckling to take into account the eccentricity of load, deterioration of elastic stiffness due to plastic yielding and imperfections.

Figure 5(b) shows a typical graph showing the allowable load of a pile and the buckling load, if unsupported. It may be observed that as the length of the pile increases the allowable load increases but the buckling load decreases by the square of the length. Thus, if unsupported for a particular length a buckling instability problem might occur for most piles. Dynamic centrifuge tests were carried out by Bhattacharya (2003) to verify the hypothesis of pile failure of buckling instability, Bhattacharya (2003), Bhattacharya et al (2004a, 2004b), Bhattacharya and Bolton (2004a, 2004b, 2004c). The tests were carried out in level grounds to avoid the effects of lateral spreading. Figure 6(a) shows the failure of piles observed in the centrifuge tests and in each case of the failure the pile head mass rotated. It is quite similar to the failure of the piled Kandla tower in Figure 6(b). Figure 6(c) shows the hinge formation in the model pile at the upper part which is similar to the observed hinge formation field case records, see Figure 6(d). Thus a failure mode observed in the field could be replicated in the centrifuge test. It shows that buckling is a feasible failure mechanism.

3. IMPLICATIONS TO PRACTICE

Buckling and bending has two different approaches in design. Current design codes are all based on bending. Bending is a stable mechanism as long as the pile is elastic, i.e. if the lateral load is withdrawn; the pile comes back to its initial configuration. This failure mode depends on the bending strength (moment for first yield, M_Y ; or plastic moment capacity, M_P) of the member under consideration. On the other hand, buckling is an unstable mechanism. It is sudden and occurs when the

elastic critical load is reached. It is the most destructive mode of failure and depends on the geometrical properties of the member, i.e. slenderness ratio, and not on the yield strength of the material.

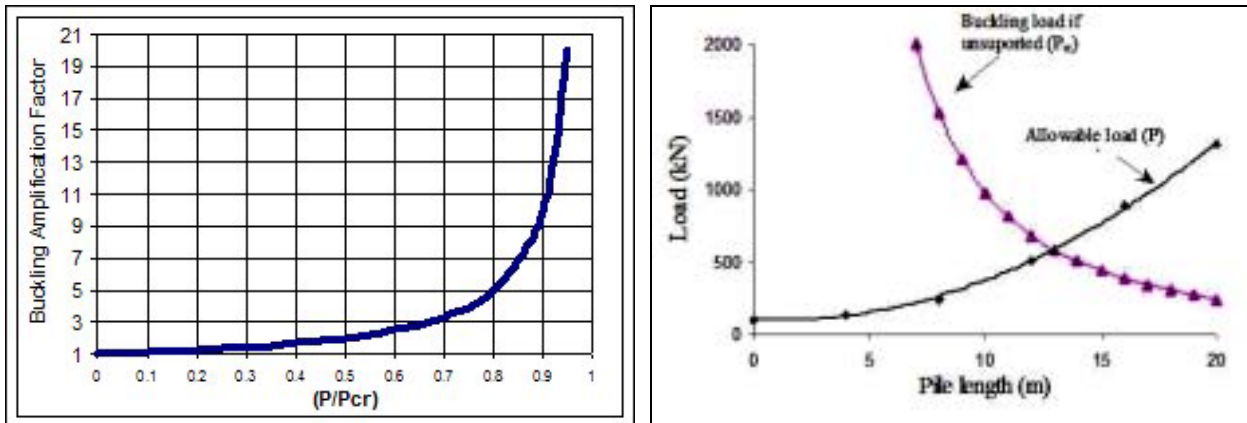


Figure 5: (a): Buckling amplification factor and normalized axial load; (b): Allowable load (P) and Buckling load (P_{cr}) of a pile, if unsupported.



Figure 6: Model test and field case history; (a): Pile foundation after the dynamic centrifuge test; (b): Failed Kandla Port tower; (c): Hinge formation in the centrifuge test; (d): Hinge formation in a building, Tokimatsu et al (1997).

Bending failure may be avoided by increasing the yield strength of the material, i.e. by using high-grade concrete or additional reinforcements, but it may not suffice to avoid buckling. To avoid buckling, there should be a minimum pile diameter depending on the depth of the liquefiable soil. This section of the paper describes a new approach. There is also a need to reconsider to safety of the existing piled foundations designed by current codes of practice i.e. based on bending mechanism.

3.1 Need of a new design method to include buckling

Figure 7(a) shows schematically the possible modes of pile failure. Details of the description can be seen in Bhattacharya (2003), Bhattacharya et al (2004a). However, it is clear that a piled foundation (a): has to sustain the axial load at all times without buckling; (b): should not form a collapse mechanism under the combined action of lateral load and axial load. Figure 7(b) shows a graph of minimum pile diameter required based on the depth of liquefiable soil from Bhattacharya (2003).

3.2 A simple method to identify the existing unsafe structures

This section of the paper will describe a way to identify the structures which may be unstable in an event of liquefaction. The examples of LPG tanks, Figure 8(a), during Kobe earthquake is taken to demonstrate the efficacy of the method. In the same site, tank 101 performed well while tank 106 failed. Let P be the axial load acting on each pile beneath the piled tank shown in Figure 8(b). It will be assumed that each pile is equally loaded. For a pile fixed at the tip and fixed in direction but free to translate at the top, the effective length (L_{eff}) is the unsupported length Figure 4(b). Considering the effect of lateral loads, it is reasonable to adopt a 35% of critical as safe load, following Figure 5(a) and

as mentioned in the text. A parameter called critical depth (H_c) is now defined to identify the unsupported length of the pile required for instability. For this type of structure (i.e. bottom part of the pile embedded firmly in non-liquefiable layer and the top part is free to translate but fixed in direction) H_c , is given by equation 2.

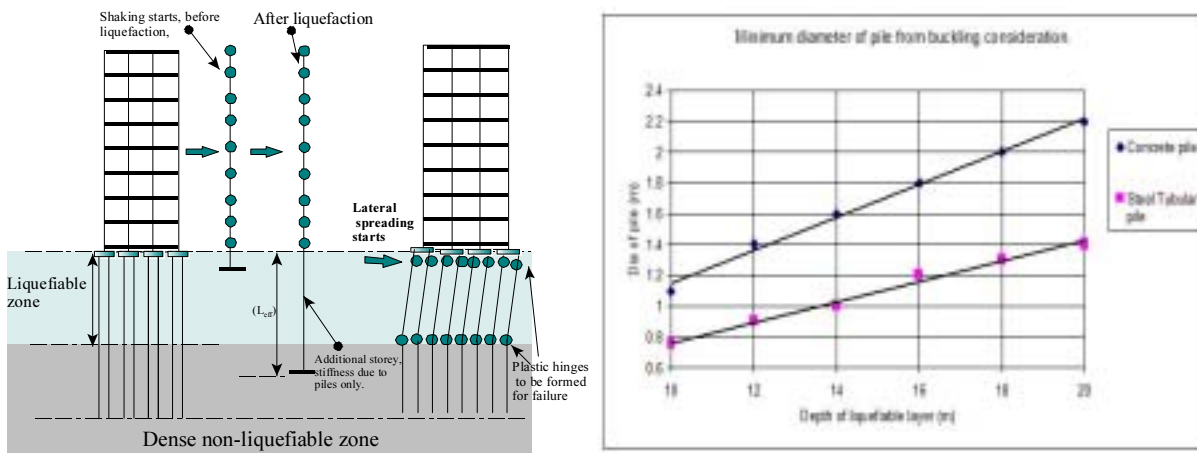


Figure 7: (a) Possible failure modes of pile foundation in a liquefiable region; (b): A proposed minimum pile diameter requirement to avoid buckling, details can be seen in Bhattacharya (2003).

$$P = 0.35P_{cr} = 0.35 \frac{\pi^2 EI}{H_c^2}, \text{ which leads to } H_c = \sqrt{\frac{3.45EI}{P}} \quad (2)$$

It must be noted that the critical depth concept is a by-product of L_{eff} but it is particularly fruitful from practical point of view to evaluate the safety of existing piled foundations prone to axial instability. A piled structure becomes unstable for $H_c < D_L$, where D_L is the depth of liquefiable layer. Table 1 estimates the critical depth for the tank foundations. P is estimated based on the allowable load concept, Bhattacharya (2003). Relevant details of the case history can be seen in Ishihara (1997). Analysis of the case history can be seen in Bhattacharya (2003).

Table 1: Estimation of critical depth

Case history	EI of the pile	P	H_c (Eq2)	D_L (Depth of liquefiable soil)	Remarks
LPG Tank 101	$1.79 \times 10^9 \text{ N.m}^2$ 1.1m dia RCC	4.1MN	38.8m	15m	Here $H_c > D_L$ and thus should be stable. It performed well
LPG Tank 106	$11.15 \times 10^6 \text{ N.m}^2$ 0.3m dia RCC hollow	0.46MN	9.14m	15m	Here $H_c < D_L$ and thus should be unstable. It failed

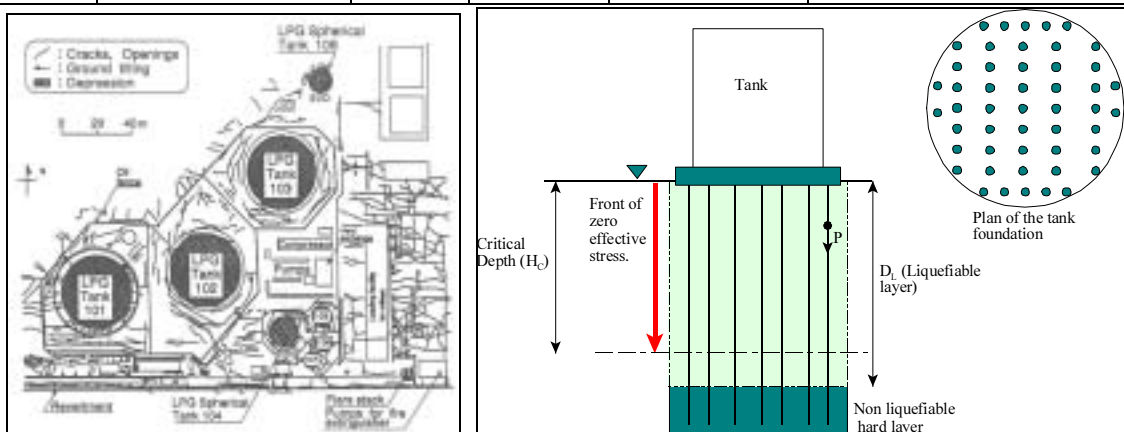


Figure 8: LPG tanks (a): Tanks 101 performed well while tanks 106,107 failed; (b): Schematic diagram of a piled tank.

The method is valid for the particular type of piled foundations mentioned in the text i.e. large pile caps or piled rafts with embedment of at least 6 times the diameter of the pile in the non-liquefied layer beneath the liquefiable layer. For other boundary conditions, the critical depth H_C will change depending on the fixity of the pile below and above the liquefiable soil. This can be easily computed based on the equation 1 and Figure 4(b) but will be of the same form as equation 2. After checking the stability against buckling, the designer needs to check against the formation of a collapse mechanism as shown in Figure 7(a). While checking against the collapse mechanism, the reduction of bending stiffness of the pile needs to be considered to take into account the effect of the axial stress.

4. CONCLUSIONS

Buckling is a feasible pile failure mechanism in areas of seismic liquefaction. To avoid buckling there is a requirement of a minimum diameter of pile based on the depth of liquefiable soil. In contrast, current understanding is based on bending mechanisms. Buckling and bending requires different approach in design. Designing against bending would not automatically suffice the buckling requirements. Thus there is a need to reexamine the safety of existing piled foundations designed based on bending mechanism. A simple method to evaluate such safety is proposed in this paper. Designers should use large diameter pile is instead of a group of small diameter pile.

References:

- Berrill, J.B., Christensen, S. A., Keenan, R. P., Okada, W. and Pettinga, J.R (2001): "Case Studies of Lateral Spreading Forces on a Piled Foundation", *Geotechnique* 51, No. 6, pp 501-517.
- Bond, A. J (1989): "Behaviour of displacement piles in over-consolidated clays", PhD thesis, Imperial College (UK).
- Bhattacharya, S. Madabhushi, S.P.G and Bolton, M.D (2004a): "An alternative mechanism of pile failure during seismic liquefaction", *Geotechnique* 54, (April/May). Also available as Technical report of Cambridge University CUED/D-SOILS/TR-324(October 2002), can be seen at http://www-civ.eng.cam.ac.uk/geotech_new/TR/TR324.pdf
- Bhattacharya, S, Madabhushi, S.P.G., Bolton, M.D, Haigh, S.K. & Soga, K (2004b): "A reconsideration of the safety of the piled bridge foundations in liquefiable soils", Accepted for publication in *Soils and Foundations*. Available as Technical Report of Cambridge University, TR 328; can be seen at http://www-civ.eng.cam.ac.uk/geotech_new/TR/TR328.pdf
- Bhattacharya, S (2004), "Pile supported structures still collapse during earthquakes. What is the missing load in the design method?" Research Report, Tokyo Institute of Technology, Japan Feb 2004.
- Bhattacharya, S and Bolton, M.D (2004a): "A fundamental omission in seismic pile design leading to collapse", *Proc 11th International Conference on Soil Dynamics and Earthquake Engineering*, 7-9th Jan, Berkeley, pp 820-827.
- Bhattacharya, S and Bolton, M.D (2004b): "Errors in design leading to pile failure during seismic liquefaction", Paper 12A-12; *Proc. 5th International Conference on Case Histories in Geotechnical Engineering*, New York, April 13-17.
- Bhattacharya, S and Bolton, M.D (2004c): "Pile failure during earthquake Liquefaction-theory and practice"; *Int. Conf on Cyclic Behavior of soil and liquefaction phenomena*, Bochum, Germany, Publisher: AA Balkema., 31st Mar-2nd Apr.
- Bhattacharya, S (2003), "Pile Instability during earthquake liquefaction"; PhD thesis, University of Cambridge (U.K).
- Hamada, M (1992): "Case Studies of liquefaction and lifelines performance during past earthquake", Technical Report NCEER-92-0001, Volume-1, Japanese Case Studies, National Centre for Earthquake Engineering Research, Buffalo, NY
- Hamada (2000): "Performances of foundations against liquefaction-induced permanent ground displacements", 12th WCEE,
- Ishihara, K (1997): Terzaghi oration: "Geotechnical aspects of the 1995 Kobe earthquake", *Proc of ICSMFE*, Hamburg.
- Ishihara, K (1993): Rankine Lecture: "Liquefaction and flow failure during earthquakes", *Geotechnique* 43, No-3, pp 351-415
- NEHRP (2000): Commentary for FEMA (USA 369) on seismic regulations for new buildings and other structures.
- NISEE: National Information Services for Earthquake Engineering, University of California, Berkeley.
- NCE (1998); *New Civil Engineers magazine*, Institution of Civil Engineers (London).
- Takata, T., Tada, Y., Toshida, I, and Kuribayashi, E (1965): "Damage to bridges in Niigata earthquake". Report No 125-5, Public Works Research Institute (in Japanese).
- Timoshenko, S.P and Gere, J.M (1961): "Theory of elastic stability", McGraw-Hill book company, New York
- Tokimatsu K. and Asaka Y (1998): "Effects of liquefaction-induced ground displacements on pile performance in the 1995 Hyogoken-Nambu earthquake", *Special issue of Soils and Foundations*, pp 163-177, Sep 1998.
- Tokimatsu K., Oh-oka Hiroshi, Satake, K., Shamoto Y. and Asaka Y (1997): "Failure and deformation modes of piles due to liquefaction-induced lateral spreading in the 1995 Hyogoken-Nambu earthquake", *Journal Struct. Eng. AIJ (Japan)*, No-495, pp 95-100.

1-G MODEL TEST ON PILE-SOIL INTERACTION IN LATERAL FLOW OF LIQUEFIED GROUND

J. Kuwano¹⁾, A. Takahashi²⁾, Y. Yano³⁾ and T. Saruwatari⁴⁾

1) Associate Professor, Department of Civil Engineering, Tokyo Institute of Technology, Japan

2) Research Associate, Dept. of Civil and Environmental Engineering, Imperial College, London, U.K.

3) Mitsubishi Jisho Sekkei Inc., Tokyo, Japan

4) Graduate Student, Department of Civil Engineering, Tokyo Institute of Technology, Japan

jkuwano@cv.titech.ac.jp

Abstract: This paper describes an experimental study on lateral resistance of a pile in liquefied sand. In order to avoid complication in interpretation of the test results and to easily observe the behavior of soil surrounding the pile, the pile was modeled as a buried cylinder that corresponded to a sectional model of the pile at a certain depth in subsoil. The deformation of the soil surrounding the cylinder was successfully observed by digital video camera. Loading rate effects on the lateral resistance of the cylinder was also investigated.

1. INTRODUCTION

Detailed observations on damage of pile foundations after the Hyogo-ken Nambu Earthquake of 1995 revealed that pile cracking and structure hinging occurred at the pile cap or the interfaces between soil layers having different lateral stiffness (e.g. Matsui & Oda, 1996; Fujii et al., 1998). This kind of damage was mainly found in sites where liquefaction took place particularly when large lateral movements of liquefied soil overlaid non-liquefied soil occurred.

The effects of large lateral soil movement, especially liquefaction-induced lateral spreading of soil, on the failure and deformation of the piles have been experimentally investigated using geotechnical centrifuges by many researchers (e.g. Abdoun & Dobry, 1998; Horikoshi et al., 1998; Satoh et al., 1998; Takahashi et al., 1998). In these researches, shaking tables were used to simulate the ground motions during earthquakes. Information derived from the shaking table tests is seen to be of value in demonstrating the actual behavior of piles and soils during earthquakes. However, the actual behavior of piles is complicated and affected by several factors. Investigating the effect of each factor from the complicated behavior observed in the shaking table tests is not a straightforward process.

In order to avoid this complication in their interpretation and to easily observe the soil surrounding the pile, the pile was modeled as a buried cylinder that corresponded to a sectional model of the pile at a certain depth in subsoil (Fig.1). Based on almost the same concept, measurement of the drag force of the buried cylinder embedded in sand was carried out by Towhata et al. (1999). However, as their tests were conducted under very low initial over burden pressure, it is very difficult to make a comparison between the test results and actual phenomena observed in the field. In order to create a realistic stress condition in the model ground, the model was prepared in a sealed container and the over burden pressure was applied to the ground surface by a rubber pressure bag.

This paper focuses on observing the deformation of the liquefied soil surrounding the pile when a large relative displacement between the pile and the soil is induced. The loading rate effect on the lateral resistance of the pile in the liquefied sand is also investigated.

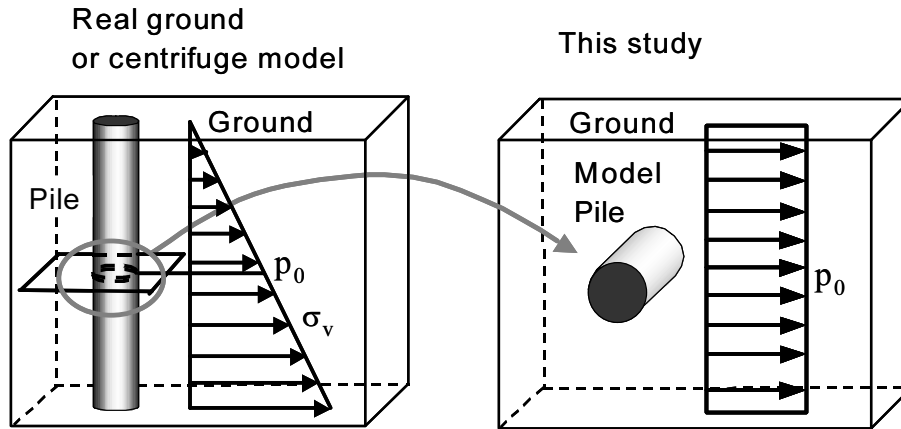


Figure 1. Modeling of pile in this study.

2. TEST PROCEDURES AND CONDITIONS

2.1 Test procedures

The model setup used in this study is schematically illustrated in Fig.2. An aluminum model container was used with inner sizes of 450mm in width, 150mm in breadth, and 250mm in height. The front face of the box was a transparent window to allow observing deformation of the model ground. A pressure bag made of rubber was attached underneath the top lid of the container to apply an over burden pressure, P_A , on the surface of the soil. A fluid tank was connected to the bottom of the box to supply and drain out fluid and to apply back pressure, P_B , to the pore fluid of the soil.

Figure 3 shows an aluminum-made-cylinder equipped with pore and earth pressure transducers. The surface of the cylinder was made smooth by the fabricator. Rubber sheets were put on both ends of the cylinder for lubrication and to prevent sand particles from getting into the gap between the cylinder and the side walls of the container. Two rods were connected to the center of the cylinder. Two load cells were inserted into the respective rods near the cylinder to avoid the influence of friction in measuring the net lateral force on the cylinder. The cylinder was actuated back and forth through the rods by an electro-hydraulic actuator. The actuator was mounted on the side wall of the model container.

Toyoura sand, uniformly graded sub-angular quartz sand ($D_{50}=0.19\text{mm}$) was used for the

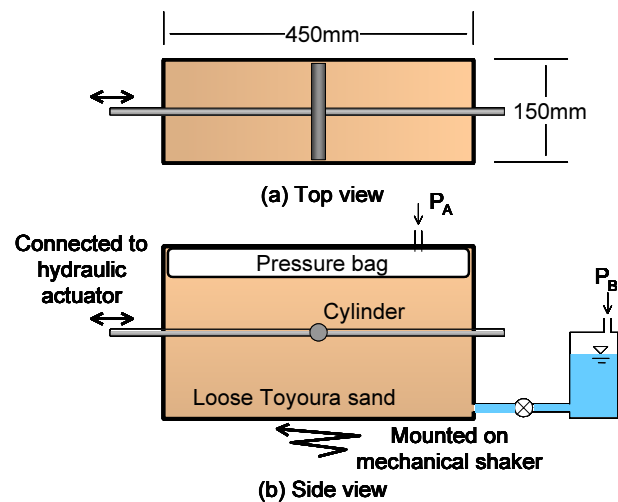


Figure 2. Schematic illustration of model

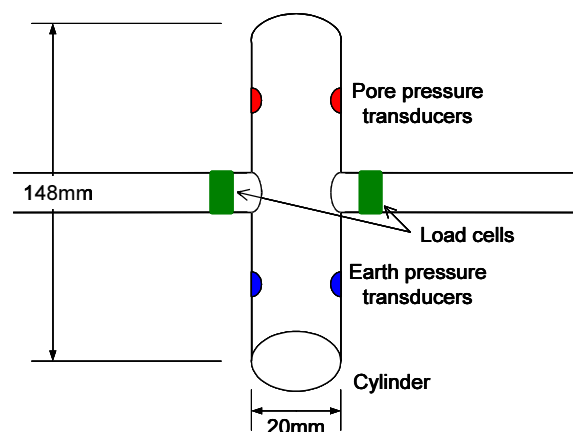


Figure 3. Schematic illustration of cylinder

Table 1. Test conditions.

Case	Pore fluid material	Back pressure P_B (kPA)	Cylinder loading rate V (mm/s)	Shaking
SW1Q	water	49	1 (monotonic)	X
SW10Q	water	49	10 (monotonic)	X
SW1	water	0	1 (monotonic)	O
SW10	water	0	10 (monotonic)	O
SW100	water	0	100 (cyclic)	O
SM1	methyl cel. sol.	0	1 (cyclic)	O
SM10	methyl cel. sol.	0	10 (cyclic)	O
SM100	methyl cel. sol.	0	100 (cyclic)	O
SM10N	methyl cel. sol.	0	10 (cyclic)	X
SM100N	methyl cel. sol.	0	100 (cyclic)	X

model. The model was prepared by the air pluviation method to achieve the relative density of 30~40%. It was saturated up to the ground surface with de-aired water or methyl cellulose solution under a negative pressure of 98kPa in a large tank by applying a vacuum. Japanese noodles 'somen' were placed between the model ground and the transparent window as markers to observe deformation of the ground. After the saturation, the top lid of the box was attached and the over burden pressure was applied to the soil under the drained condition.

Having prepared the model, the model container was set on the mechanical shaker and the electro-hydraulic actuator was attached to the container. In the tests, the horizontal shaking of the container started two seconds prior to the pile loading. This duration was enough to liquefy the model ground. A horizontal shaking was applied to the container by sinusoidal waves with a frequency of 50Hz and a maximum acceleration of approximately 5g. A period of shaking was 10 seconds. During the tests, acceleration of the container, horizontal load and displacement of the cylinder and earth pressure and pore fluid pressure around the cylinder were measured. Movement of the cylinder and the ground was recorded by a digital video camera.

2.2 Test Conditions

Table 1 shows the test conditions in this study. Effects of the ground vibration and the loading rate of the cylinder on the lateral resistance of the cylinder were investigated. In all the cases, the applied over burden pressure was $P_A=49\text{kPa}$. The loading rate of the cylinder, V , was varied from 1mm/s to 100mm/s. In the cyclic loading tests, the symmetrical triangular waves were applied in order to achieve a constant loading rate.

In cases SW1, SW10, SW100, SM1, SM10 and SM100, a horizontal sinusoidal motion was applied to the container to generate the excess pore fluid pressure in the model. Meanwhile, in cases SW1Q and SW10Q, pore pressure increase P_B of 49kPa was applied to the soil after the consolidation of the soil at $P_A=49\text{kPa}$ without ground vibration. The effective confining stress of the model became almost zero by increasing the back pressure without ground vibration on the condition that the model was subjected to almost the same stress history that the models in the other cases experienced. This stress condition is defined as artificial soil "liquefaction without ground vibration" in this study. SM1N and SM100N were the tests in which the cylinder was moved back and forth with the initial condition of no liquefaction.

At the beginning, de-aired water was used as the pore fluid. However, considering the partial drainage around the cylinder, the migration velocity of water was relatively large, as the diameter of

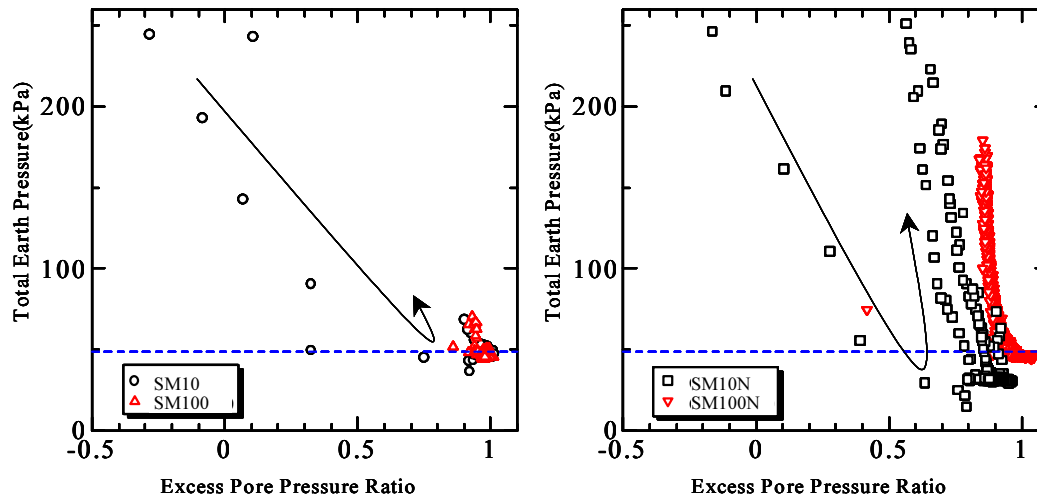


Figure 4. Total earth pressure vs. excess pore pressure on the cylinder surface (SM10, SM100, SM10N & SM100N).

the cylinder was very small compared with the actual pile. In order to resolve the problem, in the latter half of the series of the tests, the scaling laws of the centrifuge modeling were adopted, i.e. a higher viscosity fluid (methyl cellulose solution) was used as the pore fluid to avoid conflict with the scaling laws for the time of dynamic events and seepage. The viscosity of the methyl cellulose solution was 50 times higher than that of fresh water. With this similitude rule, measured lateral resistance of the 20mm-diameter cylinder corresponds to the lateral resistance of the 1m-diameter pile at a depth of 5m. Loading rate of 1mm/s corresponds to the situation of the pile in a very slow flow of liquefied soil, while that of 100mm/s corresponds to the vibration of the pile during an earthquake.

3. TEST RESULTS AND DISCUSSIONS

3.1 Earth Pressure and Lateral Resistance on the Cylinder with Excess Pore Pressure

Total earth pressure is plotted against excess pore pressure ratio in Fig.4 for the cases of SM10, SM100, SM10N and SM100N. Pressures shown here are measured on the initially loaded side surface of the cylinder and the excess pore pressure is normalized by the initial over burden pressure, $p_0 = P_A$. In case SM10, total earth pressure drastically increased in the first cycle, associated with negative excess pressure. Total earth pressure then converged almost 49 kPa in the following cycles in which excess pore pressure ratio was kept almost 1. In case SM10N also, the total earth pressure increased rapidly with the excess pore pressure drop caused by dilative behavior of soil with the movement of pile. Unlike SM10, the total earth pressure increased and decreased repeatedly in the following cycles. However, when the excess pore pressure ratio increased to be over 0.9, the total earth pressure kept almost constant value of 49 kPa without showing dilative behavior of solid ground. The ground behaved like liquid. Cases SM100 and SM100N showed almost the same tendency.

Lateral resistances of cylinder against displacement in cases SW1Q, SW10Q, SW1 and SW10 are plotted in Fig.5. The lateral resistance is the lateral force acting on the cylinder divided by a projected area of the cylinder on a vertical plane. Lateral force is the difference of forces measured by the load cells on the left and right rods. In the figure, lateral resistance, p , and displacement of the cylinder, δ , are normalized by an initial over burden pressure, $p_0 = P_A$, and the diameter of the cylinder, D , respectively. Herein the normalized displacement, δ/D , is called the reference strain, γ . Irrespective of the method inducing liquefaction, the larger loading rate makes the lateral resistance larger. Further discussion on the loading rate effect will be made later.

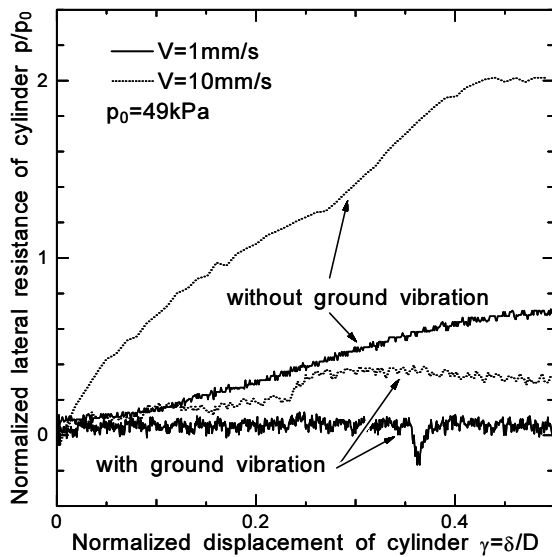


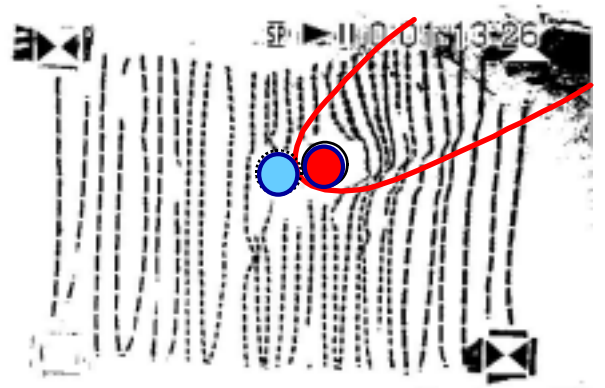
Figure 5. Lateral resistance against lateral displacement of cylinder (SW1Q, SW10Q, SW1 & SW10).

Regarding the difference in the method used to induce liquefaction, the lateral resistances for the cases without vibration of the ground are remarkably larger than those for the cases with vibration. Fig.6 shows observed deformation of the soil surrounding the cylinder just after loading. The black lines are noodle markers placed vertically on the soil before the tests. Without ground vibration, the large amount of soil in front of the cylinder moved forward resulting in a heaving of the ground surface of the front side. On the other hand, when the shaking was applied to the container, deformation of the soil was quite limited in the area adjacent to the cylinder. The difference in the soil area influenced may directly affect the lateral resistance of the cylinder as shown in Fig.5. The vibration of the ground may cause instability in the contacts of the soil particles and reduce the resistance of the surrounding soil against the movement of the cylinder.

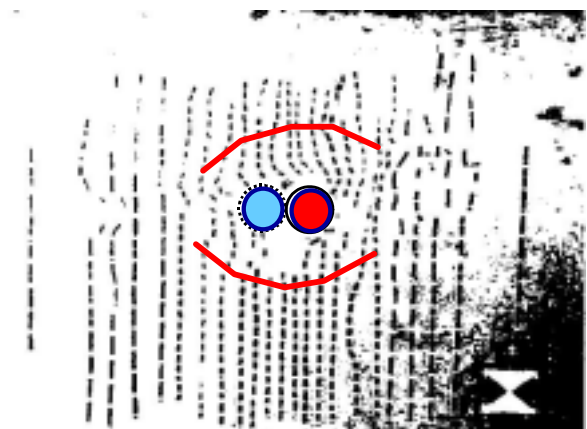
3.2 Loading Rate Effects on Lateral Resistance

Figure 7 shows the first loops of the relationship between the lateral resistance and displacement of the cylinder in cases SM1, SM10 and SM100. In these cases, the loading rate was varied from 1mm/s to 100mm/s, and the cylinder first moved toward the actuator-side, i.e. the leftward displacement is taken as negative. The initial resistance was negligibly small in all the cases. The larger lateral resistance is mobilized as the loading rate becomes higher. The lateral resistance was mobilized only after a certain amount of displacement was developed depending on the loading rate.

The point where the gradient of the loop starts to increase is here defined as a resistance transformation point. The normalized displacement at the point is referred to as the reference strain of resistance transformation point, γ_L , as shown in Fig.8. This reference strain was originally introduced by Yasuda et al. (1998) as the point that the shear strength of soil starts to recover in a post liquefaction stress-strain relation. Reference strains of resistance transformation point in the first loading are plotted against loading rate in Fig.9. In the case of the smallest loading rate, as no obvious mobilization of the lateral resistance was observed in the range of the pile displacement imposed in



(a) Without ground vibration (SW10Q)



(b) With ground vibration (SW10)

Figure 6. Deformation of surrounding soil just after loading.

this study, the reference strain must be larger than the value shown in the figure. The smaller loading rate makes the reference strain of resistance transformation point larger. This tendency may be associated with not only the dilatancy characteristics of sand but also pore fluid migration around the cylinder.

Figure 10 shows the time histories of the lateral resistance, the displacement of the cylinder and excess pore fluid pressure around the cylinder in cases SM1 and SM10. It should be noted that the base motion continued only until the end of the first half of the loading cycle in the 1mm/s loading rate case, as the period of the container shaking was 10 seconds. Excess pore fluid pressure of the soil surrounding the cylinder was measured by the pressure transducers attached to the cylinder shown in Fig.3. If we look at the first quarter cycle of the last half of the first loading cycle, in both the cases, the pore pressure on the side of the movement direction (the dotted line) once slightly increased by the sand contraction, then it showed rapid decrease due to the sand dilation. Suction force on the back side of the cylinder, while the pressure on the back side (the solid line) monotonically decreased due to the suction force.

As a result, the pore pressure decreased on both sides when the maximum displacement of the cylinder was imposed, though the pressure on the side of the direction of movement was larger than that on the other side in both the cases.

Comparing the pore pressure responses in SM1 ($V=1\text{mm/s}$) to those in SM10 ($V=10\text{mm/s}$), the decrease in the pore pressure was smaller, and the displacement of the cylinder when the excess pore fluid pressure started to decrease was larger for the smaller loading rate. It is because the suction force on the back side of the cylinder will be small when the hydraulic conductivity of the sand is sufficiently larger than the cylinder loading rate. This difference in pore pressure responses would directly affect the cylinder displacement required for the lateral resistance mobilization, i.e., the reference strain of resistance transformation point shown in Fig.9.

Lateral resistances of the cylinder at $\gamma=\delta/D=0.1, 0.2,$ and 0.4 are plotted against cylinder loading rate normalized by the soil

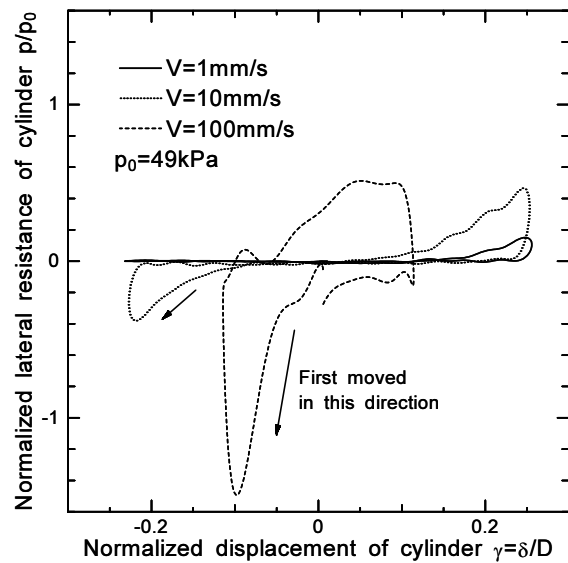


Figure 7. Lateral resistance against lateral displacement of cylinder (SM1-SM100)

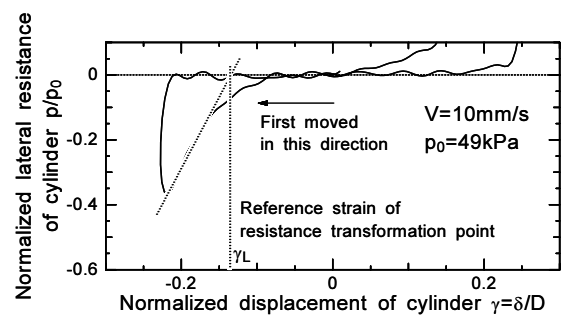


Figure 8. Definition of reference strain of resistance transformation point γ_L

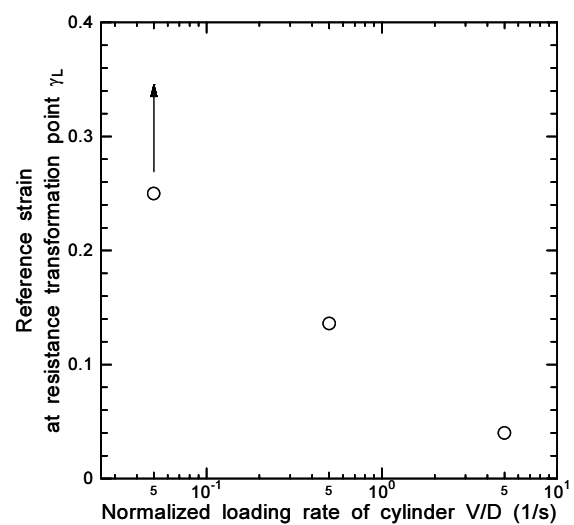


Figure 9. Reference strain of resistance transformation point against loading rate (SM1-SM100)

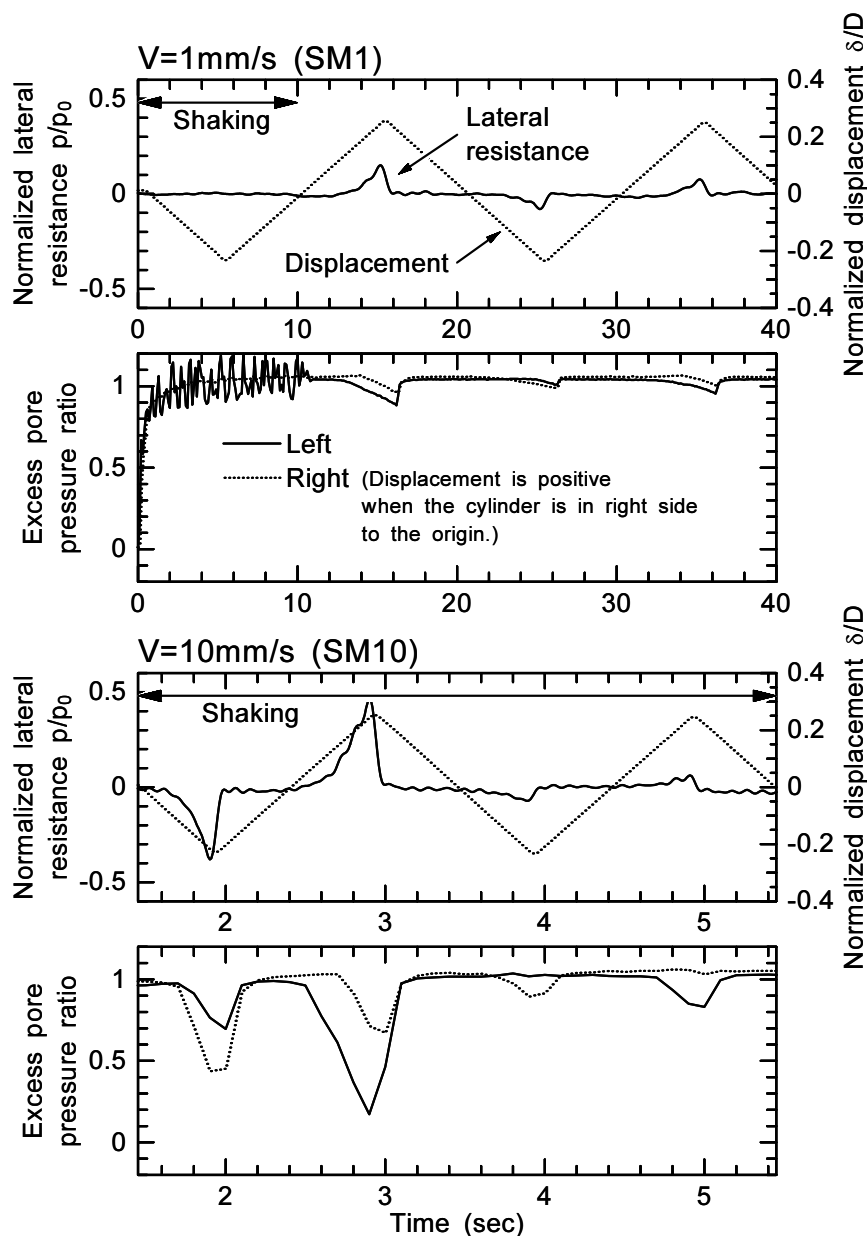


Figure 10. Time histories of lateral resistance and displacement of cylinder and excess pore pressure around cylinder (SM1 & SM10)

hydraulic conductivity in the first loading in Fig.11. The lateral resistance at $\delta/D=0.1$ becomes remarkably larger when $V/k=10^4$. The threshold V/k value for the lateral resistance at $\delta/D=0.1$ exists between 10^3 and 10^4 for the 1m-diameter pile in the medium loose Toyoura sand. This threshold V/k for the lateral resistance varies with δ/D , as the cylinder displacement required for the lateral resistance mobilization depends on V/k . Let us assume piles in a lateral spreading soil that moves 1m in 10 seconds earthquake period, i.e. $V=0.1\text{m/s}$. If the hydraulic conductivity of the liquefied soil is 10^{-5}m/s , V/k becomes 10^4 , and the large earth pressure acts on the piles. If k is larger than 10^{-4}m/s , the pressure would become smaller.

All indications in this section support that the pore fluid migration rate, i.e. the hydraulic conductivity of the soil with respect to the loading rate, is the crucial factor for mobilization of the lateral resistance of a buried structure in liquefied soil.

4. CONCLUSIONS

Lateral loading tests on the buried cylinder were conducted to study the lateral resistance of a pile in liquefied soil, focusing on observation of the deformation of the liquefied soil surrounding the pile when a large relative displacement between the pile and the soil is induced. The loading rate effect on the lateral resistance of pile in the liquefied soil was also investigated. The following conclusions were obtained in this study:

- 1) The deformation of the soil surrounding the cylinder could be successfully observed by the digital video camera through the transparent windows of the box.
- 2) Without ground vibration, the large amount of the soil in front of the cylinder moved forward, while the deformation of the soil was quite limited in the vicinity of the cylinder when shaking was applied to the model container.
- 3) The difference in the deformation mode of the soil affected the lateral resistance of the cylinder.
- 4) Larger lateral resistance is mobilized as the loading rate becomes higher.
- 5) When the loading rate is higher, the cylinder displacement required for the lateral resistance mobilization becomes smaller.
- 6) Tendencies of loading rate effect are associated with not only the dilatancy characteristics of sand but also pore fluid migration around the cylinder.
- 7) All indications in this study support that the hydraulic conductivity of the soil in relation to the loading rate is the important factor for the mobilization of the lateral resistance of piles in liquefied soils.

References:

- Abdoun, A. and Dobry, R. (1998), "Seismically induced lateral spreading of two-layer sand deposit and its effect on pile foundations," *Proceedings of the International Conference Centrifuge 98*, **1**, 321-328.
- Fujii, S., Isemoto, N., Satou, Y., Kaneko, O., Funahara, H., Arai, T. and Tokimatsu, K. (1998), "Investigation and analysis of a pile foundation damaged by liquefaction during the 1995 Hyogoken-Nambu Earthquake," *Soils and Foundations*, Special Issue on Geotechnical Aspects of the Jan. 17 1995 Hyogoken-Nambu Earthquake, (2), 179-192.
- Horikoshi, K., Tateishi, A. and Fujiwara, T. (1998), "Centrifuge modeling of a single pile subjected to liquefaction-induced lateral spreading," *Soils and Foundations*, Special Issue on Geotechnical Aspects of the Jan. 17 1995 Hyogoken-Nambu Earthquake, (2), 193-208.
- Matsui, T. and Oda, K. (1996), "Foundation damage of structures," *Soils and Foundations*, Special Issue on Geotechnical Aspects of the Jan. 17 1995 Hyogoken-Nambu Earthquake, (1), 189-200.
- Satoh, H., Ohbo, N. and Yoshizako, K. (1998), "Dynamic test on behavior of pile during lateral ground," *Proceedings of the International Conference Centrifuge 98*, **1**, 327-332.
- Takahashi, A., Takemura, J., Kawaguchi, Y., Kusakabe, O. and Kawabata, N. (1998), "Stability of piled pier subjected to lateral flow of soils during earthquake," *Proceedings of the International Conference Centrifuge 98*, **1**, 365-370.
- Towhata, I., Vargas-Mongem W., Orense, R.P. and Yao, M. (1999), "Shaking table tests on subgrade reaction of pipe embedded in sandy liquefied subsoil," *Soil Dynamics and Earthquake Engineering*, **18**(5), 347-361.
- Yasuda, S., Terauchi, T., Morimoto, H., Erken, A. and Yoshida, N. (1998), "Post liquefaction behavior of several sands," *Proceedings of the 11th European Conference on Earthquake Engineering*.

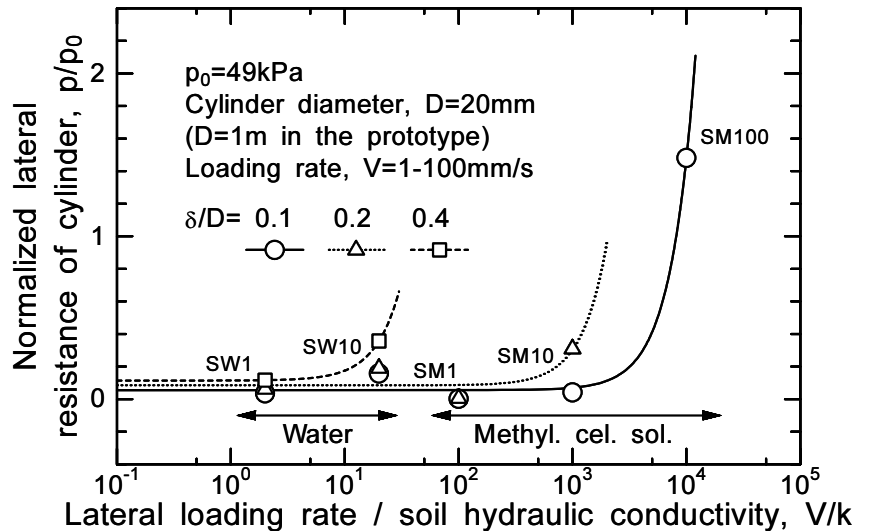


Figure 11. Relationship between lateral resistance of cylinder at $\delta/D=0.1, 0.2$ & 0.4 and cylinder loading rate over soil hydraulic conductivity in first loading.

LIQUEFACTION REMEDIATION OF SAND WITH AN EXISTING OIL TANK BY CHEMICAL GROUTING

J. Takemurai¹⁾, S. Imamura²⁾ and T. Hirano³⁾

1) Associate Professor, Department of Civil Engineering, Tokyo Institute of Technology, Japan

2) Senior Researcher, Nishimatsu Technical Research Center, Nishimatsu Construction Co., Ltd, Kanagawa, Japan

*3) Engineer, Nishimatsu Construction Co., Ltd, Kanagawa, Japan
jtakemur@cv.titech.ac.jp/ shinichiro_imamura@nishimatsu.co.jp,*

Abstract: In this study, a series of dynamic centrifuge model tests was performed to investigate the efficiency of chemical grouting as a countermeasure against liquefaction of sand deposits with an oil tank on the ground surface. Conditions mainly investigated in the tests were the grouting depth ratio to the depth of liquefiable layer and the stiffness of improved portion. The test results indicated that the grouting into the sand beneath the tank by chemical grouting was effective in reducing the maximum settlement and differential settlement of the tank and the maximum settlement decreased almost linearly with the depth of the grouting. Some differences were observed in the ground acceleration and settlement between 2D plane strain models and 3D models with a circular tank, which clearly showed the 3D effects in the behavior of the tank under seismic loading.

1. INTRODUCTION

Settlements and differential settlements of oil storage tanks caused by the liquefaction of sand deposits and the sloshing of liquid in oil storage tanks during earthquakes are of major concern in the seismic design of such structures. In Japan, since the 1995 Hyogoken Nanbu earthquake, originally the 1964 Niigata earthquake and the 1978 Miyagiken-oki earthquake (Ishihara et al., 1980), it has become an urgent matter for geotechnical engineers to implement proper countermeasures for existing oil storage tanks. Application of remedial measures against liquefaction of sand on which oil storage tanks have already existed is extremely important in Japan, because the majority of existing tanks were constructed before early 1970's when the soil liquefaction was first considered in the design of tank foundation.

Countermeasures commonly used, such as vibration method, gravel drains, sheet pile walls, are very difficult to apply due to various restriction, e.g., working space, vibration problems. Chemical grouting is one of feasible countermeasures overcoming these restrictions, making it possible to improve the soil underneath the tank with arbitrary shape in a narrow working space. However, the rational method to obtain an economical area of chemical grouting has not been established yet.

In this study, using 2D and 3D models, a series of dynamic centrifuge model tests was performed to investigate efficiency of chemical grouting as a countermeasure against the liquefaction of sand deposits with oil tanks on the ground surface. Conditions investigated in the tests were grouting depth ratio to the depth of liquefiable layer, the stiffness of improved portion and the situation where the central portion beneath the tank was remained ungrouted.

2. CENTRIFUGE MODEL TESTS

2.1 Model Preparation

The test set up for the dynamic centrifuge model is shown in Figure 1. A large laminar box, with the inner dimensions of 300mm in height, 400mm in width and 650mm in length (Imamura et al., 2002) was used. Two types of model tanks were employed in the tests in order to verify a difference between 2D and 3D models. One was circular tank for 3D condition and the other rectangular one for 2D condition. Both model tanks were essentially made of aluminum plate (1mm thickness) with the base of rubber membrane. This rubber membrane (0.5mm thickness) was used to model flexible base of oil storage tank. The circular model tank was 45mm in height and 140mm in diameter. On the other hand, the rectangular model tank has the same height, a width of 140mm and length of 400mm. The material properties of fine silica sand No.8 used in the tests are summarized in Table 1.

200mm thick model sand layer with unit weight of 15.2kN/m^3 ($D_r=50\%$) was prepared by pouring. After being flattened the surface by applying vacuum, zircon sand was laid on the surface to obtain surcharge layer of 10mm thickness, which gives a surcharge pressure of 10kPa at the centrifugal acceleration of 50g. The model tank was then placed and lead shots were put into the model tank, which could create the tank pressure of 100kPa to the surface at 50g.

The active silica was used as chemical grouting material. The solution of active silica has low viscosity giving high hydraulic conductivity before becoming gel which is stable when submerged. For the preparation of grouted sand, the same silica sand with the same relative density as model ground was pored in a box. The solution of active silica was then injected from the bottom of the box. After curing about one month, the improved sand block was removed from the box and trimmed to predetermined shape. The diameter (for 3D) or width (for 2D) of the trimmed sand block is fixed $B=160\text{mm}$, which is 20mm larger than that of the tank model, while the depth of the improvement (H') was varied from 0 to the depth of the sand layer ($H=200\text{mm}$) as described below. The trimmed sand was placed on the sand at the center of the laminar box during the preparation of sand layer, once the sand reached to the predetermined thickness. Finally, the model was aerated with carbon dioxide gas, and then was saturated with the deaerated water.

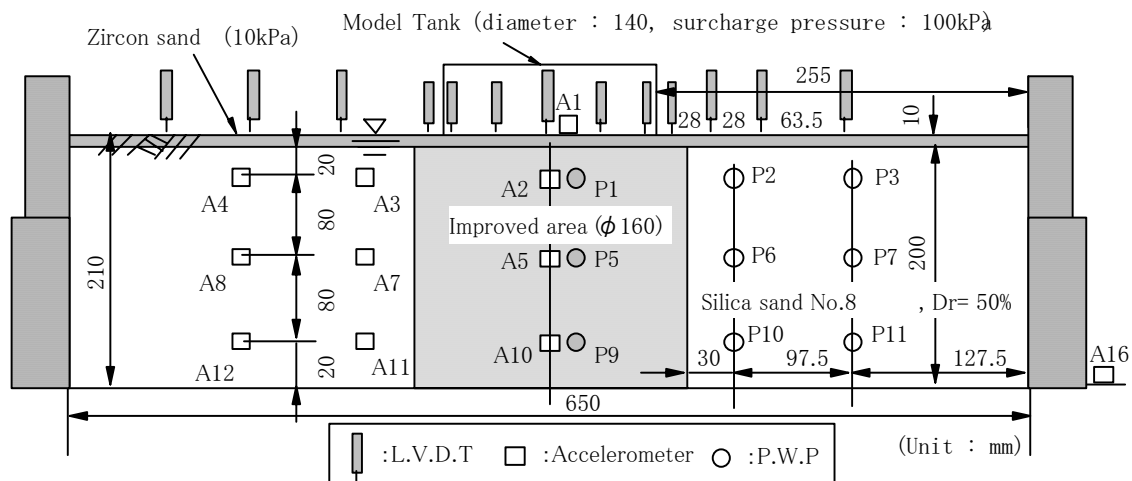


Figure 1 Test set up and location of sensors.

Table 1 Material properties of fine silica sand No.8.

Specific gravity, ρ_s	2.65
Maximum void ratio, e_{max}	1.333
Minimum void ratio, e_{min}	0.703
Coefficient of uniformity, U_c	2.927
Average grain size, D_{50} (mm)	0.1
Permeability, k (m/sec)	2.0×10^{-5}

Table 2 Test conditions

Dim	Code	Improved area	Improved depth H' (mm)	Improved ratio (H'/H)	Silica sand layer D_r (%)	q_u (kPa)	E_{50} (MPa)
3 D	IA1	No improve	—	0	52.3	—	—
	IA21	All depth to bearing stratum	200	1	43.4	120	4.38
	IA22				52.0	75	1.90
	IA31	Three quarters	150	0.75	51.9	121	3.70
	IA32				52.7	121	3.70
	IA4	Three quarters without central part	150	0.75	52.3	142	3.43
	IA51	Half	100	0.5	52.5	142	3.43
	IA52				52.6	223	11.8
2 D	IB1	No improve	—	0	48.9	—	—
	IB2	All	200	1	50.9	120	4.09
	IB3	Three quarters	150	0.75	50.9	121	4.81
	IB4	Half	100	0.5	51.5	142	7.06

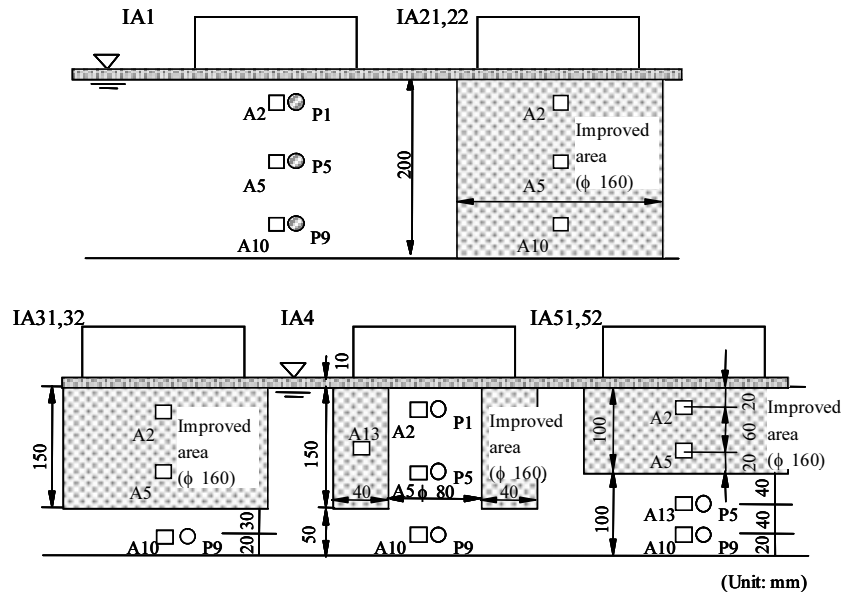


Figure 2 Configuration of improvement portion.

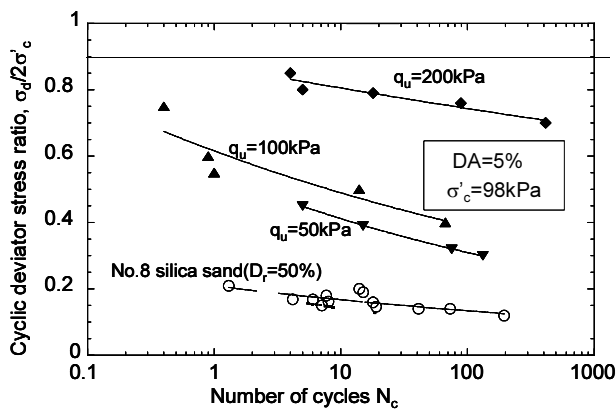


Figure 3 increase of liquefaction resistance by chemical grouting.

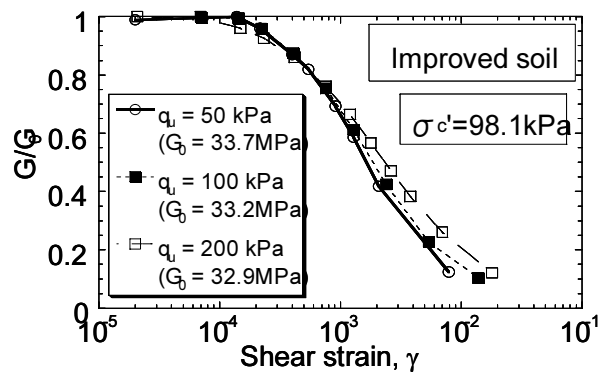


Figure 4 $G/G_0 - \gamma$ relation of grouted sand.

2.2 Test conditions and test procedures

Test conditions are summarized in Table 2, and the configurations of improvement portion are illustrated in Figure 2. 12 centrifuge model tests were conducted. Beside the 2D and 3D conditions, improvement depth (H') is the main parameter. Four different improvement depth tested were $H'/H=0$, $1/2$, $3/4$ and 1 . Whole portion underneath the tank to the improvement depth were improved, except IA4 where central portion of three quarters improvement were remained ungrouted.

Unconfined compression strengths of the improved sand were about 120kPa for almost all the cases except of IA22 and IA52, which had about 60% (75kPa) and 160% (223kPa) strengths of the others. Figures 3 and 4 show the results of undrained cyclic triaxial test and the normalized secant shear modulus (G/G_0) - shear strain (γ) relation of the grouted sand with various unconfined compression strength respectively. From these two figures it can be confirmed that liquefaction resistance of loose sand can be improved by the chemical grouting but not for the small strain stiffness.

Centrifuge acceleration employed was 50 g, under which the corresponding prototype is equivalent to a 7m diameter oil tank on 10m depth sand deposit. All tests were carried out by the dynamic geotechnical centrifuge (effective radius: 3.80m, maximum payload: 19.2MN-m/sec²) of Nishimatsu Construction Co., Ltd (Imamura et al., 1998). Input wave for the tests is shown in Figure 5. A sinusoidal wave with acceleration amplitude of 12.5g, frequency of 100Hz (20cycles) was applied to the model for duration of 0.2sec. This input motion is the horizontal acceleration of 250gal, frequency of 2Hz and duration of 10 sec in the prototype scale. Locations of various probes installed in the model are shown in Figure 1 and 2. On measurements, particular attentions were paid to the settlements of ground under the tank base, dynamic responses of the oil tank and excess pore water pressures underneath the soil improvement. Details of the tests are given by Imamura et al. (2004).

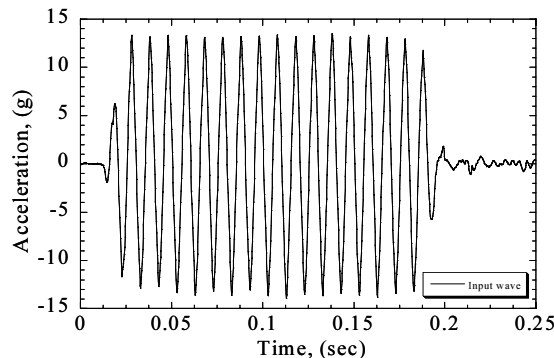


Figure 5 Horizontal input motion.

3 TEST RESULTS AND DISCUSSIONS

3.1 Variation of observed accelerations with depth in the model

Ratios of observed acceleration amplitude at the tank (A1) and the ground under the tank (A2, A5, A10) to that of the input motion for both 2D and 3D models are shown together with those of surrounding ground (A4, A8, A12) in Figure 6. In all the cases, the ratios are smaller for the shallower depth. As can be seen, there exists a considerable difference between 2D and 3D models. In 3D models, the improvement condition appears to have some influence on the variation of the ratio with the depth. The variations of the ratio in IA4 and IA51 coincide with that in IA1 except of the tank. The variation in IA21 ($H'/H=1$) was similar to that in IA31 ($H'/H=3/4$). In general the larger the improvement depth, the smaller the attenuation of the motion. On the other hand, in 2D models all the ratios in the ground with improvement are smaller than those of the case without improving and the difference in the variation of the ratio for different improvement depth is not so clear compared to the 3D models. The variation in the surrounding ground is closer to that under the tank for 2D models than 3D models. This may imply that the end wall effect is more significant in 2D model than 3D

model, because the soil in the surrounding ground is confined by the end wall and the improved soil in 2D model.

In the cases where relatively high ratio was observed below the tank, the ratio of the tank was smaller than that below. As a result, the ratios of the tank are almost the same for all improvement cases. The ratios of the tank under the improved soil are about 40 and 50 % for 2D and 3D models respectively. In the tests the improvement of sand under the tank by chemical grouting did not cause amplification of shaking motion of the tank.

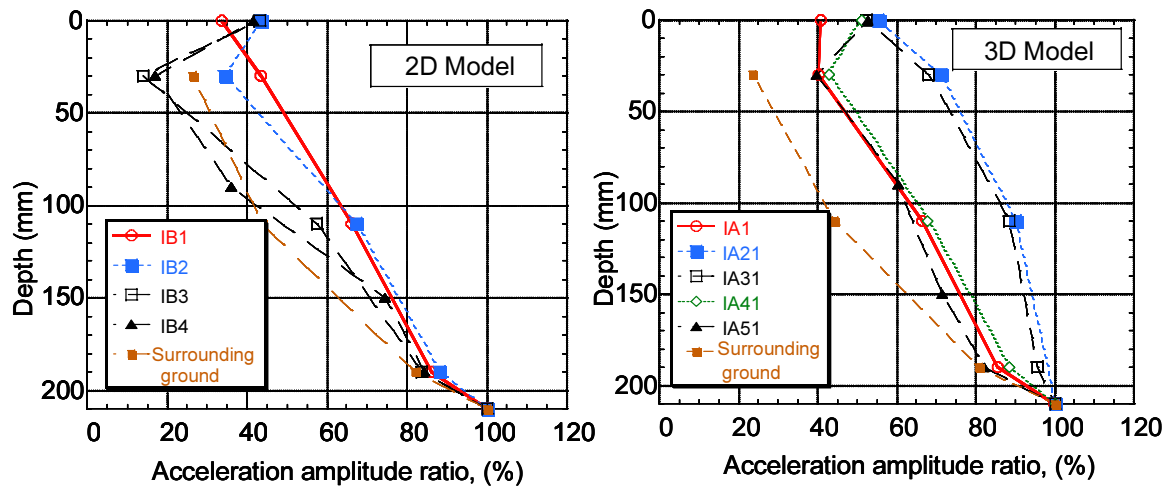


Figure 6 Variation of acceleration amplitude with depth.

3.2 Settlement under the tank

Figures 7 show the settlements at the center of the tank during shaking. The tank settled with shaking time, but no settlement occurred after shaking except of IA1 which showing small settlement after the shaking. In cases of a half depth improvement in 3D series, settlement rates increased in the middle of shaking time, while for the other cases the settlement rates decreased gradually with time. Maximum settlements normalized by tank diameter (S_{max}/D) are plotted against soil improvement ratio (V'/V) in Figure 8, where V' is the volume of the improvement sand, V is that of the cases with entire depth improvement. In Figure 9 improvement efficiency defined by $S_{max}/S_{max}(NO)$ are plotted against improvement ratio, where $S_{max}(NO)$ is the maximum settlement of the case without improvement (IB1 and IA1 for 2D and 3D cases respectively). Tank settlement is effectively reduced by grouting underneath the tank. In 3D series, the tank settlement decrease almost linearly with the improvement ratio for the case with similar strength of grouted sand. In Figures 8 and 9, the results with different strength of the grouted sand (IA22 and IA52) are also plotted. From the figures it can be also confirmed that the strength or stiffness of the grouted sand is also very important for reducing the tank settlement. The higher the strength, the smaller that settlement.

As the stiffness of the active silica gel is not so high, the gradual grouting into sand does not change the stress distribution of the ground underneath the tank. However, once the surrounding ground liquefies, the shear stresses on the vertical surface on the grouted sand diminish, resulting in the concentration of vertical stress on the grouted sand as shown in Figures 10. The concentration of the stress yields the vertical compression of grouted sand. Hence, the stiffness of the sand becomes one of dominant factor of the settlement of grouted sand underneath the tank. IA21 and IA22 were both the entire depth improvement cases, but the settlement in the latter was more than the double of that in the former. This difference can be reasonably explained by smaller E_{50} in IA22 than IA21 (see Table 2).

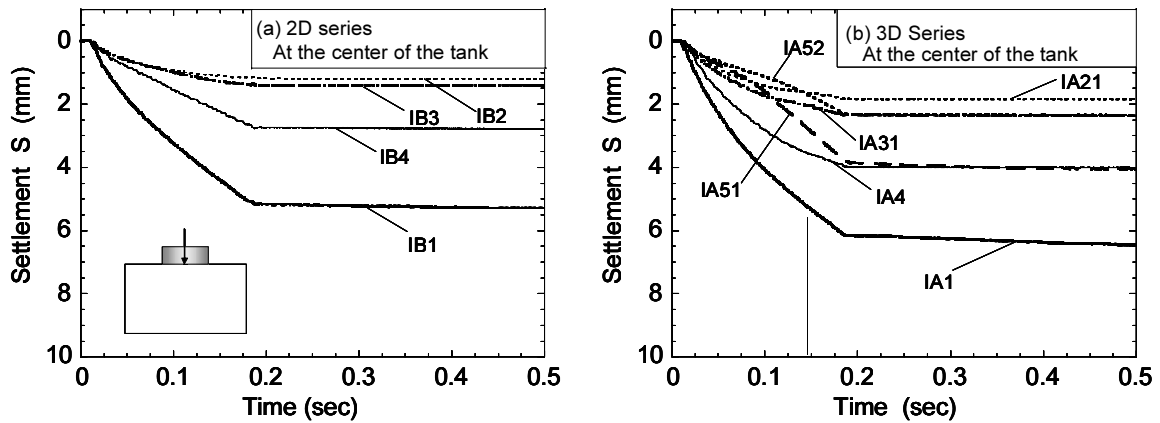


Figure 7 Settlement at the center of the tank during shaking.

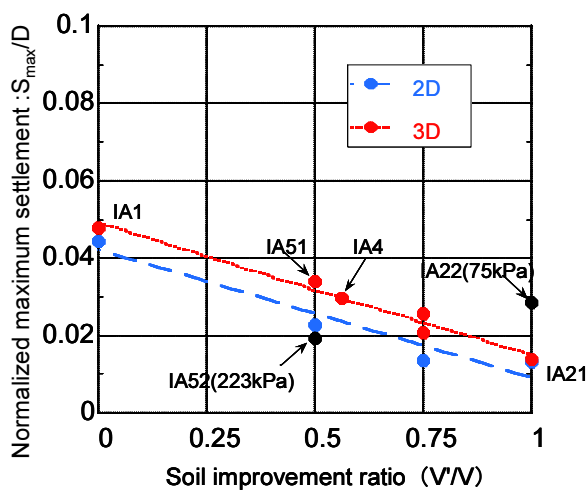


Figure 8 Relationship between soil improvement ratio and normalized maximum settlements

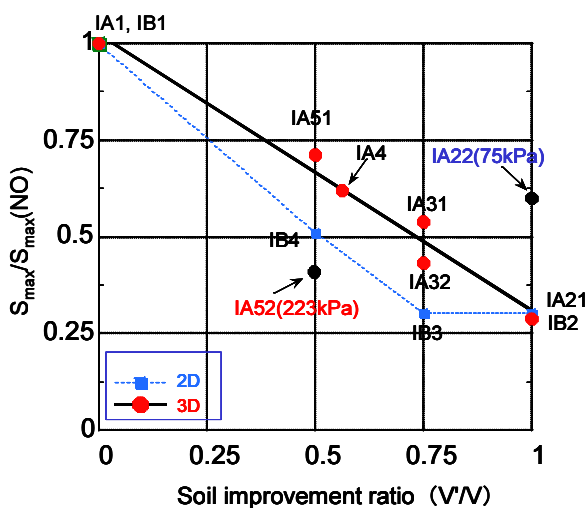


Figure 9 Correlation between soil improvement ratio and improvement efficiency ($S_{max}/S_{max}(NO)$).

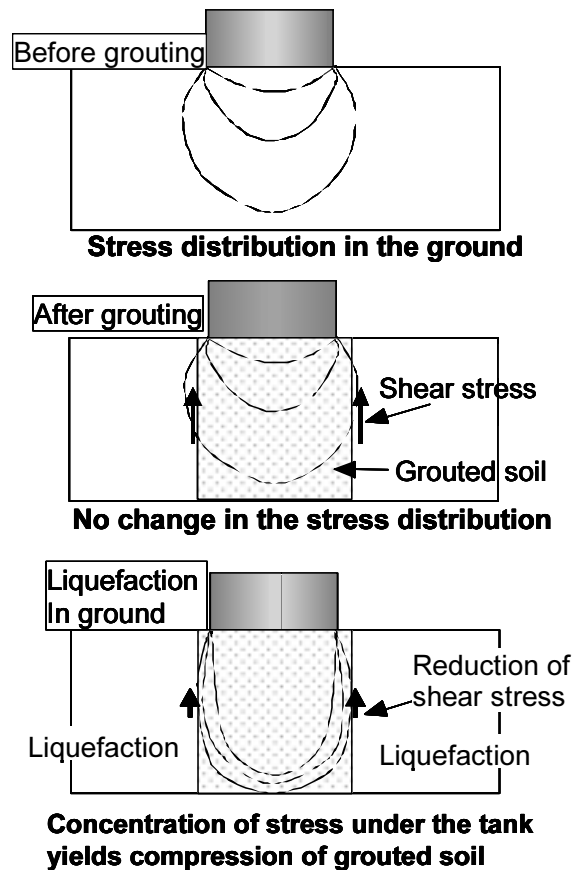


Figure 10 Change of stresses in the grouted sand underneath tank due to liquefaction of the surrounding ground

Three dimensional effect on the tank settlement can be also seen in Figures 8 and 9. The larger settlement and less improvement efficiency were obtained in 3D models than 2D models especially in the cases of a half and three quarters improvements.

Settlement profiles under the tank caused by the shaking are shown in Figures 11. In the case with three quarters depth improvement having no improved portion at the center (IA4), the settlement similar to that of IA21, IA31, about 2mm, took place on the improved portion, but the settlement at the central non-improved portion was about 4mm (60% of IA1). Two main causes of the tank settlement can be considered, one is the volume compression and the other the lateral movement of the soil beneath the tank (Kimura et al. 1995). From the fact explained above, the larger settlement at the central portion can be attributed to the volume compression of non-improved sand within the improved sand. In this test, the base of tank was modelled by rubber membrane to create perfectly flexible condition to avoid the complicated interaction between the tank and soil. However, the settlement at the central portion might be overestimated due to this modelling of tank base compared to the actual tanks with thin steel base plate.

Maximum differential settlements normalized by the tank diameter ($\delta S_{max} / D$) are plotted against the improvement ratio in Figure 12. $\delta S_{max} / D$ decreases as the improvement ratio increases, which clearly reveals the efficiency of the improvement. The differential settlement in 3D model is larger than that in 2D, especially for the cases with small improvement ratio. This may be attributed to the high freedom of displacement for 3D condition compared to 2D and the difference of the end wall

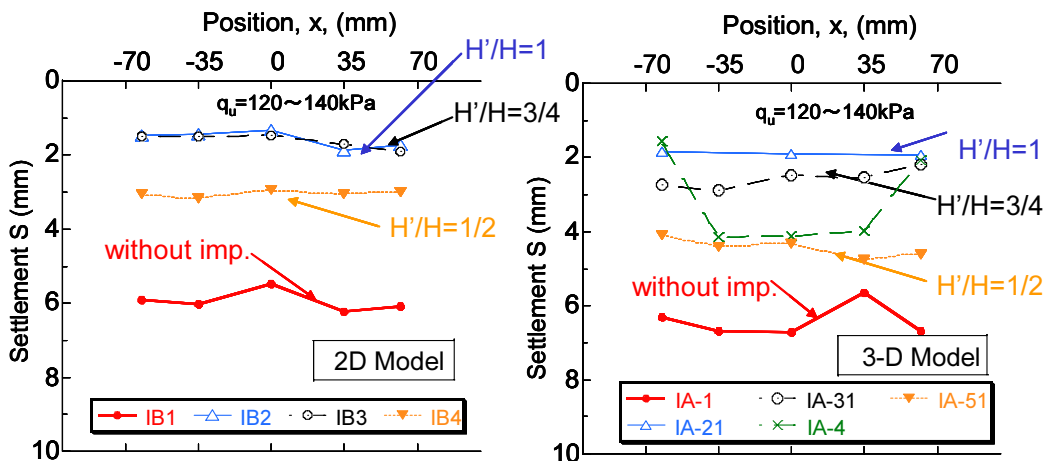


Figure 11 Settlement profiles under the tank.

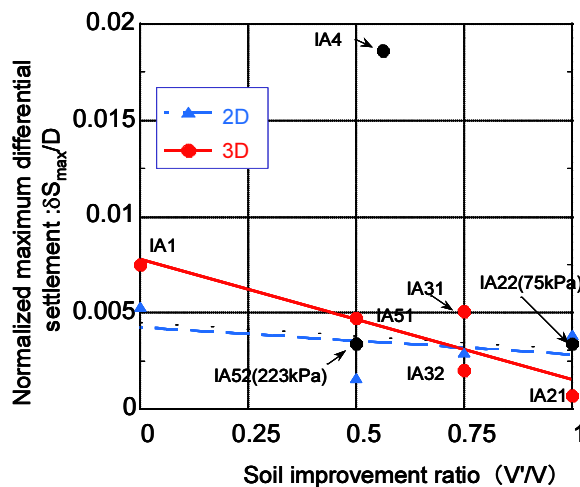


Figure 12 Relationship between and normalized maximum differential settlements.

effects as discussed before. These comparisons between 2D and 3D models confirm the importance of 3D effects in both physical modelling and numerical modelling on the seismic performance of the tank.

From the observation about the settlements under the tank, it can be concluded that the suppression of vertical and lateral displacements in the area directly beneath the tank by chemical grouting is effective in reducing the settlement and differential settlement of the tank base. In order to establish more rational way for reducing the improvement volume, it is necessary to conduct further tests where the base plate of the tank is properly modeled.

4. CONCLUSIONS

From dynamic centrifuge model tests on efficiency of chemical grouting as a countermeasure against the liquefaction of sand deposits with oil tanks, the following conclusions were drawn.

1. The suppression of vertical and lateral deformation of the area directly beneath the tank by chemical grouting is effective in reducing both settlement and differential settlements of the tank caused. If the grouted sand has the same stiffness, the maximum and differential settlements decrease almost linearly with the improvement depth.
2. From 2D models qualitatively similar results to 3D models were obtained on the effect of the improvement. However, the maximum and differential settlements were smaller in the 2D models than the 3D models. This may be attributed to the high freedom of displacement for 3D condition compared to 2D and the difference of the end wall effects, which indicating the importance of 3D effects in both physical modelling and numerical modelling on the seismic performance of the tank.
3. If the soil under the central portion of the tank are remained non-improved in order to reduce the volume of the improvement, some differential settlement may take place between improved and non-improved portion. However, the liquefaction of the non-improved sand confined by the surrounding improved sand was effectively prevented. The observed differential settlement in the test might be overestimated due to this modeling of tank base compared to the actual tanks with thin steel base plate.
4. In order to establish more rational way for reducing the improvement volume, it is necessary to conduct further tests where the base plate of the tank is properly modeled.

References:

- Imamura, S., Hagiwara, T. and Nomoto, T. (1998), "Nishimatsu dynamic geotechnical centrifuge", Proc. of Centrifuge 98, 25-30.
- Imamura, S. & Fujii, N. (2002), Observed dynamic characteristics of liquefying sand in a centrifuge, Proc. of Physical Modeling in Geotechnics, 195-200.
- Imamura, S., Hirano, T., T. Hagiwara, Takahashi, A. and Takemura, J. (2004), "Centrifuge model tests of existing oil tanks on liquefiable loose sand improved by chemical grouting", Proceeding of JSCE, Geotechnical Division, (to appear).
- Ishihara, S., Kawase, Y. and Nakajima, M. (1980), "Liquefaction characteristics of sand deposits at an oil tank site during the 1978 Miyagiken-oki Earthquake, Soils and foundations, Vol.20, No.2, pp. 97-111.
- Kimura, T., Takemura, J., Hiro-oka, A., Okamura, M. and Matsuda, M. (1995), "Countermeasures against liquefaction of sand deposits with structures", Proc of Earthquake Geo-technical Engineering (edited by Ishihara), IS-Tokyo 95, 1203-1224.

INTEGRATED NATURAL HAZARDS RISK REDUCTION - EMERGENCE OF A US APPROACH

C. Scawthorn¹⁾

*1) Professor of Lifeline Engineering, Department of Urban Management
Kyoto University, Kyoto 606 Japan
cscawthorn@quake.kuciv.kyoto-ac.jp*

Abstract: A series of developments, some unrelated to earthquake or natural hazards risk reduction, have occurred in the US which together comprise many elements of an integrated approach to natural hazards risk reduction. These developments include the Disaster Mitigation Act of 2000, the HAZUS-MH software, the requirements of GASB 34, and passage of the Sarbanes-Oxley Act of 2002. A major gap still remaining is earthquake risk reduction for homeowners, however. Additionally, while the prospects for an integrated program of natural hazards risk reduction is promising, the need for appropriate measures of risk, and risk or performance goals, are areas for needed research.

1 INTRODUCTION

Risk identification and mitigation in the US have been significantly enhanced by several recent major “risk accounting” developments. These include the passage of the Disaster Mitigation Act of 2000 (PL 106-390) and the requirements of GASB 34, both affecting public entities, the passage of the Sarbanes-Oxley Act of 2002 (PL 107-204) affecting private entities, and the development by FEMA of the HAZUS-MH software. Together, these developments are emerging as major elements of an integrated approach for natural hazards risk reduction. This paper describes each of these developments, with the goal of both clarifying the picture in the US as well as summarizing these trends for the benefit of other countries. Lastly, several a major gap in the ‘integrated program’ is identified, as well as other areas for improvement and opportunities for research.

2 DISASTER MITIGATION ACT OF 2000 (PL 106-390)

The Stafford Act of 1978 (PL 93-288) formed the basis for modern disaster management in the US, allowing for Presidential Declarations of Disaster at the request of the governor of a state, and compensation to public entities for cost of repairs arising from the disaster. Additionally, the Act allowed that the “*President may contribute up to 75 percent of the cost of hazard mitigation measures which the President has determined are cost-effective and which substantially reduce the risk of future damage, hardship, loss, or suffering in any area affected by a major disaster.*” As a result of a number of major disasters, including the 1989 Loma Prieta and 1994 Northridge earthquakes, it became apparent that the Act in some ways had an unintended effect, in that local governments sometimes put off major expenditures required for disaster mitigation. That is, rather than spend their own money to fix buildings and infrastructure before a disaster, local governments

waited for the time if and when a disaster occurred, and then received a subsidy for the repairs or replacement of the damaged facilities, as well as a windfall in the form of Hazard Mitigation Grant Program (HMGP). Examples of cost repairs largely paid for by the federal government included the extensive and expensive repairs to the San Francisco and Oakland City Halls following the 1989 Loma Prieta earthquake, and to the Los Angeles City Hall following the 1994 Northridge earthquake.

As a result, the Stafford Act was extensively amended in 2000 as the Disaster Mitigation Act of 2000 (PL 106-390, also known as **DMA 2000**). A basic requirement of DMA 2000 is that state and local governments by late 2004 develop and implement a multi-hazard mitigation plan. This requirement is not mandatory, but only those state and local governments who have approved plans will be eligible for compensation for repairs or replacement of the damaged facilities, and the 75% HMGP. Table 1 provides additional detail on these requirements. This ‘carrot and stick’ approach is quite effective, and most state and local governments are developing multi-hazard mitigation plan in compliance with DMA 2000. The multi-hazard mitigation plan has several elements (see Figure 1), including:

- a) Risk Assessment, which requires identification of the hazards such as earthquake, tsunami, flood, coastal storm, tornado, landslide and wildfire; an estimate of the vulnerability to these hazards, including potential monetary losses; and a general description of local land use and development trends so that mitigation options can be considered in future land use decisions (see Figure 2, and Figure 3).
- b) Mitigation Strategy, describing the goals of the strategy, and a coordinated set of feasible actions (see Figure 4)

The Federal Emergency Management Agency (FEMA) in order to support the implementation of these requirements has developed a series of reference materials that provide guidance for developing the plan, including.

- *State and Local Mitigation Planning How-to Guides* – intended to help States and communities plan and implement practical, meaningful hazard mitigation measures (FEMA 386-1 to FEMA 386-9)
- *Planning for a Sustainable Future* (FEMA 364) and *Rebuilding for a More Sustainable Future* (FEMA 365) – two related volumes that provide guidance for integrating sustainable practices as part of pre- and post-disaster mitigation planning efforts; and
- *FEMA Mitigation Resources for Success* (FEMA 372) – a compact disc with a compendium of FEMA resources related to mitigation practices and projects.

In addition, FEMA has prepared DMA 2000-related training and workshop materials for FEMA Regional staff, States, and local communities based on the Plan Criteria and the reference materials described above. Many communities across the US are implementing this process. Figure 5 shows an example of hazard mapping and risk identification, for tsunami hazard in Kauai County, Hawaii.

3 HAZUS-MH

HAZUS-MH was first conceived of in the early 1990’s as a standardized nationally applicable natural hazards loss estimation software tool for planning and mitigation purposes. From 1994 to the late 1990’s development of the earthquake module occurred, with the first release in 1997. Development of the flood and wind modules occurred from 1997 to 2003, and HAZUS-MH was released very recently (for copies see http://www.fema.gov/hazus/pdf/order_form_mh.pdf). While full details of the flood, wind or even just earthquake modules are beyond the scope of the present paper (see National Institute of Building Sciences, 1999 and Scawthorn et al, to appear, for more details), Figure 7 provides an overview of the earthquake loss estimation methodology.

HAZUS-MH is relevant to the present discussion because it is an emerging tool for the consistent estimation of losses, in support of the framework laid out in DMA 2000. Since its release in 1997, the earthquake module has seen considerable growth in its use, with 1,700 current users nationwide including federal agencies, states, localities, academic institutions, and private enterprises. In 2001 a study of estimated annualized earthquake losses for the United States was completed using HAZUS99 (FEMA 366), in order to analyze and compare seismic risk across regions of the United States, and finding that the Annualized Earthquake Loss (AEL) to the national building stock is \$4.4 billion per year. Other applications of HAZUS Earthquake have been for the state of South Carolina (Bouabid et al, 2002), and San Francisco (Kornfield et al, 2002). Although HAZUS Earthquake was originally intended as a planning tool, it has increasingly been utilized for response and recovery efforts. This use is especially enhanced with the availability of ShakeMaps, developed in California by the USGS [Wald et al., 1999] or by other regional strong-motion instrumentation networks.

4 SECURITY VULNERABILITY ASSESSMENTS

DMA 2000 only addresses public entities, which leaves a large gap where privately owned utility *lifelines* are concerned, such as water, wastewater, electric power and gas. Because these are privately owned, they are responsible for their own risk management, and are not compensated by the federal government should they sustain damage due to a natural hazard. In some cases, public regulators require some risk analyses, but in general this is not the case. However, as a result of 9/11, it became apparent that these vital lifelines were very vulnerable to, and needed to be protected against, intentional acts. An example is the requirement by the US Environmental Protection Agency that water utilities in the US, public or privately owned, are required to have completed Security Vulnerability Assessments (SVAs) per the schedule shown in **Table 2**. The SVA procedure is a simplified risk assessment and mitigation methodology, Figure 6, in which a significant aspect is defining the utility's goals, and the Design Basis Threat (DBT). This differs in some ways from seismic vulnerability assessments, in that for security, in actuality, these two aspects are inter-active. That is, for earthquakes, nature provides a fixed 'spectrum' of threats, while for intentional acts, the 'threat spectrum' is defined by the goals of the utility.

SVA is relevant to the present discussion only because (a) it addresses a portion of the built environment, lifelines, often not addressed by DMA 2000, and (b) in practice, some utilities took the opportunity of performing the SVA to also address other non-Security-related hazards, such as earthquake. That is, in a number of cases, the SVA methodology was employed for both security and seismic related vulnerabilities, and an integrated mitigation program developed. For seismic, the mitigation program typically was served by the SVA process in several stages – that is:

1. the SVA served as a screening methodology for seismic vulnerabilities, identifying those parts of the lifeline system that were most critical and required vulnerability reduction,
2. for those parts of the parts of the lifeline system that the SVA identified as critical and which could be readily mitigated (eg, bracing equipment), those mitigation measures were combined with the Security-related mitigation measures (eg, installation of new Security alarms, systems, or other equipment) into a rapidly implemented program
3. for those parts of the parts of the lifeline system that the SVA identified as critical and which could NOT be readily mitigated (eg, reinforcing tanks), those mitigation measures were referred more additional analysis and design, for eventual incorporation into the Capital Improvements Program.

Table 3 shows an example drawn from the author's practice, in which Security and Natural Hazards risk results are presented, while Table 4 shows the integration of these risks into a mitigation program.

5 GASB 34

Traditionally, US governmental agencies (state and local) have accounted for infrastructure assets like roads, bridges, water and sewer facilities, dams, etc. in their annual financial report during the year in which the cost of construction was incurred – so called, cash accounting. That is, the value of all other physical assets does not appear, or is “off the books”. In reality, of course, this physical infrastructure is an enormous, although depreciating, asset. A more accurate report of a government’s finances would show the existing (depreciated) value of the agency’s capital assets – so called “accrual accounting”, in which the cost, or the loss in value, of an asset is spread across the asset’s useful lifetime (eg, 20-50 years). Accrual accounting is more consistent with the reporting of other costs of doing business, and with private business practices, so that government and private business finances are more easily comparable. In order to encourage state and local governments to make the change to accrual accounting, the Governmental Accounting Standards Board (or GASB, a nonprofit entity responsible for establishing accounting standards—or generally accepted accounting practices GAAP) published GASB Statement 34, which required state and local governments to begin reporting the value of their infrastructure assets on an accrual basis, generally by 2006. The relevance of GASB 34 to the present discussion is that (a) the full economic value of local government and agency infrastructure is now valued, and (b) DMA 2000 requires its risk be accounted for. Thus, an increasing trend in US local government and agency financial accounting is the emergence of ‘natural hazard risk charges’ against the value of infrastructure. These risk charges are only now beginning to emerge in local government and agency accounting, but it can be anticipated that over time they will be noticed, and provide a further impetus for risk management.

6 SARBANES-OXLEY ACT OF 2002 (PL 107-204)

Just as the Loma Prieta and Northridge earthquakes led to DMA 2000, and the events of 9/11 led to Security Vulnerability Assessments, the several financial scandals of the last few years (Enron, Tyco, etc) led to the passage in 2002 of the Sarbanes-Oxley Act. Sarbanes-Oxley effectively calls for comprehensive, integrated ‘enterprise-wide’ risk management of publicly traded companies. That is, while the intent of Sarbanes-Oxley is largely seen as focused on corporate governance processes, disclosure practices and internal controls, compliance with Sarbanes-Oxley lays the foundation for implementing Enterprise Risk Management (ERM) capabilities that did not previously exist for many companies. Many privately-held and not-for-profit firms are also seeking to demonstrate adherence to the same standards. The result is a push by investors, policy-makers, regulators, exchanges and rating agencies towards greater transparency regarding governance, risks and internal control. The relevance of Sarbanes-Oxley to the present discussion is that a key element in ERM is the risk due to natural hazards, such as earthquakes – that is, for the first time, private companies will be required to quantify their natural hazards risk. While not statutorily required for private companies (as it is for the public sector by DMA 2000), the economically efficient management and mitigation of this risk, in concert with the comprehensive suite of risks confronting the enterprise, will be a natural outgrowth of this push for ERM.

7 CONCLUDING REMARKS

7.1 Fitting the Pieces Together

In summary, the several requirements and trends outlined above are emerging as the basis for a comprehensive program of natural hazards risk management:

- **public sector** – natural hazards identification and mitigation explicitly required by DMA 2000,

as well as implicitly by GASB 34

- **utility infrastructure** – natural hazards identification and mitigation implicitly required by Sarbanes Oxley
- **private corporations** – natural hazards identification and mitigation implicitly required by Sarbanes Oxley

7.2 Areas for Research and Improvement

While the comprehensive program of natural hazards risk management, which is pictured above as emerging in the US, is promising, there are still many gaps and areas for improvement. A few of these include:

- **Personal property** – the risk to people’s homes is the one major ‘piece’ missing from the picture outlined above. For floods, insurance has been efficiently and effectively mandated for decades via the National Flood Insurance Program (Scawthorn, 1999). Hurricane risk protection is provided at reasonable prices via the insurance industry. Earthquakes however, both in the US and Japan, are strenuously avoided by the insurance industry, so that government pools serve this need (at least in California, in the US), although not providing very good coverage or prices. Insurance is not the real answer anyway, as the 1995 Hyogo-ken earthquake demonstrated. Real risk reduction via retrofitting of buildings is required. How can this be accomplished?
- **Risk Metrics** - In all the above programs, the measure of risk is not stated, and is usually left to the entities to decide for themselves. While this has certain economic efficiencies, it also leaves each entity to ‘re-invent the wheel’, and also results in a very heterogeneous landscape of results, which precludes aggregation. Thus, oversight agencies (regulators, rating agencies) as well as investors and, in the case of DMA 2000 the federal government, are prevented from comparing performance between entities.
- **Risk Objectives** – similarly, risk objectives or performance goals are not provided, and are left to the entities to decide for themselves. The situation is similar as that with risk metrics, with each entity floundering as to appropriate objectives, and a heterogeneous final risk landscape.
- **Explicit vs. Implicit** –except for DMA 2000, most requirements for natural hazards risk are implicit. Even DMA 2000 is mostly seen as being for local governments, so that public agencies such as water utilities are sometimes overlooked. What is needed are more explicit requirements in GASB 34, Sarbanes Oxley, as well as other mandates, for natural hazards risk accounting.

References:

- Bouabid, J. et al (2002) “A Comprehensive Seismic Vulnerability and Loss Evaluation of the State Of South Carolina Using Hazus: Part I Overview And Results”, *Proceedings Seventh National Conference on Earthquake Engineering*, Earthquake Engineering Research Institute, Oakland.
- FEMA 366, 2001. “HAZUS99 Estimated Annualized Earthquake Losses for the United States”, Federal Emergency Management Agency (Washington, D.C.: FEMA 366).
- Kornfield, L. M., C. Bauman, C. Scawthorn. (2002). “San Francisco’s Program For Seismic Safety Planning: CAPSS – The Community Action Plan For Seismic Safety”. *Proceedings Seventh National Conference on Earthquake Engineering*, Earthquake Engineering Research Institute, Oakland.
- NIBS (1999). “HAZUS99 Technical Manual”. Developed by the Federal Emergency Management Agency through agreements with the National Institute of Building Sciences (NIBS), (Washington, D.C.: NIBS).
- Scawthorn, C. (1999) “Modeling Flood Events in the US”. *Proceedings of the EuroConference on Global Change and Catastrophe Risk Management*, International Institute for Advanced Systems Analysis, Laxenburg, Austria.
- Scawthorn, C., Schneider, P. and Schauer, C. (editors), to appear, “Multi-hazard Special Theme Issue”, *Natural Hazards Review*, Am. Soc. Civil Engineers, Reston.
- Wald, David J. et al, 1999. “TriNet `ShakeMaps`: Rapid Generation of Instrumental Ground Motion and Intensity Maps for Earthquakes in Southern California,” *Earthquake Spectra*, Vol. 15, No. 3, Earthquake Engineering Research Institute).

Table 1 DMA 2000 Mitigation Plan Requirements of DMA 2000

Requirements for Standard State Mitigation Plan (SSMP)	Additional Requirements for Enhanced State Mitigation Plan (ESMP) and Local Mitigation Plan (LMP)
<p>a. Plan Requirement</p> <p>SSMP: Due date is November 1, 2004*</p> <p>Standard State Mitigation Plan (SSMP) includes the requirements of the Hazard Mitigation Grant Program (HMGP) Administrative Plan. In order for a State to be eligible for HMGP funding based on 15% of the total estimated eligible Stafford Act disaster assistance, FEMA must approve the SSMP by November 1, 2004. SSMPs must be updated every 3 years.</p>	<p>ESMP: Due date is November 1, 2004*</p> <p>Enhanced State Mitigation Plan (ESMP) increase eligibility for HMGP funding from 15% to 20% of available funding. ESMPs must demonstrate that the State (§201.5(a)):</p> <ul style="list-style-type: none"> • Has developed a comprehensive mitigation program • Makes effective use of available mitigation funding • Is capable of managing the increased funding LMP: Due date is November 1, 2004* <p>Local Mitigation Plans (LMPs) must be updated every 5 years. Multi-jurisdictional plans can be used as long as each jurisdiction participates in the process and officially adopts the plan. State-wide plans will not be accepted as multi-jurisdictional plans. Up to 7% of mitigation funding can be used to support planning, including LMP development.</p>
<p>b. Planning Process (Requirements Prior to Preparation of the Plan)</p> <p>SSMP: Establish coordination with other State agencies, appropriate federal agencies, interested groups, and integrated to the extent possible with other ongoing State planning efforts as well as other FEMA mitigation programs and initiatives.</p>	<p>ESMP: Same requirements as SSMP.</p> <p>LMP: Additional requirements includes: (1) opportunity for public to comment on the LMP during development and before approval; (2) opportunity for involvement by neighboring communities, local and regional agencies supporting hazard mitigation and development activities, and businesses, academia and other private and non-profit interests; and (3) review and incorporation, if appropriate, of existing plans, studies, reports, and technical information.</p>
<p>c. Plan Content</p> <p>1. Planning Process Description SSMP: Describes the planning processes used to prepare the plan, including:</p> <ul style="list-style-type: none"> • How the plan was prepared • Who was involved • How other agencies participated 	<p>ESMP: Additional requirements include demonstrating integration to the extent practicable with (1) other State and/or regional planning initiatives, (comprehensive growth management, economic development, capital improvement, land development, and/or emergency management plans) and (2) FEMA mitigation programs and initiatives that provide guidance to State and regional agencies. (§201.5(b)(1))</p> <p>LMP: Additional requirements include describing how the public was involved.</p>

Table 1 DMA 2000 Mitigation Plan Requirements of DMA 2000 (cont.)

Requirements for Standard State Mitigation Plan (SSMP)	Additional Requirements for Enhanced State Mitigation Plan (ESMP) and Local Mitigation Plan (LMP)
<p>2. Risk Assessments SSMP: Includes:</p> <p>A statewide risk assessment that provides a “statewide overview” characterization and analysis of potential natural hazards and associated risks.</p> <p>Comparison of potential losses throughout the State to determine priorities for implementing mitigation measures (item 3 below) and prioritize jurisdictions for technical and financial support in developing more detailed local risk and vulnerability assessments.</p> <p>The risk assessment shall include:</p> <ul style="list-style-type: none"> <i>i.</i> <i>Overview of Hazards</i> Types and locations of hazards, past occurrences, and probability of future events, using maps, as appropriate. <i>ii.</i> <i>Overview and Analysis of Vulnerability</i> Overview and analysis of the State’s vulnerability to the hazards based on estimates provided in local risk assessments as well as the State risk assessment. The State will describe vulnerability in terms of the jurisdictions most threatened by the identified hazards and most vulnerable to damage and loss associated with hazard events. State owned critical or operated facilities in the hazard areas also will be addressed. <i>iii.</i> <i>Overview and Analysis of Potential Losses</i> Identification of vulnerable structures and estimate of potential dollar losses to State owned or operated buildings, infrastructure, and critical facilities located in the identified hazards areas (based on LMPs and State risk assessment). 	<p>ESMP: Same requirements as SSMP.</p> <p>LMP:</p> <ul style="list-style-type: none"> (i) Overview of Hazards and (ii) Summary of Each Hazard and its Impacts, including: <ul style="list-style-type: none"> a. Types and number of existing and future buildings, infrastructure, and critical facilities in the identified hazard areas; b. Estimate of potential dollar losses and description of how estimate was prepared (similar to iii for SSMPs); c. General description of local land use and development trends so that mitigation options can be considered in future land use decisions. For multi-jurisdictional plans, the risk assessment section must assess each jurisdiction’s risks where they vary from the risks facing the entire planning area.

Table 1 DMA 2000 Mitigation Plan Requirements of DMA 2000 (cont.)

<p>Requirements for Standard State Mitigation Plan (SSMP)</p>	<p>Additional Requirements for Enhanced State Mitigation Plan (ESMP) and Local Mitigation Plan (LMP)</p>
<p>3. Mitigation Strategy SSMP: Documents the follow elements of strategy:</p> <ul style="list-style-type: none"> i. <i>State Goals</i> Describes the State goals to guide the selection of mitigation activities to reduce potential losses identified in Item 2 above. ii. <i>State Mitigation Programs</i> Presents the State's pre- and post-disaster hazard management policies, programs and capabilities to mitigate the hazards in the area, including: An evaluation of State laws, regulations, policies and programs related to hazard mitigation and related to development in hazard-prone areas A discussion of State funding capabilities for hazard mitigation projects A general description and analysis of the effectiveness of local mitigation policies, programs and capabilities iii. <i>Analysis</i> Identifies, evaluates, and prioritizes cost-effective, environmentally sound, and technically feasible mitigation actions and activities that the State is considering and explains how each activity contributes to the overall mitigation strategy. Also, this section should link to LMPs, where specific local actions and projects are identified. iv. <i>Funding</i> Identifies current and potential sources of Federal, State, local or private funding to implement mitigation activities. 	<p>ESMP: Additional requirements should address the following: Project Implementation Capability (§201.5(b)(2)) Documents project implementation capability, identifying and demonstrating the ability to implement the plan, including: <i>i. Eligibility Criteria</i> Present established eligibility criteria for multi-hazard mitigation measures. <i>ii. Mitigation Actions</i> A system to determine the cost effectiveness of mitigation measures, consistent with OMB Circular A-94, Guidelines and Discount Rates for Benefit-Cost Analysis of Federal Programs, and to rank the measures according to the State's eligibility criteria. <i>iii. HMGP Management</i> Demonstration that the State has the capability to effectively manage the HMGP as well as other mitigation grant programs, including a record of the following: A. Meeting HMGP and other mitigation grant application timeframes submitting complete, technically feasible, and eligible project applications with appropriate supporting documentation; B. Preparing and submitting accurate environmental reviews and benefit-cost analyses; C. Submitting complete and accurate quarterly progress and <i>iv. Mitigation Assessment</i> A system and strategy by which the State will conduct an assessment of completed mitigation actions and include a record of the effectiveness (actual cost avoidance) of each mitigation action. LMP: Provides the blueprint for reducing the potential losses identified in the risk assessment, based on existing authorities, policies, program and resources and local ability to expand on and improve these existing tools. Same content as SSMP, but presented as following sub-sections focusing on the local level: (i) mitigation goals, (ii) mitigation actions, and (iii) action plan. For multi-jurisdictional plans, actions must be specific to the jurisdiction requesting FEMA approval or credit of the plan. financial reports on time; and D. Completing HMGP and other mitigation grant projects within established performance periods, including financial reconciliation.</p>

Table 1 DMA 2000 Mitigation Plan Requirements of DMA 2000 (cont.)

Requirements for Standard State Mitigation Plan (SSMP)	Additional Requirements for Enhanced State Mitigation Plan (ESMP) and Local Mitigation Plan (LMP)
<p>4. Coordination of Local Mitigation Planning Includes: <i>i. Funding</i> Describes State process to support, through funding and technical assistance, the development of LMPs. <i>ii. Timeframe</i> Describes the State process and timeframe by which the LMPs will be reviewed, coordinated, and linked to the State Mitigation Plan. <i>iii. Prioritization Criteria</i> Criteria to be used in prioritizing communities and local jurisdictions that would receive planning and project grants under available funding programs, which should include consideration for communities with the highest risks, repetitive loss properties, and most intense development pressures. Further, for non-planning grants, a principal criterion for prioritization will be the extent to which benefits are maximized according to a cost benefit review of proposed projects and their associated costs.</p>	<p>ESMP: Additional requirements to demonstrate the State's commitment to a comprehensive State mitigation program (§201.5(b)(4)), which can include any of the following: <i>i. Local Support</i> A commitment to support local mitigation planning by providing workshops and training, State planning grants, or coordinated capability development of local officials, including Emergency Management and Floodplain Management certifications. <i>ii. Statewide Support</i> A Statewide program of hazard mitigation through the development of legislative initiatives, mitigation councils, formation of public/private partnerships, and/or other executive actions that promote hazard mitigation. <i>iii. State Funding</i> State provision of a portion of the non-Federal match for HMGP and/or other mitigation projects. <i>iv. Building Code Standards</i> To the extent allowed by State law, the State requires or encourages local governments to use a current version of a nationally applicable model building code or standard that addresses natural hazards as a basis for design and construction of State sponsored mitigation projects. <i>v. Multi-year Plan</i> A comprehensive, multi-year plan to mitigate the risks posed to existing buildings that have been identified as necessary for post-disaster response and recovery operations. <i>vi. Post-disaster Recovery</i> A comprehensive description of how the State integrates mitigation into its post-disaster recovery operations. LMP: §201.6 does not require a separate section to address local coordination; however, the need for local coordination is clearly documented in the rule. The LMP should clearly document coordination processes; this could be included in section C.1 (above) or included as a separate section on coordination as for the SSMP and EMP. Multi-jurisdictional LMPs must document coordination across jurisdictions.</p>
<p>5. Plan Maintenance Process Purpose: This section includes: <i>i. Method</i> and schedule for monitoring, evaluating, and updating the plan. <i>ii. A system</i> for monitoring implementation of mitigation measures and project closeouts. <i>iii. A system</i> for reviewing progress towards goals as well as activities and projects identified in Item 3.</p>	<p>ESMP: Same requirements as SSMP. LMP: Describes: <i>i. The method</i> and schedule of monitoring, evaluating, and updating the LMP within a five-year cycle; <i>ii. The process</i> for incorporating the requirements of the LMP into other planning mechanisms, such as comprehensive or capital improvement plans, when appropriate; and <i>iii. How</i> the community will continue public participation in the LMP maintenance process. Annual reviews of the plan are recommended.</p>

Table 1 DMA 2000 Mitigation Plan Requirements of DMA 2000 (cont.)

Requirements for Standard State Mitigation Plan (SSMP)	Additional Requirements for Enhanced State Mitigation Plan (ESMP) and Local Mitigation Plan (LMP)
<p>6. Plan Adoption Process Documents formal adoption by the State before submittal to FEMA for final review and approval.</p> <p>7. Assurances Assurances for compliance with all applicable Federal statutes and regulations in effect for the periods for which it receives grant funding, in compliance with 44 CFR 13.11(c). The SSMP will be amended whenever necessary to reflect changes in State or Federal laws and statutes as required in 44 CFR 13.11(d).</p>	<p>ESMP: Same as SSMP. LMP: Documents LMP adoption by the appropriate local government body. For multi-jurisdictional plans, each jurisdiction requesting plan approval must document adoption. LMP must identify specific projects if funding is requested.</p> <p>ESMP: Should also include a demonstration that the State effectively uses existing mitigation programs to achieve its mitigation goals. (§201.5(b)(3))</p> <p>LMP: While a specific section on assurances is not identified for LMPs, assurance regarding use of the LMP to achieve mitigation goals is inferred by the rule and a section should be included.</p>
d. Review and Updates	
<p>Plans for review and revision to reflect changes in development, progress in Statewide mitigation efforts, and changes in priorities and resubmitted for approval to the appropriate Regional Director every three years. The Regional review will be completed within 45 days after receipt from the State, whenever possible. Note: Although not a requirement, FEMA also encourages States to review their plans in the post-disaster timeframe to reflect changing priorities.</p>	<p>ESMP: Same cycle as SSMPs. LMP: LMP must be submitted to the State Hazard Mitigation Officer for initial review and coordination. The State then sends LMP to the appropriate FEMA Regional Office for formal review and approval. The review process occurs as follows: The Regional review will be completed within 45 days after receipt from the State, whenever possible. Plans must be reviewed, revised if appropriate, and resubmitted for approval within five years in order to continue to be eligible for HMGF project grant funding. For States with managing authority, (that is, States with delegated approval authority for local mitigation plans), FEMA approval will not be required. Instead, States use the criteria in this part to review each LMP within 45 days of receipt, whenever possible, and provide a copy of the approved plans to the FEMA Regional Office .</p>

Source: <http://www.hazus.org/SEHUG/Kick Off Documents/Draft Job Aid-Mitigation Plan Content.pdf>

Table 2 US Community drinking water systems -- Requirements Under the Public Health Security and Bioterrorism Preparedness and Response Act of 2002

Systems serving population of:	Certify and submit Vulnerability Assessment (VA) by:	Certify Emergency Response Plan:
100,000 or greater	March 31, 2003	Six months following the completion of the vulnerability assessment *
50,000 - 99,999	December 31, 2003	
3,301 - 49,999	June 30, 2004	

Source: <http://www.epa.gov/safewater/security/community.html>

Table 3 Example Security Vulnerability Assessment Results, combining Security and Natural Hazards

SYSTEM VULNERABILITY	SECURITY		NATURAL HAZARDS																						
	Consequence of Failure (% People without water)	50%	1	75	50%	25	5	100%	5	100%	25	10%	75	50%	10%	70%	70%	1	50%	1	50%	1	50%		
Correlation Factor (See note 1)																									
North Side																									
Watershed	1%	70%	0%	7%	3%							7%	0%	7%	3%	70%	0%								
Intake Structure	1%	70%	0%	7%	3%	2%								7%	3%										
Lowlift Pump Station	1%	70%	0%	70%	26%	6%	25%	6%	1%	7%	0%			25%	9%							25%	0%		
Treatment Plant	1%	70%	0%	7%	3%				7%	0%				50%	19%										
Disinfection System	1%	70%	0%	7%	3%				7%	0%				7%	3%										
Highlift/Clearwell	1%	70%	0%	7%	3%				7%	0%				25%	9%										

Table 4 Integration of Vulnerability Assessment Findings

Hazard	Avg. Risk	Max Risk	Risk	Mitigation	Est. Cost
Floods	4%	25%	VH	Pump station reconstruction: raise station above the 500-year flood plain.	Not estimated
Earthquake	3%	19%	VH	Add shear walls, roof anchorage and other measures.	\$800,000
Security	2%	11%	VH		\$200,000
Building / Facility Fire / Explosion	1%	8%	H	Develop a standard operating procedure to address storage of flammable materials. Continue annual inspection of electrical equipment to minimize the potential for electrical fires.	Negligible
Winter Snow / Ice Storms	1%	8%	H	Further develop the capability to provide emergency power for the treatment plant and remote pump stations.	Not estimated

the hazard mitigation planning process

Hazard mitigation planning is the process of determining how to reduce or eliminate the loss of life and property damage resulting from natural and human-caused hazards. Four basic phases are described for the hazard mitigation planning process as shown in this diagram.

For illustration purposes, this diagram portrays a process that appears to proceed sequentially. However, the mitigation planning process is rarely a linear process. It is not unusual that ideas developed while assessing risks should need revision and additional information while developing the mitigation plan, or that implementing the plan may result in new goals or additional risk assessment.

organize resources

From the start, communities should focus on the resources needed for a successful mitigation planning process. Essential steps include identifying and organizing interested members of the community as well as the technical expertise required during the planning process.



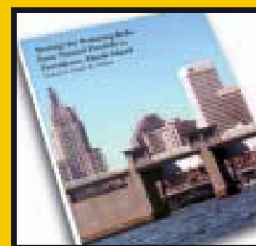
assess risks

Next, communities need to identify the characteristics and potential consequences of hazards. It is important to understand how much of the community can be affected by specific hazards and what the impacts would be on important community assets.



develop a mitigation plan

Armed with an understanding of the risks posed by hazards, communities need to determine what their priorities should be and then look at possible ways to avoid or minimize the undesired effects. The result is a hazard mitigation plan and strategy for implementation.



implement the plan and monitor progress

Communities can bring the plan to life in a variety of ways ranging from implementing specific mitigation projects to changes in the day-to-day operation of the local government. To ensure the success of an on-going program, it is critical that the plan remains relevant. Thus, it is important to conduct periodic evaluations and make revisions as needed.

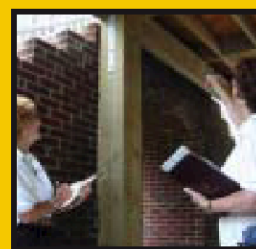


Figure 1 The Hazard Mitigation Planning Process (FEMA 386-1)

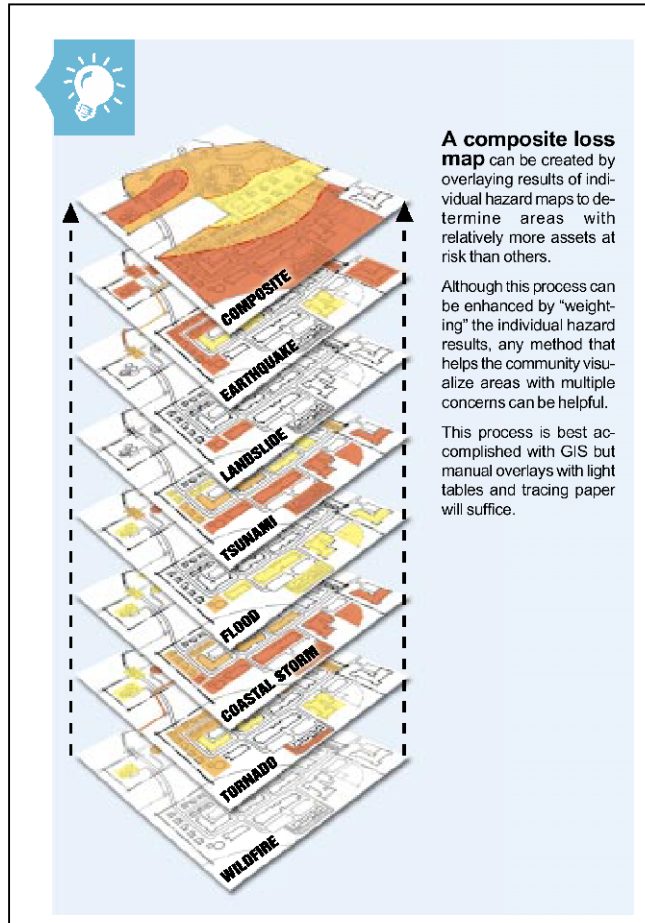


Figure 2 Composite Loss Map (FEMA 386-2)

Earthquake Professional Office Building Loss Estimation Tables

PGA (g)	Building Damage Ratio (%)**							
	Concrete Wall Construction				Steel Frame (Braced)			
	High*	Moderate*	Low*	Precode*	High*	Moderate*	Low*	Precode*
0.55	14.0	23.7	37.0	43.7	14.5	18.6	31.2	38.3
0.50	12.0	20.0	31.0	39.1	12.1	15.2	25.0	32.1
0.45	9.9	17.2	27.2	34.2	10.5	13.3	20.8	27.6
0.40	7.2	11.4	16.5	22.0	7.9	9.1	13.1	17.5
0.35	5.4	9.4	13.5	18.4	6.5	7.3	10.0	13.6
0.30	4.2	7.2	10.0	14.2	4.7	5.4	7.5	10.1
0.25	3.0	4.7	7.8	11.0	3.7	4.0	5.3	7.4
0.20	2.0	2.9	5.6	8.1	2.5	2.9	3.7	5.2
0.15	1.0	1.8	3.2	5.4	1.5	1.7	2.4	3.2
0.10	0.4	0.6	1.0	1.5	0.5	0.7	0.9	1.3
0.07	0.2	0.3	0.4	0.6	0.2	0.3	0.4	0.5
0.05	0.0	0.1	0.2	0.2	0.0	0.1	0.2	0.2
0.03	0.0	0.0	0.0	0.1	0.0	0.0	0.0	0.0

Figure 3 Earthquake Loss Estimation Tables (FEMA 386-2)

Alternative Mitigation Actions	Prevention																
	Building codes	Coastal zone management regulations	Density controls	Design review standards	Easements	Environmental review standards	Floodplain development regulations	Floodplain zoning	Forest fire fuel reduction	Hillside development regulations	Open space preservation	Performance standards	Shoreline setback regulations	Special use permits	Stormwater management regulations	Subdivision and development regulations	Transfer of development rights
Floods	■	■	■	■	■	■	■	■			■	■	■	■	■	■	■
Earthquakes	■		■	■	■	■				■	■	■		■		■	■
Tsunamis	■	■	■	■		■					■	■	■	■		■	■
Tornadoes	■			■		■						■				■	
Coastal Storms	■	■	■	■	■	■	■	■			■	■	■	■		■	■
Landslides	■		■	■	■	■			■	■	■	■	■	■		■	■
Wildfires	■		■	■	■	■			■	■	■	■		■		■	■

Alternative Mitigation Actions	Property Protection					Public Education & Awareness		
	Acquisition of hazard-prone structures	Construction of barriers around structures	Elevation of structures	Relocation out of hazard areas	Structural retrofits (e.g., reinforcement, flood-proofing, storm shutters, bracing, etc.)	Hazard information centers	Public education and outreach programs	Real estate disclosure
Floods	■	■	■	■	■	■	■	■
Earthquakes	■			■	■	■	■	■
Tsunamis	■	■	■	■	■	■	■	■
Tornadoes					■	■	■	■
Coastal Storms	■	■	■	■	■	■	■	■
Landslides	■			■		■	■	■
Wildfires	■			■		■	■	■

Figure 4 Alternative Mitigation Actions by Hazard (FEMA 386-3)

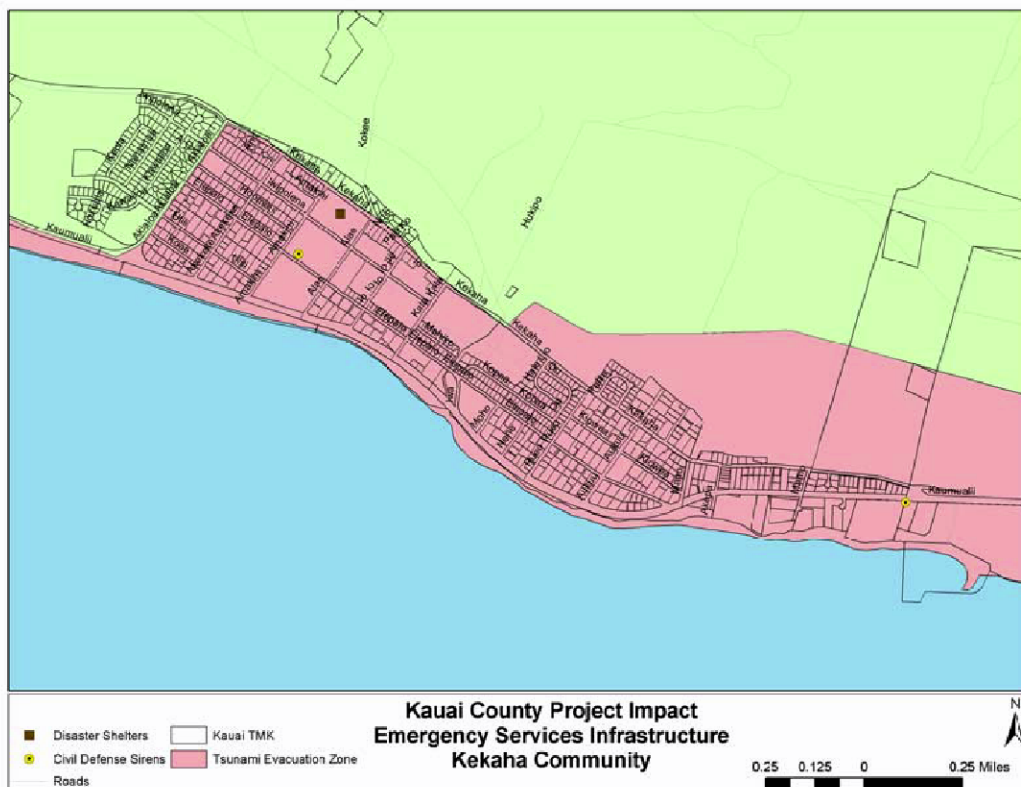
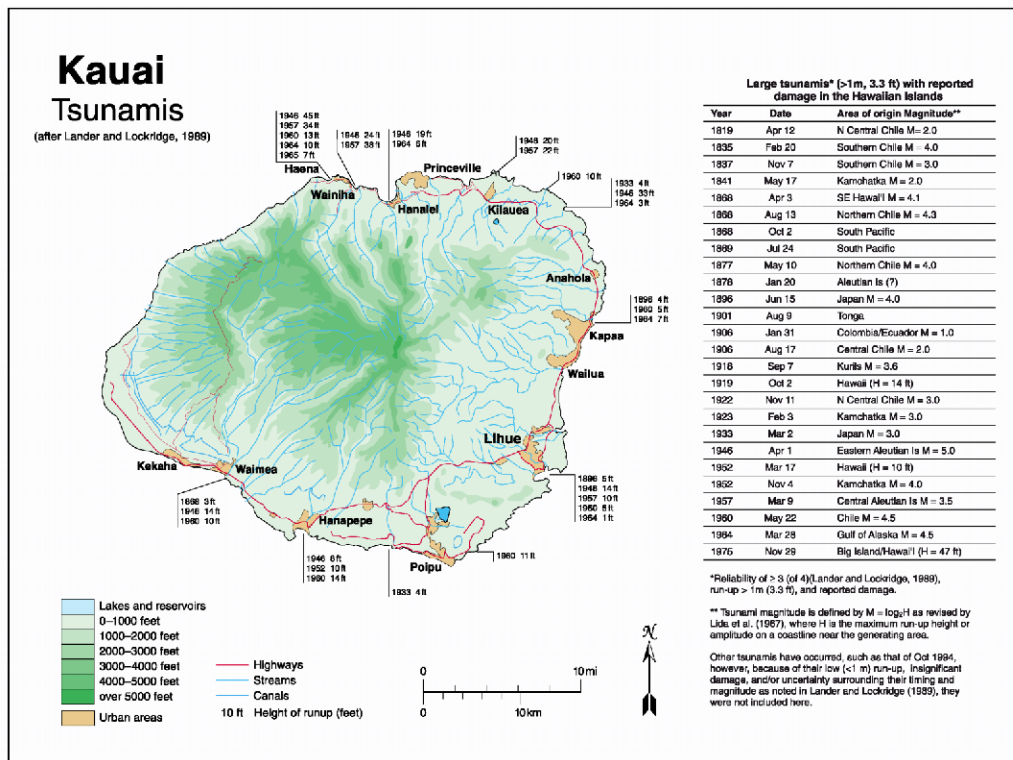


Figure 5 Kauai (Hawaii) (top) Tsunami Hazard (b) tsunami risk to emergency facilities

(source: http://www.mothernature-hawaii.com/county_kauai/planning.htm)

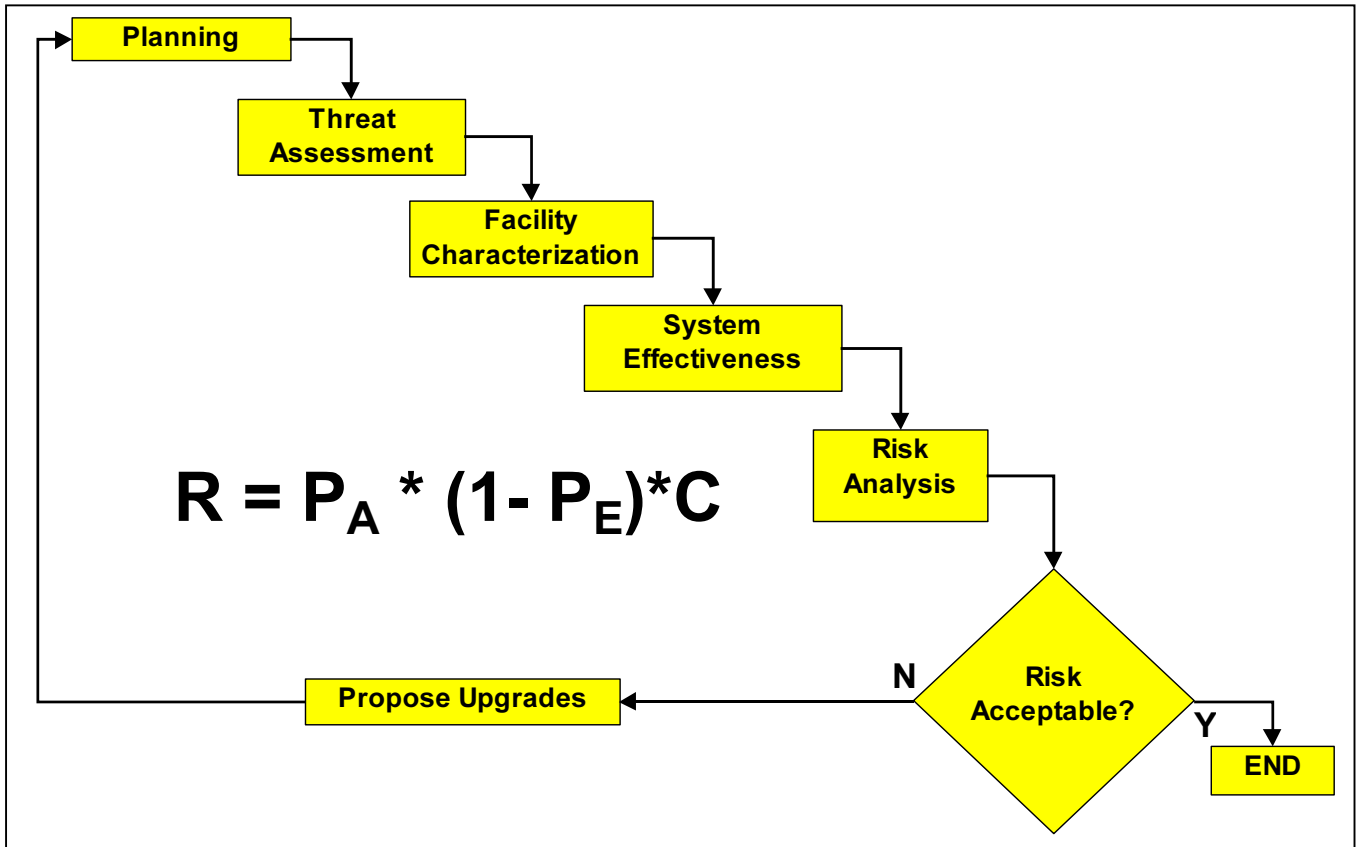


Figure 6 Security Vulnerability Assessment methodology

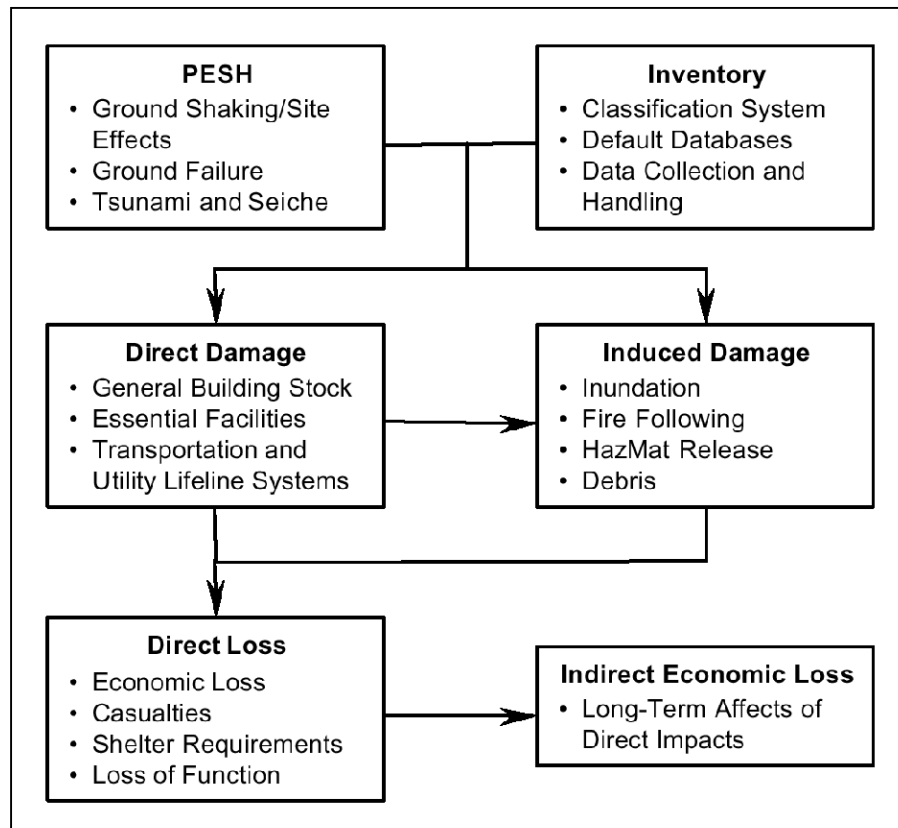


Figure 7 HAZUS Earthquake Methodology (NIBS, 1999)

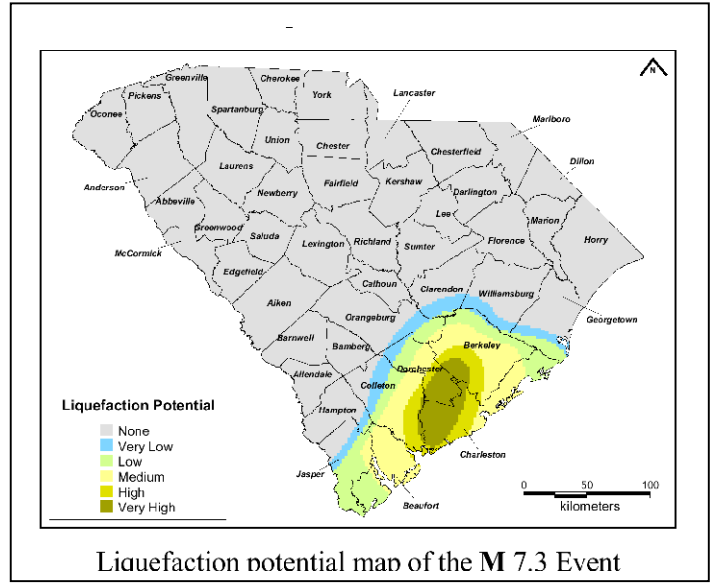
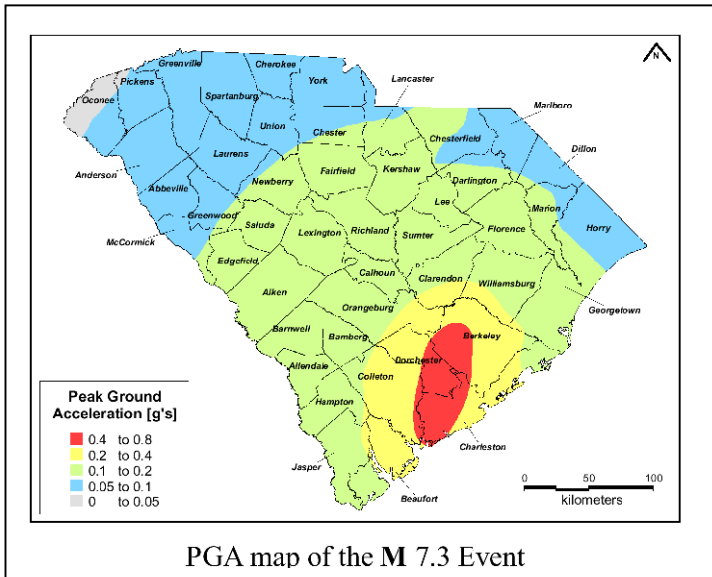


Figure 8 HAZUS results, state of South Carolina (Bouabid et al, 2002)

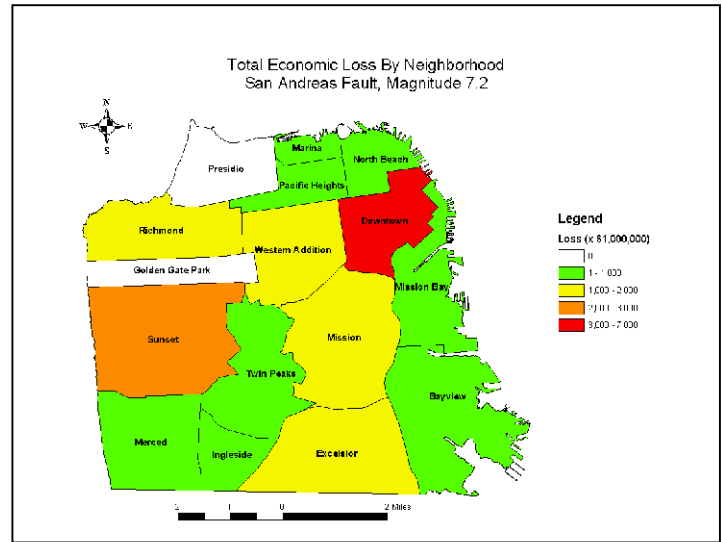
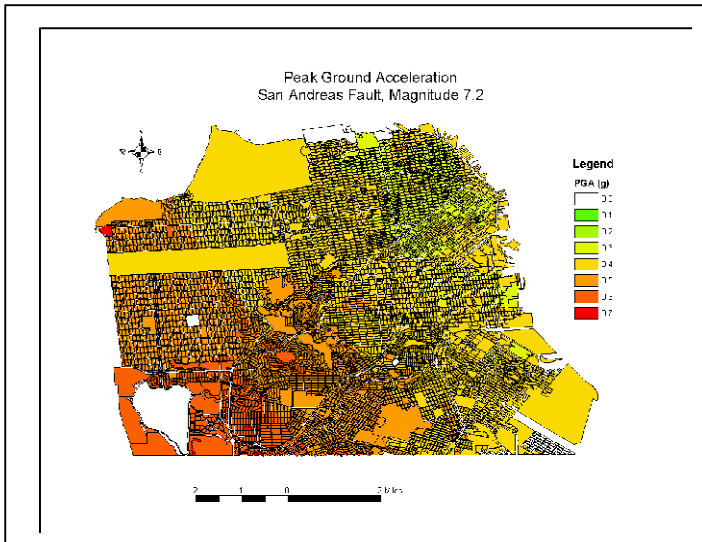


Figure 9 HAZUS results, City of San Francisco CA (Kornfield et al, 2002)

SEISMIC DESIGN: FROM BUILDINGS TO CITIES

Akira Wada

*Professor, Structural Engineering Research Center
wada@serc.titech.ac.jp*

Abstract: A human life is around 80 years. Each building will be used about 60 years. A life of the city have to be more than one thousand years. An extreme big earthquake will come to the city in every several hundred years or one thousand years. When we want to make safe city to the next big earthquake, we have to make buildings having high seismic performance structures such as seismic isolated or passive controlled structures than before.

1. Seismic design of buildings

Many studies have been carried out on a variety of earthquake resistant structures such as seismic isolated structures, passive controlled structures, strength oriented structures and ductile frame structures. Of these methods, the highest seismic performance is expected from seismic isolated structures. Structures can be designed to achieve the required performance within the limits of each of the above four structural methods, if the design earthquake ground motion can be defined.

2. Seismic design for urban city

Earthquake is a natural phenomenon. The largest problem in the seismic design of building structures is the uncertainty of future occurrence of ground motion where the building stands. When it will happen and how large it will be are totally unpredictable. The probability of occurrence of a large earthquake ground motion may be evaluated as negligible, and thus neglected in the design process on economic grounds. However, this would be a big gamble, because although the life of individual buildings may be 60 years, the life of a city may be longer than 1000 years. Individual buildings are components of a city. The seismic issues of a city cannot be solved if the seismic resistance of its individual buildings is determined only from the relationship between the life of a single building and the earthquake occurrence in this life span.

3. Level of seismic design and violation of private property rights

Nevertheless, criticism would arise from society if individual buildings were designed for the largest level of earthquake ground motion. However, if there had been no large earthquake in the period until the building was demolished after several 10s of years, the structures would have been wastefully over-designed. Actions to legally demand excessively high seismic performance are interpreted as a violation of Article 29 of the Constitution of Japan [property right]. This is a very difficult issue.

4. Leaping improvement of seismic performance that does not increase cost

New technology development needs to be advanced. It is necessary to develop new structural systems that provide a huge leap in seismic performance at the same cost as current construction methods. If the cost is not excessive, the rationale is put in place to seek no building damage against very rarely occurring large earthquake ground motions. Society could then not claim that the expenditure is wasted. As a result, safety of cities would become very high. If the life of a city were expected to be 1000 or 2000 years, it would become possible to employ that lifetime as the return period of the earthquake ground motion in design.

5. Research target

The focus of our studies is to pursue this huge leap in seismic performance. Reinforced concrete structures and steel structures introduced to Japan from Europe during the Meiji Restoration period have suffered a lot of earthquake damage in the past 100 years. In my opinion, the limit of these structures did not start to be understood until after we entered the 21st century. It is necessary to greatly improve seismic performance of cities by popularizing new technologies such as seismic isolated structures and passively controlled structures. The desired approach should be to promote building structures of higher seismic performance while maintaining generally the same cost rather than the approach of fixing the required seismic performance followed by seeking cost reduction.

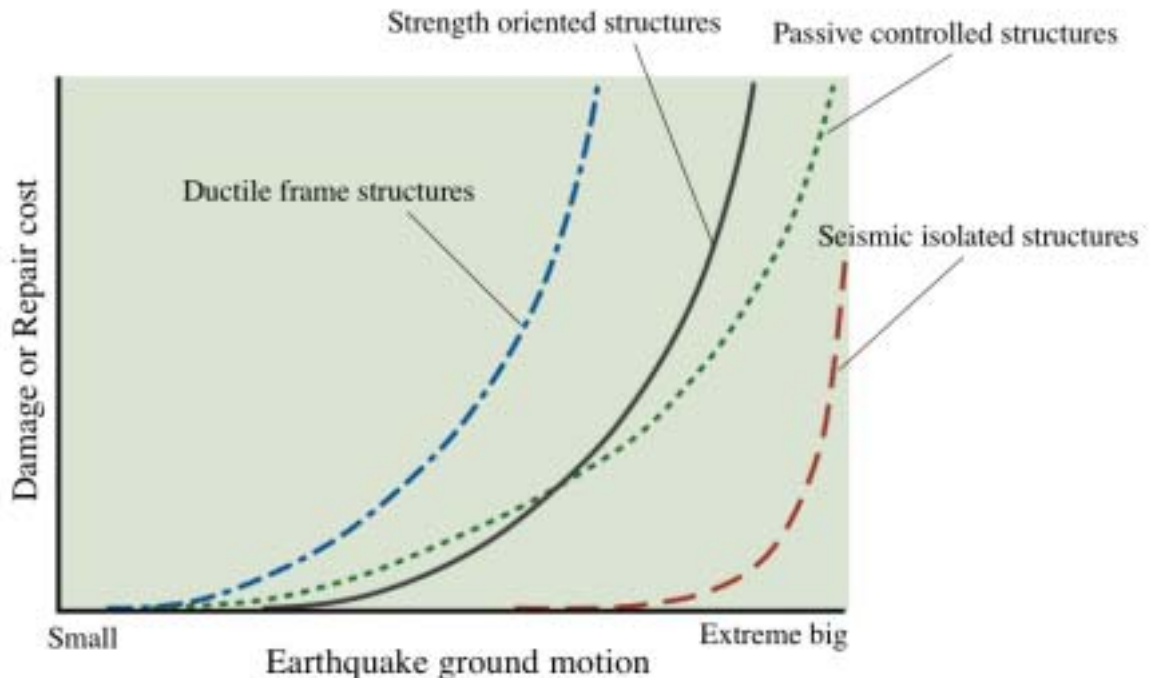


Fig. 1 Earthquake ground motion vs. Damage or Repair cost

Fig. 2 Damages of buildings in the city after big earthquake, in the case that all buildings were designed as ductile frame structure.

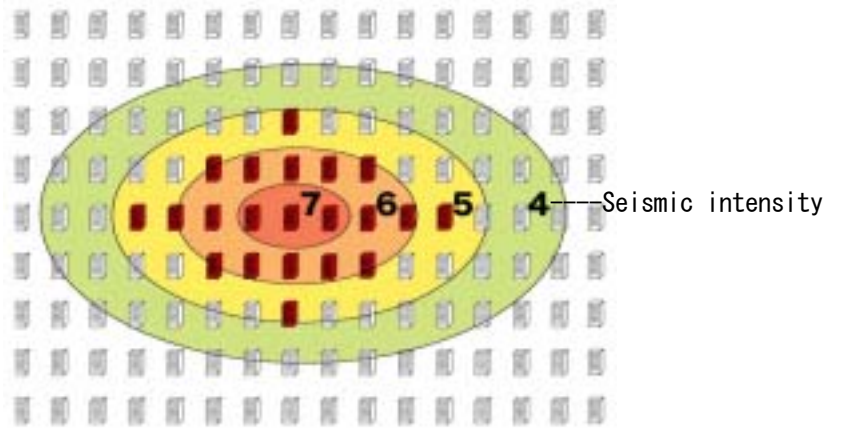


Fig. 3 Damages of buildings in the city after big earthquake, in the case that all buildings were designed as strength oriented structure.

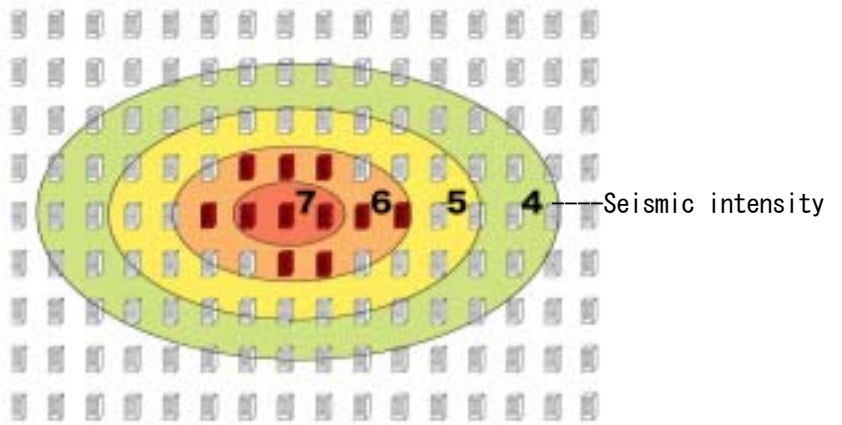


Fig. 4 Damages of buildings in the city after big earthquake, in the case that all buildings were designed as passive controlled structures.

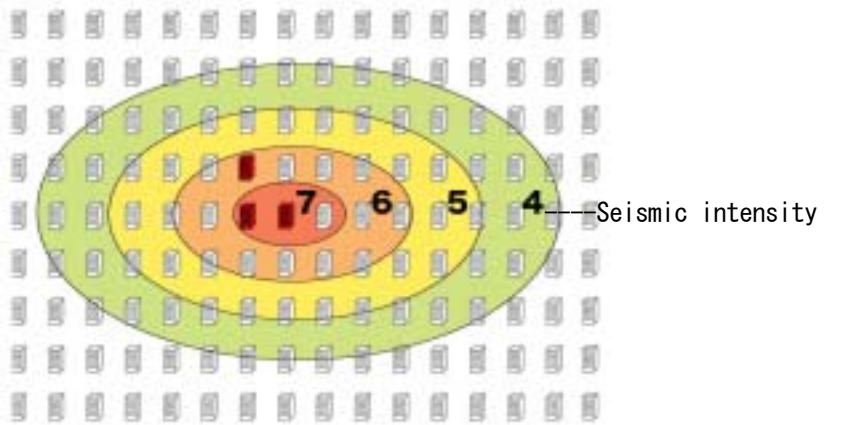
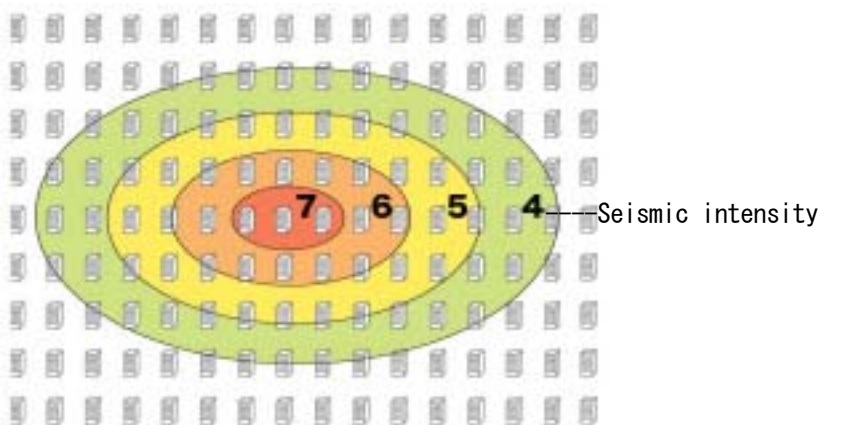


Fig. 5 Almost no Damage of building in the city after big earthquake, in the case that all buildings were designed as seismic isolated structures.



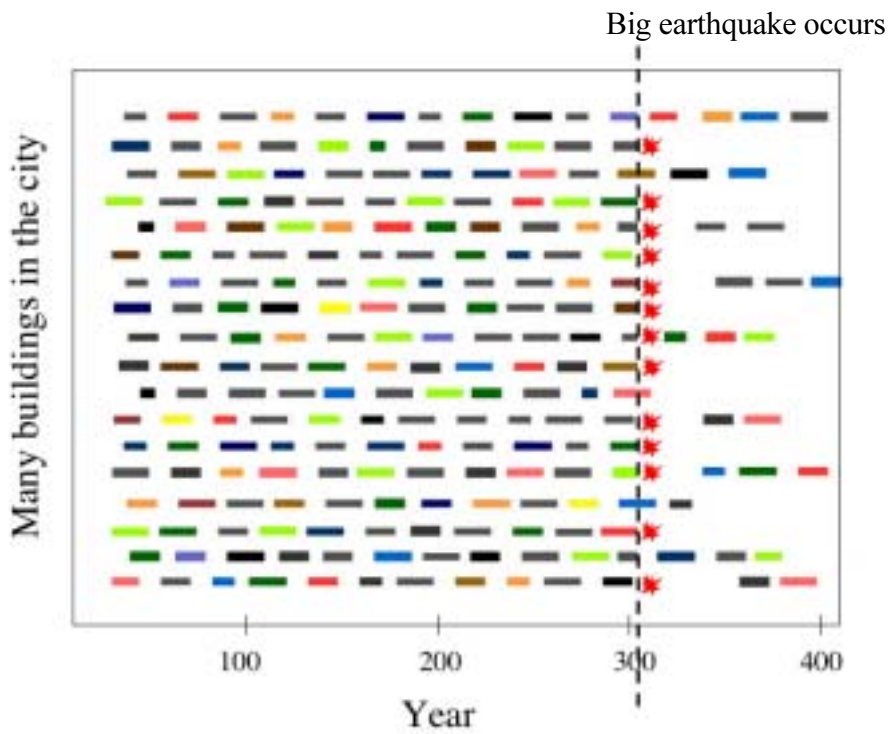


Fig. 6 Many buildings will suffer severe damages by the next big earthquake when the buildings are designed in considering with performance of the structures in 60 years and permitting of large plastic deformation of the structures.

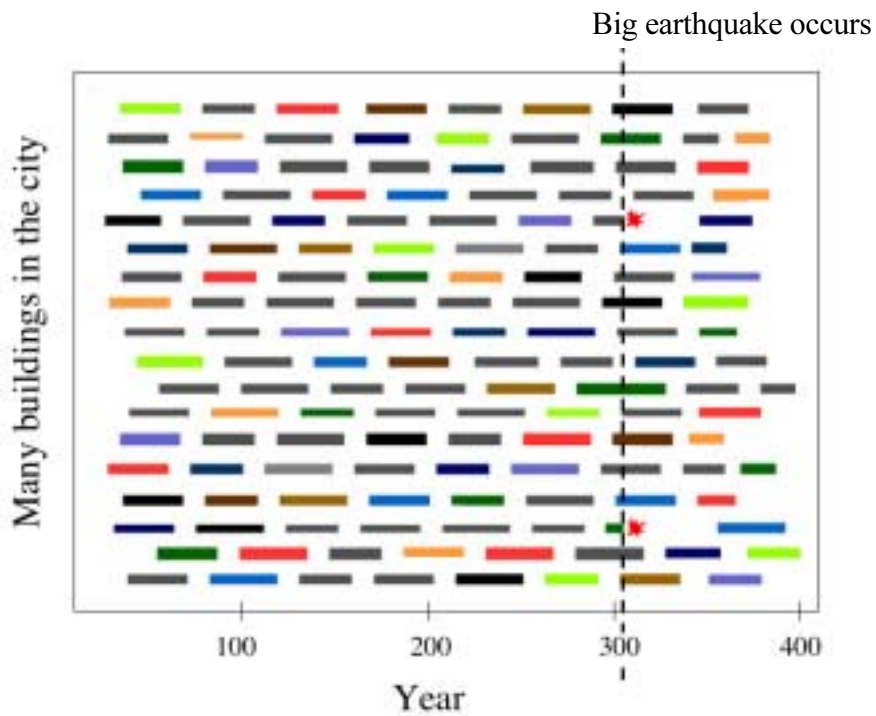


Fig. 7 Few buildings will suffer severe damages by the next big earthquake when the buildings are designed in considering with performance of the city in 1000 years and using seismic isolated or passive controlled structural system or new technologies.

An Optimal Design Problem of Infrastructure Consistent with Maintenance/Replacement Scheduling

T. Ueda ¹⁾ and **N. Yamada** ²⁾

1)Associate Professor , Department of International Development Engineering, Tokyo Institute of Technology

2)Student, Department of Civil Engineering, Tokyo Institute of Technology

tueda@plan.cv.titech.ac.jp

Abstract: Degrading of infrastructure not only results in lower service level but also in higher risk of earthquake damage. The maintenance/replacement should be well scheduled so as to maximize an economic value of infrastructure. On the other hand, the design of infrastructure should also follow the maximization principle. The design and the schedule of maintenance/replacement interact with each other. Then, we should optimize both of them in a unified framework. This paper proposes an optimal design problem consistent with maintenance/replacement scheduling. The problem is a type of bi-level programming, which contains an optimal scheduling problem at lower level and an optimal design at upper level. In the optimal scheduling, the degradation of infrastructure by fatigue is modeled as the Markov Chain Process. In the optimal design, the best material type is chosen. After we formulate a general framework for the problem, we apply it to a case in practice. The results suggest that the schedule and the design interact with each other and are very critical for the economic value of infrastructure.

1. INTRODUCTION

Degrading of infrastructure not only results in lower service level but also in higher risk of earthquake damage. The maintenance/replacement should be well scheduled so as to maximize an economic value of infrastructure. On the other hand, the design of infrastructure should also follow the maximization principle. The design and the schedule of maintenance/replacement interact with each other. Then, we should optimize both of them in a unified framework. This paper proposes an optimal design problem consistent with a maintenance/replacement strategy. The problem is a type of bi-level programming, which contains an optimal scheduling problem at lower level and an optimal design at upper level.

2. MODEL

Design of a structure is formalized as a bi-level programming. The upper level problem is to choose design variables such a material type, a size of member and a shape so as to maximize the economic value of an infrastructure. The programming at the upper level is,

$$V(X(0)) = \max_{d \in D_x} V(X(0), d) \quad (1)$$

where $V(\cdot)$ is the net present value of the infrastructure defined at the lower level, $X(0)$ the initial state of the infrastructure, d the design variable and D_x the feasible set of d .

The lower level problem is to find the rule of maintenance/replacement action $u(t)$ in any periods in time horizon indicated by $t \in \{0, \dots, T\}$. Benefit/cost flow is dependent on the state of the infrastructure $X(t)$, action $u(t)$ and the design d . The net present value, which is the objective function at the upper level, is defined as

$$V(X(0), d) = \max_{u(t) \in U} E_{X(t)} \left\{ \sum_{t=0}^T b(X(t), u(t), d)(1+\rho)^{-t} - \sum_{t=0}^T C(X(t), d)(1+\rho)^{-t} - \sum_{t=0}^T R(X(t), u(t), d)(1+\rho)^{-t} - \sum_{t=0}^T C_F(d)P_F(X(t))(1+\rho)^{-t} \right\} - I(d) \quad (2.a)$$

s.t.

$$X(t) = F(X(t-1), u(t), d, \omega) \text{ for all } t \in \{1, \dots, T\}, \quad (2.b)$$

$$X(0) = \bar{X}(0) : \text{given} . \quad (2.c)$$

$b(\cdot)$ is the benefit in the period t . ρ is the social discount rate. $C(\cdot)$ is the operation cost. $R(\cdot)$ is the cost of maintenance/replacement action. $C_F(\cdot)$ is the recovery cost when damaged by earthquake and $P_F(\cdot)$ is the probability that the structure is damaged in the unit period. $I(\cdot)$ is the initial cost or the construction cost of the structure. The state of the infrastructure $X(t)$ evolves with the state equation in (2.b). The initial state $\bar{X}(0)$ is given.

The probability of damage by earthquake is assumed to be dependent on the state $X(t)$. If the structure is more deteriorated, then the probability is higher. The state equation in the above represents the stochastic process which includes the random factor ω .

The programming described by (2.a) – (2.c) is a kind of stochastic control problem. To solve it, the Bellman's principle of optimality is often applied and therefore the Bellman's equation is employed.

3. APPLICATION

3.1 Specification of the model

In this paper, we apply the model formalized in the previous section to design of a bridge. The bridge is a steel bridge whose initial cost can be simply estimated by total weight. The design is the choice of a material type $d \in \{1, 2, 3\}$, where 1 is the strong steel, 2 the normal steel and 3 the weak steel. We first specify the state $X(t)$ in discrete form $X(t) = i(t) \in \{1, 2, 3, 4\}$. Then the action $u(t)$ is also specified as

$$u(i(t), t) = \begin{cases} 0 & \text{for do nothing} \\ 1 & \text{for do the action} \end{cases} \quad (3)$$

Functions in (2.a) and (2.b) are specified as,

$$b(X(t), u(t), d) = b\psi(1 + \lambda)^t \quad (4.a)$$

$$C(X(t), d) = \bar{c} \quad (4.b)$$

$$R(X(t), u(t), d) = \{b\psi(1 + \lambda)^t l(i(t)) + \alpha R(i(t)) + \beta(wv(d) + A_1)\}u(i(t), t) \quad (4.c)$$

$$I(d) = wv(d) + A_2 \quad (4.d)$$

$$C_F(d) = wv(d) + A_3 \quad (4.e)$$

$$\text{and } P_F(X(t)) = P_F(i(t)) \quad (4.f)$$

In (4.a), b is the annual benefit of a unit of traffic volume, ψ the initial annual traffic volume and λ the annual growth rate of traffic. In (4.b), the operation cost is simply assumed to be constant. In (4.c), the cost of maintenance/replacement action consists of $b\psi(1 + \lambda)^t l(i(t))$ the reduction of benefit where $l(i(t))$ is the rate of stopping service due to the action, $R(i(t))$ the component dependent on the state $i(t)$ and $wv(d) + A_1$ dependent on the weight of the bridge. This cost is valid when the action is done $u(i(t), t) = 1$.

The stochastic process denoted by the state equation in (2.b) is rewritten into the Markov Chain, whose transition probability matrix is given by

$$\mathbf{M}^{w.o.}(d) \frac{\psi(1+\lambda)^t}{\phi} = (P_{i,j}^{w.o.}(d))_{i,j \in \{1,2,3,4\}} \quad \text{for nothing done} \quad (5.a)$$

$$\text{and } \mathbf{M}^w = (P_{i1}^w = 1, P_{ij}^w = 0)_{i \in \{1,2,3,4\}, j \in \{2,3,4\}} \quad \text{for the action.} \quad (5.b)$$

(5.a) indicates that the probability matrix for the unit of traffic volume (a million cars per year) $\mathbf{M}^{w.o.}(d)$ must be multiplied with itself for the times $\frac{\psi(1+\lambda)^t}{\phi}$. Then in the year when traffic volume is large, the probability of deterioration becomes higher. The matrix in (5.b) means that whenever the action is done, the state always comes back to $i(t) = 1$.

The Bellman equation for the model with the specifications is

$$\begin{aligned}
& V(i(t) = i, d) \\
& = \max_{u(i(t), t) \in \{0,1\}} b\psi(1 + \lambda)^t - \bar{c} - (b\psi(1 + \lambda)^t l(i(t)) + \alpha R(i(t)) + \beta(w\nu(d) + A_1))u(i(t), t) \\
& \quad - (w\nu(d) + A_3)P_F(i(t)) \\
& \quad + \left(\frac{1}{1 + \rho}\right) \left[\sum_{j \in \{1,2,3,4\}} \{(1 - u(i(t), t))P_{i,j}^{w.o.}(d) + uu(i(t), t)P_{i,j}^w\} V(i(t+1) = j, d) \right]
\end{aligned} \tag{6}$$

Solving the Bellman equation by backward induction (See Ueda and Kimoto(2003) and Judd(1998)), we can calculate the net present value in (2.a) for each design d .

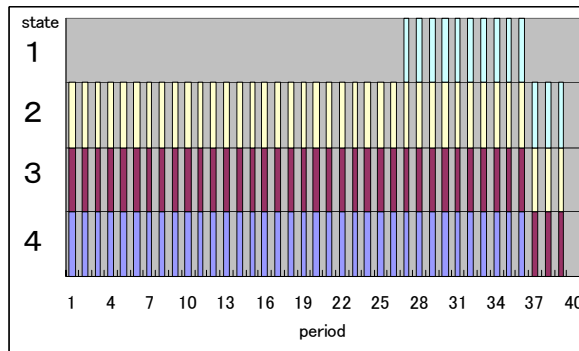
The parameters and necessary information for specified function and matrices in (4.a)-(5.b) are listed in Table 1.

(a) Material type					
	Strong (1)	Normal (2)	Week (3)		
Spec	SM570	SM490	SM400		
Cost $\nu(d)$	140,000(yen/ton)	110,000(yen/ton)	90,000(yen/ton)		
(b) Parameters for benefit and cost					
b	\bar{c}	w	$A_1 = A_2 = A_3$	$1/(1 + \rho)$	
60 (yen/car)	50000 (yen)	300 (ton)	250,000,000(yen)	0.96	
(c) Parameters for maintenance/replacement action					
State $i(t)$	Crack	Action	Cost of Action		
			$\alpha R(i(t)) + \beta(w\nu(d) + A_1)$		
1	< 10 mm	TIG Processing	5,000,000 (yen)		
2	10 mm - 15mm	Welding	10,000,000 (yen)		
3	15mm - 30 mm	Steel Plate	25,000,000(yen)		
4	30 mm <	Replacement	Initial Cost		
(d) Parameters for earthquake risk					
State $i(t)$	Probability of damage				
	$P_F(i(t))$				
1	0.05				
2	0.1				
3	0.2				
4	0.35				
(e) Matrix for Markov Chain for the unit of traffic volume (a million cars/year)					
$\mathbf{M}^{w.o.}(1) =$	$\begin{bmatrix} 0.9930 & 0.0070 \\ & 0.9915 & 0.0085 \\ & & 0.9800 & 0.0200 \\ & & & 1.0000 \end{bmatrix}$	$\mathbf{M}^{w.o.}(2) =$	$\begin{bmatrix} 0.9846 & 0.0154 \\ & 0.9840 & 0.0160 \\ & & 0.9576 & 0.0424 \\ & & & 1.0000 \end{bmatrix}$	$\mathbf{M}^{w.o.}(3) =$	$\begin{bmatrix} 0.9630 & 0.0370 \\ & 0.9580 & 0.0420 \\ & & 0.8670 & 0.1330 \\ & & & 1.0000 \end{bmatrix}$

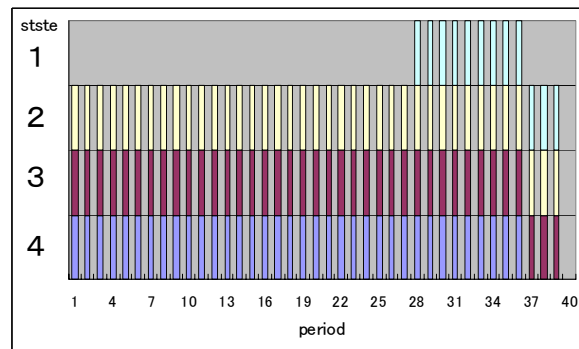
Table 1 Setting of parameters in case study

3.2 Results

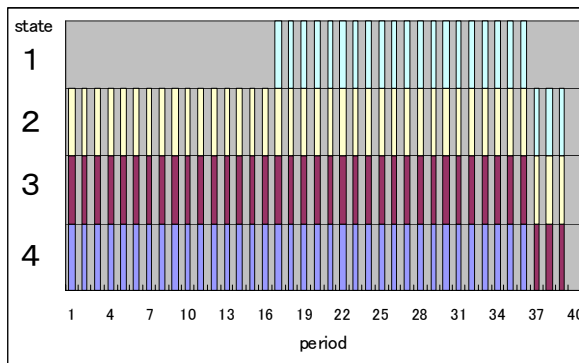
We first compare the optimal strategy of maintenance/replacement action for each material type when the annual growth rate of traffic is 6%. Figure 1 shows the strategy for each type. Each panel in the figure indicates that for example if the state in the period 4 becomes 2,3, or 4, then do the action, otherwise do noting. However, the strategy is not time invariant. Furthermore, we find differences in strategy between material types. Picking up the period 22, we find that if the state becomes 2,3, or 4, then do the action in the cases of design 1 (strong steel) and 2 (normal steel), and in contrast that if the state becomes 1, 2,3, or 4, then do the action in the cases of design 3 (week steel).



(a) Material type 1 (strong steel)



(b) Material type 2 (normal steel)



(c) Material type 3 (week steel)

Figure 1 Comparison of maintenance/replacement strategy between material types

The differences in maintenance/replacement strategy also result in differences in the net present value of the bridge as shown in Figure 2. The material type 1 (strong steel) indicates the

highest economic value, 2 (normal steel) the second and 3 (week steel) the lowest. As a solution of the upper level programming, the optimal design as material choice is the type 1 (strong steel) in this case.

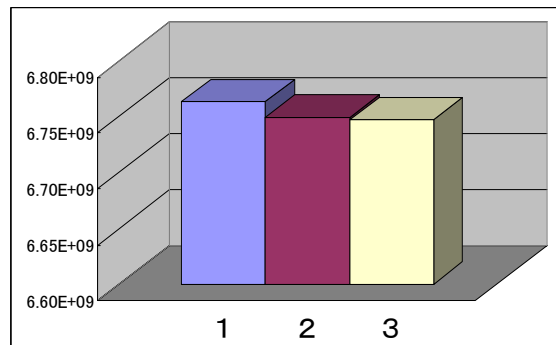


Figure 2 Comparison of the economic value of the bridge between material types for 6% traffic growth

As the society becomes more aged or has less population, the traffic volume may decrease. It is of interest that we examine the case that the annual growth rate of traffic is negative, -3%. Figure 3 shows the net present value of the bridge for each material type. In contrast to the case of 6% as already examined, the material type 3 indicates the highest economic value. The optimal design has varied from the previous case.

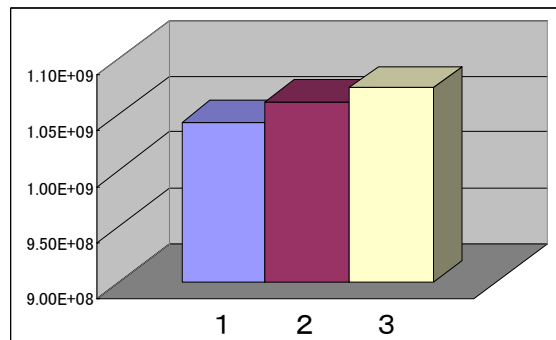


Figure 3 Comparison of the economic value of the bridge between material types for -3% traffic growth

Throughout cases in various setting of parameters, we have found that the optimal design and strategy of maintenance/replacement action interact with each other. Although the implications are still case-specific, the approach of the bi-level programming has been proved to be useful in the economic design of the infrastructure.

4. CONCLUDING REMARKS

We have proposed a bi-level programming model for the economic design of an infrastructure. The results of case studies suggest that the schedule and the design interact with each other and are very critical for the economic value of infrastructure.

We should try to enhancement of the model and examination of the model throughout more and more case studies. In particular, stochastic process of deterioration must be modeled more carefully.

References:

Ueda, T. and Kimoto, Y. (2003), MAINTENANCE AND REPLACEMENT STRATEGIES OF URBAN INFRASTRUCTURE BY DYNAMIC OPTIMIZATION, Computers for Urban Planning and Management, Sendai, (CD-R),2003

Judd, K. (1998), Numerical Methods in Economics, MIT Press

EVALUATION OF PORTFOLIO SEISMIC RISK DUE TO DIFFERENT ALLOCATIONS OF MULTIPLE BUILDINGS

H.Suwa¹⁾, A.Nobata²⁾ and M.Seki³⁾

1) Deputy Manager, Obayashi Corporation Technical Research Institute, Japan

2) Group Leader, Obayashi Corporation Technical Research Institute, Japan

3) General Manager, Obayashi Corporation Technical Research Institute, Japan

suwa.hitoshi@obayashi.co.jp, nobata.arihide@obayashi.co.jp, seki.matsutaro@obayashi.co.jp

Abstract : The purpose of this paper is to develop a method for evaluating portfolio seismic risk through a set of scenario earthquakes in and around Japan, and to compare with seismic risk of several portfolios, the contents of which are mutually different. It is quantitatively verified that value at risk such as PML is to be different because of the degree of correlation.

1. INTRODUCTION

In recent years, seismic risk analysis of building has been widely carried out in Japan for the purpose of due diligence business for real estate investment trust and so on. Seismic risk curve for a single building, which can be obtained through both seismic hazard curve at construction site and seismic loss curve of building, has been generally calculated. However, from the standpoint of risk dispersion, portfolio seismic risk, which indicates the seismic risk with respect to multiple buildings located at scattered construction sites, is to be evaluated among property insurance companies etc. Seismic hazard curve can not be used for calculating portfolio seismic risk, because this curve is only defined with respect to a single construction site. As a single earthquake may have an influence on seismic damage of multiple buildings, it is necessary to add up the seismic loss of each building due to a specific earthquake on condition that the geographical relationship between hypocenter location and each construction site is appropriately considered. Therefore the analytical method by making use of numerous scenario earthquakes, which can equivalently represent probabilistic seismic hazard at a specific construction site, is needed in order to evaluate portfolio seismic risk. The purpose of this paper is to evaluate portfolio seismic risk through a set of scenario earthquakes in and around Japan, and to quantitatively compare with seismic risk of several portfolios, the contents of which are mutually different.

2. ANALYTICAL METHOD FOR EVALUATING PORTFOLIO SEISMIC RISK

The flowchart for evaluating portfolio seismic risk curve is shown in Fig.1. It is denoted that 'n' is the order of a scenario earthquake and 'm' is the order of a building respectively. A set of scenario earthquakes in and around Japan [1] is adopted in order to calculate probabilistic seismic hazard at a construction site. The exceedance loss curve of m-th building due to n-th scenario earthquake can be obtained through integrating the seismic loss distribution of building multiplied by each small occurrence probability of seismic intensity. By repeating this calculation with respect to other buildings M times, the exceedance loss curve of multiple buildings due to n-th scenario earthquake is calculated. Moreover, by repeating this procedure with respect to other scenario earthquakes N times, the exceedance loss curve of multiple buildings due to all selected scenario earthquakes is calculated. Portfolio seismic risk curve can be evaluated through this exceedance loss curve. The detail of these procedures is

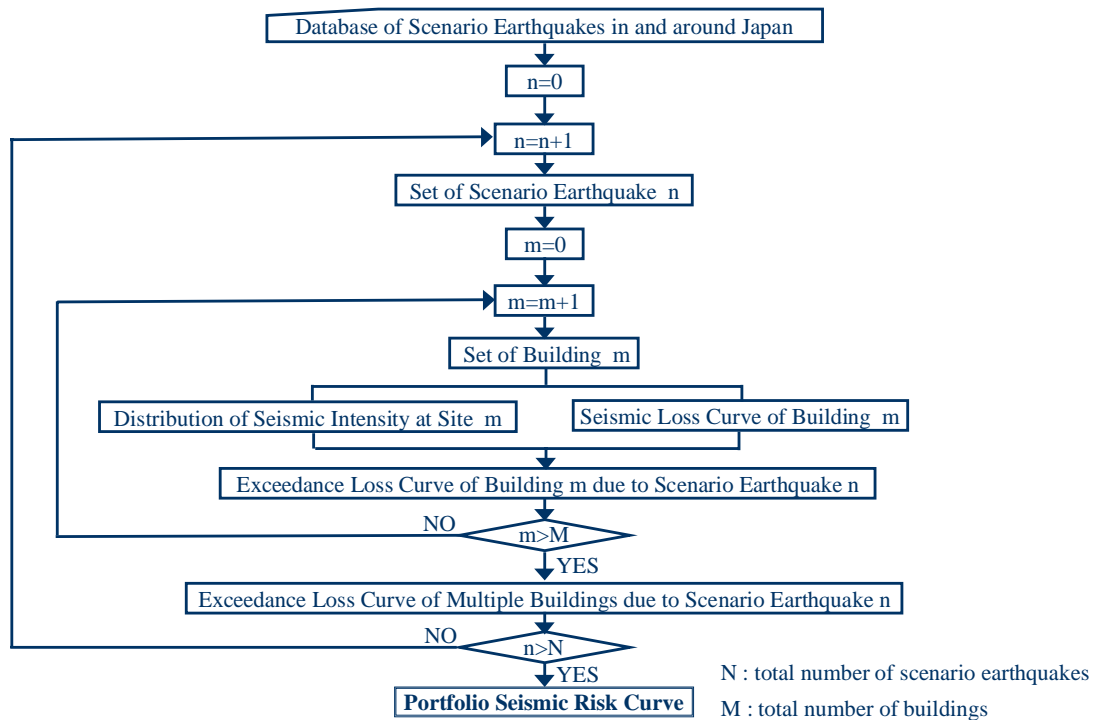


Fig.1 Flowchart for Evaluating Portfolio Seismic Risk Curve

described as follows.

2.1 A Set of Scenario Earthquakes

For seismic source model, many earthquakes which are located at inland and sea are considered. The model consists of three type seismic sources, which are plate boundaries, inland active faults and background earthquakes. For the plate boundary source, the Pacific Ocean Plate and the Philippine Sea Plate are considered. For the fault source, several major tectonic lines are considered as vertical plane sources, and others are considered as line sources. The background source is considered to explain historical earthquakes which are not related with plate boundaries or active faults.

A set of scenario earthquakes, which appropriately represent the characteristic of the above mentioned seismic source model, is developed. A scenario earthquake consists of a set of information including a name of source, a location of source, a distribution of magnitude and its annual occurrence rate. The number of scenario earthquakes should be reduced in order to make it rapid to calculate portfolio seismic risk. In this study, about twenty-eight thousand scenario earthquakes, which are located at 20km grid-points throughout Japan, are generated. The accuracy of this reduced model has been confirmed by comparing these results with the probabilistic seismic hazard curve at several principal cities.

2.2 Seismic Intensity at Construction Site

Seismic intensity at a construction site is calculated through the attenuation model, representative parameters of which are magnitude of a scenario earthquake and shortest distance from a hypocenter. The uncertainty of attenuation is modeled by lognormal distribution.

2.3 Seismic Fragility Curves of Buildings

For structural type of buildings, R/C buildings, which are modeled by shear lumped mass system, are selected in this study. In order to obtain the relationship between seismic intensity and response relative story displacement for each story, earthquake response analysis due to several simulated seismic

Table1 Parameters of Limit Drift Angle for Seismic Fragility Curve

	Minor	Intermediate	Major	Collapse
Median	1/200	1/100	1/75	1/40
Lognormal Standard Deviation	0.4	0.4	0.4	0.4

waves is carried out. Semi-continuous relationship of them is calculated by changing the level of peak ground acceleration at several points, and the relationships may be modeled by the following regression equation.

$$\delta = d_1 \times a^{d_2} \quad (1)$$

a : peak ground acceleration δ : response relative story displacement
 d_1, d_2 : coefficient of regression

Minor damage, intermediate damage, major damage, and collapse are considered for the level of damage. The shape of seismic fragility curve is modeled by lognormal distribution, and its parameters are determined as follows. The median of limit drift angle with respect to each level of damage is given through the damaged database of buildings suffered from several historical earthquakes. The lognormal standard deviation is assumed to be 0.4 for all levels of damage based on damaged ratio curves in terms of many buildings in 1995 Hyogo-Ken-Nanbu earthquake [2]. The median and lognormal standard deviation of limit drift angle with respect to each level of damage is shown in Table 1. Because the relationship between seismic intensity and response relative story displacement can be obtained from Eq.(1), the lognormal expectation and lognormal standard deviation of seismic fragility curve, in which peak ground acceleration is selected as the index of seismic intensity, are evaluated respectively from the following equation.

$$\lambda_R = \frac{1}{d_2} \times (\lambda_\delta - \ln d_1) \quad ; \quad \zeta_R = \frac{1}{d_2} \times \zeta_\delta \quad (2)$$

λ_R, ζ_R : parameters of seismic fragility curve

$\lambda_\delta, \zeta_\delta$: parameters of limit relative story displacement

2.4 Repair Costs of Buildings due to Hyogo-Ken-Nanbu Earthquake

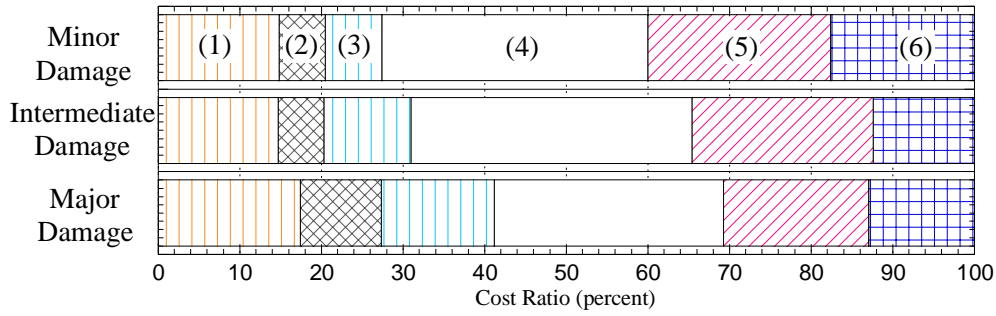
We investigated the repair cost of buildings suffered from the 1995 Hyogo-Ken-Nanbu earthquake, and made out the database of repair cost . The total number of investigated buildings are twenty-seven, and this database consists of eighteen R/C buildings, in which this number includes steel encased reinforced concrete buildings, and nine steel buildings. On the other hand, this database consists of fourteen minor damaged buildings, ten intermediate damaged buildings, and three major damaged buildings respectively. Repair costs per unit area, which are defined by repair cost of whole building over total floor area, are calculated with respect to each building. Expectations of repair cost per unit area, which are obtained through these repair costs of each building, are shown in Table 2. The cost ratios of each building work, which are normalized by sum of repair costs of each building work, are shown with respect to each level of damage in Fig.2. It is found that the cost ratio of skeleton work is around ten percent, that of finishing work is approximately thirty percent, and that of equipment work is about twenty percent regardless of the difference of level of damage. Therefore, it is significant to enhance seismic performance of finishing materials in order to decrease seismic loss effectively.

2.5 Modeling of Numerous Damaged Modes Through Event Tree

Including the level of no damage, there are five kinds of the level of damage at each story. In the case of L story building, the total combination K of damaged mode for all stories is to be 5^L . Therefore event tree analysis is adopted in order to calculate many consequences as efficiently as possible. For example, schematic diagram of event tree analysis for five story building is shown in Fig.3. At that

Table2 Expectation of Repair Cost per Unit Area (yen)

Minor	Intermediate	Major
38,800	87,400	119,000



(1) : temporary work, (2) : demolition work, (3) : skeleton work, (4) : finishing work, (5) : equipment work, (6) : other work, content of which consists of general overheads and design fee etc.

Fig.2 Cost Ratio of Each Building Work

time, the occurrence probability and the repair cost of k-th damaged mode is given in the following equations respectively.

$$P_k = \prod_{i=1}^L \{SF_{ik}(a)\} \quad ; \quad C_k = \sum_{i=1}^L C_{ik} \quad (3)$$

$SF_{ik}(a)$: damaged probability of i-th story with respect to k-th damaged mode on the condition that peak ground acceleration is a

C_{ik} : repair cost of i-th story with respect to k-th damaged mode

At that time, newly built cost is used for repair cost if any story collapses. As this procedure is carried out K times, the occurrence probability and the repair cost of all kinds of damaged mode can be calculated.

2.6 Evaluation of Exceedance Loss Curve of Each Building

Through the event tree analysis, the seismic loss distribution is obtained. By using Eq.(3), the expectation and standard deviation of this distribution is calculated by the following equations respectively.

$$\mu_C = \sum_{k=1}^K (P_k \times C_k) \quad ; \quad \sigma_C = \sqrt{\sum_{k=1}^K \{P_k \times (C_k - \mu_C)^2\}} \quad (4)$$

The occurrence probability P_0 , in which no story is damaged, and the occurrence probability P_M , in which any story collapses, are calculated in advance, and the rest distribution of seismic loss is modeled by lognormal distribution. At that time, the exceedance probability of seismic loss, in which seismic loss C is greater than c when peak ground acceleration is 'a', is formulated as follows.

$$P(C > c|a) = P_M + \{1 - (P_0 + P_M)\} \times \Phi\left(-\frac{\ln C - \lambda_C}{\zeta_C}\right) \quad (5)$$

λ_C, ζ_C : lognormal expectation and lognormal standard deviation of seismic loss distribution

$\Phi(\bullet)$: standard normal probability distribution function

As the uncertainty of seismic intensity at construction site is defined by lognormal distribution, the exceedance probability of seismic loss of each building due to a specific scenario earthquake can be formulated by using Eq.(5).

$$P(C > c|E) = \int P(C > c|a) \times f(a|E) da \quad (6)$$

$f(a|E)$: conditional probability density function of seismic intensity due to a specific scenario earthquake

2.7 Evaluation of Portfolio Seismic Risk Curve

In order to calculate the exceedance loss curve of all buildings with respect to a specific scenario earthquake, the amount of seismic loss distribution of each building is needed. This distribution can be obtained by the following equation.

$$C(E) = \sum_{m=1}^M C_m(E) \quad (7)$$

$C_m(E)$: seismic loss distribution of each building due to a specific scenario earthquake

$C(E)$: seismic loss distribution of all buildings due to a specific scenario earthquake

Annual occurrence ratio of seismic loss for all buildings due to a specific scenario earthquake is calculated by using both annual occurrence ratio of a specific scenario earthquake and Eq.(7).

$$v(C > c|E) = v \times P(C > c|E) \quad (8)$$

v : annual occurrence ratio of a specific scenario earthquake

$P(C > c|E)$: exceedance probability of seismic loss for all buildings

The annual occurrence ratio of seismic loss of all buildings due to all scenario earthquakes is given by using Eq.(8).

$$v(C > c) = \sum_{n=1}^N v(C > c|E_n) \quad (9)$$

Assuming that the occurrence of each scenario earthquake is modeled by stationary poisson process, the annual exceedance probability of seismic loss for all buildings is calculated.

$$P(C > c) = 1 - \exp[-v(C > c)] \quad (10)$$

According to Eq.(10), portfolio seismic risk curve can be obtained.

3. ANALYTICAL CONDITIONS

3.1 Analytical Conditions for Calculating Seismic Intensity

The scenario earthquakes, the magnitude of which is greater than five, are selected from a set of scenario earthquakes. The seismic intensity at engineering bedrock is calculated through Annaka's attenuation model [3]. The uncertainty of its model is given by lognormal distribution, in which the lognormal standard deviation is assumed to be 0.5.

The response spectrum at engineering bedrock is defined by that of AIJ recommendations [4]. The acceleration response spectrum in terms of soil type one is selected. The method, which fits response spectrum due to simulated seismic waves for this target response spectrum, is adopted. Several simulated seismic waves are generated by the following method, which is defined by multiplying the waves fit for the target spectrum by the Jennings type enveloped function in proportion to the level of magnitude. In addition, the level of seismic intensity of simulated seismic waves is variously changed. As a result, thirty nine simulated seismic waves at engineering bedrock are generated. In order to calculate simulated seismic waves at ground surface, equivalent linear responses through SHAKE program are carried out by using the specific soil profile in Table 3.

3.2 Analytical Model for Buildings

The five story R/C building, in which first natural period is about 0.42sec, and yielding base shear coefficient is 0.5, is assumed for the analytical model. The vertical distribution of yielding shear coefficient is given based on the A_i distribution, which indicates the vertical distribution of seismic

Table3 Soil Profile for Surface Layer

Thickness of Layer (m)	Velocity of S Wave (m/s)	Weight per Unit Volume (kN/m ³)	Type of Soil
5	120	14.0	Cohesive Soil
1	180	18.0	Cohesive Soil
6	260	20.0	Sandy Soil
10	395	20.0	Sandy Soil

Table4 Analytical Model

Story	Height of Story (m)	Floor Area (m ²)	Weight (kN)	Cracking Strength (kN)	Yielding Strength (kN)	Yielding Displacement (m)	Second Ratio of Stiffness	Third Ratio of Stiffness
5	3.5	800	9800	2215	6645	0.023	0.22	0.01
4	3.5	800	9800	3667	11002	0.023	0.22	0.01
3	3.5	800	9800	4845	14535	0.023	0.22	0.01
2	3.5	800	9800	5794	17383	0.023	0.22	0.01
1	3.5	800	9800	6533	19600	0.023	0.22	0.01

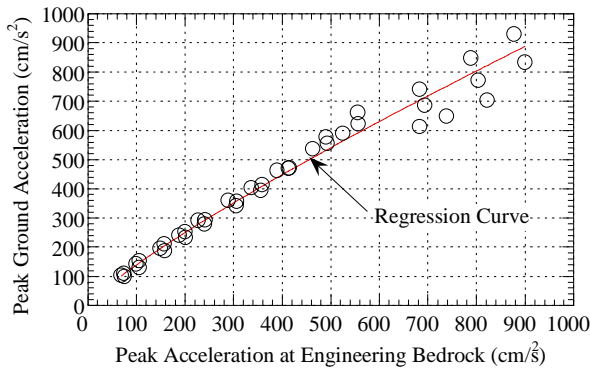


Fig.3 Relationship between Peak Acceleration at Engineering Bedrock and Peak Ground Acceleration

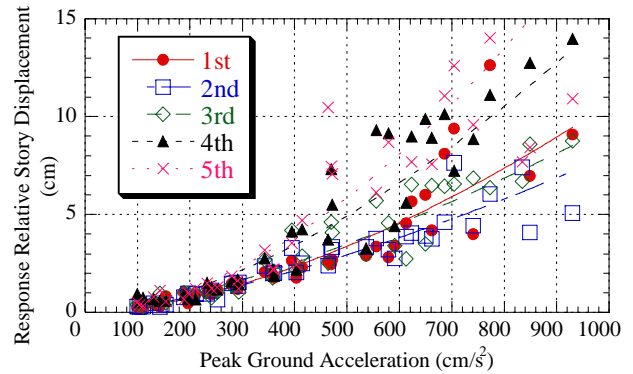


Fig.4 Relationship between Peak Ground Acceleration and Response Relative Story Displacement

shear coefficient defined by Japan building code. Takeda model is used as hysteresis restoring force characteristic. Some parameters concerning building model is shown in Table 4. The repair costs per unit area for minor damage, intermediate damage, and major damage are given through Table2. Moreover, the repair cost of collapse is given by newly built cost, in which 250,000 yen is assumed for a standard newly built cost.

3.3 Analytical Cases for Portfolio Seismic Risk

Result of portfolio seismic risk is influenced by both allocation of buildings and correlation of seismic loss. Portfolio seismic risk is generally calculated on condition that correlation of seismic loss among buildings is assumed to be independent. However, correlation of seismic intensity among multiple construction sites might exist because of a way of allocation. In order to investigate the extreme combinations, correlation of seismic loss is assumed to be independent or fully correlated. As shown in Table 4, three cases of portfolio are set to evaluate the difference due to previously mentioned factors. At that time, total number of buildings is ten, the analytical model of which are all the same. The degree of influence due to correlation may tend to be higher in Case1 rather than other cases.

4. ANALYTICAL RESULTS

4.1 Some Results

Based on the analytical condition in chapter 3.1, the relationship between peak acceleration at engineering bedrock and peak ground acceleration is obtained in Fig.3. The relationship between peak

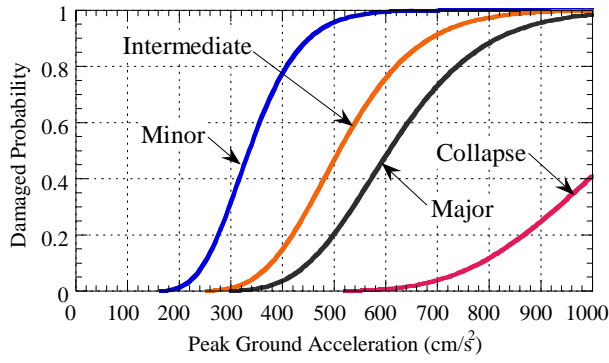


Fig.5 Seismic Fragility Curves at First Story

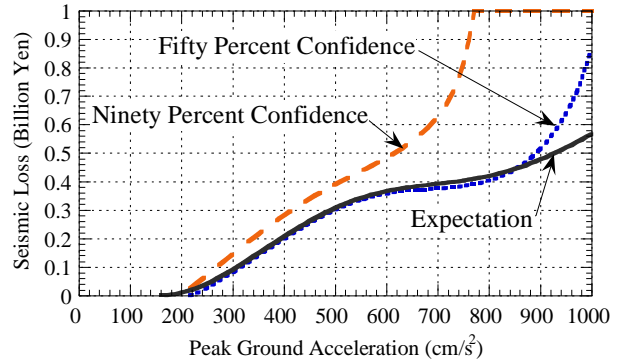


Fig.6 Seismic Loss Curve of Building

Table5 Analytical Cases of Portfolio

	Influence due to Correlation	Region	Construction Sites
Case1	High	Urban Area	Tokyo, Shinjuku, Shinagawa, Ueno, Ikebukuro, Shibuya, Meguro, Ochanomizu, Yotsuya, Komagome
Case2	Medium	Metropolitan Area	Tokyo, Shinjuku, Shinagawa, Mitaka, Hachioji, Kawasaki, Yokohama, Funabashi, Chiba, Saitama
Case3	Low	Whole Country Area	Tokyo, Kawasaki, Yokohama, Shizuoka, Nagoya, Kyoto, Osaka, Kobe, Sendai, Niigata

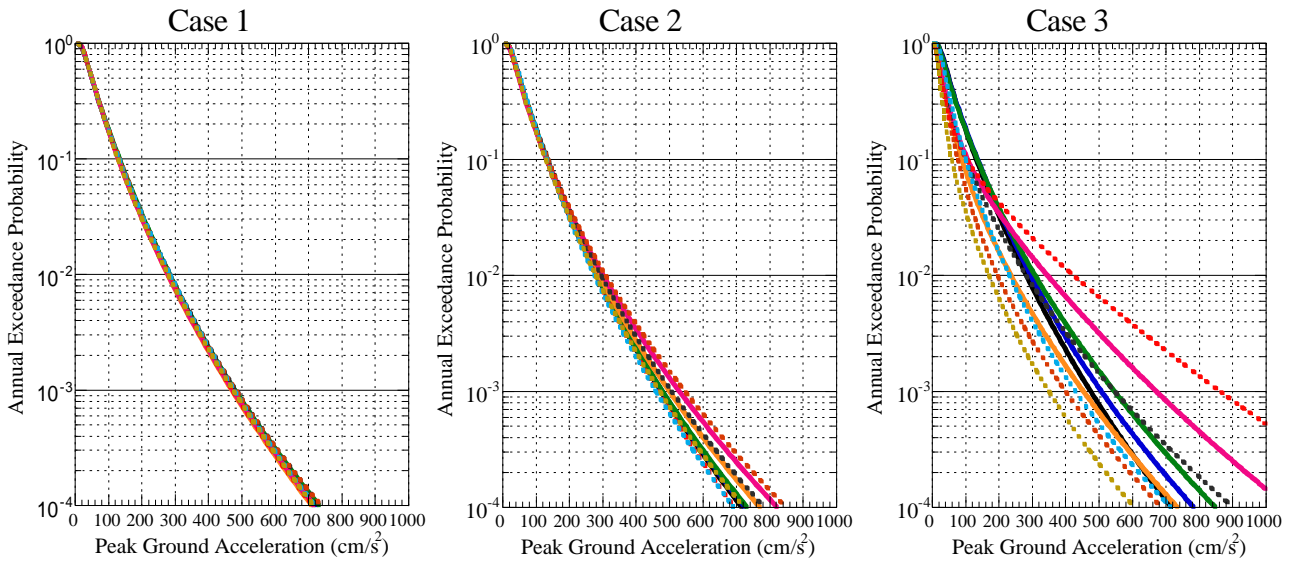


Fig.7 Seismic Hazard Curves at Each Construction Site

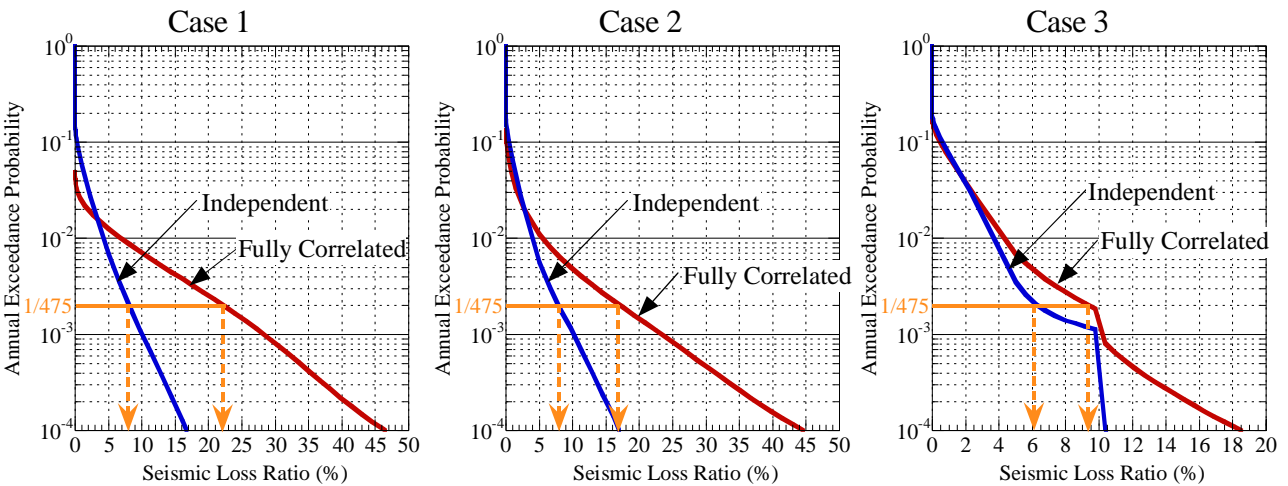


Fig.8 Comparison of Portfolio Seismic Risk Curves

Table6 Comparison of Portfolio PML (%)

	Independent	Fully Correlated
Case1	8.2	22.4
Case2	7.8	16.2
Case3	6.2	9.2

ground acceleration and response relative story displacement for each story is shown in Fig.4. In this figure, five curves denote regression equations through Eq.(1). Seismic fragility curves of first story, which denote the conditional damaged probability with respect to peak ground acceleration, are shown in Fig.5. Seismic loss curve, which denotes the relationship between peak ground acceleration and seismic loss of building, is shown in Fig.6. The seismic loss curves with respect to fifty percent confidence and ninety percent confidence, as well as expectation of it, are denoted in this figure. It is noted that the fifty percent confidence curve is relatively similar to the expectation curve until the value of peak ground acceleration is within about 900 cm/s². However beyond this value, the fifty percent confidence curve is considerably larger than the expectation curve, because the occurrence probability P_M is defined that any story collapses.

4.2 Comparison of Portfolio Seismic Risk

Seismic hazard curves at each construction site are shown in Fig.7. Seismic hazard curves in case 1 almost correspond with each other. On the other hand, seismic hazard curves in case 3 are mutually different with respect to a construction site.

Portfolio seismic risk curves with respect to each case are shown in Fig.8. The seismic loss ratio, which is normalized by the total cost of ten buildings, is used for the representation of seismic loss. It is found that portfolio seismic risk curves are different with respect to degree of correlation in all cases. In due diligence, probable maximum loss (PML) has been conventionally adopted as the checking level of seismic loss. In this study, PML is defined such that the annual exceedance probability of seismic loss is equal to one over four hundred and seventy-five. Portfolio PML with respect to each case is shown in Table 6. It is verified that as the area of allocation of multiple buildings is gradually narrow, the difference between PML of independent and that of fully correlated gets to be larger. It is likely that correlations of seismic intensity among construction sites might be high in smaller area. Therefore, annual expectation of seismic loss, the definition of which is to integrate the probability density function multiplied by seismic loss, is very useful index for representing seismic risk as well as PML.

5. CONCLUSION

From the standpoint of risk dispersion, an analytical method, which can evaluate portfolio seismic risk through a set of scenario earthquakes in and around Japan, is developed. Seismic risk of several portfolios, the contents of which are mutually different, is compared numerically through this method. As a result, it is confirmed that value at risk such as PML is to be different because of the degree of correlation. Therefore, annual expectation of seismic loss as well as PML is useful index for representing seismic risk of buildings.

References :

- [1] M.Mizutani, S.Yoshida, Y.Imazuka, M.Achiwa and M.Sato "Seismic Risk Assessment Procedures for a System Considering of Distributed Facilities, -Part One Basic Method of the Procedures-, - Part Two Seismic Hazard Modeling-, -Part Three Insurance Portfolio Analysis-", *ICOSSAR*, 2001
- [2] H.Suwa, A.Nobata and M.Seki, "Practical Seismic Risk Assessment of Existing Building By Using Damaged Database of 1995 Hyogoken Nanbu Earthquake", *AIJ Journal of Technology and Design*, No.12, 2001, pp.41-46
- [3] T.Annaka and Y.Nozaawa "A Probabilistic model for Seismic Hazard Estimation in the Kanto District", *Proc. 9th WCEE*, 1988, pp.107-112
- [4] Architectural Institute of Japan (AIJ), *AIJ Recommendations for Loads on Buildings*, 1996, pp.115

SEISMIC RESPONSE OF NONLINEAR CONTROLLED ISOLATED BRIDGES UNDER NEAR-FIELD GROUND MOTIONS

T.Y. Lee¹⁾, and K. Kawashima²⁾

1) Graduate Student, Department of Civil Engineering, Tokyo Institute of Technology, Japan

2) Professor, Department of Civil Engineering, Tokyo Institute of Technology, Japan

tylee@cv.titech.ac.jp, kawasima@cv.titech.ac.jp

Abstract: Seismic isolation has been extensively used worldwide for bridges. Considerable progress has been made in control method of civil engineering structures subjected to environmental loads in the past two decades. However, in most studies, structures except isolators are assumed to be linear elastic. This paper shows the efficiency of supplementary dampers with active control algorithm to mitigate the large deck displacement and the hysteretic behavior of column. Magnetorheological dampers (MR-dampers) are used in this numerical analysis so that arbitrary control algorithm for damping force vs. bridge response relations is introduced. Both external and internal damper allocations are implemented to evaluate the difference of performance.

1. INTRODUCTION

Seismic isolation has been extensively used worldwide for bridges. However isolated bridges inherently exhibit inelastic responses and excessive deck displacements when subjected to a strong near-field ground motion, such as Northridge Earthquake in USA, 1994, Kobe Earthquake in Japan, 1995 and Chi-Chi Earthquake in Taiwan, Duzce Earthquake in Turkey, 1999. Such large displacements enhance the difficulty of design of bridge accessory equipments, such as expansion joints and unseating prevention devices, and may affect the recovery and reconstruction after earthquakes even though collapse does not occur.

This paper shows the efficiency of supplementary dampers to mitigate the large deck displacement and the hysteretic behavior of columns. Magnetorheological (MR) fluid dampers are used in this analysis so that arbitral control algorithm for damping force vs. bridge response relations is introduced. A bridge is composed of low-damping isolation bearings and MR dampers, and it is subjected to five near-field ground motions. Both external and internal damper allocations are implemented by numerical simulation based on active optimum control with full-state feedback to evaluate their efficiency.

In most control studies, structures except isolators are assumed to be linear elastic even under strong earthquakes. However, based on the modern bridge seismic design method, bridge columns exhibit high hysteresis to dissipate more energy. In this study, hysteretic behaviors of columns are included in the analysis as well. It is found from the analysis that columns with high ductility still exhibit hysteretic behavior under extreme earthquakes and the efficiency of control force due to classical control method is not as remarkable as the one with low ductility under moderate earthquakes.

2. ISOLATED BRIDGES WITH SUPPLEMENTARY DAMPERS

Consider a n degrees of freedom nonlinear or hysteretic structure subjected to a one-dimensional earthquake horizontal ground acceleration $\ddot{u}_g(t)$. The equation of motion is given by

$$\mathbf{M} \ddot{\mathbf{u}}(t) + \mathbf{F}_D[\dot{\mathbf{u}}(t)] + \mathbf{F}_S[\mathbf{u}(t)] = \boldsymbol{\eta} \ddot{u}_g(t) + \mathbf{H} \mathbf{U}(t) \quad (1)$$

in which $\mathbf{u}(t) = [u_1, u_2, \dots, u_n]'$ is an n -vector with u_i being the displacement of the i th element; \mathbf{M} is a $(n \times n)$ mass vector. $\mathbf{F}_D[\dot{\mathbf{u}}(t)]$ and $\mathbf{F}_S[\mathbf{u}(t)]$ are nonlinear damping and stiffness vectors, respectively; $\mathbf{U}(t)$ is a r -dimensional consisting of r active control damping forces from the MR dampers, and \mathbf{H} is a $(n \times r)$ denotes the location of MR dampers. In this paper, a prime indicates the transpose of either a matrix or a vector.

In the state space, Eq. (1) can be expressed as

$$\dot{\mathbf{Z}}(t) = \mathbf{g}[\mathbf{Z}(t)] + \mathbf{B} \mathbf{U}(t) + \mathbf{W} \ddot{u}_g(t) \quad (2)$$

in which $\mathbf{g}[\mathbf{Z}(t)]$ is a $2n$ -vector which is a nonlinear function of the state vector $\mathbf{Z}(t)$ and other matrices are defined as follows:

$$\mathbf{Z}(t) = \begin{bmatrix} \mathbf{u}(t) \\ \dot{\mathbf{u}}(t) \end{bmatrix}; \quad \mathbf{g}[\mathbf{Z}(t)] = \begin{bmatrix} \dot{\mathbf{u}}(t) \\ -\mathbf{M}^{-1}[\mathbf{F}_D + \mathbf{F}_S] \end{bmatrix}; \quad \mathbf{B} = \begin{bmatrix} 0 \\ \mathbf{M}^{-1}\mathbf{H} \end{bmatrix}; \quad \mathbf{W} = \begin{bmatrix} 0 \\ \mathbf{M}^{-1}\boldsymbol{\eta} \end{bmatrix} \quad (3)$$

The LQR performance index is given by

$$J = \int_0^T [\mathbf{Z}'(t)\mathbf{Q}\mathbf{Z}(t) + \mathbf{U}'(t)\mathbf{R}\mathbf{U}(t)]dt \quad (4)$$

in which \mathbf{Q} is a $(2n \times 2n)$ symmetric positive semidefinite weighting matrix and \mathbf{R} is a positive weighting matrix.

Referring to the generalization of optimal control theory for nonlinear structures by Yang et al. (1994), minimizing the objective function, J , given by Eq. (4) subjected to the constraint of the state equation of motion, Eq. (2) yields the control damping force as follows:

$$\mathbf{U}(t) = -0.5\mathbf{R}^{-1}\mathbf{B}\mathbf{P}\mathbf{Z}(t) \quad (5)$$

$$\boldsymbol{\Lambda}_0' \mathbf{P} + \mathbf{P}\boldsymbol{\Lambda}_0 - 0.5\mathbf{P}\mathbf{B}\mathbf{R}^{-1}\mathbf{B}'\mathbf{P}\mathbf{Z}(t) = -2\mathbf{Q} \quad (6)$$

in which \mathbf{P} is the Riccati matrix where

$$\boldsymbol{\Lambda}_0 = \partial \mathbf{g}(\mathbf{Z}) / \partial \mathbf{Z} |_{\mathbf{Z}=0} \quad (7)$$

Note that Eq. (6) is approximated by neglecting the earthquake ground acceleration $\ddot{u}_g(t)$ and linearizing the structural system at the initial equilibrium point $\mathbf{Z}=0$. Since the term $\mathbf{P}\mathbf{B}\mathbf{R}^{-1}\mathbf{B}'\mathbf{P}$ is positive semidefinite, Eq. (7) can be approximated further by

$$\boldsymbol{\Lambda}_0' \mathbf{P} + \mathbf{P}\boldsymbol{\Lambda}_0 = -2\mathbf{Q} \quad (8)$$

which is known as the Lyapunov equation.

The bridge structure and isolated bearing may be idealized to be nonlinear or hysteretic. The following hysteretic model is used for both the bridge structure and isolator. The stiffness restoring

force is given by Bouc-Wen model.

$$F_{si}(t) = \alpha_i k_i x_i(t) + (1 - \alpha_i) k_i x_{yi} v_i \quad (9)$$

in which x_i = deformation of the i th element, k_i = elastic stiffness, α_i = ratio of the post-yielding to pre-yielding stiffness, x_{yi} = yielding deformation, and v_i = hysteretic variable with $|v_i| \leq 1$, where

$$\dot{v}_i = x_{yi}^{-1} \left[A_i \dot{x}_i - \beta_i |\dot{x}_i| |v_i|^{n_i-1} v_i - \gamma_i \dot{x}_i |v_i|^{n_i} \right] \quad (10)$$

in which parameters A_i , β_i , γ_i and n_i govern the scale, general shape and smoothness of the hysteresis loop. Note that the i th element is linear elastic if $\alpha_i = 1$.

3. NUMERICAL SIMULATION

A target bridge with isolators is considered as shown in Fig. 1. MR dampers are installed between the deck and the column or the deck and the abutment. When MR dampers are connected to the abutment, they are regarded as applying external force to the bridge. On the other hand, when MR dampers are connected to the deck, the damping forces are regarded as part of internal forces. The effectiveness of both allocations will be discussed respectively. Assuming that the soil is stiff, the response of bridge may be idealized as a two degree of freedom system as shown in Fig. 2. The mass of deck and column are 700T and 140T, respectively. The columns exhibit bilinear elastoplastic behavior with zero post-yield stiffness, whereas the isolator is elastomeric with low damping, Fig.3. The fundamental natural period of the entire bridge is 1.3 second. For simplicity, the damping of the system is considered as linear viscous damping and the damping ratio of 2% is assumed for the both modal shapes.

The earthquake records used in this study are JMA Kobe Observatory and JR-Takatori Station in the 1995 Kobe Earthquake, Japan, Duzce in the 1999 Duzce Earthquake, Turkey, Sylmar Parking Lot in the 1994 Northridge, USA, and Sun-Moon Lake in 1999 Chi-Chi Earthquake, Taiwan, as shown in Fig. 4. All the excitations are applied at the full intensity for the evaluation of the performance indices.

With the MR damper applying the control force to the bridge, the structural response depends on the weighting matrices \mathbf{Q} and \mathbf{R} . For this example, the \mathbf{Q} matrix is considered as a diagonal matrix with all the diagonal elements equal to 1.0. Since the \mathbf{R} weighting matrix consists of only one element and the magnitude of required control damping force mainly depends on \mathbf{R} value, \mathbf{R} value is implemented over a wide range in order to evaluate and search for the suitable \mathbf{R} value under the feasible capacity of devices. In some studies, considering that the required control force may be too large when the earthquake excitation is strong, saturated controller is adopted to bound the control force. In this study, control force will not be limited but only control force below 30% of deck weight is evaluated.

Time histories of all the response quantities have been computed within 30 seconds of the records except Chi-Chi Earthquake with 40 seconds. The generated control damping force, and the corresponding displacement and absolute acceleration of deck and column are evaluated using normalized indices. The performance index of generated control damping force is normalized by the deck weight. The performance indices of displacement and absolute acceleration are normalized by the corresponding magnitudes in the uncontrolled structure. The results of the evaluations for external damper and internal damper are presented as follows.

3.1 External damper

Time history displacement responses for JMA Kobe and Sun-Moon Lake earthquakes with \mathbf{R} of

5×10^{-12} are shown in Figs. 5 and 6. The hysteretic loops of the column and isolator are also shown in Figs. 7 and 8. The corresponding stroke and damping force hystereses of the MR damper are shown in Fig. 9. As observed from the results, displacement responses are reduced substantially from the uncontrolled responses. The column even exhibits elastic response using controlled damper under JMA Kobe record, while column displacement ductility factor decreases from 12 to 7 under Sun-Moon Lake record.

The performance indices described above with respect to weighting \mathbf{R} for five ground motions are shown in Fig. 10. The column displacement ductility factor without control is 4.1, 3.8 and 1.1 under JMA Kobe, Duzce and Sylmar records, respectively, while it is 9.2 and 11.8 under JR-Takatori and Sun-Moon Lake records, respectively, which are not shown in Fig. 10(d). The higher ductility factor in uncontrolled bridge, the higher control damping force is generated as shown in Fig. 10(a). However, even though higher control force is applied, the deck displacement under Sun-Moon Lake and JR-Takatori do not reduce to the level developed under other records except Sylmar, as shown in Figs. 10(b), and it is important to note that column still exhibits high inelastic behavior as shown in Fig. 10(d). One can attribute it to the insufficient assumption in the linearization of the bridge that the initial stiffness is used to determine the gain vector of control force.

3.2 Internal damper

Time history displacement responses of the deck and the column under JMA Kobe and Sun-Moon Lake records with \mathbf{R} of 5×10^{-12} are shown in Figs. 11 and 12. The hysteretic loops of the column and isolator are also shown in Figs. 13 and 14. The corresponding stroke and damping force hystereses of the MR damper are shown in Fig. 15. Using the controlled damper, both the deck and column displacements can be decreased, but still some inelastic deformation occurs in the column.

The performance indices with respect to weighting \mathbf{R} for five ground motions are shown in Fig. 16. As same as the external damper, the deck displacement under Sun-Moon Lake and JR-Takatori do not reduce to the level developed under other records as shown in Figs. 16(b) even though higher control force is applied as shown in Fig. 16(a). One can also attribute it to the insufficient assumption in the linearization of the bridge that the initial stiffness is used to determine the gain vector of control force. Note that column still exhibits hysteretic behavior compared to the same level of control force applied by the external damper under all ground motions except Sylmar as shown in Fig. 16(d). In addition, the decrease of deck and column displacements results in an increase of deck accelerations because the internal damping force restricts the relative displacement between the deck and the column as shown in Fig. 16(e).

4. CONCLUSIONS

The feasibility and effectiveness of MR dampers for controlling the seismic response of isolated bridges have been evaluated by numerical simulations under five strong near-field ground motions. The damper allocations investigated include the external damper and the internal damper. The following conclusions may be obtained from the results presented herein.

- (a) Both damper allocations are effective for active control in reducing the deck displacement subjected to the near-field ground motions. Especially, the external damper shows higher efficacy than the internal damper and no penalty of increasing deck acceleration. However the external damper may only be installed at the ends of bridges such as abutments. It is limited for wider application in seismic design.
- (b) The magnitude of damper force required for control depends on not only the weighting \mathbf{R} but also the intensity and characteristic of ground excitation. In addition, the performance indices extensively vary depending on ground motions so that one should pay an attention on the type

of ground motions to maintain the stability of control.

- (c) Under the control using a feasible level of damping force, the amount of mitigation of the deck displacement and the plastic deformation in the column is insufficient. Further improvement of the control method that can be applied to bridges with high nonlinearity is required.

Acknowledgements:

The authors acknowledge support from the Center for Urban Earthquake Engineering (CUEE) in Tokyo Institute of Technology.

References:

Kawashima, K. and Unjoh, S. (1994), "Seismic Response Control of Bridges by Variable dampers," *Journal of Structural Engineering*, American Society of Civil Engineers, **120**(9), 2583-2601.
 Yang, J.N., Li, Z. and Vongchavallitkul, S. (1994), "A Generalization of Optimal Control Theory: Linear and Nonlinear Control," *Journal of Engineering Mechanics*, American Society of Civil Engineers, **120**(2), 266-283.
 Yang, J.N., Wu, J.C., Kawashima, K. and Unjoh, S. (1995), "Hybrid Control of Seismic-excited bridge structures," *Earthquake Engineering and Structural Dynamics*, **24**(11), 1437-1451.

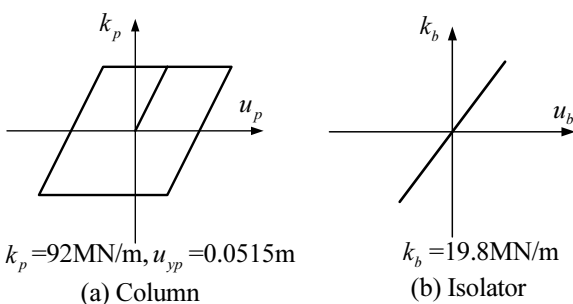
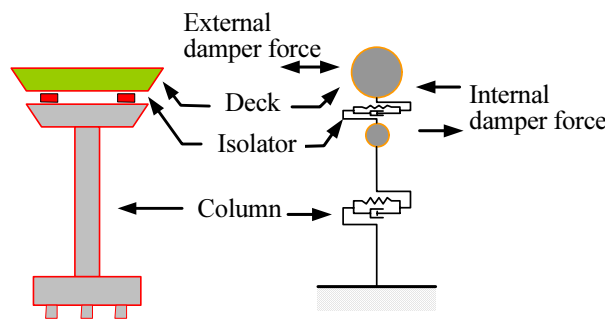
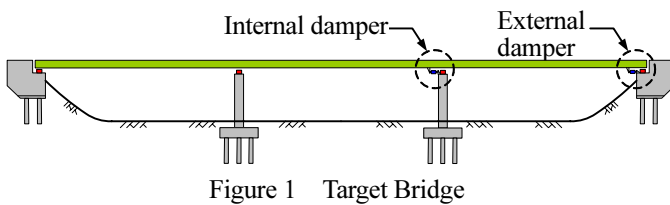
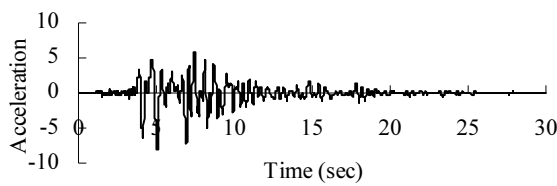


Figure 3 Material Behavior of Column and Isolator



(a) JMA Kobe Observatory

Figure 4 Ground Motions (m/sec^2)

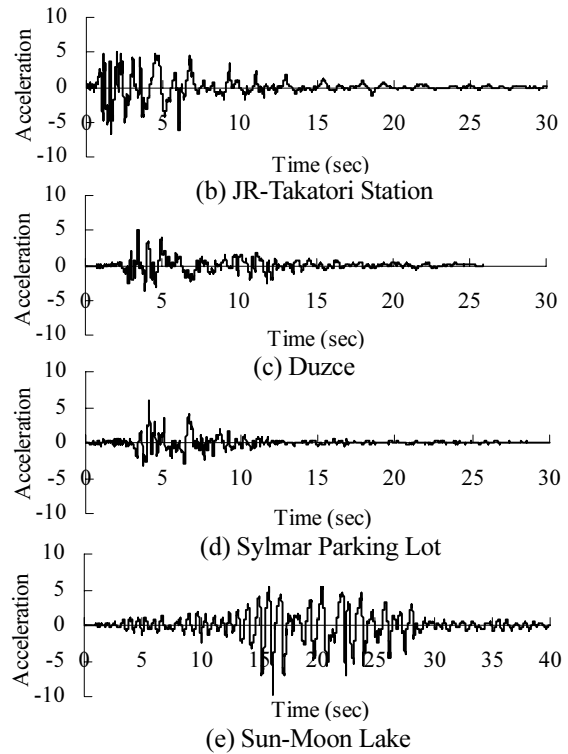
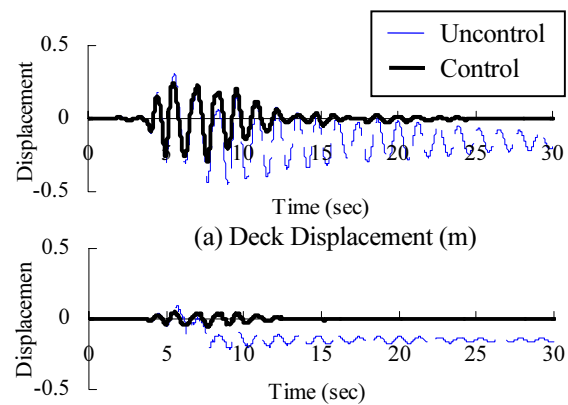


Figure 4-conti. Ground Motions (m/sec^2)



(a) Deck Displacement (m)

(b) Column Displacement (m)

Figure 5 Displacements Responses under JMA Kobe

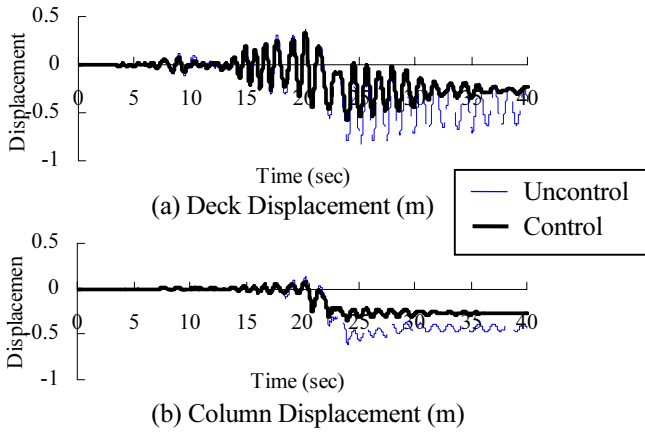


Figure 6 Displacements Responses under Sun-Moon Lake

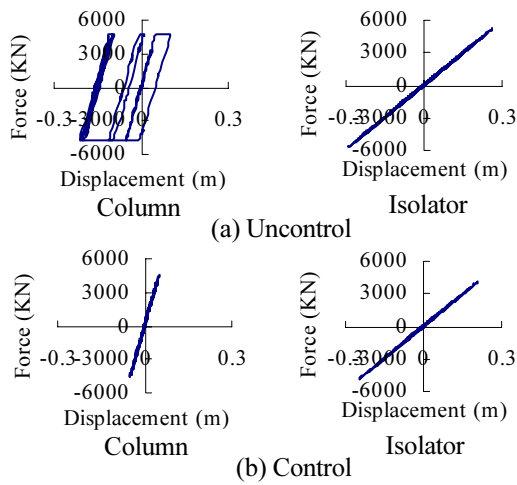


Figure 7 Hysteretic Loops under JMA Kobe

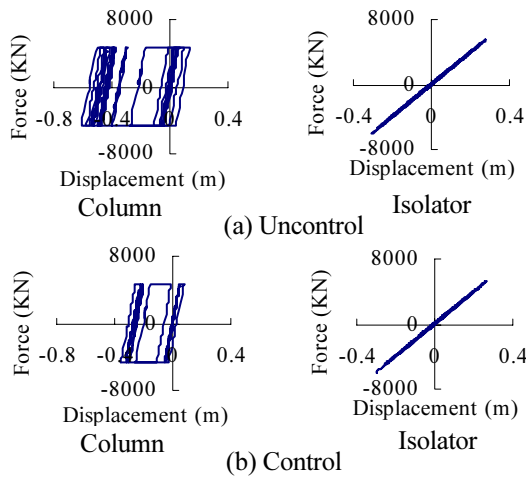


Figure 8 Hysteretic Loops under Sun-Moon Lake

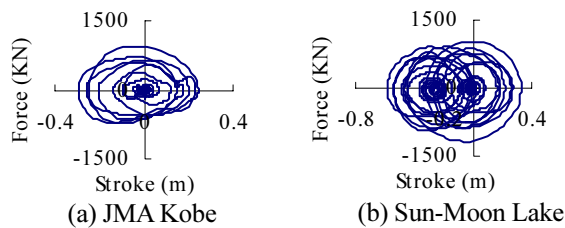


Figure 9 Damping Force v.s. Stroke Hystereses

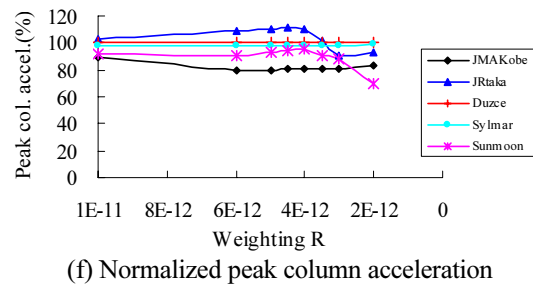
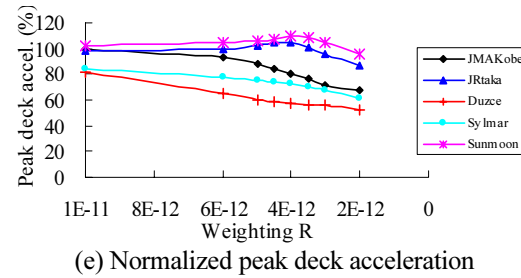
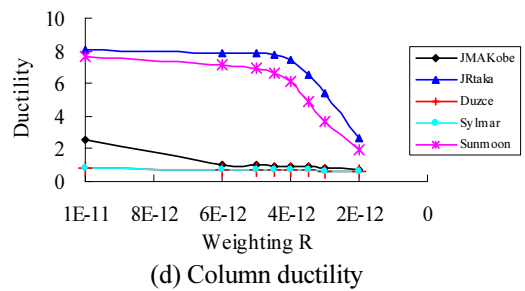
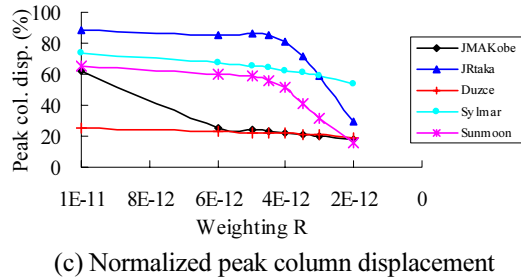
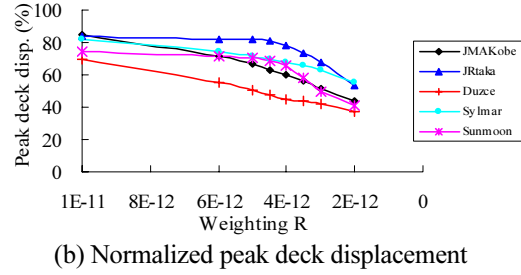
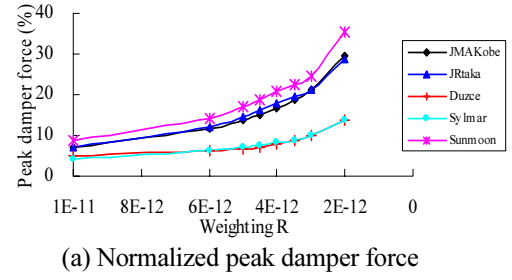


Figure 10 Performance Indices v.s. Weighting R of External Dampers under Five Excitations

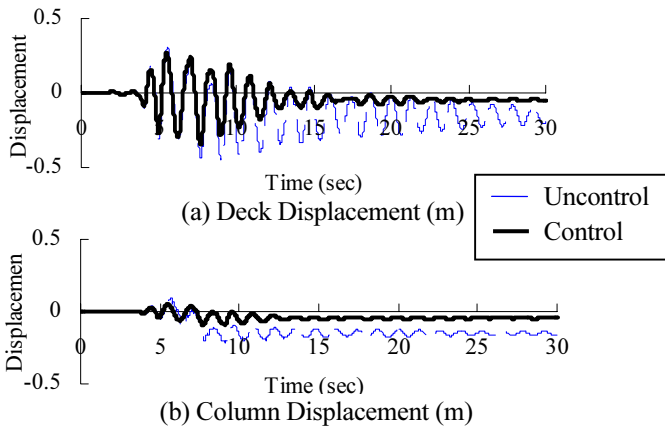


Figure 11 Displacements Responses under JMA Kobe

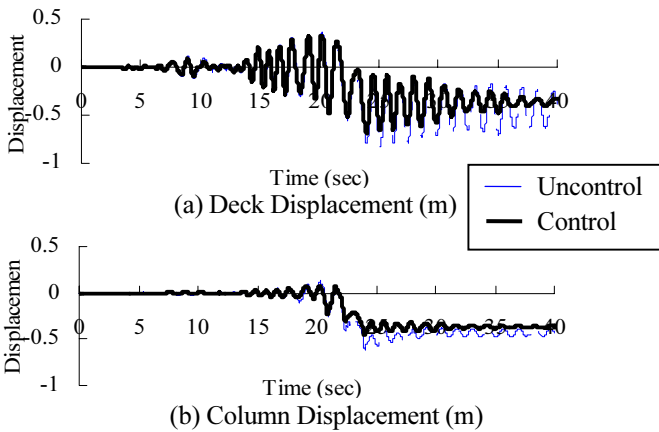


Figure 12 Displacements Responses under Sun-Moon Lake

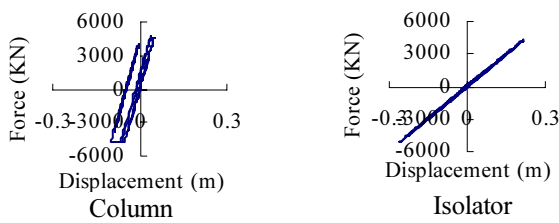


Figure 13 Hysteretic Loops under JMA Kobe

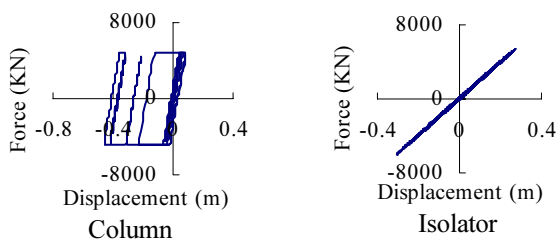


Figure 14 Hysteretic Loops under Sun-Moon Lake

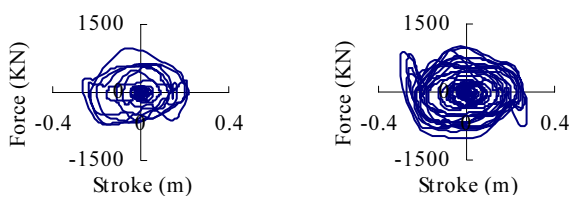
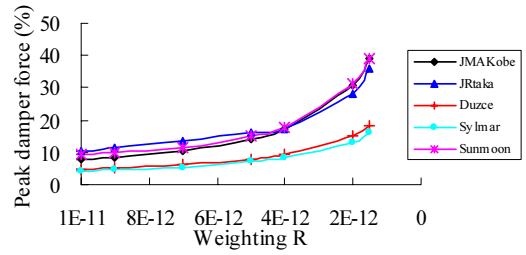
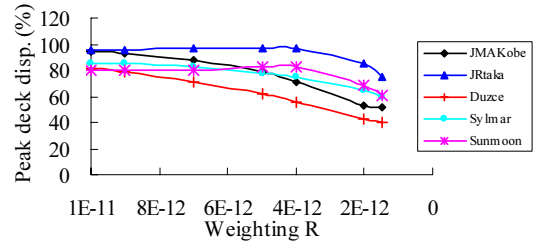


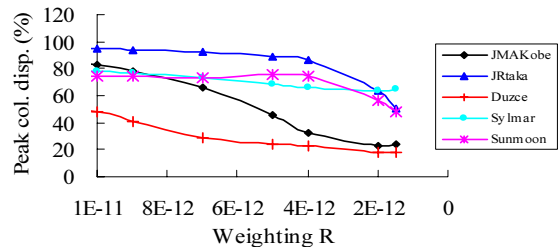
Figure 15 Damping Force v.s. Stroke Hystereses
(a) JMA Kobe (b) Sun-Moon Lake



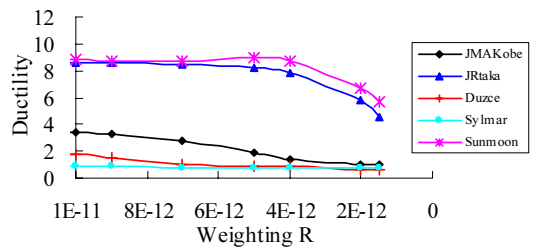
(a) Normalized peak damper force



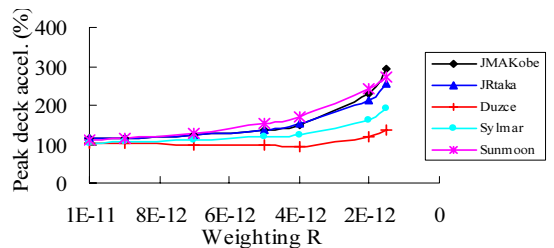
(b) Normalized peak deck displacement



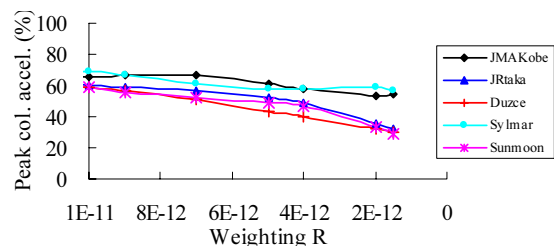
(c) Normalized peak column displacement



(d) Column ductility



(e) Normalized peak deck acceleration



(f) Normalized peak column acceleration

Figure 16 Performance Indices v.s. Weighting R of Internal Dampers under Five Excitations

SEISMIC PERFORMANCE OF REINFORCED CONCRETE C-BENT COLUMNS BASED ON A HYBRID LOADING TEST

S. Nagata¹⁾, K. Kawashima²⁾, and G. Watanabe³⁾

1) Graduate Student, Department of Civil Engineering, Tokyo Institute of Technology, Japan

2) Professor, Department of Civil Engineering, Tokyo Institute of Technology, Japan

*3) Research Associate, Department of Civil Engineering, Tokyo Institute of Technology, Japan
nseiji@cv.titech.ac.jp, kawasima@cv.titech.ac.jp, gappo@cv.titech.ac.jp*

Abstract: C-bent columns have a unique seismic performance due to the eccentricity between the column center and the point where the dead load of the superstructure and the lateral inertia force apply. This results in an extensive deterioration of the flexural capacity and an increase of residual displacement. To study the effect of the eccentricity on the seismic performance of C-bent columns, a hybrid loading test was conducted.

1. INTRODUCTION

In urban areas, there exists a number of reinforced single columns with the lateral beams being longer in one side than the other. They are called C-bent columns or inversed L-shaped columns. C-bent columns are subjected to an eccentric dead load of the superstructure and the inertia force during an earthquake. As a consequence, a side of the eccentricity (side with longer lateral beam) and the other side of the eccentricity are subjected to compression and tension, respectively, due to the dead load of the superstructure. They are called hereinafter the eccentric compression side and the eccentric tension side, respectively.

To clarify the seismic performance of reinforced concrete C-bent columns, Kawashima and Unjoh conducted a shake table test (Kawashima and Unjoh 1994), and Tuchiya et al conduct a cyclic loading test (Tuchiya et al 1999). From the studies, it was found that an extensive failure occurred at the eccentric compression side of the columns and this resulted in a large residual displacement under a strong excitation. Based on a bilateral cyclic loading test on reinforced concrete C-bent columns, Kawashima et al pointed out that the restoring force deteriorates more significantly under the bilateral loading (Kawashima et al 2003).

To study the seismic response of reinforced concrete C-bent columns under a bilateral excitation, a hybrid loading test was conducted on six model columns with two eccentricities. This paper presents the experimental behavior of the models.

2. MODEL COLUMNS AND TEST PROCEDURE

Six model columns without an eccentricity and with the eccentricities of $0.5D$ and D (D : width of the columns) were constructed as shown in Table 1. They were designed in accordance with the current Japanese seismic design codes (JRA 1996) assuming that they are “small prototype” columns. They have a 400 mm × 400mm square cross section with an effective height from the bottom to the

Table 1 Model Columns used in the Hybrid Loading Tests

Models	H-1	H-2	H-3	H-4	H-5	H-6
Eccentricities	0	$0.5D$	D	0	$0.5D$	D
Longitudinal Reinforcement Ratio (%)	1.27	1.35	1.9	1.27	1.35	1.9
Tie Reinforcement Ratio (%)	0.79	0.99	1.19	0.79	0.99	1.19
Concrete Strength (MPa)	28.7	32.1	31.3	31.2	29.1	28.6
Loading Type*	1			2		

*Loading Type=1: loading in the longitudinal direction using NS component of JMA Kobe record, and Type=2: loading in the bilateral direction using NS and EW components of JMA Kobe record

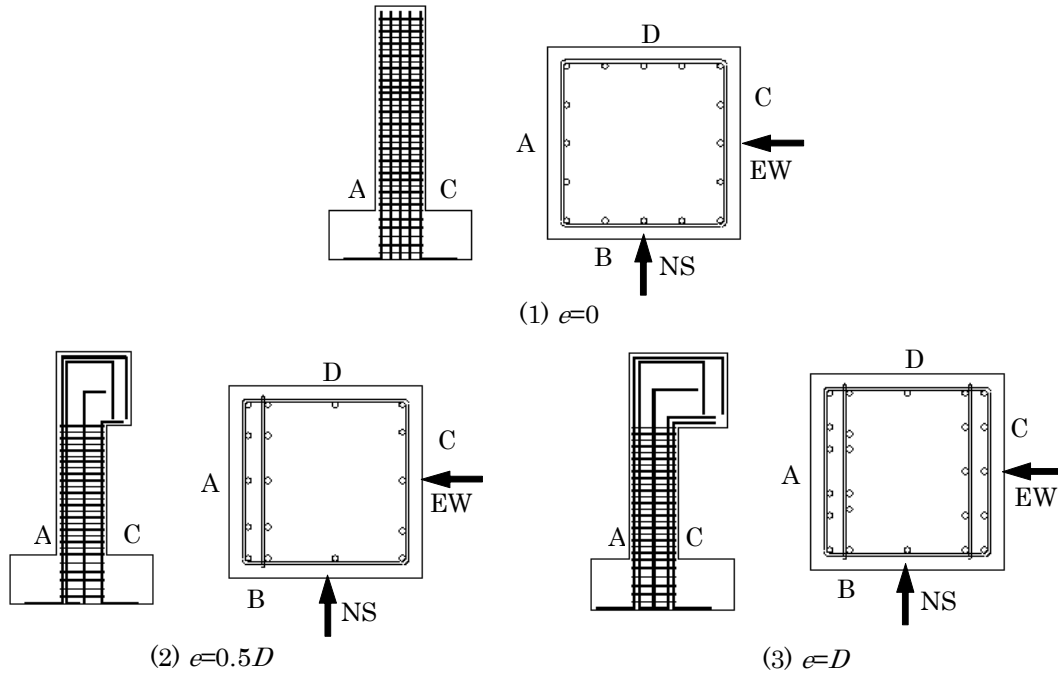


Fig. 1 Model Columns

loading point of 1350mm.

Fig. 1 shows the model columns. Deformed longitudinal bars with a 13 mm diameter (D13) are provided in double at the eccentric tension side in the column with an eccentric of $0.5D$. On the other hand, the D13 longitudinal bars are provided in double at not only the eccentric tension side but also the eccentric compression side in the column with an eccentricity of D . The compression in the eccentric compression side is so large in the column with the eccentricity of D that the double reinforcements are required in the eccentric compression side. The longitudinal reinforcement ratio is 1.27%, 1.35% and 1.90% in the columns without an eccentricity and the columns with the eccentricities of $0.5D$ and D , respectively. D6 tie bars are provided at 50 mm interval for the entire column height. They are anchored by 135 degree bent hooks. Ties are provided in the inner longitudinal bars as well. The volumetric tie reinforcement ratio is 0.79%, 0.99% and 1.19% in the columns without an eccentricity and the columns with the eccentricities of $0.5D$ and D , respectively.

The loading test was conducted using the dynamic testing facility in the Tokyo Institute of Technology. The columns were subjected to unilateral excitation in the longitudinal direction (direction perpendicular to the eccentricity) and bilateral excitation under a constant vertical load of 160 kN, which induced a stress 1 MPa at the plastic hinge of the column. The ground acceleration recorded at JMA Kobe Observatory during the 1995 Kobe earthquake was used as an input motion by scaling down its intensity to 30% of the original. NS and EW components were used in the longitudinal and transverse directions, respectively. Since the lateral actuators in the longitudinal

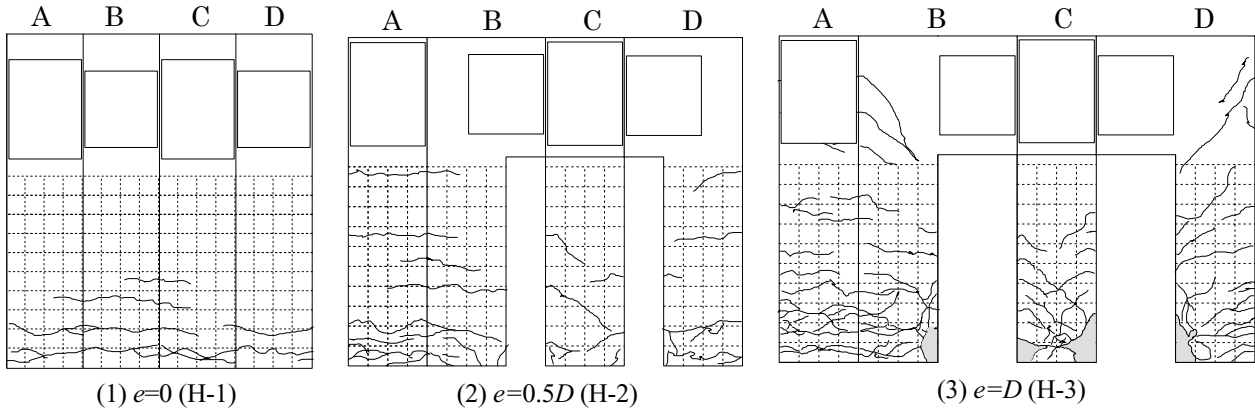


Fig. 2 Damage of the Columns after the Tests under the Unilateral Excitation

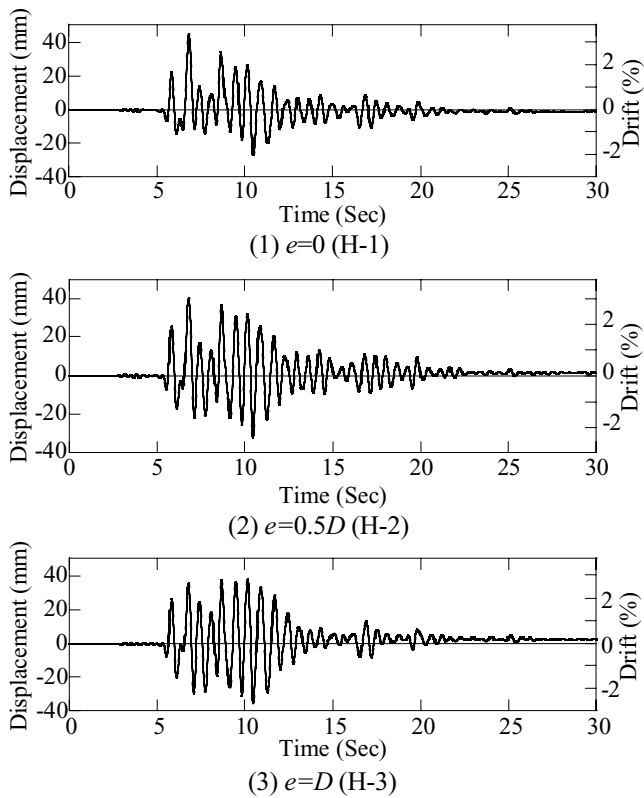


Fig. 3 Displacement Response under the Unilateral Excitation

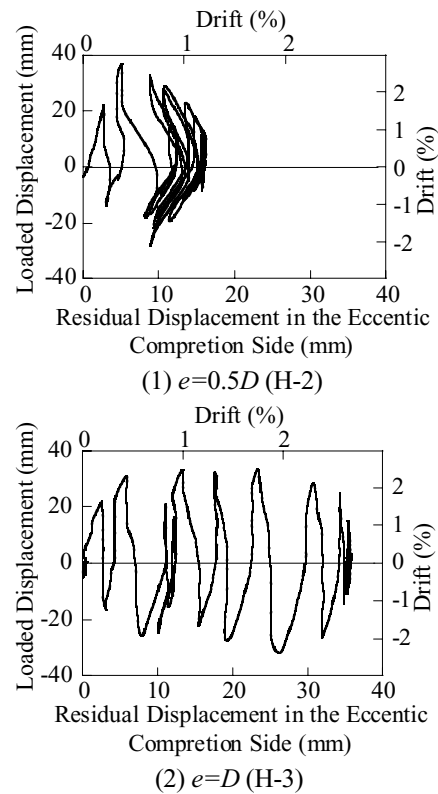


Fig. 4 Transverse Displacement of the Column under the Unilateral Excitation in the Longitudinal Direction

direction as well as the actuator in the vertical direction with an eccentricity, it is noted that a rotation occurred in the columns as a result of the eccentricity.

direction was set apart from the column center with an eccentricity, it is noted that a rotation occurred in the columns as a result of the eccentricity.

3. SEISMIC RESPONSE BASED ON A HYBRID LOADING TEST

3.1 Seismic Response under Unilateral Excitation

Fig. 2 compares damage of the column without an eccentricity (H-1) and the columns with eccentricities of $0.5D$ (H-2) and D (H-3) after the tests. Only flexural cracks occurred at all surfaces in the columns without an eccentricity and an eccentricity of $0.5D$, while spalling off of the covering concrete as well as flexural cracks occurred at the surface in compression side (B surface) in the

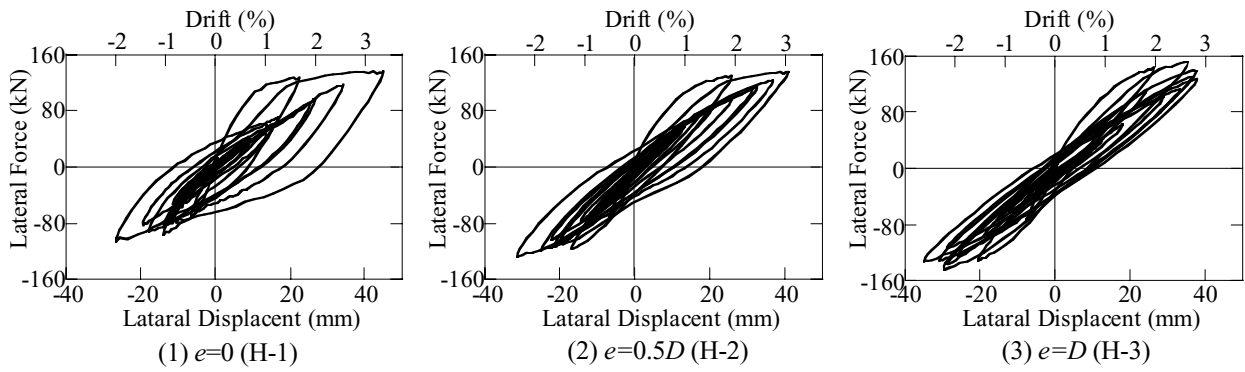


Fig. 5 Lateral Force vs. Lateral Displacement Hystereses under the Unilateral Excitation

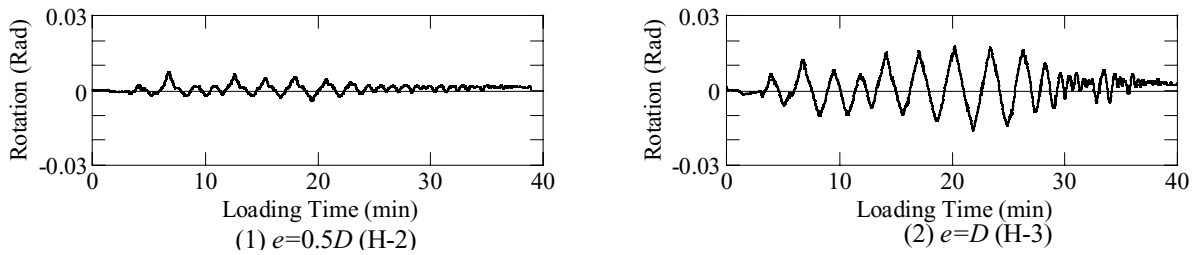


Fig. 6 Rotations of the Columns Relative to the Footings under the Unilateral Excitation in the Longitudinal Direction

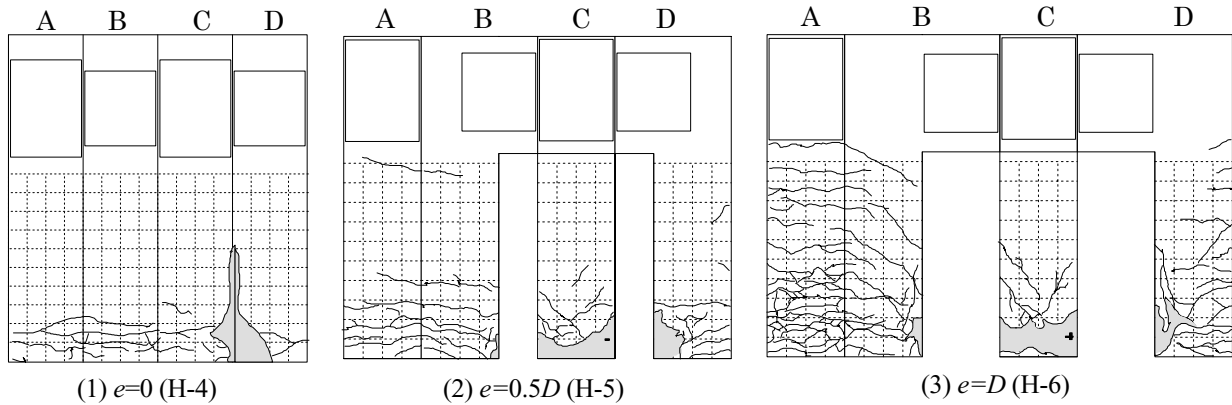


Fig. 7 Damage of the Columns after the Tests under the Bilateral Excitation

column with an eccentricity of D . Longitudinal and ties bars suffered no visible damage in the tests.

Fig. 3 shows the displacement response of the three columns. The maximum displacement was 3.4%, 3.0% and 2.9% drift in the columns without an eccentricity and with the eccentricities of $0.5D$ and D , respectively. Residual drift in the longitudinal direction was not significant in the tests. A remarkable feature of the C-bent columns under the excitation in the longitudinal direction is the drifting of the columns in the eccentricity direction as shown Fig. 4. This resulted from the failure of concrete in the eccentric compression side. The residual drift reached 1.3% and 2.7% in the columns with the eccentricities of $0.5D$ and D , respectively.

Fig. 5 shows the lateral force vs. lateral displacement hysteresis of the columns. The maximum strength was 139.5kN, 139.6kN and 152.5kN in the columns without an eccentricity and with the eccentricities of $0.5D$ and D , respectively, and was stable during the entire excitations. The eccentricity resulted in rotations of the columns as shown Fig. 6. The maximum rotation was 0.008 and 0.019 radian in the columns with the eccentricities of $0.5D$ and D , respectively. It is obvious that the rotation increases as the eccentricity increases.

3.2 Seismic Response under Bilateral Excitation

Fig. 7 compares the damage of the column without an eccentricity (H-4) and the columns with eccentricities of $0.5D$ (H-5) and D (H-6) after the bilateral excitation. Spalling off of the covering

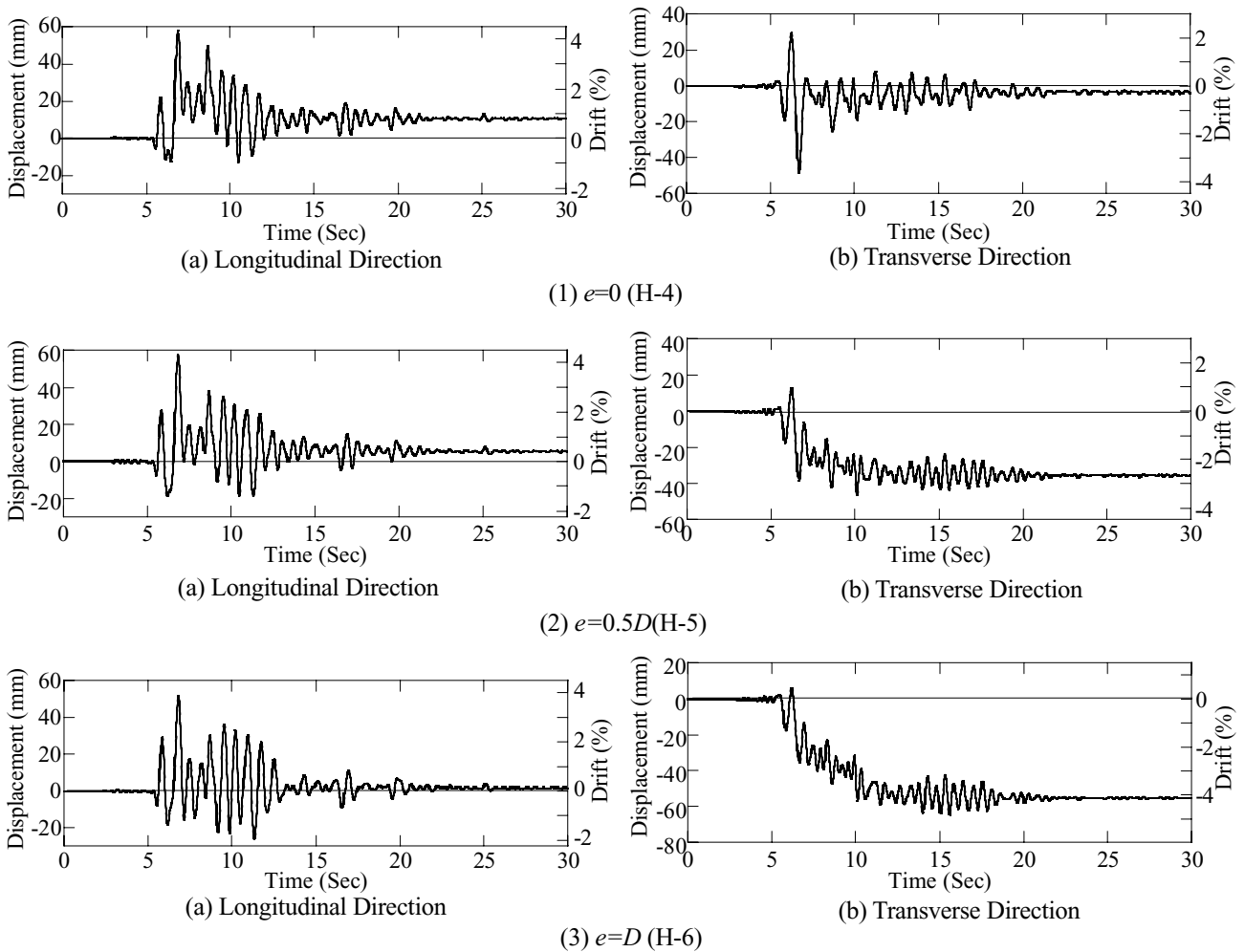


Fig. 8 Displacement Response under the Bilateral Excitation

concrete as well as flexural cracks occurred at CD corner in the column without an eccentricity, while it occurred at the surface in the eccentric compression side in the column with the eccentricities of $0.5D$ and D . Longitudinal and ties bars did not suffer visible damage in the tests. It is apparent that more extensive failure occurred in the columns under the bilateral excitation than those under the unilateral excitation.

Fig. 8 shows the displacement response of the columns under the bilateral excitation. The maximum displacement in the longitudinal direction was 4.3%, 4.2% and 3.9% drift in the columns without an eccentricity and with the eccentricities of $0.5D$ and D , respectively. The maximum displacements under the bilateral excitation were 26-40% larger than those under the unilateral excitation. Residual drift was not significant in the longitudinal direction. On the other hand, the maximum displacement in the transverse direction was -3.6%, -3.5% and -4.6% drift in the columns without an eccentricity and with the eccentricities of $0.5D$ and D , respectively. Residual drift in this direction was -2.7% and -4.1% drift in the columns with the eccentricities of $0.5D$ and D , respectively, while it was -1.3% and -2.7% drift in the columns with the eccentricities of $0.5D$ and D , respectively, under the unilateral excitation. Residual drift under the bilateral excitation was much larger than that under the unilateral excitation.

Fig. 9 shows the lateral force vs. lateral displacement hysteresis of the columns. The strength in the longitudinal direction was 116.7 kN, 129.8 kN and 133.6 kN in the columns without an eccentricity and with the eccentricities of $0.5D$ and D , respectively. The flexural strengths under the bilateral excitation were 7.0-16.4% smaller than those under the unilateral excitation. The restoring force was stable during the entire duration of the excitations. Significant deteriorations of the restoring

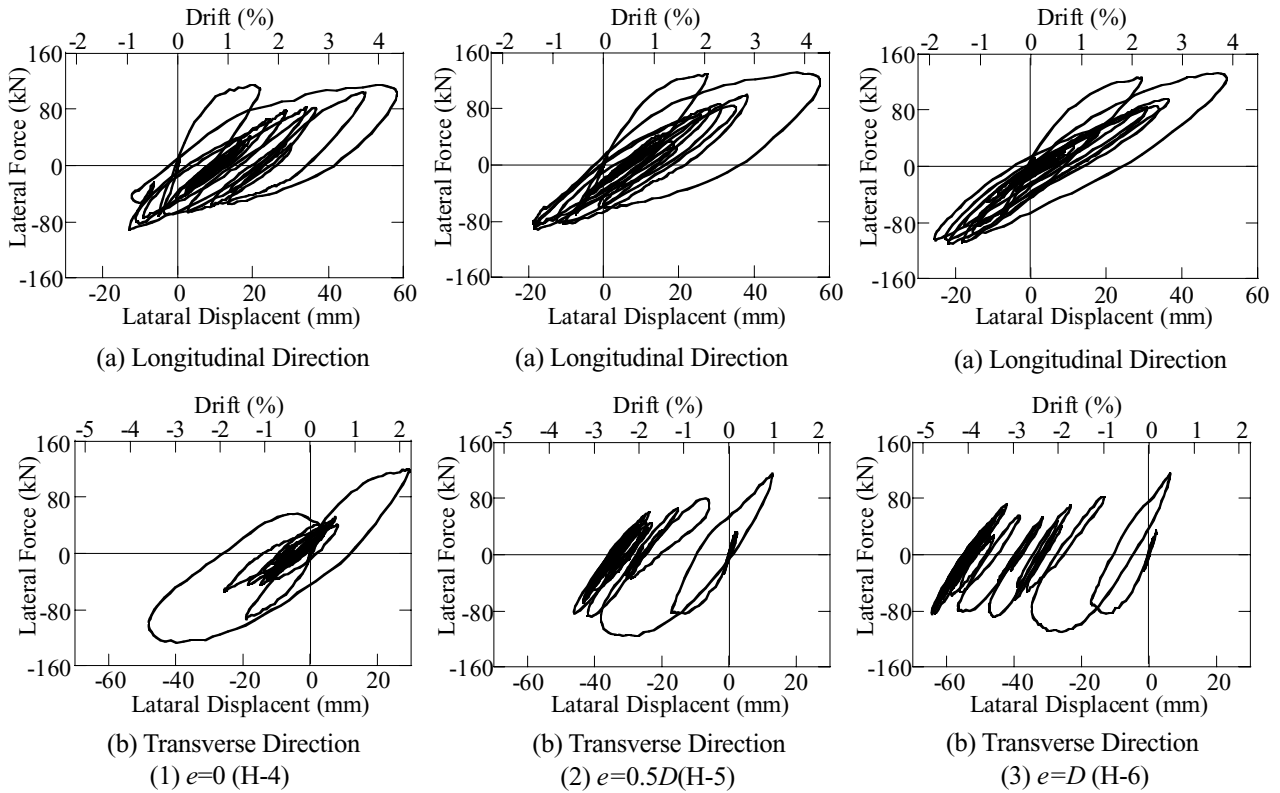


Fig. 9 Lateral Force vs. Lateral Displacement Hystereses under the Bilateral Excitation

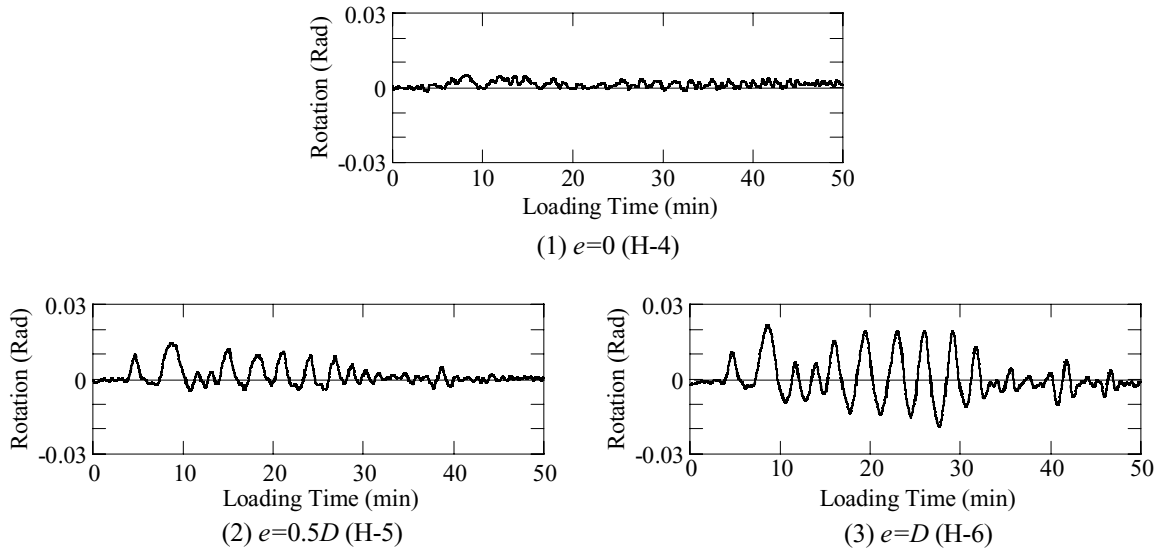


Fig. 10 Rotations of Columns Relative to the Footings under the Bilateral Excitation

force did not occur in the longitudinal direction under the bilateral excitation. The strength in the transverse direction was 120.4 kN, 116.7 kN and 116.7 kN in the columns without an eccentricity and with the eccentricities of $0.5D$ and D respectively. The restoring force deteriorated to 71% and 75% of their strength in the columns with the eccentricities of $0.5D$ and D , respectively, at 3.5% drift.

Fig. 10 shows the rotations of columns relative to the footings in the columns. The rotation occurred in the columns without an eccentricity was limited (0.005 radian). On the other hand, the maximum rotation was 0.014 and 0.022 radian in the columns with the eccentricities of $0.5D$ and D , respectively. The rotation increases as the eccentricity increases.

Table 2 Model Columns used in the Cyclic Loading Tests

Models	C-1	C-2	C-3	C-4
Eccentricities	$0.5D$	D	$0.5D$	D
Longitudinal Reinforcement Ratio (%)	1.35	1.9	1.35	1.9
Tie Reinforcement Ratio (%)	0.99	1.19	0.99	1.19
Concrete Strength (MPa)	24.3	24.9	24.3	25.5
Loading Type*	1		2	

*Loading Type=1: loading in the longitudinal direction, and Type=2: loading in the bilateral direction

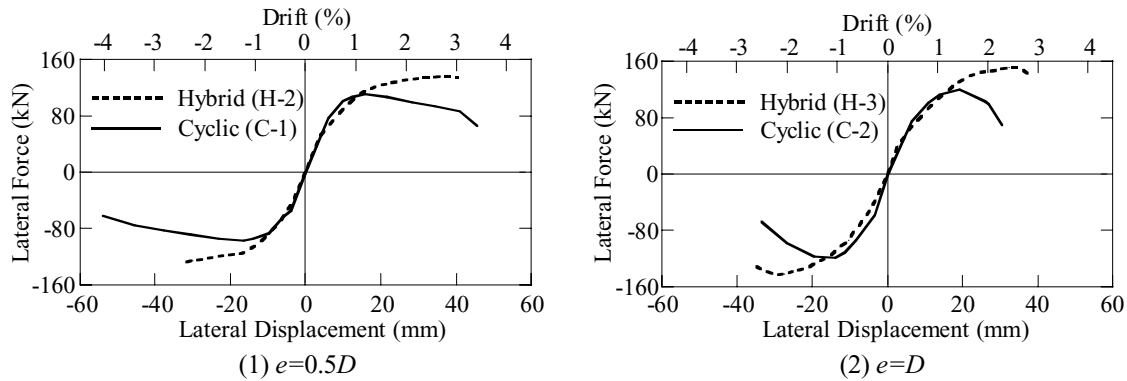


Fig. 11 Comparison of Envelope Curve of the Lateral Force vs. Lateral Displacement Hystereses under the Unilateral Loading

4. EFFECT OF LOADING HYSTERESIS

To clarify the effect of loading hysteresis, a result of cyclic loading tests of reinforced concrete C-bent columns conducted by Kawashima et al is presented here. Two columns with an eccentricity of $0.5D$ and two columns with an eccentricity of D were loaded unilaterally or bilaterally. In the bilateral loading, a rectangular orbit was used. Amplitude of the lateral displacement was stepwisely increased from 0.5% drift until failure with an increment of 0.5% drift. Three cyclic loading were conducted at each step. Due to the space limitation, only envelop curves of the lateral force vs. lateral displacement hysteresis are shown here.

Fig. 11 compares the envelops of the hysteresis between the hybrid loading test and the cyclic loading test under the unilateral excitation in the longitudinal direction. Deterioration of the flexural strength initiated at 3% and 2.5% drift in the columns with the eccentricities of $0.5D$ and D , respectively, under the cyclic loading test, while the restoring force was stable until 3% and 2.8% drift in the columns with the eccentricities of $0.5D$ and D , respectively, under the hybrid loading test. As a consequence, an extensive underestimation of the restoring force occurred at larger displacements under the cyclic loading test.

Fig. 12 compares the envelops of the lateral force vs. lateral displacement hysteresis between the hybrid loading test and the cyclic loading test under the bilateral excitation. Again, it is apparent that more extensive damage progressed in the columns subjected to the cyclic loading than those subjected to the ground motion excitation.

5. CONCLUSIONS

To clarify the seismic performance of reinforced concrete C-bent columns, a hybrid loading test was conducted. The following conclusions may be derived from the results presented herein.

- 1) Extensive failure occurs at the plastic hinge in the eccentric compression side under both the unilateral excitation and the bilateral excitation. This results in a large residual displacement in the

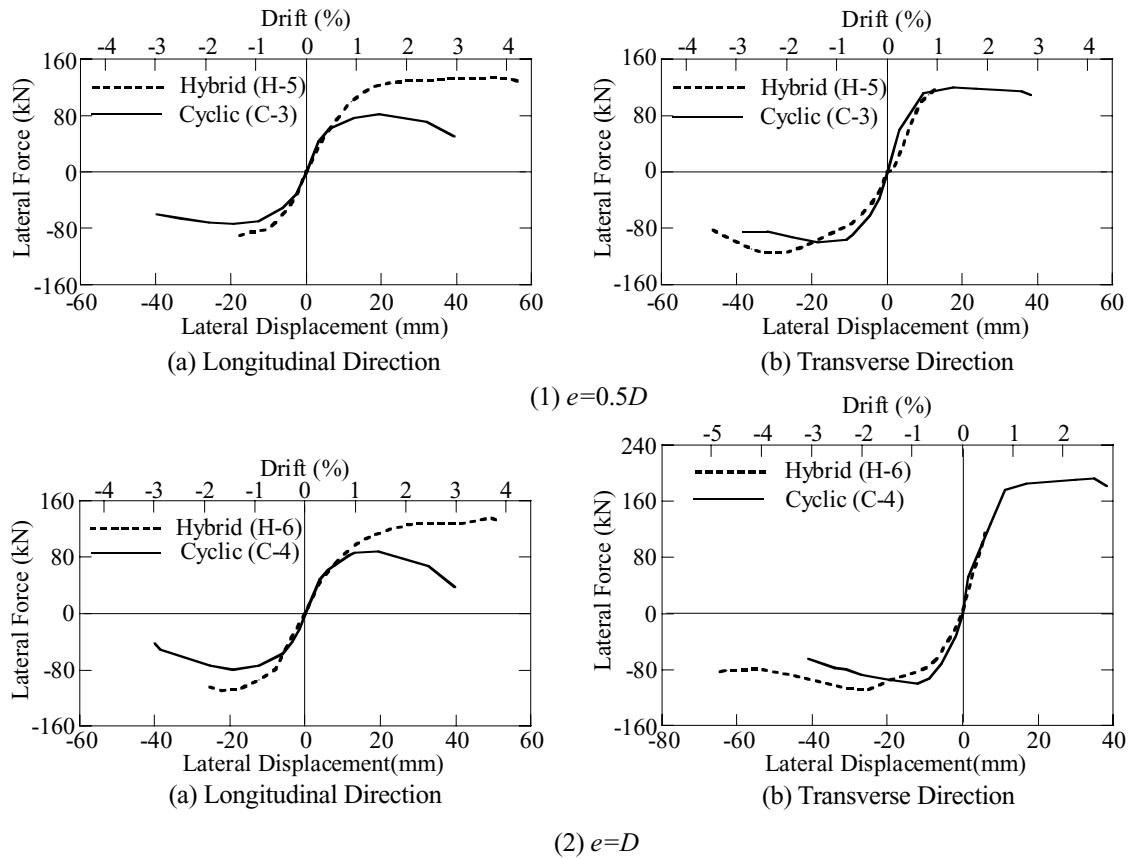


Fig. 12 Comparison of Envelope Curve of the Lateral Force vs. Lateral Displacement Hystereses under the Bilateral Loading

eccentric compression side. The failure and the residual displacement under the bilateral excitation are more extensive than those under the unilateral excitation.

- 2) The eccentricity results in rotations of the columns around their axis under both the unilateral excitation and the bilateral excitation. The rotation increases as the eccentricity is increases.
- 3) The cyclic loading test with the rectangular orbit results in more extensive deterioration of the flexural strength than that under the hybrid loading test.

Acknowledgements:

The authors express their sincere appreciation to Dr. Yabe, M., Chodai Consultants, for design of the columns. Extensive support was provided by Messrs Nakazawa, N., Shimoyamada, E., Matukawa, R., Hayakawa, R., Nakamura, G., Miyaji, K., Fukuda, T., Ichikawa, Y., Ogimoto, H. and Kijima, K. for construction of the columns and executing the tests.

References:

- Kawashima, K. and Unjoh, S (1994), "Seismic Response of Reinforced Concrete Bridge Piers Subjected to Eccentric Loading," *9th Japan Earthquake Engineering Symposium*, 1477-1482, Tokyo, Japan.
- Tsuchiya, T., Ogasawara, M., Tsuno, K., Ichikawa, E. and Maekawa, K., (1999), "Multi-axis Flexure Behavior and Nonlinear Analysis of RC Columns Subjected to Eccentric Axial Forces," *J. Materials, Concrete Structure, Pavements, JSCE*, No. 634/V-45, 131-143.
- Kawashima, K., Watanabe, G., Hatada, S. and Hayakawa, R. (2003), "Seismic Performance of C-bent Columns Based on A Cyclic Loading Test," *J. Structural Mechanics and Earthquake Engineering, JSCE*, No. 745/I-65, 171-189.
- Japan Road Association (1996), "Part V Seismic Design, Design Specifications of Highway bridges," Maruzen, Tokyo, Japan.

THREE-DIMENSIONAL NON-LINEAR EARTHQUAKE RESPONSE ANALYSIS OF REINFORCED CONCRETE STRUCTURES

K. Nishimura¹⁾, K. Takiguchi²⁾, and H. H. Nguyen³⁾

1) Assistant Professor, Dept. of Architecture and Building Engineering, Tokyo Institute of Technology, Japan

2) Professor, Dept. of Mechanical and Environmental Informatics, Tokyo Institute of Technology, Japan

3) Graduate Student, Dept. of Mechanical and Environmental Informatics, Tokyo Institute of Technology, Japan
knishimu@tm.mei.titech.ac.jp, ktakiguc@tm.mei.titech.ac.jp, huyhoang76@tm.mei.titech.ac.jp

Abstract: In this paper, three-dimensional non-linear earthquake responses of R/C structures were considered with one-mass-system. The restoring force characteristics were modeled based on the theory of plasticity, which was one of the macro models. Two types of the restoring force model were adopted. One was flexural type that could be seen in rigid frame structures, and the other was shear type that could be seen in R/C box wall structures. Parameters of the response analysis were natural period of the system and types of analysis those were three and two dimensional analyses. As a result, comparison between three and two dimensional responses, consideration of vertical response acceleration, and estimation of total energy input were carried out.

1. INTRODUCTION

An earthquake response analysis of building is one of the effective methods in order to estimate the seismic safety. One-directional analysis is popular in the seismic design, and lateral two-directional effects are often considered. However, three-directional analysis is hardly made in the seismic design instead of its necessity. In this paper, three-dimensional non-linear earthquake responses of R/C structures were considered with one-mass-system.

The restoring force characteristics can be represented with skeleton curve and hysteresis loop. It can be said that the characteristics of R/C structures can be classified into two types. One is flexural type that has large area in hysteresis loop, and the other is shear type that has small area in the loop, where the area means energy dissipation. The former one can be seen in rigid frame structures, and the later one can be seen in R/C box wall structures. The restoring force model presented by Nishimura and Takiguchi (2003), which was based on the theory of plasticity so-called analogy model that was one of the macro models, was used for both types with modification of stiffness of hysteresis loop. This model can describe axial deformation behavior on unloading that was one of the problems on analogy models of R/C structures (Takiguchi and Gao 2000).

2. RESTORING FORCE MODEL

2.1 Skeleton Curves

The two types of restoring force model, which are called F-model and S-model in this paper, are represented in tri-linear skeleton curves as shown in Figure 1. The F-model has large area and the

S-model has small area in hysteresis loops. Figure 2 shows cracking surface and yield surface those are corresponded to first and second corners of the skeleton curve, respectively. The F-model has parabola surfaces and the S-model has ellipse, and the cracking surface and the yield surface are expressed as $F^c=0$ and $F^y=0$, respectively. The characteristics of Y-axis are assumed to be the same with X-axis. A force point and a deformation point are expressed as $\{P\}=(Q_X, Q_Y, N)$ and $\{\delta\}=(\delta_X, \delta_Y, \delta_Z)$, respectively, where X and Y axes are lateral axes and Z-axis is vertical axis. The restoring force models of one-direction shown in Figure 1 were expressed when $N=cN$. The yield surfaces and the cracking surfaces obey the mixed hardening rule that consist of isotropic hardening and Prager's kinematic hardening rule (Shield and Ziegler 1958).

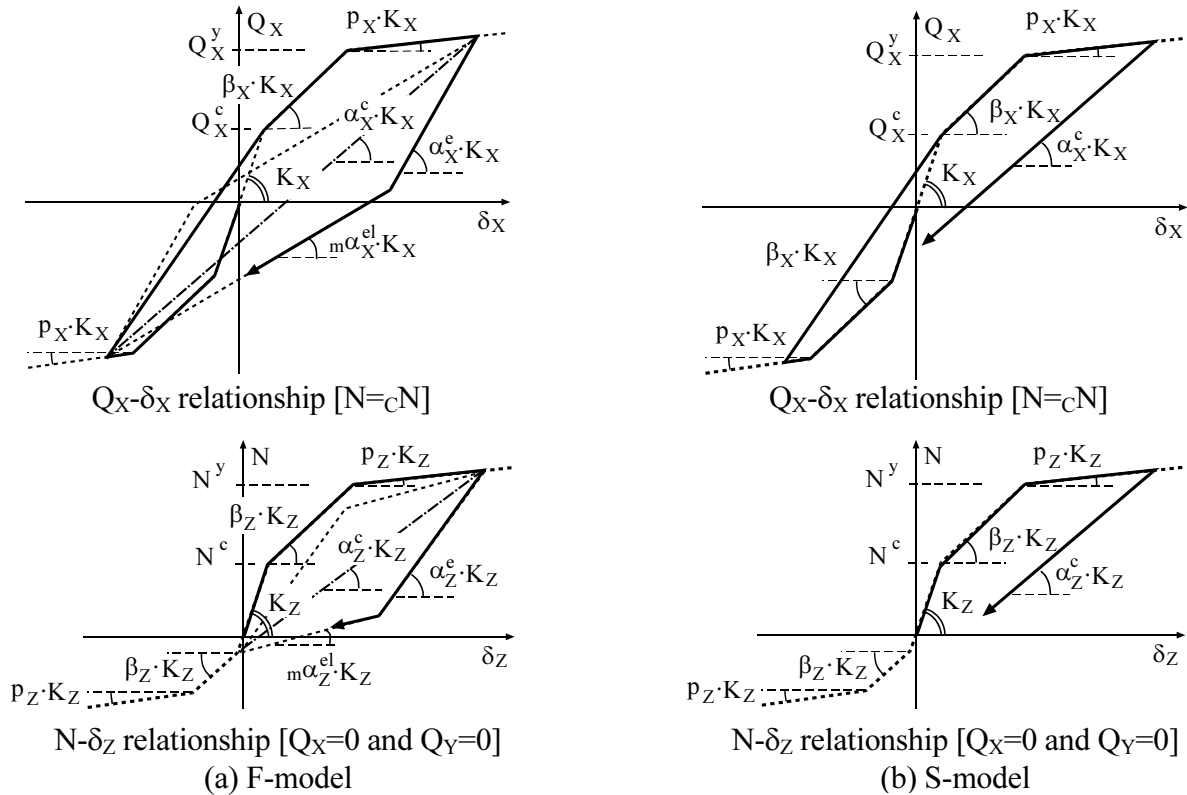


Figure 1 Restoring Force Model on One-axis

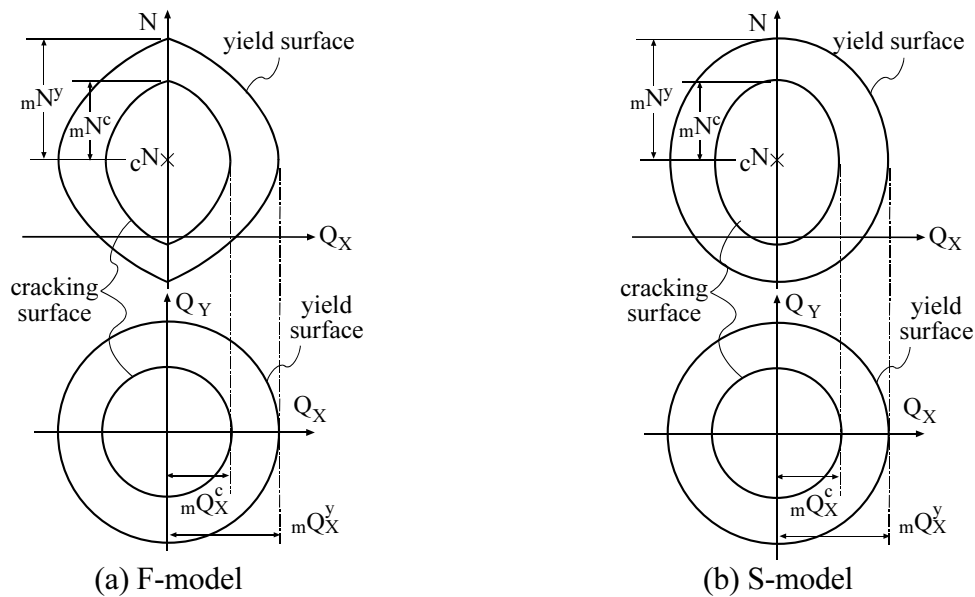


Figure 2 Cracking Surface and Yield Surface

2.2 Loading Surface

Loading surface that is corresponded to corner of hysteresis loop of F-model is assumed as $F^l=0$ (Nishimura and Takiguchi 2003). As shown in Figure 3, the loading surfaces are assumed on a virtual plane and Z-axis those are expressed as ${}_bF^l=0$ and ${}_zF^l=0$, respectively. ${}_bF^l=0$ is represented as circle where $\{{}_bP\}=({}_bQ_X, {}_bQ_Y)^T$, and ${}_zF^l=0$ decide the range of Z component of a force point.

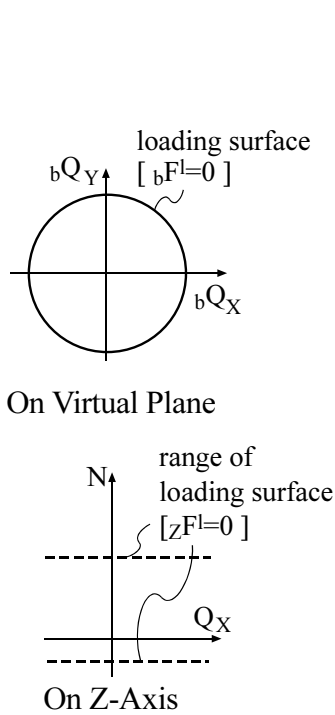


Figure 3 Loading Surface

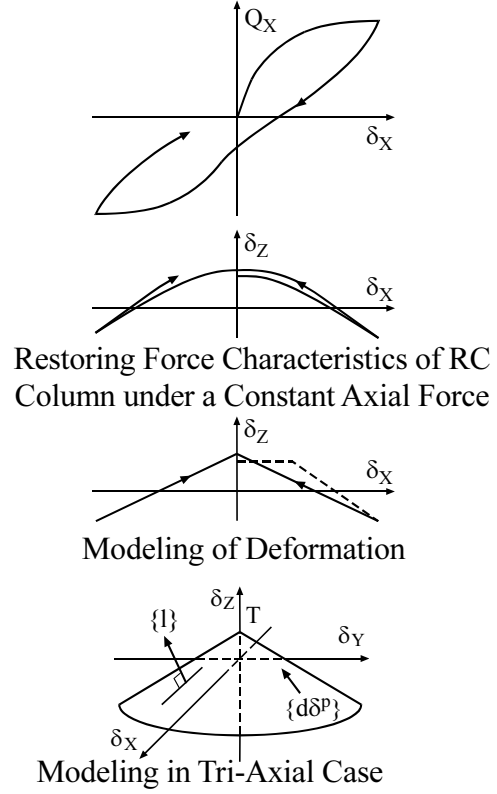


Figure 4 Model of Direction of Plastic Deformation

The force point $\{P\}$ in tri-axial force space is transformed to the point $\{{}_bP\}$ on the virtual plane with the following equation, where $\{P^l\}=({}_bQ_X, {}_bQ_Y, 0)^T$ (Nishimura and Takiguchi 2003).

$$\{dP^l\} = k_n \cdot \left[[I] - \frac{\{l\} \cdot \{n\}^T}{\{n\}^T \cdot \{l\}} \right] \cdot \{dP\} \quad (1)$$

$[I]$ is unit matrix, $\{l\}$ is normal vector of the corn shown in Figure 4, and $\{n\}$ is a unit vector lies in positive direction of Z-axis. In this paper, k_n is assumed as follows.

$$k_n = 1 - \left\{ (N - {}_cN^c) / {}_mN^c \right\}^2 \text{ for F-model, and } k_n = \sqrt{1 - \left\{ (N - {}_cN^c) / {}_mN^c \right\}^2} \text{ for S-model.} \quad (2)$$

A center of the loading surface is also transformed in the same way as the force point.

2.3 Rigidity Degradation

Elastic rigidity degradation of F-model is assumed as shown in Figure 5. The elastic rigidity before yielding is decided as a point direct to the maximum point experienced. The rigidity after yielding is decided according to ratio between maximum yield deformation and initial yield deformation those are expressed as ${}_m\delta_X^y$ and ${}_y\delta_X$ in Figure 5, respectively. The following equation is given to express these rules.

$$\alpha_X^e \cdot K_X = \alpha_X \cdot \left(\frac{m \delta_X^y}{Y \delta_X} \right)^{\gamma} \cdot K_X \quad (3)$$

α_X is the lower value between α_X^c and $imQ_X^y / (Y \delta_X K_X)$, where imQ_X^y is initial value of mQ_X^y . $m\delta_X^y$, which initial value is equal to $Y \delta_X$, is assumed to increase as yield surface expands. α_X^{el} shown in Figure 5 is assumed as follows, which is considered axial force effects by using k_n that is equal to Eqn.(2).

$$\alpha_X^{el} = k_n \cdot m \alpha_X^{el}, \text{ where } m \alpha_X^{el} = (m Q_X^c - m Q_X^l) / (m Q_X^c / \alpha_X^c - m Q_X^l / \alpha_X^e). \quad (4)$$

α_X^e of S-model is assumed as follows, which is also considered axial force effects.

$$\alpha_X^e = k_n \cdot \alpha_X^c, \text{ where } k_n \text{ is equal to Eqn.(2).} \quad (5)$$

Rigidities of Y and Z axes are calculated the same as X-axis.

2.4 Top of Corn

A top of the corn shown in Figure 4 is made smooth by parabola to have no corner as shown in Figure 6 because the corner make calculation difficult. In this paper the range of parabola is $m\delta_X^y/50$ in X-direction, and the range in Y- directions are calculated the same as X-direction.

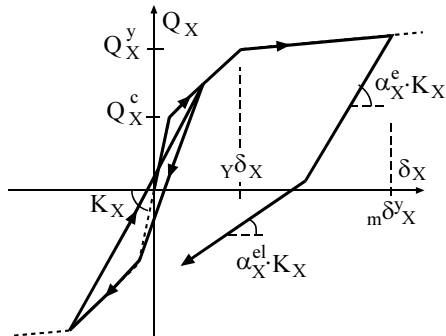


Figure 5 Rigidity Degradation

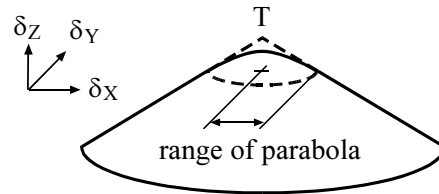


Figure 6 Top of the Corn

3. EARTHQUAKE RESPONSE ANALYSIS

3.1 Numerical Program

Earthquake responses of R/C structures were examined with the one-mass-system and the two types of restoring force model those were F-model and S-model. Newmark method [$\beta=1/4$] was used for the response analysis, and three earthquake ground motions those were Chi Chi 1999, Kobe 1995, and El Centro 1940 were inputted. Constants of the F-model and the S-model were decided based on experimental results of R/C columns (Takiguchi et al. 2001) and R/C box wall structures (Torita et al. 1998), as shown in Table 1. Coefficient of damping was calculated with damping factor and instant stiffness of the system on each step. Parameters of the analysis were natural period ranged from 0.1 to 0.6 and types of analysis those were three and two dimensional analyses. The natural period corresponds to initial elastic stiffness of the model. The restoring model of two-dimensional analysis is the same to the model of three-dimensional analysis except for having no Z-directional components.

A total plastic deformation can be given as shown in Figure 7. A total plastic deformation ratio η

on one-dimension can be estimated by Δh if p , β , and ξ . The equation shown in Figure 7 was adopted in three and two dimensional analyses. In this paper, earthquake response analyses were carried out as η get to 20.0 in F-model and 0.5 in S-model those are decided based on the past experimental study (Takiguchi et al. 2001, and Torita et al. 1998). Δh corresponded to η was calculated, and then analyses were made as Δh get to the calculated values.

Table 1 Constants of the system

	F-model	S-model
$\beta_x (= \beta_y = \beta_z)$	0.27	0.21
$p_x (= p_y = p_z)$	0.001	0.001
Axial force ratio	0.25	0.1
Ratio of yield strength to cracking strength	2.2	3.3
Axial yield strength ratio of tension to compression	0.25	0.25
Axial cracking strength ratio of tension to compression	0.1	0.1
γ shown in Eqn.3	-0.5	-
Damping factor	0.02	0.05
Ratio of vertical natural period to lateral natural period	0.3	0.3

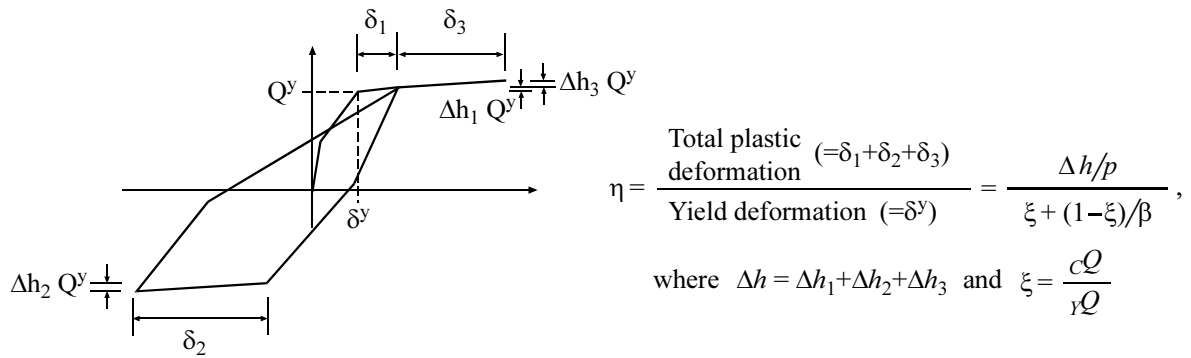


Figure 7 Total Plastic Deformation

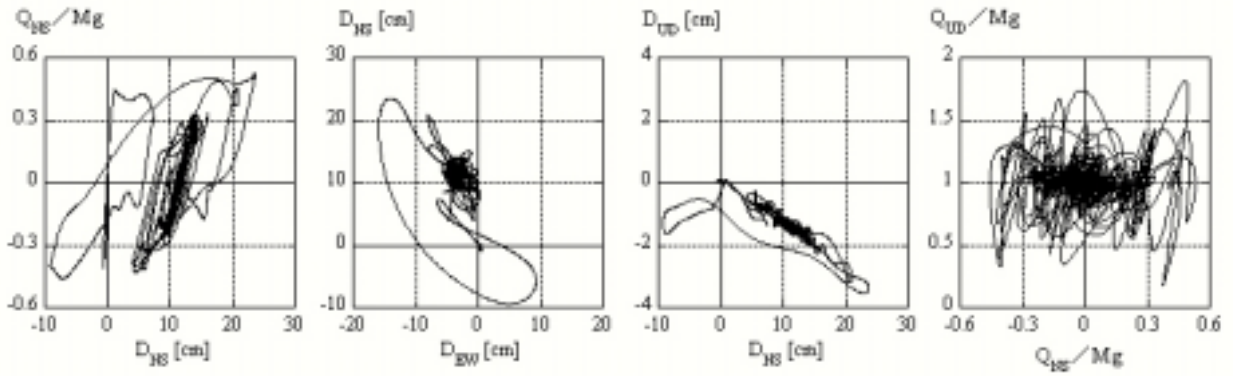
3.2 Numerical Results

Figure 8 shows responses in case of inputting Kobe ground motion. Initial natural periods of the system are 0.2 for F-model and 0.1 for S-model. UD-axis takes compressive side as positive direction. As shown in Figure 8, the restoring force model shown in this paper could represent behaviors on unloading stage, which UD-directional deformation Δ direct to compressive side.

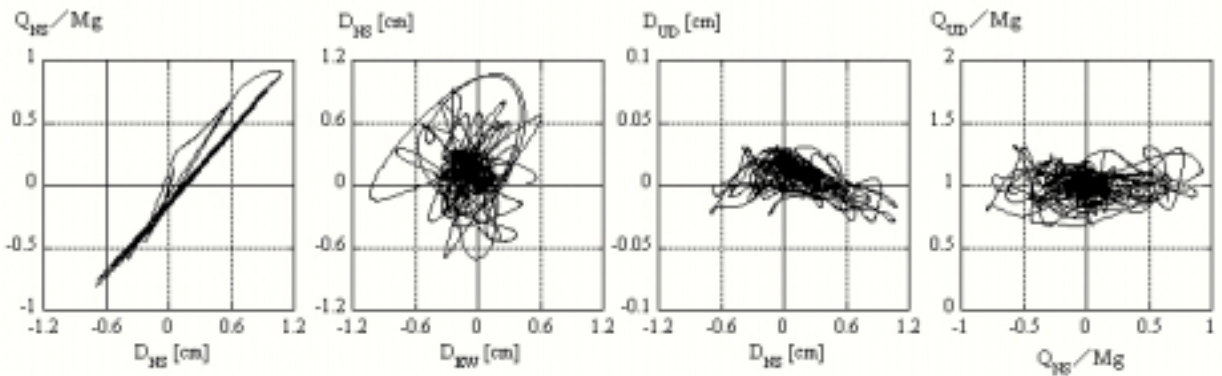
Figure 9 to 12 show numerical results when Chi Chi, Kobe, and El Centro ground motions were inputted. Circle and diamond marks represent the results of F-model and S-model, respectively. Black and White marks represent three and two dimensional analyses, respectively. D, A, A_V , V_E , and T express maximum lateral response deformation, maximum lateral absolute response acceleration, maximum vertical absolute response acceleration, equivalent velocity of total energy input (Akiyama 1985), and initial natural period of the system, respectively. D is equal to a square root of sum of δ_{NS}^2 and δ_{EW}^2 . A is calculated in the same way as D. V_E can be given as follows, where E and M are energy input and mass of the system, respectively.

$$V_E = \sqrt{2E/M} \quad (6)$$

D-T, A-T, and V_E -T relationships of three-dimensional analysis almost agree with the relationships of two-dimensional analysis as shown in Figure 9 to 11. These results indicate possibility that it is enough to consider two directional input of earthquake motion when we estimate lateral external force and maximum deformation in seismic design. It is important to know the maximum deformation to judge whether non-structural claddings of buildings can follow the deformation.



(a) F-model with 0.2 sec natural period



(b) S-model with 0.1 sec natural period
Figure 8 Responses inputted Kobe wave

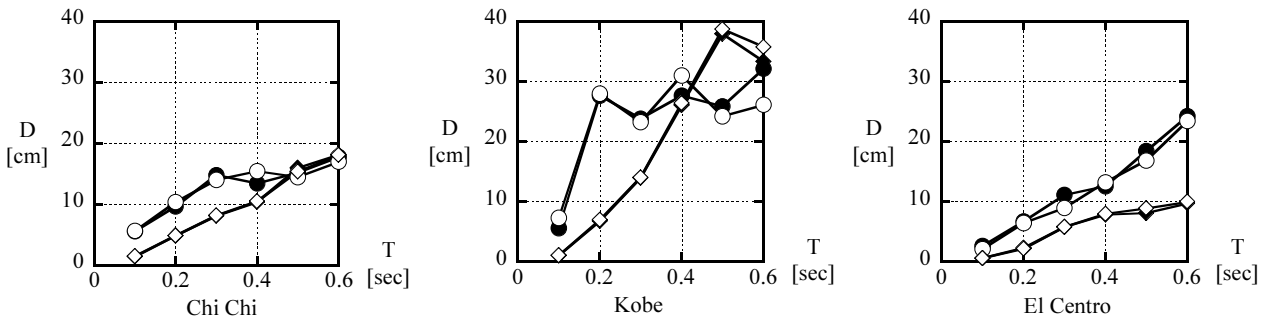


Figure 9 Maximum Lateral response deformation

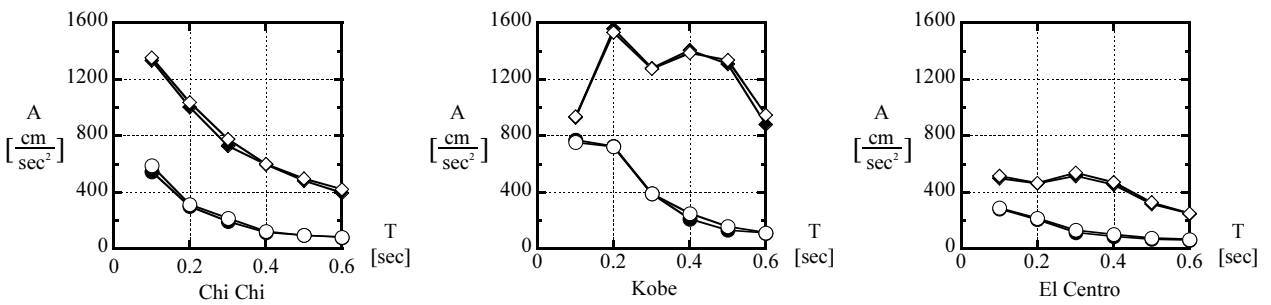


Figure 10 Maximum Lateral Absolute Response Acceleration

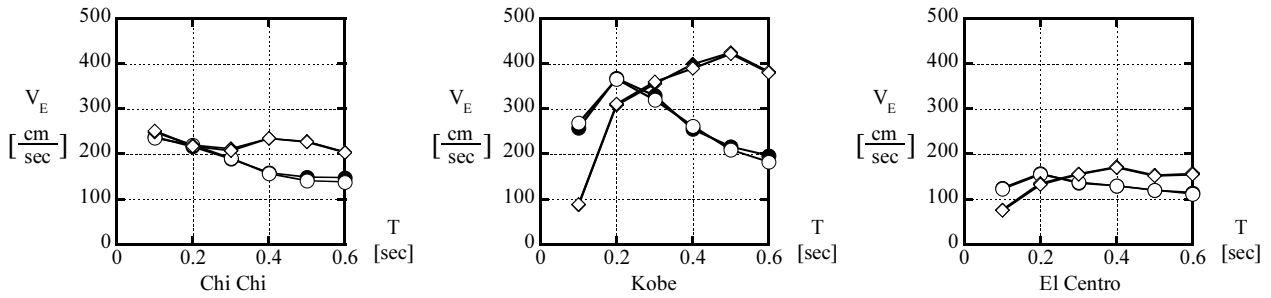


Figure 11 Equivalent Velocity of Total Energy Input

Positive and negative sides of the maximum vertical absolute accelerations are both plotted in Figure 12. As shown in this figure, the values of positive and negative side were almost equal. The biggest values were about 940 cm/sec^2 on the F-model of 0.3 sec natural period inputted Kobe wave, and about 1090 cm/sec^2 on the S-model of 0.5 sec natural period inputted Kobe wave. It can be said that the numerical results of A_V were obtained in the range of 300 to 1100 cm/sec^2 . Although this result may not be serious from the viewpoint of collapse of structures, we have to consider this result from the viewpoint of influence on inside of buildings.

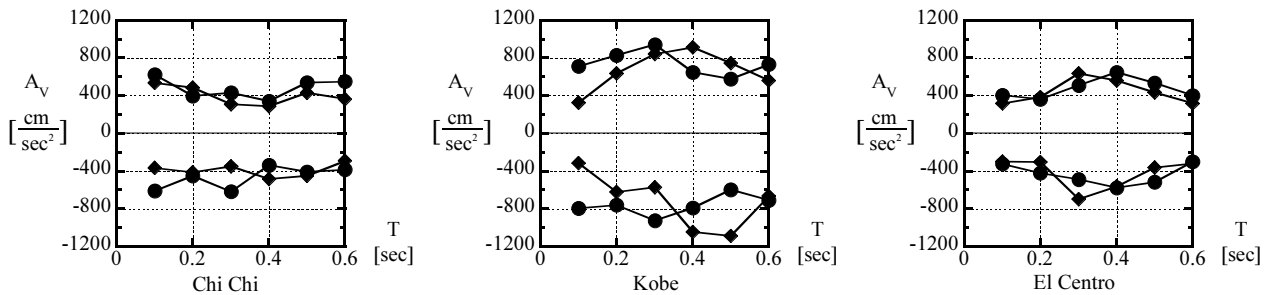


Figure 12 Maximum Vertical Absolute acceleration

3.3 Evaluation of Total Energy Input

An evaluation of the total energy input was considered with a result of elastic response analysis, which damping factor is 0.1 (Akiyama 1985). Figure 13 show V_E - T relationships where a solid curve express a result of three-dimensional elastic response analysis, which damping factor is 0.1. Circle and diamond marks are represented the results of F-model and S-model, respectively. The results were plotted by averaged period of initial period given by initial elastic stiffness and last period given by using last value of α_X^c shown in Figure 1. V_E of F-model and S-model show good agreement with the elastic analysis results. There are some differences between the results of the elastic analysis and non-linear analysis in the range of longer period, however those are safety side and those differences aren't large. Therefore, it can be said that V_E of elastic analysis at averaged natural period have possibility to be able to evaluate V_E of F-model and S-model.

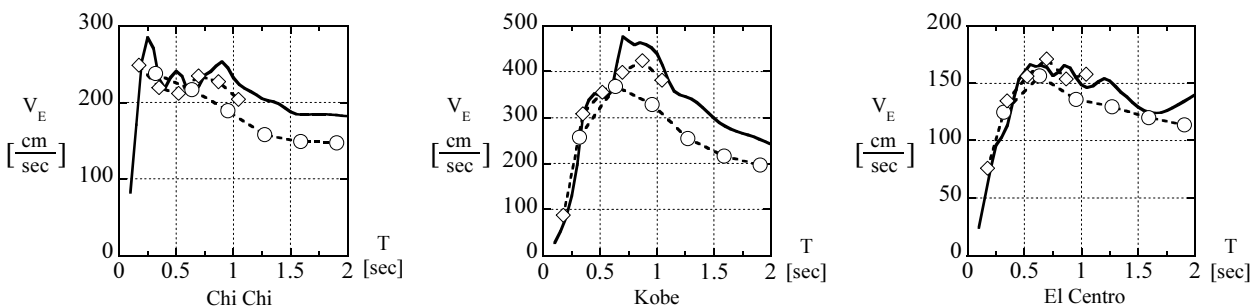


Figure 13 Estimation of Total Energy Input

4. CONCLUSIONS

Three-dimensional non-linear earthquake responses of R/C structures were examined with one-mass system. The restoring force characteristics were modeled based on the theory of plasticity, which was one of the macro models. Two types of the restoring force model were adopted. One was flexural type that had large area in hysteresis loop, and the other was shear type that had small area in the loop. The former one can be seen in rigid frame structures, and the later one can be seen in R/C box wall structures. Parameters of the analysis were natural period ranged from 0.1 to 0.6 and types of analysis those were three and two dimensional analyses. The natural period corresponds to initial elastic stiffness of the model. Chi Chi, Kobe, and El Centro earthquakes were employed for input data. As a result, the following conclusions were found.

- 1) Maximum lateral response deformation, maximum lateral absolute response acceleration, and total energy input of three-dimensional analysis were almost equal to the responses of lateral two-dimensional analysis. These results indicate possibility that it is enough to consider two directional input of earthquake motion to estimate lateral external force and maximum deformation in seismic design.
- 2) Maximum vertical absolute response accelerations of three-dimensional analyses were obtained in the range of 300 to 1,100 cm/sec². Although this result may not be serious from the viewpoint of collapse of structures, it is necessary to consider this result from the viewpoint of influence on inside of buildings.
- 3) Total energy input of elastic response analysis with 0.1 damping factor showed good agreement with result of three-dimensional non-linear response at an averaged period that was an average of two periods associated with initial elastic stiffness and last stiffness that connected two maximum points of hysteresis loop diagonally. It can be said the result of elastic response analysis with 0.1 damping factor has possibility to be able to evaluate the total energy input of three-dimensional non-linear earthquake response by using the averaged periods.

References:

- Nishimura, K. and Takiguchi, K. (2003), Tri-Axial Non-Linear Restoring Force Model of R/C Structures by Using an Analogy to the Plastic Theory, *Journal of Structural and Construction Engineering*, Architectural Institute of Japan, 566, 113-120, (in Japanese).
- Takiguchi, K., and Gao, Z. (2000), Tri-axial non-linear restoring force model of R/C structure using the theory of plasticity, *Proc. of 12th World Conference on Earthquake Engineering*, Auckland, New Zealand, Paper ID 0693.
- Shield, R. T., and Ziegler, H. (1958), On Prager's Hardening Rule. *Zeitschrift für angewandte Mathematik und Physik*, Vol.9a, 260-276
- Takiguchi, K., Nishimura, K., and Hirai, K. (2001), Experimental study on two-dimensional restoring force characteristics of R/C columns under varying axial force, *Journal of Structural and Construction Engineering*, Architectural Institute of Japan, 539, 111-118, (in Japanese).
- Torita, H., Nishikawa, T, Saito, H., Ishikawa, Y., and Kitada, Y. (1998), Study on Restoring Force Characteristics of a RC Box Wall Subjected to Diagonal Horizontal Force. *Summaries of Technical Papers of Annual Meeting AIJ*, C-2, 865-866, (in Japanese).
- Akiyama, H. (1985). "Earthquake-Resistant Limit-State Design for Buildings," University of Tokyo Press, Tokyo, Japan.

The Proposal of Simplified Truss Model for Shear Carrying Capacity of Prestressed Concrete Beams

M. Lertsamattiyakul¹⁾, J. Niwa²⁾, S. Tamura³⁾, and Y. Hamada³⁾

1) Doctoral Student, Department of Civil Engineering, Tokyo Institute of Technology, Japan

2) Professor, Department of Civil Engineering, Tokyo Institute of Technology, Japan

3) Researcher, Research and Development Center, DPS Bridge Work Co., Ltd, Japan

96b31110@cv.titech.ac.jp, jniwa@cv.titech.ac.jp, s_tamura@dps.co.jp, y_hamada@dps.co.jp

Abstract: In this study, the simplified truss model with a small number of members has been proposed for evaluating the shear carrying capacity and the failure pattern of PC slender beams without transverse reinforcement. To investigate the failure mechanism, which is influenced mainly by prestressing force and type of the stress distribution, the parametric study using FEM has been carried out. The estimated inclination of the critical stress flow and the thickness of struts assessed in terms of the width of bearing plates and the effective depth have been utilized to the proposed model. The satisfactory prediction on the shear carrying capacity and failure pattern of PC slender beams without transverse reinforcement can be obtained.

1. INTRODUCTION

With the requirements of saving in dead load resulting from the concrete section together with a high resistance in the superhigh-rise structures, prestressed concrete (PC) becomes the significant structural members. At present, it is recognized that the clear explanation and the well-predicted analytical results for the shear failure behavior of PC beams are still not achieved. For the recommended method by JSCE (2002) called the decompression moment method, the scatter of predicted results is usually observed due to the neglecting of distribution of the prestressing force. Moreover, there is another method considering the resistance at the flexural cracking as the extra value to the shear resistance due to the contribution of compression, called M_{cr} method (Ito et al. 1994). It has been observed that, even in PC slender beams where shear span to effective depth ratio, $a/d \geq 2.5$, after the diagonal cracking, the beams still maintain the resistance due to the arch action and finally fail in shear compression mode. It is found that this method cannot be used to yield the comprehensive explanation about the shear compression failure of PC slender beams and how the resistance of the flexural cracking remains until the ultimate stage. Thus, newly proposed method should be simple, accurate in prediction and able to clarify the mechanism of shear compression failure by considering the effects of prestressing forces and type of stress distribution.

In this study, the simplified truss model has been proposed to assess the shear carrying capacity of PC slender beams without transverse reinforcement. To obtain the important information for modeling, the parametric study using finite element method (FEM) of PC slender beams has been performed. The failure mechanism influenced by the variation of significant parameters has been clarified. The tendency of stress flows obtained from the analytical results is summarized and adopted to the model. The shear carrying capacity and the failure patterns of the calculated and experimental results are compared in order to confirm the applicability of the proposed model.

2. PARAMETRIC STUDY USING FEM

To investigate the failure mechanism of PC slender beams, the nonlinear FEM analysis using DIANA system has been carried out. Details of geometric properties of the analytical model are illustrated in Figure 1. The values of prestressing force, P , in the upper and lower prestressing bars are proportionally adjusted and varied in the range of 100- 400 kN. Based on the values of P and the location of applied axial force, the upper and lower fiber stresses (σ_u and σ_l , respectively) are calculated and changed in the range of -3- 6 and 1- 15 MPa, respectively. From the values of σ_u and σ_l , the types of stress distribution can be categorized into 4 types as shown in Figure 2. The shear span to effective depth ratio, a/d , the effective depth, d , and the compressive strength of concrete, f_c' , are also considered as the significant parameters and varied from 2.5- 4.5, 400- 800 mm and 40- 80 MPa, respectively. The width of beam, b , is assumed to be 200 mm for all cases. The longitudinal reinforcement ratio is set to be 1.3% ($f_{py} = 930$ MPa).

The samples of contour figures of stress flow at 90% analytical resistance at the ultimate stage (90% V_{max}) of PC slender beams under triangle with zero upper fiber stress distribution ($\sigma_u = 0$ MPa) are depicted in Figure 3. It is found that, with the increase in σ_l , the slope of the concentrated stress flow becomes steeper (Figures 3(a) and (b)). However, when the value of σ_l becomes comparatively large, the concentration of this steep stress flow becomes weak, whereas the stress flow from the loading point to the support becomes remarkable (Figures 3(c) and (d)). It implies that, not only the resistance along the diagonal crack, the stress flow curvedly transferring to the support also exists. The comparison between the differences in types of stress distribution (variation of σ_u) is expressed as the example in Figure 4. With the increase in value of σ_u , the inclination of the stress flow becomes slightly steeper (Figures 4(a) and (b)). On the other hand, the stress flow curvedly transferring to support becomes larger with the greater value of σ_u (Figures 4(c) and (d)). That means, not only the value of σ_l , but the value of σ_u also influences on the inclination of concentrated stress flow. The estimation of inclination of the concentrated

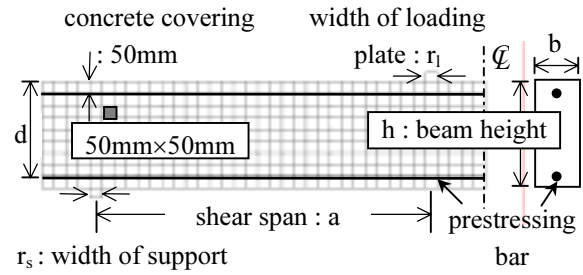


Figure 1 Finite element analytical model of PC slender beam in the parametric study

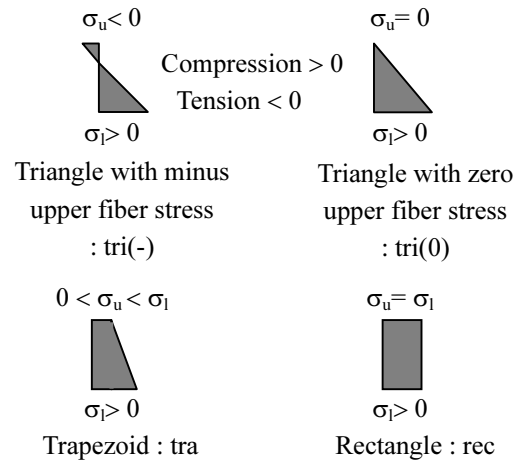


Figure 2 Types of stress distribution due to the prestressing force

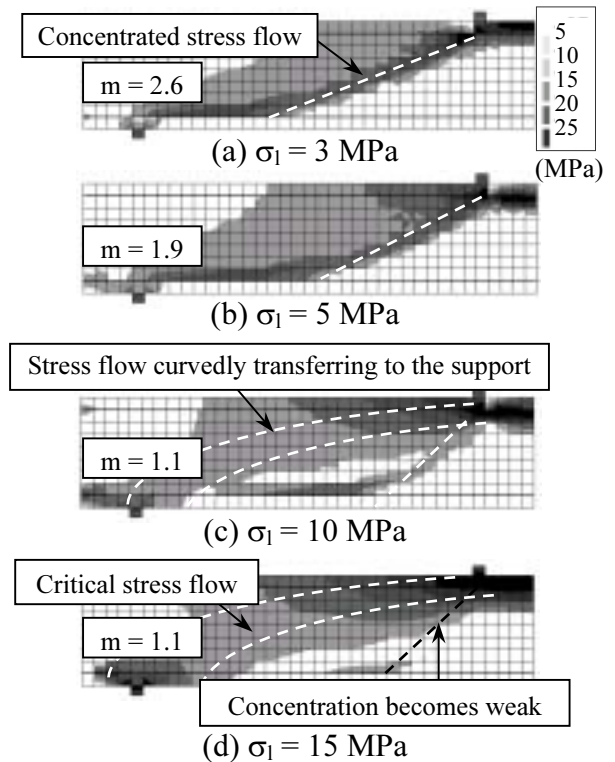


Figure 3 Analytical results with variation of σ_l where $\sigma_u = 0$ MPa ($a/d = 3.5$, $d = 400$ mm and $f_c' = 40$ MPa)

stress flow is important for predicting the failure mechanism of the beams. Therefore, the values of principal compressive stress, σ_2 , at each Gauss's point are taken into the consideration. As demonstrated in Figure 5, between the upper and lower prestressing bars, the maximum absolute values of σ_2 in each horizontal level, σ_{2i-max} , are marked. By considering the location of σ_{2i-max} as the co-ordination in X-Y axes, (x_i, y_i) , the correlation coefficient (equation in Figure 5) is employed to express the level of correlation between the values of x and y in the approximated relationship. The part of marked Gauss's points that has a high value of correlation coefficient (≥ 0.95) is selected. The relationship of the selected points is approximated and summarized in terms of m , where $m = \cot\theta$ and θ is an angle of the estimated slope. It should be noted that the value of m decreases with the increase in the value of σ_l (Figure 3) and also slightly decreases with the increase in the value of σ_u (Figure 4). For the case that the stress flow curvedly transferring to support becomes the critical path, even though the concentration of the steep stress flow becomes weak, this steep inclination is assumed to evaluate the value of m . This is in order to recapitulate the values of m in the same trend that is the value of m decreases with the increase in the value of σ_l . The relationships between the values of m and σ_l with σ_u , a/d , d , and f_c' are summarized. As the example, in Figure 6, the relationship between the values of m from FEM results (FEM) and σ_l with σ_u are summarized and approximated (Approx.). It is found that the values of m become greater with the increase in values of a/d and f_c' , while the value of d has a small effect on value of m . The equation for predicting the value of m can be expressed as in Eq. (1).

$$m = 2.55 \left(\left(1 + 0.2 \frac{\sigma_u}{\sigma_u + \sigma_1} \right) \sigma_1 \right)^{\frac{3}{5}} \left(\frac{a}{d} \right) \left(\frac{f_c'}{100} \right)^{\frac{3}{5}} \quad (1)$$

3. SIMPLIFIED TRUSS MODEL

Figure 7 demonstrates the simplified truss model with the prestressing forces in terms of the axial forces, P_1 and P_2 , developed in this study to

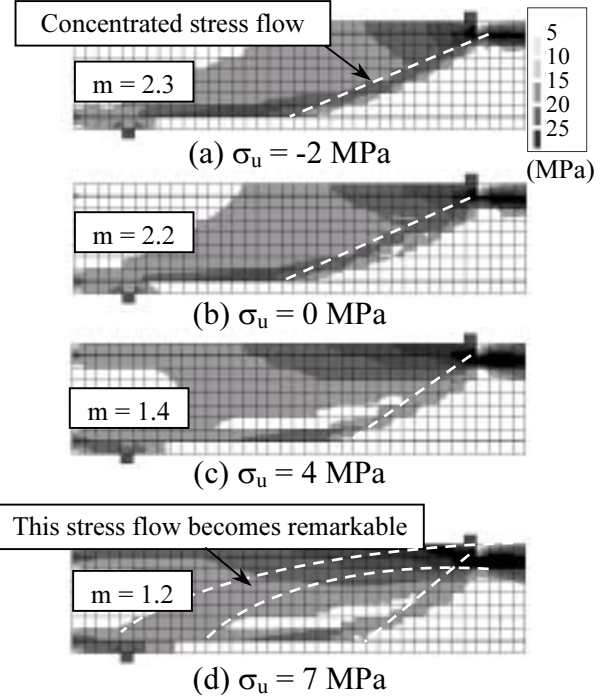
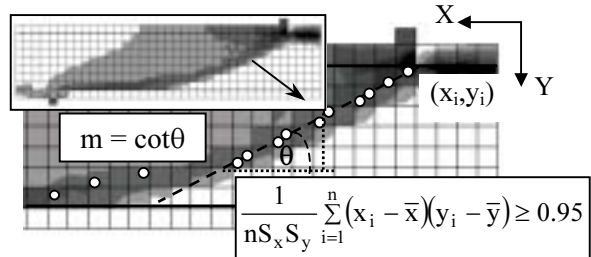


Figure 4 Analytical results with variation of σ_u where $\sigma_l = 7$ MPa ($a/d = 3.5$, $d = 400$ mm and $f_c' = 40$ MPa)



\bar{x}, \bar{y} : Mean of x and y
 S_x, S_y : Standard division of x and y
 n : Number of considered data

Figure 5 Evaluation of inclination of concentrated stress flow in terms of m

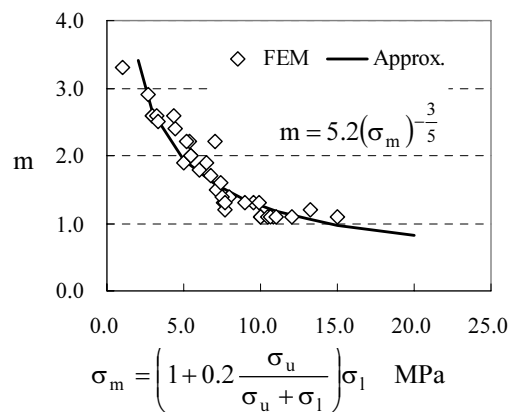


Figure 6 Relationship of m and σ_l and σ_u ($a/d=3.5$, $d=400$ mm, $f_c'=40$ MPa)

calculate the shear carrying capacity of PC slender beams without transverse reinforcement. As one of the main concepts that the model should be simple, the proposed model consists of 7 nodes and 11 members. The modeling of concrete and reinforcement are expressed as in Figure 7. After modeling by using the value of m , each member force, F_i , caused the externally applied shear force, V , can be determined by employing the principles of virtual work method. The equivalent elastic analysis has been carried out for simplicity in calculation. That is, the stiffness of concrete at the ultimate stage as the secant modulus and the concrete softening, η , are incorporated to the struts. The shear carrying capacity of the beam can easily be determined when the member force of one of 4 struts becomes greater than its capacity. The process of calculation is summarized in Figure 8. The location of two struts, [3] and [4], is simply assumed with the same horizontal distance in the level of flexural tension members as shown in the figure. The thickness of the flexural compression member is set to be $2c$, where c is the thickness of concrete cover. The thicknesses of the transverse tension members [5] and [6] are assumed to be the distance from the loading point to the middle point between members [5] and [6] and the left distance to the middle point of support, respectively. The sum of cross sectional area of reinforcements is applied as the cross sectional area of the flexural tension member. It is recognized that the thickness of strut is important for evaluating the resistance of concrete structure in shear compression failure.

3.1 Thickness of Strut

Based on FEM analytical results, compressive stresses in the vertical direction at each Gauss's points, σ_{yi} , at about 90% of V_{max} are considered. The range of $0.2d$ inner side of a beam from the upper prestressing bar is investigated. In each level, the distribution of the ratio of σ_{yi} and the maximum values in that horizontal level, σ_{yi-max} , ($\Delta_i = \sigma_{yi}/\sigma_{yi-max}$) along the beam axis is evaluated. For each horizontal level of Gauss's point in the range of $0.2d$, the horizontal width of the distribution, t_i , where $\Delta_i = 0.3$ is measured. The average value of t_i is considered as the horizontal thickness of the strut, t . The range in the vicinity area of the support above the lower prestressing bar is also treated with the same process to evaluate the horizontal width of the distribution. Figure 9 shows the examples of obtained horizontal

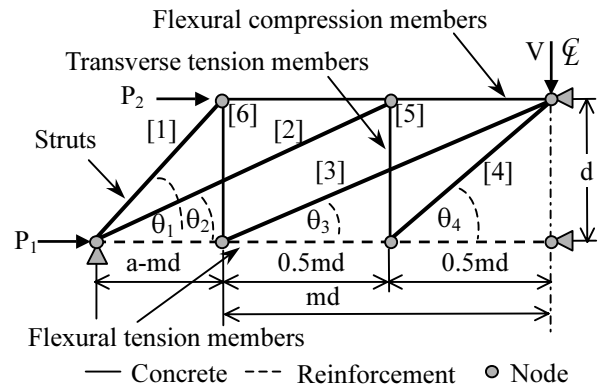


Figure 7 Simplified truss model for a PC beam without transverse reinforcement

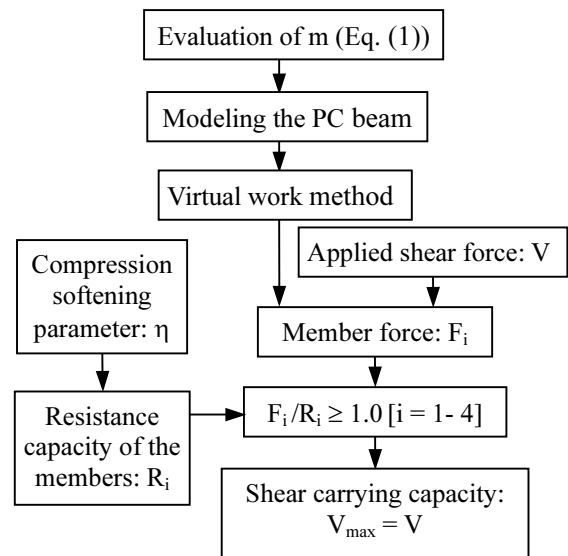


Figure 8 Process in calculating the shear carrying capacity

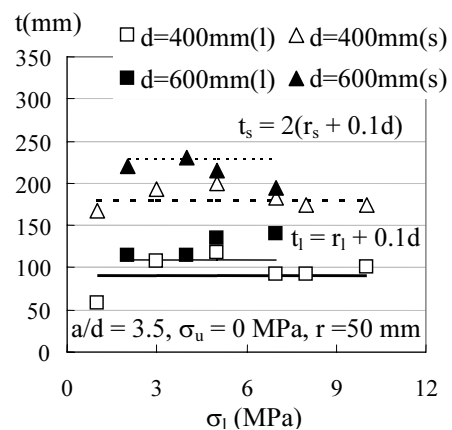


Figure 9 Example of measured and estimated t (variations of σ_1 ($\sigma_u = 0\text{MPa}$) with d)

thickness in the vicinity area of a loading point, t_l , and support, t_s , from FEM analytical results with the variations of σ_l and d . By considering the effects of bearing plates and the effective depth (Niwa 1984), the values of t_l and t_s can be simply estimated with the width of a loading plate, r_l , or support, r_s , and d as $r_l+0.1d$ and $2(r_s+0.1d)$, respectively. In the proposed model, the members [1] - [2], and members [3] - [4] are considered to be affected by support and loading plates, respectively. The cross sectional area of each strut can be assumed as the values of t_l or t_s multiplied with b and its inclination.

3.2 Division of Modeling

As discussed in the previous section, based upon the analytical study, there are 2 types of failure pattern can be observed. One takes place along the concentrated stress flow (Model 1) and the other one occurs along the stress flow curvedly transferring to the support (Model 2). By considering the value of m relating with the possible location of the critical strut, the proposed simplified truss model is divided into 2 models as depicted in Figure 10.

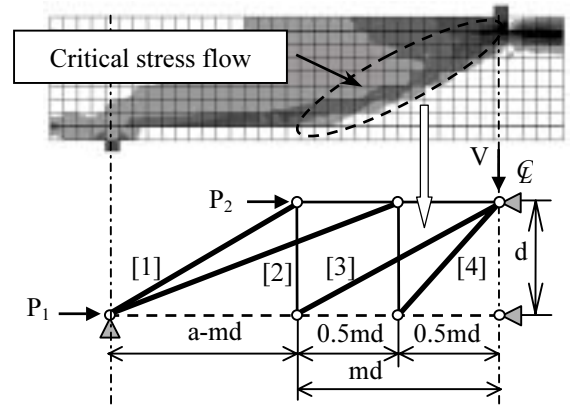
In *Model 1* ($m > 1.0$, Figure 10(a)), the distance md is adopted as the horizontal distance from the loading point to the ended node of member [3]. When $m \geq 2.0$, since the effect of a loading plate is considered to become weak, the thickness of member [3] is set to be $(a-md)\sin\theta_3$, where $d \geq a-md$. When the inclinations of struts are quite flat in case of $m \geq 2.0$, 50 mm is set to be a lower bound value of w_i avoiding the underestimation. The applied upper bound value of m is set to be $0.9a/d$ in modeling. The specimen with low up to medium level of prestressing stress is considered to match with this model.

In *Model 2* ($m \leq 1.0$, Figure 10(b)), the distance md is adopted as the horizontal distance from the loading point to the ended node of member [4]. Due to the small effect of bearing plates on the size of members [2] and [3], which are expressing the stress flow curvedly transferring to the support, the thicknesses are set to be $md\sin\theta_2$ and $(a-2md)\sin\theta_3$, where $d \geq a-2md$. Because of the inclinations of struts are quite flat, 50 mm is assumed as a lower bound value of w_i in this case. This model is considered to fit for a specimen with comparatively high prestressing stress level.

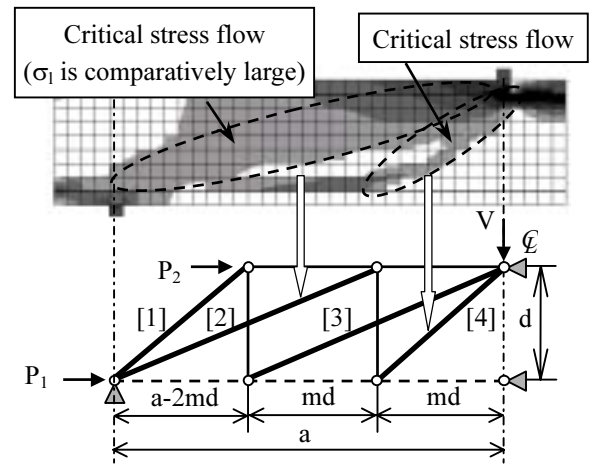
3.3 Compression Softening Parameter

In calculation of the shear carrying capacity, the value of compression softening parameter, η , affected by the existence of cracks, should be considered. For a sake of simplicity in calculation, the practical expression of η is equated with a slight variation from 0.6 to 0.4 in the range of f_c' of 30 to 100 MPa as in Eq. (2).

$$\eta = -0.3\left(\frac{f_c'}{100}\right) + 0.7 \quad (2)$$



(a) Model 1: $m > 1.0$



(b) Model 2: $m \leq 1.0$

Figure 10 Division of the proposed simplified truss model

4. COMPARISON OF CALCULATED AND EXPERIMENTAL RESULTS

The outlines of the specimens and comparisons between the experimental and calculated results in order to confirm the applicability of the simplified truss model are tabulated in Table 1. By checking the reliability of the test data by FEM as in the previous study (Tamura et al 2003) and the additional investigation, 31 cases of the experimental results from 9 references are collected (Arai et al 2000, Hamada et al 1999, Kar 1969, Kobayashi 1992, Mikata et al 2001, Mikata 2002, PWRI 1995, Sato et al 1987, Tamura et al 2001). All specimens failed by the shear compression mode of failure. The data consist of the wide ranges of geometric properties, that is, the values of a/d vary in the range of 2.4 to 5.1 and the values of d change from 140 to 1000 mm. The prestressing force in terms lower fiber stress vary from 2.0 to 21.0 MPa including all 4 types of stress distribution. In case that the roller loading was applied, the value of width of the bearing plate is set to be 50 mm in calculation. In Table 1, the number of critical strut mentioned in Figure 10 is written for each case. It is evident that the calculated results yield the well-predicted results compared with the experimental results, in many conditions of concrete properties, geometric properties, level of

Table 1 Outline of experimental data and the comparison with the calculated results

Researcher	No. #	Specimen	a/d	d (mm)	f_c' (MPa)	r_t/r_s^* (mm)	σ_u (MPa)	σ_l (MPa)	m	m** (model)	$V_{exp.}$ (kN)	η	$V_{cal.}$ (kN)	$V_{exp.}/V_{cal.}$	Failed member
Arai	1	<i>NC-40</i>	3.0	167	36.4	50/50	-0.1	4.3	1.7	1.7	41	0.59	38	1.08	3
	2	<i>NC-80</i>	3.0	167	36.4	50/50	-0.2	8.3	1.2	1.2	46	0.59	42	1.10	2
	3	<i>LC-40</i>	3.0	167	36.5	50/50	-0.1	4.3	1.7	1.7	35	0.59	38	0.92	3
	4	<i>LC-80</i>	3.0	167	36.5	50/50	-0.2	8.3	1.2	1.2	36	0.59	42	0.86	2
	5	<i>SC-40</i>	3.0	167	37.4	50/50	-0.1	4.3	1.8	1.8	27	0.59	37	0.73	3
	6	<i>SC-80</i>	3.0	167	37.4	50/50	-0.2	8.3	1.2	1.2	33	0.59	43	0.77	2
Hamada	7	<i>45LC-0</i>	3.5	300	47.0	65/150	-1.2	3.4	2.9	2.9	135	0.56	123	1.10	4
Kar	8	A-1	5.1	175	35.9	100/100	-1.0	6.0	2.5	2.5	26	0.59	23.0	1.13	2
	9	A-2	5.1	175	34.8	100/100	0.0	5.0	2.6	2.6	24	0.60	23.0	1.04	2
Kobayashi	10	<i>L5</i>	2.4	167	38.0	R/R	0.0	3.9	1.5	1.5	63	0.59	58	1.09	3
Mikata	11	P-0-20	3.2	140	41.9	R/R	0.0	2.0	3.2	2.9	49	0.57	50	0.98	2
	12	P-0-30	3.2	140	43.0	R/R	0.0	3.0	2.6	2.6	53	0.57	47	1.13	2
	13	P-0-40	3.2	140	43.0	R/R	0.0	4.0	2.1	2.1	48	0.57	49	0.98	2
	14	P-20-40	3.2	140	43.0	R/R	2.0	4.0	2.1	2.1	52	0.57	49	1.06	2
	15	P-40-40	3.2	140	43.0	R/R	4.0	4.0	2.0	2.0	48	0.57	50	0.96	2
	16	HP-0-30	3.2	140	79.6	R/R	0.0	3.0	3.7	2.9	74	0.46	72	1.03	2
Mikata	17	<i>PRC-9</i>	2.6	152	60.0	R/R	-1.0	12.2	1.1	1.1	63	0.52	83	0.76	2
	18	<i>PRC-12</i>	2.6	152	72.1	R/R	-1.7	21.1	0.9	0.9	100	0.48	105	0.95	3
PWRI	19	H3-35-30	3.0	350	92.0	100/150	-1.0	3.0	4.0	2.7	245	0.42	251	0.98	4
	20	H3-35-60	3.0	350	86.3	100/150	-2.0	6.0	2.5	2.5	284	0.44	311	0.91	4
	21	H3-35-90	3.0	350	70.3	100/150	-3.0	9.0	1.8	1.8	295	0.49	257	1.15	3
	22	H3-55-30	3.0	550	84.0	100/150	-1.0	3.0	3.8	2.7	228	0.45	282	0.81	4
	23	H3-75-30	3.0	750	88.5	100/150	-1.0	3.0	3.9	2.7	345	0.43	316	1.09	4
	24	H3-95-60	3.0	950	71.4	100/150	-2.0	6.0	2.3	2.3	586	0.49	583	1.01	3
	25	<i>L3-35-60</i>	3.0	350	40.6	100/150	-2.0	6.0	1.6	1.6	202	0.58	190	1.06	3
Sato	26	<i>3-11</i>	2.5	403	41.8	R/150	-3.1	8.9	1.1	1.1	171	0.57	193	0.89	3
	27	<i>4-6</i>	3.2	337	40.1	50/50	-5.0	14.0	1.0	1.0	170	0.58	185	0.92	3
	28	<i>4-12</i>	3.1	353	39.7	50/50	-4.7	14.5	1.0	1.0	162	0.58	190	0.85	3
Tamura	29	<i>45LC-3</i>	3.8	1000	55.1	150/150	-1.1	2.6	4.1	3.4	505	0.53	406	1.24	3
	30	<i>45LC-5</i>	3.8	1000	53.3	150/150	-2.0	5.0	2.7	2.7	569	0.54	684	0.83	2
	31	<i>60LC-5</i>	3.8	1000	68.7	150/150	-2.4	5.8	2.9	2.9	600	0.49	734	0.82	2

: Model 2 is in bold.

* : Unit is MPa *Italic characters* : Prestressed reinforced concrete beams

** : Applied values of m in modeling : Lightweight concrete

AVE.	0.97
C.V.	0.13

prestressing force and the types of stress distribution. The comparisons between the crack patterns at the ultimate stage and the failed members of the predicted results are also carried out. As the examples shown in Figure 11, the good agreement between the critical strut and the crack patterns of specimens, which are predicted to fail by the members [2], [3] and [4], can be observed. The bold dashed line represents the critical strut in each specimen. From the satisfactory prediction in case of the specimen P-40-40 as shown in Figure 11(a), it implies that this proposed simplified truss model is applicable for predicting the crack pattern even in case where σ_u is under compression (rectangular stress distribution). From Figures 11(b) and (c), it is apparent that this proposed model can be utilized to predict the failure patterns of the normal (H3-35-30) and lightweight (L5) PC slender beams. Moreover, it can also be said that the crack pattern of prestressed reinforced concrete beam can satisfactorily be estimated as shown in case L5 (Figure 11(b)).

In order to confirm the high accuracy in prediction, the calculated results of the proposed simplified truss model (*Proposed*) are compared with the calculated results of M_{cr} method (M_{cr}) (Ito et al 1994). The comparison is expressed in Figure 12 with the variation of lower fiber stress. It is found that the proposed model provides calculated results with the average value (AVE.) of 0.97 and a coefficient of variation (C.V.) of 0.13, whereas M_{cr} method yields the calculated results which AVE. = 1.18 and C.V. = 0.22. Based on these results, it can be said that the proposed model yields the better accuracy in prediction of shear carrying capacity.

5. CONCLUSIONS

The simplified truss model has been proposed based on the clarification of failure mechanism in the parametric study using FEM. With the increase in value of σ_l , the inclination of critical stress flow becomes steeper. In case of considerably high value of σ_l , the concentrated stress flow turns into the stress flow curvedly transferring to the support. It can be said that the influence on the shear failure mechanism due to σ_u

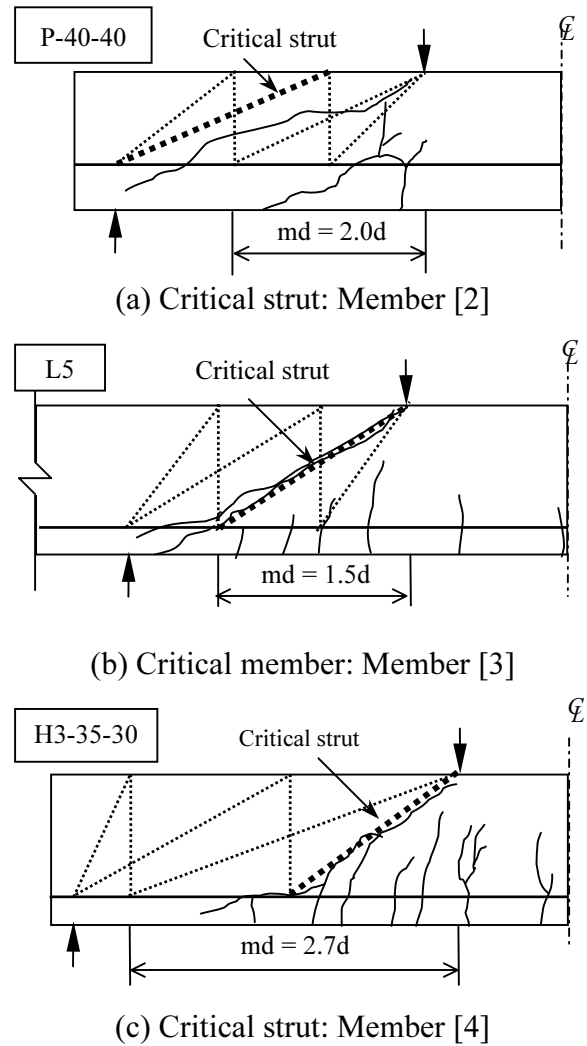


Figure 11 Examples of the critical members and actual crack patterns at the ultimate stage

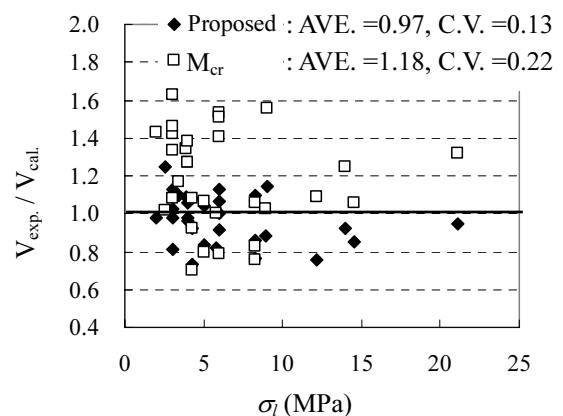


Figure 12 Comparison in shear carrying capacity between the proposed model and M_{cr} method

(types of stress distribution) cannot also be neglected. For calculating the shear carrying capacity of PC slender beams, the equivalent elastic analysis of the simplified truss model with a small degree of freedom has been performed. The thickness of the considered struts assessing from FEM results is simply estimated in terms of the width of bearing plates and the effective depth. By adopting the evaluated thickness of struts and the value of m , the excellent correlation with the experimental data can be achieved. It is apparent that the simplified truss model is applicable to evaluate the shear carrying capacity and the failure patterns of PC slender beams without transverse reinforcement.

References:

- Japan Society of Civil Engineers (JSCE) (2002), "Standard Specification for Concrete Structures," *Structural Performance Verification*.
- Ito, T., Yamaguchi, T. and Ikeda, S. (1994), "Flexural Shear Behavior of Precast Segmental PC Beam," *Proceedings of the JCI*, **16**(2), 967-972.
- Niwa, J. (1984), "Equation for Shear Strength of Reinforced Concrete Deep Beams Based on FEM Analysis," *Concrete Library of JSCE*, **4**, 283-295.
- Tamura, S., Hamada, Y., Lertsamattiyakul, M. and Niwa, J. (2003), "A Study on Shear Carrying Capacity of Evaluation Methods of Prestressed Concrete Beams with Rectangular Cross Section," *Journal of Prestressed Concrete*, **45**(6), 101-110.
- Arai, Y. and Yaginuma, Y. (2000), "Shear Behavior of PC Beams Using Light-weight Concrete," *Proceedings of The 10th Symposium on Developments in Prestressed Concrete*, 545-550.
- Hamada, Y., Tamura, S., Maehori, S. and Niwa, J. (1999), "Ultimate Shear Capacity of Prestressed Concrete Beams Using High Performance Lightweight Aggregates," *Proceedings of The 9th Symposium on Developments in Prestressed Concrete*, 739-744.
- Kar, J. N. (1969), "Shear Strength of Prestressed Concrete Beams Without Web Reinforcement," *Magazine of Concrete Research*, **21**(68), 159-170.
- Kobayashi, K. (1992), "Effects of Introducing Prestress on Shear Resistance of Concrete Beams," *Proceedings of Cement and Concrete, Japan Cement Association*, **46**, 750-755.
- Mikata, Y., Inoue, S., Kobayashi, K. and Nieda, T. (2001), "Effect of Prestress on Shear Capacity of Prestressed Concrete Beams," *Journal of Materials, Concrete Structures and Pavements, JSCE*, **669**(50), 149-159.
- Mikata, Y. (2002), "The Study on Shear Strength Characteristics of Concrete Structural Members," *Doctoral Thesis*, Dept. of Civil Eng., Osaka Institute of Technology.
- Public Works Research Institute (1995), "Study on Shear Strength of PC Beams with High Strength Concrete," *Joint Research on Design Method of High Strength Concrete Structures*, **122**.
- Sato, T., Ishibashi, T., Yamashita, H. and Takada, S. (1987), "Shear Strength and Modes of Failure of Prestressed Concrete Beams," *Proceedings of the JCI*, **9**(2), 323-328.
- Tamura, S., Hamada, Y., Maehori, S. and Niwa, J. (2001), "Shear Strength Characteristics of Large Scale PC Beams Using Super Lightweight Concrete," *Proceedings of the JCI*, **23**(3), 709-714.

NONLINEAR ANALYSIS OF REINFORCED CONCRETE VIADUCTS SUBJECTED TO SEISMIC LOADS USING 3D LATTICE MODEL

T. Miki¹⁾ and J. Niwa²⁾

1) *Doctoral Student, Department of Civil Engineering, Tokyo Institute of Technology, Japan*

2) *Professor, Department of Civil Engineering, Tokyo Institute of Technology, Japan*

mikitomo@cv.titech.ac.jp, jniwa@cv.titech.ac.jp

Abstract: Analytical study for the seismic response of RC structures subjected to earthquake motion is presented. Dynamic analysis using the 3D lattice model is performed on the actual RC structures. The 3D lattice model can offer the reasonable prediction of the shear-carrying capacity of RC columns and beams. Analytical targets are two RC rigid-frame viaducts damaged at the 1995 Hyogo-ken Nanbu Earthquake. The results of dynamic lattice model analysis are compared with the actual damages of RC viaducts. The comparison reveals the reliability of the 3D lattice model at the structural system level. It is also found that the analysis can predict the damages including both the shear failure in the columns and the buckling of reinforcement in RC columns. In addition, the influence of the vertical motions on the maximum displacement and the instable behavior due to large vertical load is clarified.

1. INTRODUCTION

Hyogo-ken Nanbu Earthquake, which occurred at January 1995 in Japan, caused the destructive collapse to various structures, including reinforced concrete (RC) structures. The observations following this earthquake show that the main causes of severe damage were due to the overestimation of both shear carrying capacity and ductility of structures. It is also found that the structures had insufficient amount of transverse reinforcement. On the other hand, it is noticed that there were many RC structures without almost any damages. The difference of the degree of damage is influenced by several factors even if the dimensions of structures and the arrangements of reinforcement are almost identical.

Many investigations for the damage of structures and the damage analyses have been carried out (Ishibashi and Okamura 1998, Committee 311 2000). The seismic performance evaluation was also performed by the frame analysis based on the moment-curvature restoring characteristics or the analysis using the fiber technique (Tsuchiya et al. 1999, 2000). The shortcoming of these models is the difficulty in predicting the behavior in the post-peak region, especially, when RC members fail in shear. In these models, moreover, the shear deformation and torsional behavior cannot be directly predicted because the in-plane deformation is not taken into account.

In this study, the 3D lattice model is used. The 3D lattice model is the objective and simple procedure, which can explain the shear resisting mechanism for RC members appropriately. The seismic response of RC rigid-frame viaducts is evaluated using the 3D nonlinear dynamic lattice model analysis. Here, the RC rigid-frames in railroad viaducts are selected as the analytical targets. The input ground motions determined by FDEL (Sugito et al. 1994) are used. The analytical results are compared with actual damages of viaducts. The interaction between the soil and the structures is not considered in the analysis.

2. ANALYTICAL MODEL

2.1 Outlines of 2D Lattice Model

The 3D lattice model is developed based on the concept of the 2D lattice model. The 2D lattice model consists of members of concrete and reinforcement, as shown in **Figure 1**. The column subjected to load from left hand side is shown. With the RC column, the concrete is modeled into flexural compression members, flexural tension members, diagonal compression members, diagonal tension members, horizontal members and two arch members. The longitudinal and the transverse reinforcements are modeled into vertical and horizontal members, respectively. The characteristic of 2D lattice model is to incorporate the diagonal tension members and the arch members of concrete into the modeling. This point is different from the conventional modified truss model. The diagonal members are regularly located with the inclined angles of 45 and 135 degrees to the longitudinal axis of the column, respectively. The arch members connecting the nodes at the opposite diagonal corners between the loading point and the bottom of the column are arranged according to the direction of internal compressive stress flows.

Figure 2 shows a schematic diagram of cross section of RC column. The concrete is divided into the truss part and the arch part. When the value of t is defined as a ratio of the width of arch part to the width of cross section, b , the widths of the arch part and the truss part are given by $b \times t$ and $b \times (1 - t)$, respectively, in which $0 < t < 1$. The value of t is determined based on the theorem of the minimization of the total potential energy for the 2D lattice model with the initial elastic stiffness. The total potential energy is obtained from the difference between the summation of the strain energy in each element and the external work. The pre-analysis using the 2D lattice model is carried out for the small provided displacement at the loading point, where the value of t has changed from 0.05 to 0.95 with an interval of 0.05. The strain energy of the 2D lattice model is accumulated one of each lattice component.

2.2 Configuration of 3D Lattice Model

In the 3D lattice model, it is assumed that the shear resisting mechanism is divided into arch action and truss action. With the 2D lattice model, the 3D RC member is modeled into 2D based on the assumption of plane stress. As illustrated in **Figure 3**, in the 3D lattice model of an RC column, four arch members are arranged connecting between the top and the end of the column at the opposite corners. The resisting mechanism of RC column subjected to one certain load

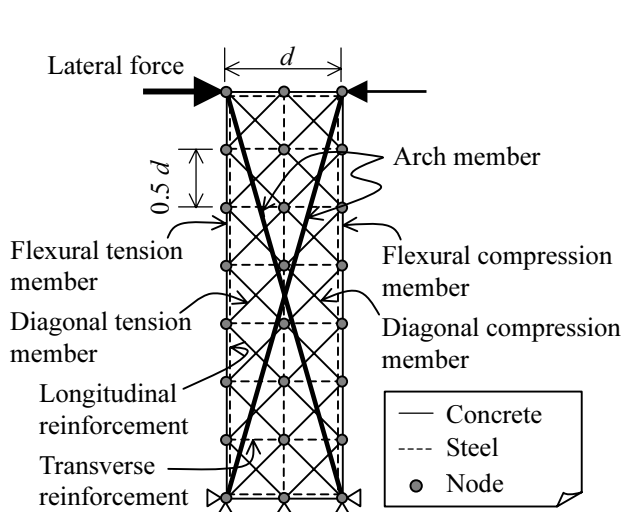


Figure 1 Outlines of 2D lattice model

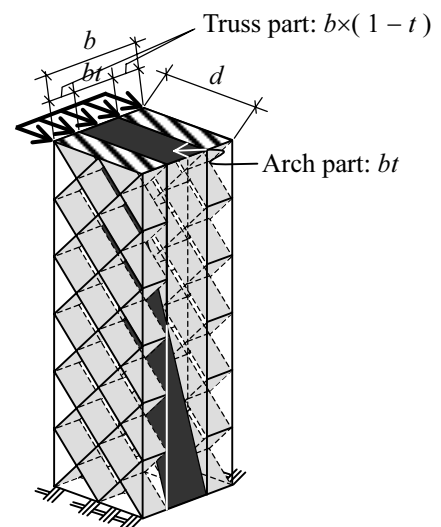


Figure 2 Cross section of RC column modeled by 2D lattice model

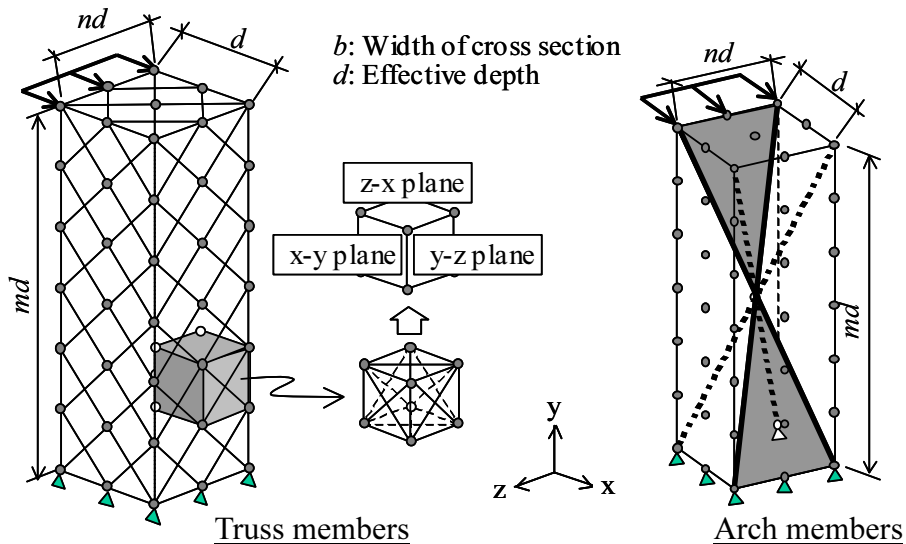


Figure 3 Discretization for 3D lattice model

consists of two arch members crossing each other. The stiffness of these arch members is assumed to be equivalent to that of two arch members in 2D lattice model. With the RC column subjected to load from the diagonal direction, it is assumed that the corner-to-corner arch action inside the RC column is idealized as a compressive strut that is represented by these arch members in the 3D lattice model.

To represent the truss action, it is assumed that 3D space is comprised of an orthogonal coordinate system that is defined by three planes, x-y plane, y-z plane, and z-x plane. Two crossed truss members are located on each truss plane so that unit element consists of 12 truss members in six truss planes as shown in **Figure 3**. In each truss plane, the in-plane 2D constitutive law of concrete, considering the softening of the compressive strength for diagonally cracked concrete depending on the transverse tensile strain, can be used.

In 2D lattice model, the value of t is defined by a ratio of the arch part width to the cross-section width of RC member as mentioned previously. Based on the assumption that the global stiffness of 3D lattice model is equivalent to one of 2D lattice model, the cross-sectional area of the arch member can be calculated. Here, the ratios of the arch part width to the width and the depth in the cross section of the column are defined as t_b and t_d , respectively. With the determination of values of t in 3D lattice model, not only the width of cross-section of the column but also the depth of cross-section of the column is varied in the pre-analysis. According to the 2D lattice model, in the 3D lattice mode the values of t_b and t_d are determined based on the theorem of minimization of the total potential energy.

2.3 Material Constitutive Models

In order to consider the effect of lateral confinement of concrete due to suitable arrangements of transverse reinforcement, the stress-strain relationship of confined concrete proposed by Mander et al. (1988) is applied to the diagonal compression members and the arch members. For cracked concrete, the compressive softening behavior of concrete proposed by Vecchio and Collins (1986) is considered. The ability of cracked concrete to resist compressive stress decreases as the transverse tensile strain increases.

With the flexural compression member, which is assumed to represent the cover concrete, the stress-strain relationship represented by the quadratic curve (Vecchio and Collins 1986) is used. With the concrete model under cyclic loading, the stress is assumed to decrease with the initial stiffness in the unloading path. In the reloading path, the stress is assumed to proceed to the

previous maximum state along with same path as unloading.

For the flexural tension members of concrete, which are located near reinforcing bar, the concrete continues to contribute the tension force even after cracking due to the bond effect between the concrete and reinforcing bars. Therefore, the tension-stiffening model (Okamura and Maekawa 1991) is applied. On the other hand, for the diagonal tension members that consist of concrete far from reinforcing bar, after the crack occurs, the concrete can be assumed to show a tension strain-softening behavior. Hence, the tension softening curve, so-called 1/4 model (Rokugo 1989), is applied. The fracture energy of concrete G_F , which is the area under the tension softening curve, is assumed to be 0.1 N/mm as a standard value of normal concrete. In both tensile models of concrete, the unloading path is assumed to decrease directly to the origin and the reloading path is assumed to behave following to the unloading path.

The envelope stress-strain curve of reinforcing bar is modeled as bi-linear in which the tangential stiffness after yielding is $0.01E_s$, where E_s denotes Young's modulus. After yielding, the stiffness of the reinforcing bar decreases when the stress stage changes from tension to compression, while the similar behavior is observed when the stress stage changes from compression to tension. In the analysis, this phenomenon, so-called Bauschinger effect, is considered by the numerically improved model of reinforcing bars (Fukuura 1997). In addition, in order to evaluate the buckling behavior of longitudinal reinforcing bars, the buckling model proposed by Dhakal (2000) is used. This model is characterized as the spatially averaged material model that accurately takes into account the inelastic behavior of buckling.

3. TARGET STRUCTURES AND LATTICE MODEL

3.1 RC Viaducts

The seismic performance evaluation is performed for two RC rigid-frame viaducts. **Figure 4** shows the dimensions and arrangements in Shimokema R5 Viaduct. Hansui R5 Viaduct has similar dimensions and arrangements as Shimokema R5 Viaduct. They are beam-slab type rigid-frame with three-span. Actual damage conditions of two viaducts after the earthquake are shown in **Figure 5** (Committee 311 2000). It was observed that there was the slight damage with crossed diagonal cracks at the upper column in Shimokema R5 Viaduct. On the other hand, in Hansui R5 Viaduct, the severe shear failure with the collapse of columns and the drops of beams and slabs were observed. The compressive strength of concrete of Shimokema R5 Viaduct was slightly stronger than that of Hansui R5 Viaduct. The material properties used in these two viaducts are summarized in **Table 1**.

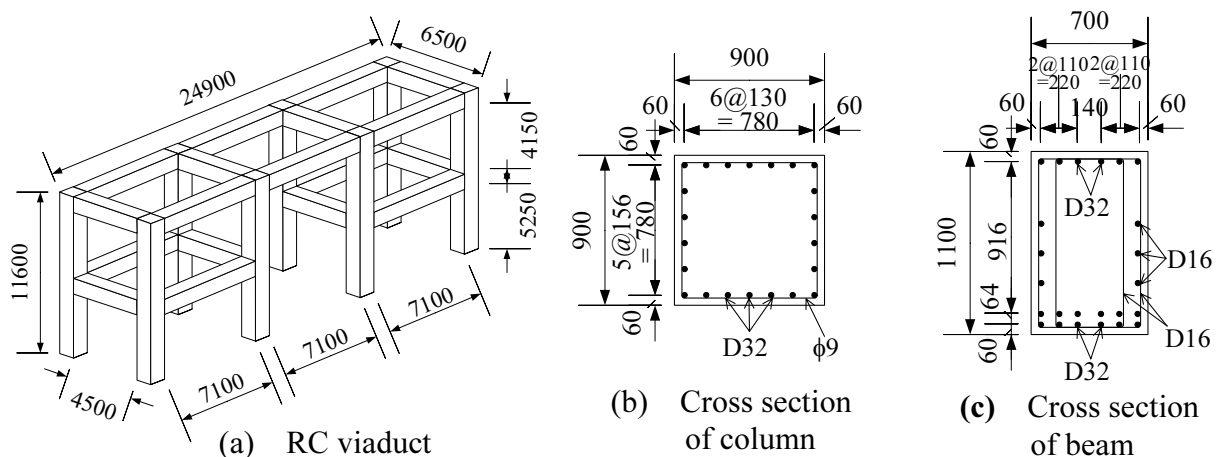
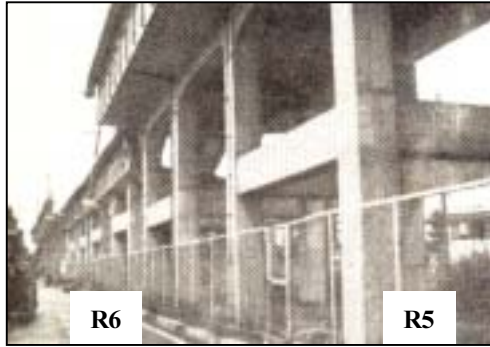


Figure 4 Dimensions and arrangements in Shimokema R5 Viaduct



(a) Shimokema R5 Viaduct



(b) Hansui R5 Viaduct

Figure 5 Damage conditions in Shimokema R5 Viaduct and Hansui R5 Viaduct

Table 1 Material properties of concrete and reinforcement

Name of RC viaducts	Concrete			Longitudinal reinforcement			Transverse reinforcement		
	f_c' (MPa)	f_t (MPa)	E_c (GPa)	f_y (MPa)	f_u (MPa)	E_s (GPa)	f_y (MPa)	f_u (MPa)	E_s (GPa)
Shimokema R5	31.7	2.43	16.8	349	533	197	296	436	204
Hansui R5	29.1	1.27	18.4	322	521	203	263	380	183

The input ground motions determined by Frequency-Dependent Equi-Linearized technique, FDEL (Sugito et al. 1994) are used. The weight of a superstructure including the slab is assumed to be 7200 kN. The self-weight of viaduct is calculated by multiplying the volume of columns and beams by the specific gravities of concrete and reinforcement.

3.2 Analytical Procedure

The three-span viaduct is treated as a unit of the analytical model. The model consists of columns and beams, while the slab is not included. In the analysis, it is assumed that the masses corresponding to the self-weight of viaducts are uniformly distributed over all nodal points, using the lumped-mass idealization. It is also assumed that there is a concentrated mass, which is equal to the weight of the superstructure and the slab, acting on the top nodes of columns and beams.

In the dynamic analysis, Newmark's method is used as a time integration scheme. For the damping, the numerical damping of Newmark's method ($\beta = 0.36$, $\gamma = 0.70$) is used. The Newton-Raphson iteration method is adopted to iterate the calculation until an adequately converged solution is obtained. With the termination of calculation, the out-of-balance force and the energy increment are compared with initial values during iteration. Here, the convergence tolerances for the out-of-balance force and energy are set to be 0.001 and 0.01, respectively.

4. DAMAGE ANALYSIS OF ACTUAL RC VIADUCTS

4.1 Seismic Response of RC Viaducts

Figure 6 shows the analytical results by the dynamic 3D lattice model for Shimokema R5 Viaduct and Hansui R5 Viaduct. The analytical results of displacement time histories and particle traces of displacement at the mid-span of an upper beam in the transverse direction are illustrated in the figure. With Shimokema R5 Viaduct, it can be observed that the stable response during 10 seconds is predicted. In the analysis, the buckling of reinforcement takes place at the bottom of the lower column. It can be also observed that the buckling of reinforcement does not occur at the top of the column and the each end of the beam. The cracks occur in the diaconal members of

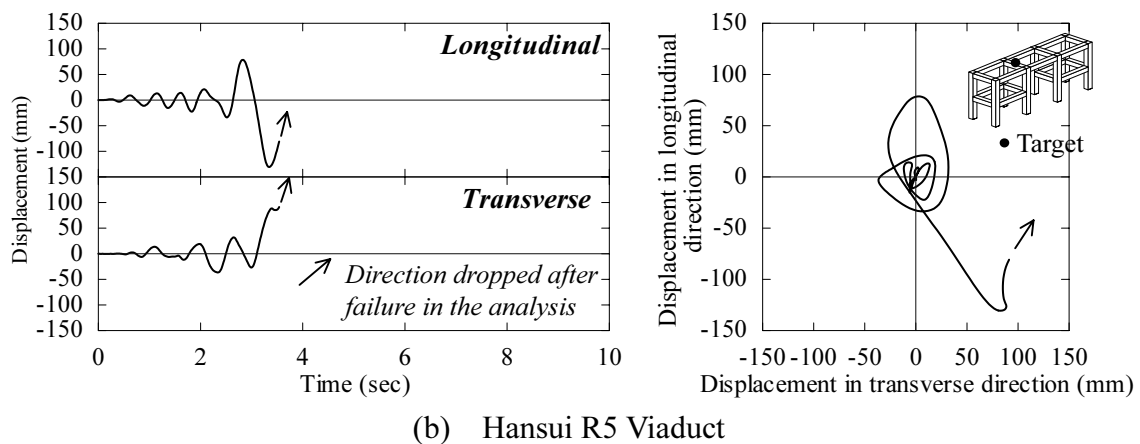
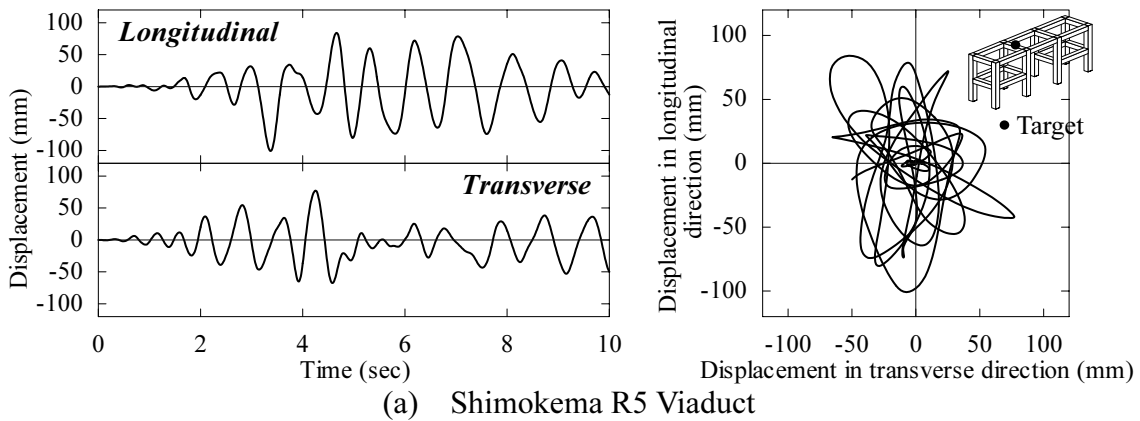


Figure 6 Analytical responses at an upper beam by the dynamic 3D lattice model

concrete at the upper and lower columns. The behavior corresponds to the actual observation after the earthquake as shown in **Figure 5** (Committee 311 2000). On the other hand, the calculation is terminated due to the divergence in the case of Hansui R5 Viaduct as shown in **Figure 6(b)**. This is caused by the compressive softening of concrete in the diagonal and flexural members at the lower column. Actually, it was observed in Hansui R5 Viaduct that the severe shear failure at the lower columns took place that induced the drops of beams and slabs. It is also found that the direction, in which the beams and slabs dropped down after the lower column fails in shear, can be clearly estimated by the particle traces of displacement in **Figure 6(b)**. As can be judged from the analytical results, Hansui R5 Viaduct fails toward transverse direction during the displacement in longitudinal direction decreases. The information about the state of deformation after the structure fails in shear is beneficial in terms of the restoration after the earthquake.

4.2 Analytical Simulation of Shear Failure of RC Viaducts

To verify the response of Hansui R5 Viaduct where the calculation in the dynamic analysis is terminated by the divergence, the detailed analytical investigation is performed. With Hansui R5 Viaduct, the elements of the lower column in the 3D lattice model are focused on. **Figure 7** shows the stress-strain relationships of concrete flexural members and the strain time histories of concrete diagonal members. In the figure, the deformed shape of 3D lattice model for Hansui R5 Viaduct is also illustrated.

It can be observed that the analysis can predict the compressive softening behavior in diagonal and flexural members of concrete. The compressive softening behavior is observed in the elements D and E in the 3D lattice model, while the tensile strain of concrete increases in the element F. This is because that the externally applied energy by the earthquake is locally

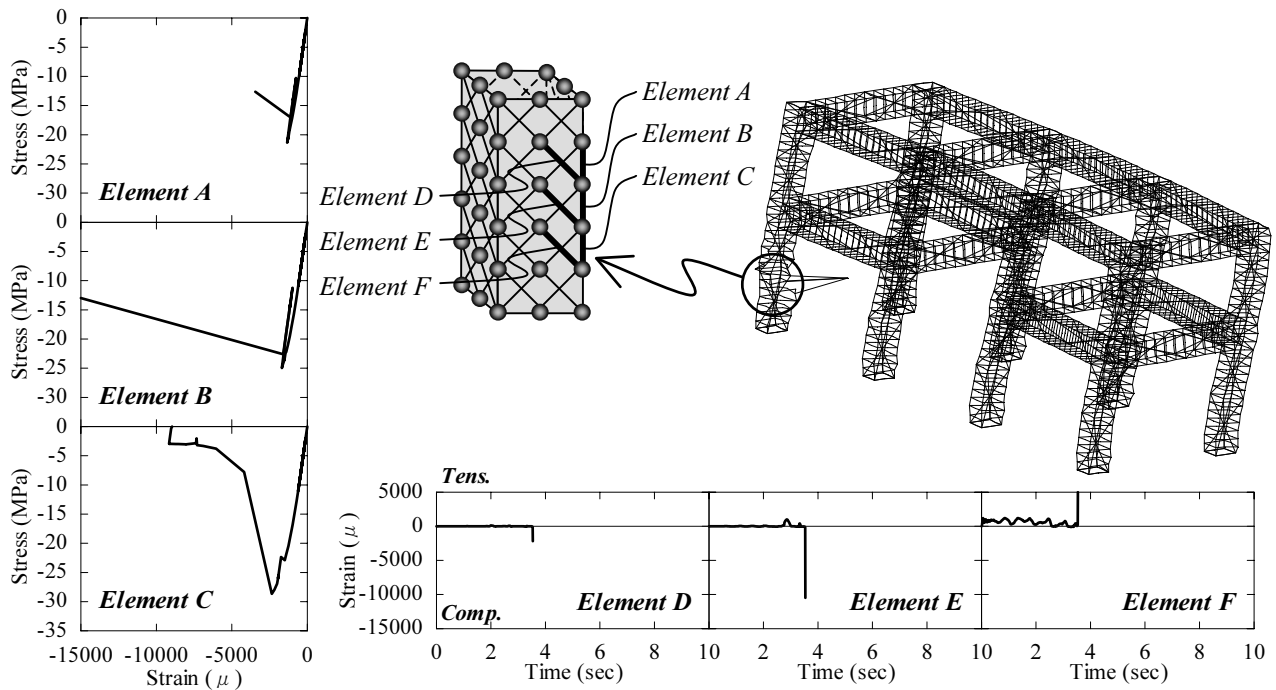


Figure 7 Elemental responses of concrete in 3D dynamic lattice model for Hansui R5 Viaduct

consumed by the elements D and E and the element F in the surrounding portion releases the stored energy into localizing elements. It is assumed that in the analysis the shear failure takes place at the column when the compression softening behavior of concrete in arch and diagonal members has been predicted. The shear failure is predicted in spite of the decrease in shear stresses transferred across diagonal cracks by the aggregate interlock. In addition, arch or diagonal members are assumed to include the severe diagonal cracks that have widely opened. Because of widely opened diagonal crack, the compressive strength of concrete shows the softening as the tensile strain perpendicular to the compressive direction increases. It is also found that the analytical response in the post-peak is milder than that in the actual brittle behavior.

4.3 Influence of Vertical Loads on Seismic Response of RC Viaducts

In order to investigate the influence of the self-weight of structure on the analytical response, two analyses are carried out. **Figure 8** shows the displacement time histories obtained by the dynamic 3D lattice model with and without vertical loads corresponding to the self-weight. It is

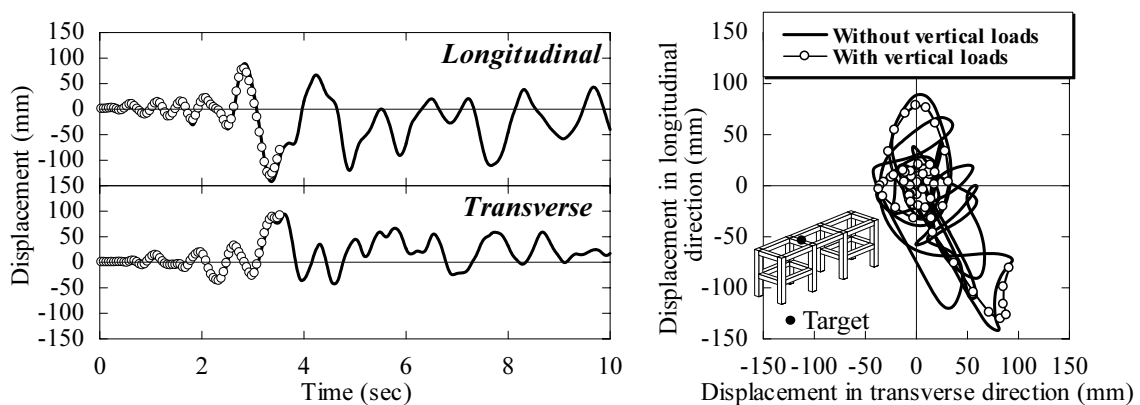


Figure 8 Analytical response of Hansui R5 Viaduct (Influence of vertical loads)

found that when the vertical loads are neglected, the analytical results of RC viaducts show the stable response during 10 seconds. The stable behavior can be observed even if the analysis considering the vertical loads predicts the shear failure. This is caused by the additional moment of $P-\Delta$ effect with the increase in the lateral displacement. It is found that the collapse mechanism takes place due to the geometrical nonlinearity, which is associated with large vertical loads. The analysis of RC viaducts shows that the flexural instability occurs with the vertical loads corresponding to the self-weight and the weight of the superstructure. Therefore, it is recommended that the geometrical nonlinearity due to the material nonlinearity at the large deformation range should be considered in predicting the allowable ductility of RC columns with heavier weight of a superstructure.

5. CONCLUSIONS

3D nonlinear analysis of actual RC rigid-frame viaducts is performed using the dynamic 3D lattice model. The comparisons between the results of dynamic analysis and the actual damages of RC viaducts prove the reliability of the 3D lattice model. It is also found that the analysis can predict damage conditions including both the buckling of longitudinal reinforcement in RC columns and their shear failure. In addition, the dynamic analysis is carried out on the verification with respect to the vertical loading, which represents the self-weight and the weight of a superstructure. The results of the analysis reveal the influence of the vertical loads on the maximum displacement. From the analysis, it is found that when the columns in RC viaducts are subjected to large deformation, the collapse takes place due to the geometrical nonlinearity. The analysis also shows that this instable behavior caused by a large vertical load appears when the lateral displacement significantly increases.

References:

- Dhakal, R.P. (2000), "Enhanced Fiber Model in Highly Inelastic Range and Seismic Performance Assessment of Reinforced Concrete." Thesis (PhD), The University of Tokyo.
- Fukuura, N. and Maekawa, K. (1997), "Computational Model of Reinforcing Bar under Reversed Cyclic Loading for RC Nonlinear Analysis." *Journal of Materials, Concrete Structures and Pavements*, JSCE, **564**(35), 291-295. (in Japanese)
- Ishibashi, T. and Okamura, H. (1998), "Study on the Design Earthquake Resistance and Degree of Earthquake Damage of Reinforced Concrete Viaducts," *Cement and Concrete Composites*, Elsevier, **19**(3), 193-201.
- Mander, J.B., Priestley, M.J.N., and Park, R. (1988), "Theoretical Stress-strain Model for Confined Concrete," *Journal of Structural Engineering*, ASCE, **114**(8), 1804-1826.
- Miki, T., Niwa, J., and Lertsamattiyakul, M. (2003), "Numerical Evaluation of Seismic Performance of Reinforced Concrete Bridge Piers Using Dynamic Lattice Model," *Concrete Library of JSCE*, **41**, 49-64.
- Niwa, J., Choi, I. C. and Tanabe, T. (1995), "Analytical Study for Shear Resisting Mechanism Using Lattice Model," *Concrete Library of JSCE*, **26**, 95-109.
- Okamura, H. and Maekawa, K. (1991), "Nonlinear Analysis and Constitutive Models of Reinforced Concrete," Gihodo-Shuppan.
- Rokugo, K., Iwasa, M., Suzuki, T., and Koyanagi, W. (1989), "Testing Method to Determine Tensile Strain Softening Curve and Fracture Energy of Concrete," *Fracture Toughness and Fracture Energy*, Balkema, 153-163.
- Subcommittee for Damage Analysis of Concrete Structures Caused by Hanshin-Awaji Great Earthquake. (Committee 311) (2000), "Verification of Procedures of Seismic Performance Evaluation based on Damage Analysis for Hanshin-Awaji Earthquake," *Concrete Engineering Series*, **36**. (in Japanese)
- Sugito, M., Goda, H., and Masuda, T. (1994), "Frequency Dependent Equi-linearized Technique for Seismic Response Analysis of Multi-layered Ground," *Journal of Geotechnical Engineering*, JSCE, **493**(27), 49-58. (in Japanese)
- Tsuchiya, S., Furuya, Y., Kim, I.H., and Okamura, H. (2001), "Seismic Performance Evaluation of RC Frames in Railroad Viaducts Using Three-dimensional Nonlinear Dynamic Analysis," *Concrete Library of JSCE*, **38**, 105-120.
- Vecchio, F.J. and Collins, M.P., (1986), "The Modified Compression Field Theory for Reinforced Concrete Elements Subjected to Shear," *ACI Journal*, **83**(2), 219-231.

Research on Weight Reduction of PC Composite Members Using Ultra High Strength Fiber Reinforced Cementitious Composites (UFC)

H. Murata¹⁾, J. Niwa²⁾, and C. Sivaleepunth³⁾

1) Master course 2nd year student, Department of Civil Engineering, Tokyo Institute of Technology, Japan

2) Professor, Department of Civil Engineering, Tokyo Institute of Technology, Japan

3) Master course 1st year student, Department of Civil Engineering, Tokyo Institute of Technology, Japan
hmurata@cv.titech.ac.jp, jniwa@cv.titech.ac.jp, chunyakom@cv.titech.ac.jp

Abstract: In the improvement of seismic performance of a bridge structure, the weight reduction of a girder is one of the significant factors. Recently, prestressed concrete (PC) composite bridge girders, which web member is made by various materials, have been developed. In this study, new PC composite structural members using Ultra High Strength Fiber Reinforced Cementitious Composites (UFC) in a web truss member are examined. UFC has high compressive strength around 200MPa, high ductility, and high durability. Due to its predominant mechanical properties, UFC is applied to the web member of PC composite bridge girders and the self-weight of girders can be significantly reduced. The aim of this research is to investigate the mechanical properties of PC composite members using UFC truss and evaluate the effect of weight reduction. Then, PC composite beams are designed and experiments and analyses are carried out. In addition, the level of weight reduction of a web member is examined.

1 Introduction

As for the improvement of seismic performance of bridge structures, the weight reduction of girders is one of the promising factors. A PC composite girder, of which web member is made of different material from a flange member, has been developed. Because of high strength of a web member, the cross sectional area of a web member can be reduced. As a result of volume reduction, the total weight of a bridge is also reduced.

Ultra High Strength Fiber Reinforced Cementitious Composites (UFC) (Sagawa et al. 2001) has been developed since 1994. This material provides high compressive strength around 200MPa with high ductility because of the existence of steel fiber reinforcement and high durability.

In this study, a PC composite girder utilizing UFC truss as web members is focused as shown in Figure 1. In case that UFC is used as a precast truss, the complexity in the construction can be solved and the total cost of construction can be reduced. Then, in order to clarify mechanical properties of this PC composite structural member, PC composite beams utilizing UFC precast truss as web members were constructed, and the loading test was carried out. Parameters to be considered in this study were the joint method and the variation of cross sectional area of UFC truss.

In addition, in order to clarify mechanical properties by analytical approach, nonlinear finite element method (FEM) analysis was performed and obtained analytical results were compared with experimental results.

Finally, the PC composite beams were compared with RC beams, which provide the same load carrying capacity, in order to discuss the reduction in weight.

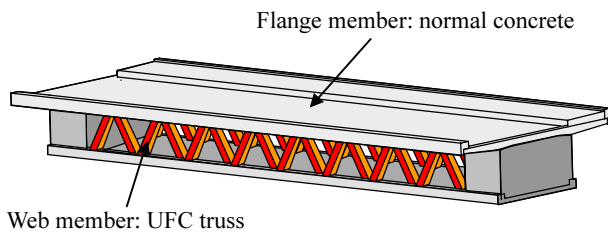
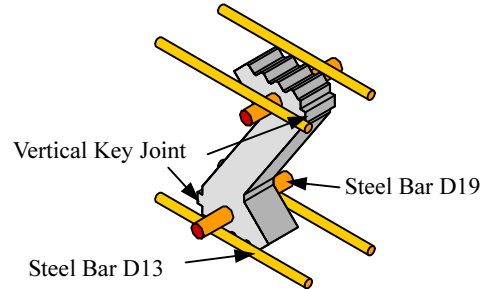
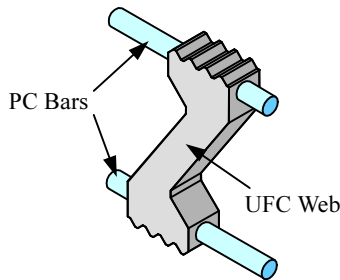


Figure 1 PC composite bridge using UFC

Table 1 Test parameters

Specimen name	Joint method (See Figure 2)		Thickness of truss b_w [mm]	
	A	B	40	60
60A	○	-	-	○
60B	-	○	-	○
40B	-	○	○	-



(a) Joint A: Penetration of PC bar with key joint (b) Joint B: Reinforcing bar with vertical key joint
Figure 2 Joint methods

2 Experiments

2.1 Experimental procedures

In this study, there were 3 specimens of PC composite beams using UFC truss as a web member: named as 60A, 60B and 40B as listed in Table 1. There were 2 parameters, which were considered in this study: joint methods between flange and web and the thickness of UFC in web. The number in the specimen name stands for the thickness of truss in mm and the alphabet A or B represents the joint method. Figure 2 illustrates two types of joint method, which are the penetration of PC bar with key joint (Joint A) and the reinforcing bar with vertical key joint (Joint B) as shown in the work by Kawaguchi et al. (2003).

The test of simply supported PC composite beams under two points load was performed to compare the applicability of the joint A (specimen 60A) and the joint B (specimen 60B). The vertical force, P , was applied monotonically to the specimen with two loading points as shown in Figure 3. In order to reduce the friction at the supports, friction-reducing pads, i.e., two Teflon sheets sandwiching the grease, were inserted between the specimen and the support plates. After determined the suitable joint method, the cross sectional area of UFC truss as a web member was discussed.

In the web of PC composite beams, UFC was introduced because of its superior strength (compressive strength = 200MPa). It results in significant weight reduction and provides nearly limitless structural member shape. The mix proportion of UFC truss member is shown in Table 2. The mixing time of UFC is about 12-14 minutes. There was no segregation and sinking of steel fiber from the matrix due to its high viscosity. After casting, the formwork was covered by plastic sheet and put into the chamber, in which the temperature was controlled at 20°C for 48 hours. After the formwork was removed, the specimens were cured again in air with 100% humidity at 90°C for 48 hours.

The outlines of experiments and properties of specimens were summarized in Figure 4 and Table 3, respectively. The shear span for all specimens was set to be 1500mm. In specimen 60A (Joint A), two $\phi 17$ PC bars (SBPR1080/1230; yield strength, $f_y = 1229$ MPa, Young's modulus, $E_s = 200$ GPa) were applied to both top and bottom flanges (one bar per each flange). The longitudinal reinforcement ratio was set to be 1.89%. In specimens 60B and 40B (Joint B), four $\phi 13$ PC bars

Table 2 Mix proportion of UFC [kg/m³]

Water	Premix	Steel fiber	Superplasticizer
180	2254	157	26

Table 3 Properties of specimens

Specimen name	60A	60B	40B
Joint method	A	B	B
Thickness of truss (b_w) [mm]	60	60	40
Effective depth [mm]	340	350	350
Shear span to effective depth ratio	4.41	4.29	4.29
Longitudinal reinforcement ratio[%]	1.89	1.86	1.86

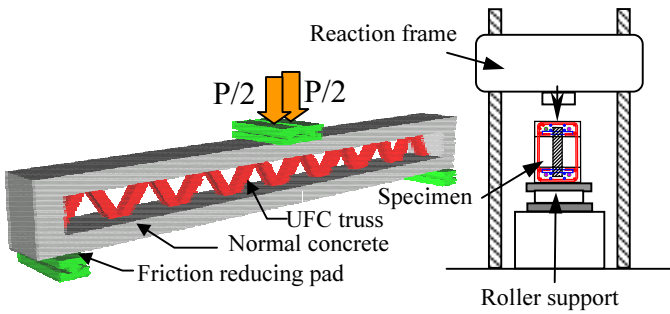


Figure 3 Flexure-shear test of PC composite beams

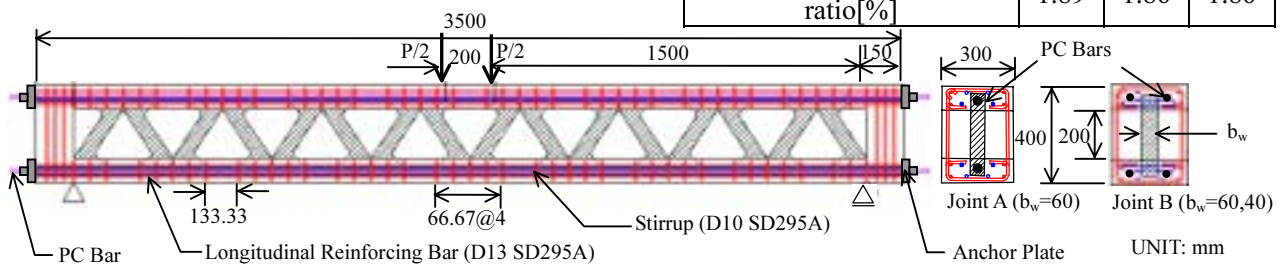


Figure 4 Outlines of experiments

Table 4 Mix proportion of concrete

Maximum size of coarse aggregate [mm]	Water-cement ratio [%]	Sand aggregate ratio [%]	Unit weight [kg/m ³]				
			Water	Cement	Fine aggregate	Coarse aggregate	Superplasticizer
15	30.0	53.3	170	567	871	765	9.1

(SBPR1080/1230; $f_y = 1243\text{MPa}$, $E_s = 201\text{GPa}$) were applied to both upper and lower flanges (two bars per each flange). The longitudinal reinforcement ratio was set to be 1.86%. For all the specimens, the stirrup (D10 SD295A, $f_y = 349\text{MPa}$, $E_s = 206\text{GPa}$) was used as the shear reinforcement in both upper and lower flanges. The shear reinforcement ratio was 0.59%.

Table 4 tabulates the mix proportion of concrete used in the flange. Before casting of concrete into the flange, the precast UFC truss web members were arranged and connected with each other by using epoxy glue. After casting the flange part, the specimens were cured for 7 days. Then, the prestressing force was applied to both upper and lower flanges in order to generate 3MPa and 5MPa in compression as the upper and lower fiber stresses, respectively. For all the specimens, grouting of cement paste was performed. After that, specimens were cured for another 7 days, thus curing period of concrete in the flange was totally 14 days before loading.

2.2 Comparison of joint methods

As the first step, the comparison of joints A and B was made. Table 5 shows the results of experiments. From the experimental results of 60A and 60B, the first peak loads, P_m (not the maximum loading capacities), were 92.5kN and 115kN, respectively. Figure 5 illustrates the load-deflection curve of beams with joint A and joint B. According to Figure 5(a), from the beginning, the curves rise up to the first peak load, P_m . It should be noted that the values of P_m of the two beams show the different results. After that the loads dropped until it reached the stable condition, and then gradually increased again. After the deflections of beams reached 13mm, the behavior of 60A and 60B was the same.

Figure 6 shows the crack patterns of specimens. First cracking loads of 60A and 60B were 69kN and 78kN, respectively. However, crack patterns of each specimen were similar (Figures 6(a) and (b)). In both cases, crack propagated in tension members of UFC truss on the left side and the failure was asymmetric. After that, cracks occurred in compression members because of the bending as a result of sliding of upper and lower flanges as shown in Figure 7.

Because the specimen 60B showed the higher loading capacity, this joint method is suitable to pursue in the study of the influence of UFC truss thickness for 40B.

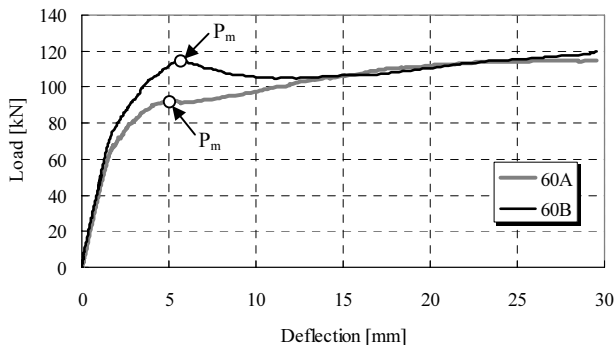
2.3 Influence of thickness of UFC truss

By comparing the thickness of UFC truss, when the cross sectional area of UFC truss used in 60B was decreased one-third of its cross sectional area, the first peak load, P_m of PC composite beam (specimen 40B) decreased about one-third of its P_m as shown in Figure 5(b). This implies that the first peak load depends on the thickness of truss.

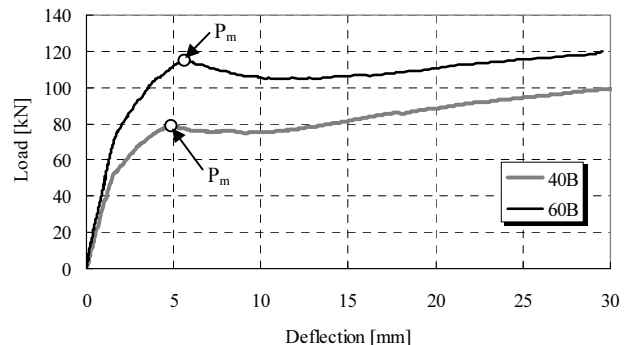
From Figure 6(b) and (c), there was not much difference on crack patterns between specimens 40B and 60B. The influence of thickness of UFC truss cannot be observed. It was also noticed that the failure was asymmetric.

Table 5 Loading capacity of PC composite beams and material strength

Specimen	First peak load P_m [kN]	Concrete in Flange			UFC in Web		
		Compressive strength [MPa]	Tensile strength [MPa]	Young's modulus [GPa]	Compressive strength [MPa]	Tensile strength [MPa]	Young's Modulus [GPa]
60A	92.5	71.2	3.2	34.3	195.1	8.8	52.9
60B	115.0	69.1	3.5	32.9			
40B	78.8	77.3	3.1	32.3	206.7	7.6	53.3



(a) Comparison of joint



(b) Comparison of truss thickness

Figure 5 Load-deflection curve

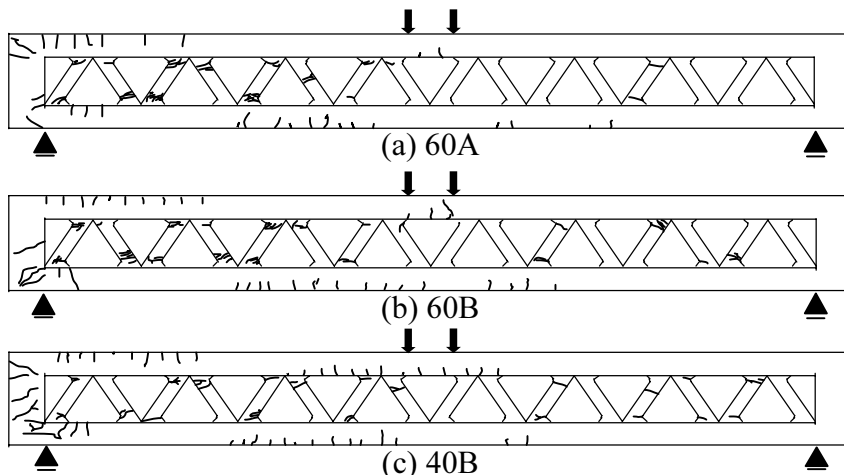


Figure 6 Crack patterns

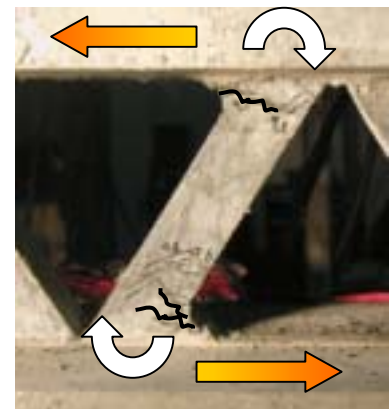


Figure 7 Cracks of compression member

3 Nonlinear FEM analyses

3.1 Analytical procedures

(1) Analytical model

For the analysis, a two dimensional nonlinear FEM tool, DIANA was applied. Figure 8 shows the mesh division. Four nodes isoparametric plane stress elements were adopted for concrete and UFC. The embedded reinforcement element was employed for reinforcements and PC bars. In consideration of asymmetry of failure, a whole of specimen was analyzed.

(2) Constitutive models

For crack model of concrete and UFC, the rotating crack model was used. For UFC, from experimental results in previous work by Kakei et al. (2003), constitutive models as shown in Figure 9 were applied. For concrete, Thorenfeldt's model was applied in compressive area (Figure 10(a)) and in tension area, concrete behaves as an elastic body with the elastic modulus, E_c , until it reaches the tensile strength, f_t . In the post peak region, Hordijk's model was applied (Figure 10(b)). Reinforcements and PC bars were assumed to be elastic bodies with elastic modulus, E_s , until it reaches yield stress, f_y , and then the stress increases gradually with $0.01E_s$ after it reaches f_y as shown in Figure 11.

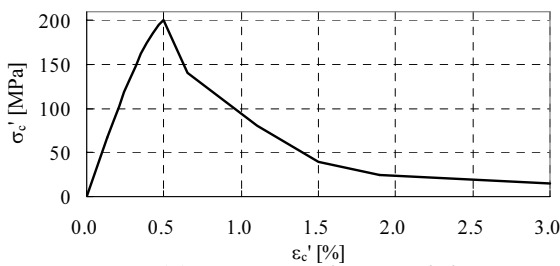
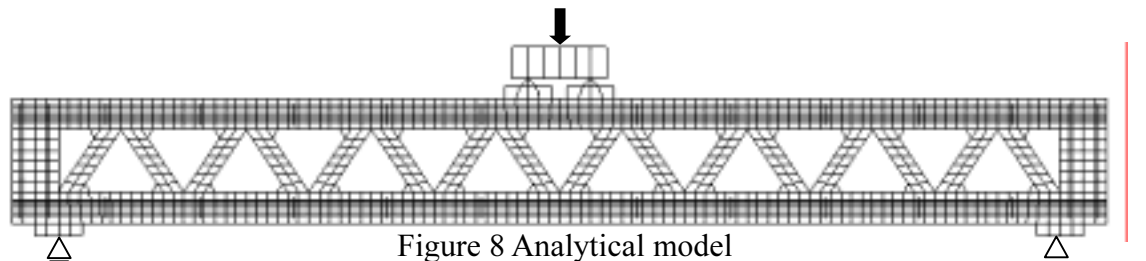
(3) Characteristics of materials

Experimental results were applied to concrete and UFC. The yield strength, f_y , of PC bars is 1250 MPa and f_y of SD295A is 340MPa. Tensile strength, f_t , of UFC on the right side is assumed to be slightly higher than that of the left side by 0.5MPa.

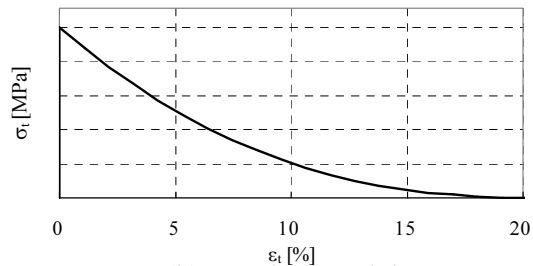
3.2 Results and discussions

(1) Load-deflection curve

Figure 12 illustrates load-deflection curves obtained by experiments and analyses. In case 60B,

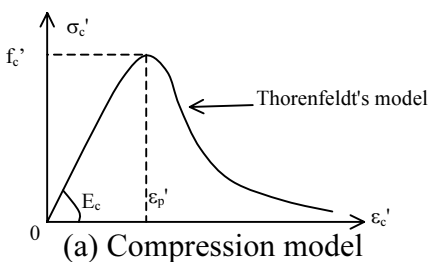


(a) Compression model

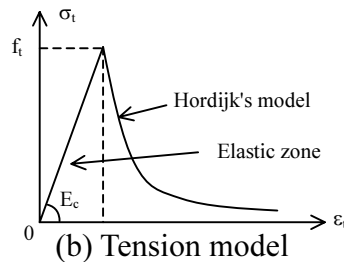


(b) Tension model

Figure 9 UFC model



(a) Compression model



(b) Tension model

Figure 10 Concrete model

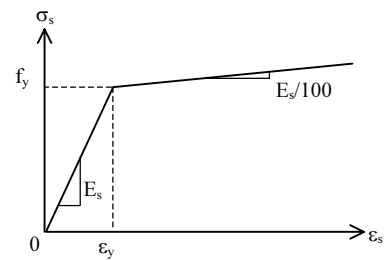


Figure 11 Model for steel bar

ultimately the compressive failure of concrete under the loading plate occurred in the analysis. However, the analysis expressed the behavior after the load fell until it reached the stable condition, and then gradually increased. Especially, the analytical first peak load, P_m , was almost consistent with the experimental one. By the way, in FEM analysis of this study, the joint between web and flange was completely bonded. Consequently, based on the agreement of value of P_m , joint B on the experiment yields the high performance of bond. For case 40B, the load-deflection curve from analysis also expresses a good prediction compared with the experimental results as shown in Figure 12(b).

(2) Crack patterns from analysis

Figure 13 shows analytical crack patterns. For all cases, it is found that cracks propagated in tension members of UFC truss on the left side similar to the experimental results. That means the failure was asymmetric. Because the compression member received bending force due to sliding of a flange member, cracks occurred in compression members like those obtained in the experiments. Therefore, it can be said that, in all cases, the analyses provide adequately predicted results compared with the experimental results.

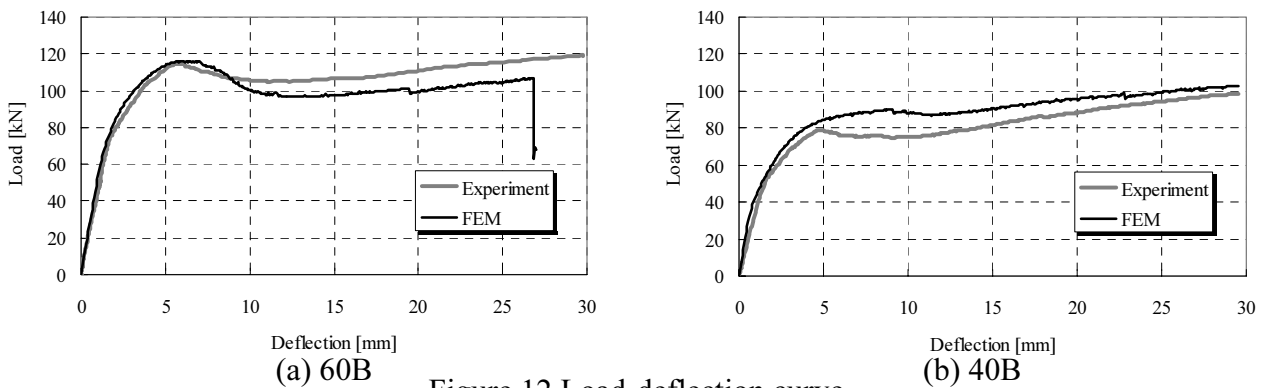


Figure 12 Load-deflection curve

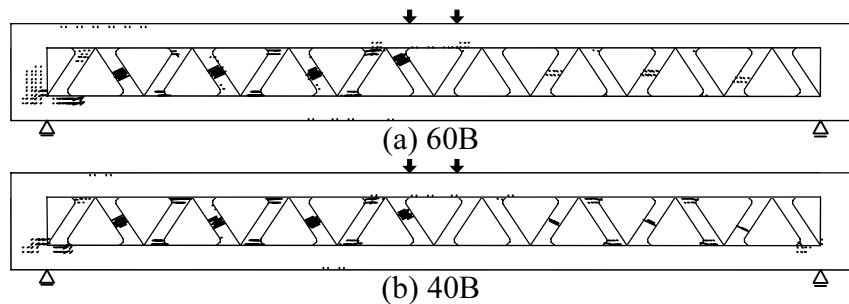


Figure 13 Crack patterns from FEM

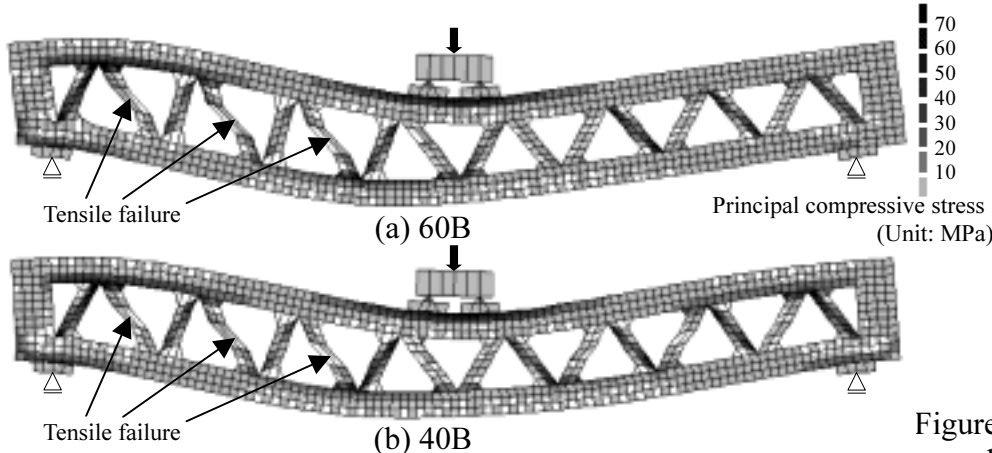


Figure 14 Principal compressive stress patterns and deformations

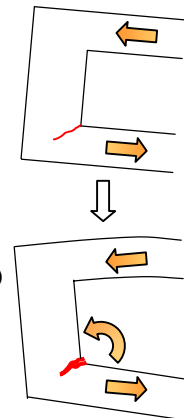


Figure 15 Mechanism of deformation at the corner of concrete frame

(3) Principal compressive stress patterns and deformations

Figure 14 shows the principal compressive stress and deformations obtained by the analysis. Deformations are exaggerated by 10 times. For all cases, from the deformations, it is shown that the tension members of UFC truss on the left side of a specimen are completely failed. However, the tension members on the right side were hardly damaged. It is found that the portion at the far left of upper flange was bended up. Moreover the compressive stress concentrated in the lower part of the upper flange. The possible reasons are as follows: (1) the edge of a concrete member was pushed by the upper flange and pulled by the lower flange, (2) in the lower corner of concrete frame, cracks occurred and opened, and (3) the upper flange member was bended (Figure 15).

From principal compressive stress patterns, for all cases, it was seen that the compressive stress of compression members of UFC truss on the right side was higher than that of the left side.

4 Comparison with RC beams

4.1 Design of RC beams

RC beams which have the same load carrying capacity as the PC composite beams (case 60B and 40B) were designed in order to examine the level of weight reduction of a web member. The characteristics of RC beams are the same as in the PC composite beams as tabulated in Table 6 and the outlines of RC beams are shown in Figure 16. The shear reinforcement ratio of RC beams was set to be 0.30%. This value is specifically the upper limit.

The shear carrying capacity, V_u , of RC beams can be obtained from the following Eqs. (1), (2), and (3) (JSCE code 2002).

$$V_u = V_c + V_s \quad (1)$$

$$V_s = \frac{A_w f_{wy} j d (\sin \alpha + \cos \alpha)}{s} \quad (2)$$

$$V_c = 0.2 (f'_c)^{1/3} \left(\frac{1000}{d}\right)^{1/4} (100 p_w)^{1/3} b_w d \quad (3)$$

where, A_w : cross sectional area of stirrup [mm^2], f_{wy} : yield strength of stirrup [MPa], j : 1/1.15, d : effective depth [mm], α : inclined angle of stirrup to axis of RC beam ($=90^\circ$), s : spacing of stirrup [mm], f'_c : compressive strength of concrete [MPa], p_w : longitudinal reinforcement ratio ($=A_s/(b_w \cdot d)$) [%], and b_w : web thickness of RC beams [mm].

Table 6 Characteristics of RC beam and its materials

Compressive strength (f'_c)	[MPa]	60
Shear span (a)	[mm]	1500
Effective depth (d)	[mm]	350
Cross sectional area of longitudinal reinforcement (A_s)	[mm^2]	1058
Yield strength of longitudinal reinforcement (f_y)	[MPa]	1250
Cross sectional area of stirrup (A_w)	[mm^2]	142.6
Yield strength of stirrup (f_{wy})	[MPa]	295

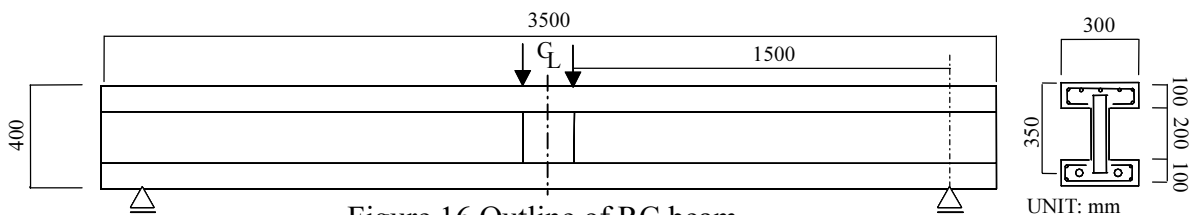


Figure 16 Outline of RC beam

Table 7 Designed results of RC beams

Specimen	Maximum load [kN]	Thickness of web of RC beam [mm]	Weight of web in PC composite beam [kg]	Weight of web in RC beam [kg]	Weight reduction rate [%]
60B	119.5	70.4	33.0	112.6	70.7
40B	99.4	55.5	22.0	88.8	75.2

By setting the value of $2V_u$ to be corresponding to the maximum loads of PC composite beams, b_w was determined. Here, the maximum load was obtained when deflections reached 30mm in the experiments (Figure 5(b)). From the densities of RC and UFC of $2.5t/m^3$, the weights of a web member of RC beams and PC composite beams were compared.

4.2 Comparison of weight

Table 7 shows the designed results of RC beams with the same load capacity as PC composite beams. It was found that the weight of a web member can be reduced to about 70-75%. That means the PC composite girder can make a large contribution to the weight reduction of a web member.

This implies that the self weight of a web member of the PC composite girder using UFC truss is enormously reduced compared with RC girders.

5 Conclusions

The study of mechanical properties of PC composite beams using UFC truss as a web member was carried out. In addition, by the experiment and the nonlinear FEM analysis, the level of weight reduction of a web member by using UFC truss was investigated in comparison with RC beams.

The conclusions of this study are as follows:

- 1) From the experimental results, it is noteworthy turned out that the reinforcing bar with vertical key joint is more suitable joint method than the penetration of PC bar with key joint.
- 2) Based on experimental results, it is proved that, by reducing one-third of UFC volume in web, the first peak load of PC composite beams also decreased by one-third.
- 3) By nonlinear FEM analysis, the mechanical behavior of PC composite beams and the stress flow can be properly predicted.
- 4) By comparing PC composite beams with RC beams having the same resistance, the weight of a web member can be reduced about 70-75% when using the UFC truss. Therefore, the seismic performance of PC composite bridge structures using UFC truss can be enormously improved.

Acknowledgments:

Sincere gratitude is expressed to Taiheiyo Cement Co., Ltd. and Oriental Construction Co., Ltd. for their cooperation.

References:

- Sagawa, Y., Matsushita, H., Tsuruta, H., and Shimoyama, Y. (2001), "Mechanical Properties of Steel Fiber Reinforced High Strength Mortar," *Proceedings of the JCI*, **23**(2), 199-204.
- Kawaguchi, T., Kakei, T., Katagiri, M., and Niwa, J. (2003), "Experimental Research on Mechanical Properties of Composite PC Members Using UHSFRCC," *Proceedings of the JCI*, **25**(2), 1987-1992.
- Kakei, T., Kawaguchi, T., Niwa, J., and Hyodo, H. (2003), "Fracture Properties of Ultra High Strength Steel Fiber Reinforced Cementitious Composites," *Proceedings of Cement and Concrete*, **57**, 230-231.
- TNO (2000), "DIANA User's manual - Nonlinear Analysis."
- JSCE (JSCE CODE) (2002), "Structural Performance Verification, Standard Specification for Concrete Structures."

Mechanism of Efflorescence on Historical Masonry Buildings Seismically Reinforced with Concrete

T.Matsuo¹⁾ and K.Tanaka²⁾

1) Graduate Student, Tokyo Institute of Technology, Japan

*2) Professor, Structural Engineering Research Center, Tokyo Institute of Technology, Japan
tmatsuo@serc.titech.ac.jp, tanaka@serc.titech.ac.jp*

Abstract: The use of concrete for the seismic reinforcement of historical masonry buildings has been related to the accumulation of alkali salts on external brickwork, resulting in accelerated decay of the original masonry. A survey of a reinforced historical building revealed that efflorescence occurs most heavily in areas that become wet due to rainfall. This mode of efflorescence was successfully reproduced using a test wall of brickwork with cement mortar backing. Efflorescence was found to accumulate most heavily on areas of the brickwork that become wettest, and efflorescence was shown to progress with repeated wetting and drying of the brickwork. The porosity of brick after the efflorescence tests was also measured using a mercury intrusion method, and it was confirmed that the porosity of brickwork in regions with heavy efflorescence is much lower than in areas with little surface efflorescence.

1. INTRODUCTION

The conservation and renovation of historical buildings through the application of modern construction techniques such as masonry, reinforced concrete, and steel-frame structures has become widespread. Most historical buildings need to be seismically reinforced using appropriate conservation and renovation methods in order to preserve the buildings, which were built predominantly in urban areas, for continued use. In the planning of reinforcement of these historical buildings, due consideration should be given to their historical value, the original method of construction, the original materials used, and the intended manner of reinforcement, as inappropriate reinforcement methods can reduce the historical value of the building and in fact promote decay.

In Japan, seismic reinforcement is necessary in many cases because the original building does not provide sufficient seismic safety. Of the various materials such as concrete, steel, synthetic resins, and high-strength fibers that have been used for seismic reinforcement, concrete is most widely used as inner wall, column or slab reinforcement. The reinforcement effect expected in such cases is quite good considering the similarity to masonry walls in terms of rigidity. However, reinforcement with concrete has been noted to cause heavy efflorescence on brickwork due to the leaching of alkali salts from the cement, resulting in extensive decay of the original structure.

This paper experimentally analyzes the mechanism of efflorescence on historical masonry buildings that have been seismically reinforced with concrete.

2. EXAMPLE OF MASONRY BUILDING REINFORCED WITH CONCRETE

Many historical masonry buildings have been reinforced with concrete in Japan. An example of such a building, built in 1890 and reinforced with inner concrete walls in 1977, was assessed in 2003 to evaluate the extent of efflorescence on exterior walls. Figures 1 and 2 show examples of the efflorescence on the exterior wall of this historical masonry building. Efflorescence was observed on most exterior walls, with a considerable accumulation below the eaves, around cornices, below window frames, and at joints between walls - areas that are likely to remain wet after rainfall. Spalling of the brickwork was also observed, as shown in Figure 3. It is supposed that this spalling is induced by the accumulation of crystalline salt residue inside the brick.

From this survey it was inferred that the mechanism of efflorescence on masonry buildings reinforced with concrete appears to be related to the movement of moisture and salt in the masonry wall.

3. MODEL TEST FOR EFFLORESCENCE

3.1 Test Wall

The model wall fabricated to attempt to reproduce the efflorescence appearing on masonry walls reinforced internally with concrete is shown in Figure 4. Brickwork was laid using cement lime mortar and allowed to cure for 28 days. A lining of cement mortar was then formed in direct contact with the brickwork. The joint mortar included a lime constituent, as commonly employed before the Second World War. The conditions of specimens are listed in Table 1.

Table 1 Absorption of brick, joint mortar and cement mortar backing

	Position of brick	Absorption of cold water (%)	Joint mortar	Cement mortar backing	
Cement mortar backing	Upper	8.0	cement:lime:sand=1:3:12 (by volume), lime:water=1:1 (by weight)	w/c=0.6, cement:sand=1:2.5	
	Lower	9.0			
No backing	Upper	9.0			
	Lower	8.6			

3.2 Test Method

Epoxy resin was applied to the surfaces as shown in Figure 5. The test procedure is outlined in Figure 6. In the test, a reservoir on the top of the specimen was

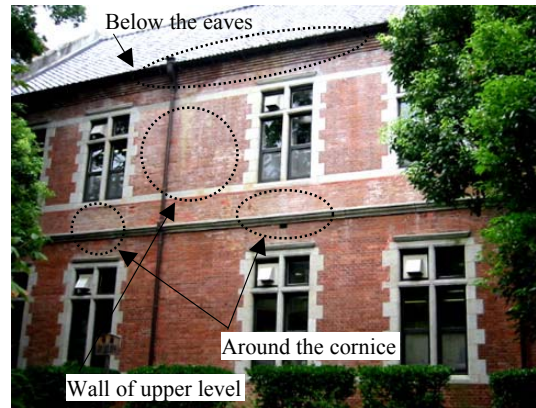


Figure 1 Efflorescence on a historical masonry building reinforced with concrete

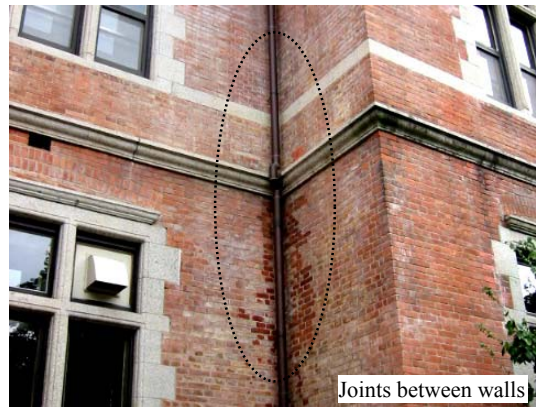


Figure 2 Efflorescence at joints between walls



Figure 3 Spalling caused by crystalline salt residue inside the brickwork

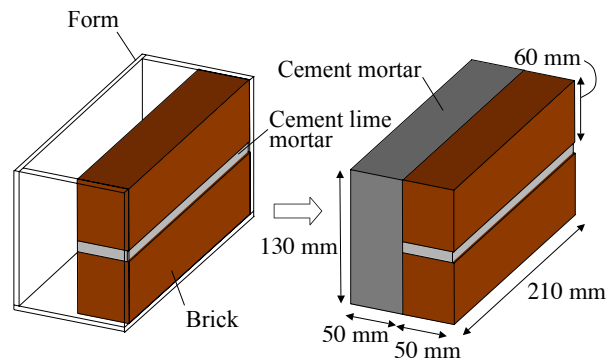


Figure 4 Test wall specimen

filled with a fixed quantity of water (300 mL), and the efflorescence was observed after the brick surface had dried. This process was repeated. The test was carried out in a thermostatic chamber maintained at 20 °C and 60% relative humidity, and airflow was applied to the brick surface to accelerate drying.

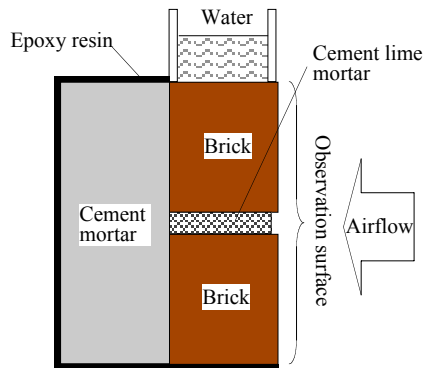


Figure 5 Summary of test method

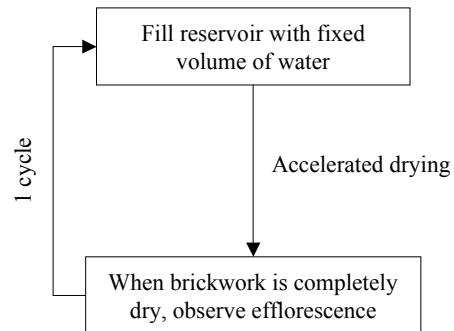


Figure 6 Procedure of test

3.3 Results

The test results are shown in Figure 7. The ratio of efflorescence area to the total exposed brickwork area (except joints) was also calculated (see Figure 8) and the results are shown in Figure 9. The efflorescence area increased with repeated wet/dry cycles. The joint mortar (cement-lime) appeared to contribute little to the efflorescence compared to the cement mortar backing, indicating that cement lime mortar supplies less salts than the cement mortar backing.

The distribution of efflorescence accumulation was not uniform, with heavy efflorescence appearing on the upper portion of the brickwork. This is attributed to a non-uniform distribution of water content in brickwork, varying from high content near the top (closest to the reservoir), to low water content near the base.

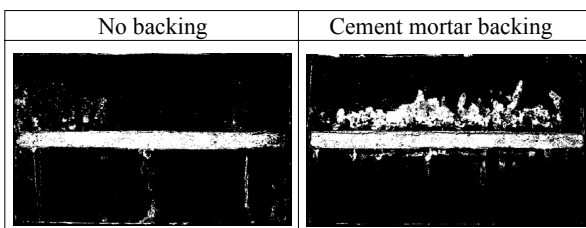


Figure 8 Example of before and after pictures (7 cycles)

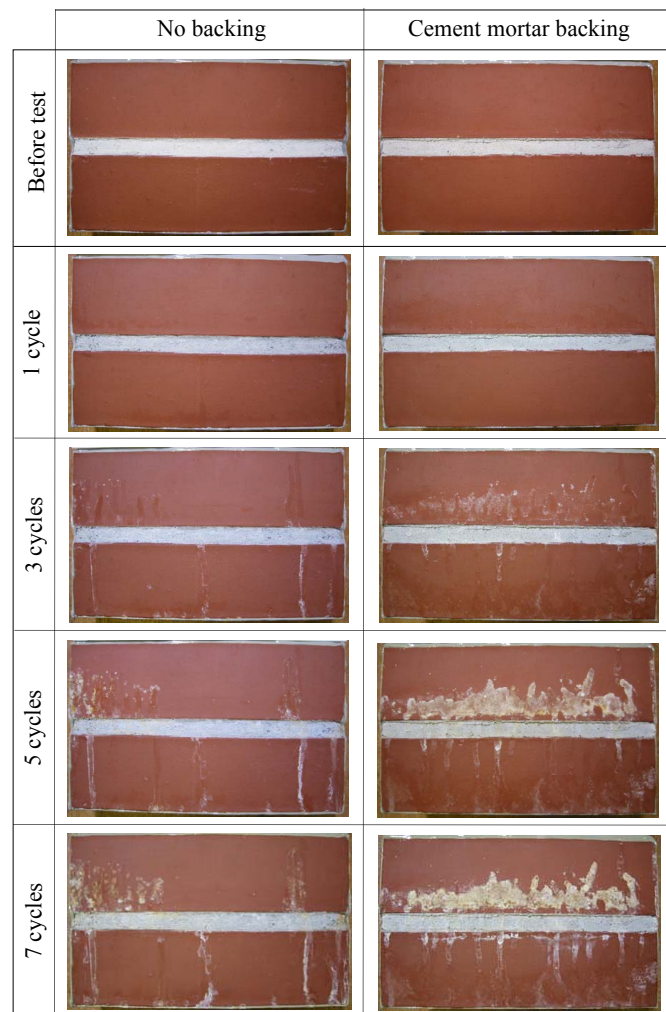


Figure 7 Test result: View of observation surface at each cycle

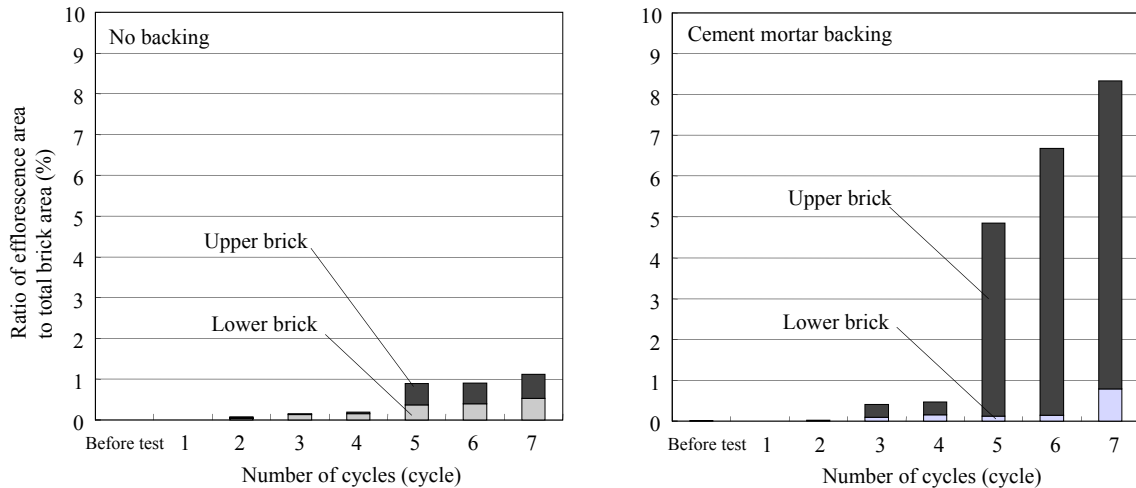


Figure 9 Ratio of efflorescence area to total brickwork surface area except joints

4. POROSITY CHANGE IN BRICK DUE TO CEMENT SALTS

4.1 Test of Efflorescence without Joint Mortar

4.1.1 Test Method

The effect of cement salts leached from the concrete reinforcement and accumulating in the masonry brickwork was investigated in more detail using a test model consisting of bricks and a cement mortar backing, without joint mortar. The specimen is shown in Figure 10. The absorption of water into the brick after 24 h immersion in cold water was 8.0% (by weight). The backing cement mortar had a water content of 0.6 and a cement:sand ratio of 1:2.5. The test configuration is shown in Figure 11. The test procedure and conditions were the same as in the previous experiments.

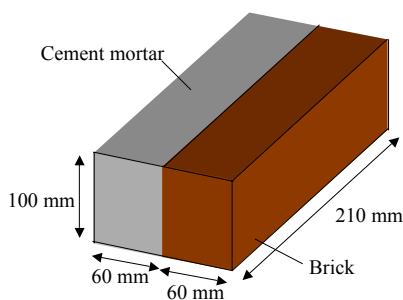


Figure 10 Test specimen

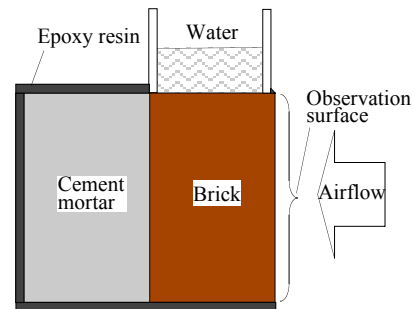


Figure 11 Test method

4.1.2 Results

Figure 12 shows photographs of the brick surface before the test and after 6 cycles. Heavy efflorescence can be seen due the cement mortar backing. Again, the distribution of efflorescence was not uniform, but in this case, heavy efflorescence accumulation occurred on the lower part of the brick. The ratio of efflorescence area to total exposed brick surface calculated from such photo pairs is shown in Figure 13. These results clearly show that efflorescence

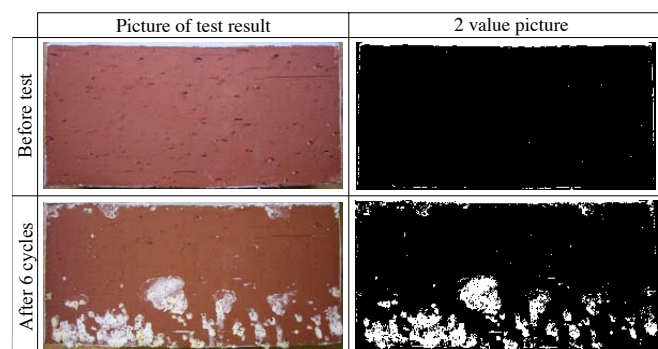


Figure 12 Test result: View of observation surface before test and after 6 cycles

accumulated progressively on the brick surface with repeated wet/dry cycles.

4.2 Porosity of Brick after Efflorescence Test

Although the cement salts could be readily seen to accumulate on the brick surface, it is also important to investigate whether cement salts are crystallizing inside the brick as well, which may be the cause of spalling and decay. This was examined by measuring the porosity of the bricks using a mercury intrusion method.

The samples for measurement were cut from two places of the specimen after the accelerating test, as shown in Figure 14, from an area exhibiting little surface efflorescence and an area with a heavy accumulation of efflorescence. The measurement results are shown in Figure 15. While pores of approximately 10 μm or more in diameter are present in the upper part of the brick (low efflorescence), the porosity of the lower part is significantly lower, from 1 μm to 10 μm . This difference in porosity between the upper and lower parts of the same brick after the efflorescence test indicates that cement salts were crystallizing inside the brick due to efflorescence, reducing the porosity of the brick in regions that exhibit heavy efflorescence on the surface.

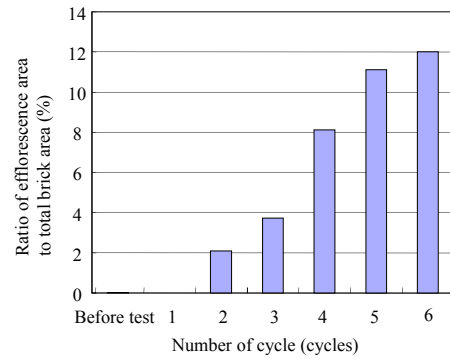


Figure 13 Ratio of efflorescence area to total brick area

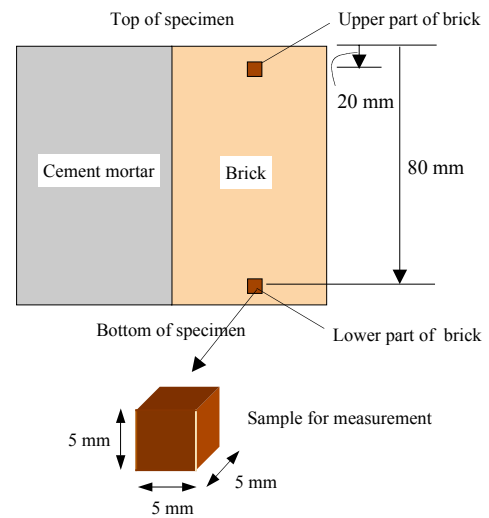


Figure 14 Position of samples for porosity measurement by mercury intrusion method

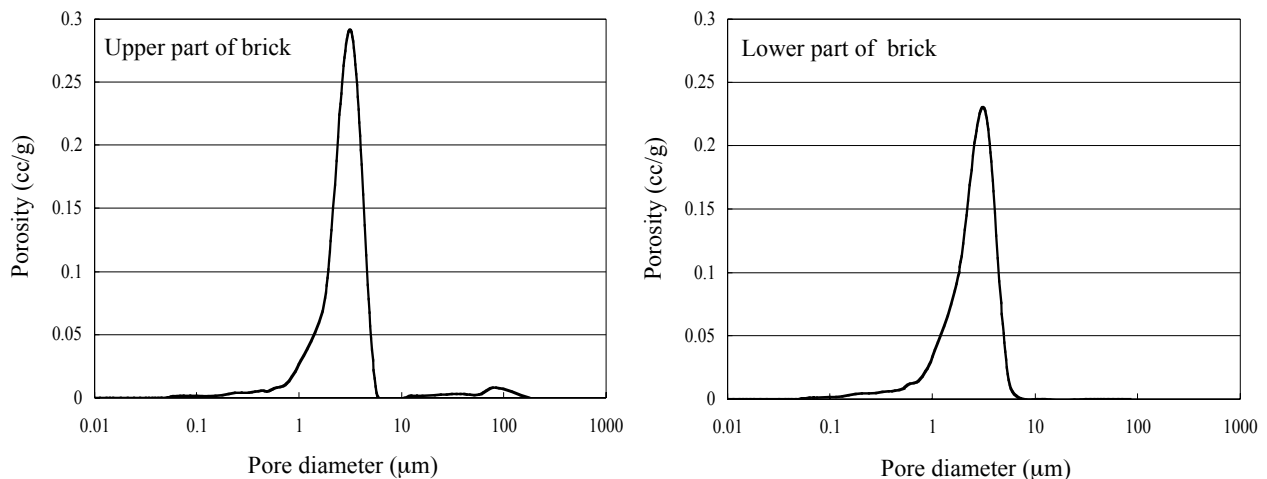


Figure 15 Porosity of bricks measured by mercury intrusion method

5. CONCLUSIONS

This study considered the mechanism of efflorescence on historical masonry buildings that have been seismically reinforced with an internal backing of concrete. A survey of a historical masonry building that had been reinforced with concrete, revealed that efflorescence occurred on most areas of exterior walls,

with particularly heavy accumulations below the eaves, around cornices, below window frames, and at joints between walls, which are area that are likely to become wet due to rainfall. An experiment using a model wall with a concrete backing successfully reproduced the efflorescence observed in the field, and showed that the efflorescence on brickwork accumulates with repeated wetting and drying of the brickwork. The distribution of surface efflorescence was not uniform, and is considered to be related to the vertical variation in water content in the brickwork. Finally, the porosity of bricks after efflorescence tests was measured using an mercury intrusion method, and it was found that the porosity of brick in areas with heavy surface efflorescence was significantly lower than that in areas exhibiting less surface efflorescence.

Acknowledgements:

This research was supported by the Tanaka Laboratory of the Structural Engineering Research Center (SERC) of the Tokyo Institute of Technology. Porosity measurements were conducted in collaboration with Dr. K. Kurumisawa of the Japan Testing Center for Construction Materials.

References:

- T. Matsuo, K. Tanaka, "Mechanism of Efflorescence on Historical Brick Buildings Reinforced with Concrete Wall", Summaries of Technical Papers of Annual Meeting Architectural Institute of Japan, 2003, pp.925-926
- Chin, I.R., "Spalling of Brick," *Masonry: Opportunities for the 21st Century*, ASTM STP 1432, D. Throop and R.E. Klingner, Eds., ASTM International, West Conshohocken, PA, 2003, pp.97-113
- Kaskel, B.S., Gerns, E.A., and DeMuth, K., "Renovation of Existing Masonry Buildings to Residential Lofts," *Masonry: Materials, Testing, and Application*, ASTM STP 1356, J.H. Brisch, R.L. Nelson, and H.L. Francis, Eds., American Society for Testing and Materials, West Conshohocken, PA, 1999, pp.140-147
- H. Nishizawa, "On Seismic Reinforcement of Brick Masonry Structures", GBRC, No.72, Oct. 1993, pp.15-26
- Chin, I.R., and Petry, L., "Design and Testing to Reduce Efflorescence Potential in New Brick Masonry Walls," *Masonry: Design and Construction, Problems and Repair*, ASTM STP 1180, J.M. Melander and L.R. Lauersdorf, Eds., American Society for Testing and Materials, Philadelphia, 1993, pp.3-21
- Kim Moon Han et al., "A Study on the Efflorescence of Brick structures and Reduceing method", Summaries of Technical Papers of Annual Meeting Architectural Institute of Japan, 1991, pp.633-634
- Tomassetti, Albert A., "Problems & Cures in Masonry," *Masonry: Components to Assemblages*, ASTM STP 1063, American Society for Testing and Materials, Philadelphia, PA. 1990, pp.324-338
- Isberner, A.W., "A Test Method for Measuring the Efflorescence Potential of Masonry Mortars," *Masonry: Research, Application, and Problems*, ASTM STP 871, J.C. Grogan and J.T. Conway, Eds., American Society for Testing and Materials, Philadelphia, 1985, pp.27-37
- Harris, H.A., "A Method to Determine Efflorescence and Water Permeance of Masonry Mortars," *Masonry: Research, Application, and Problems*, ASTM STP 871, J.C. Grogan and J.T. Conway, Eds., American Society for Testing and Materials, Philadelphia, 1985, pp.88-100
- Grimm, C.T., "Durability of Brick Masonry: A Review of Literature," *Masonry: Research, Application, and Problems*, ASTM STP 871, J.C. Grogan and J.T. Conway, Eds., American Society for Testing and Materials, Philadelphia, 1985, pp.202-234
- Young, J.E., "Backup Materials as a Source of Efflorescence," *Journal of the American Ceramic Society*, Columbus, Ohio, Vol.40, No.7, July 1957, pp.240-243
- Ritchie, T., "Study of Efflorescence on Experimental Brickwork Piers," *Journal of the American Ceramic Society*, Columbus, Ohio, Vol.38, No.10, Oct. 1957, pp.357-361

DEVELOPMENT OF PLANAR ARRAY PROBES FOR DETECTION OF THREE-DIMENSIONAL DEFECT

N. Rattanasuwannachart¹⁾, K. Takahashi²⁾, C. Miki³⁾, and S. Hirose⁴⁾

1) Graduate Student, Department of Civil Engineering, Tokyo Institute of Technology, Japan

2) Undergraduate Student, Department of Civil Engineering, Tokyo Institute of Technology, Japan

3) Professor, Department of Civil Engineering, Tokyo Institute of Technology, Japan

*4) Professor, Department of Mechanical and Environmental Informatics, Tokyo Institute of Technology, Japan
narong@cv.titech.ac.jp, kazuya@cv.titech.ac.jp, miki@cv.titech.ac.jp, shirose@cv.titech.ac.jp*

Abstract: In the present study, two types of multi-channel planar array probes have been developed. The first is planar pitch-catch array probe and the second is planar tandem array probe. Both of them are designed to detect weld defects in structural connection based on the normal-beam and angle-beam techniques, respectively. The planar pitch-catch array probe is the assembly of 16 normal-beam transducers arranged in 4-by-4 matrix, and the planar tandem array probe is the assembly of 15 angle-beam transducers arranged in 3-by-5 matrix. The ultrasonic detection system, which is designed to use with these probes, is developed for fastness and compactness. The 3D-SAFT algorithms, which are applicable and appropriate to both types of probes, are studied and developed. The 3D-SAFTs are applied to the A-scans obtained by the flaw detection system and make the interpretation of internal defect information.

1. INTRODUCTION

In the Great Hanshin Earthquake, brittle fracture caused the collapse of steel bridge piers. The results from many investigations had been reported that the brittle fracture was originally expanded from the weld defect in the structural connection. Therefore, in viewpoint of retrofitting works of the existing bridges, it is necessary to observe the internal condition and information of the structural connections, nondestructively.

Ultrasonic testing, one of techniques in nondestructive testing, has been widely used for in-situ inspection of in-service structures (Achenbach 2000). Main tasks of ultrasonic testing are to detect flaws and defects inside the structural connection and to give accurate information of defect such as shape, size, and orientation. In the conventional testing, single-probe technique is the most widely used method (Krautkrämer et al. 1983). This method refers to the procedure that uses one reversible transducer (longitudinal or shear waves) to scan for the location of defects in structures. However, this technique, sometimes, leads to the lack of information of defects, which reflect the incident waves in two or three dimensions.

Therefore, in order to increase the detectability of defects, two-probe testing techniques have been developed such as the time-of-flight diffraction (TOFD) technique and the tandem technique. In those methods, transmitter and receiver are separated and the receiver is mechanically scanned for the reflected wave.

Unfortunately, such methods face three major problems. First, scanning the probe mechanically will cause error in evaluation of position of defects. Second, during manual scanning, thickness of coupling material between the probe and specimen changes. As a result, the wave amplitude will be



Figure 1 Planar Pitch-Catch Array Probe

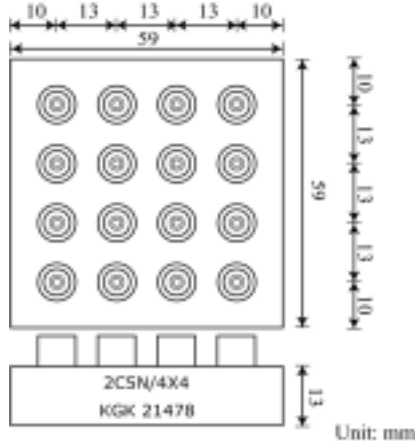


Figure 2 Geometry of Planar Pitch-Catch Array Probe

relatively changed. Third, inspection for one target area spends long time for mechanically manual scanning and recording the A-scans. Furthermore, inspection of bridge components is difficult due to the restriction of inspection time and lack of accessible space. Therefore, in order to cope with such problems, the planar array probes with the fast ultrasonic flaw detection system should be developed.

In general, the data of ultrasonic testing are presented in form of unprocessed radio frequency (RF) signals or A-scans. These A-scans are very difficult to evaluate and may lead to unreliable inspections. Therefore, image reconstruction systems have been developed and introduced to ultrasonic testing for managing and analyzing the A-scans. One of the famous imaging systems is synthetic aperture focusing technique (SAFT), which is originally used in radar system for military and surveillance missions (Soumekh 1999). With the application of the SAFT imaging, information of defect in form of images is obtained accurately and easy to evaluate with reliability.

The objectives of this study are 1) to propose multi-channel array probes in order to increase detectability of three-dimensional defects, 2) To develop the fast and compact in-situ ultrasonic flaw detection system, and 3) To propose the 3D-SAFT imaging algorithms, which are applicable to the planar array probes.

2. MULTI-CHANNEL PLANAR ARRAY PROBES AND FLAW DETECTION SYSTEM

In this study, two types of planar array probes have been developed. The first is the planar pitch-catch array probe and the second is the planar tandem array probe. Both of them are designed to use in different situations. The planar pitch-catch array probe is based on the normal-beam technique, while the planar tandem array probe is based on the angle-beam technique.

2.1 Planar Pitch-Catch Array Probe

The planar pitch-catch array probe has been developed with the assembly of 16 normal-beam transducers in form of 4-by-4 matrix as shown in Figure 1. Geometry is shown in Figure 2. This array probe has 16 channels. Each channel generates longitudinal wave with central frequency of 2MHz.

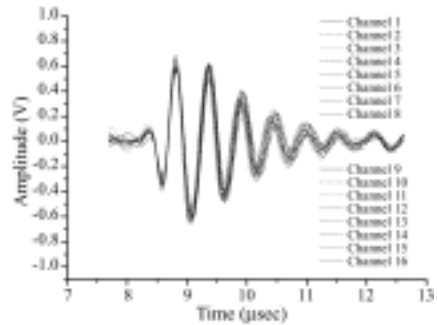


Figure 3 Longitudinal Wave Signals from The Planar Pitch-Catch Array Probe

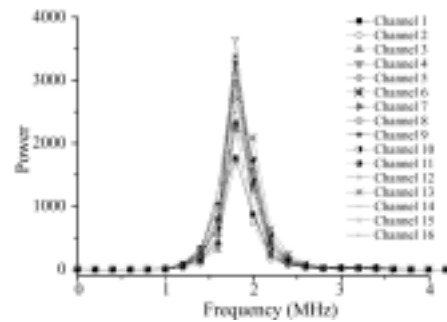


Figure 4 Spectrum of Longitudinal Wave Signals



Figure 5 Planar Tandem Array Probe

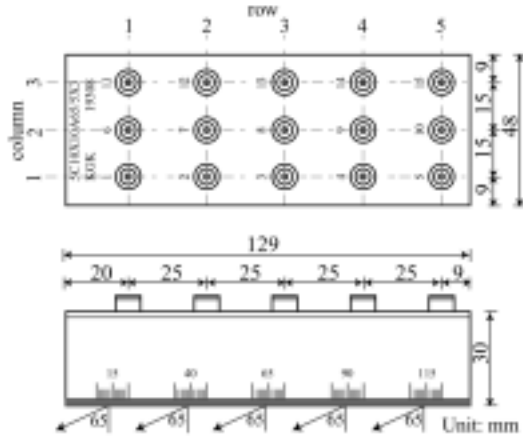


Figure 6 Geometry of Planar Tandem Array Probe

The wave signals generated from each channel are observed and shown in Figure 3. Applying Fourier transformation to these waveforms gives frequency spectrums as shown in Figure 4. Spectrums of all waveforms show almost practically agreement.

2.2 Planar Tandem Array Probe

Figure 5 is the planar tandem array probe and its geometry is shown in Figure 6. It is an assembly of 15 angle-beam transducers arranged in form of 3-by-5 matrix (3 columns and 5 rows). Each channel is reversible type and can transmit shear waves with angle of refraction of 65 degree. The waves propagate in the same direction for all channels. Each channel has central frequency of 5 MHz.

The plot of received waveforms of all channels is shown in Figure 7 and the plot of their spectrums is in Figure 8. All waveforms and spectrums show practically identical shapes.

Results from both array probes show that all waves generated from each channel have the same properties in shape and frequency. Each channel can receive waves generated from another channels. Therefore, the two-probe technique can be used properly in both probes.

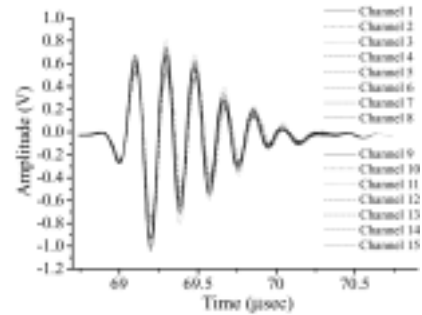


Figure 7 Shear Wave Signals from The Planar Tandem Array Probe

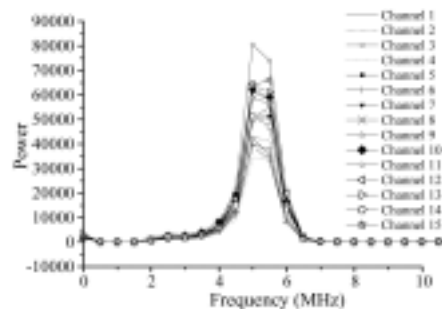


Figure 8 Spectrum of Shear Wave Signals

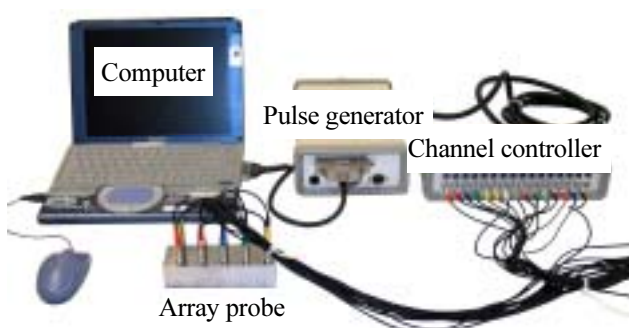


Figure 9 Ultrasonic Flow Detection System

2.3 Ultrasonic Flow Detection System

In this study, we developed the ultrasonic flaw detection system, which is compatible to the planar array probes. The system consists of personal computer, pulse generator, and channel controller. They are connected to array probe as shown in Figure 9.

Channel controller is used for controlling channels of transmitter and receiver. Personal computer is used for data acquisition and controlling pulse generator, which is used for sending wave pulses.

In our system, each channel is used for transmitting incident waves and receiving reflected waves generated from another channels. Therefore, a total of 256 and 225 files of

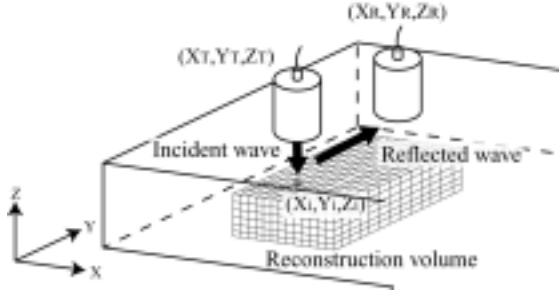


Figure 10 3D Pitch-Catch SAFT

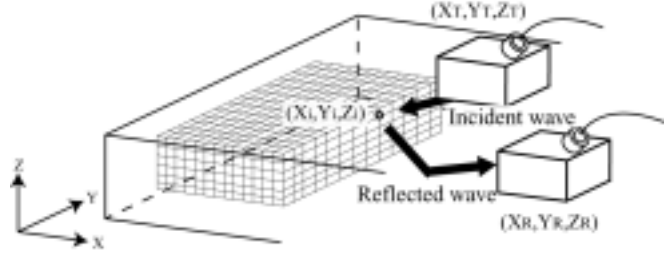


Figure 11 3D Tandem SAFT

the A-scans can be, respectively, obtained from the pitch-catch and tandem array probes without time consumption, which is appropriate for in-service inspection.

3. 3D-SYNTHETIC APERTURE FOCUSING TECHNIQUE

SAFT processing relates to many parameters, such as coordinates of probe position and reconstruction areas, direction of wave incidence, material wave velocities, received A-scans, and possible sound paths. In this chapter, the specific 3D-SAFT algorithms for the planar pitch-catch and tandem array probes are proposed.

3.1 3D Pitch-Catch SAFT

Figure 10 demonstrates the principle of the 3D pitch-catch SAFT algorithm. Reconstruction volume (volume of inspection) is divided into many voxels with their coordinates (X_i, Y_i, Z_i) . Transmitter (X_T, Y_T, Z_T) generates wave with certain direction and receiver (X_R, Y_R, Z_R) gains the A-scan of reflected waves.

Assuming the considering voxel (X_i, Y_i, Z_i) in Figure 10 is a part of defect, the incident wave is incident to and reflected at this voxel and returned to the receiver by the assumed sound path illustrated in the figure. The sound paths of incident and reflected waves are pre-assumed in the SAFT process. All possible sound paths should be considered for an A-scan of a pair of transmitter and receiver. However, many assumptions of sound paths generally result in the artefacts (ghost images), which are caused from mistake assumption of sound path. Therefore, in this pitch-catch SAFT algorithm, the sound paths of the incident and reflected waves are considered only the direct path, which is the straight-line connecting the probe to the voxel. Then, the time of flight (TOF) is determined as follows:

$$TOF = \frac{(L_{IN} + L_{REF})}{C_P} \quad (1)$$

$$L_{IN} = \sqrt{(X_T - X_i)^2 + (Y_T - Y_i)^2 + (Z_T - Z_i)^2} \quad (2)$$

$$L_{REF} = \sqrt{(X_R - X_i)^2 + (Y_R - Y_i)^2 + (Z_R - Z_i)^2} \quad (3)$$

where L_{IN} and L_{REF} are lengths of incident and reflected paths, respectively. C_P is longitudinal wave velocity of material.

Amplitude value of received A-scan is added up to that voxel with respect to the TOF as followings:

$$H(X_i, Y_i, Z_i) = f(TOF) \quad (4)$$

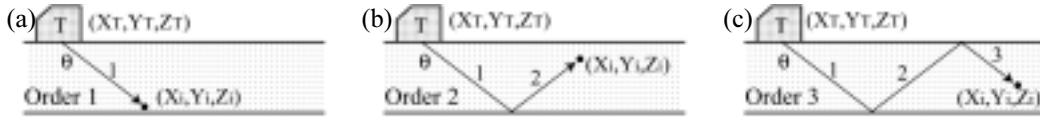


Figure 12 Dependency of Incident Path of Wave on Boundary of Specimen: a) 1st, b) 2nd, and c) 3rd Orders

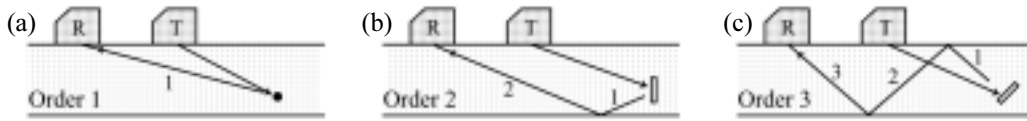


Figure 13 Dependency of Reflected Path on Defect Orientation: (a) 1st, (b) 2nd, and (c) 3rd Orders

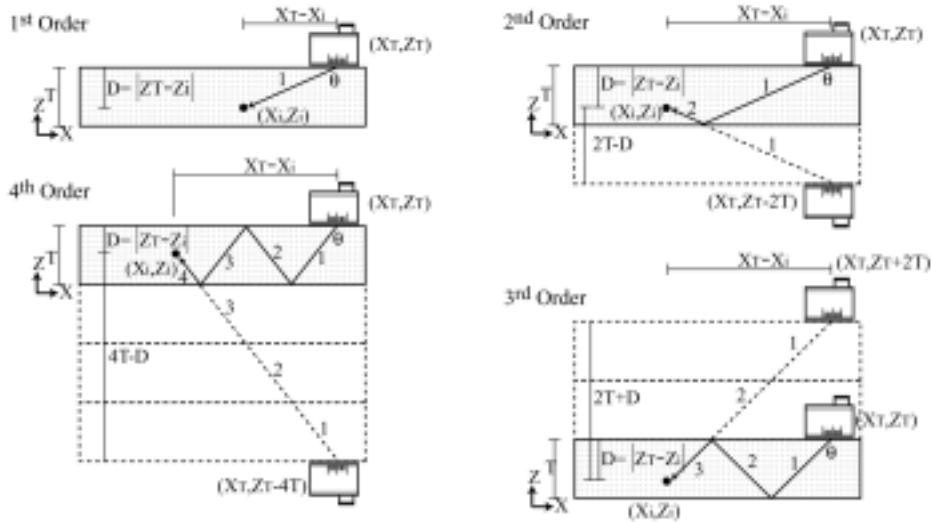


Figure 14 Determination of Lengths of Boundary-Reflected Sound Paths

where $H(X_i, Y_i, Z_i)$ is amplitude intensity at specific voxel (X_i, Y_i, Z_i) and $f(\text{TOF})$ is amplitude of considering A-scan at time TOF.

Then the summation of amplitude values at the specific voxel is done for A-scans of another pairs of transmitter and receiver from 1 to A as follows:

$$H(X_i, Y_i, Z_i) = \sum_{a=1}^A f_a(\text{TOF}) \quad (5)$$

Conducting the process in Eq. (5), the voxel, which respects to the actual defect, will be resulted in high intensity of amplitude values.

3.2 3D Tandem SAFT

In case of single-probe method, the sound paths for angle-beam technique are certain and simply assumed. However, assumption of sound path is difficult in case of tandem technique. Unlike the pitch-catch SAFT, the tandem SAFT, demonstrated in Figure 11, involves boundary condition of the test steel plate. In this section, the incident path is considered separately of the reflected path.

Incident path can be certainly determined, because the direction of wave incident in the test specimen is known. Figure 12 demonstrates the incident paths of waves to specific pixel (X_i, Y_i, Z_i) . As shown in figure, the incident path depends on the angle of refraction and boundary of test specimen. As a result, waves propagate in steel plate can have multiple reflection at boundary before the reflection at defect. Therefore, we classify the incident paths into many orders, for ease, referring to a number of straight lines composing the sound paths. For example, the incident paths are of orders 1, 2, and 3 in cases of Figures 12(a), (b), and (c), respectively.

In many testing situations, the thickness of test specimen and the angle of refraction are given. As a sequence, an order, n , of the incident path of waves, generated by transmitter (X_T, Y_T, Z_T) ,

propagating to the specific pixel can be determined using following formula:

$$\text{Order } n = \text{integral part of } \left[\frac{\sqrt{(X_T - X_i)^2 + (Y_T - Y_i)^2}}{T \times \tan \theta} \right] + 1 \quad (6)$$

where T is the plate thickness and θ is the angle of refraction.

Reflected path also depends on boundary of test object as the incident path, but it is more complicated because it additionally depends on the orientation of defects as shown in Figure 13. As same as the incident path, the reflection paths in Figures 13(a), (b), and (c) are, respectively, classified to orders 1, 2, and 3.

In order to determine lengths of sound paths of any orders, we propose an idea as demonstrated in Figure 14. Sound paths of waves, which are reflected at boundary, are unwrapped to be straight line as shown by dashed line. For odd-number orders such as 3rd order, sound path is flipped up making a straight line from voxel (X_i, Y_i, Z_i) to new probe position $(X_T, Y_T, Z_T + 2T)$. On the contrary, sound paths are flipped down in cases of even-number orders such as 2nd and 4th orders. Equation for the lengths of the sound paths for any orders (n) can be summarized as followings:

$$\text{Length of sound path at } n^{\text{th}} \text{ Order: } \sqrt{(X_T - X_i)^2 + (Y_T - Y_i)^2 + \Delta Z^2} \quad (7)$$

$$\Delta Z = \eta \cdot T + (-1)^{n+1} \cdot D \quad \begin{cases} \eta = n-1 \text{ for } n = \text{odd number} \\ \eta = n \text{ for } n = \text{even number} \end{cases} \quad (8)$$

where $D = |Z_T - Z_i|$.

As same as the principle of the SAFT in the pitch-catch method, the time of flight (TOF) is determined as follows:

$$\text{TOF} = \frac{(L_{\text{IN}} + L_{\text{REF}})}{C_s} \quad (9)$$

where C_s is the shear wave velocity. L_{IN} and L_{REF} are determined from Eq. (7).

As mentioned that the reflected path depends on test object boundary and orientation of defects, therefore, for a pair of transmitter and receiver, the order of the reflected path (n_r) is varied from 1 to appropriate numbers (N). The amplitude intensity at specific voxel (X_i, Y_i, Z_i) for a number (A) of A-scans can be written as:

$$H(X_i, Y_i, Z_i) = \sum_{a=1}^A \left(\sum_{n_r=1}^N f_a(\text{TOF}) \right) \quad (10)$$

4. APPLICATION OF 3D SAFTs TO FLAW DETECTION SYSTEM

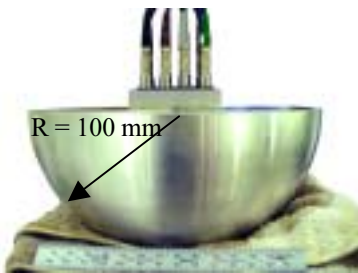


Figure 15 Experimental Setup of The Pitch-Catch Array Probe.

In this chapter, the planar array probes with the 3D-SAFTs are applied to the specimens in order to verify the validity and advantage of this system.

4.1 Graphical results of the planar pitch-catch array probe

Experimental setup and specimen are shown in Figure 15. The half spherical specimen with radius of 100 mm is used as test specimen. The bottom surface of this specimen has a curvature shape, which is supposed

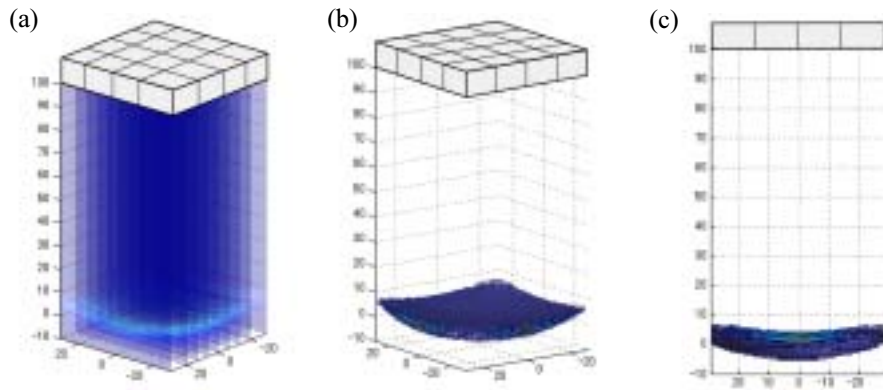


Figure 16 Images of Bottom Surface of Half Spherical Specimen: (a) Sliced-Plane Image, (b) and (c) Isosurface Images to reflect the waves in three dimensions.

The 3D pitch-catch SAFT is applied to the A-scans gained by the planar pitch-catch array probe. The graphical result of the half spherical specimen is shown in Figure 16. Figure 16(a) shows the volumetric data in form of sliced-plane image, while Figures 16(b) and (c) show by isosurface images. Both types of image interpretations show information of three-dimensional curve at specimen bottom surface.

However, the isosurface images of the volumetric data, shown in Figures 16(b) and (c), give us in-depth information of orientation, location, and shape in three dimensions. Therefore, it is strongly recommended for interpretation of the volumetric data.

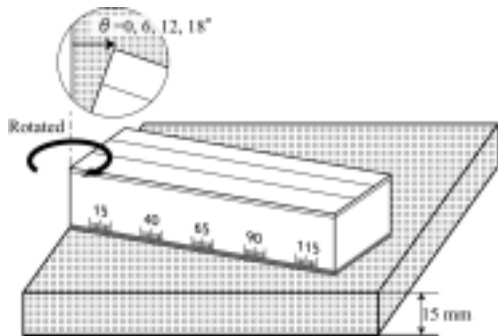


Figure 17 Experimental Setup of The Tandem Array Probe

4.2 Graphical results of the planar tandem array probe

In this section, we use the steel plate, which has 15 mm in thickness, for the experiment. Experimental setup is shown in Figure 17. Plate edge of this plate is supposed to be the planar defect. In order to confirm the detectability of three-dimensional planar defect, we rotated the probe around one corner making the plate edge angled to the probe front for 0, 6, 12, and 18 degrees.

Top views of the isosurface images for $\theta = 0, 6, 12,$ and 18 degrees are compared and shown in Figures 18(a), (b), (c), and (d), respectively. Red lines indicated in the figures are actual orientation of plate edges. In case of $\theta = 0^\circ$, isosurface image shows the same orientation with plate edge.

In cases of inclined orientation at $\theta = 6^\circ$ and 12° , isosurface images in columns 1 and 2 show very good relation with actual plate edge orientation. The reason that isosurface images in column 3 do not show good relation with actual orientation can be explained based on probe geometry. The waves generated from transmitters in column 1 can be detected by receivers in columns 2 and 3, and the waves generated from transmitters in column 2 can be relatively detected by receivers in column 3. However, the waves generated by transmitters in column 3 cannot be detected, because there is no column of receivers to detect reflected waves.

In case of $\theta = 18^\circ$, images do not relate to plate edge for all columns, because angle of plate edge to the probe front is very large so that the reflected waves cannot be efficiently detected.

Note that we cannot gain any three-dimensional information, such as orientation and shape as shown in Figures 16 and 18 by using only a single-probe technique. These results show the importance and necessity of the three-dimensional ultrasonic flaw detection system.

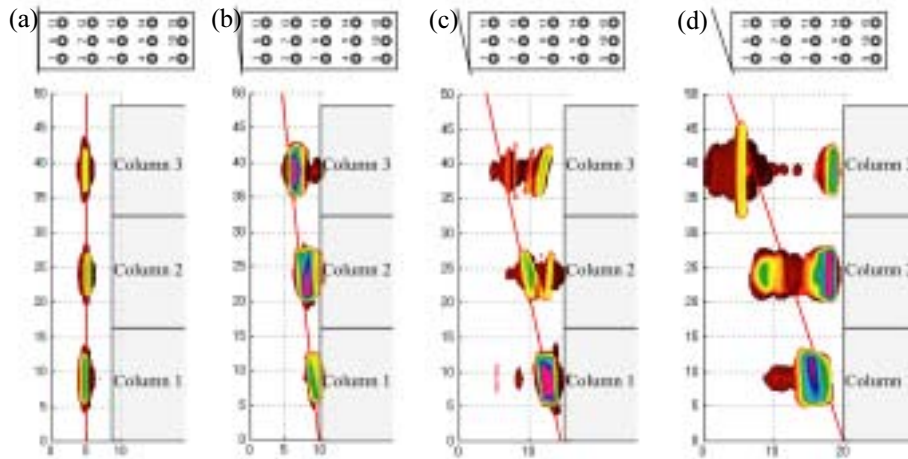


Figure 18 Comparison of Top Views of Isosurface Images of Specimen Edge at $\Theta =$ (a) 0° , (b) 6° , (c) 12° , and (d) 18°

5. CONCLUSIONS

In this study, multi-channel planar pitch-catch array probe and planar tandem array probe have been developed to improve detectability of three-dimensional defect. The ultrasonic flaw detection system and specific 3D-SAFT imaging algorithms have been particularly developed to use with these array probes.

Advantages of the planar array probes and flaw detection system are 1) no mechanical scan required, 2) saving inspection time, 3) increasing detectability of three-dimensional defect, and 4) with application of 3D-SAFT system, three-dimensional information of defect can be obtained with high accuracy.

The results of this study show great contribution to current ultrasonic detection technique that the defect information can be greatly extracted by using the planar array probe with application of 3D-SAFT.

Acknowledgements:

The authors are indebted to Dr. Eiichi Sasaki for his great valuable assistance. This study was supported by a Grant-in-Aid for Scientific Research (A)(1) under Project No. 11305034 and was one of the projects in SIG-1 of Science and Technology Research Body in Tokyo Institute of Technology

References:

- Achenbach, J.D. (2000), "Quantitative nondestructive evaluation," *International Journal of Solids and Structures*, **37**, 13-27.
- Krautkrämer, J. and Krautkrämer, H. (1983), "Ultrasonic Testing of Materials," Springer-Verlag.
- Soumekh, M. (1999), "Synthetic Aperture Radar Signal Processing," John Wiley & Sons.

PROPOSAL OF NEW STEEL STRUCTURES WHICH LIMIT DAMAGE TO CONNECTION ELEMENTS AT THE BOTTOM FLANGE OF BEAM-ENDS

S. Kishiki¹⁾, S. Yamada²⁾, T. Takeuchi³⁾, K. Suzuki⁴⁾, and A. Wada⁵⁾

1) Graduate Student, Structural Engineering Research Center, Tokyo Institute of Technology, Japan

2) Associate Professor, Structural Engineering Research Center, Tokyo Institute of Technology, Japan

3) Associate Professor, Dept. of Architecture and Building Engineering, Tokyo Institute of Technology, Japan

4) Manager, Building Construction Division, Nippon Steel Corporation, Japan

5) Professor, Structural Engineering Research Center, Tokyo Institute of Technology, Japan

kishiki@serc.titech.ac.jp, naniwa@serc.titech.ac.jp, toru@arch.titech.ac.jp,

suzuki.kazuaki1@eng.nsc.co.jp, wada@serc.titech.ac.jp

Abstract: In the Northridge (1994) and Kobe (1995) Earthquakes, some buildings suffered damage and lost their functions, although many buildings avoided collapse so as to save human life. If a heavy earthquake occurred in urban areas, the stop of the function of urban facilities would cause the severe economical loss. It is very important for structural engineers to consider restoring buildings at the early stage after an earthquake. That is to say, not only structural performances but also easy repairs after an earthquake are required for buildings. One of methods that make buildings have these abilities is the Damage-Controlled-Structure. This system consists of a mainframe and dampers. The mainframe can remain in elastic range during an earthquake, because dampers absorb the input energy of the earthquake. Today, by such a seismic design concept and developments of efficient dampers, many high-rise buildings with easy repairs are being constructed in urban area. However, in urban areas, there are many low-rise or medium-rise buildings which are not suitable for applying dampers. And even if they were buildings with dampers, high rotation capacities might be required at beam-ends of a mainframe. Since the earthquakes above occurred, a lot of studies have been carried out on beam-to-column connections, and new details at beam-to-column connections have been proposed. Nevertheless, the seismic design with these new details is based on plastic rotation capacity of principal members in a mainframe. In other words, these details cannot give easy repairs to structures.

The purpose of this study is to propose new ductile steel structure, which realizes easy repairs as well as structural performances. Main feature of this system is to limit plastic deformations (damage) to the connection elements, the weak-web-split-tee, at the bottom flange of beam-ends.

1. INTRODUCTION

In the Northridge (1994) and Kobe (1995) Earthquakes, some buildings suffered damage and lost structural functions, although many buildings avoided collapse so as to save human life. If a heavy earthquake occurs in urban areas, the loss of the function of urban facilities would cause severe economic loss. In urban areas, social and industrial activities cannot be lost for long. Therefore, it is very important for a structural engineer to consider restoring buildings soon after an earthquake. One of the methods that give buildings this ability is the Damage-Controlled-Structure (Wada et al., 1992 and Y. H. Huang, 1995) and it is shown in Fig.1. This system consists of a mainframe and dampers. The mainframe only supports gravity and can remain in elastic range during an earthquake, because dampers absorb the input energy of the earthquake. Therefore, buildings can be used continuously by repairing and exchanging dampers. Today, many high-rise buildings based on the design method of Damage-Controlled-Structure are being constructed.

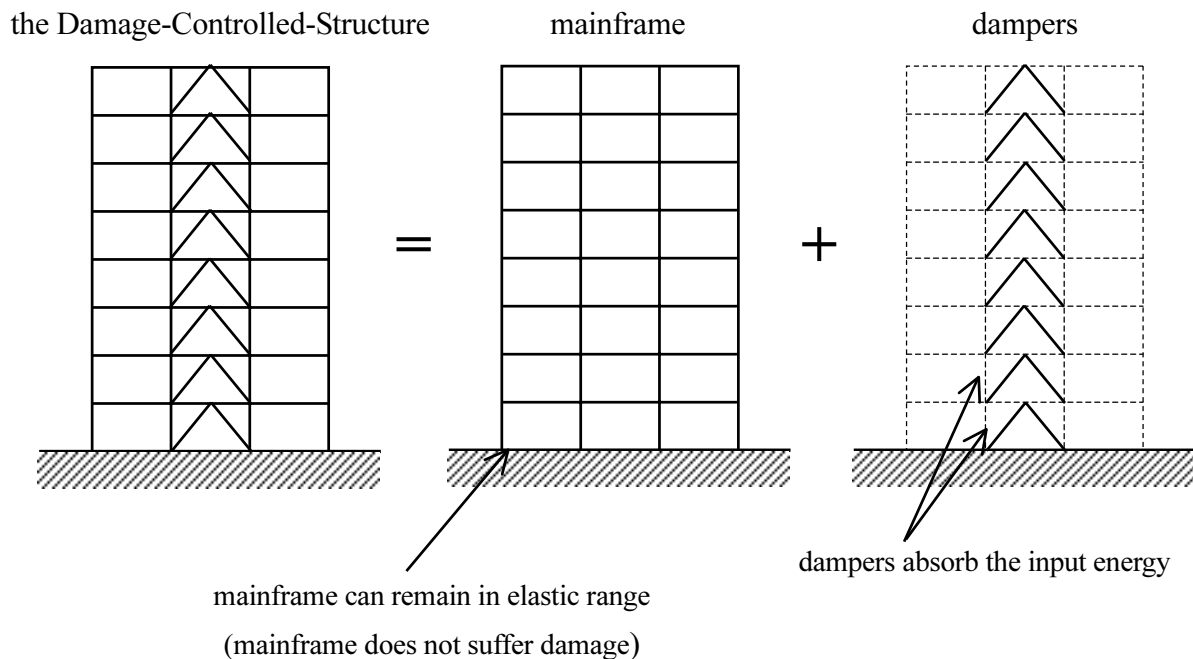


Fig.1 the Damage-Controlled-Structure (Wada et al., 1992 and Y. H. Huang, 1995)

However, in urban areas, there are many low-rise or medium-rise buildings which are not suitable for applying dampers. In the case of these buildings, naturally, energy absorption of an earthquake must be expected at the beam-ends (shown in Fig.2 (a)). And even if there were low-rise or medium-rise buildings with dampers, high rotation capacities would be required at the beam-ends of a mainframe (shown in Fig.2 (b)). It means that most low-rise or medium-rise buildings had been built based on the seismic design permitting damage at the beam-ends.

In the two earthquakes mentioned above, many steel structures suffered damage at beam-to-column connections, and some fractures of bottom flanges occurred at the beam-to-column connections. After these earthquakes, a remarkable number of studies have been made on beam-to-column connection. Some of them tried to investigate the causes of these fractures, and others proposed the new connection details to resolve the issues. Examples of the proposed details are as follows: the reduced beam section detail (RBS), the horizontal-haunch beam detail, the no-weld access hole detail, and the improved weld access hole detail. And many test results have showed us that each of them prevents a premature fracture and has a large plastic rotation capacity. As the result, The RBS detail has been recommended in the U.S. and no-weld access hole detail has been adopted in Japan. Nevertheless, seismic design with these details is based on the plastic rotation capacity of main members in the mainframe. And in those studies, little attention has been paid to repairing the connections. Consequently, we cannot easily repair the buildings when using these details. In other words, these proposed details have not been able to solve the issues that the past disasters caused.

If we can easily repair the mainframe with or without dampers, the buildings can be restored soon after an earthquake. We can do it even if they are naturally low-rise or medium-rise buildings. The purpose of this study is to propose a new ductile steel structure, which realizes not only structural performance but also easy repair after a heavy earthquake. Main feature of this system is that plastic

deformation concentrates on connection elements (the weak-web-split-tee, see 2.2.) at the bottom flange of beam-ends in the mainframe. In this paper, first, why damage has to concentrate on the connection elements at the bottom flange is shown. Next, the ability of the connection elements required in order to realize the proposed system is shown. Finally, the detail of the connection elements that satisfy the requirements is shown.

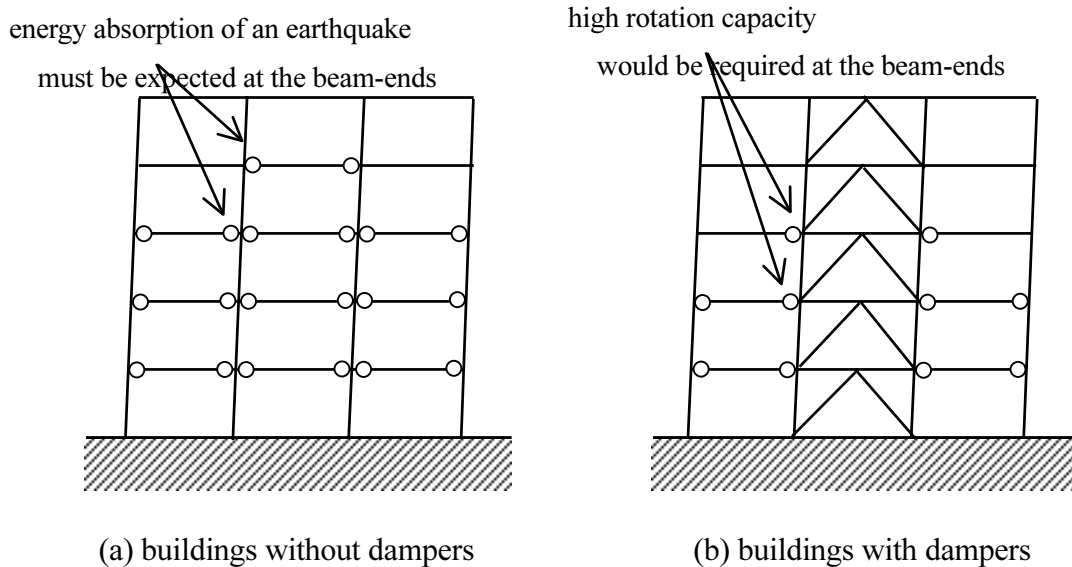


Fig.2 a seismic design based on damage at the beam-ends (low-rise or medium-rise buildings)

2. PROPOSAL OF NEW DUCTILE STEEL FRAMES

2.1 NEW DUCTILE STEEL FRAMES

There are two conditions that must be met to make structures easily repairable. One of them is to constitute structures using exchangeable members. The other is to limit damage to some of these exchangeable elements. In the Damage-Controlled-Structure, dampers on which damage concentrates are connected to a mainframe by exchangeable high-strength bolts. Naturally, beams and columns of the mainframe that are connected by high-strength bolts are more easily repairable than those that are welded. And it is thought that, by designing connection elements (Split-Tee (T-stub) or Angle) that are weaker than the beam and column, it is possible to limit damage to the connection elements. However, conventional Split-Tee (T-stub) shows different behaviors in tension and compression. This characteristic behavior prevents limiting damage to exchangeable elements. A behavior of a frame with conventional Split-Tee is shown in Fig.3. In the state of this deformation, a compression force occurs on the beam because the rotation points of left and right side differ. Consequently, at the connection, stiffness and yield strength would increase with this compression force, and local buckling on the bottom flange might be caused by this compression force. It means that the state of the

deformation with conventional Split-Tee is not suitable for limiting damage to connection elements.

With regards to limiting damage, the desirable state of the deformation with bolted connections would be shown in Fig.4. Main feature of this behavior is that plastic deformation is limited to the connection elements at the bottom flange. Consequently, The rotation points of left and right side stay at the top flange. Naturally, it avoids damage to the connection elements on the top flange, which is difficult to exchange. The point we wish to emphasize is that we can concentrate deformations of a mainframe on Split-Tee at the bottom flange, if the connection elements show the same behaviors in tension and compression (see 2.2.). By repairing and exchanging the connection elements at the bottom flange after an earthquake, buildings can continue to be used. Consequently, even if the building is not suitable for applying dampers or cannot absorb the input energy with only dampers, it can be repaired easily, such as the Damage-Controlled-Structure.

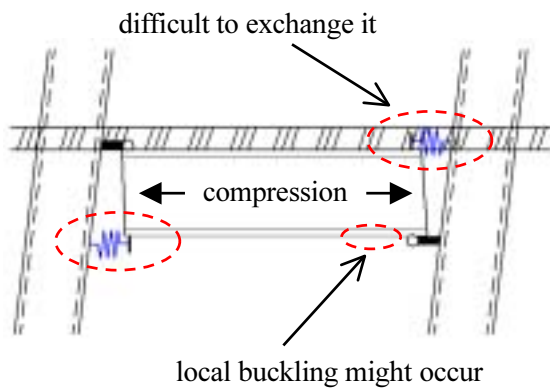


Fig. 3 The conventional deformation (with conventional Split-Tee)

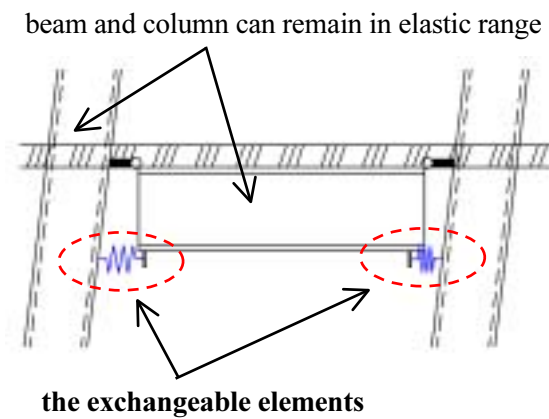
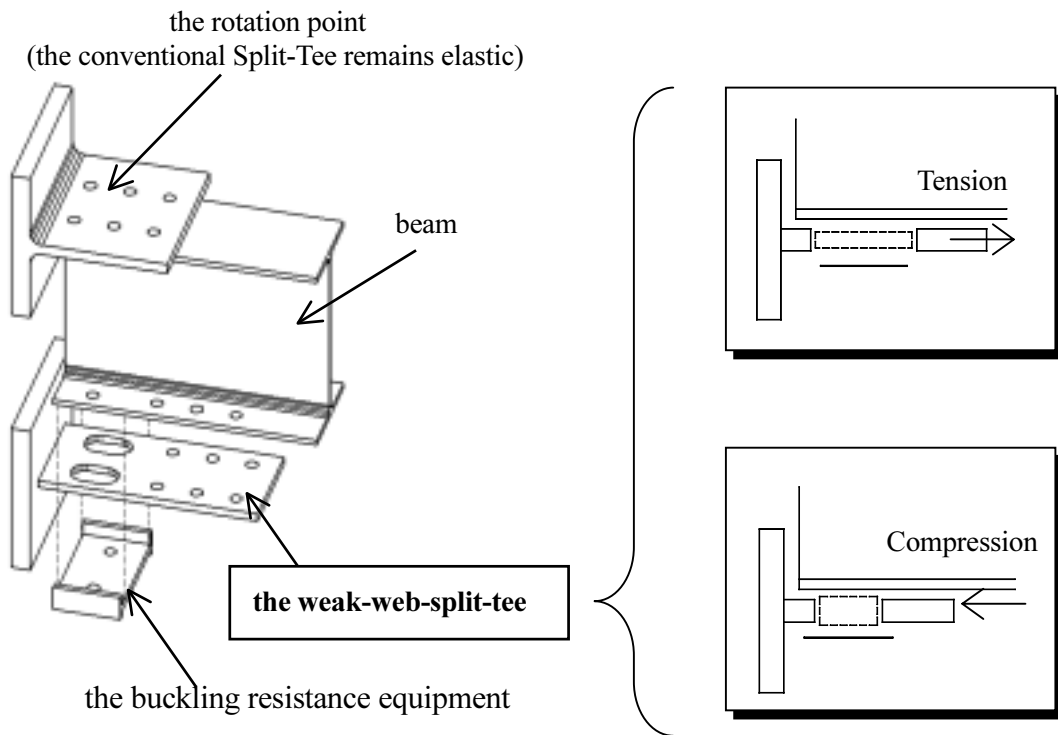


Fig. 4 The desirable deformation (with **the weak-web-split-tee** (see 2.2.))

2.2 NEW CONNECTION ELEMENTS (THE WEAK-WEB-SPLIT-TEE)

In order to form the desirable deformation to limit damage (shown in Fig.4), the damage must concentrate on the connection elements at the bottom flange. It means that the elements have to show same behavior in tension and compression. The new connection elements (shown in Fig.5), which are proposed by us, satisfy the requirement. A feature of the connection elements is that they have a reduced section at the web plate. By designing the weak section, it allows the connection to reach yield strength earlier than the beam, column, and the connection elements at the top flange. As the result, the rotation point of beam-ends would stay at the top flange, and deformation of the mainframe would concentrate on the connection elements at the bottom flange. Nevertheless, naturally, buckling occurs at the weak section when it is in compression. Therefore, we use the buckling resistance equipment shown in Fig.5 (a). Buckling of the weak web is avoided by putting the weak web between the bottom flange of the beam and the resistance equipment. By using the buckling resistance method, the Split-Tee can show the stable deformation capacities in tension and compression (shown in Fig.5 (b)).



(a) detail of beam-to-column connections

(b) behavior of the weak-web-split-tee

Fig. 5 the beam-to-column connection with the weak-web-split-tee

3. CONCLUSIONS

Many steel structures suffered damage at beam-to-column connection under the past heavy earthquakes. After these disasters, although a lot of researchers proposed new connection details, most of them paid little attention to repairing after an earthquake. In urban areas, social and industrial activities cannot stop for long, because it causes the severe economic loss. Therefore, to consider restoring buildings is very important for structural engineers and urban areas. Today, structural engineers and urban areas require buildings that can do it.

The purpose of this study is to propose the new ductile steel frames, which realize not only structural performances but also easy repair after an earthquake. Main feature of this system is limiting damage to connection elements at the bottom flange of beam-ends. In this paper, first, why damage has to concentrate on the connection elements at the bottom flange was shown. Next, the ability of the connection elements required in order to realize the proposed system was shown. Finally, the detail of the connection elements (the weak-web-split-tee, see 2.2.) that satisfy the requirements was shown.

References:

- Wada, J. J. Connor, H. Kawai, M. Iwata and A. Watanabe, "Damage Tolerant Structure", Fifth U.S.-Japan Workshop on the Improvement of Building Structural Design and Construction Practice, pp.1-13
- Y. H. Huang, "Damage Controlled Seismic Design for Tall Steel Buildings", Dr. thesis, Tokyo Institute of Technology (in Japan), 1995.

APPLICATIONS OF INELASTIC SPD METHOD FOR ESTIMATING RELATIVE DISPLACEMENT TO AVOID POUNDING OF ADJACENT BUILDINGS

B. T. Tran¹⁾ and K. Kasai²⁾

1) Graduate Student, Department of Built Environment, Tokyo Institute of Technology, Japan

2) Professor, Structural Engineering Research Center, Tokyo Institute of Technology, Japan
tthbinh@enveng.titech.ac.jp, kasai@serc.titech.ac.jp

Abstract: Pounding between closely spaced structures can be a serious hazard in seismically active metropolitan areas. Peak relative displacement between these structures can be obtained by the proposed spectral difference (SPD) rule. Unlike time history analysis method, a closed form solution can be applied to discuss trends of relative displacement of buildings in terms of periods, damping ratios, yield strength, ductility demands of the buildings as well as earthquake spectrum. In this study, practical implementation of the SPD rule through a simple procedure is proposed in order to estimate required separation to preclude pounding between adjacent structures. Validation study is conducted, using a relatively large ensemble of 33 ground motion records on a number of various adjacent building pairs that are consistent with the current code requirements for strength and stiffness. Inconsistencies of other spectrum methods and the accuracy of SPD-based method are explained through comparisons with the time history analysis results.

1. INTRODUCTION

In recent years, there has been an increased awareness of the potential impact of buildings during moderate to strong earthquakes due to insufficient separation distance (Bertero 1986, Rosenblueth and Meli 1986, Kasai and Maison 1997). Controlling the relative displacement between adjacent buildings (Fig. 1) is an important method for preventing these buildings pound each other during seismic excitation. The magnitude of the required seismic gap s_{req} can be estimated by calculating their peak relative displacement through time history analysis. However, since one cannot determine specifically the future earthquake time history, a spectrum approach that uses an ensemble from the past as well as potential earthquakes would be more reliable and preferred.

In fact, the peak relative displacement depends not only on the peak displacement of each separate structure but also on the *vibration phase*, which is associated with their elastic and inelastic responses. Therefore, the key parameters such as adjacent building's vibration periods, damping ratios, heights, ductility demands, and even hysteresis types must be taken into account for determining reasonable gap between structures. Kasai et al. (1996) presented a method called "spectral difference (SPD) rule" using response spectrum to estimate the maximum relative displacement. The method provides a closed-form solution that relates those key parameters with the buildings' relative motion. However, using directly this SPD rule requires either inelastic response spectrum or time history analysis to obtain peak inelastic displacement of each separate building.

This study is to propose a practical SPD-based method by implementing more simplifications. The proposed method employs only elastic response spectrum to approximate peak inelastic displacement of each structure. Then it considers a number of various adjacent building pairs having stiffness and strength consistent with the Japanese seismic code and an ensemble of 33 earthquakes scaled to

different levels for the validation study. The accuracy of the SPD-based method is illustrated by comparing results with time history analysis and other methods. We also clarify the trend of the peak relative displacement by explaining the complex effect of the mentioned key factors through this SPD-based method. This work aims to emphasis on the significant effect of yielding on building's phase motion and relative displacement. The study would be useful for understanding and controlling the relative displacement of adjacent structures.

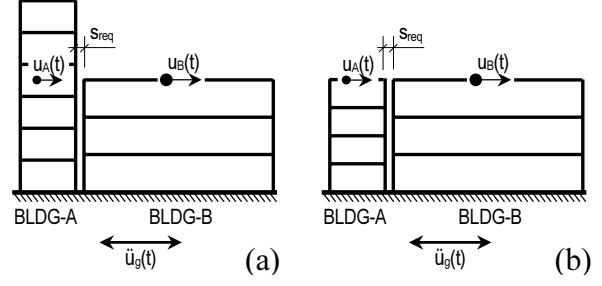


Figure 1. Relative Displacement of Adjacent Bldgs.

2. RELATIVE DISPLACEMENT AND VARIOUS ESTIMATES

2.1 Past Rules

From Fig. 1, the relative displacement $u_{rel}(t)$ between buildings A and B is $u_{rel}(t) = u_A(t) - u_B(t)$, where $u_A(t)$, $u_B(t)$ = displacement time histories at potential pounding locations. From now on, the subscripts “A” and “B” shall refer to buildings A and B, respectively.

Required separation between buildings A and B can be determined as $u_{rel}(TH) = \max |u_{rel}(t)|$, ‘TH’ indicates results from time history analysis, and pounding is avoided if the separation distance $s_{req} > u_{rel}(TH)$.

Two other methods for estimating the peak relative displacement are the absolute-sum (ABS) rule: $u_{rel}(ABS) = u_A + u_B$ and the square-root-of-sum-of-squares (SRSS) rule: $u_{rel}(SRSS) = \sqrt{u_A^2 + u_B^2}$, where u_A , u_B = the absolute peak displacements of the buildings, which can be obtained from the response spectrum. The use of the SRSS rule is stipulated in the U.S. seismic code (IBC, 2000).

2.2 Spectral Difference (SPD) Rule

Unlike the ABS and SRSS rules, the SPD rule (Kasai et al. 1996) uses a cross correlation coefficient ρ_{AB} , and

$$u_{rel}(SPD) = \sqrt{u_A^2 + u_B^2 - 2\rho_{AB}u_Au_B} \quad (1)$$

The ρ_{AB} reflects vibration phase of buildings A and B, and it was derived from a random vibration theory as follows (Kasai et al. 1996, Der Kiureghian 1980):

$$\rho_{AB} = \frac{8\sqrt{\xi_A^*\xi_B^*}(\xi_B^* + \beta^*\xi_A^*)\beta^{*1.5}}{(1 - \beta^{*2})^2 + 4\xi_A^*\xi_B^*(1 + \beta^{*2})\beta^* + 4(\xi_B^{*2} + \xi_A^{*2})\beta^{*2}} \quad (2)$$

where β^* = ratio of effective vibration periods T_B^*/T_A^* , ξ_A^* and ξ_B^* = effective damping ratios. Note that $0 \leq \rho_{AB} \leq 1$, and larger ρ_{AB} means more in-phase motion, and consequently smaller u_{rel} (Eq. 1).

Eq. 2 explains that T^* and ξ^* play a key role in vibration phase. When β^* is close to 1, and/or ξ_A^* and ξ_B^* are large, ρ_{AB} approaches 1, and in-phase motion develops. Inclusion of damping comes from the fact that damping tends to eliminate a free vibration portion of the seismic response, and mainly a forced vibration portion remains, making the two buildings vibrate similarly to the

ground motion (Kasai et al., 1996; Kasai et al., 2002).

For the buildings of bilinear hysteresis (Fig. 2a) and stiffness degrading hysteresis (Fig. 2b), the above effective properties are given as:

$$\text{Bilinear:} \quad T^* = T[1 + 0.09(\mu - 1)] \quad ; \quad \xi^* = \xi + 0.084(\mu - 1)^{1.3} \quad (3a)$$

$$\text{Degrading:} \quad T^* = T[1 + 0.18(\mu - 1)] \quad ; \quad \xi^* = \xi + 0.16(\mu - 1)^{0.9} \quad (3b)$$

where T , ξ , μ = initial elastic vibration period, initial viscous damping ratio, and peak ductility demand, respectively.

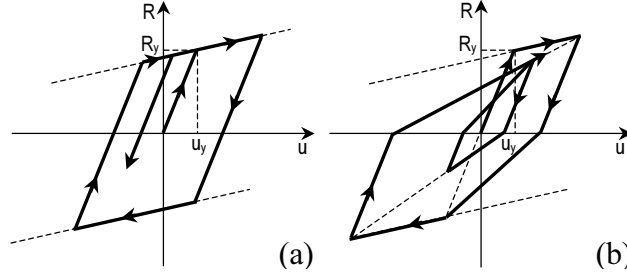


Figure 2. Hysteresis Behavior: (a) Bilinear Building Model, and (b) Stiffness Degrading Model.

3. TRENDS OF RELATIVE MOTION AND PHASE

3.1 Trends of Relative Motion

Consider two single-degree-of-freedom (SDOF) systems A and B with initial vibration periods T_A and $T_B = 1.0s, 1.3s$, and initial viscous damping ratios $\xi_A = \xi_B = 0.02$. The stiffness degrading hysteresis model (Fig. 2b) is used with strain-hardening ratio 5%. The system is designed under the three cases described below, and they are subjected to the 1940 Imperial Valley earthquake (117 El Centro station, 0.35g).

Case 1: Systems are elastic and only small damping is given. Thus, they must vibrate mostly out-of-phase.

Case 2: Systems are inelastic and designed to develop $\mu_A = \mu_B = 3$. In-phase motion is promoted due to the hysteretic damping.

Case 3: Systems are inelastic, and designed to develop distinct values of $\mu_A = 6$ and $\mu_B = 3$. Like case 2, in-phase motion develops due to hysteretic damping. In addition, although $T_B/T_A = 1.3$, different μ_A and μ_B causes $T_B^*/T_A^* \approx 1$, may lead to strong in-phase motion.

As Fig. 3a shows, Case 1 develops out-of-phase movement between the elastic systems A and B due to their different periods. In contrast, the responses of inelastic systems in Cases 2 and 3 are significantly in phase (Figs. 3b, and 3c). Fig. 3d plots $u_{rel}(t)/(u_A+u_B)$, which highlights increasing trend of the in-phase motion in the order of Cases 1, 2, and 3. Table 1 lists magnitudes of each response quantity.

The SPD, SRSS, and ABS rules are used to estimate u_{rel} of the above three cases by using the peak displacements u_A, u_B obtained from the time history analyses. In case of the SPD method, the values are also divided by the yield displacements to calculate μ_A, μ_B , and the cross correlation ρ_{AB} (Eq. 2)

Table 2 indicates superior prediction of u_{rel} by the SPD rule. The errors of the SRSS and ABS rules increase, especially when buildings exhibit large inelastic deformations. Eqs. 1 to 3 of the SPD rule, therefore, could clarify the complex effects from the initial vibration periods, viscous damping ratios, and ductility demands varied herein. This point will be further demonstrated below.

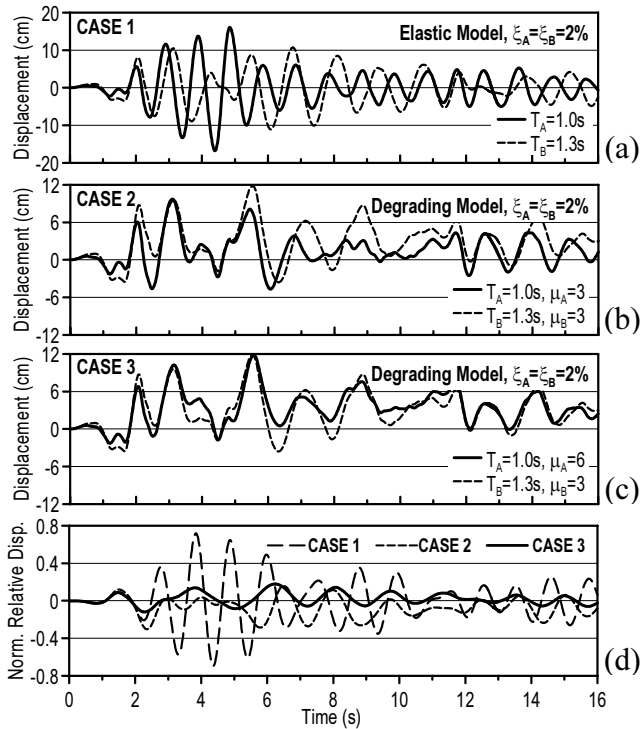


Figure 3. Time History Responses of the Systems in Three Cases.

3.2 Trends of Vibration Phase

Fig. 4 beside plots cross correlation coefficients ρ_{AB} (Eq. 2) in order to illustrate general trends of systems' phase. For elastic systems (Fig. 4a), the ρ_{AB} is high only if both $T_B/T_A \approx 1$ and $\xi_B/\xi_A \approx 1$, and it is very low otherwise. For inelastic systems, however, $T_B/T_A \neq 1$ can lead to the largest ρ_{AB} , depending on the values of μ_A and μ_B (Figs. 4c and 4d). This is because the effective period and damping, instead of initial period and damping, governs ρ_{AB} when systems are inelastic. Case 3 gives a typical example, where $T_B^*/T_A^* \approx 0.93$ (Table 2) in contrast to $T_B/T_A = 1.3$, and it gave the smallest u_{rel} among all cases (Fig. 3).

Since T^* and ξ^* are affected by the ductility demand μ , Fig. 4 provides the direct and useful information regarding the effect of μ . The peaks of the ρ_{AB} -curves are close to 1.0 for a wide range of T_B/T_A when $\mu > 2$, indicating importance of including even moderate amount of yielding.

Thus, large ρ_{AB} results even when the initial period ratio $T_B/T_A \neq 1$, and maximum ρ_{AB} is obtained when systems A and B have different μ 's. This is the reason why Case 3 shows more in-phase motion than Case 2.

Table 1. Results of Three Considering Cases.

Case	Ductility		Peak Disp. (cm)			$\frac{u_{rel}}{\max(u_A, u_B)}$	$\frac{u_{rel}}{u_A + u_B}$
	μ_A	μ_B	u_A	u_B	u_{rel}		
1	1	1	16.81	11.09	20.02	1.19	0.72
2	3	3	9.70	11.77	6.50	0.55	0.30
3	5	3	11.84	11.77	4.23	0.57	0.18

Table 2. Approximation Results Using SPD and Other Methods.

Case	Effective Parameters				ρ_{AB}	$\frac{u_{rel}(SPD)}{u_{rel}(TH)}$	$\frac{u_{rel}(SRSS)}{u_{rel}(TH)}$	$\frac{u_{rel}(ABS)}{u_{rel}(TH)}$
	T_A^*	T_B^*	ξ_A^*	ξ_B^*				
1	1.00	1.30	0.02	0.02	0.02	1.00	1.01	1.39
2	1.36	1.77	0.32	0.32	0.85	0.96	2.35	3.30
3	1.90	1.77	0.70	0.32	0.91	1.19	3.95	5.58

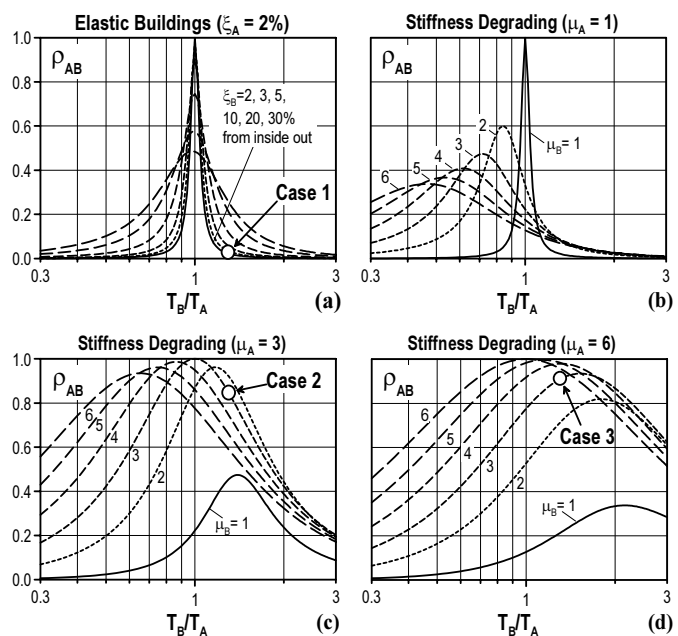


Figure 4. General Trends of Buildings' Phase.

4. SIMPLIFIED SPD-BASED METHOD

4.1 Inelastic Displacement Prediction by Elastic Spectrum

Studies have been conducted worldwide to predict inelastic response via elastic spectrum. They utilize the strong correlation between the ductility demand μ and the strength reduction factor R_μ .

$$R_\mu = \frac{Q_e}{Q_y} = \frac{\Delta_e}{\Delta_y} \quad (4)$$

where Q_y, Δ_y = yield shear and yield displacement of the system given, and Q_e, Δ_e = base shear and displacement when the system is presumed to behave elastically. The above displacements are defined at the effective height (Chopra 1995) H_{eff} of the building.

The $\mu - R_\mu$ relationships have been proposed by Newmark and Hall (1973), Uang (1992), and others. In the present study, we will utilize Nassar and Krawinkler's rule (1991) as follows:

$$\mu = 1 + \frac{R_\mu^c - 1}{c} \quad ; \quad c = \frac{T^a}{1 + T^a} + \frac{b}{T} \quad (5a,b)$$

where a and b depend on the strain-hardening ratio α .

Once Δ_e is estimated from an elastic spectrum, μ is obtained from Eqs. 4 and 5, and the peak inelastic displacement Δ at height H_{eff} is

$$\Delta = \mu \cdot \Delta_y \quad (6)$$

Following Nassar and Krawinkler (1991), Uang (1992), and Kasai et al. (2003), the damping ratio shall be 5% when using the elastic spectrum.

4.2 Step-by-Step Procedure for Simplified SPD-Based Method

For simplified prediction of u_{rel} without conducting time history analysis, we combine the SPD rule with elastic response spectrum. The height of building A is set equal to or greater than that of building B, i.e., $H_A \geq H_B$ will be considered (Fig. 1).

The procedure obtains the following parameters in order:

- (1) Elastic displacements Δ_{eA} and Δ_{eB} from elastic spectrum.
- (2) Inelastic displacements Δ_A and Δ_B using Eqs. 4 to 6.
- (3) Inelastic displacements u_A and u_B at the common critical height.
- (4) Effective periods T_A^* and T_B^* , damping ratio ξ_A^* and ξ_B^* from Eqs. 3.
- (5) Cross correlation ρ_{AB} from Eq. 2, and $s_{req} = u_{rel}(SPD)$ from Eq. 1.

In the present study, a simple straight-line building deformation mode is assumed. For step (3) above, therefore, effective height $H_{eff} = 2H/3$ is considered for each building, and the following relationship is used: $u_A = 1.5(H_B/H_A) \Delta_A$, and $u_B = 1.5 \Delta_B$

4.3 Building Models Consistent with Code

Building models to be used in the following sections will be defined here. The preliminary data required for the application of the SPD-based method are the initial period T and the yield displacement Δ_y of each building. From now on, T is assumed to coincide with that given by the Japanese Seismic Code (IAEE, 1996), i.e., $T = 0.03H$ and $T = 0.02H$, where H = total height of the building in meters, for steel building and concrete building, respectively.

Building yield shear is set to ΩQ_y , where Ω = overstrength factor, and Q_y = yield shear required by the code such as:

$$Q_y = C_0 \cdot R_t \cdot W \quad (7)$$

In Eq. 7, $C_0 = 0.25$ and 0.30 are assumed for the steel and concrete buildings, respectively. The values are somewhat arbitrary as long as $C_0 \geq 0.2$, and they are made equal to the D_s -factors (IAEE, 1996). Indeed, these higher values may better approximate the actual behavior. However, note also that the overstrength factor Ω can be varied, making the specific C_0 -value less significant.

The design spectral coefficient R_t is obtained from the formula as specified in Japanese Seismic Code (IAEE, 1996), where medium soil can be assumed. Based on these, the yield displacement Δ_y at height H_{eff} is calculated as:

$$\Delta_y = C_0 \cdot R_t \cdot g \left(T / 2\pi \right)^2 \quad (8)$$

5. VALIDATION OF SIMPLIFIED SPD-BASED METHOD

5.1 Parameters Considered for Validation

A validation study is now conducted in order to examine the accuracy of the SPD-based method, and to obtain the general trend of u_{rel} between the building pairs consisting of various steel and concrete frames. In this study, buildings have 8 different heights of 3, 6, 9, 12, 15, 18, 21, and 24 stories with a common story height of 4m. For building pairs A and B, all possible combinations of 8 different heights are considered with the condition of $H_A \geq H_B$ (Fig. 1). The total number of building pairs is 36.

Additionally, 4 cases of material type combinations for buildings A and B are assumed: steel vs. steel; concrete vs. concrete; steel vs. concrete; and concrete vs. steel, respectively. In total, the number of building pairs is 144 [(36 height combinations) x (4 material type combinations)].

For each building pair, 31 past earthquakes and 2 artificial earthquakes (Kasai et al. 2003) are used, and each record is applied in both positive and negative directions. The records cover a variety of seismic intensities, and it is reasonable to scale them to the same peak ground acceleration (PGA). Thus, 4 different PGA scales of 0.2g, 0.4g, 0.6g, and 0.8g are considered for each record. In total, the number of earthquakes considered for each building pair is 264 [(33 earthquakes) x (2 directions) x (4 PGA scales)].

Fig. 5 shows the mean acceleration spectrum and mean \pm standard deviation of 33 records scaled to 0.4g. Fig. 5 also shows $R_t \cdot g$ curve for the medium soil condition. Yield strengths of 8 steel buildings and 8 concrete buildings are also plotted, respectively.

Using the elastic spectrum of each earthquake, inelastic peak displacement is estimated, and used for all the SPD-, SRSS-, and ABS-based methods. Also, in order to obtain exact solution for u_{rel} , dynamic time history analyses are conducted using a SDOF nonlinear analysis program NONSPEC (Mahin and Lin 1983). In summary, this validation study examines a total of 38,016 cases [(144 building pairs) x (264 scaled records)].

5.2 Validation Results

For each of the cases mentioned above, the ratios of $u_{rel}(\text{SPD})$, $u_{rel}(\text{SRSS})$, and $u_{rel}(\text{ABS})$ to the

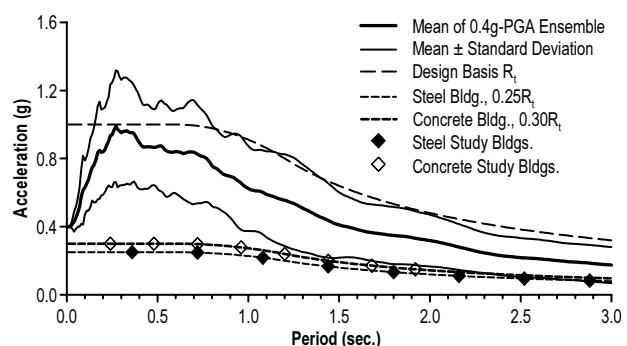


Figure 5. Mean and Deviation of 33 Acceleration Spectra (PGA=0.4g), Design Spectrum and Design Strength of Buildings.

$u_{rel}(TH)$ are obtained, and they are averaged over 36 height combinations and 2 earthquake directions per combination of material type, earthquake, and PGA scale. The average values are shown in Fig. 6.

Fig. 6 shows that $u_{rel}(SPD)/u_{rel}(TH) \approx 1$ for most cases, indicating superior accuracy of the SPD-based method. ABS- or SRSS-based method appears to be largely conservative, as the PGA scale increases. This is because they do not account for the important effect of inelastic deformation, which, under stronger earthquake causes more in-phase motion between the two buildings.

The important effect of inelastic in-phase motion is seen especially for the strong earthquakes like Kobe Japan (earthquakes 7 to 12), Iran and Northridge (earthquakes 17 to 22). These earthquakes, even scaled to the same PGA as other earthquakes, force each building to deform larger due to their higher spectral values over a wide period range, but they also produce at the same time more in-phase motion between the two buildings. Such tendencies are accurately predicted by the simplified SPD-based method.

When PGA is 0.2g, the SRSS-based method is almost as accurate as the SPD-based method. This is because the average spectrum of 0.2G earthquakes approaches the buildings' design strength spectra, as can be imagined from Fig. 5. Thus, the buildings responded almost elastically, resulting in the small effective damping and consequently the small correlation ρ_{AB} .

Note also that, unlike the other methods, the SPD-based method implicitly includes material types and corresponding hysteretic characteristics, and it always gives very stable estimates, irrespective of any material type combinations. Although we observe some scattering of its estimates for stronger earthquakes of 0.8g PGA, the standard deviation (not shown for ABS and SRSS methods) does clearly strengthen the stable degree of the SPD-based method over the ABS- and SRSS-based methods.

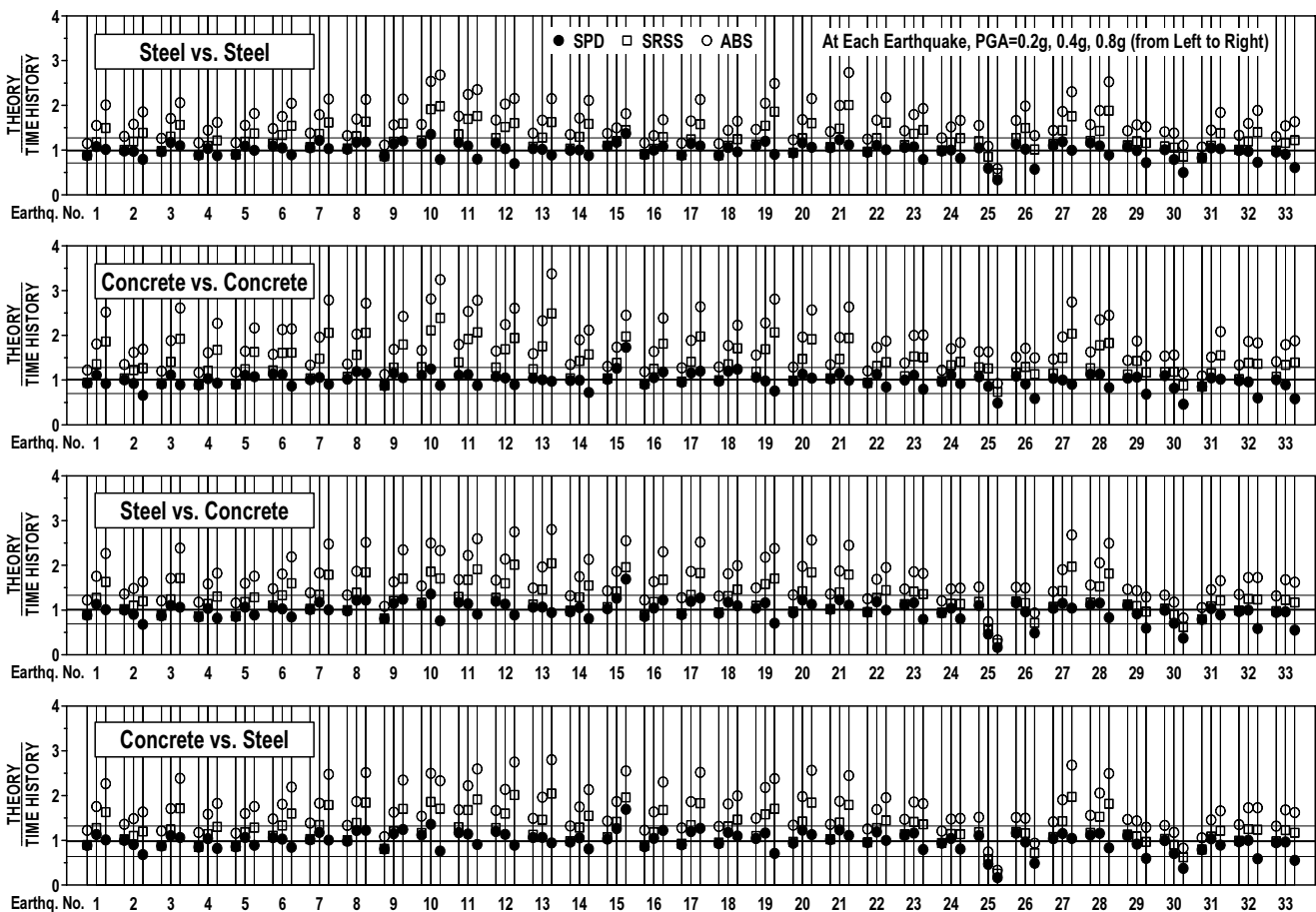


Figure 6. Average Ratios of $u_{rel}(SPD)$, $u_{rel}(SRSS)$, and $u_{rel}(ABS)$ to Exact Solution $u_{rel}(TH)$.
(Thick and thin horizontal lines represent average accuracy and average \pm standard deviation of the SPD-based method)

6. CONCLUSIONS

This paper has proposed a new method to estimate the seismic peak relative displacement between two inelastic buildings, by combining the writers' spectral difference (SPD) rule and elastic response spectrum. The conclusions are as follows:

(1) The method is validated through extensive numerical experiments using numerous code-compatible building pairs with different heights and material combinations, as well as 33 earthquakes of 2 directions, scaled to 4 different levels. The method is found to accurately estimate the relative displacement, with a narrow variability of error.

(2) Determination of relative displacement requires considerations of many factors such as; building heights, elastic vibration periods, initial yield strengths, hysteresis types, and spectrum characteristics as well as intensities of the earthquakes. Only the SPD-based method explicitly accounts for and clarifies the complex effects of these key parameters, and its use is simple.

(3) The ABS-based method is excessively conservative for the level of earthquake as well as building stiffness and strength, specified in the current code. The SRSS-based method gives a reasonably conservative estimate for moderate earthquakes, but remains incorrect for strong earthquakes because of not accounting for the relevant effect of hysteresis damping.

Acknowledgements:

The Ministry of Education, Science and Culture provided support for this study in the form of Grants-in-Aid for Scientific Research, Category C (Research Representative: Kazuhiko Kasai), and the second author's Monbu Kagakusho Scholarship. The authors gratefully acknowledge the support. The authors also thank Mr. Jagiasi for his initial participation.

References:

- Bertero, V.V. (1986), "Observation of Structural Pounding," *Proc., International Conference: the Mexico earthquake-1985*, ASCE, NY., 264-278.
- Chopra, A.K. (1995), "Dynamics of Structures: Theory and Applications to Earthquake Engineering," Prentice-Hall, Inc.
- Der Kiureghian, A. (1980), "A Response Spectrum Method For Random Vibrations," *EERC Report No. UCB/EERC-80/15*, University of California, Berkeley, California.
- IAEE (1996), "Regulations for Seismic Design, A World List – 1996," International Association for Earthq. Eng., Japan.
- IBC (2000), "International Building Code," International Code Council, Inc., Falls Church, Virginia.
- Jeng, V. and Kasai, K. (1996), "Spectral Relative Motion of Two Structures Due To Seismic Travel Waves," *J. Struct. Eng.*, ASCE, **122**(10), 1128-1135.
- Kasai, K., Ito, H., and Watanabe, A. (2003), "Peak Response Prediction for a SDOF Elasto-Plastic System Based on Equivalent Linearization Technique," *J. Struct. Constr. Eng.*, AIJ **571**(9), 53-62.
- Kasai, K., Jagiasi, R.A., and Jeng, V. (1996), "Inelastic Vibration Phase Theory For Seismic Pounding Mitigation," *J. Struct. Eng.*, ASCE, **122**(10), 1136-1147.
- Kasai, K. and Maison, B.F. (1997), "Building Pounding Damage During The 1989 Loma Prieta Earthquake," *Engineering Structures*, **19**(3), 195-207.
- Kasai, K., Motoyui, S., and Ooki, Y. (2002), "A Study on Application of Viscoelastic Dampers to a Space Frame and Response Characteristics under Horizontal Ground Motions," *J. Struct. Constr. Eng.*, AIJ **561**(11), 125-135.
- Mahin, S.A. and Lin, J. (1983), "Construction of Inelastic Response Spectra for Single Degree of Freedom Systems," *EERC Report No. UCB/EERC-83-17*, University of California, Berkeley.
- Miranda, E. (1993), "Site-Dependent Strength Reduction Factors," *J. Struct. Eng.*, ASCE, **119**(12), 3503-3519.
- Miranda E. (1994), "Evaluation of Strength Reduction Factors for Earthquake-Resistant Design," *Earthquake Spectra*, Earthquake Engineering Research Institute, **10**(2), 357-379.
- Nassar, A.A., Krawinkler, H. (1991), "Seismic Demands for SDOF and MDOF Systems," The John A. Blume Earthquake Engineering Center, Stanford University, California.
- Newmark, N.M. and Hall, W.J. (1973), "Seismic Design Criteria for Nuclear Reactor Facilities," *Report No.46*, Building Practices for Disaster Mitigation, National Bureau of Standards, U.S. Department of Commerce.
- Rosenblueth, E. and Meli, R. (1986), "The 1985 Earthquake: Causes and Effects in Mexico City," *Concrete Journal*, American Concrete Institute, **8**(5), 23-24.
- Uang, C.M. (1992), "Seismic Force Reduction and Displacement Factors," *Proceedings of 10th World Conference on Earthquake Engineering (WCEE)*, Madrid, Spain.

SIMPLIFIED PEAK RESPONSE EVALUATION AND DESIGN FOR ELASTO-PLASTICALLY DAMPED STRUCTURES

H. Ito¹⁾ and K. Kasai²⁾

1) Graduate Student, Department of Built Environment, Tokyo Institute of Technology, Japan

*2) Professor, Structural Engineering Research Center, Tokyo Institute of Technology, Japan
ihiroshi@enveng.titech.ac.jp, kasai@serc.titech.ac.jp*

Abstract: This paper proposes a practical theory for peak response evaluation method and a design approach for elasto-plastically damped structure in preliminary seismic design. The proposed theory is based on the single-degree-of-freedom (SDOF) idealization of multistory building structure, and uses the so-called “control performance curve” which simultaneously expresses the seismic performance as a function of stiffness parameter, ductility demand and seismic response spectrum. A rule to convert a SDOF design to a multi-story design and arrangement of damper stiffness over the height of structure is also presented. The accuracy of this method is validated via extensive time history simulations over a wide range of building models.

1. INTRODUCTION

In recent years passive control of building structures by incorporating various energy dissipation devices (dampers) has become common in Japan. In particular, the use of elasto-plastic (EP) damper, such as buckling-restrained brace, for passively-controlled structure have gained widespread practical applications. The EP dampers substantially reduce story drifts and member forces by adding hysteretic damping and stiffness to the primary structure (frame) under earthquake excitation. In preliminary seismic design, however, lack of comprehension of the relationship among response reduction, amount of damper and input ground motion induces an irrational approach, which requires numerous time history simulations.

Objectives of this paper are to propose a practical theory for peak response evaluation method and a design approach for elasto-plastically damped structure in preliminary seismic design, and to verify the accuracy of this method. The proposed theory employs the SDOF idealization of multistory building structure and equivalent linearization technique. A rule to convert a SDOF design to a multi-story design and arrangement of damper stiffness over the height of structure is also presented. The accuracy of this method is validated via time history simulations over a wide range of building models. Basic part of this paper is adopted in “JSSI manual for design and construction of passively-controlled buildings in Japan (2003)”.

2. DYNAMIC PROPERTIES OF SDOF EP SYSTEM

2.1 Damper and System

As Figure 1 shows, SDOF model of EP system consists of a mass and two springs which show EP

damper and frame connected in a row to the mass. EP damper is modeled as elasto-perfectly-plastic with elastic stiffness K_d and ductility demand μ_d , whereas frame behaves linearly with elastic stiffness K_f (Figure 2(a),(b)). Fundamental vibration period and damping ratio of frame are defined as T_f and h_0 . Elastic stiffness K_0 , fundamental vibration period T_0 and ductility demand μ of EP system are given by Eq. 1(a)-(c).

$$K_0 = K_f + K_d, \quad T_0 = \sqrt{\frac{K_f}{K_0}} \cdot T_f, \quad \mu = \mu_d \quad (1a-c)$$

Equivalent linear (secant) stiffness of EP system K_{eq} is

$$K_{eq} = K_f + \frac{K_d}{\mu} = \frac{1 + p(\mu - 1)}{\mu} \cdot K_0, \quad p = \frac{K_f}{K_f + K_d} \quad (2a,b)$$

where p = ratio of post-yield stiffness to elastic stiffness of the system.

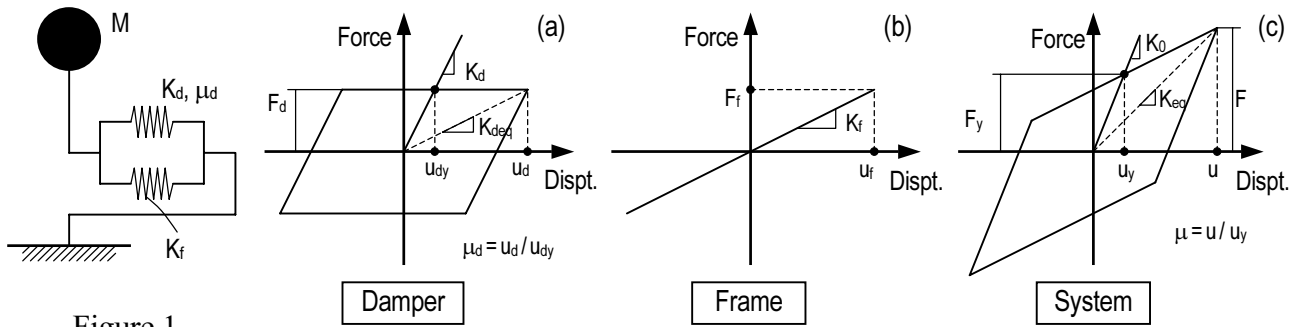


Figure 1
SDOF Model
of EP System

Figure 2 Force – Displacement Characteristic
(a)Damper, (b)Frame and (c)System

2.2 Equivalent Period and Equivalent Damping Ratio of System

According to Eq. 2(a), the equivalent vibration period T_{eq} of system is

$$T_{eq} = \sqrt{\frac{K_f}{K_{eq}}} \cdot T_f = \sqrt{\frac{p\mu}{1 + p(\mu - 1)}} \cdot T_f \quad (3)$$

The damping ratio of the EP system at ductility demand μ' can be evaluated as the energy dissipated per cycle divided by 4π times the elastic strain energy obtained from secant stiffness. We define the equivalent damping ratio h_{eq} of system as the average of the damping ratio corresponding to ductility factor μ' , considering the randomness of earthquake motion as shown in the work by Kasai et al (1998).

$$h_{eq} = h_0 + \frac{1}{\mu} \int_1^\mu \frac{2(1-p)(\mu'-1)}{\pi[1+p(\mu'-1)]} d\mu' = h_0 + \frac{2}{\mu\pi p} \ln \left[\frac{1+p(\mu-1)}{\mu^p} \right] \quad (4)$$

3. SYMPLIFIED RESPONSE EVALUATION FOR SDOF EP SYSTEM

3.1 Response Reduction Factor of Displacement and Acceleration

Peak response of the EP system will be obtained from a linear response spectrum using T_{eq} and h_{eq} indicated above. We define S_d , S_{pv} , and S_{pa} as response displacement, response pseudo velocity and response pseudo acceleration spectra, respectively. For the frame, their values are obtained from an expected seismic response spectrum, T_f and h_0 . With the response of frame, peak response of the EP system is expressed by considering following two effects due to inserting the damper.

1. The effect of vibration period change (from T_f to T_{eq}) tends to reduce response displacement and increases response acceleration.
2. The effect of hysteretic damping increase (from h_0 to h_{eq}) reduces both response displacement and response acceleration. This effect is represented by damped effect factor D_h , which is an “average” reduction of S_d , S_{pv} , and S_{pa} (Eq. 5).

$$D_h = \sqrt{\frac{1 + \alpha h_0}{1 + \alpha h_{eq}}} \quad (5)$$

where $\alpha = 25$ (for an ensemble of 31 observed earthquakes from 0.2 to 3 sec of vibration period (Kasai et al., 2003)). Peak responses of the EP system $S_d(T_{eq}, h_{eq})$ and $S_{pa}(T_{eq}, h_{eq})$ normalized to those of the frame $S_d(T_f, h_0)$ and $S_{pa}(T_f, h_0)$ are defined as displacement reduction R_d and pseudo acceleration reduction R_{pa} (for EP system acceleration reduction $R_a = R_{pa}$), respectively. Considered the two effects indicated above, also S_{pv} will be assumed to be period-independent as often assumed for a medium-long period structure. They are given as

$$R_d = D_h \cdot \frac{T_{eq}}{T_f}, \quad R_a = D_h \cdot \frac{T_f}{T_{eq}} \quad (6a,b)$$

Also, for a short period structure, S_{pa} will be assumed to be period-independent, R_d and R_a are given as

$$R_d = D_h \cdot \frac{T_{eq}}{T_f} \cdot \frac{T_{eq} + T_0}{2T_f}, \quad R_a = D_h \cdot \frac{T_f}{T_{eq}} \cdot \frac{T_{eq} + T_0}{2T_f} \quad (7a,b)$$

3.2 Control Performance Curve

The previous equations can clarify the complex interactive effects of stiffness parameter, ductility demand, vibration period, damping and seismic response spectrum on the response reduction of the EP system. Figure 3 shows the curves for drift reduction R_d and acceleration (base shear) reduction R_a of SDOF EP system under a period-independent S_{pv} , and S_{pa} , respectively. The initial damping ratio of frame is $h_0 = 0.02$.

The control performance curves for EP system depend strongly on two parameters: damper stiffness ratio K_d / K_f and ductility demand μ . In Figure 3, the point $K_d / K_f = 0$ gives the frame response $R_d = R_a = 1$. In case of independent-period S_{pv} , to a point, larger K_d / K_f (stiffer damper) leads to smaller drift (R_d) and force (R_a) (Figure 3(a)). Thereafter, the drift continues to decrease, but base shear increases sharply. Also, larger μ (lower yield strength) leads to smaller drift (R_d) and force (R_a). In case of independent-period S_{pa} , larger K_d / K_f and μ lead to smaller drift (R_d) and force (R_a) (Figure 3(b)). As indicated above, the control performance curve clearly shows the trade-off between drift and base shear, and enables to easily obtain the design solution to satisfy the desired response.

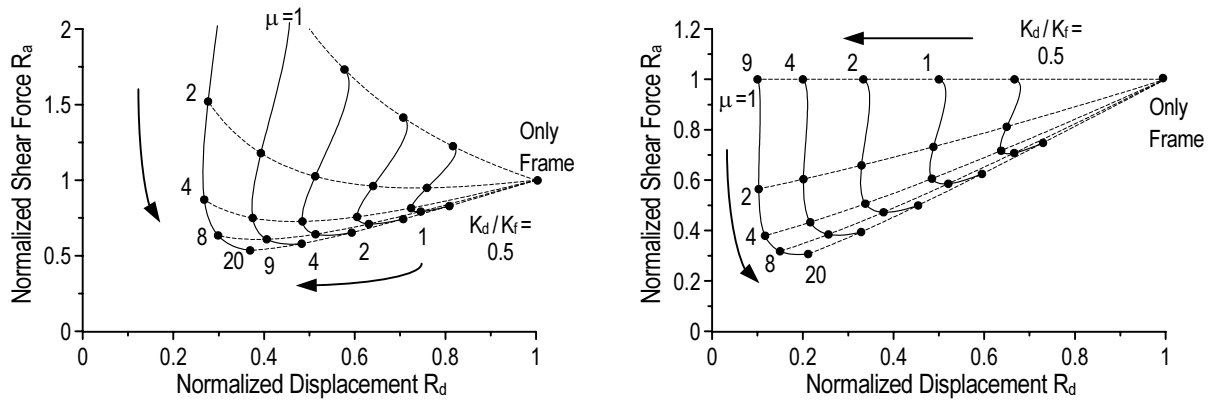


Figure 3 Control Performance Curve

4. DESIGN OF MDOF EP SYSTEM

4.1 Design Conditions of MDOF Frames

Three types of frame are considered: standard type (S-Type), upper-deformed type (U-Type) and lower-deformed type (L-Type). The frames have three different heights: 3, 12, and 24-story. Member stiffness of the frames will be reduced due to incorporating the dampers, fundamental vibration period of them are $T_f = 0.040H$ (12 and 24-story), $0.052H$ (3-story) as shown in table 1. H represents the total height of structure, mass and story height are identical for every story: $m_i = 1.2 \text{ kN}\cdot\text{sec}^2/\text{cm}$ and $h_i = 4.2\text{m}$, respectively. The initial damping ratio of frame is $h_0 = 0.02$.

Consider 12-story frame for example, three types of frame stiffness distribution are shown in Figure 4(a). The frame stiffness K_{fi} at i th-story of S-Type is designed such that story drift becomes uniform under the A_i lateral force distribution (Figure 4(b)). As Figure 4 shows, in U-Type frame, story drift increases at upper stories, whereas in L-Type frame, story drift increases at lower stories. As mentioned above, story stiffness distributions of frames are obtained such that fundamental vibration period of them are $T_f = 2.00 \text{ sec}$.

Table 1 Fundamental Vibration Period of the 3, 12 and 24-story frames

	3-story	12-story	24-story
T_f (sec)	0.65	2.00	4.00
H (m)	12.6	50.4	100.8
T_f / H	0.052	0.040	0.040

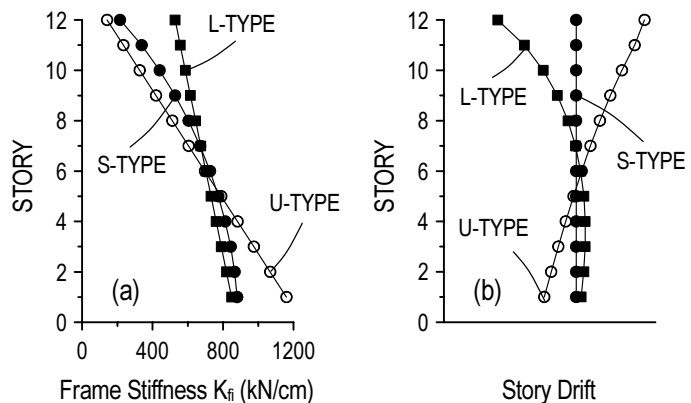


Figure 4 3 Types of 12-Story Frame Stiffness Distributions and Story Drift Distributions

The peak responses S_d , S_{pv} , and S_{pa} of SDOF idealized multi-story frame without damper are obtained from the seismic response spectrum, T_f and h_0 . With these response values, displacement u_0 and base shear F_0 of the SDOF frame are given by Eq. 8.

$$u_0 = S_d(T_f, h_0), \quad F_0 = M_{eq} \cdot S_{pa}(T_f, h_0) \quad (8a,b)$$

$$\text{where } M_{eq} = \left(\sum_{i=1}^N m_i \cdot u_{0i} \right)^2 / \sum_{i=1}^N (m_i \cdot u_{0i}^2) \quad (9)$$

where M_{eq} = equivalent mass of 1st mode and u_{0i} = deformation shape of frame, which is assumed to be linear over the height of structure regardless of frame type, because desired drift angle distribution of EP system is uniform. Considered that u_0 is displacement of the MDOF frame without damper at equivalent height H_{eq} , drift angle of the SDOF frame θ_f is given by Eq. 10(a).

$$\theta_f = \frac{u_0}{H_{eq}}, \quad H_{eq} = \sum_{i=1}^N (m_i \cdot u_{0i} \cdot H_i) / \sum_{i=1}^N (m_i \cdot u_{0i}) \quad (10a,b)$$

where H_i = height at i th-story level.

4.2 SDOF EP System Design

For the MDOF frames designed above, SDOF EP systems are designed to meet the performance criteria: yield strength levels of damper corresponds to SDOF EP system ductility demands $\mu=2, 4,$ and $8,$ and three target drift angles $\theta_{max}=1/200, 1/150$ and $1/125.$ Each frame is analyzed for BCJ-L2 artificial ground motion. Firstly, the target displacement reduction factor R_d for each frame is given by Eq. 11.

$$R_d = \frac{\theta_{max}}{\theta_f} \quad (11)$$

Secondly, determine the damper stiffness ratio K_d/K_f at the ductility demand μ to meet the target displacement reduction factor $R_d.$ From response spectrum of BCJ-L2, S_{pv} will be assumed to be period-independent in the range greater than 0.7 sec, S_{pa} will be also assumed to be period-independent in the range of shorter vibration period. Therefore, displacement reduction factors R_d for the SDOF EP system in 12 and 24-story design are obtained by Eq. 6, those of 3-story designs are also obtained by Eq. 7. It is clarified that damped effect factor D_h of BCJ-L2 artificial ground motion is much lower than an 31 ensemble of observed earthquakes in the work by Kasai et al. (2003). In this case, substitute $\alpha=75$ (BCJ-L2 artificial ground motion) for Eq. 5.

Considering the indicated above, damper stiffness ratio K_d/K_f to satisfy the target displacement reduction factor R_d can be obtained.

4.3 Conversion to MDOF EP System Design

Considering the change of equivalent stiffness of system K_{eqi} due to yielding of damper under the earthquake excitation, a rule to arrange the damper stiffness K_{di} at i th-story is proposed by Eq. 15 (Kasai et al., 2002). The following constraints are used for the conversion:

1. The equivalent damping, which is ratio of total energy dissipated by damper per cycle divided by 4π times total elastic strain energy obtained from the system secant stiffness, for MDOF EP system becomes the same as that of SDOF EP system.
2. Under the design shear force, the distributions of drift angle and ductility demand of MDOF EP system become uniform, although those of the frame without damper may be non-uniform.
3. Yield drift angle for each story is uniform.

Then, constraint 1 gives

$$\sum_{i=1}^N [K_{di}(\mu_i - 1)(\theta_i \cdot h_i / \mu_i)^2] / \sum_{i=1}^N [(K_{fi} + K_{di} / \mu_i) \cdot \theta_i^2 \cdot h_i^2] = K_d(\mu - 1) / [(K_f + K_d / \mu) \cdot \mu^2] \quad (12)$$

With constraint 2: drift angle θ_i and ductility demand μ_i at i th-story are $\theta_i = \theta$, $\mu_i = \mu$, respectively, Eq. 12 is revised by Eq. 13.

$$\frac{K_d}{K_f} = \frac{\sum_{i=1}^N (K_{di} \cdot h_i^2)}{\sum_{i=1}^N (K_{fi} \cdot h_i^2)} \quad (13)$$

where K_d / K_f = damper stiffness ratio obtained from SDOF EP system. Constraint 3 is obviously a necessary and sufficient condition for constraint 2. Also, shear drift angle is a quotient of story shear and stiffness and story height. Thus, from constraint 2

$$Q_i \cdot h_i / [(K_{di} / \mu + K_{fi}) \cdot h_i^2] = \sum_{i=1}^N (Q_i \cdot h_i) / \sum_{i=1}^N (K_{di} \cdot h_i^2 / \mu + K_{fi} \cdot h_i^2) \quad (14)$$

where Q_i = the design shear force based on A_i distribution coefficient. Substituting Eq. 13 for Eq. 14, Eq. 15 is obtained.

$$[1 + (K_{di} / \mu) / K_{fi}] / [1 + (K_d / \mu) / K_f] = \left[Q_i \cdot \sum_{i=1}^N (K_{fi} \cdot h_i^2) \right] / \left[K_{fi} \cdot h_i \cdot \sum_{i=1}^N (Q_i \cdot h_i) \right] \quad (15)$$

where $K_{di} / \mu = K_{deqi}$: equivalent stiffness of damper at i th-story corresponding to μ . For the frame with uniform story height as considered in this study, Eq. 15 indicates that the equivalent stiffness of system K_{eqi} at i th-story is proportionate to the design shear force Q_i . Consider the condition: 12-story, $\theta_{max} = 1/150$ and $\mu = 4$ for example, distributions of equivalent stiffness of damper K_{deqi} and system K_{eqi} by using the rule mentioned above are shown in Figure 5. As the frame stiffness distribution K_{fi} of S-Type is proportionate to Q_i , the ratio of equivalent stiffness of damper to frame stiffness at i th-story K_{deqi} / K_{fi} evidently becomes uniform value over the height of building. In both U-Type and L-Type frame, K_{deqi} / K_{fi} becomes high value at the story expected large deformation of frame without damper. Whereas, no damper is inserted in the first story for U-Type, and in the top three stories for L-Type.

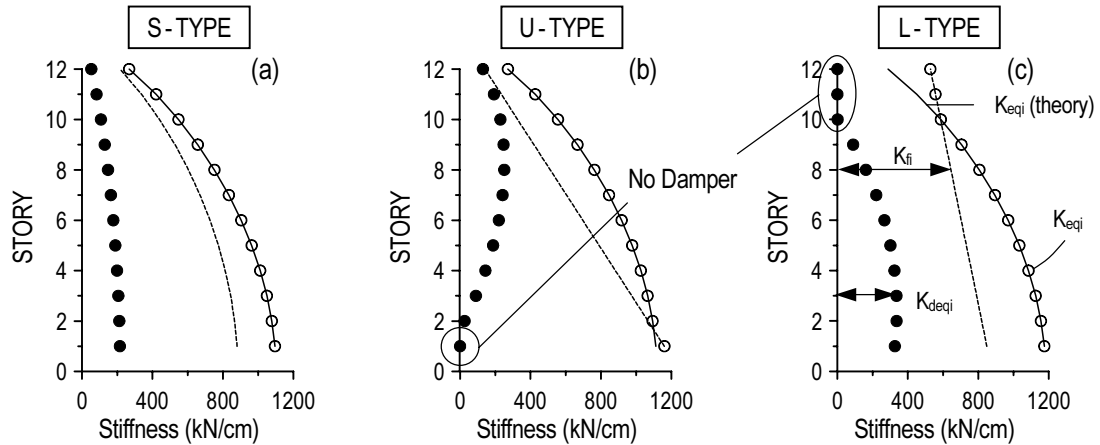


Figure 5 3 Types of Equivalent Stiffness Distributions of Damper and System (12-Story $\theta_{max} = 1/150$, $\mu = 4$)

Also, Damper force F_{dyi} at i th-story is given by Eq. 16.

$$F_{dyi} = K_{di} \cdot \Delta u_{yi}, \quad \Delta u_{yi} = \frac{\theta_{max} \cdot h_i}{\mu} \quad (16)$$

5. NUMERICAL RESULTS

Time history simulations were carried out for 81 MDOF EP systems designed above: 3 types of frame, 3 building height, 3 ductility demands, and 3 target drift angle. Simulation models are MDOF shear-bar models as shown in Figure 6. Consider the condition: 3 types of 12-story frames, $\theta_{max} = 1/150$ and $\mu = 2, 4, \text{ and } 8$ for example, the peak drift angle obtained from time history simulations and design target are shown in Figure 7. As you can see Figure 7, simulation results fairly meet design target due to inserting a sufficient amount of damper. In addition, note that distributions of peak drift angle become uniform regardless of the deformation shape of each frame without damper. Table 2 summarizes the average accuracy of the drift angle for each frame type and building height. "Average" in Table 2 indicates the total average of the ratio of simulation to design target at every story for 9 cases: 3 ductility demands, 3 target drift angle. Compared 3, 12, and 24-story systems, the peak drift angle of the taller building tends to be underestimated. The most likely reason for this issue is that the present approach neglects the contribution of higher modes in evaluating the story drift of MDOF EP system, considering first mode alone is slightly inadequate for 24-story systems.

As a whole, the proposed response evaluation method based on SDOF can provide a good estimation for response of MDOF EP system in preliminary seismic design. It demonstrates that the simple rule to arrange the damper stiffness shown in Eq. 156 can produce the uniform distribution of peak story drift under earthquake excitation.

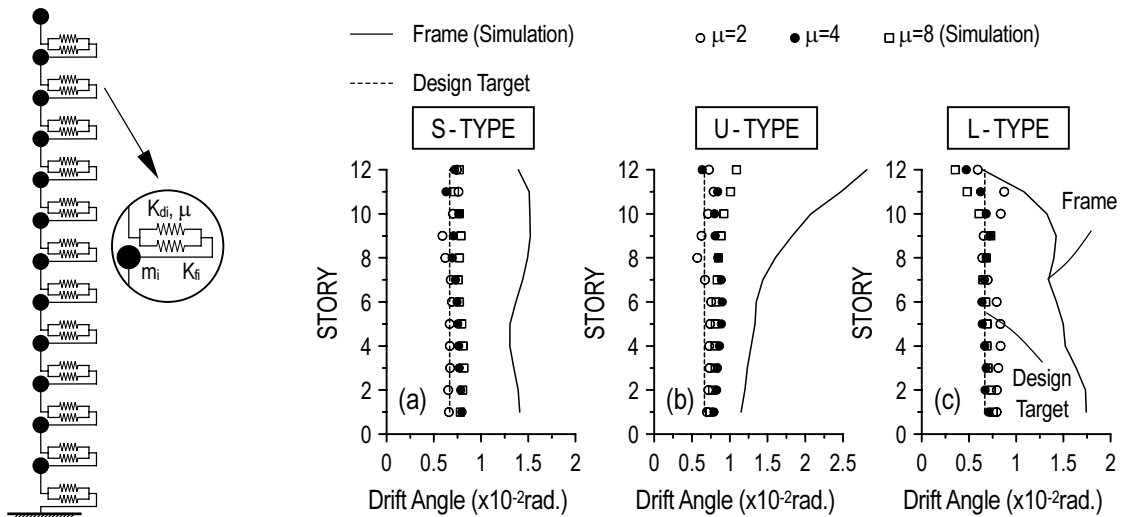


Figure 6 12-DOF Shear-bar Model

Figure 7 Comparison Simulations with Design Target on Drift Angle (12-Story, $\theta_{max} = 1/150$, $\mu = 2, 4, 8$)

Table 2 Average Accuracy of Drift Angle

	3-Story			12-Story			24-Story		
	S-Type	U-Type	L-Type	S-Type	U-Type	L-Type	S-Type	U-Type	L-Type
Average	0.890	0.909	0.864	1.102	1.177	0.998	1.229	1.190	1.074
Standard Deviation	(0.102)	(0.145)	(0.112)	(0.105)	(0.167)	(0.150)	(0.176)	(0.196)	(0.235)

6. DESIGN PROCEDURE FOR ELASTO-PLASTICALLY DAMPED STRUCTURES

Characteristics of frame: fundamental vibration period T_f , initial damping h_0 , story stiffness distribution K_{fi} , mass distribution m_i , and story height h_i and performance criteria: ductility demand μ , and target drift angle θ_{max} and design response spectrum are all given, design procedure for elasto-plastically damped structure is summarized in sequence of steps below:

1. Obtain the drift angle θ_f and base shear F_0 of SDOF frame without damper from design response spectrum, by evaluating the equivalent height H_{eq} and equivalent mass M_{eq} (Eq. 8-10).
2. Calculate the target displacement reduction factor R_d by Eq. 11.
3. Determine the damper stiffness ratio K_d/K_f at the ductility demand μ to meet the displacement reduction factor R_d by using the control performance curve.
4. Arrange the damper stiffness K_{di} at i th-story by Eq. 15.
5. Calculate the yield deformation Δu_{yi} and strength F_{dyi} of damper at i th-story by Eq. 16.
6. Determine the details of EP dampers as shown in the manual (JSSI, 2003).

7. CONCLUSIONS

This research is aimed toward developing the peak response evaluation method and design approach for elasto-plastically damped structure in preliminary seismic design. The proposed method is based on the SDOF idealization of multi-story building structure, equivalent linearization technique and a rule to convert a SDOF design to a multi-story design. The evaluation of the accuracy of this method for 81MDOF EP systems has led to the following conclusions:

1. The proposed response evaluation method based on SDOF can provide a good estimation for response of MDOF EP system in preliminary seismic design. Design by this approach fairly meets the performance criteria: target drift angle and ductility demand.
2. It demonstrates that the proposed rule to arrange the damper stiffness over the height of structure can produce the uniform distribution of peak story drift under earthquake excitation.

The present approach neglects the contributions of higher modes in evaluating the response of MDOF EP system, considering first mode alone is slightly inadequate for tall buildings such as 24-story systems. It can be further improved by including a sufficient number of modes in evaluating the drift angle.

Acknowledgements:

The Ministry of Education, Science and Culture provided support for this study in the form of Grants-in-Aid for Scientific Research (Research Representative: Hiroshi Ito) and first author receives JSPS fellowship. The author gratefully acknowledges the support.

References:

- Japan Society of Seismic Isolation (2003), "JSSI Manual for Design and Construction of Passively-Controlled Buildings in Japan"
- Kasai, K., Fu, Y., and Watanabe, A. (1998), "Passive Control Systems for Seismic Damage Mitigation," *Journal of Structural Engineering*, American Society of Civil Engineers, 124(5), 501-512.
- Kasai, K., Ito, H., and Watanabe, A. (2003), "Peak Response Prediction Rule for a SDOF Elasto-plastic System Based on Equivalent Linearization Technique," *Journal of Structural Engineering*, Architectural Institute of Japan, 571, 53-62
- Kasai, K., and Ito, H. (2002), "Stiffness Tuning Method for Design of Elasto-plastically Damped Structures," *Proceedings of the Passive Control Symposium*, Structural Engineering Research Center, Tokyo Institute of Technology, 273-282

WIND AND SEISMIC VIBRATION CHARACTERISTICS OF A TALL BUILDING MODEL USING VISCOELASTIC DAMPER

D. Sato¹⁾, K. Kasai²⁾, and T. Tamura³⁾

1) Graduate Student, Department of Built Environment, Tokyo Institute of Technology, Japan

2) Professor, Structural Engineering Research Center, Tokyo Institute of Technology, Japan

*3) Professor, Department of Environmental Science and Technology, Tokyo Institute of Technology, Japan
daiki@enveng.titech.ac.jp, kasai@serc.titech.ac.jp, tamura@depe.titech.ac.jp*

Abstract: This paper discusses the wind vibration control for a tall building using passive control dampers. Viscous damper and viscoelastic damper are considered in this study, and they are attached to a wind tunnel test model. The test set-up includes a special measurement system to obtain the damper hysteresis loop, which is extremely useful to understand the dynamic characteristics of the dampers and the model. Free vibration tests as well as wind vibration tests using uniform flow are conducted with or without the dampers. The model global response is correlated with the damper local response. Commonality of the damper responses obtained from the free vibration test and the wind tunnel test is discussed

1. INTRODUCTION

In Japan, most buildings may be designed against earthquake load. However they will sometimes encounter wind-related vibration discomfort of occupants, mainly due to excessive accelerations of the upper part of the tall buildings. In addition, in a case of tall building which is over 200 m high, it is known that wind load becomes larger than earthquake load. So when the tall buildings are designed, it is necessary to consider earthquake and wind load. A number of measures to reduce the wind-induced response of those high-rise buildings were proved effective. On the aerodynamic point of view, reduction in wind forces may be achieved by configuration control to modify the structural shape. On other point, increase of building mass, stiffness, and structural damping may provide an alternative way to reduce the wind-induced response of the structure. However, increasing building mass and stiffness is expensive and may elicit larger seismic forces. It is thus more promising to increase the structural damping by employing damper devices.

In this study, either a viscous damper or a viscoelastic damper is considered as a damping device. The first application of the viscoelastic damper was made in 1969, for the World Trade Center, New York. Although thirty years have passed since the first application, the effect of the viscoelastic damper on the wind-induced response has not been fully comprehended yet. This is due to the complex nature of meteorology and wind flows, as well as sensitivity of viscoelastic material against the frequency, temperature, and strain. On the other hand, it has been recognized that the damper has significant advantage of being effective against not only the wind but also the earthquake.

While properties of viscous or viscoelastic damper are carefully considered when predicting seismic responses of the damped building, it has not been the case for wind responses. In wind engineering, the parameters such as damping ratio and vibration period are traditionally used for response prediction. In field of seismic engineering, the prediction methods of considering the damper property are already developed. Therefore this paper adopts the method to estimate for the damper

property, and will survey if such approach can be applicable to wind vibration. Pursuant to these, the present paper addresses such a study by referring to both viscous and viscoelastic dampers.

The present study uses the viscous damper of silicone oil and the viscoelastic damper, either of which is attached to a building model. The dampers are configured to suit the model, still retaining their fundamental characteristics. The test set-up includes a special measurement system to obtain the damper hysteresis loop, which is extremely useful to understand the dynamic response of the dampers and model. Free vibration tests as well as wind vibration tests are conducted with or without the dampers. The results are discussed by relating the model global response with the damper response. Regarding wind tunnel tests, uniform flow was considered and the responses due to the use of the viscous damper are explained as an example.

2. TEST MODELS

Figs. 1(a) and (b) show the test models installed with the viscoelastic dampers and viscous dampers, respectively. From now on, they will be called as "viscoelastic damper system" and "viscous damper system". A square balsa cylinder having an aspect ratio of 6 and a side ratio of 1 is used as the building model. The plan dimension and height of the square cylinder are $B = 50 \text{ mm} \times D = 50 \text{ mm}$ and $H = 300 \text{ mm}$, respectively. The test model is mounted on a gimbal, and two coil springs are utilized to simulate the building stiffness in the cross-wind directions (Y-direction). The gimbal can rotate freely in the Y-direction. A laser displacement transducer is used to measure the Y-direction displacement of a point below the spring.

The viscoelastic damper (Fig. 1 (a)) is installed on same height of springs. So the viscoelastic damper has the same deformation to one spring deformation. The viscous damper (Fig. 1 (b)) is located under the displacement measurement point. Two load cells are connected to the bottom of each damper respectively, and the damper force is obtained by summing the values measured from them.

Viscoelastic damper (Fig. 1(a)) is made of the viscoelastic material (5 mm x 5 mm x 8 mm) and two aluminum plates (3 mm-thick) attached on its each side. ISD112 viscoelastic material (Sumitomo-3M Company) is used. When the building model vibrates, the relative motion between the two plates causes material deformation, reaction force, and consequently energy dissipation. The viscous damper (Fig. 1(b)) consists of the lever arm with an end plate, and silicon oil filled in a container. The end plate is sunk in the oil, and its in-plane motion causes shearing resistance of the oil and energy dissipation.

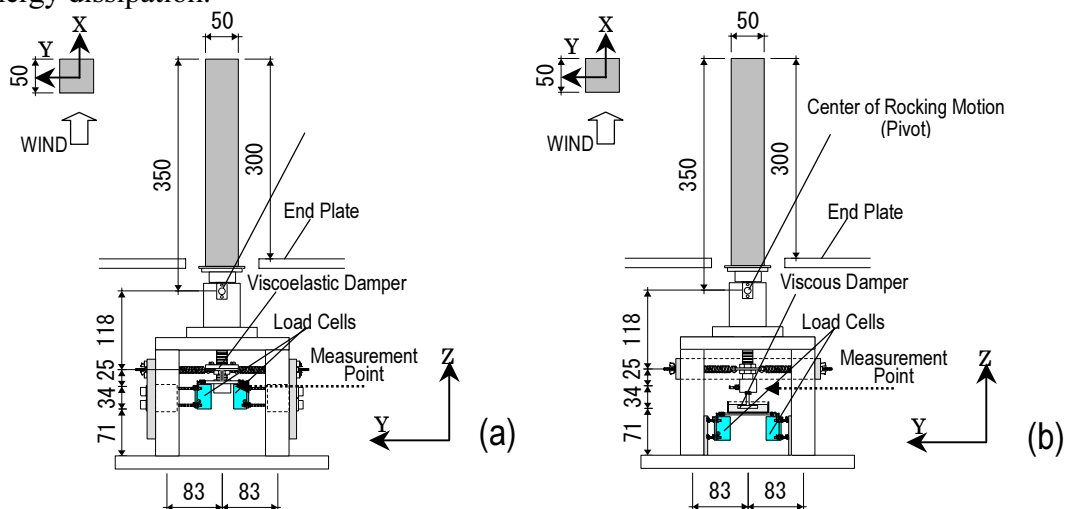


Figure 1 Test models (unit:mm): (a) Viscoelastic damper system, and (b) Viscous damper system

3. FREE VIBRATION TESTS

Free vibration tests are conducted with or without the dampers before each set of wind tunnel test. Regarding the model without the damper, the natural frequency $f_0 = 17.80$ Hz and the damping ratio $h_0 = 0.20$ % are estimated from the successive peaks of the displacement time history during free vibration. As for the model with the damper, the equivalent frequency f_{eq} and the equivalent damping ratio h_{eq} are also estimated using the same method as mentioned above. After each set of wind tunnel test, free vibration tests are conducted again to verify whether there is no damage to the system.

Damping ratio of the viscoelastic damper system is adjusted by changing the temperature of the viscoelastic damper: the material becomes softer and dissipates less energy under higher temperature. Temperature of viscoelastic damper is monitored using the infrared radiation thermometer, and the light bulbs are used to control temperature of viscoelastic. Damping ratio of the viscous damper system is adjusted by changing the amount of the silicon oil.

Figs. 2(a) and (b) show examples of the damper force F_d vs. the damper deformation u_d curves, i.e., hysteresis loops of the viscous and viscoelastic dampers, respectively. They are obtained from the free vibration tests, and the viscoelastic damper's loop has clear inclination (stiffness) compared with viscous damper's loop. Thus, viscoelastic damper adds not only energy dissipation but also the stiffness to the system.

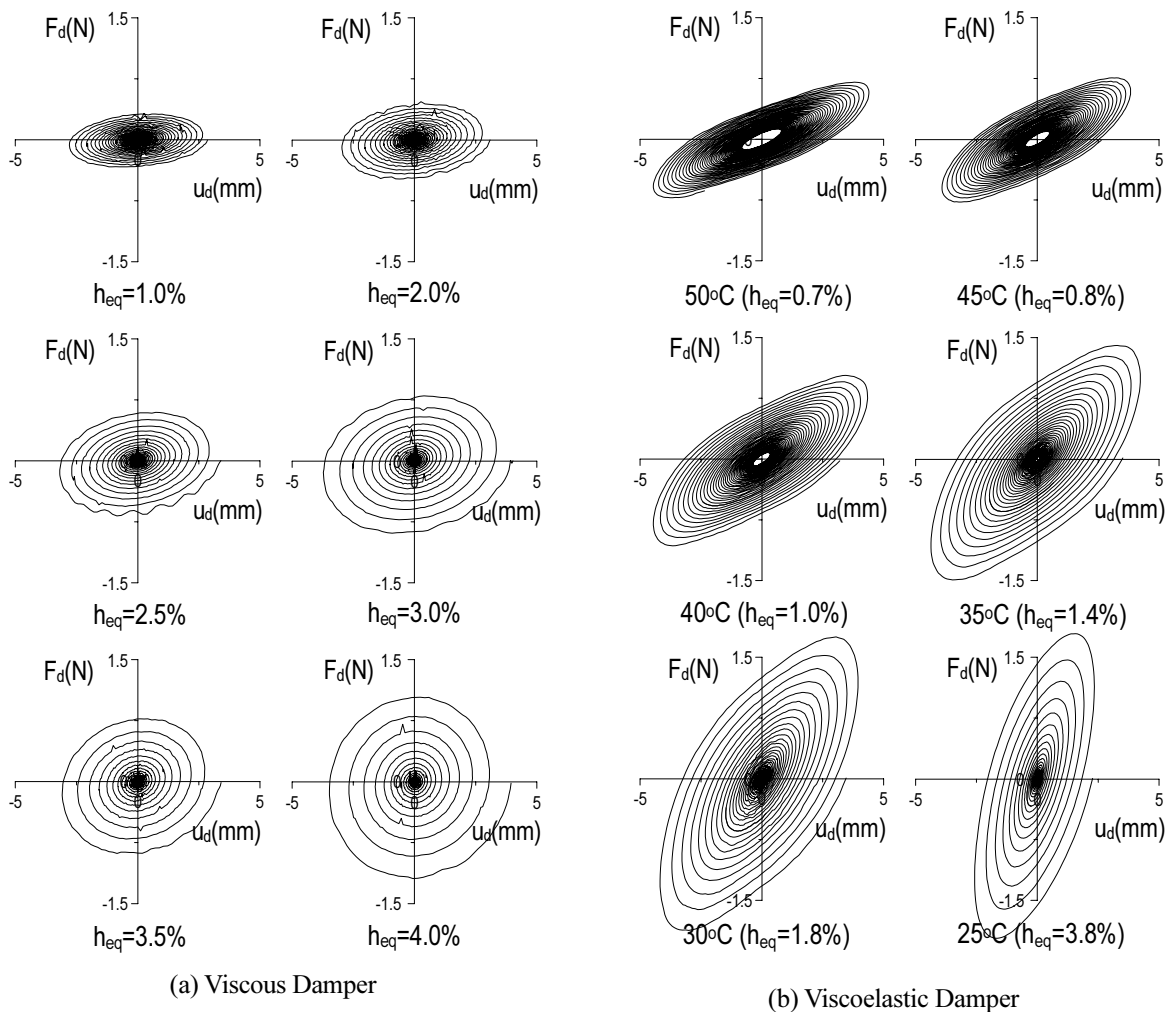


Figure 2 Results of Free Vibration Tests

To consider the effect of the damper on the system precisely, we developed a method to obtain the equivalent frequency of the system f_{eq}' and the equivalent damping ratio of the system h_{eq}' , by using the hysteresis loops of the damper. The procedure is as follows:

A hysteresis loop of the viscous and/or viscoelastic damper when undergoing steady-state response is shown in Fig. 3. The mechanical property of the damper is expressed by K_d' and η_d , the former is a storage modulus representing the stiffness (loop inclination) and the latter a loss factor representing the energy dissipation capability (loop thickness) (Kasai, K., Okuma, K. 2001).

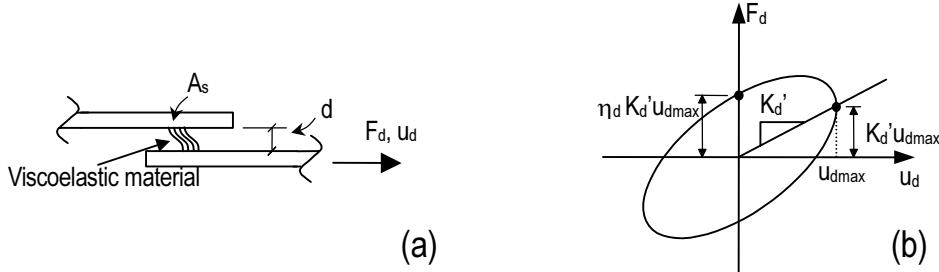


Figure 3 (a) Deformation of the Viscoelastic Damper, and (b) Force-Deformation Hysteresis Loop

K_d' and η_d can be written as in Eqs. 1a and b, using the experimental values $F_d^{(j)}$ and $u_d^{(j)}$ at the j -th step (Kasai, K., Ooki, Y., Amemiy, K., Kimura, K. 2003).

$$K_d' = \frac{n \sum F_d^{(j)} u_d^{(j)} - \sum F_d^{(j)} \sum u_d^{(j)}}{n \sum (u_d^{(j)})^2 - (\sum u_d^{(j)})^2}, \quad \eta_d = \frac{2E_D'}{\pi K_d' (u_{d \max})^2} \quad (1a, b)$$

where Σ means sum of “ n ” sets of $F_d^{(j)}$ and $u_d^{(j)}$ per one cycle of the hysteresis loop. E_D' is the energy dissipated by the damper per half cycle, and it is calculated from the area of the damper hysteresis loop.

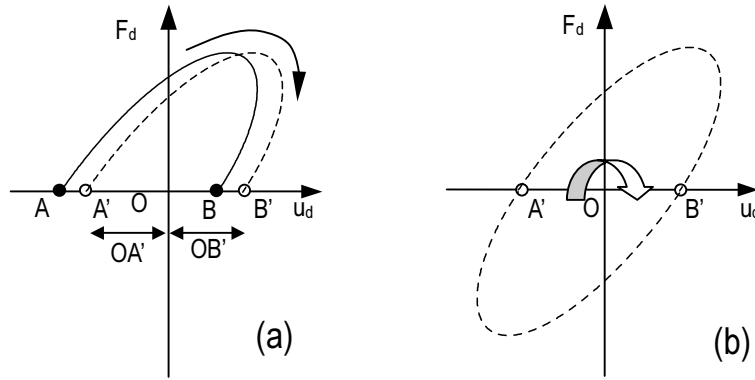


Figure 4 (a) Half Cycle, and (b) Obtained Closed Hysteresis Loop

In case of the free vibration tests, the damper force and deformation decrease in subsequent cycles, and the hysteresis loop is not necessarily closed. Thus, as shown by the solid curve in Fig. 4(a), \overline{OA} is longer than \overline{OB} , and a large calculation error appears when using Eq. (1a) and (1b) without alteration. In order to obtain a closed hysteresis loop, the solid curve is moved along horizontal axis so that $\overline{OA'} = \overline{OB'}$ (dashed curve, Fig. 4(a)), and rotated 180° about the origin “ O ” (Fig. 4(b)).

After evaluating K_d' and η_d , the equivalent storage modulus K_{eq}' and the equivalent loss factor η_{eq} of the damped system can be calculated using following equations.

$$K'_{eq} = K_s + K'_d \left(\frac{L_2}{L_1} \right)^2, \quad \eta_{eq} = \frac{\eta_d}{1 + (K_s / K'_d)(L_1 / L_2)^2} \quad (2a, b)$$

where K_s = sum of the Y-direction stiffness of the two coil springs, L_1 = distance from the pivot point to the coil springs, and L_2 = distance from the pivot point to the damper. In the present set-up, K_s = 9.42 N/mm, L_1 = 118 mm and L_2 = 118 mm (Viscoelastic damper system), = 177 mm (viscous damper system), respectively.

The equivalent frequency of system f'_{eq} and equivalent damping ratio of system h'_{eq} can be expressed as follows:

$$f'_{eq} = \frac{1}{2\pi} \sqrt{\frac{K'_{eq}}{M_{eff}}}, \quad h'_{eq} = h_0 + \frac{\eta_{eq}}{2} \quad (3a, b)$$

where M_{eff} = effective mass at the point of coil spring, and it is estimated from the free vibration tests without damper, *i.e.*, $M_{eff} = K_s / (2\pi f_0)^2$.

The above relationship is commonly used for both viscous and viscoelastic damper systems. The coefficient of viscosity C_d , often used to express the property of a viscous damper, can be written as follows:

$$C_d = \frac{\eta_d K'_d}{2\pi f'_{eq}} \quad (4)$$

The errors f'_{eq} / f_{eq} and h'_{eq} / h_{eq} are shown in Fig. 5. As defined earlier, f_{eq} and h_{eq} are the equivalent frequency and damping ratio evaluated from the displacement time history of the test model, and f'_{eq} and h'_{eq} are those calculated from the damper hysteresis loop recorded (Fig. 2) as well as Eqs. 1 to 3. As shown in Fig. 5, f'_{eq} and h'_{eq} agree well with f_{eq} and h_{eq} , respectively, validating both the measurement system and the proposed evaluation method.

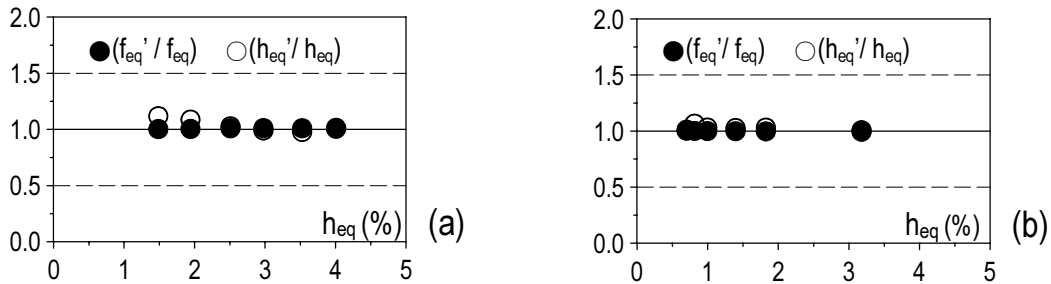


Figure 5 Error plots (a) Viscous damper system, (b) Viscoelastic damper system

4. WIND TUNNEL TEST SET UP

Wind tunnel tests are performed using the Eiffel type wind tunnel at Tokyo Institute of Technology. The cross section and length of the test section are 1000 mm x 800 mm and 7000 mm, respectively. The contraction ratio is 5 and the maximum wind speed is 25 m/s. Schematic diagram of the test set-up is shown in Fig. 6. For avoiding various noises, support structure is made very stiff and the base very heavy, thereby preventing their high-frequency vibration. The end plate is installed to reduce the effect of boundary layer on the generated uniform flows. Fig. 7(a) shows an example for the vertical distribution of U / U_H measured, where U = mean wind velocity at each elevation, and U_H = mean velocity at top of the model. The U / U_H appears to be 1.0 throughout the height of the

model. Also, Fig. 7(b) shows the vertical distribution of the turbulent intensity that was measured at the center of the turn table (Fig. 6). The boundary layer, defined to have the turbulent intensity of more than 0.3%, is located at the bottom of the model, and its depth is about 50mm, very small compared with the model height. As these indicate, the set-up accurately produces the uniform flow condition.

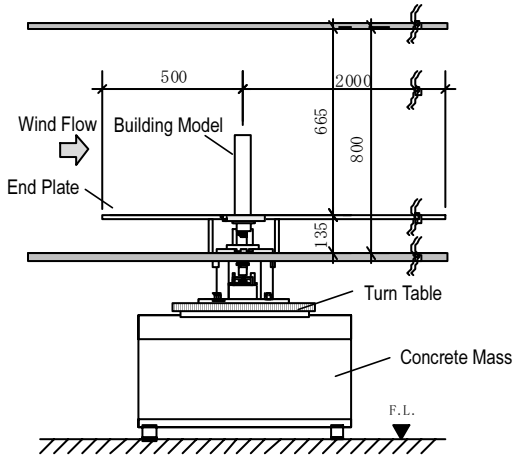


Figure 6 Schematic of the test setup in the wind tunnel. (unit:mm)

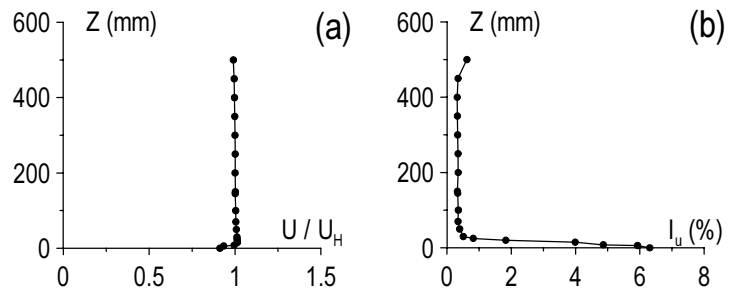


Figure 7 Vertical profile :
(a) Normalized mean velocity, and (b) Turbulent intensity

5. WIND TUNNEL TEST RESULTS

5.1 Viscous Damper System

Wind tunnel tests of the viscous damper system are performed as the first step in this study. It is general methods to use silicon oil as the damping device of the wind tunnel.

The root-mean-square (RMS) of the displacement at the measurement point (Fig. 1), namely, y_{rms} is obtained experimentally. Fig. 8 shows the RMS of the rotational angle θ_{rms} ($= y_{rms} / L_1$) against the reduced wind velocity V_r for various magnitudes of mass-damping parameter δ of the viscous damper system. Note that $V_r = U_H / (f_0 B)$, where B = width of the model. Also, δ can be expressed as follows (Amano 1995):

$$\delta = \frac{\tilde{M}}{\rho B^2 L_0} h_{eq} = \frac{K_s L_1^2}{\rho (2\pi f_0)^2 B^2 L_0^3} h_{eq} \quad (5)$$

Where, \tilde{M} = generalized mass, ρ = air density, L_0 = distance from the pivot point to the top of the model, 350mm. The parameter δ is adjusted by changing only the damping ratio h_{eq} as estimated from free vibration tests. The relation between δ and h_{eq} is indicated in Table 1. When $\delta = 0.64$ ($h_{eq} = 0.8\%$), the peak of θ_{rms} is observed at $V_r = 10.4$. As δ is increased, the peak occurred at smaller V_r , and for instance, when $\delta = 1.04$ ($h_{eq} = 1.3\%$), the peak occurred at $V_r = 9.65$. Besides, the resonant vibration is suppressed as δ was increased to 1.12 ($h_{eq} = 1.4\%$). The results agree well with those reported by Tamura et al. (2000).

Table 1 Relation between δ and h_{eq}

δ	0.64	0.72	0.80	0.88	0.96	1.04	1.12	1.28	1.44	1.60
h_{eq} (%)	0.8	0.9	1.0	1.1	1.2	1.3	1.4	1.6	1.8	2.0

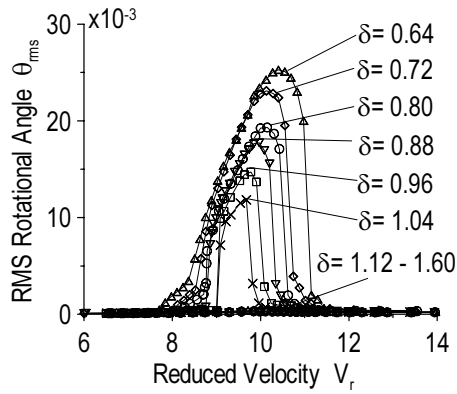


Figure 8 RMS response curve in the viscous damper system

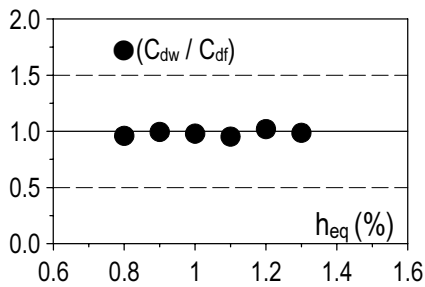


Figure 10 Comparison between C_{dw} and C_{df}

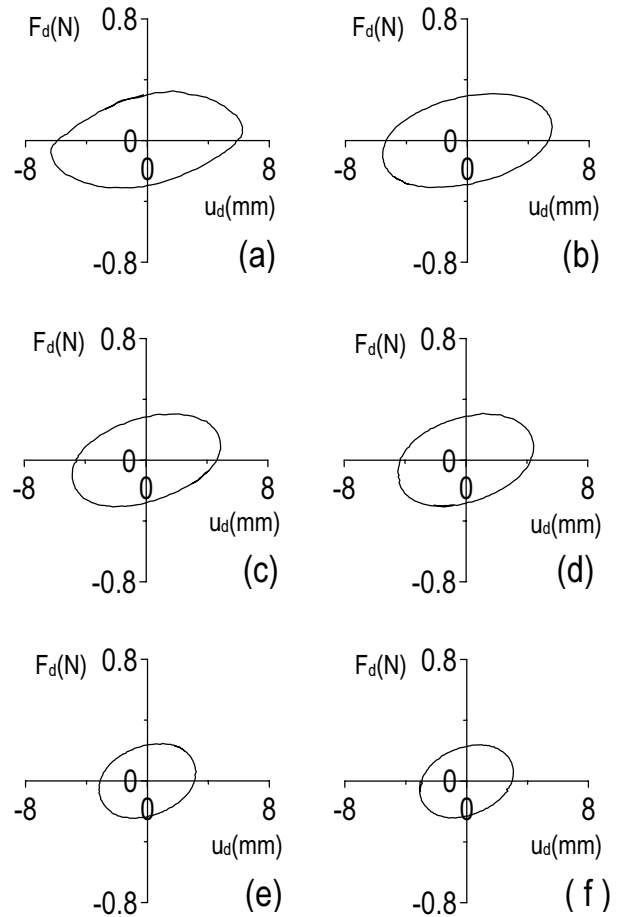


Figure 9 Damper hysteresis loops in wind tunnel tests: (a) $\delta=0.64$, (b) $\delta=0.72$, (c) $\delta=0.80$, (d) $\delta=0.88$, (e) $\delta=0.96$, (f) $\delta=1.04$

Fig. 9 shows the damper hysteresis loops recorded when RMS rotational angle was at peak. Plots of ratios C_{dw} / C_{df} are also shown in Fig. 10, where C_{df} and C_{dw} = coefficients of damper viscosity estimated from the damper hysteresis loops recorded during the free vibration test and wind tunnel test, respectively. Note that the latter was calculated from the loops at the resonance state (Fig. 8), and the alteration such as shown in Fig. 4 was not needed. As in Fig. 10, C_{df} coincides well with C_{dw} , confirming that the resonance response under uniform flow can be characterized by the property of the damper obtained from the free vibration test. In addition to this, the measurement system has made it possible to correlate the responses of the model and the damper.

5.2 Comparison with Viscous Damper System and Viscoelastic Damper System

Wind tunnel tests of the viscoelastic damper system are carried out under same damping ratio h_{eq} case of the viscose damper system. The damping ratio of the viscoelastic damper system is obtained from the free vibration test in which is carried out before the wind tunnel test, and then the viscoelastic damper temperature, which is monitored by thermometer, is decided. During wind tunnel test, the temperature is controlled adjusting the brightness of the light bulb, as maintained uniformly.

Comparing the wind tunnel test results of the viscous damper system and the viscoelastic damper system are shown in Figs. 11 (a) and (b). The result in the case of $\delta = 0.64$ is shown in Fig. 11 (a), and the result in the case of $\delta = 0.72$ is shown in Fig. 11 (b). As in Fig. 11, the value θ_{rms} at peak are similar the viscose damper system and the viscoelastic damper system, but V_r when peak θ_{rms} occurs. In case of the viscoelastic damper system, peak θ_{rms} occurs at higher V_r compare in case of viscose damper system.

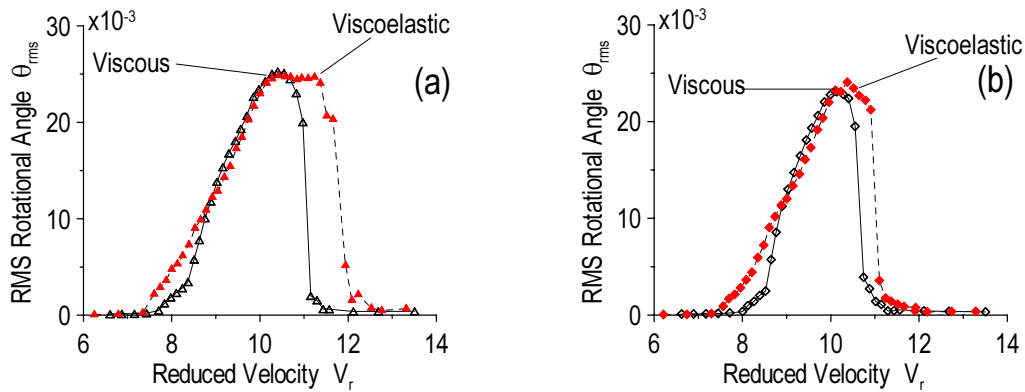


Figure 11 Comparison with the viscous damper system and the viscoelastic damper system :

(a) $\delta = 0.64$, (b) $\delta = 0.72$

6. CONCLUSION

This paper has discussed the first step of our study on wind vibration control for a tall building using passive control dampers. The objective of this study is to evaluate the wind response reduction scheme by considering significantly different characteristics of various dampers available in Japan. Viscous damper and the viscoelastic damper are considered in this study, and they are attached to a wind tunnel test model. A special measurement system was created to obtain the relationship between local damper force and deformation, essential information towards a comprehensive study on building global responses. The conclusions are as follows:

- (1) Hysteresis loops of the dampers recorded during the free vibration tests clearly indicate different dynamic properties of the viscous damper and viscoelastic damper. The proposed method to estimate the damper storage modulus and the loss factor from the loops appears to be very reliable.
- (2) Equivalent frequency and equivalent damping ratio of the damped building model can be estimated from the above-mentioned damper storage modulus and the loss factor, and they appear to agree well with those evaluated from the global displacement time history of the model subjected to free vibration.
- (3) The coefficients of the damper viscosity estimated from the free vibration tests and from the wind tunnel tests agreed well. Thus, the resonance response under uniform flow can be characterized by the property of the damper obtained from the free vibration test. Moreover, the measurement system has made it possible to correlate the responses of the model and the damper.
- (4) The viscoelastic system showed the peak RMS rotational angle at a higher value than the viscous damper system.

References:

- Kasai, K., Okuma, K. (2001), "Kelvin-Type Formulation and Its Accuracy for Practical Modeling of Linear Viscoelastic Dampers," (Part 1 One-mass system having damper and elastic/inelastic frame), *Journal of Structural and Construction Engineering*, No. 550, 71-78
- Kasai, K., Ooki, Y., Amemiya, K., Katuhiko, K. (2003), "A constitutive rule for viscoelastic materials materials combining ISO-butylene and styrene polymers," (Part 1 Liner model considering temperature and frequency sensitivities), *Journal of Structural and Construction Engineering*, No. 569, 47-54
- Amano, T. (1995), "The Effect of Corner-Cutting of Three-Dimensional Square Cylinders on Vortex-Induced Oscillation and Galloping in Uniform Flows," *Journal of Structural and Construction Engineering*, No. 478, 63-69
- Tamura, T., Okada, R., Wada, A. (2000), "Wind Tunnel Test on Dynamic Behavior Near Resonant Region for High-Rise Building Model With Hysteretic Damper," *Journal of Structural and Construction Engineering*, No. 537, pp.35-41

PORE WATER PRESSURE RESPONSE AROUND PILE AND ITS EFFECTS ON P-Y RELATION DURING LIQUEFACTION

H. Suzuki¹⁾ and K. Tokimatsu²⁾

1) Graduate Student, Dept. of Architecture and Building Engineering, Tokyo Institute of Technology, Japan

2) Professor, Dept. of Architecture and Building Engineering, Tokyo Institute of Technology, Japan

hsuzuki@arch.titech.ac.jp, kohji@o.cc.titech.ac.jp

Abstract: The effect of pore water pressure response around a pile on p-y behavior during soil liquefaction is investigated based on shaking table tests with a laminar shear box 6.0 m high and 12.0 m long. Three soil-pile-structure models having liquefiable sand deposits prepared at different densities are tested with pore water pressure transducers densely instrumented around a pile. The pore water pressure around a pile in dense sand decreases considerably with increasing relative displacement between soil and pile. This causes an increase in subgrade reaction, making the p-y behavior stress hardening. A close examination indicates that the reduction in pore water pressure is greater on the extension side than on the compression side of the soil around the pile. This is because the pore water pressure on the extension side decreases due to the combined effects of extension stress and dilatancy characteristics of the soil induced by the shear stress developed around the pile, while that on the compression side does not decrease due to the adverse effects of compression stress and dilatancy characteristics. The pore water pressure around the pile in loose sand, in contrast, does not decrease despite a larger relative displacement, making the p-y behavior stress softening.

1. INTRODUCTION

The field investigation and subsequent analyses made after the 1995 Hyogoken-Nambu earthquake indicated that ground movements could have a significant effect on damage to pile foundations. Especially, in liquefied area where the ground moves largely, the effect cannot be neglected, as most of the pile damage was associated with large ground movement.

To estimate the kinematic effect from ground movement during liquefaction, p-y behavior, defined as the relationship of subgrade reaction with relative displacement between ground and pile, has been studied based on large shaking table tests and centrifuge model tests (Tokimatsu et al. (2002 & 2001) and Wilson et al. (2000)). These studies have shown that the pore pressure reduction around a pile has a significant effect on p-y behavior; however, the response mechanism of pore pressure reduction including its variation around a pile is unknown. Toward better understanding of the mechanism of p-y behavior and its effects on pile foundations, the distribution of pore pressure around a pile should be identified.

The object of this paper is to investigate the variation of pore water pressure reduction around a pile on p-y behavior during liquefaction. Large shaking table tests are conducted for this purpose with dense instrumentation of pore water pressure transducers around a pile, together with earth pressure gauges, strain gauges, displacement transducers, and accelerometers. The effects of pore water pressure reduction and its variation around a pile on p-y relation during soil liquefaction is then examined.

2. LARGE SHAKING TABLE TESTS

To investigate qualitatively the effect of pore water pressure on p-y relation, the results of large shaking table tests, conducted on soil-pile-structure systems using the shaking table facility at the National Research Institute for Earth Science and Disaster Prevention (NIED), are used. The dimensions of the shear box on the shaking table were 5.0 m high, 12.0 m wide and 3.5 m long.

Fig. 1 shows a soil-pile-structure system used for the tests. The soil profile consisted of a top dry sand layer 0.5 m thick, a liquefiable sand layer 3 m thick and an underlying dense gravelly layer about 1.5 m thick. The sand used was Kasumigaura Sand ($e_{max} = 0.961$, $e_{min} = 0.570$, $D_{50} = 0.31$ mm, $F_c = 5.4\%$). Table 1 summarizes test series. The soil densities estimated were loose for D1, medium for DL, and dense for DS. Test series D1 had a foundation of 16.7 kN without a superstructure. Test series DS and DL had a foundation of 20.6 kN with a superstructure of 139.3 kN, whose natural period was shorter or longer than that of the ground before liquefaction. All the structure models were supported by a 2x2 steel pile group that was fixed to the container base. The piles had a diameter of 31.85 cm with a 0.6 cm wall thickness.

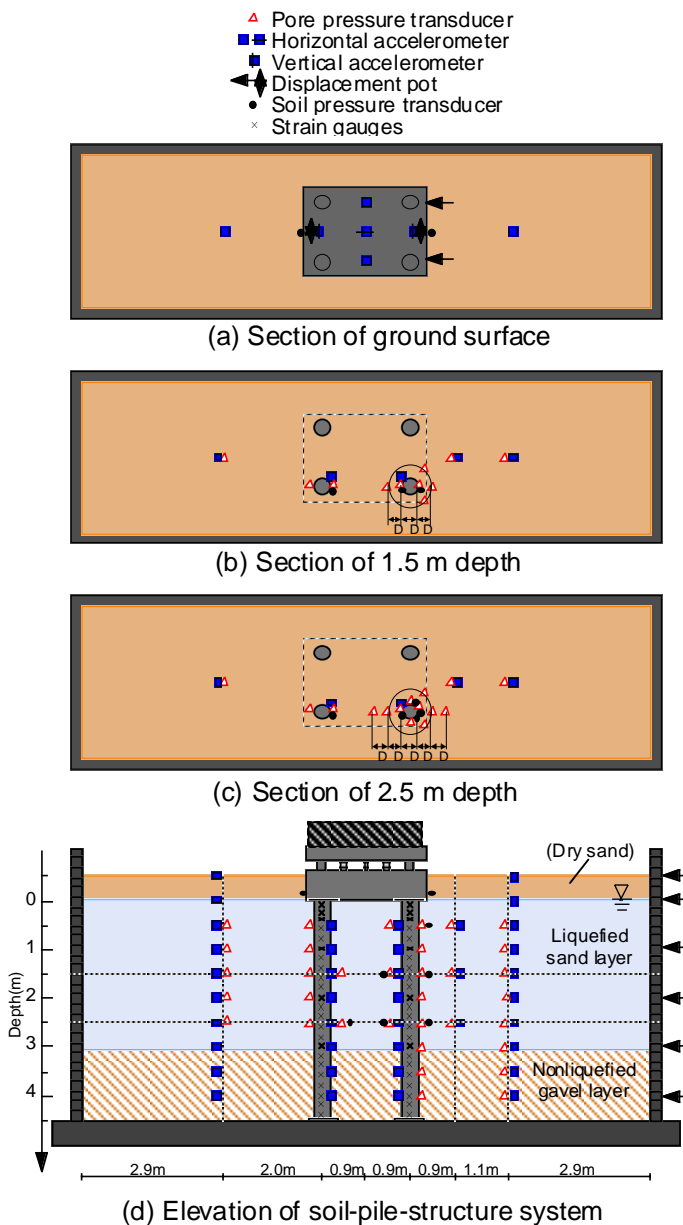


Fig. 1 Model layout

The soil-pile-structure system was densely instrumented with accelerometers, displacement transducers, strain gauges, pore water pressure transducers, and earth pressure transducers, as shown in Fig. 1. The accelerations and pore water pressures on the piles and in the ground were measured at every 50 cm with depth and the bending strains of piles at every 10-25 cm. Particularly, many pore water pressure transducers and some earth pressure transducers were installed around a pile at 1.5 and 2.5 m depth, as shown in Fig. 2.

In these tests, an artificial ground motion called Rinkai, produced as an earthquake in Southern Kanto district in Japan was used as an

Table 1 Test series

Series ID	Superstructure	Soil density
D1	No	Loose
DL	Yes ($T_b > T_g$)	Medium
DS	Yes ($T_b < T_g$)	Dense

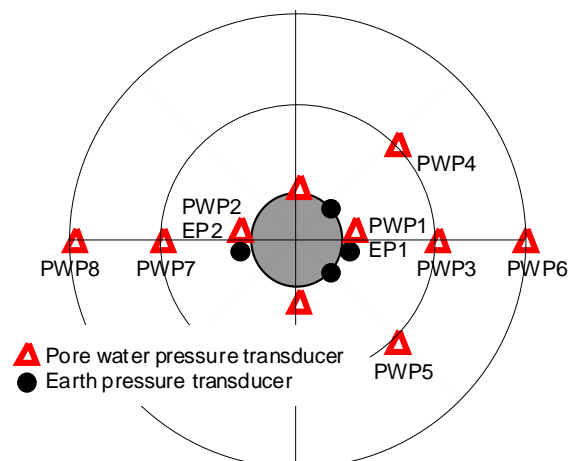


Fig. 2 Instrument on and around pile

input base acceleration to the shaking table, with a maximum acceleration of either 1.5 or 2.0 m/s². The test results evaluated in this study are those of series D1 with a peak input acceleration of 1.5 m/s², and series DL and DS with 2.0 m/s².

3. TEST RESULTS

3.1 Time History of Observed Value

To evaluate the effect of pore water pressure on p-y relation, the displacements of the ground and pile are calculated from the double integration of accelerations and the subgrade reaction from the double differentiation of bending moment with depth. Figs. 3, 4 and 5 show the time histories of the displacements of soil and pile, the relative displacement of the two, the horizontal subgrade reaction and pore water pressure ratio at 2.5 m depth in series DS, DL and D1, together with that of the input motion. The pore water pressure ratio is the average of the four values observed on the surfaces of the pile. The pore water pressure ratio increases to 1.0 in about 20 s, accompanied by an increase in relative displacement between soil and pile.

In dense sand (DS, Fig. 3), the subgrade reaction becomes large at about 20 s, at which the variation of pore water pressure ratio with time is pronounced. Both the subgrade reaction and the variation of pore water pressure ratio with time in

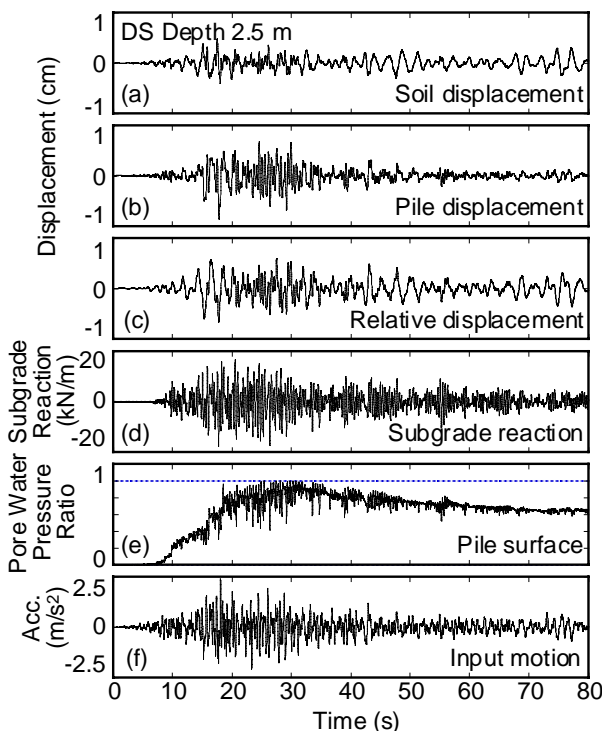


Fig. 3 Time histories at 2.5 m depth in DS

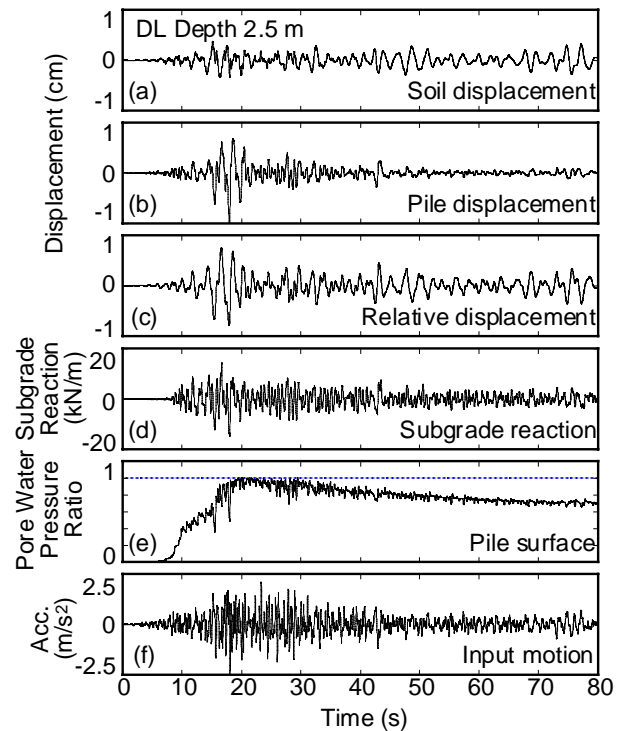


Fig. 4 Time histories at 2.5 m depth in DL

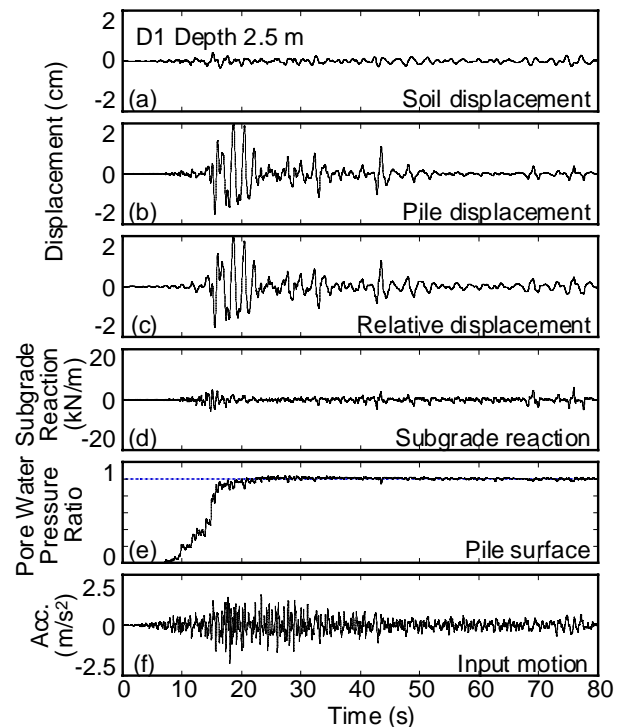


Fig. 5 Time histories at 2.5 m depth in D1

medium dense (DL, Fig. 4) to loose sand (D1, Fig. 5) are less than those in the dense sand (DS). In particular, the pore water pressure does not occur in the loose sand (D1) despite the largest relative displacement among the three tests, yielding a very small subgrade reaction.

3.2 Effect of Pore Water Pressure on p-y Relation

To estimate the effect of pore water pressure on p-y behavior, Fig. 6 shows the relationships of relative displacement between pile and soil with subgrade reaction or pore water pressure ratio at a depth of 2.5 m in series DS, for three time segments, i.e., 0-20 s, 20-50 s and 50-80 s. The subgrade reaction increases sharply with increasing relative displacement and the p-y behavior shows an inverted S-shape, probably due to the dilatancy effects of dense sand. This is well illustrated in Fig. 6(e) in which the pore water pressure in the dense sand decreases with increasing relative displacement between pile and soil.

To examine the mechanism of the large subgrade reaction observed in series DS, Fig. 7 shows the relationships between relative displacement and earth pressure increments measured with EP1 and EP2 on the surfaces of the pile (Fig. 2). The earth pressure increment at EP1 is shown in (a)-(c), and that at EP2 is shown in (d)-(f). The total earth pressure acting on the pile, given by the difference between the two, is shown in (g)-(i). The total earth pressure obtained by the earth pressure gauges is almost consistent with the value of subgrade reaction (Fig. 4) if it is divided by the pile diameter. As expected, according to Fig. 7 (a) and (d), when the earth pressure on one side increases, that on the other side decreases. This creates the compression stress state on one side and extension stress state on the other side of the pile. It is interesting to note that the change in earth pressure is larger on the extension side than on the compression side particularly in the period of 20-50 s.

It seems that the above difference in earth pressures on the extension and compression sides is due to the response of pore water pressure around a pile. Fig. 8 shows the relationships between the relative displacement and pore water pressure ratios measured at the both sides of the pile surface. The pore water pressure on the extension side reduces considerably while that on the compression side is almost unchanged or increases slightly. The trend is related to the variation of earth pressure shown in Fig. 7, suggesting that the large stress increment on the extension side could have occurred due to the large reduction in pore water pressure and the small stress increment on the compression side due to the small change in pore water pressure.

The differences in pore water pressure and earth pressure responses between compression and extension sides of a pile are probably

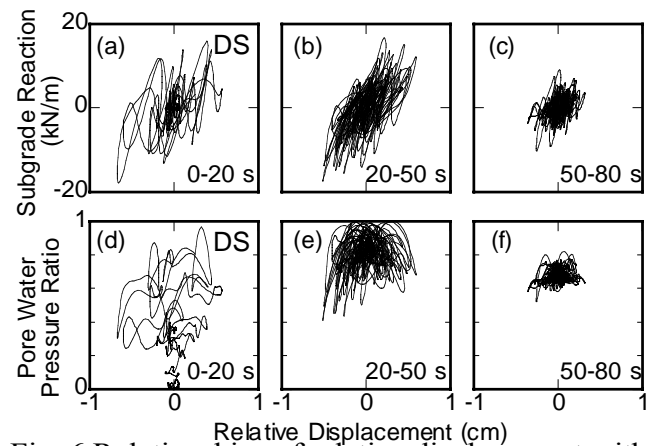


Fig. 6 Relationships of relative displacement with subgrade reaction or pore pressure ratio in DS

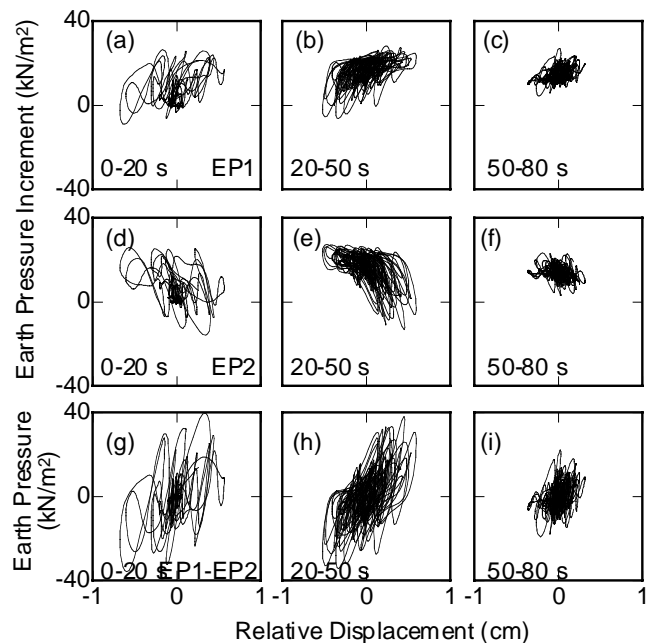


Fig. 7 Relationships between relative displacement and earth pressure in DS

caused by the difference in stress state as schematically shown in Fig. 9 (Narita et al. (2003)). With increasing relative displacement between soil and pile, not only extension and compression stresses but also shear stress develops on the front and rear sides of the pile. Noting that both extension and shear stresses can reduce pore water pressure, the reduction in pore water pressure on the extension side becomes pronounced due to the combined effects of extension stress and dilatancy characteristics of the sand induced by the shear stress. In contrast, the reduction in pore water pressure on the compression side becomes small probably because the compression stress that increases pore water pressure, tends to reduce the reduction in pore water pressure due to dilatancy of the soil induced by the shear stress.

Fig. 10 shows the relationships between relative displacement and pore water pressure ratio at distances equal to and twice the pile diameter from the pile at 2.5 m depth, after liquefaction (20-50 s). The closer the distance from the pile, the larger becomes the pore water pressure reduction for the extension stress (positive displacement in plates (a) and (b), and negative displacement in plates (c)-(f)). In addition, the reduction in pore water pressure at PWP8 is smaller than that at PWP6, in spite of the same distance from the pile of the two sensors. This is probably because the compression and extension stress from the left and right piles are canceled out in the soil inside the pile group (Figs. 1(c) and 2) where PWP8 is located. In contrast, the stress from the pile cannot be cancelled out in the soil outside the pile group where PWP6 is located. A similar trend can be seen in the pore water pressure response observed at the pile surface, as shown in Fig. 8, in which the reduction in pore water pressure measured at PWP1 in the soil outside the pile group is significantly larger than that at PWP2 inside the pile group.

3.3 Effect of Soil Density on p-y Relation

To investigate the effect of soil density on p-y relation, Figs. 11 and 12 compare the relationships of relative displacement with subgrade reaction or the pore water pressure ratio at the pile surface at 2.5 m depth in series D1 and DL having soil densities looser than that in DS. The reduction in pore water pressure is found to be smaller than that in DS, suppressing the increase in subgrade reaction. Especially, the pore pressure in D1 does not show any reduction despite its large relative displacement, yielding a very small subgrade reaction.

Figs. 13 and 14 show the relations between relative displacement and pore water pressure around the pile at 2.5 m depth in DL and D1. The pore water pressure around the pile in DL reduces slightly on the extension side, while keeping almost the same value on the compression side. The larger the distance from the pile, the smaller

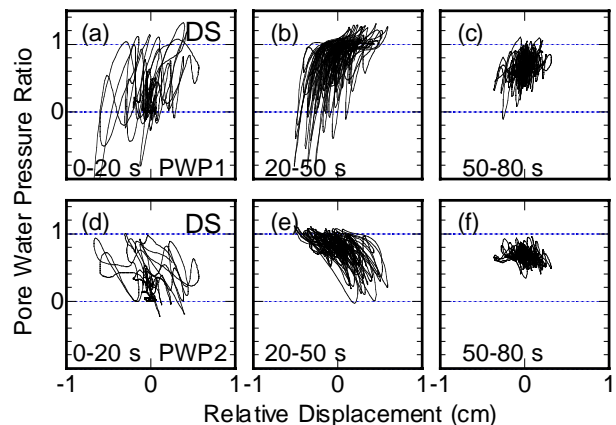


Fig. 8 Relationship between relative displacement and pore pressure ratio in DS

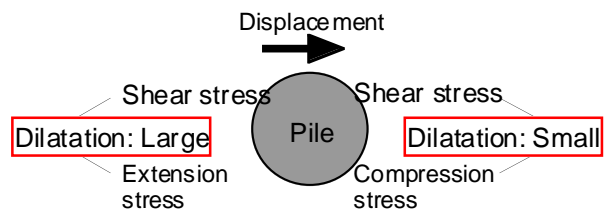


Fig. 9 Stress states around pile

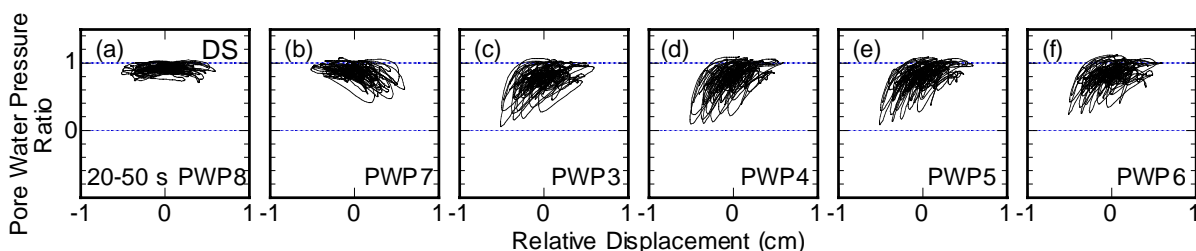


Fig. 10 Relationships between relative displacement and pore pressure ratio around pile in DS

becomes the pore pressure reduction on the extension side (Fig. 13). This trend is similar to that observed in DS. The pore water pressures around the pile in D1, in contrast, do not show any sign of reduction at any place (Fig. 14).

The above findings confirm that the soil density around the pile affects the p-y behavior during liquefaction. Namely, with increasing relative displacement, the dilative nature in dense sand reduces the pore water pressure around the pile particularly on the extension side, making the liquefied sand solid and increasing the subgrade reaction. Conversely, the contractive nature in loose sand does not induce any reduction in pore water pressure at any place around the pile, keeping the liquefied sand liquid and yielding a very small subgrade reaction.

To compare the response of pore water pressure around the pile in the tests, the reduction in pore water pressure with distance from the pile is presented in Fig. 15. The value of pore water pressure ratio is the average of those of the lowest peaks in the period range of 20-30 s. The arrow shows the direction of pile displacement. The compression stress develops in the soil on the front

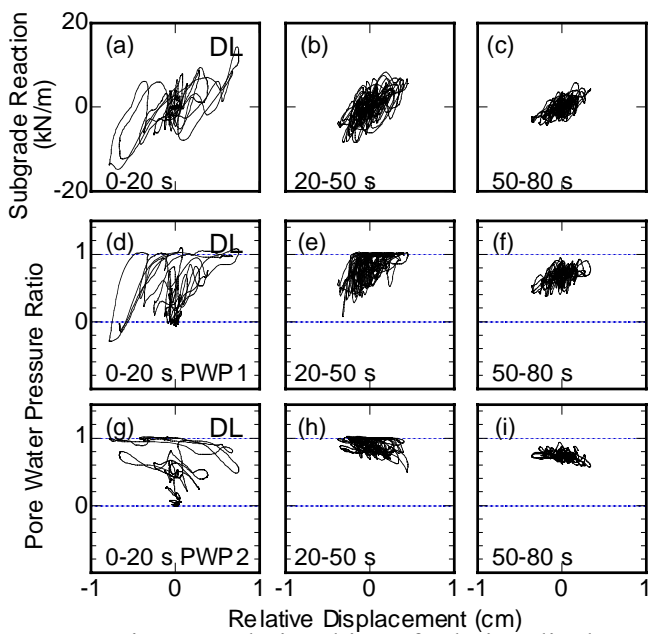


Fig. 11 Relationships of relative displacement with subgrade reaction or pore pressure ratio in DL

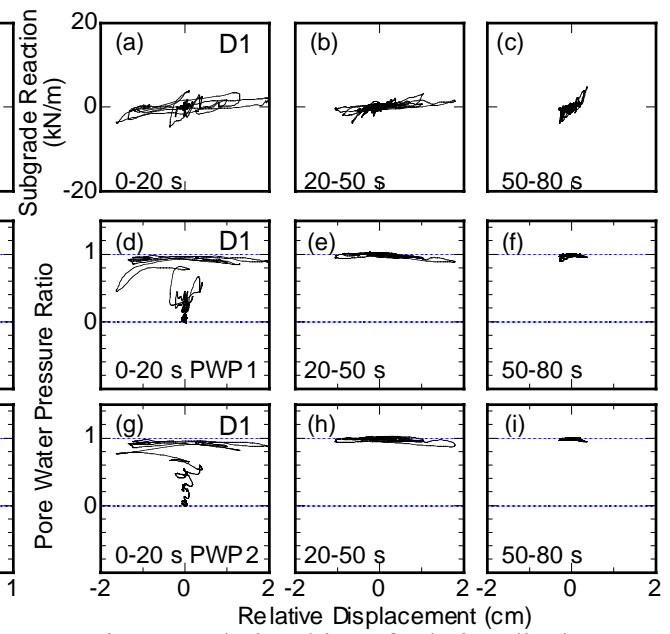


Fig. 12 Relationships of relative displacement with subgrade reaction or pore pressure ratio in D1

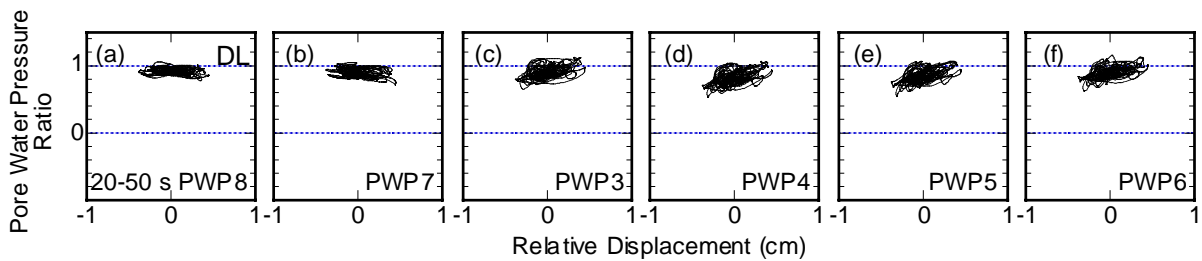


Fig. 13 Relationships between relative displacement and pore pressure ratio around pile in DL

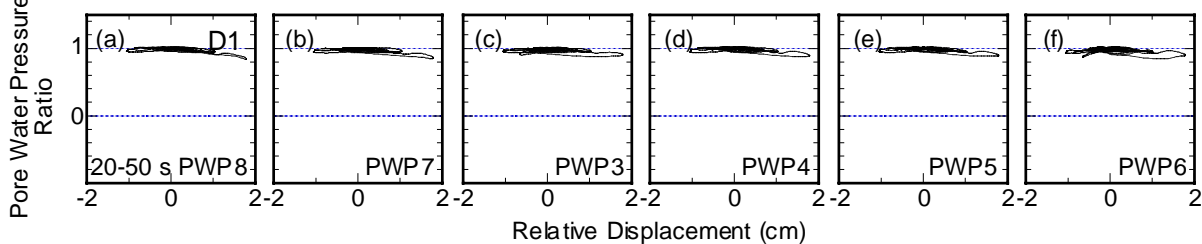


Fig. 14 Relationships between relative displacement and pore pressure ratio around pile in D1

side, while the extension stress on the rear side. The denser the soil, the more pronounced the pore pressure reduction on the extension side. It seems that the reduction in pore water pressure on the extension side depends on the direction of displacement. Namely, the pore water pressure reduction is more significant in soil outside (Fig. 15(b)) than inside (Fig. 15(a)) the pile group. This is probably because the compression and extension stresses from the left and right piles are canceled out in the soil inside the pile group. In contrast, the extension stress from the pile cannot be cancelled in the soil outside the pile group.

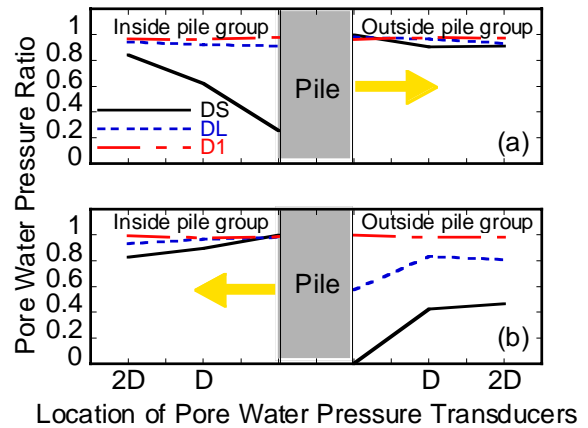


Fig. 15 Reduction in pore pressure around pile in DS, DL and D1

4. CONCLUSION

The effect of pore water pressure response on the subgrade reaction of a pile during liquefaction was investigated based on the large shaking table tests. The test results and discussions lead to the following conclusions:

- (1) The pore water pressure around a pile in dense sand decreases considerably with increasing relative displacement between soil and pile. This causes an increase in subgrade reaction, making the p-y behavior stress hardening. The pore water pressure around the pile in loose sand, in contrast, does not decrease despite a larger relative displacement, making p-y behavior stress softening.
- (2) The reduction in pore water pressure is greater on the extension side than on the compression side of the soil around the pile. This is because the pore water pressure on the extension side decreases due to the combined effects of extension stress and dilatancy of the soil induced by the shear stress, while that on the compression side does not decrease due to the adverse effects of compression stress and dilatancy of the soil.
- (3) The reduction in pore water pressure on the extension side is more remarkable in the soil outside the pile group than inside the pile group. This is probably because the compression and extension stresses from the left and right piles are canceled out in the soil inside the pile group. In contrast, the extension stress from the pile cannot be cancelled in the soil outside the pile group.

Acknowledgments

The study described herein was made possible through Special Project for Earthquake Disaster Mitigation in Urban Areas, supported by Ministry of Education, Culture, Sports, Science and Technology (MEXT). The authors express their sincere thanks to the above organization.

References

- K. Tokimatsu, H. Suzuki, Y. Suzuki & S. Fujii (2002), "Evaluation of lateral subgrade reaction of pile during soil liquefaction based on large shaking table tests" (in Japanese), *Journal of Structural and Construction Engineering*, **553**, 57-64.
- K. Tokimatsu, H. Suzuki & Y. Suzuki (2001), "Back-calculated p-y relation of liquefied soils from large shaking table tests", *Forth International Conference on Recent Advances in Geotechnical Earthquake Engineering and Soil Dynamics*, San Diego, Paper No. 6.24.
- D. W. Wilson, R. W. Boulanger & B. L. Kutter (2000), "Observed seismic lateral resistance of liquefying sand", *Journal of Geotechnical and Geoenvironmental Engineering*, **126**(10), 898-906.
- N. Narita, H. Sako & K. Tokimatsu (2003), "Effects of permeability on interaction between soil and pile during earthquake" (in Japanese), *Thirty-eight Japan National Conference on Geotechnical Engineering*, Akita, 1903-1904.

SCATTERING OF PLANE SH-WAVES BY A CIRCULAR CAVITY IN A PRE-STRESSED ELASTIC MEDIUM

S. Leungvichcharoen¹⁾ and A. C. Wijeyewickrema²⁾

1) Graduate Student, Department of Civil Engineering, Tokyo Institute of Technology, Japan

2) Associate Professor, Department of Civil Engineering, Tokyo Institute of Technology, Japan
somsak@cv.titech.ac.jp, anil@cv.titech.ac.jp

Abstract: Fundamental studies on elastic waves propagating in the presence of obstacles such as cavities, embedded footings and underground tunnels are important in earthquake engineering. Previous studies have been restricted to the case where the surrounding medium is considered to be linear elastic. In this paper, the effect of pre-stress on the scattering of plane SH-waves from a circular cylindrical cavity in a compressible isotropic elastic medium, is studied. The complex function method is employed to analyze the incremental boundary value problem. The spatial variables (x_1, x_2) are mapped on to two different complex planes, to represent the series solution of the incident waves and the scattered waves. The coefficient of each term in the series solution can be computed numerically from a set of linear simultaneous equations, which are constructed by satisfying the incremental traction free boundary condition along the surface of the cavity. Varga material is assumed in the numerical example and in the absence of pre-stress, the analytical solution for linear isotropic elastic case is recovered. Varying the values of principal stretches, the effect of pre-stress on the speed of incident SH-waves and the dynamic stress concentration factor along the surface of the cavity is clearly seen.

1. INTRODUCTION

The dynamic response due to seismic waves, of underground structures such as foundations of superstructures, transportation tunnels or pipelines, is an important engineering problem. There are many previous studies on the analysis of wave scattering problems, where linear elastic assumptions are used, e.g., analysis of SH-waves scattered from a rigid semicircular cylinder embedded in isotropic half-space (Wijeyewickrema and Keer, 1986) and dynamic stress concentration analysis for SH-wave scattering from a cavity in a linear anisotropic elastic medium (Liu 1988; Liu and Han, 1993; Han et al. 1995). However, considering that the earth is an initially stressed medium, it may be more appropriate to model the earth as a pre-stressed elastic medium. In the last two decades, wave propagation problems in pre-stressed elastic media have been extensively studied but due to the complexity of the analysis, which comes from the effects of pre-stress, analytical results of wave reflection and scattering problems, have been limited to reflection of waves from a linear plane boundary or interface only (Ogden and Sotiropoulos, 1998 and Hussain and Ogden, 2001).

In the present paper, SH-wave scattering from a circular cylindrical cavity in a compressible pre-stressed unbounded elastic medium is studied. The complex function method is employed where the fundamental equations and formulation of the problem are given in Sec. 2. The numerical results of two examples when the Varga strain energy function is assumed are given in Sec. 3, and the dynamic stress concentration factor and the non-dimensional displacement and stresses are plotted. The conclusions in Sec. 4 are useful for engineering practice and further studies are suggested.

2. FORMULATION OF THE PROBLEM

2.1 Basic Equations

Consider a homogeneous compressible isotropic elastic material with an initial unstressed state denoted by \mathfrak{B}_u , which after being subjected to pure homogeneous strains has the new configuration \mathfrak{B}_e , the pre-stressed equilibrium state. A Cartesian co-ordinate system $Ox_1x_2x_3$, with axes coincident with the principal axes of strain, is chosen for the configuration \mathfrak{B}_e . Let \mathbf{u} be a small, time dependent displacement superimposed on \mathfrak{B}_e . The incremental equations of motion for small time dependent displacements superimposed on the finite quasi-static deformation and the component of incremental nominal stress tensor \mathbf{s}_0 , can be written as (Chapter 6, Ogden, 1984)

$$A_{0jilk}u_{l,jk} = \rho\ddot{u}_i, \quad s_{0ji} = A_{0jilk}u_{k,l}, \quad (1)$$

where A_{0jilk} are the components of the fourth-order tensor of first-order instantaneous elastic moduli which relates the nominal stress increment tensor and the deformation gradient increment tensor, ρ is the material density in the current configuration and superimposed dot and comma indicate differentiation with respect to time t and spatial coordinate component in \mathfrak{B}_e , respectively.

The corresponding equations for anti-plane deformation where $u_3 = u_3(x_1, x_2, t)$ and $u_1 = u_2 = 0$ can be written as

$$A_{01313}u_{3,11} + A_{02323}u_{3,22} = \rho\ddot{u}_3, \quad s_{013} = A_{01313}u_{3,1}, \quad s_{023} = A_{02323}u_{3,2} \quad (2)$$

in which the instantaneous elastic moduli A_{01313} and A_{02323} are given in term of the strain energy function $W(\lambda_1, \lambda_2, \lambda_3)$ and the principal stretches λ_i , ($i = 1, 2, 3$) as,

$$JA_{0i3i3} = \begin{cases} (\lambda_i W_i - \lambda_3 W_3)\lambda_i^2 / (\lambda_i^2 - \lambda_3^2), & \lambda_i \neq \lambda_3 \\ \frac{1}{2}(\lambda_i^2 W_{ii} - \lambda_i \lambda_3 W_{i3} + \lambda_i W_i), & \lambda_i = \lambda_3, \end{cases} \quad (3)$$

where $W_i = \partial W / \partial \lambda_i$, $W_{ij} = \partial^2 W / \partial \lambda_i \partial \lambda_j$ and $J = \lambda_1 \lambda_2 \lambda_3$ (Roxburgh and Ogden, 1994).

The incremental nominal stress components s_{0r3} and $s_{0\theta3}$ in the cylindrical coordinate system (r, θ, x_3) where $x_1 = r \cos \theta$ and $x_2 = r \sin \theta$ can be expressed as,

$$s_{0r3} = A_{01313}u_{3,1} \cos \theta + A_{02323}u_{3,2} \sin \theta, \quad s_{0\theta3} = -A_{01313}u_{3,1} \sin \theta + A_{02323}u_{3,2} \cos \theta. \quad (4)$$

Since the complex function method is used from Eq. (4), the complex expression of non-dimensional stresses are obtained as,

$$\hat{s}_{0r3} - i\hat{s}_{0\theta3} = [\gamma^2 u_{3,1} - iu_{3,2}]e^{i\theta}, \quad \hat{s}_{0r3} + i\hat{s}_{0\theta3} = [\gamma^2 u_{3,1} + iu_{3,2}]e^{-i\theta}, \quad (5)$$

where $\gamma^2 = A_{01313}/A_{02323}$, $\hat{s}_{0r3} = s_{0r3}/A_{02323}$ and $\hat{s}_{0\theta3} = s_{0\theta3}/A_{02323}$.

2.2 Embedded Cavity and the Incident Plane SH-Wave

Consider an infinitely long circular cavity embedded in an unbounded pre-stressed elastic solid as shown in Fig. 1. The homogeneous principal stretches λ_i , ($i = 1, 2, 3$) yield the corresponding homogeneous static principal Cauchy stresses σ_i , ($i = 1, 2, 3$) (pg. 216, Ogden, 1984) and are given by,

$$\sigma_i = \lambda_i W_i / J, \quad (i = 1, 2, 3). \quad (6)$$

Since homogeneous principal stretches are assumed which yields homogeneous Cauchy stresses the internal static traction that should be applied along the inner surface of the cavity is

$$\mathbf{t}_0(\theta) = -(\sigma_1 \cos^2 \theta + \sigma_2 \sin^2 \theta) \mathbf{e}_r + (\sigma_1 - \sigma_2) \cos \theta \sin \theta \mathbf{e}_\theta, \quad (7)$$

where \mathbf{e}_r and \mathbf{e}_θ are unit basis vectors. For the equibiaxially pre-stressed $\sigma_1 = \sigma_2$ the traction $\mathbf{t}_0(\theta)$ in Eq. (7) corresponding to an internal static pressure (i.e., $p_0 = -\sigma_1$).

The incremental displacement of the incident time harmonic plane SH-wave $u_3^{(i)}(x_1, x_2, t) = U_0 e^{-i\omega t} e^{ik_\alpha(x_1 \cos \alpha + x_2 \sin \alpha)}$ can be expressed in the polar coordinate system as

$$u_3^{(i)}(r, \theta, t) = U_0 e^{-i\omega t} e^{ik_\alpha r \cos(\theta - \alpha)}, \quad (8)$$

where $\theta = \alpha$ is the direction of wave propagation, ω is an angular frequency, $k_\alpha = \omega / c_\alpha$ is wavenumber, and c_α is wave speed in this direction, i.e., $\rho c_\alpha^2 = A_{01313} \cos^2 \alpha + A_{02323} \sin^2 \alpha$ (pg. 474, Ogden 1984). Here the superscript (i) indicates the incident wave.

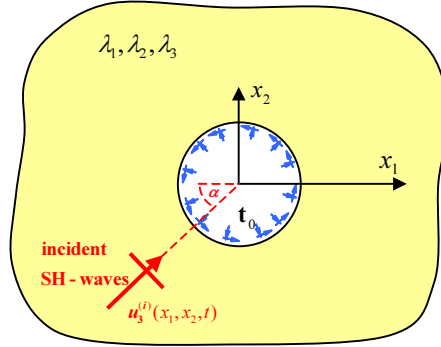


Figure 1. Unbounded pre-stressed material with cavity and the incident plane SH-wave.

Equation (8) may be expressed in the form of a Fourier series expansion (Liu, 1988) as,

$$u_3^{(i)}(r, \theta, t) = U_0 e^{-i\omega t} \sum_{n=-\infty}^{\infty} i^n e^{in(\theta - \alpha)} J_n(k_\alpha r) \quad (9)$$

where $J_n(k_\alpha r)$ is the Bessel function of order n with argument $k_\alpha r$.

To use the complex function method introduce the complex variables,

$$z = x_1 + ix_2 = r e^{i\theta}, \quad \bar{z} = x_1 - ix_2 = r e^{-i\theta}, \quad |z| = r, \quad (10)$$

which yields,

$$u_{3,1}^{(i)} = u_{3,z}^{(i)} + u_{3,\bar{z}}^{(i)}, \quad u_{3,2}^{(i)} = i(u_{3,z}^{(i)} - u_{3,\bar{z}}^{(i)}), \quad (11)$$

where $u_{3,z}^{(i)} = \partial u_3^{(i)} / \partial z$ and $u_{3,\bar{z}}^{(i)} = \partial u_3^{(i)} / \partial \bar{z}$, from which Eq. (9) can be expressed as

$$u_3^{(i)}(z, t) = U_0 e^{-i\omega t} \sum_{n=-\infty}^{\infty} i^n e^{-in\alpha} J_n(k_\alpha |z|) (z/|z|)^n. \quad (12)$$

From Eqs. (5), (11) and (12) the stress components due to the incident wave can be written as

$$\begin{aligned}
\hat{s}_{0r3}^{(i)}(z, t) &= \frac{1}{4} U_0 k_\alpha e^{-i\omega t} \left\{ [(\gamma^2 + 1)e^{i\theta} + (\gamma^2 - 1)e^{-i\theta}] \sum_{n=-\infty}^{\infty} i^n e^{-in\alpha} J_{n-1}(k_\alpha |z|) (z/|z|)^{n-1} \right. \\
&\quad \left. - [(\gamma^2 - 1)e^{i\theta} + (\gamma^2 + 1)e^{-i\theta}] \sum_{n=-\infty}^{\infty} i^n e^{-in\alpha} J_{n+1}(k_\alpha |z|) (z/|z|)^{n+1} \right\}, \\
\hat{s}_{0\theta 3}^{(i)}(z, t) &= \frac{i}{4} U_0 k_\alpha e^{-i\omega t} \left\{ [(\gamma^2 + 1)e^{i\theta} - (\gamma^2 - 1)e^{-i\theta}] \sum_{n=-\infty}^{\infty} i^n e^{-in\alpha} J_{n-1}(k_\alpha |z|) (z/|z|)^{n-1} \right. \\
&\quad \left. - [(\gamma^2 - 1)e^{i\theta} - (\gamma^2 + 1)e^{-i\theta}] \sum_{n=-\infty}^{\infty} i^n e^{-in\alpha} J_{n+1}(k_\alpha |z|) (z/|z|)^{n+1} \right\}.
\end{aligned} \tag{13}$$

2.3 Wave Scattering Solution

When the incident wave $u_3^{(i)}$ impinges on the surface of the cavity, the scattered wave $u_3^{(s)}$ is generated and the total displacement is the summation of both incident and scattered waves i.e., $u_3 = u_3^{(i)} + u_3^{(s)}$. For the scattered wave, another set of complex variables is introduced i.e.,

$$\eta = x_1 + i\gamma x_2 = r(\cos\theta + i\gamma \sin\theta), \quad \bar{\eta} = x_1 - i\gamma x_2 = r(\cos\theta - i\gamma \sin\theta), \tag{14}$$

and hence,

$$\begin{aligned}
u_{3,1}^{(s)} &= u_{3,\eta}^{(s)} + u_{3,\bar{\eta}}^{(s)}, & u_{3,2}^{(s)} &= i\gamma(u_{3,\eta}^{(s)} - u_{3,\bar{\eta}}^{(s)}), \\
u_{3,11}^{(s)} &= u_{3,\eta\eta}^{(s)} + 2u_{3,\eta\bar{\eta}}^{(s)} + u_{3,\bar{\eta}\bar{\eta}}^{(s)}, & u_{3,22}^{(s)} &= -\gamma^2(u_{3,\eta\eta}^{(s)} - 2u_{3,\eta\bar{\eta}}^{(s)} + u_{3,\bar{\eta}\bar{\eta}}^{(s)}).
\end{aligned} \tag{15}$$

Substituting Eq. (15) into Eq. (2a) yields

$$4c_0^2 u_{3,\eta\bar{\eta}}^{(s)} = \ddot{u}_3^{(s)}, \tag{16}$$

where c_0 is the SH-wave speed in x_1 -direction i.e., $\rho c_0^2 = A_{01313}$.

Following the work of Liu et al., (1982) the solution of Eq. (16), which satisfies the radiation condition when $r \rightarrow \infty$ can be written as

$$u_3^{(s)}(\eta, t) = e^{-i\omega t} \sum_{n=-\infty}^{\infty} a_n H_n^{(1)}(k_0 |\eta|) (\eta/|\eta|)^n, \tag{17}$$

where a_n , $n = 0, \pm 1, \pm 2, \dots$ are arbitrary constants and $H_n^{(1)}(k_0 |\eta|)$ is the Hankel function of order n with argument $k_0 |\eta|$ and $k_0 = \omega / c_0$.

The corresponding stress components are

$$\begin{aligned}
\hat{s}_{0r3}^{(s)}(\eta, t) &= \frac{1}{4} k_0 e^{-i\omega t} \sum_{n=-\infty}^{\infty} \left\{ a_n [(\gamma^2 + \gamma)e^{i\theta} + (\gamma^2 - \gamma)e^{-i\theta}] H_{n-1}^{(1)}(k_0 |\eta|) (\eta/|\eta|)^{n-1} \right. \\
&\quad \left. - [(\gamma^2 - 1)e^{i\theta} + (\gamma^2 + 1)e^{-i\theta}] H_{n+1}^{(1)}(k_0 |\eta|) (\eta/|\eta|)^{n+1} \right\}, \\
\hat{s}_{0\theta 3}^{(s)}(\eta, t) &= \frac{i}{4} k_0 e^{-i\omega t} \sum_{n=-\infty}^{\infty} \left\{ a_n [(\gamma^2 + \gamma)e^{i\theta} - (\gamma^2 - \gamma)e^{-i\theta}] H_{n-1}^{(1)}(k_0 |\eta|) (\eta/|\eta|)^{n-1} \right. \\
&\quad \left. - [(\gamma^2 - 1)e^{i\theta} - (\gamma^2 + 1)e^{-i\theta}] H_{n+1}^{(1)}(k_0 |\eta|) (\eta/|\eta|)^{n+1} \right\}.
\end{aligned} \tag{18}$$

The incremental boundary condition along the surface of a circular cavity with radius a is expressed as

$$\hat{s}_{0r3}^{(i)}(z, t) + \hat{s}_{0r3}^{(s)}(\eta, t) = 0, \quad \text{on } |z| = a. \tag{19}$$

Substituting Eqs. (13) and (18) into Eq. (19) yields

$$\sum_{n=-\infty}^{\infty} a_n \phi_n = \phi, \quad (20)$$

where,

$$\begin{aligned} \phi_n &= (k_0 / k_\alpha) \left\{ [(\gamma^2 + \gamma)e^{i\theta} + (\gamma^2 - \gamma)e^{-i\theta}] H_{n-1}^{(1)}(k_0 | \eta |) (\eta / | \eta |)^{n-1} \right. \\ &\quad \left. - [(\gamma^2 - 1)e^{i\theta} + (\gamma^2 + 1)e^{-i\theta}] H_{n+1}^{(1)}(k_0 | \eta |) (\eta / | \eta |)^{n+1} \right\}, \\ \phi &= -[(\gamma^2 + 1)e^{i\theta} + (\gamma^2 - 1)e^{-i\theta}] \sum_{n=-\infty}^{\infty} (i)^n e^{-in\alpha} J_{n-1}(k_\alpha | z |) (z / | z |)^{n-1} \\ &\quad + [(\gamma^2 - 1)e^{i\theta} + (\gamma^2 + 1)e^{-i\theta}] \sum_{n=-\infty}^{\infty} (i)^n e^{-in\alpha} J_{n+1}(k_\alpha | z |) (z / | z |)^{n+1}, \quad \text{on } |z| = a. \end{aligned} \quad (21)$$

Multiply both side of Eq. (20) with $e^{-im\theta}$ and integrating from $-\pi$ to π yields a set of simultaneous equations:

$$\sum_{n=-\infty}^{\infty} A_n \phi_{mn} = \phi_m, \quad m = 0, \pm 1, \pm 2, \dots \quad (22)$$

where $\phi_{mn} = \frac{1}{2\pi} \int_{\theta=-\pi}^{\pi} \phi_n e^{-im\theta} d\theta$ and $\phi_m = \frac{1}{2\pi} \int_{\theta=-\pi}^{\pi} \phi e^{-im\theta} d\theta$. The coefficients A_n , $n = 0, \pm 1, \pm 2, \dots$ can be determined numerically by solving the above system of simultaneous equations.

2.4 Dynamic Stress Concentration Factor

Along the surface of the cavity, the dynamic stress concentration factor is defined as the ratio of incremental stress along the circumference to the maximum amplitude of the incident incremental stress at the same point. For the time harmonic incident SH-wave given in Eq. (8), the maximum incremental stress is $|s_{\max}^{(i)}| = A_{02323} \gamma^2 k_\alpha U_0$. Therefore the dynamic stress concentration factor is

$$|s_{0\theta 3} / s_{\max}^{(i)}| = |\hat{s}_{0\theta 3}^{(i)} + \hat{s}_{0\theta 3}^{(s)}| / (\gamma^2 k_\alpha U_0). \quad (23)$$

3. NUMERICAL RESULTS

As mention in Sec. 2.1 the instantaneous elastic moduli A_{01313} and A_{02323} depend on the strain energy function of the material and the principal stretches. In this section compressible Varga material is assumed and the strain energy function is given as (Roxburgh and Ogden, 1994),

$$W^{(V)} = 2\mu_0 [\lambda_1 + \lambda_2 + \lambda_3 - 3 - \ln(\lambda_1 \lambda_2 \lambda_3)]. \quad (24)$$

From the definition of A_{01313} , A_{02323} , and γ in Sec. 2.1, Eq. (24) yields

$$JA_{01313} = 2\mu_0 \lambda_1^2 / (\lambda_1 + \lambda_3), \quad JA_{02323} = 2\mu_0 \lambda_2^2 / (\lambda_2 + \lambda_3), \quad \gamma = \frac{\lambda_1}{\lambda_2} \sqrt{\frac{\lambda_2 + \lambda_3}{\lambda_1 + \lambda_3}}. \quad (25)$$

In the absence of pre-stress (i.e., $\lambda_1 = \lambda_2 = \lambda_3 = 1$), Eq. (25) yields $A_{01313} = A_{02323} = \mu_0$, $\gamma = 1$ which from the orthogonal properties of $e^{-im\theta}$, $m = 0, \pm 1, \pm 2, \dots$ the linear isotropic solution (pg. 121, Pao and Mow, 1973) is recovered and the coefficient A_n in Eq. (22) can be expressed as

$$A_n = -i^n \frac{nJ_n(k_0 a_0) - k_0 a_0 J_{n+1}(k_0 a_0)}{nH_n^{(1)}(k_0 a_0) - k_0 a_0 H_n^{(1)}(k_0 a_0)}, \quad (n = 0, \pm 1, \pm 2, \dots), \quad (26)$$

where in this case $k_0 = \omega \sqrt{\rho_0 / \mu_0}$ is the wavenumber, ρ_0 and μ_0 are the material density and the shear stiffness in an undeformed configuration, respectively.

For the pre-stressed material that is equibiaxially deformed in (x_1, x_2) -plane (i.e., $\lambda_1 = \lambda_2 = \lambda$), Eq. (25) yields $A_{01313} = A_{02323} = \mu$ and $\gamma = 1$, where $\mu = 2\mu_0 \lambda_1^2 / J(\lambda_1 + \lambda_3)$ is the shear stiffness of the material in the equilibrium configuration. Since $\gamma = 1$ the coefficient A_n is still given by Eq. (26) but with $k_0 a_0$ replaced by $ka = \omega a \sqrt{\rho / \mu}$ where $\rho = \rho_0 / J$ and $a = a_0 \lambda_1^2$ are material density and radius of cavity in the equilibrium configuration, respectively. It can be seen that for the same frequency of the incident waves, the dynamic stress concentration factor $|s_{0\theta 3} / s_{\max}^{(i)}|$ in pre-stress media is different with of linear isotropic case.

Example 1: Figure 2 shows the geometry of this example when the material is equibiaxially deformed in (x_1, x_2) -plane (i.e., $\lambda_1 = \lambda_2 = \lambda$), the internal pressure $p_0 = 2\mu_0(1 - \lambda) / J$ is applied inside the cavity. The internal pressure is necessary since homogeneous stretches are assumed. The incident wave is assumed to propagate in the x_1 -direction with non-dimensional frequency $\bar{\omega} = \omega \sqrt{\rho_0 a_0^2 / \mu_0}$. The principal stretches are varying as $\lambda = 0.1, 0.5, 1.0$ and $\lambda_3 = 0.5, 1.0, 2.0$. The non-dimensional phase speed of the SH-wave $\bar{c} = \sqrt{\mu \rho_0 / \mu_0 \rho}$ and non-dimensional internal pressure $\bar{p} = p_0 / \mu_0$ which depend on the values of principal stretches are shown in Fig. 3, while the dynamic stress concentration factors are shown in Fig. 4.

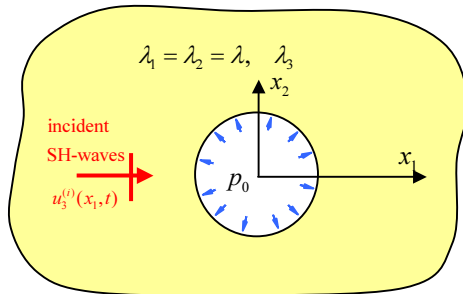


Figure 2. Geometry of Example 1.

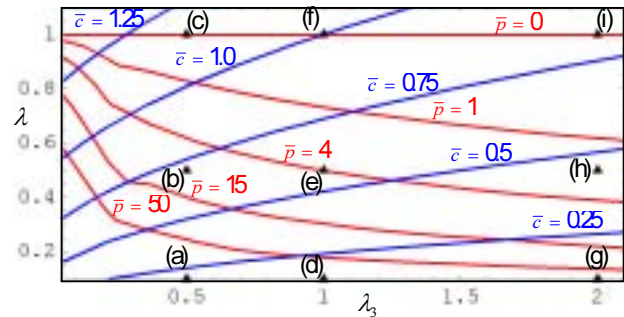


Figure 3. Contour plot of non-dimensional frequency \bar{c} and pressure \bar{p} .

It can be seen in Fig. 3 that for $\lambda_3 < \lambda < 1.0$ which simulates the pre-stressed earth when the (x_1, x_2) -plane is parallel to the horizontal ground surface, the speed of SH-waves is slower than that of the non-pre-stressed material i.e., $\bar{c} < 1.0$, while the surrounding pressure $\bar{p} > 0$.

Since the (x_1, x_3) -plane is a plane of symmetry $|s_{0\theta 3} / s_{\max}^{(i)}|$ is plotted for $0^\circ \leq \theta \leq 180^\circ$. It should be note that the maximum static stress concentration factor in the linear isotropic case is 2.0 at $\theta = 90^\circ$ (pg. 133, Pao and Mow, 1973). In this example when $\bar{\omega} = 0.1$ the maximum value of $|s_{0\theta 3} / s_{\max}^{(i)}|$ is slightly greater than 2.0 and for the higher frequencies ($\bar{\omega} = 1, 2$) the maximum values of $|s_{0\theta 3} / s_{\max}^{(i)}|$ are lower than 2.0. Therefore, the low frequency wave is an important consideration in the study of dynamic stress concentrations in pre-stress media as well as in linear elastic material. The effect of pre-stress on the distribution of $|s_{0\theta 3} / s_{\max}^{(i)}|$ is more for high frequency and less for the low frequency waves.

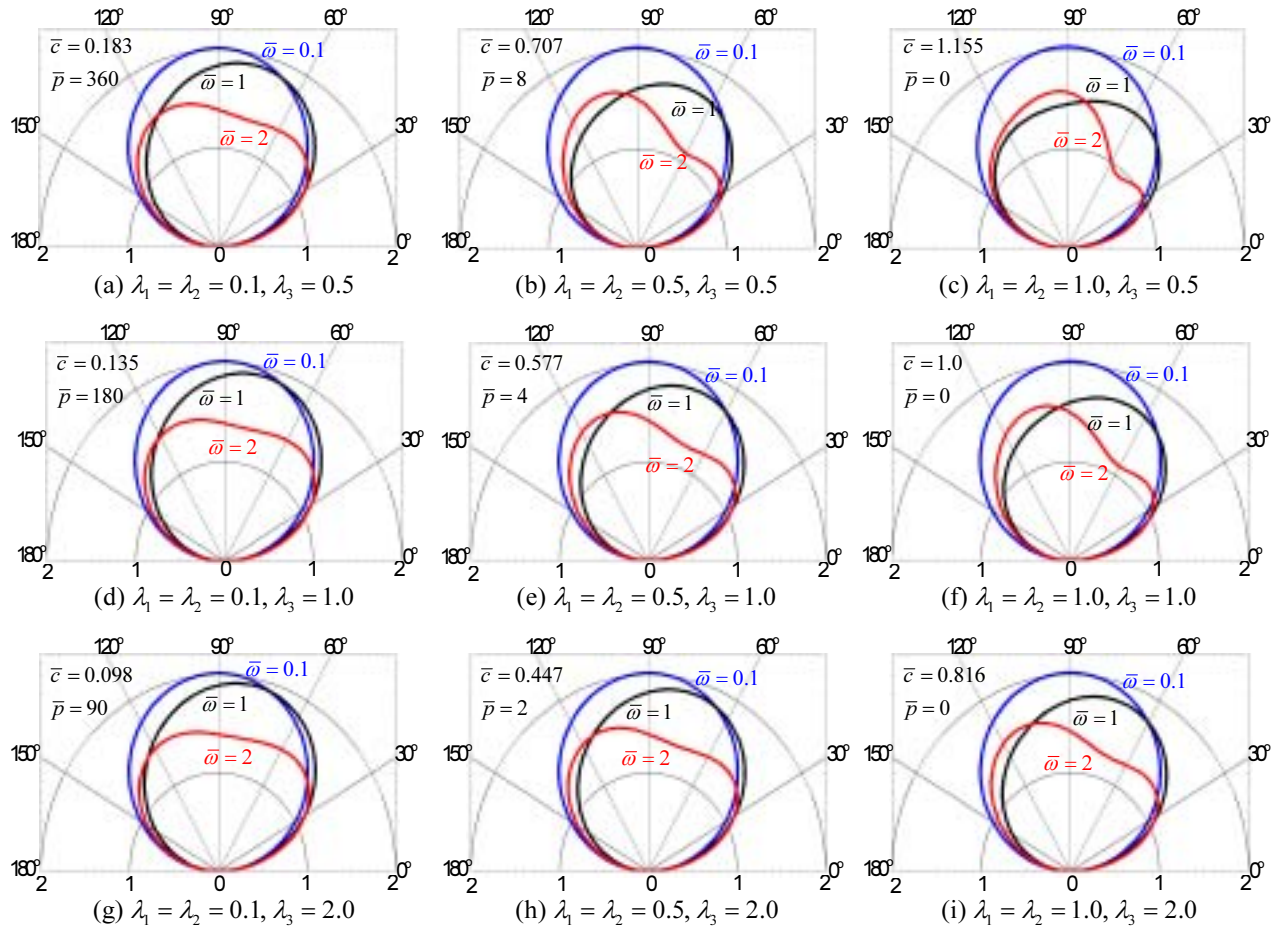


Figure 4. Dynamic stress concentration factor $\left|s_{0\theta 3}/s_{\max}^{(i)}\right|$ of Example 1.

Example 2: The Varga material is equibiaxially deformed in the (x_1, x_3) -plane with the principal stretches $\lambda_1 = \lambda_3 = \lambda = 0.9$ and $\lambda_2 = 0.7$, where the internal static traction $\mathbf{t}_0(\theta) = 3.527\mu_0 [(3\cos^2\theta + \sin^2\theta)\mathbf{e}_r - \sin 2\theta\mathbf{e}_\theta]$ is applied along the inner surface of the cavity since uniform stretches are assumed. The incident SH-wave has an incident angle $\alpha = 45^\circ$ (see Fig. 1) and non-dimensional frequency $\omega\sqrt{\rho a^2/\mu} = 0.5$. Using the method presented in Sec. 2 with $n_{\max} = 20$, the coefficients A_n , $n = 0, \pm 1, \pm 2, \dots, \pm 20$ are numerically obtained. The real and imaginary parts of the amplitude of the displacement and shear stresses along the surface of cavity and the distribution of dynamic stress concentration are plotted in Figs. 5-8.

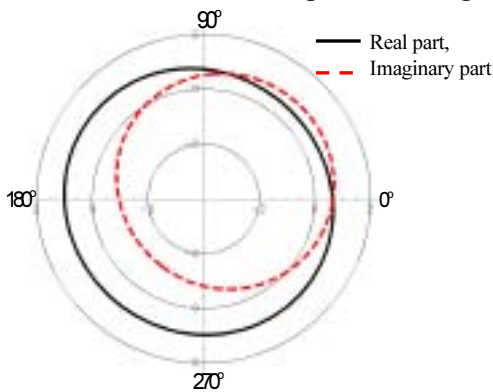


Figure 5. Non-dimensional displacement u_3/U_0 along the surface of cavity.

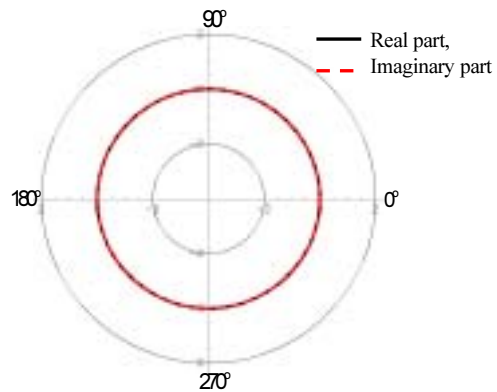


Figure 6. Non-dimensional shear stress $s_{0r3}/|s_{\max}^{(i)}|$ along the surface of cavity.

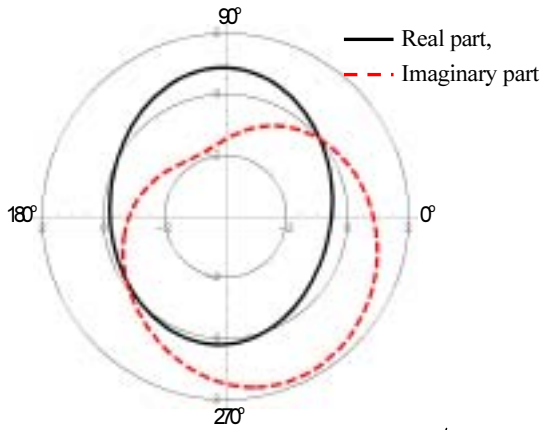


Figure 7. Dynamic stress concentration $s_{0\theta 3}/|s_{\max}^{(i)}|$.

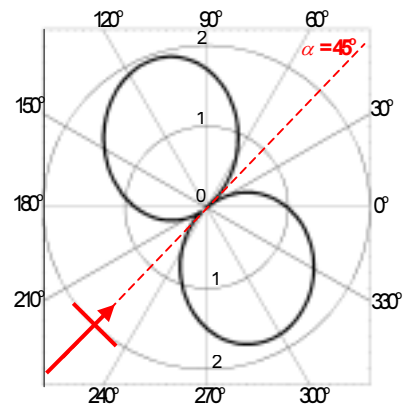


Figure 8. Dynamic stress concentration factor $|s_{0\theta 3}/s_{\max}^{(i)}|$.

Figures 5 and 7 can be used to calculate the displacement and shear stresses at any time in the period of vibration, while Fig. 6 shows that the results agree with the boundary condition at the surface of the cavity. It is seen from Fig. 8 that the position of maximum stress concentration factor is at $\theta = 110.1^\circ$ with $|s_{0\theta 3}/s_{\max}^{(i)}| = 1.939$, and the another local maximum is at $\theta = 297.3^\circ$ with $|s_{0\theta 3}/s_{\max}^{(i)}| = 1.810$ and the distribution of $|s_{0\theta 3}/s_{\max}^{(i)}|$ is not symmetric with respect to any plane or axis for this example.

4. CONCLUSIONS

Using the complex function method the scattering of plane SH-waves from a circular cylindrical cavity in a pre-stressed elastic medium is analyzed. The effect of pre-stress on the speed of plane SH-waves and the dynamic stress concentration factor can be clearly seen from the numerical results. Low frequency waves will have a higher stress concentration than the high frequency waves. The distribution of stress concentration factor for pre-stressed media is not always symmetric, except for the in-plane equibiaxially deformed case. Scattering problems for non-circular cavities and inclusions in pre-stressed elastic unbounded media or in a half-space and the scattering of in-plane waves (P and SV waves) should also be studied.

References:

- Hussain, W. and Ogden R. W. (2001), "The effect of pre-strain on the reflection and transmission of plane waves at an elastic interface," *International Journal of Engineering Science*, **39**, 929-950.
- Liu, D. (1988), "Dynamic stress concentration around a circular hole due to SH-wave in anisotropic media," *Acta Mechanica Sinica*, **4**, 146-155.
- Liu, D., Gai, B. and Tao, G. (1982), "Application of the method of complex functions to dynamic stress concentrations," *Wave Motion*, **4**, 293-304.
- Liu, D. and Han, F. (1993), "The scattering of plane SH-waves by noncircular cavity in anisotropic media," *Journal of Applied Mechanics*, **60**, 769-772.
- Han, F., Yan, W. and Liu, D. (1995), "The interaction of plane SH-waves and circular cavity surfaced with lining in anisotropic Media," *Applied Mathematics and Mechanics*, **16**, 1149-1159.
- Ogden, R. W. (1984), "Non-linear Elastic Deformation," Dover Publications, New York.
- Ogden R. W. and Sotiropoulos, D. A. (1998), "Reflection of plane waves from the boundary of a pre-stressed compressible elastic half-space," *IMA Journal of Applied Mathematics*, **61**, 61-90.
- Pao, Y.-H. and Mow, C.-C. (1973), "Diffraction of Elastic Waves and Dynamic Stress Concentrations," Crane-Russak, New York.
- Roxburgh, D. G. and Ogden, R. W. (1994), "Stability and vibration of pre-stressed compressible elastic plates," *International Journal of Engineering Science*, **32**, 427-457.
- Wijeyewickrema, A. C. and Keer, L. M. (1986), "Antiplane transient response of embedded cylinder," *ASCE Journal of Engineering Mechanics*, **112**, 536-549.

EVACUATION BEHAVIOR IN CITY FIRE FOLLOWING EARTHQUAKE

Y. Meshitsuka¹⁾, Y. Aoki²⁾, R. Ohno³⁾, T. Osaragi⁴⁾, and M. Katayama⁵⁾

1) Graduate Student, Department of Architecture and Building Engineering, Tokyo Institute of Technology, Japan

2) Professor, Department of Architecture and Building Engineering, Tokyo Institute of Technology, Japan

3) Professor, Department of Built Environment, Interdisciplinary, Tokyo Institute of Technology, Japan

4) Associate Professor, Department of Mechanical and Environmental Informatics, Tokyo Institute of Technology, Japan

5) Graduate Student, Department of Built Environment, Interdisciplinary, Tokyo Institute of Technology, Japan

meshi@mail.arch.titech.ac.jp, aoki@arch.titech.ac.jp, rohno@n.cc.titech.ac.jp,

osaragi@mei.titech.ac.jp, katamegu@enveng.titech.ac.jp

Abstract : In this study, we propose a model which describes evacuation behavior in a city fire following a strong earthquake by considering the effect of evacuees' familiarity / unfamiliarity with areas. Through some of the simulations in the model, we examine the layout of evacuation areas. As the result, it is shown that the largest number of people can evacuate in the case that all evacuation areas are placed on the center of the target city.

1 INTRODUCTION

1.1 Background and Objectives

Many studies on evacuation behavior in a city fire following a strong earthquake have been carried out (e.g., Itoigawa et al 1989). Most of these studies were based on the assumptions that everybody can take an appropriate route and evacuate to the nearest evacuation area. From the following two reasons, however, those assumptions are hardly accepted in the case that people evacuate in an unfamiliar area. The first reason is that it seems to take more time to move in an unfamiliar area by losing their way or taking roundabout route. The second reason is that people are likely to take familiar routes even if more suitable and short routes may exist, as shown in Murosaki and Yamada (1980). Hence, in this study, we construct a model which describes evacuation behavior in a city fire following an earthquake by considering of the effect of their familiarity with areas, and examine the proper layout of evacuation areas through simulations.

In the previous study, Aoki et al (1992) showed that the information boards on main evacuation routes could bring smooth evacuation. In addition, the effectiveness of pre-learning and guide-information was reported (Kaji 1989, Aoki et al 1992, Kumagai 1992, Kakei et al 2000). However, evacuees' familiarity / unfamiliarity with areas was not discussed in the previous researches.

1.2 Simulation Model

It is necessary to integrate the situation of fire spreading and behavior of evacuation, when we estimate human injuries caused by considering the phenomenon in which evacuees are surrounded and killed in the flames. It is, however, too difficult to treat the situation of fire spreading and behavior of evacuation simultaneously using the real complex road networks of cities.

From the viewpoint of practical availability and effectiveness, a grid based model was proposed (Okada et al 1979). In this model, on one hand each area is represented by a grid, and the behavior of evacuation is expressed by the number of person who move across the boundary between two adjacent grids, and all the evacuation starts directly after the earthquake. The amount of movement per unit time is determined by the total road width on a grid line. On the other hand the original point of a fire is represented on the intersection of two grid lines, and the state of fire spreading is represented on grid lines. The accuracy of these model is limited since the situation of inside of grids is simplified, while it is still useful for looking at the situation in perspective.

In this study, the Okada's model is modified by describing the evacuation behavior more accurately. In the following section, the outline of model is described. The details of this model can be found in Okada et al (1979) and Aoki et al (1992).

2 FIRE-SPREAD MODEL

Spreading of fire is considered as a kind of stochastic processes. Therefore, Monte Carlo method is appropriate for simulating fire-spreading of each building. In respect of a grid based model, however, it is not always effective to use an accurate stochastic model like the Monte Carlo method. Hence, in this study, we adapt a compact and non-stochastic model based on Hamada's formulation which was used in Okada et al (1979). In this model, we assume that the specific number of fires break out at random place after a strong earthquake, and spread at the speed V represented by equation (1):

$$V = C_w \times C_e \times K \times V_{wood}, \quad (1)$$

where C_w and C_e are the coefficient of wind and the coefficient of extinguishing respectively. In addition, K is the coefficient of prevention of surrounding buildings and V_{wood} is the fire spread speed in pure wooden urban district. The value of K is calculated as follows:

$$K = \{(a + b)(1 - c)\} \div \left\{a + \frac{b}{0.6}\right\}, \quad (2)$$

where the parameters a , b and c respectively represent the ratio of pure-wooden buildings, fire-prevention building and fire-resistant building. The above parameter C_w , C_e and V_{wood} are set up as the average state of city as follows:

$$C_w = 1.0, \quad C_e = 0.8, \quad V_{wood} = 2.3m/min.$$

3 EVACUATION MODEL

3.1 Daily Life Area (DLA)

The area where people usually move on foot is seemed to be restricted, and people seldom move to the outside of this area. In this study, this area is called Daily-Life-Area (DLA) and the effect of this area on the evacuation behavior is discussed.

DLA seems to be similar to the area surrounding the house and nearest railroad station in Tokyo or other Japanese cities. Hence, we compute DLA in the following procedures. Firstly, we draw the straight line which connects a evacuee's house and the center of district which includes a railroad station. If evacuees at Area(x_0, y_0) are in their DLA, we express $DLA(x_0, y_0) = 1$, and otherwise $DLA(x_0, y_0) = 0$. In case evacuees in an area come from two or more areas, the coordinates(x_0, y_0) of Area(x_0, y_0) is obtained from the average coordinates weighted by the number of evacuees.

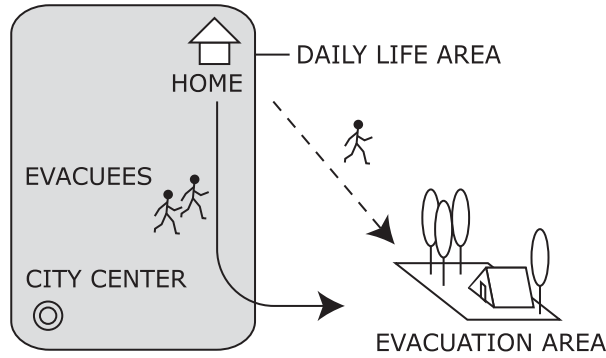


Figure 1: Daily-Life-Area

3.2 Effects of Daily Life Area in Evacuation Behavior

Evacuees staying at outside of DLA are likely to lose their way or take roundabout route, as compared with evacuees in DLA. That is, the evacuation speed at outside of DLA is expected to be less than that at inside of DLA. Therefore, we estimate the time to move across a grid line for each evacuee, denoted by T , as follows:

$$T(x, y) = \frac{(1 - \alpha DLA(x, y)) \times E(x, y)}{\sum_w C_f \times R_p(x, y, \omega)}. \quad (3)$$

In equation (3), α expresses the effect of DLA. $\alpha = 0$ shows the case that the effect of DLA is negligible, and $\alpha = 1.0$ shows the case that the effect of DLA is critical. In the following case study, the value of α is changed at intervals of 0.2 from 0.0 to 0.6. In addition, $E(x, y)$ is the number of evacuees, $R_p(x, y, \omega)$ is total width of passable road to each direction and C_f is the coefficient of fluidity of crowded people. The value of above parameter C_f is assumed to be low, i.e., $C_f = 1.0 \text{ person}/m \cdot \text{sec}$, since old people and children are included in evacuees.

3.3 Evacuation Route Selection

In this model, evacuees in the same area are treated as one group and move together. When a group of evacuees on each grid decides where to go next, the following procedures are used. Firstly

the average time to pass through each areas is estimated by equation (3). The time to pass areas in outside of DLA are excessively estimated according to the effect of DLA (α). Secondly the shortest time to reach to each evacuation area is searched, and the route is recorded. Finally the evacuation area, where the time for evacuation is shortest and the capacity is large enough, is selected. Thus, the grid which the group of evacuees moves to is determined. Note that they don't move toward the truly nearest evacuation area.

After the above procedures, the number of evacuees who move to the next grid is determined by the total road width on grid line as $M(x, y, \omega)$ by following equation (4):

$$M(x, y, \omega) = E(x, y) \times \frac{R(x, y, \omega) \cdot C_v \cdot C_f}{\sum_w R(x, y, \omega) \cdot C_v \cdot C_f}, \quad (4)$$

where $E(x, y)$ is the number of evacuees, $R(x, y, \omega)$ is total width of passable road in the each direction, C_v and C_f are the coefficient of effective road width and the coefficient of fluidity of crowded people respectively. The value of C_v is assumed to be 0.4 because many barricades on evacuation routes such as cars and various obstructions disturb their evacuation. Evacuees who reach to evacuation area are added to the number of successful evacuees. Evacuees who can't move any directions in surrounding fire are regarded as death toll.

4 CASE STUDY

The space of target city is composed of the grid data of 20×20 cells, and the size of a grid represents $500\text{m} \times 500\text{m}$. In this study, we compare the following 4 layouts of evacuation areas (see figure 2). All evacuation areas of type-A are distributed on the perimeter zone, meanwhile all evacuation areas of type-D are distributed on the central zone.

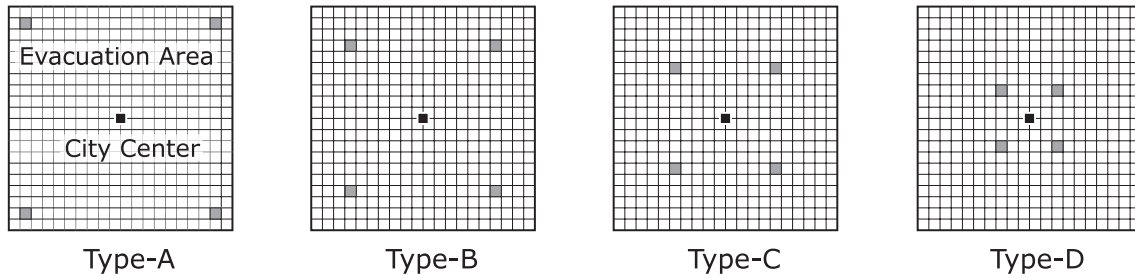


Figure 2: Layout of evacuation area

The process of evacuation is visualized in figure 3. The number of evacuees in each area is represented by the color of area. The number of evacuees who move to neighboring area is represented by the length of arrows on each grid line. Each original point of a fire is represented at one of the intersections, and fire-spread is represented on grid line.

Figure 4 shows the process of evacuation and fire-spread of each layout. Quite different movement of evacuees is observed for each layout. Figure 5 shows the relationship between the speed of evacuation and the effect of DLA(α). The ordinate is total number of evacuees who succeed in evacuation in 10 hours. It is obvious that the largest number of people can evacuate in the case of type-D. This means that if the effect of DLA is not negligible, type-D is the best among these 4 layouts.

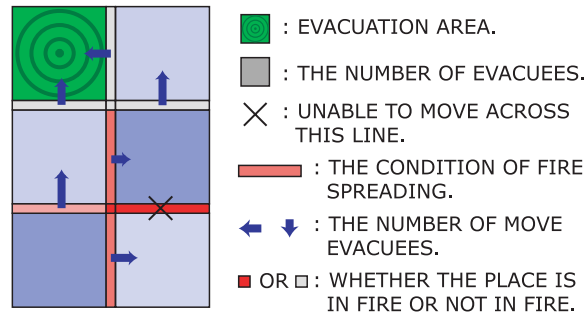


Figure 3: Visualization of evacuation process

In order to understand the detail of this result, the process of evacuation of each layout is examined. Figure 6 shows the changes of evacuation speed according to lapsed time after earthquake. The ordinate is the number of evacuees who succeeded in evacuation in 1 hour. It is shown that type-A is superior layout in 2 hours after earthquake, and type-B and type-C are superior layouts in the next 2 hours. However, type-D becomes the most superior layout after 4 hours.

5 Conclusion

The proper layout of evacuation areas are examined by considering the difference in evacuation behavior caused by evacuees' familiarity / unfamiliarity with areas. As the result of 4 layouts of evacuation areas, the largest number of people can evacuate in the case that evacuation areas are placed on the center of the city.

In Japan, evacuation areas are often located in public facilities such as large parks in the suburbs. However, according to our results of some simulations, evacuation areas should be located at the center of city, although further research is needed.

References :

- Itoigawa E., et al (1989), "Study of Real Time System for Information Processing of Post-earthquake Fire – Fire spread prediction and evacuation control –," *Report of The Building Research Institute*, Building Research Institute, **120**.
- Murosaki M. and Yamada T. (1980), "Research on A Resident's Evacuation Area Selection (In Japanese)," *Journal of the City Planning Institute of Japan*, The City Planning Institute of Japan, **15**, 259-264.
- Okada K., Yoshida K., Kashihara S. and Tsuji M. (1979), "Presumption of Human Injury in Case of Earthquake's Fire and Consideration on Its Countermeasure – Part 1 Structure of Computer Simulation Model and its Assumptions –," *Transaction of the Architectural Institute of Japan*, Architectural Institute of Japan, **275**, 141-148.
- Kaji H. (1989), "Effectiveness of Information about Damage on Resident's Safe Evacuation," *Journal of the City Planning Institute of Japan*, The City Planning Institute of Japan, **24**, 73-78.

- Kumagai Y. (1992), "Experimental Study on Arrangement of Evacuation Guidance Signs," *Journal of the City Planning Institute of Japan*, The City Planning Institute of Japan, **27**, 571-576.
- Takei H., Sato H, Iyata Y. and Sako T. (2000), "A Psychological Study on Effectiveness of Pre-learning and Guide-information in Evacuation – A Development of Evacuation Guidance-System Based on Multimedia Technology Part I –," *Journal of Architecture Planning Environment Engineering*, Architectural Institute of Japan, **535**, 139-146.
- Aoki Y., Osaragi T and Hashimoto K. (1992), "A Simulation Model of Evacuation Behavior in the Fire-Spread Urban Area Following Earthquake – Effects of Hearsay Information Process and Geographical Urban Image –," *Journal of Architecture Planning Environment Engineering*, Architectural Institute of Japan, **440**, 111-118.
- Horiuchi S., Yasuno K. and Murosaki M. (1994), "New edition : Fire Prevention Of Buildings (In Japanese)," Asakura-Shoten.

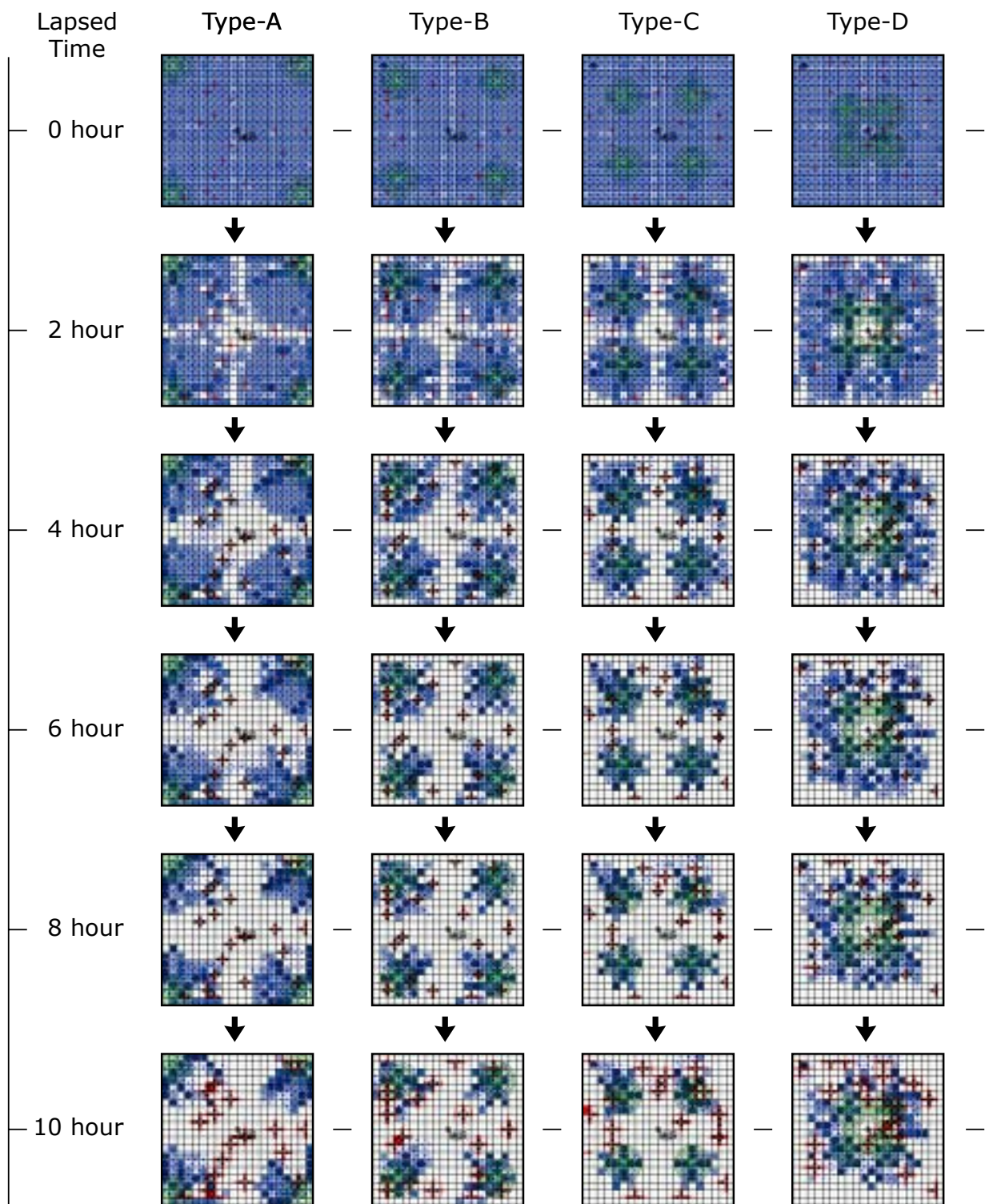


Figure 4: The process of evacuation and fire-spread ($\alpha=0.2$)

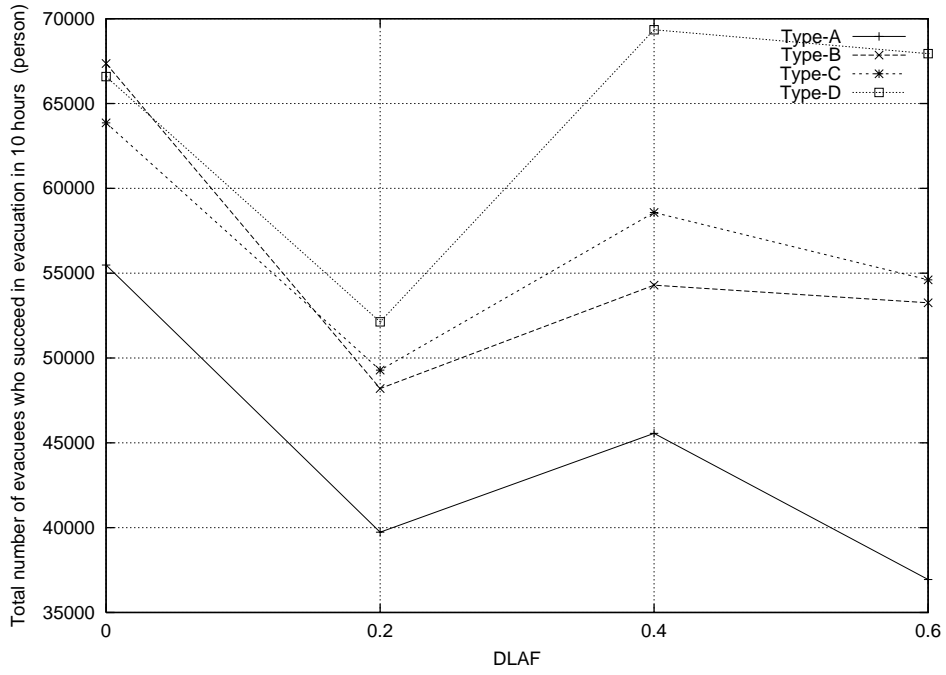


Figure 5: Total number of evacuees who succeeded in evacuation in 10 hours

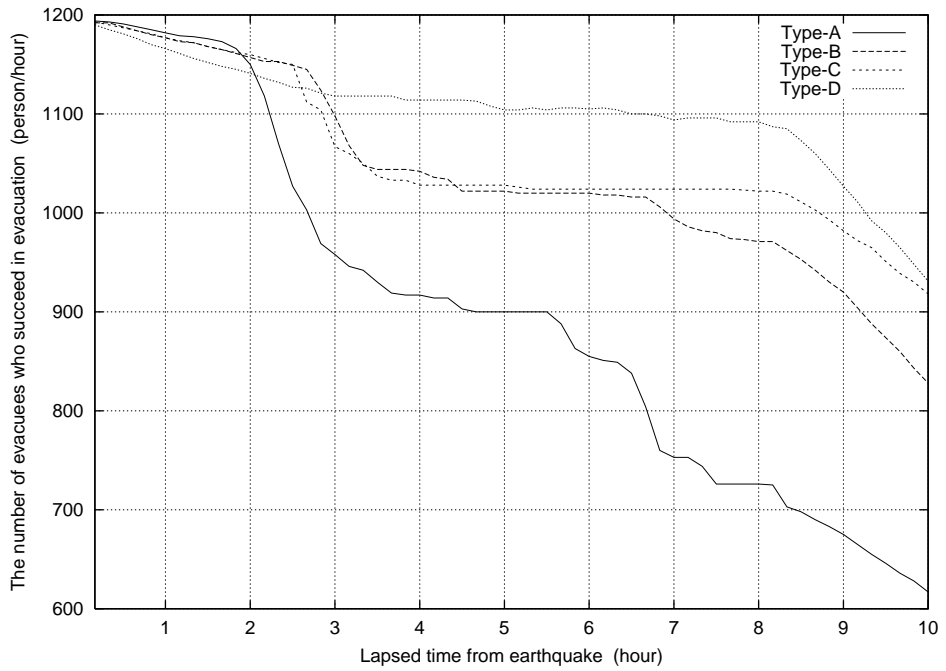


Figure 6: The changes of evacuation speed according to lapsed time after earthquake ($\alpha=0.2$)

RELATION BETWEEN RAYLEIGH WAVES AND UPLIFT OF THE SEABED FOR RAPID TSUNAMI DETECTION

S. Inoue¹⁾, T. Ohmachi²⁾

1) *Research Associate, Department of Built Environment, Tokyo Institute of Technology, Japan*

2) *Professor, Department of Built Environment, Tokyo Institute of Technology, Japan*

shusaku@enveng.titech.ac.jp, ohmachi@enveng.titech.ac.jp

Abstract: In recent years, serious damages have been caused by near field tsunamis whose arrival time is less than or equal to a few minutes after the occurrence of earthquakes. In this research, to develop a new tsunami warning system that is more quickly and more accurate than the current systems, we aimed Rayleigh wave inducing the sea surface disturbance preceding tsunami. For this purpose, we research the characteristics of Rayleigh wave and the sea surface disturbance from simulation and real data. The good correlation between the static uplift and the displacement of Rayleigh waves was found on the hanging wall side of the fault plane only.

1. INTRODUCTION

In recent years, serious damages have been caused by near field tsunamis whose arrival time is less than or equal to a few minutes after the occurrence of earthquakes. Current tsunami warning systems need at least some minutes to announce tsunami warning because they are usually based on submarine faults estimated from seismic data observed at several points. Additionally, the wave height estimated from the real time tsunami warning system does not correspond to the actual wave height in near field owing to some approximations in that estimation.

To develop a new tsunami warning system that is more quickly and more accurate than the current systems, we are trying to make use of Rayleigh wave that induces the sea surface disturbance preceding tsunami. The purpose of this study is to investigate the possibility of a tsunami warning system by means of Rayleigh wave and the sea surface disturbance. For this purpose, we study the characteristics of Rayleigh wave and the sea surface disturbance from simulation and real data.

Figure 1 shows the wave height observed at Fukaura in 1983 Nihonkai-Chubu earthquake. The main purpose of this

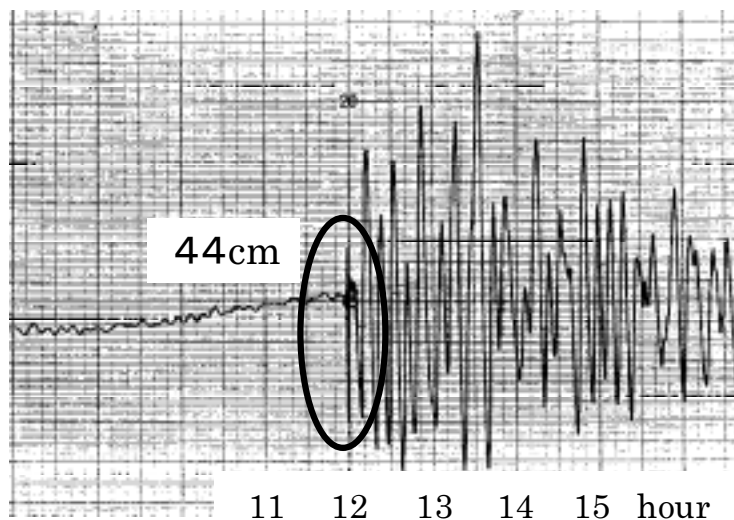


Fig. 1. Tidal record at Fukaura

instrument is to record the tide, so the chart speed is very slow. Each thick line crossing the horizontal axis indicates 1 hour. From this record, long period waves arriving after 12 o'clock can be seen. These waves are the tsunamis that attacked Fukaura. Another wave with amplitude 44cm can be seen at just 12 o'clock, which arrived 7 minutes before the tsunami. This wave is the sea surface disturbance preceding tsunami.

2. TWO-DIMENSIONAL TSUNAMI SIMULATION

The generation of the sea surface disturbance and the tsunami are evaluated by a 2-dimensional simulation. The technique in this simulation is different from conventional ones that use the static seabed displacement and long wave approximation. In the present technique, a total system consisting of the sea water and the underlying ground is assumed to be a weakly coupled system. As a simulation procedure, earthquake ground motion due to seismic fault rupturing is first simulated by the boundary element method (BEM). Then, sea water disturbance including tsunami resulting from the seismic ground motion is simulated by the finite difference method (FDM) using the ground motion velocity as an input to the sea water. In the fluid domain simulation, the governing equation is the Navier-Stokes equation, which accounts for acoustic effects (Ohmachi et al., 2001).

Figure 2 illustrates the analytical model employed. Due to its contribution to tsunami generation we assumed thrust faulting for a 30km wide segment, dipping at 30 degrees, located 7km under the seabed. This fault undergoes unilateral faulting, which means that the fault rupture starts at the bottom of the fault and propagates upward. The rupture velocity, dislocation, and rise time are as shown in Fig. 2. The water depth above the seabed is 3km, and the simulation area extends to +/- 100km from the fault.

Snapshots at several seconds after the fault rupturing are shown in Fig 3. The lower and upper surfaces represent the seabed and the sea surface, respectively. At 15sec after the fault rupturing occurs, the wave height in the near-fault area is larger than the seabed displacement. From 20 to 30 sec, Rayleigh waves are generated in the near-fault area, propagating along the seabed, to the right of the figure. The short period sea surface waves travel with the same speed as these Rayleigh waves. The profile of tsunami remaining in the near-fault area at 50 sec propagates to the both side. From this simulation, the sea surface disturbance excited by Rayleigh wave preceding tsunami can be estimated.

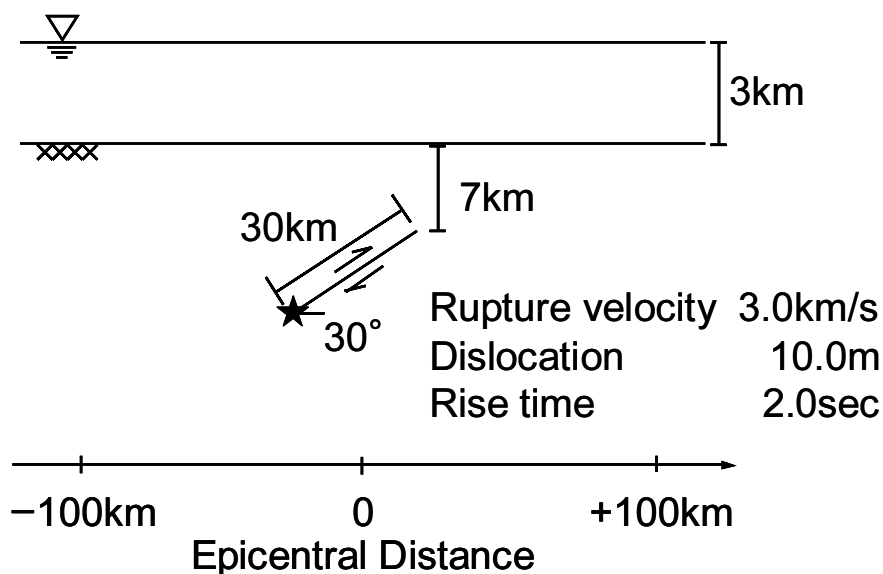


Fig. 2. A 2-D tsunami simulation model.

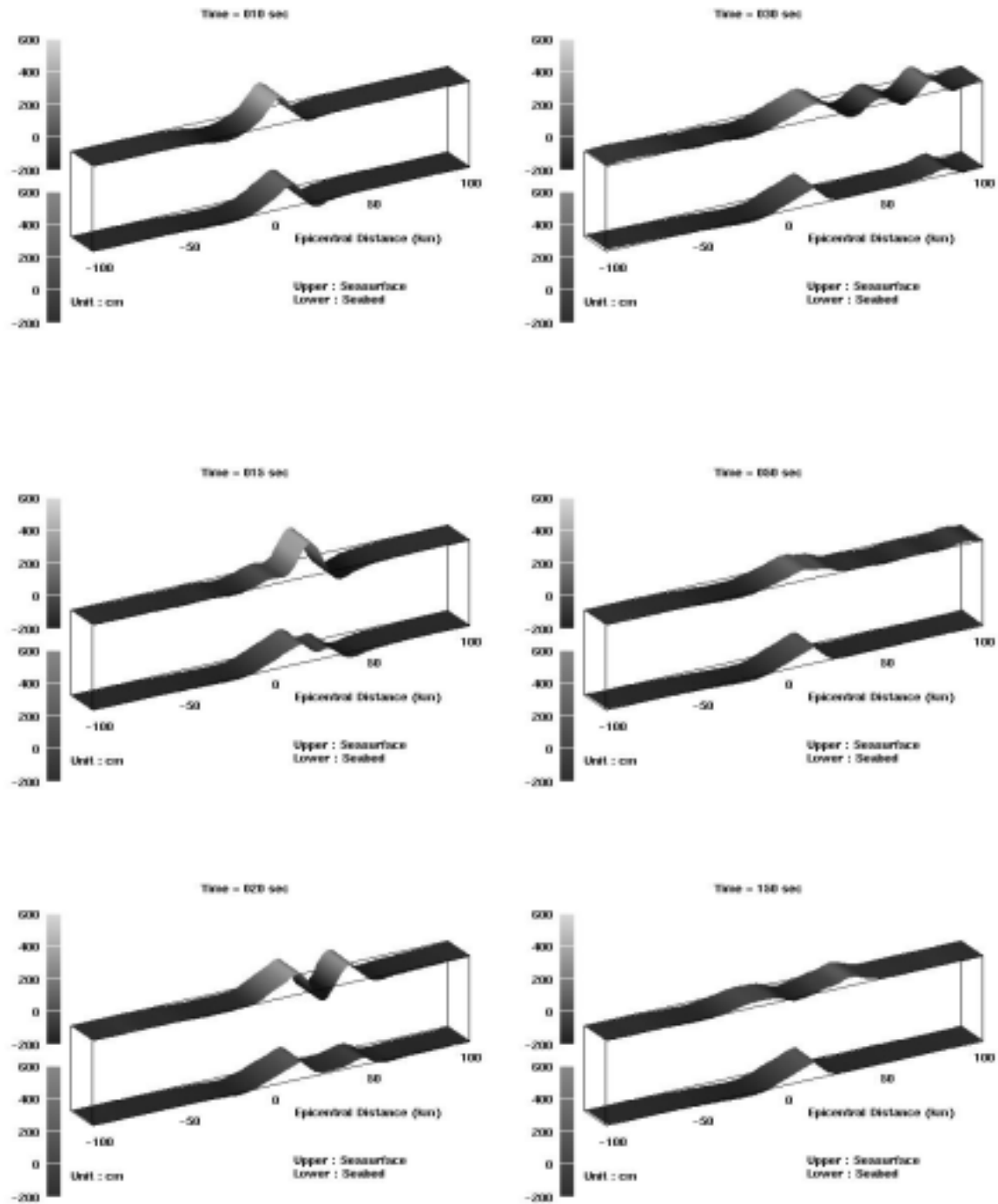


Fig. 3. Two-dimensional tsunami simulation.

3. CHARACTERISTICS OF PROPAGATION

3.1 The 1993 Hokkaido-Nansei-Oki tsunami

To develop a single-point observation system, it is needed to know how Rayleigh waves as well as the sea disturbance propagate from the source area. To investigate the characteristic of the propagation, we check the tidal records of the 1993 Hokkaido-Nansei-Oki tsunami, and the seismic data of the 1999 Chi-Chi Taiwan earthquake.

Figure 4 shows wave height distribution of sea surface disturbance observed prior to the tsunami 1993 Hokkaido-Nansei-Oki earthquake. In this figure, tidal observation points and wave height in cm are shown by black circles and numbers. A fault model proposed by Mendoza and Fukuyama(1996) has northern and southern faults. The fault projection is also shown in Fig. 4. In this model, fault rupturing starts at northern fault and propagates to the southern fault. Black stars in Fig. 4 are epicenters of the faults. From the figure, the sea surface disturbances are observed at limited points from Iwanai to Noshiro. These points extend to the south. It is because the sea surface disturbances are induced by Rayleigh waves, which becomes larger gradually as fault rupturing propagates from Northern fault to Southern fault. The Rayleigh wave propagates in the ground, so the sea surface disturbance is observed at Mori where tsunami did not arrive.

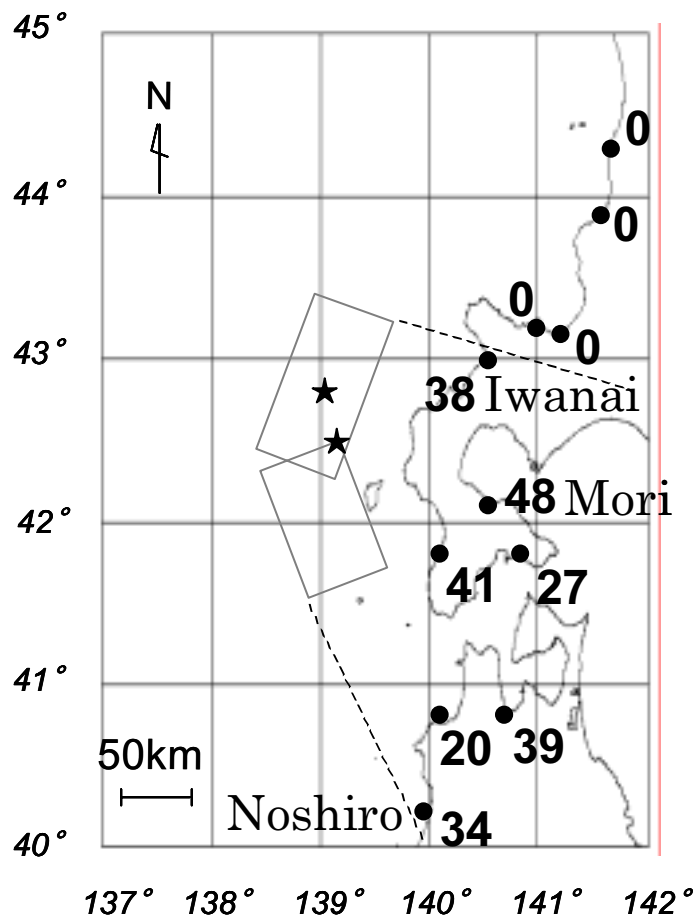


Fig. 4. Wave height distribution of sea surface disturbance.

3.2 The 1999 Chi-Chi Taiwan earthquake

The 1999 Chi-Chi Taiwan earthquake is due to low angle thrust-faulting with $M_s = 7.6$ (USGS), occurred in central Taiwan on September 20, 1999. Though thrust-faulting subduction earthquake causes tsunami frequently, for this reason, we use this earthquake in this study.

Digital seismic acceleration data that contains 441 points all around Taiwan were provided by Lee et al (2001). Figure 5 shows these observation stations and the fault projection proposed by Kikuchi et al. (2000). This fault model is low angle thrust faulting, and slopes down to the east. To find displacement by Rayleigh waves, the vertical acceleration records were integrated with a bandpass filter from 2 to 20 sec.

The distribution of maximum displacement is shown in Fig. 6. From this figure, the displacement is larger on the northwest side of the fault than the other side. Moreover larger displacement is limited to the front of the fault. The epicenter of this earthquake is located at around the center of this fault. We thought that the Rayleigh wave increased in the amplitude gradually on the west side as fault rupturing propagates in shallow area, while the Rayleigh wave does not increase on the east side that fault rupturing propagated in deep area. From the result, it can be thought the Rayleigh wave showed directionality that the amplitude increased in the direction of fault rupturing and in the front area of the fault.

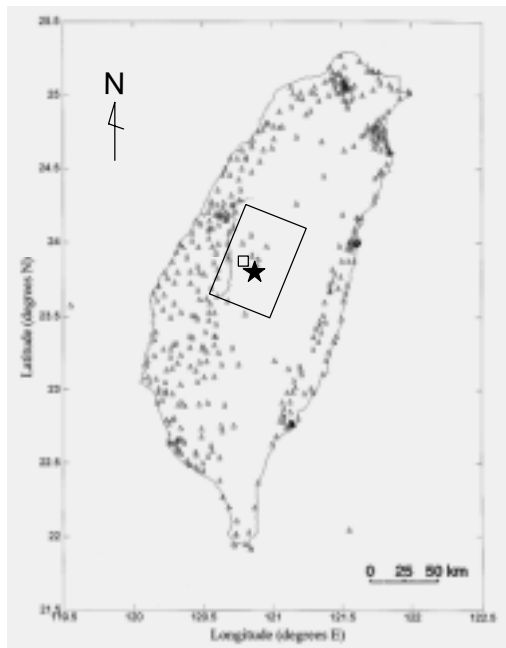


Fig. 5. Observation points and projection of the fault plane (Lee et al ,2001).

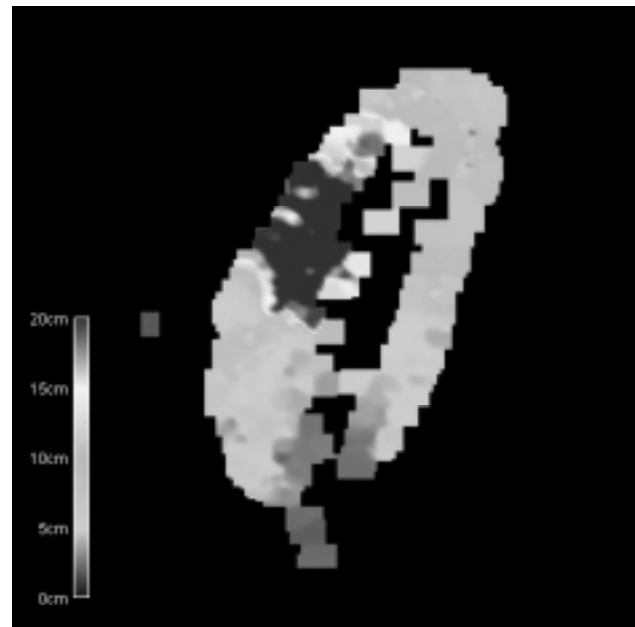


Fig. 6. Distribution of maximum displacement.

3. CORRELATION BETWEEN THE AMPLITUDE OF GROUND MOTION AND VOLUME OF SEA-BED UPLIFT

To investigate possibility of tsunami warning by means of Rayleigh waves and the sea surface disturbance, next we investigate the relationship between the coseismic ground displacement and the volume of the seabed uplift. First, we define the dynamic maximum displacement and volume of the uplift as shown in Fig. 7. The Volume of the uplift is a part of uplift relative to an observation point (-50km) expressed as a shadow part in the left figure. The dynamic displacement of the ground is the

displacement reduced from the maximum displacement to static displacement in Fig. 7.

Figure 8 shows the relationship between the dynamic displacement and the volume in cases of dip angles 30, 45, 60 degree when depth of the fault changes. In the left figure, we can see their correlation looks linear. Similarly, right figure in Fig. 8 shows their relationship when width of the fault changes. The correlation looks almost linear. The linear correlation is found on the hanging wall side in near field area. But, the relation is not linear far field area, or on the foot wall side.

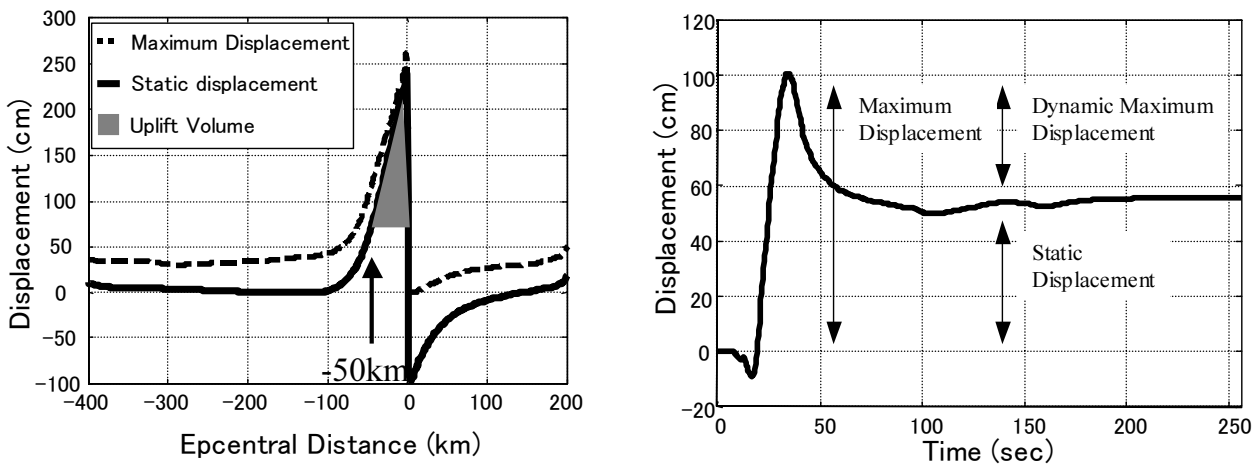


Fig. 7. Uplift Volume of ground and dynamic maximum displacement.

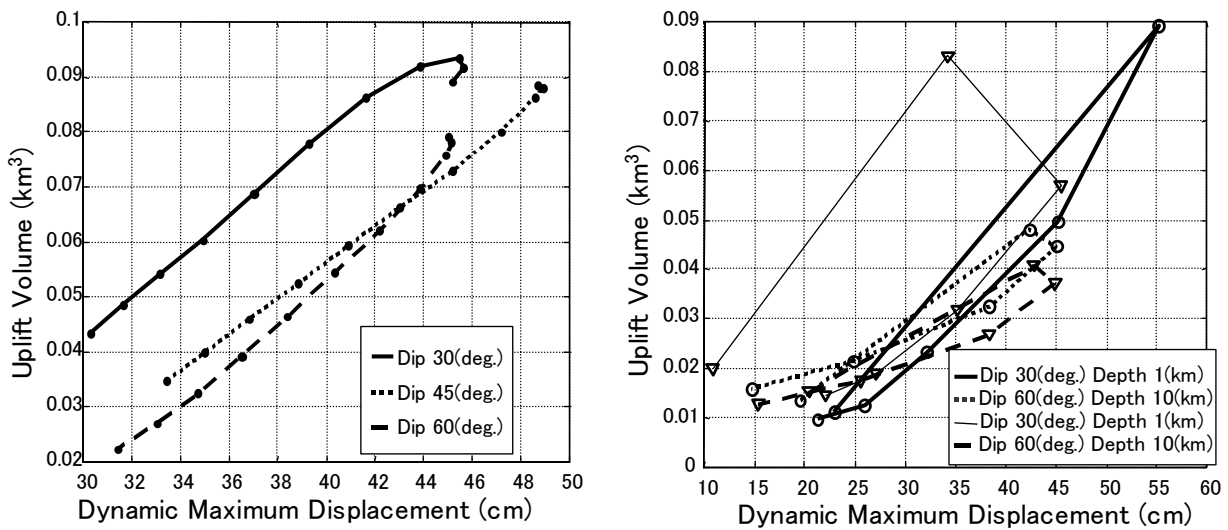


Fig. 8. A correlation between uplift volume and dynamic maximum displacement.

4. CONCLUSIONS

As conclusions, we can point out the followings:

1. Rayleigh waves excite the sea surface disturbance that propagates faster than tsunamis.
2. Rayleigh waves show directionality, from which the amplitude increases in the direction of fault rupturing and in the front area of the fault.
3. A correlation between the dynamic maximum displacement and volume of uplift is almost linear in the near-filed area of hanging wall side.

References:

- Ohmachi, T., H. Tsukiyama and H. Matsumoto(2001) : “Simulation of tsunami induced by dynamic displacement of seabed due to seismic faulting”, *Bull. Seism. Soc. Am.*, 91, 6, pp. 1898-1909.
- Mendoza, C. and E. Fukuyama(1994) : “The July 1993 Hokkaido-Nansei-Oki, Japan, earthquake : Coseismic slip pattern from strong-motion and teleseismic recordings”, *J. Geophys. Res.*, Vol. 101, pp. 791-801
- Lee, W. H. K., T. C. Shin, K. W. Kuo, K. C. Chen and C. F. Wu(2001) : “CWB free-field strong-motion data from the 921 Chi-Chi earthquake” : *processed acceleration files on CD-ROM*, Central Weather Bureau, Taiwan.
- Kikuchi, M., Y. Yagi and Y. Yamanaka(2000) : “Source process of the Chi-Chi, Taiwan earthquake of September 21, 1999 inferred from teleseismic body waves”, *Bull. Earthq. Res. Inst.*, Vol. 75, pp. 1-13.

UPDATING OF GIS BUILDING INVENTORY DATA FOR EARTHQUAKE DAMAGE ASSESSMENT USING HIGH-RESOLUTION SATELLITE IMAGE – APPLICATION TO METRO MANILA, PHILIPPINES –

H. Miura¹⁾, S. Midorikawa²⁾ and K. Fujimoto³⁾

1) Graduate Student, Department of Built Environment, Tokyo Institute of Technology, Japan

2) Professor, Department of Built Environment, Tokyo Institute of Technology, Japan

3) Research Associate, Department of Built Environment, Tokyo Institute of Technology, Japan

hmiura@enveng.titech.ac.jp, smidrik@enveng.titech.ac.jp, kazu@enveng.titech.ac.jp

Abstract: The GIS building inventory data in Metro Manila, Philippines is updated by using the satellite remote sensing data in order for the reliable earthquake damage assessment. The distribution of mid-rise and high-rise buildings is captured by the application of the building detection method using the high-resolution satellite images. The distribution of low-rise buildings is estimated from the land cover classification based on the time-series middle-resolution satellite images. The building damage due to a scenario earthquake is assessed by means of simplified procedure considering the seismic capacity of the buildings. The result shows that the damage of low-rise buildings is concentrated at lowland areas while the damage of high-rise buildings are slight to moderate at most of the areas.

1. INTRODUCTION

Influx of population to urban areas is a common problem faced by developing countries. The number of mega-cities, which are vulnerable to disasters, is increasing. The disaster mitigation activities in mega-cities should be strengthening immediately. The earthquake loss estimation is indispensable to efficient earthquake disaster mitigation planning. The GIS (Geographic Information System) building inventory data is a basic data to practice the reliable loss estimation. Due to the rapid growth in the urban area, the number of buildings has been swelling. Not only the number of low-rise buildings, but also that of high-rise buildings is increasing especially in developed commercial zones. However, the system for updating GIS data continuously is hardly established in developing countries. As a result, the number of buildings that are not included in the GIS data is increasing.

Satellite remote sensing can capture land cover information in urban areas widely and continuously. Recently, high-resolution satellite images (e.g., IKONOS, QuickBird) with the ground resolution 1m or less have been available at relatively low cost. Individual building in an urban area can be identified in the images. Therefore, the high-resolution satellite images are useful to grasp the distribution of mid-rise and high-rise buildings that are difficult to identify the individual location in middle-resolution satellite images (e.g., Landsat, SPOT). In this paper, the method for automatic detection of newly constructed buildings from a high-resolution satellite image is applied in Metro Manila, Philippines in order to grasp the distribution of mid-rise and high-rise buildings. Combining the result together with the distribution of low-rise buildings estimated from the land cover classification based on the time-series Landsat images, the up-to-date building inventory data is

constructed. The building damage assessment due to a scenario earthquake is conducted by means of simplified procedure based on the seismic capacity of the buildings and the computed ground motion.

2. SOCIAL CONDITION AND DATA SOURCES IN METRO MANILA

Metro Manila, the capital of Philippines, consists of seventeen cities and municipalities including Manila, Makati, Quezon and Marikina. The population concentration and the urban sprawl have been strongly observed. As shown in Fig. 1, about fifty years ago the urbanized area was less than 100km² with a population of 1.6 million, but now is expanded to more than 600km² with a population of 10 millions (Doi and Kim (1998)). In the downtown such as Manila, densely built-up area with low-rise and mid-rise buildings has been developed. In the commercial zones such as Makati and Ortigas, many high-rise buildings have been constructed. According with the sprawl of urbanized area, new commercial zones have been expanded.

In Metro Manila, the GIS base map was constructed based on the topographic map with a scale of 1/10,000 edited in 1987. In the base map, the footprints of the buildings and the congested housing areas are included. The building survey was conducted in the major commercial zones such as Makati, Manila, Ortigas and Quezon (Midorikawa *et al.* (2002)). The number of the buildings whose footprints are shown is about 280,000. In Metro Manila, the total number of the buildings is about 910,000 as of 1989 (Sarausad (1993)). The difference of the numbers suggests that about 630,000 buildings are located in the congested areas. Thus, assuming that the 630,000 low-rise buildings are uniformly distributed in the congested areas, they are added in the GIS data. However, the buildings that are newly constructed after 1989 are not included in the GIS data.

The satellite IKONOS color images with 1m ground resolution are used in this study in order to grasp the distribution of newly constructed mid-rise and high-rise buildings. These images are composed of 3 bands with visible (Red, Green, Blue) range and 1 band with near infrared (NIR) range. Figure 2 shows the coverage areas of the images. These images cover 75 percent of Metro Manila.

3. FLOW OF UPDATING GIS BUILDING INVENTORY DATA

In order to assess the earthquake damage appropriately, it is necessary to grasp the up-to-date building distribution. Figure 3 shows the flow of updating GIS building inventory data employed in this study. The distribution of mid-rise and high-rise buildings is captured by the high-resolution satellite images, while the distribution of low-rise buildings is estimated from the middle-resolution satellite images.

Individual location and their height of mid-rise and high-rise buildings are detected from IKONOS images using the method proposed by the authors (Miura and Midorikawa (2003)). The locations of the newly constructed buildings are detected from the difference between the image and the GIS data. In this method, the edges are extracted from the image in order to detect the boundaries of the buildings. The shadow area, the vegetation area, the existing building area, the road area and the water area are extracted as “the known areas” from the image and the GIS data. After the elimination of the edges in the known areas, the image analysis is conducted for discriminating building edges from the others. Considering that edges of a building are always neighbored to their shadow, the edge pixels neighbored to the shadow pixels in the direction of the sun are identified as the building edges. The regions including the building edges are finally extracted in the analysis. The numbers of stories of the buildings are estimated using the shadow length observed in the image.

The up-to-date distribution of low-rise buildings is estimated from the land cover classification based on the time-series Landsat images by Yamazaki *et al.* (2003). They classified the built-up areas into the three categories according to the developing period. Considering that the newest

built-up areas almost correspond with the distribution of the buildings that are constructed after the edit of the GIS data, we estimated the distribution and amount of the low-rise buildings. Combining the results of the analysis, the GIS building inventory data is updated.

4. DISTRIBUTION OF MID-RISE AND HIGH-RISE BUILDINGS

First, we examine the applicability of the proposed method (Miura and Midorikawa (2003)) to the data in Metro Manila. Figure 4 (a) shows a part of the IKONOS image acquired in 2001/9/28. The area covers recently developed commercial zone in the northeastern part of Makati. The high-rise buildings shown in the circles in Fig. 4(a) are newly constructed after the edit of GIS data.

We apply the method to the data shown in Fig. 4(a). Figure 4(b) shows the result of the analysis. The rectangles indicate the locations of correctly detected buildings. The triangles and the circles represent the location of mis-detected objects and un-detected buildings, respectively. All of the high-rise buildings shown in Fig. 4(a) are detected correctly. Figure 5 shows the result arranged according to the building size and the number of stories. A lot of low-rise buildings whose sizes are under 25m are observed in the image. Using the proposed method, it is difficult to detect such low-rise and small buildings individually. However, almost 90% of the mid-rise and high-rise buildings are detected successfully.

We estimate the numbers of stories using the shadow lengths observed in the image. The number of stories is calculated using the shadow length, the sun elevation and the average floor height set as 3.2m. The result shows that most of the buildings are estimated successfully within the error range of 2 stories.

The proposed method is applied to the whole area of the images shown in Fig. 2. Figure 6 shows the result of the analysis. The regions indicate the locations of detected buildings. About 2,600 newly constructed buildings are detected from the images. The numbers of stories of the buildings are estimated using their shadow lengths. The number of the mid-rise buildings (4-9F), that of the high-rise buildings (10-30F) and that of the super high-rise buildings (31F-) are 666, 202 and 24, respectively. In order to provide quantitative assessment of the analysis, the un-detected buildings are extracted by the visual interpretation with the images. The detection percentage of mid-rise and high-rise buildings is computed as shown in Table 1. The result shows that all the detection percentages are more than 90%. All the footprints of the newly constructed buildings are included in the GIS data.

5. DISTRIBUTION OF LOW-RISE BUILDINGS

It is difficult to detect the individual location of low-rise buildings accurately using the proposed method. Yamazaki *et al.* (2003) revealed the distribution of built-up area in Metro Manila using time-series Landsat images (30m-resolution). They classified the built-up areas into the three categories according to the developing period (-1972, 1972-1992, 1992-). The older built-up areas before 1992 almost coincide with the building distribution of the existing GIS data. The built-up areas after 1992 correspond with the building distribution developed after the edit of the GIS data. We compare the number of the buildings of the existing data and the built-up areas. The number of the buildings in the existing data is about 910,000 while the number of pixels in the built-up areas before 1992 is about 330,000. Therefore, the number of buildings that are located in the one pixel is estimated at three. Considering that the number of pixels in the built-up areas after 1992 is about 130,000, the number of the buildings in the built-up area after 1992 is estimated at about 380,000. Assuming that the most of the estimated buildings consist of low-rise buildings and the low-rise buildings are uniformly distributed in the built-up areas, they are added in the GIS data. Combining

the distribution of mid-rise and high-rise buildings and that of low-rise buildings, the building inventory data is updated. The total number of the buildings is estimated at about 1,290,000, which almost corresponds with the result of the recent survey by JICA *et al.* (2003).

6. ESTIMATION OF BUILDING DAMAGE

Using the updated GIS building inventory data, building damage assessment due to a scenario earthquake is conducted considering the seismic capacity of the buildings. The flow of building damage estimation is shown in Fig. 7. The ground motion due to a scenario earthquake was computed by the hybrid simulation method with the 3-D underground structure model and the soil response analysis using the surface soil profiles (Yamada *et al.* (2003)). The building response is evaluated by the capacity spectrum method. The buildings in Metro Manila are classified into several categories. The nonlinear response of the buildings is estimated from the capacity curves and the ground motion spectrum. The damage state for each building category is determined by the building response and the fragility curve. Multiplying the damage state of each building category and the updated building inventory data, the distribution of the building damage is computed.

The building types proposed by Vibrametrics, Inc. (2003a) are used in this study. They classified the buildings into three major categories; CHB (concrete hollow block), C1 (concrete moment frame building) and C2 (concrete shear wall building), and twenty detailed categories considering the possible height range and the design vintage for each structural type. Taking account of the height range and the typical design vintage, we classify the buildings into seven categories shown in Table 2. The capacity curves and the fragility curves proposed by Vibrametrics, Inc. (2003a, b) are used in the capacity spectrum method.

The West Valley Fault is selected as the source of a scenario earthquake because the fault is closer to the central part of Metro Manila. The computed peak ground velocity on the surface due to the scenario earthquake (M 6.7) is shown in Fig. 8 (a). The large ground motion is computed in the areas that are located on the thick soft soil such as Coastal lowland and Marikina valley.

The number of the damaged buildings is computed by multiplying the damage ratio and the number of the buildings. Figure 8 (b) shows the distribution of low-rise buildings (1-3F) with the complete or extensive damage level. The damage of low-rise buildings is concentrated in Coastal lowland and Marikina valley. The number of the damaged buildings is about 180,000, which corresponds with almost 15% of the low-rise buildings in Metro Manila.

The distribution of mid-rise buildings (4-7F) with the complete or extensive damage level is shown in Fig. 8 (c). The damage is concentrated in Manila. About 20% of mid-rise buildings are damaged because a lot of mid-rise buildings are located in Manila. The distributions of high-rise buildings with the moderate damage level are shown in Fig. 8 (d)-(f). The building damages for the higher types are relatively slight. Most of the high-rise buildings may suffer less than moderate damage level. One of the reasons is the spectral characteristic of ground motion. The magnitude of the scenario earthquake (6.7) is not large enough to generate the strong ground motion with longer period, which contributed to the response of higher buildings.

7. CONCLUSIONS

The GIS building inventory data in Metro Manila, Philippines is updated by using the satellite remote sensing data in order for the reliable earthquake damage assessment. The distribution of mid-rise and high-rise buildings is captured by the application of the building detection method using the IKONOS images. The distribution of the low-rise buildings is estimated from the land cover classification based on the time-series Landsat images. The building damage due to a scenario

earthquake is assessed by means of simplified procedure considering the seismic capacity of the buildings. The result shows that the damage of low-rise buildings is concentrated at lowland areas while the damage of high-rise buildings are slight to moderate at most of the areas.

Acknowledgements:

The authors acknowledge Ass. Prof. Hiroaki Yamanaka (Tokyo Institute of Technology) and Dr. Masashi Matsuoka (Earthquake Disaster Mitigation Research Center) for providing the ground motion simulation data and the land cover classification data, respectively. This study was done as a part of the Development of Earthquake and Tsunami Disaster Mitigation Technologies and Their Integration For the Asia-Pacific Region (EqTAP) project.

References:

Doi, K. and Kim, K. (1998), "Role of Strategic Modeling Approach in the Formulation of the Framework of Sustainable Metropolitan Policies," *Proc. 1st Workshop on Environment Conservation of Metro Manila*, pp.13-25

Japan International Cooperation Agency (JICA) et al. (2003), "Earthquake Impact Reduction Study for Metropolitan Manila, Republic of the Philippines," Progress Report 2

Midorikawa, S. et al. (2002), "Preliminary Assessment of Building Damage Due to A Scenario Earthquake in Metro Manila, Philippines," *Proc. 7th U. S. National Conference on Earthquake Engineering*, Paper No. LE-1f, (CD-ROM)

Miura, H. and Midorikawa, S. (2003), "Automated Building Detection from High-Resolution satellite Image for Updating GIS Building Inventory Data," *Journal of Society Safety Science*, No.5, pp.37-44 (in Japanese)

Sarausad, F. (1993), "Infrastructure Condition in Metro Manila," *Disaster Prevention and Mitigation in Metropolitan Manila Area*, pp.93-107

Vibrametrics, Inc. (2003a), "Survey of Experts' Judgment on Earthquake Capacity of Selected Building Types in Metro Manila," EqTAP Metro Manila Case Study, Final Report

Vibrametrics, Inc. (2003b), "Development of Fragility Curves for Selected Building Types," EqTAP Metro Manila Case Study, Final Report

Yamada, N. et al. (2003), "Strong Ground Motion Simulation in Metro Manila," *Journal of Structural Engineering*, Vol.49B, pp.1-6 (in Japanese)

Yamazaki, F. et al. (2003), "Urban Classification of Metro Manila for Seismic Risk Assessment Using Satellite Images," *The 5th Multi-Lateral Workshop on Development of Earthquake and Tsunami Disaster Mitigation Technologies and Their Integration for the Asia-Pacific Region*, EDM Technical Report No.16, Earthquake Disaster Mitigation Research Center, NIED, (CD-ROM)

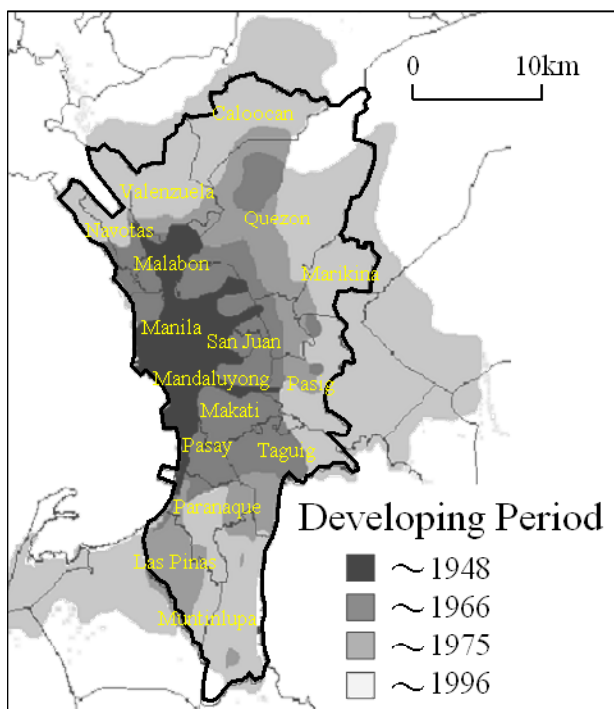


Fig.1 Urban development in Metro Manila

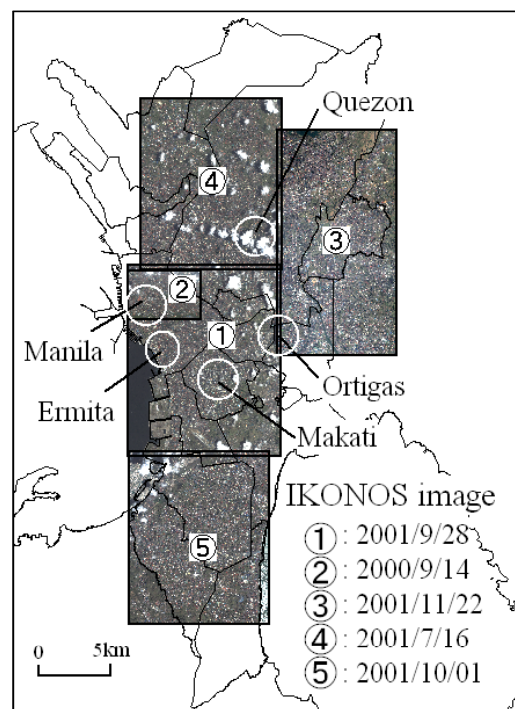


Fig.2 Coverage area of IKONOS images

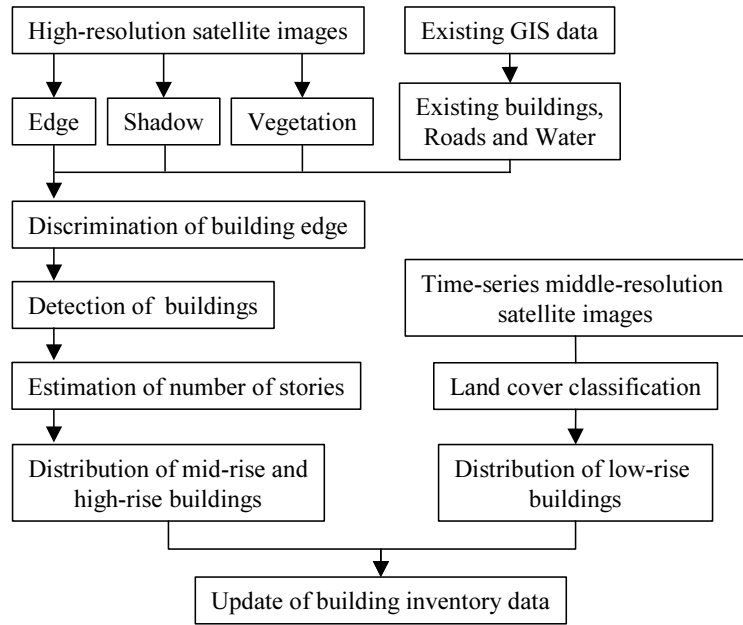


Fig.3 Flow of updating GIS building inventory data

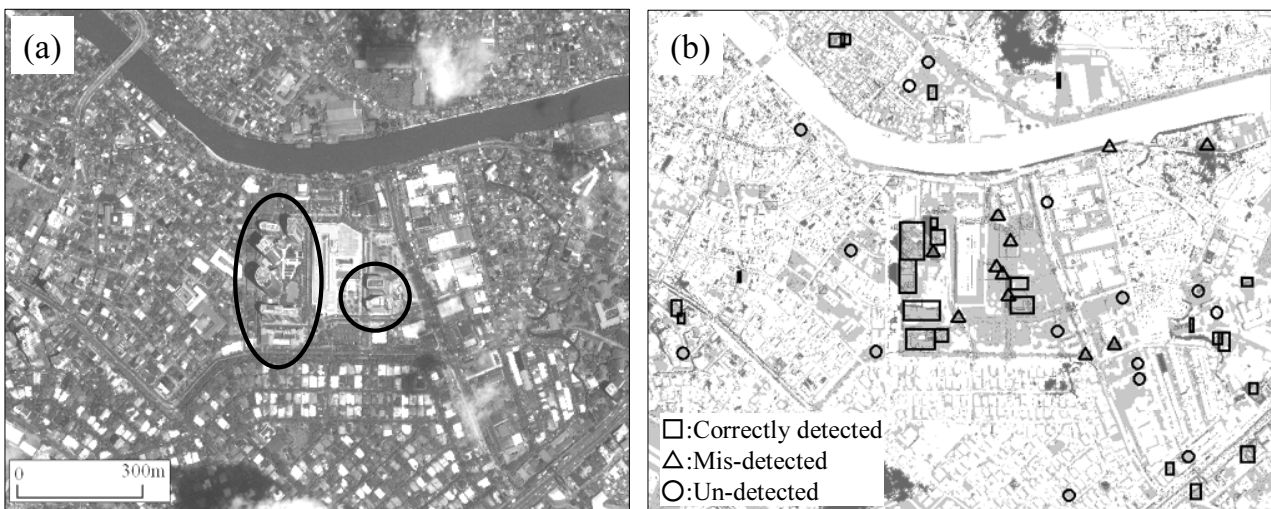


Fig.4 (a) IKONOS image in the developed commercial zone
(b) Result of the image analysis

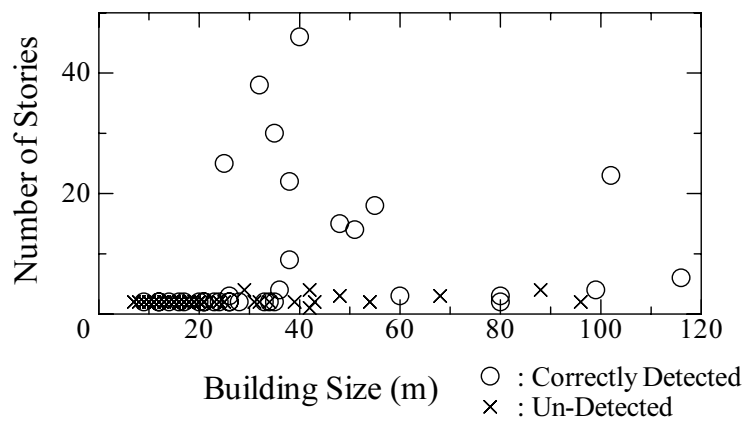


Fig.5 Relationship between building size and number of stories

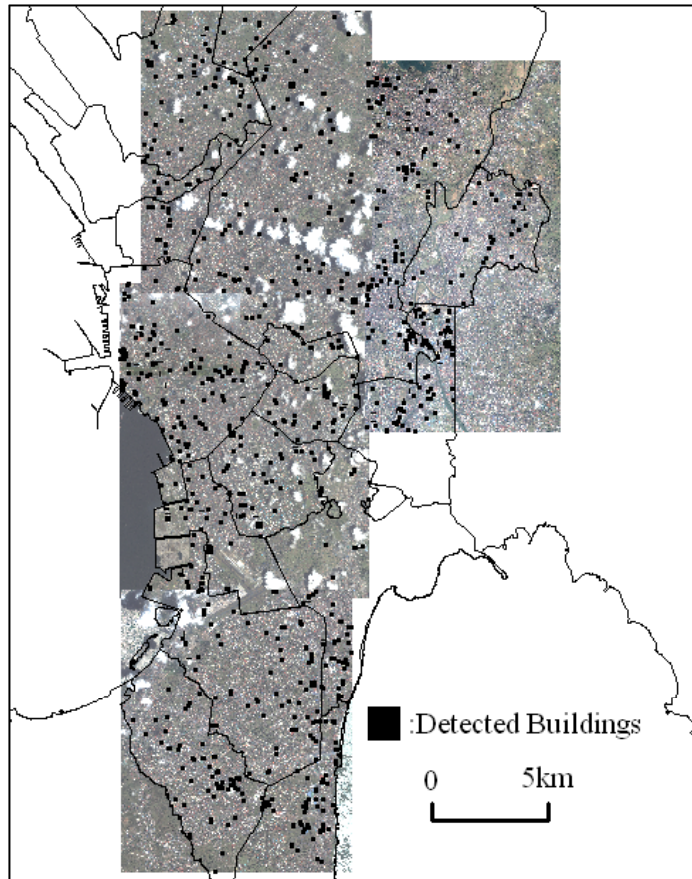


Fig.6 Locations of detected buildings

Table 1 Detection percentage of the analysis

The number of stories	Detected	Un-detected	Detection percentage
4-9	666	74	90%
10-30	202	7	97%
31-	24	0	100%

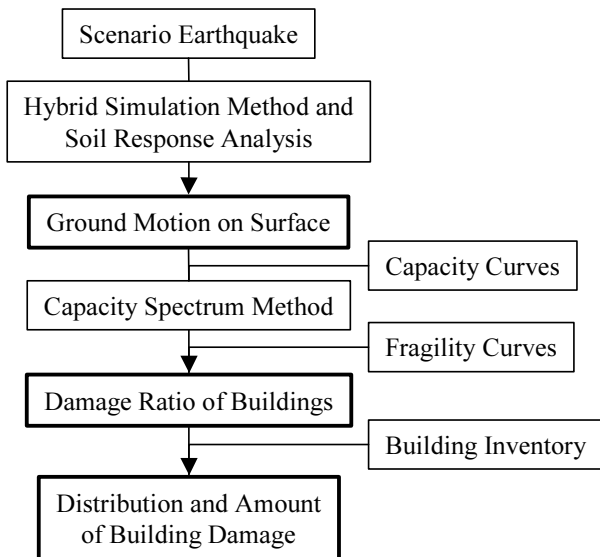


Fig.7 Flow of building damage estimation

Table 2 Building types used in this study

Building Type	Structural Type	Number of Stories	Design Vintage
CHB	Concrete Hollow Block	1-3	Sub-Type 3
CIL	Concrete Moment Frame Building	1-3	Sub-Type 3
C1M		4-7	Sub-Type 3
C1H		8-15	Sub-Type 2
C2V		16-25	Sub-Type 1
C2E	Concrete Shear Wall Building	26-35	Sub-Type 1
C2S		36-	Sub-Type 1

Sub-Type 1 : Constructed after 1992
 Sub-Type 2 : Constructed from 1972-1991
 Sub-Type 3 : Constructed before 1971

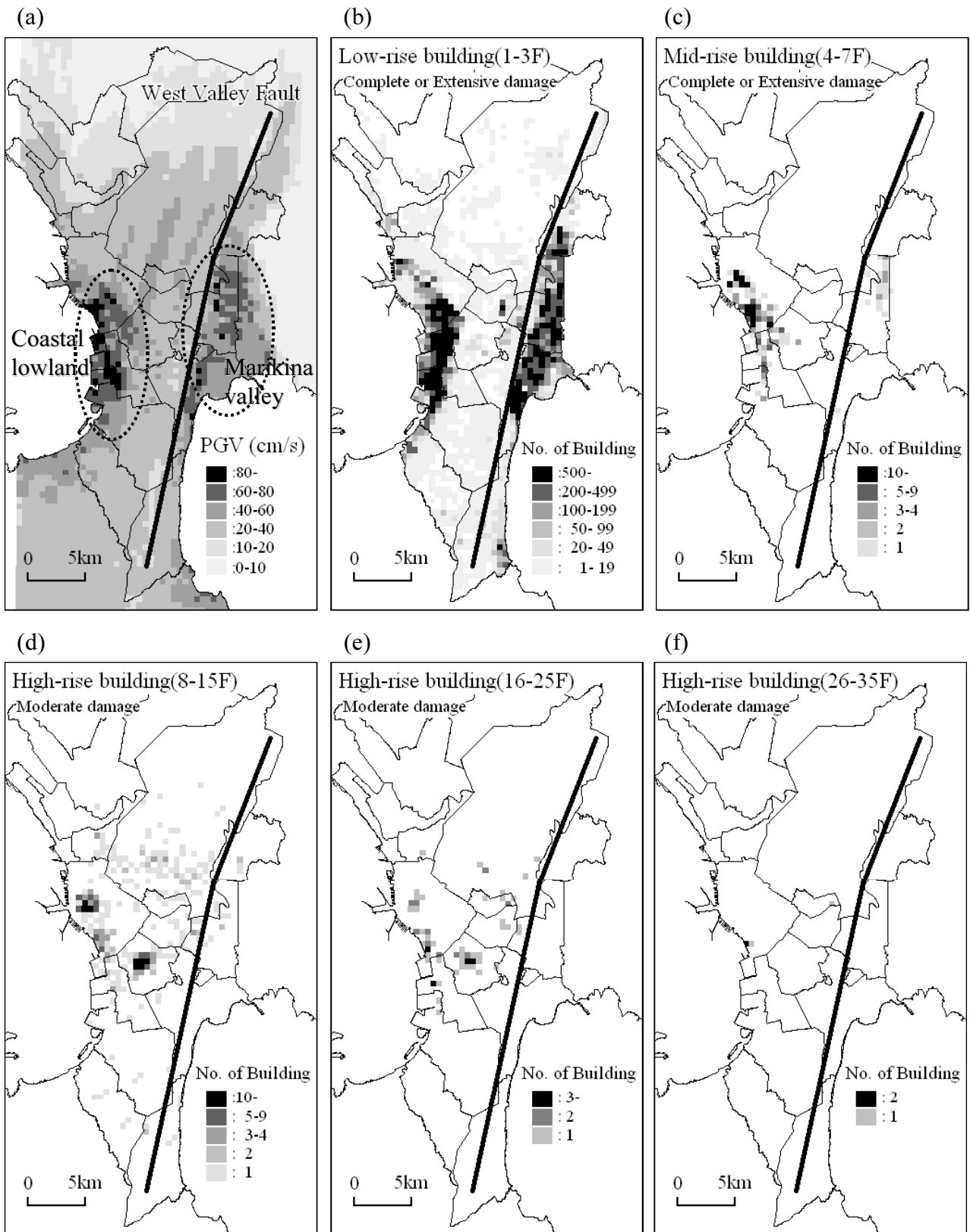


Fig.8 (a) Peak ground velocity on surface
 (b) Distribution of low-rise building with complete or extensive damage
 (c) Distribution of mid-rise building (4-7F) with complete or extensive damage
 (d) Distribution of high-rise building (8-15F) with moderate damage
 (e) Distribution of high-rise building (16-25F) with moderate damage
 (f) Distribution of high-rise building (26-35F) with moderate damage

Preliminary Evaluation of Surface Soil Response applying the H/V Spectral Ratio Technique to Microtremor Data within Dhaka City, Bangladesh

A. S. M. Maksud Kamal¹⁾, S. Midorikawa²⁾, F. Yamazaki³⁾, and M. Ansary⁴⁾

1) Graduate student, Department of Built Environment, Tokyo Institute of Technology, Japan

2) Professor, Department of Built Environment, Tokyo Institute of Technology, Japan

3) Professor, Department of Urban Environment Systems, Chiba University, Japan

4) Associate Professor, Civil Engineering Department, BUET, Bangladesh

kamal@enveng.titech.ac.jp, smidorik@enveng.titech.ac.jp, yamazaki@tu-chba-u.ac.jp, ansaryma@yahoo.com

Abstract: The geomorphological map of Dhaka city area with eighteen geomorphic units and four categories of landfills created by the authors previously employed as a major source of data used in this study. Data compiled from 140 boreholes provided information that allowed characterization of nine of the geomorphic units under analysis in terms of representative soil profiles and SPT-N values. Further analysis of overall shape of the SPT-N curves corresponding to these representative soil profiles suggested the possibility of regrouping them into four general patterns. Estimation of the site response through the evaluation of the predominant periods and corresponding amplification factors relied on the application of the horizontal to vertical spectral (H/V) technique employing 58 microtremor recordings distributed over twelve of the geomorphic units. Consideration of the similarity of the overall shape of the resulting transfer functions, predominant periods, and maximum amplification ratios suggested classification of the sites into three typical patterns. These H/V patterns displayed good correlation with the derived representative soil profiles. The compilation of a more extensive microtremor and borehole dataset covering all geomorphic units proved necessary for the further precise development of this work.

1. INTRODUCTION

The infrequent occurrence of destructive earthquakes does not permit the compilation of enough data to support the estimation of the distribution of damages in the future. To overcome this lacking, different authors proposed the use of alternative sources of excitation, such as, distant earthquakes, small near earthquakes, explosions, aftershocks and microtremors. The use of microtremors, an idea pioneered by Kanai *et. al.* (1954) turns into one of the most appealing approaches in site effects studies, due to its relatively low economic cost, and the possibility of recordings without strict spatial or time restrictions (Rodriguez and Midorikawa, 2002). The H/V spectral ratio technique of microtremors gained popularity in the early nineties, after the publication of several papers (Nakamura; 1989; Field and Jacob, 1993; Lermo and Shavez-Garcia, 1994) claiming the ability of this technique to estimate the site response of soft sedimentary deposits satisfactorily. The method is rather attractive in developing countries characterized by a moderate seismicity, where only very limited resources are available for seismic hazard studies.

Bangladesh is a country characterized by a moderate seismicity with almost no resources is available for large scale seismic hazard studies. The objective of this study was to evaluate the site response using H/V spectral ration of microtremors in terms of peak period and corresponding amplification within Dhaka city area (Figure-1), Bangladesh. This work was important for the nation, as a recent study conducted by Cardona *et. al* (2001) on twenty cities of

the world showed Dhaka appeared to have one of the highest values of earthquake disaster risk index (EDRI) mainly due to its inherent vulnerability of building infrastructures, high population density and poor emergency response and recovery capacity. Dhaka is positioned in the central part of Bangladesh, on a northwest-southeast elongated and southeastward tilted tectonically uplifted Pleistocene terrace. Regionally, Bangladesh is a part of the Bengal Basin, originated as a result of intra-plate movements involving the Indian, Tibetan and Burmese plates between Cretaceous to Holocene period.

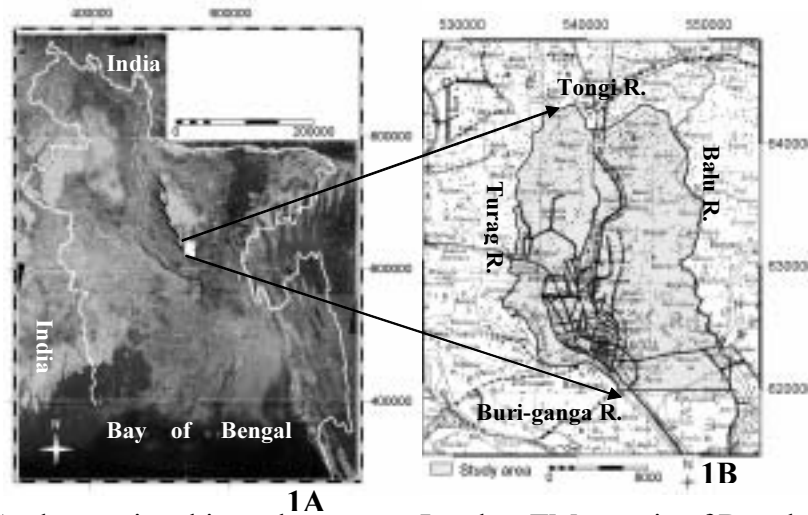


Figure 1A): Study area in white polygon on a Landsat TM mosaic of Bangladesh, 1B): Dhaka city area within the four river system as shown on Bangladesh topographic map no. 79I

2. DATA USED

The geomorphological map of Dhaka city with eighteen units and four categories of thickness of the landfills (Figure 2) were created by the authors (Kamal and Midorikawa, 2003), through the combined analysis of old aerial photographs acquired in 1954, borehole data, and satellite images of Landsat TM⁺ of bands (30 m resolution) 5, 4 and 3 and IRS-1D PAN (5.8 m resolution) taken in 2002 and 2000 respectively was used a major source of data in this study. The soil profiles of 140 boreholes with their SPT-N value curves were compiled and subsequently simplified them into patterns. Fifty-eight microtremors recording was measured at the ground surface with a three components velocity meter and processed to derive their spectral ratios (H/V). The H/V spectral ratio curves were analyzed and differentiated into three patterns. A simple flow chart of the materials and procedures used in this study shown in Figure 3:

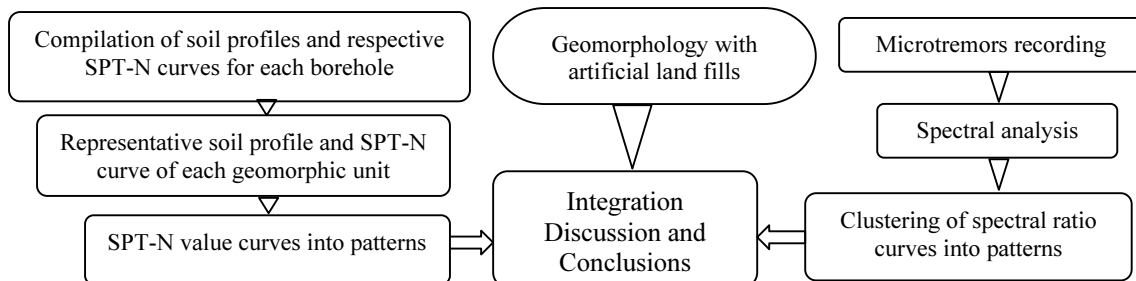


Figure 3: Simple flowchart of methodology

In the ‘integration, discussion and conclusion’ scheme, we overlaid the sites of the derived patterns of both boreholes and microtremors as the point information on the geomorphological map and examined the correlation among them.

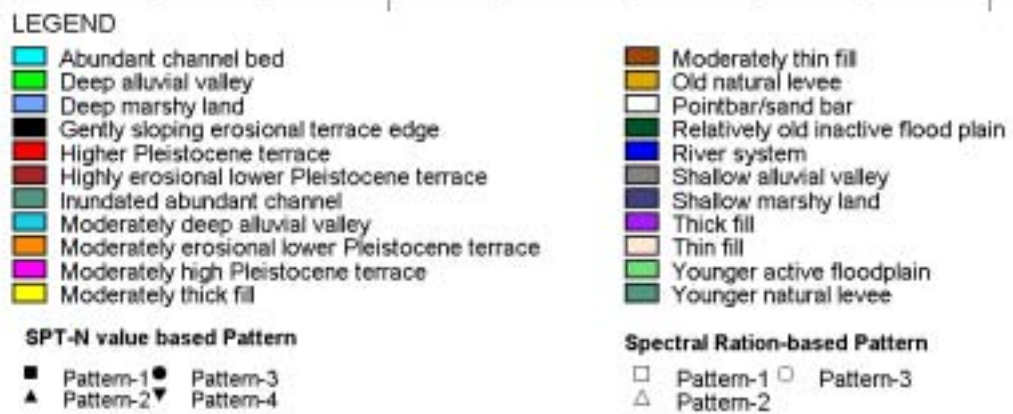
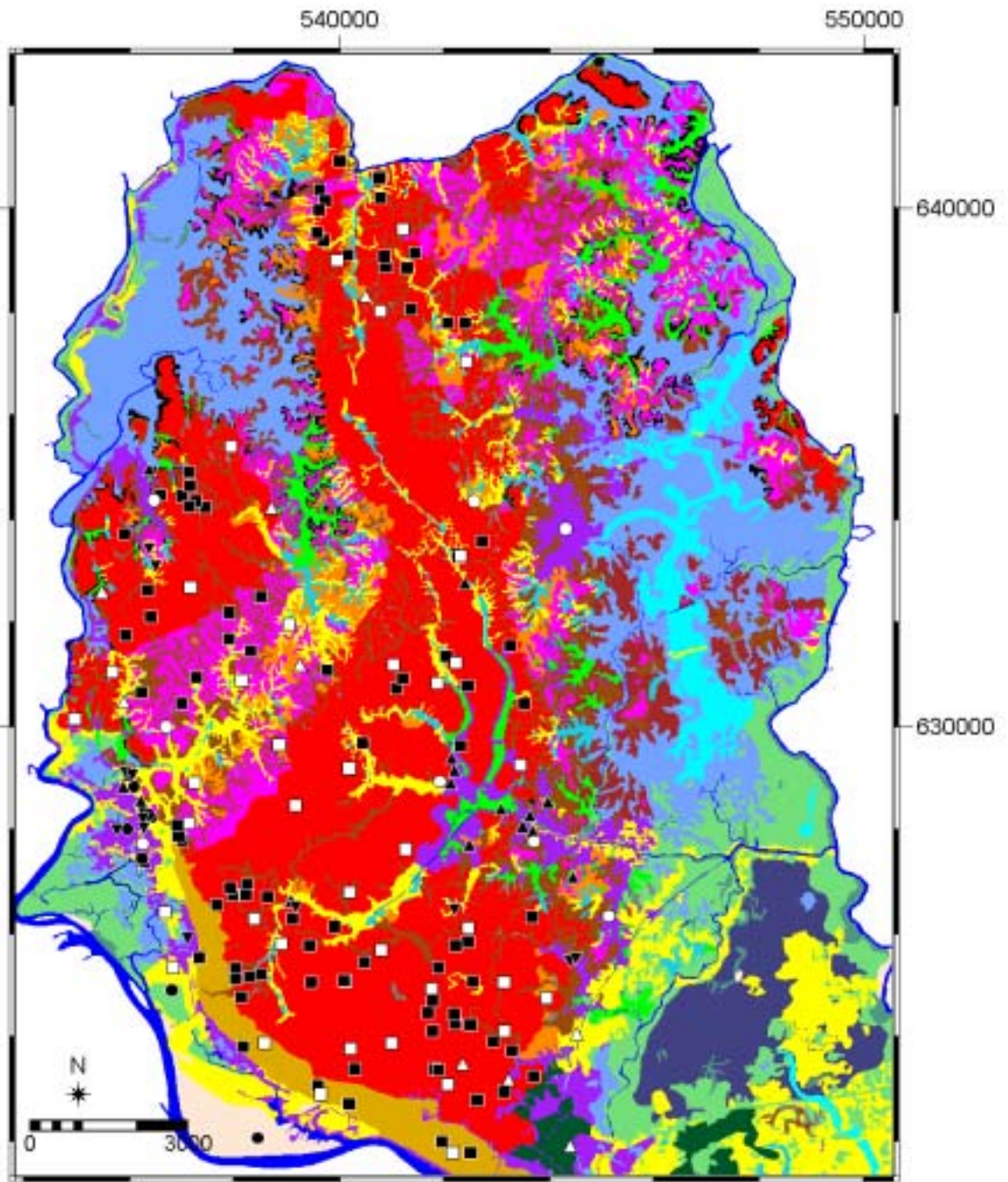


Figure 2: Geomorphological map with Landfills. Both the patterns derived from SPT-N values of boreholes and spectral-ratios of microtremors were superimposed in this map.

3. BOREHOLE DATA ANALYSIS

We compiled the soil-profile and SPT-N value curves of 140 boreholes which were randomly distributed on the nine geomorphic units out of eighteen. All the SPT-N curves of a geomorphic unit were overlaid in a plot which provided the information of the representative soil profiles and corresponding SPT-N value of that geomorphic unit. Figure 4 below showed the representative soil profiles with SPT-N curves of the nine investigated geomorphic units.

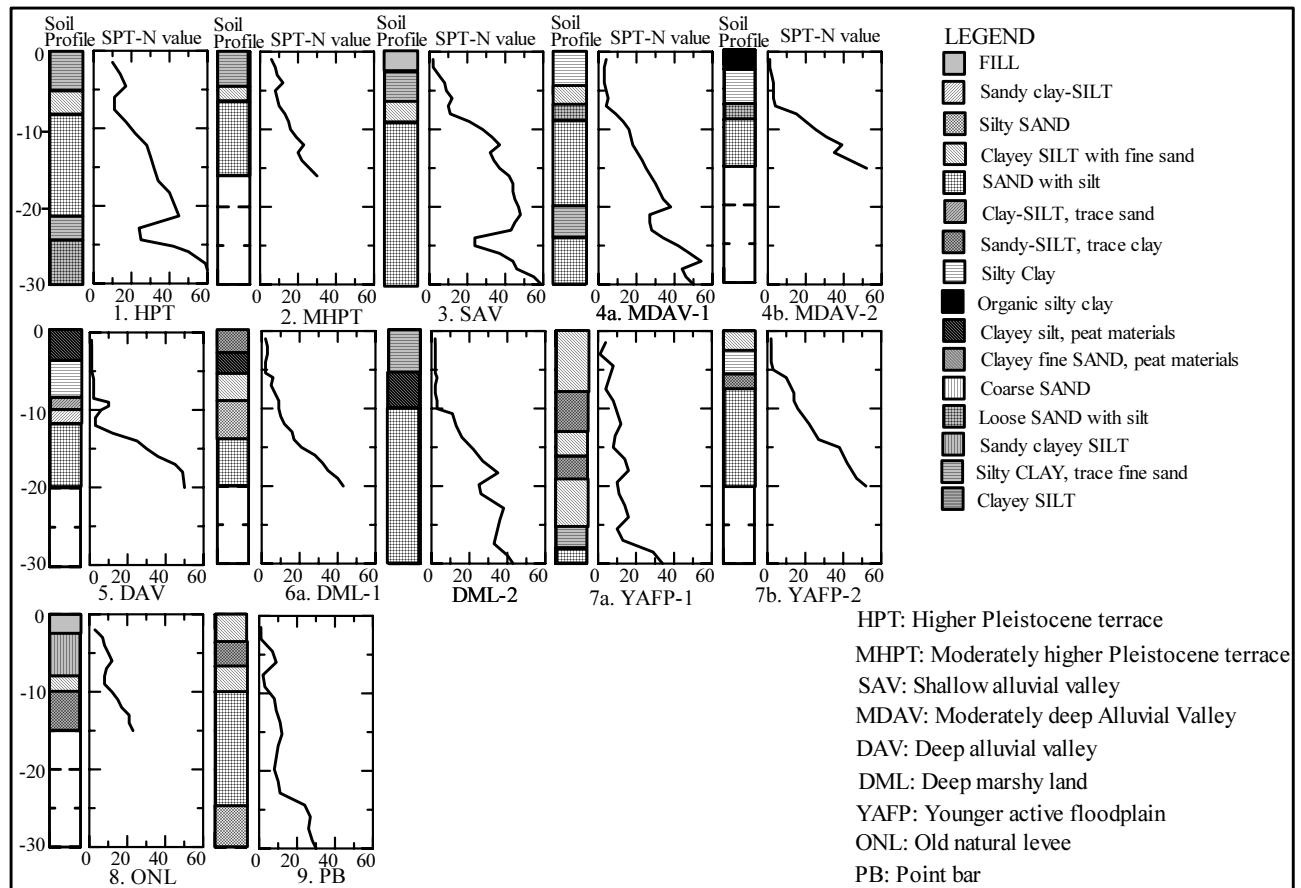


Figure 4: The representative soil profiles and SPT-N value of boreholes

In Figure 4, some geomorphic units showed more than one representative soil profiles. For instance, the younger active floodplain showed two representative soil profiles plotted as YAFFP-1 and YAFFP-2. The demonstration of SPT-N value curves of the boreholes of younger active floodplain justified two distinct appearances of YAFFP-1 and YAFFP-2, named as ‘category 1’ and ‘category 2’ respectively as shown in Figure 5. Thus, 140 boreholes of nine geomorphic units came-out into thirteen representative soil profiles and corresponding SPT-N value curves.

To investigate the relationship among the geomorphic units and to find-out the possibility in order to further simplify the thirteen representative soil profiles, we overlaid their SPT-N curves in a plot (Figure 6). It was observed that some SPT-N value curves closely correspond with each other. As an example, the curve of Higher Pleistocene terrace showed its close association with the curves of Moderately high Pleistocene terrace, Old natural levee and Shallow alluvial valley. Thus, based on the close association of representative SPT-N value curves, we grouped these four geomorphic units into a ‘pattern’. The thirteen representative soil profiles with SPT-N value curves, thus, simplified into four different patterns (Figure 7) for the nine geomorphic units of the study area. The association of the derived patterns with the geomorphic units was given below:

Pattern-1: The geomorphic unit of Higher Pleistocene terrace, Moderately higher Pleistocene terrace, Old natural levee and Shallow alluvial Valley.

Pattern-2: Category-2 of Deep marshy land, category-2 of Moderately deep alluvial valley and Deep alluvial valley.

Pattern-3: Category-1 of younger active floodplain and Point bar deposits.

Pattern-4: Category-1 of Moderately deep alluvial valley, Category-1 of deep marshy land and category-2 of Younger active floodplain.

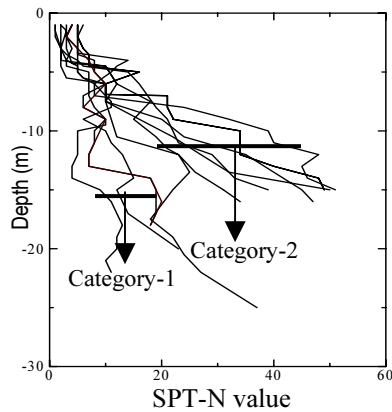


Figure 5: SPT-N value curves of category-1 and 2 of *Younger active floodplain*

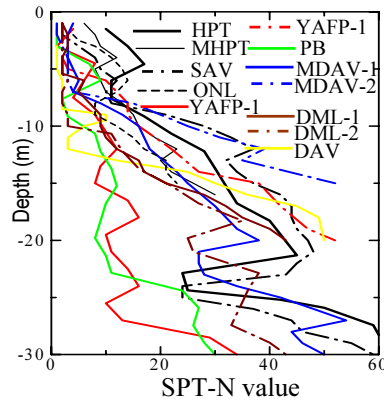


Figure 6: Thirteen representative SPT-N value curves of nine geomorphic units

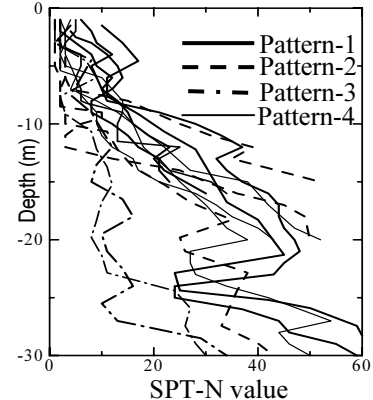


Figure 7: SPT-N value curves of four different patterns

4. SPECTRAL ANALYSIS FOR H/V RATIOS OF MICROTREMORS

As mentioned before, 58 microtremors records were measured on twelve geomorphic units. Each record comprises of three components, viz., EW, NS and UD. For spectral analysis we took three noise-free portions of 20.48s of the recordings as the instrumental sampling frequency was 100Hz. However, to determine at which frequency of the spectrum, the sedimentary packages caused the larger amplifications we applied first Fourier transform on the time domain records, then smoothed the corresponding spectra and finally applied the spectral ration (H/V) technique to derive transfer functions. The applied sequences were given below:

(1) At first, we calculated the Fourier spectra of the two horizontal and the vertical components. As the Fourier spectra of the two horizontal components looked alike, their horizontally combined spectra were calculated to obtain the maximum Fourier amplitude spectrum as a complex vector in the horizontal plane. While that of the UD component provided the vertical motion spectra.

(2) Smoothing of the spectra: After Fourier transformation, we digitally filtered the combined horizontal and vertical spectra applying a logarithmic window (Konno and Ohmachi, 1998; Rodriguez and Midorikawa, 2002) with a bandwidth coefficient equal to 15. This filtering technique was applied to reduce the distortion of peak amplitudes.

(3) Calculation of the soil response functions: The smoothed combined horizontal spectrum was divided with the vertical counterpart (H/V) which provided the desired predominant period and corresponding amplification factor of the investigated portions (20.48s) of records.

(4) After calculating three sets of the H/V ratios at each site, they were normalized to obtain a relatively non-biased site specific H/V ratio.

All the 58 records of microtremors were analyzed to obtain the predominant periods and corresponding amplification factors of the sites following the above sequences of analyses using a microtremor record measured on the Higher Pleistocene terrace as shown in Figure 8. From the tri-axial waveform W, three noise-free portions A, B, C having 20.48s long were selected for analysis in Figure 8. In the plots A(f), B(f), and C(f), the horizontal to vertical motion Fourier spectra were shown after smoothing by logarithmic window (width coefficient $b=15$). The plots

D, E and F showed the soil response functions, where as, G represented the normalized H/V ratios after averaging D, E and F.

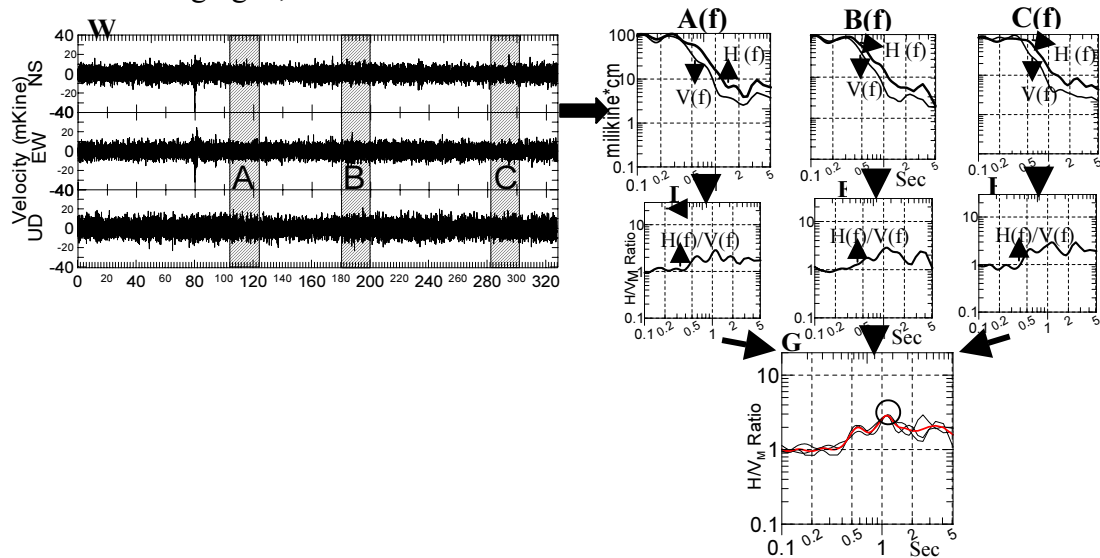


Figure 8: Flow of calculation process applied to obtain the transfer functions (H/V ratios).

The circle on the H/V curves in G showed the predominant period 1.13s and corresponding amplification factor 2.87 after averaging. The predominant period indicates the frequency of the spectrum under which the near-surface soft sediment amplifies the earthquake ground motion, which is often referred as the site effects. The degree of damage caused by earthquake shaking is larger when the predominant period of the sites appears near the period of the structure.

5. PATTERN RECOGNITION OF H/V CURVES

We observed that some of the H/V curves looked alike in shape even their measuring sites were located on different geomorphophic units. So, in order to increase the simplicity of the analysis, we classified the fifty-eight H/V spectral ratio curves of twelve geomorphic units into the cluster of three ‘patterns’ (Figure 9) based upon: (1) the shape of the overall amplification spectra within the frequency range of interest; and (2) The coincidence between predominant periods and maximum spectral ratios. The descriptions of the patterns were as follows:

Pattern 1: We observed that the amplification spectra of 39 sites belonging to the six geomorphic units viz., Higher Pleistocene terrace, Moderately higher Pleistocene terrace, Old natural levee, Old inactive floodplain, Shallow Alluvial Valley and some sites on Younger active floodplain represented a unique shape and their predominant periods around 1.0s with a standard deviation of 0.13. We found that on Higher Pleistocene terrace, the amplification was less than 3, where as, on the other geomorphic units of this pattern, the amplification factor fluctuates in an order of 3-5.

Pattern-2: There were nine sites in pattern 2 under five geomorphic units, namely, Moderately erosional lower Pleistocene terrace, Gently sloping erosional terrace edge, Inundated abundant channel, and some sites on Moderately deep alluvial valley as well as Younger active floodplain. The predominant period in this pattern was rather higher, in an average of around 1.86s. In the five sites of first three geomorphic units of this pattern the amplification factors were around 4, where as, in the four sites of the last two, the amplification factors were higher fluctuating around 6-7.5

Pattern-3: The sites of this pattern were located on eight thick soft sediments, belonging four geomorphic units, namely, Deep marshy land, Deep alluvial valley, Moderately deep alluvial valley and Younger active floodplain. There were two mode of predominant period observed in

this pattern. The short period mode fluctuated around 0.56s where as long period mode showed a typical 1.57s. The amplification factors were observed around 3.25 and 3-6 in short and long period modes respectively. In the Figure 9 below, the amplification spectra of each pattern and their calculated average were shown.

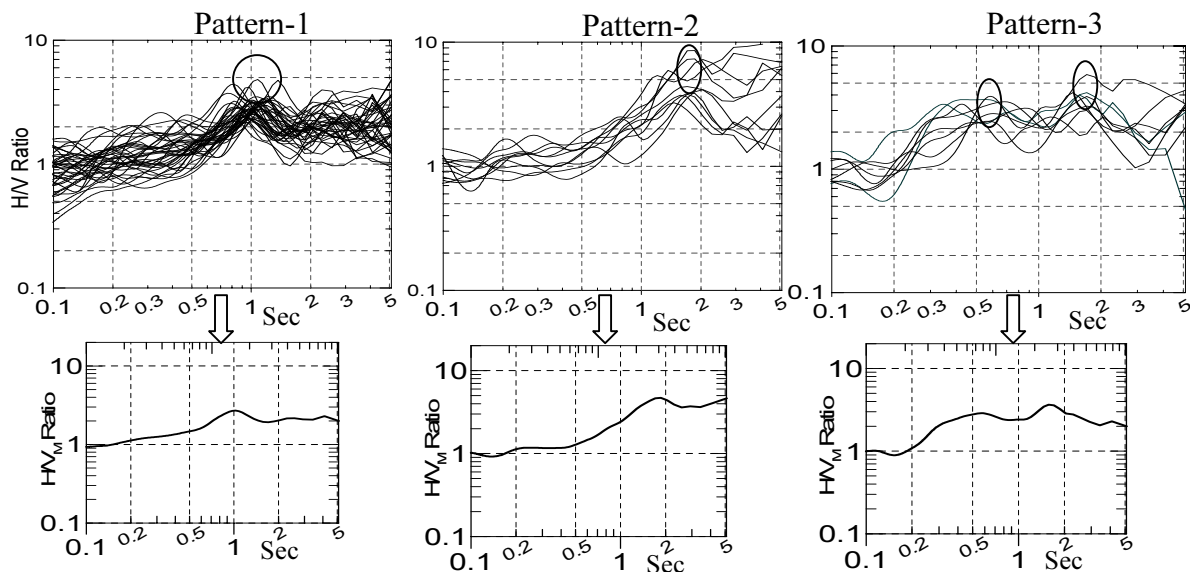


Figure 9: Spectral ratio curves and their normalized average shape as obtained from the analyses microtremors records on nine geomorphic units.

6. DISCUSSIONS AND CONCLUSIONS

We superimposed both the patterns derived from the borehole and microtremor data on the geomorphological map units as shown in Figure 2 in order to investigate whether the spatial distribution of sites under the SPT-N value-based patterns correspond with the spectra ration-based patterns.

It was observed that the spatial distribution of most the data comprising both the pattern-1 nicely corresponds with each other. The geomorphological units comprising these patterns included 99 boreholes and 39 microtremor data out of the total investigated amount of 140 and 58 respectively. The surface soil of these units was encountered comparatively stiffer than that of other geomorphic units. Although, the predominant period on these units were around 1.0 s but we observed the fluctuation of amplification in an order of 3-5 in the geomorphic units belonging to this pattern. This phenomenon can be explained by the inspections of Figure 10.

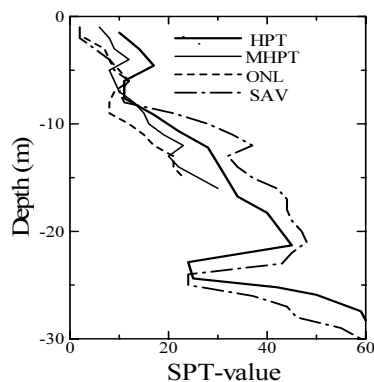


Figure 10: Four representative SPT-N value curves of pattern-1

The figure demonstrated that the SPT-N value of the top-soil of Higher Pleistocene terrace (HPT) was relatively higher than that of other geomorphic units of this pattern. The legend of SPT-N value curves in Figure 10 was organized from top to bottom according to the decrease of surface soil stiffness of the respective geomorphic units. The HPT, MHPT, ONL and SAV stood for Higher Pleistocene terrace, Moderately high Pleistocene terrace, Old natural levee and Shallow alluvial valley respectively. According to legend, the surface sediments of Higher Pleistocene terrace was very stiff, where as, shallow alluvial valley and Old natural levee represented less stiffness in surface soils. The Moderately higher Pleistocene terrace stood in between the above mentioned three

geomorphic units. The variations in the stiffness from hard to relative softness of the surface soil would be responsible for the fluctuations of amplification factors in the geomorphic units of this pattern. The SPT-N based 'pattern-1' showed that other than the above mentioned four units, Old inactive floodplain and three sites of Younger active floodplain belong to this pattern. Due to the lacking of borehole data, we could not correlate this pattern with SPT-N value based pattern-1.

The pattern-3 of the microtremor seems to be corresponded with pattern-2 of boreholes. The spatial distribution of these patterns incurred the geomorphic units, namely, Deep marshy land, some sites of Deep alluvial valley and Moderately deep alluvial valley. The representative soil profile with SPT-N curves in figure 4 suggested that the sites of these patterns showed a good impedance contrast in the near-surface strata at a depth of around 10 m. We assumed that this near-surface velocity contrast was the responsible for the developments of first mode of peak around 0.56. Due to the shallow depth of borehole, we could not explain the reason of another peak around 1.57 s. The amplification factors fluctuated in an order of 4-7, such a fluctuation of amplification was difficult to explain using this small amount of preliminary dataset.

The pattern-2 of microtremor did not show any specific relation with the borehole patterns. The pattern 3 and 4 of the boreholes included the sites which were under the geomorphic units of younger active floodplain, Point bar, Moderately deep alluvial valley and Deep marshy land. The representative soil profile showed the intercalation of many sub-soil strata in the sites of these patterns.

The amount of the data under the spectral ratio-based patterns 2 and 3 and SPT-N value curve-based patterns 2, 3 and 4 were not sufficient enough in this preliminary stage to draw a conclusion about their relationship. These spatial ratio-based and SPT-N value curve-based patterns included 19 and 41 sites of investigation. The compilation of a more extensive microtremor and deep borehole (more than 30 m depth) dataset covering all geomorphic units proved necessary from this preliminary investigation to draw the convincing conclusion among the relationship in the patterns of microtremor and boreholes with respect to geomorphic units.

References:

- Kanai, K. Tanaka, T. and Osada K. (1954), "Measurements of Micro-tremors 1. *Bulletin Earthquake Research Institute*, Tokyo University, 32, 199-210.
- Rodriguez, V. S. H. and Midorikawa, S. (2002), "Applicability of the H/V Spectral Ratio of Microtremors in Assessing Site Effects on Seismic Motion," *Earthquake Engineering and Structural Dynamics*, 31, 261-279.
- Nakamura, Y. (1989), "A Method for Dynamic Characteristics of Sub-surface Using Microtremors on the Ground Surface," *Quick Report of Railway Technical Research Institute*, 30(1)-25-33 (in Japanese).
- Field, E. H. and Jacob K. H. (1993), "The Theoretical Response of Sedimentary Layers to Ambient Seismic Noise," *Geophysical Research Letter*, 20, 2925-2928.
- Lermo, J. and Chavez-Garcia, F. J. (1994), "Are Microtremors Useful in Site Response Evaluation?," *Bulletin of Seismological Society of America*, 84, 1350-1364.
- Cardona, C. Davidson, R. and Villacis, C. (1999), "Understanding Urban Seismic Risk Around the World- A Final Report on the Comparative Study," *A project of the United Nations RADIUS Initiative, IDNDR, published by Geo-Hazards International*.
- Kamal, A. S. M. M, and Midorikawa, S. (2003) "GIS-based Landfill Mapping of Dhaka City Area, Bangladesh, Using Remote Sensing Data," *Proceedings on the Second International Symposium on New Technologies for Urban Safety of Mega Cities in Asia*, University of Tokyo, Japan.
- Konno, K. and Ohmachi, T. (1998), "Ground-motion Characteristics Estimated from Spectral Ratio between Horizontal and Vertical Components of Microtremor," *Bulletin of the Seismological Society of America*, 88(1), 228-241.
- Rodriguez, V. H. S. and Midorikawa, S., (2003), "Comparison of Spectral Ratio Technique for Estimation of Site Effects Using Microtremor Data and Earthquake Motions Recorded at the Surface and in Boreholes," *Earthquake Engineering and Structural Dynamics*, 32, 1691-1714.

A STUDY ON THE EFFECTS OF SURFACE WAVES GENERATED IN DEEP SEDIMENTARY BASINS DURING A MAJOR EARTHQUAKE

K. Eto ¹⁾, K. Motoki ²⁾ and K. Seo ³⁾

1)Graduate student, Department of Built Environment, Tokyo Institute of Technology, Japan

2)Research Assoc., Department of Built Environment, Tokyo Institute of Technology, Japan

3)Prof., Department of Built Environment, Tokyo Institute of Technology, Japan

eto@enveng.titech.ac.jp, kmoto@enveng.titech.ac.jp, seo@enveng.titech.ac.jp

Abstract: In the Kanto basin, when we consider the case of next great earthquake, long period component will appear as the result of surface waves excited by deep sedimentary layers. By a series of Izu earthquakes on July 2000, the surface waves about 10 seconds predominate extremely at the central Boso peninsula in eastern part of the Kanto basin. In compared with the dispersion curve of group velocity calculated with underground structural model by Yamada et al. (2003), we confirmed that this phenomenon was amplified by the deep sedimentary layers at the central Boso peninsula. These amplified surface waves have the potential to cause the disaster of large structures, e.g. fuel tank.

1. INTRODUCTION

In the Kanto basin, when we consider the case of next great earthquake, long period component will appear as the result of surface waves excited by deep sedimentary layers. Consequently, we must understand this phenomenon to evaluate earthquake ground motions for larger structures. Several researchers have studied on the effect of long period motions at the Kanto basin; Kinoshita *et al.*(1992) and Zama(1992) pointed out that Love waves generated from edge of the Kanto basin are dominant in the long period later arrivals observed around Tokyo-bay area. Koketsu *et al.*(2000) showed the propagation of the 5 seconds low-pass filtered motions by 384 strong motion instruments across the Kanto sedimentary basin and its surroundings. They identified wave fronts with abrupt changes in the amplitude and trajectory of ground motion. On the other hands, Koketsu *et al.*(1992) made the 3D structural model of the Kanto basin. Miura *et al.*(2000, 2001) made the 3D underground structure by PS converted wave in Yokohama city to examine the characteristics of Love wave propagation. 3D simulation of the 1923 great Kanto earthquake are performed by Sato *et al.*(1999). Yamada *et al.*(2003) tried the simulation of earthquake motions and constructing new 3D underground structural model at the Kanto basin.

In this paper, we found out about the peculiar amplification characteristics for the prediction of the surface waves in the central Boso peninsula using a series of Izu earthquake on July 2000.

2. RISK OF SURFACE WAVES IN THE DEEP SEDIMENTARY BASIN

Earthquakes have never taken place larger than magnitude 7 after the great 1923 Kanto earthquake at the Kanto basin, many large structures, high-rise, base-isolated buildings and fuel

tanks, with long natural period have been constructed in decades. Strong earthquake motions have not subjected such kind of large structures. Figure 1 shows the distribution of these structures. Many structures concentrate around the Tokyo-bayside. Especially, the fuel tank at the industrial area around Tokyo-bay has the various natural periods based on the size of tank and liquid volume. Taking the recent disaster, in 2003 Tokachi-oki earthquake, some fuel tanks burned for two days at Tomakomai. Figure 2 shows the wave plot with EW component from strong motions site near the epicenter to Tomakomai, and long period motions were amplified around Tomakomai. It has been proposed that long period components are excited by deep sediment to seismic bedrock. Thus, the survey of deep underground structures and the amplification characteristics of long period earthquake motions have been important problems in case of next great earthquake associated with Tokai-earthquake and South-Kanto earthquake. In this paper, we used the strong motions data of two earthquakes observed on July 2000 at K-Net and SK-Net in the Kanto basin (Fig.3).

3. EFFECTS OF SURFACE WAVES GENERATED IN DEEP SEDIMENTARY BASIN

3.1 Features of Surface Waves in The Kanto Basin on July 2000 earthquakes

Many researchers have studied the propagation of long period strong motions in the southern part of the Kanto basin. For example, Fig.4 shows the trajectories of horizontal velocity using observed earthquake motions at the southern part of Tokyo by Koketsu *et al.* (2000). Similarly, we made the trajectories map including the Boso peninsula to understand the propagation at all of Kanto basin (Fig.5). Trajectories were made for long-period motions filtered from 6 to 12 s. We reconfirmed that surface waves generated from two different directions, the epicenter and the western mountain area in the Kanto basin from Fig.5. Besides, we remarked that two earthquakes have the different feature in terms of the amplification between the eastern and western part of Tokyo-bayside. Thus, we focused on this peculiarity, and separated Tokyo-bayside into three areas; western, northern and eastern, to compare with the surface waves characteristics. Figure 6 shows velocity Fourier spectra at each area with 15 July 2000 (EQ.1) and 30 July 2000 (EQ.2). And the wave-plots of time histories filtered around dominant periods on EQ.2 are shown Fig.7. These spectra have the eminent peak with long period, but their predominant periods are not same on each earthquake. In the case of EQ.1 (Fig6 (a)-(c)), predominant periods at the almost sites are from 7 to 9s, and only eastern area have the wide band periods including 10s. These components still remain the high amplitude even around northern area. In the case of EQ.2 (Fig6 (d)-(f)), almost sites have the predominant period between from 8 to 12s. The amplitude at western area and northern area are same, but ICH, CHB014 and SOD at the eastern area are higher than other area. The group velocity at the eastern area inferred from Fig.7 is slower than western area. As the surface waves propagate toward northern part of the Boso peninsula, they are amplified gradually.

3.2 Peculiar Case of Amplification Characteristics at The Boso Peninsula

As mentioned in the preceding section, the amplification characteristics at the eastern area of Tokyo-bayside are different from other area. Figure 8 shows the comparison of the multiple filtered ground motions with three sites, CHB023, CHB015 and CHB014. Earthquake motions on EQ.1 and EQ.2 are composed of the different wave band. Collections of marked periods are two; from 6 to 8s and from 9 to 12s. In periods of the former, Fig.8 (d)-(f) did not contain these phases, and amplitude of these phases at CHB014 is not higher than CHB023 in Fig.8 (a)-(c). That is to say, Love waves of the period from 6s to 8s were hardly excited at the Boso peninsula in the case of July 2000 earthquakes. The other hands, surface waves with period range from 9s to 12s were amplified much higher than other periods as these phases propagate toward northern parts of Boso peninsula. Next,

we use the 3D underground structural model in the Kanto basin by Yamada *et al.* (2003) shown Fig.9 to consider about this cause. The central part of the Boso peninsula have the most deepest sedimentary to the seismic bedrock. Also above layers with an S-wave velocity of 1.7km/s and 1.0 km/s are deeper than other area. Figure 10 is the dispersion curve of Love wave group velocity calculated using structural model by Table.1 excerpted from Fig9. Airy phase in which surface waves are excited can be seen around 10s. Therefore, these Love waves are amplified highly by these deep sedimentary layers located at central the Boso peninsula.

4. EXPECTATED SURFACE WAVES DURING MAJOR EARTHQUAKE

The scale of predicted magnitude for next major earthquakes at the Kanto basin is larger than 7. Figure 11 shows the observed spectral acceleration amplitude at bedrock by Ohta *et al.*(1976). The larger the magnitude of earthquake is, the longer periods surface motions are excited at the epicenter. Earthquakes of magnitude 7 or more have the prevailing energy with period of 10s. Thus, if the major earthquake occurs near the Kanto basin, the earthquake motions with predominant period of 10 seconds will be amplified at the central Boso peninsula. These motions will affect to the fuel tank and large bridge rather than high-rise and base-isolated buildings.

5. CONCLUSION

We examined the effects of surface waves generated in Kanto basin on a series of Izu earthquake on 15 July and 30 July 2000. Firstly, we remarked that two earthquakes have the different feature in terms of the amplification between the eastern and western part of Tokyo-bayside. Especially, the amplitude with period of 10s at the central Boso peninsula was much higher than other area. Next, we calculated the Love wave group velocity using the model of deep underground structure to consider this phenomenon. In the result, we confirmed that surface waves amplified by the deep sedimentary layers at the central Boso peninsula. These long period motions have the potential to cause the disaster of large structures, e.g. fuel tank.

Acknowledgments:

Observed Strong motions in this paper by National Research Institute of Earth Science and Disaster Prevention, K-NET and Seismic Kanto Research Project, ERI, Univ. Tokyo, SK-NET.

Reference:

- Kinoshita, S., Fujiwara, H., Mikoshiba, T., and Hoshino, T., (1992), "Secondary Love waves observed by a strong motion array in the Tokyo lowlands, *J. Phys. Earth*, **40**, 99-116.
- Zama, S. (1992) "Characteristics of long-period ground motions in Tokyo bay area, Japan", Proc. 10th World Conf. Earthq. Eng., 593-598.
- Koketsu, K. and Kikuchi, M. (2000) "Propagation of seismic ground motion in the Kanto basin, Japan", SCINENCE, **288**, 1237-1239.
- Koketsu, K. and Higashi, S. (1992) "Three-dimensional topography of sediment / basement interface in Tokyo metropolitan area, central Japan", *Bull. Seism. Soc. Am.*, **82**, 2328-2349.
- Miura, H., Midorikawa, S. and Kinoshita S. (2000) "Characteristics of Love wave propagation in the southern part of the Kanto basin", Proc. 6th Intern. Conf. Seismic Zonation, No.00019
- Miura, H. and Midorikawa S., "Effects of 3-D deep underground structure on characteristics of rather long-period ground motion –Examination in and around Yokohama City –", *JISIN*, **54**, 381-395. (in Japanese)
- Sato, T., R. W. 10Graves, and P. G. Somerville (1999), "Three-dimensional finite-difference simulations of long-period strong-motions in the Tokyo metropolitan area during the 1990 Odawara Earthquake (MJ 5.1) and the Great 1923 Kanto Earthquake (MS 8.2) in Japan", *Bull. Seism. Soc. Am.*, **89**, 579-607.
- Yamada, N. and Yamanaka, H. (2003) "Ground motion simulations of moderate earthquakes for comparison of performance of 3D subsurface structural models in Kanto plain for strong motion prediction", *JISIN*, **56**, 111-123. (in Japanese)
- Ohta, Y., and Kagami, H., (1976) "Ultimate values of period and amplitude on seismic input motions in relation to a large-scale structure, **249**, 53-60. (in Japanese)

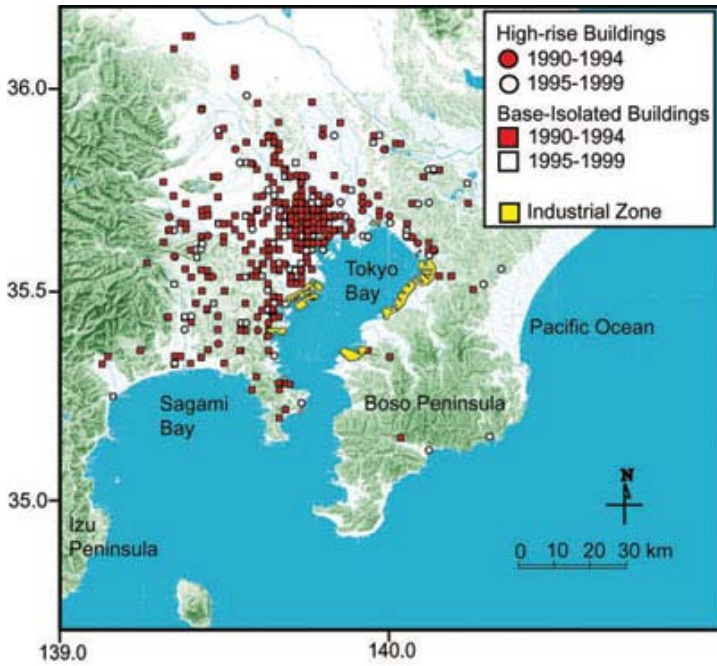


Figure 1 Distribution of large structures with long natural period, high-rise, seismically isolated buildings and fuel tanks.

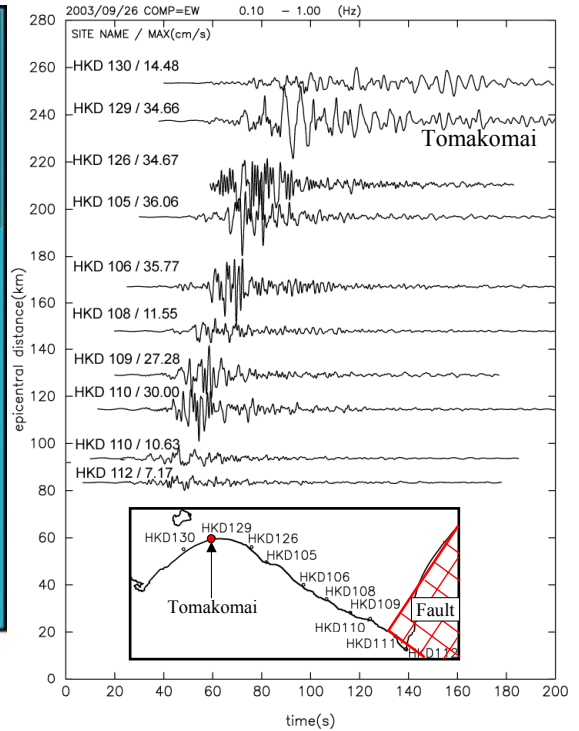


Figure 2 The velocity waves of E-W component with period of 1 to 10s from near fault site to Tomakomai on 2003 Tokachi-oki earthquake.

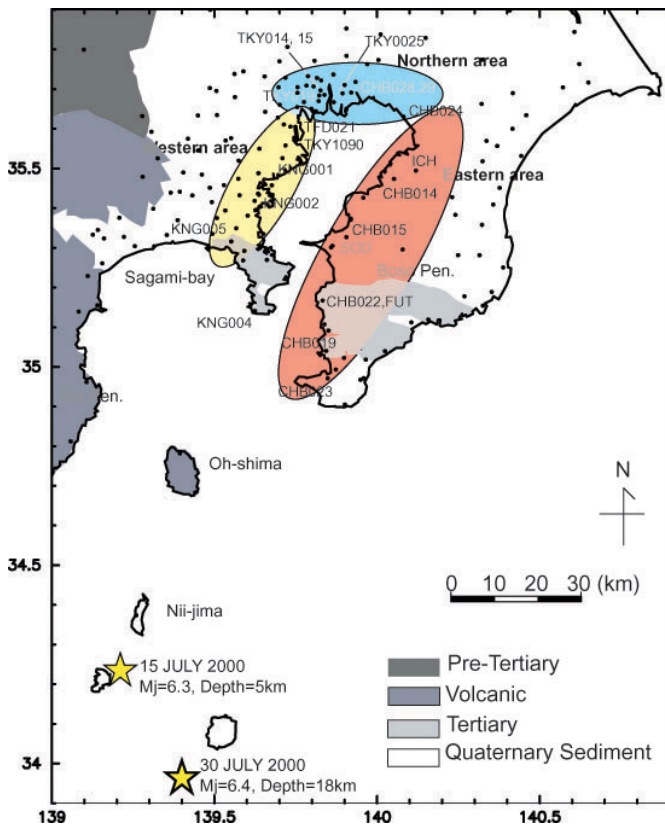


Figure 3 The strong motion sites observed on July 2000 earthquakes at the K-Net and SK-Net in the Kanto basin

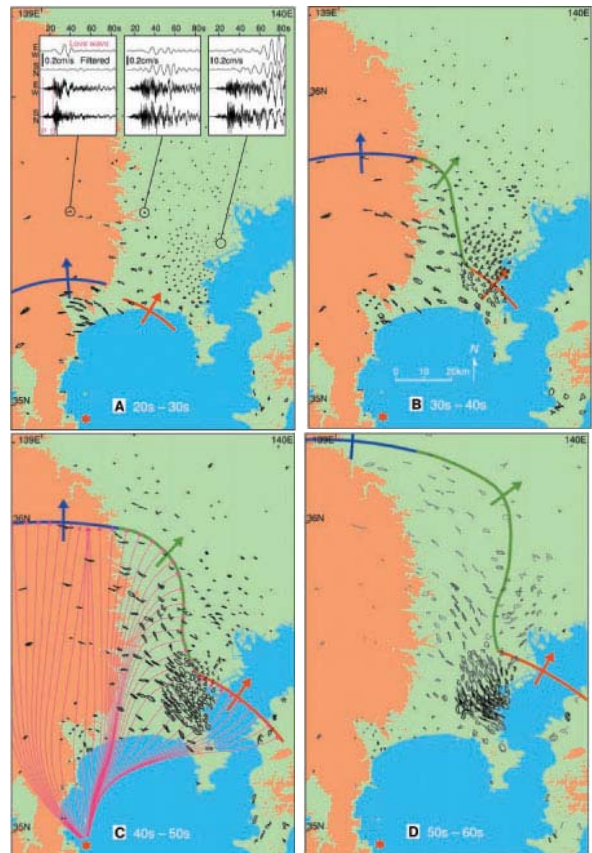
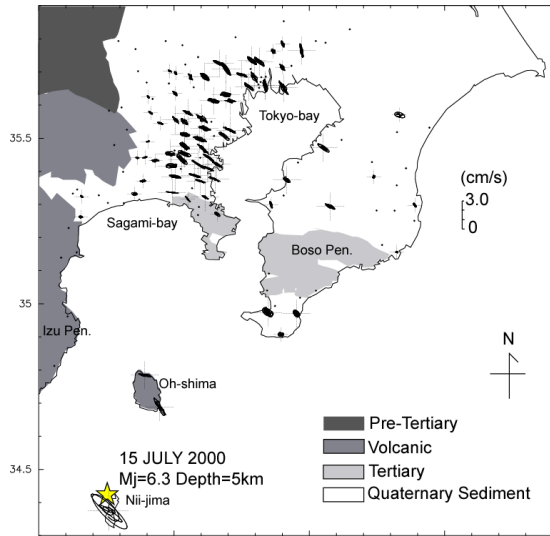
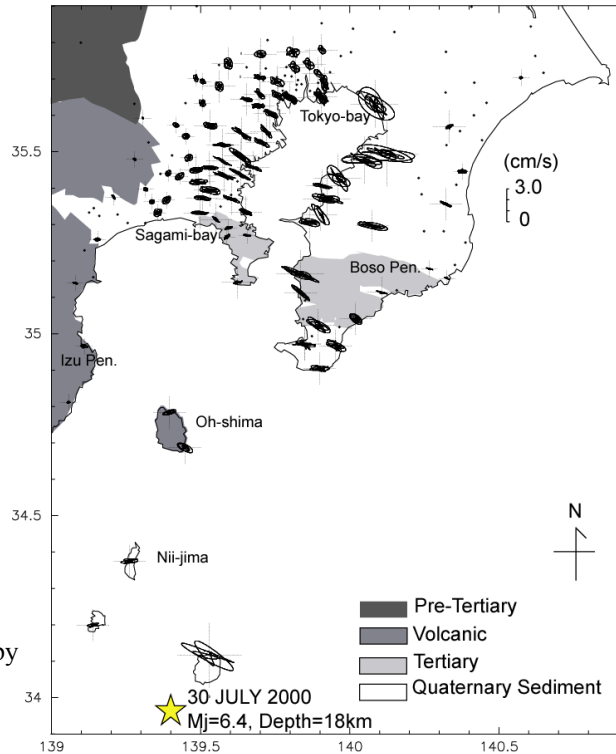


Figure 4 The trajectories of horizontal velocity at the southern part of the Kanto basin using the southwest of Tokyo earthquake 3 May 1998 (M5.7) by Koketsu *et al.* (2000)

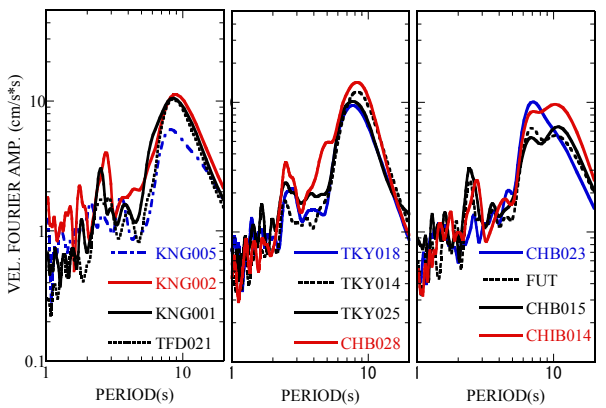


(a) 15 July 2000 (M6.3, Depth=5km)

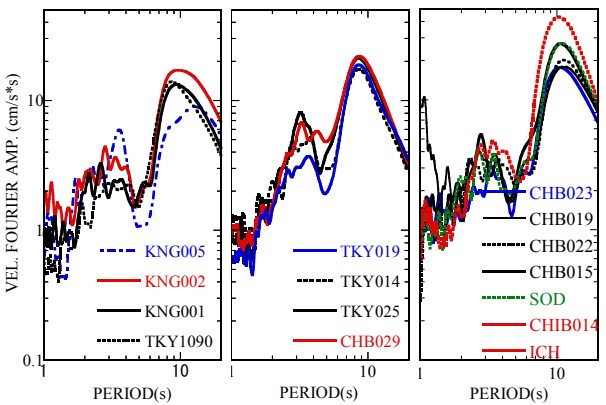


(b) 30 July 2000 (M6.4, Depth=18km)

Figure 5 Trajectories map in the Kanto basin by a series of Izu earthquakes on July 2000; (a) 15 July 2000, (b) 30 July 2000

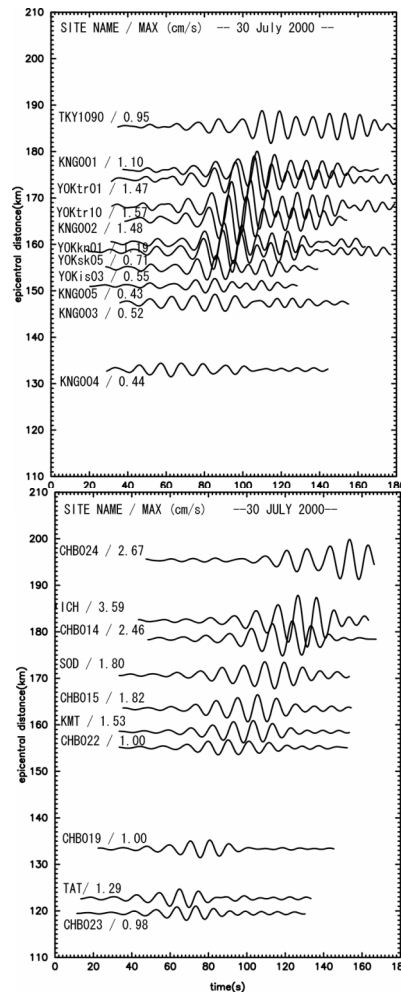


(a) Western area (b) Northern area (c) Eastern area



(d) Western area (e) Northern area (f) Eastern area

Figure 6 Fourier spectra of ground motions on July 2000 earthquakes; (a) – (c) : 15 July 2000 (d) – (f) : 30 July 2000



(a) Western area

(b) Eastern area

Figure 7 Velocity wave pest-up with period of 7 to 12 s on 30 July 2000

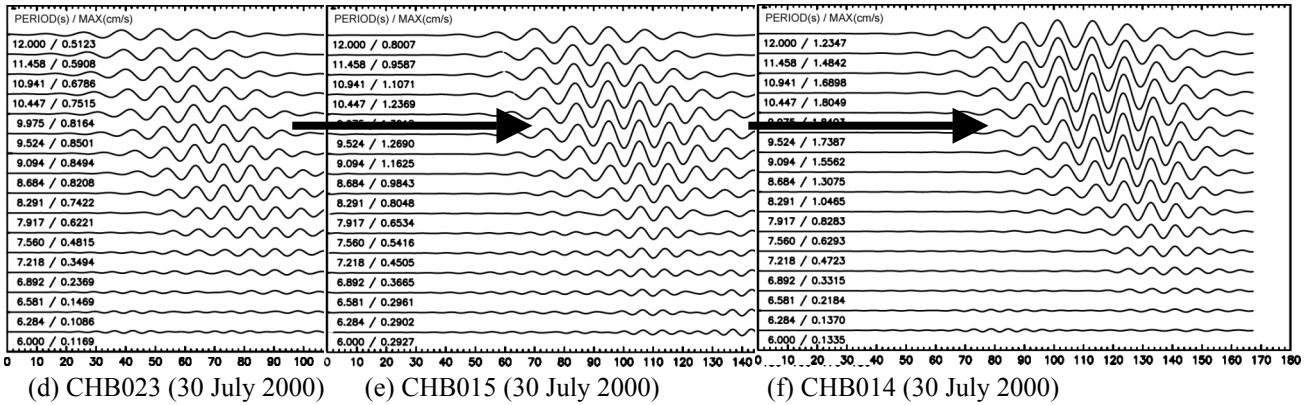
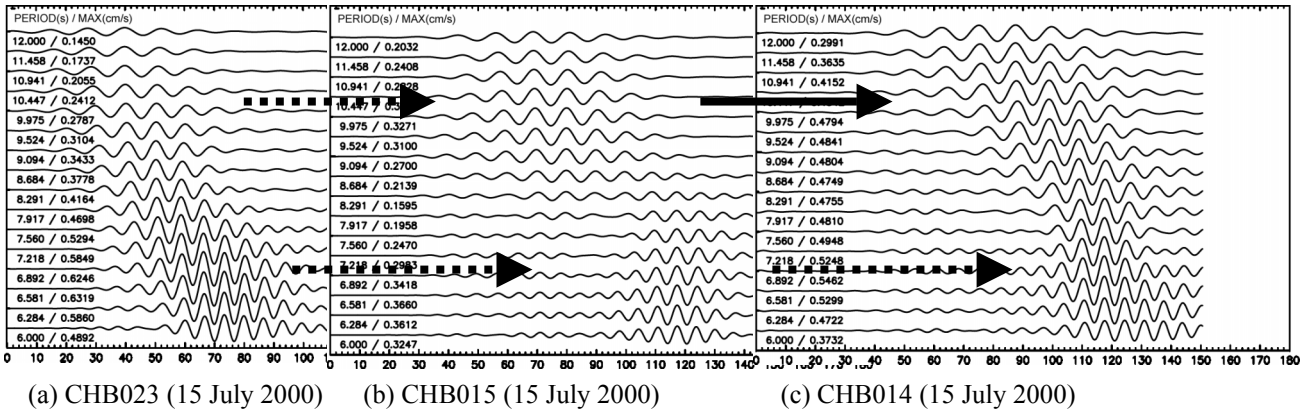


Figure 8 Observed ground motions with multiple filtered from 6 to 12 s at the CHB023, CHB015 and CHB014

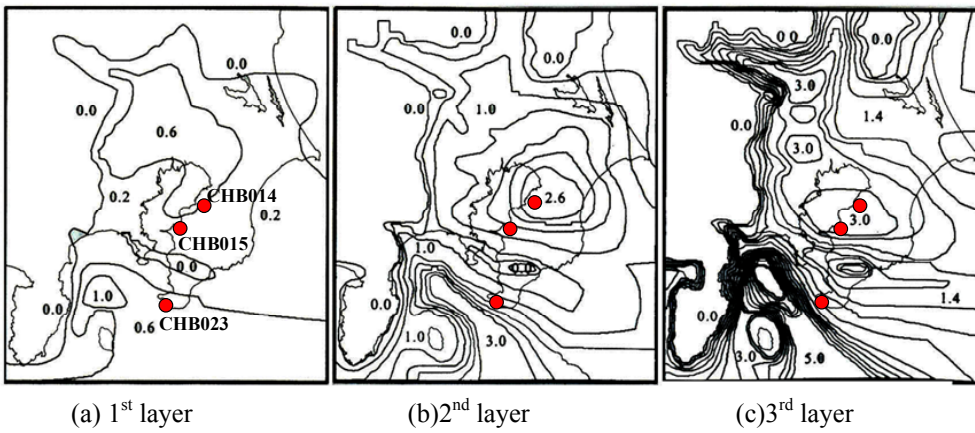


Figure 9 3D underground structural model in the Kanto basin by Yamada *et al.* (2003) and Location of strong motion sites, CHB023, CHB015 and CHB014. Each number shows the depth of km.

Table.1 Physical parameters at the CHB014 from Fig.9

Layer	Depth (km)	Vs(km/s)	$\rho(g/cm^3)$	Q
1	0.6	0.5	1.9	100
2	2.6	1.0	2.1	100
3	3.0	1.7	2.3	150
4	-	3.0	2.5	300

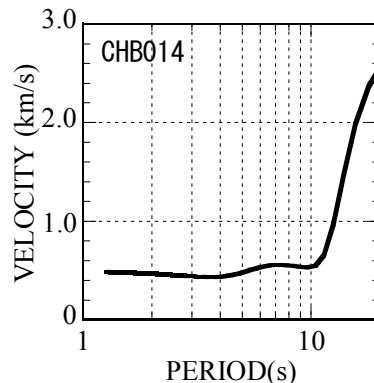


Figure 10 Dispersion curve of Love wave group velocity at CHB014

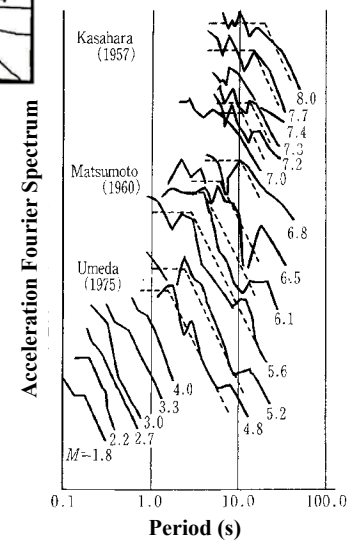


Figure 11 Observed acceleration spectrum on rock site by Ohta *et al.* (1976).

EFFECTS OF DEEP SUBSURFACE STRUCTURES ON SEISMIC WAVE PROPAGATION NEAR THE EDGE OF SEDIMENTARY PLAIN

K. Saguchi¹⁾, K. Motoki²⁾, and K. Seo³⁾

- 1) *Graduate Student, Dept. of Built Environment Interdisciplinary Graduate School of Science and Engineering, Tokyo Institute of Technology, Japan*
- 2) *Research Associate, Dept. of Built Environment Interdisciplinary Graduate School of Science and Engineering, Tokyo Institute of Technology, Japan*
- 3) *Professor, Dept. of Built Environment Interdisciplinary Graduate School of Science and Engineering, Tokyo Institute of Technology, Japan*
k-sagu@enveng.titech.ac.jp, kmoto@enveng.titech.ac.jp, seo@enveng.titech.ac.jp

Abstract: Significant later phases following the S-wave arrivals in horizontal components often appear in the ground motions recorded in the sedimentary plain. In this paper, we discuss the propagation process of ground motions generated by a shallow earthquake through the analysis of seismograms recorded on rock and sediment sites. To accomplish it, we first deployed a temporary stations for seismic refraction prospecting to clear up the boundary between the mountain range and the edge of the sedimentary plain in the southwestern edge of the Kanto Plain. Accordingly, we employed the recordings of seismic waves generated by explosions to model the subsurface structures applying travel time analysis. We also applied a 2D finite difference method to simulate the later phases during an earthquake observed at the sediment sites using the subsurface structures derived from the seismic prospecting process. The results indicate that when considering basin excited waves, the characteristics of the simulated waveforms including the later phases display good agreement with the observed seismograms.

1. INTRODUCTION

It is essential to understand propagation characteristics of seismic motion in sedimentary basin in order to estimate the damage distribution from an earthquake. It has been recognized that the long-period ground motions, which consist mainly of surface waves, become larger in amplitude on sedimentary basins and longer in duration than at its margins. This is of great engineering concern. Because many large cities have a number of large-scale structures, such as high-rise buildings, long-spanned bridges and huge oil tanks in the world, including Tokyo Metropolitan area is located in a large sedimentary basin.

Tanaka et al. (1980) has reported that surface waves with a period of around 8 seconds are predominant in seismograms recorded at station on sediments in Tokyo during large earthquake. On the other hand, Toriumi et al. (1984) has pointed out that surface waves are generated secondary in the edge of basin by using seismograms from array observations. Therefore, it is necessary to consider underground structures not only particular observation sites but also process of propagation of seismic motion in order to clarify the propagation characteristics of the long-period ground motions.

In this study, seismic waves from the explosions are used to investigate the deep underground structure down to seismic basement in the Sagami area, which located at boundary between mountain region and the edge of the Kanto plain. The purpose of our investigation was to clear up the nature of the boundary between mountain region and the edge of basin, and the propagation characteristics are

discussed at this region using seismograms recorded on rock site and sediment sites due to the July 11, 2003 earthquake that occurred at the western part of Kanagawa prefecture (M=4.1,H=21km).

2. EARTHQUAKE OBSERVATION AT SOUTHWESTERN EDGE OF THE KANTO PLAIN

The southwestern part of the Kanto plain is depicted in Figure 1 with the observation points and the surface geology conditions. The Sagamihara area, located about 50km southwestern of Tokyo where is a diluvial terrace on the north side, and the Kanto Mountains, which is on the sedimentary rocks on the northwest side of this terrace.

Velocity type strong motion seismometers with three orthogonal components each were installed are 7 sites in this area. The stations ASK and AKW are located at the western part of the plain on a hard rock. YKY and FCN are located around the same area at the edge of the plain in the sediment.

Figure 2 shows an example of the horizontal components with velocity seismograms recorded at this region during the July 11, 2003 earthquake that occurred at the western part of Kanagawa prefecture (M=4.1,H=21km). Significant later phases appear following the first S-wave arrivals in horizontal components, especially transverse component at YKY and FCN. Such phenomena can be seen only in seismograms of earthquakes that occurred between the western part of Kanagawa prefecture and the eastern Yamanashi prefecture areas. The focal depth of these earthquakes is comparatively shallow (less than about 30km).

Kinoshita(1985) found seismograms observed during earthquake with the same shape from records at Fuchu array observation on the Kanto plain. As the results of analyses of characteristics of seismograms, by using apparent velocity method and Hilbert transform method. It was observed that the train of impulsive later phases was produced by multiple reflections of SH-wave at the upper boundary of dipping basement around the edge. Kurita(1996) found the significant later phase observed during the August 5, 1990 earthquake that occurred at the western part of Kanagawa prefecture (M=5.1,H=13.6km) at FCN. As the results of analyses of characteristics of seismograms, by using polarization analysis method and travel time analysis method. This phase was generated at the edge of sedimentary plain due to time difference between onset of first S-wave and first later phase. However, it has not resulted in detailed examination in propagation process because the underground structure at the edge of plain was not cleared.

3. DEEP SUBSURFACE STRUCTURES NEAR THE EDGE OF THE KANTO PLAIN

A seismic refraction prospecting was carried out in the southwestern part of the Tokyo Metropolitan area in January 15, 2000, for purpose of earthquake disaster prevention to clarify the deep underground structure down to the seismic basement. The explosions were denoted at 3 sites; Zama (SP1), Hiratsuka (SP2) and Tamagawa (SP3) are shown in Figure 3. The charge sizes were 500kg, 300kg and 50kg for SP1, SP2 and SP3, respectively.

In this experiment, we observed an explosion from SP1 by 9 stations on a 20km from Zama shot point to north observation line (N-Line), and 30 stations on a 25km east to west line (EW-Line) (Saguchi et al, 2000). EW-Line is on the line of one of the Yumenoshima explosions, of which research group made a series of seismic prospecting by exploding dynamite underground at Yumenoshima for more than twenty five times since 1975 (Research Group on Underground Structure in the Tokyo Metropolitan Area, 1989). The other group observed an explosion from SP1 by 40 stations and SP2 by 9 stations on a 15km from Zama shot point to south observation line (S-Line) along the Sagami River crossing the Hiratsuka shot point (Maeda et al, 2000). Locations of more than 70 observation stations in detail are shown in Figure 4. Digital recorders with a 200Hz sampling

recorded vertical component of ground velocity. Sensors we used geophones with a natural frequency of 4.5Hz were used for N-Line, and 2.0Hz were used for EW-Line. Synchronized time was carried out by GPS almost of stations.

Vertical component seismograms along the N-Line, the S-Line and the EW-Line released from SP1 are shown in Figure 5, respectively. The amplitudes, which were traced in Figure 5, are normalized by its maximum of each amplitude. The quality of the data is quite well and clear first arrivals corresponding to a refracted wave from seismic basement can be traced up to offsets of more than 10km along the N-Line (Figure 5(a)). The apparent P-wave velocity of the first arrivals is 5.3km/s in this section, and the intercept times are about 1.0s. On the other hand, these are not appeared along the S-Line (Figure 5 (a)), indicated that the upper layers of seismic basement are thicker than N-Line. Instead, the layer that has apparent velocity of 4.0-4.5km/s whose intercept times are about 0.5s is refracted wave from a shallow layer is recognized in both of sections. Along the S-Line, vertical component of seismic wave released from SP2 were obtained. The basin area along the EW-Line (Figure 5(b)), the apparent P-wave velocity of the first arrivals corresponding to a refracted wave from the identical layer is 3.8km/s, and the intercept times are about 0.5s. On the other hand, the mountain area crops out Cretaceous rock in this section have an apparent velocity greater than 7.0km/s. It is consider that there are interpreted as refracted wave from the seismic basement. In additionally, many later phases are recognized in all of the section. Travel time diagram for P-wave initial onsets along the line are shown in Fig. 4. Authors must follow the format details given in this section.

P-wave velocity profiles obtained from the travel time diagrams along the line are shown in Figure 6. As a primary process, the method of differences (Hagiwara, 1938) was applied to the travel time data obtained from the travel time diagrams along the S-Line, since the method is useful for understanding a general structure and also estimates approximated P-wave velocities of layer. As shown in Figure 7 (a), it consists of two layers with P-wave velocities of 2.2 and 4.3km/s from results of this method in this section. At the Zama shot point, the thickness of the upper sedimentary layer with P-wave velocity of 2.2km/s is about 0.7 km, and thinner than one at the Hiratsuka shot point. And second one with velocity of 4.3km/s. Then as a secondary process, we constructed a P-wave velocity model with three layers using by time term method along the N-Line (Figure 7 (b)) based on the result from the S-Line profile. Finally, the underground structure with a P-wave velocity along the EW-Line (Figure 7 (c)) was revealed using by time term method. It was confirmed that the basement structure of the boundary in the mountain region inclines drastically to the edge of the basin. The depth of basement in this area is about two or three hundred meters.

4. NUMERICAL SIMULATION BY FINITE-DIFFERENCE METHOD

In this study, the 2-D finite difference method is used to perform a numerical simulation. We are interested in significant later phases generation and propagation within sedimentary layers, and a observed seismogram on the rock site can be regarded as an input wave to sedimentary layers. Therefore, the velocity record of transverse component, which observed at AKW station on a hard rock, the July 11, 2003 earthquake that occurred at the western part of Kanagawa prefecture (M=4.1,H=21km), is used as input wave. The main portion of the seismogram consists of SH wave and Love waves, and set the input wave as plane wave with 45-degree incidence. It is determined by simple horizontally layered crustal structure shown in Figure 9a, which is assumed near AKW. In the computation, a band pass filter with periods from 1 to 5 second was applied considering the stable condition. This filtered record with duration of 5 second is shown in Figure 8, in which the main portion of the ground motions is included, is used as the input wave. An underground structural model for the profile along the EW-line in Figure 4 is depicted in Figure 9a, and the computed velocities on the ground surface along this line are shown Figure 9b. Three phases appear in the computed velocities, and these phase corresponds first SH-wave, multiple reflections of SH-wave and excited

wave from the edge of plain, respectively. In this figure, it seems that the multiple reflections of SH-wave at the upper boundary of dipping basement is remarkable less than 35km from the epicenter, but excited wave which have an apparent velocity of 1.1km/s is remarkable more than 35km from the epicenter. The comparison between the observed and the synthetic seismograms at each station on the sedimentary is shown in Figure 10. According to the arrival time of each phase can be compared, it regard observed significant phases as the multiple reflections of SH-wave at the upper boundary of dipping basement at STN, YKY and FCN station. To a contrary, it turns out that the excited wave has appeared predominantly at OGM station.

5. CONCLUSIONS

The deep subsurface structure in the southwestern part of the Kanto plain was revealed by travel time analysis. The main results from our experiment are as follows the underground structure along the N-Line consists with three layers. The P-wave velocities of these layers are 2.3, 4.3 and 5.3km/s, respectively. But along the S-Line and the EW-Line, the layer with P-wave velocity of 5.3km/s was not found. Therefore, we estimate the profile along the EW-Line using by time term method based on the layer with P-wave velocity of 4.3km/s along the EW-Line. It was confirmed that the basement structure of the boundary in the mountain region inclines drastically to the edge of the plain. The depth in this area is 200 to 300 hundred meters.

We also applied a 2D finite difference method to simulate the later phases during an earthquake observed at the sediment sites using the subsurface structures derived from the seismic prospecting process. The results indicate that when considering then as basin excited waves, the characteristics of the simulated waveforms, including the later phases, display good agreement with the observed seismograms. It seems that the excited wave from edge of plain is remarkable more than 10km from the southwestern edge of the Kanto plain.

Acknowledgements:

The authors wish to express their thanks to Prof. T. Enomoto, Kanagawa Univ., Prof. N. Abeki and Mr. T. Maeda, Kanto Gakuin Univ. and Prof. K. Masaki, Aich Inst. of Tech. for making data available to the authors. They are also grateful to the public officials at Kanagawa Pref., Sagamihara City, Kawasaki City, and Yokohama City for support during this experiment. The authors would like to thank Dr. N. Yamada, Disaster Prevention Research Institute Koto University and Associate Prof. H. Yamanaka, Tokyo Inst. of Tech for making program of a finite different method available to the authors.

References:

- Hagiwara, T. (1938), Travel time curve analysis for the structure with the irregular basement interface, *Zisin*, **10**, 463-468, (in Japanese).
- Kinoshita, S. (1985), Propagation of total reflected phase SH pulses in a dipping layer. *Zisin*, **38**, 597-608, (in Japanese).
- Maeda, T., Maeda, N. and Abeki, N. (2000), Exploration of the underground structure along the line from Zama to Hiratsuka using seismic refraction method, *Abstract of 2000 Japan Earth and Planetary Science Joint Meeting*, Tokyo, Japan, June 25-28, (in Japanese).
- Neidell, N. S. and M. T. Taner (1971), Semblance and other coherency measures for multichannel data, *Geophysics*, **36**, 482-497.
- Research Group on Underground Structure in the Tokyo Metropolitan Area (1989), *Technical Report on the Yumenoshima seismic refraction experiment*, Earthquake Res. Inst., University of Tokyo.
- Saguchi, K., Seo, K., and Kurita, K. (2000), On the Seismic in the Southwestern Part of the Kanto Plain -Underground Structure in Sagamihara Area, Kanagawa Prefecture-, *Abstract of 2000 Japan Earth and Planetary Science Joint Meeting*, Tokyo, Japan, June 25-28, (in Japanese).
- Tanaka, T., Yoshizawa, S. and Osawa, Y. (1980), Characteristics of strong earthquake ground motion in the period range from 1 to 15 seconds, *Proc. of the 7th World Conf. On Earthquake Engineering*, **vol. 2**, Istanbul, Turkey, September 8-13, 609-616.
- Toriumi, I., Ohba, S. and Murai, N. (1984), Earthquake motion characteristics of Osaka plain, *Proc. of the 7th world Conf. on Earthquake Engineering*, **vol. 2**, San Francisco, California, July 21-28, 465-472.

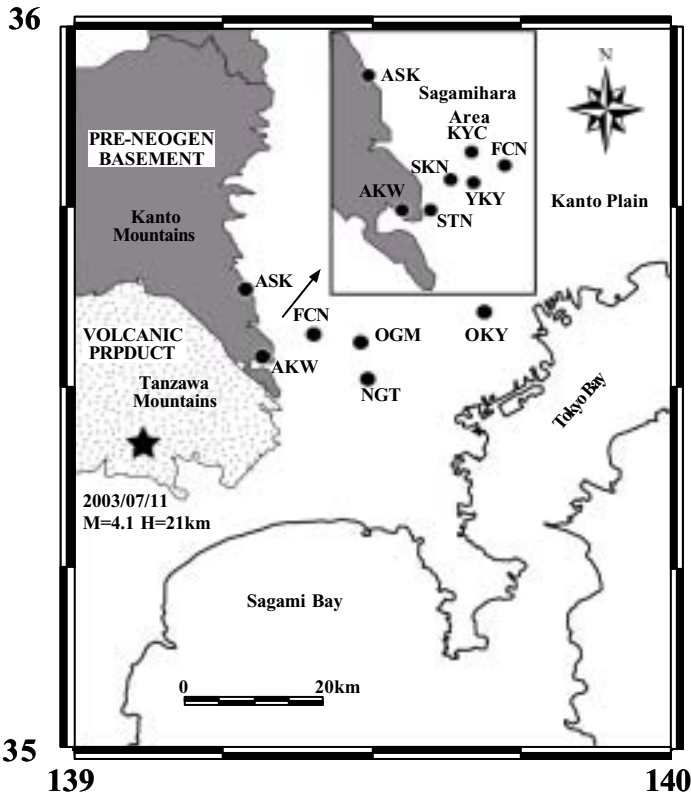


Figure 1. Map of the studied filed, the southwestern part of the Kanto plain, Japan. The solid circles indicate observation sites. The star shows the epicenter of earthquake.

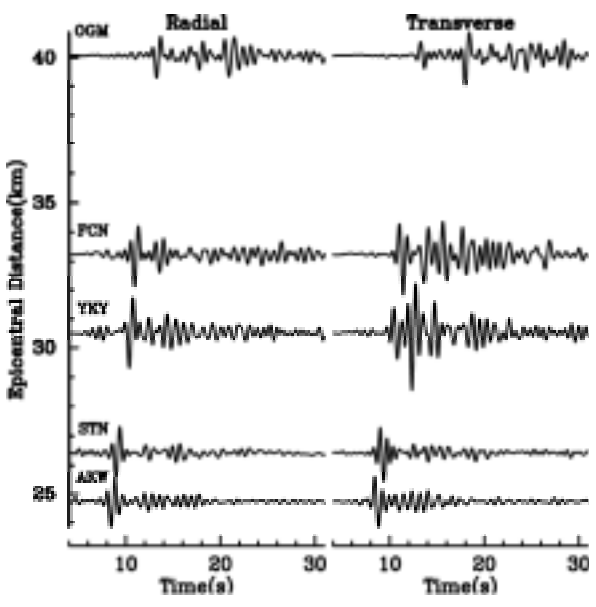


Figure 2. Horizontal velocities observed near southwestern edge of the Kanto plain during the earthquake on July, 11 in 2003. Each trace is filtered in a period range from 1 to 5 seconds.

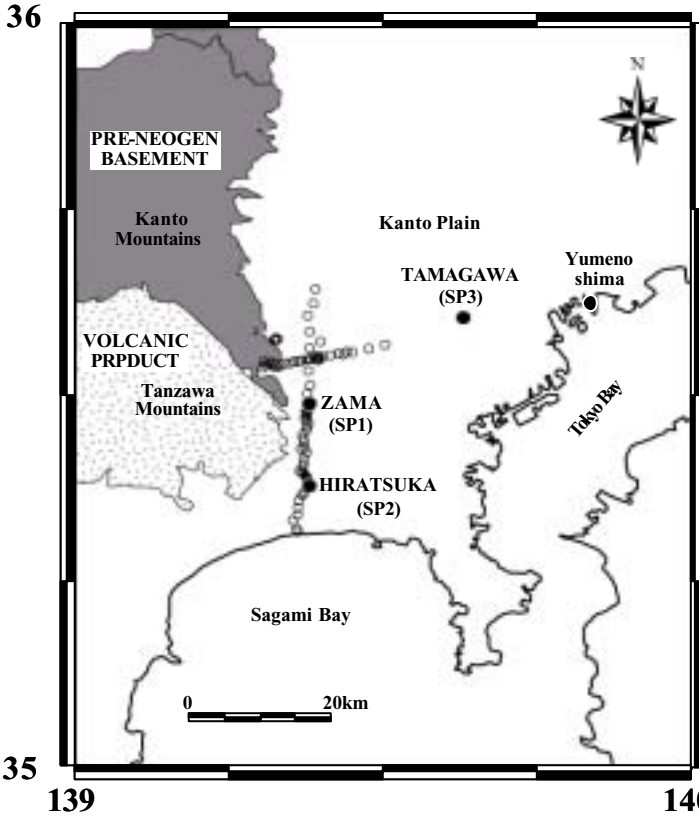


Figure 3. Map of the studied filed, the southwestern part of the Kanto plain, Japan. The solid circles and circles show explosion points and observation stations, respectively.

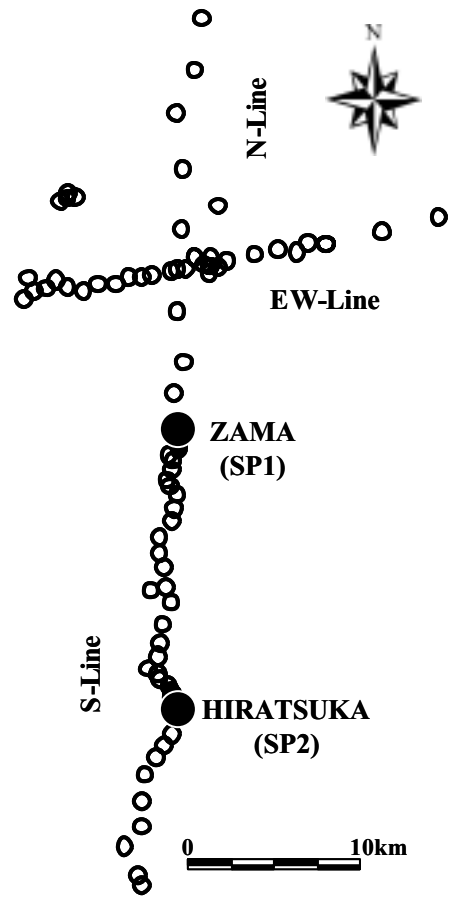


Figure 4. Map of the studied filed with the observation stations and surveying lines. NLine located from Zama shot point to the north. S-Line located from Zama shot point to the south

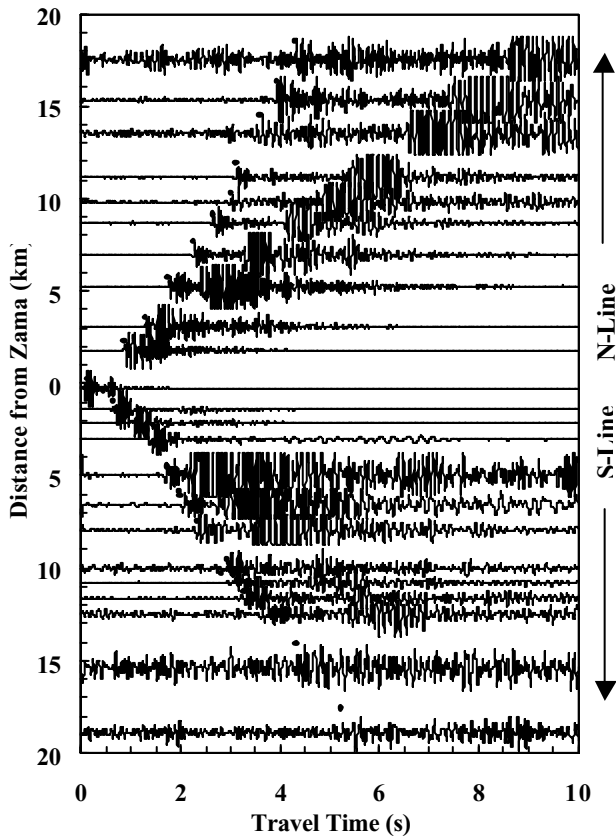


Figure 5. (a) Seismograms observed at the stations along the N-Line and the S-Line during the Zama explosion. Each trace is normalized to its maximum amplitude.

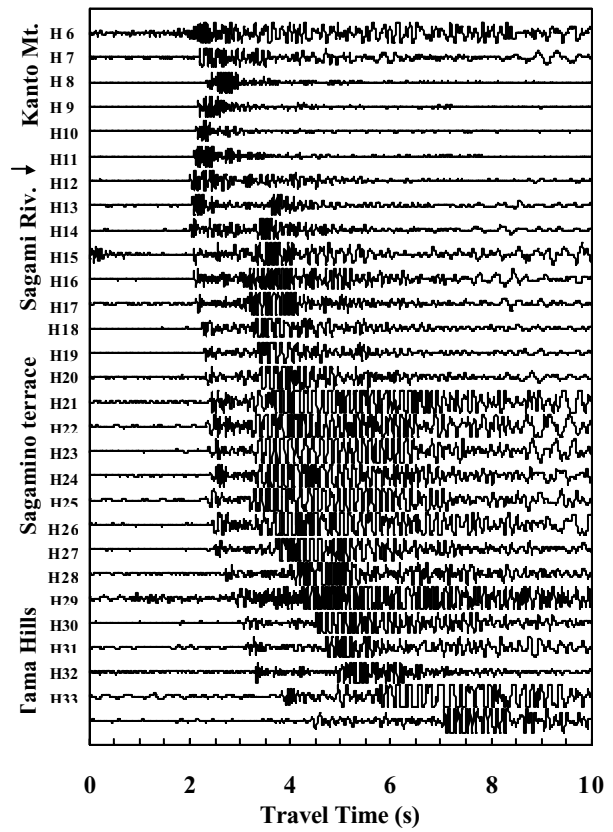


Figure 5. (b) Seismograms observed at the stations along the EW-Line during the Zama explosion. Each trace is normalized to its maximum amplitude.

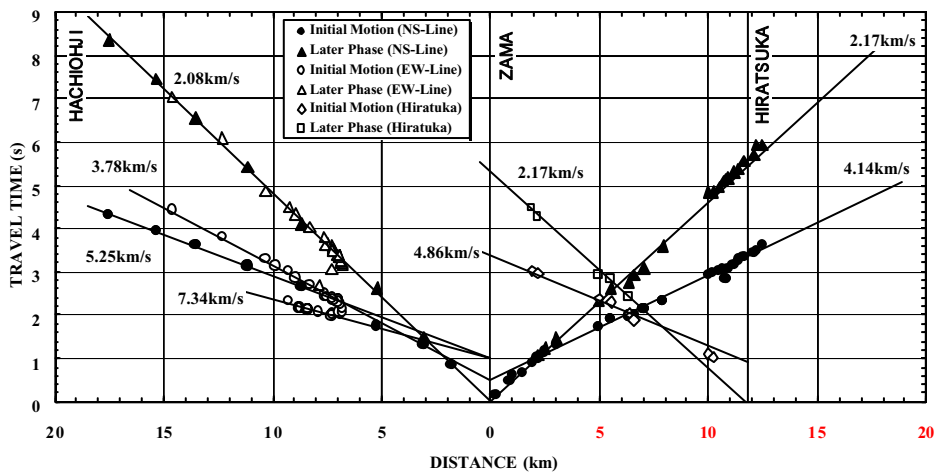


Figure 6. Travel time diagram on Hiratsuka-Hachiohji line. Solid circles and triangles show arrivals of initial and later phases for the Zama explosion, respectively. Open circles and triangles show arrivals of initial and later phases for the Hiratsuka explosion, respectively. Open squares show arrivals of initial and later phases for the Hiratsuka explosion, respectively.

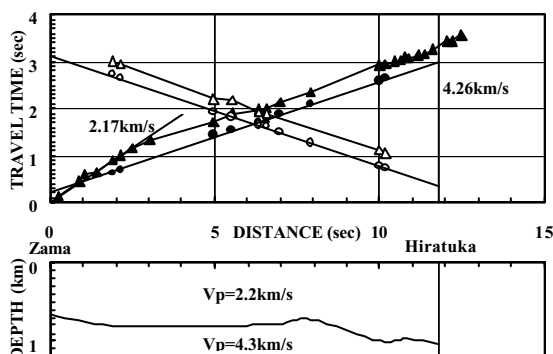


Figure 7. (a) Under ground structure obtained from the method of differences for the S-Line. Observed travel times are shown by triangles.

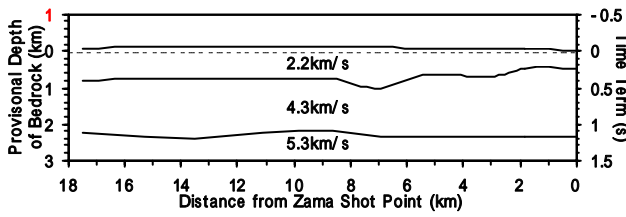


Figure 7. (b) Under ground structure obtained based on profile for the N-Line.

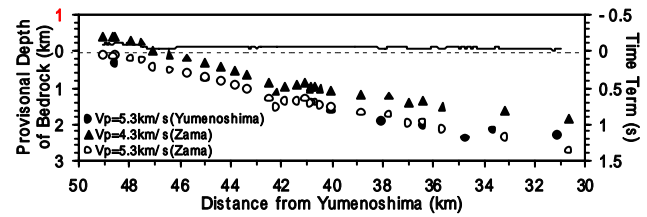


Figure 7. (c) Comparison of time terms on the EW-Line derived from Zama explosion.

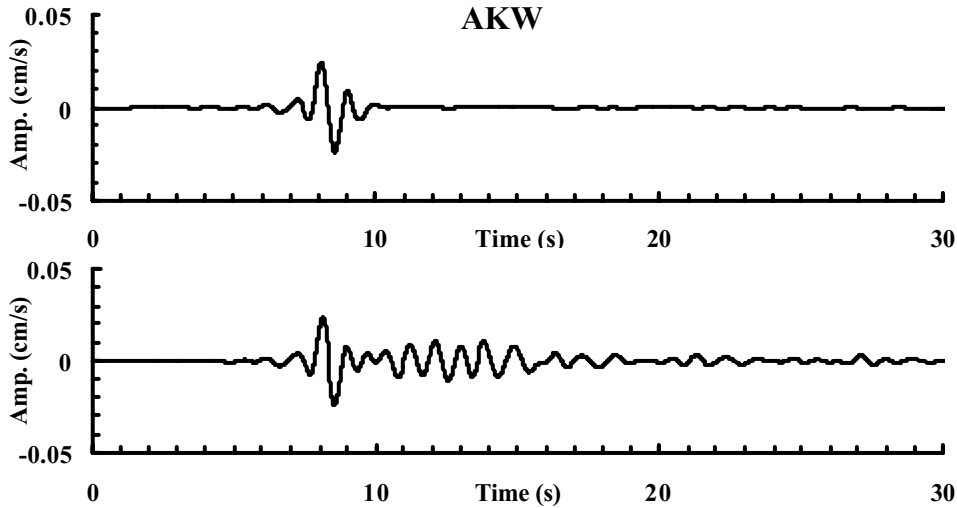


Figure 8. Input wave for calculate the waveforms using finite difference method. Upper: The only first motion observed at AKW with band pass filter in period range from 1 to 5 seconds. Lower: All data observed at AKW.

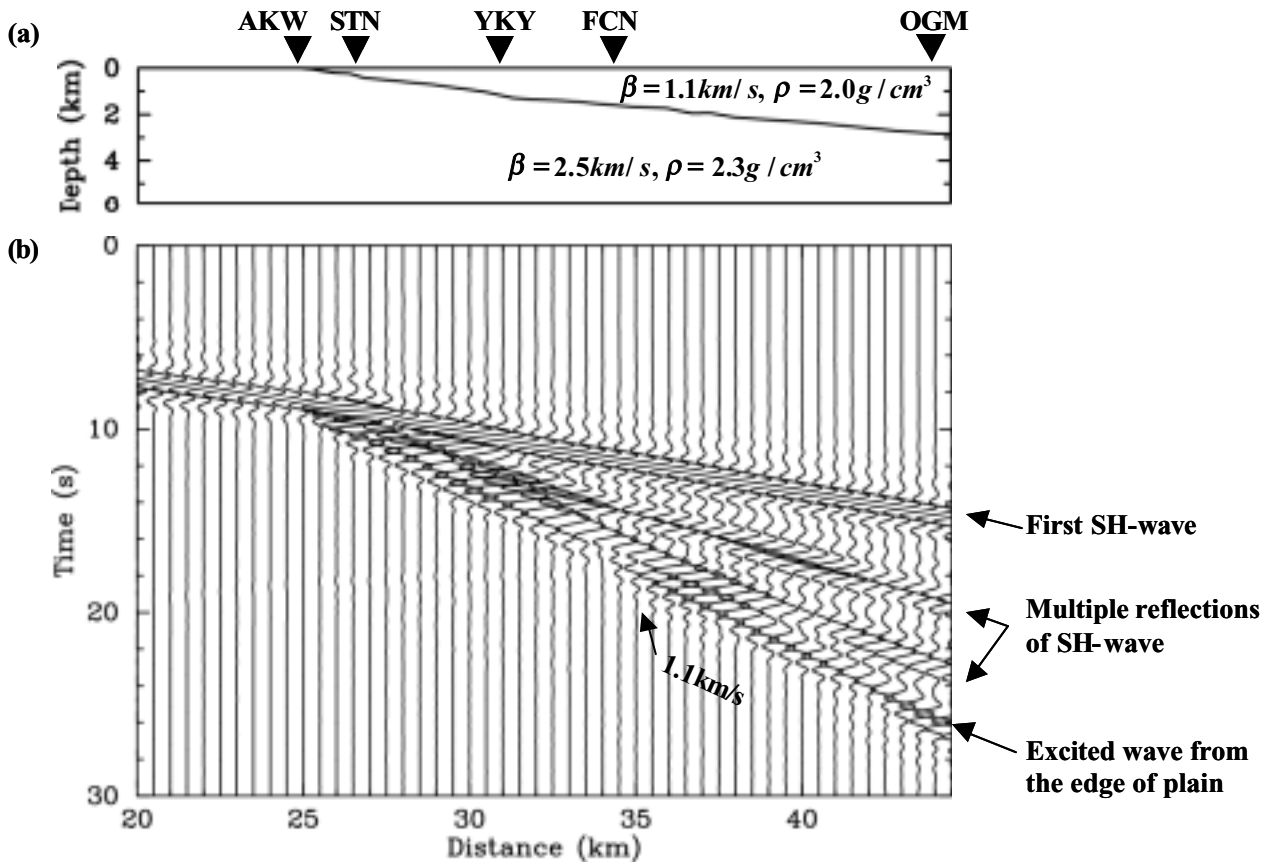


Figure 9. (a) Underground structure model along EW-line in Figure 4. (b) Synthetic velocity seismograms on the surface of the model. Each trace is normalized to maximum of all traces.

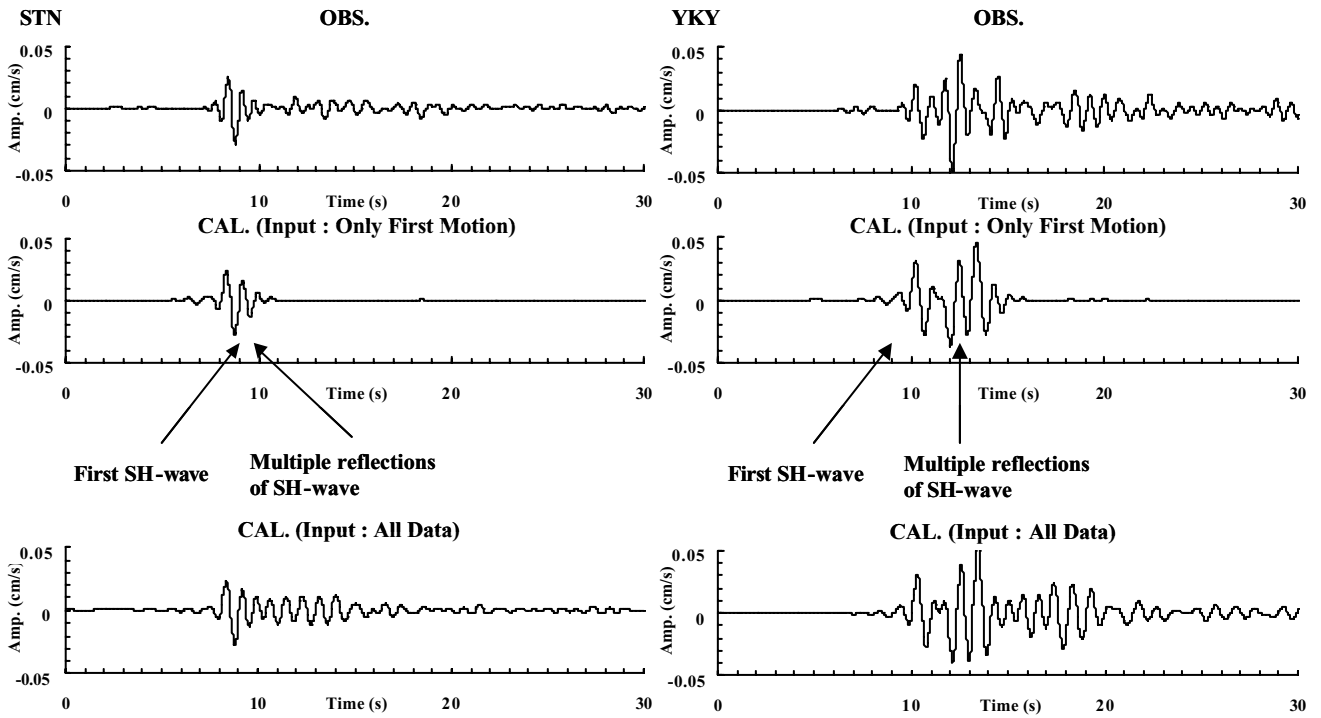


Figure 10 (a) Comparison of observed and synthetic velocities for STN (Left) and YKY (Right). Band pass filter with period from 1 to 5 seconds for the observed velocity records. Upper: Observed velocity. Middle: Synthetic velocity using the only first motion observed at AKW as an input. Lower: Synthetic velocity using all data observed at AKW as an

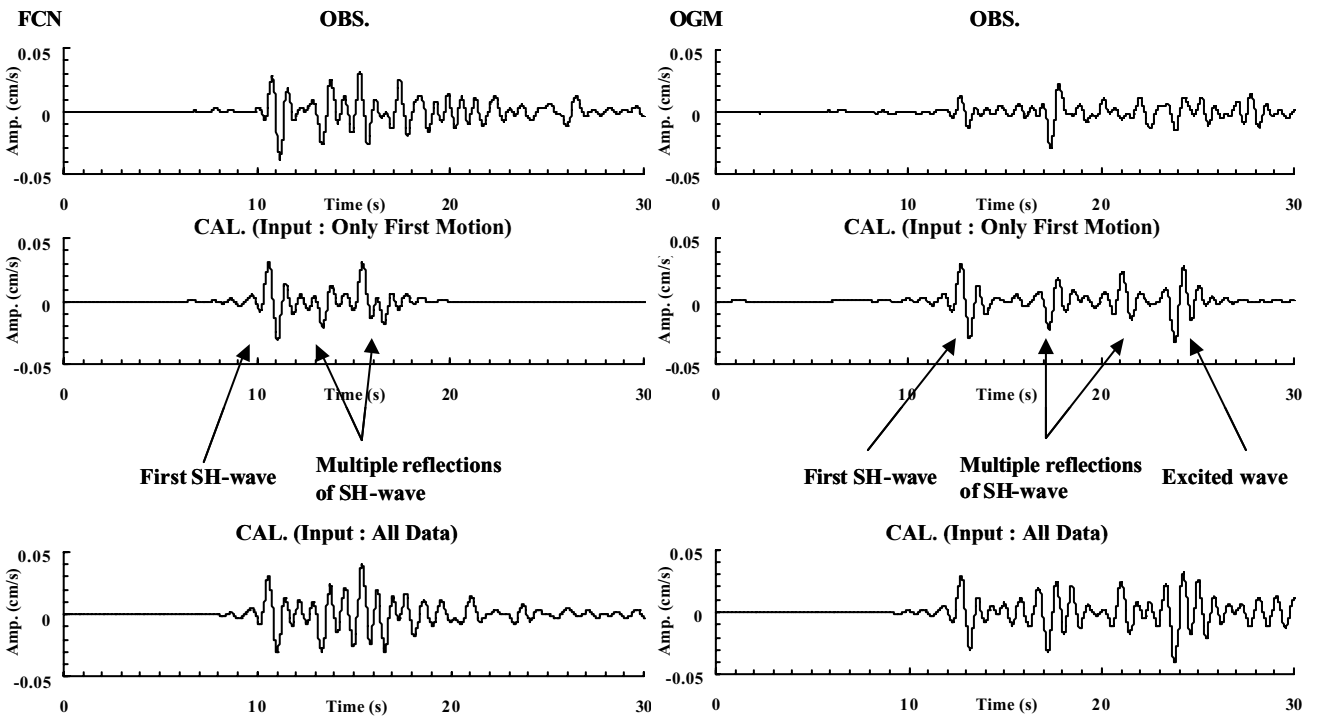


Figure 10 (b) Comparison of observed and synthetic velocities for FCN (Left) and OGM (Right). Band pass filter with period from 1 to 5 seconds for the observed velocities. Upper: Observed velocity. Middle: Synthetic velocity using the only first motion observed at AKW as an input. Lower: Synthetic velocity using all data observed at AKW as an input.

MODERN URBAN SEISMIC NETWORK IN BUCHAREST, ROMANIA

A. Aldea¹⁾, T. Kashima²⁾, D. Lungu³⁾, R. Vacareanu⁴⁾, S. Koyama⁵⁾, C. Arion⁶⁾

1) Lecturer, Technical University of Civil Engineering, Bucharest &
Chief of Division, National Centre for Seismic Risk Reduction, Bucharest, Romania

2) Senior Researcher, Building Research Institute, Tsukuba, Japan

3) Professor, Technical University of Civil Engineering, Bucharest &
General Director, National Building Research Institute, Bucharest, Romania

4) Associate Professor, Technical University of Civil Engineering, Bucharest &
Director, National Centre for Seismic Risk Reduction, Bucharest, Romania

5) Senior Researcher, National Institute for Land and Infrastructure Management, Tsukuba, Japan

6) Chief of Division, National Centre for Seismic Risk Reduction, Bucharest, Romania

aldea@mail.utcb.ro, kashima@kenken.go.jp, lungud@mail.utcb.ro, vradu@mail.utcb.ro, koyama@nilim.go.jp

Abstract: The paper presents the main characteristics of ground motions recorded in Bucharest during strong and moderate earthquakes from the intermediate depth Vrancea seismic source, and the existing seismic instrumentation in Bucharest, Capital City of Romania, with emphasis on the recently installed seismic network (2003) of the *National Centre for Seismic Risk Reduction NCSRR* in the frame of the Technical Cooperation Project "Seismic Risk Reduction for Buildings and Structures" with *Japan International Cooperation Agency*. This new network with digital instruments has three components: stations for ground motion attenuation analysis (6 stations outside Bucharest), stations for site effects assessment in Bucharest (7 sites instrumented with free field and borehole sensors at 2 depth levels, between 25m and 153m), and stations for structural monitoring in Bucharest (4 instrumented buildings). The paper also presents preliminary site response assessment based on seismic records from the new network, and building characteristics derived from building records.

1. INTRODUCTION

Located in the alluvial Romanian Plain and crossed by two rivers, Bucharest, the capital city of Romania suffers from earthquakes originating from Vrancea intermediate depth (focal depth 60÷170km) earthquakes. There is a significant variability of ground shaking characteristics within the city, and it is considered that deep sediments of variable thickness and composition are responsible for the site effects observed in Bucharest.

The main characteristic of ground motions in Bucharest is the long predominant period of soil vibration, the city being characterised in international scientific literature as "Large city with Mexico-city effect" (The World Map of Natural Hazards, *Munich Re*, 1998). The relatively high seismic hazard, the peculiarities of ground motion, the existing building stock with many pre-code vulnerable buildings, the concentration of economical, political, administrative and cultural activities, all of these make Bucharest as one of the cities with the highest seismic risk in Europe.

Seismic instrumentation is essential for the proper establishment of input ground motion for design of new buildings and for seismic evaluation and retrofitting of existing buildings. The development of seismic instrumentation, in terms of quantity and quality, represents a continuous concern and effort of Romanian and foreign institutions and/or projects.

2. SEISMIC GROUND MOTIONS RECORDED IN BUCHAREST

The history of strong ground motions recorded in Bucharest started with the March 4, 1977 (moment magnitude $M_W=7.5$) earthquake. The 1977 earthquake killed 1,424 people and injured 7,598 in Bucharest, most of them in the 31 buildings that collapsed. One accelerogram was recorded on a SMAC-B Japanese instrument from *INCERC (National Building Research Institute)* seismic network. The record was digitised and processed by the *Observational Committee of Strong Motion Earthquake of the Building Research Institute, Japan, 1978*. The main characteristic of the record was the large spectral amplification at long periods. "The field study of the Romanian earthquake of 1977 suggests that strong ground motions, for engineering purposes, may differ considerably from those currently adopted for design on the basis of US West Coast-type of recordings." (Ambraseys, 1977). Fig.1 presents the spectral acceleration *SA* - spectral displacement *SD* spectra of the record.

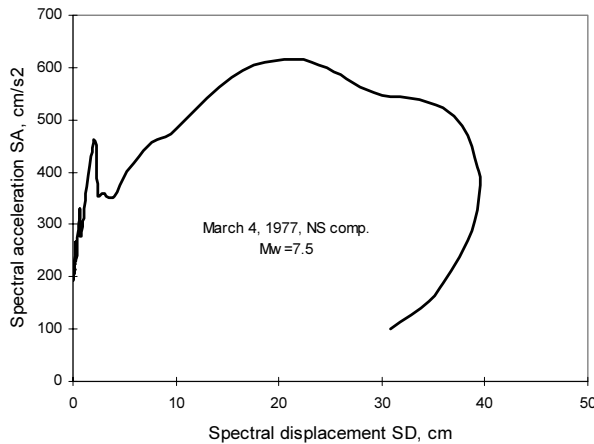


Fig.1 *SA-SD* spectra of 1977 *INCERC* record

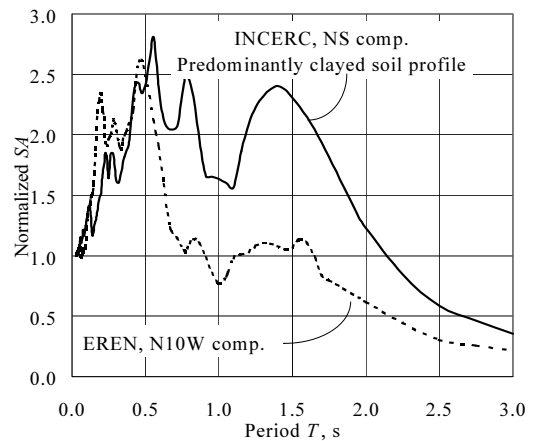


Fig.2 Normalised *SA* spectra for 1986 event recorded at *INCERC* station (East of Bucharest) and *EREN* station (North of Bucharest)

Three other important earthquakes were later recorded in Bucharest: August 30, 1986 ($M_W=7.2$) and May 30&31, 1990 ($M_W=7.0$ & 6.4) Vrancea earthquakes. The records were obtained in three seismic networks: *INCERC* – 24 records, *INFP (National Institute for Earth Physics)* – 2 records and *GEOTEC (Institute for Geotechnical and Geophysical Studies)* – 3 records.

These records indicated that there is a significant difference in the ground shaking characteristics within the city and from one earthquake to another (mobility with magnitude). For exemplification, in Fig.2 is presented the variation of normalised acceleration response spectra at two sites during 1986 earthquake (Lungu *et al.*, 1997), and in Fig. 3 is presented the microzonation of Bucharest in terms of peak ground acceleration *PGA* for 1986 earthquake (Lungu *et al.*, 2000). There is a clear difference between the Eastern, Central and Southern Bucharest and the rest of the city. In this part of Bucharest the *PGA* has lower values and the control period has higher values in comparison with North and Western side where *PGA* reaches the highest values and the control period is lower. This is explained by the difference in the subsoil conditions. The long control period of response spectra is a characteristic of Bucharest and it appears just in case of moderate and strong Vrancea earthquakes (Lungu *et al.*, 1997, 2000). The quite large spectral values at long periods are not just a local phenomenon, the microzonation of *SA* for 1986 event showing in the city a practically uniform distribution of the *SA* ordinates at $T=1.5s$ at values of about $200cm/s^2$ (Aldea *et al.*, 2003).

HAZUS 99 underlines that it's demand spectrum does not apply for the combinations of source and site conditions characterised by significant amplifications at periods larger than 1 second, case in which *HAZUS* spectrum over-estimate the spectral acceleration at low periods and under-estimate it at long periods. Mexico-city and Bucharest city (Figure 1) are such special cases.

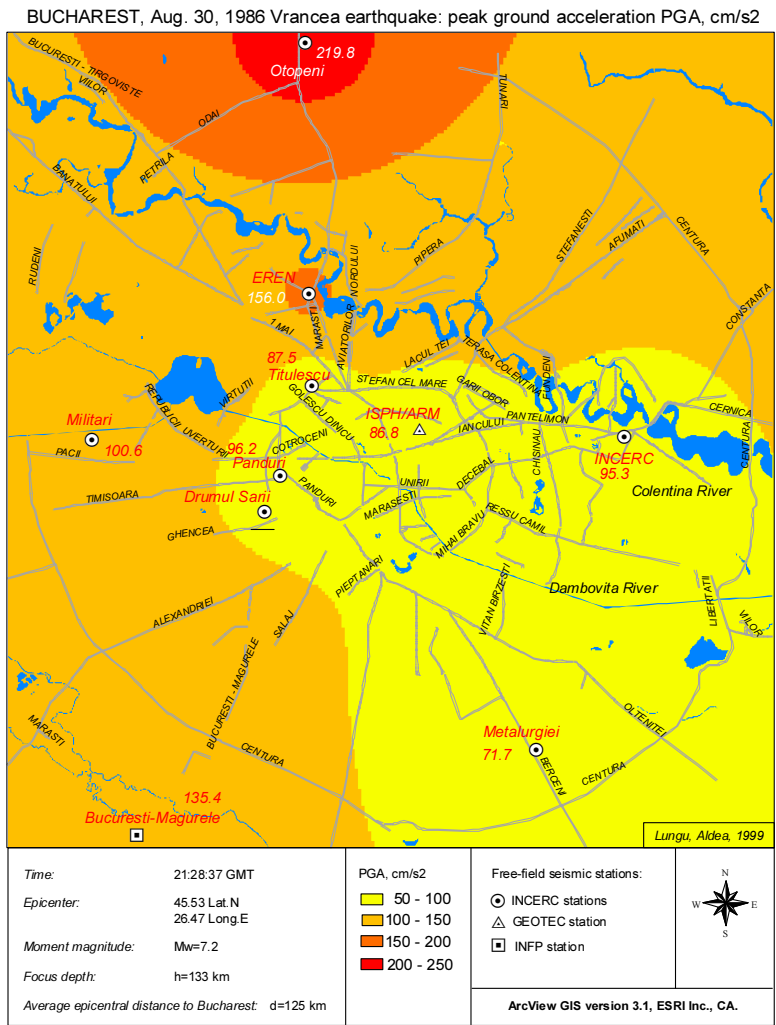


Fig.3 Bucharest – August 30, 1986 Vrancea earthquake: microzonation of PGA

3. SEISMIC NETWORKS IN BUCHAREST

The three networks with analog instruments of *INCERC*, *INFP* and *GEOTEC* continue to function in Bucharest and a significant effort for developing a digital network was done by all institutions. *INCERC* installed 9 Romanian digital instruments in the '90s, and in 2003, with the support of *State Inspectorate for Construction* also installed 7 *Etna Kinematics* instruments. In the frame of the *SFB 461 German Science Foundation Project* at *Karlsruhe University* with *Technical University of Civil Engineering UTCB*, *INFP* and *INCERC*, *Karlsruhe University* installed in the last decade 15 *K2 Kinematics* instruments that are operated by *INFP*. In 2003 a new seismic network was created: in the frame of the *Japan International Cooperation Agency JICA Technical Cooperation Project "Reduction of Seismic Risk for Buildings and Structures"*, the *National Centre for Seismic Risk Reduction NCSRR* installed in Bucharest 7 free field stations and instrumented 4 buildings with *K2 Kinematics* instruments. The total number of stations in Bucharest is now 56. The distribution within the city of these instruments is presented in Fig.4.

4. NCSRR SEISMIC NETWORK IN BUCHAREST

The *National Centre for Seismic Risk Reduction NCSRR* seismic network was installed in 2003 by staff from *OYO Japan*, *NCSRR* and *UTCB*. The *Kinematics* equipment was donated by *JICA*. All the stations are *K2 Kinematics* and, for the moment, they are stand-alone stations.



Fig.4 Bucharest – existing seismic networks in 2003

The NCSRR network has 2 components in Bucharest: (i) free-field instrumentation for site effect assessment (7 sites with sensors at ground surface and in two boreholes) and (ii) building instrumentation (4 buildings). A brief description of the network is presented in Table 1 and Table 2. At all the free-field stations the soil profile of the boreholes is known. Down-hole tests were performed by NCSRR and Tokyo Soil and their results will be soon published. Laboratory tests are underway. All these data will allow the numerical modelling of site response.

Table 1 NCSRR seismic stations for site effect assessment

No.	Site	Station ID	Surface sensor location	Depth of sensor in shallow borehole, m	Depth of sensor in deep borehole, m	Type of equipment
1	UTCb Tei	UTC1	free field	-28	-78.4	K2 + FBA-23DH
2	UTCb Pache	UTC2	1 storey building	-28	-66	
3	NCSRR/INCERC	INC	1 storey building	-24	-153	
4	Civil Protection Hdq.	PRC	1 storey building	-28	-68	
5	Piata Victoriei	VIC	free field	-28	-151	
6	City Hall	PRI	free field	-28	-52	
7	Municipal Hospital	SMU	free field	-30	-70	

Table 2 NCSRR seismic stations in buildings

No.	Site	Station ID	Station & sensor 1 location	Sensor 2	Sensor 3	Sensor 4	Bldg. data	Type of equipment
1	Stefan cel Mare 1	BLD1	11 th floor	12 th floor	5 th floor	1 st floor	RC frame '80s	K2 +
2	Stefan cel Mare 2	BLD2	Basement	7 th floor	4 th floor	Free field	RC frame '60s	Episensor
3	National Television	TVR	14 th floor	15 th floor	basement	-	RC frame '60s	ES-T
4	BRD-SG Tower	BRD	19 th floor	3 rd basement	-	-	RC dual 2003	

4.1 Available data

Ambient vibration measurements were performed at all sites using the *Kinematics* equipment. Some outputs of these measurements are herein presented.

At all the free-field stations sites microtremor measurements were done with velocity sensors and equipment made by *Tokyo Soil* and *Buttan Service*, Japan, donated by *JICA* to *NCSRR*. Microtremor velocity data is under analysis.

Four small earthquakes were recorded by *NCSRR* network, three originating from Vrancea source: October 5, 2003 ($M_W=4.6$, $h=143km$), December 24, 2003 ($M_D=3.8$, $h=86km$) and January 21, 2004 ($M_b=4.7$, $h=111km$), and one from Bulgaria: December 17, 2003 ($M_D=4.5$, $h=10km$), and a total of 14 records were obtained.

4.2 Preliminary site response assessment

Using earthquake records, the H/V spectral ratio technique was compared with the borehole top/bottom spectral ratio technique. Both techniques are commonly used nowadays for the assessment of site response, especially for identifying the predominant periods of ground vibration.

H/V spectral ratio has to be tested in Bucharest, since the classical and reliable spectral ratio that uses a reference rock site is not applicable. In Bucharest area there is no outcropping bedrock, and the bedrock is believed to be at about 800÷1000m depth, the city being located on deep sediments. The H/V single station spectral ratio, despite a lack in theoretical justification, was tested successfully by an increasing number of authors (for example Lermo *et al.* 1993). The basic assumption is that the vertical component of ground motion is not affected by site effects.

The technique that uses borehole records (Surface-Borehole Spectral Ratio SBSR) is considered by some authors as the most reliable (Atakan, 1995), while others do not recommend it since "the downhole sensors records not only the incident waves coming from the source, but also waves reflected from the surface" (Safak, 1997). In our case, the method is used only for comparison, the main limitation coming from the fact that the borehole sensor is not located on the bedrock, and consequently the spectral ratio may characterise just the response of the soil profile corresponding to the borehole depth.

In Fig. 5 are presented the H/V ratio and the SBSR for NCSRR/INCERC site, for Dec.17, 2003 event, and in Fig.6 the same ratios for Jan.21, 2004 earthquake. The borehole sensor (B2) is located at -153m. Majority of the ratios indicates a first major peak around 0.8Hz. The SBSR are more clear and show a similar pattern for both earthquakes, identifying also the higher vibration modes. These results are in agreement with previous studies indicating for INCERC site a predominant frequency of ~0.75Hz in case of March 4, 1977 earthquake (Lungu *et al.*, 1997) and 0.87 Hz as a mean of H/V ratio for several small earthquakes (Aldea, 2001).

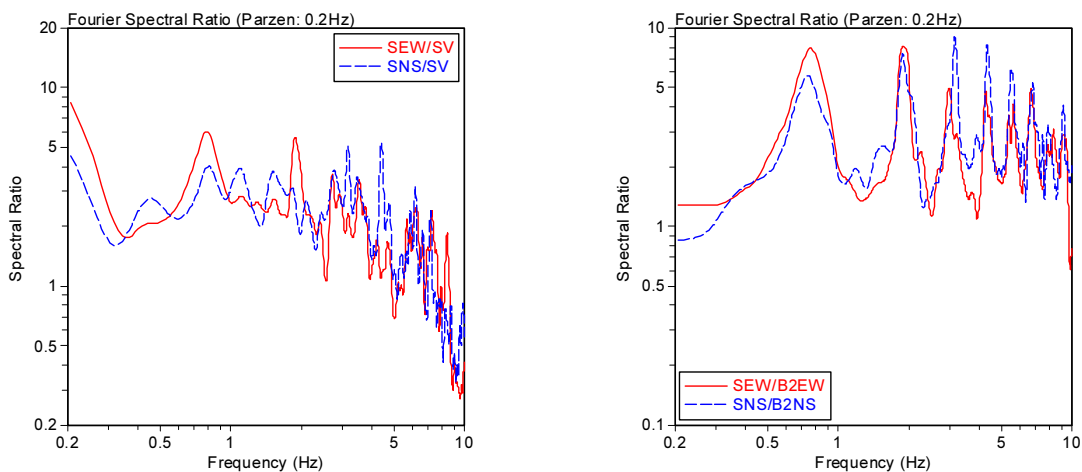


Fig.5 NCSRR/INCERC site, Dec.17, 2004 event: H/V ratio (left) and SBSR (right)

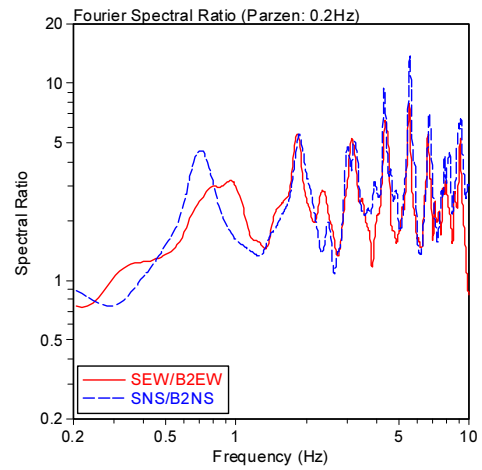
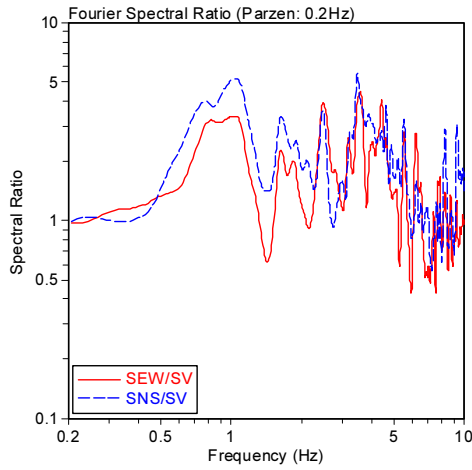


Fig.6 NCSRR/INCERC site, Jan.21, 2004 event: H/V ratio (left) and SBSR (right)

In Fig. 7 are presented the H/V ratio and the SBSR for UTC2 site, for Dec.17, 2003 event, and in Fig.8 the same ratios for Jan.21, 2004 earthquake. The borehole sensor (B2) is located at -70m .

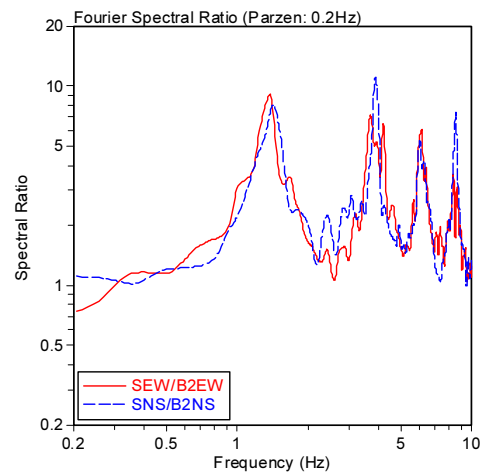
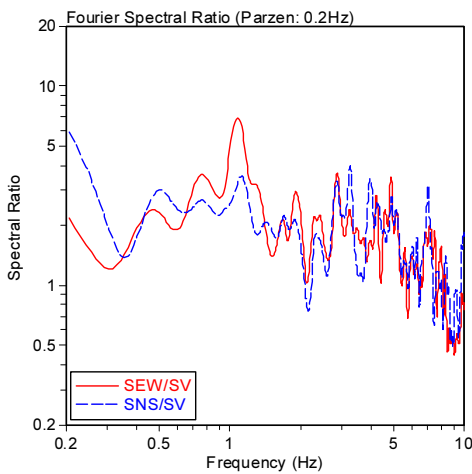


Fig.7 UTC2 site, Dec.17, 2004 event: H/V ratio (left) and SBSR (right)

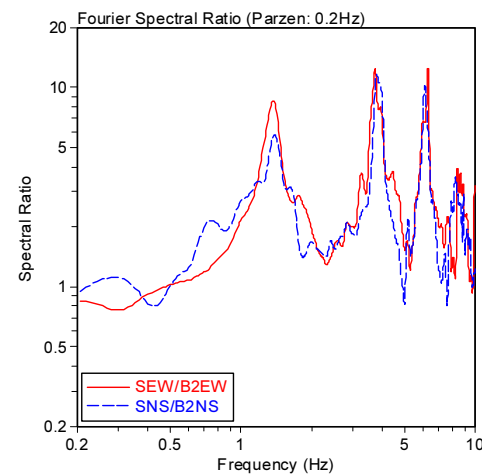
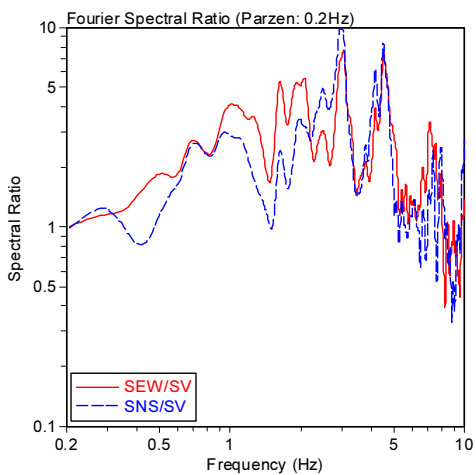


Fig.8 UTC2 site, Jan.21, 2004 event: H/V ratio (left) and SBSR (right)

The SBSR ratios are very much similar for both earthquakes, clearly identifying a predominant frequency of 1.5Hz at UTC2. The H/V spectra are less clear, and the predominant peak is at 1-1.2Hz.

The analysis of more data, completed by numerical modelling and by H/V Nakamura (1989) method (for microtremors) will allow an improved assessment of site response in Bucharest.

4.3 Preliminary building response assessment

In the case of instrumented buildings, the ambient vibration at bottom/basement represents an input signal that is amplified by the building. The top vibration includes the building vibration and, if soil-structure interaction exists, it also includes the contribution of rocking and sway. A soil-structure interaction assessment for the instrumented buildings has not yet been performed, and in the followings, the identified frequencies are considered as the frequencies corresponding to the vibration modes of the building.

In Fig.9 are presented the Fourier spectra of ambient vibration records at the top of the *Romanian National Television TVR* (14 storeys). The spectra indicate clearly the main period of vibration for each direction of the building, and also the higher modes of vibration can be identified: 0.85Hz, 3Hz, 5Hz for NS direction, and 0.75Hz, 2.9Hz, 5Hz for EW direction.

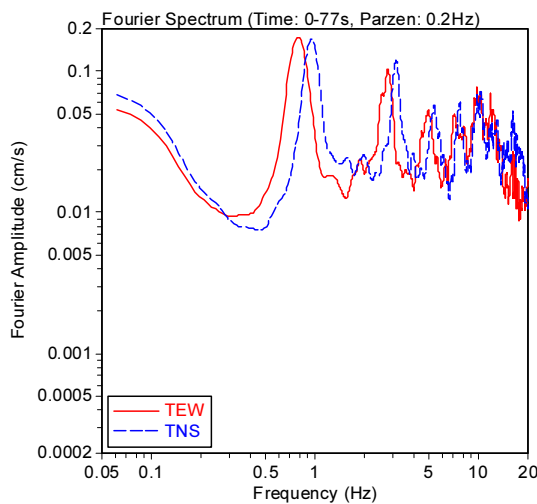


Fig.9 Fourier spectra of ambient vibration at *TVR* building

In Fig.10 are presented the Fourier spectra of ambient vibration records at the top of the *BRD-SG* Tower (20 storeys). The spectra indicate clearly the main period of vibration for each direction of the building: 1.5Hz for NS direction and 1Hz for EW direction. These values are in agreement with a previous microtremor study done at *UTCB* for the *BRD-SG* building in 2002.

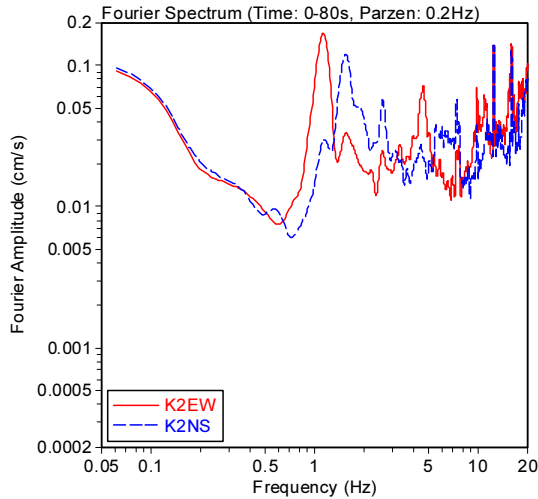


Fig.10 Fourier spectra of ambient vibration at *BRD-SG* building

Fig. 11 presents top/basement Fourier spectral ratios for earthquake records at BLD 2 station, indicating the main periods of vibration of the building: 2.2Hz for NS direction and 2.5Hz for EW.

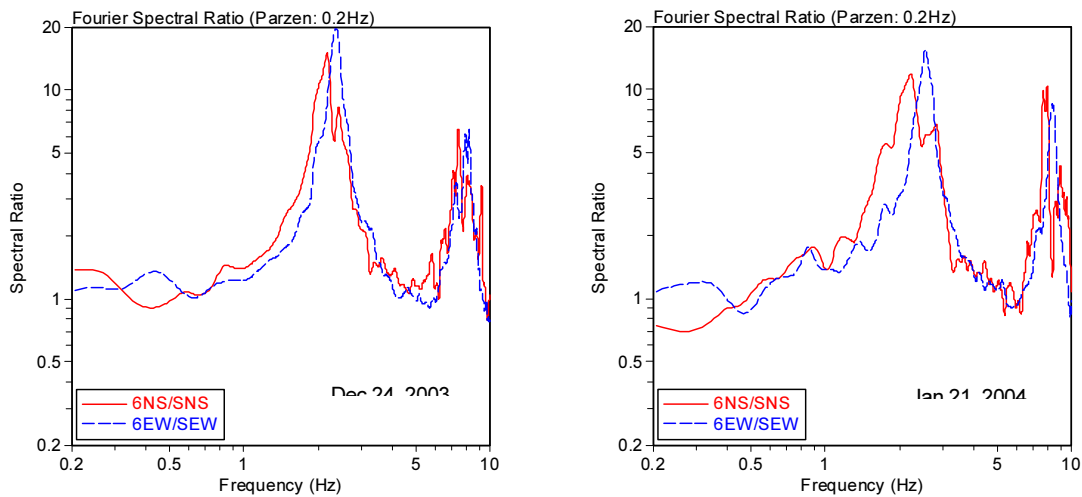


Fig.11 Top/basement Fourier spectral ratio for earthquake records at BLD2 seismic station

5. CONCLUSIONS

Bucharest city is one of the well instrumented cities in Europe, but efforts are still needed for having an entirely digital network, for a better distribution of seismic stations and for a modern communication of recorded data allowing in the future the development of near-real time shake maps. The *NCSRR* seismic network offers remarkable conditions for a better understanding of site response by providing seismic data in 14 boreholes at seven sites with the city. The network will also help the understanding of RC structures behaviour during earthquakes.

Acknowledgements:

The authors acknowledge *Japan International Cooperation Agency JICA* for supporting seismic risk reduction efforts in Romania by establishing the Project "Reduction of Seismic Risk for Buildings and Structures" that includes the donation of

seismic observation equipment. The authors acknowledge support from *Japan Ministry of Education, Culture, Sport, Science, and Technology (MEXT)* for establishing the *Center for Urban Earthquake Engineering (CUEE)* in *Tokyo Institute of Technology*. The support has made possible this international conference, as well as international joint research projects and exchange programs with foreign universities.

References:

- ***Kenchiku Kenkyu Shiryo No.20, 1978. Digitized Data of Strong Motion. Earthquake accelerograms in Romania (March 4, 1997) by Observational Committee of Strong Motion. *Building Research Institute*, Japan, 254 p
- ***Munich Re, 1998. World Map of Natural Hazards
- Aldea, A., Lungu, D., Arion, A., 2003. "GIS microzonation of site effects in Bucharest based on existing seismic and geophysical evidence", *6ème Colloque National AFPS 2003*, July, Palaiseau, France, 8p., CD-ROM
- Aldea, A., 2001. "Assessment of Site Response in Eastern Bucharest, Romania". *Bulletin of the International Institute of Seismology and Earthquake Engineering IISEE*, Vol. **36**. Tsukuba, Japan, 13p.
- Ambraseys, N.N., 1977. Long-period effects in the Romanian earthquake of March 1977, *Nature*, **268**, July, p.324-325
- Atakan, K., 1998. A review of the type of data and the techniques used in empirical estimation of local site response., *Proceedings of the International Conference Effects of Surface Geology 1998*, Japan, p.1451-1460
- Lermo, J., F.J.Chavez-Garcia, 1993. "Site effect evaluation using spectral ratios with only one station", *Bull. Seism. Soc. Am.*, Vol.**83**, No.5, p.1574-1594
- Lungu, D., Aldea, A., Arion, C., Demetriu, S., Cornea, T., 2000. Microzonage Sismique de la ville de Bucarest - Roumanie, *Cahier Technique de l'Association Française du Génie Parasismique*, No.**20**, p.31-63
- Lungu, D., T.Cornea, A.Aldea, C.Nedelcu, A.Zaicenco, 1997. Seismic microzonation of the city of Bucharest-Romania. Technical Rep. for Association Française du Génie Parasismique, 2Vol., 91p.+69p.
- Nakamura, Y., 1989. A method for dynamic characteristics estimation of subsurface using microtremor on the ground surface. *QR Railway Technical Research Institute*, Vol.**30**. No.1, p.25-33
- Safak E., 1997. "Models and methods to characterize site amplification from a pair of records". *Eq.Spectra*, **13**(1), p.97-129

Center for Urban Earthquake Engineering (CUEE) Tokyo Institute of Technology

Suzukakedai Office ■

Department of Built Environment
Tokyo Institute of Technology
4259 Nagatsuta-cho, Midori-ku, Yokohama, Japan 226-8502
Tel: +81-(0)45-924-5576 Fax: +81-(0)45-924-5574

O-okayama Office ■

Department of Architecture and Building Engineering
Tokyo Institute of Technology
2-12-1 O-okayama, Meguro-ku, Tokyo, Japan 152-8552
Tel: +81-(0)3-5734-3200 Fax: +81-(0)3-5734-3200

Email:office@cuee.titech.ac.jp
URL:<http://www.cuee.titech.ac.jp>